SLAC-R-361

SLAC – 361
CONF – 8907134
UC-414
(T/E)

PROCEEDINGS

OF

SUMMER INSTITUTE ON PARTICLE PHYSICS

July 10-21, 1989

PHYSICS AT THE 100 GeV MASS SCALE

Program Directors

Gary J. Feldman

Frederick J. Gilman

David W. G. S. Leith

Ed. by Eileen C. Brennan

Sponsored by Stanford University and Stanford Linear Accelerator Center under contract with the U.S. Department of Energy. Contract DE-AC03-76SF00515.

January 1990

Printed in the United States of America. Available from National Technical Information Service, U.S. Department of Commerce, 5285 Port Royal Road, Springfield, VA 22161.









PREFACE

The seventeenth annual SLAC Summer Institute on Particle Physics was held from July 10 to 21, 1989. First results from the SLC and increased luminosity from hadron colliders inspired the topic of "Physics at the 100 GeV Mass Scale." Experimental and theoretical aspects of this topic were explored by a total of 305 participants from 10 countries. The school portion of the Institute featured lectures on this subject by M. Chanowitz, K. Ellis, I. Hinchliffe, R. Hollebeek, M. Levi, M. Peskin, M. Shapiro, and M. Swartz. Another series of lectures discussed accelerator technology for building new hadron and e^+e^- machines. These talks were presented by H. Edwards, R. Ruth, R. Siemann, and M. Tigner.

The afternoon discussion session were very much enhanced and enlivened by presenting supplementary material and by posing probing questions to the lecturers. We are indebted to the following people for serving as provocateurs: M. Berger, A. Cooper, C. Dib, A. Hsieh, R. Kauffman, D. Kennedy, J. Kent, S. Komamiya, H. Lu, R. Miller, K. Oide, L. Rivkin, C. Simopoulos, R. VanKooten, and M. Woods.

The topical conference was highlighted by first results on Z production at the SLC, electroweak measurements and top quark search results from CDF and CERN, and results on CP violation from Fermilab and CERN experiments.

We thank Eileen Brennan for organizing and running the meeting, and with great persistence, editing these Proceedings. She and her staff contributed much to the success of the meeting both through their hard work and their good humor. Their efforts, coupled with the excellent lectures and stimulating discussions, made for an interesting and most enjoyable meeting.

Gary Feldman
Frederick J. Gilman
David W. G. S. Leith
Program Directors

TABLE OF CONTENTS

Part II. **TOPICAL CONFERENCE** (continued) page

APPENDIX

Heavy Quarks – Experimental

Robert Hollebeek
University of Pennsylvania

1989 SLAC Summer School Lectures

1 Introduction

The purpose of these lectures, given at the 1989 SLAC Summer School, was to discuss the experimental aspects of heavy quark production. Since a companion set of lectures on the theoretical point of view were to be given by Keith Ellis, I gave some thought to what in particular should be the "experimental viewpoint". One obvious answer is that an experimentalist should gather together the measurements which have been made by various groups, compare, contrast and tabulate them, and if possible point out the ways in which these measurements confirm or contradict current theories. I have tried to do this, although the reader who expects to find here the latest of all experimental measurements should probably be forewarned that the field is moving extremely rapidly. In some cases, I have added and update materials where crucial new information became available after or during the summer of 1989, but not in all cases. I have concentrated on trying to select those measurements which are at the moment most crucial in refining our understanding of heavy quarks as opposed to those which merely measure things which are perhaps too complicated to be enlightening at the moment.

While theorists worry primarily about production mechanisms, cross sections, QCD corrections, and to some extent about signatures, the experimentalist must determine which measurements he is interested in making, and which signatures for heavy quark production are realistic and likely to produce results which will shed some new light on the underlying production model without undo theoretical complications. Experimentalists also need to evaluate the available experimental equipment, both machines and detectors to find the best way to investigate the properties of heavy quarks. In many cases, the things which we would like to measure are severely restricted by what we *can* measure. Nevertheless, many properties of heavy quark production and decay can be measured, and the results have already taught us much about the weak interactions and QCD.

2 B Physics

The Standard Model of the Electro-Weak interactions contains at least 18 parameters. These include 3 coupling constants, 6 quark masses, 3 lepton masses, 4 real Kobayashi-Maskawa (K-M) parameters, 1 weak phase angle, and one Higgs mass. One could probably add more, for example, 3 neutrino masses, more lepton generations, the assumption that the K-M matrix is not Unitary, or more complex Higgs structures, but this is probably already enough parameters for one model. Of the 18 parameters, 13 can be measured without information from the b quark or t quark systems. The coupling constants of the strong, electromagnetic and weak forces, 4 of the quark masses, the lepton masses, and some of the K-M parameters are already known with varying degrees of precision. The missing 5 parameters (for which we need the heavy quark systems) are the two heavy quark masses, the two K-M parameters which represent their couplings to the other quarks, and the Higgs mass. Of these, all but the last can be directly addressed by experiments using heavy quarks. The b system is accessible at current machines, but the t quark has not yet been detected. If the t quark remains unseen, we can still measure all of the parameters except the t quark and Higgs masses, however, we will not be able to test many ideas about higher order corrections in the electro-weak model (where the t quark mass is important) nor will we be able to measure the KM parameter corresponding to the t quark coupling except indirectly through the b system. We will begin this section on B physics by exploring just how far we can go using information from the b system alone, and turn later to the t quarks.

2.1 Measurements using b Quarks

There are three different types of measurements which one could think of doing in the b system. The first is to measure the properties of the b quark as it is found in the B meson. We could for example measure its lifetime and its decay modes and compare them to standard model calculations. For the decay modes, the simplest place to start would be to measure the semileptonic decay widths, because these are the most straight-forward of the theoretical calculations. Each decay mode measurement could be compared to calculations, and values of the K-M parameters extracted. These types of experiments have been underway for several years, and will form the bulk of what we can say about the present experimental situation.

A second type of measurement is the analog of measurements which have been made for some time in the $K^0\bar{K}^0$ system. In it, we would try to measure the rate at which transitions are made between neutral B mesons and their anti-particles. These flavor oscillations would give further information about the K-M angles and together with searches for rare decays of the B meson might tell us about the presence of contributions from fourth generations. These experiments are the focus of much of the current planning for experiments to be performed in the next few years. Finally, the B meson system may exhibit CP violation. If it does, it will be extremely useful as another example of this poorly understood phenomenon.

Studies of the first type, that is decay modes of the B meson, have primarily been done at the CESR and DORIS machines. Lifetime studies have been done at the PEP and PETRA machines because, of course, to measure the B lifetime requires the production of B mesons which have been boosted in the lab frame which can only be done at the higher energies available at the latter machines. Oscillations of the B system are being studied at all machines including many recent efforts at hadron machines where the number of produced B's can be very large and where the signature of same-sign dileptons is relatively clean.

Most of what has been learned about the decays of B mesons has come from measurements of the Upsilon 4S system studied at CESR and DORIS which produces B^0 and B^+ mesons (in this and future cases, I will not bother to mention the charge conjugate states). Other studies include those of the B_s and B_c which, together with the B^0 and B^+, are produced at hadron machines and higher energy e^+e^- machines. The production ratios of these states are not always well known and depend on the masses of the mesons and the constituent quarks.

Let us focus first on measurements of the K-M matrix parameters from these systems. If the K-M matrix parameterization of quark mixing using a 3 by 3 matrix is an accurate description of nature, and if there are in fact only 3 generations of quarks, then the 3 quark system is closed; i.e. we do not expect transitions from these states to as yet unobserved exotics and/or fourth generation objects.

In this case, there should be no probability leakage to such states, and the 3 by 3 KM matrix should be unitary. The weak eigenstates (d',s',b') are mixtures of the pure states (d,s,b) with the mixing described by the KM matrix. If we consider transitions from a state u through all possible intermediate states (d,s,b) and back to a different state u', the unitarity of the KM matrix guarantees that

$$\sum_j V_{ij} V^*_{kj} = \sum_j V^*_{ji} V_{jk} = \delta_{ik} \quad .$$

Note that if this were not the case, we would have flavor changing neutral currents (FCNC) in second order in the weak interactions, and also that the above relation gives us a relationship between elements of the KM matrix, or equivalently a way to test whether the matrix is unitary or whether there is room for exotic contributions. If we start with the u quark for example, and make transitions to the d,s,b intermediate states and back to the u quark, we have have the following experimental information.

$$\begin{aligned} V_{ud} &= 0.9747 \pm 0.0011 \\ V_{us} &= 0.221 \pm 0.002 \end{aligned} \quad .$$

This implies that

$$V_{ud}^2 + V_{us}^2 = 0.999 \pm 0.002$$

which we could combine with the unitarity relation

$$V_{ud}^2 + V_{us}^2 + V_{ub}^2 = 1$$

to deduce a value for V_{ub}. Unfortunately the errors are large enough that V_{ub} could well be zero. We could try the same thing for the c quark, and eventually can do the same with the t quark when we find it. In the c quark case, we would find values of V_{cd} primarily from neutrino charm production, and values of V_{cs} from dimuon production or the semileptonic decay of charmed mesons.

Another interesting relationship between the KM matrix elements can be derived from the off-diagonal terms in the unitarity relation. For the terms where $i \neq k$, an equation is obtained for products of KM elements of the form $a+b+c=0$. If the three terms are thought of as sides of a triangle, this relationship becomes

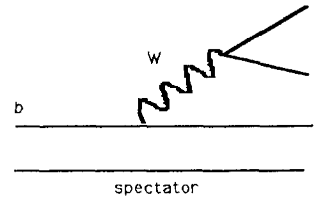

Figure 1: Feynman diagram for a spectator type decay of a B meson.

the basis for what is known as the "Unitarity Triangle". The relation can be further simplified using $V_{ud} \approx 1$ and $V_{tb} \approx 1$.

2.2 The Spectator Model

In order to relate the KM parameters to experimental measurements, we need a model for the heavy quark decay. The simplest model for the decay of a heavy quark inside a heavy meson is to assume that the quark is quasi-free and decays weakly. The other (lighter) quark is not affected by the decay. The Feynman diagrams for these decays would then look like figure 1. One simple consequence of this picture is that since different types of B mesons (B^0, $\overline{B}^0$, B^+, B^-, B_c, B_s, etc.) differ only in their spectator quark composition, all types would have the same semileptonic decay partial widths. Complications arise due to QCD corrections which link the spectator quark with the b quark, QCD corrections due to interactions between the spectator quark and the final state quarks from the virtual W decay, and the annihilation and W exchange diagrams shown in figure 2.

Annihilation diagrams are not possible for the neutral B's because an annihilation graph there would require FCNC. For charged B's, both types of diagrams are possible. The annihilation graph is expected to be helicity suppressed as in π decays, but this suppression may be overcome to some extent by the emission of soft gluons. Overall, the total corrections to the simple spectator picture are expected to be largest for the neutral B's, leading to longer charged B lifetimes and larger charged B semileptonic branching ratios. The semileptonic and total widths within the spectator model are given by

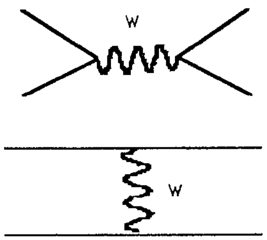

Figure 2: Annihilation and W exchange diagrams for B decay.

$$\Gamma_{s\ell} \approx \frac{G_F^2 m_b^5}{192\pi^3}\left(0.86|V_{ub}|^2 + 0.48|V_{cb}|^2\right)$$

$$\Gamma_{tot} \approx \frac{G_F^2 m_b^5}{192\pi^3}\left(7.55|V_{ub}|^2 + 3.92|V_{cb}|^2\right) \quad .$$

It is clear from the formulae that the semileptonic branching ratio and the lifetime are very sensitive to the choice of the b quark mass. One can consider two quite different methods of estimating this mass, illustrated best by looking at the Upsilon resonance and the B mesons. Since the Upsilon contains two b quarks in a bound state, we might estimate the b quark mass to be slightly more than half the Upsilon mass. B mesons on the other hand contain a single heavy b quark bound to a lighter quark. The mass of the b quark would then be approximately equal to that of the lightest of the B mesons. The calculation of the lifetime of the b quark gives an example of this mass dependence. (See Barger and Phillips **Collider Physics**). The lifetime is given by

$$\tau_b \approx \frac{\tau_\mu}{5.8|V_{cb}|^2} \frac{\left(\frac{m_\mu}{m_b}\right)^5}{I\left(\frac{m_c^2}{m_b^2}\right)}$$

where the factor 5.8 in the above expression comes from counting the available decay modes using

$$\mathrm{e} + \mu + 3\mathrm{d} + \frac{1}{5}(\tau + 3\mathrm{s}) \quad .$$

The $\frac{1}{5}$ is approximate and is due to the phase space suppression of the heavier tau and strange quark modes. The two different choices mentioned above for the

Table 1: Expected B meson decay rates in the spectator model for two b quark mass choices.

$b \to q$	$W^- \to$	Decay rate $[\frac{G_F^2 m_b^5}{192\pi^3}\|V_{qb}\|^2]$	
		current mass	constituent mass
$(b \to c)$	$\bar{u}d$	1.89	1.26
$(b \to c)$	$\bar{u}s$	0.09	0.06
$(b \to c)$	$\bar{c}s$	0.81	0.24
$(b \to c)$ + Hadrons		2.79	1.56
$(b \to c)$	$e^-\bar{\nu}_e$	0.48	0.36
$(b \to c)$	$\mu^-\bar{\nu}_\mu$	0.48	0.36
$(b \to c)$	$\tau^-\bar{\nu}_\tau$	0.12	0.09
$(b \to c)$ + Leptons		1.08	0.81
$(b \to u)$	$\bar{u}d$	3.42	3.08
$(b \to u)$	$\bar{u}s$	0.18	0.16
$(b \to u)$	$\bar{c}s$	1.90	1.20
$(b \to u)$ + Hadrons		5.50	4.44
$(b \to u)$	$e^-\bar{\nu}_e$	0.86	0.84
$(b \to u)$	$\mu^-\bar{\nu}_\mu$	0.86	0.82
$(b \to u)$	$\tau^-\bar{\nu}_\tau$	0.32	0.35
$(b \to u)$ + Leptons		2.05	2.02

b quark mass yield

$$\mathrm{m}_b \approx m_B = 5.27$$

$$m_b = \tfrac{1}{2} m_\Upsilon = 4.73$$

$$\tau_b = \left\{\begin{smallmatrix}1.2\\1.8\end{smallmatrix}\right\} 10^{-12}\left(\frac{0.05}{|V_{cb}|}\right)^2$$

$$\Gamma_{b\to e} = \left\{\begin{smallmatrix}1.2\\0.8\end{smallmatrix}\right\} 10^{11}\left(\frac{|V_{cb}|}{0.05}\right)^2 \quad .$$

Fortunately, the b quark mass is known to about 10% so that the decay partial widths can be calculated with an uncertainty of about 50%. Note that including corrections to the spectator model may require changes to the effective b quark mass required in a calculation. (See Table 1.)

2.3 B Meson Detection (non-semileptonic)

The semileptonic and hadronic decays of the B system offer two quite different ways to study the spectator model and its extensions. The semileptonic decays are in principle cleaner, since for example there is no possibility of spectator to final state quark interactions, but they have the disadvantage of occurring at a lower

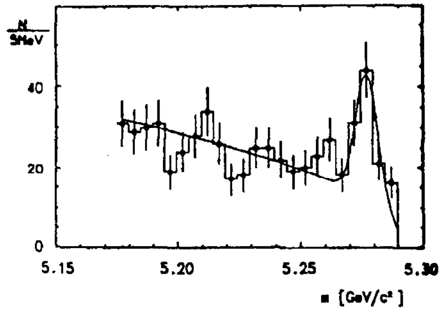

Figure 3: ARGUS B meson reconstruction using D^* decays.

rate. We will start then by looking at the hadronic decay modes. The purpose will be to investigate possible non-spectator effects by looking for differences in the B^0 and B^+ lifetimes, to measure the KM parameter V_{ub} by looking for decays which do not contain charm, and to study mixing and CP violation.

The reconstruction of B decays can be facilitated by looking for modes which contain a D^* decay. Examples would be

$$\begin{aligned} \overline{B}^0 \quad &\rightarrow \quad D^{*+}\pi^- \\ & \qquad D^{*+}\pi^-\pi^0 \\ & \qquad D^{*+}\pi^-\pi^-\pi^+ \end{aligned}$$

$$\begin{aligned} B^- \quad &\rightarrow \quad D^{*+}\pi^-\pi^- \\ & \qquad D^{*+}\pi^-\pi^-\pi^0 \end{aligned}$$

with D's detected as

$$D^* \rightarrow D^0\pi^+$$

$$\begin{aligned} D^0 \quad &\rightarrow \quad K^-\pi^+ \\ & \qquad K_s^0\pi^+\pi^- \\ & \qquad K^-\pi^+\pi^0 \\ & \qquad K^-\pi^+\pi^+\pi^- \quad . \end{aligned}$$

Figure 3 shows the result of such an analysis from the ARGUS collaboration. In this technique, one is taking advantage of a well-known trick for finding D meson decays using the soft pions from the D^* decay.[1] Similar results from the CLEO collaboration are shown in figure 4.[2] In this data, several modes without D^* decays are also used as are the decays of B to ΨK and ΨK^*. From these figures, it is clear that even though the number of produced B's is large, the number of fully reconstructed events is small. Several decay modes must be used together to gather a sufficiently large sample of B decays. In these techniques, it is extremely important to have a detector with good momentum resolution. For example, the results shown for the CLEO detector were obtained with

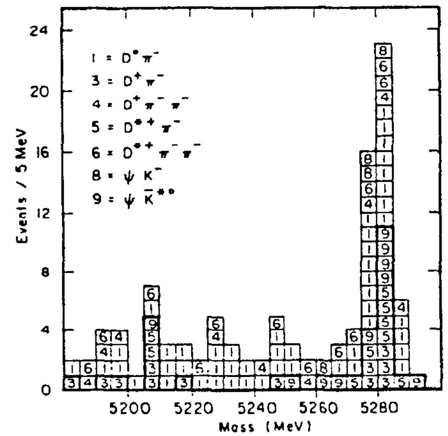

Figure 4: CLEO B meson reconstruction.

$$\left(\frac{\delta p}{p}\right)^2 = (.007p)^2 + (.006)^2$$

which is excellent for a large tracking detector.

To reduce combinatorial backgrounds, π's and K's are identified using dE/dx and/or time-of-flight. For π^0 reconstruction, typically only γ's with energy greater than 40 MeV are used. The track momentum resolution is then further improved by using constrained kinematic fits to the masses of the D, and any neutral K's or π's and sometimes by using constrained fits to the known position of the beam. Finally, the event is constrained to the beam energy which is usually well known in an e^+e^-machine. If in addition, the B's are the result of decays from a narrow resonance such as the $\Upsilon(4S)$, an improvement of roughly a factor of ten can be

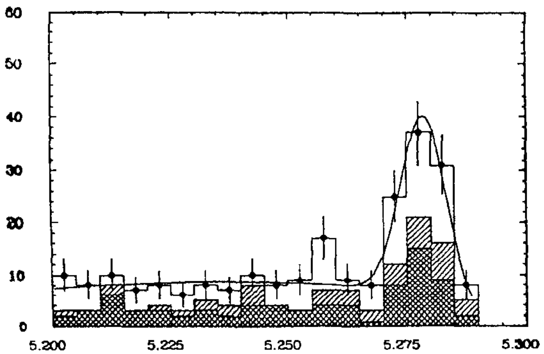

Figure 5: Mass distribution of B candidates from $B \to D^{*+}\ n\pi(n = 1-3)$, hatched area, $B \to J\Psi K\ n\pi(n = 1,2)$,shaded area, and $B \to D^{*}, D^{+}\ n\pi(n = 1,2)$,open area.

gotten by constraining to the mass of that state yielding a mass resolution as good as a few MeV.

A further technique which can be used to detect B's is to use decay modes which contain the easily recognizable decays of the J/Ψ. For example, the decay $B \to \Psi K n\pi$ can be found by detecting e or μ pairs from the decay of the Ψ. These modes are of interest for another reason. Later, we will discuss the important question of whether the KM parameter V_{bu} is zero. Decays involving V_{bu} do not produce charm, but in trying to measure decays of the B system where no charm has been produced, corrections will have to be applied for the Ψ decays as well as any other decays of the B where there is no *apparent* charm content. Figure 5 shows the relative contributions of these decays compared similar ones with explicit charm in the form of D mesons. [3]

If the source of the B's is the 4S resonance, there is some uncertainty in the relative rate of 4S decays to charged and neutral B's. Various models yield production ratios between 50:50 and 60:40 depending primarily on the mass difference between the charged and neutral B mesons. Earlier measurements of this mass difference yielded about $2 \pm 1\ MeV$ which gives a charged to neutral production ratio of 55:45. Assuming this ratio, table 2 shows the measured branching ratios

Table 2: Branching ratios for B decays assuming 55:45 charged to neutral production.

DecayMode	*ARGUS*	*CLEO*
$\overline{B}^0 \to D^{*+}\pi^-$	$0.35 \pm 0.18 \pm 0.13$	$0.37\ {}^{+0.26+0.16}_{-0.15-0.11}$
$\overline{B}^0 \to D^{*+}\pi^-\pi^0$	$2.0 \pm 1.0 \pm 1.0$	

for various decays of the B mesons. More recent measurements of the mass difference (see this volume) are consistent with zero and would give production ratios of 50:50.

2.4 B Decays to Charm – Measuring V_{bc}

One way to measure the KM parameter V_{bc} is to try to determine the average number of charm particles resulting from each produced B meson. We would need to measure

$$\begin{array}{lcl} B & \to & D^0 + X \\ B & \to & D^+ + X \\ B & \to & D^* + X \\ B & \to & D_s^+ + X \\ B & \to & \Lambda_c + X \\ B & \to & \Psi + X \end{array}$$

with a suitable correction for the fact that the last mode contains two charmed quarks. To see how this looks in our model, we begin with the spectator diagrams involving b to c transitions as shown in figure 6.

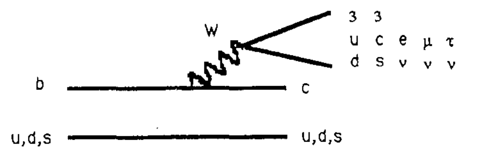

Figure 6: Spectator diagrams for b to c transitions with 9 possible final states (the 3 is for color).

Note that from the diagram it is easy to see that there is one charm quark produced per b quark decay plus an additional 3/9 coming from the cs decay modes. These heavier modes are phase-space suppressed and the result is that

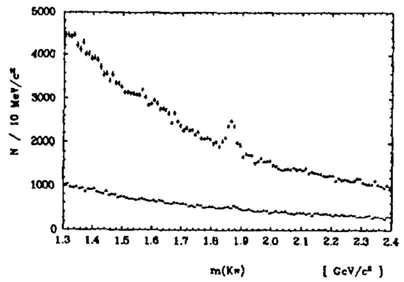

Figure 7: Inclusive D's from B decays at the 4S.

there are approximately 1.2 charmed quarks produced per B meson decay. If instead of the b to c transition, we had started from the b to u transition, the only source of c quarks is the 3/9 coming from cs decays of the virtual W which when phase-space suppressed yields approximately .2 c's per B. If the ratio of $b \to u$ to $b \to c$ is known,

$$\alpha = \frac{\Gamma(b \to u)}{\Gamma(b \to c)}$$

we can predict the number of charmed objects which will be produced per B decay, or more interestingly, we can measure the number of charmed objects per B decay and try to learn something about V_{bu} from

$$\frac{N_c}{N_B} \approx \frac{1.2 + 0.2\alpha}{1 + \alpha} \quad .$$

The charm quarks are detected most easily by using modes such as $D \to K\pi$. Corrections will need to be applied for the phase-space suppression of the heavier modes (which we have thus far approximated by changing 3/9 to 0.2), decays to charmed bound states, and unreconstructed decays of the D mesons (some of which can be corrected for by using well known branching ratios of the D's). Figure 7 shows the type of spectra obtained for inclusive D's using the 4S as a source of B's. The branching ratios determined from these measurements are shown in table 3. We will return to the determination of α after discussing the D meson momentum spectrum and the corrections for Ψ production.

An additional benefit of measuring the inclusive decays of D mesons from B decays is that the momentum spectrum of the D mesons contains information about the details of the quark fragmentation process. The source of D mesons is dominated by the transition $b \to c$, with the c quark combining with the spectator to form the D meson system. Since the relatively heavy c quark gets most of the momentum of the parent b, this leads to a fairly hard spectrum of D's, but the D meson momentum spectrum will be softened by the emission of gluons from the spectator quark during the formation of the D. Figure 8 shows the momentum spectrum of D mesons measured by the CLEO collaboration.[4] The general conclusion is that the data lie midway between the models with hard fragmentation, and those with very soft fragmentation.

We can also use the decays of the B to a D_s to probe fragmentation. In this case, the strange quark can be either one that comes from the virtual W, or it can be from a pair of strange quarks produced in the fragmentation. Again, the momentum distribution of the produced D_s's can distinguish between these two effects. One might expect that the production of the heavier strange quark pairs would be suppressed in the fragmentation, and this seems to be born out by the data (figure 9).

Table 3: Inclusive D's from B decays.

Decay Mode	*ARGUS*	*CLEO*
$B \to D^0X$, $D^0 \to K^-\pi^+$	$0.0196 \pm 0.0015 \pm 0.0025$	$0.021 \pm 0.0015 \pm 0.0021$
$B \to D^0X$	$0.466 \pm 0.071 \pm 0.063$	$0.5 \pm 0.061 \pm 0.067$
$B \to D^+X$, $D^+ \to K^-\pi^+\pi^+$	$0.0189 \pm 0.0027 \pm 0.0032$	$0.019 \pm 0.004 \pm 0.002$
$B \to D^+X$	$0.208 \pm 0.046 \pm 0.031$	$0.209 \pm 0.049 \pm 0.031$

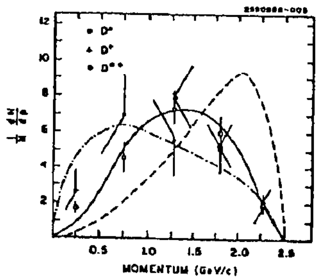

Figure 8: Momentum spectrum of D's from B decays measured by the CLEO collaboration.

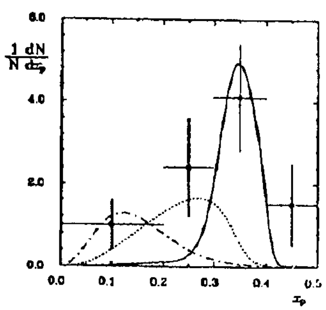

Figure 9: D_s momentum spectrum from B decays.The models are for $s\bar{s}$ pair production, three body production and two body production of D_s's.

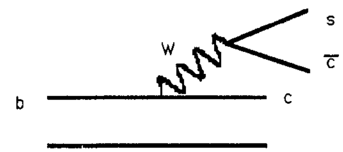

Figure 10: Diagram for $c\bar{c}$ production in B decay.

2.5 J/Ψ Production from B Decays

Since J/Ψ's can be easily identified, they also make useful probes of the fragmentation of B mesons. Their momentum spectrum can be used in the same way as the D, and the D_s, and since fragmentation production of heavy $c\bar{c}$ pairs is highly suppressed, they should arise primarily from diagrams involving the b to c transition. The decays of the B mesons to Ψ's have been mentioned before as important for the measurement of the b to u transition since when counting the number of charm quarks per B decay, hadronic decay modes of the Ψ would for example seem to contribute to the charmless decay modes. This can be corrected for by measuring Ψ decays to leptons and then making a correction using the known branching ratios for Ψ to hadronic final states (all of which have no *apparent* charm). The Ψ's are also important for the study of CP violation since some CP eigenstate decay modes involve Ψ's.

In the spectator model, the only diagram which would yield a $c\bar{c}$ pair is the one shown in figure 10. The cs mode of the W is 3/9 of the total but is again phase-space suppressed to about 20% . The probability that a $c\bar{c}$ pair will produce a Ψ bound state is

$$\langle c\bar{c}|J/\Psi\rangle \approx 0.6 \quad .$$

The Ψ state is a color singlet so there is an additional color suppression factor of 1/9 since the c and $\bar{c}$ quarks have uncorrelated colors. As shown in figures 11-12, this channel yields a very good experimental signature.[5,6,7,8]

It is possible that the radiation of soft but colored gluons could cancel the color suppression mechanism, but the expected rate with color suppression is

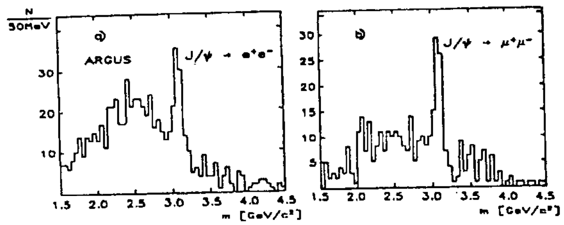

Figure 11: ARGUS: $e^+e^-$and $\mu^+\mu^-$ mass spectra in $\Upsilon(4S)$ decays.

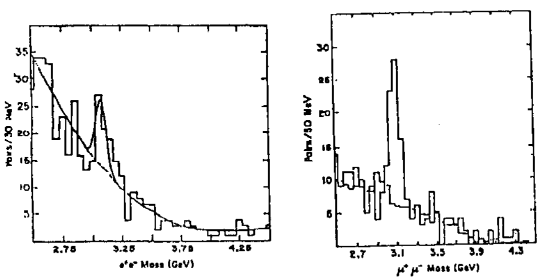

Figure 12: CLEO: $e^+e^-$and $\mu^+\mu^-$ mass spectra in $\Upsilon(4S)$ decays.

about 1.3% which is in good agreement with the experimental numbers:

$$\begin{array}{lcc} & CLEO & ARGUS \\ BR(B \to \Psi X) & 1.09 \pm 0.16 \pm 0.21\% & 1.07 \pm 0.16 \pm 0.22\% \end{array}$$

The same mechanism which produces $B \to \Psi$ can also produce states like Ψ' and χ_c or η_c. The Ψ' state can be detected experimentally by looking for $\Psi' \to \Psi\pi\pi$ and is found to be about 0.3 %. The other states are estimated to contribute a branching ratio of 0.8%.

Using this information, we can return to the estimate of the number of c's produced per B meson. Note that the observed charm production rates saturate the branching ratio leaving only small room for a contribution from b to u transitions (see table 4). If we use the quantity α defined previously, we conclude that α is less than 0.2 which is actually not very restrictive for V_{bu} compared to measurements done using the semileptonic decays of B's to be described in the next section.

Table 4: Branching ratios used to find the number of c quarks produced per b decay.

	CLEO Branching Ratio%	ARGUS BranchingRatio%
$B \to D^0X$	$50.0 \pm 6.1 \pm 6.7$	$46.6 \pm 7.1 \pm 6.3$
$B \to D^+X$	$20.9 \pm 4.9 \pm 3.1$	$23.2 \pm 5.3 \pm 3.5$
$B \to D_s$	$19 \pm 5 \pm 4$	$16 \pm 4 \pm 3$
$B \to$ *charmed baryon* $+ X$	$8.2 \pm 1.4 \pm 2.0$	$7.6 \pm 1.4 \pm 1.8$
$2 * B \to \Psi, \Psi', \chi_c$ *or* $\eta_c + X$	4.2 ± 1.0	4.2 ± 1.0
sum	$102 \pm 10 \pm 9$	$98 \pm 10 \pm 8$

2.6 Semileptonic B Decays

We will now concentrate on the semileptonic decay modes of the B mesons, i.e. those modes where the virtual W in the spectator model decays only to e's,μ's,or τ's. The relations between the branching ratio, the lifetime, and the semileptonic decay width in the spectator model are

$$\mathrm{BR} = \frac{\Gamma_{s\ell}}{\Gamma_{tot}} = \Gamma_{s\ell}\,\tau$$

$$\Gamma_{s\ell} \approx \frac{G_F^2 m_b^5}{192\pi^3}\left(a|V_{ub}|^2 + b|V_{cb}|^2\right) \quad .$$

The spectator model predicts the same rate Γ for e,μ,or τ modes except for phase-space effects. To verify this prediction, we would like to measure the branching ratio and lifetime for each of the different types of B mesons separately since non-spectator effects can affect charged and neutral B's differently. Non-spectator effects are expected for example to reduce the neutral B lifetime. The major problem at the moment however is that these quantities have only been measured for a mixture of B's.

Semileptonic decays are also useful for setting limits on the b to u transition by using the momentum spectrum of the charged leptons. The basic idea is that the maximum momentum of a lepton from a $b \to u$ decay should be higher than that from $b \to c$ decay because of the kinematics (i.e. due to the c-u quark mass difference). We can thus look for a small number of high momentum leptons as a signature of the $b \to u$ decays. The kinematic limit for the electron momentum in the semileptonic decay of a B at rest to a charmed quark is approximately 2.4 GeV. The experimental lepton spectra are shown in figure 13. [9,10,11]

Corrections need to be applied for lepton sources other than B's which can be obtained by taking data off the 4S resonance. The presence of these continuum electrons is the primary limit to the sensitivity of this type of search. Leptons from τ's and Ψ's must also be subtracted. Further, B mesons from 4S decays are not quite at rest, so the lepton spectra are corrected assuming the B's are produced with a $\sin^2$ angular distribution. Finally, the standard model V-A matrix element is used to predict the lepton spectra. Fits are used to derive limits for the $b \to u$ transition, and the data are consistent with being dominated by the b to c transition:

$$90\%\mathrm{CL}\ \ \text{Limits for}\ \ \frac{\mathrm{BR}(b\to u\ell\nu)}{\mathrm{BR}(b\to c\ell\nu)}$$

$$\begin{array}{ll} CLEO & < 0.08 \\ ARGUS & < 0.12 \\ CB & < 0.13 \ . \end{array}$$

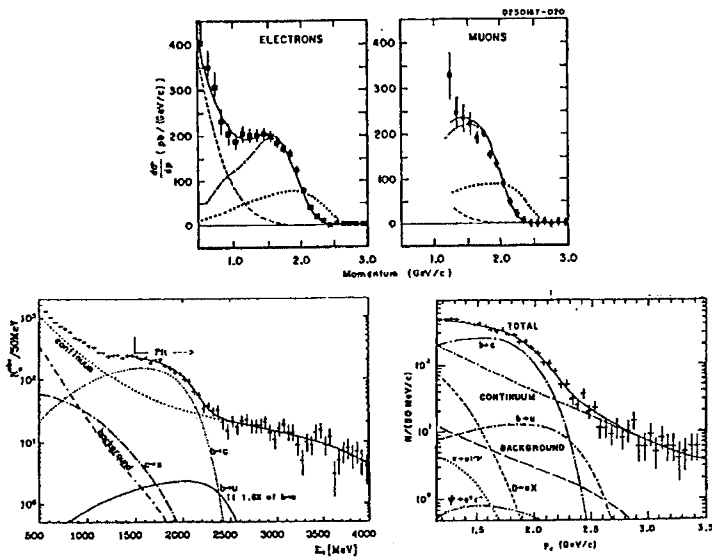

Figure 13: Lepton spectra from semileptonic B decays.

The best limit of 8% gives the KM constraint

$$\frac{|V_{ub}|}{|V_{cb}|} < 0.21 \quad .$$

2.7 B's from PEP and PETRA

At higher energy machines such as PEP and PETRA, the b quark production is a smaller fraction of the total cross section than it is at the 4S resonance. Also there is no on/off resonance technique to be used to compare and contrast the behavior of the b quarks from that of the rest of the quarks. Cuts which are often inefficient need to be used to enhance the fraction of b jets. The chief advantage of these machines however is that the B mesons have much higher momenta which makes measurements of the B lifetime possible. The semileptonic branching ratios measured at these machines (see table 5) are in good agreement with those from the 4S resonance.

Table 5: Semileptonic B branching ratios measured at PEP and PETRA.

	$BR(b \to l^- \bar{\nu} X)$ [%]	$BR(c \to l^+ \nu X)$ [%]	l
TASSO	$11.7 \pm 2.8 \pm 1.0$	$8.2 \pm 1.2^{+2}_{-1}$	μ
TASSO	$11.1 \pm 3.4 \pm 4.0$	$9.2 \pm 2.2 \pm 4.0$	e
MARKJ	$8.8 \pm 0.7 \pm 1.1$	$12.4 + 1.3 \pm 2.0$	μ
CELLO	$8.8 \pm 3.4 \pm 3.5$	$12.3 \pm 3.4 \pm 3.5$	μ
CELLO	$14.1 \pm 5.8 \pm 3.0$		e
JADE	$11.7 \pm 1.6 \pm 1.5$	$7.8 \pm 1.6 \pm 1.5$	μ
MAC	$12.3 \pm 1.8(\pm 0.8^{+1.7}_{-1.3})$	$9 \pm 3.$	μ
MAC	$11.3 \pm 1.9 \pm 3.0$	8 ± 3	e
MARKII	$12.6 \pm 5.2 \pm 3.0$	$8.3 \pm 1.3 \pm 3.0$	μ
MARKII	$13.5 \pm 2.6 \pm 2.0$	$6.6 \pm 1.4 \pm 2.0$	e
DELCO	$14.9^{+2.2}_{-1.9}$	$11.6^{+1.1}_{-0.9}$	e
TPC	$15.2 \pm 1.9 \pm 1.2$	$6.9 \pm 1.1 \pm 1.1$	μ
TPC	$11.0 \pm 1.8 \pm 1.0$	$9.1 \pm 0.9 \pm 1.3$	e

2.8 B Lifetime Measurements

Lifetimes are currently measured for the average mix of charged and neutral B's produced in e^+e^-interactions. Eventually we would like to measure the lifetimes of individual types of B's to determine whether non-spectator diagrams have an effect. The primary cuts used in the analysis are to find high thrust events which contain leptons with both high momentum along the thrust axis and high trans-

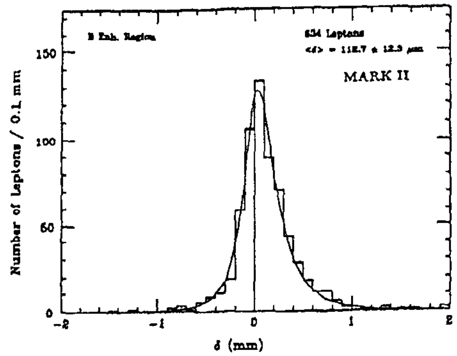

Figure 14: Impact parameter distribution for B lifetime measurements from MarkII.

verse momentum relative to the thrust axis. The first cut enhances the b quark fraction because of the harder decay spectrum for b leptonic decays, and the second selects b's because the transverse momentum relative to the thrust axis has a maximum which is $m_q/2$ and therefore higher for b's. The quantity which is measured is the impact parameter of the lepton relative to the beam location. A typical set of data is shown in figure 14. While the distribution is only shifted slightly from zero, the mean of the distribution can be determined quite accurately. Similar results are obtained by the Mark II, DELCO, JADE, HRS, and TASSO groups. The combined result for the B average lifetime is

$$\tau_B = 1.18 \pm 0.14 \; 10^{-12} \; sec \; .$$

Since this lifetime can be calculated in the spectator model, the KM parameters become constrained by this measurement to satisfy the relation

$$\tau_B = 0.86|V_{ub}|^2 + 0.48|V_{cb}|^2 \approx 0.0011 \pm 0.0003 \quad .$$

Using the previous bound

$$0 < \frac{V_{ub}}{V_{cb}} < 0.21$$

from the lepton spectrum measurements, we get $V_{cb} \approx 0.047$. Note that while the s to u transition is about 0.2 in the standard model, the b to c transition is a factor of 4 smaller. This is one of the reasons why despite the heavier mass and large phase-space for heavy b decays, the lifetime is still relatively long.

2.9 Charmless B Decays

As has been mentioned several times before, it is important to measure the KM parameter V_{ub}. The attempt to detect these transitions has already been mentioned in the context of measuring the total amount of produced charm per B decay with corrections for $c\bar{c}$ states, and the detection of leptons past the kinematic endpoint for b to c transitions. Another way of testing for charmless B decays is to find an exclusive final state which can only be produced by b to u transitions. In the context of the spectator model, if the b quark converts to a u quark with charged current interactions (no FCNC), then the B meson will decay in the simplest case to a two body mode containing a π or ρ or some other similar resonance. Table 6 shows the upper limits obtained by the CLEO and ARGUS groups for these simple modes. By far the most sensitive channel is $B \rightarrow \rho l \nu$ (note the large coefficient in the table 6 prediction column) where the upper limit

Table 6: CLEO and ARGUS charmless B decay limits.

DecayMode	*CLEO*	*ARGUS*	*Prediction*
$B^0 \rightarrow \pi^+\pi^-$	0.03	0.04	$0.21\left(\frac{V_{ub}}{0.05}\right)^2$
$B^0 \rightarrow \rho^+\pi^-$	0.61		$0.56\left(\frac{V_{ub}}{0.05}\right)^2$
$B^- \rightarrow \pi^0\pi^-$	0.23		$0.06\left(\frac{V_{ub}}{0.05}\right)^2$
$B^- \rightarrow \rho^0\pi^-$	0.02	0.07	$0.22\left(\frac{V_{ub}}{0.05}\right)^2$
$B^0 \rightarrow \rho^0\rho^0$	0.05		$0.01\left(\frac{V_{ub}}{0.05}\right)^2$
$B^0 \rightarrow \pi^+a_1(1270)^-$	0.12		
$B^0 \rightarrow \pi^+a_2(1320)^-$	0.16		
$B^- \rightarrow \rho^0a_1(1270)^-$	0.32		$0.33\left(\frac{V_{ub}}{0.05}\right)^2$
$B^- \rightarrow \rho^0a_2(1320)^-$	0.23		
$B^0 \rightarrow p\bar{p}$	0.02	0.013	
$B^- \rightarrow \rho^0\ell^-\nu$	0.25	0.22	$3.9\left(\frac{V_{ub}}{0.05}\right)^2$

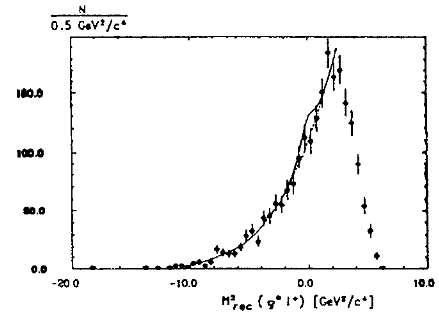

Figure 15: Recoil mass spectrum in $B \rightarrow \rho l\ X$ with the expected contribution from $B \rightarrow \rho l \nu$ for the limit set for V_{ub} of 0.012 .

of 0.22 corresponds to a limit on V_{ub} of 0.012. This channel can be searched for by looking for a zero mass object recoiling against the $\rho\ l$ system in a B decay. The recoil mass spectrum for the data [12] is shown in figure 15, the small bump at zero being the amount consistent with the upper limit of 0.012.

Similar limits to those obtained with the lepton spectrum endpoint can be derived by looking at $B \rightarrow D^* l \nu$

$$\frac{|V_{ub}|}{|V_{cb}|} < 0.22 \quad .$$

2.10 $p\bar{p}$ Modes

One of the most interesting, and also perhaps the most controversial measurements has been the ARGUS observation of $B \rightarrow p\bar{p}\pi^-$ and $B \rightarrow p\bar{p}\pi^-\pi^+$ because it provides direct evidence that V_{ub} is non-zero. This is extremely important because if $V_{ub} = 0$ in the KM model, there is no CP violation in the B system. Further, since CP violation is proportional to V_{ub}, if this parameter is large, perhaps CP violation in the B system will be easier to see. The data from ARGUS [13] for these two modes have not been confirmed by the CLEO group. In particular, the combined modes from ARGUS give a branching ratio of $(7.8 \pm 1.7)10^{-4}$ while the upper limit from the CLEO data is 3.6 10^{-4}. If taken at face value, the original

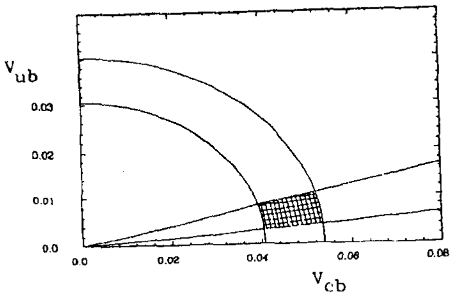

Figure 16: Constraints on V_{ub} and V_{cb}. The elliptical constraints come from the B lifetime, the upper limit on the ratio from lepton endpoint measurements, and the lower limit from the ARGUS $p\overline{p}$ result.

ARGUS data provide a lower limit on the KM parameter [14,15]

$$\frac{|V_{ub}|}{|V_{cb}|} > 0.08 \quad .$$

Putting all of the constraints which we have discussed together, one obtains figure 16 where as mentioned, the lower limit for V_{ub} awaits confirmation. The elliptical constraint in figure 16 comes from the B lifetime, the upper limit on the ratio of V_{ub} to V_{cb} comes from the lepton endpoint measurement, and the lower limit on the ratio comes from the ARGUS $p\overline{p}$ measurement.

2.11 $B\overline{B}$ Oscillations

In the neutral K system, it is known that there are transitions between K and $\overline{K}$ states. These could in principle also exist in the D,B,or T systems, but are believed to be large only in the B system. The rapid decrease in the lifetime of the B meson as a function of the b quark mass is partially offset by the smallness of the V_{cb} KM matrix element which gives the neutral B system a long enough lifetime that this kind of mixing can occur.[16,17] As in the K system, the Feynman diagrams responsible for these transitions are the box diagrams shown in figure 17.

The calculation of the matrix element for the B_d transition assuming the box

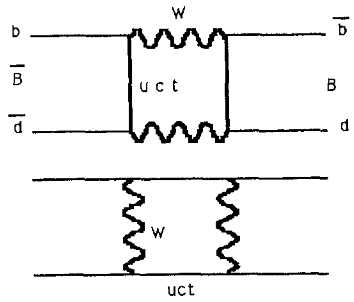

Figure 17: Box diagrams for $B\overline{B}$ mixing.

diagram with a t quark exchange would contain the KM parameters

$$V_{tb}^{2}V_{td}^{2}$$

whereas for B_s transitions, it would be

$$V_{tb}^{2}V_{ts}^{2}$$

which we would expect to be larger since V_{ts} is probably larger than V_{td}. Thus we would expect the largest mixing in the B_s system.

The Hamiltonian for the $B\overline{B}$ system is

$$\mathrm{H}\begin{pmatrix} B^0 \\ \overline{B}^0 \end{pmatrix} = \begin{bmatrix} M - \frac{i\Gamma}{2} & M_{12} - \frac{i\Gamma_{12}}{2} \\ M_{12}^{*} - \frac{i\Gamma_{12}^{*}}{2} & M - \frac{i\Gamma}{2} \end{bmatrix} \begin{pmatrix} B^0 \\ \overline{B}^0 \end{pmatrix}$$

where the off-diagonal terms in the mixing matrix are

$$\mathrm{M}_{12} = \left\langle \mathrm{B}^0 | \mathbf{H} | \overline{\mathrm{B}}^0 \right\rangle \quad .$$

There are two CP eigenstates

$$|\mathrm{B}_{1,2}\rangle = \tfrac{1}{\sqrt{2}}\left(|\mathrm{B}_0\rangle \pm |\overline{\mathrm{B}}_0\rangle\right)$$

$$M_{1,2} = M \pm \tfrac{\Delta M}{2}$$

$$\Gamma_{2,1} = \Gamma \pm \tfrac{\Delta\Gamma}{2} \quad .$$

The mixing is usually described by a mixing parameter r where r=0 denotes no mixing. The equations are exactly the same as those encountered in the K meson system except that to a good approximation in the B system, $\Delta\Gamma \approx 0$, so that $\Gamma_1 = \Gamma_2$ can be used to simplify many of the equations involved. The probability that if you start with a B, you find a B at a later time t for example is given by

$$W_B(t) \approx \frac{1}{2}e^{-\Gamma t}(1 + cos(\Delta M t))$$

which shows that the B's will oscillate in time in a way which may be useful in investigations of CP violation.

There are several different ways in which CP violation can arise in the B system. The interested reader should start with the 1987 Berkeley SSC study, **Experiments, Detectors, and Experimental Areas for the Supercollider**, pp706-717 for a nice summary.

3 Hadronic Production of B's

So far we have concentrated almost entirely on results obtained from B's produced at e^+e^- machines. But B's are also produced at hadron machines, and experiments are underway to study B production using fixed targets at the Tevatron, and using collider experiments at $Sp\bar{p}S$ and the Tevatron. Since b's are produced by the strong interactions at hadron machines, the production cross sections can be very large provided they are not limited by threshold effects (which are however important for the present fixed target experiments). As usual at hadron machines, one needs to know a bit more about QCD to actually calculate the production cross section, but much progress has been made in this area in the past year including higher order corrections to the cross section.

Details of the QCD calculations and corrections can be found in the series of lectures at this school by Keith Ellis.[18] Considerable effort is underway at the moment to experimentally verify the calculations of both the total b production cross section and the momentum spectrum of the B's. So far, little has been done in the way of detecting exclusive decays of B's, although this situation may change in the next series of collider runs as detectors begin to implement silicon vertex detectors. The major technique used currently is to detect electrons or muons from semileptonic B decays. Both the total cross section and the transverse momentum spectrum of produced b quarks can in principle be deduced from the observed lepton spectra.

For an experimentalist, the issue of higher order QCD corrections is important for two reasons. First the corrections affect the total b production cross section. Due to large uncertainties in the gluon structure function at small x, together with large contributions to the total cross section from gluon-gluon diagrams, the total cross section is quite uncertain. Measurements will eventually settle this issue and perhaps allow a comparison with QCD. The second effect of the corrections is to change the shape of the p_t spectrum of the b quarks. This is actually important because whatever Monte Carlo is used by the experimentalist to estimate efficiencies and backgrounds, the result can be very sensitive to the assumed p_t shape. Before doing any detailed QCD calculations, one can estimate the importance of this effect by using a Monte Carlo which does lowest order QCD and then tries to add selected diagrams and processes believed to be important at high p_t . Figure 18 shows the p_t spectrum of produced b quarks in such a calculation. Note that the cross section *magnitude* changes most at high p_t as higher order effects are added, but that the *shape* (i.e. slope) changes most at low p_t . This result is also found in more detailed calculations and is important because the high p_t region is the interesting region if one is worried about b backgrounds to heavier quark signatures or other exotics. If the shape is unchanged by higher order corrections, then the major uncertainty in efficiency and background calculations becomes just the magnitude of b production cross section at high p_t . The distributions can then be normalized to the detected cross section at high p_t .

As usual in QCD issues, the interpretation of experimental results depends to some extent on the way in which the produced quark fragments to form hadrons. In the case of leptons from B mesons, higher order corrections and variations in the fragmentation models can lead to different amounts and distributions of particles accompanying the lepton. This is a problem for electrons, because it is typical to use the amount of energy in a cone around the electron as a signature of the effective mass of the parent quark. Heavier quarks can produce leptons with larger transverse momentum relative to the decay axis; the maximum being $m_q/2$. Thus these "isolation" cuts can be used to discriminate against leptons from

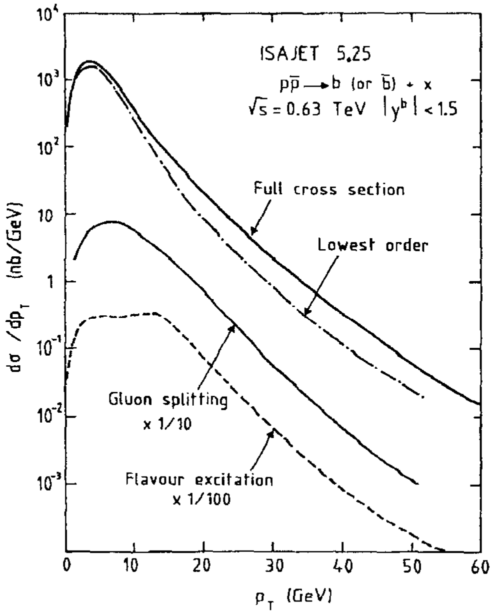

Figure 18: Isajet calculations of the b quark p_t spectrum, UA1 collaboration.

lighter quark backgrounds. A Monte Carlo calculation must be used to correct for inefficiencies due to the isolation cut which leads to some sensitivity to the choice of a fragmentation model. The assumptions in the Monte Carlo can be checked by using muon data which do not require such isolation cuts provided the muon system is thick enough.

Monte Carlo's also need to make assumptions about how the b quarks fragment into B mesons and other hadrons. The quark fragmentation functions in Isajet for example are assumed to follow the Peterson form [19]

$$f(z) = \frac{1}{z}\left[1 - \frac{1}{z} - \frac{\varepsilon}{1-z}\right]^{-2},$$

where ϵ is related to the quark masses by

$$\varepsilon_q \approx \frac{k}{m_q^2}.$$

The Peterson formula illustrates the important point that for a heavy quark b which decays into a heavy meson B with other light hadrons, the B meson (just due to momentum conservation) will carry most of the momentum. This effect becomes more pronounced as the quark gets heavier. One consequence is that the inclusive x spectrum of B mesons from b decay (where x is the fraction of the b momentum carried by the B) will be strongly peaked towards 1 and that this peaking will be even stronger for t decays.

The Peterson et al. argument is quite simple. Consider the transition $b \rightarrow B + h$ where the B meson takes a fraction x of the b quark momentum. The quantum mechanical amplitude for this transition will be proportional to $\frac{1}{\Delta E}$ where

$$\Delta E = E_B + E_h - E_b \ .$$

If we use $m_b \approx m_B$ and

$$\begin{aligned} E_B^2 &= m_B^2 + x^2p^2 \\ E_h^2 &= m_h^2 + (1-x)^2p^2 \\ E_b^2 &= m_b^2 + p^2 \end{aligned}$$

we obtain

$$\Delta E \propto 1 - \frac{1}{x} - \frac{\varepsilon}{1-x}$$

with

$$\varepsilon = \frac{m_h^2}{m_b^2}$$

which is the Peterson form. Since the harder meson spectrum will also result in a harder lepton spectrum, we expect that the spectrum of leptons from B decay and other heavy quarks will be harder than that of light quarks due to this effect. The ϵ value determined from the spectrum of D^*'s yields the solid curve shown in figure 19.[20] These data confirmed the stiffening of the x spectra in the c quark system.

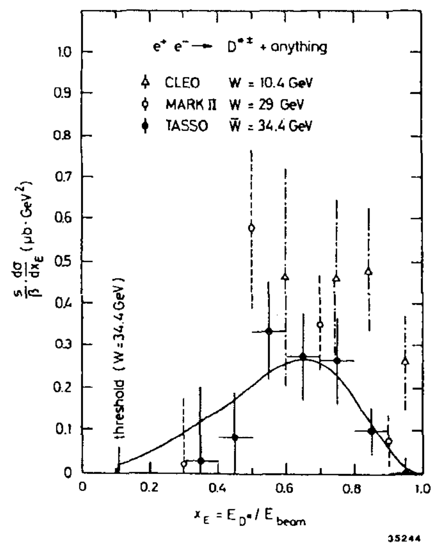

Figure 19: D^* spectrum used to extract an ϵ parameter.

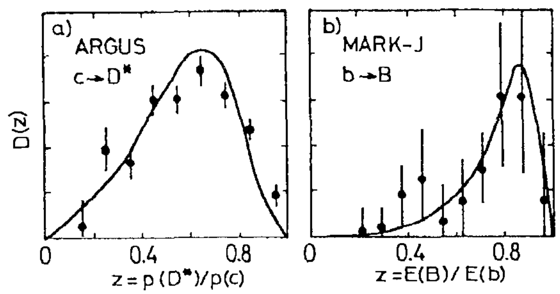

Figure 20: Comparison of c and b fragmentation illustrating the hardening of the spectrum for heavier quarks.

Figure 20 shows a comparison of data from c and b quarks with fits for ϵ of 0.18 and 0.018 respectively ([21,22]) which agrees with the expected $1/m_q^2$ dependence.

3.1 Checking the p_t Spectrum

It is important to be able to measure the shape of the p_t spectrum for b production both to check higher order QCD calculations and to verify the assumptions embedded in experimental Monte Carlos. In order to do this, different samples of leptons and various techniques have been used to detect low, medium, and high p_t b production.[23]

Figure 21 shows the results of these measurements from the UA1 collaboration using four different techniques. The lowest p_t point comes from measuring the μ pair decay mode of J/Ψ's. The total inclusive cross section for Ψ's with $p_t > 5$ GeV and rapidity less than 2 is found to be

$$\sigma B\,(p\bar{p} \to J/\psi + X) = 7.5 \pm 0.7(\text{stat}) \pm 1.2(\text{syst})\ \text{nb}$$

where most of the cross section is due to charm or χ_c state production. In order to determine what fraction of this is due to b's, the momentum of the Ψ is measured relative to the adjacent jet activity. The transverse component of this momentum is limited to $m_q/2$ and thus will extend to larger values for b's than it does for lighter quarks just as in the case of the lepton spectra discussed earlier. This allows

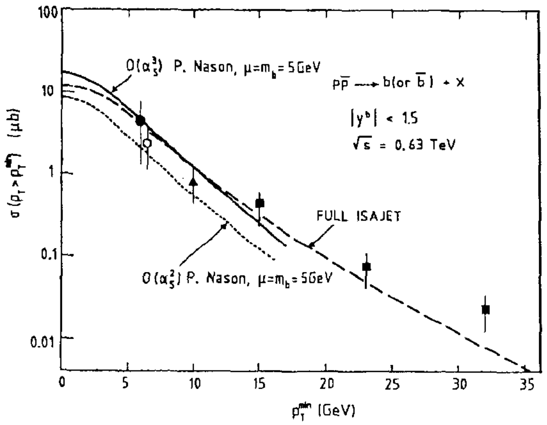

Figure 21: UA1 measurements of the p_t spectrum of b production together with $\mathrm{O}\left\{\alpha_s^3\right\}$ and Isajet predictions.

the contribution from the b quarks to be separated from the lighter contributions. The result is

$$\sigma \mathrm{B}\left(\mathrm{p}\overline{\mathrm{p}} \rightarrow \mathrm{b} \rightarrow \mathrm{J}/\psi + \mathrm{X}\right) = 1.8 \pm 0.6 \pm 0.9\mathrm{nb} \quad .$$

This provides a measurement of the B spectrum which due to the p_t cut on the $\Psi's$ and the steeply falling p_t distribution is at a p_t of just slightly more than the 5 GeV p_t cut.

The second measurement also comes from measuring dimuons but at higher mass. The sources of dimuons are Drell-Yan production, Upsilon production, and decay in flight backgrounds. By looking at the dimuon "p_t relative" distribution (i.e. the p_t of the dimuon relative to the nearby jet activity), it is determined that the b to c parent ratio is 92:8 for this sample. Dimuons below the Ψ can also be used for this purpose, and provided one cuts on the dimuon p_t (relative to the beam this time), the sample is dominated by $b \rightarrow c\mu, c \rightarrow s\mu$. Finally at somewhat higher p_t 's (15 and above), the inclusive muon p_t distribution can be used to determine the b spectrum. The pt-rel distribution indicates that about 76% of this sample comes from b parents. At the highest p_t 's, (above 25 GeV), the lepton spectra become dominated by leptons from W's and this technique can no longer be used. Corrections are applied to the data for each p_t bin for the fraction of b parents. These fractions are

$\mathrm{p_t}$ range	b fraction(%)
10 – 15	76
15 – 20	76
20 – 25	43

Looking again at figure 21, there are several lessons to be learned. First, the shape of the calculated higher order cross section (labeled P.Nason et al.) is very similar to the lowest order and this reduces the systematic errors in the measurement. Second, the cascade type Monte Carlo (Isajet) seems to be a good approximation to the shape of the p_t spectrum. Finally, the largest uncertainty in the total b cross section comes from the uncertainties in the extrapolation to low p_t values. The observable part of the b cross section is reasonably well known. The UA1 group concludes that the cross section is

$$\sigma\left(\mathrm{p}\overline{\mathrm{p}} \rightarrow \mathrm{b} \text{ or } \overline{\mathrm{b}} + \mathrm{X}, |\mathrm{y}| < 1.5\right) = 14.7 \pm 4.7\mu\mathrm{b}$$
$$\sigma\left(p\overline{p} \rightarrow b\overline{b} + X\right) = 10.2 \pm 3.3\mu b \quad .$$

Note there is a factor of two required for the *b or* $\overline{b}$ cross section so that the *observed* part of the cross section is about 72% (i.e.14.7/(2*10.2)).

4 B Factories

There have been many recent studies of the capabilities of various types of machines designed specifically to produce large numbers of B mesons.[24,25,26,27, 28,29] The types of designs range from very high current linear colliders to high luminosity e^+e^-storage rings optimized for the production of collisions in the Upsilon region. Studies have also been done on the capabilities of existing B factories such as the Cornell storage rings, or the Tevatron collider and even the Tevatron fixed target program, all of which produce very large numbers of B's. Other plans include CESR upgrades,[30] a machine at PSI[28] (designed but turned down by the Swiss government), a linear collider design at Frascati,[31] and a machine with two different beam energies (asymmetric machines) at SLAC,[32,33].

The primary goal for all of these studies has been the potential for observing CP violation in the B system. It is widely believed that the observation of this effect in a second system (the first being of course the K system) might provide important clues to the origin of this poorly understood phenomenon. The potential for observing CP violation is usually used to determine roughly the machine parameters, but opinions vary about exactly how many B's need to be produced or how many need to be detected to achieve this goal. While optimists might claim that 10^7 B's would be sufficient, pessimists would claim 10^9. Unfortunately, the design constraints for all machines make achieving 10^8 rather difficult. There are of course always other good pieces of physics which can be investigated by machines which produce large numbers of B's, for example, measurements of the KM matrix elements to high precision, investigations of $B\overline{B}$ mixing, and particularly studies which test the b$\to$t coupling. At the present, few designs if any have a guaranteed ability to test CP.

The largest B samples at present come from the CLEO detector. An integrated luminosity there of 350 pb^{-1} represents 7 10^5 $B\overline{B}$'s at the 4S. Average detection efficiencies are about 0.001. In trying to study the $B\overline{B}$ system, one obvious problem for e^+e^-machines is that the B's at the 4S are produced almost at rest in the lab frame. The decay products from the B and the $\overline{B}$ are thus intermingled which causes combinatorial background problems for the reconstruction of the B or $\overline{B}$. To study CP violation, it is necessary to tag a B or $\overline{B}$, and then reconstruct the $\overline{B}$ or B which accompanies it. Thus in the detector design, a premium must be placed on particle identification in the low momentum region (up to 2.5 GeV, the maximum for B decay) to help in the reconstruction of the B final states. Most studies of new machines to produce large numbers of B's are thus accompanied by suggestions for sophisticated new detectors.

The current CESR luminosity of about 2 10^{32}, with a cross section of about 1 nb gives 2 10^6 $B\overline{B}$ per year assuming a running year of 10^7 seconds. This is clearly not quite what we would like, although the possibility exists of accumulating a significant sample by running for several years and accomplishing modest improvements in luminosity and/or detector performance.

The asymmetric machine designs are considerably more ambitious in their goals for produced B's requiring in excess of 10^8 per year. The reason for having a machine with two different beam energies to study the B system is quite simple. If the two energies are not the same, then the produced B mesons will not be at rest in the lab frame, but will be travelling with some momentum directed along the beam axis. If the B and the $\overline{B}$ decay at different proper times, then their decay vertices will be separated along the beam axis, and a good vertex detector with resolution in this direction (not the usual dimension in which vertex detectors have good resolution) will be able to assist in separating the decay products of the two B mesons. For the traditional storage ring approach, B's produced at the 4S have a β of 0.06 and a mean decay path of only 20 microns. In contrast, a machine which produced B's with $\beta\gamma \approx 1$ would yield decay lengths of 400μ. If this separation can be detected, then the rates of B and $\overline{B}$ decay to various channels can be measured as a function of the time difference between the two decays.

Decays of B's to CP eigenstates are particularly useful.[34,35] If for example the state f is a CP eigenstate, and there is mixing, then the amplitude for B$\to$f and B$\to$ $\overline{B}$ $\to$f will interfere, the phase from the KM matrix being opposite for an initial B or $\overline{B}$. The mixing of B's and $\overline{B}$'s can be studied by using decay modes which identify the initial B or $\overline{B}$ such as the leptonic decays (after corrections $\sim 6\%$ for wrong sign leptons from cascade decays b$\to$c$\to$ e,μ instead of b$\to$ e,μ) or charged K mesons. Like sign K's or leptons indicate mixing.

Detection of CP violation can be done by using events which contain both a B decay to a CP eigenstate and also have a second B which can be tagged. In the presence of CP violations, rates for $B\overline{B}$'s where tagged B's have subsequent decays of another object to a CP eigenstate will differ from decays of $B\overline{B}$'s where decays to CP eigenstates have subsequent decays to tagged B's. Note that this method actually tests T violation and hence CP via the CPT theorem. Events with CP eigenstates and subsequent $\overline{B}$ decays have the same phase and can be added to the sample and compared to tagged $\overline{B}$'s with subsequent CP eigenstate formation. Schematically we compare

$$B\overline{B} \to BX, X \to CP$$
$$B\overline{B} \to CP\ X, X \to \overline{B}$$

with

$$\mathrm{B\overline{B}} \rightarrow \mathrm{CP\ X, X} \rightarrow \mathrm{B}$$
$$\mathrm{B\overline{B}} \rightarrow \mathrm{\overline{B}X, X} \rightarrow \mathrm{CP}\ .$$

Suggested CP eigenstates include D^+D^- and ΨK_s as well as events where the Ψ is replaced by χ, ω, ρ, ϕ and/or the K_s is replaced by K_L. The ΨK_s has an excellent experimental signature when the Ψ decays to $\mu\mu$ or ee, and the K_s decays to $\pi\pi$. The ARGUS collaboration measures a rate of about 1 detected event per 100 pb^{-1} in this mode.[36,37] The measurement of the asymmetry due to CP violation requires perhaps 100 such events. The total number of $\mathrm{B\overline{B}}$'s required can be estimated from

$$\mathrm{N}_{B\overline{B}} \approx \frac{1}{\epsilon\ BR}\left(\frac{s}{A}\right)^2$$

where ϵ is the detection efficiency, BR the B$\rightarrow \Psi K_s$ branching ratio, A the asymmetry and s the desired statistical significance. As you can see, for a 10% asymmetry, branching ratio of 3 10^{-4} and 10% efficiency, we required a few 10^7 events for a 3σ effect.

4.1 Detector Requirements

Detector requirements for precision B experiments at e^+e^-colliders are quite stringent. High precision tracking is required over large solid angle for the reconstruction of multibody final states. The tracking should also have dE/dx capabilities to aid in K meson recognition for kinematic fits. Independent particle ID for $e\ \mu\ \pi\ K\ p$ (using for example time-of-flight, Cherenkov or RICH counters) is also required. Because of the need to also reconstruct π^0's for D and D* reconstruction, the low energy cut off for photon detection is important. The reconstruction efficiency for D*'s for example decreases rapidly with this parameter (see figure 22). This requires that the electromagnetic calorimetry be constructed inside the coil to minimize soft photon inefficiencies. Vertex detection is required with good resolution along the beam axis for CP violation techniques in asymmetric machines, and good resolution transverse to the beam to aid in D and B tagging. Strip chamber vertex detectors would thus be inadequate.

Soft charged pion detection from D$^*\rightarrow D\pi$ is important. In a 1.5T field, 90% efficiency for reconstructions requires detection of tracks down to 30 MeV which corresponds to a track which curls up within 7 cm. Finally, the collection of large samples of order 10^8 events corresponds to an average trigger rate (for a 10^7 sec year) of about 10Hz. If the signal is only 10% of the total rate at the trigger level, the trigger rate would be 100Hz. Thus, given the complexity of the detector, DAQ systems with high speed and good buffers are required.

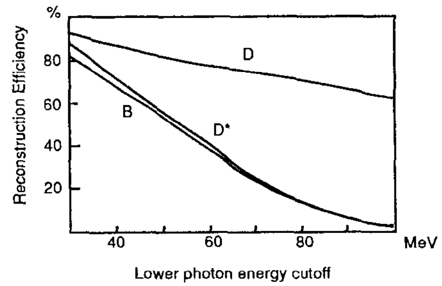

Figure 22: D* reconstruction efficiency versus minimum detectable photon energy, calculated for the ARES detector at the proposed Frascati linear collider.

4.2 B's at the Tevatron

Large samples of B mesons are currently being produced at the Tevatron both in the collider and fixed target modes. Detection and separation of these events from lighter quark backgrounds is however a non-trivial problem to say the least. The primary characteristics of these events which can be used to distinguish them from backgrounds are the increased probability of a lepton trigger, larger maximum p_t of the lepton relative to the remaining soft hadronic particles – a characteristic difficult to use in a trigger, and finally the presence of extended vertices. The latter aspect of these events is also difficult to use in a trigger since sufficiently rapid vertex reconstruction and read-out is usually not available. Instead, several groups have tried to implement triggers which find extended vertices by utilizing the growth in charged multiplicity and hence of target ionization which occurs after a B meson decays.

Experiment E771 at Fermilab is typical of such an experiment. Based on an

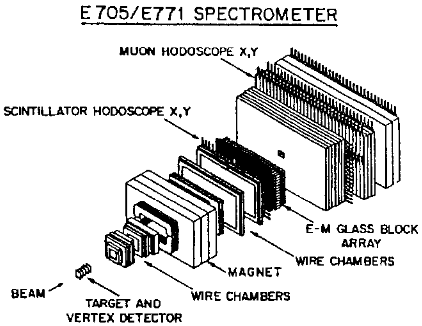

Figure 23: E771 Spectrometer

existing spectrometer from E705 (see figure 23), a vertex strip detector is added which is used as both a target and a vertex detector. A beam energy of 900 GeV will be used with an interaction rate of 3 10^6 and a muon plus vertex trigger. The total $B\overline{B}$ cross section is uncertain, but estimated to be $\sim$ 10nb yielding about 10^6 $B\overline{B}$'s produced in a year (2 10^6 sec for extracted FNAL beams). This is similar to current production levels at CESR. This number of produced $B\overline{B}$'s should yield about 1000 events from B$\rightarrow$ Ψ X which would give 5-10 identified B$\rightarrow$ Ψ K_s events. To study CP, the opposite sign B must be tagged, the efficiency for which is about 1%. Thus to obtain a statistically significant sample, say 100-1000 events requires an increase in rate of 10^3 to 10^4. One order of magnitude can come from running longer, the rest needs to come mostly from increased interaction rates on target.

The primary limitation for the target interaction rates in these "open geometry" experiments comes from the rate capabilities of wire chambers and the induced radiation damage to the target/vertex detector. The former can be alleviated by constructing chambers with small wire spacings and running at low wire gain. Damage to the silicon planes of the vertex detector can perhaps be reduced by running the detector at lower temperatures and by using rad-hard electronics. Radiation doses to the target silicon from beam particles alone would correspond to 1mrad per 10^6 interaction rate per year of running.[38] Radiation damage from secondaries will at least double this, thus running at higher interaction rates will require corresponding increases in the area of the beam at the target to keep radiation damage per square centimeter to reasonable levels.

An alternative to the open geometry is being pursued by the E-789 experiment ("Son of 605") which uses a semi-closed geometry to achieve the potential of running at interaction rates approaching 10^{10} by 1992. Closed geometry means that most of the incoming particles are absorbed by a thick beam dump which allows the experiment to run at high rates. While this should produce a recognizable signal in $B \rightarrow \pi^+\pi^-$, the closed geometry precludes tagging the other B and thus this technique while useful for the study of B's, cannot be used for CP. Nevertheless, knowing the $B \rightarrow \pi^+\pi^-$ branching ratio will be an important input to the design of future CP experiments. Dihadrons from B decay are measured in a double arm spectrometer, while vertices of high p_t particles which make it through the beam dump used to absorb soft particles can be measured with a silicon microvertex detector with fast readout consistent with separating interactions with a resolving time of one RF bucket to reduce confusion from multiple interactions.

Another experiment, E687, will run in the tagged photon beam and will concentrate on muon final states, with approximately 1000 tri-muon events expected for a years run. Finally, E791, the successor to E691(charm photoproduction) and E769(charm hadroproduction) will attempt to run with a trigger which requires only 6 GeV E_t in a calorimeter! The experimental design calls for writing 5000 events per second to tape, with offline analysis to be performed later to extract a signal! This experiment can only run at interaction rates of about 10^5 but may be able to see 50 fully reconstructed B events after final analysis of all of the data on tape from a year's run is completed.

5 Bottom as Background to Top

While bottom quarks as we have seen are interesting in their own right, they are also an important background to the search for the top quark. Because of their higher mass relative to the light u,d,c,s quarks, bottom quarks will be the dominant sources of isolated leptons at high p_t which is exactly where we would like to look for evidence of the top quark. This problem has led to extensive Monte Carlo studies by UA1,UA2 and CDF of the properties of the leptons coming from b decays. As the lower limit for the top quark increases toward the W mass, this background becomes less significant however because the p_t spectrum of leptons from b's falls very rapidly, and for heavier top, one can increase the lower cut on the p_t of the required lepton until there is little b background. Nevertheless, it is important to know as much as possible about the b as a background to the top search.

The recent calculations of P.Nason, S.Dawson, and K.Ellis [39] have now provided us with α_s^3 corrections in QCD for the b total cross section as well as the differential cross section as a function of p_t . The most uncertain parts of the p_t spectrum are the lowest and highest regions. In the future we will also need the higher order cross sections as a function of both p_t and rapidity so that experimental acceptance corrections can be made for the unseen part of the cross section either outside of y_{max} which is typically 1-2 or below pt_{min} which is typically a few GeV. For most experimental top quark searches, the low p_t region, while dominating the uncertainty in the total cross section, is unimportant because of relatively high minimum p_t requirements for the leptons used in the analysis. As far as backgrounds to the lepton spectrum at moderate p_t are concerned, at Tevatron energies, the dominant source of high p_t electrons and muons (other than those from W's and Z's) is however bottom production. Overlaps, misidentifications, conversions, decays in flight etc. do not dominate. Charmed quarks contribute less in this region (especially to isolated electrons) because both the higher b mass and the harder b fragmentation relative to c fragmentation enhance the b spectrum above that of the c quark which has a similar production cross section.

For the experimentalist, the b backgrounds for lepton signals for top or other exotics must be analyzed with the help of a Monte Carlo generator containing the latest theoretical information, and an event simulator which can take into account the finite acceptance of the apparatus, and the variations in efficiencies across the detector due to the device and the trigger. To get around the problem of the poorly known total cross section for b's, the Monte Carlo is used to predict the relation between the produced b spectrum and the daughter lepton spectra. The

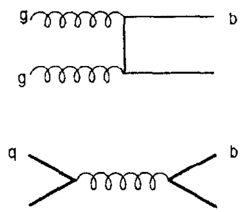

Figure 24: Lowest order diagrams for b production in $p\overline{p}$.

b cross section at high p_t is then normalized to the observed spectrum [40]:

$$\sigma_b = \sigma_\mu \left[\frac{\sigma_b}{\sigma_\mu}\right]_{MC} .$$

The Monte Carlo contains the assumptions about the fragmentation of virtual b's to B and B* mesons, the (V-A) semileptonic decay spectra of the B mesons, and the lepton decay kinematics including finite mass effects. To this must be added a set of structure functions and the higher order QCD matrix elements. For the latter, there are two quite different methods being used. The more traditional is used in Isajet and consists of using the lowest order diagrams plus cascade shower development and a fragmentation model. The second method includes higher order diagrams combined with some of the fragmentation features of the former. Care must be taken in the second approach not to double count the part of the higher order corrections which may be included in the fragmentation model (final state gluon emission for example.) In general, the diagrams shown in figure 24 involving the production of b's directly from lowest order processes are quite easy to generate, but the diagrams in figure 25 which involve "flavor excitation" or "gluon splitting" require several hundred hours of computing on IBM3090 class computers to generate reasonable samples. The reason that gluon splitting is important is that the total interaction cross section is dominated by $gg \to gg$, and even though the probability of gluon branching to $b\overline{b}$ is small, the $gg \to gg$ total cross section is measured in mbarns, and we are interested in backgrounds at the nb level. Further, as we will see in the next section, top searches often require leptons plus additional jets, and the gluon splitting contribution is enhanced by the jet requirement.

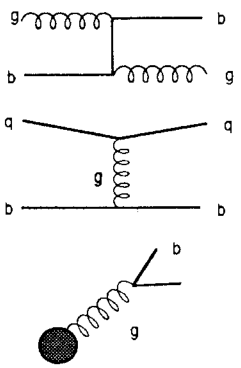

Figure 25: Gluon splitting and flavor excitation contributions to b production in $p\overline{p}$.

6 t Quark Physics

The top quark has been the object of intensive searches during the past year by many groups. This important ingredient in the standard model of particle physics however remains unseen. Searches for it or its discovery will eventually provide further important constraints on the parameters of the standard model and the elements of the KM matrix. The presence of a light top quark would produce an obvious threshold effect in the hadronic cross section at e^+e^-machines, as was the case for the c and b quarks. That such an effect was not observed, (see figure 26) has allowed a limit of $M_t > 30.4$ GeV to be set by the AMY and VENUS groups at Tristan.[41] Similar studies of the decays of the Z to high sphericity events at the SLC require $M_t > 40.7$ GeV. Both of these possibilities had already been excluded by the early measurements of the UA1 collaboration at CERN which (through techniques similar to those described later) set a lower bound of 41 GeV.

During the summer of 1989, UA1 and UA2 at CERN quoted mass limits for the top quark of (M_t >61,67 GeV 95%CL) respectively,[42] while CDF results extended these limits to exclude the range

$$40 < M_t < 77 \quad 95\%CL$$

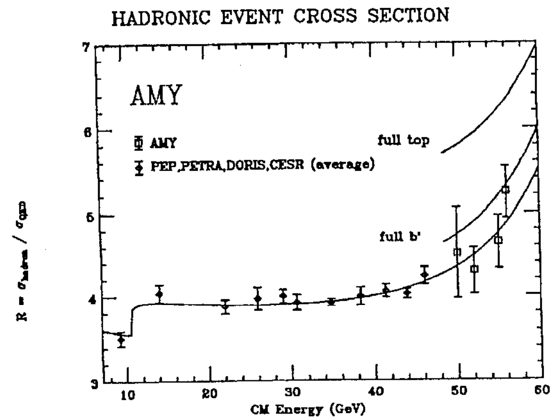

Figure 26: Expected behavior of the hadronic event cross section with and without top.

from a search which uses an electron plus jets final state, and

$$28 < M_t < 72 \quad 95\%CL$$

from an electron muon final state. For the purpose of this review, I will concentrate on the most recent results from CDF which place the most stringent limits to date on the top quark mass.

Despite the fact that the top quark has not been found, evidence or prejudice for its existence is quite strong. In the standard model, the b quark is produced in e^+e^-annihilation with a forward backward asymmetry which is given by

$$A^b_{FB}(s) = \frac{9\ G_F\ a^b}{16\pi\ \sqrt{2}\alpha}\ \frac{sM_Z^2}{M_Z^2 - s}\ .$$

The measurement of this b quark asymmetry [43,44] in e^+e^-annihilation shows that the b quark has the expected asymmetry for a member of a left-handed doublet and right-handed singlet structure indicating that it should have a partner, namely the top quark. The measured value of the b quark asymmetry yields

$$a^b = -1.08 \pm 0.29\ .$$

If the b quark were alone in a singlet structure, one would expect zero for this parameter.

6.1 Indirect constraints on the top mass

A number of indirect constraints on the top quark mass are available. For example, the observation of $B_d\ \overline{B_d}$ mixing implies an upper bound on the top quark mass of approximately 180 GeV.[45,46,47] An additional indirect method involves the use of the ratio [48]

$$R = \frac{\sigma_W\ \mathrm{BR(W \to e\nu)}}{\sigma_Z\ \mathrm{BR(Z \to ee)}}$$

where

$$\frac{\mathrm{BR(W \to e\nu)}}{\mathrm{BR(Z \to ee)}} = \left(\frac{\Gamma(W \to e\nu)}{\Gamma_{W tot}}\right) / \left(\frac{\Gamma(Z \to ee)}{\Gamma_{Z tot}}\right) .$$

The ratio of cross sections for W and Z production can be predicted reliably from theory as can the leptonic decay partial widths of the W and Z leaving a dependence in R on the t mass due to its influence on the total widths of the Z and W. Many systematics cancel, such as the uncertainty due to higher order corrections in the absolute W and Z cross sections. The value of R varies from the low mass region where the top contributes to both the W and Z decays, through an intermediate region where it contributes only to the W, and finally a high t mass region where the t becomes too heavy to contribute to either partial width. While previous measurements of this ratio were thought to favor low top quark masses, more recent data presented at the EPS Madrid conference give

$$\mathrm{CDF} \quad 10.3 \pm 0.8 \pm 0.5$$

$$\mathrm{UA2} \quad 10.3^{+1.5}_{-1.0}$$

and are consistent with heavy top masses.

6.2 t Quark Production

At Tevatron energies ($\sqrt{s} = 1.8\ TeV$), the production of t quarks is dominated by the production of $t\bar{t}$ states. This situation differs from that found at the lower energies available at CERN where $W \to t\bar{b}$ also contributes significantly to t production. The difference (see figure 27) is due to the faster rise of the t production cross section with energy relative to the W production cross section.[49] The expected behavior of the t cross section as a function of the top quark mass for these two energies including higher order corrections by Nason, Dawson, and Ellis [39] is well reproduced by the Monte Carlo Isajet as was the case for the b quarks. This Monte Carlo will be used later for acceptance calculations.

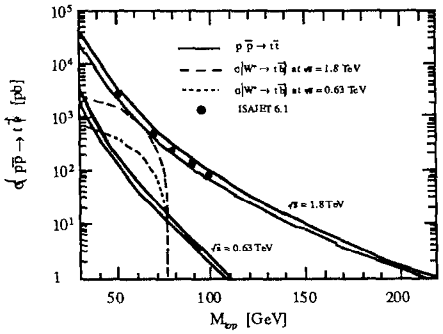

Figure 27: Contributions to top production from $t\bar{t}$ production and W decays at CERN and Tevatron energies. The upper and lower $t\bar{t}$ curves use DFLM structure functions with μ = m/2, Λ = 250 MeV and μ = 2m, Λ = 90 MeV respectively.

Since $t\bar{t}$ production dominates at the Tevatron, each event has two t quark decays. The standard model of t quark decays predicts that for a $t\bar{t}$ system, roughly 44% of the decays will be to fully hadronic final states with as many as 6 final state jets when each of the t's decays in its hadronic mode. While these rates are attractive, the calorimeter performance, the ability to reconstruct jets, and the copious QCD background in this channel limit the experimenter's ability to utilize this mode. An additional 15% of the $t\bar{t}$ final states for each of the leptons e, μ, τ, will have leptonic decays of one of the t quarks and the hadronic decay of the other, leading to a lepton, as many as four jets and missing E_t ($\not{E}_T$) due to the neutrino from the decay of a virtual or real W. The total for all of these single leptonic decays is then 45%. The remaining decay modes consist of 1% for ee, $\mu\mu$, and $\tau\tau$ pairs (each of which suffer from significant Drell-Yan backgrounds) and 2% for non-identical lepton pair final states. These lepton pair events will contain as many as two additional jets and missing E_t .

The searches by the CDF collaboration were done using the electron plus jets final state and the electron plus muon final state. The electron plus jets mode has the advantage of higher rate than the $e\mu$ channel and can therefore probe heavier masses. The $e\mu$ channel has the largest di-lepton rate, does not suffer from Drell-Yan backgrounds, and can be used effectively at low masses where acceptances in the electron jet channel are uncertain.

7 Lepton Detection

Since the hadronic decay of both t's in a $t\bar{t}$ final state is masked by QCD backgrounds, the remaining methods of top quark detection depend heavily on semileptonic decays involving either electrons or muons, so the following section is devoted to the techniques used for lepton (primarily electron) detection in the hadron machine environment. Tau decays are particularly difficult for the detector to trigger on, and are not used heavily at the present time.

The subject of lepton detection has a rather long history dating back to attempts at the AGS, ISR and other machines to measure the ratio (e/π) of electron to pion production to see if there were anomalous sources for leptons. The ratio is roughly 10^{-4} for low energy particles, so one looks for techniques which can separate charged pions from the random overlap of a charged track with an energetic π^0 or the early charge exchange of a $\pi^\pm$ with rejections of 10^4. The standard techniques used in early experiments were:

1. (E/P) : comparisons of the electromagnetic energy deposition (E) and the track momentum P,
2. Cherenkov detectors and transition radiation detectors, set to trigger on electrons but not π's,
3. Pre-shower detectors, triggering on the early shower development of electrons relative to π's,
4. Track to shower position matching.

Because the interaction length λ_π of pions is much longer than the radiation length of electrons X_0, technique 1 discriminates against high momentum pions which then leave only a portion of their energy in the electromagnetic calorimeter and give low values of E/P. It also discriminates against random overlaps with low momentum tracks which give large E/P values (as well as some small ones). Technique 2 was useful in the early ISR and AGS studies but is difficult to implement for the larger solid angle and momentum range of modern detectors like UA1,UA2, and CDF. The UA2 detector does however use a transition radiation detector as part of their electron signal. Pre-shower detectors are also used in UA2. They make use of the fact that electron showers develop very rapidly, thus by requiring large energy deposited in the first few radiation lengths of an electromagnetic calorimeter, electrons can be separated from pions. Similar techniques can be used if the electromagnetic detector is segmented in depth. In the limit of many samples, the longitudinal shower profile could be compared to that expected for an electron.

Technique 4 is extremely powerful against random overlaps. The object is to compare the position of the candidate electron track as it enters the calorimeter to the position of the deposited energy inside the calorimeter. This type of technique comes in several different varieties. Earliest applications used the transverse segmentation of the shower detector (L), to measure the shower position with resolution $L/\sqrt{12}$. Improving this resolution by decreasing L can be mechanically difficult, or very expensive, so newer techniques involve using a finely segmented preshower detector, or as in the case of CDF, imbedding a wire chamber within the calorimeter near shower max. The wire chamber is useful because it can measure not only the transverse *position* of the shower, but also its width and transverse *shape*, which provides additional electron discrimination.

For a detector which has a hadronic calorimeter surrounding the electromagnetic detector, it is also possible to detect interacting pions and overlaps by requiring that the energy deposited in the hadron calorimeter towers directly behind the electromagnetic shower be small. For electrons, the longitudinal shower shape has a tail which could extend into the hadron calorimeter, but in order to have good resolution, the electromagnetic detector is made thick enough so that this tail is typically a few percent. In contrast, interacting pions, and even interacting pions which overlap with energy in the electromagnetic section from π^0's, will leave substantial amounts of energy in the hadronic calorimeter. Thus the ratio of hadronic to electromagnetic energy (had/em) can be required to be small for an electron.

7.1 Isolation

There is a good deal of argument over whether the next cut is a means of detecting electrons, or should be treated as a means of verifying that the electrons detected in the final sample come from a particular source. The cut is called isolation, and for the sake of t quark searches, I will treat it as a cut. The heavier the quark, the more transverse momentum the decay lepton will have relative to the remaining heavy meson decay products. The maximum transverse momentum of the lepton relative to the meson momentum vector will be $M_{HQ}/2$. For bottom quarks, the maximum momentum is about 2.5 GeV, so many of the leptons from b quarks will be accompanied by additional particles from the semileptonic b quark decay. These particles will have transverse momenta which are typically 0.3-1.0 GeV with respect to the meson momentum vector. For heavier top quarks, the scale of $M_{HQ}/2$ is large enough that most leptons will be well separated from any other decay products. (Note that the degree of separation depends only on kinematics, and thus there is little systematic uncertainty associated with the use of isolation as a cut for detecting t's.)

Because of this difference between the bottom and heavier quarks, it is possible to separate leptons from the two sources by looking at their isolation distributions: i.e. determining the amount of energy which accompanies the lepton within a fixed cone of solid angle. It turns out that the amount of energy in a random cone (which might be considered noise for this technique) is small relative to that expected for most bottom decays, so that the effect is not obscured by the "Minimum Bias event" which is the random debris in a hadron collision. The minimum bias event (or in the case of the SSC, the pile-up of several such events) does limit how small the cut which can be used for t quarks can be while maintaining good efficiency.

Isolation can thus be viewed as a means of discriminating against light (i.e. b) quark backgrounds for the top quark search, or as a means of verifying that the detected signal comes from heavy quarks. When the limits on the top quark mass were in the 30-40 GeV range, potential backgrounds from B meson decays were substantial, and it was important to use the shape of the isolation distribution as proof that the b background had been properly eliminated. As the limits on the t quark mass have increased, however, it became more and more safe to treat the isolated lepton as just another cut required for the detection of leptons coming specifically from heavy objects.

It is important to realize when looking at isolation distributions, that many of the cuts inherent in other parts of the analysis, or the properties of the detector may place implicit isolation requirements on the signal. For example, the E/P cut contains an implicit isolation cut because the calorimeter energy E is summed over a cell of finite size in the electronic readout. This cell size, together with the magnitude of the upper limit on the E/P cut is an implicit isolation requirement. The same comment applies to the had/em cut and even to things like shower matching or transverse shower profiles, since nearby energy depositions can cause a true electron to fail these cuts when accompanied by other particles.

7.2 Muons

All of the assumptions which go into the use of the isolation properties as a cut can be checked to some extent by using muons instead of electrons. Most leptons from B mesons for example will be buried in the middle of the jet of other hadrons from the B decay. Despite this fact, the muon can be detected if it is energetic enough to go through the hadron calorimeter and into a good muon system. If the muon system is thick enough to independently identify muons and there are no decay in flight backgrounds, there is little if any implicit isolation requirement. If on the other hand the muon system is thin (as it is in the CDF case), it may be necessary to require isolation in the form of small em and/or hadronic energy to extract signals from inclusive muon triggers. In the latter case, this again represents an implicit isolation requirement. Thus if the experiment you would like to do requires the detection of leptons from B mesons, there is an advantage to using muons but only if the muon system is thick enough to detect muons independent of other cuts.

7.3 Novel Techniques

The importance of electron detection is clear both for present experiments and for future LHC or SSC scale experiments. Several new techniques and detector configurations are worth highlighting before we return to t quark detection. The UA2 experiment uses a scintillating fiber detector (SFD) in front of the electromagnetic calorimeter to measure the track position at the entry to the calorimeter to high accuracy. The comparison between track and shower position yields resolutions of $\sigma_{R\Phi} = 0.4mm$ and $\sigma_Z = 1.1mm$ (see figure 28). For SSC designs, transition radiation detectors have been discussed which would be constructed from straw tubes with $Xe\ CH_4$ gas and 50 radiators for a total thickness of only 0.33% of a radiation length. Even more novel is the suggestion to use the synchrotron radiation from

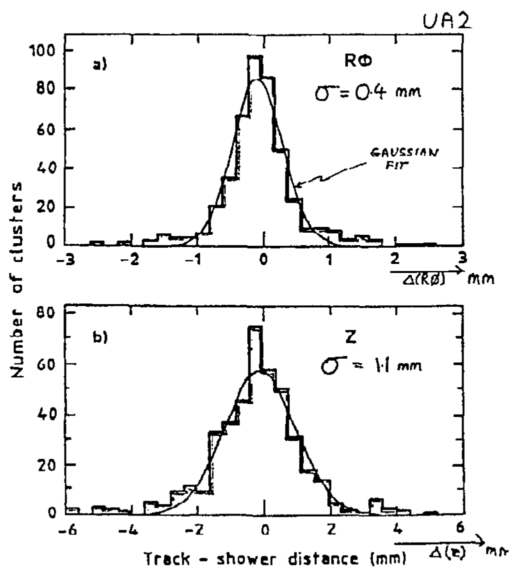

Figure 28: Comparison of track and shower positions in UA2.

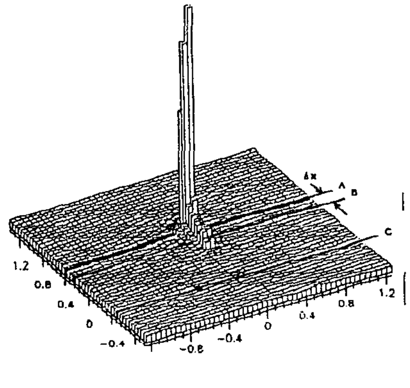

Figure 29: Synchrotron tail and energy deposited from a 200 GeV electron in less than one X_0 of lead.

electrons in a strong magnetic field to identify electrons. Figure 29 shows [50] the results of a simulation which indicates that a finely segmented calorimeter of one radiation length thickness would be sufficient to detect the radiative tail from electrons in an SSC detector. The size of the tail is determined by the bending in the magnetic field, and its position relative to the electron shower determines the charge of the electron. This type of detector is being used in the AMY detector at Tristan. Note that it can also be used as a thin pre-radiator and as a means of measuring the shower entry position.

7.4 CDF Electron Detection

The CDF analysis uses the following quantities to identify electrons: E/P (the ratio of the shower energy to the track candidate momentum), *had/em* (small leakage of energy from the electromagnetic to the hadronic sections of the calorimeter), $\Delta x, \Delta z$ (the shower to track matching parameters measured using strip chambers positioned at a depth of 6 radiation lengths within the electromagnetic calorimeter), χ^2_x, χ^2_z (the shower profiles near shower max), and LSHR (a chi-square like parameter describing the shower sharing between adjacent calorimeter towers).

The electron detection techniques can be tested by using the electrons from

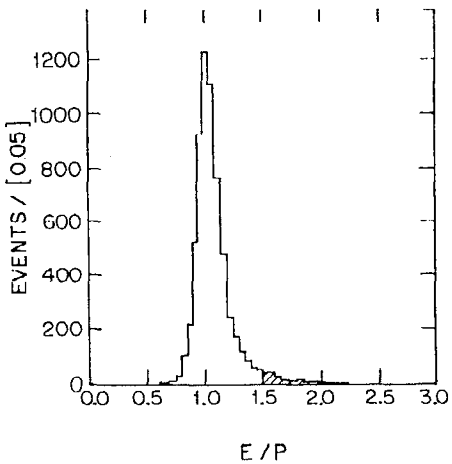

Figure 30: CDF E/P distribution for electron candidates with $E_t > 15$ GeV. The hatched area is removed by the standard cuts.

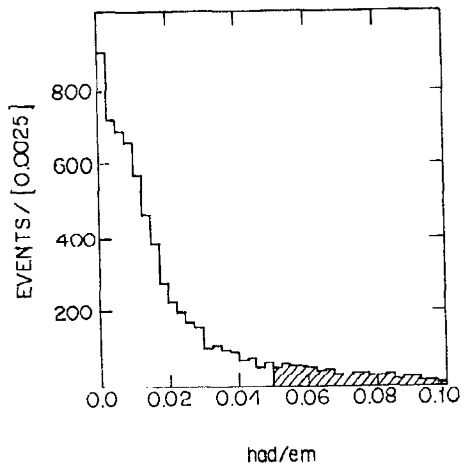

Figure 31: CDF *had/em* distribution for electron candidates with $E_t > 15$ GeV. The hatched area is removed by the standard electron cuts.

W decay, identified conversions, and electrons from the inclusive electron trigger. The distributions of the E/P and *had/em* parameters are shown in figures 30-31 for electron candidates with $E_t > 15\ GeV$.

A further cut called the border tower cut is the isolation cut and can be used to discriminate against electrons from parent b quarks. In this cut, the energy in towers immediately adjacent to the electron is summed and required to be less than 2 GeV. The number of towers summed in this manner depends on the shape of the electron cluster but ranges between 8 and 12. This cut requires the electron to be isolated and is efficient for heavy t quarks because the large mass of the t quark leads to increased separation on average between the decay electron and any associated jet activity.

7.4.1 Conversion Detection

One of the general conclusions to be derived from studying the E/P and other distributions for various electron cuts within the CDF data, is that the electron candidate samples are dominated by sources of *real* electrons. However, these electrons include a contribution from converted γ's which is as large as 30% at low p_t . Thus it is important to design algorithms which are effective in removing conversions.

Pairs of tracks (one of which is an electron candidate) are selected which have opposite charges and low invariant mass. Also, the CDF vertex time projection chamber (VTPC) is used to identify candidate tracks which have fewer than the expected number of hits in this innermost chamber. This independent method for finding photon conversions from the outer wall of the VTPC can be used to correct for conversions in the inner wall and to determine the efficiency of the conversion detection method which depends on finding low mass opposite charge track pairs. The conversion samples with well-separated electron pairs can be used to further test the response of the detector to real electrons. Figure 32 shows the fraction of expected VTPC hits found for opposite and same sign charge pairs. The peak at small hit fraction in the opposite sign distribution is due to conversions.

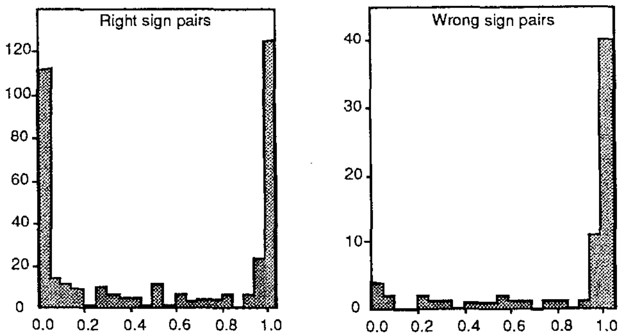

Figure 32: Fraction of expected hits in the CDF VTPC tracker for opposite and same sign charge pairs.

Another source of real electrons and thus potential background for a top quark search begins to dominate for high p_t leptons. This is the production of electrons from the decays of W's and Z's. The lepton p_t from the decay of these objects is high because of the large mass of the W and Z. Leptons from Z's are easily removed from the sample by eliminating all events which have a second electromagnetic cluster which forms an invariant mass greater than 70 GeV with the candidate electron. W's are much harder to remove, and we will find later that the chief background to electron plus jet searches for top is W + jet production.

Additional checks of the electron response can be made with the electrons from identified W decays, i.e. those events with both a high p_t electron and large $\not{E}_T$. The E/P distribution from such a sample is shown in figure 33 and illustrates both the cleanliness of the signal, and the presence of a small tail at higher E/P due to hard synchrotron radiation which lowers the value of P detected by the tracking chamber, while having a smaller effect on E because most of the radiated energy is deposited in the same calorimeter cell with the electron shower. Note that the W Monte Carlo which includes this and other effects in the simulation, does an excellent job of reproducing the shape of the E/P distribution.

One final method of verifying the performance of the cuts used to define electron samples is to use test beam data. Figure 34 shows the distribution in the

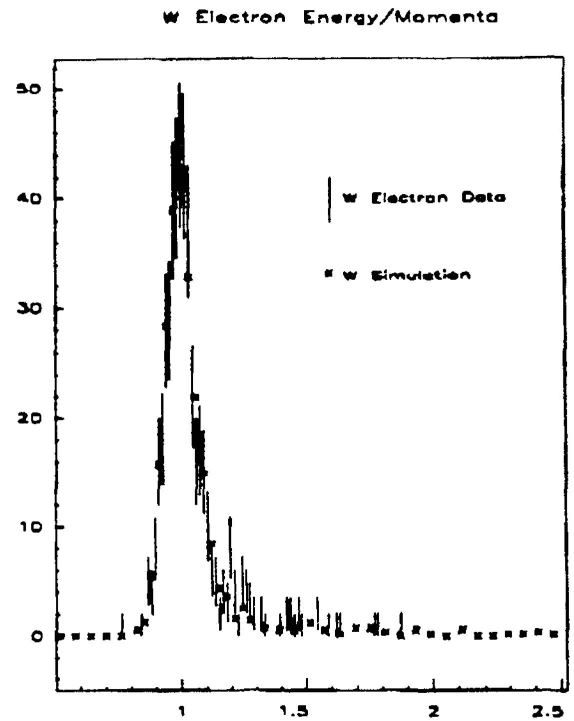

Figure 33: The E/P distribution from a W sample.

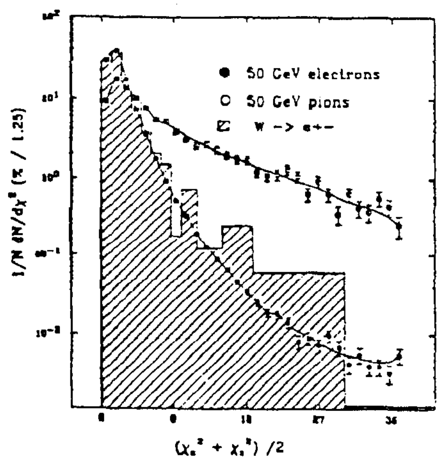

Figure 34: The strip chamber χ^2 distribution for 50 GeV π and electron showers in the test beam data compared to a sample of electrons from W's.

χ^2 variable used to test the transverse shower shape of an electron in the strip chambers which are within the CDF detector. The points shown are from test beam pions and electrons, while the solid histogram is the distribution found for W events in the data.

7.5 Cut Efficiencies

The efficiencies of the cuts used to define electrons can be measured using a combination of Monte Carlo electron sample, and test beam techniques. In most cases, the efficiencies and cuts depend to some extent on the type of analysis which is needed in the sense that one must balance the need for very clean signals and excellent pion rejection with the need for an efficiency large enough to provide a reasonable size sample of final events.

For top quark searches, combined efficiencies times branching ratios are typically a percent or less for leptonic channels. Thus in order to detect the presence of a top quark, the number of produced events must be somewhere between 100 and 1000. The top cross section for the CDF detector with an integrated luminosity of about 4 pb^{-1} would allow a mass limit of approximately 80 GeV for an effective sensitivity of 0.1% and a limit of about 125 GeV for a sensitivity of 1%. In the final analysis, the efficiency is close to 1%, but with proper account for uncertainties in the theoretical cross section for top production and the systematic uncertainties in detection efficiency, we will see that the effective sensitivity is closer to 0.1%. Table 7 lists the rough individual efficiencies for the cuts which

Table 7: Rough efficiencies for cuts made in a top analysis.

Criteria	*Efficiency*
$\lvert\eta\rvert \leq 1.1$	68%
$h/em \leq 0.07$	99%
Isolation	74%
Track	88%
Track to strip	95%
shower pattern	98%
$E_t \geq 6\ GeV$	95%

are made on an electron for aMonte Carlo $t\bar{t}$ sample.

7.6 $t\bar{t} \rightarrow e\ +\ jets$

For the electron plus jets search for the top quark, the techniques used at the Tevatron and CERN differ because of the different relative contributions of t production from W decays and direct t production. For a light enough t quark, it would be possible for a real W to decay into $t\bar{b}$. In this case, semileptonic decay of the t or b will yield an event with an electron, $\not\!\!E_T$ and at least one fairly energetic jet. Backgrounds arise from W + 1 jet production and $b\bar{b}$ production. Present limits from CDF [51] however, are large enough to exclude significant W to t decays.

At the higher energies available at the Tevatron, the dominant production mechanism is $t\bar{t}$. Detection in the e + jets mode is due primarily to the semileptonic decay of one of the t's although there is also a contribution from electrons from the b quarks resulting from the t decays. With one semileptonic decay, the signature is an electron, $\not\!\!E_T$, and at least 4 jets, although as pointed out later, depending on the mass of the top, two of the jets may be quite soft.

In order to effectively use these signatures for the top quark, it is necessary to detect and count the number of jets produced in association with the electron and $\not\!\!E_T$. Figure 35 shows the energy deposition from a pair of 200 GeV jets and illustrates that at these energies, jets are easily distinguishable, and are well-

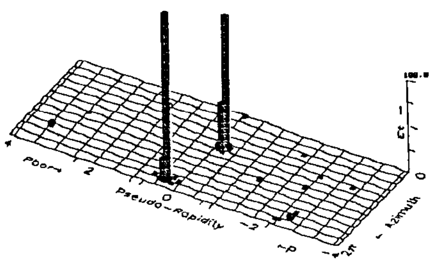

Figure 35: Energy deposition from two 200 GeV jets

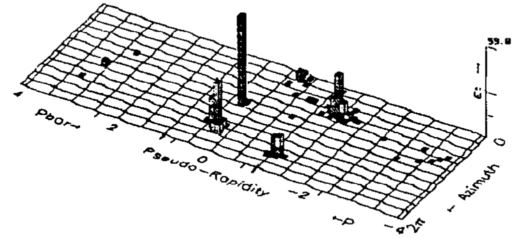

Figure 36: A top-like event, probably due to W production.

defined objects. The primary problem for the top search is that the jets are on average about 20-25 GeV, and thus it is necessary to know the detection efficiency at lower energies and the jet energy scale, i.e. $E_{observed}/E_{produced}$ for these lower energy jets. An example of an event which looks like top, but is most likely from W plus jet production is shown in figure 36. The tall narrow tower is the electron with E_t of 63 GeV, and the $\not\!\!E_T$ is 34 GeV.

8 CDF Electron Plus Jets Search

The electron plus jets search proceeds by requiring a "golden" electron candidate, i.e. a cluster in the central electromagnetic calorimeter with $E_t > 12$ GeV, *had/em* less than 0.05, E/P less than 1.5, track to strip matches of less than 1.5 cm in xy and 3 cm in z, and good shower profiles. The distributions in figures 30-31 indicate that very little background remains in the sample from overlaps or charged pion interactions after these cuts. About 30% of the inclusive electrons above E_t of 12 GeV come from γ conversions and π^0 Dalitz decays. These are removed as discussed previously by requiring a track in the VTPC, and by removing any candidate with a second track which forms an invariant mass pair with mass less than 0.5 GeV. Electrons from Z^0 decays are removed by looking for a second EM cluster which forms an invariant mass greater than 70 GeV. At least two jets with $E_t > 10$ GeV and $|\eta| < 2$ are required.

The distribution of $\not\!\!E_T$ versus E_t shows (see figure 37) that the remaining

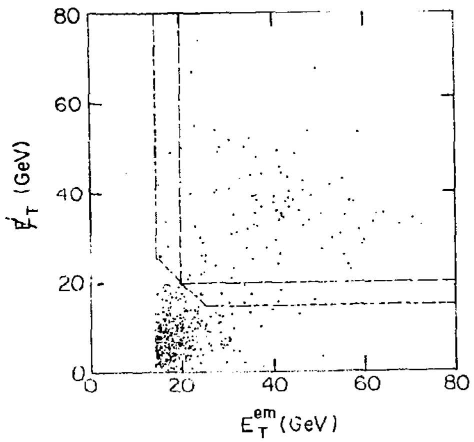

Figure 37: $\not{E}_T$ versus E_t for electron + $\geq$ 2 jet events.

sample of events comes primarily from events with large $\not{E}_T$ and large E_t due to W production, and lower $\not{E}_T$,E_t events which in general also show poor isolation and are consistent with the kinematic properties expected for events due to bottom production.

Two fiducial regions in the $\not{E}_T$, E_t plane are defined, one with $\not{E}_T > 20$ GeV and $E_t > 20$ and a second with $\not{E}_T$,$E_t > 15$ but $\not{E}_T + E_t > 40$ GeV. See figure 37. The looser cut is more efficient for low mass top, but lets in more background from light quarks. It is used to extend the search to lower top masses where the rates are large. The tighter cuts are used at higher masses.

The method used to search for top quark production in the electron plus 2 or more jet sample is to use the electron E_t and the missing transverse energy, $\not{E}_T$, to calculate a transverse mass and then to compare this distribution to that expected for W and top production. The expected transverse mass distribution for W's is generated by Monte Carlo, but checked by studying the electron plus one jet sample which should in fact be dominated by W production. The observed distribution for this sample is then compared to a W+1 jet prediction from the PapagenoMonte Carlo[52] and found to be in excellent agreement. One might well ask whether the agreement in the W+1 jet sample is relevant to the search which is dominated by W+2 jet backgrounds, but the detector resolution in transverse mass for the W+2 jet sample is similar to the resolution for the W+1 jet sample, and it is this transverse mass resolution which is most crucial for the final result.

Table 8: Fitted value for parameter a and expected number of top events.

M_{top}	a	$n_{t\bar{t}}$
40	$0.07 \pm 0.05 \pm 0.02$	130 ± 44
50	$0.06 \pm 0.05 \pm 0.03$	123 ± 31
60	$0.11 \pm 0.08 \pm 0.04$	101 ± 22
70	$0.00 \begin{smallmatrix}+0.12\\-0.00\end{smallmatrix} \pm 0.11$	43 ± 8
80	$0.00 \begin{smallmatrix}+0.27\\-0.00\end{smallmatrix} \pm 0.17$	32 ± 5

In this analysis, the electron plus two or more jet sample is found to have a transverse mass distribution which agrees with that expected for a pure W sample. The rate of events observed in this class is within 30% of the predicted rate from the Papageno Monte Carlo which is within the theoretical uncertainty of about 30-50%.[53] The transverse mass distribution for top decays where the top mass is below threshold for real W production, is quite different from that for W's. In general, it tends to peak at lower transverse masses. This fact is used to fit the observed experimental distribution to the expected shape due to the sum of contributions from the W plus jets and from top. A binned maximum-likelihood fit is used to fit to the form

$$\mathrm{dN/dM_t = aT\,(M_t) + bW\,(M_t)} \quad .$$

The results of the fits are shown in table 8 and figure 38 where the coefficients a and b would be 1 if the predicted source agreed in rate with the Monte Carlo prediction.

To interpret the fit as a limit for top production, the following systematic errors are included: 1% for electron energy calibration, 20% for jet energy scale uncertainties, 5% electron selection uncertainties, and 15% luminosity uncertainty. In addition, the fragmentation parameters of the top quark in the Isajet Monte

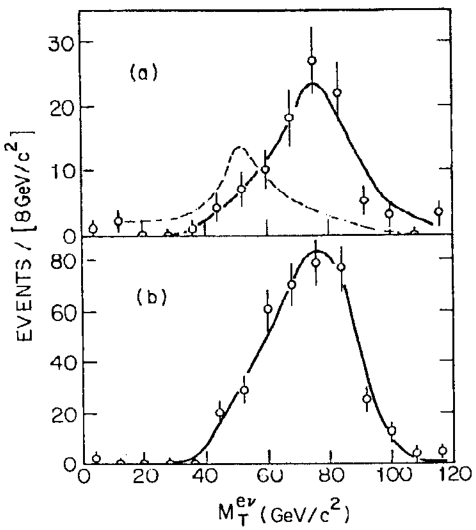

Figure 38: The transverse mass distributions for (a) 70 GeV top (dashed) and Papageno (solid) for ≥ 2 jets and (b) ≥ 1 jet.

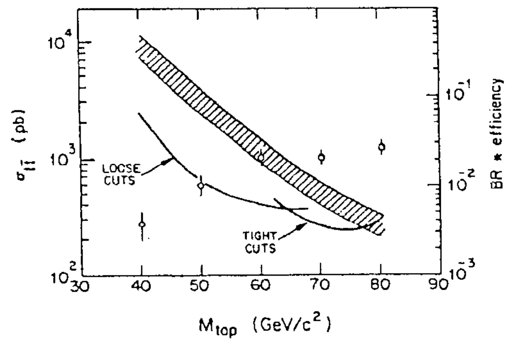

Figure 39: The 95% CL upper limit from the electron plus jets search and the acceptance (right hand scale)

Carlo have been varied,[54] and uncertainties of 50% and 20% have been used for initial state radiation and the underlying event contributions to the jet rate respectively. Each of these quantities is varied in theMonte Carlo,and the resultant effect on the fit (which depends on M_t) is taken as the systematic error due to this parameter. These errors are added in quadrature. The resulting upper limit for t production is shown in figure 39 where the top production cross section which has been assumed is the lower bound from Altarelli et al.[55] The results of the fit exclude the range

$$40 < M_t < 77 \quad excluded \quad 95\%cl \ .$$

Additional information concerning the candidate events such as the jet-jet mass distribution for 2 jet events, and the distribution of the number of jets in the observed events are also consistent with a pure W sample. Although these latter distributions and also the angular correlations between the jets have not been used in the present analysis, they can be used to extend the sensitivity of the search in the future.

9 Top Detection using Dilepton Signatures

Since at the Tevatron the dominant production of top quarks is via $t\bar{t}$ production, the simplest signature for this cross section is the presence of dileptons from the semileptonic decay of both the t and the $\bar{t}$. (It should be kept in mind that depending on the cuts as much as 30% of such a signal may be contributed by cascade decays where one of the leptons comes from b decay.) In this mode, backgrounds to the electrons, especially at low p_t , come from the usual conversions and overlap backgrounds . In the muon case, there are decays in flight and punch thru backgrounds. In addition to these backgrounds, dileptons can also arise from $b\bar{b}$ production with the subsequent leptonic decay of both b's. This background can be effectively eliminated by isolation requirements on the leptons.

The possible modes for a dilepton search are

1. e^+e^- : good trigger, but backgrounds from Drell-Yan and Z's
2. $\mu^+\mu^-$: same as electrons, but easier to check isolation cuts
3. $\tau^+\tau^-$: poor trigger, $\not{E}_T$ from τ decays sometimes cancels
4. $e\tau$: low background, poor τ detection efficiency
5. $\mu\tau$: same problems as $e\tau$
6. $e\mu$: probably the best of the dilepton modes.

Rates for all of the dilepton modes are low compared to single lepton modes, and rates for identical leptons such as 1-3 are half those of 4-6. Detection efficiencies for τ's are at present quite low so that together with the low dilepton branching ratio this effectively eliminates 3-5 as viable search methods. In addition, the channels 1-3 suffer from Drell-Yan backgrounds, making all but the last mode unsuitable for the discovery of top, although each channel can be used independently to help confirm or deny the presence of a top signal. Figure 40 shows the expected signal from $t\bar{t}$ production per 1 pb^{-1} and 5 GeV mass bin for the e^+e^-channel. While the signal is expected to extend up to approximately $2m_t$, at low m_{ee}, it is obscured by Drell-Yan backgrounds and at high m_{ee} it is obscured by the presence of the

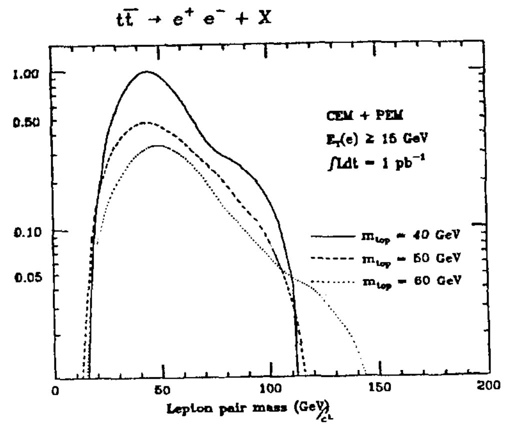

Figure 40: Expected rate in events per 5 GeV/c^2 from $t\bar{t} \rightarrow e^+e^-$.

Z! The best place to look for top turns out to be in the valley between these two phenomena which would restrict the search to intermediate masses. With additional cuts against Z and Drell-Yan kinematics (and hence further reduced sensitivity), it may be possible to probe higher masses in the future.

9.1 $t\bar{t} \rightarrow \mu\ e$

The CDF electron muon search for top uses the same electron sample discussed previously for the electron jet mode except that the electron E_t requirement is 12 GeV and the E/P cut is 1.4. Because backgrounds are smaller in this final state, the isolation cut is not applied. In the central region, $\eta < 0.65$, a track with impact parameter $< 0.5cm$, and $p_t > 5$, which matches a muon chamber stub with $\Delta R\phi < 10cm$ is required. The difference in slope between the central track and the muon stub must be less than 0.1, and the calorimeter must have less than 2 GeV in the EM section and <6 GeV in the hadronic section consistent with a minimum ionizing track. In the region $0.65 < \eta < 1.2$, the requirement of a muon stub is removed. In this case, the track p_t is required to be more than 10 GeV and

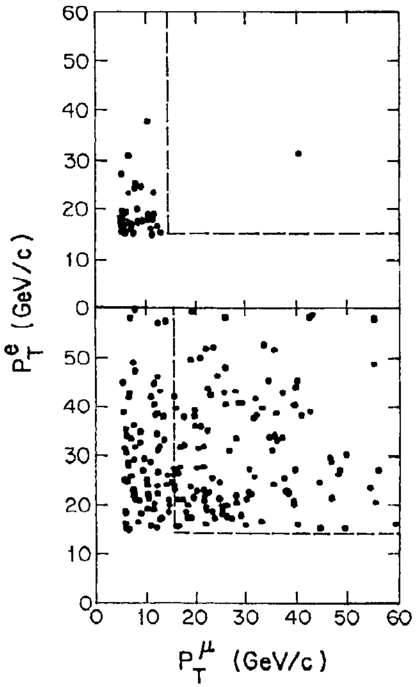

Figure 41: $e\mu$ (a) data and (b) 70 GeV top for 80 pb^{-1}

the total calorimeter energy associated with the muon candidate less than 5 GeV in a cone of radius 0.4 about the track. Note that many of these cuts involve implicit isolation requirements.

The events in the remaining sample cluster at low electron and muon E_t as would be expected for light quark production with the electron and muon being typically back-to-back. To reject these backgrounds, the electron and muon are both required to have $E_t > 15$ and to be of opposite sign. One event remains in the sample. (See figure 41.)

Expected rates from background sources are 1 event from $Z \to \tau\tau$, 0.15 events from WW production, 0.05 events from WZ production, and of order 1 event or less from b quark jets though this rate is uncertain due to uncertainties in the b quark production cross section. The assumed systematic errors are 1% for electron calibration, 5% for electron selection efficiency, 15% luminosity uncertainty, and 20% acceptance uncertainty. The limit is determined by finding the mean of a Poisson distribution that when convoluted with the total systematic error yields a probability of 5% for observing zero or one event. This analysis excludes a top quark in the range 28 $GeV < M_t < 72$ GeV at 95%CL.

10 Verification of the Detection Efficiencies

The electron and jet detection efficiencies are crucial to the top quark searches discussed so far. It is important therefore to be able to verify that the electrons in theMonte Carlo simulations used for efficiency studies correctly mimic the properties of electrons in the real data. The jet detection efficiencies also need to be verified, and here again one needs to rely on theMonte Carlo parameterization of the jets and the response of the detector to them.

A number of techniques have been used to verify that the jet detection techniques used in the CDF electron plus jet search for top are efficient and to verify that the jet energy scale is correct. Since the jet detection efficiency enters twice for a two jet event, the overall detection efficiency can be quite sensitive to errors in the jet energy scale. This sensitivity is less than might be expected however for heavy M_t because the leading jets tend to be well over the 10 GeV threshold used for jet counting. Thus a small shift in scale does not change the rate by large factors. The CDF acceptance varies by 5% for example if the threshold is changed to 12 GeV. Monte Carlo studies have shown that the $E_t > 10$ GeV threshold used in this analysis corresponds roughly to a produced jet of 15 GeV E_t .

The response of the detector depends on the charged to neutral ratio in the jet as well as the fragmentation spectra and the detector response. Fortunately, much is known about these parameters. We know for example from e^+e^-annihilation that the fragmentation of b quarks is not significantly different from other jets at these energies. Thus even though the top final states contain a significant number of b jets, the Monte Carlo parameterization of their fragmentation is probably reasonable. The e/π response of the calorimeter to individual particles is verified by using samples of low momentum charged tracks which are well isolated from jet activity. These tracks provide a source of in-situ test beam particles.

Three samples are used to further verify the jet response of the detector.

1. the inclusive electron sample (dominated by electrons from b's)

2. Z+jet events (low statistics since $N_W/N_Z \approx 10$)

3. γ+jet events .

These samples can all be used to balance the p_t of a known electron, Z or γ against a jet on the opposite side to determine the jet energy scale.

In the case of the inclusive electrons for example, the primary source is believed to be (even after isolation cuts) $p\overline{p} \to b\overline{b}$. Assuming that the $\overline{b}$ decays to a jet and the b decays to an electron, and using the fact that the $b\overline{b}$ production is dominated by low p_t $b\overline{b}$ pairs, one would expect to see the p_t of the electron balanced by the p_t of the jet after making a suitable correction for the fraction of the parent b quark momentum carried by the decay electron. The CDF inclusive electron sample has 12,000 events with $E_t > 12$ GeV, and can be used for detailed studies not only of the jets, but also of the electron properties. Further confirmation of the prediction that this sample is rich in b production comes from the observation of an enhancement of 62 ± 17 events in right sign $K\pi$ pairs around the D meson mass with 5 ± 11 seen in wrong sign pairs.

The Z+jets sample is interesting for a number of reasons. First, the Z p_t can be precisely calculated from the Z$\to e^+e^-$mode. This p_t will be balanced by the p_t of the observed jets in the event and the jet p_t and Z p_t can be compared as in the case of the inclusive electron sample. One might worry about corrections due to undetected jets from initial state gluon radiation, but these average to zero. The second interesting use of the Z's is in estimating the background to top searches from W+multi-jet production. W+njet Monte Carlos are constantly improving, but there are problems. For example, W+(0,1)jets is included in Monte Carlos like Isajet, W+2 jets can be calculated from the matrix elements imbedded in the Papageno Monte Carlo, and calculations of the matrix elements for W+3 jets are in progress. The complexity of the calculation of the matrix element however increases so rapidly with the number of jets that there is little hope of having a W+4 jet expression any time soon. This is actually rather unfortunate because the rate of $t\overline{t} \to$e+4jets is quite large, and without this calculation, it is not possible to estimate the contamination in the sample due to W+4 jet production.

Fortunately, the Z+njet production is very similar to W+njet, the Feynman diagrams being the same. There are several obvious differences namely

- Z statistics are limited (1/10 the number of W's)

- The mass of the Z and W are different

- Z's come from $u\overline{u}$, and $d\overline{d}$ while W's come from $u\overline{d}$ and $d\overline{u}$.

The last point is important because the proton has a u to d ratio which increases slightly as you go up in x (i.e. go to higher p_t) and this effect may enhance the production of larger njet slightly. Even with this caveat, the Z's are an extremely useful calibration and test signature. In order to dispel the popular myth that such events are somehow "dirty" at hadron machines, figure 42 shows a typical Z event which at low p_t has only a few extra tracks from the "minimum bias event". Z events can be extracted from the inclusive electron samples with minimal cuts on the second electron. Figure 43 shows the mass spectrum obtained from such a sample with the additional requirement of a second electromagnetic cluster, but no other electron cuts. Note the high mass candidates are essentially free of background.

The p_t spectrum of the Z sample obtained in this way can be compared to the predictions of the Isajet Monte Carlo which includes both the lowest order matrix elements and an effective contribution from some of the higher order diagrams due to the inclusion of initial state radiative gluon corrections. The comparison is shown in figure 44, and shows excellent agreement. Figure 45 shows the result of comparing the jet p_t with the Z p_t in a selection of Z + 0 or 1 jet events to determine the jet p_t scale. The expected ratio is approximately 0.6 due to the average response of the hadron calorimeter to the jet energy deposition. The jet efficiency can also be estimated in such a plot by counting the number of times

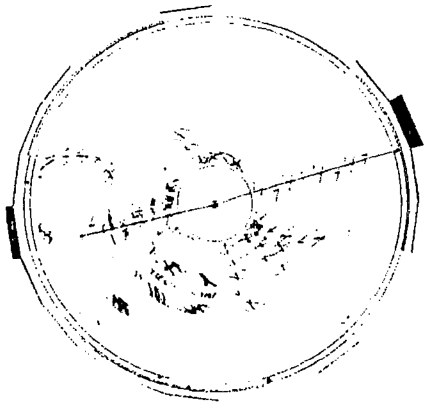

Figure 42: Typical Z event in the hadron environment.

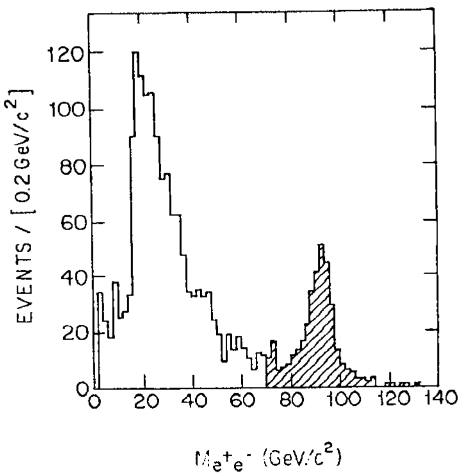

Figure 43: Invariant mass distribution of inclusive electrons combined with a second electromagnetic cluster.

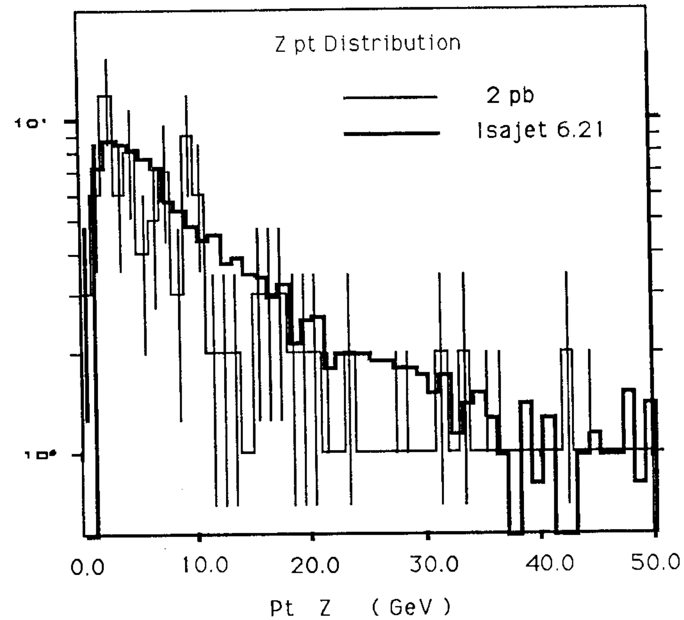

Figure 44: Partial (2 pb−1) Z p_t spectrum from CDF compared to Isajet 6.21.

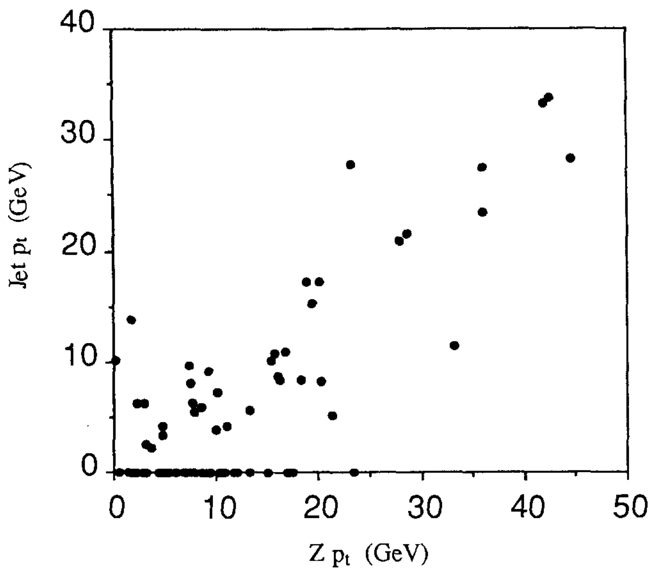

Figure 45: Jet p_t versus Z p_t for Z + 0 or 1 jet events. This distribution can be used to verify the jet energy scale. The slope of 0.6 shown is the expected detector response.

that a Z occurs with no jet as indicated by the points on the plot with no observed jet energy. This is only a lower limit to this efficiency because a correction needs to be applied for those events where the Z p_t is balanced by a low p_t forward jet or by several jets. Jets shown in the plot are restricted to lie in the region $|\eta| \leq 2$, and events with more than 1 jet are not plotted.

It is clear from the plots, that the technique of using Z's to calibrate the detector is at present limited by the Z statistics. This technique will however become very important in SSC detectors. The typical "Snowmass year" for an SSC detector is one in which the recorded luminosity is 10^4 pb^{-1}. The Z cross section is about 70 nb (20nb within η of 1.5) yielding several events per second in the e^+e^-decay mode, which is sufficient for detailed studies of the detector response.

10.1 Direct Photons

The detection of direct photon events, i.e. events with a photon which is not the decay product of a π^0 or some other resonance, is interesting both as a physics process which can indicate new physics, and as a further means of calibrating the detector response. The response of the detector to a well-isolated photon (or in fact a well-isolated π^0) depends only on the electromagnetic calorimeter response and usually has quite a small calibration error. As in the case of the Z, events where the p_t of the photon is balanced by a jet can be used to calibrate the jet response in the hadron calorimeter at low jet p_t . Unlike the Z, statistics are not limited. The major problems are the theoretical uncertainties due to the degree of isolation of the photon. Three possible types of Feynman diagrams contribute to the production as shown in figure 46. The annihilation and Compton diagrams are the most useful because they produce well-isolated photons, but the Bremsstrahlung diagrams yield many more events because the glue-glue luminosity is much greater than that of the quark-antiquark or quark-glue structure function combinations. Such photons are not useful for calibration both because of the need to balance the p_t of the photon against that of two other jets, and the fact that one of the jets is likely to be quite close to the photon and thus there will be some uncertainty about exactly how much of the deposited energy in the photon

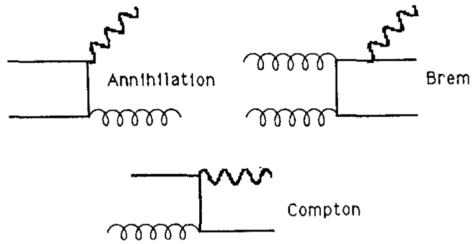

Figure 46: Feynman diagrams for direct photon production.

is in fact coming from the tails of the transverse spread of the nearby jet. Some rejection of these events can be had by cutting out events with jet activity in the same hemisphere as the photon.

11 t Quark Fragmentation

As discussed before for the b quark, the lepton spectrum and the degree of lepton isolation will be determined by the way in which the t quark hadronizes. As in the case of the b quark, the heavy t quark will yield a fragmentation spectrum which, via momentum conservation, will tend to produce T mesons with momentum fraction z near one. When the T mesons are finally detected, this sample will provide a further test of the Peterson form of the fragmentation spectrum. Following this form, the Isajet Monte Carlo uses

$$\frac{\epsilon_q}{m_q^2}$$

for the ϵ parameter with the default values shown in table 9. In this model note that constant ϵ_q values still lead to harder fragmentation spectra as the quark mass increases due to the $1/m_q^2$ behavior of ϵ. Larger values of ϵ_q however have the effect of softening the lepton spectra and thus decreasing the experimental efficiency. There is no firm theoretical estimate of the possible variation which should be used for systematic errors on the ϵ parameter, but given the success of the Peterson formula in describing the c and b systems, it seems reasonable to use the range 1.5-0.5. A study of the effect of this variation[56,51] has shown that the decrease in efficiency for the electrons in the CDF top search is at least partially compensated at low mass by an increased efficiency in the $\not{E}_T$ cut. Table 10 shows the ratio of the rates for top candidates assuming ϵ_t values of 1.5 and 0.5 for events passing various cuts.

Table 9: Default values for ϵ_q

Quark	ϵ_q
c	0.8
b	0.5
t	0.5

Table 10: Ratio of the rates for ϵ_t values of 1.5 and 0.5

$\epsilon = 1.5/\epsilon = 0.5$ rates	$M_t = 40$	$M_t = 70$
Standard electron	0.92	0.97
Twojets	0.89	0.98
E_t, $\not{E}_T > 15$ $E_t + \not{E}_T > 40$	1.07	0.99

12 Higher Mass t Quark Detection

Present limits from the electron plus jets search of CDF indicate that the top mass is greater than 77 GeV. The electron jet search and the dilepton searches from CDF will be extended in the next Tevatron run, but meanwhile it is good to investigate other search methods and see what the limitations are to extending the present searches.

The region from $m_t = M_W + m_b \approx 86$ to $m_t \approx 95$ is a particularly difficult one for the electron plus jet search. The reason is that as we have seen, the chief background to the search is the production of W+multi-jets. In this mass region, the t quark begins to decay into real W's, but due to the light mass of the b quark relative to the W, the b quark is very soft and is often below the jet detection threshold. There are of course two W's in the event, so there are still several jets, but the kinematics of the two b quarks are changing rapidly across this region. As a function of top mass then, the electron plus at least two jets detected rate decreases rapidly at around 86 GeV in a way which depends on the W width and the b quark mass. Once the minimum is reached however, the experimental acceptance as a function of top quark mass remains relatively constant as the top mass increases because the decrease in the $t\bar{t}$ cross section with mass is compensated by the rising efficiency due to the harder and harder b quark spectrum.[57]

The sensitivity of present searches could be improved by requiring more than two jets in the electron jet search. The W background decreases by roughly α_s, while the t rate decreases somewhat more slowly. For 80 GeV top quarks for example, one would expect to detect roughly equal numbers of electrons plus two, three, and four jet events. The major uncertainty becomes the increased systematic uncertainty associated with detecting more jets. Other methods of improving the search sensitivity include placing cuts on the leading jet-jet invariant mass for electron plus two or more jet events. This new information will certainly improve the sensitivity slightly, but will require increased reliance on the details of the W+jetMonte Carlo. The electron + four jet rate is probably quite clean. Unfortunately, there is no W+4 jet Monte Carlo, and too few Z+4jet events to determine how clean this sample is. Even if we had a Monte Carlo for e plus 4jet production, there would still be uncertainties due to the possible presence of one or fewer jets coming from initial state effects. In any case, the efficiency of this channel decreases even more rapidly than the two jet case near 86 GeV.

Baer et al.[58] have suggested an interesting variant of the W to Z ratio test for top discussed previously under indirect top search methods. The basic idea is to make the same ratio test, but to divide the ratio test into bins of various numbers of jets. Figure 47 shows the variation of this ratio as m_t increases above 70 GeV. This method is using the same information as would be used by requiring more than two jets or by including the njet distribution in some sort of likelihood fit. That is, it points out that the chief contribution of top quarks will be to produce W-like events with extra jets. The main difference is that at the expense of the

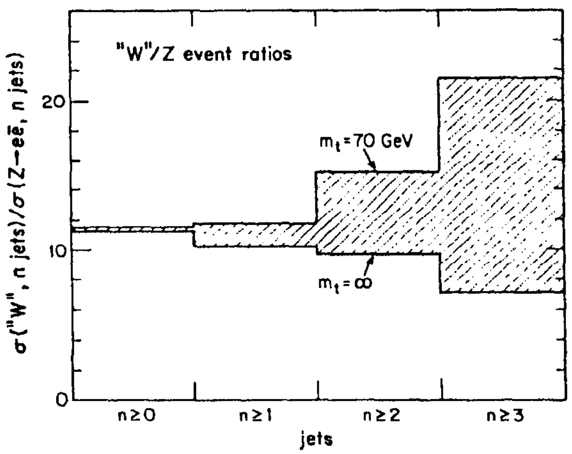

Figure 47: W/Z expected event ratio as a function of the number of jets (partons).

poor statistics in the Z+2,3 jet rates, the uncertainty in initial state radiative effects has been removed since they should be the same for the real W's and the Z. Any extra rate in the "W" 's would signal the presence of top. Note also that the real experimental ratio probably does not vary smoothly in going across the region just above M_W because the number of partons which are detected as jets is changing for the reasons discussed previously.

12.1 Multi-W Production

Despite the presence of W plus multi-jet backgrounds, the real signature for heavy top production is the presence of *two* W's. There is of course a standard model background from WW and WZ production which however from the point of view of an experimentalist, would be interesting to study anyway. Note that the standard model WW rate depends crucially on cancellations arising from the Higgs mechanism! Figure 48 shows that the rates for WW and WZ topologies are strongly dependant on the top quark mass. The rates for SSC scale machines are enhanced by 2-3 orders of magnitude by the presence of top in the 130 GeV range.

The absolute rate for $t\bar{t}$ production for masses of order 100 GeV is small enough that extending present searches would only be possible if the detection efficiency were somehow increased. One obvious way to do this is to pick a branching ratio for the final state which is higher, i.e. replace the electron $\not{E}_T$ signature with jets. Changing from the electron decay of the real W to jet modes increases the branching ratio and therefore the efficiency by a factor of about 9. The final state is $t\bar{t} \rightarrow WWb\bar{b} \rightarrow jjjjb\bar{b}$. Without the isolated lepton however, the signature is overwhelmed by QCD multi-jet production. Even the QCD 4 jet rate with pairs of jets with m^2 above 60 GeV is one to two orders of magnitude larger than the expected signal, depending on the cuts. Future generations of experiments may be able to extract a signal by optimizing the hadron calorimeter resolution (which improves signal to noise), and perhaps some level of b quark tagging either by vertices or soft leptons or both.

The success or failure of detecting $t\bar{t}$ production in the multi-jet channel depends crucially on the calorimeter resolution. A 100 GeV top quark for example has a production cross section of about 100 pb so that for CDF integrated lumi-

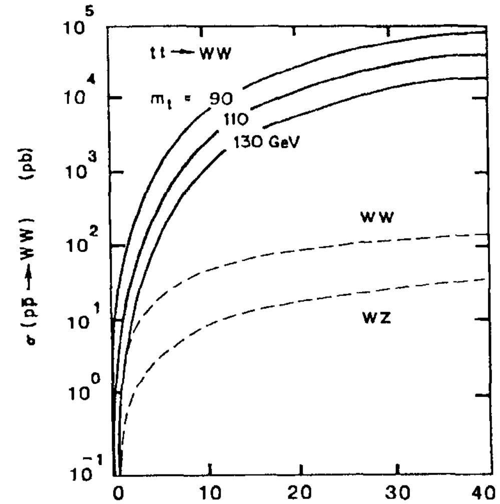

Figure 48: $p\bar{p} \rightarrow W^+W^-X$ for $m_t = 90, 110, 130$ GeV. The dashed curves give the standard model rates for WW and WZ production.

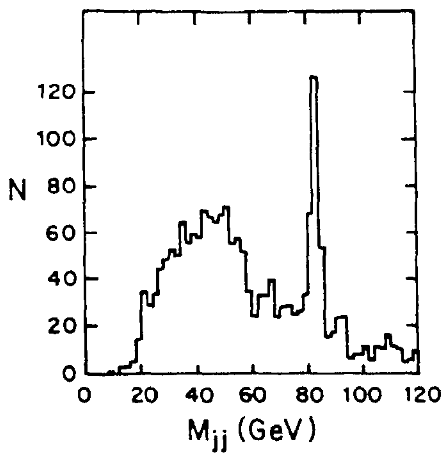

Figure 49: Mass combinations for partons with $p_t > 15$ in $p\bar{p} \to W^+W^-X$ for $m_t = 100$ GeV.

nosities of 4.7 pb^{-1}, there are almost 500 events produced with about half $((6/9)^2)$ of them decaying into the four jet channel. Figure 49 illustrates the jet-jet mass combinations calculated at the parton level for the case $m_t = 100$. Further elimination of false combinations can be done by eliminating some of the 6 combinations that occur in a 4 jet event and by selecting events in which there are two distinct combinations which are both within resolution of the W mass. While this works well at the parton level, it is less successful when one deals with detected jet energies and angles to calculate the jet-jet mass. Comparisons between the parton and detected jet angles [59] indicate that the FWHM is $\Delta\phi < 2$ degrees and in $\Delta\eta < 0.3$. The major problem is not with the angular measurements, it is with the energy measurement of the jet. Hadron calorimetric measurements as bad as $150\%/\sqrt{E}$ can completely wash out the parton level peak and thus destroy the signal. There are many ways to degrade the performance of a hadron calorimeter. Dead regions, variations in response due to non-uniform construction techniques or aging of the medium, radiation damage, inability to control the channel to channel calibration, inadequate segmentation, noisy electronics, poor multi-event recognition due to slow time response, lack of compensation (i.e. differing hadronic and electromagnetic response), poor sampling fractions, low signal levels and intrinsic noise all contribute, and one of the greatest challenges for SSC detectors will be to simultaneously optimize all of these factors.

13 Top Quarks at HERA

The HERA machine will collide 30 GeV electrons with 820 GeV protons for a center-of-mass maximum energy of $\sqrt{s} = 314$ GeV. Note that this would in itself limit top searches to the region $m_t < 157$ GeV. The center-of-mass energy of an individual electron quark collision will be lower than $\sqrt{s}$ and will be determined by

$$\hat{s} = xs$$

where x is the fraction of the proton's momentum being carried by the constituent quark or gluon which is struck by the electron. The relative discovery reach of machines depends on the luminosity, the underlying coupling strength of the colliding particles, and the available c.m. energy. With infinite luminosity, one can probe all the way out to x=1 for a clean signature, but for comparisons of HERA with the Tevatron, we will use $x = \frac{1}{3}$. This latter estimate comes from the ability to easily see 600 GeV mass jet-jet pairs at the Tevatron where the total c.m. energy is 1800 GeV and the available energy goes like $\hat{s} = x_1x_2$ s. One might expect then to see top up to roughly $157/\sqrt{3}$ or 92 GeV at HERA. To further compare the discovery potential for top of HERA and the Tevatron, we also need to compare the integrated luminosities. The projected luminosity for HERA is 200 pb^{-1} per year, but this has to be degraded by roughly a factor of α due to the electromagnetic coupling of the electron. Thus we can see that this luminosity is roughly equivalent to one third the luminosity accumulated in the last Tevatron run (5 pb^{-1}). These rough arguments indicate that top quark searches for heavy top will be difficult at HERA, but to go further we need to look in detail at the production cross sections and the signatures.

There are two possible ways to produce heavy quarks at an ep machine. The first, shown in figure 50a requires Qq mixing and has a very small cross section.

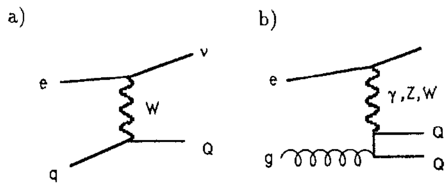

Figure 50: Heavy quark production processes in ep.

The process shown in figure 50b (boson-gluon fusion) dominates.[60] The relative contributions from γ and W exchange depend on the top quark mass as shown in figure 51 with weak and electromagnetic contributions being equal at about 60 GeV.

The main problem however is that while the cross section for $m_t = 60$ is 0.13 pb for $\bar{t}b$ and 0.09 for $t\bar{t}$, the $b\bar{b}$ cross section is $4\ 10^5$. Isolation cuts and p_t cuts (less than 1 GeV in $\Delta R = 0.4$ and $p_t > 8$) yield a b:t ratio of 100:1. This is further improved by requiring $\not{E}_T > 10$ GeV but by this time the t rate is so small that a 5 year run only yields 10 events for a top mass of 80 GeV. [61,62]

Dilepton modes with both leptons isolated are cleaner. Since the major source is $t\bar{t}$ production due to the isolation requirement, a further cut on the sum E_t in the event can be made. The signal to noise at this point is only 1/1000. Cuts on the p_t of each lepton of 10 and 5 respectively yield a signal to noise of 1 at $m_t = 40$. Again however, the rates at higher masses are not high enough. As in the $p\bar{p}$ case, further progress might be possible by looking for non-leptonic decay modes since this increases the available statistics. Cuts required involve using circularity, cutting on sum E_t , requiring at least 4 jets, and anti-selecting on isolated leptons. At this level, the rates appear to be too small to cut hard enough against the $\gamma q \to qg$ background. Basically the backgrounds are large and the signals are small. If the top quark had been as light as 40 GeV, the cross sections might have been large enough for the required cuts, but with current limits on the top mass, it is unlikely that t production in ep is large enough to be found at HERA.

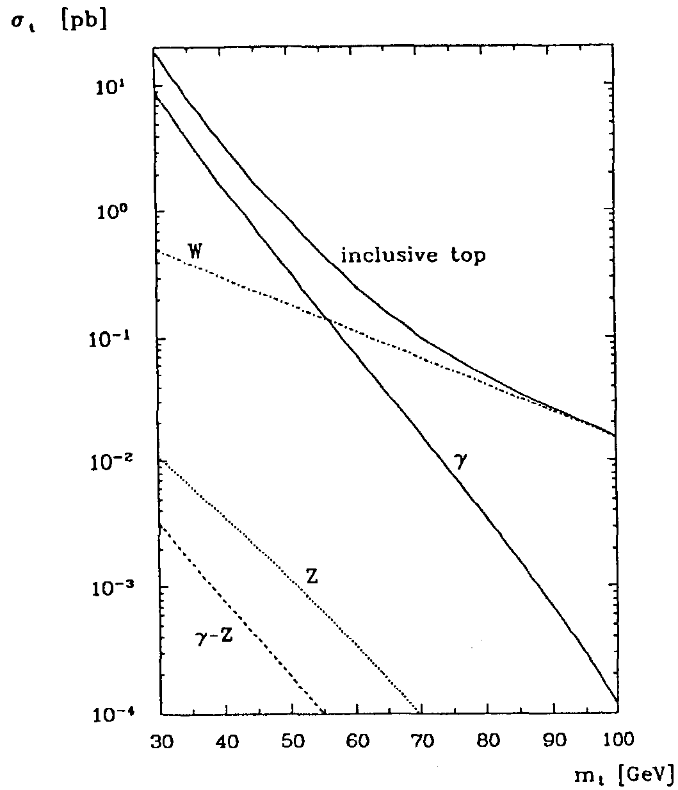

Figure 51: Top production contributions in ep versus m_t.

14 Conclusions

The top quark has successfully eluded detection for another year with the highest lower limits for its mass being 77 GeV from the CDF electron plus jets search. Hopefully it can't avoid being detected much longer! Its discovery will not only confirm our basic 3 doublet picture of the quark generations, but will also provide us with the crucial parameter (m_t) needed at present for high precision tests of our understanding of the standard model. No reason to believe for the moment that the t does not exist, if anything, the b quark asymmetry indicates that it must. Charged Higgs decay modes of the t however could easily hide it from many of the current search techniques. Otherwise, if the mass is less than about 150 GeV it should show up in the 1991 or 1993 Tevatron collider runs. If it's heavier, we'll have to wait for the SSC.

In b physics, the standard model together with the spectator model of b decays continues to describe the physics well. Significant constraints between different elements of the KM matrix are beginning to arise, and the next major frontier in this area will be the investigation of CP violation. In this respect, the evidence seems to favor a non-zero value for the $b \rightarrow u$ transition which if it had been zero would have eliminated CP violation from the B system. Assuming CP violation is large enough, the B meson system will provide valuable new measurements to add to those already gathered in the K system to investigate this poorly understood phenomena.

I think it is clear that we are learning and will continue to learn a great deal about the standard model and potential deviations from it by studying the heavy b and t quarks. They are unique in the sense that their mass allows us to flavor tag their presence in hadronic final states (via large lepton p_t) and that their mass is large enough to make perturbative QCD reasonably valid. So, armed with a good experimental technique and a good theoretical calculation, we are certain to make further progress.

References

[1] H. Albrecht et al.(ARGUS collaboration),Phys.Lett.**185B**(1987)218.

[2] CLEO collaboration, Phys.Rev.**D36**(1987)1289.

[3] C.Bebek et al.(CLEO collaboration),Phys.Rev.**D36**(1987)1289.

[4] D.Bortoletto et al.(CLEO collaboration),Phys.Rev.**D35**(1987)19.

[5] H.Albrecht et al.(ARGUS collaboration),Phys.Lett.**162B**(1985)395.

[6] H.Albrecht et al.(ARGUS collaboration),Phys.Lett.**199B**(1987)451.

[7] P.Haas et al.(CLEO collaboration),Phys.Rev.Lett.**55**(1985)1248.

[8] M.S.Alam et al.(CLEO collaboration),Phys.Rev.**D34**(1986)3279.

[9] S.Berends et al.(CLEO collaboration),CLNS-87/78,May 1987.

[10] K.R.Schubert et al.(ARGUS collaboration),Proceedings of the XXIII Int. Conf. on HEP(Berkeley,1986)781.

[11] K.Wachs et al.(Crystal Ball collaboration),DESY 87-084,July1987.

[12] H.Schroder(ARGUS collaboration),Proc, of the 23rd Rencontre de Moriond,1988.

[13] H.Albrecht et al.(ARGUS collaboration),Phys.Lett.**209B**(1988)119.

[14] M.Gronau,J.Rosner,EFI 87-55(1987).

[15] N.Deshpande,J.Trampetic,A.Soni,OITS-370(1987).

[16] H.Albrecht et al.,Phys.Lett.**192B**(1987)245.

[17] M.Artuso et al.,Phys.Rev.Lett.**62**(1989)2233.

[18] R.K.Ellis,1989 SLAC Summer School,"Heavy Quarks - Theoretical".

[19] C.Peterson et al.,Phys.Rev.**D27**(1983)105.

[20] S.L.Wu,Phys.Rpts.**107**(1984)213.

[21] See Barger and Phillips,**Collider Physics**, figure 6.8 .

[22] Proceedings, International Europhysics Conference, Bari,Italy(1985).

[23] UA1 Collaboration,Phys.Lett **200B**(1988)380.

[24] H.Kolanoski,DESY 88-121,August,1988.

[25] Foley et al.,Snowmass Summer Study,(1987)701.

[26] Snowmass Summer Study,1988.

[27] D.Stork,ed.,Proc. of the UCLA Workshop on Linear Collider $B\overline{B}$ Factories.

[28] PSI design report,PSI preprint PR-88-09.

[29] The Physics Program of a High-Luminosity Asymmetric B Factory, SLAC-353,LBL-27856,CALT-68-1588,October,1989.

[30] K.Berkelman,CLNS 87/101.

[31] U.Amaldi,G.Coignet,NIM,**A260**(1987)7.

[32] J.Rees,SLAC/AP-67,1988.

[33] Feasibility Study for an Asymmetric B Factory based on PEP,LBL Pub-5244,SLAC-352,CALT-68-1589,October,1989.

[34] I.Dunietz,J.Rosner,Phys.Rev.**D34**(1986)1404.

[35] I.Bigi,A.Sanda,Nucl.Phys.**B281**(1987)41.

[36] M.S.Alam et al.,Phys.Rev.**D34**,3279(1986).

[37] H.Albrecht et al.,Phys.Lett.**199B**(1987)451.

[38] W.Selove,UPR-176E,Oct.1989.

[39] P.Nason,S.Dawson and R.K.Ellis,Nucl.Phys.**B303**(1988) 607.

[40] UA1 Collaboration,Phys.Lett.**B213**(1988)405.

[41] Eva Low, AMY Collaboration, 1989 EPS Conference,Madrid.

[42] UA1,2 combined 95% limits,1989 EPS Conference,Madrid.

[43] The JADE Collaboration, DESY 88-154(1988).

[44] W.W.Ash et al.,Phys.Rev.Lett.**58**(1987)1080.

[45] U.Amaldi et al.,Phys.Rev.**D36**(1987)1385.

[46] G.Costa et al.,Nucl.Phys.**B297**(1988)244.

[47] J.Ellis and G.Fogli,Phys.Lett.**213B**(1988)526.

[48] P.Colas, D.Denegri, C.Stubenrauch, DPhPE 88-02.

[49] See for example Barger and Phillips,**Collider Physics**, figure 10.23.

[50] P.Cushman and R.Rusack,ECFA Study Week,CERN 89-10.

[51] F.Abe et al.(CDF Collaboration),Phys.Rev.Lett.**64**(1990)142.

[52] I.Hinchliffe,report in preparation,Papageno V2.71.

[53] M.Mangano,S.Parke Fermilab Pub 84/106-T(1989).

[54] The epsilon parameter was changed by a factor of 3.

[55] G.Altarelli,M.Diemos,G.Martinelli, P.Nason, Nucl.Phys.**B308**(1988)724.

[56] P.Sinervo,CDF Note 1016.

[57] P.Sinervo, private communication.

[58] H.Baer et al.,MAD-PH-445.

[59] R.Hollebeek, P.Sinervo, CDF Note 617.

[60] G.Ingelman,G.A.Schuler,Z.Phys.**C40**(1988)299.

[61] G.Ingelman,G.A.Schuler,J.F.deTroconiz,DESY 88-143.

[62] R.A.Eichler,Z.Kunszt,Nucl.Phys.**B308**(1988)791.

THE THEORY OF HEAVY FLAVOUR PRODUCTION

R. K. Ellis

Fermi National Accelerator Laboratory
P.O. Box 500, Batavia, Illinois 60510, USA

The theory of heavy quark production in hadronic reactions is reviewed. Rates for the production of charm, bottom and top quarks at energies of current interest

1. Lecture 1

1.1 The QCD parton model

The treatment of heavy quark production which I shall present relies on the QCD improved parton model. This model is generally applicable to high energy processes which involve a hard interaction. The parton model as originally envisaged by Feynman[1] provides a physical picture of a high energy scattering event in a frame in which the hadron is rapidly moving. In such a frame the hard interaction leading to the scattering event occurs on a time scale short compared to the scale which controls the evolution of the parton system. The characteristic evolution time for the parton system has been dilated by the Lorentz boost to the rapidly moving frame. During the hard interaction the partons can be treated as though they were effectively free. Only in such a frame does it make sense to talk about a number density of partons. The number of partons of type i with a momentum fraction between x and $x + dx$ is given by a distribution function $f_i(x)$.

Much of the structure of the parton model can be demonstrated to follow from the QCD Lagrangian, but with certain significant modifications. The QCD parton model has been introduced by Hinchliffe in his lectures[2]. I shall therefore only review the salient features of the model. The QCD parton model expresses the cross section σ for a hard scattering with characteristic momentum scale Q as

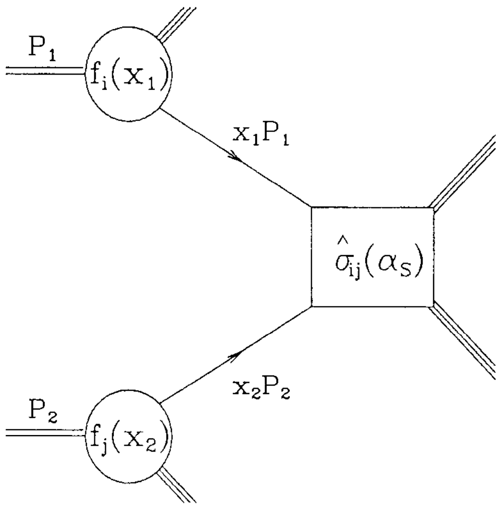

Figure 1: The parton model picture of a high energy scattering.

follows,

$$\sigma(P_1, P_2) = \sum_{i,j} \int dx_1 dx_2 \; f_i(x_1, \mu) f_j(x_2, \mu) \; \hat{\sigma}_{ij}(\alpha_S(\mu), x_1 P_1, x_2 P_2) \qquad (1.1)$$

This formula is illustrated in Fig. 1. The short distance cross section $\hat{\sigma}$ is evaluated at rescaled values of the incoming hadron momenta P_1 and P_2. The sum on i and j runs over the light quarks and gluons. μ is an arbitrary scale which should be chosen to be of the order of the hard momentum scale Q. Note that the impulse approximation is used in Eq. 1.1. Interference terms which involve more than one active parton per hadron are not included. They require the transfer of the large momentum Q from one parton to another. Such interactions lead to terms which are suppressed by powers of the large scale Q and are not shown in Eq. 1.1.

The important features which distinguish QCD from the naive parton picture are as follows. The short distance cross section is now calculable as a systematic expansion in the strong coupling α_S because of the property of asymptotic freedom. The short distance cross section is defined to be the perturbatively evaluated parton cross section from which the mass singularities have been factorised. For details of this factorisation procedure I refer the reader to Ref. [3]. The physical purpose of this procedure is to remove the long distance pieces (which are signalled by the presence of mass singularities) from the hard scattering cross section and place them in the parton distribution functions. The short distance cross section then contains only the physics of the hard scattering. In the Born approximation the short distance cross section is just the normal perturbatively calculated parton cross section, since no mass singularities occur in lowest order. The Born approximation is sufficient in many circumstances to extract the qualitative features of the physics predicted by the parton model. I shall therefore not explain the factorisation procedure in detail.

In QCD the parton distribution functions depend on scale μ in a calculable way as determined by the Altarelli-Parisi Equation [4]; $f_i(x, \mu)$ is the number of partons in the infinite momentum frame carrying a fraction between x and $x + dx$ of the momentum of the incoming hadron and with a transverse size greater than $1/\mu$. The scale μ which occurs both in the running coupling and in the parton distributions, should be chosen to be of the order of the hard interaction scale Q in order to avoid large logarithms in the perturbative expansion of the short distance cross section.

The doubly differential form of the parton model result will also be necessary for our purposes. Consider a hard scattering process in which two incoming hadrons of momenta P_1 and P_2 produce an observed final state with two partons of momenta p_3 and p_4. The predicted invariant cross section is,

$$\frac{E_3 E_4 \, d\sigma}{d^3p_3 d^3p_4} = \sum_{i,j} \int dx_1 dx_2 f_i(x_1, \mu) f_j(x_2, \mu) \left[\frac{E_3 E_4 \, d\hat{\sigma}(\alpha_S(\mu), x_1 P_1, x_2 P_2)}{d^3p_3 d^3p_4} \right]. \qquad (1.2)$$

I shall discuss the sensitivity of the physical predictions to the input parameters in detail in the second lecture. Suffice it to say at this point that the distributions of quarks and gluons in the proton are determined experimentally, mainly by the analysis of deeply inelastic lepton hadron scattering experiments. At present these experiments determine the form of the light quark distributions, and to a lesser extent the form of the gluon distribution function, in a range of $x \geq 10^{-2}$ and $\mu < 15$ GeV.

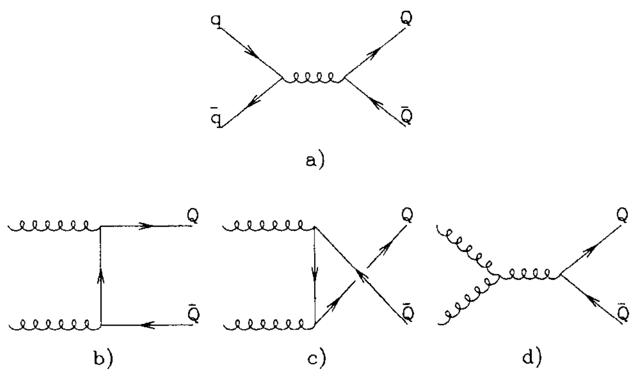

Figure 2: Lowest order Feynman diagrams for heavy quark production.

1.2 The theory of heavy quark production

The dominant parton reactions leading to the production of a sufficiently heavy quark Q of mass m are,

$$\begin{aligned} &(a)\quad q(p_1) + \bar{q}(p_2) \rightarrow Q(p_3) + \overline{Q}(p_4) \\ &(b)\quad g(p_1) + g(p_2) \rightarrow Q(p_3) + \overline{Q}(p_4)\ , \end{aligned} \tag{1.3}$$

where the four momenta of the partons are given in brackets. The Feynman diagrams which contribute to the matrix elements squared in $O(g^4)$ are shown in Fig. 2. The justification of the use of perturbation theory in the calculation of heavy quark cross sections relies on the fact that all the propagators in Fig. 2 are off-shell by an amount at least m^2. The invariant matrix elements squared[5,6] which result from the diagrams in Fig. 2 are given in Table 1. The matrix elements

Process	$\overline{\sum}\lvert M\rvert^2$
$q\,\bar{q} \rightarrow Q\,\overline{Q}$	$\frac{V}{2N_c^2}\left(\tau_1^2+\tau_2^2+\frac{\rho}{2}\right)$
$g\,g \rightarrow Q\,\overline{Q}$	$\frac{1}{2VN_c}\left(\frac{V}{\tau_1\tau_2}-2N_c^2\right)\left(\tau_1^2+\tau_2^2+\rho-\frac{\rho^2}{4\tau_1\tau_2}\right)$

Table 1: Lowest order processes for heavy quark production. $\overline{\sum}|M|^2$ is the invariant matrix element squared with a factor of g^4 removed. The colour and spin indices are averaged (summed) over initial (final) states.

squared have been averaged (summed) over initial (final) colours and spins, (as indicated by $\overline{\sum}$). In order to express the matrix elements in a compact form, I have introduced the following notation for the ratios of scalar products,

$$\tau_1 = \frac{2p_1.p_3}{s},\quad \tau_2 = \frac{2p_2.p_3}{s},\quad \rho = \frac{4m^2}{s},\quad s = (p_1+p_2)^2. \tag{1.4}$$

The dependence on the $SU(N_c)$ colour group is shown explicitly, ($V = N_c^2 - 1$, $N_c = 3$) and m is the mass of the produced heavy quark Q.

In the Born approximation the short distance cross section is obtained from the invariant matrix element in the normal fashion[7].

$$d\hat{\sigma}_{ij} = \frac{1}{2s}\,\frac{d^3p_3}{(2\pi)^3 2E_3}\,\frac{d^3p_4}{(2\pi)^3 2E_4}(2\pi)^4\delta^4(p_1+p_2-p_3-p_4)\, g^4\overline{\sum}|M_{ij}|^2. \tag{1.5}$$

The first factor is the flux factor for massless incoming particles. The other terms come from the phase space for two-to-two scattering.

I shall now illustrate why it is plausible that heavy quark production is described by perturbation theory[8]. Consider first the differential cross section. Let us denote the momenta of the incoming hadrons, which are directed along the z direction, by P_1 and P_2 and the square of the total centre-of-mass energy by S where $S = (P_1+P_2)^2$. The short distance cross section in Eq. 1.2 is to be evaluated at rescaled values of the parton momenta $p_1 = x_1P_1$, $p_2 = x_2P_2$ and hence the square of the total parton centre-of-mass energy is $s = x_1x_2S$, if we ignore the masses of the incoming hadrons. The rapidity variable for the two final state partons is defined in terms of their energies and longitudinal momenta as,

$$y = \frac{1}{2}\ln\left[\frac{E+p_z}{E-p_z}\right]. \tag{1.6}$$

Using Eqs. 1.2 and 1.5 the result for the invariant cross section may be written as,

$$\frac{d\sigma}{dy_3 dy_4 d^2p_T} = \frac{\alpha_S^2(\mu)}{s^2}\sum_{ij} x_1 f_i(x_1,\mu) x_2 f_j(x_2,\mu)\overline{\sum}|M_{ij}|^2. \tag{1.7}$$

The energy momentum delta function in Eq. 1.5 fixes the values of x_1 and x_2 if we know the value of the p_T and rapidity of the outgoing heavy quarks. In the centre of mass system of the incoming hadrons we may write the components of the parton four momenta as $((E, p_x, p_y, p_z))$

$$\begin{aligned} p_1 &= \sqrt{S}/2(x_1,0,0,x_1) \\ p_2 &= \sqrt{S}/2(x_2,0,0,-x_2) \\ p_3 &= (m_T\cosh y_3, p_T, 0, m_T\sinh y_3) \\ p_4 &= (m_T\cosh y_4, -p_T, 0, m_T\sinh y_4)\,. \end{aligned} \tag{1.8}$$

The transverse momentum in the final state has been arbitrarily routed along the x-direction. Applying energy and momentum conservation we obtain,

$$x_1 = \frac{m_T}{\sqrt{S}}(e^{y_3}+e^{y_4}),\quad x_2 = \frac{m_T}{\sqrt{S}}(e^{-y_3}+e^{-y_4}),\quad s = 2m_T^2(1+\cosh\Delta y). \tag{1.9}$$

The transverse mass of the heavy quarks is denoted by $m_T = \sqrt{(m^2+p_T^2)}$ and $\Delta y = y_3 - y_4$ is the rapidity difference between the two heavy quarks.

Using Eqs. 1.7 and 1.9, we may write the cross section for the production of two massive quarks calculated in lowest order perturbation theory as,

$$\frac{d\sigma}{dy_3 dy_4 d^2p_T} = \frac{\alpha_S^2(\mu)}{4m_T^4(1+\cosh(\Delta y))^2}\sum_{ij} x_1 f_i(x_1,\mu)\, x_2 f_j(x_2,\mu)\,\overline{\sum}|M_{ij}|^2. \tag{1.10}$$

Expressed in terms of m, m_T and Δy the matrix elements for the two processes in Table 1 are,

$$\overline{\sum}|M_{q\bar{q}}|^2 = \frac{V}{2N_c^2}\Big(\frac{1}{1+\cosh(\Delta y)}\Big)\Big(\cosh(\Delta y)+\frac{m^2}{m_T^2}\Big) \tag{1.11}$$

$$\overline{\sum}|M_{gg}|^2 = \frac{1}{VN_c}\Big(\frac{V\cosh(\Delta y)-1}{1+\cosh(\Delta y)}\Big)\Big(\cosh(\Delta y)+2\frac{m^2}{m_T^2}-2\frac{m^4}{m_T^4}\Big)\,. \tag{1.12}$$

Note that, because of the specific form of the matrix elements squared, the cross section, Eq. 1.10, is strongly damped as the rapidity separation Δy between the two heavy quarks becomes large. It is therefore to be expected that the dominant contribution to the total cross section comes from the region $\Delta y \approx 1$.

I now consider the propagators in the diagrams shown in Fig. 2. In terms of the above variables they can be written as,

$$\begin{aligned} (p_1+p_2)^2 &= 2p_1.p_2 &&= 2m_T^2(1+\cosh\Delta y) \\ (p_1-p_3)^2-m^2 &= -2p_1.p_3 &&= -m_T^2(1+e^{-\Delta y}) \\ (p_2-p_3)^2-m^2 &= -2p_2.p_3 &&= -m_T^2(1+e^{\Delta y})\,. \end{aligned} \tag{1.13}$$

Note that the denominators are all off-shell by a quantity of least of order m^2. It is this fact which distinguishes the production of a light quark from the production of a heavy quark. When a light quark is produced by these diagrams the lower cut-off on the virtuality of the propagators is provided by the light quark mass, which is less than the QCD scale Λ. Since propagators with small virtualities give the dominant contribution, the production of a light quark will not be calculable in perturbative QCD. In the production of a heavy quark the lower cut-off is provided by the mass m. It is therefore plausible that heavy quark production is controlled by α_S evaluated at the heavy quark scale.

Note also that the contribution to the cross section from values of p_T which are much greater than the quark mass is also suppressed. The differential cross section falls like m_T^{-4} and as m_T increases the parton flux decreases because of the increase of x_1 and x_2. Since all dependence on the transverse momentum appears in the transverse mass combination, the dominant contribution to the cross section comes from transverse momentum of the order of the mass of the heavy quark.

Thus for a sufficiently heavy quark we expect the methods of perturbation theory to be applicable. It is the mass of the heavy quark which provides the large scale in heavy quark production. The transverse momenta of the produced heavy quarks are of the order of the heavy quark mass and they are produced close in rapidity. The heavy quarks are produced predominantly centrally because of the rapidly falling parton fluxes. Final state interactions which transform the heavy quarks into the observed hadrons will not change the size of the cross section. A possible mechanism which might spoil this simple picture would be the interaction of the produced heavy quark with the debris of the incoming hadron. However these interactions with spectator partons are suppressed by powers of the heavy quark mass[9,10]. For a sufficiently heavy quark they can be ignored.

The theoretical arguments summarised above do not address the issue of whether the charmed quark is sufficiently heavy that the hadroproduction of charmed hadrons in all regions of phase space is well described by only processes (a) and (b) and their perturbative corrections.

Integrating Eq. 1.5 over all momenta we can obtain the total cross section for the production of a heavy quark. In general the total short distance cross section can be expressed as,

$$\hat{\sigma}_{ij}(s,m^2) = \frac{\alpha_S^2(\mu)}{m^2}\mathcal{F}_{ij}\Big(\rho,\frac{\mu^2}{m^2}\Big), \quad \alpha_S = \frac{g^2}{4\pi}. \tag{1.14}$$

Equation 1.14 completely describes the short distance cross section for the production of a heavy quark of mass m in terms of the functions $\mathcal{F}_{ij}$. The indices i and j specify the types of the annihilating partons. These short distance cross sections can be used directly to predict the total heavy quark cross section using Eq. 1.1. The dimensionless functions $\mathcal{F}_{ij}$ have a perturbative expansion in the coupling constant. The first two terms in this expansion can be expressed as follows,

$$\mathcal{F}_{ij}\Big(\rho,\frac{\mu^2}{m^2}\Big) = \mathcal{F}_{ij}^{(0)}(\rho) + 4\pi\alpha_S(\mu)\Big[\mathcal{F}_{ij}^{(1)}(\rho) + \overline{\mathcal{F}}_{ij}^{(1)}(\rho)\ln\big(\frac{\mu^2}{m^2}\big)\Big] + O(\alpha_S^2). \tag{1.15}$$

The energy dependence of the cross section is given in terms of ρ and β,

$$\rho = \frac{4m^2}{s}, \quad \beta = \sqrt{1-\rho}. \tag{1.16}$$

The lowest order functions $\mathcal{F}_{ij}^{(0)}$ defined in Eq. 1.15 are obtained by integrating Eq. 1.5 using the results of Table 1. The results are,

$$\mathcal{F}_{q\bar{q}}^{(0)}(\rho) = \frac{V\pi\beta\rho}{24N_c^2}\Big[(2+\rho)\Big]$$

$$\mathcal{F}_{gg}^{(0)}(\rho) = \frac{\pi\beta\rho}{24VN_c}\Big[3[\rho^2+2V(\rho+1)]\mathcal{L}(\beta) + 2(V-2)(1+\rho) + \rho(6\rho - N_c^2)\Big]$$

$$\mathcal{F}_{gq}^{(0)}(\rho) = \mathcal{F}_{g\bar{q}}^{(0)}(\rho) = 0$$

$$\mathcal{L}(\beta) = \frac{1}{\beta}\ln\Big(\frac{1+\beta}{1-\beta}\Big) - 2\,. \tag{1.17}$$

Note that the quark gluon process vanishes in lowest order, but is present in higher orders.

Using the results in Table 1 we can also calculate the average values of the transverse momentum squared. The $q\bar{q}$ contribution to the p_T^2 weighted cross section is,

$$\int dp_T^2\, p_T^2\, \frac{d\hat{\sigma}_{q\bar{q}}}{dp_T^2} = \frac{\alpha_S^2\pi\beta^3 V}{60N_c^2}\Big[3+2\rho\Big] \tag{1.18}$$

and the gg contribution is

$$\int dp_T^2\, p_T^2\, \frac{d\hat{\sigma}_{gg}}{dp_T^2} = \frac{\alpha_S^2\pi\beta}{120VN_c}\Big[2V\Big[7\beta^2(2+3\rho) - 15\rho(1+2\rho)\mathcal{L}(\beta)\Big] - 15\rho^3\mathcal{L}(\beta)$$

$$-6(5\rho+2)\beta^4\Big] \tag{1.19}$$

with $\mathcal{L}(\beta)$ defined in Eq. 1.17. The results of Eqs. 1.14 and 1.17 allow us to calculate the average value of p_T^2:

$$\Big\langle p_T^2\Big\rangle = \frac{1}{\sigma}\int dp_T^2\, p_T^2\, \frac{d\sigma}{dp_T^2}\,. \tag{1.20}$$

This leads to an average transverse momentum of order of the heavy quark mass. This is illustrated in Fig. 3 for the particular case of pN collisions. For all values of the beam energy which are sufficiently far above threshold to have a sizeable number of events, the average value of p_T^2 is of the order of m^2. As shown in Fig. 3 p_T^2 continues to have a small dependence on μ, because of the μ dependence in the structure functions.

Far above threshold the average transverse momentum squared grows approximately linearly with $\sqrt{S}$:

$$\Big\langle p_T^2\Big\rangle \approx m\sqrt{S}\,. \tag{1.21}$$

The net transverse momentum of the produced heavy quark pair reflects the distribution of transverse momenta of the incoming partons and is therefore small.

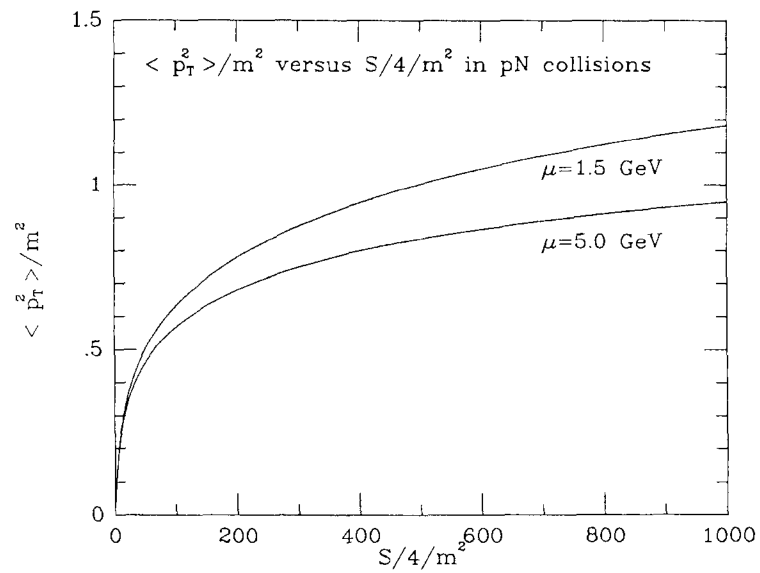

Figure 3: The average value of p_T^2 in heavy quark production.

1.3 Parton luminosities

Consider a generic hard process initiated by two hadrons of momenta P_1 and P_2 and $S = (P_1 + P_2)^2$:

$$\sigma(S) = \sum_{i,j} \int_0^1 dx_1 \int_0^1 dx_2 \; f_i(x_1, \mu) f_j(x_2, \mu) \; \hat{\sigma}_{ij}(\alpha_S(\mu), x_1 P_1, x_2 P_2). \tag{1.22}$$

In many circumstances the flux of partons with a given invariant mass squared will play a major role in the determination of the cross section. It is therefore convenient to define a parton luminosity L as a function of $\tau = s/S$ where s is the invariant mass squared of the partons:

$$\tau \frac{dL_{ij}}{d\tau} = \frac{1}{1+\delta_{ij}} \int_0^1 dx_1 dx_2 \; [(x_1 f_i(x_1, \mu) \; x_2 f_j(x_2, \mu)) + (1 \leftrightarrow 2)] \delta(\tau - x_1 x_2). \tag{1.23}$$

Hence any parton cross section can be written as,

$$\sigma(S) = \sum_{i,j} \int_{\tau_0}^1 \frac{d\tau}{\tau} \left[\mathcal{L}_{ij}(\tau, s) \right] \left[s \sigma_{ij} \right] \tag{1.24}$$

$$\mathcal{L}_{ij}(\tau, s) = \left[\frac{\tau}{s} \frac{dL_{ij}}{d\tau} \right] \tag{1.25}$$

where $s = x_1 x_2 S$. $\mathcal{L}$ has the dimensions of a cross section. The second object in square brackets in Eq. 1.24 is dimensionless. It is approximately determined by powers of the relevant coupling constants. Hence knowing the luminosities, we can roughly estimate cross sections. For this purpose we show the parton luminosities for gg, $u\bar{u}$ and $d\bar{d}$ in Figs. 4, 5 and 6. The luminosities are shown at the present energies of the CERN and FNAL $p\bar{p}$ colliders and at the energies of the proposed UNK collider($\sqrt{S} = 6$ TeV, $p\bar{p}$), the LHC ($\sqrt{S} = 17$ TeV, pp) and the SSC ($\sqrt{S} = 40$ TeV, pp).

As an example of the use of these plots we examine the flux of partons with $\sqrt{s} = 100$ GeV. Since for heavy quark production $s \approx 4m_T^2$ this value is appropriate for the production of a quark of mass $m \approx 35$ GeV. From Figs. 4, 5 and 6 we find that,

$$\begin{aligned} &\mathcal{L}_{gg} = 1 \times 10^4 \text{pb}, \;\; \mathcal{L}_{u\bar{u}} = 1.5 \times 10^4 \text{pb}, \;\; \mathcal{L}_{d\bar{d}} = 2 \times 10^3 \text{pb}, \;\; \sqrt{s} = 0.63 \text{ TeV} \\ &\mathcal{L}_{gg} = 3 \times 10^5 \text{pb}, \;\; \mathcal{L}_{u\bar{u}} = 5 \times 10^4 \text{pb}, \;\; \mathcal{L}_{d\bar{d}} = 2 \times 10^4 \text{pb}, \;\; \sqrt{s} = 1.8 \text{ TeV} \end{aligned} \tag{1.26}$$

Note that $\mathcal{L}_{gg}$ is about 30 times larger at the Tevatron than at the CERN $Sp\bar{p}S$. The quark-antiquark luminosities at CERN are about the same size as the gluon-gluon luminosity, whereas they are a factor of ten smaller than the gluon-gluon luminosities at the Tevatron. We conclude that the production of a 35 GeV top quark at the Tevatron is dominated by gluon-gluon fusion. At CERN energies both the gluon-gluon and the quark-antiquark mechanisms are important. The cross section is expected to be about 10 times bigger at FNAL than at CERN. The estimate for the cross section for the production of a 35 GeV heavy quark at the Tevatron is ($\alpha_S \approx 0.1$),

$$\sigma \approx \alpha_S^2 \times 3 \times 10^6 \text{pb} \approx 3 \times 10^4 \text{pb}. \tag{1.27}$$

In later sections we shall see that this rough estimate is confirmed by a more detailed analysis.

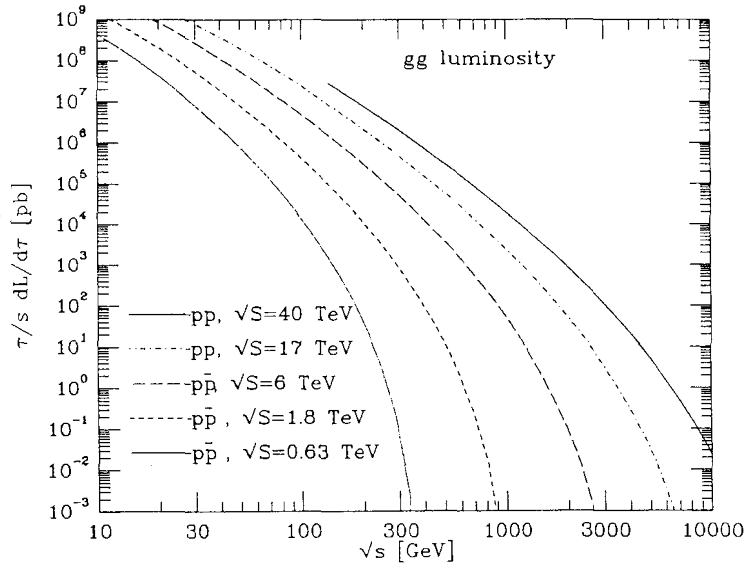

Figure 4: Luminosity plot for gluon-gluon.

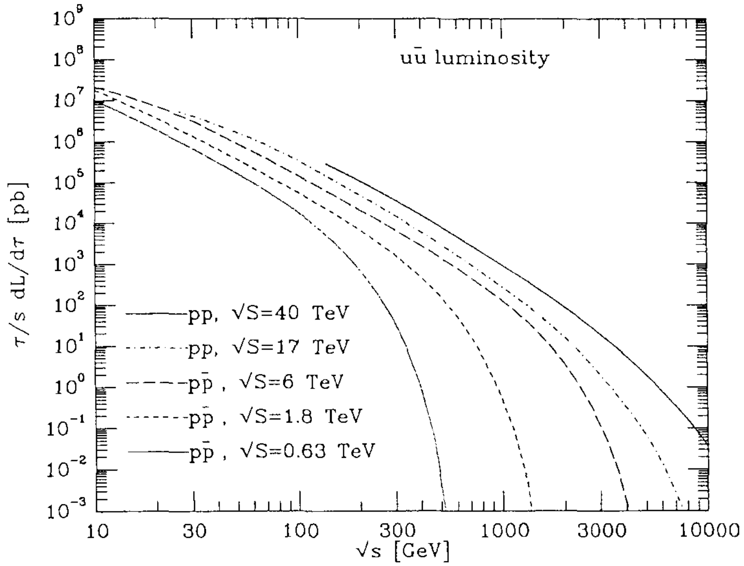

Figure 5: Luminosity plot for up quark-up antiquark.

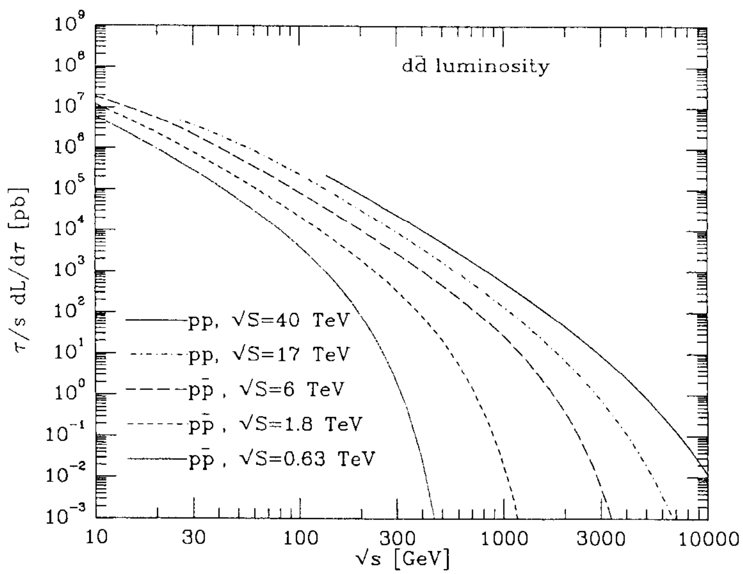

Figure 6: Luminosity plot for down quark-down antiquark.

1.4 Higher order corrections to heavy quark production

The lowest order terms presented above are the beginning of a systematic expansion in the running coupling:

$$\hat{\sigma}_{ij}(s,m^2) = \frac{\alpha_S^2(\mu)}{m^2} \mathcal{F}_{ij}\Big(\rho, \frac{\mu^2}{m^2}\Big) . \tag{1.28}$$

Equation 1.28 completely describes the short distance cross section for the production of a heavy quark of mass m in terms of the functions $\mathcal{F}_{ij}$, where the indices i and j specify the types of the annihilating partons. The dimensionless functions $\mathcal{F}_{ij}$ have the following perturbative expansion,

$$\mathcal{F}_{ij}\Big(\rho, \frac{\mu^2}{m^2}\Big) = \mathcal{F}^{(0)}_{ij}(\rho) + 4\pi\alpha_S(\mu)\Big[\mathcal{F}^{(1)}_{ij}(\rho) + \overline{\mathcal{F}}^{(1)}_{ij}(\rho)\ln(\frac{\mu^2}{m^2})\Big] + O(g^4) \tag{1.29}$$

where ρ is defined in Eq. 1.16. The functions $\mathcal{F}^{(1)}_{ij}$ are completely known[11]. Examples of the types of diagrams which contribute to $\mathcal{F}^{(1)}_{ij}$ are shown in Fig. 7. The full calculation involves both real and virtual corrections. For full details I refer the reader to Ref. [11]. The gluon-gluon contribution is also considered in Ref. [12].In order to calculate the $\mathcal{F}_{ij}$ in perturbation theory we must perform both renormalisation and factorisation of mass singularities. The subtractions required for renormalisation and factorisation are done at mass scale μ. The dependence on μ of the non-leading order term is displayed explicitly in Eq. 1.29.

Note that μ is an unphysical parameter. The physical predictions should be invariant under changes of μ at the appropriate order in perturbation theory. If we have performed a calculation to $O(\alpha_S^3)$, variations of the scale μ will lead to corrections of $O(\alpha_S^4)$:

$$\mu^2 \frac{d}{d\mu^2}\sigma = O(\alpha_S^4) . \tag{1.30}$$

Using Eq. 1.30 we find that the term $\overline{\mathcal{F}}^{(1)}$ which controls the μ dependence of the higher perturbative contributions is fixed in terms of the lower order result $\mathcal{F}^{(0)}$.

$$\overline{\mathcal{F}}^{(1)}_{ij}(\rho) = \frac{1}{8\pi^2}\Bigg[4\pi b \mathcal{F}^{(0)}_{ij}(\rho) - \int_\rho^1 dz_1\, \mathcal{F}^{(0)}_{kj}(\frac{\rho}{z_1})P_{ki}(z_1) - \int_\rho^1 dz_2\, \mathcal{F}^{(0)}_{ik}(\frac{\rho}{z_2})P_{kj}(z_2)\Bigg] \tag{1.31}$$

In obtaining this result I have used the renormalisation group equation for the

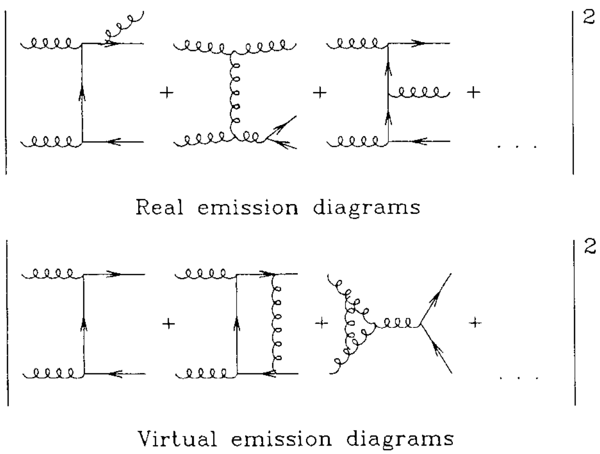

Figure 7: Examples of higher order corrections to heavy quark production.

running coupling,

$$\mu^2 \frac{d}{d\mu^2}\alpha_S(\mu) = -b\alpha_S^2(1 + b'\alpha_S + \ldots)$$
$$b = \frac{33 - 2n_f}{12\pi}, \quad b' = \frac{153 - 19n_f}{2\pi(33 - 2n_f)} \tag{1.32}$$

and the Altarelli-Parisi equation,

$$\mu^2 \frac{d}{d\mu^2} f_i(x,\mu) = \frac{\alpha_S(\mu)}{2\pi} \sum_k \int_x^1 \frac{dz}{z} P_{ik}(z) f_k(\frac{x}{z},\mu) \; . \tag{1.33}$$

This illustrates an important point which is a general feature of renormalisation group improved perturbation series in QCD. The coefficient of the perturbative correction depends on the choice made for μ, but the μ dependence changes the result in such a way that the physical result is independent of the choice made for μ. Thus the μ dependence is formally small because it is of higher order in α_S. This does not assure us that the μ dependence is actually numerically small for all series. A pronounced dependence on μ is a signal of an untrustworthy perturbation series.

I shall illustrate this point by showing the μ dependence found in two cases of current interest. Firstly in Fig. 8, I show the μ dependence found for the hadroproduction of a 100 GeV top quark in leading and non-leading order. The inclusion of the higher order terms leads to a stabilisation of the theoretical prediction with respect to changes in μ. The situation for the bottom quark is quite different. In Fig. 9 the scale dependence of predicted bottom quark cross section is shown. The cross section is approximately doubled by the inclusion of the higher order corrections, which do nothing to improve the stability of the prediction under changes of μ. It is apparent that the prediction of bottom production at collider energies is subject to considerable uncertainty.

I now turn to the question of flavour excitation. A flavour excitation diagram is one in which the heavy flavour is considered to reside already in the incoming hadron. It is excited by a gluon from the other hadron and appears on shell in the final state. An example of a flavour excitation diagram is shown in Fig. 10a. Note that in calculating the flavour excitation contribution the incoming heavy quark is treated as it were on its mass shell. If we denote the momentum transfer between the two incoming partons as q, the parton cross section will contain

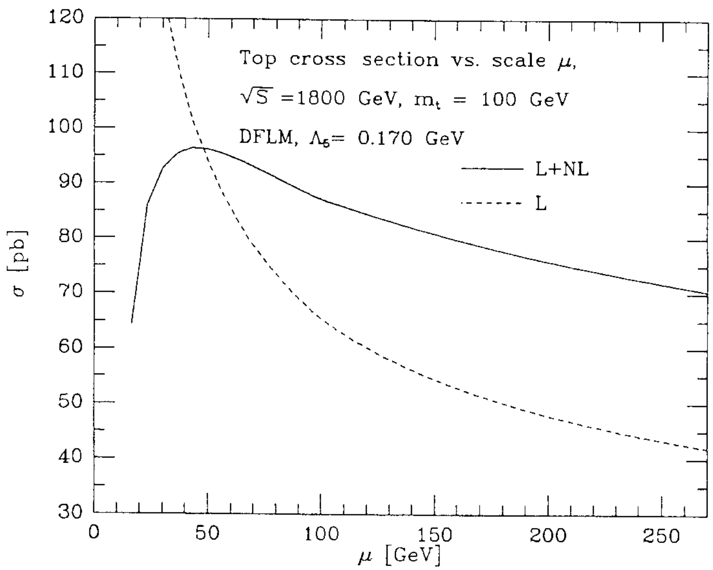

Figure 8: Scale dependence of the top quark cross section in second and third order.

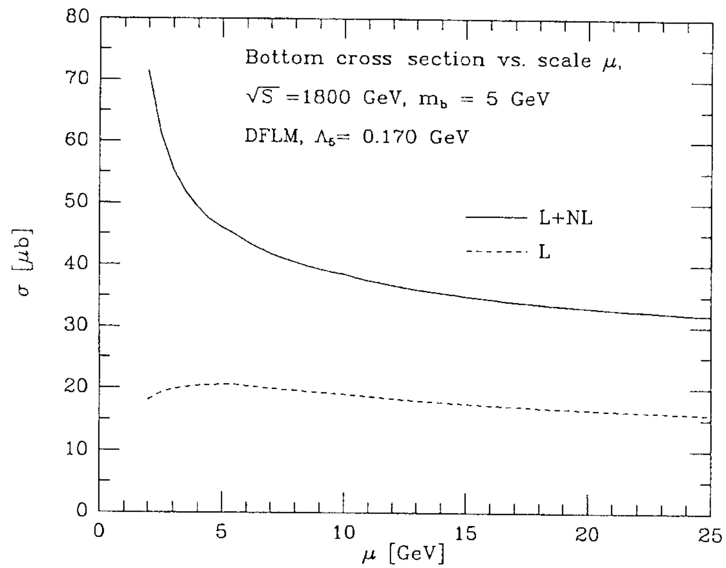

Figure 9: Scale dependence of the bottom quark cross section in second and third order.

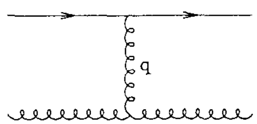

a) Example of flavour excitation graph

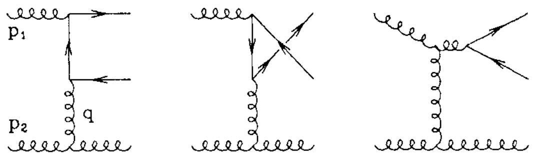

b) Graphs containing spin-one exchange in the t-channel

Figure 10: Graphs relevant for discussion of flavour excitation.

a factor $1/q^4$ coming from the propagator of the exchanged gluon. Therefore these graphs appear to be sensitive to momentum scales all the way down to the hadronic size scale. This casts doubt on the applicability of perturbative QCD to these processes.

In the following I shall sketch an analysis[8] which leads to an important conclusion. When considering the total cross section, flavour excitation contributions should not be included. The net contribution of these sorts of diagrams are already included as higher order corrections to the gluon-gluon fusion process. This analysis begins from the observation that the flavour excitation graph is already present as a subgraph of the first two diagrams shown in Fig. 10b. Does the flavour excitation approximation accurately represent the results of these diagrams? In particular is the $1/q^4$ pole, which is the signature of the presence of the flavour excitation diagrams, present in these diagrams?

I shall now indicate why the $1/q^4$ behaviour is not present in the sum of all three diagrams indicated in Fig. 10b. Let us denote the 'plus' and 'minus' components of any vector q as follows,

$$q^+ = q^0 + q^3, \quad q^- = q^0 - q^3, \quad q^2 = q^+ q^- - q_T . q_T . \tag{1.34}$$

We choose the upper incoming parton in Fig. 10b to be directed along the 'plus' direction, $p_1 = p_1^+$ and the lower incoming parton to be directed along the 'minus' direction, $p_2 = p_2^-$. In the small q^2 region the 'plus' component of q is small, because the lower final state gluon is on shell

$$(p_2 - q)^2 = 0, \quad q^+ = \frac{q^2}{2p_2^-} \tag{1.35}$$

since in the centre-of-mass system $p_1^+ \approx p_2^- \approx \sqrt{S}$. In the low q^2 region the 'minus' component of q is determined from the condition that production is close to threshold.

$$(p_1 + q)^2 \approx 4m^2, \quad q^- \approx \frac{m^2}{p_1^+}, \text{ where} \tag{1.36}$$

q^- is therefore also small in the fragmentation region in which $p_1^+ \approx \sqrt{S}$. We therefore find that in the fragmentation region of upper incoming hadron,

$$q^2 = q^+ q^- - q_T . q_T \approx -q_T . q_T . \tag{1.37}$$

The current J to which the exchanged gluon of momentum q couples is determined by the upper part of the three diagrams. In the fragmentation region only the 'plus' component is large:

$$q^\mu J_\mu = q^+ J^- + q^- J^+ - q_T.J_T = 0, \quad J^+ \approx \frac{q_T.J_T}{q^-} \tag{1.38}$$

where the Ward identity is a property of the sum of all three diagrams. The explicit term proportional to q_T in the amplitude shows that one power of the $1/q^2$ is cancelled in the amplitude squared.

This cancellation only occurs when the soft approximation to J^+ is valid. This requires the terms quadratic in q to be small compared to the terms linear in q in the denominators in the upper parts of the diagrams in Fig. 10b. The momentum q^- must not be too small:

$$q^2 < 2p^+ q^- \approx m^2. \tag{1.39}$$

We therefore expect the soft approximation to be valid and some cancellation to occur when $q^2 < m^2$. For further details I refer the reader to Ref. [8]. The calculation of Ref. [11] provides an explicit verification of this cancellation in the total cross section.

1.5 Heavy quarks in jets

A question of experimental interest is the frequency with which heavy quarks are found amongst the decay products of a jet. Since hadrons containing heavy quarks have appreciable semi-leptonic branching ratios such events will often lead to final states with leptons in jets. If we wish to use lepton plus jet events as a signature for new physics we must understand the background due to heavy quark production and decay.

This issue is logically unrelated to the total heavy quark cross section. As discussed above the total cross section is dominated by events with a small transverse energy of the order of the quark mass. Jet events inhabit a different region of phase space since they contain a cluster of transverse energy $E_T \gg m_c, m_b$. This latter kinematic region gives a small contribution to the total heavy quark cross section. A gluon decaying into a heavy quark pair must have a virtuality $k^2 > 4m^2$ so perturbative methods should be applicable for a sufficiently heavy quark. The number of $Q\bar{Q}$ pairs per gluon jet is calculable[13] using diagrams such as the one shown in Fig. 11. The calculation has two parts. Firstly one has to calculate $n_g(E^2, k^2)$, the number of gluons of off-shellness k^2 inside the original gluon with off-shellness E^2. Secondly, one needs the transition probability of a gluon with off-shellness k^2 to decay to a pair of heavy quarks.

The number of gluons of mass squared k^2 inside a jet of virtuality E^2 is given by,

$$n_g(E^2, k^2) = \left[\frac{\ln(E^2/\Lambda^2)}{\ln(k^2/\Lambda^2)}\right]^a \frac{\exp\sqrt{[(2N_c/\pi b)\ln(E^2/\Lambda^2)]}}{\exp\sqrt{[(2N_c/\pi b)\ln(k^2/\Lambda^2)]}} \tag{1.40}$$

where

$$a = -\frac{1}{4}\left[1 + \frac{2n_f}{3\pi b}(1 - \frac{V}{2N_c^2})\right] \tag{1.41}$$

and b is the first order coefficient in the expansion of the β function, Eq. 1.32. The correct calculation of the growth of the gluon multiplicity Eq. 1.40 requires the imposition of the angular ordering constraint which takes into account the coherence of the emitted soft gluons[14].

$R_{Q\bar{Q}}$ is the number of $Q\bar{Q}$ pairs per gluon jet. Ignoring for the moment gluon branching calculated above, we obtain:

$$R_{Q\bar{Q}} = \frac{1}{4\pi}\int_{4m^2}^{E^2} \frac{dk^2}{k^2}\alpha_S(k^2) \int_{z_-}^{z_+} dz \left[z^2 + (1-z)^2 + \frac{2m^2}{k^2}\right] \tag{1.42}$$

where the integration limits are given by $z_\pm = (1 \pm \beta)/2$ with $\beta = \sqrt{(1 - 4m^2/k^2)}$. The term $(z^2 + (1-z)^2)/2$ is recognisable as the familiar Altarelli-Parisi branching probability for massless quarks. Integrating over the longitudinal momentum fraction z we obtain,

$$R_{Q\bar{Q}} = \frac{1}{6\pi}\int_{4m^2}^{E^2} \frac{dk^2}{k^2}\alpha_S(k^2)\left[1 + \frac{2m^2}{k^2}\right]\sqrt{1 - \frac{4m^2}{k^2}}\ . \tag{1.43}$$

The final result including gluon branching for the number of heavy quark pairs per gluon jet is,

$$R_{Q\bar{Q}} = \frac{1}{6\pi}\int_{4m^2}^{E^2} \frac{dk^2}{k^2}\alpha_S(k^2)\left[1 + \frac{2m^2}{k^2}\right]\sqrt{1 - \frac{4m^2}{k^2}}\ n_g(E^2, k^2)\ . \tag{1.44}$$

The predicted number of charm quark pairs per jet is plotted in Fig. 12 using a value of $\Lambda^{(3)} = 300$ MeV and three values of the charm quark mass. Also shown

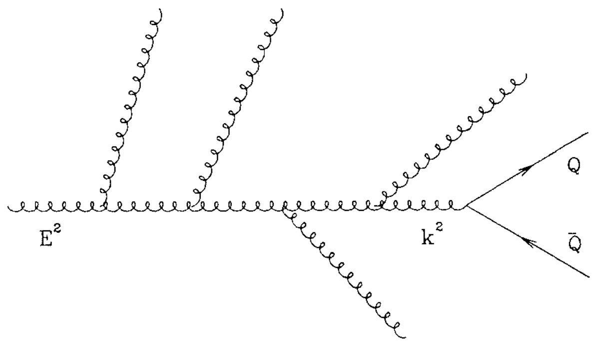

Figure 11: Heavy quark production in jets.

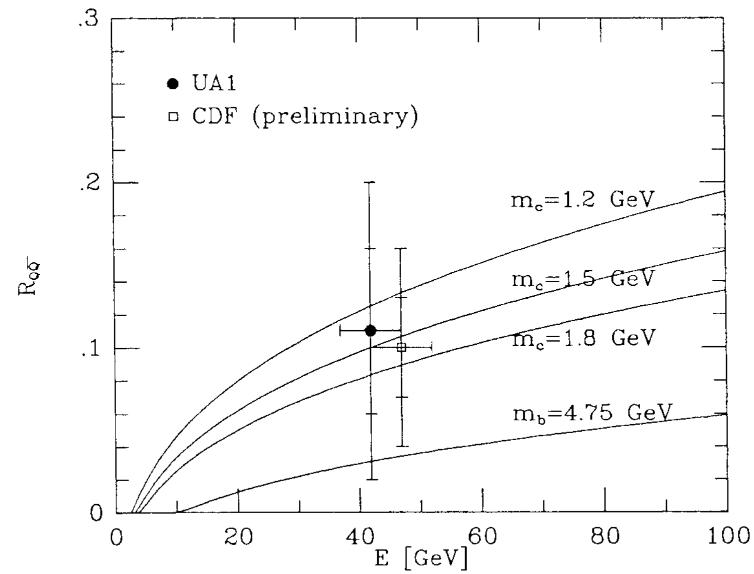

Figure 12: Heavy quarks in jets compared with UA1 and CDF data.

plotted is the number of bottom quarks per jet with $\Lambda^{(4)} = 260$ MeV. The data point shows the number of D^* per jet as measured by the UA1 collaboration[15] and by the CDF collaboration[16]. Note that these results depend on the values used for the branching ratios ($D^* \to D\pi$) and ($D \to K\pi$). CDF uses the values of the Mark III collaboration [17] whereas UA1 uses the values quoted by the Particle Data Group. In order compare these numbers with the $c\bar{c}$ pair rates, a model of the relative rates of D and D^* production is also needed. For example, if all spin states are produced equally one would expect the charged D^* rate to be 75% of the total D production rate. The points in Fig. 12 needed to corrected upward for unobserved modes before they can be compared with the curves for the total $c\bar{c}$ pair rate.

2. Lecture 2

2.1 Phenomenological predictions

In this second lecture I will illustrate the application of Eqs. 1.1 and 1.2 to the production of hadrons containing heavy quarks. It is evident that in order to have a reliable estimate of the cross section one needs information on the running coupling, the form of the parton distributions and a calculation of the short distance cross section as a perturbation series in the coupling constant.

To give an idea of the order of magnitude uncertainty to be expected in these estimates, I show a partial compilation[18] of coupling constant measurements in Fig. 13. Also shown plotted is the expected theoretical form for several values of the QCD parameter Λ. By convention α_S is determined from the QCD parameter Λ by the following solution of Eq. 1.32.

$$\alpha_S(\mu) = \frac{1}{b\ln(\mu^2/\Lambda^2)}\left[1 - \frac{b'}{b}\frac{\ln\ln(\mu^2/\Lambda^2)}{\ln(\mu^2/\Lambda^2)} + \ldots\right]. \tag{2.1}$$

b and b', which are also given in Eq. 1.32, depend on the number of active light flavours. Consequently Λ also depends on the number of active flavours. The relationship between the values of Λ for different numbers of flavours can be determined by imposing the continuity of α_S at the scale $\mu = m$, where m is the mass of the heavy quark. Here Λ is the QCD parameter in the $\overline{MS}$ renormalisation scheme with five active flavours. It is apparent from Fig. 13, that the value of α_S

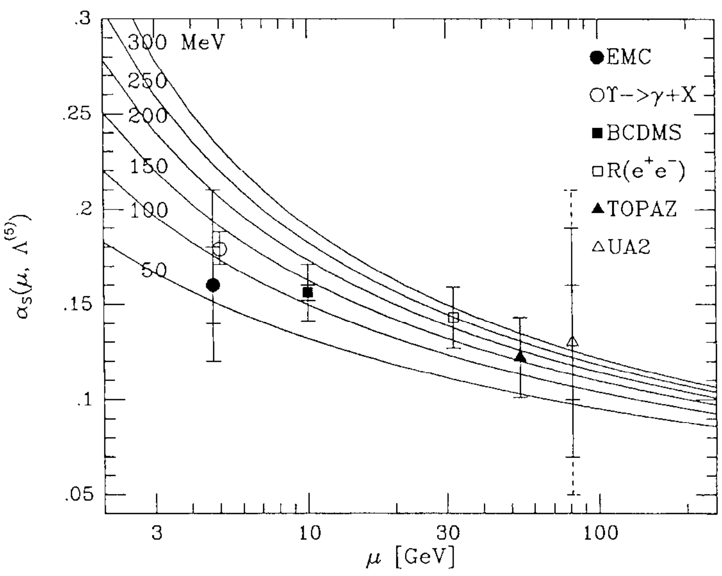

Figure 13: Behaviour of the running coupling.

is still subject to a considerable uncertainty. For definiteness I shall consider Λ to lie in the following range,

$$100 \text{ MeV} < \Lambda^{(5)} < 250 \text{ MeV} \tag{2.2}$$

but clearly other less restrictive interpretations of the data are possible. With this spread in the value of Λ the variation of α_S at $\mu = 100$ GeV is as follows,

$$0.104 < \alpha_S(\mu = 100 \text{ GeV}) < 0.118. \tag{2.3}$$

The uncertainty in α_S is larger at lower values of μ. It appears squared in any estimate of the heavy quark cross section.

The extraction of Λ from deep inelastic scattering is correlated with the form assumed for the gluon distribution function. A given set of data can be described by a stiff gluon distribution function and a large value of Λ, or by a softer gluon distribution and a smaller value of Λ. In order to make an estimate of the uncertainty due to the form of the gluon distribution function, I shall use three sets of distribution functions due to Diemoz, Ferroni, Longo and Martinelli[19]. These distribution functions have $\Lambda^{(5)} = 100$, 170 and 250 MeV and appropriately correlated gluon distribution functions.

The value of the heavy quark mass is the principal parameter controlling the size of the cross section. This dependence is much more marked than the $1/m^2$ dependence in the short distance cross section expected from Eq. 1.14. As the mass decreases, the value of x at which the structure functions must be supplied becomes smaller (*cf.* Eq. 1.9) and the cross section rises because of the growth of the parton flux.

The approach which I shall take to the estimate of theoretical errors in heavy quark cross sections is as follows[20]. I shall take Λ to run in the range given by Eq. 2.2 with corresponding variations of the gluon distribution function. I shall arbitrarily choose to vary the parameter μ in the range $m/2 < \mu < 2m$ to test the sensitivity to μ. Lastly, I shall consider quark masses in the ranges,

$$\begin{aligned} 1.2 &< m_c < 1.8 \text{ GeV} \\ 4.5 &< m_b < 5.0 \text{ GeV}\,. \end{aligned} \tag{2.4}$$

I shall consider the extremum of all these variations to give an estimate of the theoretical error.

We immediately encounter a difficulty with this procedure in the case of charm. Variations of μ down to $m/2$ will carry us into the region $\mu < 1$ GeV in which we certainly do not trust perturbation theory. An estimate of the theoretical error on charm production cross sections is therefore not possible. In preparing the curve for charm production I have taken the lower limit on μ variations to be 1 GeV.

The dependence on the value chosen for the heavy quark mass is particularly acute for the case of charm. In fact, variations due to plausible changes in the quark mass, Eq. 2.4, are bigger than the uncertainties due to variations in the other parameters. I shall therefore take the aim of studies of the hadroproduction and photoproduction of charm to be the search for an answer to the following question. Is there a reasonable value for the charm quark mass which can accommodate the majority of the data on hadroproduction? In Fig. 14 I show the theoretical prediction for charm production. Note the large spread in the prediction. Also shown plotted is a compilation of data taken from Ref. [21] which suggests that a value of $m_c = 1.5$ GeV gives a fair description of the data on the hadroproduction of D's. After inclusion of the $O(\alpha_S^3)$ corrections, the data can be explained without recourse to very small values of the charmed quark mass[20].

This conclusion is further reinforced by consideration of the data on photoproduction of charm. The higher order corrections to photoproduction $O(\alpha\alpha_S^2)$ have been considered in Ref. [22]. After inclusion of these higher order terms we obtain predictions for the total cross section as a function of the energy of the tagged photon beam. The principal uncertainty derives from the value of the heavy quark mass, so I have plotted the minimum cross section which is obtained by varying Λ and the scale μ within the range 1 GeV $< \mu < 2m$ for three values of the charm quark mass. The comparison with the data on the photoproduction of charm[23,24], shown in Fig. 15, indicates that charm quark masses smaller than 1.5 GeV do not give an acceptable explanation of the data.

In conclusion within the large uncertainties present in the theoretical estimates, the $D/\bar{D}$ production data presented here can be explained with a mass of the order of 1.5 GeV. This is not true of all data on the hadroproduction of charm, especially the older experiments. For a review of the experimental situation I refer the reader to Ref. [25].

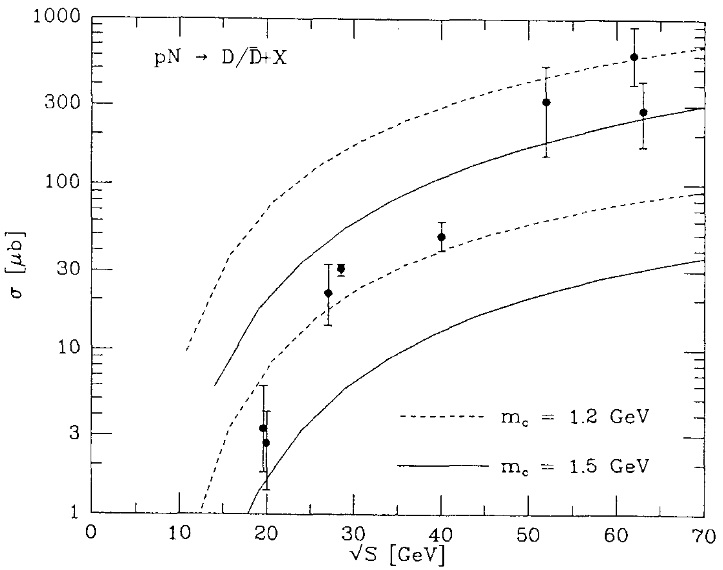

Figure 14: Data on hadroproduction of $D/\bar{D}$ compared with theory.

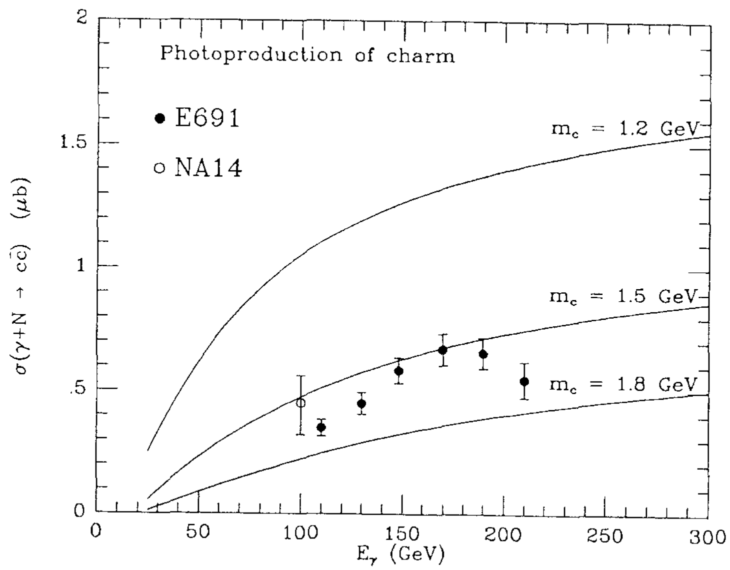

Figure 15: Data on photoproduction of charm compared with theoretical lower limits.

2.2 Results on the production of bottom quarks

The theoretical prediction of bottom quark production is very uncertain at collider energies. This has already been briefly mentioned in the discussion of Fig. 9. The cause of this large uncertainty is principally the very small value of x at which the parton distributions are probed. In fact, at present collider energies the bottom cross section is sensitive to the gluon distribution function at values of $x < 10^{-2}$. Needless to say the gluon distribution function has not been measured at such small values of x. An associated problem is the form of the short distance cross section in the large s region. The lowest order short distance cross sections, $\mathcal{F}^{(0)}$, given in Eq. 1.17, tend to zero in the large s region. This is a consequence of the fact that they also involve at most spin $\frac{1}{2}$ exchange in the t-channel as shown in Fig. 2. The higher order corrections to gg and gq processes have a different behaviour because they involve spin 1 exchange in the t-channel. The relevant diagrams are shown in Fig. 10b. In the high energy limit they tend to a constant[11]. Naturally these high s contributions are damped by the small number of energetic gluons in the parton flux, but at collider energies the region $\sqrt{s} \gg m$ makes a sizeable contribution to bottom cross section. The fact that this constant behaviour is present in both $\mathcal{F}^{(1)}$ and $\overline{\mathcal{F}}^{(1)}$ indicates the sensitivity of the size of this term to the value chosen for μ. There is therefore an interplay between the size of this term and the small x behaviour of the gluon distribution function.

At fixed target energies the cross section for the production of bottom quarks is theoretically more reliable. The μ dependence plot has a characteristic form similar to Fig. 8 and it is possible to make estimates of the theoretical errors. A compilation of theoretical results[26] and estimates of the associated theoretical error is shown in Table 2. The experimental study of the production of bottom quarks in hadronic reactions is still in its infancy, but Table 2 also includes the limited number of experimental results on total bottom production cross sections.

The calculations of Ref.[11] also allow us to examine the p_T and rapidity distributions of the one heavy quark inclusive cross sections. Although the prediction of the total cross section at collider energy is uncertain, it is plausible that the shape of the transverse momentum and rapidity distributions is well described by the form found in lowest order perturbation theory. The supporting evidence [31] for this conjecture is shown in Fig. 16, which demonstrates that the inclusion of the first non-leading correction does not significantly modify the shape of the transverse momentum and rapidity distributions. At a fixed value of μ, the two curves lie on top of one another if the lowest order is multiplied by a constant factor. Similar results hold also for the shape of the top quark distribution[31]. The UA1 collaboration have provided experimental information on the transverse distribution of the produced bottom quarks. In Fig. 17 comparison of the full α_S^3 prediction with UA1 data is made. The data is plotted as a function of the lower cutoff on the transverse momentum of the b quark. At lower values of k the agreement is satisfactory, but the experimental points lie somewhat above the theoretical curve at high k. It would be nice to have an independent confirmation of this experimental result. An inability to predict the value of the bottom cross section for large transverse momenta p_T, casts doubt on our ability to predict the top quark cross section for $m_t \approx p_T$. However in view of the difficulties of the experimental analysis, this discrepancy is probably not yet a cause for alarm.

The corresponding prediction for the shape of the bottom production cross section at the Tevatron is shown in Fig. 18.

m_b [GeV]	σ (theory)	Theoretical error	Experimental data
$\sqrt{S}$ = 41 GeV, pp			
4.5	23 nb	+21 -15	
5.0	9 nb	+8.4 -5.9	
$\sqrt{S}$ = 62 GeV, pp			
4.5	142 nb	+98 -80	BCF[27], $150 < \sigma < 500$ nb
5.0	66 nb	+47 -38	
$\sqrt{S}$ = 630 GeV, $p\bar{p}$			
4.5	19 μb	+10 -8	UA1[28], 10.2±3.3 μb
5.0	12 μb	+7 -4	
$\sqrt{S}$ = 24.5 GeV, πN			
4.5	7.6 nb	+4.7 -3.8	WA78[29], $\sqrt{S}$= 24.5 GeV, 2 ±0.3±0.9 nb
5.0	3.1 nb	+1.5 -1.5	NA10[30], $\sqrt{S}$= 23 GeV, 14+7-6 nb

Table 2: Cross section for bottom production at various energies.

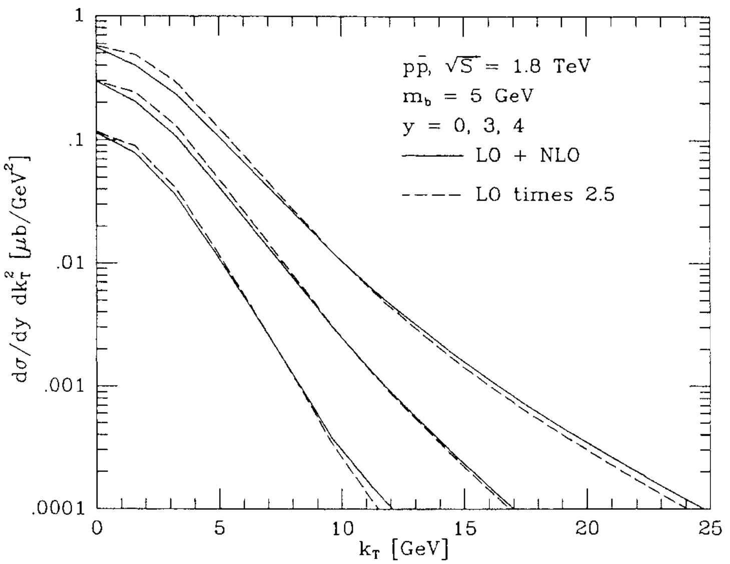

Figure 16: The shape of the cross section for bottom quark production.

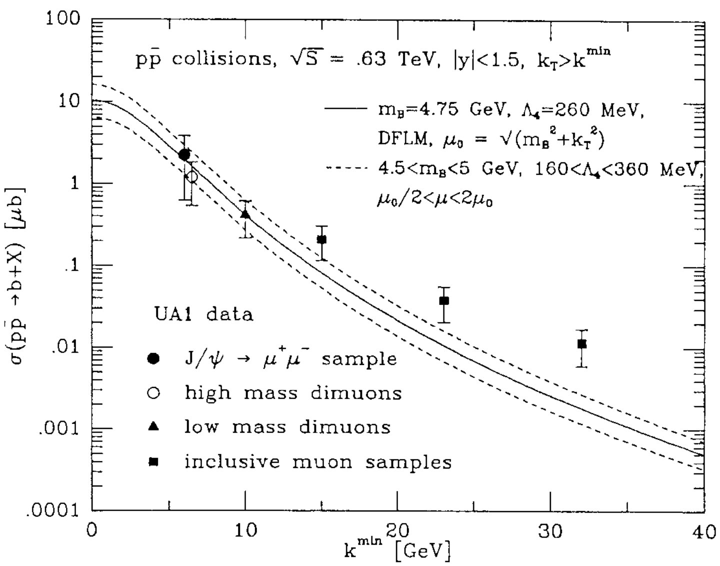

Figure 17: The cross section for bottom quark production at CERN energy.

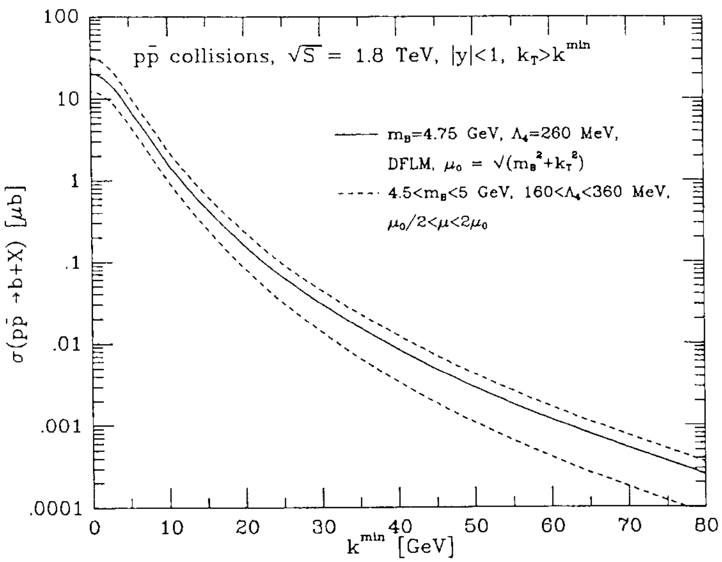

Figure 18: The cross section for bottom quark production at FNAL energy.

2.3 Decays of the top quark

Consider first of all the decay of a very massive top quark which decays into an on-shell W-boson and a b-quark. The process has a semi-weak rate. In the limit in which $m_t \gg m_W$ the width is given by,

$$\Gamma(t \to bW) = \frac{G_F m_t^3}{8\pi\sqrt{2}} |V_{tb}|^2 \approx 170 \text{ MeV} |V_{tb}|^2 \left(\frac{m_t}{m_W}\right)^3 . \tag{2.5}$$

When the top quark is so heavy that the width becomes bigger than a typical hadronic scale the top quark decays before it hadronises. Mesons containing the top quark are never formed.

This should be compared with the conventional top quark decay for $m_t < m_W - m_b$ which is a scaled up version of μ decay,

$$\Gamma(t \to be\bar{\nu}) = \frac{G_F^2 m_t^5}{192\pi^3} |V_{tb}|^2 \approx 2.3 \text{ keV} |V_{tb}|^2 \left(\frac{m_t}{40\text{GeV}}\right)^5 . \tag{2.6}$$

The top branching ratio to leptons is given in the simplest approximation by counting modes for the W decay. Assuming the decay channel to $t\bar{b}$ is forbidden because $m_t > m_W - m_b$, the branching ratio is given by counting over the decay modes $e\bar{\nu}_e$, $\mu\bar{\nu}_\mu$, $\tau\bar{\nu}_\tau$ and three colours of $u\bar{d}$ and $c\bar{s}$:

$$\text{BR}(W^+ \to e^+\bar{\nu}) = \frac{1}{3+3+3} \approx 11\% . \tag{2.7}$$

It is important to investigate unconventional decays of the top quark, especially if they alter the branching ratio into the leptonic decay mode. The leptonic decay mode is the basis of most searches for the top quark. A simple extension of the standard model involves the introduction of a second Higgs doublet. Top quark decay in this model has been investigated in Ref. [32]. In order to avoid strangeness changing neutral currents[33] one must couple all quarks of a given charge to only one Higgs doublet. After spontaneous symmetry breaking we are left with one charged physical Higgs and three neutral Higgs particles. The dominant decay mode of the top quark is not to a leptonic mode, but rather to the charged Higgs,

$$\Gamma(t \to b\eta^+) > \frac{1}{4\pi v}\frac{m_b}{m_t^2}(m_t^2 + m_b^2 - m_\eta^2 + 2m_t m_b)\lambda(m_t, m_b, m_\eta) \tag{2.8}$$

where v is the normal vacuum expectation value and $\lambda(a,b,c) = \sqrt{((a^2 - b^2 - c^2)^2 - 4b^2c^2)}$. In turn, the η^+ decays predominantly to $c\bar{s}$ and $\tau\nu_\tau$. If the vacuum expectation value of the two Higgs fields is taken to be equal the branching fraction into $c\bar{s}$ is found to be 64% and $\tau\nu_\tau$ is 31%[32].

2.4 The search for the top quark

The belief that the top quark must exist is based both on theoretical and experimental evidence. The theoretical motivation is that complete families are required for the cancellation of anomalies in the currents which couple to gauge fields. Hence the partner of the b, τ and ν_τ must exist to complete the third family.

An anomaly occurs in a theory because symmetries present at the classical level are destroyed by quantum effects. They typically involve contributions to the divergence of a current which is conserved at the classical level. If the gauge currents are anomalous, the Ward identities, which are vital for the proof that the gauge theory is renormalisable, are destroyed.

Anomalies occur in the simple triangle diagram with two vector currents and one axial vector current. Elimination of the anomalies for a particular current in the lowest order triangle diagram is sufficient to ensure that the current remains anomaly free, even after the inclusion of more complicated diagrams. If the currents which interact at the three corners of the triangle couple to the matrices L^a, L^b and L^c for the left-handed fields, and to the matrices R^a, R^b and R^c for the right-handed fields, the vector-vector-axial vector triangle anomaly is proportional to,

$$A = \mathrm{Tr}\,[R^a\{R^b, R^c\}] - \mathrm{Tr}\,[L^a\{L^b, L^c\}]. \tag{2.9}$$

For the specific case of the $SU(2)_L \times U(1)$ theory of Weinberg and Salam we have the following weak isospin and hypercharge assignments for the third family ($Q = T_3 + Y$),

$$\begin{aligned}
&t_L,\ T_3 = \tfrac{1}{2}, Y_L = \tfrac{1}{6}, \qquad && t_R,\ T_3 = 0,\ Y_R = \frac{2}{3}, \\
&b_L,\ T_3 = -\tfrac{1}{2}, Y_L = \tfrac{1}{6}, && b_R,\ T_3 = 0,\ Y_R = -\frac{1}{3}, \\
&\nu_L,\ T_3 = \tfrac{1}{2}, Y_L = -\tfrac{1}{2} && \\
&\tau_L,\ T_3 = -\tfrac{1}{2}, Y_L = -\tfrac{1}{2}, && \tau_R,\ T_3 = 0,\ Y_R = -1.
\end{aligned} \tag{2.10}$$

Substituting these couplings into Eq. 2.9, with all combinations of the $SU(2)$ matrices T^a or the $U(1)$ matrices Y we obtain the form of the anomaly for the gauge currents of the Weinberg-Salam theory. Two of the resulting traces of the couplings vanish for each fermion separately,

$$\mathrm{Tr}\, T^a\{T^b, T^c\} = 0, \ \ \mathrm{Tr}\, T^a\{Y_L, Y_L\} = 0\,. \tag{2.11}$$

The other two traces vanish only for a complete family[35]

$$\mathrm{Tr}\,(Y_R^3 - Y_L^3) = 0, \ \ \mathrm{Tr}\, Y_L\{T^a, T^b\} = 0\,. \tag{2.12}$$

It should be noted that there are still anomalies in global (non-gauged) currents in the Weinberg-Salam model. For example the normal isospin current corresponding to a global symmetry (in the absence of quark masses) is anomalous. It is this anomaly which is responsible for π^0 decay.

The experimental reason to believe in the existence of the top quark is the measurement of the weak isospin of the bottom quark. The forward backward asymmetry of b-jets in e^+e^- annihilation[34] is controlled by $a_e a_b$, the product of the axial vector coupling to the electron and the b quark. The produced b and $\bar{b}$ quarks are identified by the sign of the observed muons to which they decay. The measurement is therefore subject to a small correction due to $B^0 - \bar{B}^0$ mixing. Assuming that the axial coupling to the electron has its standard value the measured weak isospin of the left-handed b quark is[34],

$$T_3 = -0.5 \pm 0.1\,. \tag{2.13}$$

The simplest hypothesis is that the bottom quark is in an $SU(2)$ doublet with the top quark, although more complicated schemes are certainly possible.

Thus assured that the top quark exists, we must only find it. The expected cross section for the process

$$p + \bar{p} \to t + \bar{t} + X \tag{2.14}$$

is shown in Fig. 19. The cross section is calculated using the full $O(\alpha_S^3)$ calculation of [11] and the method of theoretical error estimate described in the previous sections, (*cf.* [20]). In addition, production of top quarks through the decay chain $W \to t\bar{b}$ is also shown. Note the differing proportions of the two

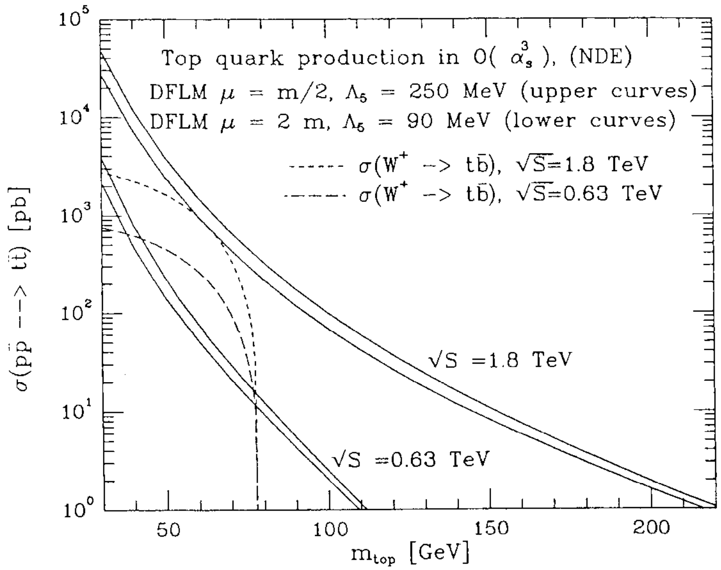

Figure 19: The cross section for top quark production at CERN and FNAL.

modes at CERN and FNAL energies. At $\sqrt{S} = 1.8(0.63)$ TeV the $t\bar{t}$ production is predominantly due to gluon-gluon annihilation for $m_t < 100(40)$ GeV. On the other hand the W production comes mainly from $q\bar{q}$ annihilation at both energies. This explains the more rapid growth with energy of the $t\bar{t}$ production shown in Fig. 19.

From Fig. 19 the range of top quark masses which can be investigated in current experiments can be derived. In a sample of 5 inverse picobarns about 2500 $t\bar{t}$ pairs will be produced if the top quark has a mass of 70 GeV. One can observe the decays of the top quark to the $e\mu$ channel or to the $e+$ jets channel. With a perfect detector the numbers of events expected is,

$$\begin{aligned} \text{Number of } e\mu \text{ events} &= \quad 2 \times .11 \times .11 \times 2500 \approx 50 \\ \text{Number of e + jet events} &= \quad 2 \times .11 \times .66 \times 2500 \approx 300 \end{aligned} \tag{2.15}$$

The e plus jets channel gives a more copious signal and does not require muon detection, but the background is larger due to the process $p\bar{p} \to W + jets$. This background may become less severe with increasing top mass as the jets present in top decay become more energetic.

Let us assume that a limit of about 80 GeV will be set with the data from the 1988-1989 collider run. If the efficiency of extracting the signal from the data does not change with the mass of the top quark, we can expect to improve the limit by an additional 40 GeV above the present limit, by increasing the luminosity accumulated at the Tevatron by a factor of 10. Note however that the efficiency of the $e+$ multi-jets channels will increase for a heavier top quark. As the mass of the top quark increases the b quark jets occurring in its decay will be recognised in the detector as fully-fledged jets. This occurs with no extra price in coupling constants. The background due to normal W+jets production is suppressed by a power of α_S for every extra jet. It will become less important if we look in the channel with an electron and three and four jets.

References

[1] R. P. Feynman, Photon Hadron Interactions, W. A. Benjamin, Reading, Mass (1972).

[2] I. Hinchliffe, these proceedings.

[3] R. K. Ellis, Proceedings of the 1987 Theoretical Advanced Study Institute in Elementary Particle Physics, edited by R. Slansky and G. West, (World Scientific).

[4] G. Altarelli and G. Parisi, *Nucl. Phys.* **B126** (1977) 298 .

[5] M. Gluck, J.F. Owens and E. Reya, *Phys. Rev.* **D17** (1978) 2324 ;
B. Combridge, *Nucl. Phys.* **151** (1979) 429 .

[6] R. K. Ellis, *Strong Interactions and Gauge Theories,* edited by J. Tran Thanh Van, Editions Frontières, Gif-sur-Yvette, 1986, p. 339.

[7] J. D. Bjorken and S. D. Drell, Relativistic Quantum Fields, McGraw Hill, New York (1964).

[8] J. C. Collins, D. E. Soper and G. Sterman, *Nucl. Phys.* **B263** (1986) 37 .

[9] S. J. Brodsky, J. C. Collins, S.D. Ellis, J. F. Gunion and A. H. Mueller, in *Proc. 1984 Summer Study on the Design and Utilization of the Superconducting Super Collider*, Fermilab, Batavia, Illinois, 1984, p. 227.

[10] S. J. Brodsky, J. F. Gunion and D. E. Soper, *Phys. Rev.* **D36** (1987) 2710 .

[11] P. Nason, S. Dawson and R. K. Ellis, *Nucl. Phys.* **B303** (1988) 607 .

[12] W. Beenakker *et al.*, *Phys. Rev.* **D40** (1989) 54 .

[13] A. H. Mueller and P. Nason, *Phys. Lett.* **157B** (1985) 226 .

[14] A. Bassetto, M. Ciafaloni and G. Marchesini, *Phys. Rep.* **100** (1983) 201 and references therein.

[15] M. Ikeda, Proceedings of the 8th Topical Workshop on Proton Antiproton Collider Physics,Castiglione della Pescaia (1989).

[16] F. Abe *et al.*, Fermilab preprint, Fermilab-PUB-89/171-E, (1989).

[17] J. Adler *et al.*, *Phys. Lett.* **208B** (1988) 152 ;
J. Adler *et al.*, *Phys. Rev. Lett.* **60** (1988) 89 .

[18] R. K. Ellis, Proceedings of the XXIV Conference on High Energy Physics, Munich, August 1988.

[19] M. Diemoz *et al.*, *Zeit. Phys.* **C39** (1988) 21 .

[20] G. Altarelli *et al.*, *Nucl. Phys.* **B308** (1988) 724 .

[21] U. Gasparini, Proceedings of the XXIV Conference on High Energy Physics, Munich, August 1988.

[22] R. K. Ellis and P. Nason, *Nucl. Phys.* **B312** (1989) 551 .

[23] J. C. Anjos *et al.*, *Phys. Rev. Lett.* **62** (1989) 513 .

[24] R. Forty, Proceedings of the XXIV Conference on High Energy Physics, Munich, August 1988.

[25] S. P. K. Tavernier, *Rep. Prog. Phys.* **50** (1987) 1439 .

[26] P. Nason, Proceedings of the XXIV Conference on High Energy Physics, Munich, August 1988.

[27] L. Cifarelli *et al.*, (BCF collaboration) *Nucl. Phys.* **Proc. Suppl. 1B** (1988) 55.

[28] C. Albajar *et al.*, *Zeit. Phys.* **C37** (1988) 505 ;
C. Albajar *et al.*, *Phys. Lett.* **B213** (1988) 405 .

[29] M. G. Catanesi *et al.*, (WA78 collaboration), *Phys. Lett.* **202B** (1988) 453.

[30] P. Bordalo *et al.*, (NA10 collaboration), *Zeit. Phys.* **C39** (1988) 7 .

[31] P. Nason, S. Dawson and R. K. Ellis, preprint FERMILAB-Pub-89/91-T, *Nucl. Phys. B* (in press).

[32] S. Glashow and E. Jenkins, *Phys. Lett.* **196B** (1987) 233 .

[33] S. Glashow and S. Weinberg, *Phys. Rev.* **D15** (1977) 1958 .

[34] S. L. Wu, Proceedings of the Lepton Photon Symposium, Hamburg, August 1987;
W. Bartel *et al.*, *Phys. Lett.* **146B** (1984) 437.

[35] C. Bouchiat, J. Iliopoulos and P. Meyer, *Phys. Lett.* **38B** (1972) 519 ;
D. J. Gross and R. Jackiw, *Phys. Rev.* **D6** (1972) 477 .

ssi89-003

SLAC–PUB–5219
March 1990
E/T

Precision Experiments in Electroweak Interactions*

MORRIS L. SWARTZ

Stanford Linear Accelerator Center
Stanford University, Stanford, California, 94309

Presented at the Seventeenth SLAC Summer Institute:
Physics at the 100 GeV Mass Scale,
Stanford Ca., July 10-21, 1989

⋆ Work supported by the Department of Energy, contract DE–AC03–76SF00515.

Table of Contents

1. Introduction

The electroweak theory of Glashow, Weinberg, and Salam (GWS) has become one of the twin pillars upon which our understanding of all particle physics phenomena rests. It is a brilliant achievement that qualitatively and *quantitatively* describes all of the vast quantity of experimental data that have been accumulated over some forty years. Note that the word *quantitatively* must be qualified. The low energy limiting cases of the GWS theory, Quantum Electrodynamics and the V−A Theory of Weak Interactions, have withstood rigorous testing. The high energy synthesis of these ideas, the GWS theory, has not yet been subjected to comparably precise scrutiny.

The recent operation of a new generation of proton-antiproton ($p\bar{p}$) and electron-positron (e^+e^-) colliders has made it possible to produce and study large samples of the electroweak gauge bosons $W^\pm$ and Z^0. We expect that these facilities will enable very precise tests of the GWS theory to be performed in the near future. In keeping with the theme of this Institute, *Physics at the 100 GeV Mass Scale*, these lectures will explore the current status and the near-future prospects of these experiments.*

* In other words, we will use the title of this school as an excuse to ignore the many lower-energy, neutral current tests of the GWS theory. The two lecture format of this presentation precludes a more exhaustive treatment of the field.

LECTURE I

2. Parameters of the Standard Model

The minimal Standard Model contains some 21 empirical parameters. They are listed in Table I with their approximate values.

Table I

Parameter	Description	Approximate Value
g_s	SU(3) coupling constant	1.3 @ 34 GeV
g	SU(2) coupling constant	0.63
g'	U(1) coupling constant	0.35
$\langle\phi\rangle$	VEV of the Higgs field	174 GeV
M_H	Higgs boson mass	?
m_{ν_e}	electron neutrino mass	< 12 eV
m_{ν_μ}	muon neutrino mass	< 0.25 MeV
m_{ν_τ}	tau neutrino mass	< 35 MeV
m_e	electron mass	0.511 MeV
m_μ	muon mass	106 MeV
m_τ	tau mass	1.78 GeV
m_u	up-quark mass	5.6 MeV
m_d	down-quark mass	9.9 MeV
m_s	strange-quark mass	199 MeV
m_c	charm-quark mass	1.35 GeV
m_b	bottom-quark mass	5 GeV
m_t	top-quark mass	?
$\sin\theta_{12}$	K-M Matrix parameter	0.217-0.223
$\sin\theta_{23}$	K-M Matrix parameter	0.030-0.062
$\sin\theta_{13}$	K-M Matrix parameter	0.003-0.010
$\sin\delta$	K-M Matrix parameter	?

The dynamics of electroweak *Physics at the 100 GeV Mass Scale* are determined (at tree level) by three of the parameters: the SU(2) coupling constant (g), the U(1) coupling constant (g'), and the vacuum expectation value of the Higgs field ($\langle\phi\rangle$). The complete specification of the electroweak sector of the Standard Model requires that all three parameters be *precisely* known. The values of these quantities are extracted from the measurement of three related quantities: the electromagnetic fine structure constant (α), the Fermi coupling constant (G_F), and the mass of the Z^0 boson (M_Z). The current values of these quantities are listed in Table II.

Table II

The current values of the physical parameters that determine the determine the electroweak sector of the Standard Model.

Quantity	EW Parameters	Current Value	Precision (PPM)
α	$\frac{1}{4\pi}\frac{g^2 g'^2}{g^2+g'^2}$	$[137.0359895(61)]^{-1}$	0.045
G_F	$\frac{1}{\langle\phi\rangle^2\sqrt{8}}$	$1.16637(2)\times10^{-5}$ GeV^{-2}	17
M_Z	$\sqrt{\frac{g^2+g'^2}{2}}\,\langle\phi\rangle$	91.16(3) GeV	320

The value of α is extracted from a very precise measurement of the anomalous magnetic moment of the electron.[1] The value of G_F is derived from the measured value of the muon lifetime.[2] The first precise measurements of the Z^0 mass have been made quite recently.[8] Although M_Z is determined with far less accuracy than are α and G_F, it is expected to remain the most well-determined Standard parameter for the foreseeable future. It is clear that the measurement of a fourth physical quantity should overconstrain the determination of the electroweak parameters. We should therefore be able to *test* the electroweak sector of the Standard Model.

Unfortunately, the expression given in Table II that relates M_Z to g, g', and $\langle\phi\rangle$ is valid only at tree-level. Since M_Z is measured at a substantially larger energy scale than are α and G_F, we must include virtual electroweak corrections in order to extract accurate values for the electroweak parameters. In principle, this requires a knowledge of all of the parameters listed in Table I. In practice, a dispersion relation is used to determine the dominant correction (due to low mass fermion loops) from the low energy e^+e^- total cross section. The largest remaining corrections depend upon the top quark mass (strongly) and the Higgs boson mass (weakly). A reasonably precise test of the Standard Model therefore requires at least two more experimental measurements (ideally a measurement of m_t would be one of them).

At high energies, all of the proposed tests of the Standard Model fall into one of two categories:

1. An improved measurement of the W boson mass,

$$M_W^2 = \frac{g^2}{2} \langle \phi \rangle^2 (1 + \delta_{RC}^W), \tag{2.1}$$

   where M_W is the W boson mass and δ_{RC}^W accounts for the virtual electroweak corrections.

2. A measurement of the ratio of the vector and axial vector parts of the Z^0 coupling to a fermion-antifermion ($f\bar{f}$) pair. The vector and axial vector coupling constants (v_f and a_f, respectively) are given by the following expression,

$$\begin{aligned} v_f &= \tau_3^f - 4Q_f \frac{g'^2}{g^2 + g'^2} \\ a_f &= -\tau_3^f \end{aligned} \tag{2.2}$$

   where τ_3^f is twice the third component of the fermion weak isospin and Q_f is the fermion charge.

The Standard Model tests that fall into the second category measure one combination of coupling constants. At tree-level, this combination is the well-known electroweak parameter $\sin^2\theta_w$,

$$\sin^2\theta_w = \frac{g'^2}{g^2 + g'^2}. \tag{2.3}$$

To good approximation, the virtual corrections that affect each quantity in the category can be absorbed into the definition of $\sin^2\theta_w$. We can therefore use the tree-level $\sin^2\theta_w$ sensitivities of the second-category quantities to compare their sensitivities to the electroweak parameters and loop corrections.

3. Experiments at Hadron Colliders

High energy physics, like most fields of scientific endeavor, follows trends that are determined as much by psychology as by logic. In the decade of the 1970's, the electron-positron collider was preeminent. The great success of the SPEAR storage ring at SLAC lead to the construction of larger projects at DESY, SLAC, Cornell, and KEK. The experimental program at the CERN ISR (which was the world's only hadron-hadron collider) was rather slow in hearing fruit and never did produce a major discovery.*

In the 1980's, the situation was somewhat reversed. The large program of moderate energy e^+e^- storage rings (25-60 GeV in the cm frame) produced no major discoveries.† On the other hand, the observation of the $W^\pm$ and Z^0 bosons at the CERN Sp$\bar{\text{p}}$S Collider provided fairly dramatic evidence that the GWS theory of electroweak interactions is substantially correct. This has lead to the great popularity of high energy hadron-hadron colliders and to the plans for the building of the SSC in the US and the LHC at CERN. Perhaps some discovery at SLC/LEP will cause the pendulum to swing the other way?

At the current time, there are two active hadron colliders in the world, the Sp$\bar{\text{p}}$S at CERN and the Tevatron collider at Fermilab. The parameters of the two machines are summarized in Table III. Note that substantial upgrades of the Tevatron collider are being proposed for the next several years.

⋆ The observation of large transverse momentum scattering processes did lend support, along with data from electron-nucleon scattering experiments, to the parton model of hadrons.

† The observation of an increased fraction of three-jet events in the total hadronic cross section was strong supporting evidence for Quantum Chromodynamics. The reader is requested to consider whether these data could have been termed *the discovery of the gluon* in the absence of a very detailed theory and several very detailed simulations.

Table III

Machine	Energy	Peak Luminosity	Integrated Luminosity
Sp$\bar{p}$S	630 GeV	3×10^{30}cm^{-2}sec^{-1}	6.7 pb^{-1}
Tev I	1.8 TeV	1×10^{30}cm^{-2}sec^{-1}	4.7 pb^{-1}
Tev I(1995)	1.8 TeV	5×10^{31}cm^{-2}sec^{-1}	300 pb^{-1}?

3.1. Experimental Details

There are four experiments that are active or in preparation at the Sp$\bar{p}$S and the Tevatron: the UA1 and UA2 experiments at CERN, and the CDF and D0 experiments at Fermilab. The main features of the these experiments are as follows:

1. Large Solid Angle Calorimeters - each experiment utilizes a calorimeter that covers the entire azimuth in a region of polar angle that extends to within $\sim 5°$ of the beam direction. These devices are usually segmented transversely and longitudinally. The longitudinal segmentation permits the separation of electron and photon showers from hadron showers. The energy resolution of these devices is typically $\delta E/E \sim 0.15/\sqrt{E}$ (E in GeV) for electromagnetic showers and $\delta E/E \sim 0.80/\sqrt{E}$ for hadronic showers. Additionally, the overall energy scale of a typical calorimeter is uncertain to $\lesssim$ 1% for electromagnetic showers and $\sim$ 3.5% for hadronic showers.

2. Magnetic Spectrometers - The UA1 and CDF experiments contain large charged particle tracking systems that are immersed in magnetic fields. They are capable of reconstructing transverse momenta with resolutions in the range $\delta P_t/P_t \sim$(0.001-0.005)$\cdot P_t$ (where P_t is in GeV). Although these resolutions are inferior to those of the calorimeters for high energy electrons, the CDF collaboration have managed to control the momentum scale uncertainty to a few tenths of a percent. The UA2 and D0 experiments have charged particle tracking systems but are not capable of charged particle momentum reconstruction.

3. Muon Spectrometers/Identifiers - The UA1, CDF, and D0 experiments have magnetized iron shielding for the identification and measurement of muon tracks. The momentum resolution of these systems is poor as compared with the inner tracking systems mentioned above.

4. Triggers - All four experiments need fairly sophisticated, calorimeter-based triggers to ignore the large rate (~ 100 kHz) of ordinary hadronic interactions. The triggers normally require that preselected patterns of transverse energy* be deposited into the calorimeter. The energy thresholds are adjusted to reduce the trigger rates to a few Hertz.

Observable Quantities

As the energies of storage rings and collider complexes have increased, the importance of observing individual final-state hadrons has declined. This is particularly true in hadron colliders. The experimentally observable and measurable quantities are as follows:

1. Hadron Jets - the signature of a quark or gluon jet in a typical detector is a cluster of energy in the calorimeter. The transverse and longitudinal extent of the energy deposition is much larger than that associated with an electron or photon. A large number of charged tracks is usually required to originate from a vertex and point to the cluster.

2. Electron - the signature of an electron in a typical detector is a cluster of energy in the calorimeter of small transverse and longitudinal extent. A charged track must be associated with the cluster. The track-calorimeter matching is improved with the use of high granularity preshower detectors, high granularity layers in the calorimeter, or position sensitive detectors embedded in the calorimeter. The UA1 and CDF experiments also require that the momentum of the charged track (as measured by magnetic deflection)

---

* Transverse energy is defined as the product of the energy deposited into a calorimeter segment and the sine of the polar angle subtended by the segment.

agree with the energy that is measured in the calorimeter. All of the experiments require that electron candidates pass an isolation criterion of some description (typically, less than a few GeV of energy must be detected in a cone of 15°-40° about the track-cluster).

3. Muons - the signature of a muon is a charged track that penetrates the iron muon identifier. The track is required to match to a charged track in the central detector. The central track must not show any sign of a *kink* that could be associated with the decay of a pion or kaon. The energy measured in the calorimeter must be consistent with the passage of a minimum ionizing particle. Additionally, the muon candidate must pass an isolation criterion that is similar to the one applied to electron candidates.

4. Neutrinos - the large coverage of the calorimeters permits the reconstruction of the net transverse momentum vector of the entire event (relative to the beam axis). The measurement of the net longitudinal momentum of the event requires calorimetric coverage to quite near the beam direction and is not practical. Since the transverse momentum of the initial state is zero, the total event transverse momentum measures the total transverse momentum of all non-interacting particles. Neutrinos with large transverse momenta can be identified and tagged by this technique. The missing transverse momentum (P_t^{miss}) resolution of a typical detector is given by the following expression,

$$\delta P_{T_{x,y}}^{miss} = (0.5 \rightarrow 0.7) \cdot \sqrt{E_t^{obs}} \text{ GeV}$$

   where x, y are the directions that are orthogonal to the beam axis and where E_t^{obs} is the total transverse energy that is observed in the calorimeter (the energy of each cell weighted by the sine of the polar angle).

It is clear that large P_t electrons and (in the case of CDF) muons are much better measured quantities than are jets or neutrinos. The most serious backgrounds to large transverse momentum charged leptons are due to low multiplicity hadronic jets. The rejection power of the selection criteria is typically several $\times$ 10^4. The efficiency to detect a large P_t lepton is typically 50% to 75% depending upon the detector and the selection criteria.

3.2. Gauge Boson Production

All the electroweak tests that have been performed at hadron colliders involve the measurement of gauge boson properties. It is important to remember that gauge boson production in these machines is a small part of the total cross section. The signatures and cross sections for gauge boson production are compared with those of hadronic processes in Table IV.

Table IV

Process	Signature	σ(0.63 TeV)	σ(1.8 TeV)
Soft Collision	E_t = 5-10 GeV 15-25 charged tracks	$\sim 6\times 10^7$ nb	$>6\times 10^7$ nb
Hard Collision	Two large P_t jets back-to-back azimuthally	~600 nb (P_t^j>30 GeV)	~3000 nb (P_t^j>32 GeV)
$p\bar{p} \to W \to q\bar{q}$	Two large P_t jets back-to-back azimuthally	~3 nb	~15 nb
$p\bar{p} \to Z \to q\bar{q}$	Two large P_t jets back-to-back azimuthally	~1 nb	~5 nb
$p\bar{p} \to W \to \ell\nu$	Large P_t lepton	~0.5 nb	~2.5 nb
$p\bar{p} \to Z \to \ell\ell$	Two large P_t leptons	~0.05 nb	~0.25 nb

Note that the hadronic final states of the gauge bosons have a signature that is very similar to that of the dominant large P_t scattering process. For this reason, all precise gauge boson measurements make use of the leptonic final states.

Drell-Yan Mechanism

The hadronic production of the $W^\pm$ and Z^0 bosons occurs via the well-known *Drell-Yan* mechanism which is illustrated in in Figure 1. The incident proton and antiproton have momenta k_1 and k_2, respectively. A parton carrying a fraction

x_1 of the proton momentum collides with a parton carrying a fraction x_2 of the antiproton momentum. The two lowest order subprocesses that produce gauge bosons are shown in parts a) and b). The dominant subprocess is the $q\bar{q}$ annihilation diagram shown in part a). Note that the emitted gluon is optional and is shown only to illustrate the production mechanism for gauge boson transverse momenta. The second subprocess is the Compton scattering of a quark and gluon. This process is higher order in α_s than the basic process (without initial state gluon radiation) and is important when the longitudinal or transverse momentum of the gauge boson is large.

The parton-parton center of mass energy, $\sqrt{\hat{s}}$, has a simple relationship to the hadron-hadron center of mass energy $\sqrt{s}$,

$$\hat{s} = x_1 x_2 s = \tau s \tag{3.1}$$

where the definition of τ is obvious. If the gauge boson transverse momentum $P_t^{W,Z}$ is small as compared with its mass, the gauge boson longitudinal momentum is given by the following simple expression,

$$P_L^{W,Z} = P_{beam} \cdot (x_1 - x_2), \tag{3.2}$$

where P_{beam} is the beam momentum.

Assuming that the annihilation subprocess dominates the cross section, we can therefore write the lowest order differential cross section as,

$$\frac{d\sigma_0}{dx_1 dx_2} = \frac{1}{N_c} \sum_{i,j} \left[\frac{q_i^1(x_1)\bar{q}_j^2(x_2)}{x_1 x_2} + \frac{\bar{q}_j^1(x_1) q_i^2(x_2)}{x_1 x_2} \right] \hat{\sigma}_{ij}(x_1 x_2 s), \tag{3.3}$$

where: $q_i^1(x_1)/x_1$ is the probability of finding a quark of species i in the proton with momentum fraction x_1; N_c is a color factor (3) to account for the probability of finding a quark-antiquark pair in a color-neutral state; and $\hat{\sigma}_{ij}(\hat{s})$ is the cross section for the annihilation of quark species i and j with a $q\bar{q}$ cm energy of $\hat{s}$.

The QCD radiative corrections to equation (3.3) are quite substantial. Real gluon emission produces large gauge boson transverse momenta. At a center of mass energy of 630 GeV, the average gauge boson transverse momentum is approximately 7 GeV. In the absence of gluon radiation, the natural scale of the gauge boson transverse momentum would be that of the Fermi momentum of a quark in a nucleon (a few hundred MeV). Additionally, the QCD vertex corrections change the size of the cross section by a factor that is between one and two. Nevertheless, equation (3.3) correctly describes many of the features of gauge boson production and gives the correct scale of the cross section.

3.3. W Boson Physics

As an example of the Drell-Yan mechanism, let's consider the process $p\bar{p} \to W^{\pm} \to \ell^{\pm}\nu$. The cross section for the process $q\bar{q} \to W^{\pm} \to \ell^{\pm}\nu$ in the $q\bar{q}$ cm frame can be written as,

$$\frac{d\hat{\sigma}}{d\Omega}(q_\ell cos\theta^*) = \frac{\alpha^2}{64\sin^4\theta_w} \cdot \frac{\hat{s}}{(\hat{s}-M_W^2)^2 + \Gamma_W^2\hat{s}^2/M_W^2} \cdot (1 - q_\ell\cos\theta^*)^2, \tag{3.4}$$

where: θ^* is the polar angle of the charged lepton relative to the quark direction; q_ℓ is the lepton charge; and Γ_W is the W boson width. The large angular asymmetry is a consequence of the V-A coupling of the W to all fermions. Note that electrons are emitted preferentially in the quark direction and positrons in the antiquark direction.

The lowest order Drell-Yan cross section for the production of the W^- boson follows from the substitution of equation (3.4) into equation (3.3),

$$\begin{aligned}\frac{d\sigma_0}{d\Omega} = \frac{1}{3}\int dx_1 dx_2 \delta(x_1x_2 - \hat{s}/s)\Bigg[&\frac{d_p(x_1)\bar{u}_{\bar{p}}(x_2)}{x_1x_2}\frac{d\hat{\sigma}}{d\Omega}(-\cos\theta^*) \\ &+ \frac{\bar{u}_p(x_1)d_{\bar{p}}(x_2)}{x_1x_2}\frac{d\hat{\sigma}}{d\Omega}(\cos\theta^*)\Bigg]\end{aligned} \tag{3.5}$$

where $u_h(x)$ [$d_h(x)$] is the momentum distribution of u [d] quarks in hadron h. The antiquark-antiproton distribution $\bar{u}_{\bar{p}}(x)$ is required to be identical to the quark-proton distribution $u_p(x)$ by CPT invariance. The sea quark distributions $\bar{u}_p(x)$

and $d_{\bar{p}}(x)$ are approximately equal and are unimportant except at small values of x. The angular asymmetry that is associated with the $\bar{u}_p(x_1)d_{\bar{p}}(x_2)$ factor has the opposite sense because the $q\bar{q}$ axis reverses direction with respect to the parent hadrons. Note that the delta function explicitly applies the constraint given in equation (3.1). The average value of x_1 or x_2 is therefore $x_{avg} \sim M_W/\sqrt{s}$. At larger values of x_{avg} (lower energy colliders), the valence quark distributions dominate equation (3.5) and the lepton angular asymmetry is large. As x_{avg} becomes smaller, the wrong-sign sea quark terms dilute the asymmetry.

Since the u-quark distribution of the proton is *harder* than is the d-quark distribution (there are two valence u quarks to one d quark), we expect that W^- bosons are slightly boosted in the antiproton direction, and that W^+ bosons are slightly boosted in the proton direction. The scaled longitudinal momentum distribution $x_2 - x_1$ of W^- bosons produced at $\sqrt{s} = 630$ GeV is shown in Figure 2. The average boost along the antiproton direction is fairly small, $x_2 - x_1 = 0.06$. However, the distribution is quite broad. The average value of the absolute value $|x_2 - x_1|$ is 0.22 which corresponds to an average longitudinal momentum of 68.2 GeV.

The Detection of W Bosons

As we have already discussed, there are serious QCD backgrounds to the detection and measurement of W bosons via their hadronic decays. It is necessary to search for the charged lepton-neutrino final states. The QCD background is suppressed both by the leptonic selection criteria and by the missing P_t signature of the neutrino.

The identification of charged leptons and neutrinos is greatly aided by the two-body nature of the W decay. This becomes clearer if we consider the transformation of the lepton angular distribution from the W center-of-mass frame to the laboratory frame. Let the cm angular distribution be described by some (analytic) function f,

$$\frac{dN}{d\cos\theta^*} = f(\cos\theta^*). \tag{3.6}$$

In the laboratory frame, most of the W boson momentum is along the beam axis. Therefore, the transverse momentum distribution of the charged leptons is the same in both frames. The lepton transverse momentum P_t^ℓ has a simple relationship to the cm emission angle,

$$P_t^\ell = \frac{M_W}{2}\sin\theta^*. \tag{3.7}$$

Changing variables from $\cos\theta^*$ to P_t^ℓ, equation (3.6) becomes

$$\frac{dN}{dP_t^\ell} = \frac{1}{\sqrt{1-4P_t^{\ell 2}/M_W^2}} f(\pm\sqrt{1-4P_t^{\ell 2}/M_W^2}). \tag{3.8}$$

There is a singularity in the P_t^ℓ distribution at $M_W/2$! This so-called *Jacobian peak* (after the Jacobian of the transformation) implies that most of the leptons and neutrinos emerge with the largest transverse momenta.

The singularity in the P_t^ℓ distribution as described by equation (3.8) is unphysical and is moderated by three effects:

1. The parent W boson has a finite width, $\Gamma_W \sim 2.1$ GeV.
2. The detector has finite resolution.
3. The parent W is produced with non-zero transverse momentum.

These effects are incorporated into a simulation of the process $p\bar{p} \to W \to e\nu$ at $\sqrt{s} = 630$ GeV. The P_t^e distribution is presented for three different phenomenological W boson transverse momentum distributions in Figure 3. The average values of P_t^W are zero (the dashed curve), 7 GeV (the dashed-dotted curve), and 14 GeV (the solid curve). The energy resolution of the detector is assumed to be $\delta E/E = 0.15/\sqrt{E}$. Note that the P_t^e distribution is very sensitive to the W transverse momentum distribution.

The Jacobian peak is a feature of transverse momentum distributions of the charged leptons and of the neutrinos. Since the backgrounds that affect the identification of charged and neutral leptons decrease rapidly with increasing P_t, most experiments select W candidates by requiring that P_t^ℓ and P_t^ν be larger than 20 GeV. The electron and neutrino transverse momentum distributions for the 1203 $W \rightarrow e\nu$ event sample of the UA2 Collaboration[9] are shown in Figure 4. The background from misidentified two-jet events is estimated to be less than 1%.

In practice, W bosons are detected by their decays into $e\nu$ and $\mu\nu$ final states. The $\tau\nu$ final state cannot be detected with high efficiency (the efficiency is in the range 10%-15%). This is because a large fraction of τ decays appear as low multiplicity hadronic jets. One must use very restrictive cuts to eliminate low multiplicity QCD events. A second difficulty is that neutrinos are detected from an imbalance in the total transverse momentum of the event. Since all τ decays contain at least one neutrino, the missing P_t distribution is softened considerably. The P_t^ν requirement is therefore less efficient. Although the identification of τ lepton final states is difficult, the leptonic decays of the τ's do contaminate the $e\nu$ and $\mu\nu$ final states. For electron or muon transverse momenta above 20 GeV, the τ contamination is in the range 3%-4%.

W Mass Measurement

It is clear from equation (3.8) and from Figure 3 that the position of the Jacobian peak in the P_t^ℓ distribution is determined by the mass of the W boson. Figure 3 also illustrates the difficulty in the extraction of M_W from a fit to the distribution. The P_t^ℓ distribution is very sensitive to the P_t^W distribution which is neither well-known nor well-measured. The solution to this problem is to use the so-called transverse mass variable, $M_t^{\ell\nu}$. The transverse mass is the two-dimensional analog of the normal three-dimensional one,

$$M_t^{\ell\nu} \equiv \sqrt{2P_t^\ell P_t^\nu(1-\cos\Delta\phi_{\ell\nu})} \tag{3.9}$$

where P_t^ν is the neutrino transverse momentum and $\Delta\phi_{\ell\nu}$ is the azimuthal angle between the lepton and neutrino P_t vectors. Although M_t is not a Lorentz-invariant quantity, it is quite insensitive to the P_t^W distribution. This is shown in Figure 5. The $M_t^{e\nu}$ distributions are plotted for the three P_t^e distributions shown in Figure 3. The average values of P_t^W are zero (the dashed curve), 7 GeV (the dashed-dotted curve), and 14 GeV (the solid curve). The resolution of the neutrino P_t along the x and y axes is assumed to be $\delta P_{t,xy}^{\nu} = 0.5\sqrt{E_T}$ GeV. Note that the $M_t^{e\nu}$ distribution is very insensitive to the details of the P_t^W distribution.

Note also that the $M_t^{e\nu}$ distributions are much more sharply peaked than are the P_t^e distributions. The transverse mass should therefore be a more sensitive measure of the W mass. We can quantify this observation by analyzing the expected results of likelihood fits to the P_t^e and $M_t^{e\nu}$ distributions. Let f and g be P_t^e and $M_t^{e\nu}$ likelihood functions that are normalized in the region of sensitivity. In practice, the regions 25 GeV $< P_t^e <$ 50 GeV and 50 GeV $< M_t^{e\nu} <$ 100 GeV are used to measure M_W. The functions f and g are therefore defined as follows,

$$f(P_t^e, M_W) = \frac{\frac{dN}{dP_t^e}}{\int_{25}^{50} dP_t^e \frac{dN}{dP_t^e}} \qquad g(M_t^{e\nu}, M_W) = \frac{\frac{dN}{dM_t^{e\nu}}}{\int_{50}^{100} dM_t^{e\nu} \frac{dN}{dM_t^{e\nu}}}. \tag{3.10}$$

The M_W precision of likelihood fits to the measured distributions can be estimated from the following expressions,

$$\begin{aligned} \delta M_W &= \left[N_d \int_{25}^{50} dP_t^e \frac{\left(\frac{\partial f}{\partial M_W}\right)^2}{f} \right]^{-\frac{1}{2}} & \delta M_W &= \left[N_d \int_{50}^{100} dM_t^{e\nu} \frac{\left(\frac{\partial g}{\partial M_W}\right)^2}{g} \right]^{-\frac{1}{2}} \\ &= \frac{14}{\sqrt{N_d}} \text{ GeV} & &= \frac{8.1}{\sqrt{N_d}} \text{ GeV} \end{aligned} \tag{3.11}$$

where N_d is the number of detected events. The numerical results given in the second line are derived by numerically differentiating and integrating the $\langle P_t^W \rangle =$ 7 GeV distributions in Figures 3 and 5. Note that the transverse mass distribution has substantially more analyzing power than does P_t^e distribution. Note also that our simulation of the missing P_t resolution is somewhat optimistic. The analyzing power of the $M_t^{e\nu}$ distribution is probably not a good as indicated by equation (3.11).

The transverse mass distribution has the advantages that it is less sensitive to the W boson P_t distribution and more sensitive to the W boson mass than is the lepton transverse momentum distribution. These advantages are the result of adding more information to the problem (the neutrino P_t). Unfortunately, the additional information is accompanied by an additional uncertainty. We must understand the resolution function for the missing P_t vector. In practice, the increase in the systematic uncertainty that is associated with the use of the P_t^ν information is more than compensated by the reduced sensitivity to the P_t^W distribution.

The shapes of the $M_t^{\ell\nu}$ and P_t^ℓ distributions near the Jacobian peaks are sensitive to the proton structure functions. The lineshape of the W resonance and the accepted lepton transverse momentum distribution are both affected by the structure functions. The lineshape is given by the convolution of the relativistic Breit-Wigner resonance form (given in equation (3.4)) with the quark structure functions (see equation (3.5)). Since the structure functions fall sharply with increasing x, the $M_t^{\ell\nu}$ and P_t^ℓ distributions are steepened above the peak values. The acceptance effect is caused by the boosting of the W along the beam axis. The acceptance for a lepton that is emitted with a *backward angle* (in the W rest frame) relative to the boost direction is larger than the acceptance for a lepton that is emitted with the symmetric forward angle. Since P_t^ℓ is completely correlated with the emission angle, the accepted P_t^ℓ and $M_t^{\ell\nu}$ distributions are sensitive to the choice of proton structure functions. The dependence of the predicted distributions upon the structure functions leads to an uncertainty on the fit value of M_W of roughly 100 MeV.

The best current measurement of the W boson mass is the one derived from the 1203 event sample of the UA2 Collaboration,[9]

$$M_W = 80.79 \pm 0.31(\text{stat}) \pm 0.21(\text{syst}) \pm 0.81(\text{scale})\ \text{GeV}.$$

The systematic error has roughly equal contributions from uncertainties on the transverse momentum resolution, the quark distribution functions, and the statistical precision of the Monte Carlo that was used to calculate the shape of the $M_t^{e\nu}$ distribution. There are smaller contributions to the systematic error from the leakage energy from the underlying event into the electron clusters, from uncertainties on the final state radiative corrections, and from the uncertainty on the electron energy resolution function. Note that the largest single uncertainty is due to the 1% energy scale uncertainty of the UA2 electromagnetic calorimeter. The error is quoted separately because it cancels in the ratio of the W and Z masses.

W Angular Distribution

We have already seen that the angular distribution of the leptons emitted in W decay is expected to be strongly asymmetric *in the $q\bar{q}$ center-of-mass frame.* It is clearly important to verify that this is indeed true for the 81 GeV particle that has been observed. Unfortunately, the $q\bar{q}$ center-of-mass frame is generally not well determined. The reasons for this are:

1. The $q\bar{q}$ axis is coincident with the $p\bar{p}$ axis only when the W is produced with zero transverse momentum. A non-zero value for P_t^W implies that one or both of the incident quarks emitted gluons in the collision process. The solution to this problem is to use the Collins-Soper definition of the $q\bar{q}$ cm frame.[10] The bisector of the proton and antiproton directions in the W rest frame is chosen as the $q\bar{q}$ axis. This definition is therefore *correct on average* but fails on an event by event basis.

2. The use of the Collins-Soper frame requires that we know the W boson rest frame. However, since the neutrino longitudinal momentum is not measured, we do not have enough information to reconstruct the W rest frame. The solution to this problem is to constrain the mass of the lepton-neutrino system to the W mass (ignoring the finite width of the W). This yields two solutions for the neutrino longitudinal momentum P_L^ν. Since the W longitudinal momentum is $P_L^W = P_L^\ell + P_L^\nu$, there are two solutions for P_L^W. In the

Collins-Soper frame, the two solutions correspond to opposite sign solutions for $\cos\theta^*$. In many cases, the W is highly boosted on the laboratory frame and one solution is unphysical ($P_L^W > \sqrt{s}/2$). These unambiguous events are normally used to measure W boson angular asymmetry.

The UA1 collaboration has performed this analysis with their old (767 nb^{-1}) sample of $W \to e\nu$ events.[11] They have used only the 149 events that have an unambiguous solution for P_L^W and a measured value of P_t^W less than 15 GeV. They correct the measured distribution for the biases that are introduced by the selection process. The resulting distribution is plotted in Figure 6. The solid curve shows the expected $(1 - q_e \cos\theta^*)^2$ distribution. It agrees well except near $q_e \cos\theta^* = 1$ where the wrong-sign sea quark contribution is large (see equation (3.5)).

3.4. Z^0 Boson Physics

The cross section for the process $p\bar{p} \to Z^0 \to \ell^+\ell^-$ can be calculated from the zeroth order Drell-Yan formalism given in equation (3.3). The cross section for the point process $q\bar{q} \to Z^0 \to \ell^+\ell^-$ is straightforward to calculate from the Standard Model couplings,

$$\begin{aligned}\frac{d\hat{\sigma}_q}{d\Omega}(c) = \frac{\alpha^2}{4\hat{s}}\Bigg\{ & Q_q^2(1+c^2) \\ & - \frac{Q_q}{2\sin^2 2\theta_w}\mathrm{Re}\Gamma(\hat{s})\Big[vv_q(1+c^2) + 2aa_qc\Big] \\ & + \frac{1}{16\sin^4 2\theta_w}|\Gamma(\hat{s})|^2\Big[(v^2+a^2)(v_q^2+a_q^2)(1+c^2) + 8vav_qa_qc\Big]\Bigg\}\end{aligned} \tag{3.12}$$

where: $c \equiv \cos\theta^*$ is cosine of the polar angle of the lepton relative to the quark direction; $\Gamma(\hat{s}) = \hat{s}/(\hat{s} - M_Z^2 + i\Gamma_Z\hat{s}/M_Z)$ is the normalized Z propagator; Γ_Z is the Z^0 width; and where the coupling constants (defined in equation (2.2)) without subscript, v and a, refer to the leptonic couplings. The first term within the braces describes the process of pure γ exchange, the second term describes the Z^0-γ interference, and the third term describes pure Z^0 exchange. The γ

exchange term is quite small and can be ignored. The interference term vanishes at $\hat{s} = M_Z^2$ and can be ignored except when calculating the angular distribution (because $aa_q \gg vv_q$).

The lowest order Drell-Yan cross section for the Z^0 production follows from the substitution of equation (3.12) into equation (3.3),

$$\begin{aligned}\frac{d\sigma_0}{d\Omega} &= \frac{1}{3}\int dx_1 dx_2 \delta(x_1 x_2 - \hat{s}/s) \cdot \\ &\left\{ \frac{u_p(x_1)\bar{u}_{\bar{p}}(x_2)}{x_1 x_2}\frac{d\hat{\sigma}_u}{d\Omega}(c) + \left[\frac{s_p(x_1)\bar{s}_{\bar{p}}(x_2)}{x_1 x_2} + \frac{d_p(x_1)\bar{d}_{\bar{p}}(x_2)}{x_1 x_2}\right]\frac{d\hat{\sigma}_d}{d\Omega}(c) \right. \\ &\left. \frac{\bar{u}_p(x_1)u_{\bar{p}}(x_2)}{x_1 x_2}\frac{d\hat{\sigma}_u}{d\Omega}(-c) + \left[\frac{\bar{s}_p(x_1)s_{\bar{p}}(x_2)}{x_1 x_2} + \frac{\bar{d}_p(x_1)d_{\bar{p}}(x_2)}{x_1 x_2}\right]\frac{d\hat{\sigma}_d}{d\Omega}(-c) \right\}\end{aligned} \tag{3.13}$$

where $s_h(x)$ is the strange (sea) quark structure function.

Note that the angular distribution of the outgoing lepton is a function of the ratio of the rates $u\bar{u}$ annihilations and $d\bar{d}$ annihilations (because $d\hat{\sigma}_u/d\Omega$ is quite different from $d\hat{\sigma}_d/d\Omega$). Like the W case, there is also a dilution effect coming from the wrong-sign sea quarks.

Z Boson Detection

The presence of a second charged lepton makes the detection of the decay $Z^0 \to \ell^+\ell^-$ extremely straightforward for electron and muon final states. On the other hand, the detection of τ final states is quite difficult without the missing P_t signature of the W decays. At the current time, no experiment has published a signal for the process $p\bar{p} \to Z^0 \to \tau^+\tau^-$. In the case of electrons, it is necessary to require that only one of the *legs* of the Z candidate satisfy very restrictive identification criteria. Taking all lepton pair masses between 60 and 120 GeV, the background from misidentified hadronic events is typically less than 1%.

Measurement of M_Z

The mass of the Z boson is extracted from the observed lepton-lepton mass ($M_{\ell\ell}$) distribution. The observed $M_{\ell\ell}$ distribution is the convolution of the underlying Breit-Wigner lineshape, the quark structure functions, and the experimental resolution. The leptonic daughters of the Z are sufficiently energetic that the energy resolution associated with electromagnetic calorimeters ($\delta E/E \sim 0.15/\sqrt{E}$) is better than that associated with magnetic spectrometers ($\delta(1/P_t) \sim 0.001\ \mathrm{GeV}^{-1}$) by roughly a factor of two. We therefore expect the electron final states to offer better statistical analyzing power than do the muon final states. We can quantify the difference by comparing the expected results of fits to the M_{ee} and $M_{\mu\mu}$ distributions. Let $z(M_{\ell\ell}, M_Z)$ be the likelihood function for the observed lepton pair mass distribution normalized over the interval 60 GeV $< m_{\ell\ell} <$ 120 GeV,

$$z(M_{\ell\ell}, M_Z) \equiv \frac{\frac{dN}{dM_{\ell\ell}}}{\int_{60}^{120} dM_{\ell\ell} \frac{dN}{dM_{\ell\ell}}}. \tag{3.14}$$

The M_Z precision of a likelihood fit to the measured distribution can then estimated from the following expression,

$$\delta M_Z = \left[N \int_{60}^{120} dM_{\ell\ell} \frac{\left(\frac{\partial z}{\partial M_Z}\right)^2}{z} \right]^{-\frac{1}{2}} = \begin{cases} \frac{2.9}{\sqrt{N}}\ \mathrm{GeV}, & \text{for electrons} \\ \frac{4.1}{\sqrt{N}}\ \mathrm{GeV}, & \text{for muons} \end{cases} \tag{3.15}$$

where N is the number of detected events. The electrons are expected to be better by roughly 30%.

In practice, only well-measured lepton pairs are used to extract M_Z. The existing experiments are well instrumented only at relatively large values of polar angle ($|\theta| \gtrsim 20°$). The probability that both leptons are detected in this region is about 70% at $\sqrt{s} = 630$ GeV and 47% at $\sqrt{s} = 1800$ GeV. The magnetically measured masses of 123 muon pairs and 65 electron pairs of the CDF collaboration[12] are shown in Figure 7. Although the momentum resolution of the CDF magnetic spectrometer is inferior to the energy resolution of the CDF calorimeter, the momentum/energy scale is more precisely known (an uncertainty of 0.22% is claimed). The magnetic spectrometer is used to directly measure the muon pair masses and to calibrate the electromagnetic calorimeter with low energy electrons (from b quark decay). Performing likelihood fits to the 123 μ-pair sample and to a sample of 73 calorimetrically measured electron pairs, the following the measurements of M_Z were obtained,

$$M_Z = 90.7 \pm 0.4 \text{ (stat)} \pm 0.2 \text{ (syst) GeV (muons)}$$

$$M_Z = 91.1 \pm 0.3 \text{ (stat)} \pm 0.4 \text{ (syst) GeV (electrons).}$$

The systematic error on the muon result is dominated by the momentum scale uncertainty of the magnetic spectrometer. The systematic error quoted for the electron measurement is due largely to uncertainties in the calorimeter calibration. The combined result is

$$M_Z = 90.9 \pm 0.3 \text{ (stat + syst)} \pm 0.2 \text{ (scale) GeV}$$

where the scale uncertainty has been quoted separately.

The UA2 Collaboration have also recently published a result that is based upon a sample of 90 electron pair events,[9]

$$M_Z = 91.49 \pm 0.35\text{(stat)} \pm 0.12\text{(syst)} \pm 0.92\text{(scale) GeV},$$

where dominant contributions to the systematic error are due to leakage of energy from the underlying event into the electron clusters and to uncertainties in the detector response to the process $Z^0 \to e^+e^-\gamma$.

3.5. M_W, M_Z and the Standard Model

The ratio of the W and Z boson masses is an interesting quantity for very practical reasons. We have seen that lepton energy scale uncertainties lead to substantial uncertainties on the gauge boson masses. These particular uncertainties cancel in the ratio M_W/M_Z. Since M_Z has been precisely measured in e^+e^- experiments (which cannot measure M_W at the current time), the electroweak information contained within M_W is also contained within the mass ratio.

The best measurement of M_W that is currently available is contained within the M_W/M_Z measurement of the UA2 Collaboration,[9]

$$\frac{M_W}{M_Z} = 0.8831 \pm 0.0048(\text{stat}) \pm 0.0026(\text{syst}).$$

Taking the current weighted world average value[8] for M_Z ($M_Z = 91.160 \pm 0.0029$ GeV), they quote a rescaled W mass value of,

$$M_W = 80.49 \pm 0.43(\text{stat}) \pm 0.24(\text{syst}) \text{ GeV}.$$

The ratio M_W/M_Z directly determines the parameter $\sin^2\theta_w$ as defined by Sirlin,[13]

$$\sin^2\theta_w \equiv 1 - \left(\frac{M_W}{M_Z}\right)^2 = 0.220 \pm 0.008(\text{stat}) \pm 0.005(\text{syst}).$$

The Sirlin definition of $\sin^2\theta_w$ is related to the Z^0 mass by a very well-known expression,[14]

$$M_Z^2 = \frac{A^2}{(1-\Delta r)\sin^2\theta_w \cos^2\theta_w}, \tag{3.16}$$

where Δr contains the effects of electroweak radiative corrections ($\Delta r = 0$ at tree level), and A is a constant,

$$A = \left[\frac{\pi\alpha}{\sqrt{2}G_F}\right]^{\frac{1}{2}} = 37.2805 \pm 0.0003 \text{ GeV}.$$

Using the SLC/LEP value for M_Z and their own result for M_W/M_Z, the UA2 group derive a result for Δr,

$$\Delta r = 0.026^{+0.029}_{-0.032}.$$

Their result is consistent with a large value of m_{top} (100-200 GeV).

3.6. Future Measurements of M_W and M_Z

We have seen that the mass ratio M_W/M_Z has the advantage that the uncertainty on the leptonic energy scale cancels in the ratio. The remaining systematic errors are due largely the differences in the techniques that are used to extract the masses. These techniques have been developed to minimize the statistical error of the result. The Tevatron experiments expect to accumulate significantly larger data samples in the next few years (the current CDF sample could increase by a factor of order fifty). The increased size of the samples should be adequate to saturate the current systematic errors.* One must therefore ask if it is possible to reduce the systematic uncertainties by using techniques with less statistical sensitivity.

The obvious approach is to extract the Z mass from the transverse mass technique. In this case, the uncertainties associated with the P_t^ν resolution, the underlying event, and the electron energy resolution would largely cancel in the mass ratio. The remaining uncertainties would be those due to the differences in radiative corrections and structure functions.

The question of whether to discard one leg of a Z event has been much discussed (over coffee). It is clear that a strong correlation exists between the transverse momenta of the two leptons. It would be difficult to assess the effect of the correlation on the result. However, it is very likely that this question will remain academic. In the current experiments, the number of Z candidates with two well-measured legs is somewhat smaller than the number with only one well-measured leg (the CDF group uses 73 well-measured electron pairs to determine M_Z and 193 events with one well-measured leg to determine the Z cross section[15]). The use of second well-measured legs would therefore add only a small statistical advantage (in the CDF example, the statistical error would be improved by only 17%).

Scaling the current CDF samples[15] of $W \to e\nu$ candidates (1828 events) and

---

⋆ It would also permit the detailed study and reduction of the current systematic errors. For instance, a large sample of Z^0 decays should help understand the missing P_t resolution from the study of the hadronic system that recoils against the (well-measured) lepton pair.

one-legged $Z \to ee$ events (193) by a factor of 50, we can use equation (3.11) to estimate the statistical error on M_W/M_Z that might be achieved in the future. Assuming that only one leg from each Z event is used, we estimate the error on the ratio to be

$$\delta\left(\frac{M_W}{M_Z}\right) \sim 0.0009.$$

Assuming that M_Z is known to 30 MeV, this corresponds to an error on M_W of 83 MeV. It is clear than a 100-150 MeV measurement of M_W is possible if the remaining systematic error can be controlled to a comparable level.

3.7. The Z^0 Angular Distribution

The angular distribution of the leptons in the $q\bar{q}$ center-of-mass frame is given by equations (3.12) and (3.13). Although the net expression is fairly complicated, it has the following form,

$$\frac{d\sigma}{d\Omega^*} = \frac{A}{2}(1 + \cos^2\theta^*) + B\cos\theta^* \tag{3.17}$$

where the complexity is hidden in the definitions of the constants A and B. If the initial state hadrons were monoenergetic quarks of energy $M_Z/2$, we could write A and B as

$$\begin{aligned} A &= \frac{\alpha^2}{512\sin^4 2\theta_w} \cdot \frac{1}{\Gamma_Z^2} \cdot 2(v^2 + a^2)(v_q^2 + a_q^2) \\ B &= \frac{\alpha^2}{512\sin^4 2\theta_w} \cdot \frac{1}{\Gamma_Z^2} \cdot 8 v a v_q a_q. \end{aligned} \tag{3.18}$$

It is often quite useful to consider the so-called *forward-backward asymmetry* which measures the ratio of the B and A terms. It is defined as follows,

$$\begin{aligned} A_{FB}(x) &\equiv \frac{\int_0^x d\cos\theta^* \frac{d\sigma}{d\cos\theta^*} - \int_{-x}^0 d\cos\theta^* \frac{d\sigma}{d\cos\theta^*}}{\int_{-x}^x d\cos\theta^* \frac{d\sigma}{d\cos\theta^*}} \\ &= \frac{4x}{3+x^2} \cdot \frac{3}{4} \cdot \frac{B}{A} = F(x) \cdot \frac{3}{4} \cdot \frac{B}{A} \end{aligned} \tag{3.19}$$

where x is an integration limit and the function $F(x)$ is normalized such that

$F(1) = 1$. The forward-backward asymmetry is the ratio of the difference in the cross sections for finding the lepton in the quark and antiquark hemispheres to the total cross section. The effect of limited detector acceptance in polar angle is described by the function $F(x)$ where x is the maximum value of $\cos\theta^*$. By convention, the symbol A_{FB} describes the asymmetry for complete polar angle coverage ($A_{FB} = A_{FB}(1)$).

The forward-backward asymmetry is sensitive to the couplings of the Z^0 to incident quarks and the final state leptons. For the simple example of monoenergetic quarks of energy $M_Z/2$, the asymmetry has the form,

$$A_{FB} = \frac{3}{4} \cdot \frac{-2va}{v^2 + a^2} \cdot \frac{-2v_q a_q}{v_q^2 + a_q^2} = \begin{cases} 0.063 & \text{for } u\text{-quarks} \\ 0.089 & \text{for } d\text{-quarks} \end{cases} \tag{3.20}$$

where we have assumed that $\sin^2\theta_w = 0.234$. Note that the lepton and quark vector coupling constants are sensitive functions of $\sin^2\theta_w$ (see equation (2.2)). The Z^0 forward-backward asymmetry is therefore useful for testing the Standard Model.

The actual $p\bar{p}$ initial state is a mixture of $u\bar{u}$ and $d\bar{d}$ states. The measured asymmetry should therefore fall between the above extremes (as determined by the u and d quark structure functions and by the quark couplings to the Z^0). Or should it? We expect that a number of effects should reduce the measured asymmetry:

1. As in the case of the W angular distribution, there are *wrong-sign* sea-quark pairs that dilute the asymmetry. Note that a correct analysis of this effect depends upon a good knowledge of the low-x quark structure functions.

2. The electroweak interference terms are important when $\hat{s} \neq M_Z^2$. This effect is also sensitive to the quark structure functions.

3. The acceptance of a real experiment is finite ($x < 1$). The actual acceptance depends upon the longitudinal momentum distribution of the Z which is sensitive to the quark structure functions.

4. The actual $q\bar{q}$ axis is unknown. Although we can use the average direction (the Collins-Soper definition), there will be an inevitable dilution of the asymmetry.

It appears that the measured value of A_{FB} might be quite sensitive to uncertainties in the quark structure functions of the proton. To investigate the above effects, we have performed a Monte Carlo simulation with several different sets of structure functions. It is assumed that our experiment can reconstruct leptons with polar angles larger than 20°. We find that the reconstructed value of A_{FB} is 0.050 ± 0.002 where the uncertainty reflects the variation of the result with structure function parameterizations. This result does not vary between Sp$\bar{\text{p}}$S and Tevatron energies. Given our list of structure function dependent dilution effects, the uncertainty seems remarkably small. Note that our simulation does not include the correct mechanism for the generation of Z^0 transverse momentum. The smearing of the angular distribution due to the initial state gluon bremsstrahlung (which produces non-zero P_t^Z) is not correctly simulated. This may result in a large uncertainty in the reconstructed asymmetry. The sensitivity of the resolved asymmetry to variations in $\sin^2\theta_w$ is given by the following expression,

$$\delta\sin^2\theta_w = \frac{1}{3.7} \cdot \delta A_{FB}. \tag{3.21}$$

The only measurement of A_{FB} that is currently in print was performed by the UA1 Collaboration[11] with 33 events,

$$A_{FB} = \frac{3}{4} \cdot (0.06 \pm 0.24) = 0.045 \pm 0.18$$

which they convert into a measurement of $\sin^2\theta_w$,

$$\sin^2\theta_w = 0.24^{+0.05}_{-0.04}.$$

It is likely that CDF will be able to produce a measurement in the near future with a precision,

$$\delta A_{FB} \sim \frac{1}{\sqrt{N}} \sim 0.07$$

where N is the number of Z candidates. The corresponding precision on $\sin^2\theta_w$ would be approximately $\delta\sin^2\theta_w \sim 0.020$.

Although neither the UA1 nor the likely CDF results are likely to be very significant, future high-luminosity measurements could reach the $\delta\sin^2\theta_w \sim 0.003$ level if the uncertainty associated with the $q\bar{q}$ axis can be controlled.

LECTURE II

4. Experiments at Electron-Positron Colliders

During the last year, two high energy electron-positron colliders have begun operation. The SLAC Linear Collider (SLC) began physics operation in April of 1989 and had produced a sample of about 600 Z^0 events by early 1990. The LEP project began operation in October of 1989 and had produced samples of approximately 30,000 Z^0 events in each of four detectors by early 1990. The current and future parameters of the two machines are summarized in Table V.

Table V

Machine	Date	Energy	Peak Luminosity
SLC	1989	$\lesssim$ 100 GeV	$\sim 1.4\times10^{28}\mathrm{cm}^{-2}\mathrm{sec}^{-1}$
SLC	1992	$\lesssim$ 100 GeV	$\sim 6\times10^{29}\mathrm{cm}^{-2}\mathrm{sec}^{-1}$
LEP I	1989	$\lesssim$ 100 GeV	$\sim 2\times10^{30}\mathrm{cm}^{-2}\mathrm{sec}^{-1}$
LEP I	1990	$\lesssim$ 100 GeV	$\sim 1\times10^{31}\mathrm{cm}^{-2}\mathrm{sec}^{-1}$
LEP II	1994?	$\lesssim$ 200 GeV	$\sim 3\times10^{31}\mathrm{cm}^{-2}\mathrm{sec}^{-1}$

The luminosity of the SLC is expected to improve by a factor of approximately forty in the next two years. The SLC has a spin polarized electron source that is expected to provide a 40% degree of polarization at the beam collision point. The polarized electron beam should begin operation during 1990. The LEP machine was operated routinely at 20% of its design luminosity during its first run. It seems likely that the design luminosity of 10^{31} $\mathrm{cm}^{-2}\mathrm{sec}^{-1}$ will be achieved during the next year. Although there are serious plans to produce longitudinally polarized beams in LEP, it appears to be difficult to achieve a high degree of longitudinal polarization ($\gtrsim$ 30%) with good luminosity. In the longer term, the energy of LEP will be upgraded to a value above the threshold for W pair production.

4.1. Experimental Details

There are a total of six experiments that are currently operating at or being prepared for SLC and LEP. At the SLC, the Mark II detector is currently in operation and will be replaced by the SLD detector later this year. There are four active experiments at the LEP collider: ALEPH, DELPHI, L3, and OPAL. A complete description of the six detectors would be extremely tiresome. All of them share the a number of common features and capabilities:

1. High Resolution Magnetic Spectrometers - all of the experiments contain charged particle tracking systems that are immersed in magnetic fields. They are capable of reconstructing track directions and transverse momenta. The transverse momentum resolution is typically $\delta P_t/P_t \sim$(0.001-0.002)$\cdot P_t$ (where P_t is in GeV) in the region of polar angle $|\cos\theta| < 0.8$.

2. Electromagnetic Calorimetry - all of the experiments have electromagnetic calorimeters. These range from gas sampled devices with resolutions $\delta E/E \sim 0.30/\sqrt{E}$ (E in GeV) to lead glass and BGO calorimeters with sub-percent resolutions over a large range of energies.

3. Muon Spectrometers/Identifiers - all of the experiments except L3 have magnetized iron shielding for the identification and measurement of muon tracks. The momentum resolution of these systems is poor as compared with the inner tracking systems mentioned above. The L3 detector handles muons in an *inside-out* manner. The muon identification is achieved by penetration of the unmagnetized hadron calorimeter. The muons are momentum analyzed in a huge magnetic spectrometer that is external to the identification shielding and has much higher momentum resolution than the internal tracking system.

4. Vertex Detectors - since the Z^0 is a fairly copious source of b and c quarks, all of the experiments have high precision tracking systems at small radius. The resolution of these systems is typically a few 10's of microns per track measurement.

5. Triggers - since the total (accepted) cross section in an e^+e^- experiment is quite small, a trigger is necessary to find bunch crossings that contain events. The SLC and LEP experiments all contain electronic hardware that can find drift chamber tracks and calorimeter energy depositions during the interval between bunch crossings (22.5 μsec at LEP, 8.3 msec at SLC). Typically, any event containing two or more charged tracks or a calorimeter energy deposition larger than approximately 5 GeV is recorded.

6. Specialties - in addition to the common elements, most of the experiments have some special strengths and features. The following is a partial list:

   (a) Ring Imaging Cerenkov Devices - DELPHI and SLD use ring imaging Cerenkov devices to identify long-lived hadrons.

   (b) High Resolution Vertexing - Mark II and SLD make use of the small SLC beam and the small SLC vacuum chamber with very high resolution microvertex detectors.

   (c) Muon Measurement - as already mentioned, L3 has been optimized for the measurement of muon final states.

   (d) DE/DX - the ALEPH and DELPHI have time projection chambers as their primary tracking systems. These devices are capable of very good measurements of the charged-particle energy loss due to ionization of the chamber gas. This information can be used to identify long-lived charged particles at low momentum.

   (e) Hadron Calorimetry - the SLD calorimeter is expected to have good energy resolution for hadronic final states.

The Electron-Positron Environment

Unlike the situation with hadron colliders, the most copious processes in a high energy e^+e^- collider are also the most interesting ones. The signatures and relative sizes of the various processes are indicated in Table VI. The most serious background to Z^0 production is due to the various two-photon processes. The two-photon background is rather trivial to remove from the data sample (a total energy cut is sufficient to suppress it by several orders of magnitude).

Table VI

Event Type	Signature	$\sigma(\sqrt{s} = M_Z)$
$e^+e^- \to Z^0 \to$ hadrons	2-3 jets $\gtrsim$ 20 charged tracks	~30 nb
$e^+e^- \to e^+e^-$ (small angle)	45 GeV clusters in small angle *tagger*	~50-200 nb (dep on acceptance)
$e^+e^- \to e^+e^-\ell^+\ell^-$ $e^+e^- \to e^+e^-h^+h^-$	Transversely balanced low energy track pairs	~7-8 nb (dep on acceptance)
$e^+e^- \to Z^0 \to \mu^+\mu^-$	back-to-back high energy tracks	~1.5 nb
$e^+e^- \to Z^0 \to \tau^+\tau^-$	acolinear track pairs 1-3 combinations	~1.5 nb

4.2. Mass and Width of the Z^0

We have already discussed the importance of a high precision measurement of the mass of the Z^0. The width of the Z^0 has a tree-level dependence upon the parameters of the Standard Model and the particle content of the theory. The total width is the sum of the partial widths for the decay into each fermion-antifermion final state,

$$\Gamma_Z = \sum_f \Gamma_{f\bar{f}} = \frac{G_F M_Z^3}{24\pi\sqrt{2}} \sum_f C_f(v_f^2 + a_f^2), \tag{4.1}$$

where $\Gamma_{f\bar{f}}$ is the partial width for the decay $Z^0 \to f\bar{f}$ and the constant C_f is defined as

$$C_f = \begin{cases} 1 + \frac{3\alpha}{4\pi} Q_f^2 & \text{for leptons} \\ 3 \cdot \left[1 + \frac{3\alpha}{4\pi} Q_f^2 + \frac{\alpha_s}{\pi}\right] & \text{for quarks.} \end{cases}$$

Note that the expression of each partial width in terms of M_Z has the advantage that the m_{top} and m_{Higgs} dependences are minimized. The partial widths for a generation of quarks and leptons are listed in Table VII. The last line shows the expected total width for three lepton flavors and five quark flavors. A small phase space suppression factor is included for the $b\bar{b}$ final state.

Table VII

Final State	$\Gamma_{f\bar{f}}$
$\nu\bar{\nu}$	166 MeV
$\ell^+\ell^-$	83 MeV
$u\bar{u}$	297 MeV
$d\bar{d}$	383 MeV
2.75 Generations	2.481 GeV

The actual measurement of M_Z and Γ_Z is made by measuring the cross section for the process $e^+e^- \to Z^0 \to f\bar{f}$ for a number of center-of-mass energies about the Z^0 pole. The theoretical Z lineshape is then fit to the measured cross section points to extract the desired parameters. This technique is illustrated in Figure 8 which shows the result of an actual measurement by the Mark II Collaboration.[3]

The theoretical lineshape was discussed in great detail by Michael Peskin in a lecture at this institute.[16] He showed that the tree-level lineshape for the process $e^+e^- \to Z^0 \to f\bar{f}$ is well-approximated by a relativistic Breit-Wigner form,

$$\sigma_f^0(s) = \frac{12\pi}{M_Z^2} \cdot \frac{s\Gamma_{ee}\Gamma_{f\bar{f}}}{(s - M_Z^2)^2 + \Gamma_Z^2 s^2/M_Z^2}. \tag{4.2}$$

Equation (4.2) does not apply to the process $e^+e^- \to e^+e^-$ which occurs via both s-channel and t-channel subprocesses.

The electron and positron radiate real photons rather copiously in a hard collision. The lineshape is strongly affected by the initial state radiation. This effect can be treated in a Drell-Yan-like formalism by introducing an electron structure function. The electron structure function $D(x, s)$ is defined as the probability that an electron (positron) radiates a fraction $1 - x$ of its initial energy during the collision (of cm energy $\sqrt{s}$).* The radiatively corrected cross section can then be written as,

$$\sigma_f(s) = \int dx_1 dx_2 D(x_1, s) D(x_2, s) \sigma_f^0(\hat{s} = x_1 x_2 s), \tag{4.3}$$

where x_1 and x_2 the electron and positron energy fractions. The leading term of the electron structure function has the form,

$$D(x, s) \simeq \frac{\beta}{2}(1-x)^{\frac{\beta}{2}-1}, \tag{4.4}$$

where the dimensionless constant β is the effective number of radiation lengths for the process,

$$\beta \equiv \frac{2\alpha}{\pi}\left[\ln\left(\frac{s}{m_e^2}\right) - 1\right] \simeq 0.11.$$

The effect of the convolution described in equation (4.3) is to reduce the peak cross section by ~25% and to shift the peak of the cross section by roughly 120 MeV from the pole position.

It is convenient to write the radiatively corrected cross section in a form that is close to the underlying Breit-Wigner form,

$$\sigma_f(s) = \frac{12\pi}{M_Z^2} \cdot \frac{s\Gamma_{ee}\Gamma_{f\bar{f}}}{(s - M_Z^2)^2 + \Gamma_Z^2 s^2/M_Z^2} \cdot [1 + \delta_{RC}(s)], \tag{4.5}$$

where the effects of the radiative corrections are contained in $\delta_{RC}(s)$. Using equation (4.1), we can expression all of the quantities that appear in equation (4.5) in terms of a single parameter, M_Z. Note that this choice of parameters minimizes the sensitivity of the lineshape to higher-order terms in m_{top} and m_{higgs}.

Equation (4.5) is the basis for the measurement of a number of Z resonance parameters. The analysis is usually performed with several sets of constraints:

⋆ Note that the electron structure function is defined as a number distribution unlike the hadron structure functions which are defined as normalized momentum distributions. The e^+e^- cross sections therefore lack the factors of x^{-1} that appear in the hadronic cross sections.

1. All resonance parameters are constrained to their Standard Model values. In this case, the only free parameter is M_Z. The measurement can be performed with any or all of the final states (the e^+e^- final states must be excluded or fit to the correct form).

2. The visible partial widths are constrained to their Standard Model values and the invisible width is allowed to vary as a free parameter. The total width Γ_Z is decomposed into visible and invisible portions,

$$\begin{aligned}\Gamma_Z &= \sum \Gamma_{q\bar{q}} + 3\Gamma_{\ell^+\ell^-} + 3\Gamma_{\nu\bar{\nu}} \\ &= \Gamma_{vis} \qquad\qquad\qquad + \Gamma_{inv},\end{aligned} \tag{4.6}$$

   where the visible width Γ_{vis} contains all hadronic final states and all charged lepton pairs, and Γ_{inv} contains the neutrino decays and any additional unobserved particles. Any or all of the final states can be used to perform the measurement (with the usual caveat about electrons). The data are therefore fit to a function of two parameters (M_Z and Γ_{inv}),

$$\sigma_f(s) = \frac{12\pi}{M_Z^2} \cdot \frac{s\Gamma_{ee}\Gamma_{f\bar{f}}}{(s - M_Z^2)^2 + (\Gamma_{vis} + \Gamma_{inv})^2 s^2/M_Z^2} \cdot [1 + \delta_{RC}(s)]. \tag{4.7}$$

3. The resonance parameters of the total hadronic cross section are not constrained to their Standard Model values. The hadronic cross section is described by the model-independent form,

$$\sigma_{had}(s) = \frac{s\Gamma_Z^2\sigma_{had}^0}{(s - M_Z^2)^2 + \Gamma_Z^2 s^2/M_Z^2} \cdot [1 + \delta_{RC}(s)], \tag{4.8}$$

   where the free parameters are: M_Z, Γ_Z, and the tree-level hadronic peak cross section σ_{had}^0. The Standard Model prediction for the tree-level peak cross section is,

$$\sigma_{had}^0 = \frac{12\pi}{M_Z^2} \cdot \frac{\Gamma_{ee}\Gamma_{had}}{\Gamma_Z^2} \simeq 41.5 \text{ nb}^{-1}. \tag{4.9}$$

4. None of the partial widths given in equation (4.5) are constrained to their Standard Model values. This analysis is most elegantly performed by fitting

the hadronic and leptonic final states separately but simultaneously. If the electron final states (and the appropriate lineshape) are not used, it is necessary to invoke lepton universality, $\Gamma_{ee} = \Gamma_{\mu\mu} = \Gamma_{\tau\tau}$. Assuming universality, the fit involves four parameters (M_Z, Γ_Z, Γ_{had}, and $\Gamma_{\ell\ell}$).

Scanning Theory

A hadron collider gives the experimenter a free energy scan. The hadron structure functions are quite broad in that reasonable quark-quark luminosity is produced over a large range of energies. The electron structure functions have an integrable singularity at $x = 1$. Most of the e^+e^- luminosity is produced near the nominal value of $\sqrt{s}$. The experimenter can therefore choose the most efficient energy scan to optimize the measurement he/she wishes to measure. Note that an optimal scanning strategy requires some *a priori* knowledge of the parameters that one desires to measure. In the earliest runs of the SLC, the Z^0 mass was not well known and it was necessary to search for an enhancement in the event rate. Once M_Z became somewhat constrained, it was possible to choose very efficient operating points. The presence of the Standard Model as a predictor of widths and couplings made this task much easier.

Let us consider a hypothetical scan of N energy-luminosity points:

$$E_b = E_1, E_2, ..., E_N$$
$$\int \mathcal{L}dt = L_1, L_2, ..., L_N.$$

We assume that a cross section σ_i is measured at each point,

$$\sigma_{measured} = \sigma_1, \sigma_2, ..., \sigma_N.$$

The M parameters a_j ($j = 1, M$) of our theoretical lineshape $\sigma(E)$ can be extracted from a χ^2 fit to the measured points. The quantity χ^2 is defined as,

$$\chi^2 \equiv \sum_{i=1}^{N} \frac{[\sigma_i - \sigma(E_i)]^2}{(\delta\sigma_i)^2}, \tag{4.10}$$

where $\delta\sigma_i$ is the error on the i^{th} measurement.

The best estimate of the parameters $(\bar{a}_j)$ is the one that minimizes χ^2. The parameter errors are found from a Taylor expansion of χ^2 about the minimum value,

$$\begin{aligned} \chi^2 &= \chi^2(\bar{a}) + \frac{1}{2} \sum_{j,k=1}^{M} \frac{\partial^2 \chi^2}{\partial a_j \partial a_k}(a_j - \bar{a}_j)(a_k - \bar{a}_k) \\ &= \chi^2(\bar{a}) + \sum_{j,k=1}^{M} (\mathbf{C}^{-1})_{jk}(a_j - \bar{a}_j)(a_k - \bar{a}_k) \end{aligned} , \tag{4.11}$$

where the matrix $\mathbf{C}^{-1}$ is the inverse of the parameter covariance matrix. The error hyperellipsoid is determined by changing χ^2 by one unit about the minimum value. It is straightforward to show that the parameter errors are given by the diagonal elements of the covariance matrix $\mathbf{C}$,

$$(\delta a_j)^2 = \mathbf{C}_{jj}. \tag{4.12}$$

Averaging equation (4.11) over many experiments, the inverse matrix can be expressed in the following form,

$$(\mathbf{C}^{-1})_{jk} = \sum_{i=1}^{N} \frac{1}{(\delta\sigma_i)^2} \cdot \left[\frac{\partial\sigma}{\partial a_j}(E_i)\right] \cdot \left[\frac{\partial\sigma}{\partial a_k}(E_i)\right]. \tag{4.13}$$

Although equation (4.13) is quite general, it is useful to express the cross section errors in terms of the luminosity and the theoretical cross section. Ignoring the statistical errors on the luminosity measurements,* we can express the cross section errors as $(\delta\sigma_i)^2 = \sigma(E_i)/L_i$. Equation (4.13) can then be written as,

$$(\mathbf{C}^{-1})_{jk} = \sum_{i=1}^{N} \frac{L_i}{\sigma(E_i)} \cdot \frac{\partial\sigma}{\partial a_j}(E_i) \cdot \frac{\partial\sigma}{\partial a_k}(E_i) = \sum_{i=1}^{N} L_i \cdot S(E_i, a_j) \cdot S(E_i, a_k), \quad (4.14)$$

where we define the so-called *sensitivity function* $S(E, a_j)$ as

$$S(E, a_j) \equiv \frac{1}{\sqrt{\sigma(E)}} \cdot \frac{\partial\sigma}{\partial a_j}(E). \quad (4.15)$$

If the lineshape is a function of a single parameter or if the off-diagonal elements of the inverse matrix $\mathbf{C}^{-1}$ are small, the parameter errors have a particularly simple form,

$$(\delta a_j)^{-2} \simeq \sum_{i=1}^{N} L_i \cdot \Big[S(E_i, a_j)\Big]^2. \quad (4.16)$$

Equation (4.16) *implies that the error δa_j is minimized when the integrated luminosity is concentrated in regions of scan energy where $|S(E, a_j)|$ is large.* Note that $|S(E, a_j)|$ is large where the derivative $|\partial\sigma/\partial a_j|$ is large and where the cross section is small.

The correlations between the parameters are described by the off-diagonal elements of the matrices $\mathbf{C}^{-1}$ and $\mathbf{C}$ (the error ellipsoid is unrotated if they vanish). *The presence of non-zero correlation always increases a parameter error beyond the value given in equation* (4.16).† It is clearly important to minimize the off-diagonal elements by our choice of the scan point luminosities.

Equations (4.14) and (4.12) predict the complete parameter error matrix in terms of the theoretical lineshape and the scan point luminosities. *Note that it is assumed that χ^2 is well-defined ($N > M$) and that a sufficient number of events is collected at each point that the errors are Gaussian.*

⋆ This assumption is quite valid for the measurement of non-resonant cross sections.

† The presence of non-zero correlation allows the error associated one parameter to *leak* into the error associated with another parameter.

Since any cross section measurement has an associated normalization uncertainty, it is important to consider the sensitivity of the final result to systematic shifts in the measured cross sections. Expanding the theoretical cross section in parameter space about the best estimates $\bar{a}_j$, it is straightforward to derive the average shift in a parameter Δa_j caused by shifts in the measured cross sections $\Delta\sigma_i$,

$$\langle \Delta a_j \rangle = \sum_{k=1}^{M} \mathbf{C}_{jk} \cdot \sum_{i=1}^{N} L_i \cdot \frac{\Delta\sigma_i}{\sigma_i} \cdot \frac{\partial \sigma}{\partial a_k}(E_i). \qquad (4.17)$$

It is clear that we would like to choose the energies and luminosities to minimize the parameter errors and the correlations between the parameters. We can be guided in this task by examining the energy dependence of the functions $S(E, a_j)$.

As an example of the usefulness of the sensitivity functions, let us consider the measurement of the model-independent parameters of the hadronic cross section. For simplicity, we assume that values of M_Z, Γ_Z, and $\sigma^0_{had}(M_Z^2)$ are 91 GeV, 2.5 GeV, and 40 nb, respectively. The sensitivity functions for M_Z, Γ_Z, and $\sigma^0_{had}(M_Z^2)$ are plotted in Figures 9-11 as functions of $E - M_Z$. The maximum sensitivity to M_Z occurs at the scan energies -0.8 GeV and +1.0 GeV about the pole. Note that there is little sensitivity to Γ_Z at these points. The maximum sensitivity to Γ_Z occurs at points that are approximately ± 2 GeV about the pole. If we choose our energy-luminosity points symmetrically about the pole, the sum of the products $S(E_i, M_Z) \cdot S(E_i, \Gamma_Z)$ will tend to cancel since $S(E, M_Z)$ is odd about the pole and $S(E, \Gamma_Z)$ is even about the pole. The maximum sensitivity to σ^0_{had} occurs at the pole. The same odd-even effect that cancels the M_Z-Γ_Z correlation will cancel the M_Z-σ^0_{had} correlation. The Γ_Z-σ^0_{had} correlation cannot be cancelled by a choice of scan energies. However, it is not intrinsically large since $S(E, \Gamma_Z)$ is small in the energy region where $S(E, \sigma^0_{had})$ is large.

In general, a scan strategy that is based upon equations (4.14) and (4.12) is a problem in linear programming. The scan planner must decide how important various parameters are and what constraints must be satisfied. Nevertheless, fairly simple considerations lead to the conclusion that a minimal Z-pole scan should include points at 0, ± 1, and ± 2 GeV about the pole.

Event Selection

The selection of hadronic and leptonic events was done by the five experiments with five different sets of criteria. While these criteria differ in detail, they do contain a number of common features. The selection of hadronic events usually involves the following requirements:

1. The event is required to contain five or more charged tracks. This requirement is sometimes relaxed to three or more tracks. In this case, one must be careful to exclude $\tau^+\tau^-$ events from the sample.

2. The event is required to have a visible energy (track momenta and/or calorimeter energy) that is larger than 10% of the center-of-mass energy. The principal reason for this requirement is to suppress two-photon events.

3. Most of the analyses require that substantial energy be observed in both hemispheres about the detector midplane (polar angle $\theta = 90°$). This requirement suppresses beam-gas events.

4. The time of the event must be consistent with the time of a beam crossing (to suppress cosmic ray events).

The detection efficiency for hadronic events is typically $\sim$95% with an uncertainty of 0.5-1%. The residual background contamination is typically at level of a few parts in 10^3 (mostly from $\tau^+\tau^-$ events).

Leptonic events are selected by a set of criteria that are similar to the following:

1. Electron Final States

   (a) The event is required to have two tracks. Some analyses require that the acolinearity angle be less than 5°.

   (b) There must be energy depositions in the electromagnetic calorimeters that match the tracks (spatially and/or in energy-momentum). The total energy of the calorimeter clusters must be a large fraction ($\gtrsim 80\%$) of the center-of-mass energy.

2. Muon Final States

   (a) The event is required to have two tracks. Some analyses require that the acolinearity angle be less than $5°$. The momenta of each track must be $\gtrsim 60\%$ of the beam momentum.

   (b) The energy deposition in the calorimeter that is associated with each track must be consistent with the passage of a minimum ionizing particle.

   (c) At least one track is required to penetrate the muon shielding and be detected in the outer tracking system.

3. Tau Final States

   (a) The event is required to have a visible energy that is larger than $\sim$10% of the center-of-mass energy.

   (b) The event is required to have between two and six tracks. Dividing the event into two thrust hemispheres, the legal track configurations are: one track recoiling against one track (1-1), one track recoiling against three tracks (1-3), or three tracks recoiling against three tracks (3-3).

   (c) The track momenta of two-track events are required to be $\lesssim 60\%$ of the beam momentum.

   (d) The invariant masses of the charged tracks in each hemisphere must be less than 2 GeV.

The detection efficiencies for lepton pairs are strongly affected by the acceptance of the tracking, calorimetric, and muon identification systems. Typically, electrons are selected with the largest efficiency ($\sim 70\%$). The typical detection efficiencies for muon and tau pairs are 60% and 50%, respectively. The uncertainties on the efficiencies are typically about 2%. The background contamination from hadronic events, two-photon events, and miscategorized lepton pairs ranges from $\sim$1% for electron pairs to $\sim$5% for tau pairs.

Luminosity Measurement

The experimental luminosities are inferred from measurements of the process $e^+e^- \to e^+e^-$ at small scattering angles (25-150 milliradians). In the small angle region, this process is dominated by t-channel exchange of photons and is independent of the parameters of the Z^0 system. The tree-level differential cross section has the form,

$$\frac{d\sigma_{lum}}{d\theta} \simeq \frac{4\pi\alpha^2}{s} \cdot \frac{1}{\theta^3}, \tag{4.18}$$

where the scattering angle θ is assumed to be small. An accurate determination of the luminosity requires that the radiative corrections be included in equation (4.18). Nevertheless, equation (4.18) does illustrate one of the difficulties in the measurement of the luminosity. The measured cross section σ_{lum}^{meas} is a sensitive function of the angular acceptance of the detector edges,

$$\sigma_{lum}^{meas} \simeq \frac{2\pi\alpha^2}{s}\left(\frac{1}{\theta_1^2} - \frac{1}{\theta_2^2}\right), \tag{4.19}$$

where θ_1 and θ_2 are the angles of the inner and outer detector edges.

Each of the SLC/LEP detectors contains a luminosity monitor that consists of two cylindrical electromagnetic calorimeters designed to detect e^+e^- pairs in the very forward regions (from 25-60 milliradians at the inner edges to ~150 milliradians at the outer edges). In order to control the angular acceptance well, each device is either highly segmented or contains an integral tracking system to measure the scattering angle of each particle. The accepted cross section for these devices is in the range 25-150 nb. In some cases, the statistical error on the luminosity determination is a bit worse than that on the number of hadronic events (the radiatively corrected cross section for hadronic events is ~30 nb). The systematic error on the luminosity measurement is usually dominated by the uncertainty on the accepted cross section and on the effect of higher-order radiative corrections. The systematic errors range from 1.3% to about 5%.

The uncertainty on the luminosity determination must be combined with the uncertainty on the detection efficiency to yield an overall normalization uncertainty for a cross section measurement. The overall normalization uncertainties are typically several percent.

Experimental Results

The current results of the five SLC/LEP experiments[3-7] are listed in Table VIII. The Mark II, ALEPH, DELPHI, L3, and OPAL results are based upon exposures of 17, 850, 53.9, 627, and 1247 nb^{-1}, respectively.

Table VIII

The results of the Z^0 mass and width analyses of the SLC/LEP experiments.

Experiment	M_Z (GeV)	Γ_Z (GeV)	Γ_{inv} (MeV)	σ^0_{had} (nb)	$\Gamma_{\ell\ell}$ (MeV)
Mark II[3]	91.14(12)	$2.42(^{+45}_{-35})$	460(100)	42.0(40)	$92.0(^{+170}_{-160})$
ALEPH[4]	91.18(4)	2.54(6)	501(26)	41.4(8)	83.9(22)
DELPHI[5]	91.06(9)	2.42(21)	400(107)	42.8(58)	—
L3[6,17]	91.16(4)	2.54(5)	548(29)	39.8(9)	83.0(24)
OPAL[7]	91.16(3)	2.54(5)	453(44)	41.2(11)	81.9(20)
Average	91.16(3)	2.54(3)	506(17)	40.8(5)	82.9(13)

The following notes apply to the information that is presented in Table VIII.

1. The Mark II value for the leptonic partial width is determined from the product of the measured[18] ratio $\Gamma_{\ell\ell}/\Gamma_{had}$ and the theoretical value for Γ_{had}.

2. The ALEPH Collaboration quote their result for Γ_{inv} in terms of the number of neutrinos N_ν as defined by the following

$$\Gamma_{inv} = N_\nu \cdot \Gamma_{\nu\nu} = N_\nu \cdot 166 \text{ MeV}. \tag{4.20}$$

They derive N_ν from an analysis of Γ_Z and σ^0_{had}. Note that this procedure is entirely equivalent to the use of equation (4.7) in a constrained fit. We convert their result to Γ_{inv} for display purposes.

3. The Delphi Collaboration do not use σ^0_{had} as a fit parameter but instead scale the Standard Model value with a free normalization parameter. We convert their result for the normalization parameter into a value for the peak cross section.

4. The averages that are listed in the last line are calculated by weighting each measurement appropriately with its error. The common energy scale error was correctly included in the averaging procedure. All other errors are assumed to be uncorrelated (which is undoubtedly incorrect).

The measurements of the resonance parameters that are shown in Table VIII agree remarkably well with the Standard Model predictions. Using equation (4.20) we estimate the number of light neutrino species to be,

$$N_\nu = 3.04 \pm 0.10,$$

which is the best evidence for the three generation model (note that neutrino species of mass larger than $M_Z/2$ are not ruled out). The only apparent discrepancy between the measurements and the expectations is that Γ_Z seems a bit larger than expected (by ~60 MeV). There are several possible explanations for this. We list them in descending order of likelihood: 1) it is a statistical fluctuation (the probability of a fluctuation is not small enough to establish a discrepancy); 2) there is a correlating effect (like the energy of a scan point differed from its nominal value); 3) the QCD corrections to the hadronic partial widths need more work; 4) there is a new particle in the final state. It is even possible that several of these explanations are valid.

Systematic Errors

The various resonance parameters vary in their sensitivity to the energy scale and normalization uncertainties. The determination of M_Z depends completely on the accelerator energy scale. The 27 MeV uncertainty on the LEP energy scale and the 40 MeV uncertainty on the SLC energy scale apply directly to mass measurements made at the two machines. The model-independent determinations of M_Z

are completely insensitive to the normalization uncertainty. The model constrained determinations of M_Z have a slight sensitivity to the normalization uncertainty. These uncertainties are typically a few MeV or less (even with the model constraints, most of the M_Z information is derived from the resonance shape).

The peak cross section and the invisible width are strongly affected by normalization uncertainty. This can be seen from an inspection of equation (4.7). The invisible width enters the cross section as a component of the total width. The influence of the total width is maximized when the center-of-mass energy is $s = M_Z^2$. The effect of the normalization uncertainty $\delta\sigma$ upon the invisible width is approximately,

$$\delta\Gamma_{inv} \simeq 1.5 \text{ GeV} \cdot \left(\frac{\delta\sigma}{\sigma}\right).$$

The measurement of Γ_Z depends almost entirely upon the measurement of the resonance shape. It is therefore insensitive to the absolute energy and normalization errors. It is sensitive to point-to-point errors in the energy and luminosity. These are typically much smaller than the absolute errors.

The measurement of the leptonic width is sensitive to the absolute normalization uncertainty. The peak leptonic cross section is proportional to the square of the leptonic width. The percentage uncertainty on $\Gamma_{\ell\ell}$ is therefore one half of the percentage uncertainty on the normalization.

4.3. Mass and Width of the W

The measurement of the W boson mass and width will become possible in the second phase of LEP operation. The installation of superconducting RF cavities will permit the beam energy to be increased to a value above the threshold for the process $e^+e^- \to W^+W^-$.

High Energy e^+e^- Cross Sections

The tree-level expression for the W-pair cross section is somewhat complex.[19] The inclusion of initial state radiation (as in equation (4.3)) and finite widths for the final state W bosons involves a four dimensional convolution of the tree-level expression. We therefore choose to present only the result of a Monte Carlo integration. The cross section for the process $e^+e^- \to W^+W^-$ is plotted in Figure 12 as a function of $E_b - M_W$ where E_b is the single beam energy. The mass and width of the W are assumed to be 80 GeV and 2.1 GeV, respectively. Note that three curves are plotted: the dashed curve is the basic tree-level cross section; the dashed-dotted curve is the cross section including the effect of initial state radiation; and the solid curve is the cross section including initial state radiation and the effect of a finite W width. The inclusion of initial state radiation reduces the size of the cross section. The finite W width produces non-zero cross section at energies below the nominal threshold at $E_b = M_W$.

The basic $e^+e^- \to f\bar{f}$ cross section for five quark and three lepton flavors increases from about 7 units of R at center-of-mass energies below the Z^0 pole to 10 units of R at energies above the Z^0 pole.* At $\sqrt{s} = 160$ GeV, the tree-level cross section is approximately 34 pb. Unfortunately, the initial state radiative corrections increase this number enormously. Although the photon structure functions decrease greatly as x is decreased from 1, the Z pole is sufficiently large that the convolution given in equation (4.3) is several times larger than the tree-level cross section. The process $e^+e^- \to \gamma Z^0$ therefore dominates the visible cross section at W-pair threshold. Using equation (4.3), we estimate the size of the visible cross section to be ~150 pb at $\sqrt{s} = 160$ GeV.

<u>$e^+e^- \to W^+W^-$ Threshold Scan</u>

There are several different techniques that can be used to measure the W mass at LEP II. It is possible to extract M_W from the measured distributions of jet masses or lepton energies. These methods are are described in Reference 20. The technique that we'll discuss here is the measurement of the threshold behavior of the W pair cross section.

⋆ The unit of R is the cross section for $e^+e^- \to \gamma^* \to \mu^+\mu^-$. Numerically, the cross section has the value $\sigma_R = 86.8$ nb-GeV$^2/s$.

It is clear than the W mass can be extracted from the *step* in the cross section that is shown in Figure 12. Since there is a large background from ordinary processes, it is necessary to apply selection criteria to the data to improve the signal-to-noise ratio. The background processes produce mostly two- and three jet hadronic events or lepton pair events that are often highly boosted along the beam direction. The visible energy of the background is often small as compared with $\sqrt{s}$. The W-pair events appear most often as four-jet events (~44% of W-pairs) or as an energetic lepton and two jets (~44% of W-pairs). The authors of Reference 20 have studied a number of selection criteria to reduce the background cross section to less than ~1 pb while retaining ~75% of the four-jet and ~45% of the lepton+two-jet events (we assume that τ leptons cannot be used and that one third of the remaining events are eliminated by the isolation cut used to suppress heavy flavor events). Assuming that the residual background is due to the large $\sqrt{\hat{s}}$ continuum, the measured cross section would have the following form,

$$\sigma_{meas}(E_b) = \varepsilon\sigma_{ww}(E_b) + \frac{B}{(2E_b)^2}, \tag{4.21}$$

where: ε is the efficiency to identify a W-pair event ($\varepsilon \simeq 0.53$); $\sigma_{ww}(E_b)$ is the cross section plotted in Figure 12; and B is a constant that represents the residual background (which presumably scales as $1/s$).

subsectionSensitivity Functions

We can analyze the M_W and Γ_W sensitivity of a cross section scan of the W pair threshold by using the scanning theory that was discussed in the last section. Numerically differentiating the measured cross section (as defined in equation (4.21)), it is straightforward to calculate the sensitivity functions for M_W, Γ_W, and the background constant B. For the purpose of this exercise, we assume that $B = 1\ \text{pb} \cdot (2M_W)^2$ or that the background cross section is 1 pb at W-pair threshold.

The sensitivity function $S(E_b, M_W)$ is plotted in Figure 13 as a function of $\epsilon_b = E_b - M_W$. Note that the maximum sensitivity occurs at $\epsilon_b \simeq 0.5$ GeV.

The sensitivity function $S(E_b, \Gamma_W)$ is shown in Figure 14 as a function of ϵ_b. As one would expect, it peaks just below the nominal threshold ($\epsilon_b = -1$ GeV) where the width-induced *tail* in the cross section is largest. The function $S(E_b, \Gamma_W)$ decreases rapidly as E_b is increased. It passes through zero near $\epsilon_b = 1$ GeV and plateaus above $\epsilon_b = 3$ GeV. The sensitivity in the plateau region is due to the reduction in the cross section caused by the finite width (see Figure 12). The maximum value of $|S(E_b, \Gamma_W)|$ is smaller than the maximum value of the mass sensitivity function by a factor of three. A good measurement of Γ_W will clearly require a substantial commitment of luminosity to a point of very small cross section. Note that the product $S(E_b, M_W) \cdot S(E_b, \Gamma_W)$ is an odd function about the point $\epsilon_b = 1$ GeV. In principle, the M_W-Γ_W correlation can be cancelled by measuring the cross section on both sides of this point. The functions $S(E_b, M_W)$ and $S(E_b, \Gamma_W)$ are not large in the region $\epsilon_b > 1$ GeV. The cancellation of the correlation therefore requires a substantial commitment of luminosity to a relatively insensitive region.

The function $S(E_b, B)$ is plotted as a function of ϵ_b in Figure 15. As one would expect, the background sensitivity is largest at small beam energy and decreases dramatically as E_b increases through the W pair threshold. Note that it is possible to cancel the B-Γ_W correlation but that it is not possible to cancel the B-M_W correlation.

Scan Strategies

It is clear that precise measurements of M_W and Γ_W require that LEP be operated in regions of small cross section. Since all other studies of the W-pair system require a large sample of data, there will be considerable pressure to operate the machine on the cross section plateau at the largest available energy. In order to estimate how precisely M_W and Γ_W could be measured in a 1-2 year run (500 pb^{-1}), we assume that 50% of the luminosity is dedicated to operating at the largest available energy (we assume that $\epsilon_b = 15$ GeV or $\sqrt{s} = 190$ GeV is achieved) and the remaining 50% is dedicated to operation in the threshold region.

It is instructive to first consider an extremely unrealistic scan scenario. We assume that we will measure only one parameter and that the other parameters are precisely known. In this case, we need only one scan point in the threshold region for a constrained fit. We choose to allocate the entire 250 pb^{-1} luminosity to operation at the most mass-sensitive point ($\epsilon_b = 0.5$ GeV) or at the most width-sensitive point ($\epsilon_b = -1$ GeV). Using equation (4.16) we estimate the precision of these measurements to be

$$\delta M_W = 92 \text{ MeV} \quad \text{or} \quad \delta\Gamma_W = 286 \text{ MeV}.$$

The M_W measurement would be a very desirable result. The Γ_W measurement is not competitive with the recent indirect determinations that have been published by the CDF and UA2 collaborations,[15,21]

$$\Gamma_W = (0.85 \pm 0.08) \cdot \Gamma_Z = 2.19 \pm 0.20 \text{ GeV (CDF)}$$
$$\Gamma_W = (0.89 \pm 0.08) \cdot \Gamma_Z = 2.30 \pm 0.20 \text{ GeV (UA2)}.$$

Since the width cannot be measured to an interesting level, it is clearly unwise to design a scan to measure Γ_W. We therefore concentrate on the measurement of M_W.

A real measurement of M_W will require that the background constant B be varied as a fit parameter. Unfortunately, the B-M_W correlation cannot be canceled by a clever choice of scan points. It is therefore necessary to measure both parameters well.

The number of scan points is somewhat arbitrary. A minimum of three points are required to constrain the two parameter problem. The presence of a high energy point implies that only two points are needed in the threshold region. Equation (4.14) implies that several closely spaced points in a region of large sensitivity are equivalent to a single point in the same region. We can therefore analyze the optimization of the M_W measurement by considering a two-point threshold measurement.

An optimal scan must include an energy point in a region of large background sensitivity $|S(E_b, B)|$ and a point near the maximum of the mass sensitivity function $|S(E_b, M_W)|$. We choose the scan point energies to be $\epsilon_b = -5$ GeV and $\epsilon_b = 0.5$ GeV, respectively.* The apportionment of the available luminosity between the two points is a straightforward problem in one-dimensional optimization. We find that the error δM_W has a very broad minimum about the ratio of luminosities, $L(0.5 \text{ GeV})/L(-5 \text{ GeV}) \simeq 2/1$. If the luminosities of the -5 GeV and 0.5 GeV points are 85 pb^{-1} and 165 pb^{-1}, respectively, the minimum value of the error δM_W is approximately 155 MeV.

A two-point threshold scan is somewhat risky. It is safer to bracket the region of maximum M_W sensitivity with several scan points. We therefore construct an optimal four-point scan (a five-point measurement when the $\epsilon_b = 15$ GeV point is included) by assigning one third of the 165 pb^{-1} (55 pb^{-1}) to each of three points: $\epsilon_b = 0$ GeV, 0.5 GeV, and 1.0 GeV. It is instructive to compare this scan (Scan 1) with a slightly modified version. The modified version (Scan 2) is created by shifting the luminosity from the $\epsilon_b = 0$ GeV point to $\epsilon_b = -1$ GeV. We expect the second scan strategy to improve the width measurement at the expense of the mass measurement. Finally, we note that our modified scan strategy is similar to the scan strategy that was studied in Reference 20 (which we label Scan 3). The authors of Reference 20 assigned 100 pb^{-1} to each of the following five points: $\epsilon_b = -5$ GeV, -1 GeV, 0 GeV, 1 GeV, and 15 GeV.

Using equation (4.14) and the sensitivity functions, the performance of each scan scenario can be estimated. The expected number of detected events and the expected precisions δM_W, $\delta\Gamma_W$, and δB are listed in Table IX for each of the three scan strategies. The presence of a high energy point in each strategy reduces the M_W-Γ_W correlation sufficiently that the M_W precision obtained from the three parameter fit is essentially identical to that obtained from a two-parameter fit.

$\star$ Varying the energy of the second point about $\epsilon_b = 0.5$ GeV verifies that the B-M_W correlation does not shift the point of maximum M_W sensitivity.

As one might expect, the third scan strategy which allocates 400 pb^{-1} to the threshold measurement provides the most precise M_W measurement, $\delta M_W =$ 150 MeV. *The M_W precision obtained from the optimized mass scan (Scan 1) is worse by 7%. Note however, that Scan 1 produces nearly 60% more events than does Scan 3.* Surprisingly, the second scan strategy provides a slightly better width measurement than does the third strategy. This occurs because the second scan produces a smaller B-Γ_W correlation than does the third scan strategy.

It is clear from equation (4.21) that the functions $S(E_b, a_j)$ are sensitive to the level of residual background and to the W-pair detection efficiency. We investigate these effects by reducing the background constant to $B = 0.5 \text{ pb} \cdot (M_W)^2$ and by increasing the detection efficiency to $\varepsilon_{ww} = 0.70$. The results are listed in Table IX. The error δM_W is improved by approximately 20 MeV in the case that the background is reduced by a factor of two. The mass error is improved by approximately 30 MeV when the efficiency is increased. Note that the optimal luminosity ratio $L(0.5 \text{ GeV})/L(-5 \text{ GeV})$ is nominally sensitive to both effects. However, the optimal region is so broad that the use of a 2/1 ratio degrades the result by less than 1%.

Table IX

The predicted results of three different five-point measurements of the W-pair threshold. Scan 1 is optimized for the measurement of M_W. Scan 2 is an attempt to improve the measurement of Γ_W. Scan 3 is identical to the threshold scan used in Reference 20. The results are presented for several assumptions about the level of residual background B and the W-pair detection efficiency.

Quantity	Scan 1	Scan 2	Scan 3
L[-5 GeV] (pb^{-1})	85	85	100
L[-1 GeV] (pb^{-1})	0	55	100
L[0 GeV] (pb^{-1})	55	0	100
L[0.5 GeV] (pb^{-1})	55	55	0
L[1 GeV] (pb^{-1})	55	55	100
L[15 GeV] (pb^{-1})	250	250	100
$B = 1.0$ pb $\cdot [2M_W]^2$ $\varepsilon_{ww} = 0.53$			
Number of Events	2951	2912	1863
δM_W (MeV)	160	176	150
$\delta\Gamma_W$ (MeV)	531	482	492
δB (pb $\cdot [2M_W]^2$)	0.12	0.12	0.12
$B = 0.5$ pb $\cdot [2M_W]^2$ $\varepsilon_{ww} = 0.53$			
Number of Events	2737	2698	1627
δM_W (MeV)	137	154	130
$\delta\Gamma_W$ (MeV)	508	450	448
δB (pb $\cdot [2M_W]^2$)	0.096	0.098	0.098
$B = 1.0$ pb $\cdot [2M_W]^2$ $\varepsilon_{ww} = 0.70$			
Number of Events	3760	3709	2309
δM_W (MeV)	130	144	123
$\delta\Gamma_W$ (MeV)	453	407	410
δB (pb $\cdot [2M_W]^2$)	0.12	0.13	0.13

Systematic Errors

The measurement of the W-pair threshold is affected by systematic uncertainties on the energy scale and cross section normalization. The energy scale uncertainty affects the M_W measurement directly. Assuming that the fractional error on the beam energy scale is constant, the uncertainty on M_W should be comparable to the one that applies to the M_Z measurement. By 1994, this uncertainty is expected to be ~20 MeV.

The sensitivity of the results given in Table IX to normalization errors can be estimated from equation (4.17). Taking the first scan strategy as an example, we estimate that the uncertainties on the parameters are related to an overall normalization uncertainty $\delta\sigma/\sigma$ as follows,

$$\begin{aligned}\delta M_W &= -2.26\ \text{GeV} \cdot \frac{\delta\sigma}{\sigma} \\ \delta\Gamma_W &= -19.3\ \text{GeV} \cdot \frac{\delta\sigma}{\sigma}.\end{aligned}$$

The normalization error must be controlled to the 3% level to avoid inflating the M_W error.

Sensitivity to Assumptions

Our analysis assumes that we have complete *a priori* knowledge of the W resonance parameters. Although the characteristic width in E_b space of the M_W-sensitive region is larger than the current uncertainty on M_W, our precision estimates are likely to be somewhat optimistic. It is possible to alter the results by $\lesssim$10% by varying the resonance parameters over reasonable intervals.

Conclusions

Despite the uncertainties on the ultimate W-pair detection efficiency and residual background contamination, several conclusions can be drawn from this analysis:

1. The most sensitive scan region for the measurement of M_W is ϵ_b = 0-1 GeV. *The mapping of the entire threshold shape would produce a less precise measurement.*

2. It is not possible to remove the correlation between the background parameter and M_W by a clever choice of scan point energies. This implies that a scan point of energy below the nominal threshold is quite important. If the energy is chosen to be $\epsilon_b = -5$ GeV ($E_b = 75$ GeV), an M_W-optimized scan strategy would allocate twice as much integrated luminosity to the M_W sensitive region as is allocated to the low energy point.

3. A measurement of M_W at the $\lesssim$160 MeV level is possible with the dedication of a large integrated luminosity (250 pb^{-1}) and good control of the background contamination.

4. The measurement of Γ_W to an interesting level is difficult or impossible. It is probably unwise to attempt anything more than a cursory measurement.

4.4. Forward-Backward Asymmetries

In the next several years, several asymmetries of the Z^0 cross section will be used to test the electroweak portion of the Standard Model. Note that all of these tests work by measuring the ratio of the vector and the axial vector couplings of the Z^0 to the fermionic current. As was described in the Introduction, this implies that the sensitivities of the various tests can be characterized in terms a single parameter $\sin^2\theta_w$. Note that this parameter differs from the Sirlin definition that was used to describe the ratio M_W/M_Z.

Let us begin by considering the cross section for the process $e^+e^- \to f\bar{f}$. We assume the electron and positron beams can be longitudinally polarized. The beam polarizations, P^- and P^+, are described in terms of a helicity basis ($P = +1$ describes a right-handed beam, $P = -1$ describes a left-handed beam). We can then write the tree-level cross section in the cm frame as follows,

$$\frac{d\sigma_f}{d\Omega} = \frac{\alpha^2 N_c^f}{64 s \sin^4 2\theta_w} \cdot \left\{(1 - P^+P^-)[\sigma_u^{\gamma Z} + \sigma_u^Z] + (P^+ - P^-)[\sigma_p^{\gamma Z} + \sigma_p^Z]\right\} \quad (4.22)$$

where: the unpolarized partial cross sections due to γZ interference and pure Z

exchange are defined as,

$$\sigma_u^{\gamma Z} = -8Q_f \sin^2 2\theta_w \mathrm{Re}[\Gamma(s)] \left[(1+\cos^2\theta^*)vv_f + 2\cos\theta^* aa_f\right]$$
$$\sigma_u^Z = |\Gamma(s)|^2 \left[(1+\cos^2\theta^*)(v^2+a^2)(v_f^2+a_f^2) + 8\cos\theta^* vav_f a_f\right];$$

θ^* is the angle of the outgoing fermion relative to the incident electron; the polarized partial cross sections due to γZ interference and pure Z exchange are defined as,

$$\sigma_p^{\gamma Z} = 8Q_f \sin^2 2\theta_w \mathrm{Re}[\Gamma(s)] \left[(1+\cos^2\theta^*)av_f + 2\cos\theta^* va_f\right]$$
$$\sigma_p^Z = -|\Gamma(s)|^2 \left[(1+\cos^2\theta^*)2va(v_f^2+a_f^2) + 2\cos\theta^*(v^2+a^2)2v_f a_f\right];$$

the constant N_c^f is the color factor (3) for quark final states; and where the normalized Z propagator is defined in equation (3.12). Note that we've assumed that the masses of all final state fermions are small as compared with $\sqrt{s}$ and that the unpolarized cross section for pure photon exchange is small as compared with the pure Z and interference terms. In the case that the beams are unpolarized ($P^+ = P^- = 0$), equation (4.22) is identical to the expression that we used to describe the cross section for the process $q\bar{q} \to Z^0, \gamma \to \ell^+\ell^-$ (equation (3.12)).

We have already defined the forward-backward asymmetry in the context of the process $q\bar{q} \to \ell^+\ell^-$ (see equation (3.19)). The asymmetry is defined in exactly the same way for the process $e^+e^- \to f\bar{f}$. For unpolarized electrons and positrons, the form of the asymmetry at the Z^0 pole is identical to the form that was given in equation (3.20),

$$A_{FB}^f(x) = F(x)\cdot A_{FB}^f = F(x)\cdot\frac{3}{4}\cdot\frac{-2va}{v^2+a^2}\cdot\frac{-2v_f a_f}{v_f^2+a_f^2} = F(x)\cdot\frac{3}{4}\cdot A_{LR}\cdot A_{LR}^f, \quad (4.23)$$

where the function $F(x) = 4x/(3+x^2)$ accounts for incomplete coverage of the detector in $x = \cos\theta^*$ space, and A_{LR}^f is defined as a particular combination of coupling constants,

$$A_{LR}^{f} \equiv \frac{-2v_f a_f}{v_f^2 + a_f^2}. \tag{4.24}$$

The forward-backward asymmetries are fairly sensitive to $\sin^2\theta_w$ due to the presence of the vector coupling constants (see equations (2.2) and (2.3)). The expected size and sensitivity to $\sin^2\theta_w$ of each asymmetry is listed in Table X (assuming that the appropriate value of $\sin^2\theta_w$ is 0.233).

Table X

Fermion Type	A_{FB}^{f} ($\sin^2\theta_w = 0.233$)	Sensitivity to $\sin^2\theta_w$
u-quark	0.063	$\delta A_{FB}^{u} \simeq 4.2\delta\sin^2\theta_w$
d-quark	0.089	$\delta A_{FB}^{d} \simeq 5.6\delta\sin^2\theta_w$
charged lepton	0.012	$\delta A_{FB}^{\ell} \simeq 1.6\delta\sin^2\theta_w$

Table X illustrates a *Peter Principle* of experimental physics, *the most easily measured quantities are usually the least interesting ones.* The forward-backward asymmetry for muons is undoubtedly the most straightforward one to measure but is the least sensitive to $\sin^2\theta_w$. The identification and measurement of quark jets is more difficult. The DELPHI Collaboration[22] have studied the flavor tagging of simulated of hadronic jets (which makes use of the particle identification capability of their detector). The identification criteria, tagging efficiency, level of residual background, and the corresponding uncertainty on A_{FB}^{f} are listed in Table XI. They find good consistency between several different fragmentation models. The obvious (and difficult to answer) question is whether nature agrees with the fragmentation models to the same level of consistency. It is clear that believable results must be based upon very detailed experimental fragmentation studies.

Table XI

The result of a Monte Carlo study of the flavor tagging of hadronic jets with DELPHI detector.[22]

Flavor	Significant Criteria	Efficiency	Background	δA^f_{FB}
b-quark	$\ell^\pm K^\pm$ pairs, $P_\ell P_K > 25$ GeV^2	11.2%	16.1%	0.0013
c-quark	$\ell^\pm K^\mp$ pairs, reconstruct D^*	8.1%	32.2%	0.0013
s-quark	high momentum $K^\pm$,K^0_s,K^{0^*}	2.9%	45.5%	0.0026
u-quark	high momentum protons	1.4%	30.5%	0.002

Initial State Radiative Corrections

We have already seen that the emission of initial state radiation causes the effective center-of-mass energy $\sqrt{\hat{s}}$ to be skewed from the nominal value. At tree-level, the electroweak interference term causes a shift in the asymmetry as the energy varies away from M_Z. Ignoring a small term in the denominator, the energy dependence of the asymmetry can be expressed as follows,

$$A^f_{FB}(\hat{s}) \simeq A^f_{FB}(M_Z^2) - 6Q_f \sin^2 2\theta_w \Big(1 - \frac{M_Z^2}{\hat{s}}\Big) \frac{a a_f}{(v^2 + a^2)(v_f^2 + a_f^2)}. \qquad (4.25)$$

The interference term becomes large as $\sqrt{\hat{s}}$ varies from M_Z. Note that a shift $\Delta\sqrt{\hat{s}} = -148$ MeV is sufficient to cancel the tree-level muonic forward-backward asymmetry!

The energy dependence of the forward-backward asymmetries is plotted[23] Figure 16. Note that the d-quark forward-backward asymmetry is the least sensitive to changes in $\sqrt{\hat{s}}$. The steep energy dependence of the leptonic forward-backward asymmetries implies that they are quite sensitive to uncertainties on the initial state radiative corrections. The uncertainty on A^μ_{FB} is currently estimated[24] to be 0.001. The corresponding uncertainties on the quark asymmetries are much smaller.

QCD Corrections

The quark forward-backward asymmetries are affected by QCD corrections to the $Zq\bar{q}$ vertex and by real gluon emission (which produces three-jet events). The QCD corrections have been computed to first order in α_s by Kleiss, Renard, and Verzegnassi.[25] They find that the corrected asymmetry $A^q_{FB}(\alpha_s)$ can be described in terms of the tree-level asymmetry as follows,

$$A^q_{FB}(\alpha_s) = A^q_{FB}(\alpha_s = 0)\left[1 - \eta\frac{\alpha_s}{3\pi}\right], \tag{4.26}$$

where the parameter η is four if all two- and three-jet events are used. If the three-jet events (according to a purely theoretical definition) are excluded, the parameter η decreases to one. The value of η that is appropriate to a real experiment must therefore be in the range 1-4. This leads to an uncertainty that is a few percent of the native asymmetry.

Statistical Uncertainties

The statistical uncertainty that is associated with the measurement of an asymmetry A is given by the following expression,

$$\delta A = \left[\frac{1 - A^2}{N}\right]^{1/2} \simeq \frac{1}{\sqrt{N}}, \tag{4.27}$$

where the number of events N is assumed to be large enough that a Gaussian treatment is applicable. Note that most asymmetries are small as compared with unity so that the A^2 term in the numerator can be ignored.

Bottom Line

The LEP experiments are expected to accumulate a sample of 6×10^6 hadronic Z^0 decays (which corresponds to an integrated luminosity of 200 pb^{-1}) in the next several years. Combining the expected statistical and systematic errors, the precision of the various forward-backward asymmetry measurements can be predicted. The total uncertainty δA^f_{FB} and the corresponding uncertainty on $\sin^2\theta_w$ are listed in Table XII.

Table XII

The expected precision of measurements of the forward-backward asymmetries with a sample of 6×10^6 Z^0 events.

Asymmetry	δA_{FB} (all effects)	$\delta\sin^2\theta_w$
A^μ_{FB}	0.003	0.0020
A^u_{FB}	0.01	0.0030
A^s_{FB}	0.007	0.0016
A^c_{FB}	0.007	0.0021
A^b_{FB}	0.006	0.0010

Note that the b-quark asymmetry offers the most sensitive test of the Standard Model. This particular asymmetry has a particular difficulty that must be addressed. The measured asymmetry can be diluted by the mixing of neutral B mesons. A complete reconstruction of each B meson or baryon would permit the exclusion of the B^0_d and B^0_s mesons from the asymmetry measurement. Unfortunately, this is beyond the capability of most detectors. The tagging of b-jets is more easily done with large P_t (with respect to the jet axis) leptons. The measured asymmetry $A^b_{FB}(meas)$ is then related to the native quark asymmetry by the following expression,

$$A^b_{FB}(meas) = (1-2\chi_m)\cdot A^b_{FB}, \tag{4.28}$$

where χ_m is the mixing-induced probability of measuring a wrong-sign lepton. The parameter χ_m can be extracted from a measurement of the ratio of the number of same-sign lepton pairs to the total number of lepton pairs,

$$\frac{N(\ell^+\ell^+)+N(\ell^-\ell^-)}{N(\ell\ell)} = 2\chi_m(1-\chi_m),$$

where the notation is obvious. Note that χ_m is not the actual mixing parameter but is a phenomenological average quantity that depends upon the neutral meson fractions and upon the selection criteria.

A reasonable value for χ_m is in the range $\sim$0.1. Therefore, a sample of 6×10^6 hadronic Z^0 decays would produce several thousand same-sign lepton pairs. This number should be adequate to correct the measured asymmetry for mixing effects without inflating the combined error greatly.

4.5. The Left-Right Polarization Asymmetry

At the beginning of this lecture, we mentioned that the SLC will have a polarized electron beam with a degree of polarization $P_0 \simeq 40\%$. There are also plans to produce longitudinally polarized electron and positron beams at LEP. These enterprises are designed to measure the polarization dependent part of the total cross section as defined in equation (4.22). The forward-backward asymmetries are defined to select the part of the e^+e^- cross section that is odd under spatial reflection. The left-right polarization asymmetry is designed to select the part of the cross section that is odd in difference of the beam polarizations $P^+ - P^-$. It is therefore useful to define a generalized beam polarization P_g that is proportional to $P^+ - P^-$ and has a convenient normalization,

$$P_g \equiv \frac{P^+ - P^-}{1 - P^+P^-}. \tag{4.29}$$

Note that P_g is positive whenever the electron beam is left-handed and/or the positron beam is right-handed. It is negative whenever the reverse is true. The generalized polarization becomes unity when either beam is completely polarized. The positron beam of the SLC is unpolarized. The generalized polarization therefore has the simple form, $P_g = -P^-$.

The left-right polarization asymmetry is defined as the ratio of the difference of the total Z^0 production rates with left-handed and right-handed beams to the total rate. This can be expressed more precisely as,

$$A_{LR} \equiv \frac{\sum_f \left\{ \int_{-x_f}^{x_f} dc\sigma_f(c, P_g = +1) - \int_{-x_f}^{x_f} dc\sigma_f(c, P_g = -1) \right\}}{\sum_f \left\{ \int_{-x_f}^{x_f} dc\sigma_f(c, P_g = +1) + \int_{-x_f}^{x_f} dc\sigma_f(c, P_g = -1) \right\}}, \tag{4.30}$$

where: $c \equiv \cos\theta^*$; $\sigma_f(c, P_g)$ is shorthand for the differential cross section $d\sigma_f/d\Omega^*$; $\pm x_f$ are integration limits that depend upon fermion type; and where the sum is taken over all visible final state fermions except electrons (to exclude the t-channel scattering process). Note that the integrals must be taken over symmetric limits (which is a natural property of most e^+e^- detectors).

Substituting equation (4.22) (actually, the version of equation (4.22) with finite final state masses) into equation (4.30) it is straightforward to show that the left-right asymmetry takes the following form **on the Z^0 pole**,

$$A_{LR} = \frac{-2va \sum_f \int_{-x_f}^{x_f} dc[(v_f^2 + a_f^2)(1 + \beta_f^2 c^2) + (v_f^2 - a_f^2)(1 - \beta_f^2)]}{(v^2 + a^2) \sum_f \int_{-x_f}^{x_f} dc[(v_f^2 + a_f^2)(1 + \beta_f^2 c^2) + (v_f^2 - a_f^2)(1 - \beta_f^2)]},$$

where β_f is the velocity of the final state fermion in the $f\bar{f}$ center-of-mass frame. Cancelling the common factor, we recover a familiar expression,

$$A_{LR} = \frac{-2va}{v^2 + a^2} = \frac{2(1 - 4\sin^2\theta_w)}{1 + (1 - 4\sin^2\theta_w)^2}. \tag{4.31}$$

A number of conclusions can be drawn from this derivation:

1. A_{LR} depends upon the Z^0-electron couplings alone. The dependence on the final state couplings cancels in the ratio.

2. A_{LR} is independent of the detector acceptance. This remains true even if each final state fermion is accepted differently.

3. A_{LR} is independent of final state mass effects (which would cause β_f to differ from unity).

4. All of the visible final states except the electron pairs can be used to measure A_{LR}. The measurement therefore utilizes about 96% of the visible decays. The various other Standard Model tests that are performed on the Z^0 pole make use of much smaller fractions of the event total ($\sim$ 4% for the muonic forward-backward asymmetry, $\sim$ 0.9% for the τ polarization measurement, and $\sim$ 4% for the b-quark forward-backward asymmetry).

5. A_{LR} is very sensitive to the electroweak mixing parameter $\sin^2\theta_w$. This is shown graphically in Figure 17. Small changes in A_{LR} are related to changes in $\sin^2\theta_w$ by the following expression,

$$\delta A_{LR} \simeq -8\delta\sin^2\theta_w. \tag{4.32}$$

For $M_Z = 91.17$ GeV, the asymmetry is expected to be in the range 13%-15%.

Radiative Corrections

The left-right asymmetry has the property that it is insensitive to a large class of relatively uninteresting real and virtual radiative corrections and is very sensitive to an interesting set of virtual electroweak corrections. This behavior can be summarized as follows:

1. The left-right asymmetry is very insensitive to initial state radiative corrections. The emission of real photons by the incident electron and positron causes a smearing of the center-of-mass energy of the $f\bar{f}$ system ($\sqrt{\hat{s}}$). The left-right asymmetry is quite insensitive to small changes in $\sqrt{\hat{s}}$. The energy dependence of A_{LR} is compared with those of several forward backward asymmetries in Figure 16. The size of the initial state radiative correction to A_{LR} is calculated to be[26] $\delta A_{LR} \simeq 0.002$ (this is a 2% correction to the asymmetry). The uncertainty on the correction to A_{LR} is smaller by an order of magnitude.

2. The QCD corrections to the left-right asymmetry vanish entirely to all orders in the strong coupling constant α_s at the leading order in the electromagnetic coupling constant α. The leading QCD corrections to A_{LR} are the (extremely small) corrections to the weak vector boson box diagrams.

3. The theoretical uncertainty on A_{LR} is completely dominated by the uncertainty on the renormalization of the electromagnetic coupling constant to the Z^0 mass scale. The current value of this uncertainty is[27] $\delta A_{LR} \simeq 0.002$.

4. The left-right asymmetry is quite sensitive to virtual electroweak corrections and to the presence of new particles. The sensitivity of the asymmetry to the top quark mass (m_{top}) and the Higgs boson mass (m_{Higgs}) will be discussed in the last section of this document.

Experimental Errors

At the SLC, the measurement of A_{LR} is performed by randomly flipping the sign of the beam polarization on a pulse-to-pulse basis and by counting the number of Z^0 events that are produced from each state. The measured asymmetry, A_{LR}^{exp}, is related to the theoretical asymmetry, A_{LR}, by the following expression,

$$A_{LR}^{exp} \equiv \frac{N_Z(P_g = +P_0) - N_Z(P_g = -P_0)}{N_Z(P_g = +P_0) + N_Z(P_g = -P_0)} = P_0 A_{LR}, \tag{4.33}$$

where P_0 is the magnitude of the beam polarization ($P_0 \sim 0.40$), and $N_Z(P)$ is the number of Z^0 events logged with beam polarization P. Since the left-handed and right-handed Z^0 cross sections are measured simultaneously, any systematic effects due to variations in detector livetime, luminosity, beam energy, beam position, etc., are cancelled in the ratio of the cross sections. This technique was used successfully to measure a very small polarized asymmetry ($\sim 10^{-5}$) in electron-deuteron scattering in 1978.[28] The dominant systematic error is expected to be the uncertainty on the beam polarization measurement. We expect that the SLC Compton polarimeter is capable of measuring the beam polarization with a precision of 1-2% ($\delta P_0/P_0 =$ 1-2%).

There are a number of consistency checks that can be made with the SLC polarization hardware. It is possible to reverse the circular polarization optics of the electron source laser to search for systematic problems in that system. The polarity of the spin rotation system can be reversed to check for systematic problems in the damping rings. The polarization direction of each polarimeter target is reversible. The beam polarization can be measured separately with each target polarization direction (and must be consistent). Finally, the left-right asymmetry for small-angle Bhabha scattering is *very small* ($\sim 10^{-4}$). The luminosity monitors therefore provide an important check that the left-handed and right-handed luminosities are equal (the left-right asymmetry of the Bhabha signal must be consistent with zero).

Assuming that the dominant systematic error is the beam polarization uncertainty, the combined statistical and systematic uncertainty on A_{LR} is given by the following expression,

$$\delta A_{LR} = \left[A_{LR}^2 \left(\frac{\delta P_0}{P_0} \right)^2 + \frac{1 - (P_0 A_{LR})^2}{P_0^2 N_{tot}} \right]^{1/2}, \tag{4.34}$$

where N_{tot} is the total number of Z^0 events. The expected precision of the A_{LR} measurement and the corresponding precision on $\sin^2\theta_w$ are listed in Table XIII for several values of N_{tot}. Note that the statistical uncertainty dominates the total error in the region $N_{tot} \leq 10^6$. At $N_{tot} = 3 \times 10^6$, the statistical and systematic components are comparable.

Table XIII

The expected error on A_{LR} and $\sin^2\theta_w$ as a function of the number of Z^0 events. The left-right asymmetry is assumed to be $A_{LR} = 0.135$ (which is in the middle of the range that is expected for $M_Z = 91.17$ GeV). The beam polarization is assumed to be $P_0 = 0.40$ and the precision of the polarization monitoring is assumed to be $\delta P_0/P_0 = 0.01$.

N_{tot}	δA_{LR}	$\delta\sin^2\theta_w$
100K	0.008	0.0010
300K	0.005	0.0006
1M	0.003	0.00035
3M	0.002	0.00025

Note that a measurement of A_{LR} with 10^5 events determines $\sin^2\theta_w$ to a level that is comparable to a measurement of A^b_{FB} that is based upon 6×10^6 hadronic Z^0 decays.

4.6. The τ-Lepton Polarization Asymmetry

The left-right polarization asymmetry measures a combination of coupling constants that is particularly sensitive to $\sin^2\theta_w$. It is obvious to ask whether there is comparable information in the degree of polarization of the final state fermions. We define the final state polarization of a fermion as the difference in the cross sections to produce right-handed and left-handed particles,

$$P_f(\cos\theta^*) \equiv \frac{\frac{d\sigma}{d\Omega}(f_R) - \frac{d\sigma}{d\Omega}(f_L)}{\frac{d\sigma}{d\Omega}(f_R) + \frac{d\sigma}{d\Omega}(f_L)}, \tag{4.35}$$

where the notation is obvious. Assuming that the incident electron and positron are unpolarized, it is straightforward to show that the final state polarization is given by the following expression,

$$P_f(\cos\theta^*) = -\frac{2A_{LR}\cos\theta^* + A^f_{LR}(1+\cos^2\theta^*)}{(1+\cos^2\theta^*) + 2A_{LR}A^f_{LR}\cos\theta^*},$$

where the combination of coupling constants A^f_{LR} was defined in equation (4.30).

At any given angle, the polarization of the final state fermion depends upon A_{LR} (the natural Z^0 polarization) and the final state couplings A^f_{LR}. The dependence upon the initial state couplings can be removed by integrating the numerator and denominator of equation (4.35) over symmetric limits. The average value of the final state fermion polarization is then given by the following simple expression,

$$\langle P_f \rangle = -A^f_{LR}. \tag{4.36}$$

The fermion species that is the most obvious candidate for use as a final state polarimeter is the τ-lepton. It decays via a pure $V-A$ current* into low multiplicity final states. Since $\langle P_\tau \rangle$ is formally equivalent to the left-right asymmetry, the measurement of the average τ polarization has some of the same advantages that are inherent in the measurement of A_{LR}:

1. $\langle P_\tau \rangle$ is very sensitive to the electroweak mixing parameter $\sin^2\theta_w$. This is shown graphically in Figure 17. Small changes in $\langle P_\tau \rangle$ are related to changes in $\sin^2\theta_w$ by the following expression,

$$\delta\langle P_\tau \rangle \simeq 8\delta\sin^2\theta_w. \tag{4.37}$$

   For $M_Z = 91.17$ GeV, the average polarization is expected to be in the range 13%-15%.

2. The measured value of $\langle P_\tau \rangle$ is independent of the detector acceptance (assuming that τ^- and τ^+ are accepted equally).

3. The theoretical value of $\langle P_\tau \rangle$ is insensitive to initial state radiative corrections. The energy distributions of the final state decay products are affected slightly by the initial state radiation (which has a small effect on the measured polarization).

⋆ Experimentally, the V-A character of τ decays is not well established. The best measurement of the Michel ρ parameter is[12] $\rho = 0.73 \pm 0.07$ which is consistent with the $V-A$ value of 0.75 but does not rule out significant deviations.

4. $\langle P_\tau \rangle$ is very sensitive to the interesting virtual electroweak corrections. It is affected by the same theoretical error that affects the interpretation of A_{LR}.

The τ as a Polarimeter

The dominant decay modes of the τ-lepton are the four single-prong modes listed in Table XIV.

Table XIV

Decay Mode	Branching Ratio
$e^- \bar{\nu}_e \nu_\tau$	17.5±0.4%
$\mu^- \bar{\nu}_\mu \nu_\tau$	17.8±0.4%
$\rho^- \nu_\tau$	22.3±1.1%
$\pi^- \nu_\tau$	10.8±0.6%
4-mode total	68.4±1.37%

The two leptonic modes are 3-body decays and the two hadronic modes are even simpler 2-body decays. We can consider these decays in the rest frame of the τ. It is assumed that the τ spin is oriented along the z axis. It is straightforward to show that the angular distribution of the charged hadron from the 2-body decay $\tau^\pm \to h^\pm \nu$ is given by the following expression,

$$\frac{1}{N}\frac{dN}{d\cos\theta^*} = \frac{1}{2} \cdot (1 - \alpha_h P_\tau Q_\tau \cos\theta^*), \tag{4.38}$$

where: θ^* is the angle between the spin direction and the hadron direction; P_τ is the τ polarization; Q_τ is the charge of the τ; and the constant α_h is given by the following expression,

$$\alpha_h = \begin{cases} 1, & \text{for } h = \pi \\ \frac{m_\tau^2 - 2m_\rho^2}{m_\tau^2 + 2m_\rho^2} = 0.457, & \text{for } h = \rho \end{cases}$$

where m_τ and m_ρ are the τ and ρ masses, respectively. Ignoring the lepton mass, the energy-angle distributions of the 3-body leptonic decays are given by the following expression,

$$\frac{1}{N}\frac{d^2N}{dyd\cos\theta^*} = y^2[3 - 2y - P_\tau Q_\tau(1 - 2y)\cos\theta^*], \tag{4.39}$$

where y is the scaled energy of the outgoing lepton $y = 2E_\ell/m_\tau$.

Equations (4.38) and (4.39) show that the angular distributions of the τ decay products are sensitive to P_τ. Unfortunately, the τ-leptons that are produced in Z^0 decay are not at rest but have the beam energy (as smeared by the initial state radiation). In the case of the 2-body decays, we have a sufficient number of constraints to calculate $\cos\theta^*$ from the observed hadron momentum. Unfortunately, the non-observation of the two neutrinos from the leptonic decays makes this impossible for the 3-body decays. We therefore consider the laboratory energy distributions of the observed particles.

Let x_τ be the ratio of the observed energy of the τ decay product to the beam energy. It is then straightforward to derive a simple relationship between x_τ and $\cos\theta^*$ *that is valid for the 2-body decays*,

$$x_\tau = \frac{E_h}{E_b} = \frac{1}{2}\cdot\left[1 + z + (1 - z)\cos\theta^*\right], \tag{4.40}$$

where z is the ratio of square of the hadron mass to the square of τ mass, $z \equiv m_h^2/m_\tau^2$. Changing variables from $\cos\theta^*$ to x_τ, equation (4.38) can be expressed as the laboratory energy distribution,

$$\frac{1}{N}\frac{dN}{dx_\tau} = \frac{1}{1 - z}\cdot\left[1 - \alpha_h P_\tau Q_\tau\left(\frac{2x_\tau - 1 - z}{1 - z}\right)\right], \tag{4.41}$$

where x_τ is constrained to the interval $z \leq x_\tau \leq 1$.

For the 3-body leptonic decays, we can express x_τ in terms of y and $\cos\theta^*$,

$$x_\tau = \frac{y}{2}\cdot(1 + \cos\theta^*), \tag{4.42}$$

where the lepton mass is ignored. Changing variables from $\cos\theta^*$,y to x_τ,y and integrating over all values of y (note that the allowed range for y is 0-x), equation

(4.39) can be expressed as a laboratory energy distribution,

$$\frac{1}{N}\frac{dN}{dx_\tau} = \left[\frac{5}{3} - 3x^2 + \frac{4}{3}x^3\right] - P_\tau Q_\tau \left[\frac{1}{3} - 3x^2 + \frac{8}{3}x^3\right]. \tag{4.43}$$

Statistical Sensitivity

The sensitivity of the laboratory energy distributions given in equations (4.41) and (4.43) to the average τ polarization P_τ (note that we've simplified the notation) that is expected from the Standard Model is shown in Figure 18 for the $\tau \to \ell\nu\nu$ and the $\tau \to \pi\nu$ decays. The curves correspond to the polarization that is expected for $\sin^2\theta_w = 0.20, 0.23, 0.25, 0.30$, respectively. At $\sin^2\theta_w = 0.25$, the average polarization is zero, and the π spectrum is flat. Note that the π final state seems much more sensitive than do the leptonic final states.

There are generally two approaches to the extraction of P_τ from the measured x_τ distributions. The first is to fit the measured distributions to the functions defined in equations (4.41) and (4.43). The second approach is to measure the first moments of the x_τ distributions. It is straightforward to calculate the average value of x_τ for each distribution,

$$\langle x_\tau \rangle = a + bP_\tau Q_\tau = \begin{cases} \frac{1}{2}(1+z) - \frac{1}{6}\alpha_h P_\tau Q_\tau (1-z), & \text{2-body decays} \\ \frac{7}{20} + \frac{1}{20}P_\tau Q_\tau, & \text{3-body decays.} \end{cases} \tag{4.44}$$

Numerically, the mean values of x_τ for the $\pi\nu$, $\rho\nu$, and $\ell\nu\nu$ final states are,

$$\langle x_\tau \rangle_\pi = 0.50 - 0.17 \cdot P_\tau Q_\tau$$
$$\langle x_\tau \rangle_\rho = 0.59 - 0.062 \cdot P_\tau Q_\tau$$
$$\langle x_\tau \rangle_\ell = 0.35 - 0.050 \cdot P_\tau Q_\tau.$$

The average x_τ distribution for the $\pi\nu$ final state has the most sensitivity to P_τ.

A third technique that can be applied only to the 2-body decays is to convert the measured value of x_τ into a value of $\cos\theta^*$ (using equation (4.40)) and to form the forward-backward asymmetry of the emitted hadrons,

$$A^*_{FB} \equiv \frac{N_h(Q_\tau\cos\theta^* < 0) - N_h(Q_\tau\cos\theta^* > 0)}{N_h(Q_\tau\cos\theta^* < 0) + N_h(Q_\tau\cos\theta^* > 0)} = \frac{\alpha_h}{2} \cdot P_\tau \cdot \cos\theta^*_{max}, \tag{4.45}$$

where N_h is the number of detected hadrons with a positive or negative value for the product $Q_\tau\cos\theta^*$ and where $\cos\theta^*_{max}$ is the maximum accepted value of $\cos\theta^*$ (this is the appropriate form of the acceptance function F that was defined for the Z forward-backward asymmetries).

In order to evaluate the statistical precision that is possible with each of the three techniques, we assume that our ideal detector has complete acceptance (this is to avoid considerable complexity). The uncertainty on the measurement of $\langle x_\tau\rangle$ is given by standard error of the mean which is the ratio of the variance of the distribution Δx_τ and the square root of the number of events N that are used to measure the distribution. The precision that is obtainable from a likelihood fit is given by an expression that we've used several times (see equation (3.14)). The precision of a measurement of A^*_{FB} is given by $N^{-1/2}$. These estimates are listed in Table XV.

Table XV

Technique	Expected Error	δP_τ (2-body)	δP_τ (3-body)
$\langle x_\tau\rangle$	$\frac{1}{b}\frac{\Delta x}{\sqrt{N}}$	$\frac{1}{\alpha_h}\sqrt{\frac{3}{N}}$	$\simeq\sqrt{\frac{20}{N}}$
$\mathcal{L}(x_\tau)$	$[N\int dx_\tau(\frac{\partial\mathcal{L}}{\partial P_\tau})^2/\mathcal{L}]^{-1/2}$	$\frac{1}{\alpha_h}\sqrt{\frac{3}{N}}$	$\simeq\sqrt{\frac{20}{N}}$
A^*_{FB}	$\frac{2}{\alpha_h}\frac{1}{\sqrt{N}}$	$\frac{1}{\alpha_h}\frac{2}{\sqrt{N}}$	not applicable

Note that the measurement of the average $\langle x_\tau\rangle$ determines P_τ as precisely as a full likelihood fit to the x_τ distribution. The measurement of A^*_{FB} for the 2-body decays is less sensitive than either of the other techniques. Using the expressions given in Table XV, we can estimate the statistical precision of an ideal experiment. (In reality, a minimum energy cut is necessary to reject background, hence the entire range of x_τ cannot be used.) Assuming that our experiment acquires a sample of 6×10^6 hadronic events, a total of 2.49×10^5 $\tau^+\tau^-$ pairs would be produced. We assume that the overall selection efficiency is 60%. The number of produced and observed events for each decay mode are listed in Table XVI. The estimated error on P_τ from each mode is listed in the last column. We conclude that the $\pi\nu$ and $\rho\nu$ final states are the most statistically sensitive decay modes.

Table XVI

Decay Mode	Produced Events	Observed Events	δP_τ
$\tau \to \pi\nu$	5.38×10^4	3.23×10^4	0.0096
$\tau \to \rho\nu$	1.11×10^5	6.66×10^4	0.0147
$\tau \to e\nu\nu$	8.79×10^4	5.28×10^4	0.0195
$\tau \to \mu\nu\nu$	8.79×10^4	5.28×10^4	0.0195

Systematic Errors

There are several sources of systematic uncertainty in the measurement of the average τ polarization. The two most sensitive final states are quite similar. The $\rho^\pm$ meson decays into a pair of pions, $\pi^\pm\pi^0$. The $\rho\nu$ final state therefore differs from the from the $\pi\nu$ final state only by the presence of an additional π^0. The dominant systematic uncertainty is due to contamination of the $\pi\nu$ sample by the $\rho\nu$ final state. Other systematic errors are the uncertainty on the energy scale of the decay products (from radiative effects and detector calibration uncertainties) and an uncertainty due to detector biases. The combined systematic error has been estimated to be in the range[29] $\delta P_\tau \simeq 0.005$-$0.008$.

Bottom Line

The measurement of the average polarization of the τ-leptons in Z^0 decay is a reasonably sensitive test of the Standard Model. It appears that the polarization could be measured to the 0.012 level with a sample of 200 pb^{-1} at LEP. This corresponds to an uncertainty on the effective $\sin^2\theta_w$ of 0.0015.

5. Conclusions

The recent measurements of the mass of the Z^0 have determined the parameters of the electroweak portion of the Standard Model at tree-level. Precise measurements of other physical quantities will test the electroweak theory at the loop level. The most promising of these are the measurements of the W boson mass that will be performed by experiments at the Tevatron and at LEP II and the measurements of the ratio the vector and axial-vector couplings of the Z^0 that will be performed with a variety of techniques at the SLC and LEP I. It is interesting to compare the sensitivities of these measurements to loop-level corrections.

We have seen that measurements of M_W to a level of precision $\delta M_W \simeq$ 100-150 MeV are possible in the next several years. The dependence of M_W upon the top quark mass is shown in Figure 19. The solid curves enclose the 68.3% confidence region that is expected for a ± 20 MeV uncertainty on M_Z (it is assumed that $M_Z = 91.17 \pm 0.20$ GeV) as m_{top} is varied from 60 GeV to 240 GeV. The Higgs boson mass is assumed to be 500 GeV. The 68.3% confidence interval that corresponds to a ± 100 MeV measurement is shown as a solid error bar. The theoretical error that is due to the uncertainty on the renormalization of the electromagnetic coupling constant to the W mass scale is also shown. Note that a measurement error $\delta M_W = \pm 100$ MeV corresponds to an uncertainty on m_{top} of roughly 16 GeV. The analagous dependence of M_W upon m_{Higgs} is shown in Figure 20. The dashed curves enclose the 68.3% confidence region that is expected as m_{Higgs} is varied from 100 GeV to 900 GeV. The top quark mass is fixed to 150 GeV. Note that future measurements of M_W are unlikely to constrain the Higgs mass.

The ratio of the vector and axial-vector couplings of the Z^0 is best determined from measurements of the b-quark forward-backward asymmetry and the left-right polarization asymmetry. Note that the precision of a measurement of A^b_{FB} that is based upon a sample of 6×10^6 hadronic Z decays is comparable to a measurement of A_{LR} that is based upon 10^5 Z decays. We therefore use the left-right asymmetry as a standard to determine the loop-level sensitivity of this class of measurements.

The experimental confidence intervals that are presented in Table XIII are compared with the theoretical expectation for A_{LR} in Figures 21 and 22. The solid curves in Figure 21 enclose the 68.3% confidence region that is expected for m_{Higgs} = 500 GeV and m_{top} varying between 60 GeV and 240 GeV. The finite width of the region is due to a ± 20 MeV uncertainty on the Z^0 mass (we assume $M_Z =$ 91.17 ± 0.02 GeV). The solid curves in Figure 22 enclose the 68.3% confidence region that is expected for $m_{top} = 150$ GeV and m_{Higgs} varying from 100 GeV to 900 GeV. The size of the theoretical error on A_{LR} (± 0.002) is shown as the dotted vertical error bar in each figure. The sizes of the experimental 68.3% confidence intervals that correspond to the various values of N_{tot} are indicated by the solid vertical error bars. Since the τ polarization asymmetry is formally equivalent to A_{LR}, we plot the confidence region that is expected from a measurement with a 6M Z^0 sample. It is clear that A_{LR} is quite sensitive to m_{top}. A measurement with 300K Z^0 events constrains the top quark mass to a region of roughly $\delta m_{top} = \pm 17$ GeV which is comparable to a 100 MeV determination of M_W. The sensitivity to m_{Higgs} is clearly much smaller. A very high statistics measurement of A_{LR} could provide, at best, an indication of m_{Higgs}.

It is important to note that the sensitivities of M_W and the Z pole asymmetries to higher order corrections and to new physical processes are quite different. They are, to a large degree, quite **complementary**. This is particularly true if deviations from the Standard Model expectations are found. In that case, several precise measurements would be required to constrain the space of new physical possibilities. An example of this complementarity is shown[30] in Figure 23 for the case that the Standard Model is extended to include a 500 GeV, χ-type Z' boson.[31] The contours show the expected values of M_W and A_{LR} as m_{top} is varied from 50 GeV to 200 GeV (m_{Higgs} is fixed to 100 GeV). The three contours in each group correspond to the three values of the Z^0 mass, $M_Z = 91.17 \pm 0.02$ GeV. Each group represents a different value of the $Z^0 - Z'$ mixing parameter $\sin\theta_m$. The four groups correspond to the four values $\sin\theta_m = 0.0, -0.005, -0.010, -0.015$ (top to bottom). The precision expected from a 300K event measurement of A_{LR} and a

100 MeV measurement of M_W is shown by the error bars in the corner of the plot. It is clear that the unfolding of deviations from the Standard Model expectations is greatly aided by the presence of several different high precision measurements.

Acknowledgements: The author would like to thank Michael Peskin, Gary Feldman, and Guy Blaylock for several useful and informative discussions. Additionally, Guy deserves special thanks for his careful scrutiny this manuscript.

REFERENCES

1. E.R. Cohen and B.N. Taylor, *Rev. Mod. Phys.* **59**, 1121 (1987).
2. *Review of Particle Properties*, G.P. Yost et al., *Phys. Lett.* **B204**,1 (1988).
3. G. Abrams et al., *Phys. Rev. Lett.* **63**, 2173 (1989).
4. D. Decamp et al., *Phys. Lett.* **B231**, 519 (1989) and *Phys. Lett.* **B235**, 399 (1990).
5. P. Aarnio et al., *Phys. Lett.* **B231**, 539 (1989).
6. B. Adeva et al., *Phys. Lett.* **B231**, 509 (1989) and L3 Preprint #004, December(1989).
7. M.Z. Akrawy et al., *Phys. Lett.* **B231**, 530 (1989).
8. The quoted value is a weighted average (assuming a 27 MeV LEP energy scale uncertainty) of the results given in References 3-7.
9. J. Alitti et al., CERN-EP/90-22, March 1990.
10. J.C. Collins and D.E. Soper, *Phys. Rev.* **D16**, 2219 (1977).
11. C. Albajar et al., *Z. Phys.* **C44**, 15 (1989).
12. F. Abe et al., *Phys. Rev. Lett.* **63**, 720 (1989).
13. A. Sirlin, *Phys. Rev.* **D22**, 971 (1980).
14. W.J. Marciano and A. Sirlin, *Phys. Rev.* **D29**, 945 (1984).
15. F. Abe et al., *Phys. Rev. Lett.* **62**, 154 (1990).
16. M. Peskin, SLAC-PUB-5210, March 1990.
17. B. Adeva et al., L3 preprint 005, February 1990.
18. G.S. Abrams et al., *Phys. Rev. Lett.* **63**, 2780 (1989).
19. T. Muta, R. Najima, and S. Wakaizumi, *Mod. Phys. Lett.* **A1**, 203 (1986).

20. P. Roudeau et al., *Proceedings of the ECFA Workshop on LEP 200*, edited by A. Böhm and W. Hoogland, CERN 87-08, June 1987, pg 85.

21. J. Alitti et al., CERN preprint CERN-EP/90-20, February 1990.

22. J. Drees, K. Mönig, H. Staeck, and S. Überschär, Vol. I *Polarization at LEP*, CERN 88-06, September 1988, pg 317.

23. A. Blondel, B.W. Lynn, F.M. Renard, and C. Verzegnassi, Montpellier preprint PM/87-14, March 1987.

24. M. Böhm and W. Hollik, Z Physics at LEP 1, CERN 89-08, Sept. 1989, Vol I, pg 203.

25. R. Kleiss, F.M. Renard, and C. Verzegnassi, *Nucl. Phys.* **B286**, 669 (1987).

26. D. Kennedy, B.W. Lynn, and C.J.C. Im, *Nucl. Phys.* **B321**, 83 (1989).

27. H. Burkhardt, F. Jegerlehner, G. Penso, and C. Verzegnassi, Vol. I *Polarization at LEP*, CERN 88-06, September 1988, pg 145.

28. C.Y. Prescott et al., *Phys. Lett.* **77B**, 347 (1978); and *Phys. Lett.* **84B**, 524 (1979).

29. F. Boillot and Z. Was, *Z. Phys.* **C43**, 103 (1989).

30. The author is grateful to M. Peskin for providing this calculation.

31. P. Langacker, R.W. Robinett, and J.L. Rosner, Phys. Rev. D30, 1470 (1984).

FIGURE CAPTIONS

1) The Drell-Yan mechanism for the production of W and Z bosons in $p\bar{p}$ collisions. The incident proton and antiproton have momenta k_1 and k_2, respectively. A parton carrying the fraction x_1 of the proton momentum collides with a parton carrying the fraction x_2 of the antiproton momentum. The two lowest order subprocesses that produce gauge bosons are shown in parts a) and b).

2) The scaled longitudinal momentum distribution $x_2 - x_1$ for W^- bosons produced at $\sqrt{s} = 630$ GeV. The mean of the distribution is 0.06 indicating that the average longitudinal momentum is along the antiproton direction. Note that $x_2 - x_1 = 0.4$ corresponds to a W boson longitudinal momentum of 125 GeV.

3) The electron transverse momentum distribution from W bosons produced at $\sqrt{s} = 630$ GeV. The P_t^e distribution is shown for three phenomenological W boson transverse momentum distributions. Top to bottom, the average values of the W boson transverse momentum are: 0 GeV (dashed curve), 7 GeV (dashed-dotted curve), and 14 GeV (solid curve).

4) The electron and neutrino transverse momentum distributions of 1203 $W \to e\nu$ candidates measured by the UA2 Collaboration[9].

5) The transverse mass distributions corresponding to the P_t^e distributions shown in Figure 3. Top to bottom, the average values of the W boson transverse momentum are: 0 GeV (dashed curve), 7 GeV (dashed-dotted curve), and 14 GeV (solid curve). The neutrino P_t resolution is assumed to be $\delta P^{\nu}_{t,xy} = 0.5\sqrt{E_t}$ GeV along the x and y axes.

6) The angular distribution of electrons from W decay as measured by the UA1 collaboration[11].

7) The electron and muon pair mass distributions in the Z^0 region that have been measured by the CDF Collaboration.[12]

8) The Z^0 lineshape as measured by the Mark II Collaboration.[3] The dashed curve is the result of a single parameter fit (for M_Z). The results of two and three parameter fits are indistinguishable and are shown as the solid curve.

9) The sensitivity function for M_Z as a function of center-of-mass energy about the Z pole, $E - M_Z$.

10) The sensitivity function for Γ_Z as a function of center-of-mass energy about the Z pole, $E - M_Z$.

11) The sensitivity function for $\sigma^0_{had}(M_Z^2)$ as a function of center-of-mass energy about the Z pole, $E - M_Z$.

12) The cross section for the process $e^+e^- \to W^+W^-$ as a function of $E_b - M_W$. The mass and width of the W are assumed to be 80 GeV and 2.1 GeV, respectively. Note that three curves are plotted: the dashed curve is the basic tree-level cross section; the dashed-dotted curve is the cross section including the effect of initial state radiation; and the solid curve is the cross section including initial state radiation and the effect of a finite W width.

13) The sensitivity function for M_W as a function of the single beam energy about the W pair threshold $E_b - M_W$.

14) The sensitivity function for Γ_W as a function of the single beam energy about the W pair threshold $E_b - M_W$.

15) The sensitivity function for the background parameter B as a function of the single beam energy about the W pair threshold $E_b - M_W$.

16) The forward-backward asymmetries for leptons, u-quarks, and d-quarks are plotted as a functions of the center-of-mass energy about the Z^0 pole. The asymmetries are also shown for the case that the incident beams are polarized. The energy dependence of the left-right asymmetry and an improved polarized forward-backward asymmetry $\tilde{A}^f_{FB}$ (from Reference 23) are also shown. The Z^0 mass is assumed to be 94 GeV. Note that the unimproved

forward-backward asymmetries are much more sensitive to the center-of-mass energy than are the improved ones and the left-right asymmetries.

17) The left-right asymmetry A_{LR} is plotted as a function of $\sin^2\theta_w$ and M_Z (for some choice of m_t and m_h). The leptonic forward-backward asymmetry A^{FB} is shown for comparison.

18) The normalized laboratory energy distributions of the observed decay products of polarized τ-leptons. Figure (a) shows the energy distribution for the $\tau \to \ell\nu\nu$ decay. The various curves correspond to the polarization that is expected for $\sin^2\theta_w = 0.20, 0.23, 0.25, 0.30$. Figure (b) shows the same curves for the decay $\tau \to \pi\nu$. Note that $\sin^2\theta_w = 0.25$ corresponds to zero net polarization.

19) The W boson mass as a function of the top quark mass. The Higgs boson mass is assumed to be 500 GeV. The solid curves enclose the 68.3% confidence region that is expected for a ± 20 MeV uncertainty on M_Z (we assume M_Z $= 91.17 \pm 0.02$ GeV) as m_{top} is varied from 60 GeV to 240 GeV. The size of the experimental 68.3% confidence interval (± 100 MeV) is indicated by the solid vertical error bar. The size of the theoretical error (± 25 MeV) is also shown.

20) The W boson mass as a function of the Higgs boson mass. The top quark mass is assumed to be 150 GeV. The dashed curves enclose the 68.3% confidence region that is expected for a ± 20 MeV uncertainty on M_Z (we assume $M_Z = 91.17 \pm 0.02$ GeV) as m_{Higgs} is varied from 100 GeV to 900 GeV. The dotted vertical error bar shows the size of the theoretical error (± 25 MeV) on M_W. The size of the experimental 68.3% confidence interval (± 100 MeV) is indicated by the solid vertical error bar.

21) The left-right asymmetry as a function of the top quark mass (m_{top}). The Higgs boson mass (m_{Higgs}) is assumed to be 500 GeV. The solid curves enclose the 68.3% confidence region that is expected for a ± 20 MeV uncertainty on M_Z (we assume $M_Z = 91.17 \pm 0.02$ GeV) as m_{top} is varied from 60 GeV

to 240 GeV. The dotted vertical error bar shows the size of the theoretical error (± 0.002) on A_{LR}. The sizes of the experimental 68.3% confidence intervals that are expected for the various values of N_{tot} are indicated by the solid vertical error bars. The confidence interval that is expected from a measurement of the τ polarization asymmetry with 6M Z^0 events is also shown.

22) The left-right asymmetry as a function of the Higgs boson mass. The top quark mass is assumed to be 150 GeV. The dashed curves enclose the 68.3% confidence region that is expected for a ± 20 MeV uncertainty on M_Z (we assume $M_Z = 91.17 \pm 0.02$ GeV) as m_{Higgs} is varied from 100 GeV to 900 GeV. The dotted vertical error bar shows the size of the theoretical error (± 0.002) on A_{LR}. The sizes of the experimental 68.3% confidence intervals that are expected for the various values of N_{tot} are indicated by the solid vertical error bars. The confidence interval that is expected from a measurement of the τ polarization asymmetry with 6M Z^0 events is also shown.

23) The expected values of M_W and A_{LR} are shown as m_{top} is varied from 50 GeV to 200 GeV (m_{Higgs} is fixed to 100 GeV) for the case that the Standard Model is extended to include a χ-type Z' boson (see Reference 13). The mass of the Z' boson is assumed to be 500 GeV. The three contours in each group correspond to the three values of the Z^0 mass, $M_Z = 91.17 \pm 0.02$ GeV. The dots along each contour indicate the points $m_{top} = 50$, 100, 150, 200 GeV. The four groups of contours show four values of the $Z^0 - Z'$ mixing parameter, $\sin\theta_m = 0.00$, -0.005, -0.01, -0.015. The precision expected from a 300K event measurement of A_{LR} and a 100 MeV measurement of M_W is shown by the error bars in the corner of the plot.

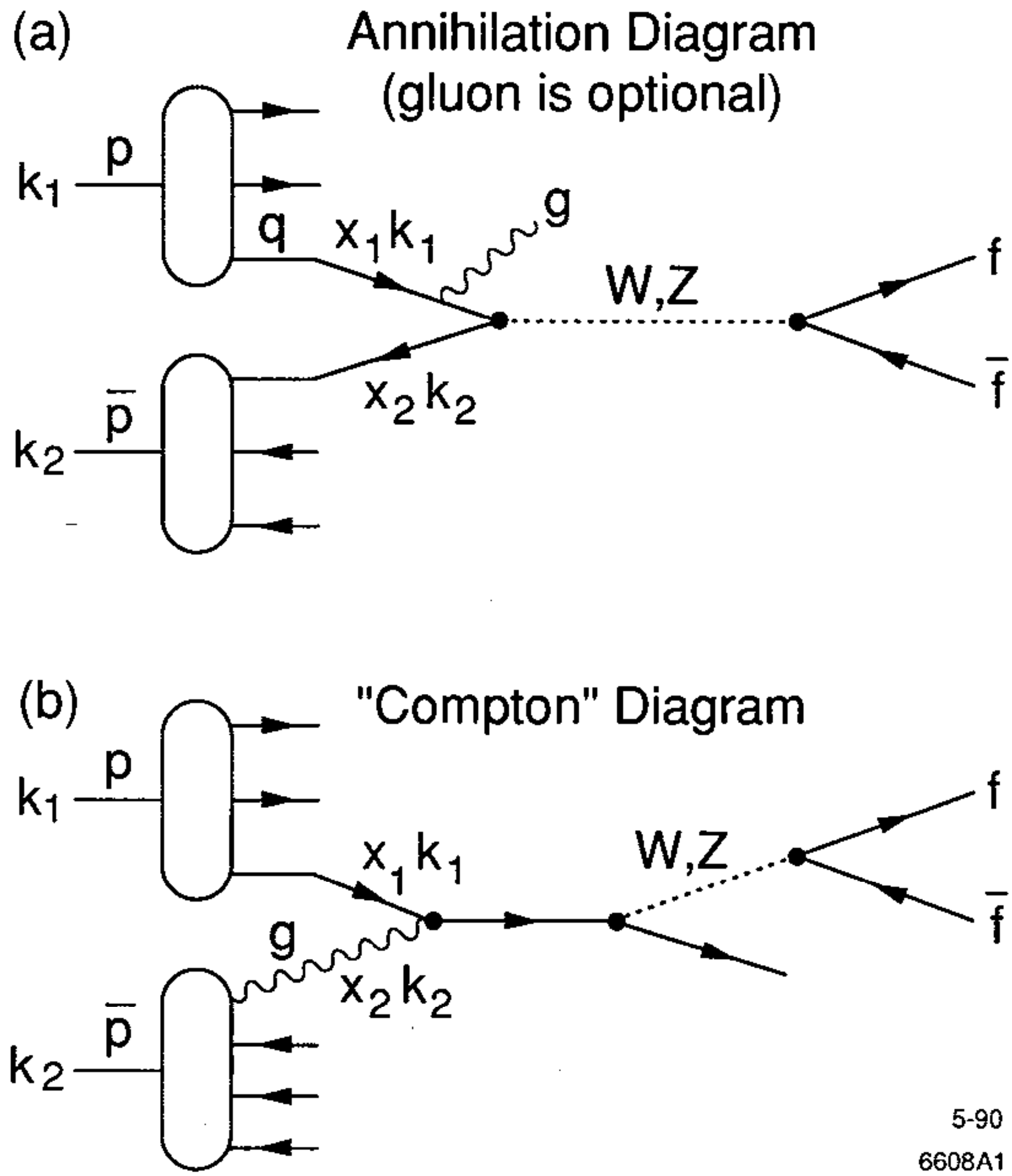
(a)
Annihilation Diagram
(gluon is optional)
p
k1
q
x1 k1
g
W,Z
f
f̄
x2 k2
p̄
k2
(b)
"Compton" Diagram
p
k1
x1 k1
W,Z
f
f̄
g
x2 k2
p̄
k2
5-90
6608A1

Fig. 1

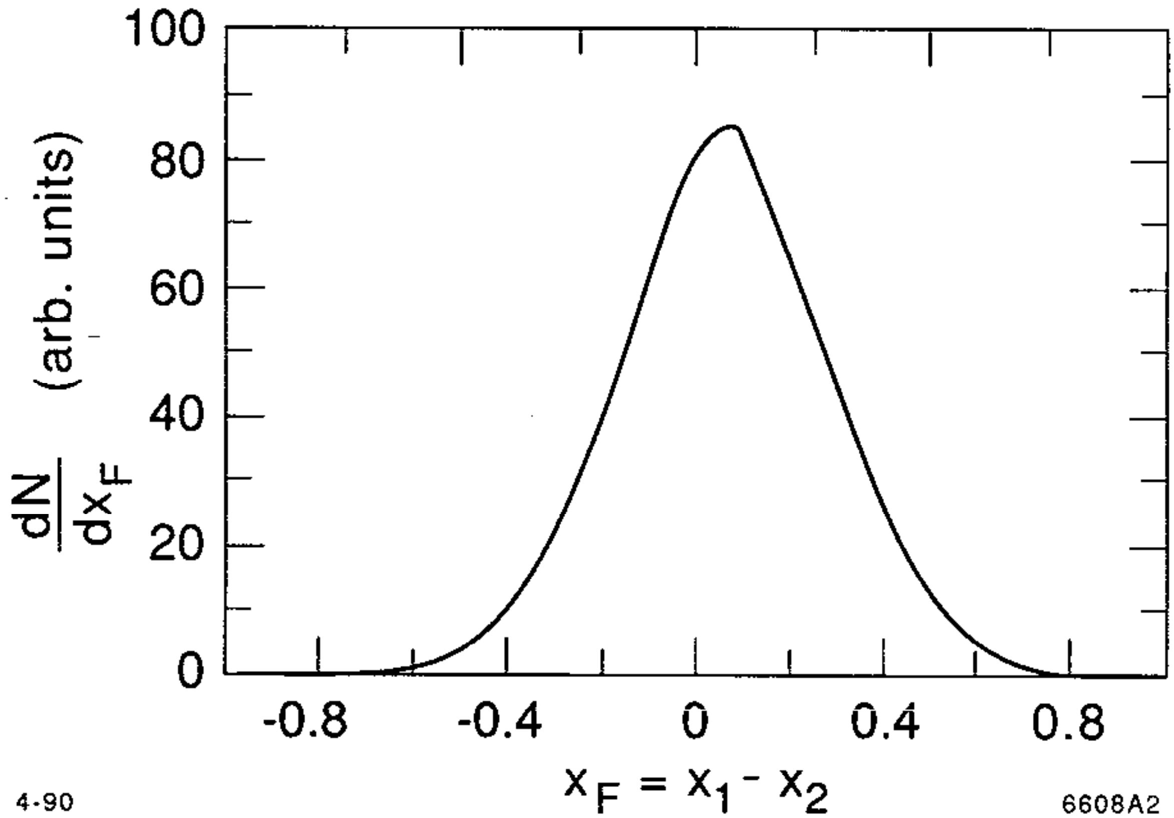

Fig. 2

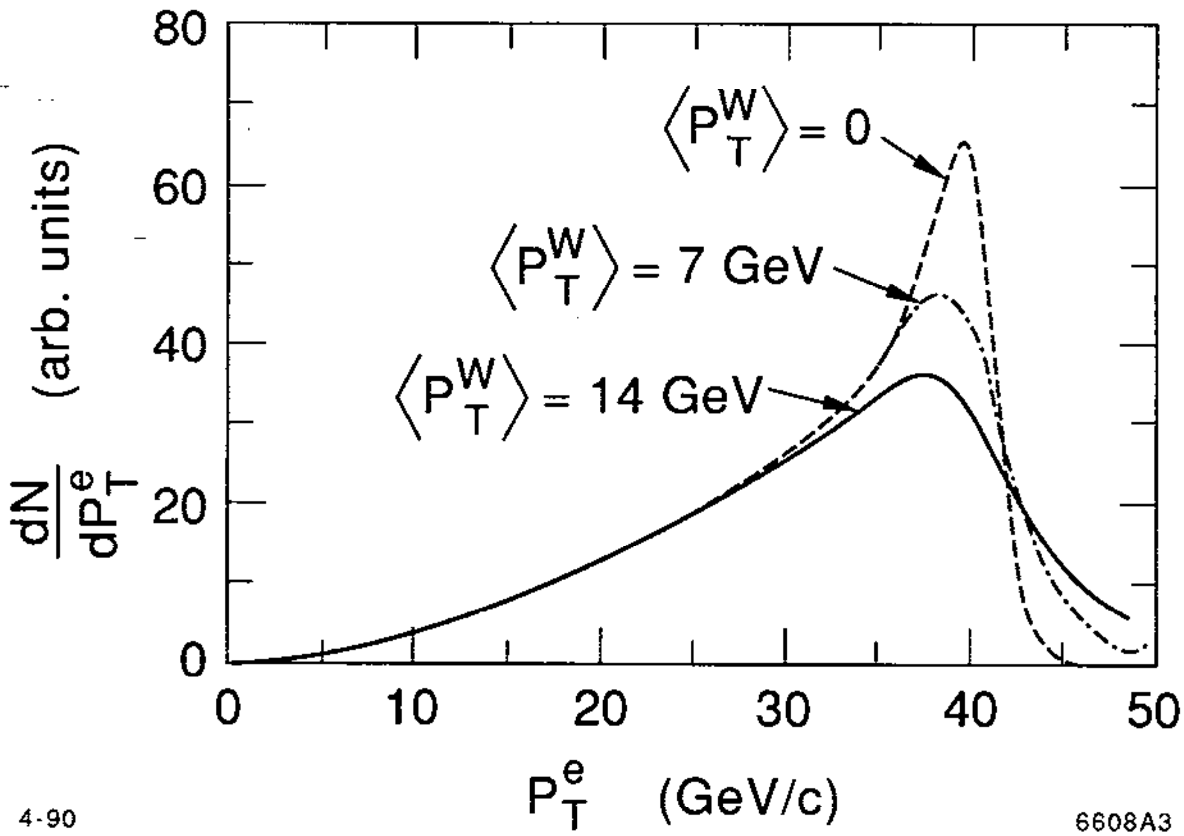

80
60
40
20
0
0
10
20
30
40
50
$\frac{dN}{dP_T^e}$ (arb. units)
P_T^e (GeV/c)
$\langle P_T^W \rangle = 0$
$\langle P_T^W \rangle = 7$ GeV
$\langle P_T^W \rangle = 14$ GeV
4-90
6608A3

Fig. 3

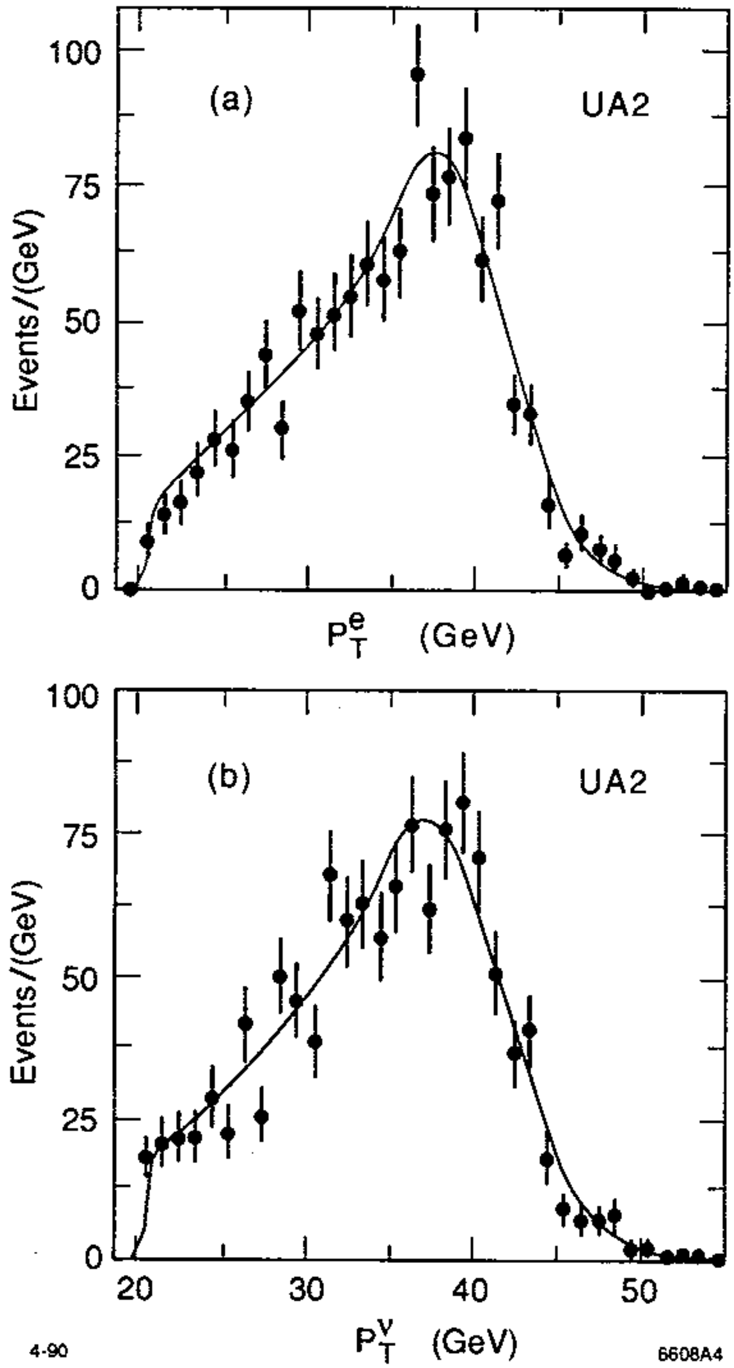
100
75
50
25
0
Events/(GeV)
(a)
UA2
P_T^e (GeV)
100
75
50
25
0
Events/(GeV)
(b)
UA2
20
30
40
50
P_T^ν (GeV)
4-90
6608A4

Fig. 4

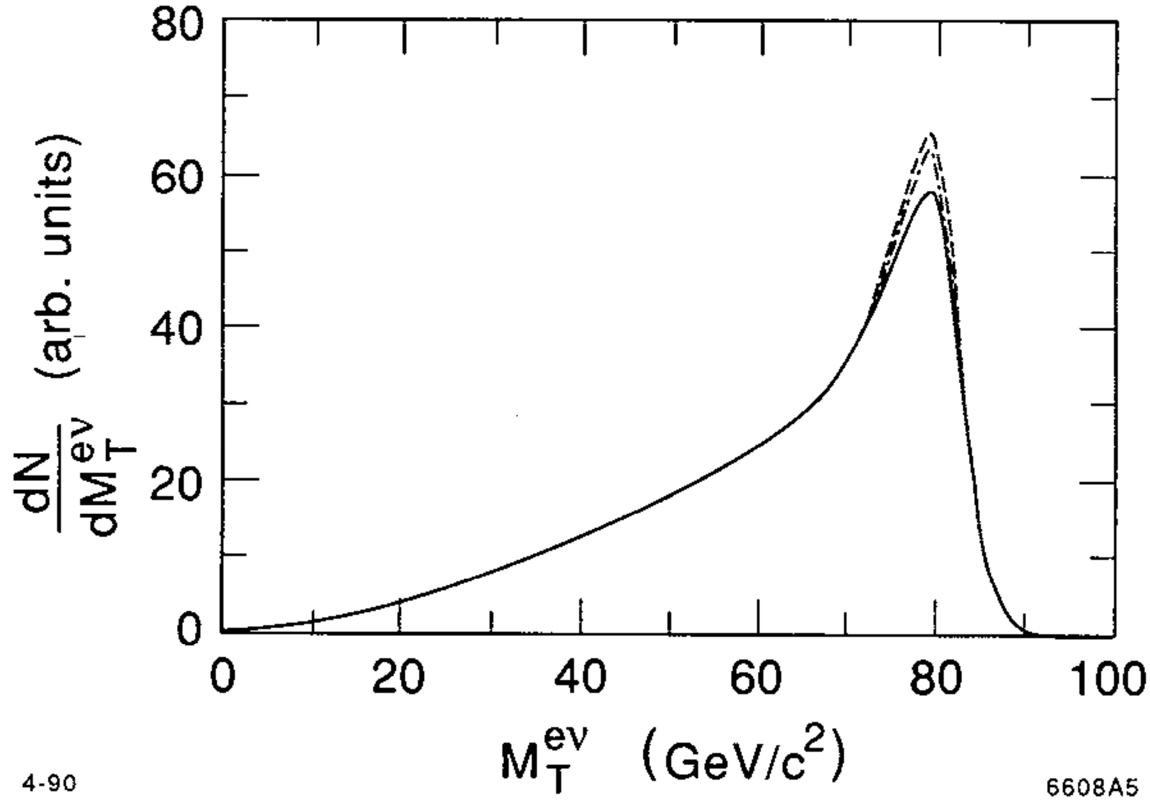

80
60
40
20
0
0
20
40
60
80
100
$\frac{dN}{dM_T^{e\nu}}$ (arb. units)
$M_T^{e\nu}$ (GeV/c^2)
4-90
6608A5

Fig. 5

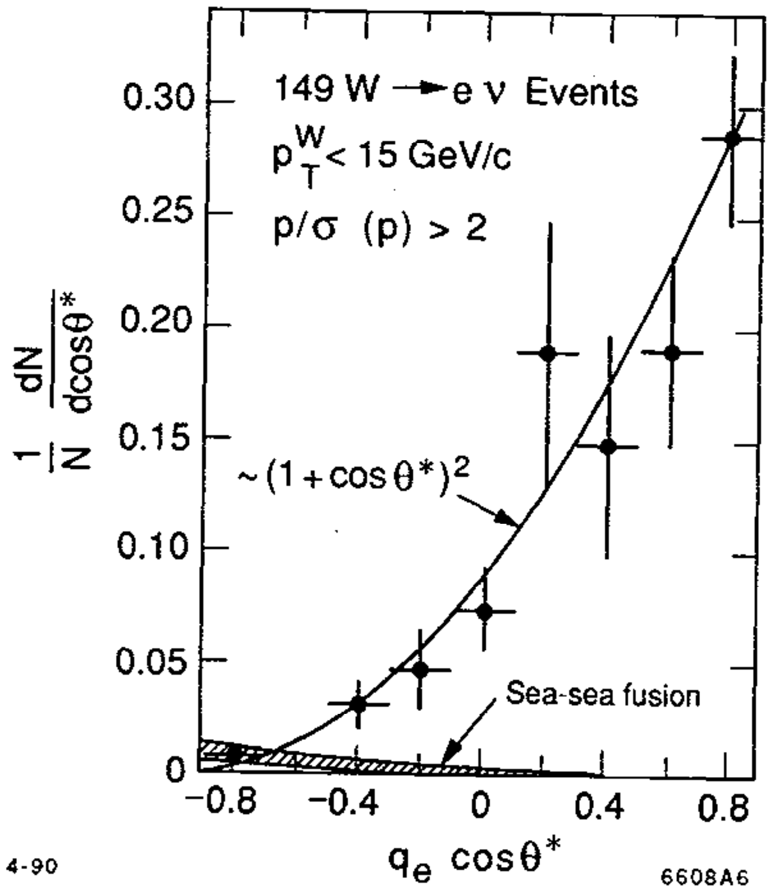

149 W → e ν Events
$p_T^W < 15$ GeV/c
p/σ (p) > 2
$\frac{1}{N}\frac{dN}{d\cos\theta^*}$
0.30
0.25
0.20
0.15
0.10
0.05
0
~(1+cos θ*)²
Sea-sea fusion
−0.8
−0.4
0
0.4
0.8
$q_e \cos\theta^*$
4-90
6608A6

Fig. 6

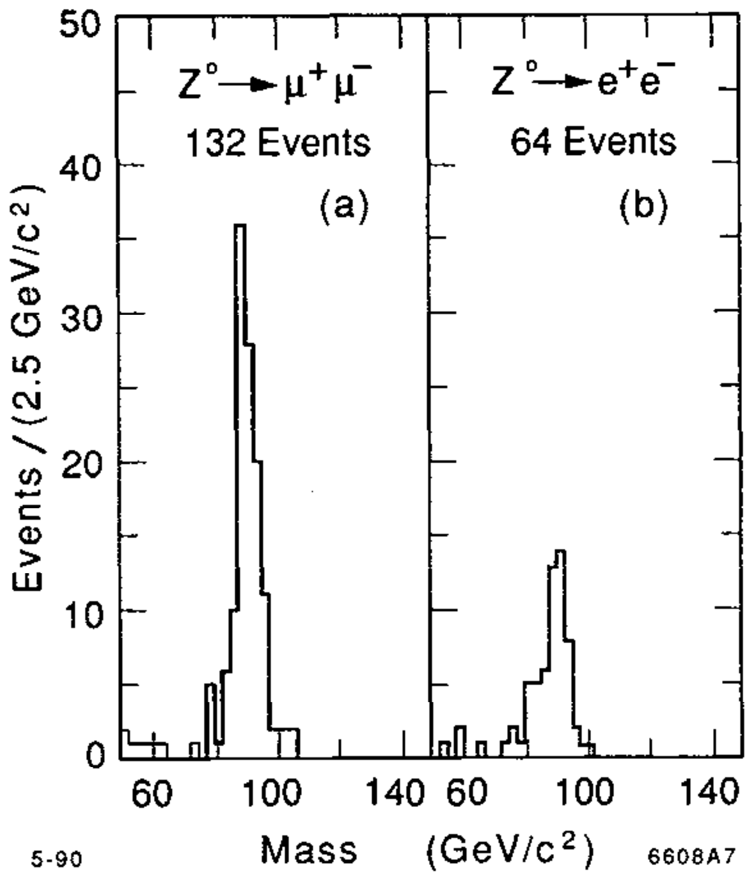

50
40
30
20
10
0
Events / (2.5 GeV/c²)
Z° → μ⁺μ⁻
132 Events
(a)
Z° → e⁺e⁻
64 Events
(b)
60
100
140
60
100
140
5-90
Mass (GeV/c²)
6608A7

Fig. 7

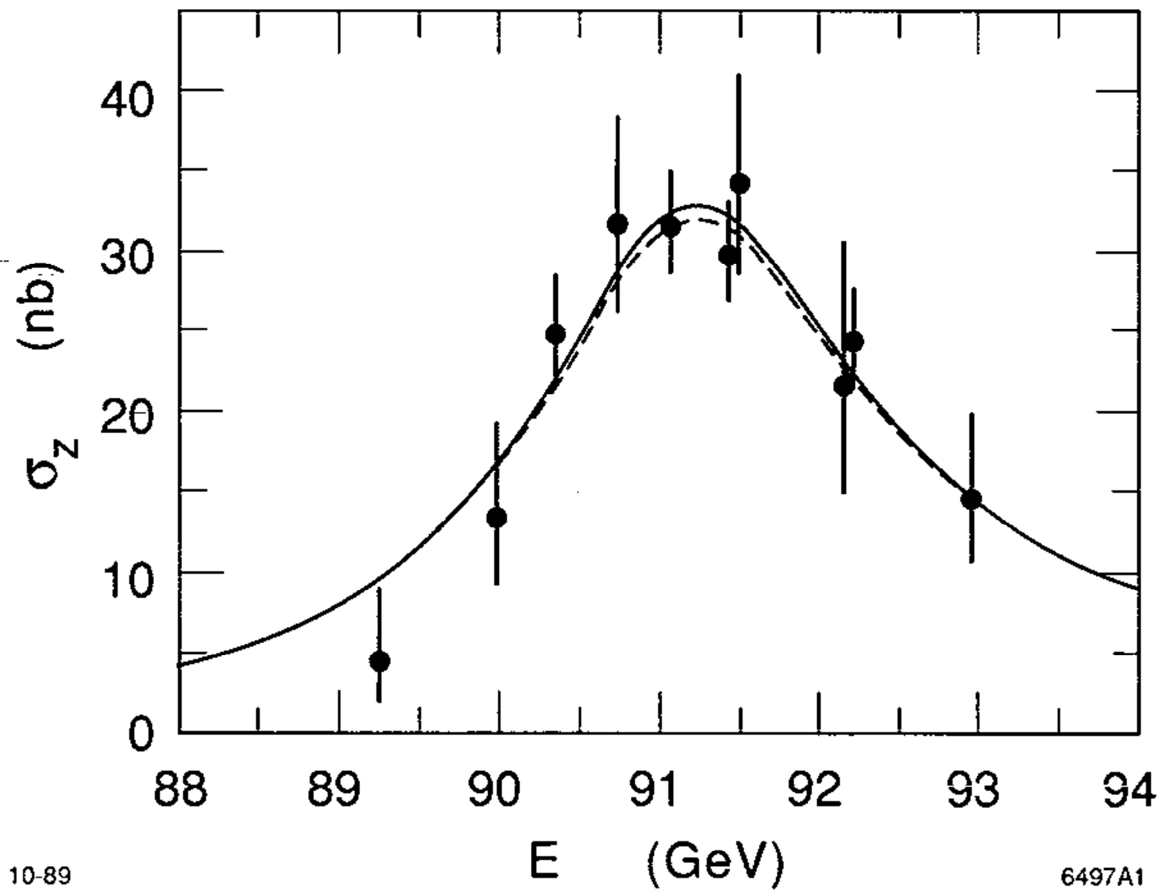

Fig. 8

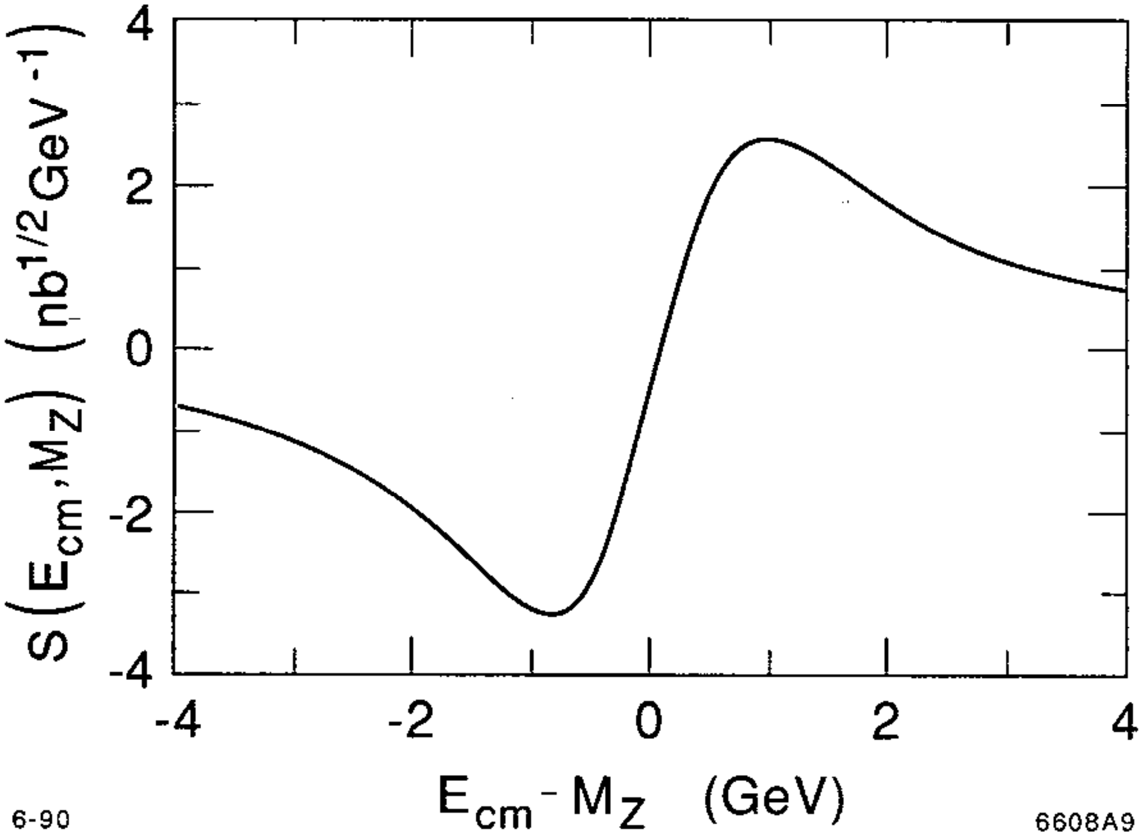

Fig. 9

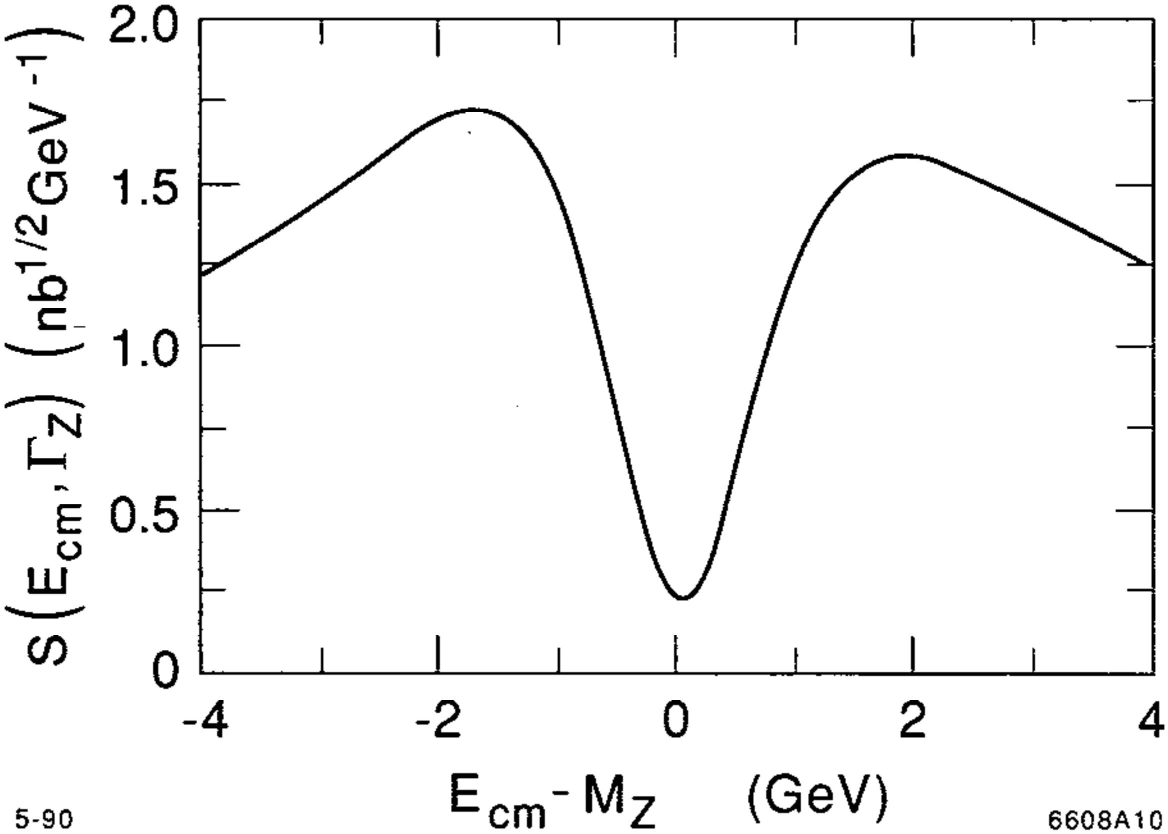

2.0
1.5
1.0
0.5
0
$S(E_{cm}, \Gamma_Z)$ $(nb^{1/2}GeV^{-1})$
-4
-2
0
2
4
$E_{cm} - M_Z$ (GeV)
5-90
6608A10

Fig. 10

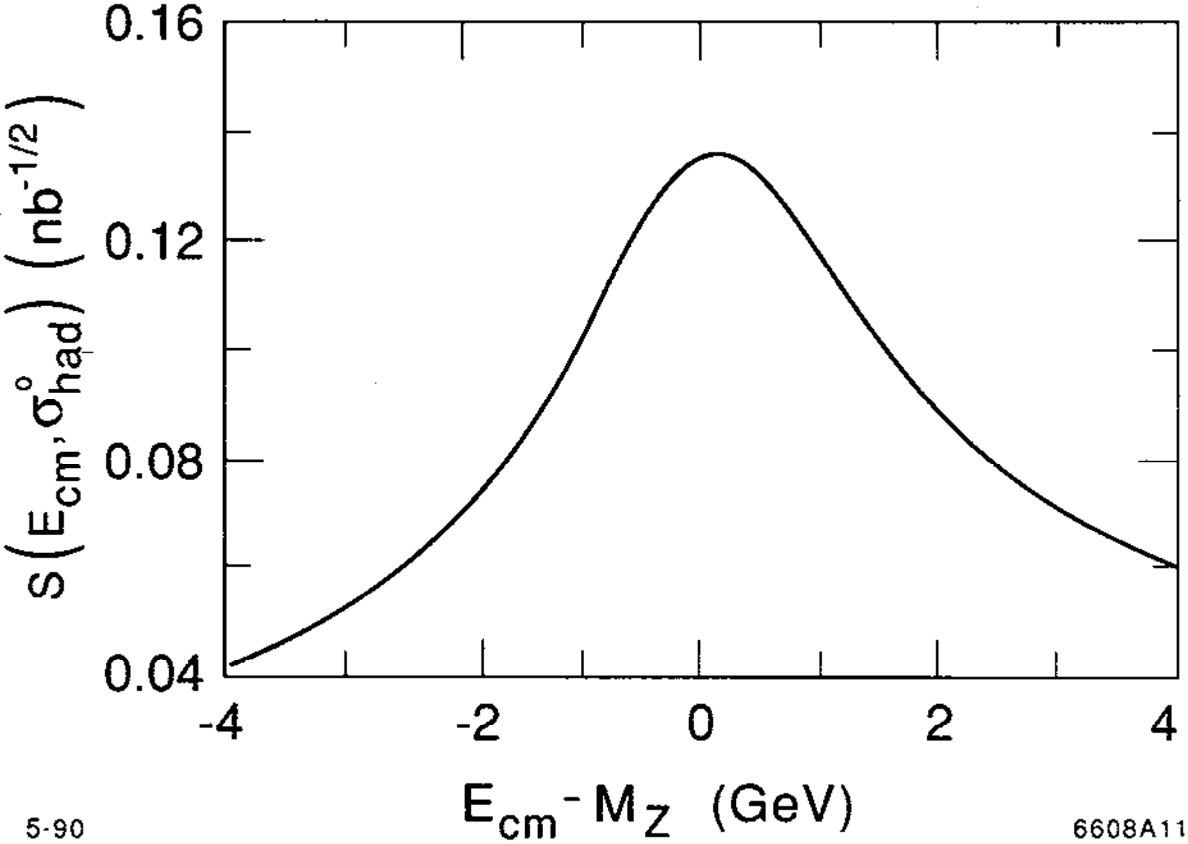
0.16
0.12
0.08
0.04
$S(E_{cm}, \sigma^{o}_{had})$ $(nb^{-1/2})$
-4
-2
0
2
4
$E_{cm} - M_Z$ (GeV)
5-90
6608A11

Fig. 11

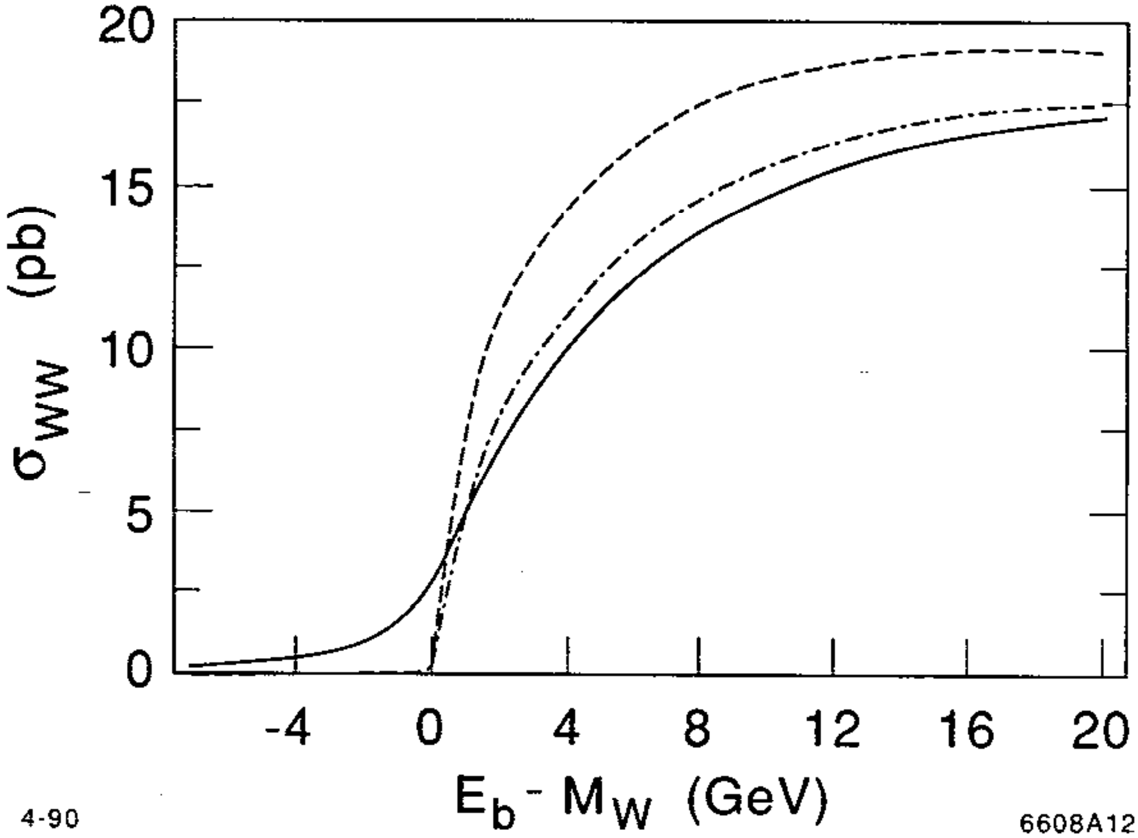

Fig. 12

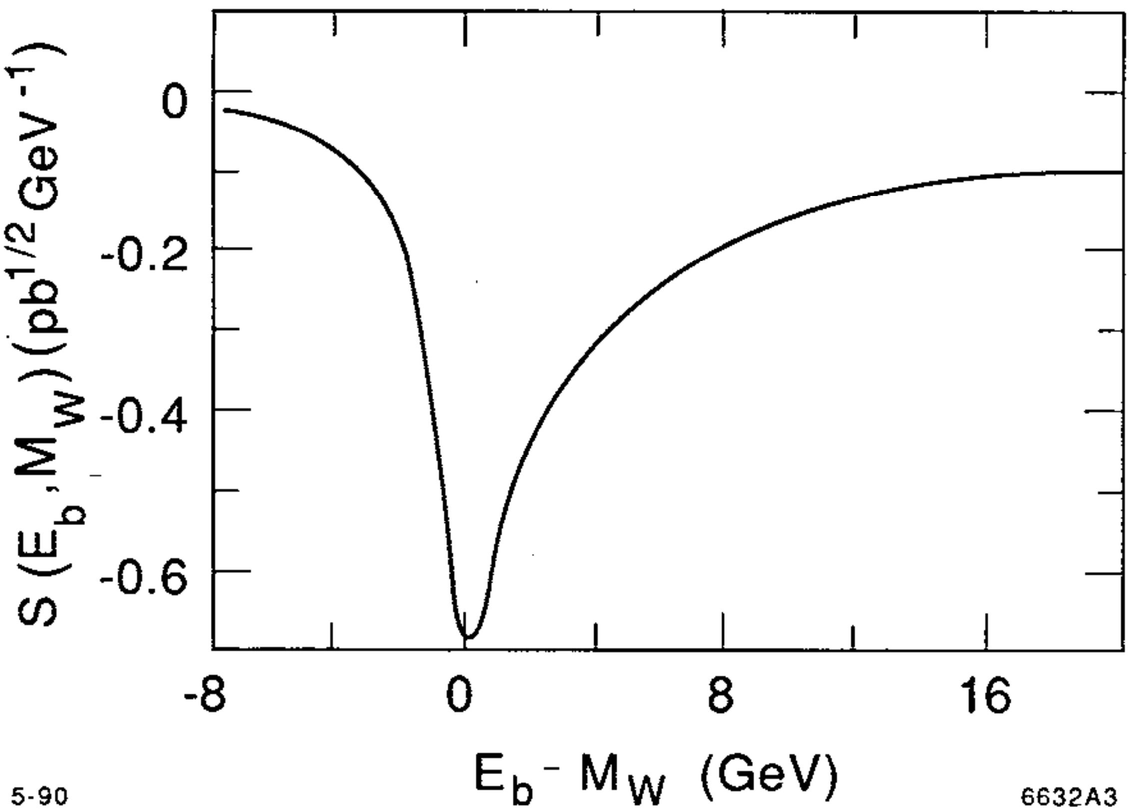

Fig. 13

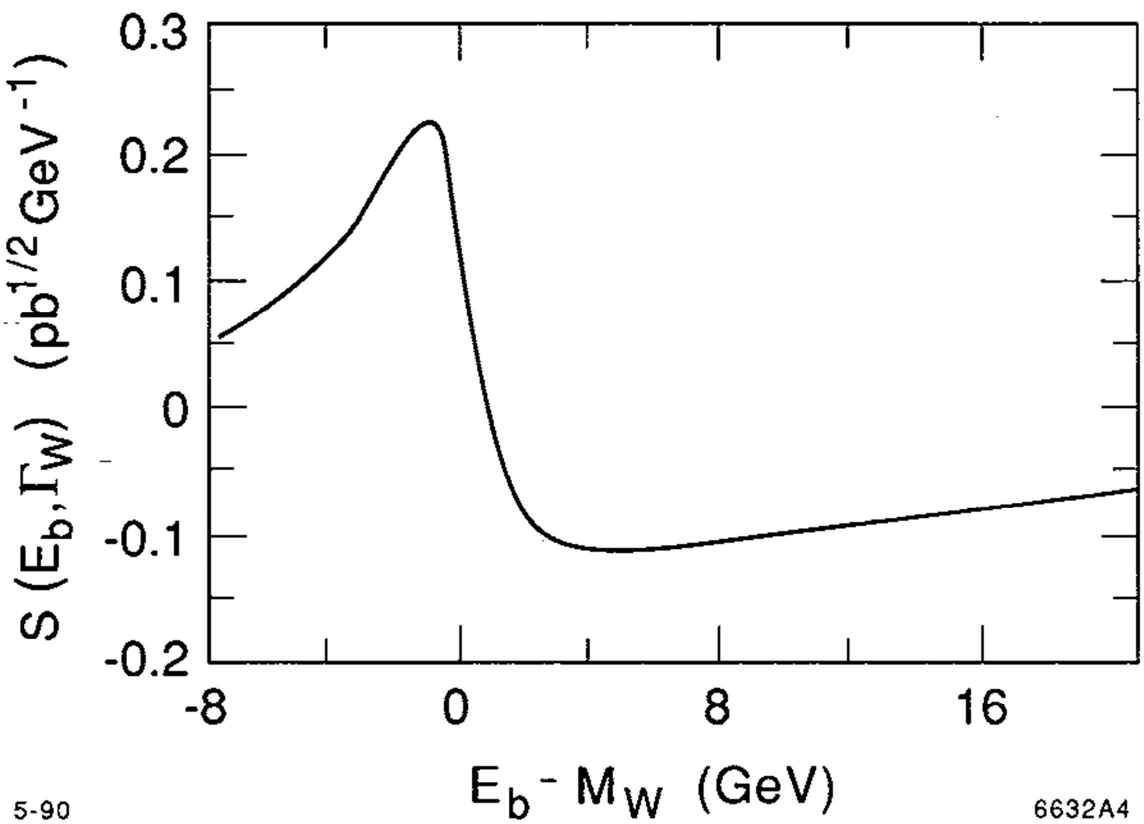

Fig. 14

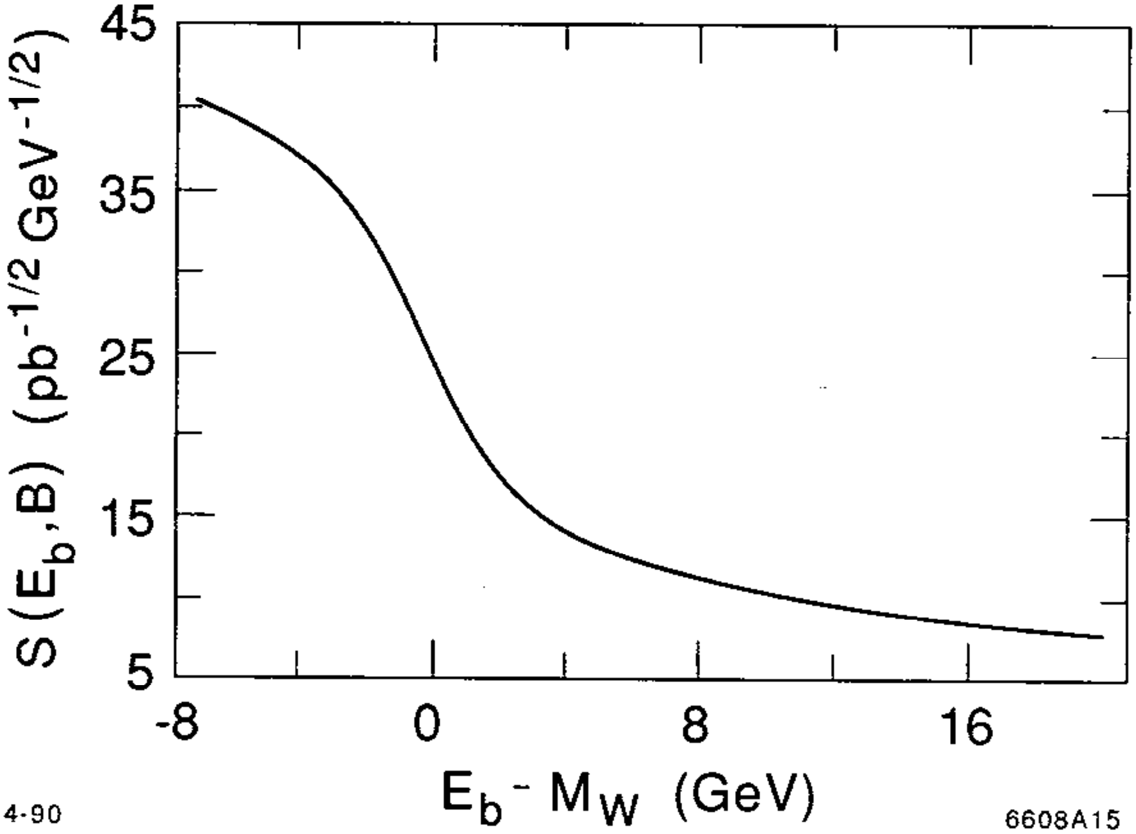

Fig. 15

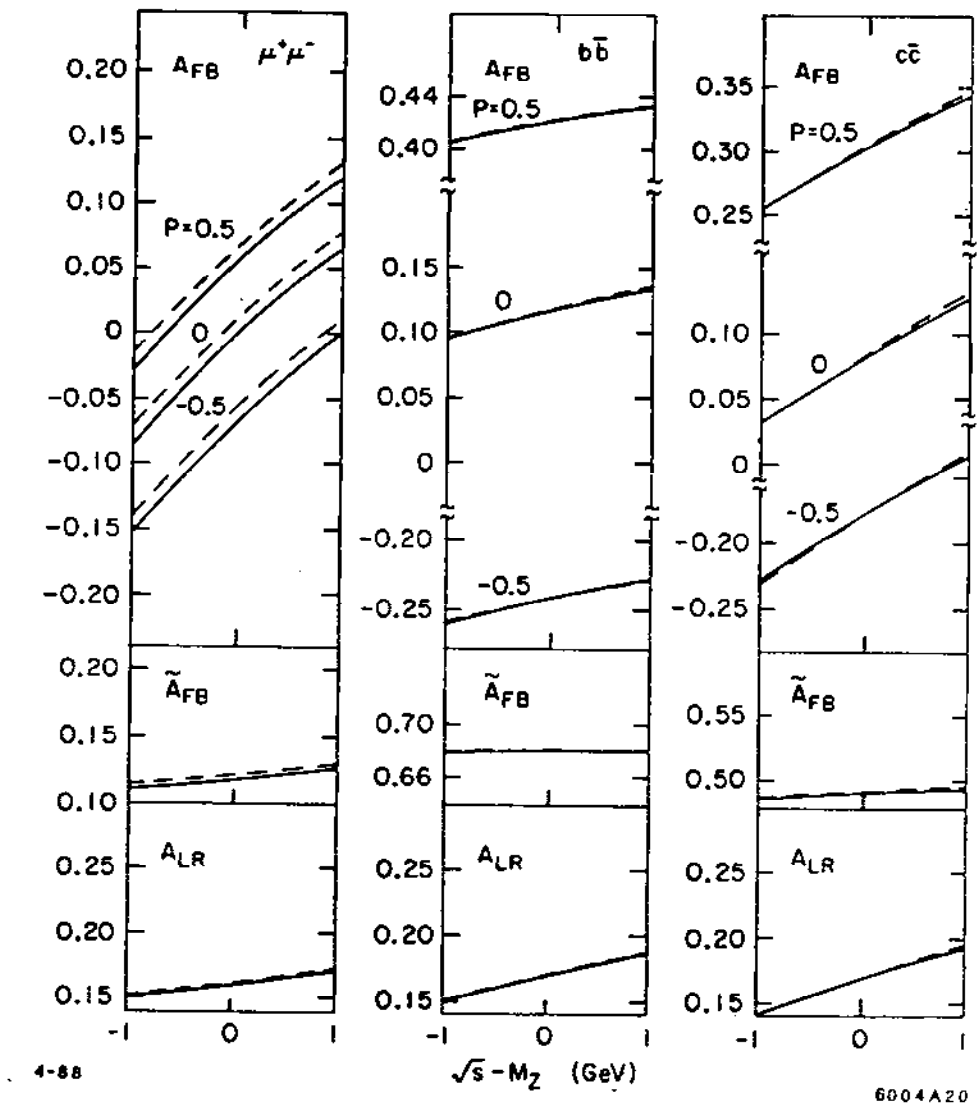

A_{FB}
$\mu^+\mu^-$
P=0.5
0
-0.5
$b\bar{b}$
$c\bar{c}$
$\tilde{A}_{FB}$
A_{LR}
$\sqrt{s} - M_Z$ (GeV)
4-88
6004A20

Fig. 16

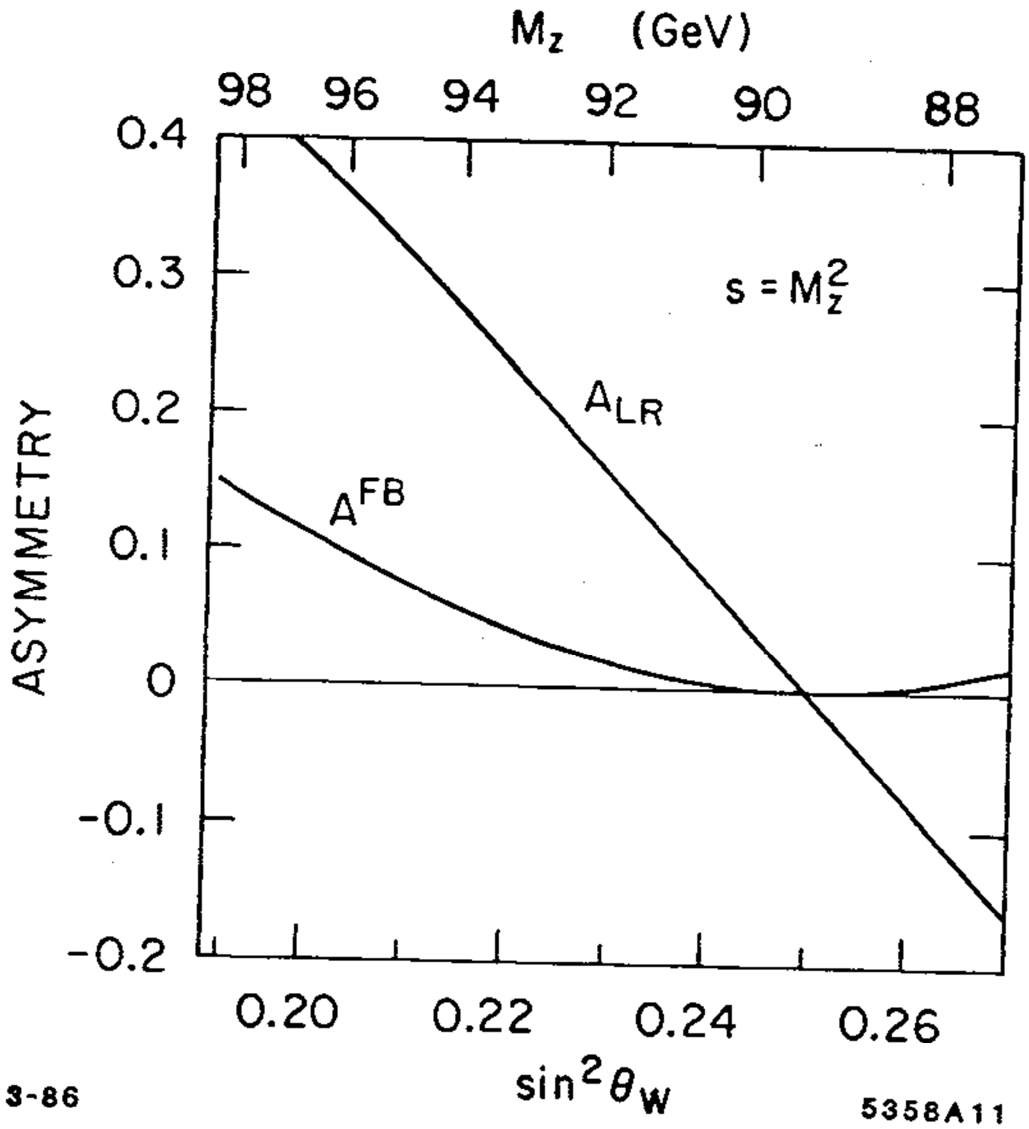

M_z (GeV)
98 96 94 92 90 88
0.4
0.3
0.2
0.1
0
-0.1
-0.2
ASYMMETRY
$s = M_z^2$
A_{LR}
A^{FB}
0.20 0.22 0.24 0.26
$\sin^2\theta_W$
3-86
5358A11

Fig 17

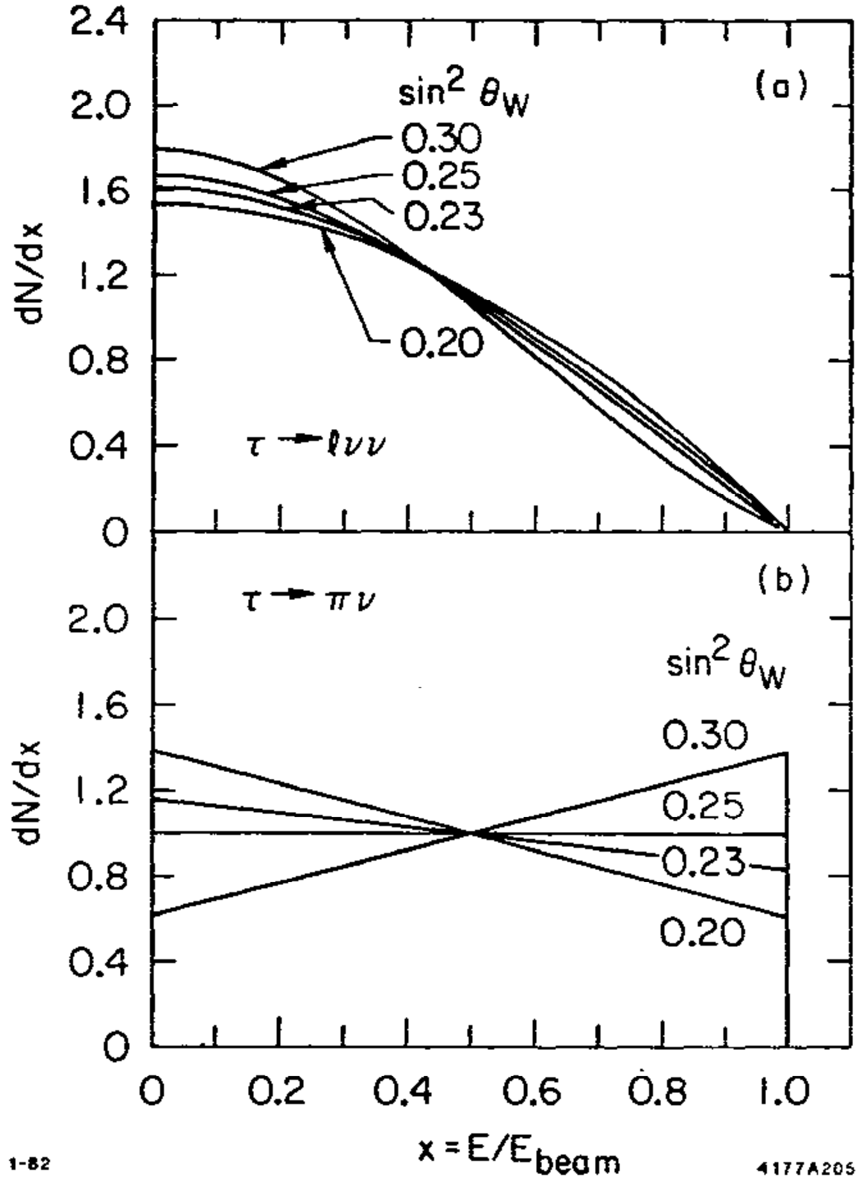

(a)
$\sin^2\theta_W$
0.30
0.25
0.23
0.20
$\tau \to \ell\nu\nu$
(b)
$\tau \to \pi\nu$
$\sin^2\theta_W$
0.30
0.25
0.23
0.20
dN/dx
$x = E/E_{beam}$
1-82
4177A205

Fig. 18

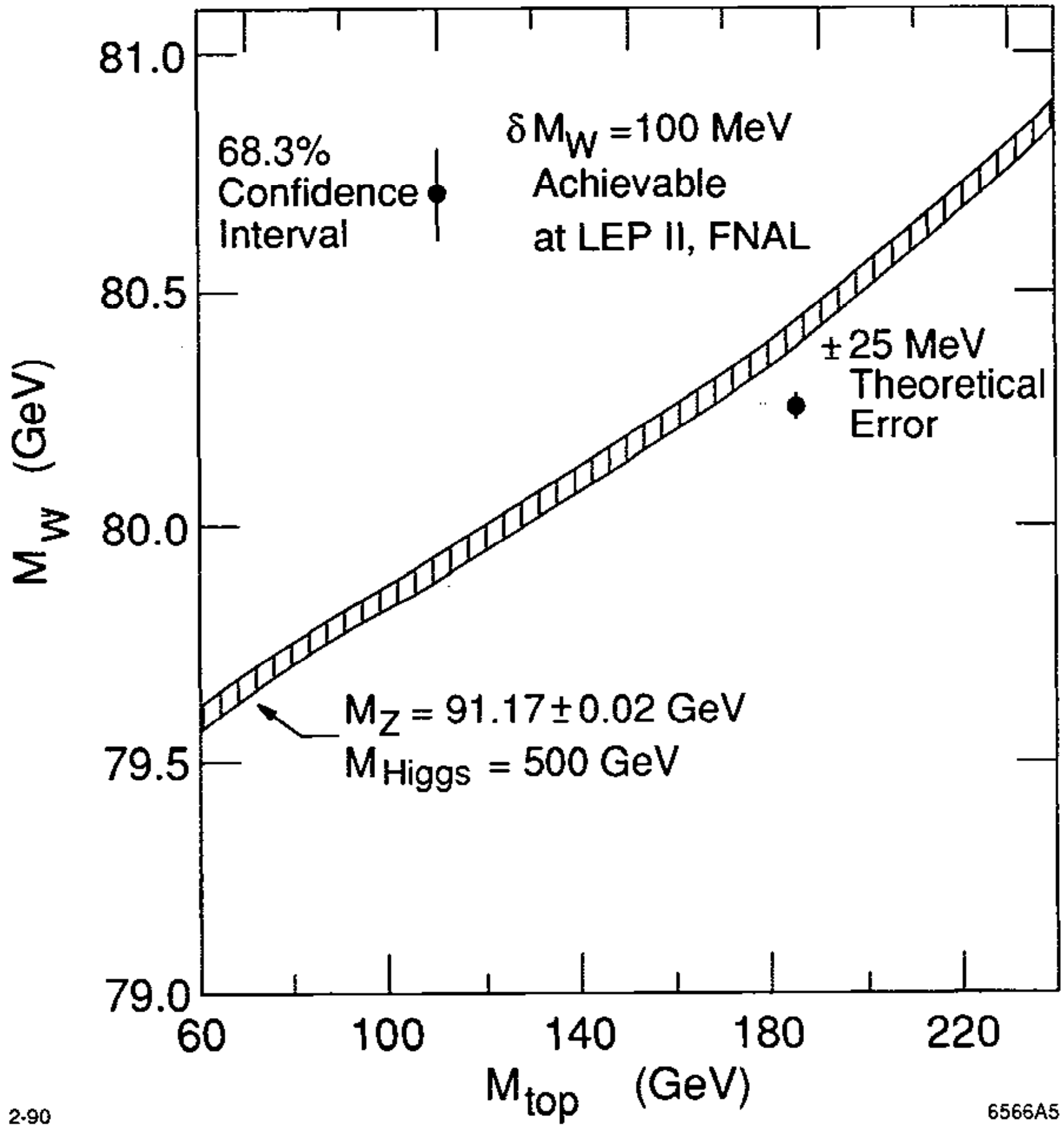

81.0
80.5
80.0
79.5
79.0
60
100
140
180
220
M_W (GeV)
M_{top} (GeV)
68.3%
Confidence
Interval
δM_W =100 MeV
Achievable
at LEP II, FNAL
±25 MeV
Theoretical
Error
M_Z = 91.17±0.02 GeV
M_{Higgs} = 500 GeV
2-90
6566A5

Fig. 19

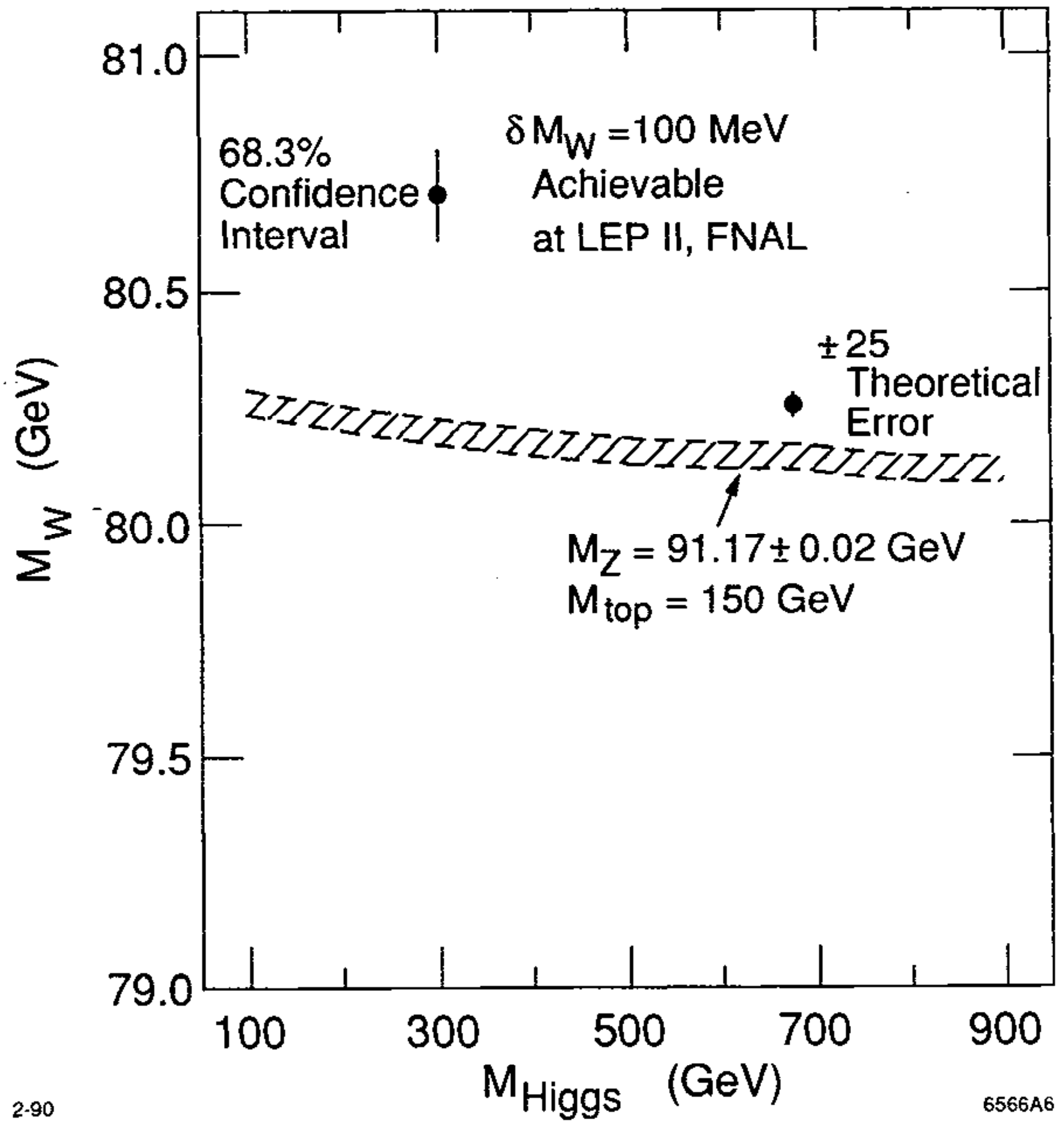
81.0
80.5
80.0
79.5
79.0
100
300
500
700
900
M_W (GeV)
M_Higgs (GeV)
68.3%
Confidence
Interval
δM_W =100 MeV
Achievable
at LEP II, FNAL
±25
Theoretical
Error
M_Z = 91.17±0.02 GeV
M_top = 150 GeV
2-90
6566A6

Fig. 20

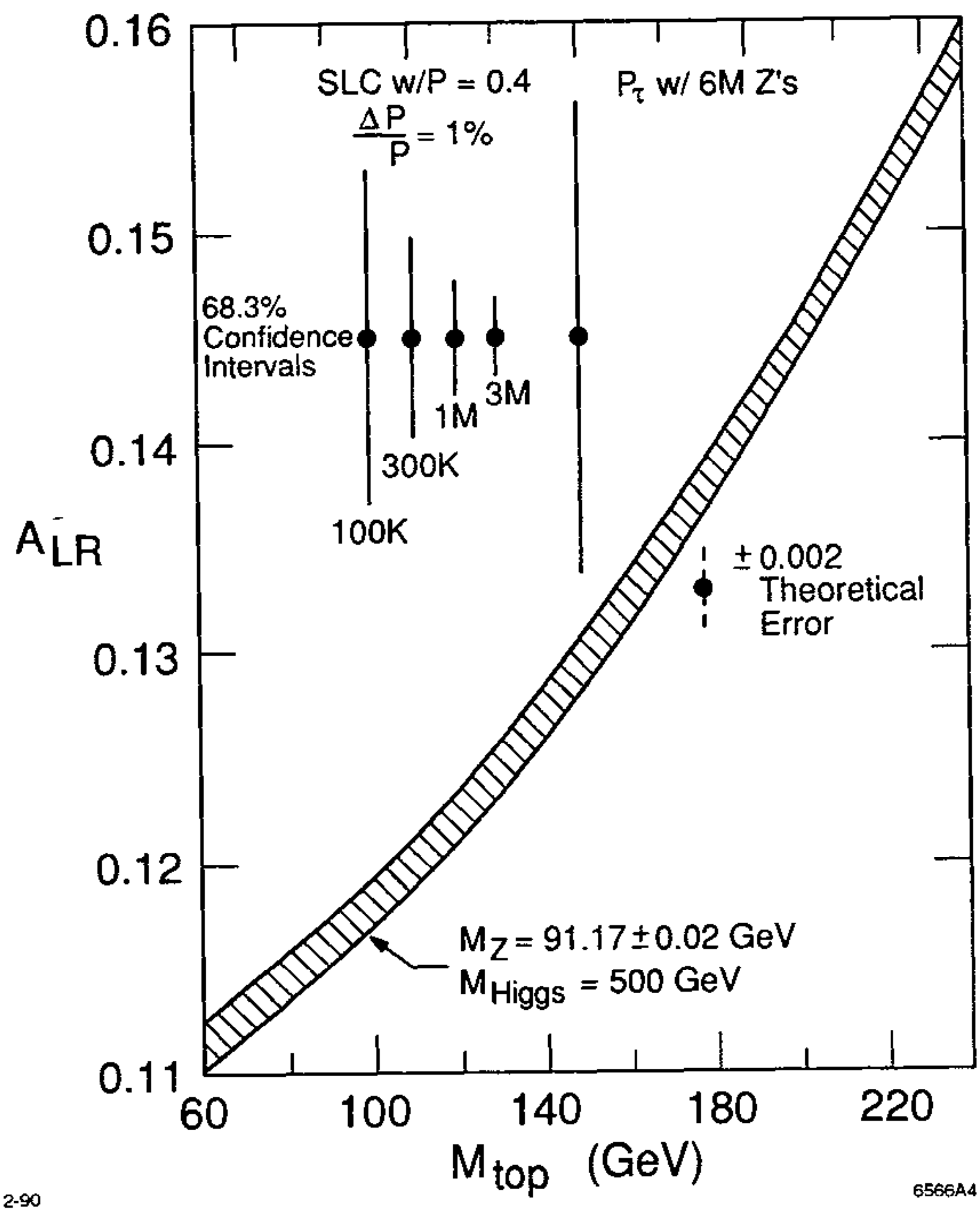

2-90

6566A4

Fig. 21

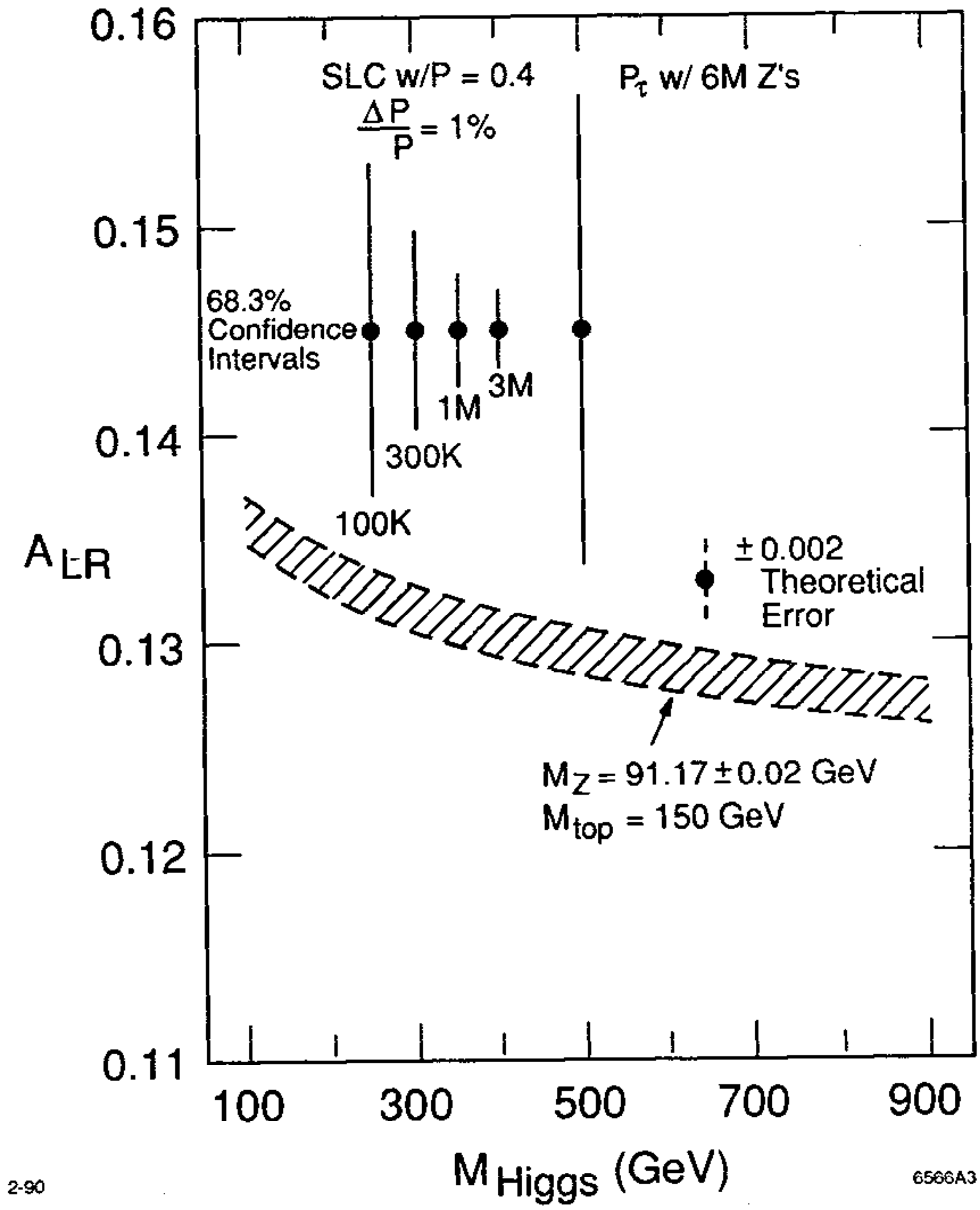

0.16
0.15
0.14
0.13
0.12
0.11
SLC w/P = 0.4
ΔP/P = 1%
Pτ w/ 6M Z's
68.3% Confidence Intervals
100K
300K
1M
3M
± 0.002 Theoretical Error
MZ = 91.17 ± 0.02 GeV
Mtop = 150 GeV
ALR
100
300
500
700
900
MHiggs (GeV)
2-90
6566A3

Fig. 22

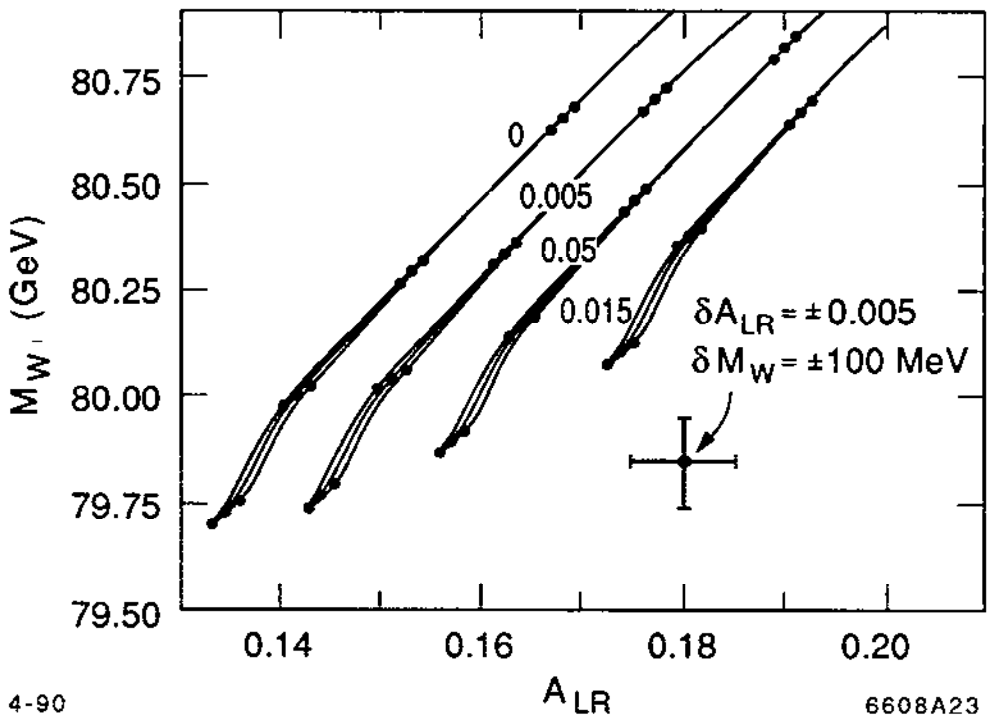

80.75
80.50
80.25
80.00
79.75
79.50
M_W (GeV)
0
0.005
0.05
0.015
$\delta A_{LR} = \pm 0.005$
$\delta M_W = \pm 100$ MeV
0.14
0.16
0.18
0.20
A_{LR}
4-90
6608A23

Fig. 23

Theory of Precision Electroweak Measurements

MICHAEL E. PESKIN*

Stanford Linear Accelerator Center
Stanford University, Stanford, California 94309

Lectures presented at the Seventeenth SLAC Summer Institute
Physics at the 100 GeV Mass Scale
Stanford, California, July 10 – 21, 1989

⋆ Work supported by the Department of Energy, contract DE-AC03-76SF00515.

TABLE OF CONTENTS

1. Introduction

From Bequerel's discovery of radioactivity almost a century ago, the study of weak interactions has matured through a series of well-defined stages. The most recent of these began in the early 1970's with the experimental discovery of neutral currents and the theoretical discovery of renormalizable gauge theories with massive vector bosons. These discoveries led to a study of the neutral current effects through a wide variety of processes and, eventually, to a remarkable convergence of the data to the predictions of the now-standard weak interaction model of Glashow, Weinberg, and Salam.

Last summer, this era of the study of weak interactions ended and a new era began. Instead of data dominated by results on effective interactions at relatively low energy, we are beginning to see the most important data come from direct measurements of the weak gauge bosons. Instead of measurements to an accuracy in the weak interaction parameter $\sin^2\theta_w$ of 10^{-2}, we can look forward to accuracies of 10^{-4}. And, most importantly, instead of looking forward to the convergence of all measurements to the predictions of a particular model, we can look forward to the discovery of *disagreements* between weak interaction experiments, at a level of detail that might give clues to new phenomena at higher energies.

In these lectures, I will review the theoretical concepts needed to understand the goals and implications of experiments in this new era of weak interactions. I will explain how to compute the most important order-α radiative corrections to weak interaction processes and discuss the physical implications of these correction terms. I hope that this discussion will be useful to those—experimentalists and theorists—who will try to interpret the new data that we will soon receive.

Of course, these brief lectures can only provide an overview of the the subject. The field of precision weak interactions, like any other area of precision measurement, is full of technical complication. Fortunately, one has available original papers of great beauty, beginning with the pioneering works of Sirlin[1,2] and Veltman,[3,4] and a number of recent excellent reviews. Among these, the article of Hollik[5] is a particularly complete and instructive summary of the theory, and the 1989 LEP study volume[6] reviews the most recent numerical results. I hope that my lectures will complement these works by providing an entryway into this field not only for those who seek to be experts but for all those who would like to understand its new stage of development.

These lectures are organized as follows: In Section 2, I will review the structure of the standard weak interaction model at zeroth order. In Section 3, I will discuss the measurement of the Z^0 boson mass in e^+e^- annihilation. This measurement is affected by radiative corrections to the form of the Z^0 resonance, and so I will review the theory of the resonance line shape. In Section 4, I will briefly review the modifications of the properties of the Z^0 which would be produced by additional neutral gauge bosons. In Section 5, I will review the theory of the renormalization of weak interaction parameters such as $\sin^2\theta_w$, concentrating especially on the contributions of the top quark and other heavy, undiscovered particles. Section 6 will give some conclusions and prospects.

2. The Standard Electroweak Model

Let us begin by recalling the basic zeroth order relations between boson masses and coupling constants in the Glashow-Weinberg-Salam weak interaction model. I will refer to this theory from here on as the standard model.

The construction of the standard model begins with the coupling of of fermions to gauge bosons of the group $SU(2)\times U(1)$. This interaction is specified by the minimal coupling

$$\mathcal{L} = \bar{f} i \not{D} f ,$$

where the gauge-covariant derivative introduces the three $SU(2)$ gauge bosons, A^a_μ, and one boson B_μ associated with the $U(1)$:

$$D_\mu = \partial_\mu - i(gA^a_\mu\tau^a + g'B_\mu Y). \tag{2.1}$$

The parameters g, g' are the coupling constants of the two groups, $\tau^a = \sigma^a/2$, and Y denotes the $U(1)$ charge, or hypercharge.

The gauge bosons of the standard model acquire masses by spontaneous breaking of the gauge symmetry. The simplest way to achieve this breaking is by introducing a scalar field $\phi(x)$, the Higgs field. This is a complex doublet under $SU(2)$ with hypercharge $Y=\frac{1}{2}$. The kinetic term of the ϕ field, which contains the gauge fields via minimal coupling, then includes a term

$$\mathcal{L} = |D_\mu\phi|^2 \quad \rightarrow \quad \phi^\dagger(gA\cdot\tau + g'BY)^2\phi . \tag{2.2}$$

If ϕ acquires a vacuum expectation value

$$\langle\phi\rangle = \begin{pmatrix} 0 \\ v/\sqrt{2} \end{pmatrix} ,$$

and we introduce this vacuum expectation value into (2.2), we find the gauge field mass term

$$\frac{1}{2}\left((\frac{g}{2})^2[(A^1)^2+(A^2)^2]+[\frac{gA^3-g'B}{2}]^2\right)v^2 .$$

The mass eigenstates are then

$$\begin{aligned} W^\pm &= \frac{A^1 \mp iA^2}{\sqrt{2}} & m_W &= \frac{g}{2}v \\ Z &= \frac{gA^3-g'B}{\sqrt{g^2+g'^2}} & m_Z &= \frac{\sqrt{g^2+g'^2}}{2}v \\ A &= \frac{g'A^3+gB}{\sqrt{g^2+g'^2}} & m_\gamma &= 0 . \end{aligned} \tag{2.3}$$

It is convenient to define a weak interaction mixing angle θ_w by

$$\cos\theta_w = \frac{g}{\sqrt{g^2+g'^2}} \qquad \sin\theta_w = \frac{g'}{\sqrt{g^2+g'^2}} .$$

The standard electric charge is given by

$$e = \frac{gg'}{\sqrt{g^2+g'^2}} = g\sin\theta_w = g'\cos\theta_w .$$

The formulae above imply the important relation

$$\frac{m_W^2}{m_Z^2} = \cos^2\theta_w . \tag{2.4}$$

Experimentally, this relation holds to within 1% accuracy, and so it is important to understand its origin. In this analysis, (2.4) would seem to be a special consequence of the assumption that the Higgs field ϕ is the agent which breaks $SU(2)\times U(1)$. But it may be shown that (2.4) holds at zeroth order in any model in which the field which acquires the vacuum expectation value is an isodoublet, and in a class of more general models, including models without elementary scalar fields, characterized by Sikivie, Susskind, Voloshin, and Zakharov.[7] The essential feature of these models is the presence of an unbroken $SU(2)$ global symmetry in the Higgs sector. Throughout these lectures, I will assume that the Higgs sector is constructed in such a way that (2.4) holds at leading order. My analysis will not otherwise depend on the nature of the Higgs sector except in Section 5, where I will specifically discuss the dependence of radiative corrections of the mass of the scalar Higgs boson in the simplest symmetry-breaking scheme.

Once the theory has been defined in terms of the three parameters g, g', and v, one can work out the predictions of the theory for a whole variety of weak interaction processes. The leading-order predictions for the weak boson masses have already been given above. To discuss the interactions mediated by these bosons, it is useful to rewrite the basic gauge-covariant derivative (2.1) in terms of the mass eigenstates:

$$\begin{aligned}(gA_\mu^a\tau^a+g'B_\mu Y) =& \frac{e}{\sqrt{2}\sin\theta_w}\left(W_\mu^+\tau^+ + W_\mu^-\tau^-\right) \\ &+ \frac{e}{\sin\theta_w\cos\theta_w}Z_\mu(I^{3L}-Q\sin^2\theta_w)+eA_\mu Q \end{aligned} . \tag{2.5}$$

In this equation, $\tau^\pm = \tau^1 \pm i\tau^2$, I^{3L} is the third component of weak isospin, and $Q = I^{3L}+Y$ is the electric charge. The photon then couples to the usual electromagnetic current. The W couples to the charged current of left-handed fermions

$$J_\mu^+ = \overline{L}\gamma_\mu\tau^+L+\cdots = \overline{\nu}_L\gamma_\mu e_L+\cdots , \tag{2.6}$$

where $f_L = \frac{1}{2}(1-\gamma^5)f$ denotes the left-handed component. The Z^0 couples to a neutral current of the particular form

$$J_\mu^Z = J_\mu^{3L} - \sin^2\theta_w J_\mu^Q , \tag{2.7}$$

in which J_μ^{3L}, J_μ^Q are, respectively, the weak isospin and electric charge currents. The unusual properties of the Z^0 and the weak neutral current all follow directly

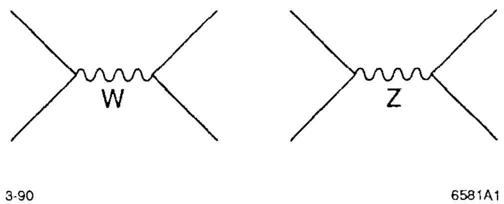

Figure 1. Diagrams contributing to effective low-energy weak interactions.

from the chirally asymmetric Z^0 charge $(I^{3L} - \sin^2\theta_w Q)$. (I will label the weak isospin I^{3L} henceforth simply as I^3.)

At high energies, the interactions of fermions with the Z^0 and W currents are made visible in the strength and angular dependence of the weak boson decays to the various species. At energies well below the Z^0 and W masses, however, experiments probe the effective four-fermion interaction which results from Z^0 and W exchange. This interaction, corresponding to the Feynman diagrams of Fig. 1, can be written in the compact form

$$\mathcal{L}_{eff} = \frac{4G_F}{\sqrt{2}}\left[J_\mu^{+L}J_\mu^{-L} + \left(J_\mu^{3L} - J_\mu^{Q}\sin^2\theta_w\right)^2\right] . \tag{2.8}$$

Due to the relation (2.4), the prefactor in this expression is identical for the W and Z contributions:

$$\frac{G_F}{\sqrt{2}} = \frac{e^2}{8\sin^2\theta_w m_W^2} = \frac{e^2}{8\sin^2\theta_w\cos^2\theta_w m_Z^2} . \tag{2.9}$$

Over the past decade, the dependence of this effective interaction on helicity and flavor has been tested in neutrino and electron scattering processes and found to be in agreement with experiment to accuracies of 5-10%. The convergence of low-energy scattering data to the standard model is well described in the reviews of Kim, *et al.*,[8] Amaldi, *et al.*,[9] and Costa, *et al.*[10]

Current and future experiments work at a higher level of precision. To compare these to theory, we must replace the lowest-order relations that I have quoted so far with more complete predictions which take into account order-α radiative corrections. It is necessary to work out carefully how each of the relations I have written between underlying parameters and observables is altered by radiative effects. Already, though, we can understand the basic features that will emerge from this program of calculation.

Because the lowest-order relations contain three free parameters—g, g', and v—one must make three high-precision measurements to determine the predictions of the theory. Only the fourth measurement can give a sensitive test. Before this past summer, only two standard model observables were known with high precision. These were the value of the basic electric charge

$$\alpha = (137.0359895(61))^{-1} ,$$

obtained from precision QED measurements such as the electron $(g-2)$ and from the measurement of the Josephson effect, and the value of the Fermi constant, the prefactor of (2.8),

$$G_F = 1.16637(2) \times 10^{-5}\ (\mathrm{GeV})^{-2} ,$$

obtained from the muon lifetime. Now, however, experiments at SLC and LEP have reported a very precise value of the Z^0 mass[11–15]

$$m_Z = 91.150(30)\ \mathrm{GeV} . \tag{2.10}$$

This corresponds to a precision of 3×10^{-4}. Future experiments at LEP might make further small reductions of the error. At the same time, these experiments and those at the $p\bar{p}$ colliders promise the precision measurement of additional quantities—the W mass and the angular and polarization asymmetries of Z^0 decays—will finally allow the standard model to be put to a stringent test.

On the other hand, the standard model implicitly contains many parameters which do not appear explicitly in the lowest-order relations. These include the quark and lepton masses and the masses and couplings of Higgs bosons. These additional parameters affect the size of radiative corrections and thus influence the precision comparison of weak interaction experiments. This adds some uncertainty to the predictions of the standard model. But, conversely, it allows us to view these comparisons as windows into the content of the standard model, illuminating properties of heavy quarks and the Higgs sector which are otherwise difficult to view experimentally.

3. The Z^0 Resonance Line-Shape

Before beginning a general analysis of higher-order weak interactions, I would like to discuss the specific problem of the Z^0 boson mass measurement in e^+e^- annihilation. Since the Z^0 creates an enormous resonance in the e^+e^- total cross section, one can measure the Z^0 mass at least roughly by locating the peak of this resonance. However, the shape of the resonance is distorted by radiative corrections, and this effect must be understood to use the position of the resonance in a precise determination of weak parameters. In this section, I will discuss the physics of this effect.

3.1. The Z^0 Resonance at Leading Order

It is a standard exercise to compute the cross section for e^+e^- annihilation into the various species of fermion pairs. Since this will be a useful starting point for our analysis, let me recall the basic formulae, at least in the limit where the various fermion masses can be neglected. In this limit, fermion helicity is conserved in the couplings of fermions to gauge bosons. Thus it is most convenient to quote the cross sections for e^+e^- states of definite helicity ($e_L^-e_R^+$ or $e_R^-e_L^+$) to annihilate to new fermions of fixed helicity ($f_L\overline{f}_R$ or $f_R\overline{f}_L$). These polarized cross sections are

$$\begin{aligned}\sigma(e^+e^-\to f\overline{f}) &= \frac{4\pi\alpha^2}{3s}\\ &\cdot\left|Q_eQ_f+\frac{(I_e^3-Q_e\sin^2\theta_w)(I_f^3-Q_f\sin^2\theta_w)}{\sin^2\theta_w\cos^2\theta_w}\,\frac{\overline{Z}\cdot s}{(s-m_Z^2+is\Gamma_Z/m_Z)}\right|^2,\end{aligned} \tag{3.1}$$

where I^3 and Q denote the weak isospin and electric charge of the fermions involved ($Q_e=-1$).

In writing (3.1), I have set the imaginary part in the denominator to $(s\Gamma_Z/m_Z)$ rather than the more usual $(m_Z\Gamma_Z)$. This reflects the fact that the imaginary part arises as the imaginary part of a loop insertion in the Z^0 propagator, as shown

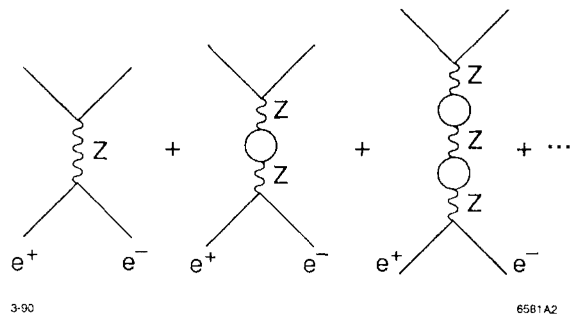

Figure 2. Feynman diagrams whose summation produces the Breit-Wigner denominator of the Z^0 propagator.

in Fig. 2. The loop diagram contains no heavy masses and is proportional to s. This produces a minor kinematical perturbation of the Z^0 resonance. I have also introduced a renormalization factor $\overline{Z}$ into the Z^0 propagator. This factor will remain very close to 1; its origin will be discussed in Section 5.7.

The total cross section for e^+e^- annihilation is built up out of the helicity cross sections according to

$$\sigma_{\text{tot}} = \frac{1}{4} \sum_{pols.} \sum_{f} \sigma(e^+e^- \to f\bar{f}) \cdot N_f \ . \tag{3.2}$$

The factor N_f denotes the effective number of species of flavor f: For leptons, $N_f = 1$; for quarks, $N_f = 3$, plus the enhancement due to QCD. More precisely, for quarks,

$$N_f = 3(1 + \frac{\alpha_s}{\pi} + \ldots) = 3.12 \pm .01 \text{ at } s = m_Z^2 \ , \tag{3.3}$$

corresponding to $\alpha_s(m_Z^2) = 0.12 \pm 0.01$. Figure 3 shows the total cross section for e^+e^- annihilation to hadrons predicted by (3.2).

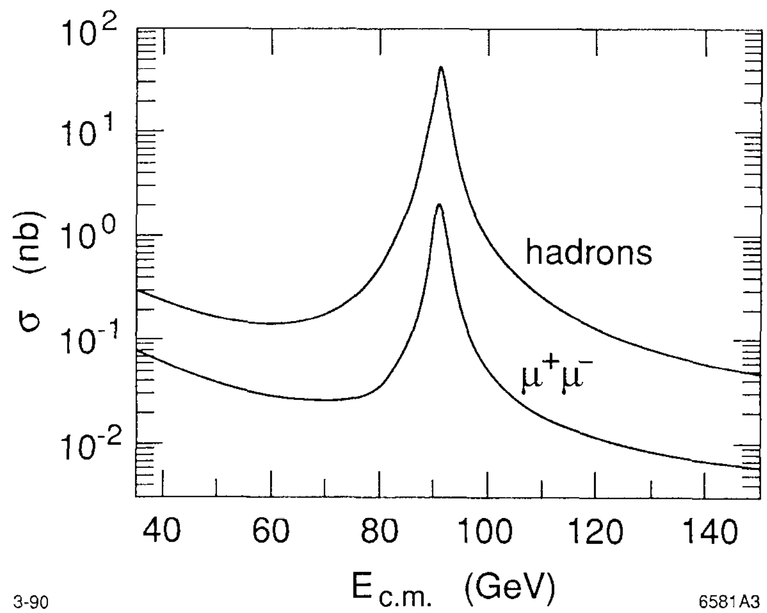

Figure 3. Total cross section, in units of R, for e^+e^- annihilation to hadrons and to muon pairs.

The helicity-dependence of the annihilation cross section also gives rise to asymmetries in fermion pair production. The forward-backward asymmetry is given by

$$A_{FB} = \frac{3}{4} \cdot \frac{(\sigma(e_L^- \to f_L) + \sigma(e_R^- \to f_R)) - (\sigma(e_L^- \to f_R) + \sigma(e_R^- \to f_L))}{\sigma(e_L^- \to f_L) + \sigma(e_R^- \to f_R) + \sigma(e_L^- \to f_R) + \sigma(e_R^- \to f_L)} . \quad (3.4)$$

The polarization asymmetry, between the cross sections of left- and right-handed electrons, may be computed as

$$A_{LR} = \frac{(\sigma(e_L^- \to f_L) + \sigma(e_L^- \to f_R)) - (\sigma(e_R^- \to f_L) + \sigma(e_R^- \to f_R))}{\sigma(e_L^- \to f_L) + \sigma(e_L^- \to f_R) + \sigma(e_R^- \to f_L) + \sigma(e_R^- \to f_R)} . \quad (3.5)$$

I will evaluate these formulae using the Z^0 mass given in (2.10) and the following values for the other parameters: $\alpha = 1/129$, $\sin^2\theta_w = 0.235$, $\overline{Z} = 1.01$. I will defend these latter choices in Section 5.7. The dependence of these asymmetries on energy, over a wide energy range around the Z^0 resonance, is shown in Figs. 4 and 5. The leading-order values of the total cross section and the weak asymmetries just in the neighborhood of the Z^0 resonance are shown in Figs. 6, 7, and 8. Notice that, just at the Z^0 resonance, the polarization asymmetry becomes independent of the final-state flavor and simply represents the asymmetry in the left- and right-handed electron couplings to the Z^0 boson.

Equation (3.1) predicts that the Z^0 resonance has a simple Breit-Wigner form:

$$\sigma(s) = \sigma^0_{\text{peak}} \cdot \left| \frac{s\Gamma_Z/m_Z}{s - m_Z^2 + is\Gamma_Z/m_Z} \right|^2 , \quad (3.6)$$

where the zeroth-order peak cross section is related to the total width and the partial widths into initial and final channels by

$$\sigma^0_{peak} = \frac{12\pi}{m_Z^2} \frac{\Gamma(Z^0 \to e^+e^-)\Gamma(Z^0 \to f\bar{f})}{\Gamma^2_{\text{tot}}} . \quad (3.7)$$

The various partial widths are given by

$$\Gamma_Z^f = \overline{Z} \frac{\alpha m_Z}{6\sin^2\theta_w \cos^2\theta_w} \sum_{L,R} (I_f^3 - Q_f \sin^2\theta_w)^2 \cdot N_f . \quad (3.8)$$

The prefactor $\overline{Z}$ is the Z^0 propagator renormalization from (3.1). Evaluating these

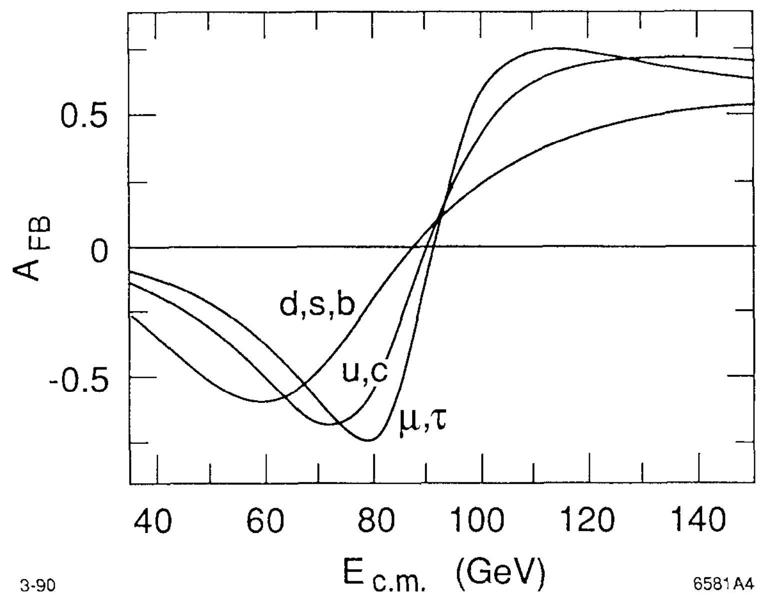

Figure 4. Forward-backward asymmetry A_{FB} for e^+e^- annihilation to charged leptons, u quarks, and d quarks.

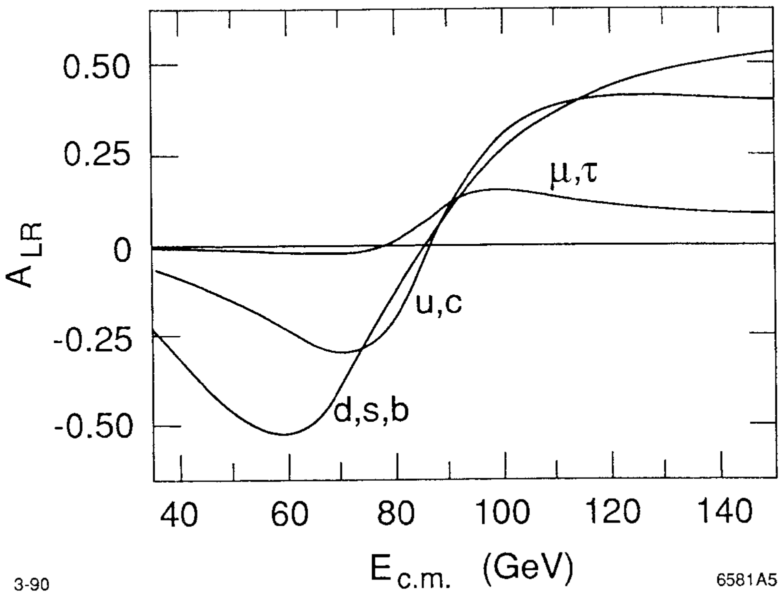

Figure 5. Polarization asymmetry A_{LR} for e^+e^- annihilation to charged leptons, u quarks, and d quarks.

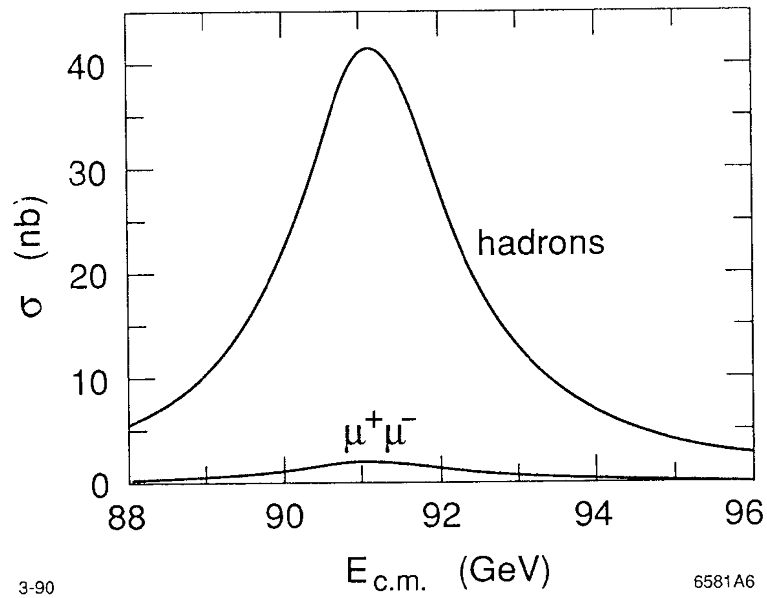

Figure 6. Total cross section for e^+e^- annihilation in the vicinity of the Z^0, to leading order in α.

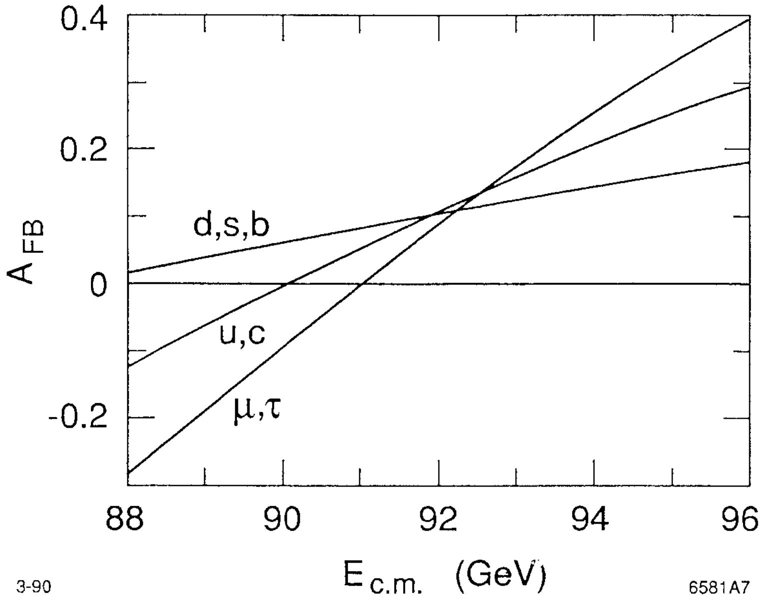

Figure 7. Forward-backward asymmetries in e^+e^- annihilation in the vicinity of the Z^0, to leading order in α.

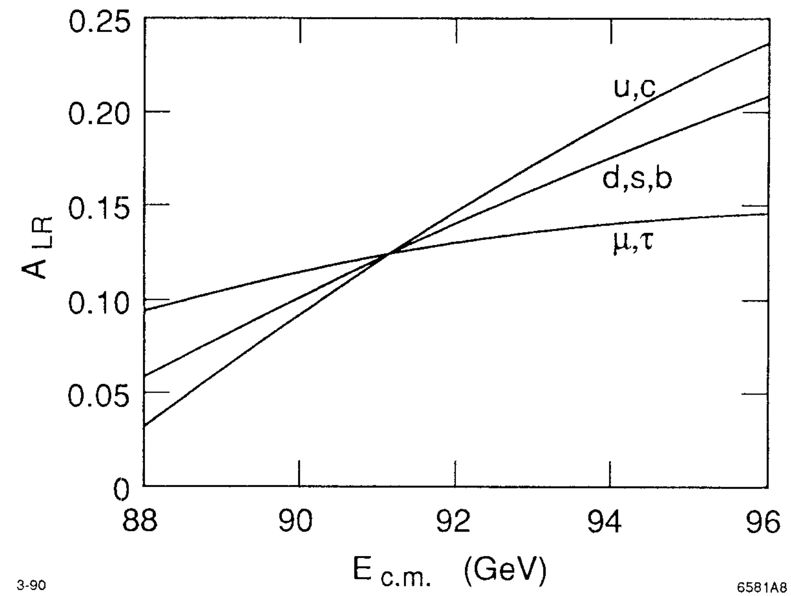

Figure 8. Polarization asymmetries in e^+e^- annihilation in the vicinity of the Z^0, to leading order in α.

formulae using the parameters listed below (3.5), we find the following the partial width for each fermion species:

e, μ, τ:	83 MeV
ν_e, ν_μ, ν_τ:	166 MeV
u, c:	294 MeV
d, s, b:	381 MeV

making up a total width of 2.48 GeV.

3.2. The General Influence of Radiative Corrections

Now that we have constructed a precise picture of the Z^0 resonance according to the leading order expressions of the standard model, we may ask how this picture is changed by radiative corrections. It is useful to think that radiative corrections produce two distinct effects: First, corrections to the Z^0 propagator and vertex shift the parameters of the resonance—the mass, the width, and the peak cross section. Second, corrections producing radiation from the initial electron and positron change the shape of the resonance by smearing out the peak toward higher energy.

At some level, these effects blend into one another; however, the most important radiative corrections can be separated into two distinct classes. Let me label the diagrams shown in Fig. 9(a), the diagrams for real photon emission from the initial electron and positron lines, and the virtual photon diagram needed to cancel their infrared divergences, as 'soft' radiative corrections. These diagrams are essentially QED effects, since the typical momentum of virtual lines is much less than m_Z. Let me label the diagrams shown in Fig. 9(b), the diagrams involving Z^0 propagator corrections and the weak interaction contributions to the vertex, as 'hard'. In these diagrams, the typical momentum of virtual lines is of order m_Z, so that weak and electromagnetic contributions appear on the same footing. As the figure suggests, the hard radiative corrections give renormalized resonance parameters which provide the input to the calculation of the smearing of the peak

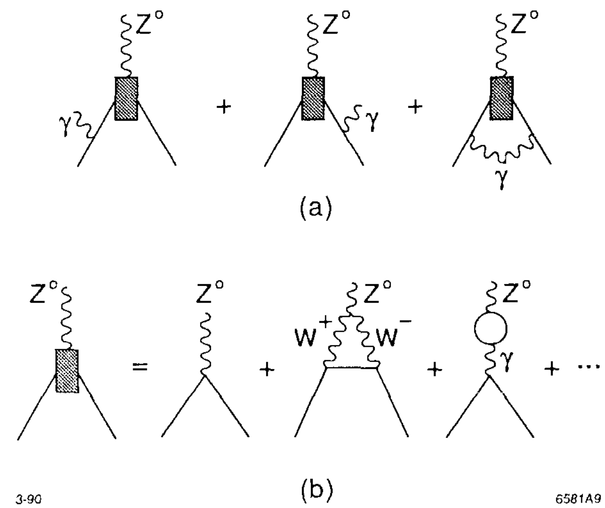

Figure 9. Classes of diagrams contributing to the shape of the Z^0 resonance: (a) 'soft' radiative corrections discussed in Section 3; (b) 'hard' radiative corrections discussed in Section 5.

by radiation. In this section, I will treat these resonance parameters as fixed and discuss the effect of radiation in determining the Z^0 line shape. We will return to the hard contributions, and determine their effect, in Section 5.

3.3. Soft Radiative Corrections: Order α

At leading order in α, QED affects the Z^0 resonance through the diagrams of Fig. 10. The evaluation of these diagrams leads to the famous Bonneau-Martin formula[16] for radiative corrections to a narrow resonance. In quoting this formula, I will drop the contributions from vacuum polarization diagrams, for example, the last diagram of Fig. 9(b); As that figure indicates, I will include these later with the hard corrections.

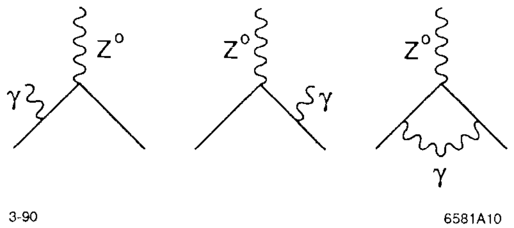

Figure 10. QED corrections to the Z^0 line shape, in the leading order in α.

The first two diagrams of Fig. 10 produce the following correction to the total cross section:

$$\Delta\sigma(s) = 2\int_0^1 dx \left[\frac{\alpha}{2\pi}\left(\log\frac{s}{m_e^2} - 1\right)\left(\frac{1+(1-x)^2}{x}\right)\right]\sigma_0(s(1-x)) \ . \tag{3.9}$$

The quantity in brackets is just the Weiszacker-Williams radiation spectrum expected in any electromagnetic scattering process; the variable x is the photon momentum fraction: $x = k/E$, where k is the photon momentum and E is the electron beam energy. The actual e^+e^- annihilation takes place at the reduced center-of-mass energy given by $\hat{s} = s(1-x)$. The integral in (3.9) diverges at the limit $x \to 0$. This is a standard phenomenon in QED; the divergence can be removed by performing an analysis to all orders in α, but, more simply, it cancels in the total cross section at any given order. Let us temporarily control it by introducing a fictitious photon mass λ, which gives an artificial lower limit to the integral. The divergence as $\lambda \to 0$ is cancelled in the total cross section by the contribution of the third diagram of Fig. 10, which diverges as

$$-2\cdot\frac{\alpha}{2\pi}\left(\log\frac{s}{m_e^2} - 1\right)\cdot 2\log\frac{E}{\lambda}\cdot\sigma_0(s) \tag{3.10}$$

for small λ. Collecting the full contribution from the three diagrams, we find

$$\begin{aligned}\sigma_{tot}(s) = &\left[1 + \frac{2\alpha}{\pi}\left\{(\log\frac{s}{m_e^2} - 1)(\log\frac{\lambda}{E} + \frac{3}{4}) + (\frac{\pi^2}{6} - \frac{1}{4})\right\}\right]\sigma_0(s) \\ &+ \frac{\alpha}{\pi}(\log\frac{s}{m_e^2} - 1)\int_{\lambda/E}^1 \frac{dx}{x}(1+(1-x)^2)\,\sigma_0(s(1-x)) \ ,\end{aligned} \tag{3.11}$$

which is finite in the limit $\lambda \to 0$.

The Bonneau-Martin formula (3.11) is compared to the zeroth-order Z^0 line shape in Fig. 11. The correction is formally of order α but, even after the cancellation of infrared divergences, it is enhanced by two large logarithms. First, there is the logarithm from the Weiszacker-Williams formula, which implies that the strength of the radiation is given by the dimensionless parameter

$$\beta = \frac{2\alpha}{\pi}(\log\frac{s}{m_e^2} - 1)\Big|_{s=m_Z^2} = 0.108 \ . \tag{3.12}$$

There is a second logarithm which arises from the fact that the two lines of (3.11) are mismatched when s is on the resonance but $s(1-x)$ is not. The full size of the correction is then

$$-\beta\cdot\log\frac{m_Z}{\Gamma_Z} \cong -0.39 \ . \tag{3.13}$$

This is indeed a very large correction; it indicates that we must compute to higher order in α to understand the Z^0 line shape quantitatively.

3.4. Multiple Photon Radiation

The systematic calculation of QED diagrams to the next order in α is a very complicated task. To make a precise analysis, one must of course perform the complete calculation. However, it would aid our understanding more to isolate those contributions which are producing the large corrections, understand their origin, and sum them up, if possible, to all orders in α.

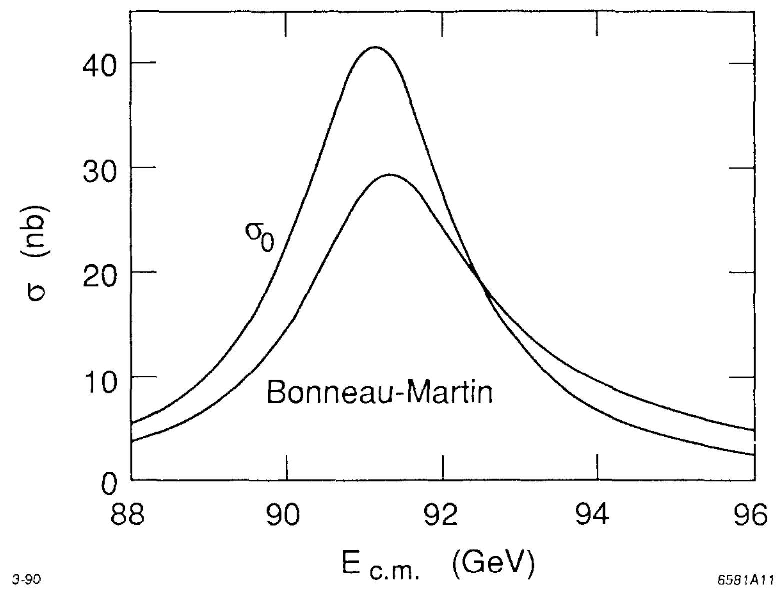

Figure 11. The effect of order α initial-state radiation corrections on the Z^0 line shape. The order α curve is computed from (3.11).

Why is the QED correction so large? The problem is not with the size of α, which is as small as one could wish; rather, it is that α is enhanced by large logarithms. In quantum field theory, large logarithms always have a physical origin; they arise when one compares quantities with two very different characteristic energies in an indelicate way. By understanding the origin of the large logarithms, we can see how to tame them.

The identification and summation of large logarithms is a major part of our understanding of perturbative QCD. Let me give two examples. Consider first the QCD correction to the total cross section for $e^+e^- \to$ hadrons, given by the diagrams of Fig. 12(a). In these diagrams, all particles have typical momenta of order the electron beam energy. Since all momenta are at the same scale, no large logarithms should appear. Indeed, the standard QCD result for the total hadronic cross section is

$$\sigma = \frac{4\pi\alpha^2}{3s} \sum Q_f^2 \cdot 3 \cdot \left(1 + \frac{\alpha_s}{\pi} - \frac{33 - 2n_f}{12}\left(\frac{\alpha_s}{\pi}\right)^2 \log\frac{s}{\mu^2} + \ldots\right). \tag{3.14}$$

The term of order α_s has no large logarithm. The next term in the expansion does have a large logarithm if α_s is defined at a scale μ very different from s, to account for the scale dependent renormalization of this coupling constant. The related process of Drell-Yan production of electron pairs, $p\bar{p} \to e^+e^-$ has an additional complication. In this process, as a result of the diagrams shown in Fig. 12(b), the quark and antiquark which annihilate have typical transverse momentum of order $\sqrt{q^2}$, where q is the momentum of the virtual photon. The amplitude for a quark in the proton, with typical transverse momentum 300 MeV, to give rise to such a highly virtual state contains powers of the logarithm of the ratio of these transverse momentum scales. The effect of these logarithms is to produce an evolution of the quark distribution in the proton with $\log q^2$; this evolution is just that described by the Altarelli-Parisi equations.[17]

The problem of computing the Z^0 line shape is the QED analogue of this latter situation. The large logarithms in (3.13) appear when we relate the off-shell

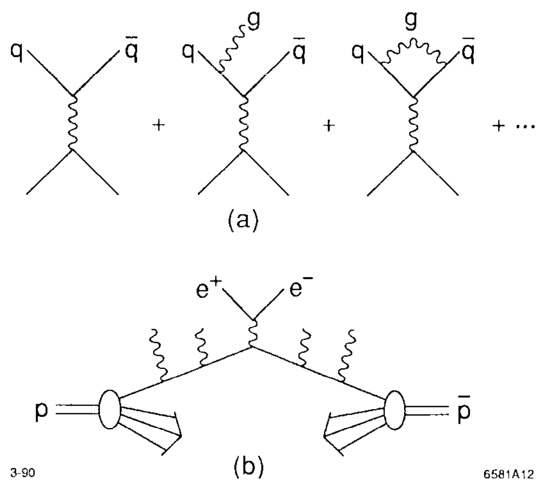

Figure 12. Two examples from QCD of the summation of large logarithms: (a) $e^+e^- \to$ hadrons; (b) $p\bar{p} \to e^+e^-$.

electron which finally annihilates into the Z^0 to the on-shell electron from which the process begins. To control these logarithms, we should reinterpret (3.11) as the first step of an evolution process by which the virtual electron emerges from the external electron. This strategy for calculating the Z^0 line shape was first advocated by Fadin and Kuraev.[18] However, it should be noted that these authors, and also Altarelli and Parisi, took their inspiration from the QED evolution equation constructed by Gribov and Lipatov[19] in their classic work on deep inelastic scattering.

Let $D_e(z,s)$ be the electron distribution function, the probability that the annihilating electron has fraction z of the original beam energy. If there is no radiation from the initial electron, we would have

$$D_e(z) = \delta(z-1) \; . \tag{3.15}$$

Order by order in α, this result receives radiative corrections. I will now argue that (3.11) may be interpreted as providing the order α correction to (3.15). In this reinterpretation, we view (3.11) as a step in a process rather than as a simple correction; this will allow us to represent this process by an evolution equation which will generate the most important corrections to all order.

To make this reinterpretation of (3.11), let us divide this equation into three parts. The second line of the equation represents the effect of radiation in moving electrons and positrons from the full energy to an energy fraction $(1-x)$. Assigning half of this contribution to the electron and half to the positron, we may represent it as

$$\Delta D_e(z) = \int dx \left[\frac{\beta}{4} \cdot \frac{1+(1-x)^2}{x}\right] D_e\left(\frac{z}{(1-x)}\right) \; . \tag{3.16}$$

As electrons radiate photons and move to lower energy, we should expect to find fewer electrons at the full beam energy. The fractional depletion should be found by integrating over x the probability of radition to energy fraction $(1-x)$:

$$\frac{\Delta D_e(z,s)}{D_e(z,s)} = -\frac{\beta}{4}\int_{\lambda/E}^{1} \frac{dx}{x}(1+(1-x)^2) = -\frac{\beta}{4}(\log\frac{E}{\lambda} + \log\frac{E}{\lambda} - \frac{3}{2}) \; . \tag{3.17}$$

Indeed, (3.11) contains exactly this depletion, in the term

$$\Delta\sigma(s) = -\beta(\log\frac{E}{\lambda} - \frac{3}{4})\sigma_0(s) \; . \tag{3.18}$$

The magnitude of (3.18) is double that of (3.17) in order to account the effect on the electron and on the positron. We have now given a physical interpretation to most of the pieces in (3.11). The only pieces of (3.11) not included in the above accounting are the terms

$$\Delta\sigma(s) = \left(1 + \frac{2\alpha}{\pi}(\frac{\pi^2}{6} - \frac{1}{4})\right)\sigma_0(s) \; ; \tag{3.19}$$

these last terms give a correction to the e^+e^- annihilation vertex which is explicitly of order α, with no enhancement by large logarithms.

The two terms (3.16) and (3.18) may be considered as the contributions of first order in β to an evolution process in which an electron radiates and moves down to lower energy fraction. The evolution parameter is β, and thus the evolution progresses further the higher the energy or the further the electron must go off-shell. We may assemble the two pieces as the kernel of an integral equation for $D_e(z,s)$:

$$\frac{\partial}{\partial\beta}D_e(z,s) = \frac{1}{4}\int_0^{(1-z)} dx\left[\frac{1+(1-x)^2}{x} - A\delta(x)\right]\cdot D_e\left(\frac{z}{(1-x)},s\right) . \tag{3.20}$$

The subtracted term depletes the electron distribution at the higher energy, the Weizsacker-William term fills in the distribution of electrons after radiation. Both terms are singular at $x = 0$, and, though this singularity is difficult to write mathematically, it is easy to describe and implement in a computation. After one cuts off the divergences in some way, the coefficient A is fixed by the requirement that the total probability does not change:

$$\int dz D_e(z,s) = 1 , \tag{3.21}$$

for any value of s.

In QCD, we have no explicit solution of the evolution equation for quark distributions. In QED, however, the situation is much more promising. First, the initial condition for the evolution equation is known: at $\beta = 0$, $D_e(z)$ reduces to the delta function in (3.15). Second, the evolution parameter β is still rather small at the Z^0, so we can imagine solving the (3.20) in an expansion in β.

We can obtain a good first approximation to the solution by concentrating on the region near $z = 1$. Let us try as an ansatz

$$D_e^{(0)}(z,s) = \frac{\beta}{2}(1-z)^{\beta/2-1} . \tag{3.22}$$

This function satisfies (3.21) and contracts to a delta function at $z = 1$ when $\beta \to 0$. Its derivative is

$$\frac{\partial}{\partial\beta}D_e^{(0)} = \frac{\beta}{4}\log(1-z)\cdot(1-z)^{\beta/2-1} + \frac{1}{2}(1-z)^{\beta/2-1} . \tag{3.23}$$

The most singular term of the integral in (3.20) is

$$\frac{1}{2}\int_\eta^{(1-z)} \frac{dx}{x} D_e\left(\frac{z}{(1-x)}\right) . \tag{3.24}$$

In writing this expression, I have cut off the integral at a lower limit η. Inserting $D_e^{(0)}$ into this term, and approximating near $z = 1$, we find

$$\frac{1}{2}\int_\eta^{(1-z)} \frac{dx}{x}\frac{\beta}{2}((1-z)-x)^{\beta/2-1} \sim \frac{\beta}{4}\log\frac{(1-z)}{\eta} \tag{3.25}$$

The logarithm of $(1-z)$ matches the desired form (3.23); the logarithm of η is a rescaling of the original distribution function and so is naturally cancelled when A in (3.20) is chosen to preserve the normalization of $D_e(z)$. In fact, since $D_e^{(0)}(z,s)$ satisfies (3.21), the correct choice of A will reproduce the second term of (3.23). In this way, we can see that the function $D_e^{(0)}(z,s)$ actually gives the correct dependence on z in the limit $z \to 1$ and thus is a good first approximation to the exact electron distribution.

Fadin and Kuraev began with this function as a first approximation and systematically computed corrections to it as a series in β:

$$D_e(z,s) = \frac{\beta}{2}(1-z)^{\beta/2-1}(1+\frac{3}{8}\beta) - \frac{1}{4}\beta(1+z) + \cdots . \tag{3.26}$$

The distribution function (3.26) is displayed, and compared to the Weiszacker-Williams distribution, in Fig. 13. An exact evaluation of the distribution function $D_e(z)$ would also include effects of pair-production (Fig. 14), which require additional terms in the evolution equation. The first such contributions are of order α^2 and so are omitted here, though they may be found in Ref. 18.

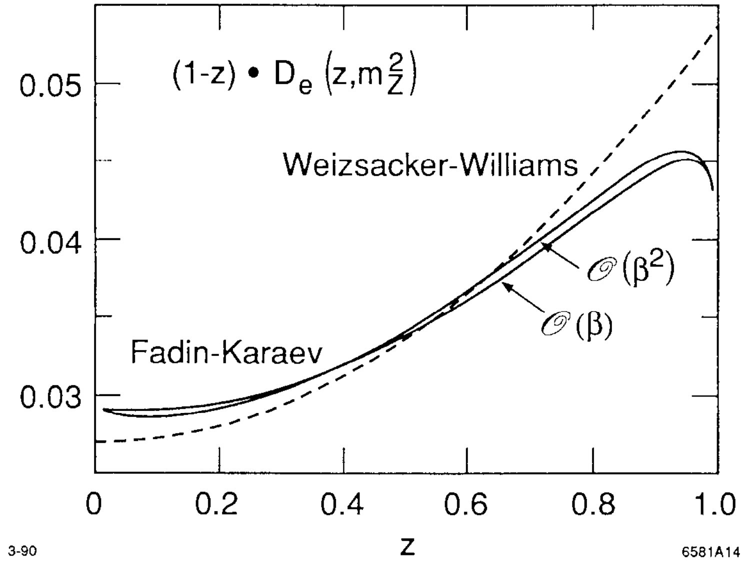

Figure 13. The distribution $D_e(z,s)$ of the energy fraction carried by a virtual electron.

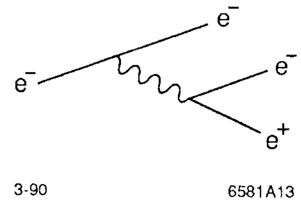

Figure 14. An additional contribution to the electron distribution function from pair-production.

To compute the Z^0 line shape, we must compute the cross section as a function of s, given this distribution in energy fraction for the electron and position. That is,

$$\sigma = \int_0^1 dz_1\ D_e(z_1) \int_0^1 dz_2\ D_e(z_2)\ \sigma^0(\hat{s})\ , \tag{3.27}$$

where $\hat{s} = z_1 z_2 s$. It is useful to work out more explicitly the distribution of the effective electron-positron collision energy. This may be described by computing

$$\begin{aligned} &\int_0^1 dz_1\ D_e(z_1) \int_0^1 dz_2\ D_e(z_2)\ \delta((1-x) - z_1 z_2) \\ &\quad = \beta x^{\beta-1}(1+\frac{3}{4}\beta) - \beta(1-\frac{x}{2}) + \cdots\ . \end{aligned} \tag{3.28}$$

In (3.28), I have inserted x to represent the fraction of total radiated energy. Using the distribution function in x, and restoring the order-α correction to the annihilation vertex written in (3.19), we find the following formula for the radiatively corrected cross section:

$$\sigma = \int_0^1 dx \left[\beta x^{\beta-1}(1+\frac{3}{4}\beta) - \beta(1-\frac{x}{2})\right] \cdot \left[1 + \frac{2\alpha}{\pi}\left(\frac{\pi^2}{6} - \frac{1}{4}\right)\right] \sigma_0\left(s(1-x)\right)\ . \tag{3.29}$$

One might view this as an improved version of the Bonneau-Martin formula (3.11) in which the logarithms are exponentiated to powers of x. The formula (3.29) is compared to the zeroth- and first-order approximations to the cross section in Figs. 15 and 16. Cahn[20] has pointed out that the integral over x in (3.29) can be carried out analytically for a Breit-Wigner resonance, and the resulting formula has been useful in analyzing data on the shape of the Z^0 resonance.

In the past few years, there has been considerable further theoretical effort to refine the calculation fo QED effects on the Z^0 line shape. Fadin and Kuraev actually carried out this analysis to order α^2. The complete order-α corrections to $e^+e^- \to \mu^+\mu^-$ have been computed by Berends, Burgers, and van Neerven.[21] Other higher-order analyses have been carried out by many authors and are reviewed by Berends in Ref. 22. A useful comparison of calculations of the Z^0 line shape at various levels of approximation has been given by Alexander, Bonvicini, Drell, and Frey.[23] Their results (computed assuming $m_Z = 93$ GeV) are reproduced in Fig. 17. These authors estimate the theoretical errors in the extraction of the mass, width, and peak cross section of the Z^0 arising from residual uncertainties in this calculation at well below 1%.

3.5. Extraction of the Resonance Parameters

Since the QED radiative corrections broaden the Z^0 peak and smear it asymmetrically, it is not useful to quote the resonance parameters in terms of the observed peak position or the visually extracted width. Rather, one should parametrize a zeroth-order cross section in terms of a resonance position, width, and peak height, integrate this cross section together with the effects of radiation by inserting it into (3.29) (or a higher-order formula for the soft radiative corretions), and compare the result to the data. Since (3.29) does not include hard radiative corrections, the effects of these corrections will be included in the fitted resonance parameters. These effects must be taken into account in comparing the extracted parameters to other weak interaction measurements and to deeper theoretical predictions.

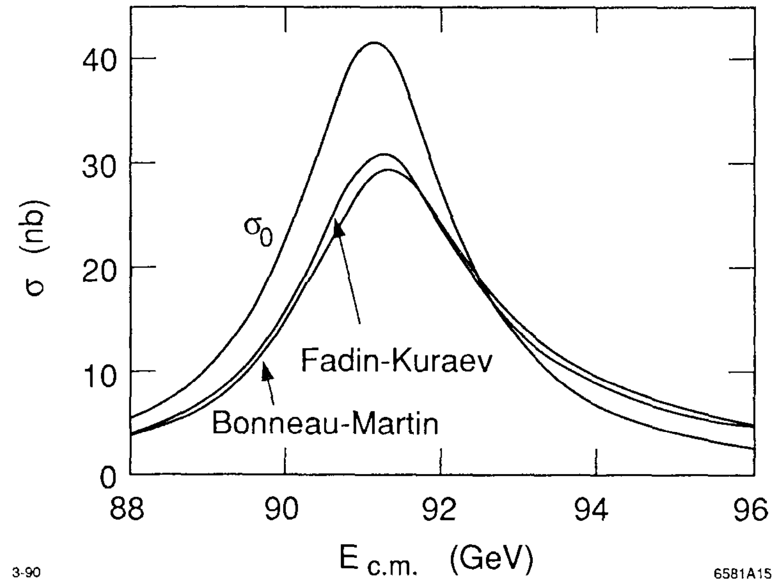

Figure 15. Total cross section for e^+e^- annihilation to hadrons in the vicinity of the Z^0, computed in zeroth order, first order (eq. (3.11)), and from the Fadin-Kuraev formula (3.29).

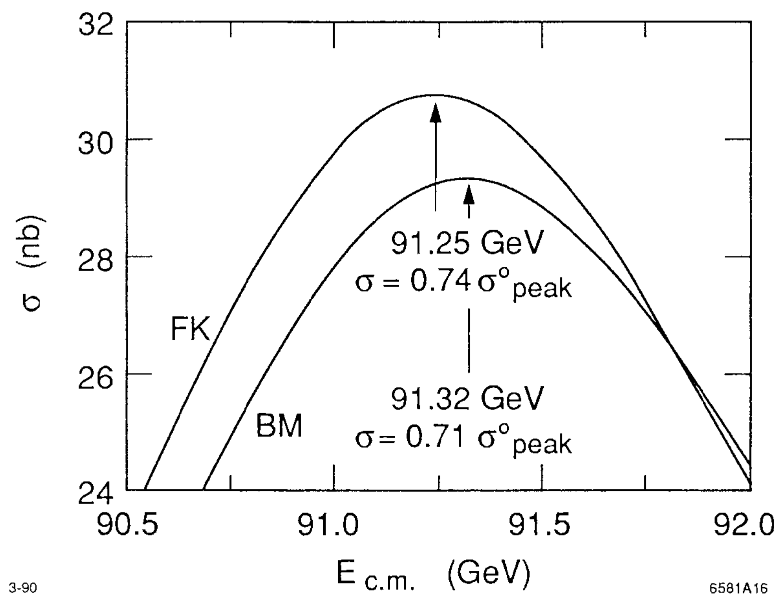

Figure 16. Magnification of Fig. 15 in the vicinity of the Z^0 peak. For each of the two radiative correction formulae, I have indicated the shift of the location of the peak and the decrease in the peak height from the zeroth-order value.

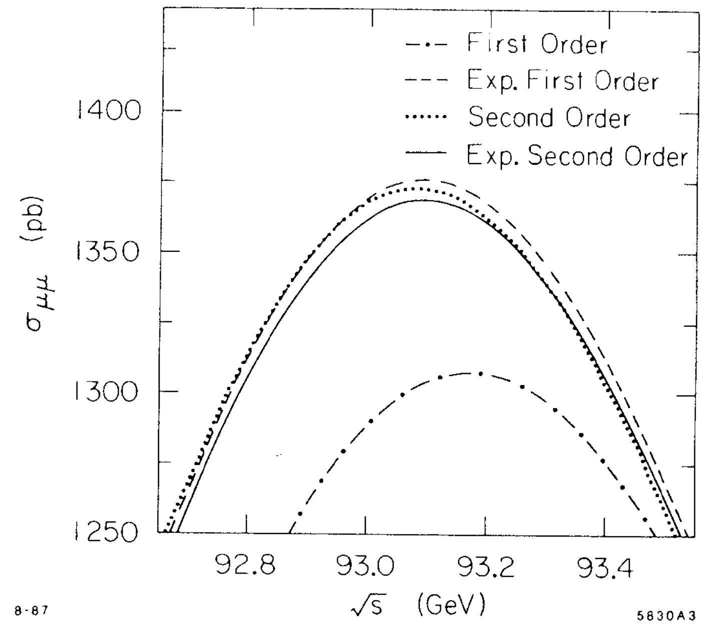

Figure 17. Comparison of the Z^0 line shape calculation at different levels of approximation, from Ref. 23.

To show the utility of this theory, I have displayed in Fig. 18 a calculation of the total cross section for e^+e^- annihilation to hadrons in the vicinity of the Z^0, obtained by inserting (3.1), with the parameters used in Section 3.1, into the radiative correction formula (3.29). The result is compared to the recent cross section measurements of the ALEPH experiment.[13] The mass of the Z^0 has, of course, been obtained from fitting such a curve to the data; however, the peak height and width of the Z^0 have been calculated from the standard model. The detailed agreement of theory and experiment for the line shape is quite remarkable.

In addition to its effects on the resonance line shape, initial-state radiation has other important effects on weak interaction experiments at the Z^0. In experiments which depend on specific exclusive final states, the effect of experimental cuts may be modified by radiation. For example, in the measurement of the forward-backward asymmetry in $e^+e^- \to \mu^+\mu^-$, a strict collinearity cut changes the shape of the Z^0 resonance slightly by suppressing its tail. The values of asymmetries measured at the Z^0 peak are affected by the smearing of the e^+e^- annihilation energy which arises from radiation. In Figs. 19 and 20, I have redrawn the plots of A_{FB} and A_{LR} versus beam energy taking into account the effects of radiation by computing the various helicity cross sections using (3.29) before forming the asymmetry. Notice that the various quantities A_{LR} are relatively weakly affected by radiation, but that the forward-backward asymmetry in $e^+e^- \to \mu^+\mu^-$ is very strongly perturbed. This effect was pointed out by Bohm and Hollik in ref. 24.

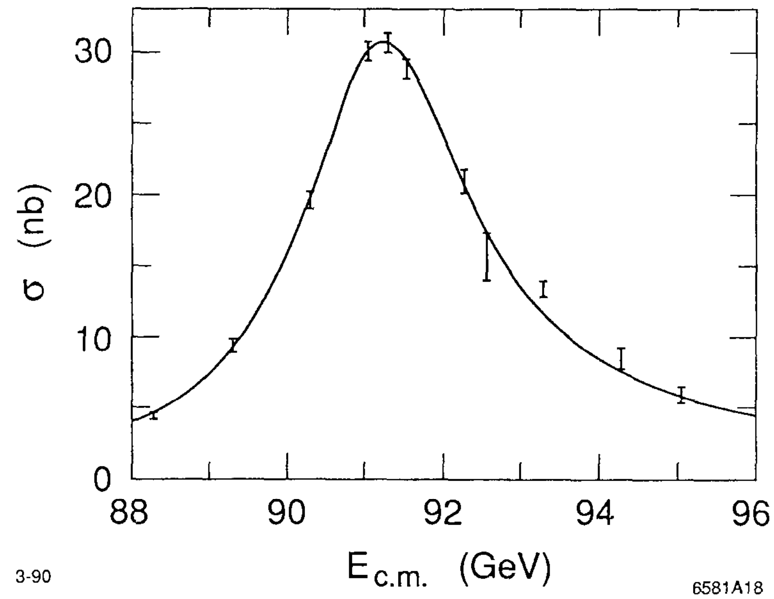

Figure 18. Total cross section measurements on the Z^0 peak reported by the ALEPH experiment,[13] compared to the line shape computed from (3.29).

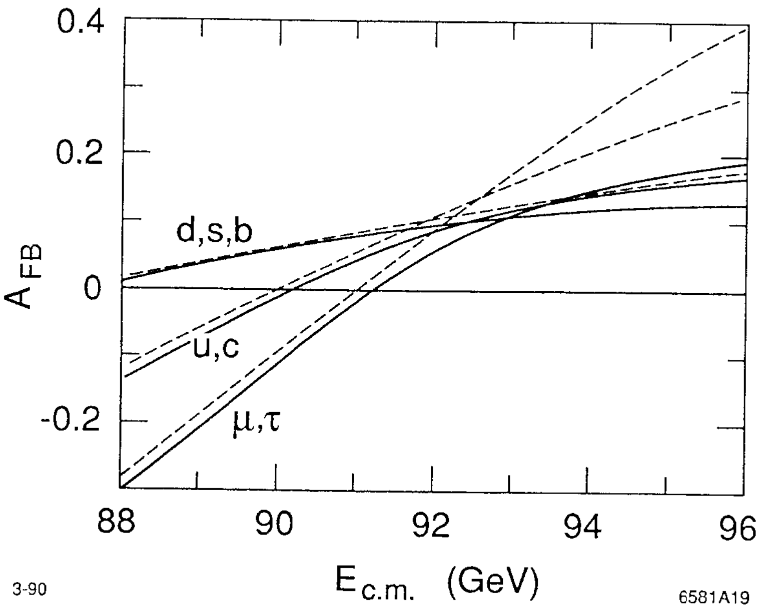

Figure 19. Forward-backward asymmetries in the vicinity of the Z^0 resonance, computed at lowest order (dashed curves) and including soft radiative corrections according to (3.29) (solid curves).

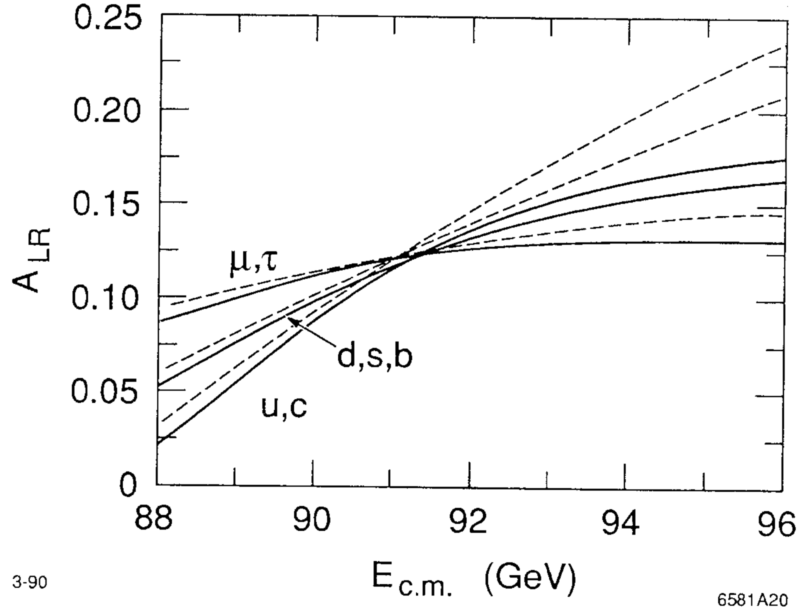

Figure 20. Polarization asymmetries in the vicinity of the Z^0 resonance, computed at lowest order (dashed curves) and including soft radiative corrections according to (3.29) (solid curves).

4. Extension of the Weak Interaction Gauge Group

Now that we have seen how to obtain the values of the Z^0 resonance parameters, we should analyze the implications of the values of these parameters for the standard model and its variants. In principle, any particle which couples to $SU(2) \times U(1)$ can appear in loop diagrams correcting the weak boson propagators and vertices and thus can modify the leading-order predictions of the standard model in order α. In the next section, I will discuss such loop corrections in a systematic framework. However, it is possible—even with our present detailed experimental knowledge—that the gauge group of the weak interactions is somewhat larger than that of the standard model. In this case, one expects variations from the standard model predictions even at leading order in α. In this section, I will briefly discuss the effects of a new heavy weak boson in modifying the properties of the Z^0 resonance.

4.1. An Extension from E_6 Grand Unification

If there does exist a second weak vector boson $Z^{0\prime}$, it should mix, at some level, with the standard Z^0. This mixing will induce a modification of the zeroth-order Z^0 current; instead of (2.7), the physical Z^0 will couple to a rotated current

$$J^Z_\mu = \cos\theta_m \left[J^{3L}_\mu - \sin^2\theta_w J^Q_\mu\right] + \sin\theta_m J^{Q'}_\mu \ , \tag{4.1}$$

where the second term is the current of a charge Q' which is orthogonal (in some extended space) to the $SU(2) \times U(1)$ charges of the standard model. This addition will cause modifications of the Z^0 asymmetries and partial widths. These modifications are independent of the mass of the $Z^{0\prime}$, depending only on the mixing angle θ_m. Of course, they also depend on the explicit form chosen for Q'.

It would be wonderful to understand the systematics of the effect of the modified current (4.1) for the most general charges Q'; however, I do not know how to present such an analysis compactly. Instead, I will restrict myself to a specific class of models which have been used by many authors as a laboratory for exploring the effects of a $Z^{0\prime}$. As is well known, grand unification in $SU(5)$ contains precisely the gauge bosons of the standard model, plus additional heavy bosons which mediate proton decay. However, this grand unification group may be extended to $SO(10)$ and further to E_6, producing at each stage one extra neutral boson whose charge commutes with the standard model gauge group. These bosons, or at least some linear combination of them, might well have a mass in the region of a few hundred GeV. Langacker, Robinett, and Rosner[25] have presented a specific scheme in which they consider one arbitrary linear combination of these two addition neutral bosons to represent the $Z^{0\prime}$. The linear combination is characterized as second mixing angle θ, which is essentially unconstrained. This leads to a family of models with

$$Q' = \sin\theta_w \left(\cos\theta \cdot \frac{1}{2\sqrt{6}}\chi + \sin\theta \cdot \frac{1}{6}\sqrt{\frac{5}{2}}\psi\right) \ . \tag{4.2}$$

In this formula, χ and ψ are quantum numbers, which, for the various species of fermion, take the values

	$(\nu, e)_L$	e_R	$(u, d)_L$	u_R	d_R
χ	3	1	-1	1	-3
ψ	1	-1	1	-1	-1

(A transparent derivation of these quantum numbers from E_6 may be found in Ref. 26.) By adjusting the parameter θ in (4.2), we can sweep through a variety of structures for the $Z^{0\prime}$ charges. This gives some robustness to this scheme of phenomenology.

I should note that there are strong experimental constraints on the size of the mixing angle θ_m. For most values of θ ($\cos\theta \geq 0$), low-energy neutral current experiments restrict θ_m to roughly the range $-0.05 < \theta_m < 0$. The precise allowed regions, for some specific choices of θ, are displayed in the papers of Amaldi, *et al.*, Ref. 9 and Costa, *et al.*, Ref. 10.

In addition, the recent precise measurements of the W boson mass by the

CDF and UA2 collaborations[27] put a further, and rather model-independent, constraint on θ_m. It is expected that a second charged weak boson cannot appear with a mass below a few TeV, since otherwise it would give a large enhancement of K_L-K_S mixing.[28] Assuming, then, that there is no new light W, the mass of the W should be unperturbed from its standard model value, while the mass of the Z^0 is affected by mixing with the $Z^{0\prime}$. The unperturbed mass of the Z^0, m_{Z0}, may then be recovered from m_Z, $m_{Z'}$, and the mixing angle θ_m using the simple properties of two-level mixing. One finds:

$$m_{Z0}^2 = m_Z^2 \cos^2\theta_m + m_{Z'}^2 \sin^2\theta_m \ . \tag{4.3}$$

The value of m_{Z0} obtained in this way must be related to the measured value of m_W through the usual standard model calculation (reviewed in Section 5.6). To understand this constraint, I have taken the average of the CDF and UA2 values of m_W:

$$m_W = 80.22 \pm 0.35 \text{ GeV} \ , \tag{4.4}$$

raised the value by 1 σ, computed the corresponding unperturbed Z^0 mass as described in the next section, and plotted in Fig. 21 the contour in the plane of $\sin\theta_m$ versus $m_{Z'}$ along which this calculation agrees with the value of m_{Z0} from (4.3). The region inside the contour is allowed at probable confidence. This constraint turns out to be quite sensitive to the value of the top quark mass, since, as I will explain in Section 5.6, a heavy top quark tends to decrease the Z-W mass splitting. This method for constraining θ_m was introduced by Langacker in Ref. 29; he pointed out there that this same constraint is an upper bound on θ_m in models with several $Z^{0\prime}$s if $m_{Z'}$ is taken to be the mass of the lightest $Z^{0\prime}$.

A second effect of the mixing between the Z^0 and $Z^{0\prime}$ is a change in the relation between m_Z and the value of $\sin^2\theta_w$ which enters the prediction of the Z^0 resonance cross sections and asymmetries. In the results of the next section, I have taken this effect into account by computing m_{Z0} from (4.3) and using this value to

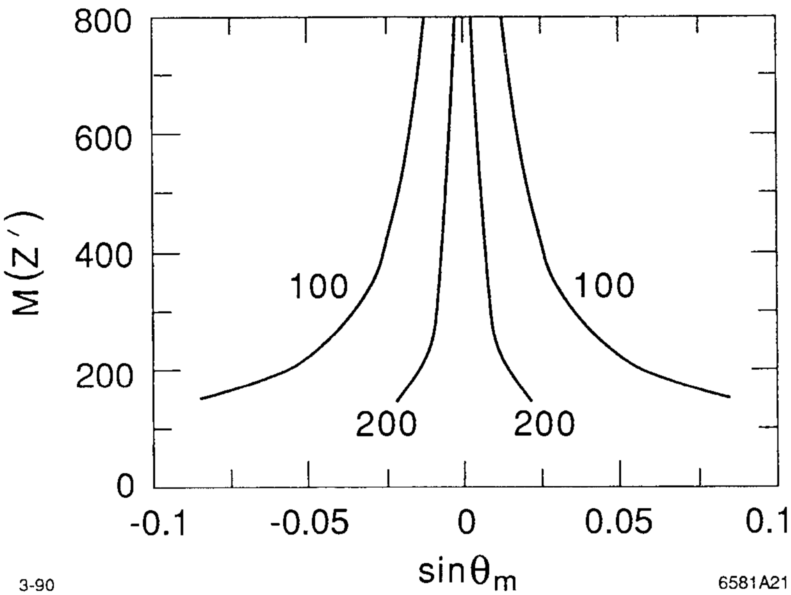

Figure 21. Probable confidence allowed region for θ_m, for $m_t = 100$, 200 GeV, based on the value (4.4) for the W mass.

extract $\sin^2\theta_w$, assuming $m_{Z'} = 500$ GeV. This correction has only a minor effect on these calculations.

4.2. Observable Consequences of an Extended Gauge Group

Now that we have defined a model with extended gauge symmetry, let us compute the effects of this model on the properties of the Z^0. Cvetič and Lynn[30] have suggested that the Z^0 asymmetries are particularly sensitive to the mixing of the Z^0 with a $Z^{0\prime}$. More recently, Altarelli and collaborators[31] have sketched out a systematic program of experiments to search for the effects of a $Z^{0\prime}$. My analysis will concentrate on the simplest observables that they discuss.

If, for each left- or right-handed species, we let

$$Q_Z = \cos\theta_m(I^3 - Q\sin^2\theta_w) + \sin\theta_m Q' \tag{4.5}$$

the relation (3.8) for the Z^0 partial widths is modified to

$$\Gamma_Z^f = \frac{\alpha m_Z}{6\sin^2\theta_w\cos^2\theta_w} \sum_{L,R}(Q_Z)^2\cdot N_f\ . \tag{4.6}$$

From this equation, we can compute the zeroth-order peak cross section of the Z^0, using (3.7), and the polarization asymmetries into various species, using

$$A_{LR}^f = \frac{\Gamma(Z\to f_L\overline{f}_R) - \Gamma(Z\to f_R\overline{f}_L)}{\Gamma(Z\to f_L\overline{f}_R) + \Gamma(Z\to f_R\overline{f}_L)}\ . \tag{4.7}$$

On the Z^0 pole, the forward-backward asymmetries are given by the simple relations

$$A_{FB}(e^+e^-\to f\overline{f}) = \frac{3}{4}A_{LR}^e A_{LR}^f\ . \tag{4.8}$$

In comparing the predictions of models with extended gauge groups to experiment, it is important to compute quantities which are directly observable, avoiding as much as possible the necessity for using standard model calculations of unmeasured quantities. For example, since the partial width of the Z^0 to neutrinos depends on the mixing with the $Z^{0\prime}$, one should compare the directly measured ratio of leptonic to hadronic branching fractions of the Z^0, rather than using the Z^0 branching fraction to leptons, which is inferred from this quantity by adding the calculated neutrino partial width to the denominator. In this spirit, I have considered the effects of the $Z^{0\prime}$ on four of the most accessible Z^0 resonance parameters—the zeroth-order total hadronic cross section, the total width of the resonance, the ratio of leptonic to hadronic branching fractions, and the polarization asymmetry from e^+e^-. In Figs. 22, 23, and 24, I have plotted these quantities against one another for $(-\pi/2)\le\theta\le(\pi/2)$, for the values $\theta_m = -0.01, -0.02, -0.03$. The standard model reference values, obtained for $m_t = 100$ GeV, $m_H = 100$ GeV, $\alpha_s(m_Z^2) = 0.11\pm0.01$, is indicated by the stars. The lines through these stars indicate the variation of the standard model prediction as m_t is varied from 50 to 200 GeV. This dependence will be discussed in detail in Section 5.7. Notice that observables involving leptons are particularly sensitive to the effects of a $Z^{0\prime}$, since the couplings of the charged leptons to the standard Z^0 are relatively weak. The standard and nonstandard predictions are compared to recent measurements from LEP. It is clear that measurements at the Z^0 will soon dramatically constrain, and may perhaps discover, the influence of a $Z^{0\prime}$.

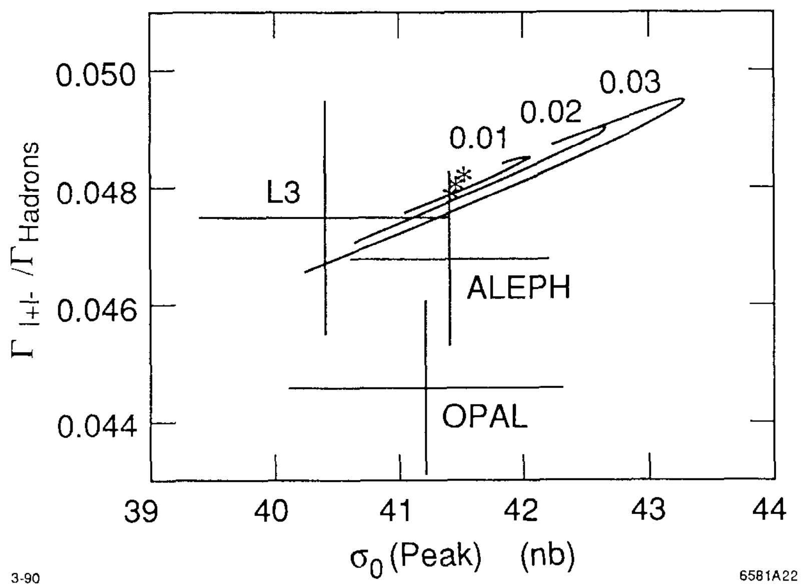

Figure 22. Effect of Z^0–$Z^{0\prime}$ mixing on the rapport between the Z^0 peak hadronic cross section and the ratio of leptonic and hadronic branching fractions. The stars denote the range of the standard model predictions. The three curves correspond to $\theta_m = -0.01, -0.02, -0.03$; each sweeps out the region $-\pi/2 < \theta < \pi/2$. The predictions are compared to data from recent publications of the ALEPH[13], L3,[14] and OPAL[15] experiments at LEP.

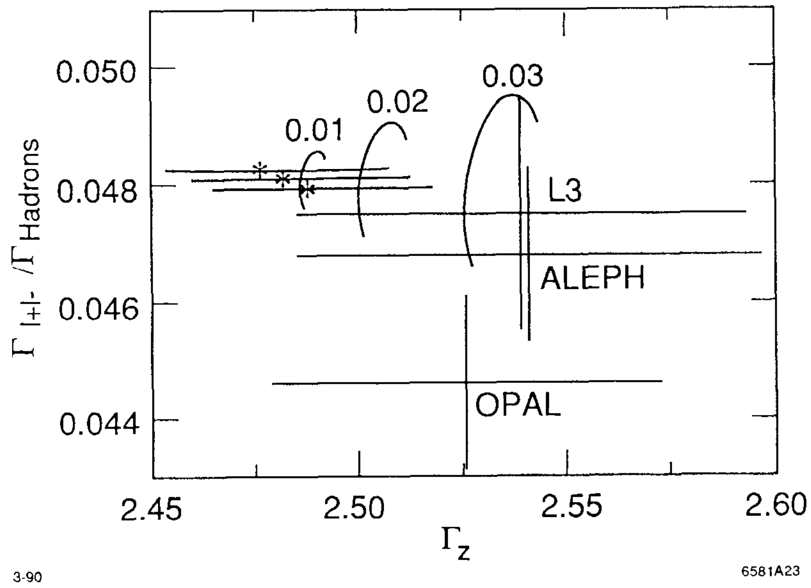

Figure 23. Effect of Z^0–$Z^{0\prime}$ mixing on the rapport between the Z^0 total width and the ratio of leptonic and hadronic branching fractions. The notation is as in Fig. 22. The horizontal lines show the effect on the standard model prediction of a variation in m_t from 50 to 200 GeV and a variation in $\alpha_s(m_Z^2)$ from 0.10 to 0.12. The stars indicate the cases $m_t = 100$ GeV. The m_t effect was included in Fig. 22, but it was almost invisible there.

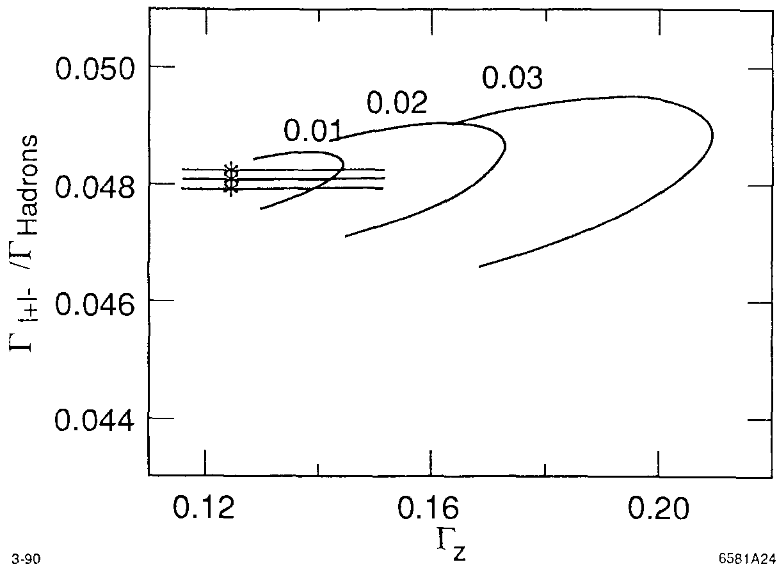

Figure 24. Effect of Z^0–$Z^{0\prime}$ mixing on the rapport between the polarization asymmetry A_{LR} and the ratio of leptonic and hadronic branching fractions. The notation is as in Fig. 23.

5. Renormalization of Weak Interaction Parameters

For the remainder of these lectures, I will assume that the standard $SU(2) \times U(1)$ model is the correct picture of weak interactions at zeroth order. However, the new precision experiments make it necessary to compute order α radiative corrections in order to allow a detailed comparison of theory with experiment. This gives us an opportunity to use these radiative corrections to probe the standard model in detail, and even to look beyond it. The opportunity comes from two sources. First, the typical size of radiative corrections is no longer a small number in the era of weak boson experiments. Indeed,

$$\frac{\alpha}{4\pi} \cdot m_Z \sim \ 100 \text{ MeV} , \tag{5.1}$$

an accuracy already reached for the Z^0 mass and soon within reach for the W mass. Second, as I will explain in this section, radiative corrections from specific sources are often larger than this simple estimate, as a result of the essential chirality of the standard model. These two points apply equally—and the second may apply even more strongly—to radiative corrections due to undiscovered heavy species.

In this section, I will review the theory of these order-α corrections to weak interaction parameters, the corrections which I termed 'hard' in the discussion of Section 3.2. I will explain how these corrections may be calculated and how they influence measureable quantities. The effect of the top quark in weak radiative corrections is particular easy to understand. Since its influence is large and also quite topical, I will use this effect as my main illustrative example.

5.1. Renormalization of α

The prototype of hard radiative corrections is the electromagnetic vacuum polarization. Let us begin by studying this correction, which gives a momentum-dependent renormalization of the electric charge. This correction provides a conceptually simple renormalization effect to introduce our program. It also has some practical significance for precision calculations in weak interactions.

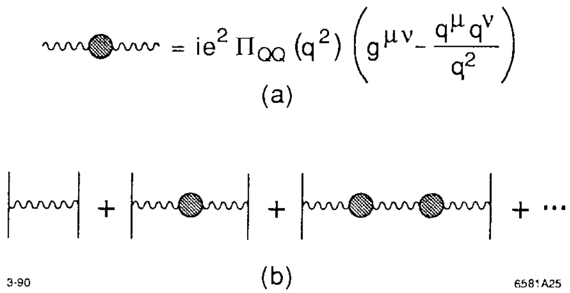

Figure 25. Conventions for the electromagnetic vacuum polarization.

I will define the electromagnetic vacuum polarization $\Pi_{QQ}(q^2)$ as the coefficient of $g^{\mu\nu}$ in the photon self-energy, as indicated in Fig. 25(a). I have extracted from Π_{QQ} the coupling constant e^2; throughout this section, unembellished coupling constants e, g will refer to *bare* parameters from the standard model Lagrangian. The full kinematic structure $(g^{\mu\nu} - q^\mu q^\nu/q^2)$ follows from the conservation of the electromagnetic current. Since the photon self-energy has no zero-mass pole, we must have $\Pi_{QQ} \sim q^2$ as $q^2 \to 0$. Then it is convenient to define

$$\Pi'_{QQ}(q^2) = \frac{\Pi_{QQ}}{q^2} . \tag{5.2}$$

(In textbooks on QED, it is $(e^2\Pi'_{QQ})$ that is usually called the vacuum polarization. My notation differs from this in order to treat vacuum polarization diagrams for the photon and the heavy gauge bosons on the same footing.)

If the photon self-energy corrections are summed up to all orders, as suggested in Fig. 25(b), one finds the complete photon propagator

$$\frac{-ie^2}{q^2}\left(1 + e^2\Pi_{QQ}\frac{1}{q^2} + \ldots\right) g^{\mu\nu} = \frac{-ig^{\mu\nu}}{q^2} \cdot \frac{e^2}{(1 - e^2\Pi'_{QQ})} . \tag{5.3}$$

The form of this equation suggests that we should define a running electric charge

$$e_*^2(q^2) = \frac{e^2}{1 - e^2\Pi'_{QQ}(q^2)} . \tag{5.4}$$

The value of α measured from the electron $(g-2)$ or the Josephson effect is the coefficient of $1/q^2$ in the photon propagator at $q^2 = 0$; that is $4\pi\alpha = e_*^2(q^2 = 0)$. Replacing the bare coupling constant e by α using this relation, and also setting $4\pi\alpha_*(q^2) = e_*^2(q^2)$, we have

$$\frac{1}{4\pi\alpha_*(q^2)} = \frac{1}{4\pi\alpha} - \left[\Pi'_{QQ}(q^2) - \Pi'_{QQ}(0)\right] . \tag{5.5}$$

The vacuum polarization Π'_{QQ} due to a fermion loop is ultraviolet divergent; however, this divergence cancels in the difference of vacuum polarization amplitudes which appears in (5.5). This equation can thus be the basis for concrete physical predictions.

It is interesting to use (5.5) to compute the change in the value of the effective electric coupling as q^2 changes from 0 to m_Z^2. Let us approximate Π_{QQ}, for each fermion flavor, by the simplest 1-loop diagram, and evaluate this diagram in the limit $m_Z^2 >> m^2$. (I will present a more general formula in the next section.) This gives

$$\frac{1}{\alpha_*(m_Z^2)} - \frac{1}{\alpha} \cong -\sum_f \frac{1}{3\pi}\, Q_f^2 N_f \left[\log\frac{m_Z^2}{m_f^2} - \frac{5}{3}\right] , \tag{5.6}$$

where Q_f is the electric charge and N_f is the factor (3.3). Evaluating this expression for the various quarks and leptons (using current algebra masses for the quarks), we find

	e	μ	τ	u	d	s	c	b
mass (MeV)	0.5	106	1784	5.5	8	150	1200	5000
$\Delta(\alpha_*^{-1})$	2.4	1.3	0.7	2.5	0.6	0.4	1.0	0.1

so that in all $\alpha^{-1} - \alpha_*^{-1}(m_Z^2) \sim 8$. A more accurate estimate, presented just below, gives a 6% upward renormalization of α. Intuitively, one would expect that it is the value of α at m_Z^2, rather than at 0, which should enter the evaluation of standard model predictions for the weak boson masses. For example, the relation between the Fermi constant and the W mass, in leading order, is

$$\frac{G_F}{\sqrt{2}} = \frac{e^2}{8\sin^2\theta_w m_W^2} \ . \tag{5.7}$$

If $\alpha_*(m_Z^2)$ is used in this relation instead of α to compute m_W from G_F, the prediction for m_W is shifted upward by 3%. Almost ten years ago, Marciano and Sirlin[32,33] showed by detailed calcuation that this large shift indeed appears in the standard model radiative corrections to m_W.

Since the electromagnetic vacuum polarization is such an important contribution to weak interaction radiative corrections, it is worth a digression to explain how it may be evaluated more exactly. Our estimate above was adequate for the leptons, but for the quarks it was little more than a guess. However, the quark contribution to Π_{QQ} can be evaluated accurately by using the optical theorem to relate the hadronic corrections to forward Bhabha scattering, indicated in Fig. 26(a), to the total cross section for $e^+e^- \to$ hadrons. This yields

$$\mathrm{Im}\ \Pi'_{QQ}(q^2) = \frac{1}{12\pi} R(q^2) \tag{5.8}$$

where $R(q^2)$ is the usual ratio of e^+e^- cross sections to hadrons versus muon pairs. Thus, Π'_{QQ} aquires an imaginary part for real positive values of q^2. It follows that, when this function is considered as an analytic function of q^2, it has a discontinuity across the real q^2 axis given by Disc $\Pi'_{QQ} = 2i\mathrm{Im}\ \Pi'_{QQ}$. This allows us to use (5.8) to evaluate a Cauchy integral for Π'_{QQ} about the contour in the q^2 plane indicated in Fig. 26(b):

$$\Pi'_{QQ}(q^2) = \oint \frac{ds'}{2\pi i} \frac{1}{s'-q^2} \Pi_{QQ}(s') \ . \tag{5.9}$$

Inserting (5.8) into (5.9), and subtracting the same integral evaluated at $q^2 = 0$

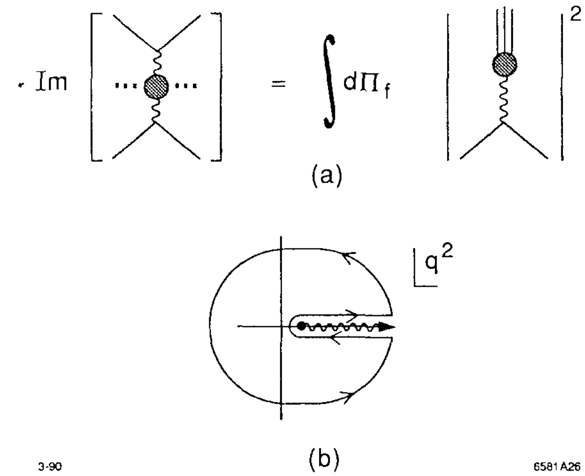

Figure 26. Evaluation of the hadronic contribution to the electromagnetic vacuum polarization.

we find

$$e^2\Pi'_{QQ}(q^2) - e^2\Pi'_{QQ}(0) = \frac{\alpha}{3\pi} P \int_0^\infty ds' R(s') \left[\frac{1}{s'-q^2} - \frac{1}{s'}\right] \ . \tag{5.10}$$

A recent evaluation of the integral (5.10) from the measured e^+e^- annihilation cross section by Burkhardt, Jegerlehner, Penso, and Verzegnassi[34] gives the result

$$\left[\alpha^{-1} - \alpha_*^{-1}(m_Z^2)\right]_{\text{hadronic}} = 3.95 \pm 0.12 \ . \tag{5.11}$$

Combining this with a more accurate evaluation of the lepton vacuum polarization diagrams, one finds

$$\alpha_{*,o}^{-1}(m_Z^2) = 128.77 \pm 0.12 \ . \tag{5.12}$$

(The subscript o indicates that this value of α_* takes into account only the renormalization effects due to observed quarks and leptons, and not the possible additional effects due to the top quark and other heavy species.) The relative error in $\alpha_{*,o}(m_Z^2)$ is 9×10^{-4}. This error is dominated by the uncertainties in the e^+e^- total cross section measurements from 2 GeV to the J/ψ and from 4 GeV to the highest energies of SPEAR.

In calculating weak interaction radiative corrections, we will also encounter vacuum polarization diagrams for weak gauge bosons, and these contain similar corrections from hadronic intermediate states. However, as Lynn, Penso, and Verzegnassi[35] have explained, the most important of these contributions are actually proportional to (5.11). The remaining terms are small and are dominated by contributions from the well-studied vector mesons ω and ϕ.

5.2. The Structure of Vacuum Polarization Amplitudes

To evaluate more general weak radiative corrections, we will need to discuss a wider variety of vacuum polarization amplitudes. Thus, in Fig. 27, I have presented in a standard notation the vacuum polarization amplitudes of the photon, Z^0, and W, and the amplitude for photon–Z^0 mixing. In this figure, and henceforth, I use the abbreviations

$$\sin^2\theta_w \rightarrow s^2\ , \quad \cos^2\theta_w \rightarrow c^2$$

in writing the values of loop amplitudes. It is most useful to break up the Z^0 vacuum polarizations into the contributions of electromagnetic and weak isospin currents (replacing the Z^0 current by (2.7)), and this has been done in setting the conventions shown. For later convenience, I have written the W vacuum polarization as a matrix element of weak isospin currents J_μ^{1L}.

If we wish to evaluate the effect of the top quark on weak interaction parameters, we must compute the contributions to this vacuum polarization amplitudes from top and bottom quark loops. In general, the contribution from heavy fermions is well approximated by the simplest fermion loop diagram, shown in Fig. 28(a).

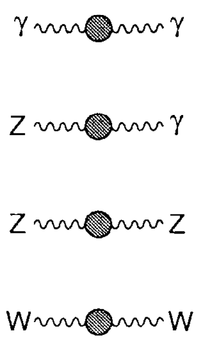

$$= i\ e^2\ \Pi_{QQ}\ g^{\mu\nu} + \cdots$$

$$= i\ \frac{e^2}{cs}\ (\Pi_{3Q} - s^2\,\Pi_{QQ})\, g^{\mu\nu} + \cdots$$

$$= i\ \frac{e^2}{c^2s^2}\,(\Pi_{33} - 2s^2\,\Pi_{3Q} + s^4\,\Pi_{QQ})\, g^{\mu\nu} + \cdots$$

$$= i\ \frac{e^2}{s^2}\ \Pi_{11}\ g^{\mu\nu} + \cdots$$

3-90
6581A27

Figure 27. Vacuum polarization diagrams arising in the evaluation of weak interaction radiative corrections.

The evaluation of this diagram for vector currents is a standard exercise in QED. However, for the weak interactions, we also need to consider chiral currents, and these add some interesting complications. Let me, then, display separately the contributions to the fermion loop diagram from left- and right-handed currents, and allowing the particle and antiparticle in the diagram to have different masses. These terms take a relatively simple form when expressed as Feynman parameter integrals

$$\Pi_{LL}(m_1^2, m_2^2, q^2) = \Pi_{RR}(m_1^2, m_2^2, q^2)$$

$$= -\frac{4}{(4\pi)^2}\int_0^1 dx \log\left[\frac{\Lambda^2}{M^2 - x(1-x)q^2}\right]\cdot\left(x(1-x)q^2 - \frac{1}{2}M^2\right)$$

$$\Pi_{LR}(m_1^2, m_2^2, q^2) = \Pi_{RL}(m_1^2, m_2^2, q^2)$$

$$= -\frac{4}{(4\pi)^2}\int_0^1 dx \log\left[\frac{\Lambda^2}{M^2 - x(1-x)q^2}\right]\cdot\left(\frac{1}{2}m_1 m_2\right) , \tag{5.13}$$

where

$$M^2 = x m_1^2 + (1-x) m_2^2 . \tag{5.14}$$

The parameter Λ is an ultraviolet cut-off (though actually these expressions are most easily obtained using dimensional regularization). Adding these four contributions, with equal mass fermions, we find the vacuum polarization of vector currents

$$\Pi_{VV}(m^2, m^2, q^2) = -\frac{8}{(4\pi)^2}\int_0^1 dx \log\left(\frac{\Lambda^2}{m^2 - x(1-x)q^2}\right)\cdot x(1-x)q^2 \tag{5.15}$$

which is the standard QED result. The approximate formula (5.6) is simply obtained from the limit $q^2 >> m^2$ of this expression. The integrals in (5.13) and (5.15) are straightforward to evaluate analytically; detailed expressions are given, for example, in ref. 5.

The various vacuum polarization amplitudes shown in Fig. 27 are straightforwardly reconstructed from these functions. For a fermion doublet of weak isospin $\frac{1}{2}$, fermion masses m_u, m_d, and electric charges Q_u, Q_d ($Q_u = Q_d + 1$), the four

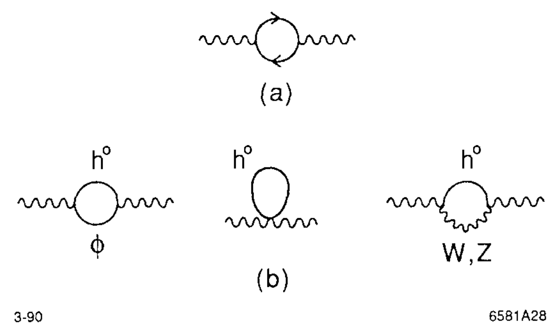

Figure 28. Contributions to the vacuum polarization amplitudes from (a) heavy fermions, (b) the Higgs boson of the minimal standard model.

amplitudes are given by

$$\begin{aligned}
\Pi_{QQ}(q^2) &= Q_u^2\,\Pi_{VV}(m_u^2, m_u^2, q^2) + Q_d^2\,\Pi_{VV}(m_d^2, m_d^2, q^2)\\
\Pi_{3Q}(q^2) &= \frac{1}{2}Q_u\,(\Pi_{LL} + \Pi_{LR})(m_u^2, m_u^2, q^2) - \frac{1}{2}Q_d\,(\Pi_{LL} + \Pi_{LR})(m_d^2, m_d^2, q^2)\\
&= \frac{1}{4}\left[Q_u\,\Pi_{VV}(m_u^2, m_u^2, q^2) - Q_d\,\Pi_{VV}(m_d^2, m_d^2, q^2)\right]\\
\Pi_{33}(q^2) &= \frac{1}{4}\left[\Pi_{LL}(m_u^2, m_u^2, q^2) + \Pi_{LL}(m_d^2, m_d^2, q^2)\right]\\
\Pi_{11}(q^2) &= \frac{1}{2}\,\Pi_{LL}(m_u^2, m_d^2, q^2) .
\end{aligned} \tag{5.16}$$

For quarks, multiply these expressions by 3 colors.

The amplitude Π_{VV} in (5.15) vanishes at $q^2 = 0$, in accordance with our earlier argument. In fact, only one vector current is needed to achieve this cancellation, so Π_{LV}, and therefore the term Π_{3Q} in the photon-Z^0 mixing amplitude, also vanishes at $q^2 = 0$. However, the purely chiral vacuum polarizations do not in general vanish at zero momentum. From (5.13), we see that the zero-momentum limit of Π_{LL} is not only nonzero but actually increases with the masses of the fermions in the loop:

$$\begin{aligned} \Pi_{LL}(m_t^2, m_t^2, q^2) &\cong \frac{2}{(4\pi)^2} m_t^2 \log \frac{\Lambda^2}{m_t^2} \\ \Pi_{LL}(m_t^2, m_b^2, q^2) &\cong \frac{2}{(4\pi)^2} m_t^2 \left(\log \frac{\Lambda^2}{m_t^2} + \frac{1}{2}\right) , \end{aligned} \tag{5.17}$$

for $m_t^2 >> q^2$, m_b^2. This unusual behavior has important physical consequences, as we will see below.

For completeness, I also display the contributions to the various vacuum polarizations from the Higgs boson of the minimal standard model, which appears in the diagrams shown in Fig. 28(b). These are

$$\begin{aligned} \Pi_{QQ}(q^2) &= \Pi_{3Q}(q^2) = 0 \\ \Pi_{33}(q^2) &= -\frac{1}{4(4\pi)^2} \int_0^1 dx \log \left[\frac{\Lambda^2}{x m_H^2 + (1-x) m_Z^2 - x(1-x) q^2} \right] \\ &\qquad \cdot \left((1-2x)^2 q^2 + 4 m_Z^2 + (1-2x)(m_Z^2 - m_H^2) \right) \\ \Pi_{11}(q^2) &= -\frac{1}{4(4\pi)^2} \int_0^1 dx \log \left[\frac{\Lambda^2}{x m_H^2 + (1-x) m_W^2 - x(1-x) q^2} \right] \\ &\qquad \cdot \left((1-2x)^2 q^2 + 4 m_W^2 + (1-2x)(m_W^2 - m_H^2) \right) , \end{aligned} \tag{5.18}$$

where m_H is the mass of the Higgs scalar.

5.3. Renormalization of Weak Interaction Asymmetries: I

Armed with this technical information, we are ready to study the radiative correction to some particular experiment. Let begin with a rather simple example, the correction due to the top quark to the prediction of weak interaction asymmetries at the Z^0 resonance. In particular, I would like to focus on the renormalization of the polarization asymmetry A_{LR}, defined as

$$A_{LR} = \frac{\sigma(e_L^- e^+ \to Z) - \sigma(e_R^- e^+ \to Z)}{\sigma(e_L^- e^+ \to Z) + \sigma(e_R^- e^+ \to Z)} . \tag{5.19}$$

The particular asymmetry A_{LR} is an important quantity for two reasons. First, it is observable not only in its own right but also as an ingredient in the various forward-backward asymmetries at the Z^0. The leading order relation

$$A_{FB}^f = \frac{3}{4} A_{LR}^e A_{LR}^f \tag{5.20}$$

is true to all orders for the contribution of the Z^0 resonance. More generally, I will argue below, all weak interaction asymmetries measure the same radiative correction amplitude, up to some unimportant residual effects. A_{LR} is thus representative of a class of radiative corrections that we would like to investigate.

Second, among the various weak asymmetries, A_{LR} is the most sensitive to radiative corrections. The formula for A_{LR} in the standard model at leading order is

$$A_{LR} = \frac{8\left(1/4 - \sin^2\theta_w\right)}{1 + \left(1 - 4\sin^2\theta_w\right)^2} \cong 8(1/4 - \sin^2\theta_w) . \tag{5.21}$$

Evaluating this expression with the parameters of Section 3.1, we find $A_{LR} \cong 0.13$. But A_{LR} is an asymmetry, and, better, the asymmetry of a total cross section with respect to changes in the polarization of a physically isolated source. This means that almost all systematic errors cancel in the measurement of A_{LR}, so that, with enough statistics, it should be possible to measure this asymmetry to 1% or so of its value. To convert this error to an error on $\sin^2\theta_w$, one should divide by the factor of 8 in (5.21), giving the possibility of achieving an accuracy

$$\delta \sin^2\theta_w \sim 2\times 10^{-4} \ . \tag{5.22}$$

With this promised precision in mind, let us evaluate the contribution of the top quark to A_{LR}. The basic ingredients of the calculation are displayed in Fig. 29. The leading order vertex for e^+e^- annihilation into a Z^0 follows directly from (2.7). The corrected polarization asymmetry may be found from the ratio of the terms proportional to I^{3L} and Q in the complete, radiatively corrected vertex. In the second line of 29, this ratio has been labelled s_*^2. The corrected value of A_{LR} is obtained by replacing $\sin^2\theta_w$ by s_*^2 in (5.21). This complete vertex gets contributions from the various diagrams shown in the third line of 29, some of which are rather complicated to compute. However, since there are no direct couplings between the top quark and the electron, the top quark enters the renormalization of this vertex only through the last diagram shown in Fig. 29, the vacuum polarization diagram involving photon-Z^0 mixing.

This particular simplification occurs quite generally for radiative corrections due to heavy or exotic particles. Because exotic particles often have no direct couplings to light fermions, and in all other cases these couplings are highly constrained, it is usually true that the only important effects of heavy particles on the weak interactions of light quarks and leptons occur by the indirect effects of these particles through their vacuum polarization amplitudes. An interesting example is the case of supersymmetric particles.[36,37] The diagrams involving the direct coupling of leptons to their superpartners turn out to be quite small, while the largest corrections come from the vacuum polarization of the t quark and the $\tilde{t}$ squark. In Ref. 38, contributions arising through vacuum polarization amplitudes were termed 'oblique' radiative corrections. As we continue this analysis, we will see that such corrections are not only numerically important but also quite easy to understand in a systematic way.

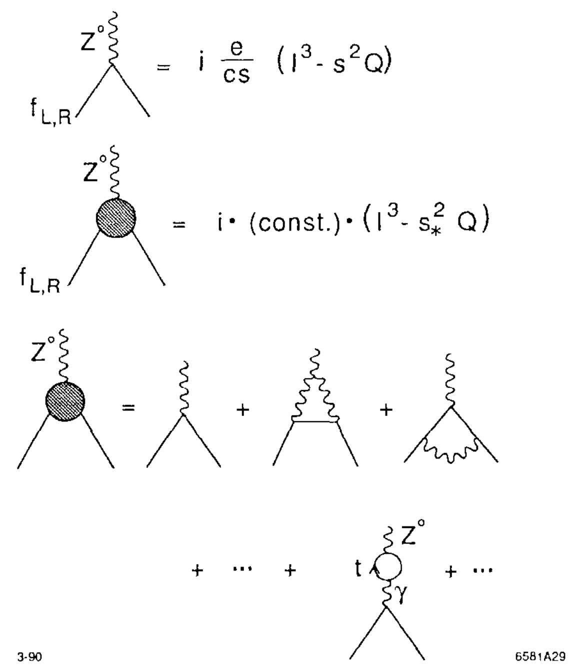

Figure 29. Calculation of the 1-loop renormalization of weak interaction asymmetries at the Z^0.

In principle, we might try to illustrate this in the calculation of A_{LR}, by adding together the leading order diagram and the oblique contribution of the vacuum polarization amplitude for photon-Z^0 mixing. The result is

$$\frac{e}{cs}\left(I^3 - \left[s^2 - e^2(\Pi'_{3Q} - s^2\Pi'_{QQ})\right]Q\right) , \tag{5.23}$$

and so we can identify

$$s_*^2 = \sin^2\theta_w - e^2(\Pi'_{3Q}(m_Z^2) - \sin^2\theta_w \Pi'_{QQ}(m_Z^2)) \ . \tag{5.24}$$

Unfortunately, this result is a disaster; the two vacuum polarization amplitudes are both ultraviolet divergent, and so the answer makes no physical sense.

5.4. An Exhortation on $\sin^2\theta_w$

In a renormalizable quantum field theory, the appearance of ultraviolet divergences in a physical amplitude is a sign that we are asking the wrong question. In the previous section, we computed the radiative correction to the polarization asymmetry by computing the shift of the left-right asymmetry of electron-positron-Z^0 vertex from its value in leading order. But this leading order value is a ratio of bare parameters; it cannot be measured directly. To make a physically meaningful statement, we must predict the value of the asymmetry from other measureable weak interaction quantities.

One straightforward way to structure such a prediction is the following: First, imagine measuring $\sin^2\theta_w$ using other observables of the weak interactions, for example, α, G_F, and m_Z. We may consider the evaluation (5.21) using this value of $\sin^2\theta_w$ as giving a reference value. We may then predict the deviation of the actual value of A_{LR} from this reference value by computing a set of Feynman diagrams. This process depends, in its intermediate stages, on the exact definition of $\sin^2\theta_w$ in terms of observable quantities. Many different definitions are possible, and I will discuss a few of these below. The final result of the process is a prediction for A_{LR} in terms of α, G_F, and m_Z, and this result will of course be independent of the definition of $\sin^2\theta_w$ used. In principle, we might simply discard $\sin^2\theta_w$ and speak only about relations between directly measureable quantities. This purist attitude has been advocated recently by Passarino.[39] I must admit, though, that I find the value of $\sin^2\theta_w$ a useful point of reference, if I know exactly what it means.

The most common definition of $\sin^2\theta_w$ in the literature on weak interaction radiative corrections is one introduced by Sirlin,[2] which elevates the leading order mass relation (2.4) to a definition

$$\sin^2\theta_w|_S \equiv 1 - \frac{m_W^2}{m_Z^2} \ . \tag{5.25}$$

This definition is technically very useful, but I feel uncomfortable with it, for two reasons. First, the mass of the W cannot be measured with the highest precision, so that in practice one must compute m_W in terms of m_Z, α, and G_F in order to apply this definition. This problem is exacerbated by the fact that the Feynman diagrams which renormalize the W–Z mass splitting depend rather strongly on the top quark mass, through the relation (5.17). Thus, the use of this definition introduces a strong dependence on m_t into processes such as the weak asymmetries at the Z^0, which do not otherwise contain this singular dependence. Similarly, the value of $\sin^2\theta_w|_S$ depends on other new physics which might be added to the standard model.

Another possibility is to define $\sin^2\theta_w$ as a ratio of coupling constants renormalized by minimal subtraction.[32,40] In this way, we define the weak interaction couplings just as the strong interaction coupling α_s is defined in QCD. This definition has the advantage of removing the strong dependence on the top quark mass. It has a further advantage for theorists who wish to predict the value of $\sin^2\theta_w$ from grand unified theories, since that computation is done most naturally in this framework.[41] However, this definition gives up the clear physical picture which is available when $\sin^2\theta_w$ is constructed from quantities which are directly measureable. In some sense, using $\sin^2\theta_w|_{\overline{MS}}$ introduces into the weak interactions all the conceptual problems that experimenters—and theorists—have in understanding the meaning of α_s or $\Lambda_{\overline{MS}}$.

As a compromise between these two viewpoints, let me propose a new standard for $\sin^2\theta_w$—the Z^0 standard: Define θ_w and $\sin^2\theta_w$ by the formula:

$$\sin 2\theta_w|_Z \equiv \left(\frac{4\pi\alpha_{*,o}(m_Z^2)}{\sqrt{2}G_F m_Z^2}\right)^{1/2} \ . \tag{5.26}$$

In this formula, $\alpha_{*,o}(m_Z^2)$ is the value of α_* at the Z^0 mass, including the renormalization due to observed quarks and leptons, as determined in Section 5.2. Regardless of the definition of α, the formula is a correct lowest-order relation in the standard model and may then be the basis for a definition to all orders. The use of $\alpha_{*,o}(m_Z^2)$ rather than α incorporates into the formula the Marciano-Sirlin renormalization effect described below (5.7); this is the largest renormalization effect coming from the conventional states of the standard model.

The value of $\sin^2\theta_w|_Z$ is now known extremely precisely; in fact, the error in this quantity is a good measure of the real accuracy of our understanding of the standard model, before theoretical uncertainties due to the top quark mass and other types of new physics are included. Using the value of the Z^0 mass given in (2.10) and the value of $\alpha_{*,o}(m_Z^2)$ from (5.12), we have

$$\sin^2\theta_w|_Z = 0.2317(4) \ . \tag{5.27}$$

The error in $\sin^2\theta_w|_Z$ arises from

$$\Delta\sin^2\theta_w|_Z \cong 0.3\left(\frac{\Delta\alpha_*}{\alpha_*}, 2\,\frac{\Delta m_Z}{m_Z}\right) = (3.1,\ 2.2)\times 10^{-4} \ . \tag{5.28}$$

Let me stress again that, by definition, $\sin^2\theta_w|_Z$ is independent of the mass of the top quark, the Higgs boson, or any other type of new physics. The dependence on these parameters is introduced when $\sin^2\theta_w|_Z$ is used to predict the values of other observables of the weak interactions, such as the W boson mass or the polarization asymmetry A_{LR}.* It is my hope that the use of $\sin^2\theta_w|_Z$ as a standard will clarify conceptually the process of using precision weak interaction measurements to constrain or to discover new physical processes.

---

* This sentiment accords with Taylor's Dogma:[42] "One should not apply to the data a radiative correction which depends on the masses of undiscovered particles."

5.5. Renormalization of Weak Interaction Asymmetries: II

Now that we have clarified the meaning of the parameter $\sin^2\theta_w$, we can see that the calculation we were performing at the end of Section 5.3 was misguided. There, we tried to compute the difference between s_*^2, the measureable ratio of the I^3 and Q terms in the weak neutral current, to the bare parameter $\sin^2\theta_w$, which is not directly observable. A more meaningful calculation would be to compute the difference of two quantities which are completely defined by experiment, for example, to compute

$$s_*^2 - \sin^2\theta_w|_Z \ . \tag{5.29}$$

Let us, then, assemble the complete contribution to (5.29) arising from top and bottom quark loop diagrams.

We may take the shift of s_*^2 from its bare value to be that given in (5.24). With no extra effort, we might evaluate this vertex at a general value of q^2, where q is the momentum of the Z^0. The parameter $s_*^2(q^2)$ is given by

$$s_*^2 = \frac{g'^2}{g^2+g'^2} - e^2[\Pi'_{3Q}(q^2) - s^2\Pi'_{QQ}(q^2)] \ . \tag{5.30}$$

But to compute (5.29), we must also work out the shift of $\sin^2\theta_w|_Z$ from its bare value. To do this, we need the shifts of α, G_F, and m_Z. Figure 30(a) shows the shift of α:

$$4\pi\alpha = e^2(1 + e^2\Pi'_{QQ}(0)) \ . \tag{5.31}$$

(To be careful, we should exclude here the contribution of the b quark loop to (5.31), since this effect was already included when we exchanged α for $\alpha_{*,o}(m_Z^2)$.) Figure 30(b) shows the shift of m_Z^2:

$$m_Z^2 = \frac{1}{4}(g^2+g'^2)v^2\left(1 + \frac{1}{m_Z^2}\,\frac{e^2}{s^2c^2}\left(\Pi_{33} - 2s^2\Pi_{3Q} + s^4\Pi_{QQ}\right)(m_Z^2)\right) \ . \tag{5.32}$$

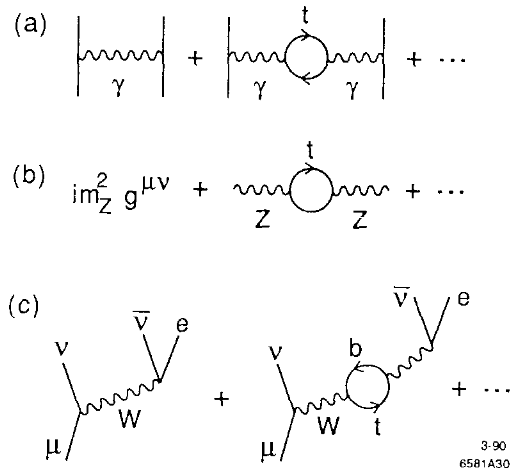

Figure 30. Shifts of the quantities needed to define $\sin^2\theta_w|_Z$ generated by 1-loop diagrams involving the t quark.

Figure 30(c) shows the shift of G_F, as it would be extracted from μ decay:

$$\frac{G_F}{\sqrt{2}} = \frac{1}{2v^2}\left(1 - \frac{1}{m_W^2}\frac{e^2}{s^2}\,\Pi_{11}(0)\right) . \tag{5.33}$$

Note that in each case, the contribution of t and b comes only from vacuum polarization diagrams. In the language of Section 5.3, all of these contributions are purely 'oblique'.

We can now compute the shift of $\sin^2\theta_w|_Z$ from its bare value with only a bit of algebra. In general,

$$\delta(\sin^2\theta_w) = 2sc\delta\theta_w = \frac{2sc}{2\cos 2\theta_w}\,\delta\sin 2\theta_w = \frac{2s^2c^2}{c^2-s^2}\,\frac{\delta\sin 2\theta_w}{\sin 2\theta_w} . \tag{5.34}$$

Then, inserting the shifts of α, G_F, and m_Z^2,

$$\begin{aligned}\sin^2\theta_w|_Z &= \frac{g'^2}{g^2+g'^2} + \frac{2s^2c^2}{c^2-s^2}\cdot\frac{1}{2}\left(\frac{\delta\alpha}{\alpha} - \frac{\delta G_F}{G_F} - \frac{\delta m_Z^2}{m_Z^2}\right)\\ &= \frac{g'^2}{g^2+g'^2} + \frac{s^2c^2}{c^2-s^2}\\ &\quad\cdot\left[e^2\Pi'_{QQ}(0) + \frac{e^2}{s^2c^2}\frac{\Pi_{11}(0)}{m_Z^2} - \frac{e^2}{s^2c^2m_Z^2}(\Pi_{33} - 2s^2\Pi_{3Q} + s^4\Pi_{QQ})(m_Z^2)\right] .\end{aligned} \tag{5.35}$$

By combining this result with (5.30), we find following contribution to (5.29) from 1-loop diagrams involving the top quark:

$$\begin{aligned}s_*^2(q^2) &= \sin^2\theta_w|_Z\\ &+\left\{\frac{e^2}{c^2-s^2}\left[\frac{\Pi_{33}(m_Z^2) - 2s^2\Pi_{3Q}(m_Z^2) - \Pi_{11}(0)}{m_Z^2} - (c^2-s^2)\,\frac{\Pi_{3Q}(q^2)}{q^2}\right]\right.\\ &\left.+\frac{e^2s^2}{c^2-s^2}\left[s^2\Pi'_{QQ}(m_Z^2) - c^2\Pi'_{QQ}(0) + (c^2-s^2)\,\Pi'_{QQ}(q^2)\right]\right\} .\end{aligned} \tag{5.36}$$

In fact, this formula did not make of any special property of the top quark, other than that it does not couple directly to light quarks and leptons. The formula (5.36) holds for any oblique weak interaction radiative correction.

We should immediately check that our new analysis solves the problem of ultraviolet divergences which was raised at the end of Section 5.3. Recall from Section 5.2 that the vacuum polarization amplitudes $\Pi_{33}(q^2)$ and $\Pi_{11}(q^2)$ contain two separate divergent terms, in their value at $q^2 = 0$ and in their first derivative at this point. However, each divergence of Π_{33} is related to a divergent term in Π_{11} by weak isospin symmetry. In particular,

$$\Pi_{33}(0) = \Pi_{11}(0) + \text{finite} ; \quad \Pi_{3Q}(0) = \Pi_{QQ}(0) = 0 . \tag{5.37}$$

This formula insures that the divergent terms from $\Pi_{33}(0)$ and $\Pi_{11}(0)$ cancel in (5.36). The divergences in the first derivatives are also related by weak isospin symmetry:

$$\frac{d}{dq^2}\,\Pi_{33}(0) = \frac{d}{dq^2}\,\Pi_{11}(0) = \frac{d}{dq^2}\,\Pi_{3Q}(0)\ . \tag{5.38}$$

The last part of this relation follows from the fact that $Q = I^3 + Y$; thus $\Pi_{3Q} = \Pi_{33} + \Pi_{3Y}$. Since the weak hypercharge is orthogonal to I^3, the second piece of this expression has no divergence in its first derivative. The first derivative of any Π at a different value of q^2 differs from the value at $q^2 = 0$ only by finite terms. Then the relation (5.38) implies that (after a bit of algebra) these divergent terms also cancel out of (5.36). Finally, the divergent terms in the last line of (5.36) assemble into differences of first derivatives of Π_{QQ}, and these are again finite. Thus, the relation (5.36) is a completely well-defined theoretical prediction, which may now be compared to experiment.

Let us, then, evaluate (5.36) and examine the properties of this relation. The formula is easily evaluated numerically by inserting the formula of Section 5.2 for vacuum polarization amplitudes. In Fig. 31, I have plotted the prediction for $s_*^2(m_Z^2)$ in the standard model as a function of the top quark mass, for fixed Higgs boson mass, and as a function of the Higgs mass, for fixed m_t.

The next few sections contain many figures similar to Fig. 31 which give the dependence of various weak interaction parameters on m_t and m_H, so it is worth pausing to clarify the conventions reflected in these figures. The figures include not only the effects of m_t and m_H but also the additional 1-loop corrections of the standard model. However, these additional corrections are added in a rather simplistic way, by introducing fixed shifts of s_*^2 and other basic quantities. The explicit procedure is spelled out in Section 5.10. This gives a simple calculational scheme, which I hope that you can straightforwardly reproduce. However, the simplicity of the method limits the accuracy to about 0.5% in $\sin^2\theta_w$. The best current calculations of weak readiative corrections are reported in Ref. 6; these results are typically good to 0.1% in $\sin^2\theta_w$. A calculation at this level is not recommended as an educational exercise, but it is essential to extract the full information from a precision experiment. The three curves in each set reflect

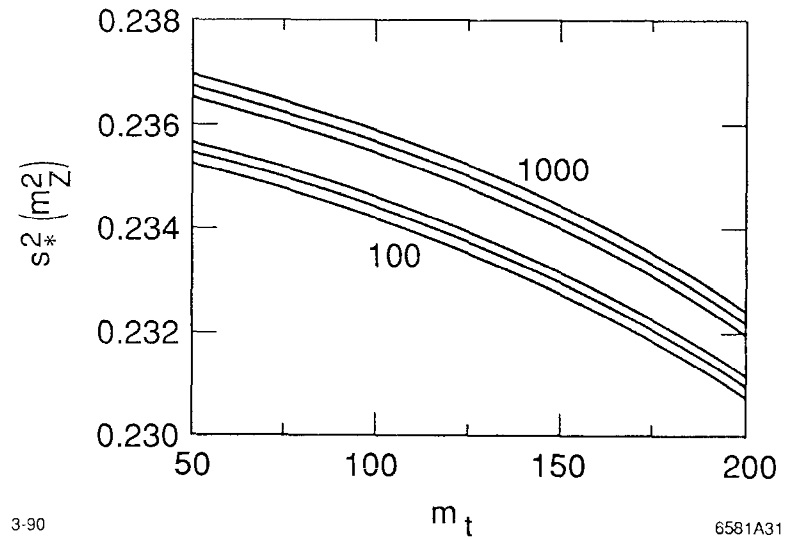

Figure 31. Dependence of $s_*^2(m_Z^2)$ on m_t and m_H predicted by (5.36), using the known value of m_Z. The two bands show the result of varying m_t, with m_H held fixed at the two values 100 GeV, 1000 GeV. The width of each band reflects the 1 σ error in m_Z.

the 1 σ uncertainty in the Z^0 mass value (2.10). In the present situation, where the dominant uncertainty in $\sin^2\theta_w|_Z$ comes from the renormalization of α, this understates the true errors by about a factor of two. Hopefully, new data on low-energy e^+e^- annihilation cross sections will decrease this uncertainty and make these errors appropriate for future comparisons.

The results of Fig. 31 may be translated into predictions for the weak asymmetries. Thus, in Figs. 32 and 33 I display the predictions for A_{LR} and for the forward-backward asymmetries at the Z^0 in $e^+e^- \to b\bar{b}$ and $e^+e^- \to \mu^+\mu^-$. The solid curves apply to the idealized situation in which the hard amplitudes are evaluated at the resonance peak. The dashed curves show the effect of including soft radiative corrections according to (3.29) and evaluating the expressions at the true peak cross section $m_Z + 100$ MeV. This soft radiative correction is a small perturbation of A_{LR} and A^b_{FB}, but is has a large effect on A^μ_{FB}.

We argued in Section 5.3 that A_{LR} is exceptionally sensitive to effects which perturb $\sin^2\theta_w$, and that is borne out here. Since the polarization asymmetry for b quarks at the Z^0 is close to 1, we would expect from (5.20) that this forward-backward asymmetry would behave quite similarly to A_{LR}, and this, again, is clear from Fig. 32. In principle, this forward-backward asymmetry might be used as a substitute for the measurement of A_{LR}. The use of this measurement brings two new difficulties. First, the b forward-backward asymmetry is diluted by B-$\overline{B}$ mixing; for a precision measurement, the mixing parameter x of the B_d-$\overline{B}_d$ system and the fraction of B_s production must be known to about 10%. Second, this asymmetry suffers a QCD correction:[43]

$$A^b_{FB} \to A^b_{FB} \cdot \left(1 - \frac{\alpha_s}{\pi}\right) . \tag{5.39}$$

Neither of these effects would seem to be an obstacle to measuring A^b_{FB} to an accuracy of 3×10^{-3}. Another possible substitute for a precision measurement of A_{LR} is the forward-backward asymmetry to lepton pairs. However, we see from Fig. 33 that this quantity is unfortunately very small, so that its measurement will be hindered at an earlier stage by systematic errors.

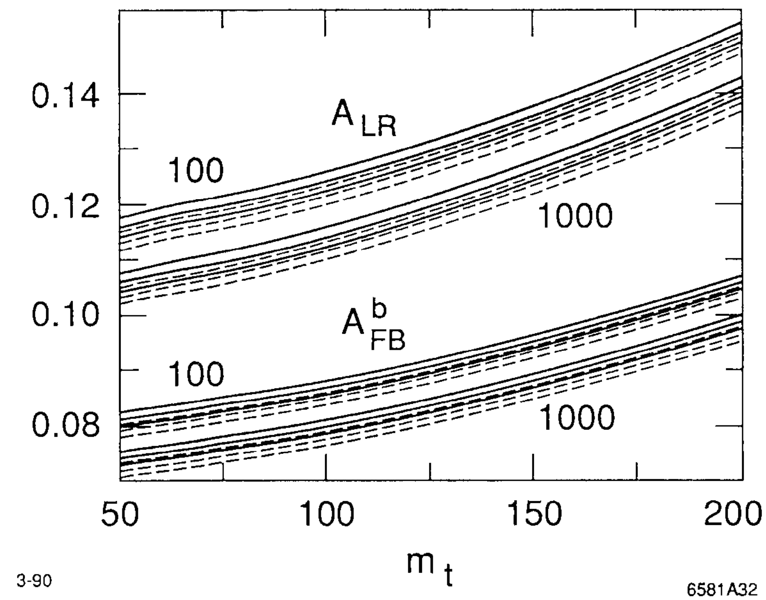

Figure 32. Dependence of A_{LR} and A^b_{FB} on m_t and m_H. The notation is as in Fig. 31. The dashed curves reflect the inclusion of soft radiative corrections, computed with (3.29).

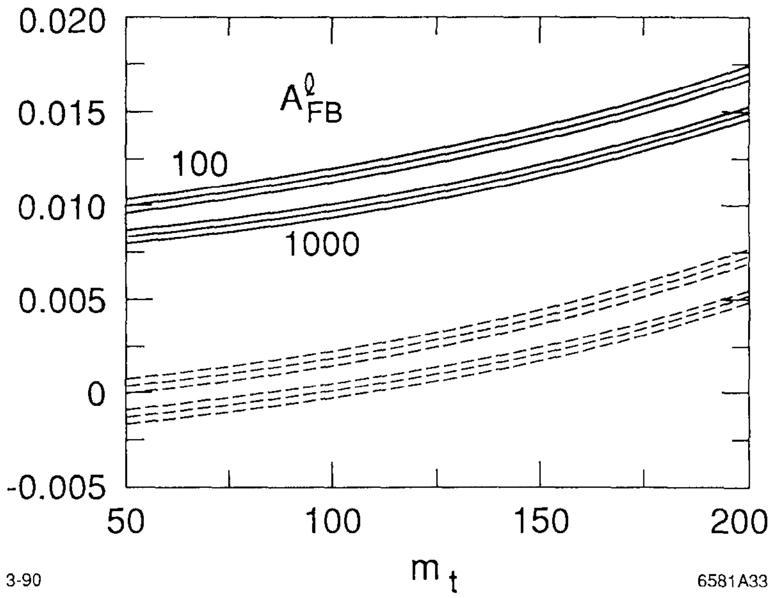

Figure 33. Dependence of A^{ℓ}_{FB}, the lepton forward-backward asymmetry, on m_t and m_H. The notation is as in Fig. 32.

For large values of the top quark mass, the parameter s_*^2 decreases quadratically with m_t. Let us evaluate this dependence using the relation

$$e^2\big(\Pi_{33}(0) - \Pi_{11}(0)\big) \cong -\frac{3\alpha}{16\pi} m_t^2 \ , \tag{5.40}$$

which follows from (5.17). This singular dependence on m_t cancels out of all other differences of vacuum polarization amplitudes. Thus,

$$s_*^2(m_Z^2) \cong \sin^2\theta_w|_Z - \frac{3\alpha}{16\pi}\frac{1}{(c^2 - s^2)}\frac{m_t^2}{m_Z^2} \ . \tag{5.41}$$

Because this dependence comes from vacuum polarizations which originate in the renormalization of m_Z and G_F, rather than in (5.30), this quadratic sensitivity to m_t may properly be considered an artifact of the definition of $\sin^2\theta_w|_Z$. This dependence does not appear, for example, in the comparison of s_*^2 with $\sin^2\hat{\theta}_w$. However, this dependence is also a true aspect of the precision calculation of s_*^2 from m_Z and, as I have pointed out, the effect is quite observable experimentally for large m_t. The quadratic dependence on m_t is expected to be independent of q^2. This is illustrated in Fig. 34, where I have displayed the dependence on m_t and m_H of $s_*^2(0)$. This quantity is measureable from the ratio of cross sections for neutrino-electron and antineutrino-electron scattering. It also plays a role in the radiative corrections to deep-inelastic neutrino scattering, as I will discuss below.

The physical origin of this quadratic dependence on m_t is easily described. In the standard model, a heavy top quark cannot be weakly coupled. Since the mass of the top quark originates from the top quark coupling λ_t to the Higgs field, its coupling must grow with m_t according to

$$m_t = \frac{\lambda_t}{\sqrt{2}} v \ , \tag{5.42}$$

where v is the Higgs field vacuum expectation value. If the weak bosons were replaced by Higgs fields, the top quark vacuum polarization diagrams would be of

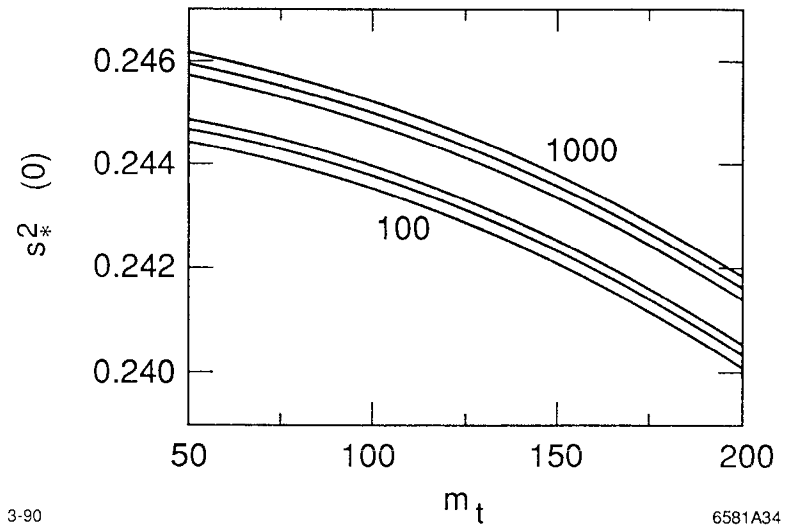

Figure 34. Dependence of $s_*^2(0)$ on m_t and m_H. The notation is as in Fig. 31.

order

$$\frac{\lambda_t^2}{4\pi} = \frac{2m_t^2}{4\pi v^2} = \frac{g^2}{8\pi}\frac{m_t^2}{m_W^2} . \tag{5.43}$$

But, when the weak bosons receive mass through the Higgs mechanism, they do absorb components of the Higgs multiplet to form their longitudinal polarization states. Thus, (5.43) should also correctly estimate the contribution of a heavy top quark to the vacuum polarization diagrams of weak gauge bosons. Indeed, (5.41) is precisely of this order.

From (5.40), one might conclude that the large radiative corrections due to m_t are a manifestation of weak isospin violation. However, (5.36) has the curious property that, even if the masses of t and b are set equal and then taken to infinity, the effect of this doublet of quarks does not vanish. Rather, it approaches the constant value

$$s_*(m_Z^2) = \sin^2\theta_w|_Z + \frac{3\alpha}{24\pi}\frac{1}{(c^2 - s^2)} . \tag{5.44}$$

The asymptotic value is quite closely approximated already when $m_t = m_b = m_Z$. In principle, then, after the top quark mass is known so that this contribution may be computed and subtracted, the measurement of s_*^2 from A_{LR} will be sensitive to additional generations of quarks and leptons, all of whose members are very heavy. The error quoted in (5.22) is slightly less than the contribution of one new quark doublet.

It would be wonderful if (5.36) were also sensitive to the mass of the Higgs boson. Unfortunately, the antisymmetric factor $(1-2x)$ under the integral in (5.18) implies that the quadratic dependence on m_H cancels out. Indeed, Veltman[3] has demonstrated a *screening rule* which states that no 1-loop corrections to processes involving light fermions depend more strongly than logarithmically on m_H.

5.6. Renormalization of the W Boson Mass

Using the method of the previous section, we can assemble the effect of the top quark loop diagrams—or any other oblique correction—on the W boson mass. The direct renormalization of m_W is

$$m_W = \frac{g^2 v^2}{4} + \frac{e^2}{s^2}\Pi_{11}(m_W^2) \ . \tag{5.45}$$

However, to make a physical prediction, we must compare m_W to another physically observable quantity. To do this, we may make use of the simple lowest-order relation (2.4) between m_W, m_Z, and $\cos^2\theta_w$. Taking the shift of m_Z from (5.32) and the shift of $\cos^2\theta_w|_Z$ from (5.35), we may compute

$$\begin{aligned} m_W^2 &= m_Z^2 \cos^2\theta_w|_Z \\ &- \frac{e^2c^2}{s^2(c^2-s^2)}\left[\Pi_{33}(m_Z^2) - 2s^2\Pi_{3Q}(m_Z^2) - \frac{s^2}{c^2}\,\Pi_{11}(0) - \frac{c^2-s^2}{c^2}\,\Pi_{11}(m_W^2)\right] \\ &- \frac{e^2s^2m_W^2}{c^2-s^2}\left[\Pi'_{QQ}(m_Z^2) - \Pi'_{QQ}(0)\right] \ . \end{aligned} \tag{5.46}$$

By using (5.37) and (5.38), you may easily show that this expression is free of ultraviolet divergences, just as we found for (5.36).

The dependence of m_W on m_t and m_H is plotted in Fig. 35. Once we have computed m_W from m_Z, we can construct $\sin^2\theta_w|_S$, the value of $\sin^2\theta_w$ as defined from the ratio of weak boson masses. The dependence of this quantity of the top quark and Higgs boson masses at fixed m_Z is shown in Fig. 36. The dependence on m_t is much more pronounced than that of s_*^2. By applying (5.40), it is easy to see that the quadratic dependence on m_t is

$$m_W^2 - m_Z^2\cos^2\theta_w|_Z \ \cong \ \frac{3\alpha}{16\pi}\frac{c^2}{s^2(c^2-s^2)}m_t^2 \ . \tag{5.47}$$

The formula (5.46) may be viewed as a formula for the difference $(\sin^2\theta_w|_S - \sin^2\theta_w|_Z)$ as a function of m_t, m_Z, and other parameters. Using this formula, it is easy to convert the relation (5.36), which governs the radiative corrections to weak asymmetries, to a formula based on $\sin^2\theta_w|_S$. I will quote only the asymptotic dependence of this relation for large m_t:

$$s_*^2(q^2) - \sin^2\theta_w|_S \ \cong \ +\frac{3\alpha}{16\pi}\frac{1}{s^2}\frac{m_t^2}{m_W^2} \ . \tag{5.48}$$

Another measure of the ratio of the W and Z^0 masses is the relative strength of the charged and neutral weak currents near $q^2 = 0$. If we include the 1-loop oblique corrections to the lowest-order formula (2.8), this equation is modified to the form

$$\mathcal{L}_{eff} = \frac{4G_F}{\sqrt{2}}\left[J_\mu^{+L}J_\mu^{-L} + \rho_*(0)\left(J_\mu^{3L} - J_\mu^Q s_*^2(0)\right)^2\right] . \tag{5.49}$$

The overall coefficient is, by definition, G_F. The factor $\rho_*(0)$ arises from the difference between vacuum polarization corrections to the W and Z propagators. Since $\Pi_{3Q}(0) = \Pi_{QQ}(0) = 0$, this difference reduces to

$$\rho_*(0) = 1 - \frac{e^2}{s^2c^2m_Z^2}(\Pi_{33}(0) - \Pi_{11}(0)) \ . \tag{5.50}$$

This quantity is quite sensitive to large m_t, behaving as

$$\rho_*(0) \cong 1 + \frac{3\alpha}{16\pi}\frac{1}{s^2c^2}\frac{m_t^2}{m_Z^2} \ . \tag{5.51}$$

I hesitated to use the symbol ρ in the previous paragraph. Veltman[4] originally defined the 'ρ-parameter'

$$\rho = \frac{m_W^2}{m_Z^2\cos^2\theta_w} \tag{5.52}$$

to call attention to the zeroth-order relation $\rho = 1$ in the standard model (eq. (2.4)), and to compute the corrections to this relation, using yet another definition of $\sin^2\theta_w$. Since that time, the literature on weak interaction radiative corrections

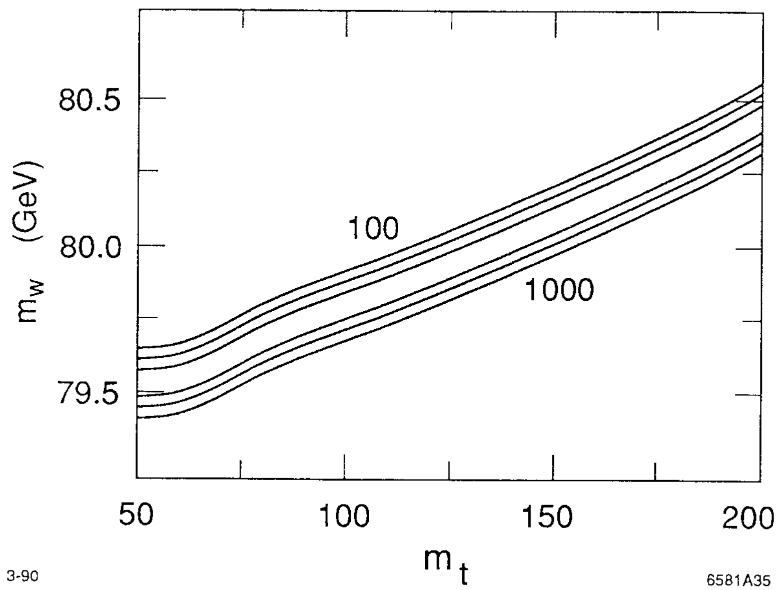

Figure 35. Dependence of m_W on m_t and m_H, for m_Z fixed at its measured value. The notation is as in Fig. 31.

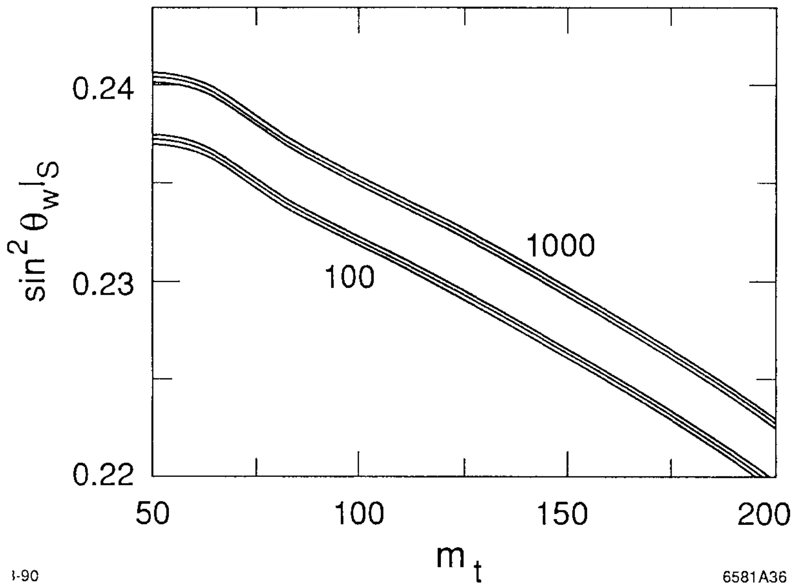

Figure 36. Dependence of $\sin^2\theta_w|_S$ on m_t and m_H, for m_Z fixed at its measured value. The notation is as in Fig. 31.

has been filled with a bewildering variety of definitions of ρ as ratios of the W and Z^0 propagators at many different kinematic points. By this time, it is probably most sensible to drop the use of ρ altogether, except (as in the usage of Amaldi, *et al.*, Ref. 9) to parametrize models in which the relation (2.4) is violated at zeroth order. I ask your indulgence, though, for my use of $\rho_*(0)$ to represent a particular, precisely defined, amplitude which is measureable in the ratio of neutral to charged current neutrino scattering. The notation meshes with a general analysis of the weak neutral current which I will present in the next section.

5.7. Renormalization of Neutral Current Amplitudes

As we analyze the observables of the weak interactions one by one, it is natural to raise the question of whether different observables measure essentially the same weak interaction renormalizations, or, conversely, which observables we must measure to cover the complete set of possible renormalization effects. This question is most easily addressed by turning to a somewhat more abstract framework. Kennedy and Lynn[44] have shown how to construct a general formalism for treating the renormalization of any process which involves photon or weak boson exchange between light fermions by writing an effective interaction which generalizes the zeroth order formula (3.1). In the notation of Kennedy and Lynn, we would write the effective neutral current amplitude in the form

$$\begin{aligned}\mathcal{M}^{NC}_{\text{eff}} &= e_*^2 Q \frac{1}{q^2} Q' \\ &+ \frac{e_*^2}{c_*^2 s_*^2}(I_3 - s_*^2 Q)\frac{Z_*}{q^2 - M_*^2}(I^{3\prime} - s_*^2 Q')\end{aligned} \tag{5.53}$$

where (I^3, Q) and $(I^{3\prime}, Q')$ are the quantum numbers of the external fermions and all starred quantities are functions of q^2.

It is straightforward to verify that (5.53) takes account of all 1-loop oblique corrections to the scattering of two light fermions by the photon and the Z^0. The diagrams we must consider are shown in Fig. 37. To lowest order, the parameters e_*^2, s_*^2, M_*^2, Z_* in (5.53) may be taken to equal $4\pi\alpha$, $\sin^2\theta_w|_Z$, m_Z^2, and 1, respectively; we define $c_*^2 = 1 - s_*^2$ to all orders. If we expand the starred functions to first order in their deviations from these values, add in the 1-loop diagrams which shift $\sin^2\theta_w|_Z$ according to (5.35), and compare the resulting expression to the 1-loop corrections, shown in Fig. 37, we find a general expression for the four starred functions in terms of vacuum polarization amplitudes. For $e_*^2(q^2)$ and $s_*^2(q^2)$, we find exactly the relations (5.5) and (5.36). The remaining functions $M_*^2(q^2)$ and $Z_*(q^2)$ may be readily worked out. If we introduce

$$\Pi_{ZZ} = \frac{e^2}{s^2c^2}(\Pi_{33} - 2s^2\Pi_{3Q} + s^4\Pi_{QQ}) \ , \tag{5.54}$$

these functions may be expressed as

$$\begin{aligned}q^2 - M_*^2(q^2) &= (q^2 - m_Z^2)\Big(1 + \frac{d}{dq^2}\Pi_{ZZ}\big|_{q^2=m_Z^2}\Big) - \big(\Pi_{ZZ}(q^2) - \Pi_{ZZ}(m_Z^2)\big) \\ Z_*(q^2) &= 1 + \frac{e^2}{s^2c^2}\frac{d}{dq^2}(\Pi_{33} - 2s^2\Pi_{3Q} + s^4\Pi_{QQ})\Big|_{q^2=m_Z^2} \\ &\quad - e^2\Pi'_{QQ}(0) - \frac{e^2(c^2 - s^2)}{s^2c^2}\big(\Pi'_{3Q}(q^2) - s^2\Pi'_{QQ}(q^2)\big) \ .\end{aligned} \tag{5.55}$$

The function $M_*^2(q^2)$ has been arranged to satisfy

$$M_*^2(m_Z^2) = m_Z^2 \quad ; \qquad \frac{d}{dq^2}M_*^2\big|_{q^2=m_Z^2} = 0 \ . \tag{5.56}$$

These two functions provide two new and independent finite combinations of vacuum polarization amplitudes.

In writing these formulae—and the formulae for s_*^2 above, I have assumed that the various vacuum polarization integrals are real. If this is not true (that is, if some intermediate state can be produced at the Z^0, we should take the real part of each vacuum polarization integral Π except for the term $\Pi_{ZZ}(q^2)$ in the first line

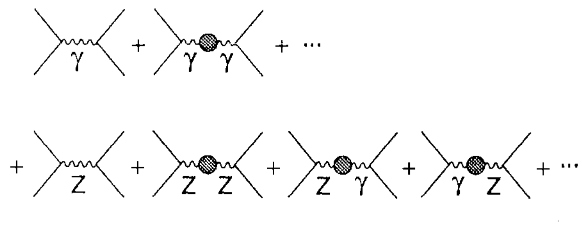

Figure 37. Feynman diagrams contributing 1-loop oblique corrections to the scattering of light fermions by the photon and the Z^0.

of (5.55). The imaginary part of this correction will then generate the Z^0 width, which would then appear in (5.53)as

$$M_*(m_Z^2) = m_Z^2 + im_Z\Gamma_Z \ . \tag{5.57}$$

Kennedy and Lynn have shown that, even though the standard model weak radiative corrections involve vertex and box diagrams as well as vacuum polarization graphs, the most important of these corrections can also be written in the form (5.53). Terms which cannot be shoehorned into this form (for example, nontrivial form factors of box diagrams) are small—a several tenths percent corrections—at the Z^0 and below. (The one important counterexample to this general statement will be discussed in Section 5.8.) Thus, the effective neutral current amplitude (5.53) is a very useful way to summarize the effect of radiative corrections both from within the standard model and from new physical processes.

The Kennedy-Lynn effective amplitude is sometimes described as merely a 'scheme', that is, yet another definition of $\sin^2\theta_w$. I hope this discussion, and the analysis to follow, clarifies that it is actually a general phenomenology of weak interaction renormalizations, and a very useful one. The starred parameters can be predicted in any scheme by trading $\sin^2\theta_w|_Z$ in the formulae above for any other definition of $\sin^2\theta_w$.

The effective amplitude (5.53) clarifies which aspects of the neutral current coupling can be measured with precision at the Z^0. In essence, experiments at the Z^0 measure values of the starred parameters at $q^2 = m_Z^2$, and, of these, the only nontrivial ones are $s_*^2(m_Z^2)$ and $Z_*(m_Z^2)$. We have already seen that $s_*^2(m_Z^2)$ governs the weak interaction asymmetries at the Z^0. The factor $Z_*(m_Z^2)$ renormalizes the Z^0 propagator; it also multiplies the Z^0 width. In fact, the effective amplitude justifies the expressions (3.1) and (3.8) for the total cross section and the partial widths at the Z^0, with the parameters of this formula evaluated as

$$\alpha \to \alpha_*(m_Z^2)\ ; \quad \sin^2\theta_w \to s_*^2(m_Z^2)\ ; \quad \overline{Z} \to Z_*(m_Z^2)\ . \tag{5.58}$$

The values quoted in Section 3.1 correspond to $m_t = m_H = 100$ GeV.

It is unfortunately difficult to extract the value of Z_* from experiment. It is much easier to obtain an accurate value of the peak cross section of the Z^0 resonance than to obtain an accurate value of the width. (It is the measurement of the peak cross section, for example, which gives the strong constraint on the number of neutrino generations.) But the factor $Z_*(m_Z^2)$ cancels out of the peak cross section, because it appears in the numerator of the second term of (5.53), as well as in the factor Γ_Z in the denominator.

The dependence of the Z^0 width on m_t and m_H is shown in Figs. 38 and 39. In Fig. 38, I have blown up the standard model prediction from Fig. 23, showing the theoretical uncertainty due to the QCD corrections to the effective number of colors N_f and the variation as m_t is raised from 50 to 200 GeV. In Fig. 39, I have plotted directly the variation of Γ_Z with the top quark and Higgs boson masses.

The rather narrow focus of Z^0 resonance experiments, in terms of their sensitivity to the parameters of the weak effective amplitude, highlights the importance of obtaining orthogonal measures of weak interaction radiative corrections from other sources, by precision measurements of m_W and of the low-energy parameters $s_*^2(0)$ and $\rho_*(0)$. However, even though the Z^0 experiments must concentrate on the extraction of the single parameter $s_*^2(m_Z^2)$, it is likely that this measurement will

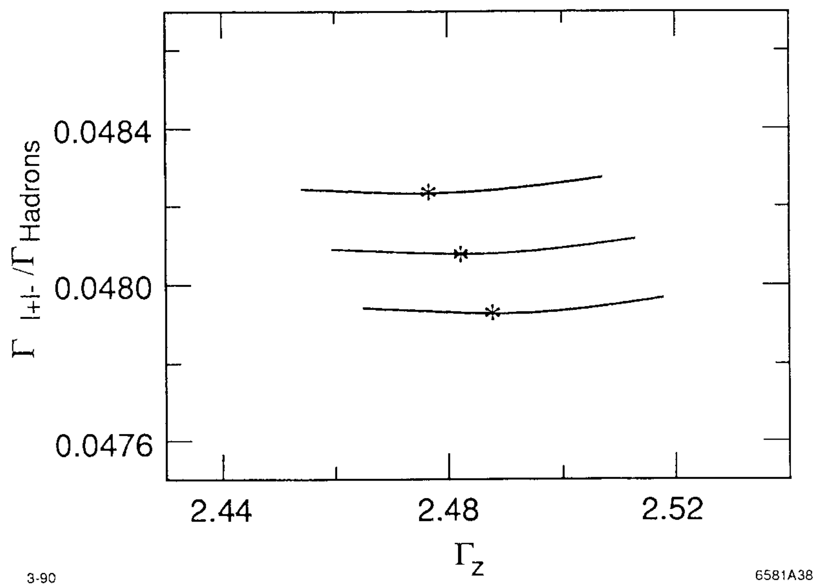

Figure 38. Enlargement of the standard model prediction from Fig. 23, showing the dependence on m_t, varied from 50 to 200 GeV, and on the QCD correction to the hadronic widths, which is varied over the 1 σ error in (3.3).

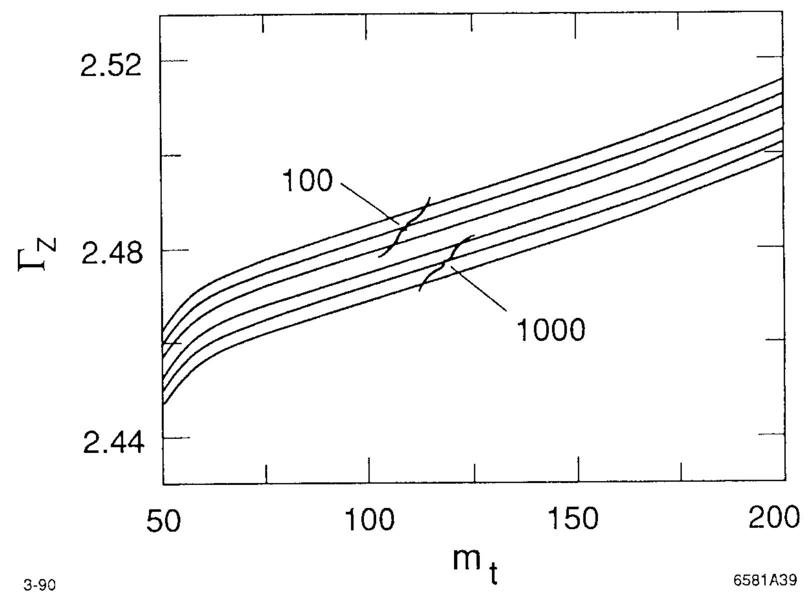

Figure 39. Dependence of the Z^0 total width on m_t and m_H. The notation is as in Fig. 31.

give the single most incisive test of the radiative corrections to the standard model. Perhaps it is fortunate that this parameter can be measured in many different and complementary ways.

5.8. A Renormalization Unique to the t Quark

There is one interesting example of a weak interaction renormalization which falls outside the scope of the effective amplitude (5.53), specifically because it involves the top quark and can be enhanced by a power of (m_t^2/m_W^2) when m_t is large. This is the one direct correction which involves the top quark: the renormalization due to t of the vertex for $Z^0 \to b\bar{b}$. The correction arises from the diagrams shown in Fig. 40, plus the additional diagrams required to make a gauge-invariant set. This correction is particularly interesting because it has the t quark as its specific origin. Up to this point, all of the renormalizations we have studied receive contributions from general vacuum polarization diagrams; in some sense, they are integrals over all types of new physics. We have concentrated on the contributions of the top quark and the Higgs boson, but this has been mainly for pedagogical reasons; it is not unlikely that s_*^2 and other weak parameters also receive contributions from other types of new physics. In an unlucky situation, these contributions might even be of the opposite sign. It is fortunate, then, that there is one correction which can arise only from the top quark and allows an unambiguous test of the rapport between the value of the top quark mass (when it is eventually measured) and a weak interaction 1-loop correction.

The diagrams of Fig. 40 and their partners have been evaluated by Akhundov, Bardin, and Riemann,[45] Bernabéu, Pich, and Santamaría,[46] and Beenakker and Hollik.[47] I will quote only the asymptotic formulae here and refer you to these papers for more exact results. Their effect is simply described by noting that these diagrams involve W exchange and so, if we ignore the mass of the b, they couple only to the left-handed components of the b quark. Thus, the effect of these

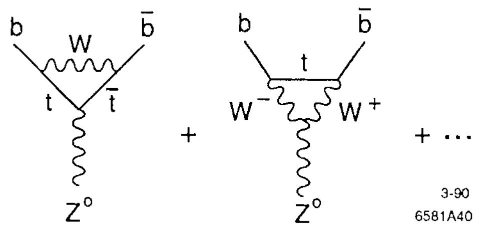

Figure 40. Renormalization of the vertex for $Z^0 \to b\bar{b}$, due to 1-loop diagrams involving the top quark.

diagrams is a multiplicative renormalization of the vertex for $Z^0 \to b_L\bar{b}_R$:

$$\mathcal{M} = \frac{-ie_*^2}{c_*s_*} Z_\mu \bar{b}\gamma^\mu b_L \cdot \left[\left(\frac{1}{2} - \frac{1}{3}s_*^2\right) - F\right] , \tag{5.59}$$

where, in the limit of large m_t,

$$F \cong \frac{\alpha}{16\pi}\frac{1}{s^2}\frac{m_t^2}{m_W^2} \tag{5.60}$$

In principle, this correction alters the relation between $s_*^2(m_Z^2)$ and the forward-backward asymmetry at the Z^0 for $e^+e^- \to b\bar{b}$. However, since the Z^0 couples much more strongly to b_L than b_R, a small change in the larger coupling has an insignificant effect on the polarization asymmetry A_{LR}^b and, through this, on A_{FB}^b. The size of the effect is indeed of order 10^{-4} in A_{FB}^b. However, the correction does noticeably affect the Z^0 branching fraction to $b\bar{b}$ if the top quark mass is large. In Fig. 41, I have plotted the variation of the ratio $\Gamma(Z^0 \to b\bar{b})/\Gamma(Z^0 \to \text{hadrons})$ with m_t. The individual partial widths are affected by the dependence of Z_* and s_*^2 on m_t, as was illustrated for the total width in Fig. 39. However, Z_* cancels in this ratio, and most of the dependence on s_*^2 cancels as well. I have illustrated this in Fig. 41 by comparing the m_t dependence of the Z^0 branching fractions to

$b\bar{b}$ and $d\bar{d}$. The latter is essentially flat as a function of m_t. Thus, a measurement of the Z^0 branching fraction to $b\bar{b}$ is almost entirely a measure of the top quark vertex correction.

Unfortunately, this is a tough experiment. The magnitude of the effect is a 4% decrease in the $b\bar{b}$ fraction for a t quark mass of 200 GeV. If the measurement is done by tagging b quarks with leptons, the leptonic branching ratio must be known to 1%. If the b quarks are identified by their vertices, the lifetime must be known to a few percent. This measurement thus challenges both the large data sets that will be available at LEP and the precision vertex information that will be provided by the SLC. I hope that careful experimenters will take up this challenge and isolate this curious but interesting effect.

5.9. Determination of $\sin^2\theta_w$ from Neutrino Scattering

No review of precision measurements in weak interactions would be complete without some discussion of the constraints imposed by experiments on neutrino-nucleon deep-inelastic scattering. It is fair to say that the precision study of the weak neutral current really began with the precision measurement of the ratio of neutral to charged current neutrino cross sections by the CDHS[48] and CHARM[49] experiments. Deep inelastic scattering has new difficulties which are not shared by experiments on the weak gauge bosons. These all stem from the fact that the target is a nucleon, and so the analysis of the scattering process eventually falters on our uncertain quantitative understanding of QCD. However, it is amazing to me what accuracy can actually be achieved by a combination of clever insights and careful analysis. Since the analysis of these deep inelastic scattering experiments is rather subtle, I have no room for a complete discussion here. For those who wish further information, I recommend the most recent paper of the CDHS collaboration,[50] which also gives references to the earlier literature.

The deep inelastic scattering experiments have concentrated on measuring the

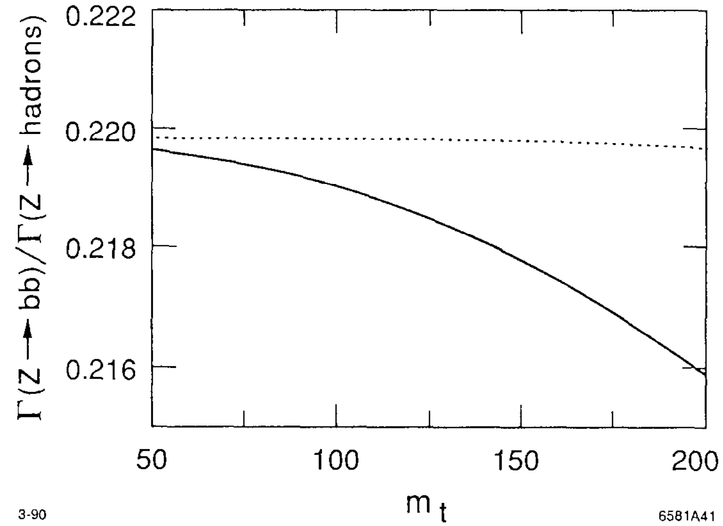

Figure 41. Dependence of the Z^0 width to $b\bar{b}$, as a fraction of the total Z^0 width to hadrons, as a function of m_t. The solid line includes the $b\bar{b}Z$ vertex corrections; the dashed line shows the result of omitting this effect, while retaining the top quark renormalization of $s_*^2(m_Z^2)$.

ratio of neutral to charged current cross sections

$$R^\nu = \int dxdy \frac{d\sigma(\nu, NC)}{dxdy} \Big/ \int dxdy \frac{d\sigma(\nu, CC)}{dxdy} , \tag{5.61}$$

where x and y are the standard dimensionless kinematic variables and the integral is taken over the experimental acceptance. These cross sections are readily estimated in the naive parton model: If $f_q(x)$ is the parton distribution of the species q in the proton, the cross sections, for neutrino-proton scattering, at lowest order in weak interactions, are proportional to

$$\begin{aligned} \frac{d\sigma(\nu, CC)}{dxdy} &= \frac{G_F{}^2 sx}{\pi}\Big(f_d(x) + (1-y)^2 f_{\bar u}(x)\Big) \\ \frac{d\sigma(\nu, NC)}{dxdy} &= \frac{G_F{}^2 sx}{\pi}\Big([(\frac{1}{2} - \frac{2}{3}\sin^2\theta_w)^2 f_u(x) + (\frac{1}{2} - \frac{1}{3}\sin^2\theta_w)^2 f_d(x)] \\ &\quad + (1-y)^2 [(\frac{2}{3}\sin^2\theta_w)^2 f_u(x) + (\frac{1}{3}\sin^2\theta_w)^2 f_d(x)] \\ &\quad + (1-y)^2 [(\frac{1}{2} - \frac{2}{3}\sin^2\theta_w)^2 f_{\bar u}(x) + (\frac{1}{2} - \frac{1}{3}\sin^2\theta_w)^2 f_{\bar d}(x)] \\ &\quad + [(\frac{2}{3}\sin^2\theta_w)^2 f_{\bar u}(x) + (\frac{1}{3}\sin^2\theta_w)^2 f_{\bar d}(x)]\Big) , \end{aligned} \tag{5.62}$$

plus contributions from heavier quark species. In the neutral current cross section, the two sets of terms for each quark refer to left- and right-handed species, respectively. The two prefactors are identical by virtue of (2.9). However, this is the only simplification available, and otherwise the integrands of (5.61) are complicated functions of x and y. When we include the QCD corrections to (5.62), these integrands will also depend on Q^2. How, then, can we extract any information to 1% accuracy?

The required strategy was set out in a beautiful paper by Llewellyn Smith.[51] In this paper, Llewellyn Smith encourages us to think about a world containing only u and d quarks. This allows three important simplifications in the computation of R^ν. First, if we consider, instead of the proton, an isoscalar target, $f_u = f_d$, $f_{\bar u} = f_{\bar d}$, and the only x-dependence in the ratio of the two parton model cross sections above occurs through the function $f_q(x)/f_{\bar q}(x)$. In fact, the only x- and y-dependence appears in the particular combination

$$\frac{(1-y)^2 + f_q/f_{\bar q}}{1 + (1-y)^2 f_q/f_{\bar q}} . \tag{5.63}$$

The second simplification occurs if we recognize that (5.63) is precisely the parton model expression for the ratio of antineutrino versus neutrino charged current cross sections. Thus, if we define

$$r = \frac{\sigma(\bar\nu, CC)}{\sigma(\nu, CC)} , \tag{5.64}$$

R^ν can be expressed, within the parton model, as $R^\nu = R^\nu_{\mathrm{LS}}(\sin^2\theta_w)$, where $R^\nu_{\mathrm{LS}}(\sin^2\theta_w)$ is the simple function

$$R^\nu_{\mathrm{LS}}(\sin^2\theta_w) = \frac{1}{2} - \sin^2\theta_w + \frac{5}{9}\sin^4\theta_w(1+r) . \tag{5.65}$$

Similarly, the ratio of neutral to charged current antineutrino cross sections is equal to

$$R^{\bar\nu}_{\mathrm{LS}}(\sin^2\theta_w) = (\frac{1}{2} - \sin^2\theta_w)r + \frac{5}{9}\sin^4\theta_w(1+r) . \tag{5.66}$$

I have quoted these results as applying to the theoretical total cross sections; however, they apply equally well if the differential cross sections in the numerator and denominator are integrated over the same experimental acceptance. Thus, the dependence of R^ν on acceptance is completely summarized in the parameter r, which can be directly measured. It is noteworthy that r is rather different for the two CERN neutrino experiments:

$$r = \begin{cases} 0.393 \pm 0.014 & \text{CDHS} \\ 0.456 \pm 0.011 & \text{CHARM} \end{cases} , \tag{5.67}$$

reflecting the lower energy threshold of the CHARM detector.

These two insights produce a remarkable simplification, but they have been derived within the naive parton model, and so they would not be of much use without the crucial third step: In a world with only u and d quarks, the above expression for R^ν can be derived *using isospin arguments only* by directly comparing strong interaction matrix elements. Thus, this expression is insensitive to QCD corrections.

In a realistic setting, one must of course correct the Llewellyn Smith expression for R^ν to take account of the non-isoscalar components of the target, the presence of strange quarks in the proton, and the soft radiative corrections. However, all of these are small corrections to a well-understood basic formula. The most troublesome correction is that due to charm production. Since the energy region of the CERN experiments overlaps the charm threshold, charm is produced at relatively low energy and so the production must be described phenomenologically, with parameters fit to the experimental data. This produces a sizeable systematic error, of order ± 0.003, in the final determination of $\sin^2\theta_w$.

Once these corrections have been made, the value of R^ν may be compared to the theoretical prediction, modified by the inclusion of hard radiative corrections. Using (5.49) (and making the oversimplification that $Q^2 << m_W^2$), these give

$$R^\nu = \rho_*(0)^2 R^\nu_{\rm LS}(s_*^2(0)), \tag{5.68}$$

where $R^\nu_{\rm LS}$ is the function given in (5.65) and ρ_*, s_*^2 are the effective amplitudes defined in the previous sections. The dependence of (5.68) on m_t and m_H, for the CDHS value of r, is shown in Fig. 42.

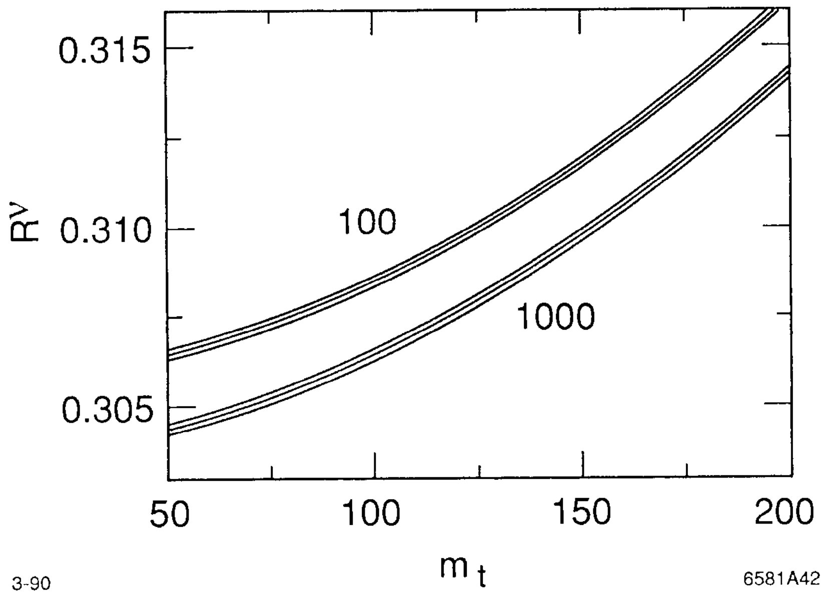

Figure 42. Dependence of R^ν on m_t and m_H, using the CDHS value of the parameter r. The notation is as in Fig. 31.

5.10. Reconciliation of Weak Interaction Measurements

In the previous few sections, we have seen how to compute the weak interaction radiative corrections to a variety of observable quantities. Many of these predictions depended rather strongly on the mass of top quark. It is thus important to ask two questions: First, are the observed values of these quantities simultaneously consistent with a single value of $\sin^2\theta_w$? Second, is this consistency contingent on some limits on the top quark mass, so that it actually constrains the possible range of values for m_t?

To address this question, we first need to know the value of the standard model radiative corrections due to conventional species—light quarks and leptons and weak gauge bosons. It is impossible to give a complete computation of these effects—or even to summarize the result—compactly. (For a rather complete discussion, see ref. 6.) However, because these effects are relatively small compared to the sensitivity of current experiments, one may account them roughly by quoting the relation of the parameters of the effective amplitude to $\sin^2\theta_w|_Z$ for particular values of m_t and m_H. For $m_t = 40$ GeV, $m_H = 100$ GeV:

$$\begin{aligned} \sin^2\theta_w|_S &= \sin^2\theta_w|_Z + 0.0050 \\ s_*^2(0) &= \sin^2\theta_w|_Z + 0.013 \\ s_*^2(m_Z^2) &= \sin^2\theta_w|_Z + 0.0036 \\ Z_* &= 1.009 \\ \rho_*(0) &= 1.000 \quad . \end{aligned} \tag{5.69}$$

Given these offsets, one can then compute the dependence of observables on m_t, m_H, and other corrections using the formulae I have presented in previous sections. I have cribbed these offsets from the current version of the program EXPOSTAR, described in Ref. 52. Because the effective amplitude does not include non-oblique corrections in an exact way, the actual values required for these offsets may vary by about 10% depending on the particular process considered; in addition, the corrections actually depend on $\sin^2\theta_w$ and in (5.69) are simply evaluted near the physical value. This method is too crude to use in analyzing a particular precision experiment, but it is useful to give a quantitative feeling for the sensitivity of each experiment to standard and nonstandard radiative corrections.

To assess the consistency of our present weak interaction measurements, Ellis and Fogli[53] have suggested making the following plot: Given the highly accurate values of α and G_F, plus one additional measurement, one can compute the value of $\sin^2\theta_w|_S$. This computation of course depends on m_t, m_H—and on the assumption that there are no other large corrections from beyond the standard model. Assuming the standard model and fixing m_H, one may then plot the extracted value of $\sin^2\theta_w|_S$ as a function of m_t. In Fig. 43, I have constructed this plot by taking each of the three best-measured weak boson parameters—m_Z, the ratio m_W/m_Z, and R^ν—as third input. The bands correspond to 1 σ measurement errors, and I have assumed $m_H = 100$ GeV. For m_Z and m_W, I have used the values (2.10) and (4.4). (Note that m_W/m_Z determines $\sin^2\theta_w|_S$ directly.) For R^ν, I have used the value

$$R^\nu = 0.3081 \pm 0.004 \ , \tag{5.70}$$

which I obtained by converting the CHARM measurement of R^ν to the value appropriate for the CDHS value of r. The calculation is simple, but instructive for anyone who wishes to understand this subject in detail, and I hope I have provided enough information here that you can reproduce it straightforwardly. For comparison, I have reprinted in Fig. 44 a 'professional' version of this analysis done by Paul Langacker.[54] The main difference between the two figures comes in the band from neutrino scattering, where Langacker has included the world sample of neutrino and antineutrino experiments, taken proper account of the Q^2-dependence of the radiative correction, and refitted the charmed quark mass as $\sin^2\theta_w$ varies. It is also instructive to replot this analysis against the variable $\sin^2\theta_w|_Z$, and this is done in Fig. 45.

The results of this analysis are striking. The ratio m_W/m_Z gives a horizontal band in the Ellis-Fogli plot. The band due to R^ν is also almost horizontal, by virtue

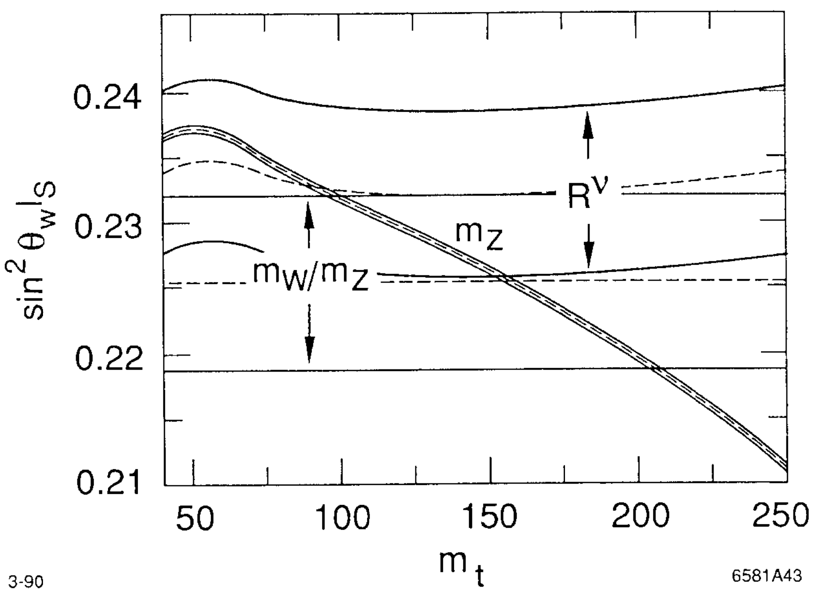

Figure 43. Interval in $\sin^2\theta_w|_S$ allowed at 1 σ confidence based on the measured values of m_Z, m_W/m_Z, and R^ν. The intervals are plotted as a function of m_t, assuming $m_H = 100$ GeV.

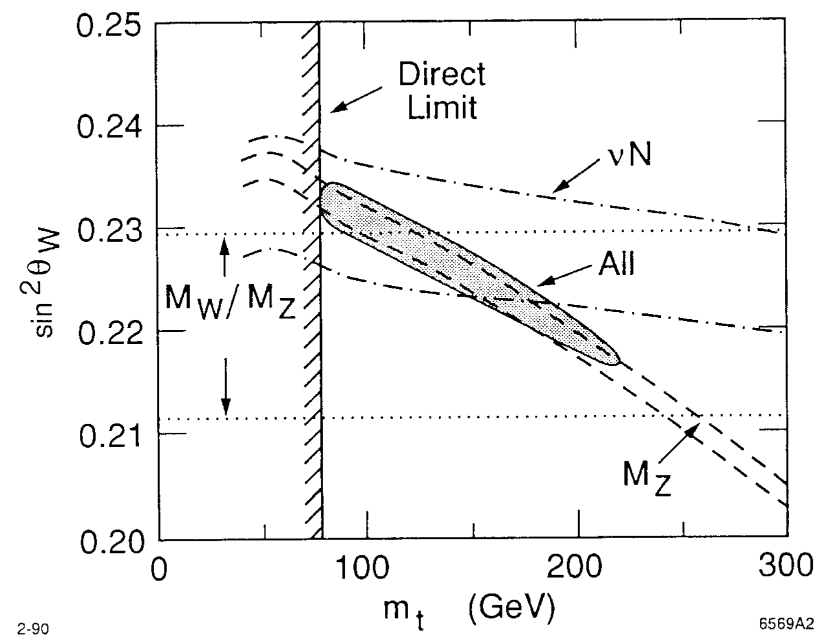

Figure 44. Interval in $\sin^2\theta_w|_S$ allowed at 1 σ confidence based on the measured values of m_Z, m_W/m_Z, and neutrino deep-inelastic cross sections, from Ref. 54. The intervals are plotted as a function of m_t, assuming $m_H = 100$ GeV. The shaded region is the 90% confidence allowed region in the plane of $\sin^2\theta_w|_S$ versus m_t.

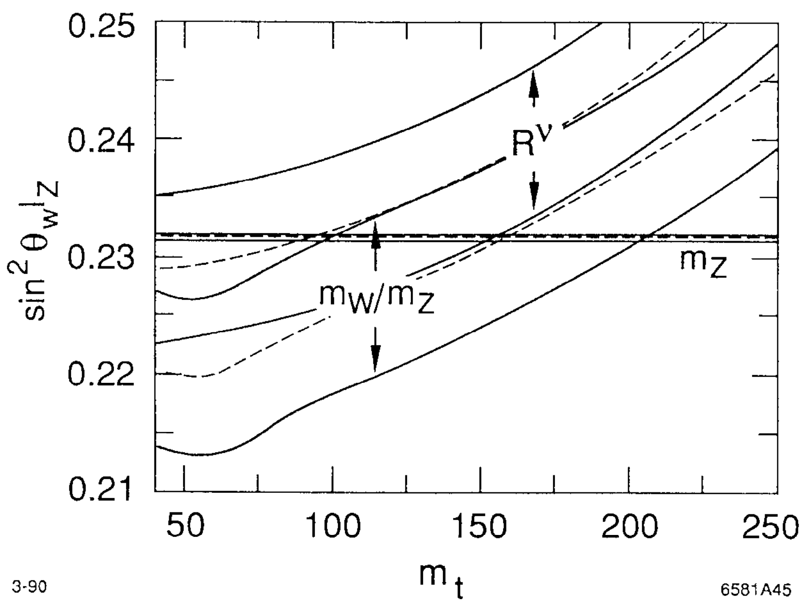

Figure 45. Interval in $\sin^2\theta_w|_Z$ allowed at 1 σ confidence based on the measured values of m_Z, m_W/m_Z, and R^ν. The notation is as in Fig. 43.

of the accidental compensation of the strong m_t dependence of $\rho_*(0)$ by the strong m_t dependence of the relation between $s_*^2(0)$ and $\sin^2\theta_w|_S$. On the other hand, the band from m_Z falls sharply on this plot, reflecting the steep dependence of $\sin^2\theta_w|_S$ on m_t shown in Fig. 36. Bands extracted from direct measurements of $s_*^2(m_Z^2)$ (from Z^0 asymmetries) or $s_*^2(0)$ (from electron-neutrino scattering) will have a similar steep decrease across the plot. The Z^0 mass measurement becomes seriously inconsistent with the neutrino measurements for $m_t > 200$ GeV. At a somewhat lower level of confidence, the measurements of m_Z and m_W become inconsistent if the top quark mass is too low. In Ref. 54, Langacker has reported a 90% confidence interval 51 GeV $< m_t <$ 186 GeV for m_H = 100 GeV; these limits are weakened slightly by variation of the Higgs boson mass. Ellis and Fogli[53] have, somewhat less conservatively, quoted the result $m_t = 132 \pm 34$ GeV. The result that the top quark mass is bounded from above by the consistency of weak interaction radiative corrections is not new; for example, the 1987 analysis of Amaldi, *et al.*,[9] gave the restriction $m_t <$ 180 GeV at 90% confidence. However, in the new data this restriction arises not as the integrated effect of many different experiments but rather as the direct contradiction of two well-measured observables.

How can we obtain more precise information on the top quark and other sources of weak interaction radiative corrections? To indicate the expectations for the near future, I have presented in Fig. 46 the expectation for the mid-1990's, when m_W has been measured to ± 50 MeV at the Tevatron or at LEP II. I have also added a band from A_{LR}, which I assume has been measured to ± 0.003 at the SLC. I cannot judge how much high-statistics neutrino scattering experiments at Fermilab can improve the value of $\sin^2\theta_w$ extracted from R^ν. At the moment, a large part of the error in this measurement is systematic, though this systematic error should be diminished by using the new high-energy neutrino beam from the Tevatron to measure the deep inelastic cross section well above charm threshold. However, I have indicated the effect of a measurement of $R^{\bar\nu}$, the neutral to charged current ratio in antineutrino-nucleon scattering, to ± 0.003. This measurement is difficult, since the systematic uncertainties of R^ν are larger for antineutrinos; however, it is a powerful probe of m_t and other effects that renormalize $\rho_*(0)$, since the function $R^{\bar{\nu}}_{\mathrm{LS}}$ defined in (5.66) is almost independent of $\sin^2\theta_w$ in the region of physical interest.

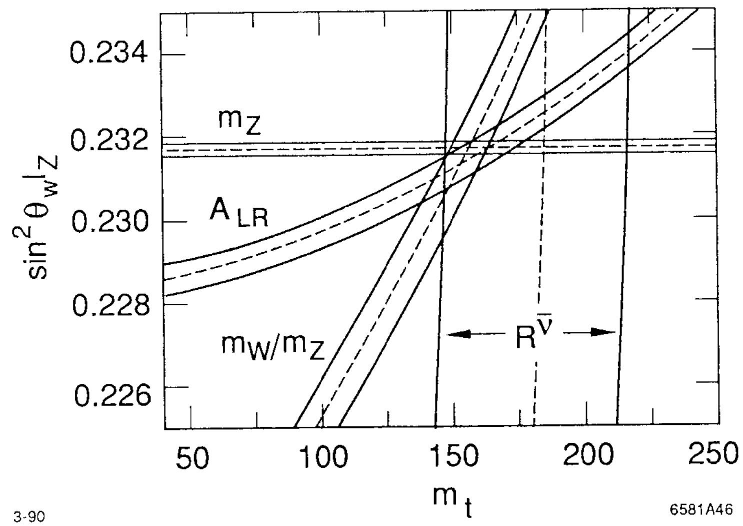

Figure 46. Future prospects for constraints on $\sin^2\theta_w|_Z$. The 1 σ confidence intervals are plotted versus m_t as in Fig. 43. The bands indicated come from m_Z, m_W/m_Z, A_{LR}, and $R^{\bar{\nu}}$. The expected errors in these quantities are described in the text; the central values are, of course, chosen arbitrarily.

6. Conclusions and Prospects

The comprehensive analyses discussed in the previous section bring this review to a natural conclusion. We began by discussing the general features of the standard model and the detailed properties of the lowest order predictions. We then made a lengthy digression on the extraction of the Z^0 mass from the resonance line-shape. Following this, we computed a certain class of weak interaction radiative corrections and saw how these influence the detailed predictions of the electroweak theory. Along the way, I included a brief discussion of the effects of an extended gauge sector, to remind you that new physics may appear not only in the loops, but also in the lowest order formulae.

When the top quark is eventually discovered and its mass measured, we will have an interesting confrontation between this mass value and the size of precisely measured weak corrections. However, it is possible, and even almost expected, that this comparison will fail. Through the example of the top quark loop corrections, we have seen that the weak interactions may be strongly perturbed by loop effects of heavy species. These effects may in fact be our first view of new physics beyond the standard model. In the last two figures, I have presented two manifestations of an additional quark doublet which might appear at very large mass. Figure 47 shows the effect of this doublet on the m_W and A_{LR}, assuming that m_Z is well known and that the top quark contribution is known and subtracted. Figure 48 shows a more futuristic application of weak interaction radiative corrections in the context of future, very high energy e^+e^- colliders. At energies of order 1 TeV in the center-of-mass, a heavy quark doublet of mass m_Q which is still above threshold produces a radiative correction to the amplitude for $e^+e^- \to W^+W^-$, for which the enhancement factor m_Q^2/m_W^2 expected from (5.43) constitutes a substantial modification of the differential cross section.[55] In both cases, the measurement of 1-loop corrections allows a glimpse of physics at energies well beyond the nominal collision energy of the e^+e^- reaction.

I have high hopes, then, for this new era of precision weak interaction exper-

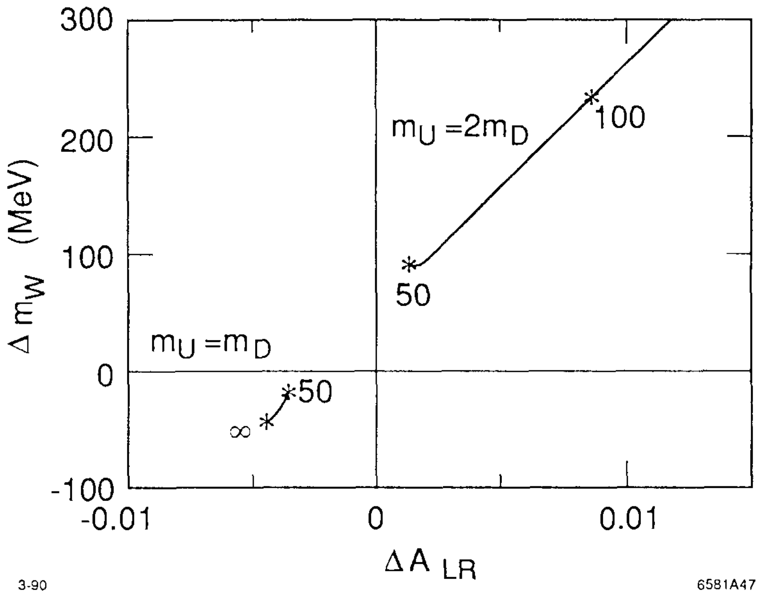

Figure 47. Effect of a heavy quark doublet (U, D) on the rapport between A_{LR} and m_W, as a function of the mass of the D. The effects are plotted as shifted from the standard model prediction. The two curves refer to $m_D/m_U = 0.5$ and $m_D/m_U = 1$. The value of m_D at the starred points is indicated.

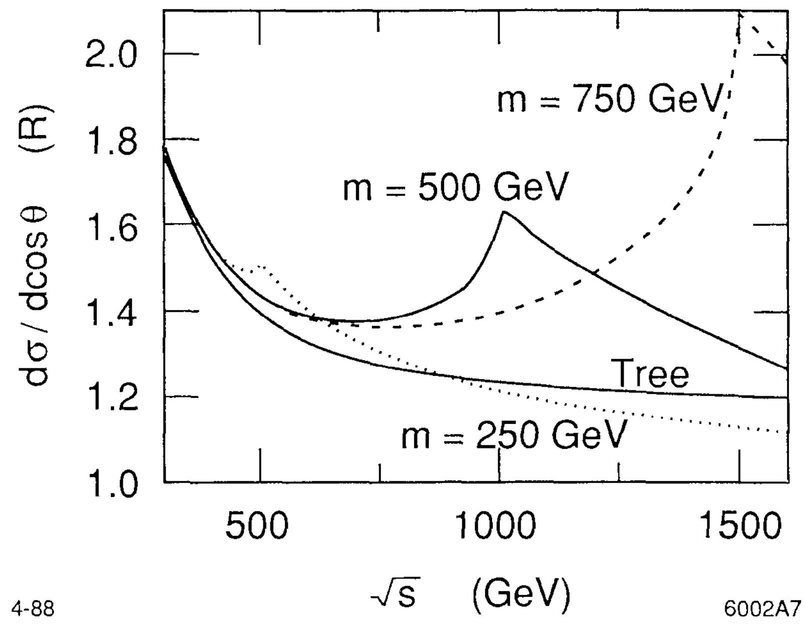

Figure 48. *Effect of a heavy quark doublet on the differential cross section for* $e^+e^- \to W^+W^-$, *at* $\cos\theta = 0$. *The various curves assume* $m_D = m_U = m$; *the cross section is computed in units of R.*

iments, in which the weak interactions become a tool to probe for the next scale of fundamental physics. I wish my experimental colleagues the skill, perseverence, and, above all, the good luck to follow this road to its promised end.

Acknowledgements:

I am grateful to many colleagues, at SLAC and elsewhere, for discussions which have contributed to my understanding of this subject. Among these people, I am particularly grateful to Gary Feldman, Traudl Hansl, Emlyn Hughes, Paul Langacker, Bryan Lynn, and Morris Swartz for sharing their considerable expertise on the topics discussed here, and to Yossi Nir and Tatsu Takeuchi, for their patient criticism of the manuscript.

REFERENCES

1. A. Sirlin, *Nucl. Phys.* **B71,** 29 (1974), *Nucl. Phys.* **B100,** 291 (1975).
2. A. Sirlin, *Phys. Rev.* **D22,** 971 (1980).
3. M. Veltman, *Acta Phys. Pol.* **B8,** 475 (1977).
4. M. Veltman, *Nucl. Phys.* **B123,** 89 (1977).
5. W. Hollik, DESY preprint DESY 88–188 (1988), to appear in *Fortschr. Phys.*
6. *Z Physics at LEP 1,* Vol. 1, G. Altarelli, R. Kleiss, and C. Verzegnassi, eds. CERN Report CERN 89–08 (1989).
7. P. Sikivie, L. Susskind, M. Voloshin, and V. Zakharov, *Nucl. Phys.* **B173,** 189 (1980).
8. J. E. Kim, *et al., Rev. Mod. Phys.* **53,** 211 (1981).
9. U. Amaldi, *et al., Phys. Rev.* **D36,** 1385 (1987).
10. G. Costa, *et al., Nucl. Phys.* **B297,** 244 (1988).
11. J. Alexander, *et al.* (Mark II), *Phys. Rev. Lett.* **63,** 2173 (1989).
12. P. Aarnio, *et al.* (DELPHI), CERN preprint CERN-EP/89–134 (1989).
13. D. Decamp, *et al.* (ALEPH), CERN preprint CERN-EP/89–169 (1989).
14. L3 Collaboration, L3 preprint # 004 (1989).
15. M. Z. Akrawy, *et al.* (OPAL), CERN preprint CERN-EP/90–27 (1990).
16. G. Bonneau and F. Martin, *Nucl. Phys.* **B27,** 381 (1971).
17. G. Altarelli and G. Parisi *Nucl. Phys.* **B126,** 298 (1977).
18. E. A. Kuraev and V. S. Fadin, *Sov. J. Nucl. Phys.* **41,** 466 (1985).
19. V. N. Gribov and L. N. Lipatov, *Sov. J. Nucl. Phys.* **15,** 438 (1972); L. N. Lipatov, *Sov. J. Nucl. Phys.* **20,** 94 (1974).
20. R. N. Cahn, *Phys. Rev.* **D36,** 2666 (1987).
21. F. A. Berends, G. J. H. Burgers, and W. L. van Neerven, *Phys. Lett.* **185B,** 395 (1987).
22. F. A. Berends, in ref. 6.
23. J. Alexander. G. Bonvicini, P. Drell, and R. Frey, *Phys. Rev.* **D37,** 56 (1988).
24. M. Bohm and W. Hollik, *Nucl. Phys.* **B204,** 45 (1982).
25. P. Langacker, R. W. Robinett, and J. L. Rosner, *Phys. Rev.* **D30,** 1470 (1984).
26. M. E. Peskin, in *Proceedings of the Fifteenth SLAC Summer Institute on Particle Physics (August, 1987),* E. C. Brennan, ed. SLAC Report No. 328 (1987).
27. Talks presented at the 1990 meeting of the Division of Particles and Fields of the APS, Dallas (January, 1990). These results are still preliminary.
28. G. Beall, M. Bander, and A. Soni, *Phys. Rev. Lett.* **48,** 848 (1982).
29. P. Langacker, *Phys. Rev.* **D30,** 2008 (1980).
30. M. Cvetič and B. W. Lynn, *Phys. Rev.* **D35,** 51 (1987).
31. G. Altarelli, R. Casalbuoni, D. Dominici, F. Feruglio, and R. Gatto, CERN preprints CERN-TH-5591/89 (1989), 5626/90 (1990).
32. W. Marciano, *Phys. Rev.* **D20,** 274 (1979).
33. W. Marciano and A. Sirlin, *Phys. Rev.* **D22,** 2695 (1980).
34. H. Burkhardt, F. Jegerlehner, G. Penso, and C. Verzegnassi, *Z. Phys.* **C43,** 497 (1989).
35. B. W. Lynn, G. Penso, and C. Verzegnassi, *Phys. Rev.* **D35,** 42 (1987).
36. E. Eliasson, *Phys. Lett.* **147B,** 65 (1984).
37. J. A. Grifols and J. Sola, *Nucl. Phys.* **B253,** 47 (1985).
38. B. W. Lynn, M. E. Peskin, and R. G. Stuart, in *Physics at LEP,* J. Ellis and R. Peccei, eds. CERN Report CERN 86–02 (1986).

39. G. Passarino, *Phys. Lett.* **B228,** 89 (1989).

40. S. Fanchiotti and A. Sirlin, *Phys. Rev.* **D41,** 319 (1990).

41. W. Marciano and A. Sirlin, *Phys. Rev. Lett.* **46,** 163 (1981).

42. R. E. Taylor, personal communication.

43. J. Jersak, E. Laermann, and P. M. Zerwas, *Phys. Lett.* **98B,** 363 (1981), *Phys. Rev.* **D25,** 1218 (1982).

44. D. Kennedy and B. W. Lynn, *Nucl. Phys.* **B322,** 1 (1989).

45. A. A. Akhundov, D. Yu. Bardin, and T. Riemann, *Nucl. Phys.* **B276,** 1 (1986).

46. J. Bernabéu, A. Pich, and A. Santamaría, *Phys. Lett.* **200B,** 569 (1988).

47. W. Beenakker and W. Hollik, *Z. Phys.* **C40,** 141 (1988).

48. H. Abramowicz, *et al.*, *Phys. Rev. Lett.* **57,** 298 (1986), *Z. Phys.* **C35,** 443 (1987).

49. J. V. Allaby, *et al.*, *Phys. Lett.* **177B,** 446 (1986), *Z. Phys.* **C36,** 611 (1987).

50. A. Blondel, *et al.*, CERN preprint CERN/EP 89-101 (1989).

51. C. H. Llewellyn Smith, *Nucl. Phys.* **B228,** 205 (1983).

52. D. Kennedy, B. W. Lynn, C. J. C. Im, and R. G. Stuart, *Nucl. Phys.* **B321,** 83 (1989).

53. J. Ellis and G. Fogli, *Phys. Lett.* **213B,** 526 (1988), **232B,** 139 (1989).

54. P. Langacker, *Phys. Rev. Lett.* **63,** 1920 (1989).

55. C. Ahn, M. E. Peskin, B. W. Lynn, and S. Selipsky, *Nucl. Phys.* **B309,** 221 (1988).

Applications of QCD to Hadron-Hadron Collisions: Experimental. *

Marjorie D. Shapiro
Harvard University
Cambridge, Massachusetts 02138

Abstract

QCD results from Hadron-Hadron Colliders are reviewed from an experiment point of view. Among the topics discussed are experimental constraints on detector design, methods of finding and measuring jets, dijet production, multijet processes, Drell-Yan processes (including $W^{\pm}$ and Z^0 production) and the production and detection of direct photons.

Hadron colliders provide an important laboratory for testing the Standard Model of Strong and Electroweak interactions. Because such colliders have the highest available center-of-mass energy ($\sqrt{s}$), they probe the shortest accessible length scales and hence provide a unique opportunity both to study the fundamental fields of the standard model and to search for deviations from the behavior predicted by the standard model. Since the $p\bar{p}$ cross section is dominated by strong interaction processes, a thorough understanding of QCD phenomena is essential for interpreting collider results. These lectures discuss the experimental aspects of QCD in the hadron collider environment.

1 Phenomenological Overview

1.1 Particle Production in Soft Processes

The total $p\bar{p}$ cross section at current collider energies is dominated by *soft* processes. Because most $p\bar{p}$ interactions involve low momentum transfers, we cannot describe the bulk of the cross section using perturbative QCD. It is therefore

*This work was supported by the Director, Office of Energy Research, Office of High Energy and Nuclear Physics, Division of High Energy Physics of the U.S. Department of Energy under Contract DE-AC02-76ER03064.

necessary to parameterize σ_{tot} with a phenomenological model. Many such models currently exist, most notably fireball, multi-peripheral and Regge models.[1] While the quantitative predictions of these parameterizations can differ, they all share two common features. First, because the momentum transfer in most $p\bar{p}$ collisions is small, particles are produced with limited transverse momentum (p_t) with respect to the incoming $p\bar{p}$ direction. Second, because there are no real dynamical constraints in the problem, the particles have a distribution of longitudinal momenta with respect to the beamline ($p_{||}$) that is determined chiefly by the available phase space.

The three dimensional phase space element can be expressed in terms of p_t and $p_{||}$:

$$\frac{d^3p}{\mathrm{E}} = d\phi \frac{dp_t^2}{2} \frac{dp_{||}}{\mathrm{E}} \tag{1}$$

where ϕ is the azimuthal angle. Hence the invariant single particle cross section can be written:

$$\mathrm{E}\frac{d\sigma}{d^3p} = \frac{1}{\pi}\frac{d\sigma}{dp_t^2dy} \tag{2}$$

where the rapidity y is defined as

$$y \equiv \frac{1}{2}\ln\left(\frac{\mathrm{E}+p_{||}}{\mathrm{E}-p_{||}}\right) \tag{3}$$

so that $dy = dp_{||}/\mathrm{E}$. Defined in this manner, y is an extremely useful variable. First, (as seen above) rapidity is the natural phase space element. Second, y transforms simply under longitudinal boosts. Given a frame F' moving with velocity v in the beam (z) direction, a particle with rapidity y in the laboratory frame will have rapidity y' in frame F' such that

$$y' = y - y_f \tag{4}$$

where $y_f \equiv \tanh^{-1}(v/c)$. This equation immediately shows that the rapidity *difference* between 2 particles is Lorentz invariant with respect to longitudinal boosts. Note that in the case where particle masses can be neglected $y \approx -\ln\tan(\theta/2)$ where θ is the angle the particle's momentum makes with respect to the beamline. This angular variable is called *pseudorapidity* (η):

$$\eta \equiv -\ln\tan(\theta/2)\,. \tag{5}$$

Because it is independent of mass and therefore requires only an angular measurement, η rather than y is the variable most commonly used at hadron colliders.

Since rapidity is a natural phase space element, the distribution of particles should be essentially flat in this variable. This fact is demonstrated in Figure 1a which shows the charged particle multiplicity $dN_{ch}/d\eta$ as a function of pseudorapidity for several center-of-mass energies. These data were taken using "minimum bias" triggers, triggers sensitive to the complete non-diffractive cross section. At all center-of-mass energies, the cross section shows almost no dependence on η. The value of $dN_{ch}/d\eta$ grows with increasing center-of-mass energy (see Figure 1b), reflecting the larger total multiplicity observed at higher $\sqrt{s}$. (Note that the flat rapidity "plateau" must end at some value of η_{max}. This value is set by the kinematic limit $\eta_{max} \sim \ln(2\mathrm{E}/m)$ where m is the mass of the produced particle, usually a pion.)

As can be seen in Figure 2, the single particle p_t spectrum falls rapidly for minimum bias events. However, as the center-of-mass energy increases, a high p_t tail becomes apparent in the data. The effect is also observed (see Figure 3) in the behavior of the cross section $d\sigma/d\Sigma_{E_t}$ where E_t is the *total transverse energy* observed in the event:

$$\Sigma_{E_t} \equiv \sum_i E_i \sin\theta_i \tag{6}$$

where E_i is the energy in the calorimeter cell with center at position θ_i and where the sum is taken over all calorimeter cells. This non-exponential tail at high transverse energy indicates the presence of a component of the cross section that does not result from the soft physics described above. This new physics is the onset of hard scattering, which will be the topic of the remainder of these lectures.

1.2 Large Momentum Transfer Processes

Because α_s becomes small at high momentum transfers, high p_t scattering is well described by perturbative QCD [2]. This process is presented schematically in Figure 4. In this picture, the initial hadrons are treated as a set of quasi-free partons (quarks and gluons) that scatter to produce large p_t partons in the final state. The momentum distributions of the initial partons are described by a set of structure functions $f_i(x)$ which specify the probability for finding a parton of type i in the proton carrying a fraction of the proton's total momentum that is between x and $x + dx$. In the naive parton model, the structure functions *scale* (are independent of the momentum transfer in the hard scattering process). QCD corrections introduce a "non-scaling behavior." The incoming hadrons are seen as beams of partons where the quark and gluon momentum distributions are each described by an initial distribution $f_i(x, M_0^2)$ that has been measured in some reference process (*i.e.* deep inelastic scattering). These structure functions then evolve to the scale appropriate to the hard scattering process of interest (M^2) via the emission of nearly collinear quarks and gluons. This evolution is described by

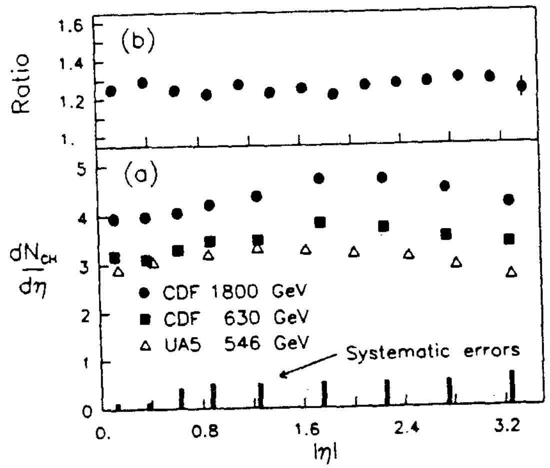

Figure 1: a) The charged particle pseudorapidity distribution $dN_{ch}/d\eta$ as a function of the pseudorapidity η as measured by CDF ($\sqrt{s} = 1800, 630$ GeV) and by UA5 ($\sqrt{s} = 546$ GeV) [3]. In all cases, the statistical uncertainty is smaller than the plotted point. An estimate of the systematic uncertainty for the CDF data is shown on the lower edge of the plot.
b) The ratio of $dN_{ch}/d\eta$ at 1800 GeV to that at 630 GeV.

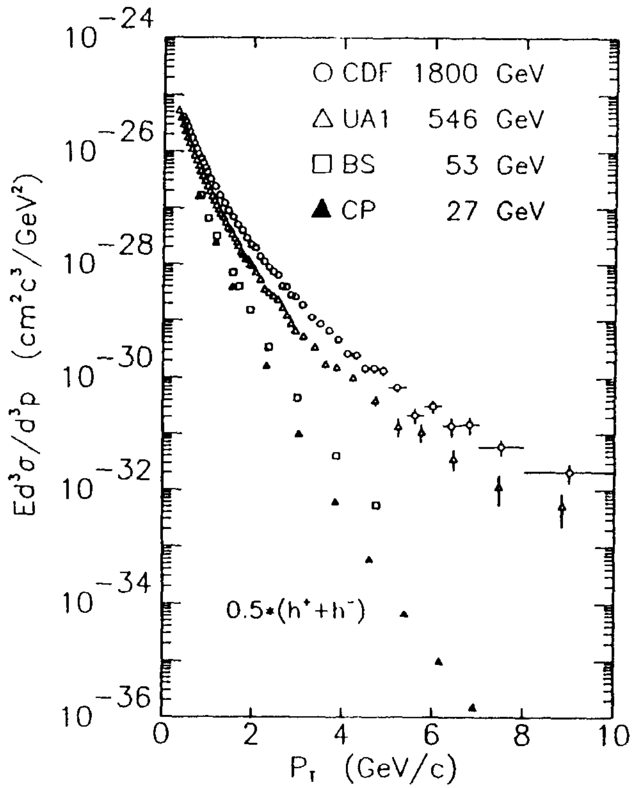

Figure 2: The energy dependence of the single particle invariant cross section $Ed^3\sigma/d^3p$ as measured by the CDF ($\sqrt{s} = 1800$ GeV) [4], UA1 ($\sqrt{s} = 546$ GeV) [5], British-Scandinavian ($\sqrt{s} = 53$ GeV) [6] and Chicago-Princeton ($\sqrt{s} = 27$ GeV) [7] collaborations.

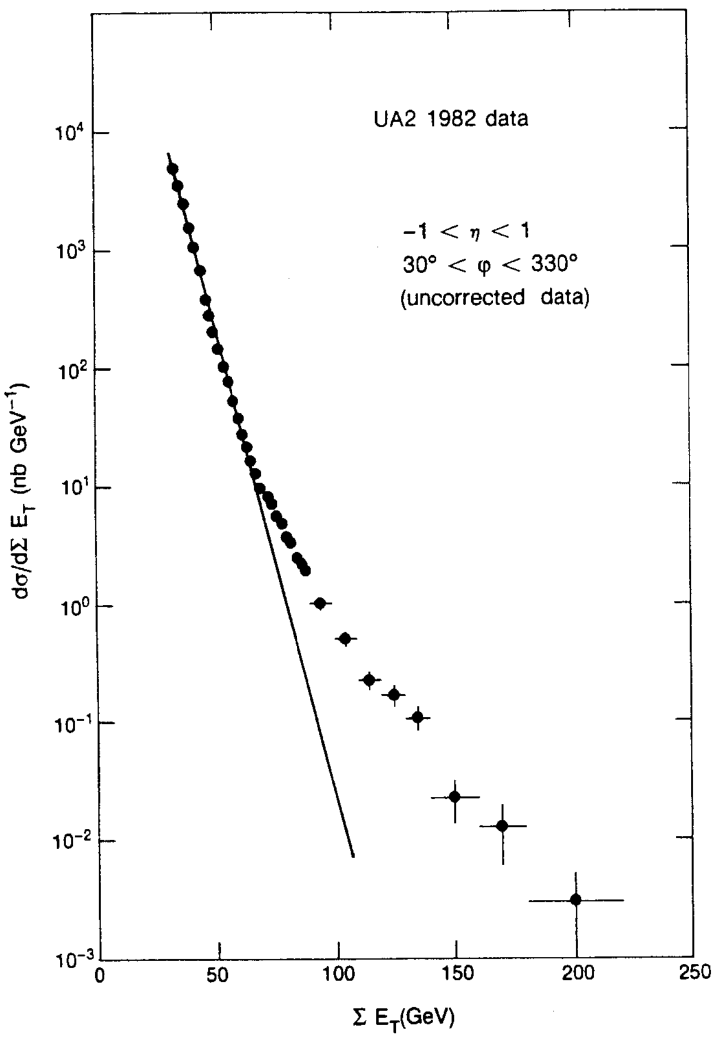

Figure 3: The observed distribution of $d\sigma/d\Sigma_{E_t}$ as a function of Σ_{E_t} as measured by the UA2 experiment.[21] The solid line shows the exponential falloff at low ΣE_t.

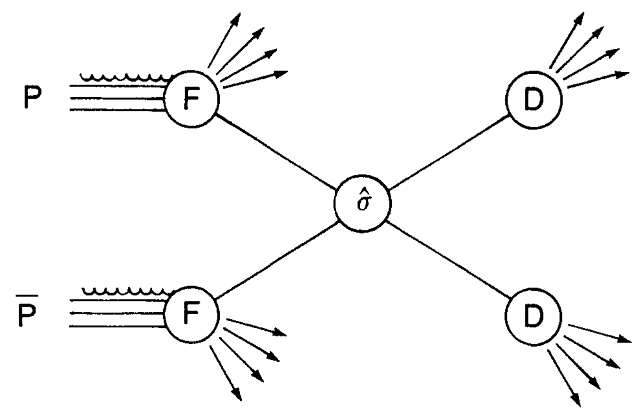

Figure 4: A schematic view of parton-parton scattering.

the Altarelli-Parisi equations [8].

The hard scattering process is represented by the following parton model formula:

$$\sigma \sim \sum_{ij} \int dx_1 dx_2 \hat{\sigma}_{ij} f_i(x_1, M^2) f_j(x_2, M^2). \tag{7}$$

Here i and j label the types of incoming partons (gluons and the various flavors of quarks and antiquarks) and $f_i(x, M^2)$ is the parton structure function for parton species i. The invariant mass of the parton-parton system ($\sqrt{\hat{s}}$) is related to the hadron-hadron center-of-mass energy ($\sqrt{s}$) by $\hat{s} = x_1 x_2 s$. The parton cross section σ_{ij} can be calculated using perturbative QCD and is expressed as an expansion in $\alpha_s(\mu)$:

$$\hat{\sigma}_{ij} = A\alpha_s^n(\mu)(1 + B\alpha_s(\mu)\ldots) \tag{8}$$

The scales M and μ are of the same order as the momentum transfers in the parton scattering process. If the final state contains color, the outgoing partons again can radiate nearly collinear quarks and gluons. These quarks and gluons then fragment into color-singlet hadrons.

As previously indicated, the proton structure functions must be measured in some reference process. In general, quark and antiquark distributions are measured in deep inelastic scattering experiments. Since these experiments are not directly sensitive to the gluon distributions, these are usually inferred (using momentum-sum rules) from the variation of the antiquark distributions with the momentum transfer Q^2. Extraction of the gluon structure function is therefore sensitive both to the value of α_s used in the calculation (since this controls the rate of evolution of the gluon distribution) and to the functional form used to characterize the initial gluon distribution.

Many parameterizations of the proton structure functions exist. Among the most common are Eichten *et al* [9] (EHLQ) set 1 and 2, Duke and Owens (DO) [10] set 1 and 2, Martin, Roberts and Stirling (MRS) [11] and Diemoz, Ferroni, Longo and Martinelli (DFLM) [12]. These parameterizations differ from each other in that they fit different experimental data and make different assumptions about the behavior of the gluon distribution at low x. EHLQ and DO result from lowest order QCD calculations, while MRS and DFLM structure functions are calculated to next-to-leading order. The uncertainties in the proton structure function represent a *systematic* error on all QCD predictions.[13]

Figure 5a shows the lowest order diagrams that contribute to parton-parton scattering in $p\bar{p}$ collisions, while Figure 5b gives some of the important next-to-leading order corrections. At Tevatron energies, the cross section is dominated by gluon-gluon scattering. This is true first because color factors enhance the gluon

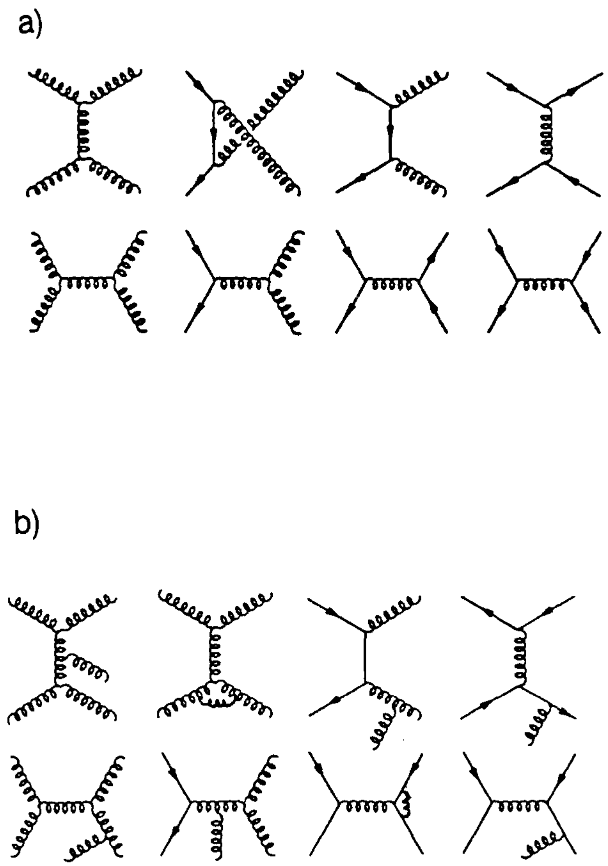

Figure 5: a)The diagrams that contribute to parton-parton scattering in lowest order QCD.
b) Some of the diagrams that contribute to parton-parton scattering in next-to-leading order.

cross section relative to quarks and second because the gluon structure functions dominate at low x, where the cross section is largest. Independent of Q^2, all important contributions to the cross section are t-channel. Thus, the angular distribution in the center-of-mass is similar to Rutherford scattering:

$$\frac{d\sigma}{d\hat{t}} = \frac{|M|^2}{16\pi\hat{s}^2} \tag{9}$$

where $\hat{t}$ and $\hat{s}$ are the normal Mandelstam variables, evaluated in the hard scattering center-of-mass:

$$\hat{s} = (p_1^\mu + p_2^\mu)^2 \tag{10}$$

$$\hat{t} = (p_1^\mu - p_3^\mu)^2 \tag{11}$$

$$\hat{u} = (p_2^\mu - p_3^\mu)^2. \tag{12}$$

Here p_1^μ and p_2^μ are the four momenta of the initial partons and p_3^μ and p_4^μ are the four momenta of the scattered partons. Note that the production of high p_t leptons must occur through diagrams involving quarks and must involve at least one electroweak coupling constant. Examples of leptonic production mechanism involving virtual photons are shown in Figure 6a while weak production mechanisms are shown in Figure 6b. The rates for these processes are therefore reduced relative to parton scattering by several orders of magnitude (see Figure 7).

The lowest order QCD calculation provides a reasonable description of the inclusive jet and boson cross sections. There is, however, always an ambiguity in the overall normalization of the lowest order calculation. The ambiguity results from the fact that the calculated rate depends on the choice of momentum scale μ used to evaluate α_s and the choice of scale M used in the evaluation of the quark and gluon structure functions. While these scales should be of order p_t of the hard scattering process, there is no fundamental reason to choose p_t rather than $p_t/2$ or $2p_t$ (and in fact no fundamental reason to choose the same scale for μ and M). If an exact calculation to all orders in perturbation theory were done, then these differences in choice would not change the final answer, but would merely change the relative contributions of terms in the perturbative expansion. If only the lowest order term is included, uncertainties due to this ambiguity are typically about a factor of two. This theoretical uncertainty can be reduced (typically to about 30%) if a next order calculation is done. The contribution of the next-to-leading order term has been calculated in several cases: the total cross section for W/Z production and for Drell-Yan scattering ($p\bar{p} \to e^+e^-$, $\mu^+\mu^-$) [14], the cross section for producing an isolated high transverse momentum photon

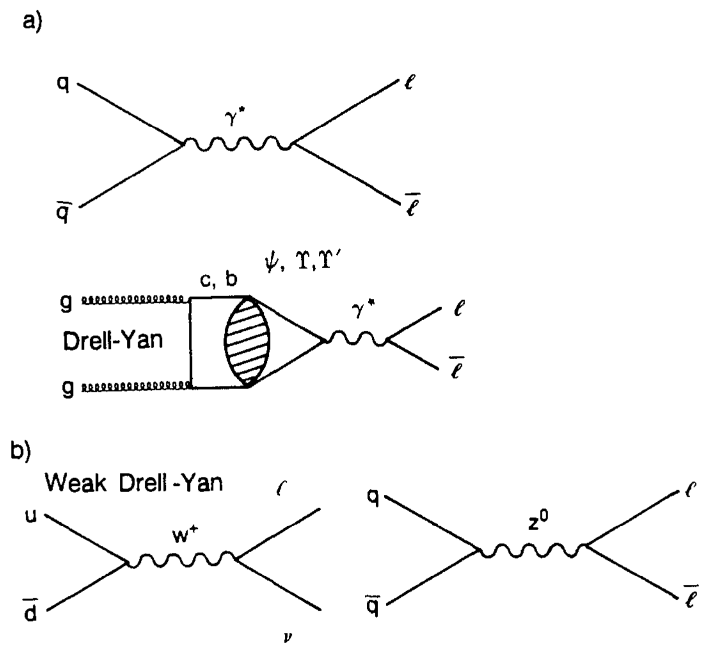

Figure 6: a) The lowest order electromagnetic diagrams that contribute to high p_t lepton production.
b) The lowest order weak diagrams that contribute to high p_t lepton production.

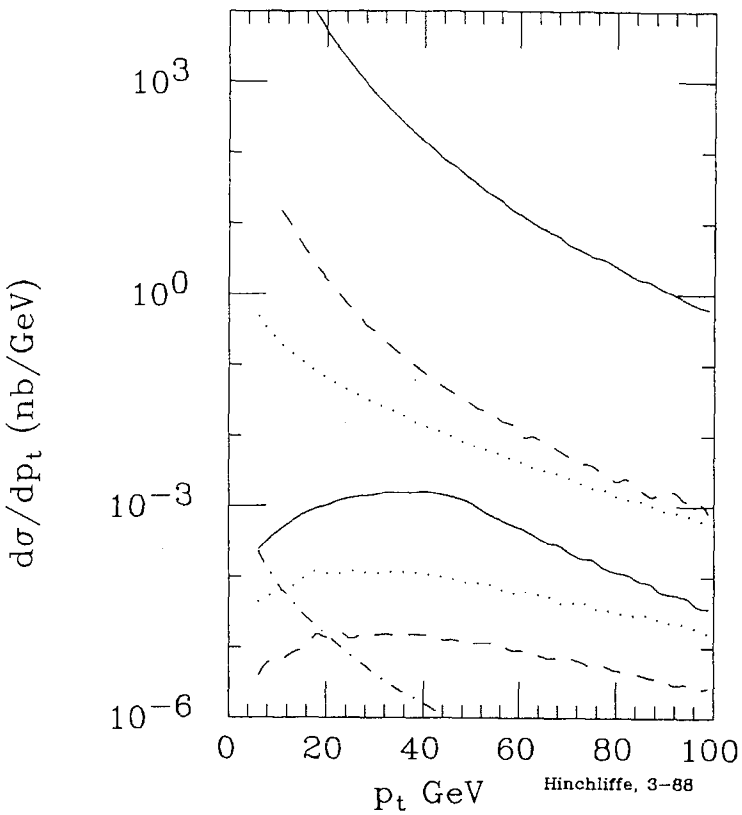

Figure 7: The production cross section for a variety of $p\bar{p}$ physics processes as a function of p_t of the hard scattering system. Going from largest to smallest cross section the processes are:
a) Jet production
b) γ + jet
c) W^+ + jet
d) W^+ from top production
e) $W^+ + \gamma$
f) $W^\pm$ pair
g) $W^+ + Z$

[15] and the total cross section for producing a heavy quark antiquark pair [16]. In the case of jet production, all the next-to-leading order diagrams have been evaluated [17] and a consistent calculation of the single jet inclusive cross section is underway [18]. In general, higher order terms do not have a big effect on the shape of inclusive distributions, which has led to the use of the term "K-factor," defined as the ratio of the lowest order to next order calculation. This term is extremely misleading since the value of the factor depends critically on the choice of momentum scale used in the lowest order calculation. There are also exceptional cases where the next order calculation can introduce changes in predicted event topology. For example, in bottom quark production where the process $g \to b\bar{b}$ does not contribute until next-to-leading order, the angular correlation between the b and $\bar{b}$ is significantly altered by this term.

1.3 Jet Production

The creation of colorless hadrons from a colored parton is a soft process. Therefore, the hadrons are produced with limited p_t with respect to the initial parton direction, forming collimated "jets" of particles. The hadron p_t with respect to the jet axis is typically of order a few hundred MeV. Because these hadrons follow the initial parton direction, there is a correspondence between the observed hadron jets and the colored objects produced in the hard scattering process. This principle of "local parton-hadron duality" is a central assumption of our theory.

Equation 7 and the principle of local parton-hadron duality provide a good description of hard scattering events. In general, these events appear in our detector as two "beam jets" and two or more high p_t scattered objects. The beam jets are remanents of the initial p and $\bar{p}$ after the hard scattering has occurred. These remanents interact via soft processes and therefore produce particle distributions that look a great deal like the soft minimum bias events discussed in Section 1.1. The presence of a hard scattering in the event can result in a higher overall multiplicity, but the "underlying event" in hard scattering processes is well described by a flat rapidity distribution of low p_t particles. This fact can be seen in Figure 8, which shows the ratio of the observed multiplicity in events containing a W boson to the multiplicity in minimum bias events.

High p_t jets, however, can be observed as localized clumps of energy. For example, Figure 9 shows a two jet event as measured in CDF. The plot shows an η - ϕ grid representing the CDF calorimeter segmentation. The height of each tower is proportional to the transverse energy deposited in that tower. All cells containing at least 0.5 GeV of transverse energy are shown. The two jets in the

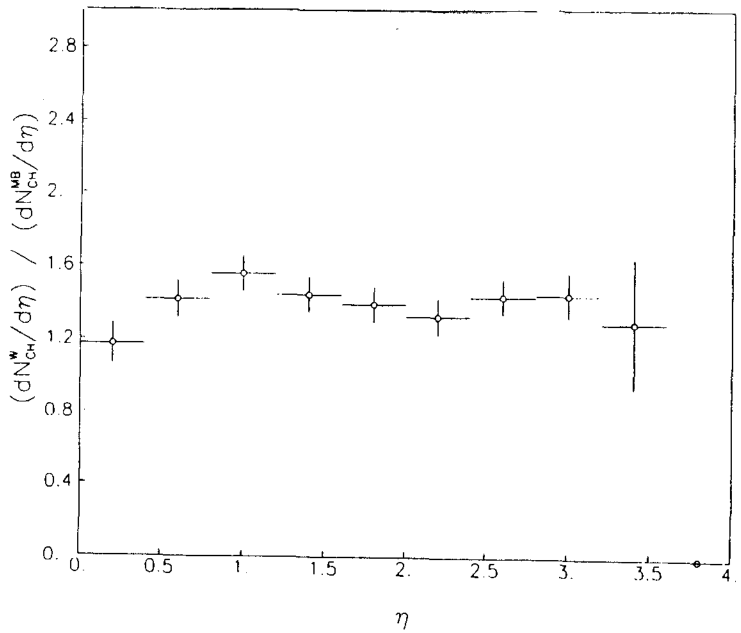

Figure 8: The ratio of the charged multiplicity $dN_{ch}/D\eta$ for events containing a $W \rightarrow e\nu$ decay to that observed in minimum bias triggers In the W events, the electron from the W decay is not included in the distribution.

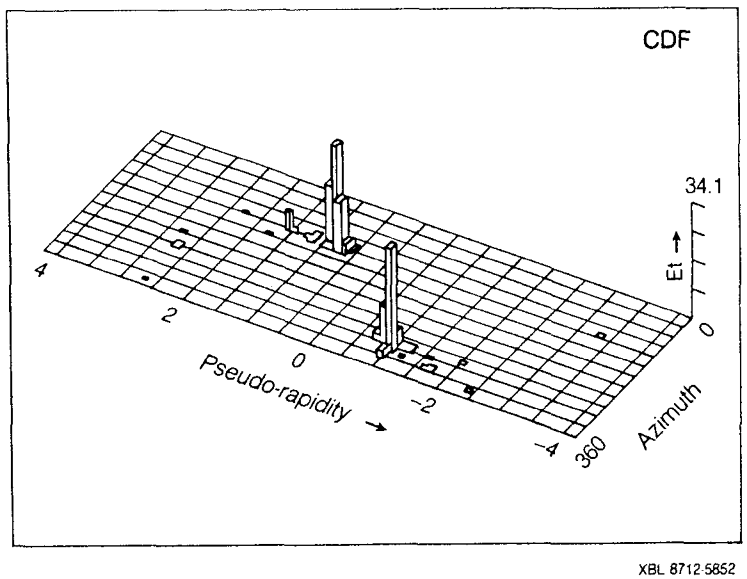

Figure 9: A two jet event as measured in CDF.

event are separated by 180° in ϕ and balance in p_t. This is the pattern expected for elastic scattering of two partons. Note that the 0.5 GeV tower cut effectively eliminates all energy from the soft underlying event.

Jets were first unambiguously observed in $p\bar{p}$ collisions by the UA2 experiment in 1982. Using a simple "cluster algorithm" that combined neighboring calorimeter cells, the UA2 group observed that for large Σ_{E_t} most of the total energy observed in their calorimeter was deposited in two back-to-back clusters. Figure 10 shows the fraction of the total observed transverse energy found in the highest (h_1) and two highest (h_2) clusters as a function of the total transverse energy in the event. At high transverse energies, most of the event E_t is found in the two highest clusters. Figure 11 shows the distribution of the difference in azimuth of the two highest E_t clusters in events with ($\Sigma_{E_t} \geq 60$ GeV). The peaking at $\phi = 180°$ is what we expect from a hard $2 \rightarrow 2$ scattering process.

The longitudinal momentum distribution of the hadrons in the high p_t jets is governed by phase space factors. The mathematical formalism developed in Section 1.1 holds in this case as well. Hadrons in jet events have a roughly flat distribution in rapidity when that rapidity is measured *relative to the jet axis*. We derive here an expression for the distribution of hadrons in a jet when this distribution is measured in laboratory coordinates.[19] Let us begin with a jet that has its axis pointing in the $\hat{n}$ direction with coordinates y_0 and ϕ_0 for its rapidity and azimuthal position respectively. This jet contains a particle with momentum $\vec{p}$. In the laboratory frame, the particle has the following coordinates: transverse momentum p_t, rapidity y and azimuthal position ϕ (see Figure 12). We can calculate the transverse momentum of this particle with respect to the jet axis:

$$p_t^{\text{wrt jet}} = \vec{p} - (\vec{p} \cdot \vec{n})\hat{\mathrm{n}}\,. \tag{13}$$

Transforming into the laboratory frame, we find

$$\begin{aligned} p_t^{\text{wrt jet}} &= E_t\{\hat{\mathrm{l}} \sin(\phi - \phi_0) - \hat{\mathrm{m}}[\sinh(y - y_0) - \cos(\phi - \phi_0)]\} & (14) \\ &\approx \mathrm{E}_t\{\hat{\mathrm{l}}(\phi - \phi_0) - \hat{\mathrm{m}}(y - y_0)\}\,. & (15) \end{aligned}$$

Thus, particles with constant p_t with respect to the jet axis are distributed about a circle in y - ϕ space where the radius of the circle is proportional to p_t and where y is measured relative to the beamline. In the laboratory frame, a jet looks like circle in $y\phi$ space with the density of particles falling off rapidly with radius. Since typical p_t's with respect to the jet axis are a few hundred MeV, for jets with E_t above 10 GeV a circle of radius 0.7 should enclose a large fraction of the particles in the jet and a circle of radius 1.0 should contain almost all. We shall use this result later.

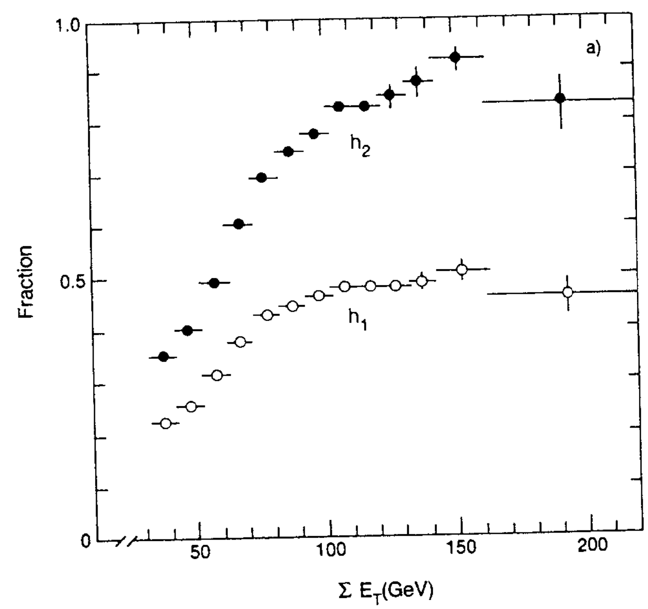

Figure 10: The fraction of the total transverse energy observed in the highest (h_1) and two highest (h_2) clusters as a function of the total transverse energy of the event, as measured by the UA2 experiment.

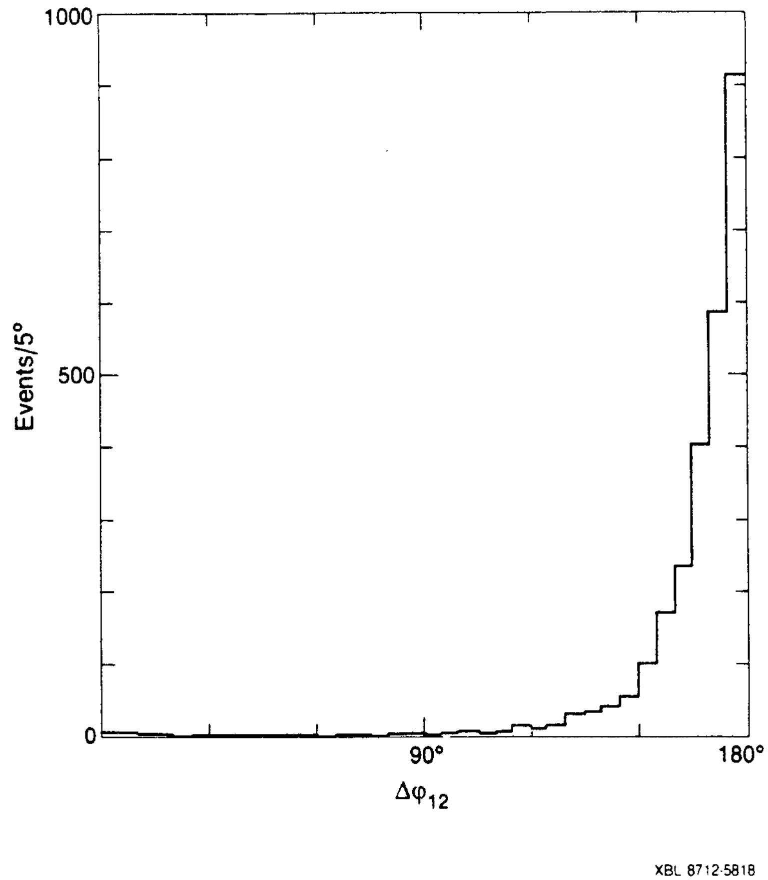

Figure 11: The distribution of the difference in azimuth between the two highest E_t clusters in events with ($\Sigma E_t \geq 60$ GeV), as measured by the UA2 experiment.

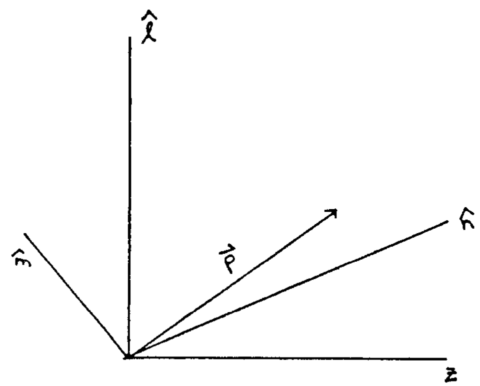

Figure 12: The coordinate system used to discuss jet fragmentation. A jet with its axis pointing into the $\hat{n}$ direction and has rapidity y_0 and azimuthal position ϕ_0. This jet contains a particle with transverse momentum p_t, rapidity y and azimuth ϕ in the laboratory frame. The laboratory coordinate system is defined by the unit vectors $\hat{z}$, $\hat{l}$ and $\hat{m}$.

2 Experimental Considerations and Detector Design

The large collider detectors currently in operation are expected to perform a wide range of measurements. Among the goals of these general purpose facilities are:

- To measure the differential cross section for hard scattering processes. Such measurements not only test strong interaction theory, but by looking for deviations from QCD predictions also search for unexpected new physics signals.
- To study electroweak couplings by measuring the mass of the $W^{\pm}$ and Z^0 bosons and by studying angular distributions and asymmetries of the boson decay products.
- To search for new particles such as heavy quarks, new gauge bosons and supersymmetric particles.
- To further constrain the range of allowable structure functions and to investigate the high energy behavior of quark and gluon fragmentation functions.

In order to study the phenomena listed above, it is necessary to have a detector that measures quarks and gluons (jets), electroweak bosons (photons, W's and Z's) and neutral, non-interacting particles (neutrino's, supersymmetric particles) over a large range of momenta. Because the total inelastic cross section is so large relative to the hard scattering rate, significant event selection must be done at the trigger level. In addition, since the rate for QCD jets is several orders of magnitude larger than for other hard scattering processes (again, see Figure 7), the tails of the jet distributions can become significant backgrounds for other measurements. These considerations place several requirements on any multipurpose detector designed to run at a hadron collider.

The high energies reached in hadron colliders necessitates the use of calorimetric detectors. The high multiplicity environment implies that the detector should have good segmentation. The fact that inclusive production is in general flat in rapidity and uniform in ϕ (for a constant E_t cut) means that rapidity, or more conveniently, pseudorapidity, and ϕ are natural segmentation variables and that a large solid angle coverage is highly desirable. Because the jet rate dominates all other processes, a high level of rejection against jet events is necessary when studying electrons, muons and missing energy signals. In the case of muons and electrons, this means that high quality tracking information is important. In a high rate environment, this information should be available at the trigger level. Good calorimeter resolution and the absence of cracks also are necessities to eliminate mis-measured jets as a major source of missing transverse energy.

Typically, collider detectors are primarily calorimetric, with large sampling type calorimeters. These detectors have good resolution at high energy and are sensitive both to charged and neutral particles. A high level of transverse segmentation is desirable. In most cases many longitudinal samples are ganged in depth to form projective "towers" in η-ϕ. Some longitudinal segmentation, however is essential. Calorimeters are typically divided into "electromagnetic" and "hadronic" depths, often constructed with different materials. The electromagnetic and hadronic segments can also be further sub-divided to give additional information about the longitudinal shower development.

The resolution of a sampling calorimeter has a contribution due to sampling fluctuations between the absorber and active medium. This resolution generally scales with energy as follows:

$$\frac{\sigma_E}{E} = \frac{\sigma_0}{\sqrt{E}}. \tag{16}$$

The deposited energy E is measured in GeV and the intrinsic resolution σ_0 is typically 14% for electromagnetic calorimetry and between 80% and 120% for hadronic calorimetry. The hadronic resolutions quoted here include not only the effect of sampling statistics, but also the fact that for most calorimeters the intrinsic response to pions and to electrons are not the same. Since a typical hadronic shower contains a mixture of charged and neutral pions, this difference in response results in a worsening of resolution. In the past few years, much progress has been made in understanding the physics of calorimeter response. [20] By appropriately choosing the thickness of the absorber and active medium, large improvements in the hadronic resolution are possible. "Compensating Calorimeters" can now be designed with $\sigma_0 \sim 35\%$.

Tracking chambers are an essential ingredient of collider detectors, providing a necessary tool for lepton and photon identification. The high overall multiplicity in hadronic collisions means that tracking detectors must have good two track resolution and must provide high quality extrapolation to calorimeters and muon detectors. While a momentum measurement can aid in background rejection and is necessary for some physics studies (such as the measurement of jet fragmentation functions or the reconstruction of final state particles such as K^0's, D^0's, etc), it is not essential for a collider detector. Two of the four large collider detectors (UA2 and D0) have no magnetic field.

The large collider detectors all run with a number of triggers at the same time. A prescaled minimum bias trigger provides a representative sample nondiffractive events. Jet triggers select hard scattering events either by requiring a minimum Σ_{E_t} in the calorimeters or requiring a localized cluster of energy above a specified E_t. Electron triggers require an electromagnetic cluster with little hadronic energy behind it and often incorporate a tracking requirement as well. Muon triggers require a set of hits in the muon chamber that point back to the interaction region. Here again, a track requirement can also be imposed.

Figures 13 and 14 show the UA1 and UA2 detectors respectively. These detectors began operating at the CERN SPS in 1982. The initial center-of-mass energy was 546 GeV, with later running at 630 GeV. Data taking continued with these detectors through 1985, at which time both detectors began substantial upgrades which were intended to coincide with luminosity upgrades of the CERN collider. The upgraded UA2 detector is shown in Figures 15. Improvements include a substantial increase in the pseudorapidity coverage (the original detector covered only to $|\eta| \leq 1$) and the addition of transition radiation detectors, a vertex detector and a scintillating fiber detector to aid in electron identification. The improved capabilities of the UA2 detector will be discussed in Section 4.1.2. UA2 has been operating with their upgraded detector since 1987. The UA1 upgrade involved replacement of the hadronic calorimeter with a "compensating" Uranium-warm liquid calorimeter and is still underway. Figure 16 shows the CDF experiment which has been operating at the Fermilab Tevatron ($\sqrt{s} = 1.8$ TeV) since 1987. The D0 detector (Figure 17) will begin operation at Fermilab in 1991.

3 Jet Physics

Jet production is the dominant high p_t process at the CERN and Tevatron colliders. The study of such jet events allows high statistics tests of the QCD model of strong interactions. The basic assumption of these measurements is that observed jet cross sections and angular distributions closely follow those of the partonic processes. This assumption relies on our ability to define a prescription for finding jets that is both experimentally well defined and well matched to the theoretical calculation of interest.[22] There is no qualitative problem in finding jets in events with large transverse energy; these jets can be clearly seen in event displays. However, as we shall see below, there are numerous subtleties and ambiguities involved in quantifying the study of jets.

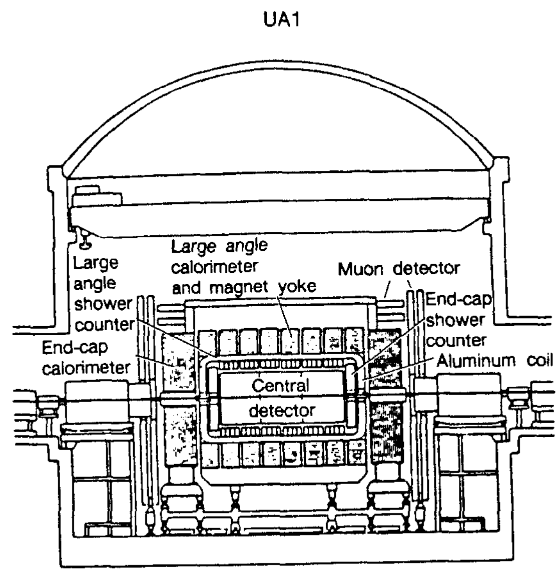

Figure 13: The UA1 detector.

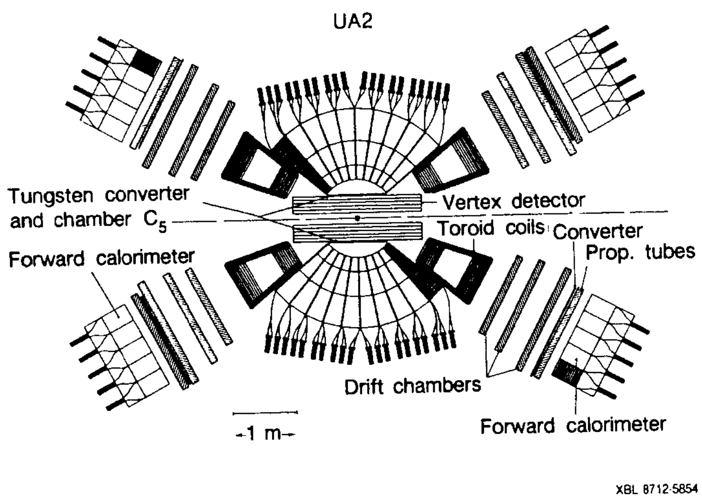

Figure 14: The UA2 detector.

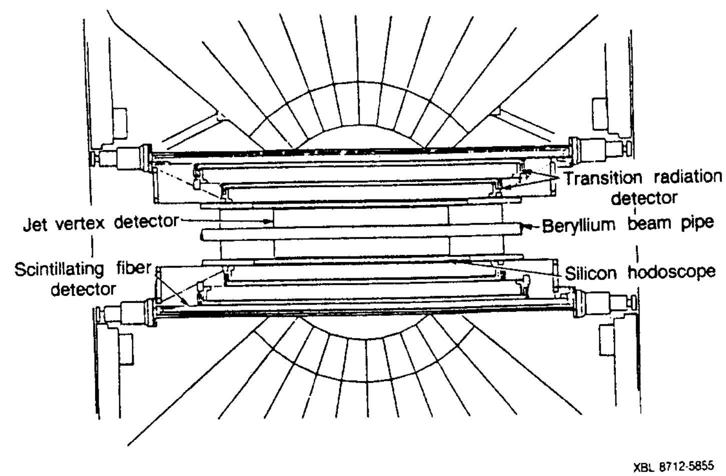

Figure 15: The upgraded UA2 detector.

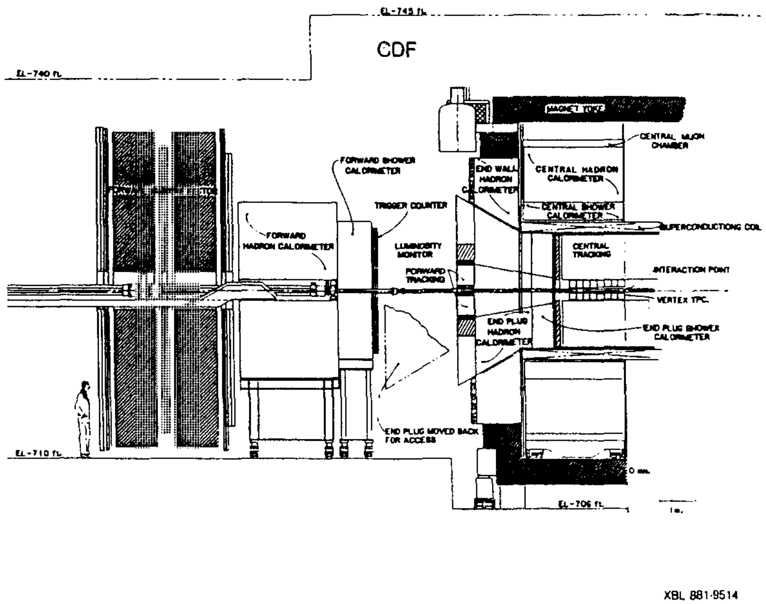

Figure 16: The CDF detector.

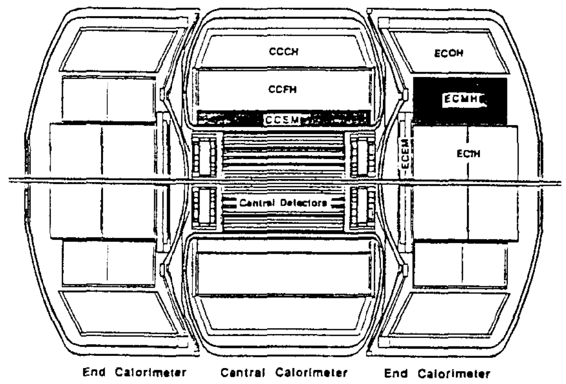

Figure 17: The D0 detector.

3.1 Cluster Finding and Jet Definition

A good jet finding algorithm must meet certain experimental and theoretical criteria. From the experimental standpoint this means that the algorithm must be easily evaluated in terms of quantities measured in the detector (E_t, η and ϕ), must be robust against fluctuations (caused by fragmentation effects, energy deposition from the underlying event or finite energy resolution), should be free of pathologies and should give stable results independent of event topology. On the theoretical side, the algorithm should be linear in energy (and therefore not sensitive to the details of fragmentation), should handle the merging of nearby jets in a straightforward manner and must provide a cluster position and energy that correlates well with the initial parton direction and energy.

We have seen in Section 1.3 that in the laboratory frame jets appear to be circles in η - ϕ space. Many cluster finding algorithms have been designed with this fact in mind. Let us take as a "typical" example, the CDF cluster finding algorithm. It is an iterative *fixed cone* algorithm that begins by looking for contiguous clumps of energy, called "pre-clusters," and then gathers all the energy within a fixed distance from these pre-clusters. The pre-clustering stage begins by combining contiguous towers with $E_t > 1$ GeV. This relatively high tower threshold is designed to eliminate clusters formed from fluctuations in the soft underlying event. Any pre-cluster with $E_t > 3$ GeV is considered a "seed" for the cluster finder. A circle in η - ϕ space is drawn around each seed. The radius of this circle is a parameter of the algorithm; the default radius is 0.7. Now, all towers inside the circle and with E_t above 100 MeV are included in the cluster. (Once a good seed has been found, a low tower threshold is used to allow the algorithm to gather the maximum fraction of the jet energy and therefore have the best possible energy resolution. The 100 MeV threshold is well above the electronic noise level for the calorimeters in CDF.) The position of each cluster is recalculated using the E_t weighted centroid of all towers in the cluster. A new circle is then drawn about the recalculated cluster position and the procedure is iterated until stable. If two clusters have more than 75% of their towers in common, the clusters are merged. When a tower is shared by two unmerged clusters, it is uniquely assigned to the cluster that is closest in η - ϕ space.

The energy and momentum of each cluster is determined using the following equations:

$$\begin{aligned} E_{\text{cluster}} &= \textstyle\sum_i E_i \\ E_{t\,\text{cluster}} &= \textstyle\sum_i E_i \sin\theta_{\text{centroid}} \\ \vec{p}_{\text{cluster}} &= \textstyle\sum_i E_i \hat{\mathbf{n}}_i \\ p_{t\,\text{cluster}} &= \sqrt{p^2_{x\,\text{cluster}} + p^2_{y\,\text{cluster}}} \end{aligned} \tag{17}$$

where the sums are taken over all towers in the cluster and where $\hat{\mathbf{n}}_i$ is a unit vector normal to the direction of tower i. Note that with the definitions above clusters have non-zero invariant mass, typically of order 10 GeV. One can think of this mass as the invariant mass of the parton produced in the hard scattering process along with all the soft "final state" gluons radiated from it.

The CDF group has studied the performance of this algorithm using both Monte Carlo data and real collider data. To understand the algorithm's pattern recognition efficiency, they have inserted jets from one event into the raw data from a second jet event and compared the results of the jet finder before and after the insertion. They have measured as a function of the η - ϕ separation of the initial clusters what fraction of the time the two clusters were merged by the algorithm and have also measured how much the cluster energy and position change for those cases where the two clusters are not merged. The results of this study show that the algorithm is quite well behaved. The fraction of clusters merged shows a sharp cutoff at a radius about 0.15 units outside the cone size used in the algorithm (see Figure 18). Clusters at smaller radii are almost always merged, while those at larger radii are almost never combined. When the clusters are not merged, the energy and position of the clusters do not change significantly from their original values. In 99% of the events, the change in measured E_t is less then 1 GeV. The efficiency of the algorithm has been studied using Monte Carlo data and has been verified using the recoil jets in direct photon events. Figure 19 shows the probability of finding a jet cluster as a function of the original parton p_t. The plot also shows how often a statistical fluctuation in the $p\bar{p}$ underlying event is misinterpreted as a "fake" jet as a function of the observed cluster p_t. Such studies indicate that jets can be found with high reliability if their transverse momentum is above 10-15 GeV/c.

While pattern recognition is a relatively straight-forward problem in jet physics, translating from observed jet energy to initial partonic energy is more problematic. Jet energy must be corrected for several effects, the most important of which are detector non-linearities, energy deposition from the underlying event and losses outside the clustering cone.

The UA1, UA2 and CDF detectors are not compensating calorimeters. Therefore, these detectors respond differently to electromagnetic energy from electrons,

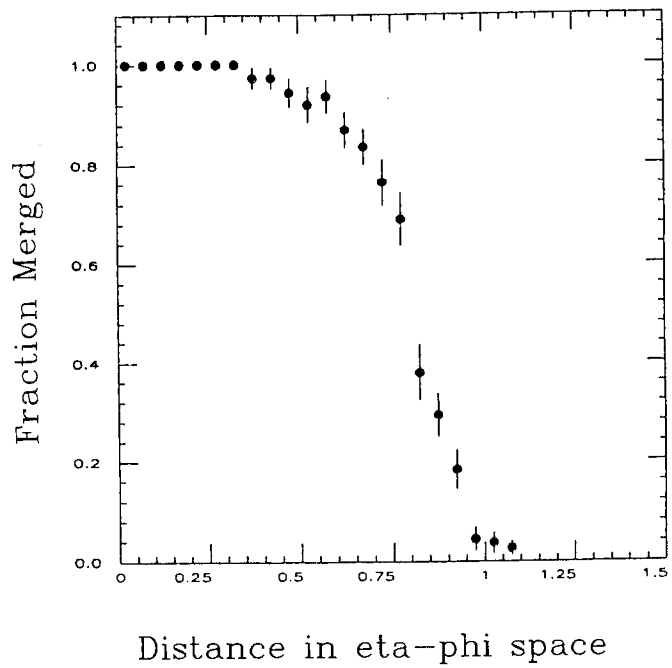

Figure 18: The probability that two jets separated by a distance $R = \sqrt{\Delta\eta^2 + \Delta\phi^2}$ will be merged by the CDF cluster finding algorithm as a function of R. This plot was made using jets in the range $25 < E_t < 35$ GeV.

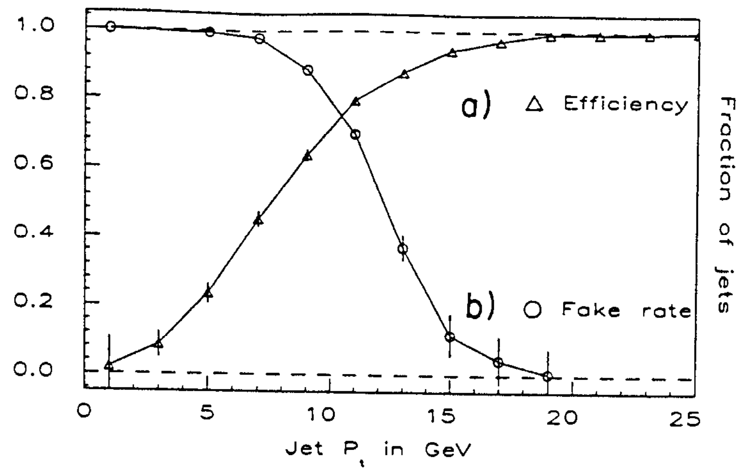

Figure 19: a) The efficiency for finding a jet cluster as a function of the original parton transverse momentum.
b) The probability that as "fake" cluster is created from a statistical fluctuation in the underlying event as a function of the cluster transverse momentum. Both plots are derived using the Isajet Monte Carlo.

photons and π^0's than to the hadronic energy from charged pions. At low momenta all three calorimeters exhibit substantial non-linearities in their response to charged pions. The size of this effect is shown in Figure 20, which plots the ratio of the observed calorimeter energy to the measured track momentum as a function of track momentum for the CDF central calorimeter. These non-linearities cause the observed jet energy to be systematically lower than the initial parton energy. This effect can, of course, be corrected *on average* if the charged particle momentum spectrum within the jets is known. The jet energy resolution is also degraded, however, due to event-to-event fluctuations in the shower development. These problems are expected to be reduced significantly for the next generation of detectors. D0, for example, has a Uranium-Liquid Argon calorimeter where the ratio of electron response to pion response is quite close to unity. This ratio is shown for a D0 test module in Figure 21.

In addition to the purely detector effects described above, there are physics effects that change the observed jet energy. These are the addition of energy from the underlying event and the loss of energy outside the cluster cone. The size of these effects can be seen in Figure 22. Here jet events are selected and are rotated in azimuth so that the highest energy jet is defined to be at $\phi = 0°$. The transverse energy in the event is then plotted as a function of ϕ. Since the cross section is dominated by dijet events, two high E_t peaks are observed at $\phi = 0°$ and $\phi = 180°$. The flat energy distribution between these jets represents the mean contribution from particles from the underlying event. Using these data, we estimate a mean energy deposit of about 1 GeV per unit rapidity per radian. This figure also demonstrates the effect of energy loss outside the fixed cone used by the cluster finder . The results indicate that for a cone size of 0.7, an energy of about 2 GeV is lost outside the jet cone. Studies by both the CDF and UA1 groups have shown that neither the underlying event energy or the energy loss outside the cone have significant dependence upon the observed jet E_t.

All collider detectors currently in operation must correct the observed cluster energy using a map that depends on p_t and η. The size of the correction varies with jet p_t, both because the detector non-linearities are most important in the low p_t region and because the cluster and underlying event corrections (in GeV) are independent of jet p_t. Typical systematic uncertainty associated with this correction (and the contributions to this uncertainty) are summarized in Figure 23.

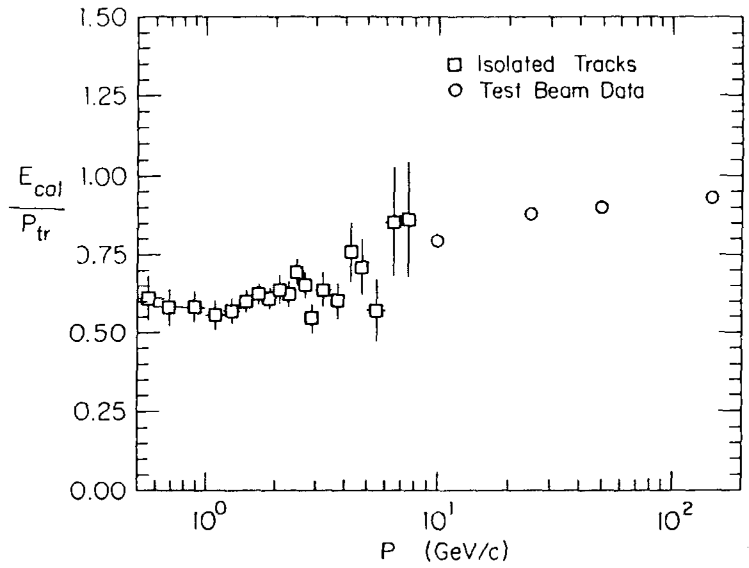

Figure 20: The ratio of the observed energy in the calorimeter to the measured track momentum as a function of track momentum for isolated tracks in minimum bias events, as measure by CDF. The plot show a substantial non-linearity at low energy.

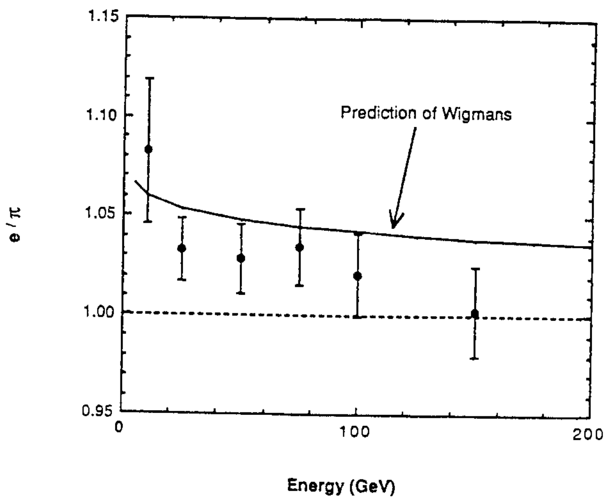

Figure 21: The ratio of the pion response to the electron response for the D0 calorimeter as a function of incident energy. The data points were measured in a test beam. The curve is a prediction of the model of Wigmans *et. al.*

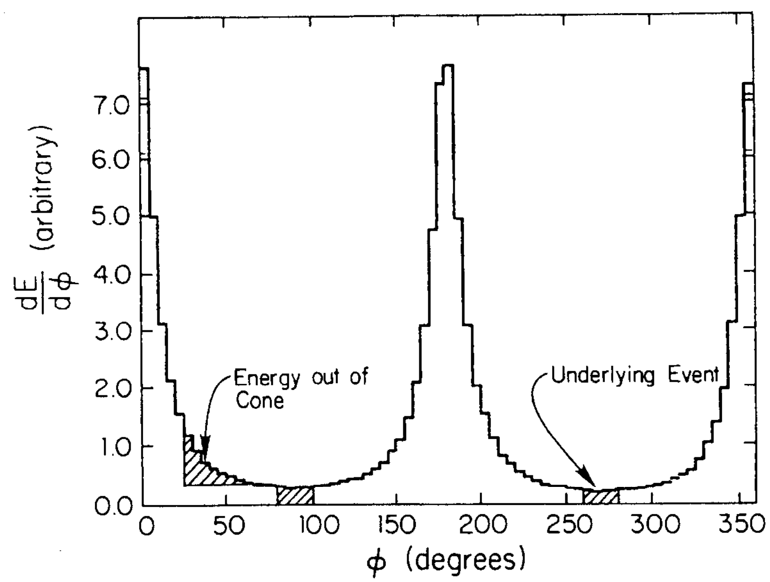

Figure 22: The distribution of energy in jet events as a function of ϕ, the azimuthal position with respect to the leading jet axis. The two peaks at $\phi = 0°$ and $\phi = 180°$ result from the dominant two jet structure. The flat region between the jets indicates the mean energy flow due to the underlying event.

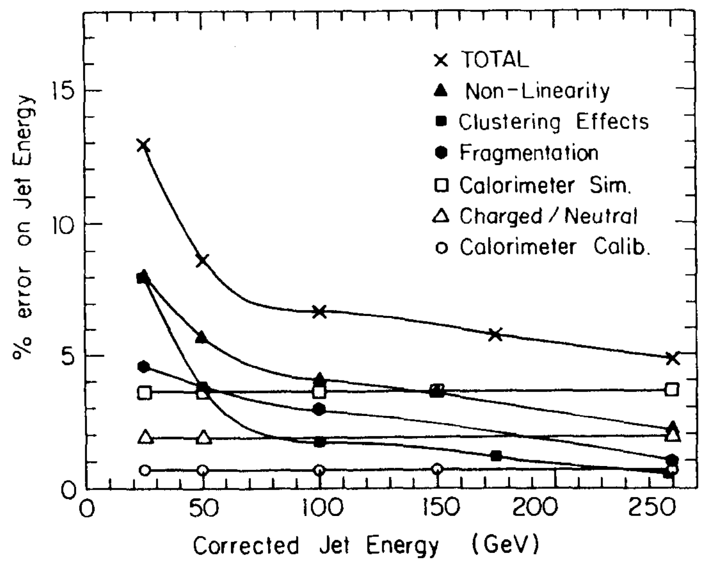

Figure 23: The contributions to the systematic uncertainty in jet energy scale as a function of jet E_t. The size of the overall uncertainty varies from 15% to 5% as a function of transverse energy.

3.2 The Single Jet Cross Section and Compositeness Limits

At all values of p_t, the jet cross section is dominated by the t-channel exchange of a gluon. Because the matrix elements for all the dominant diagrams are similar, the relative rates of quark-quark, quark-gluon and gluon-gluon scattering are determined by the structure functions and by color factors. A low $\hat{s}$ gluon scattering dominates, while quark diagrams become important at high $\hat{s}$.

The similarity of the t-channel matrix elements allows us to write the jet cross section using a *single effective subprocess approximation* [23]:

$$\frac{d\sigma}{dp_t dy_1 dy_2} = F(x_A)F(x_B)\sigma_{\hat{s}ES}(AB \to 1,2) \tag{18}$$

where

$$F(x) = G(x) + \frac{4}{9}\Sigma_{i=1}^{6}(Q_i(X) + \overline{Q}_i(x)). \tag{19}$$

UA1 and UA2 have extracted $F(x)$ using inclusive jet data and have compared the resulting values to QCD predictions. The results of such a comparison are shown in Figure 24 and demonstrate that the jet cross section at low x cannot be explained by quark-antiquark scattering alone but is in good agreement with the full QCD calculation. This plot give clear evidence for the non-Abelian nature of QCD and the existence of a three gluon coupling.

Figure 25 shows the inclusive jet cross section measured by the CDF collaboration. The error bars plotted on the data points include both statistical errors and that portion of the systematic uncertainty that is depends on E_t. In addition, an overall normalization uncertainty is shown as a separate error bar. The curves shown with the data represent the predictions of leading order QCD with a variety of structure functions and a range of scales ($p_t/2 > \mu > 2p_t$) for evaluation of the strong coupling constant. Both the overall rate and the shape of the curve are in good agreement with theory.

The measurement of $d\sigma_{\rm Jet}/dE_t$ can be used to study models of quark compositeness. If quarks are made of more fundamental objects, their strong coupling will be modified to include a form factor:

$$\mathcal{F}(Q^2) = (1 + Q^2/\Lambda_c^2)^{-1}. \tag{20}$$

Picking a simple assumption of color-singlet isoscalar exchange between left-handed quarks [9], the Lagrangian for this interaction is:

$$\mathcal{L} = \pm\frac{g^2}{2\Lambda_c^2}(\overline{u}_L\gamma^\mu u_L + \overline{d}_L\gamma^\mu d_l)(\overline{u}_L\gamma_\mu u_L + \overline{d}_L\gamma_\mu d_l) \tag{21}$$

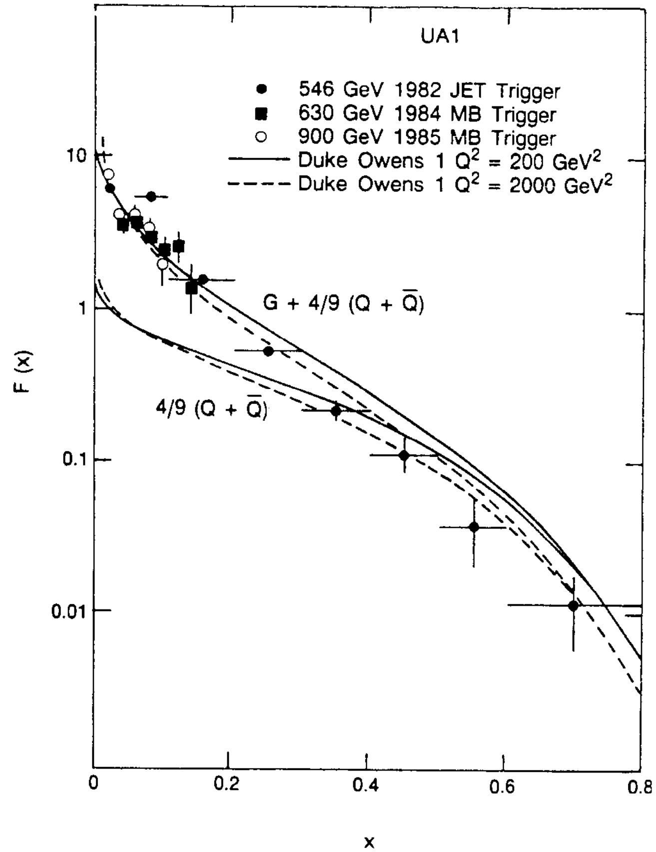

Figure 24: The effective structure function as measured by the UA1 experiment. The curves show the QCD predictions at two values of scale, with and without the gluon contribution.

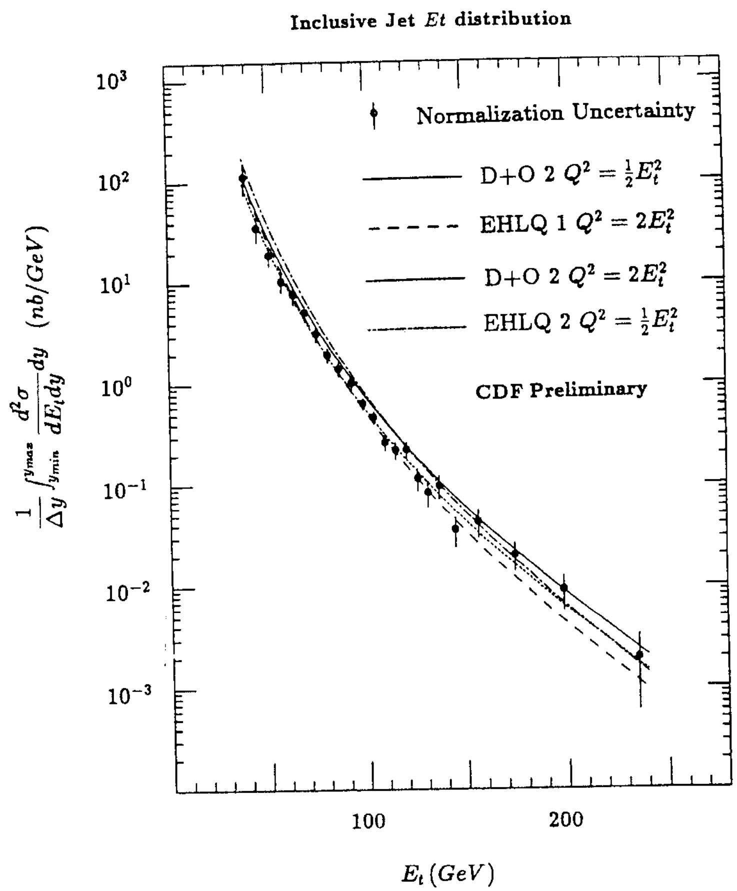

Figure 25: The single jet inclusive cross section as a function of jet E_t. The curves show the predicted QCD rate for several of structure function parameterizations and for several choices of scale in the evaluation of α_s.

where $g^2/4\pi \equiv 1$. For energies far below Λ_c, this term acts like an effective four Fermi interaction. The inclusive cross section will contain a term that is independent of $\hat{s}$, causing a flattening of the cross section as a function of E_t, *ie.* an excess of events in the high E_t region.

Figure 26 shows a preliminary measurement of $d\sigma/dE_t$ from the CDF experiment along with the predictions of QCD and predictions for the composite model described above with values of Λ_c set to be 700 GeV and 1000 GeV. Although a compositeness limit has not yet been set using this data, it is clear that values of Λ_c below about a TeV are excluded. Published results from an earlier and much smaller data set yielded a 95% confidence level limit of 695 GeV.[24]

3.3 Two Jet Angular Distribution

The majority of hard scattering events contain two back-to-back jets. This di-jet system can be described in terms of of 6 independent variables, three boost variables that transform to the hard scattering center-of-mass (β_x, β_y and β_z) plus three other variables (measured in the center-of-mass): $\hat{s}$, the invariant mass of the hard scattering system, ϕ the azimuthal position of one of the jets and $\cos\theta^*$, the scattering angle of one of the jets with respect to the beamline. The distributions in two of these six variables, β_z and $\hat{s}$, are determined by the structure function distributions in the proton. A third variable, ϕ shows no dynamical structure for unpolarized beams.

The transverse boosts β_x and β_y result from higher order QCD processes. These boosts are often described by the phrase "intrinsic k_t" and are caused by the emission of additional gluons during the hard scattering process. In all collider experiments, the observed dijet k_t results from two sources, the intrinsic k_t caused by gluon emission and experimental effects such as finite energy resolution. The UA2 group has developed a technique for separating these effects. Dijet events are selected and the k_t vector is decomposed into components along and perpendicular to the bisector of the p_t vectors of the two jets (see Figure 27a). The k_{t_ξ} component, which is perpendicular to the bisector, is dominated by detector resolution. The k_{t_η}, which is parallel to the bisector, is dominated by QCD effects. Figures 27b and c show that these two components are well modeled by a Monte Carlo that generates intrinsic k_t with a distribution of the form $dN/dk_t^2 = e^{-\alpha k_t^2}$ and then reproduces the expected energy and angular resolution of the calorimetry. The mean value of k_t is about 5 GeV.

Because there is a t-channel pole in the cross section, $\cos\theta^*$ follows a Rutherford-

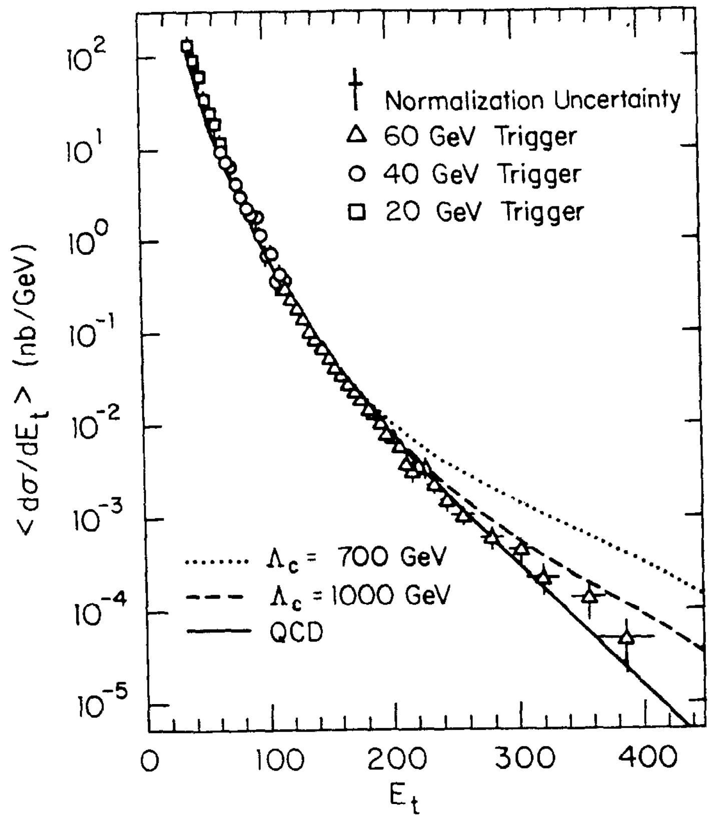

Figure 26: The inclusive cross section from 1.4 pb^{-1} of CDF data. The predictions of QCD (Duke and Owens, set II structure functions with $Q^2 = 0.5E_t^2$ and QCD modified by compositeness terms with $\Lambda_c = 0.7$ TeV and 7.0 TeV.

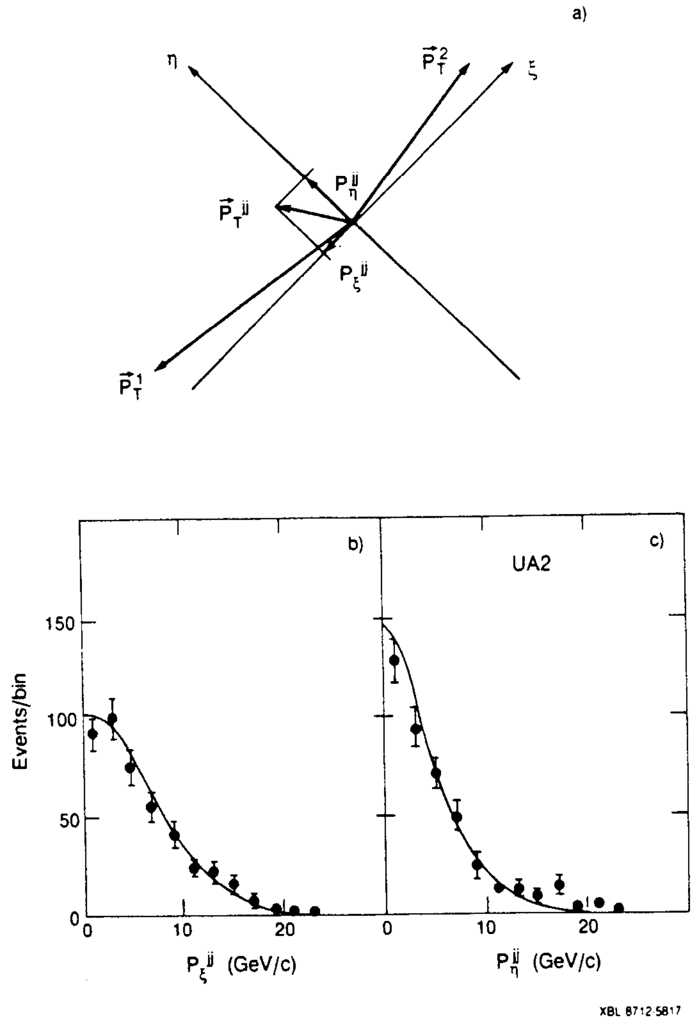

Figure 27: a) The coordinate system UA2 used to define k_t for a dijet system. b) The k_{t_ξ} and c) k_{t_η} components as measured by UA2 for dijets. The curves are the results of a Monte Carlo calculation using a mean intrinsic k_t of 5 GeV.

like shape:

$$\frac{d\sigma}{d\cos\theta^*} \sim \alpha_s^2(\mu)\,\hat{s}\,\frac{1}{1-\cos^2\theta^*}. \tag{22}$$

This shape is the angular distribution expected for a fixed cutoff in parton invariant mass and for a fixed range in the boost parameter β_z. The experimentally observed variables in a 2 jet system, however, are η_1 and η_2, the pseudorapidities of the two jets and p_t, the transverse momentum of one of the jets (the two balance transverse momentum in the center-of-mass). It is, of course, possible to express these experimentally accessible variables in terms of the orthogonal variables of the theory:

$$\begin{array}{llll} \eta_{\rm boost} & \equiv -\ln\beta_z & = & \frac{1}{2}(\eta_1+\eta_2) \\ \eta^* & \equiv \frac{1}{2}(\eta_1-\eta_2) & & \\ \hat{s} & \equiv \mathrm{M_{jj}} & = & 2p_t\cosh\eta^*. \end{array} \tag{23}$$

Note that η^* is related to the scattering angle in the center-of-mass by the equation

$$\cos\theta^* = \tanh\eta^* \tag{24}$$

The method used to measure $\cos\theta^*$ is to pick a set of cuts that gives uniform coverage in $\eta_{\rm boost}$ and $\hat{s}$ space for a given range in η^*. This insures that the acceptance corrections are small and not highly dependent on the $\eta_{\rm boost}$ and $\hat{s}$ spectra.[25] Figure 28 shows the measured $\cos\theta^*$ distribution as measured by UA1.

3.4 Three Jet Angular Distributions

The production of three jet events is common at collider energies. These events result when a hard gluon is produced via initial or final state bremsstrahlung.[26] The three jet fraction is a strong function of the minimum p_t cut on the third jet, but typically 20% of all jet events show a third jet.

The scattering of three massless partons can be described by nine independent variables. As in the two jet case, there are 3 boost variables (β_x, β_y and β_z). The distribution of energy in the center-of-mass is described by three internal variables: $\hat{s}$, the invariant mass of the three jet system, and x_3 and x_4, the energy fractions of the leading and sub-leading jet. In addition, the orientation of the three jet system can be described by three Euler-like angles: θ^*, the angle between the leading jet and the beamline, ϕ^*, the azimuthal position of the leading jet, and ψ^*, the angle of rotation about the leading jet axis (ψ^* is the angle between the plane formed by the leading jet and the beam line and the plane formed by the two subleading jets). The angular distribution in ϕ is flat, but the ψ^* distribution

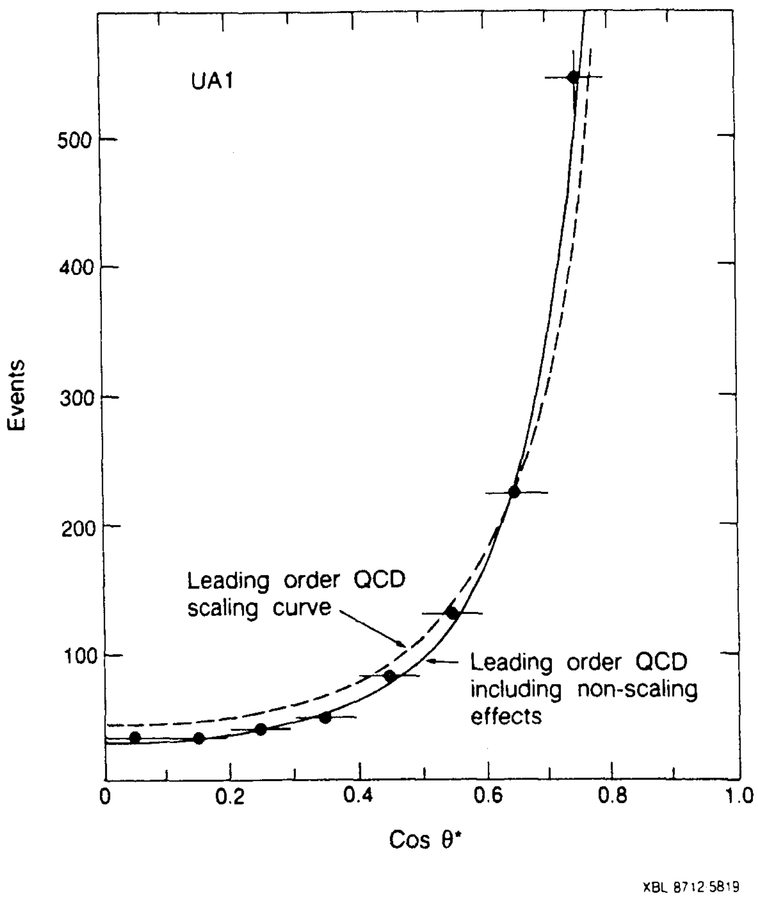

Figure 28: The distribution of $\cos\theta^*$ for two jet events as measured by the UA1 collaboration. Cos(θ^*) is the jet scattering angle with respect to the beamline in the center-of-mass of the dijet system. The curve shows the predictions of a lowest order $2 \to 2$ QCD calculation.

peaks at 0° and 180°. This structure is the result of singularities in the cross section for radiation being emitted along the beamline. (The regions of ψ^* near 0° and 180° are also experimentally difficult to measure because the p_t of the softest jet decreases rapidly as the three jet system is rotated into a configuration where the three jets are planar with the beamline.)

Because the structure of two and three jet events are so similar, we expect the scattering angle of the *leading* jet (the highest energy jet in the center-of-mass frame) to have a distribution that is similar to the two jet distribution described above. Figure 29 shows the comparison as measured by the UA2 collaboration. As expected, the shape for both 2 and 3 jet final states is dominated by the t-channel pole.

Figure 30 shows the distributions of the variables $x3$ and $x4$ as measured by the CDF experiment. The solid lines show the shapes these distributions would have in a phase space model, while the diamonds show the predictions of a QCD calculation. For both variables, QCD provides a good description of the data while significant deviations from the phase space model are seen. These plots indicate that three jet events result from a bremsstrahlung process.

4 Electroweak Physics

A thorough study of the standard model requires measurement of the production or scattering cross sections for all known gauge bosons. Thus, in addition to study jets, it is essential to identify W and Z bosons (typically through their leptonic decays) and photons. The dominant background for lepton and photon events is the tail of the large jet signal. Typically, rejection factors of 10^5 are necessary. Such factors are best obtained by combining calorimetric and tracking information and by using physics-dependent kinematic and topological cuts. In these lectures, we will give several examples of how such rejections are obtained.

4.1 Lepton Identification

At current collider energies, leptons from the decay of bottom quarks are produced with low to moderate p_t; even leptons from W's and from Z's have transverse momenta much lower than the typical QCD jets that we study. One of the challenges in hadron colliders is to study leptons over the widest possible range of p_t. The large jet production cross section forces the experimenter to reject the majority of background events at the trigger level. In CDF, for example, the electron trigger had a threshold of $p_t = 12$ GeV/c while the jet trigger threshold was $p_t = 60$

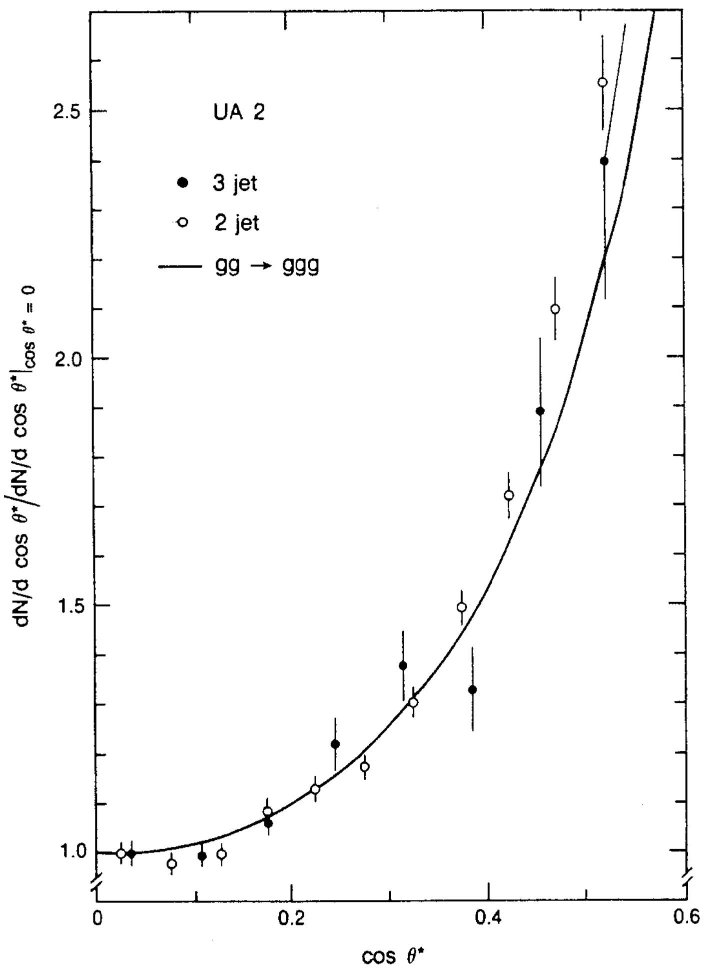

Figure 29: The distribution of the scattering angle relative to the beamline for the leading jet in 2 and 3 jet events, as measured by the UA2 collaboration. The curve is the expected distribution for the process $gg \rightarrow ggg$.

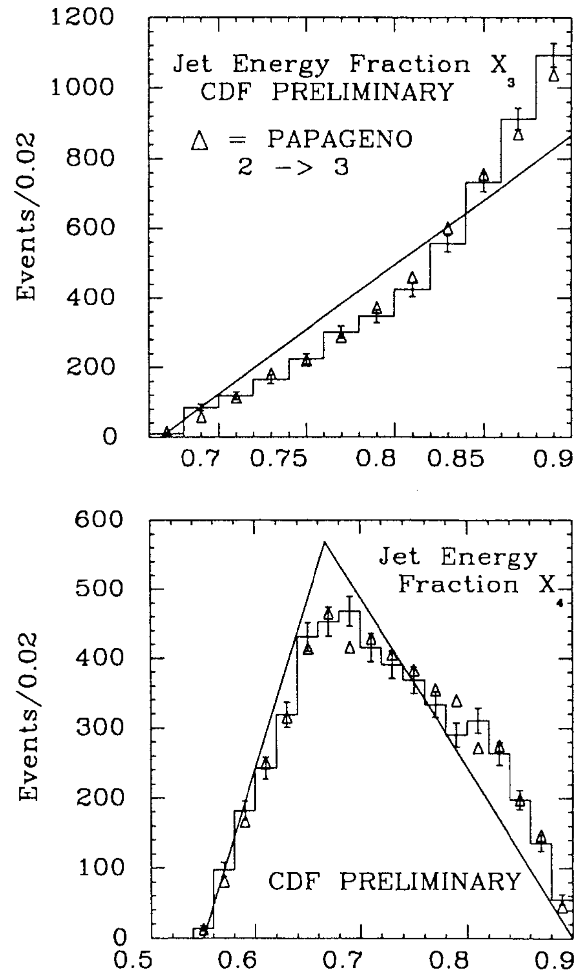

Figure 30: The distributions of the variables $x3$ and $x4$ as measured by CDF. The solid lines are the predictions of a phase space model while the diamonds show the QCD predictions.

GeV/c. For electrons, this rejection is typically done using a calorimetric trigger that requires a significant localized deposit of energy in the electromagnetic calorimeter with little leakage into the hadron compartment behind it. Further rejection can be obtained by requiring a stiff track point at the cluster. For muons, the technique is to require a track to pass through a large number of interaction lengths of iron without interacting. The dominant background in this case is pion and kaon decay in flight.

4.1.1 Electron Identification in a Magnetic Detector (CDF)

The CDF central electron trigger requires an electromagnetic energy deposit of $E_T > 12$ GeV within a "trigger tower" ($\delta\eta = 0.2, \delta\phi = 15°$) in association with a track of $p_t > 6$ GeV/c. Leakage into the hadron compartment of $< 10\%$ is also required in the trigger. This sample contains significant background from π^0-$\pi^\pm$ overlap, early showering charged pions and conversions and Dalitz pairs. These backgrounds are rejected in the following manner:

- Gas proportional chambers with cathode strip readout ("strip chambers") imbedded in the calorimeter near shower maximum provide an accurate measurement of the shower position. This position can be compared to the extrapolated track position (as measured using the Central Tracking Chamber).
- Events containing a single charged track and multiple π^0's are rejected by requiring the transverse spread of the electromagnetic cluster be consistent with that expected for an electron. The lateral shape is measured in the calorimeter by studying the fraction of the energy deposited in the towers surrounding that where the electron candidate hit. A measurement of this shape is also gotten from the strip chambers, where a χ^2 test to the electron hypothesis is made in both the wire and the strip projections.
- A requirement is made that the track momentum (p) and calorimeter energy deposit (E) be consistent (a typical cut is $E/p < 2$).
- Conversion electrons and Dalitz pairs are identified using the tracking chambers. The CDF algorithm is estimated to be 80% efficient at finding conversions.

The efficiency of the CDF cuts was measured using a sample of W electrons. The W candidates were selected by requiring an electromagnetic cluster and a missing transverse energy of at least 25 GeV. The high missing E_t requirement leads to a very pure signal; the background is estimated to be of order 1%. Figure 31 shows for this sample the following quantities:

1. Hadron leakage (E_{had}/E_{em}).
2. Transverse shower spread as measured using the calorimeter. The variable shown is proportional to the logarithm of the ratio of the observed to the expected energy outside the central tower where the electron hit.
3. The χ^2 distribution for an electron hypothesis, as measured using the cathode strips of the strip chambers.
4. The χ^2 distribution for an electron hypothesis, as measured using the anode wires of the strip chambers.
5. The match (in cm) between the $r\phi$ position measured in the strip chambers and that measured with the central tracking chamber.
6. The match (in cm) between the z position measured in the strip chambers and that measured with the central tracking chamber.

None of these quantities were used in the selection. The standard electron cuts used by CDF are indicated by arrows. Checks of these efficiencies using photon conversions indicate little momentum dependence for $E_t > 15GeV$.

All central calorimeter modules in CDF were calibrated in a high energy test beam. These calibrations were maintained *in situ* with radioactive sources and light flashers. However, the ultimate calibration of the electromagnetic detector was performed using the CDF data itself. First, the energy deposited in the calorimeter was compared to the momentum seen in the central tracking chamber for a large sample ($\approx$ 17,000) of low energy electrons. This E/p measurement was used to set the *relative* calibration of the individual calorimeter modules. Then, the overall energy scale was determined by requiring that the E/p as measured using electrons in $W \to e\nu$ events agree with the predictions of a simulation that includes radiative effects(see Figure 32).

4.1.2 Electron Identification in a non-Magnetic Detector (UA2)

The UA2 detector does not have a magnetic field and hence cannot use E/p as a tool for selecting electrons or for calibration. Nevertheless, the experiment has excellent electron identification. As in the magnetic detectors, the major

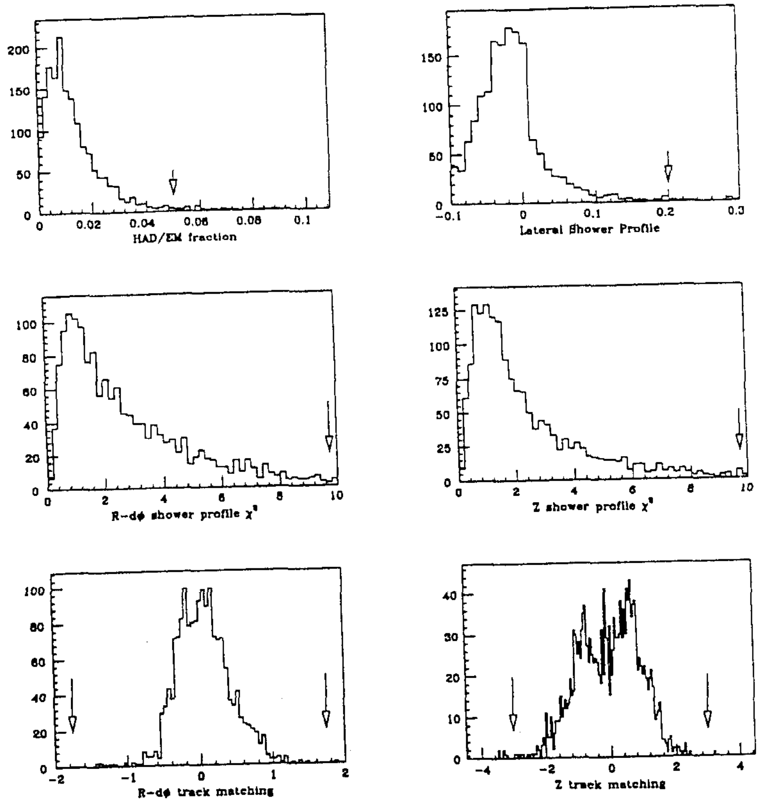

Figure 31: Electron properties for a sample of W electron candidates from CDF. The sample was selected using a missing E_t trigger. None of these quantities were used in the selection. The standard electron cuts used by CDF are indicated by arrows.

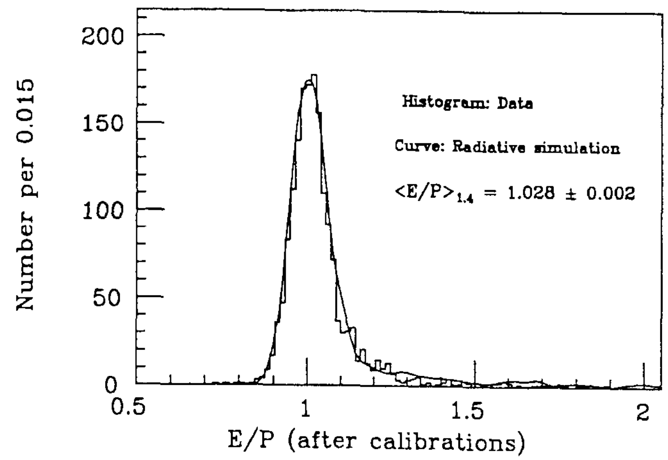

Figure 32: The E/p distribution for W decay electrons compared to a radiative simulation. These data were used to set the overall electromagnetic calorimeter scale for the CDF experiment.

methods for rejecting background are 1) requiring the electron candidate has both longitudinal and transverse shower development consistent with that expected for a single electromagnetic shower and 2) requiring a good matching between the position of the electromagnetic cluster and the extrapolated track position at the face of the calorimeter. In UA2's case this track position is measured using a preshower converter consisting of 1.5 radiation lengths of tungsten followed by a proportional chamber to provide finely segmented detection. Because no *in situ* calibration via E/p measurements is possible in UA2, the tracking and maintenance of test beam calibrations is essential for this experiment. UA2 has calibrated all of its calorimeter towers using 10 GeV electron, pion and muon test beams. The estimated scale error for the electromagnetic detector is $\pm1.5\%$ with module-to-module variations having a spread of $\pm2.5\%$.

The electron identification described above was sufficient for UA2 to cleanly select W and Z electrons. However, in an effort to improve the background rejection for lower energy and less isolated electrons from top and bottom, a major upgrade was performed. The remaining background to prompt high p_t electrons in the original UA2 consisted primarily of $\pi^0\pi^\pm$ overlaps and Dalitz decays and conversions. The upgraded UA2 has improved the background rejection by adding the following:

- A cylindrical drift chamber (Jet Vertex Detector). Its purpose is measure tracks close to the beam interaction point.
- A highly segmented silicon hodoscope. The hodoscope rejects conversion pairs by making a dE/dx measurement.
- A scintillating fiber detector (SFD). It provides a measurement of the track position immediately in front of the central calorimeter and SFD serves as a preshower counter.
- A transition radiation detector (TRD). This provides an independent method for separating electrons and pions.

Figure 33 shows a comparison of the charge (as measured in minimum ionizing units) observed in the SFD for test beam pions and electrons. Clearly, the two peaks are well separated. The additional background rejection due to the combination of all UA2 upgrades is about a factor of 20.

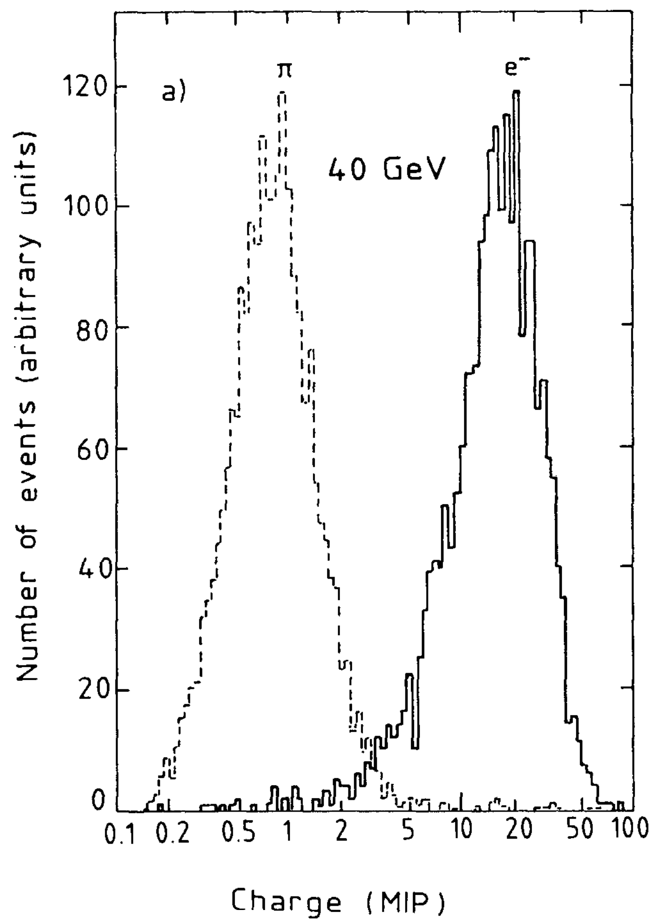

Figure 33: The preshower pulse height distribution of 40 GeV pions and 40 GeV electrons as measured with the UA2 SFD in a test beam.

4.2 Muon Identification (UA1)

Muons in the UA1 detector are measured using two sets of chambers separated by 60 cm. Each set contains planes of drift chambers and limited steamer tubes. The coverage is 70% of the full solid angle and the detector sits behind about 9 interaction lengths of iron.

The UA1 muon trigger requires a muon "stub" consisting of at least 3 out of 4 possible hits in the chamber. The stub must point back to the interaction region within a cone of ±150 mrad. The thickness of the absorber and the pointing requirement translate to an effective p_t cut of about 2 GeV on the muon trigger.

Muon candidates are selected by requiring a good match between the muon stub and a track measured in the central drift chamber. For isolated muons, a requirement that the energy deposited in the calorimeter be consistent with minimum ionizing deposition can also be applied. The major source of background in the UA1 muon sample is the decay of pions and kaons. The size of the background is quite dependent on the physics process being studied. The background goes down rapidly with p_t. In addition, since most hadrons are produced within jets, an *isolation* cut will significantly improve the signal to noise.

In both electron and muon channels, requiring isolation can provide additional background rejection *for certain physics signals.* When a lepton is produced in the decay of a heavy particle (in this context, heavy means that the particle's mass is large when compared to the mean production p_t), it will be spacially separated from the remaining decay products (see Figure 34). This is the case in W and Z decay and in the semileptionic decay of a heavy top quark. This is not the case for lighter particles; *eg.* the leptons produced in the decay of a b quark are likely to be non-isolated. Isolation is generally imposed on a leptonic signal by limited the amount of energy surrounding the lepton candidate, for example by placing a cut on the amount of energy depositied in a cone surrounding the lepton candidate.

4.3 Neutrino Identification

Electroweak decays often involve the production of neutinos. Since these particles cannot be detected directly, their presence must be inferred by the presence of a large momentum imbalance in the event. Since any realistic detector must by necessity have holes in the forward and backward region to allow the beam to enter and exit the apparatus, no detector is capable of measuring the energy flow in the beam direction. Instead, the technique for finding non-interacting neutral particles involves the search for large missing transverse momentum.

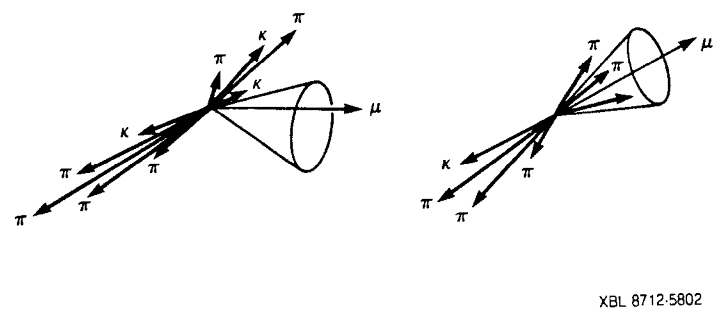

Figure 34: Examples of isolated and non-isolated muon signals.

Calorimetric detectors have the advantage that they are sensitive both to charged and to neutral particles. They therefore are the most satisfactory for missing momentum measurements. Because a calorimeter measures energy rather than momentum, the term "missing E_t" ($\not{E}_t$) is usually used to describe the magnitude of the missing transverse momentum. We define the missing transverse energy by the relation

$$\not{E}_t \equiv -\sum_i \vec{\mathrm{E}}_{t,i} = -\sum_i \mathrm{E}_{t,i}\hat{\mathrm{n}}_i \tag{25}$$

where the sum is over towers in the calorimeter and where $\hat{\mathrm{n}}_i$ is the normal to the tower center and is pointing outward. Similarly, the total transverse energy in the event is defined to be

$$\mathrm{E}_t \equiv \sum_i |\mathrm{E}_{t,i}| . \tag{26}$$

Figure 35 shows an event with large $\not{E}_t$. It is a candidate for the decay $W \to e\nu$. A high p_t electron is observed in the calorimeter. No other signal appears to balance the transverse momentum.

A missing E_t analysis is sensitive to all types of detector imperfections. The major background for $\not{E}_t$ analyses are mismeasurement of jet events due to finite detector resolution, loss of energy in cracks and loss of jets down the beamline. For both the UA1 and CDF experiments, and for the upgraded UA2 detector, mismeasured jets are the primary source ofmissing E_t.

For sampling calorimeters the resolution, in general, scales with the square root of the incident energy (see Equation 16). If the missing E_t resolution is dominated by calorimeter effects, then we would expect the fractional $\not{E}_t$ resolution to scale as $1/\sqrt{E_t}$. The UA1 group and later the CDF group have studied the $\not{E}_t$ resolution and have found that this form holds. They have therefore defined the "missing E_t significance" to be:

$$N_\sigma = \frac{\not{E}_t}{\sqrt{\Sigma E_t}} . \tag{27}$$

Figure 36 shows the distribution of missing E_t significance for jet events and for W candidates, as measured by CDF. There is a clear separation between the two. Typically, analyses that require a significant amount of missing transverse energy will require $N_\sigma > 3$.

4.4 W Production

Figure 37a shows the lowest order diagram for $W^\pm$ production at hadron colliders. The diagrams for producing a Z^0 in $p\bar{p}$ collisions are identical (except for the

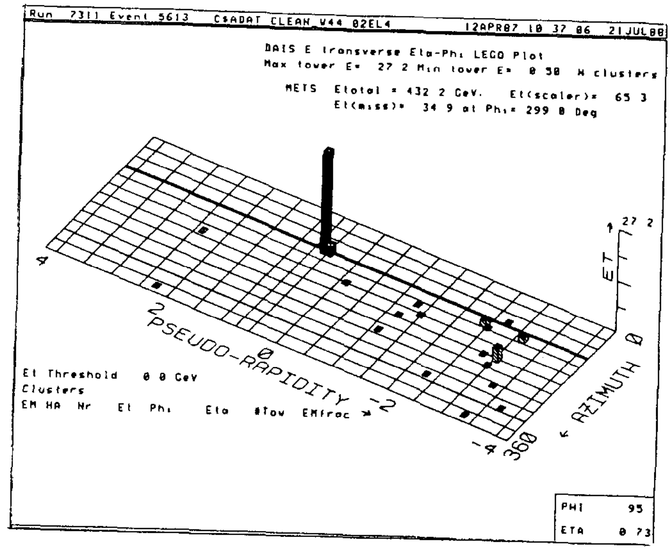

Figure 35: A W event as seen in the CDF detector.

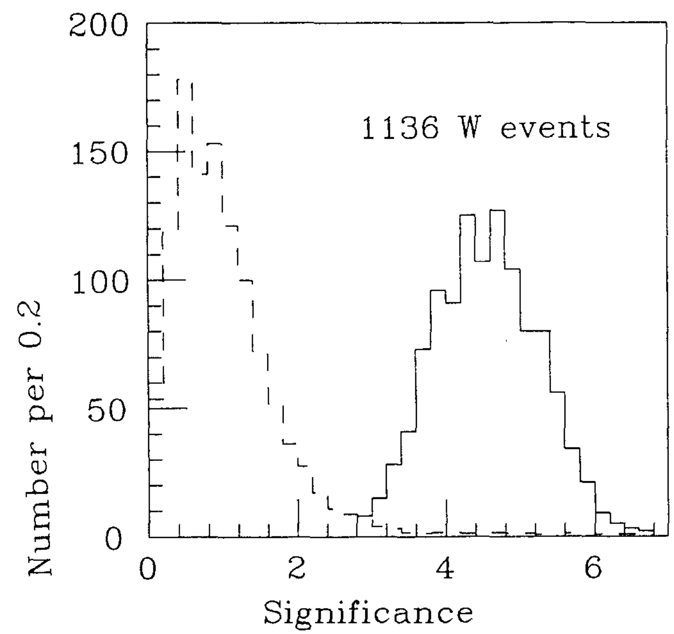

Figure 36: The distribution of the missing E_t significance N_σ for jet events and for W candidates as measured by CDF.

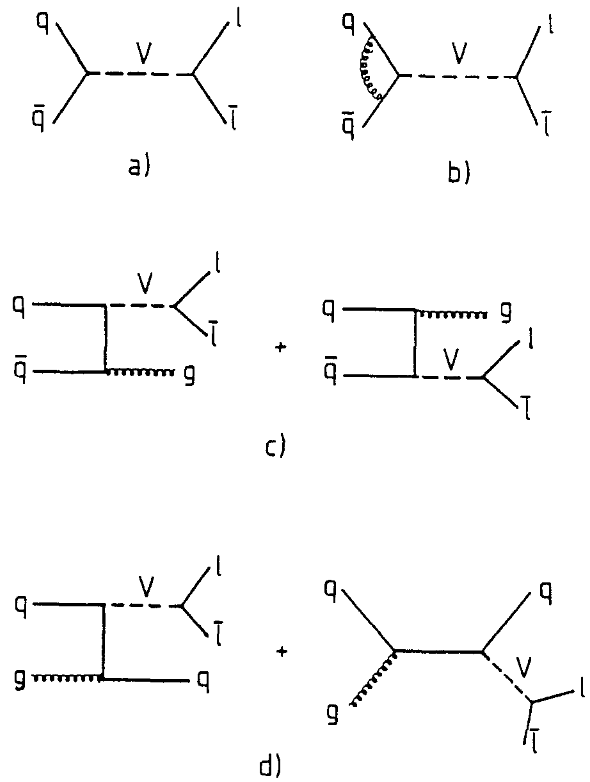

Figure 37: Feynman diagrams for vector boson (V) production. a)The lowest order Drell Yan diagram.
b) The next order virtual correction.
c) The QCD annihilation diagram with gluon radiation.
d) The QCD Compton process.

charges of the quarks involved) to those for W production. The W boson is produced via $q\bar{q}$ annihilation [27] and therefore to lowest order, has no transverse momentum. Thus, for W's that decay leptonically (*eg.* $W \to e\nu$) we find $\vec{p}_{t_e} = -\vec{p}_{t_\nu}$. This feature of W decays can be seen in Figure 38. Here, a clean W sample is selected by requiring both electron and neutrino transverse energies above 25 GeV. It can be seen from the plot that the electron and neutrino transverse energies are highly correlated.

The next to leading order calculation of the W production cross section (see Figure 37b) has been completed and has produced the following results [28]: The total cross section changes by an overall factor $K \cong 1 + \frac{8\pi}{9}\alpha_s(M_w^2)$. In addition, the W is no longer required to have zero p_t. A correct treatment of the transverse momentum spectrum for W's requires a non-perturbative treatment of multiple soft gluon emission, which is handled via resummation techniques.[29] The mean transverse momentum of the W is of order 10 GeV. Figure 39 shows the measured W production cross section at SPS and Tevatron energies. The hatched band shows the allowed range of theoretical predictions. The data at both center-of-mass energies are in good agreement with these predictions. Figure 40 shows the transverse momentum distribution of W candidates, as measured by the UA1 collaboration.[30] The thick curve show the QCD prediction (due to soft gluon resummation).[29] The thin line shows an extrapolation of this curve based on the ISAJET Monte Carlo.[31] Again, the agreement with theory is excellent.

The angular distribution of W decays is determined by helicity conservation and the spin 1 nature of the W (see Figure 41). For W^+ production, the e^+ is preferentially produced along the $\bar{d}$ direction and the angular distribution in the center-of-mass is:

$$\frac{d\sigma}{d\cos\theta} \sim \frac{\hat{s}(1+\cos\theta)^2}{(\hat{s}-M_w^2)^2 + (\Gamma_w M_W)^2} \tag{28}$$

where M_W and Γ_W are the mass and decay width of the W respectively. A transformation of variables allows us to find the electron p_t distribution (here we use the lowest order calculation where the W transverse momentum is constrained to be 0). In the center-of-mass frame, the e and ν are back-to-back and balance p_t. Then, $p_t^2 = \frac{1}{4}\hat{s}\sin\theta^2$. Changing variables from $\cos\theta$ to p_t, means evaluating the Jacobean

$$\frac{d\cos\theta}{dp_t^2} = -\frac{2}{\hat{s}}(1 - 4\frac{p_t^2}{\hat{s}})^{-\frac{1}{2}} = -\frac{2}{\hat{s}\cos\theta} \tag{29}$$

since

$$\frac{d\sigma}{d\cos\theta} = \frac{3}{8}\hat{\sigma}(1+\cos\theta)^2 \tag{30}$$

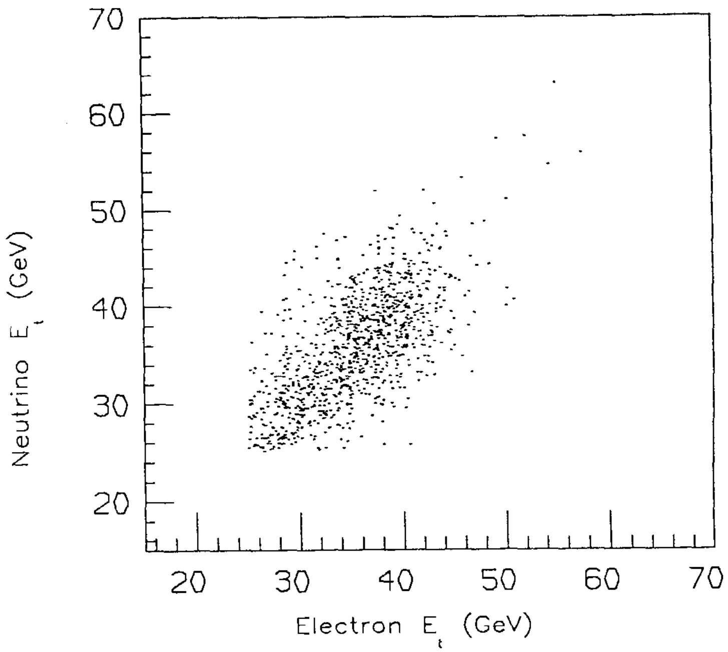

Figure 38: A scatter plot of $\not{E}_t$ as a function of electron E_t for all W candidates as measured by the CDF experiment.

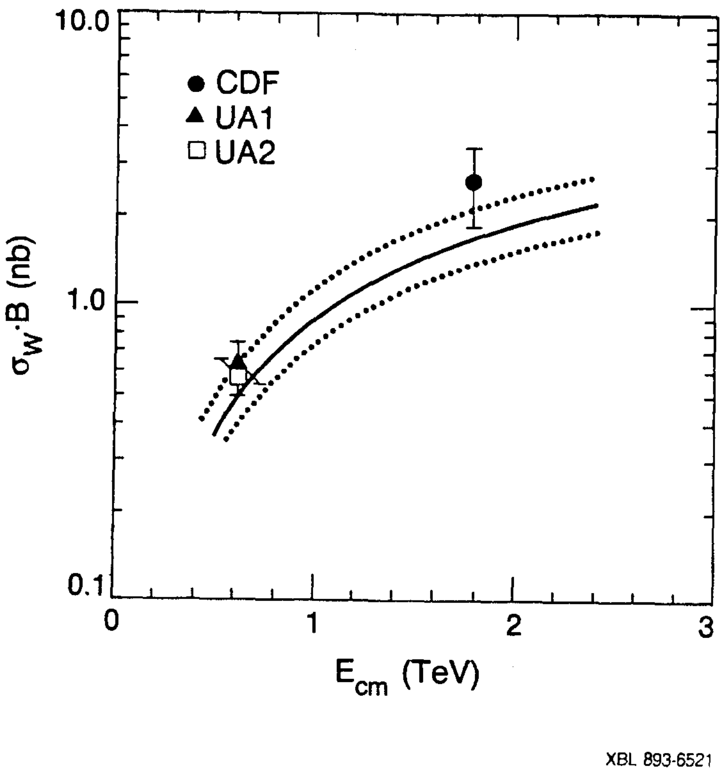

Figure 39: The product of the W production cross section times branching ratio to electrons as a function of center-of-mass energy. The hatched area shows the allowed range of theoretical predictions.

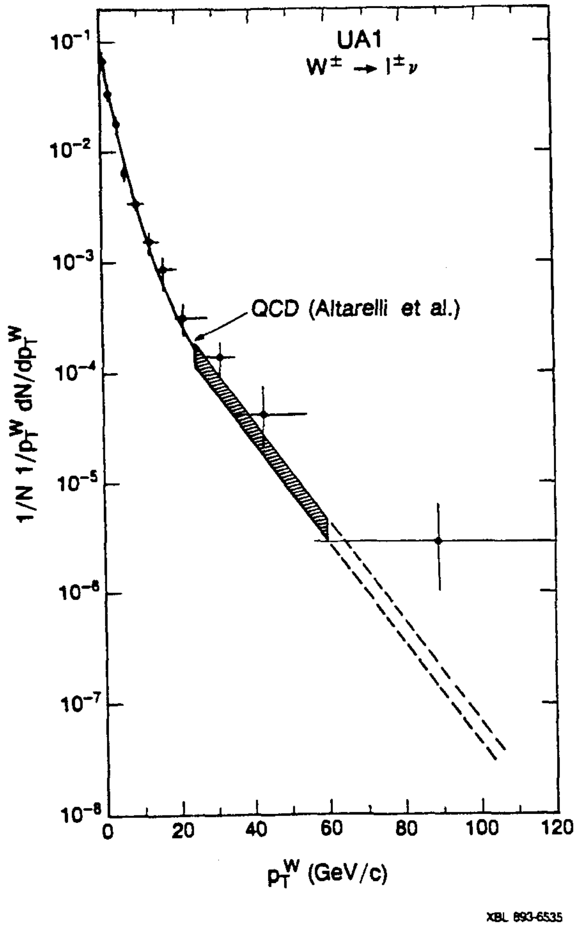

Figure 40: The W transverse momentum spectrum.

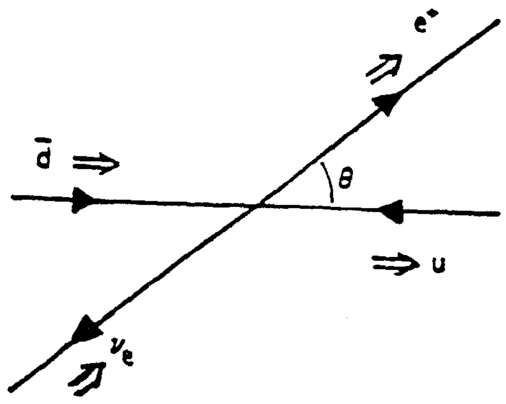

Figure 41: Figure showing how the angular decay of W bosons is affected by helicity conservation. A W^+ will preferentially decay along the $\bar{d}$ direction.

we can write

$$\frac{d\sigma}{dp_t^2} = \frac{3}{4}\frac{\hat{\sigma}}{\hat{s}}\frac{1+\cos^2\theta}{\cos\theta} = \frac{3}{2}\frac{\hat{\sigma}}{\hat{s}}\frac{1-2p_t^2/\hat{s}}{(1-4p_t^2/\hat{s})^{\frac{1}{2}}} \tag{31}$$

where the term linear in $\cos\theta$ cancels due to the fact that θ and $\pi-\theta$ contribute equally at any given p_t. Therefore, the electron p_t spectrum follows the form

$$\frac{d\sigma}{dp_t} \sim \frac{1+cos^2\theta}{\cos\theta} \sim \frac{1-2p_t^2/\hat{s}}{(1-4p_t^4/\hat{s})^{\frac{1}{2}}} \tag{32}$$

and the cross section diverges for $\theta = \pi/2$ (and $p_t = \sqrt{\hat{s}}/2$). This divergence results from the Jacobean factor and is called the *Jacobean Peak*. When Equation 32 is integrated over all values of $\hat{s}$, the presence of the Breit-Wigner removes the singularity but leaves a sharp peaking at $p_t = \sqrt{\hat{s}}/2$. Higher order diagrams give the W non-zero p_t and smear out this peak. In order to best determine the mass of the W, it is necessary to find a variable that is less sensitive to the smearing. The natural choice is the *transverse mass.*

If a W is produced with transverse momentum, this will affect both decay products equally. The $e\nu$ transverse mass is then defined to be

$$m_T^2 = (|p_{t_e}| + |p_{t_\nu}|)^2 - (\vec{p_{t_e}} + \vec{p_{t_\nu}})^2. \tag{33}$$

When p_t of the $W = 0$, we find $m_T = 2\,|p_{t_e}| = 2\,|p_{t_\nu}|$ and $d\sigma/dm_T^2 = 4d\sigma/dp_t^2$. The transverse mass depends on the p_t of the W only to order $(p_t/M_W)^2$, making it a more suitable variable for measuring M_W. Figure 42 shows the W transverse mass distribution as measured by CDF. When fitting for the W mass, CDF has chosen to select a clean W sample by requiring that the event have no additional clusters (in addition to the electron candidate) with $E_t > 7$ GeV. The curve is a fit to the data using a model that includes the predicted QCD cross section and angular distribution and the effect of finite detector resolution. The (preliminary) value of the mass obtained in this way is $m_w = 80.0 \pm .2 \pm .6$ where the first error is statistical and the second is systematic.

4.5 Z Production

The production of a Z with its subsequent decay into two leptons provides an extremely clean signal. Figure 43 shows the dilepton mass distribution for a) muons and b) electrons. The value of the mass obtained from combining these distributions is $90.9 \pm 0.3 \pm 0.2$ GeV where the first error is a combined statistical and systematic error, excluding overall energy scale, and the second reflects the uncertainty in the absolute calibration.[32] Although the accuracy obtained here

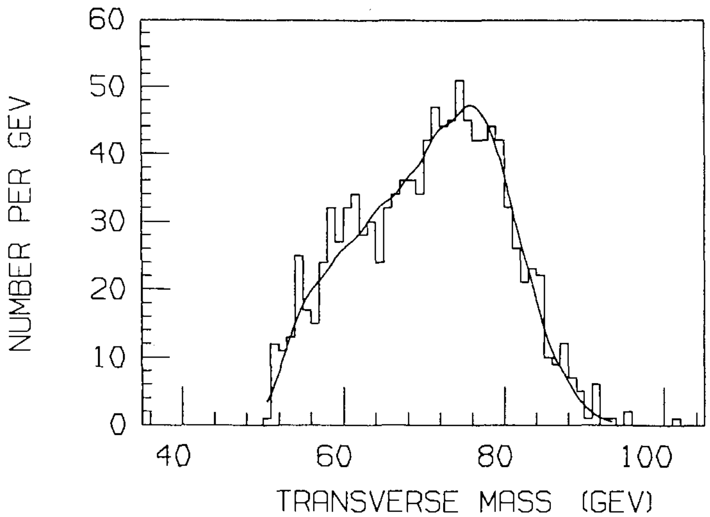

Figure 42: The W transverse mass distribution as measured by CDF. The sample used for this analysis required that the events contain no jets with E_t above 7 GeV.

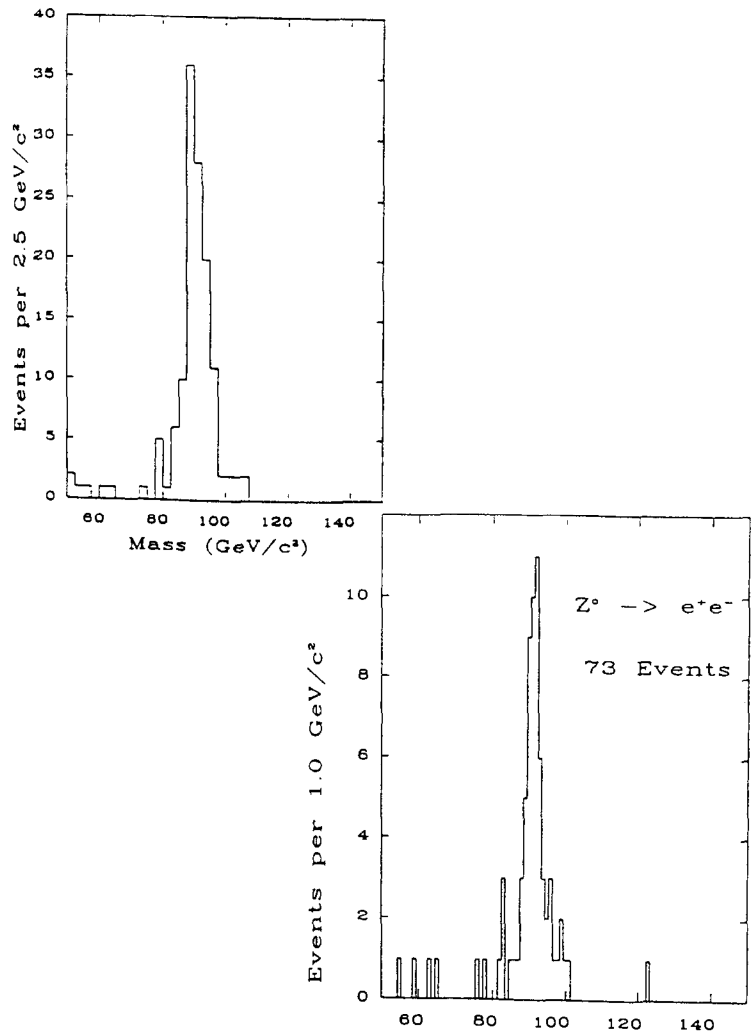

Figure 43: The Z mass peak as measured in a) muon and b) electron samples by the CDF collaboration.

is impressive for a hadron collider, the mass obtained in e^+e^- colliders is clearly much more precise. This measure therefore becomes an important calibration signal for the hadron machines.

5 Direct Photon Production

Figure 44 shows the lowest order diagrams that contribute to the production of an isolated direct photon. Because the gluon structure function peaks in the low x region where the cross section is largest, the diagram containing an initial gluon line dominates at collider energies. The annihilation term ($q\bar{q} \to \gamma g$) contributes only about 20% to the total cross section, while the Compton term ($qg \to \gamma q$) contributes 80% . Since the quark structure functions are known to much better precision than the gluon structure functions, the cross section for direct γ production (along with a set of quark structure functions) can in principle be used to measure the structure function of the gluon. In practice, theoretical uncertainties exists from two sources. First, although the next-to-leading order calculation has been done,[15] there is an overall uncertainty of about 30% in the cross section resulting from the dependence of the result on the scale μ used in the evaluation of α_s. Second, there is an additional source of photons, bremsstrahlung from an initial or final quark line. While these bremsstrahlung terms in general produce non-isolated photons (events where the γ is close to some hadronic energy), the overall production rate is large an the tails of this distribution are non-negligible. In spite of these uncertainties, the direct γ signal provides and interesting measurement that is sensitive to the gluon distribution in the proton.

At CDF, the direct photon sample is analyzed using pulse height information from a set of "strip chambers" imbedded in the central electromagnetic calorimeter modules. A multiwire proportional chamber with segmented cathode readout is located within each central calorimeter wedge at a longitudinal position corresponding to the maximum longitudinal energy deposition (shower maximum) for electromagnetic showers. The wires of the chamber sample the shower profile perpendicular to the beamline (x) while the cathode strips sample the shower along the beamline (z). In both directions, the sampling size is about 1.5 cm (the typical fwhm photon shower profile being 0.6 cm). The signal from an isolated photon will appear as a narrow peak in the x and z views and the energy in these two views will match.The conversion of a π^0 will usually appear as a single, wider peak since the opening angle is in general smaller than the two cluster resolution of the chamber.

The general strategy used to measure $d\sigma/dp_t$ for direct photon production

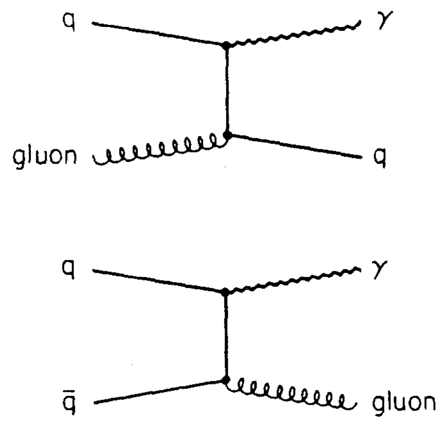

Figure 44: The lowest order QCD diagrams for production of an isolated high p_t photon.

is to search the central calorimeter for isolated electromagnetic clusters with *no* tracks pointing at them and to then statistically separate π^0 and γ signals using the pulse height information in the strip chambers. The strip chamber data is used to form a χ^2 indicating the probability that a given cluster is consistent with the shape expected for a single shower. The transverse shape used in this analysis was determined from test beam analysis of electron signals and has been verified using W and Z candidates. The expected shape for π^0 clusters is determined by combining superposed test beam electron showers. A good fraction of the "π^0" sample so produced has a large χ^2 when tested against a photon hypothesis. Figure 45 shows the efficiency for having a χ^2 value of less than 4 for both γ and π^0 events as a function of the transverse energy of the electromagnetic cluster. A statistical separation between π^0 and γ can be successfully used for photons with transverse momenta of less than 40 to 50 GeV. Above this momentum, the ability to separate the signals is not adequate. (The analysis presented here assumes the the background consists exclusively of π^0's. Work is currently under way to evaluate the effects of η^0 and multiple π^0 production on the systematic uncertainties in this measurement.)

The UA2 experiment uses a completely different technique to find direct photons.[33] Here, photons are separated for π^0 and η decays statistically using a method based on the probability of conversion in a 1.5 radiation length preradiator that proceeds the electromagnetic calorimeter. The conversion probability ϵ_γ is calculated as a function of photon momentum using the EGS Monte Carlo and these calculations are checked against electron test beam data. The conversion probability for a π^0 can then be expressed

$$\epsilon_\pi = 1 - \frac{1-\epsilon_{\gamma_1}}{1-\epsilon_{\gamma_2}} \tag{34}$$

and the fraction of direct photon candidates can be written

$$f_\gamma = \frac{\epsilon_\pi - \alpha}{\epsilon_\pi - \epsilon_\gamma} \tag{35}$$

where α is the fraction of photon candidates where a conversion has occurred in the preradiator. The advantage of this method is that it is reliable even at large p_t, unlike the CDF technique which looses resolving power once the two photons from the π^0 begin to merge.

The direct photon cross sections for UA2 and for CDF are shown in Figure 46. The error bars include both statistical and systematic uncertainties. The shape of the QCD curves represent the prediction of the lowest order calculation; these curves have been normalized to agree with the UA2 data. The "K-factor" needed

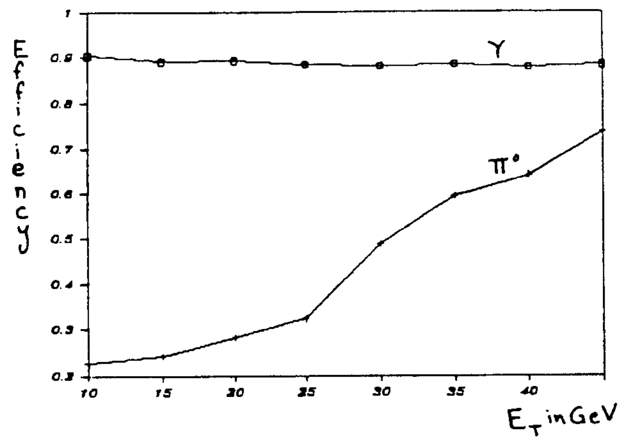

Figure 45: The efficiency for having a χ^2 value of less than 4 for both γ and π^0 candidates as a function of the transverse energy of the electromagnetic cluster for the CDF detector.

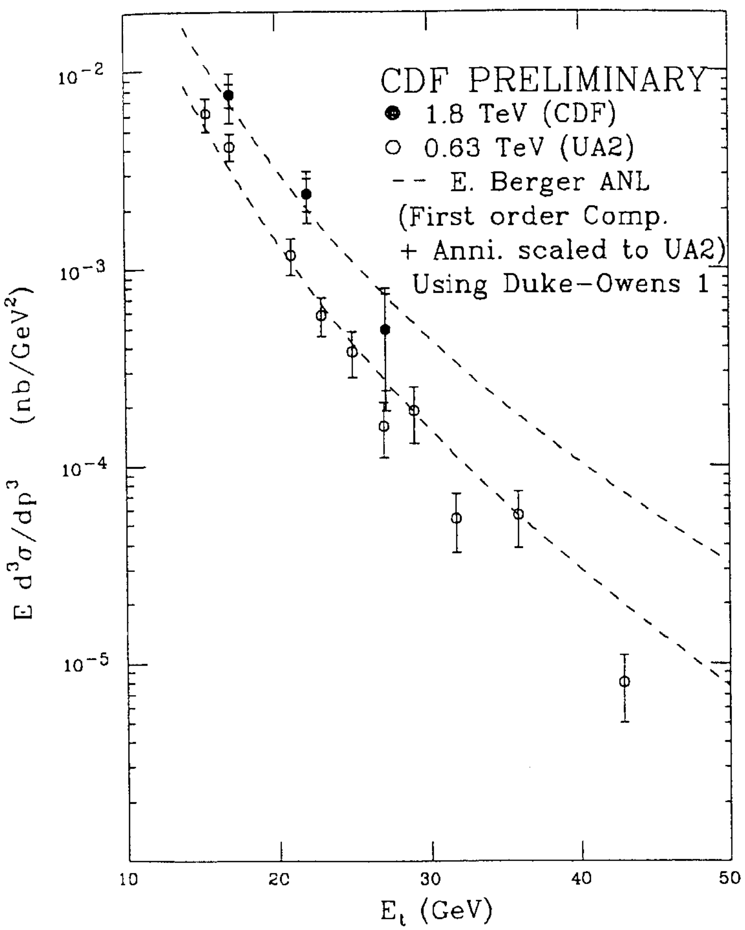

Figure 46: The invariant cross section for direct γ production as a function of the p_t of the photon. Data from the UA2 collaboration/citeUA2-photon is plotted as well. The curve shows the prediction of a lowest order QCD calculation, normalized to agree with the UA2 data.

for this normalization is in reasonable agreement with next-to-leading order calculations.

6 Conclusions

QCD provides an excellent description of the production cross sections for quarks, gluons and electoweak bosons. The agreement between theory and experiment extends over many orders of magnitude. The success of the Standard Model allows us to reliably predict backgrounds for more exotic process.

References

[1] V.A. Abramovskii, O.V. Kanchelli and V.N. Gribov in Proc. 16^{th} International Conference on High Energy Physics, FNAL (1983), Vol 1, p. 363.

[2] For a review of the QCD parton a model see G. Altarelli *Phys. Rev.* **81C**, 1 (1982).

[3] C.G. Alner *et al.*, *Phys. Rev.* **154**, 247 (1987).

[4] F. Abe *et al.*, *Phys. Rev. Lett.* **61**, 1819 (1988).

[5] G. Arnison *et al.* *Phys. Lett.* **118B**, 167 (1982).

[6] B. Alper *et al.* *Nucl. Phys.* **B87**, 19 (1975).

[7] D. Anreasyan *et al*, *Phys. Rev.* **D19**, 764 (1979).

[8] G. Altarelli and G. Parisi, *Nucl. Phys.* **B126**, 298 (1977).

[9] E. Eichten *et al.*, *Rev. Mod. Phys.* **56**, 579 (1984).

[10] D. Duke and J. Owens *Phys. Rev.* **D30**, 49 (1984).

[11] A.D. Martin, R.G. Roberts and J. Stirling, *Phys. Rev.* **D37**, 1161 (1988).

[12] M. Diemoz, F. Ferroni, E. Longo, and G. Martinelli, CERN-TH-4757 (1987).

[13] For a more detailed review of structure function parameterizations, see I. Hinchliffe and M. Shapiro, *Report of the QCD Working Group* in DPF Summer Study on High Energy Physics in the 1990's, Snowmass, Colorado, July 1988.

[14] G. Altarelli, *et al.*, *Nucl. Phys.* **B143**, 521 (1978), Erratum *Nucl. Phys.* **B146**, 544 (1978).

[15] P. Aurenche, R. Baier, A. Douiri and D. Schiff, *Phys. Lett.* **169B**, 441 (1986), *Phys. Lett.* **140B**, 87 (1984).

[16] S. Dawson, R. K. Ellis and P. Nason, *Nucl. Phys.* **B303**, 607 (1988).

[17] R.K. Ellis and J.C. Sexton, *Nucl. Phys.* **B269**, 445 (1986).

[18] S. Ellis, Z. Kunszt and D. Soper.

[19] R. Schwitters, 1983 SLAC Summer Institute, SLAC Report no 267 p. 115.

[20] R. Wigmans, CERN EF 86-18, submitted to NIM;
Bruckmann, DESY 86-155, Pisa meeting.

[21] Bengtsson and Åkesson, Paris 1982;
Bengtsson and Åkesson, Phys. Lett. **120B**, 233 (1983).

[22] For a discussion of the issues involved in jet definition, see I. Hinchliffe and M. Shapiro, *Report of the QCD Working Group* in DPF Summer Study on High Energy Physics in the 1990's, Snowmass (1988).

[23] See, for example J.F. Owens *Rev. Mod. Phys.* **59**, 465 (1987).

[24] Abe *et al.*, *Phys. Rev. Lett.* **62**, 612 (1989).

[25] UA1 Collaboration: Phys. Lett. **158B**, 494 (1985);
F. Ceradini, *Proceedings of the XXIII International Conference on High Energy Physics*, 16-23 July 1986, Berkeley, California, S. Loken, ed. (World Scientific, Singapore, 1987), Vol. II, p. 1051.

[26] F. A. Berends, *et al.*, *Phys. Lett.* **103B**, 124 (1982).

[27] Y. Yamaguchi, *Nuovo Cim.* **43A**, 193 (1966); S.D. Drell and T.M. Yan, *Phys. Rev. Lett.* **25**, 316 (1970).

[28] G. Altarelli, K. Ellis, M. Greco and G. Martinelli, *Nucl. Phys.* **B246**, 12 (1984); G. Altarelli, K. Ellis and G. Martinelli, *Zeit. fur Physik* **C27**, 617 (1985).

[29] Altarelli, *et al.*, *Nucl. Phys.* **B157**, 461 (1979).

[30] Albajar, *et al.*, CERN-EP/88-168 (1988).

[31] F. Paige and S. Protopopescu, in Proc. of 1986 Snowmass Summer Study on the Physics of the SSC, Ed. R. Donaldson FNAL (1987).

[32] Abe *et al*, *Phys. Rev. Lett.* **63**, 720 (1989).

[33] Costantini, *et al.* 7^{th} *Topical Workshop on Proton-Antiproton Collider Physics*, (World Scientific, Singapore, 1987), page 345.

Applications of QCD to Hadron-Hadron Collisions: Theoretical. *

Ian Hinchliffe
Lawrence Berkeley Laboratory
University of California
Berkeley, California 94720

Abstract

I discuss some current problems associated with the applications of QCD to event rates in high energy collisions. Emphasis is given to the current ambiguities and uncertainties that exist in estimates of signals and backgrounds.

1 Introduction

In these lectures, I shall provide an introduction to perturbative QCD and its uses in calculating rates at hadron-hadron colliders. Since QCD processes account for most of the background for new physics at such colliders, it is important to understand the uncertainties in these predicted rates. Given the limited time available I have had to be selective in the topics discussed.† I will begin with a discussion of the one parameter of QCD, namely, its coupling constant. I shall then discuss the parton model in some detail. After a discussion of the appropriate kinematical variables I shall discuss the uncertainties and ambiguities inherent in QCD calculations. I shall then discuss some aspects of jet physics and will end with a discussion of underlying (minimum bias) events.

2 QCD and the parton model

The QCD Lagrangian may be written as follows:

$$-\frac{1}{4}F^i_{\mu\nu}F^i_{\mu\nu}+\sum_j\bar{\psi}_j(i\not{D}-m_j)\psi_j. \tag{1}$$

The sum on j runs over quark flavors and,

$$F^i_{\mu\nu}=\partial_\mu G^i_\mu-\partial_\nu G^i_\mu-igf_{ijk}G^j_\mu G^k_\mu \tag{2}$$

*This work was supported by the Director, Office of Energy Research, Office of High Energy and Nuclear Physics, Division of High Energy Physics of the U.S. Department of Energy under Contract DE-AC03-76SF00098.

†For a more detailed discussion see ref. [1]

and

$$D_\mu = \partial_\mu - ig\, t^i\, G^i_\mu\,. \tag{3}$$

Here t^i are the 3×3 representation matrices and the structure constants f_{ijk} are given by $[t_i, t_j] = i f_{ijk} t_k$.

Apart from the quark masses, which have their origin in the Weinberg-Salam model of weak interactions, the theory has only one fundamental parameter, the coupling constant g. It is this coupling constant that provides us with an expansion parameter. If calculations are undertaken beyond the leading order in the coupling constant, ultra-violet divergences are encountered. These divergences must be regulated and reabsorbed into the fundamental parameters of the theory, *i.e.* the theory must be renormalized and a renormalized coupling constant defined. The easiest scheme for regulating and defining a coupling constant is the modified minimal subtraction scheme ($\overline{MS}$) [2]. The ultra violet divergences are regulated by calculating with the theory in n dimensions [3].

In order to understand the procedure, let us calculate a physical process $P(Q^2)$, which depends on some energy scale Q; P could, for example, represent a cross-section. It is convenient to choose the quantity P to be dimensionless; this can always be done by multiplying it by an appropriate power of Q. If we neglect quark masses, calculate in n dimensions then

$$P(Q^2) \sim \left[\frac{2A}{4-n} - A\gamma_E + A\log 4\pi - F(\mu, Q^2, g)\right]. \tag{4}$$

Here A is some constant and F a function that is finite when $n = 4$. The scale μ is introduced so that the coupling constant g remains dimensionless in n dimensions, *viz.*,

$$g \to g\mu^{(4-n)/2}\,. \tag{5}$$

The ultra-violet divergences appear as singularities at $n = 4$. The $\overline{MS}$ scheme is defined by removing the terms of the form $1/(n-4)$, γ_E and $\log 4\pi$. Then P has the form

$$P(Q^2) = F(Q^2/\mu^2, \alpha)\,. \tag{6}$$

I have replaced g by α: $\alpha \equiv g^2/4\pi$ and the coupling constant is now in the $\overline{MS}$ scheme. The scale μ is arbitrary so that a physical quantity cannot depend upon its value

$$\frac{dP}{d\mu} = 0 \tag{7}$$

which implies

$$\left(\mu^2 \frac{\partial F}{\partial \mu^2} + \beta(\alpha)\frac{\partial F}{\partial \alpha}\right) = 0\,. \tag{8}$$

Here $\beta(\alpha)$ is defined by

$$\beta(\alpha) \equiv \mu^2 \frac{\partial \alpha}{\partial \mu^2}\,. \tag{9}$$

We can introduce a momentum-dependent coupling $\alpha(t)$ via

$$t \equiv \int_\alpha^{\alpha(t)} \frac{dp}{\beta(p)} \tag{10}$$

where $t = \log(Q^2/\mu^2)$. Then Equation 8 has the solution

$$F(t, \alpha) = F(1, \alpha(t))\,. \tag{11}$$

Hence the only dependence on the scale Q or t is carried by $\alpha(t)$. We can expand β as a power series in α.

$$\beta = -b\frac{\alpha}{4\pi} - b'\left(\frac{\alpha}{4\pi}\right)^2 + \ldots \tag{12}$$

Hence $\alpha(\mu^2)$ has the following form:

$$\alpha(\mu^2) = \frac{4\pi}{b\log(\mu^2/\Lambda^2)} + \ldots \tag{13}$$

Here $b = 11 - 2n_f/3$ where n_f is the number of quark flavors with mass less than μ. We can regard the fundamental parameter of QCD either as $\alpha(Q_0^2)$ or as the scale Λ. Notice that as μ becomes small, α becomes large. Therefore, perturbation theory cannot be used to discuss processes which involve momentum flows as small as a few times Λ.

Other renormalization schemes are possible, for example one could not subtract the γ_E and $\log 4\pi$ terms. A physical quantity is, of course, independent of the renormalization scheme. However, if the perturbation series is terminated at some finite order in the coupling constant, the values of P (P_N) calculated to this order in two difference schemes will differ

$$P_N(\bar{\alpha}) \neq P_N(\alpha) = P_N(\bar{\alpha}) + 0(\alpha^{N+1})\,. \tag{14}$$

Since the coupling constant of QCD is not very small and most processes are not known to a very high order, these differences can be significant.

As a specific example of QCD process, consider the total cross-section for $e^+e^- \to$ hadrons at center-of-mass energy $\sqrt{s}$. In the one photon approximation (see Figure 1) this is given by

$$\sigma_{had} = \frac{8\pi\alpha_{em}^2}{3s^2} \sum_n (2\pi)^4 \delta(q - q_n) \langle 0|j_\mu|n\rangle \langle n|j_\mu|0\rangle \tag{15}$$

where j_μ is the electromagnetic current of the quarks

$$j_\mu = \sum_i e_i \bar{\psi}_i \gamma_\mu \psi_i. \tag{16}$$

If we introduce the photon self-energy function $\Pi^{\mu\nu}$

$$\Pi_{\mu\nu}(q) = i \int d^4x e^{iqx} \langle 0 \,| T(j_\mu(x) j_\nu(0)) |\, 0 \rangle. \tag{17}$$

Defining $\Pi_{\mu,\nu}(q) = (g_{\mu,\nu}q^2 - q_\mu q_\nu) = \Pi(Q^2)$ then

$$\sigma_{had} = \frac{16\pi^2 \alpha_{em}^2}{s} Im\, \Pi(s). \tag{18}$$

A dimensionless quantity is $R(s)$ defined by

$$R(s) = \frac{\sigma_{had}}{\sigma(e^- e^+ \to \mu^+ \mu^-)} \ . \tag{19}$$

The previous argument implies that $R = R(\alpha(s))$. If we calculate R using perturbation theory we get

$$R = \sum e_i^2 \left(1 + \frac{\alpha_s}{\pi} + B\left(\frac{\alpha_s}{\pi}\right)^2 \ldots\right) \tag{20}$$

where the sum runs over all quarks (electric charge e_i) of mass less than $\sqrt{s}/2$ and B is a scheme-dependent constant which is small in the $\overline{MS}$ scheme [4].

In order to discuss processes which involve hadrons in the initial state, we must discuss the parton model. Consider the case of electron-proton scattering, where the cross-section can be written as

$$\frac{d\sigma}{dxdy} = \frac{4\pi\alpha_{em}^2 s}{Q^4}\left[\frac{1+(1-y)^2}{2} 2xF_1(x,Q^2) + (1-y)(F_2(x,Q^2) - 2xF_1(x,Q^2))\right] \tag{21}$$

The variables are defined as follows (see Figure 2): q is the momentum of the exchanged photon and P is the momentum of the target proton and k is that of the incoming electron

$$\begin{aligned} Q^2 &= -q^2 \\ \nu &= \tfrac{q \cdot P}{m_p} \\ x &= \tfrac{Q^2}{2m_p\nu} \\ y &= \tfrac{q \cdot p}{k \cdot p} \\ s &= 2p\cdot k + m_p^2 \end{aligned} \tag{22}$$

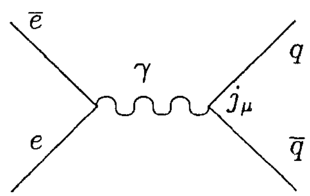

Figure 1: Feynman graph for $e^+e^- \to$ hadrons.

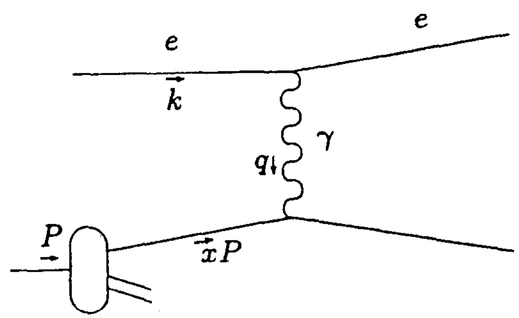

Figure 2: Diagram illustrating the variables in deep inelastic scattering (see Equation 21): electron + proton → electron + anything.

where m_p is the proton mass. I have neglected parity violating effects which arise from the exchange of a Z boson instead of a photon.

In the naive parton model the proton is viewed as being made up of a set of non-interacting partons. The structure functions F_1 and F_2 are related to the probability distribution $q_i(x)$ which represents the probability of finding a parton of type i (quark or gluon) inside the proton with fraction x of the proton's momentum, and the scattering cross-section for such a virtual photon from a parton:

$$F_1 = \frac{F_2}{2x} = \sum_i \int_x^1 \frac{dy}{y} q_i(y)[e_i^2 \delta(x/y - 1)] \tag{23}$$

where e_i is the charge of parton of type i. The δ-function appears from the cross-section for $q + \gamma \to q$ and corresponds to the constraint that the massless quark in the final state is on mass-shell. Let us consider QCD corrections to this scattering. At next order in α_s, there are contributions from gluon emission which lead to the final state $q + g$ and also from virtual gluons (see Figure 3). To order α_s Equation 23 is replaced by

$$F_1 = \sum_i \int_x^1 \frac{dy}{y} q_i(y) \left[e_i^2 \delta\left(\frac{x}{y} - 1\right) + \sigma_i\left(\frac{x}{y}, Q^2\right)\right] \tag{24}$$

with

$$\sigma_i(z, Q^2) = \frac{\alpha_s}{2\pi} e_i^2 \left[t P_{qq}(z) + f(z) + 0\left(\frac{1}{Q^2}\right)\right] \tag{25}$$

and

$$P_{qq}(z) = \frac{4}{3} \frac{(1+z^2)}{1-z} \tag{26}$$

for $z \neq 1$. Here $t = \log(Q^2/\mu^2)$ and the scale μ has appeared from dimensional regularization (I have dropped terms proportional to $1/(n-4)$). The μ dependence arises because σ_i is not finite in four dimensions. In the cases discussed previously, the divergences arose from large momentum flows inside loop diagrams (ultra-violet divergences). In this case these divergences cancel. Individual Feynman diagrams can also have divergences when momentum flows become very small or particles are collinear. The former (soft) divergences cancel between the real and the virtual diagrams but the collinear ones do not. It is these divergences that appear as singularities in the calculation of F_1 and are responsible for the μ dependence in Equation 25. In order to see the origin of the problem consider the graph of Figure 3 and work in a frame where $k_\mu = (k, k, 0, 0)$.

If the transverse momentum of the gluon (p) relative to k is small then we can take $p = (\eta k + k_\perp^2/2\eta k,\ \eta k,\ k_\perp\ 0)$. (Terms of order $k_\perp^2$ are neglected.) The internal quark line now has invariant mass squared $r^2 = (k-p)^2 = k_\perp^2/\eta$, so that

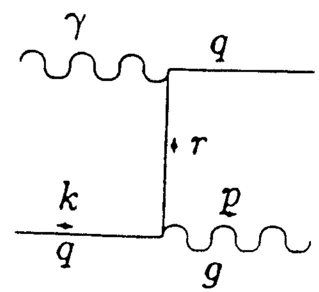

Figure 3: Diagram contributing to the process $q + \gamma \to X$ at order α_s.

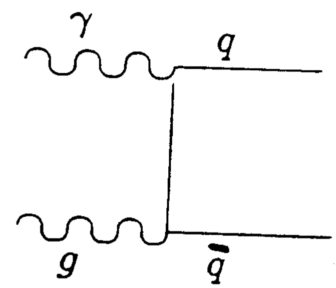

Figure 4: Diagram showing $g + \gamma \to q + \bar{q}$.

the squared amplitude from the graph will contain $1/k_\perp^4$. Now, at very small $k_\perp$ helicity conservation forbids the emission of a real gluon from a quark line, so that one factor of $k_\perp^2$ appears in the numerator. We now have for the total cross-section $q + \gamma \to q +$ anything, a contribution

$$\sigma \sim \frac{\alpha_s}{2\pi} \int \frac{dk_\perp^2}{k_\perp^2} \tag{27}$$

which gives rise to a logarithmic singularity. Notice that for a massive quark the singularity becomes $\log(Q^2/m_q^2)$.

We have obtained a result which depends on μ (or contains the large $\log(Q^2/m_q^2)$ if quark masses are retained). This is not physically meaningful. But Equation 24 contains the unknown quantity $q_i(y)$. We can define

$$q_i(x,t) = q_i(x) + \frac{\alpha_s t}{2\pi} \int_x^1 \frac{dy}{y} q(y) P_{qq}\left(\frac{x}{y}\right). \tag{28}$$

Hence

$$F_1 = \sum_i \int_x^1 e_i^2 \frac{dy}{y} q_i(y) \left[\delta\left(\frac{x}{y} - 1\right) + \frac{\alpha_s}{2\pi} f\left(\frac{x}{y}\right)\right] + 0(\alpha^2). \tag{29}$$

The t dependence can be eliminated at the cost of introducing a t-dependent structure function.

I have so far considered an oversimplification of the true problem. To order α_s there is an additional partonic process, namely *gluon* $+ \gamma \to q + \bar{q}$ (see Figure 4). This process also contains a log (Q^2/μ^2) arising from the propagation of the internal quark close to its mass shell. This singularity results in the replacement of Equation 24 and 25 by

$$\begin{aligned} F_1(x,t) \;&= \int_x^1 \frac{dy}{y} \Big[\sum_i e_i^2 q_i(y) \left[\delta(\tfrac{x}{y}) + \tfrac{\alpha_s}{2\pi}\left[tP_{qq}(\tfrac{x}{y}) + f_q(\tfrac{x}{y})\right]\right. \\ &\quad + (\textstyle\sum_i e_i^2) g(y) \tfrac{\alpha_s}{2\pi}\left[tP_{qg}(\tfrac{x}{y}) + f_g(\tfrac{x}{y})\right]\Big] \end{aligned}$$

with $P_{qg}(x) = 1/2(x^2 + (1-x)^2)$. The t dependence can be absorbed by defining

$$q_i(x,t) = q_i(x) + \frac{\alpha_s}{2\pi} t \int_x^1 (q_i(y) P_{qq}(\frac{x}{y}) + g(y) P_{qg}(\frac{x}{y})) \frac{dy}{y} \tag{30}$$

so that the quark and gluon distributions ($q_i(x)$ and $g(x)$) are now coupled. This equation can be recast in the more familiar form (Altarelli-Parisi equations) [5]

$$\frac{dq_i(x,t)}{dt} = \frac{\alpha_s(t)}{2\pi} \int_x^1 (q_i(y) P_{qq}(\frac{x}{y}) + g(y) P_{qg}(\frac{x}{y})) \frac{dy}{y}. \tag{31}$$

The equation for the evolution of the gluon distribution is

$$\frac{dg_i(x,t)}{dt} = \frac{\alpha_s(t)}{2\pi} \int_x^1 (q_i(y) P_{gq}(\frac{x}{y}) + g(y) P_{gg}(\frac{x}{y})) \frac{dy}{y}. \tag{32}$$

Given data from which $q_i(x, t_0)$ and $g(x, t_0)$ can be obtained as functions of x for a fixed t_0, these equations for the evolution of $q(x,t)$ and $g(x,t)$ with t can be solved to obtain them for all t. Note that structure functions at x_1 and t_1 depend only on those at $x > x_1$ provided $t_1 > t_0$. Since these equations are valid only to lowest order in α_s, t_0 must be sufficiently large for $\alpha_s(t_0)$ to be small enough so that the perturbation series can be trusted. If the equations are used to extrapolate to $t > t_0$ the series will become more trustworthy. The order α_s^2 terms in the Altarelli-Parisi equations are known and are included in some parameterizations of $q_i(x,t)$ (see below). The structure functions fall to zero as x tends to 1 (see Figure 5).

Before leaving the Altarelli-Parisi equations, I would like to discuss the behaviour of the structure functions at very small values of x. As the energy available increases it becomes possible to reach smaller and smaller values of x at fixed Q^2. Consider the behaviour of the gluon distribution at small x. We can neglect the generation of gluons from quarks since the gluon density is larger at small x (see Figure 5). The Altarelli-Parisi equation simplifies to

$$\frac{d}{dt} g(x,t) = \frac{\alpha_s}{2\pi} \int_x^1 \frac{dy}{y} g(y,t) P_{gg}\left(\frac{x}{y}\right). \tag{33}$$

Furthermore $P_{gg}(x)$ may be approximated by

$$P_{gg}(x) = \frac{6}{x}. \tag{34}$$

Equation 33 can be recast as

$$-x \frac{d^2(xg(x,t))}{dx\,dlogt} = \frac{12}{b} xg(x,t). \tag{35}$$

Here I have eliminated $\alpha_s(q^2)$ using Equation 13. Equation 35 can be solved to give

$$xg(x,Q^2) \propto exp\Big(\sqrt{\frac{48}{b} log(1/x) loglog(Q^2)}\Big). \tag{36}$$

The growth of this at small x is very rapid. It is eventually cut off when the equations break down [6]. We can estimate the position of this breakdown as follows. The Altarelli Parisi equations describe the growth of incoherent parton showers: the shower initiated by one parton is independent of that of the other

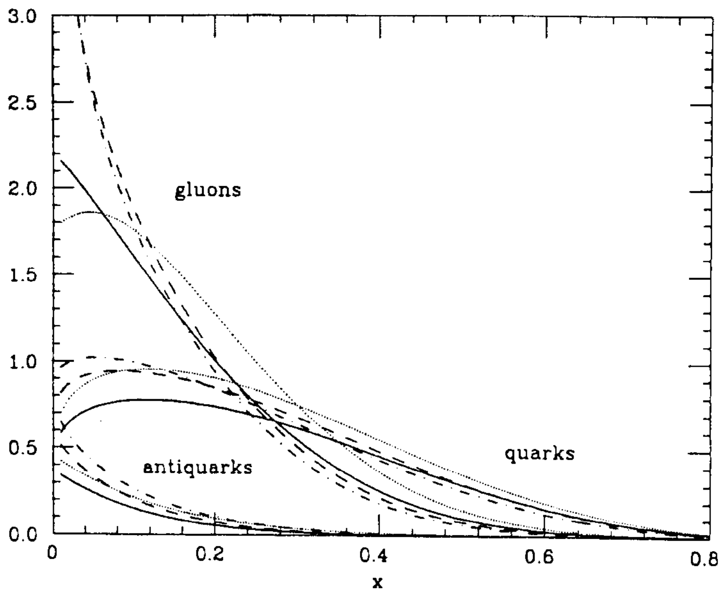

Figure 5: Diagram showing the behavior of the quark and gluon distributions as functions of x for various Q^2. Plotted is $xf(x)$ for gluons, quarks and antiquarks (summed over quark flavors). The solid (dotted) lines correspond to the structure functions of Reference [24]([20]) at $Q^2 = 5$ GeV^2. The dashed (dot-dashed) lines correspond to these structure functions evolved to $Q^2 = 25$ GeV^2 using QCD.

partons. This assumption must eventually break down. Let us view the proton in a frame which is moving extremely fast, the appropriate frame for the parton picture. The proton looks like a pancake with area $1/m_\pi^2$. Viewed on a scale Q^2 it contains a set of partons each of size $1/Q$. The fractional area occupied by partons is

$$\frac{xg(x,Q^2)m_\pi^2}{Q^2}. \tag{37}$$

Provided this fraction is small the partons are not densely packed and the incoherent approximation is correct. If the fraction is of order one, the incoherent approximation breaks down and the growth of $g(x, Q^2)$ is cut off.

A vital property of QCD is that the distribution functions defined by Equation 28 are universal. In order to illustrate this, consider the Drell-Yan process in proton-proton collisions. In the naive parton model, the cross-section for the production of a $\mu^+\mu^-$ pair of invariant mass M in a proton-proton collision (the Drell-Yan process) with total center-of-mass energy $\sqrt{s}$ is given by

$$\frac{d\sigma}{dM^2} = \frac{4\pi\alpha_{em}^2}{9M^2s}\int dx_1dx_2[\sum_i q_i(x_1)\bar{q}_i(x_2)e_i^2\delta(x_1x_2 - M^2/s) + (1 \Leftrightarrow 2)]\,. \tag{38}$$

Here $\bar{q}$ is an antiquark distribution. The fundamental process is quark-antiquark annihilation into $\mu^+\mu^-$. Consider the corrections to this at order α_s. As in the case of ep scattering these can involve either virtual or real gluons (see Figure 6). These corrections modify Equation 38, *viz.*,

$$\begin{aligned}\frac{d\sigma}{dM^2} &= \tfrac{4\pi\alpha_{em}^2}{9M^2s}\int \tfrac{dx_1}{x_1}\tfrac{dx_2}{x_2}\,[[e_i^2 q_i(x_1)\bar{q}_i(x_2) + (1 \Leftrightarrow 2)]\\ &\quad\left[\delta(1-z) + \theta(1-z)\tfrac{\alpha_s}{2\pi}[2P_{qq}(z)t + f'(z)]\right]\\ &\quad +[\textstyle\sum_i e_i^2(q_i(x_1) + \bar{q}_i(x_1))G(x_2) + (1 \Leftrightarrow 2)]\\ &\quad \left[\theta(1-z)\tfrac{\alpha_s}{2\pi}[P_{qg}(z) + f''(z)]\right]\end{aligned} \tag{39}$$

where $z = M^2/(sx_1x_2)$ [7]. The last part of the expression arises from the process $g + q \to \mu^+\mu^- + q$.

If we replace $q(x)$ by $q(x,t)$ defined by Equation 28 then the resulting expression will have no t's appearing explicitly, *viz.*,

$$\frac{d\sigma}{dM^2} = \frac{4\pi\alpha_{em}^2}{9M^2s}\int dx_1dx_2[e_i^2q_i(x_1,t)\bar{q}_i(x_2,t)\delta(x_1x_2 - M^2/s) + (1 \Leftrightarrow 2) + \mathcal{O}(\alpha_s(Q^2))] \tag{40}$$

where the order $\alpha_s(Q^2)$ terms contain no powers of t. This absorption of the singular terms into $q(x,t)$ is known as factorization; it is a universal property

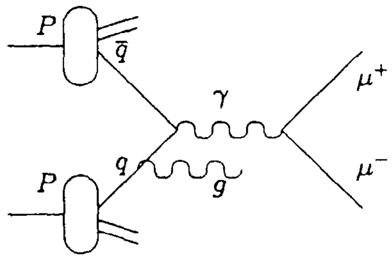

Figure 6: Feynman graph illustrating an order α_s contribution to the Drell-Yan process (see Equation 39).

which guarantees that hard processes can be reliably calculated in perturbative QCD and that the same set of structure functions should be used for all processes [8].

In summary, all cross-sections involving the transfer of large momentum (greater than 10 GeV) or the production of heavy particles can be calculated using the parton model. The cross-sections are given by

$$\sigma = \sum_{i,j} \int dx_1 dx_2 f_i(x_1, Q^2) f_j(x_2, Q^2) \hat{\sigma_{ij}} \tag{41}$$

where the sum runs over the parton types (quarks and gluons) and $\hat{\sigma_{ij}}$ is the cross-section involving partons that is calculated using perturbative QCD. Many partonic processes involve $2 \to 2$ processes of the type $a+b \to c+d$. In these cases is is useful to write the partonic cross-section in terms of Mandelstam variables: $s = (p_a + p_b)^2$, $t = (p_a - p_c)^2$, and $u = (p_b - b_c)^2$.

3 Structure of hadron-hadron events

Particle production in pp interactions is best described in terms of a particle's transverse momentum (P_t, a two dimensional vector in the plane orthogonal to the beam) and its rapidity. The latter is defined by

$$y = \frac{1}{2} log(\frac{E + P_l}{E - P_l}) \tag{42}$$

where P_l is the component of the particle's momentum along the beam direction. Also useful is the pseudorapidity (η) defined in terms of the angle that the particle makes with the beam (θ) by

$$\eta = -log(tan(\theta/2)). \tag{43}$$

For a massless particle $\eta = y$. For a particle of mass M, the maximum rapidity is $y_{max} = log(\sqrt{s}/M)$. In terms of these variables the invariant phase space element is

$$\frac{d^3p}{E} = p_t dp_t dy d\phi \tag{44}$$

where ϕ is the azimuthal angle and $p_t = |P_t|$. Rapidity is an additive quantity in the following sense. If a particle A is produced with rapidity y_A in the pp center-of-mass and decays so that one of its decay products (B) has rapidity y_B in the rest frame of A, then the rapidity of B in the pp center-of-mass frame is $y_A + y_B$.

The dominant part of the cross-section in pp or $p\bar{p}$ collisions at currently available energies consists of production of particles (so called minimum bias events) that are distributed approximately uniformly in rapidity and have a transverse momentum spectrum that falls rapidly with increasing p_t. As $\sqrt{s}$ increases from 630 GeV to 1.8 TeV, the average value of p_t rises from 432 ± 4 MeV to 495 ± 14 MeV, while $dn/d\eta$ increases by a factor of 1.27 ± 0.4 from its value of $3.30 \pm .15$ at 630 GeV[53].

The production cross-section for heavy particles at hadron colliders is also flat in rapidity near $y = 0$. The reason for this can be understood from the example of W production, the cross section for which has the following form

$$d\sigma \sim dx_1 dx_2 q(x_1, M_W^2)\overline{q}(x_2, M_W^2)\delta(x_1 x_2 - M_W^2/s). \tag{45}$$

The longitudinal momentum of the W is $(x_1 - x_2)\sqrt{s}/2$ and its transverse momentum is zero. Hence if we define $\tau = x_1 x_2$, we can write x_1 and x_2 in terms of the rapidity (y_W) of the W:

$$x_1 = \sqrt{\tau} e^{y_W}, \quad x_2 = \sqrt{\tau} e^{-y_W} \tag{46}$$

and $dx_1 dx_2 = dy_W d\tau$. The structure functions can be parameterized approximately by

$$f(x) \sim x^a (1-x)^b. \tag{47}$$

Hence

$$\frac{d\sigma}{dy} \sim \tau^a (1 + \tau - \sqrt{\tau} \cosh y_W)^b. \tag{48}$$

Hence $d\sigma/dy_W$ is almost constant if $\sqrt{\tau}\cosh y_W \lesssim 0.1$. In the case of W production the Tevatron $\sqrt{\tau} \sim 0.04$ and hence $d\sigma/dy_W$ should be approximately flat for $|y| \lesssim 1.5$. Figure 7 shows the cross-section. It can be seen from this figure that the naive expectation is in agreement with the exact calculation.

4 Uncertainties in Predicted Rates

I will now turn to the errors and uncertainties inherent in QCD predictions at hadron–hadron colliders. In order to calculate a cross-section, one needs; structure functions; α_s; the partonic cross-section and a jet definition if the process has jets in the final state. The current value of $\Lambda_{\overline{MS}}$ quoted by the Particle Data Group[10] is 180 ± 95 MeV. The corresponding $\alpha_s(Q)$ is shown as a function of Q in Figure 8. It can be seen that the corresponding uncertainty in α_s is order 15% independent of Q. Since a cross-section for n jets in a hadron–hadron collision is proportional to α_s^n, it will be uncertain by $n \times 15\%$. The situation is slightly better in e^+e^- collisions where the uncertainty is of order $(n-2) \times 15\%$.

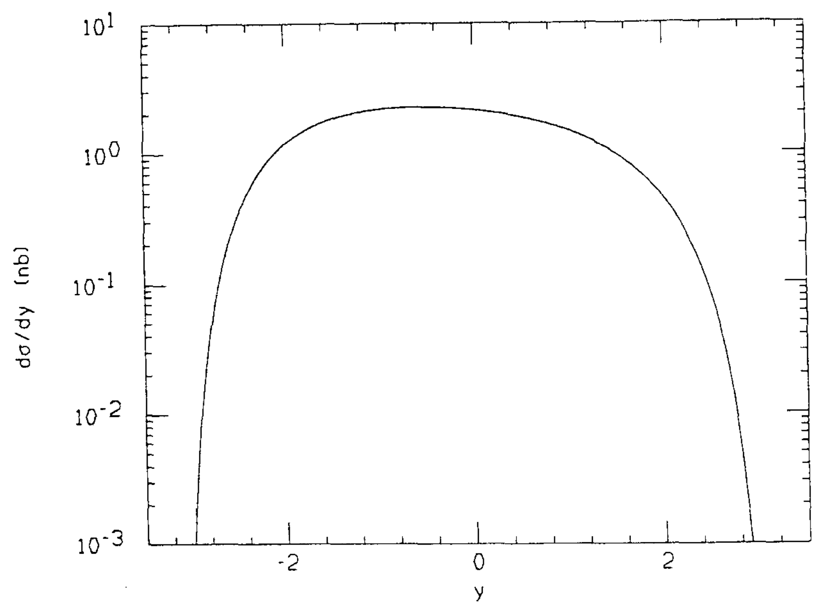

Figure 7: Figure showing the cross-section $d\sigma/dy_W$ for the production of a W^+ as a function of the rapidity of the W^+ in $p\overline{p}$ interactions at $\sqrt{s} =$ 1.8TeV.

A detailed discussion of the determination of the distribution functions and an estimate of the errors in them can be found in Ref. [11]. The existing parameterizations arise from fits to deep inelastic scattering data (with occasional input from Drell-Yan and photon production in hadron collisions). One of the major difficulties with such fits is the systematic disagreement between different data sets. This problem is illustrated in Figure 9 which shows a comparison of $F_2(x, Q^2)$ as measured by EMC[12], BCDMS[13] and SLAC[14] data on a hydrogen target. The EMC and BCDMS experiments cover the same kinematic range but do not agree. BCDMS is higher at small x and lower at large x than EMC. The ratio of them is approximately independent of Q^2. It is not clear which of these data provides a better extrapolation of the SLAC data into the range of larger Q^2. A comparison of the EMC[15] data on an iron target with the BCDMS[16] data on carbon reveals similar systematic differences. The results of these two measurements show systematic differences that are larger than the quoted errors [17]. When using these data to extract distribution functions, a choice must be made between them.

There are many sets of distribution functions coming from fits to the data using lowest order QCD. The most frequently used of these are the two sets of Duke and Owens [18] (DO1 and DO2) which were based on data from EMC [15], SLAC [14] and CDHS [20] [25] (the latter were renormalized in an attempt to deal with the systematic differences in the data sets, see above), and Eichten *et al.* [19] (EHLQ1 and EHLQ2) based primarily on the CDHS data [20]. These pairs correspond to different shapes for the gluon distribution and consequently different values of α_s (or Λ). As usual, the gluon distribution with more support at large x (harder distribution) corresponds to the larger value of α_s (EHLQ2 and DO2). Parameterizations of these distribution functions are given in the papers and can easily be applied to a variety of other processes.

Recently, fits using next-to-leading order QCD have emerged. Diemoz, Ferroni, Longo and Martinelli (DFLM) [21] used neutrino data from BEBC [22], CCFRR [23], CHARM [24] and CDHS [20] [25]. They also provide different fits corresponding to different values of α_s. They give sets of distribution functions corresponding to a range of $\Lambda^{\ddagger}$ viz $\Lambda = 160,\ 260,\ 360$ MeV. These fits are used to estimate the uncertainties in top quark rates at the Tevatron and $Sp\bar{p}S$ colliders [26].

Martin, Roberts and Stirling (MRS) [27] have used EMC data together with

‡Here we are quoting a Λ that corresponds to 4 flavors, in the range $m_{charm} < Q < m_{bottom}$ the formula for α_s is $\alpha_s(Q^2) = \frac{12\pi}{25\log(Q^2/\Lambda^2)}[1 - \frac{462}{625}\frac{\log\log(Q^2/\Lambda^2)}{\log(Q^2/\Lambda^2)}]$. See reference [10] for a summary of the behavior of this formula as a threshold is crossed.

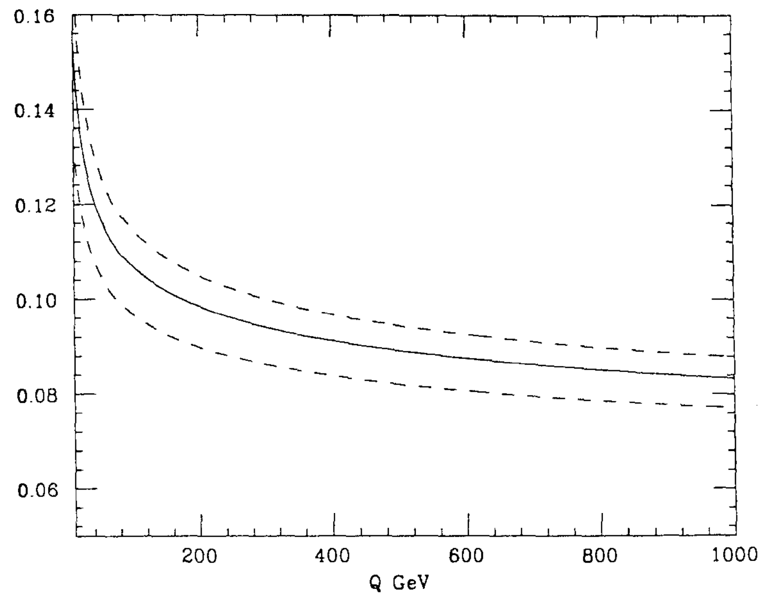

Figure 8: Figure showing $\alpha_s(Q)$ as a function of Q. The solid line indicates the central value quoted by the Particle Data Group[10], the dashed lines indicate the range of uncertainty.

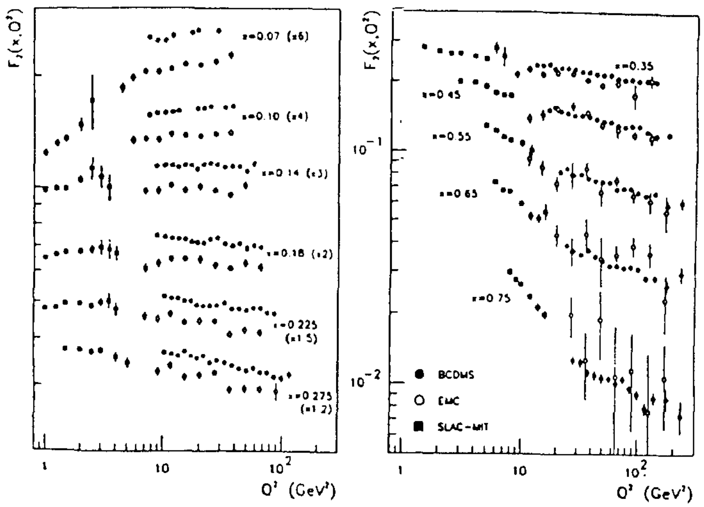

Figure 9: A comparison of $F_2(x, Q^2)$ measured in muon scattering from a proton target from the BCDMS[13] (closed dots) and EMC[12] collaborations (open circles). Also shown are data at small Q^2 (boxes) from the electron scattering experiment[14] at SLAC.

that from CDHSW and CCFRR to which they apply a renormalization of order 10%, to remove the systematic disagreement with EMC. They present three fits that differ in the form of $xg(x, Q^2 = 4GeV^2)$.

$$\begin{aligned} xg(x, Q^2 = 4GeV^2) \quad & \sim (1-x)^5 \quad && (set\ 1) \\ & \sim (1-x)^4(1+9x) \quad && (set\ 2) \\ & \sim x^{-1/2}(1-x)^4(1+9x) \quad && (set\ 3). \end{aligned} \tag{49}$$

They then use data from J/ψ production [28] and photon production [29] at large transverse momentum, processes that are sensitive to the shape of the gluon distribution (see below), in an attempt to distinguish between the sets. They conclude that the soft gluon distribution of *set 1* is preferred.

Set 1 has been[30] refitted using the BCDMS [13] [16] data instead of EMC [12] [15]. Here they find that the neutrino data and BCDMS are compatible and that a renormalization of the former is not needed. These authors have compared the predictions from these two sets of distributions with the data on Drell–Yan production at the ISR [31]. The BCDMS fit is preferred, but the order α_s QCD corrections to the Drell–Yan rate are quite large [7] and the α_s^2 terms are not known so any definite conclusion seems premature.

Existing deep-inelastic scattering data do not extend below $x \sim 0.01$ and cover a very small range of Q^2 at small x. This is a potential problem since for some applications it is necessary to know the parton distributions in this region. Recall that $x_1 x_2 > \hat{s}/s$ where $\hat{s}$ (s) is the center-of-mass energy squared in the parton-parton (hadron-hadron) system. It is traditional to assume that the gluon distribution obeys

$$\lim_{x \to 0} xg(x, Q_0^2) = const. \tag{50}$$

for some scale Q_0 of order a few GeV. However this form is unstable. When evolved to higher Q^2, it develops rapidly into a steeper form (see Figure 10). As we have seen(see Equation 36) at very small x and large Q^2, it is possible to solve the Altarelli–Parisi equations analytically. This solution is singular as $x \to 0$. It is also possible to sum to all orders in α_s the most singular terms at small x and large Q^2. This gives

$$\lim_{x \to 0, M \to \infty} xg(x, Q^2) \sim x^{-\delta} \tag{51}$$

where, $\delta = 12\alpha_s \log(2)/\pi$, which is an even more singular form [6]. It has been suggested [6] that one should use a form for $xg(x, Q_0^2)$ that is more like the asymptotic form:

$$xg(x, Q_0^2) \sim 1/\sqrt{x} \tag{52}$$

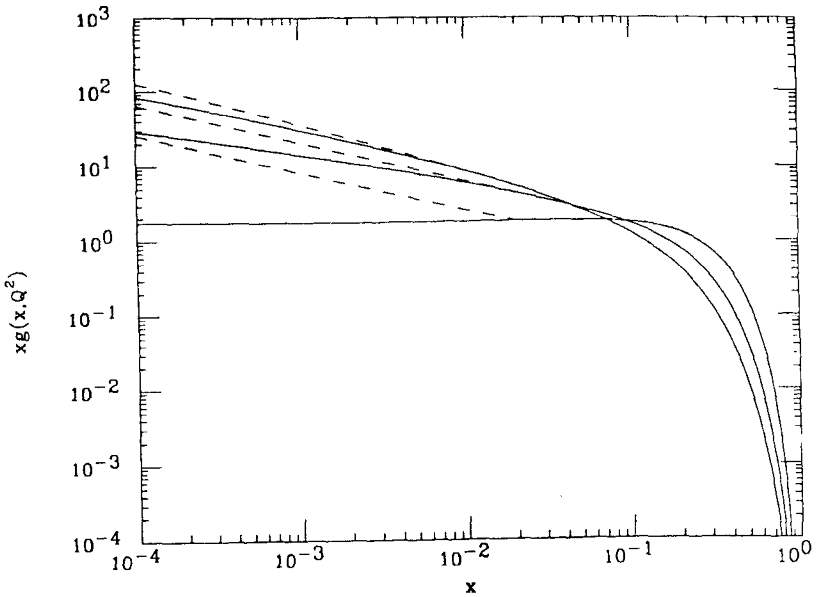

Figure 10: A comparison of the gluon distributions for fixed Q^2 as a function of x. The solid lines are EHLQ set 2 and the dashed are EHLQ2′ (see text). The higher (lower) curve at small x corresponds to $Q^2 = 50(5)$ GeV^2.

is most commonly used. This argument provides the motivation for *set 3* of the MRS structure functions. It is not clear that this form is a better assumption than the traditional one, or below what value of x this form should hold. Notice that the momentum sum rule provides almost no constraint since the amount of momentum carried by gluons in the region $x < 0.01$ is small, whichever form is used there. Figure 10 compares the resulting gluon distributions at higher Q^2 that evolve from different forms at M_0^2. The two starting forms are equal for $x > 0.02$ ($Q_0^2 = 5GeV^2$) and have the forms of Equations 50 and 52 at smaller x; the first of these is the EHLQ set 2 (see above). We will refer to the other as EHLQ2′ and will use it below to illustrate rates from such an extreme choice. As can be seen from Figure 10, the differences become less important at large Q^2. The uncertainties in predicted rates due to the small x problem are therefore serious only for processes sensitive to small x and small Q^2.

In order to assess the uncertainties in predicted rates quantitatively it is necessary to have set of structure functions that take into account the errors in the data that were used in making the fits. In the absence of such fits, one can attempt to estimate the uncertainties by using a range of structure functions that are compatible with existing data. Figure 11 shows the cross-section for the production of a photon at large transverse momentum. The relevant partonic processes are $g + q \to \gamma + q$ and $q + \bar{q} \to \gamma + g$. It can be seen from this plot that the uncertainties associated with the choice of structure functions are of order 25%.

Even if the structure functions and α_s were known exactly there would be some uncertainty in the QCD rates since the choice of scale Q at which they are evaluated in Equation 41 is arbitrary. If the partonic process were calculated to all orders in α_s then a change in Q would not change the result; it would merely adjust the relative sizes of the different terms in the α_s expansion. To see this note that

$$\alpha_s(Q') = \alpha_s(Q)(1 - \frac{33-2f}{6\pi}\log(Q/Q')\alpha_s(Q) + O(\alpha_s(Q)^2)) \tag{53}$$

and that (see Equation 30)

$$f(x, Q'^2) = f(x, Q^2) + O(\alpha_s(Q)). \tag{54}$$

Hence, a complete discussion of the Q^2 dependence of the calculated rates is only possible for processes where the next-to-leading order corrections to the partonic rate ($\hat{\sigma}$) is known. In the absence of such information one can vary Q^2 over a reasonable range and estimate the change in the predicted rate. The scale Q should be of order of the momentum transfer in the hard scattering process. For

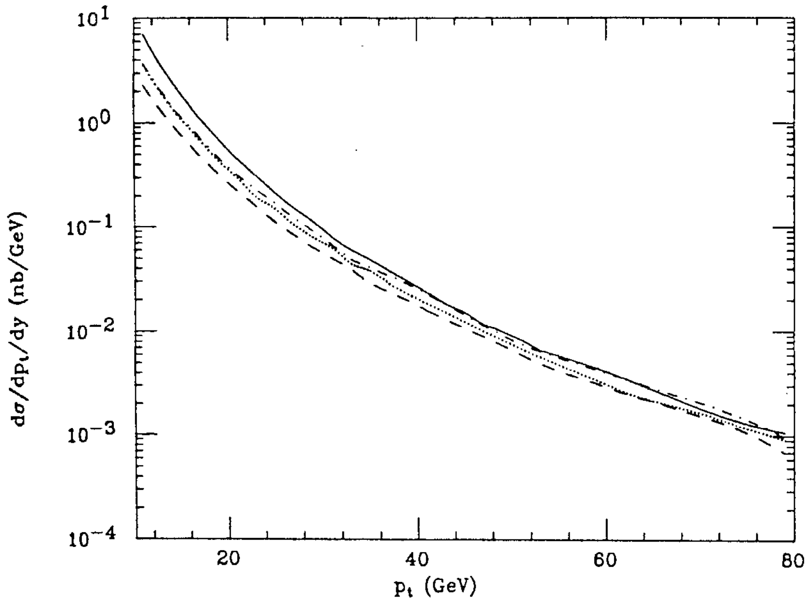

Figure 11: The cross-section $d\sigma/dp_t dy$ for the production of a photon at $y = 0$ in $p\overline{p}$ collisions at $\sqrt{s} = 1.8$ TeV for $M = \mu = p_t$. The solid, dashed, dotted, and dot–dashed lines correspond to MRS2, EHLQ2 and DFLM (Λ = 260 MeV) and EHLQ2′ distribution functions respectively.

example, in the case of W production is should be of order the W mass or, in the case of photon production at large transverse momentum, it should be of order p_t.

One would expect that the Q^2 dependence of an estimated rate would be reduced if the next order corrections to $\hat{\sigma}$ are known. Keith Ellis will discuss this in the context of the production of top and bottom quarks [32]. Here I will discuss the transverse momentum distribution of W bosons. The lowest order process that contributes to the production of W bosons is $q\overline{q} \rightarrow W$. Since the incoming partons have very small (less than a few hundred MeV) transverse momentum, this process can only produce W bosons with very small transverse momentum. There are two processes at order α_s namely $q\overline{q} \rightarrow W + g$ and $gq \rightarrow W + q$ that can produce W's at large p_t; the transverse momentum of the W is balanced by that of the outgoing quark or gluon. The rate from $q\overline{q}$ is given by [33]

$$\frac{d\sigma}{dp_t dy} = 2p_t \int_{x_{min}}^{1} dx \frac{u(x, M_W^2)\overline{d}(x_1, Q^2)\sigma(\hat{s}, \hat{t}, \hat{u})}{xs + u - M_W^2} \tag{55}$$

with

$$\begin{aligned} x_1 &= \frac{-xt - (1-x)M_W^2}{xs + u - M_W^2} \\ x_{min} &= -u/(s + t - M_W^2) \\ \sigma(s, \hat{t}, u) &= \frac{2\pi\alpha_{em}\alpha_s(Q^2)}{9sin^2\theta_W} \frac{(t - M_W^2)^2 + (u - M_W^2)^2}{stu}. \end{aligned}$$

Here the hatted variables apply to the partons and the unhatted to the hadrons. The W is produced with transverse momentum p_t and rapidity y. § The rate from the qg initial state can be obtained from this by crossing. At next order on QCD there are contributions from $q\overline{q} \rightarrow Wgg$ for example. The rate from all of the order α_s^2 processes has been computed [34] and is shown in Figure 12 as a function of Q for $p_t = 100GeV$ at $\sqrt{s} = 1.8$ TeV in $p\overline{p}$ collisions. If Q is allowed to vary over a reasonable range from $p_t/2$ to $2p_t$, it can be seen from this figure that the lowest order rate varies by a factor of order 1.8 while the order α_s^2 result changes only be a factor of 1.3. This result is typical and is to be expected if the

§Since the W is observed via its decay to $e\nu$ more useful experimentally is the cross-section for fixed momentum of the e. This is obtained by using the matrix element for $\overline{u}(p_u) + d(p_d) \rightarrow e(p_e) + \overline{\nu}(p_\nu) + g(p_g)$ which is given summed (averaged) over final (initial) spins and colors by

$$|M|^2 = (\frac{G_F}{\sqrt{2}})^2 \frac{2048\alpha_s M_W^6 \pi}{9(p_u - p_e - p_\nu)^2 (p_d - p_e - p_\nu)^2} \frac{(p_\nu p_u)^2 + (p_e p_d)^2}{((p_e + p_\nu)^2 - M_W^2)^2 + M_E^2 \Gamma_W^2}.$$

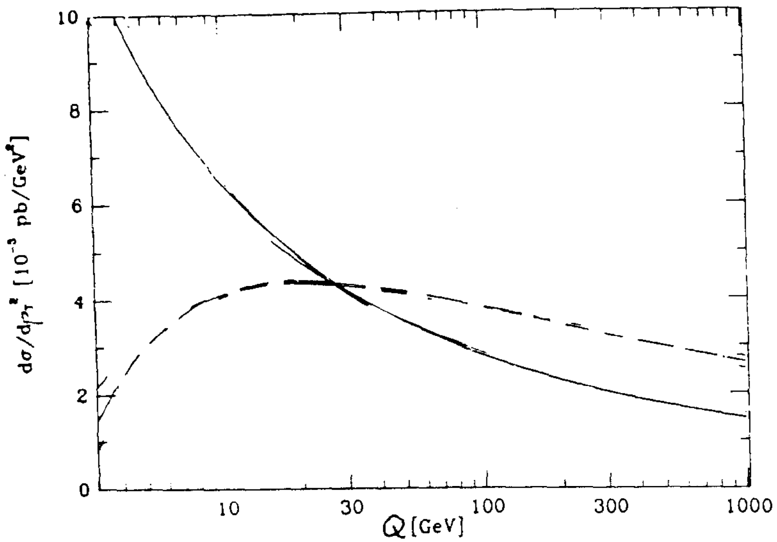

Figure 12: The dependence of the cross-section $d\sigma/dp_t^2$ for the production of a W boson with $p_t = 100$ GeV in $p\bar{p}$ interactions at $\sqrt{s} = 1.8$ TeV upon the scale Q. The solid (dashed) line is the order α_s (α_s^2) result. The DFLM ($\Lambda = 260$ MeV) structure functions are used [21] [34].

QCD perturbation theory is reliable. (Bottom quark production at the Tevatron is an exception, here the Q dependence increases in next-to-leading order [32].)

To summarize, for a process that does not require the definition of a jet the uncertainties on the cross-section are of order 25% from structure functions (more if the process has a partonic center-of-mass energy that is less than about 40 GeV and a value of $\hat{s}/s$ less than about 10^{-4}), of order 50% from the choice of Q^2 scale if next-to-leading order QCD effects are not known and order $15n$% if the partonic process is order α_s^n. In the cases where hadronic jets are measured it is necessary to define a jet.

5 Jets and their Definition

It is well known from the analysis of e^+e^- data that the details of jet fragmentation and of the experimental jet finding algorithm can significantly effect any detailed interpretations of jet measurements, and, in particular, of attempts to use such analyses to extract the value of α_s [35].

The products from a partonic hard scattering event can include quarks and gluons as well as photons and W bosons. While the latter can be observed directly in an experiment, the former cannot. What is observed is a narrow jet of hadronic particles whose direction and total energy correlate with that of the produced quark or gluon. The simplest model of such a jet is as follows. Consider a quark with four momentum $(E, P, 0, 0)$. This will fragment into n hadrons with momenta $(E_i, p_i, p_{t_i} cos\phi_i, p_{t_i} sin\phi_i)$. The distribution of particles is then given by

$$\frac{dN}{dy_i dp_{t_i} d\phi_i} = f(y_i) e^{-a p_{t_i}^2} \tag{56}$$

where the rapidity distribution $f(y_i)$ is approximately constant out to its maximum value ($y_{max} \propto log E$) where it falls rapidly to zero. This model predicts that the jets become narrower as E increases since the average value of p_{t_i} does not increase while the average value of the momentum (p_i) parallel to the quark direction does. Furthermore the average multiplicity of particles within a jet ($< n >$) will be proportional to $log E$. The average value of the transverse momentum is of order 300 MeV which is similar to the scale at which $\alpha_s(Q^2)$ becomes large and QCD perturbation theory can no longer be used.

This simple model provides a reasonable description of jets at $E \lesssim$ GeV. At higher energy the width of a jet expressed in terms of its opening angle δ does not decrease as fast with energy as the naive model indicates. (The model predicts $tan\delta \sim \frac{\langle n\rangle\langle p_t\rangle}{E}$). In order to understand this let us consider e^+e^- annihilation into hadrons.

At lowest order in QCD, α_s^0, the final state consists of a $q\overline{q}$ pair and one would therefore naively expect to find that the final state was dominated by 2–jet events. At next order we can get a state with an additional gluon (terms of this type contribute to the order α_s terms in Equation 20). Since the quarks and gluons hadronize into jets of particles, this would seem to imply that the ratio #(3jets)/#(2jets) should be of order α_s. This is only partially true since it is necessary to define what is meant by a jet. Consider the final state of two quarks and a gluon illustrated by Figure 13. The Feynman graph contains an internal propagator which gives rise to a factor of $1/(p_2+p_3)^2$; this factor becomes singular when either the gluon becomes very soft, i.e. $p_3 \rightarrow 0$, or when it moves parallel to the outgoing quark p_2. In the calculation of the inclusive cross-section, these singularities are cancelled by the divergences also present in the radiative corrections to the final state of quark and antiquark (see Figure 14).

These soft and collinear divergences correspond precisely to those parts of phase space where a detector would only detect two jets. Consider an idealised detector consisting of a set of elements each of which covers an angular cone of opening angle δ and has an energy threshold ϵ. This detector will be incapable of resolving two jets if one of them is very soft (energy ϵ or less), or if the two jets have an angular separation which is less than δ. We can define the f to be the fraction of total cross-section in which all but a fraction ϵ of the total energy is deposited into two cones of opening angle δ. Then to order α_s,

$$(1-f) = \frac{\sigma_{3-jet}}{\sigma_{total}} \tag{57}$$

provides a definition of the three jet fraction.

We can calculate this fraction as follows. Working in the center-of-mass of the e^+e^- system and defining $x_i = 2E_i/\sqrt{s}$, where E_i is the energy of the outgoing quark or antiquark(see Figure 13),the differential cross-section for the three parton final state can be written as

$$\frac{1}{\sigma_{total}}\frac{d\sigma}{dx_1dx_2} = \frac{2\alpha_s}{3\pi}\frac{x_1^2+x_2^2}{(1-x_1)(1-x_2)}\,. \tag{58}$$

Notice that this is singular when either x_1 or x_2 is zero which corresponds to the configuration where the gluon is soft ($x_1 \sim x_2 \sim 1$) or hard and parallel to one of the quarks (either $x_1 \sim 1$ or $x_2 \sim 1$). Hence [36]

$$(1-f) \;= \int_{\epsilon,\delta}\frac{1}{\sigma_{total}}\frac{d\sigma}{dx_1dx_2}$$

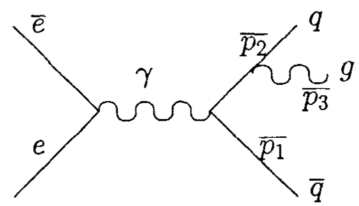

Figure 13: Feynman diagram showing a contribution to the three jet final state described by Equation 58.

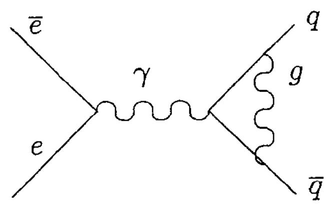

Figure 14: Feynman diagram showing a virtual correction to the total cross-section in e^+e^- annihilation.

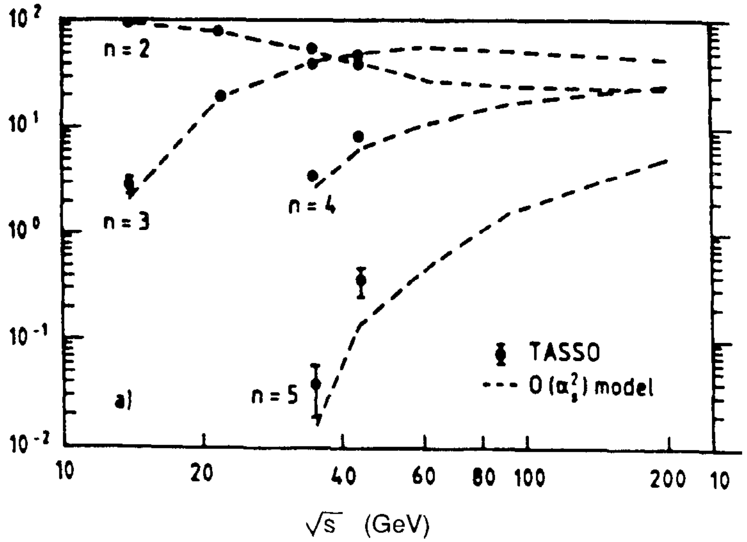

Figure 15: The relative sizes of the 2, 3,4,and 5 jet cross-section in e^+e^- annihilation as a function of $\sqrt{s}$[37] .

$$= \frac{4\alpha_s}{3\pi}(4log(1/\delta)log(1/2\epsilon) - 3log(1/\delta) + \pi^2/3 - 7/4).$$

Notice that as ϵ and δ become very small the logarithms in this expression can become very large. Ultimately the perturbation expansion in α_s breaks down since there are terms in next order which are of order $\alpha_s^2 log^2(1/\delta)$. Since this is not small compared with $\alpha_s log(1/\delta)$, the expansion is not reliable. The situation can then be improved by resumming these large logarithms to all orders.

The "fraction of three jet events" is therefore seen to depend on the jet definition. Furthermore this result shows that jets shrink only logarithmically as the energy rises (recall that α_s fall logarithmically with the energy). Another example of a jet definition in e^+e^- is as follows [37]. Suppose that n particles are produced with momenta p_i and form the invariant mass of pairs of particles:

$$M_{ij}^2 = (p_i + p_j)^2. \tag{59}$$

If $M_{ij} < M_{cut}$ then combine particles i and j into a pseudoparticle a: $p_a = p_i + p_j$. There are now $n-1$ "particles". Iterate the procedure until no more particles can be combined. Th number of jets in the event is then equal to the number of remaining pseudoparticles. Then the n–jet cross-section varies as

$$\sigma^n \sim \alpha_s^{n-2}(M_{cut}) log^{n-2}(\sqrt{s}/M_{cut}) \; . \tag{60}$$

Hence if M_{cut} is held fixed the 3 jet fraction will increase with $\sqrt{s}$. This is illustrated in Figure 15.

In a hadron-hadron collision the total energy in the parton scattering is not known *a priori* and hence the parameter ϵ is irrelevant. One could define jets in terms of a fixed angular cone. Experimentally and theoretically the best definition is in terms of a cone in rapidity and azimuth. Choose some direction then define the energy of a jet in that direction to the energy inside a cone of fixed ΔR defined by

$$\Delta R = \sqrt{(\delta\phi)^2 + (\Delta\eta)^2} \tag{61}$$

where $\Delta\phi$ and $\Delta\eta$ are the distance of the energy flow from the jet direction in azimuth and rapidity. There is some minimum value of ΔR that arises from the hadronization of a single parton and from the finite resolution of detectors; a value of order 0.7 is often used [38]. I will assume that $\Delta R < \pi/2$.

At order α_s^2 there are processes such as $g + g \to g + g$ and $q + q \to q + q$ that give rise to two partons in the final state in a hadron-hadron collision. If these partons emerge at large p_t, they will give rise, after hadronization, to jets of hadrons. At this order the two partons must be separated by $\Delta\phi = \pi$, and hence the final state will consist of 2 jets. The jet cross-section predicted by perturbative QCD is given simply by these $2 \to 2$ processes and does not depend on ΔR. The rate does depend rather strongly on the choice of Q^2; see Figure 16.

At order α_s^3 there are three parton final states arising from processes such as $g+g \to g+g+g$. This partonic final state could give rise to either a 2-jet or 3-jet final state depending upon the separation between the partons. *i.e.*

$$\frac{\#3-jet}{\#2-jet} \sim \alpha_s f(\Delta R). \tag{62}$$

The inclusive jet cross-section calculated to this order will now depend on ΔR. This is shown in Figure 17. As expected the Q^2 dependence of the cross-section is reduced when the order α_s^3 terms are included; the range of uncertainty shown on Figure 16 is reduced by about one third [39]. Notice that this calculation must include not only the three-parton final states, but also the virtual (order α_s^3) corrections to the two-parton final states. This is necessary because there are infra-red divergences in the three-parton final state that arise when one parton is very soft. These divergences cancel against those in the virtual diagrams.

Many searches for new physics in hadron-hadron collisions are limited by background from multi-jet final states. For example, one method of searching for the top quark [40] is to look for a lepton and jets arising from the production of a $t\bar{t}$ pair followed by the decays $t \to e^+\nu b$ and $\bar{t} \to \bar{b}d\bar{u}$. The background to this arises (at least for top masses larger than 60 GeV or so) for the final state $W + jets$. It is therefore vital to have good estimates of the multi-jet rates.

It is possible to use a partonic calculation to compare jet data with QCD or to estimate background rates. In this case, the theoretical prediction is taken from a partonic calculation done to some fixed order in α_s. It is important to realize that such a calculation depends not only on α_s but also on the cut-off parameters p_0 and R_0 that go into the definition of a jet. A fully correct treatment of this is, in fact, only possible in the context of a complete higher order calculation (*c.f.* previous paragraph). If one needs, for example, the four jet final state that occurs at order α_s^4, one must calculate the two loop corrections to the 2-jet final state and the one loop corrections to the 3-jet final state. In practice, the tree level results can be used (α_s^2 for 2-jet, α_s^3 for 3-jet *etc.*) together with the cutoffs. While these results can be used for estimating rates, they cannot be used for making precise QCD tests involving the comparison of final states with different numbers of jets. Recently there has been much progress in calculating these tree level rates. The exact partonic matrix elements are known for all the processes contributing to 3-parton [41] and 4-parton [42] final states. An algorithm has also been developed [43] that enables the n-parton matrix elements

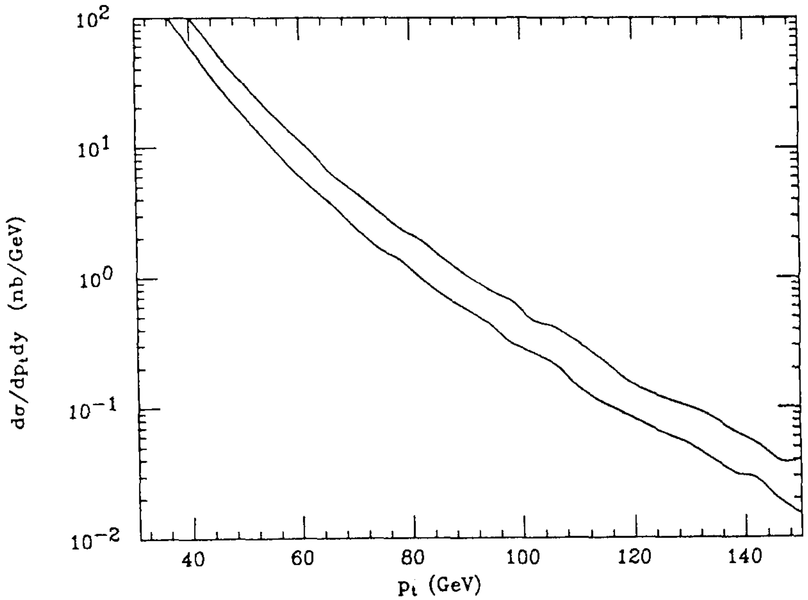

Figure 16: The cross-section $d\sigma/dp_\perp dy$ for the production of a jet at $y=0$ in $p\bar{p}$ collisions at $\sqrt{s}=1.8$ TeV. The curves correspond to the EHLQ2 set distribution functions with $\mu = M = p_t/2$ (upper curve) and $\mu = M = 2p_t$ (lower curve).

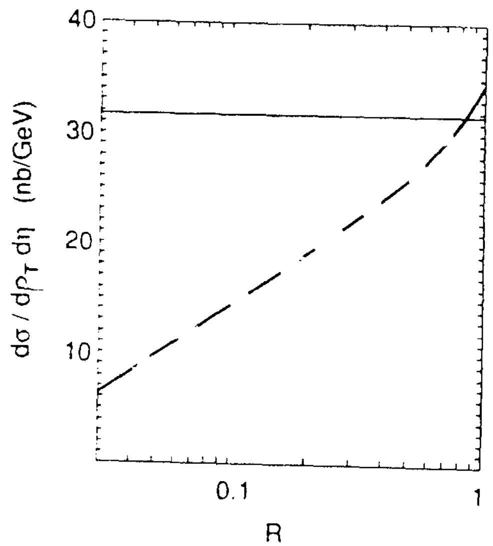

Figure 17: Inclusive jet cross-section $d\sigma/d\eta dp_t$ for $p_t = 50GeV$ and $\eta = 0$ in $p\bar{p}$ collisions at $\sqrt{s} = 1.8\ TeV$ as a function of the jet definition parameter ΔR. The solid (dashed) line is the order α_s^2 (α_s^3) result. The calculation was carried out in a modified version of QCD without quarks [39].

to be computed recursively. The exact matrix elements are very complicated and slow to evaluate for more than three jets. Nevertheless, approximations [44] have been developed that are accurate to 10% or better for the 4–jet and 3–jet final states and can be extended with some confidence to the final states with five or more jets. These fixed order calculations should be reliable provided that all of the jets are of approximately the same p_t. If $\alpha_s(p_t^{max})log(p_t^{max}/p_t^{min}) \sim 1$ or $\alpha_s log(2\pi y_{max}/\Delta R) \sim 1$, then the parton calculation ceases to be reliable. Here p_t^{max} (p_t^{min}) is the transverse momentum of the stiffest (softest) parton, y_{max} is the range of rapidity covered by the detector and ΔR is the separation in rapidity–phi space of the closest two partons. The latter criterion is always irrelevant given the segmentation present in current detectors.

If such a partonic calculation is to be used to compare with data, either the experimental data must be corrected back to "partonic energies", or the results of the calculation must be fed into a Monte Carlo event generator that fragments the final state quarks and gluons into the hadrons seen in the detector. The advantage of this technique is that the true QCD matrix element is used. The disadvantage is that the calculation does not include the effects of additional gluon radiation and hence of "jet broadening". There is another difficulty in that an n-jet final state is attributed to a 2 →n-parton calculation. After such a state is hadronized and passed through a jet finding algorithm, it may appear as an $(n-1)$–jet final state. Since such states are supposed to be produced by the $2 \to (n-1)$–parton scattering, there is a double counting problem.

An alternative method of calculation involves using a QCD inspired Monte Carlo generator (ISAJET [45], PYTHIA [48] or HERWIG [49] for example). Such generators usually start with the lowest order $2 \to 2$ calculation and then use a classical branching process to radiate more partons from these ones. This generates a multiparton final state in the so-called leading log approximation.

In order to understand how this approximation works, consider the process $g+g \to g+g+g$ which gives rise to a three parton final state. Label the momenta as follows

$$g(-p_1) + g(-p_2) \to g(p_3) + g(p_4) + g(p_5). \qquad (63)$$

Then the matrix element squared for this process can be written as (summed over all spins and colors)

$$|M|^2 = N^3(N^2-1)\sum_{i>j}(p_ip_j)^4)\sum_{perms}\frac{1}{(p_1p_2)(p_2p_3)(p_3p_4)(p_4p_5)(p_5p_1)} \qquad (64)$$

where N=3. Consider the limit in which p_4 and p_5 become parallel. Then $p_4p_5 \to$

0. Then define $p_a = p_4 + p_5$ and $z = |p_4| / |p_a|$

$$|M|^2 = \frac{N^3(N^2-1)}{(p_4p_5)z(1-z)}(1+Pz^4+P(1-z)^4)\sum_{i>j}(p_ip_j)^4)\sum_{perms}\frac{1}{(p_1p_2)(p_2p_3)(p_3p_a)(p_ap_1)} \tag{65}$$

where the sum on i and j runs over 1,2 and 3 only, we have dropped terms that are finite as $p_4p_5 \to 0$ and P is given by

$$P = \frac{\sum_{i=1,3}(p_ap_i)^4}{\sum_{i,j=1,3;i>j}(p_ip_j)^4}. \tag{66}$$

Using momentum conservation one can show that $P = 1$. We can now write

$$|M|^2 = \frac{1}{(p_ap_a)}P_{gg}(z)\,|M_2|^2 \tag{67}$$

where P_{gg} is the Altarelli-Parisi splitting function and M_2 is the matrix element for the process $g(-p_1) + g(-p_2) \to g(p_3) + g(p_a)$ viz

$$|M_2|^2 = N^2(N^2-1)\frac{s^4+t^4+u^4}{stu}\left(\frac{1}{s}+\frac{1}{t}+\frac{1}{u}\right). \tag{68}$$

This result, which can be generalized, is the basis of the "leading log approximation".

The leading log approximation calculates $|M|^2$ for a $2 \to n$ process by selecting the pair of partons (l and m) with the lowest invariant mass and writing (as above $p_a = p_l + p_m$, and $z = |p_l| / |p_a|$

$$|M(2\to n)|^2 \approx \frac{1}{(p_ap_a)}P_{ij}(z)\,|M(2\to n-1)|^2. \tag{69}$$

The procedure is then iterated so that the final expression is in terms of a number of Altarelli-Parisi factors and $M(2 \to 2)$. This approximation is good when $log(\sqrt{\hat{s}}/p_t)$ or $log(\Delta R)$ is large, where ΔR is the separation of a pair of partons.

This approximation for generating multiparton final states is used by the QCD inspired Monte Carlo generators (ISAJET [45], PYTHIA [48] or HERWIG [49] for example). Such generators usually start with the lowest order $2 \to 2$ calculation. They treat the outgoing partons as being off shell (*i.e.* they have an invariant mass of order p_t) and then allow them to "decay" with a branching probability given in terms of the Altarelli-Parisi functions. (for a review see [50]). The advantages of this approach are that it can reproduce many jet final states and that it will automatically include any jet broadening effects caused by gluon radiation. It also has no inherent problem in normalizing the rates for different numbers of jets. The hadron (or parton) can be passed through a jet algorithm and the number of jets determined. The disadvantage of the method is that the leading log approximation does not reproduce the exact calculation for wide angle radiation (typical errors can be as large as a factor of 2 or 3 in rate) and so may not provide a good basis for comparing to multi-jet data. It is also very difficult to include higher order QCD corrections in a fully correct manner.

6 Underlying Events

In a hadron–hadron collision, events that do not contain a hard scattering make up the dominant part of the cross-section at currently available energies. These events ("minimum bias") consist of hadrons of small transverse momentum distributed uniformly in azimuth and approximately uniformly in rapidity. Since the properties of these events are not calculable in QCD, the various Monte–Carlo generators use models to simulate them. ISAJET [45] uses a Regge model [51]; PYTHIA [48] builds up the event from a large number of parton–parton scatterings each of which produces an outgoing parton of very small p_t; HERWIG [49] uses a phenomenological model based on the UA5 data [52]. All of these models contain parameters which are adjusted so that they correctly describe the data at the $Sp\bar{p}S$ collider.

When these generators are used to predict the minimum bias structure at higher energies, it is not guaranteed that they will agree, either with each other or with the data. Figure 18 shows the pseudo-rapidity distribution predicted for $p\bar{p}$ collisions at $\sqrt{s}$=1.8 TeV. It can be seen from this figure that the Monte-Carlo generators do not agree with each other and that PYTHIA provides the best agreement with the CDF data [53]. HERWIG is in reasonable agreement with the data, while ISAJET is somewhat low. However, in the PYTHIA case we have not included the contribution from the "double–diffractive" process. Including this process will lower the multiplicity slightly. It is needed at $\sqrt{s} = 630$ GeV to bring the generated values closer to those of ISAJET, HERWIG and the UA5 data. ISAJET and HERWIG do not have "double–diffractive" as a separate process. If the jet final states are also included in the HERWIG predictions, better agreement is obtained [54].

In a hadron–hadron hard scattering event, such as the production of jets or W bosons, the initial state partons in the hard scattering have evolved off shell by an amount of order the momentum transfer in the hard scattering. This evolution occurs by the emission of quarks and gluons all of which have limited transverse momentum with respect to the beam direction. These quarks and gluons then turn into hadrons of limited p_t distributed approximately uniformly in rapidity. One therefore expects that the multiplicity of particles in the underlying event (*i.e.* that part of the event that is separated in $\phi - \eta$ space from the products of the hard scattering) should be larger in events which contain a hard scattering than in events which do not. This qualitative feature is seen in the data [55]. A comparison of this effect in the different Monte–Carlo generators is shown in Figure 19 which also shows data from CDF [53]. A comparison of this figure with Figure 18 shows that there are indeed more particles in the underlying event when a W is produced but that the distribution remains of approximately the same shape in pseudo–rapidity.

Acknowledgment

This work was supported by the Director, Office of Energy Research, Office of High Energy and Nuclear Physics, Division of High Energy Physics of the U.S. Department of Energy under Contract DE-AC03-76SF00098. Accordingly, the U.S. Government retains a nonexclusive, royalty-free license to publish or reproduce the published form of this contribution, or allow others to do so, for U.S. Government purposes.

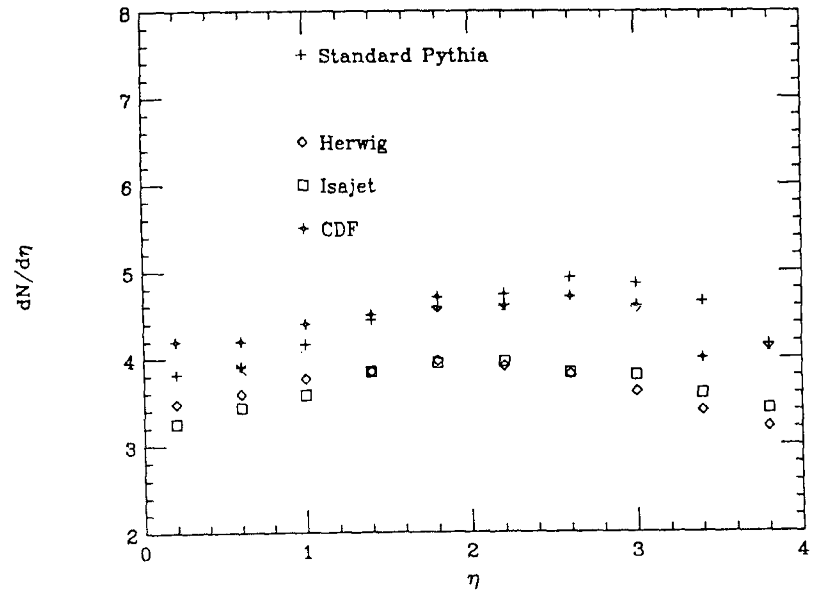

Figure 18: The distribution of multiplicity with respect to pseudo–rapidity, $dN/d\eta$, for events with no hard scattering (minimum bias) in proton–antiproton collisions at $\sqrt{s}$=1.8 TeV. The predictions of Monte–Carlo generators are compared with the CDF data [53].

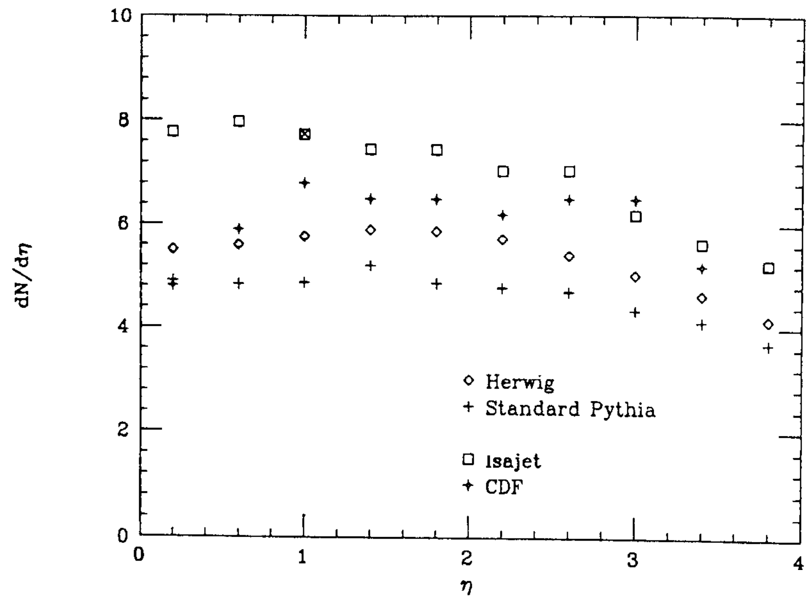

Figure 19: The pseudo–rapidity distribution $dN/d\eta$ for events in which there is a W (that decays to $e\nu$) in proton–antiproton collisions at $\sqrt{s}$=1.8 TeV. The predictions of Monte–Carlo generators are compared with the CDF data [53]. The electron from the W decay is not included.

References

[1] For a review of the QCD parton a model see G. Altarelli *Phys. Rev.* **81C**, 1 (1982),. or A. H. Mueller Lectures at the 1985 TASI (Yale University) (World Scientific Publishing Singapore, 1986). For a review of collider physics, see V. D. Barger and R.J.N. Phillips "Collider Physics" (Addison Wesley).

[2] W.A. Bardeen et al., *Phys. Rev. D* **18**, 3998 (1978).

[3] G. 't Hooft and M. Veltman, *Nucl. Phys. B* **44**, 189 (1972);
C.G. Bollini, J.J. Giambiagi and A. Gonzáles Domínguez, *Nuovo Cim.* **31**, 551 (1964);
J. Ashmore, *Nuovo Cim. Lett.* **4**, 289 (1972);
G.N. Cicuta and E. Montaldi, *Nuovo Cim. Lett.* 4:329 (1972).

[4] M. Dine and J. Saperstein *Phys. Rev. Lett.* **43**, 688 (1979),W Celmaster and R J. Gonsalves *Phys. Rev. Lett.* **44**, 560 (1979).

[5] G. Altarelli and G. Parisi, *Nucl. Phys.* **B126**, 298 (1977).

[6] J. Collins in "Supercollider Physics" Ed. D. Soper, World Scientific publishing (1987).

[7] G. Altarelli, *et al.*, *Nucl. Phys.* **B143**, 521 (1978), Erratum *Nucl. Phys.* **B146**, 544 (1978).

[8] A. H. Mueller, *Phys. Rev.*, **D18**, 3705 (1978). J. Collins, D. Soper and G. Sterman, *Nucl. Phys.* **B223**, 81 (1983),*Phys. Lett.*,**109B**, 388 (1983). R. K. Ellis, *et al.*, *Nucl. Phys.*, **B152**, 285 (1979).

[9] F. Abe *et al.*, *Phys. Rev. Lett.* **61**, 1819 (1988).

[10] R.M. Barnett, I. Hinchliffe and J. Stirling in Review of Particle Properties *Phys. Lett.* **204B**, 1 (1988).

[11] J. Morfin and W.-K. Tung, in Proceeedings of the 1988 Snowmass Summer Study, Ed. S. Jensen. World Scientific (1989).

[12] V. Papavassiliou (EMC collaboration) Proc. of Int. Europhysics Conference on High Energy Physics, Uppsala (1987).

[13] A. Benvenuti *et al.*, *Phys. Lett.* **195B**, 91 (1987).

[14] A. Bodek *et al.*, *Phys. Rev.* **D20**, 1471 (1979).

[15] J.T. Aubert *et al., Nucl. Phys.* **B293**, 740 (1987); **B272**, 158 (1986), **B259**, 189 (1985); or M. Arneodo *et al., Nucl. Phys.* **B264**, 739 (1986).

[16] A. Benvenuti *et al.,* JINR–E1–87–689, 699 (1987).

[17] See, for example, F.J. Sculli, Talk at 1988 Arles Conference, June 1988, and R. Voss in Proc. of 1987 International Symposium on Lepton and Photon Interactions at High Energies, Hamburg 1987.

[18] D. Duke and J. Owens *Phys. Rev.* **D30**, 49 (1984).

[19] E. Eichten *et al., Rev. Mod. Phys.* **56**, 579 (1984).

[20] H. Abramowicz, *et al., Zeit. fur Physik* **C17**, 283 (1983).

[21] M. Diemoz, F. Ferroni, E. Longo, and G. Martinelli, CERN–TH–4757 (1987).

[22] D. Allasia *et al., Phys. Lett.* **135B**, 231 (1986); *Zeit. fur Physik* **C28**, 321 (1985).

[23] D. B. MacFarlaneet al., *Zeit. fur Physik* **C26**, 1 (1984).

[24] J.V. Allaby, *et al., Phys. Lett.* **197B**, 281 (1987), CERN EP/87/225. F. Bergsma *et al., Phys. Lett.* **123B**, 269 (1983), **153B**, 111 (1985).

[25] H. Abramowicz, *et al., Zeit. fur Physik* **C35**, 443 (1987); B. Vallage, Thesis submitted to Université de Paris Sud (1984).

[26] G. Altarelli, *et al.,* CERN–TH–4978 (1988).

[27] A.D. Martin, R.G. Roberts and J. Stirling, *Phys. Rev.* **D37**, 1161 (1988).

[28] J.A. Branson *et al., Phys. Rev. Lett.* **38**, 1331 (1977); K.J. Anderson *et al., Phys. Rev. Lett.* **42**, 944 (1979); E.J. Siskind *et al., Phys. Rev.* **D21**, 628 (1980).

[29] T. Akesson, *et al., Zeit. fur Physik* **C34**, 293 (1987).

[30] A.D. Martin, R.G. Roberts and J. Stirling, *Phys. Lett.* **207B**, 205 (1988).

[31] D. Antreasyan *et al., Phys. Rev. Lett.* **48**, 302 (1982).

[32] R.K. Ellis, these proceedings.

[33] F. Halzen and W. Scott, *Phys. Rev.,* D18, 3378 (1978).

[34] P.B. Arnold and H. Reno *Nucl. Phys.* **B319**, 37 (1989)

[35] See, for example, S.L. Wu in *Proc. of International Symposium on Lepton-Photon Interactions*, Hamburg (1987) and references therein.

[36] G. Sterman and S. Weinberg, *Phys. Rev. Lett.,* **39**, 1436 (1977).

[37] W. Braunschwieg, *et al. Phys. Lett.* **214B**, 286 (1988).

[38] M.D. Shapiro, these proceedings.

[39] S. Ellis, D. Soper and Z. Kunszt, *Phys. Rev.* **D40**, 2188 (1989).

[40] R. Hollebeek, these proceedings.

[41] F. A. Berends, *et al., Phys. Lett.* **103B**, 124 (1982).

[42] S.J. Parke and T.R. Taylor, *Nucl. Phys.* **B269**, 410 (1986); Z. Kunszt, *Nucl. Phys.* **B271**, 333 (1986); J.F. Gunion and J. Kalinowski, *Phys. Rev.* **D34**, 2119 (1986).

[43] F.A. Berends and W.T. Giele, *Nucl. Phys.* **B306**, 759 (1988).

[44] C.J. Maxwell, *Phys. Lett.* **192B**, 190 (1987), Durham preprint DTP-88/32 (1988); Z. Kunszt and W.J. Stirling, *Phys. Rev.* **D37**, 2439 (1988); S.J. Parke and M. Mangano FNAL–Pub–88/92–T (1988).

[45] F. Paige and S. Protopopescu, in Proc. of 1986 Snowmass Summer Study on the Physics of the SSC, Ed. R. Donaldson FNAL (1987).

[46] EUROJET, B. van Eijk, in Proc. of the 5^{th} International Workshop on $p\bar{p}$ Interactions, St. Vincent, Italy (1985).

[47] PAPAGENO, I. Hinchliffe, in preparation.

[48] H-U. Bengtsson and T. Sjostrand, *Comp. Phys. Comm.* **46** 43, (1987).

[49] G. Marchesini and B.R. Webber, CAVENDISH preprint 88/7 (1988).

[50] B. R. Webber *Ann. Rev. Nucl. and Part. Sci.* **36**, 253 (1986).

[51] V.A. Abramovskii, O.V. Kanchelli and V.N. Gribov in *Proc.* 16^{th} International Conference on High Energy Physics, FNAL (1983), Vol. 1, p.363.

[52] C.G. Alner, *et al., Phys. Rep.* **154**, 247 (1987).

[53] CDF collaboration presented by J. Proudfoot at the 7^{th} Topical Workshop on $p\bar{p}$ Interactions, Fermilab, June 20–24, 1988, ANL–HEP–CP–88-61.

[54] I am greatful to Michelangelo Mangano for bringing this to my attention.

[55] C. Albajar, *et al.*, CERN–EP/88-29.

W^+W^- Interactions and the Search for the Higgs Boson

MICHAEL E. LEVI *

Lawrence Berkeley Laboratory
1 Cyclotron Road, Berkeley, California 94720

Lectures presented at the SLAC Summer Institute on Particle Physics
Stanford, California, July 10 - 21, 1989

---

* This work was supported by the Director, Office of Energy Research, Office of High Energy and Nuclear Physics, Division of High Energy Physics, of the U.S. Department of Energy under contract number DE-AC03-76SF00098.

1. Introduction

Since the original paper by Peter Higgs[1] in 1964, which was only a page and a half long, the number of publications on the topic of the Higgs particle has grown year by year and threatens to overwhelm us. If only for this reason it has become imperative that we find the Higgs. In this lecture series we will begin with a general review of the standard model Higgs and a summary of existing experimental limits on Higgs masses. We will then discuss Higgs searches at e^+e^- machines which are just coming on line, e.g. SLC and LEP, and proceed to work our way up to TLC, CLIC, and the SSC, where we will introduce the topic of W^+W^- interactions. The range of Higgs masses we cover will span six orders of magnitude from MeV to TeV. Non-minimal Higgs searches will not be dealt with in this lecture series; instead see the excellent theoretical reviews of both minimal and non-minimal model Higgs.[2,3,4]

2. Minimal Standard Model

2.1. $SU(2)_L \times U(1)_Y$

To begin, here is a thumbnail sketch of the standard model. The standard model of electroweak interactions unifies the electromagnetic and weak forces into one formalism, and (aside from the masses of particles) with only a single free parameter. The $SU(2)_L \times U(1)_Y$ model was first proposed by Glashow[5] and later by Salam and Ward.[6]

In the model there are three known generations of leptons, with the left-handed components appearing in doublets. These are the left-handed electron and its neutrino, and left-handed muon and its neutrino, and the left-handed tau and its neutrino:

$$\begin{pmatrix} \nu_e \\ e \end{pmatrix}_L \quad \begin{pmatrix} \nu_\mu \\ \mu \end{pmatrix}_L \quad \begin{pmatrix} \nu_\tau \\ \tau \end{pmatrix}_L .$$

The right-handed components of the electron, muon and tau appear as singlets:

$$e_R \quad \mu_R \quad \tau_R .$$

Similarly, the quarks come in doublets: up/down , charm/strange, and top/bottom.

$$\begin{pmatrix} u \\ d' \end{pmatrix}_L \quad \begin{pmatrix} c \\ s' \end{pmatrix}_L \quad \begin{pmatrix} t \\ b' \end{pmatrix}_L$$

$$\begin{matrix} u_R & c_R & t_R \\ d_R & s_R & b_R \end{matrix}$$

The weak interactions between these particles consist of charged and neutral currents. The charged currents are mediated by the W^+ and W^- which couple to the left-handed components, and can change, for example, a down-quark to an up-quark. The neutral currents, which couple to both left and right-handed components, are mediated by the Z° and photon. The W^+ can be thought of as a raising operator, the W^- the lowering operator, and the Z° and photon diagonal in these interactions as shown in the figure below:

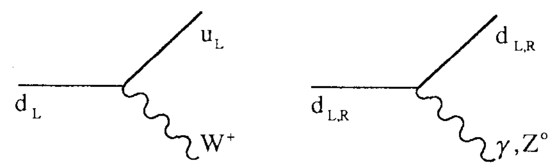

Fig 1. Diagrams for charged and neutral currents.

2.2. Electroweak Gauge Fields and Couplings

The $SU(2)_L \times U(1)_Y$ gauge group consists of an SU(2) triplet of isovector gauge fields $\vec{V}_\mu$ and an U(1) isoscalar gauge field B_μ. In the minimal model the gauge symmetry is spontaneously broken and the particle fields are given a mass by a single complex doublet of elementary Higgs scalar fields. Only a linear combination of the broken gauge generators corresponding to the electric charge, $Q = T_3 + \frac{Y}{2}$ (in units of e, where T_3 is the third component of weak isospin and Y is the weak hypercharge), remains unbroken. The resulting physical particle fields are a mixture of the gauge fields:

$$W_\mu^\pm = \frac{1}{\sqrt{2}}\left(V_\mu^1 \pm iV_\mu^2\right)$$
$$Z_\mu^o = -\sin\theta_w B_\mu + \cos\theta_w V_\mu^3$$
$$A_\mu = \cos\theta_w B_\mu + \sin\theta_w V_\mu^3 \quad ,$$

where A_μ is identified with the photon and $W_\mu^\pm$ and Z_μ^o with the massive weak gauge bosons. In the electroweak theory these gauge fields start out as massless fields and therefore with only two polarization states. When the $W^\pm$ and Z^o acquire mass they will each acquire a longitudinal degree of freedom.

There are two fundamental coupling constants, g for the weak isospin group SU(2), and g' for the weak hypercharge group U(1). The ratio of these couplings defines the weak mixing angle $\tan\theta_w \equiv g'/g$. They are related to the electromagnetic coupling $e = g\cdot\sin\theta_w$, where $\sin\theta_w = g'/\sqrt{g^2+g'^2}$, and the boson masses $M_w^2 = \pi\alpha/G_F\sqrt{2}\sin^2\theta_w$ and $M_z^2 = M_w^2\cos^2\theta_w$. In the model the fields couple universally to fermions. The left-handed components of the fermion wavefunction are doublets and the right-handed components are singlets under the weak isospin group. The couplings to the left and right-handed states are given by $g_L = T_3 - Q\sin^2\theta_w$, $g_R = -Q\sin^2\theta_w$.

2.3. The Gell-Mann Nishijima Relation

The $SU(2)_L \times U(1)_Y$ model as originally proposed by Weinberg was only applied to leptons; however, the standard model is extended to include the quark generations with only flavor diagonal currents.[7] The weak isospin and hypercharge assignments are given in Table 1, where Q=T3+Y/2 from the Gell-Mann Nishijima relation.[8]

Given that relationship, the quarks and leptons have the following quantum number assignments: the electron neutrino and the electron have weak isospin of 1/2 and hypercharge of -1: that results in a charge of 0 and -1, respectively, as one expects. Likewise, the up and down quarks, with weak isospin of 1/2, and hypercharge of 1/3 , have charges of 2/3 and -1/3.

	T	T_3	$Y/2$	Q
$\begin{pmatrix}\nu_e \\ e\end{pmatrix}_L$	½	$\begin{pmatrix}1/2 \\ -1/2\end{pmatrix}$	−1/2	$\begin{pmatrix}0 \\ -1\end{pmatrix}$
e_R	0	0	-1	-1
$\begin{pmatrix}u \\ d\end{pmatrix}_L$	½	$\begin{pmatrix}1/2 \\ -1/2\end{pmatrix}$	1/6	$\begin{pmatrix}2/3 \\ -1/3\end{pmatrix}$
u_R	0	0	2/3	-1/3
d_R	0	0	-1/3	-1/3

Table 1. Weak isospin and hypercharge assignments of quarks and leptons.

2.4. Spontaneous Symmetry Breaking

The breaking of $SU(2)_L \times U(1)_Y$ is performed by the Higgs mechanism which is now described. The minimal standard model is a spontaneously broken gauge theory which means that the symmetry of $SU(2)_L \times U(1)_Y$ is broken into $U(1)_{em}$, for example, by the selection of a preferred direction in weak isospin-hypercharge space. This direction is determined by the appearance of a non-vanishing vacuum expectation value. The nonvanishing vacuum expectation value is constructed by introducing a complex weak isodoublet of scalar fields, with hypercharge of 1.

$$\Phi = \frac{1}{\sqrt{2}}\begin{pmatrix} \phi_1 + i\phi_2 \\ \phi_3 + i\phi_4 \end{pmatrix} \equiv \begin{pmatrix} \phi^+ \\ \phi^0 \end{pmatrix}$$

Since this is a complex isodoublet, there are four real scalar fields and consequently four additional degrees of freedom in the gauge theory. The scalar fields have the weak isospin and hypercharge assignments shown in the table below.

	T	T_3	$Y/2$	Q
ϕ^+	$1/2$	$1/2$	$1/2$	1
ϕ^0	$1/2$	$-1/2$	$1/2$	0

Table 2. Weak isospin and hypercharge assignments of the scalar fields.

These scalar fields have self interactions, described in the most general way, by the scalar potential $V = \mu^2|\Phi|^2 + \lambda|\Phi|^4$. For $\mu^2 < 0$, the ground state occurs at $|\Phi|^2 = -\mu^2/2\lambda$, and this becomes the ground state of the vacuum as shown in Fig. 2. Therefore it breaks the symmetry, because there is now a preferred direction.

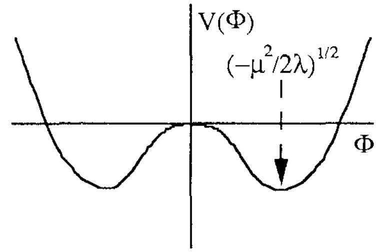

Fig. 2. Higgs scalar field effective potential for $V = \mu^2|\Phi|^2 + \lambda|\Phi|^4$ and $\mu^2 < 0$. For $\mu^2 > 0$ the ground state has a minimum at $|\Phi|^2 = 0$, while for $\mu^2 < 0$ the degenerate ground state of the vacuum has a minimum at $|\Phi|^2 = -\mu^2/2\lambda$. The degenerate vacuum with a non-zero vacuum expectation value is the hallmark of a spontaneously broken symmetry.

The $SU(2)_L \times U(1)_Y$ theory is a gauge theory with two symmetry transformations that interest us here. One is the SU(2) invariance under infinitesimal rotations, with the transformation property

$$\Psi(x) \to \Psi(x) + \frac{i}{2}\alpha(\vec{x})\cdot\vec{\tau}\ \Psi(x),$$

where $\vec{\tau}$ are Pauli spin matrices and are the generators of SU(2) isospin, and $\alpha(\vec{x})$ is an infinitesimal rotation vector in isospin space. The other symmetry is the U(1) invariance under a phase transformation, $\Psi(x) \to \Psi(x)\, e^{i\alpha(x)}$, where $\alpha(x)$ is the infinitesimal phase.

From Noether's theorem[9] we know that there is a conservation law for every symmetry transformation under which the theory is invariant. The conservation law for phase invariance is just simply charge conservation. This symmetry is unbroken in the theory and it is for this reason that the photon is left massless ($U(1)_{em}$ is unbroken). The invariance under rotation is just the conservation of the weak isospin. It is these three phases of isospin rotation, $\alpha(\vec{x})$, that get selected by the symmetry breaking. Whenever a continuous symmetry is broken, massless spin-0 particles appear,[10] one for each of the three real phases of $SU(2)_L$ weak isospin that were fixed by by the symmetry breaking. This is known as the Goldstone Theorem,[11] and the three spin-0 particles are known as Goldstone bosons. The scalar fields Φ are in addition to the massless gauge fields that become the W^+, W^-, γ, and Z°. Prior to symmetry breaking these gauge fields only have two transverse polarization states because they are massless.

In the gauge symmetry breaking by the Higgs mechanism, the self-interactions of the scalar field Φ both generate spontaneous symmetry breaking and give masses to the gauge quanta. In this mechanism, the Goldstone bosons go into the longitudinal degrees of freedom of the gauge fields, and those gauge fields then acquire a mass. In the minimal standard model, there are two fields, a charged field and a neutral field. The two fields have a weak isospin of 1/2, and a hypercharge of 1. The charged field, has charge 1, and the neutral field has charge 0.

We began with four scalar fields (four degrees of freedom) and four massless gauge quanta, for a total of twelve degrees of freedom (one degree of freedom for each polarization state), after symmetry breaking, we have one spin-0 particle left over, i.e. the Higgs boson, nine degrees of freedom in the three massive charged W's and Z, and two degrees of freedom in the massless photon.

2.5. *Electroweak Effective Lagrangian and Interactions*

Now in this theory, the Higgs mass is given by $M_H = \sqrt{-2\mu^2}$. Since μ^2 is not defined anywhere in the standard model, the mass of the Higgs is unknown and is a free parameter. In order to reproduce the weak interactions, one makes certain identifications. For example, the modulus of the vacuum expectation value of $v = \sqrt{-\mu^2/\lambda}$ is related to G_F by the relation $v = \left[\sqrt{2}G_F\right]^{-1/2} \cong 246\ \mathrm{GeV}$. And the masses of the intermediate vector bosons are related to the scalar field vacuum expectation value by the following:

$$M_w = \frac{1}{2} g v$$
$$M_z = \frac{1}{2} g_z v = \frac{M_w}{\cos\theta}.$$

In this manner one can retain all the aspects of the low energy effective weak Lagrangian,

$$L^{\mathrm{weak}}_{\mathrm{effective}} = \frac{G_F}{\sqrt{2}}\left\{J^\mu_+ J_{-\mu} + \rho\, J^\mu_{NC}\, J_{\mu NC}\right\}$$

where $J^\mu = J^\mu_{EM} + J^\mu_3$, $J^\mu_\pm$ are the charged currents, J^μ_{NC} are the neutral currents, J^μ_{EM} is the electromagnetic current, J^μ_3 is the weak current, and ρ is the ratio of the neutral current to charged current interaction strengths. By definition and before radiative corrections are applied, the ρ parameter is equal to 1 in the minimal standard model. There are other possibilities in non-minimal models. The Higgs boson also appears in the theory in a separate effective Lagrangian, such that the Higgs boson and the other bosons can all interact with themselves, because they all are carriers of weak isospin. This produces the Feynman diagrams shown in Figs. 3-5, beginning with the Higgs coupling to two fermions shown in the figure below.

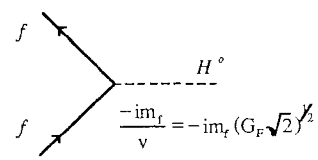

Fig. 3. Diagram for Higgs coupling to fermions.

This strength of this process is proportional to $m_f\sqrt{G_F}$. In addition there are the trilinear couplings shown in Fig. 4

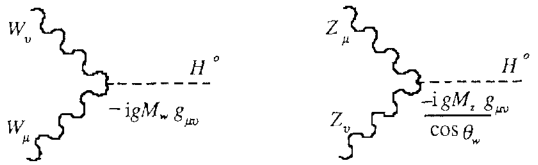

Fig. 4. Diagrams for Higgs coupling to massive gauge bosons.

where the weak coupling given by $g^2 = 4\sqrt{2}G_F M_w^2$. In the unitary gauge there are also the quartic-couplings shown in Fig 5, which couple two W's to two W's or two W's to two photons.

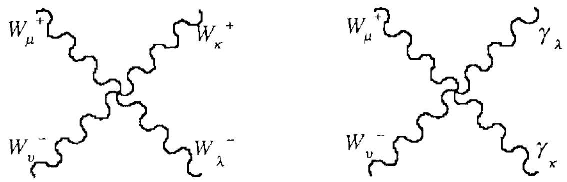

Fig. 5. Quartic couplings.

3. The ρ Parameter

3.1. Minimal Standard Model ρ Parameter

As already stated, the ρ parameter is the ratio of the neutral current to the charged current couplings in the low energy theory and has the following definition:

$$\rho \equiv \frac{M_w^2}{M_z^2 \cos^2\theta_w} .$$

In the minimal standard model, before radiative corrections, ρ is by definition one because we began with a complex doublet of scalar fields which satisfied the relation $(2T+1)^2 - 3Y^2 = 1$. What that simply says is that the $SU(2)_L$ weak isospin be $T=1/2$, and the hypercharge equal $Y=\pm 1$, for that complex doublet. However, there does not have to be one isodoublet to satisfy ρ=1. There could be 2, 3, or more, or one could have a larger group, where $T \neq 1$ or $Y \neq 1$, such as T=3 and Y=4. There is a wide spectrum of possible solutions, none of which we will discuss here, which are covered extensively in the literature.[2]

3.2. Experimental Measurements of the ρ Parameter

Experimentally, ρ has been measured and is accurately known to be close to unity. It has been measured in a variety of experiments, the easiest of which to perform are, perhaps, the W and Z measurements. The world average[12] of ρ=0.998 ± 0.0086 is shown in Fig. 6.

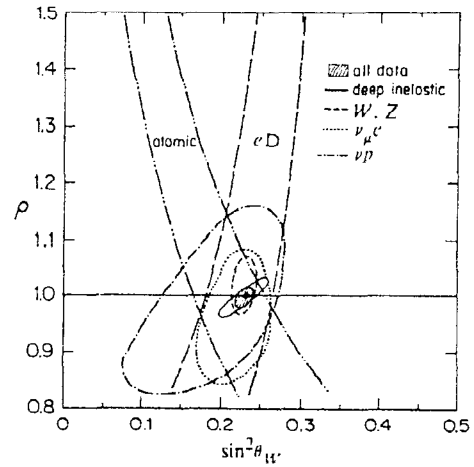

Fig. 6. Measurements of weak interaction parameters in shown plotted as a function of ρ vs. $\sin^2\theta_w$, also shown is the fitted average of experiments. Figure is from Ref. [12].

Therefore we know that we are on the right track, having started out with something that looked like a weak isodoublet. Though there are more complicated possibilities, we will confine ourselves to the minimal model with $\rho=1$ in these lectures.

4. Unitarity Bound

We do not know much about the Higgs boson mass, but there are some theoretical bounds.[13] Although it is not precisely defined in the theory, we do know from unitarity that there is an upper limit on the Higgs mass. Unitarity simply states that in a scattering process, the flux coming out cannot be greater than the flux of particles going into the scattering process. The scattering amplitudes have to be less than one. If one considers the process of $W_L^+W_L^- \to Z_L^\circ Z_L^\circ$, which proceeds through a Higgs boson intermediate state, and computes the scattering amplitude,[14] it comes out to be: $|M|^2 \cong G_F M_H^2/8\pi\sqrt{2}$ for $s >> m_H^2$. Requiring $|M|^2 < 1$, and solving for M_{H°, the unitarity limit is reached at M_{H°=1.7 TeV. Of course this limit only applies to the minimal standard model Higgs.

5. Low Energy Experimental Mass Limits

Given that the upper bound is 1.7 TeV, what is the lower bound? This brings us to the subject of existing experimental limits. I will discuss five experiments, which I have selected from a pedagogical viewpoint. I have chosen the most recent results from the SINDRUM, NA-31, and CLEO experiments, which were presented this year, and two older, but very interesting experiments on muonic atoms and forbidden transitions in nuclear states. The mass range which is excluded by these experiments extends from zero to about twice the τ lepton mass, or 3.4 GeV. The range that these measurements cover is shown pictorially in Fig. 7.

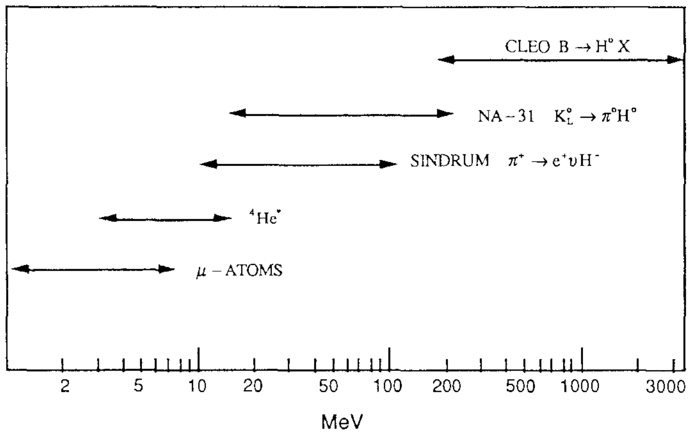

Fig. 7. Excluded regions of minimal standard model Higgs masses for selected experiments.

5.1. Higgs Coupling to Photons and Leptons

Before going into these measurements, it is instructive to discuss how the Higgs boson couples to leptons and photons. Knowledge of the coupling enables one to compute the rates. The coupling of the Higgs to the W's and Z's will be discussed later when we discuss higher-energy experiments.

The coupling to fermions is quite straightforward. As mentioned previously, in the Feynman graph for the Higgs coupling to two fermions the strength of the coupling is proportional to the mass of the fermion. The invariant amplitude is given by $|M|^2 = m_f^2 G_f \sqrt{2} \cdot 2m_h^2$, and after applying the Golden rule,

$$\frac{d\Gamma}{d\Omega} = \frac{|M|^2}{64\pi^2 m_H} = \frac{G_F m_H m_f^2}{16\pi^2\sqrt{2}},$$

and integrating over all phase space to get the decay rate, one obtains a very simple relationship for the decay rate of the Higgs into two fermions, such as two electrons or two muons, given in general by:

$$\Gamma(H \rightarrow f\bar{f}) = \frac{G_F m_H m_f^2}{4\pi\sqrt{2}} C_f \beta_f^3 ,$$

where C_f is the color factor (1 for leptons and 3 for quarks).

Since the decay width is proportional to the square of the fermion mass, the Higgs boson is most likely to decay to the heaviest fermion pair which is kinematically accessible. Therefore the coupling to two electrons is quite weak since they are so light. As an example of this we compute the production rate at an e^+e^- machine if one were to sit on a Higgs mass resonance and produce Higgs bosons.[14] (This assumes that one already knows the Higgs mass to high accuracy because the width is very small.)

$$\sigma(e^+e^- \rightarrow H) = \frac{4\pi\Gamma(H \rightarrow e^+e^-)\Gamma(H \rightarrow \text{all})}{m_H^2\, \Gamma(H \rightarrow \text{all})^2}$$

The result of the calculation yields 2 picobarns, assuming a Higgs mass of 10 GeV. When you compare that to the continuum cross section, 86.8nb/s(GeV^2), you find that the signal to background is about 1:1700. So, it is very difficult to find the Higgs directly from e^+e^- production.

The coupling of the Higgs to photons must proceed through higher order graphs. There is no direct coupling because the photon has no weak isospin. The process goes through a triangle graph shown in Fig. 8, which is theoretically well-understood and was first calculated[15] in 1949 for the case of π° decay, $\pi^\circ \rightarrow \gamma\gamma$:

$$\Gamma(\pi^\circ \rightarrow \gamma\gamma) = \left(\frac{\alpha}{2\pi}\right)^2 \left[N_c(e_u^2 - e_d^2)\right]^2 \frac{m_\pi^3}{8\pi} \frac{1}{f_\pi^2}$$

where N_c is the number of colors, f_π is the pion form factor, and e_u and e_d are the up and down quark charges.

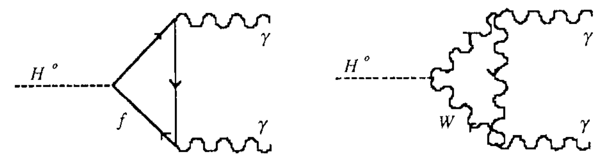

Fig. 8. Diagrams for the decay of a Higgs boson into two photons.

When we compute the same set of graphs for $H \rightarrow \gamma\gamma$, shown in Fig. 8, we come up with a very similar factor,[16,17]

$$\Gamma(H \rightarrow \gamma\gamma) = \left(\frac{\alpha}{2\pi}\right)^2 \left[7 - \frac{4}{3}\sum_f Q_f^2\, I\, C_f\right]^2 \frac{M_H^3}{8\pi} \frac{G_F}{4\sqrt{2}} \qquad \text{for } M_H << M_w$$

where instead of the pion decay constant we now have G_f. However there are a few more complications, due to additional graphs such as one in which virtual W's run around in the loop which is responsible for the factor of 7 in the above equation. For the contributions from quarks in the loop Q_f is the charge of the quark or fermion, and the factor I=1 for $m_f \gg M_{H^\circ}$ and I=0 for $m_f \ll M_{H^\circ}$. So $\Gamma(H \rightarrow \gamma\gamma)$ is an interesting decay width because it is sensitive to physics above the mass of the Higgs. We can imagine that if the Higgs were relatively light and one was able to measure $H \rightarrow \gamma\gamma$ very accurately it would probe physics far above the scale in which one is operating. Nonetheless, this decay rate, $\approx \alpha^2 G_F m_H^3$, is small due to the factor of α^2.

For Higgs masses below 1 MeV, the Higgs can only decay to two photons. If the mass is over 1.022 MeV it will decay to two electrons, until it hits twice the muon mass at which point it will decay primarily to two muons, and so on. The branching ratios for Higgs decay are shown in Fig. 9 as a function of Higgs mass.

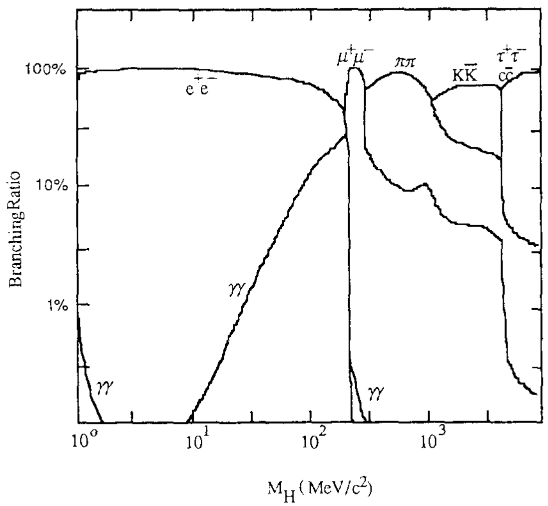

Fig. 9. Branching ratio for decays of a light minimal model Higgs boson . Figure is from Ref. [16].

5.2. Higgs Mass Limit from Muonic Atoms

The first experiment I want to discuss is interesting because it excludes a very light Higgs mass, in fact it excludes vanishingly small Higgs masses. In this respect it is unique, to my knowledge. The idea behind this experiment is that in a muonic atom, one can compute the radius of the muon's orbit about the nucleus; it is about 250 fermis in the lowest principle quantum state:

$$r = \frac{n^2}{Z\alpha m_\mu} \cong \frac{250 n^2}{Z} \text{ (fermi)}$$

where Z is the charge of the nucleus and n^2 is the principal quantum number. From dimensional arguments, one can also compute the range of the Higgs potential; it has a range of around 197 fermis for a mass of m_H=1 MeV, or more generally,

$$\frac{1}{m_H} \approx \frac{197(\text{fermi})}{m_H(\text{MeV})}.$$

The Higgs can therefore mediate an interaction between a muon and the nucleus because the range of the interaction looks like a long range force. In fact, it is an interaction very much like the Coulomb interaction. From this point of view it is as though the charge of the nucleus had shifted by some small value,[3]

$$Z\alpha \to Z\alpha\left[1+\frac{1}{Z\alpha}\cdot\frac{\varepsilon m_N m_\mu A}{4\pi}\sqrt{2}G_F\right]$$

where A is the atomic number, and ε is a QCD correction factor (approximately 0.3).

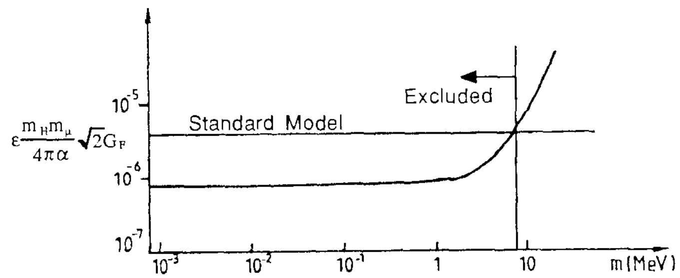

Fig. 10. Ratio of Higgs mediated muon-nucleon coupling to the electromagnetic coupling as a function of the Higgs boson mass for muonic transitions in atom ^{24}Mg and ^{28}Si [Ref. 18]. The region above the curve is excluded by the experiment. The straight line denotes the standard model expectation for the coupling as a function of the Higgs boson mass. Higgs mass values of less than 8 MeV are excluded by this experiment.

The energy levels scale with the square of the charge, $\approx (Z\alpha)^2$, so the shift turns out to be a small 4×10^{-6} shift in the energy levels. It is a very small shift but the experimental limit is well below that. The experimental result is given as a limit on the ratio of the Higgs mediated muon-nucleon coupling to the electromagnetic coupling[18]:

$$\left|\varepsilon\frac{m_N m_\mu A}{4\pi\alpha}\sqrt{2}G_F\right| < 0.8\cdot10^{-6} \quad \text{for} \quad M_H < 1\,\text{MeV}$$

The experimental limit cuts off at a Higgs mass for which the range of the interaction falls short of the muonic radius, which occurs at 8 MeV. From this result we know that the mass of the Higgs is greater than 8 MeV. The experimental result is shown in Fig. 10.

5.3. Limits from Forbidden Nuclear Transitions in ^{4}He

Measurements have also been made in nuclear decay, using an excited state of ^{4}He which is in a $J^P=0^+$ state.[19] The decay to the ground state, which is 20.1 MeV lower, is a forbidden transition (from 0^+ to 0^+). But the transition is allowed if a Higgs particle is produced instead of a photon. A light Higgs would only decay to two electrons, so the idea is to detect the two electrons from the Higgs decay. The idea is that since the Higgs only couples to objects with weak isospin, it behaves more or less like an neutrino. It has very weak interactions with matter, and this property is exploited in the experimental setup shown in Fig. 11.

One manufactures large quantities of the excited state of ^{4}He by striking a proton beam on a tritium target, followed by a 10 cm block of uranium or lead shielding. The Higgs will traverse through 10 cm uranium because it has very weak interactions, while other particles are absorbed. The energy spectrum is plotted in Fig. 12b) following, using a sodium iodine detector located after the uranium filter. In Fig. 12a) a calibration signal from 20 MeV captured γ rays is shown. The result of this experiment is shown in Fig. 13. No signal was detected in this experiment, excluding the region from 3 MeV to 14 MeV.

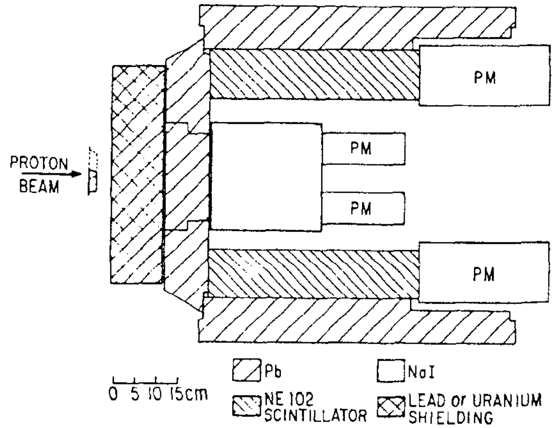

Fig. 11. Schematic view of the experimental apparatus. The figure is reproduced from Ref. [19].

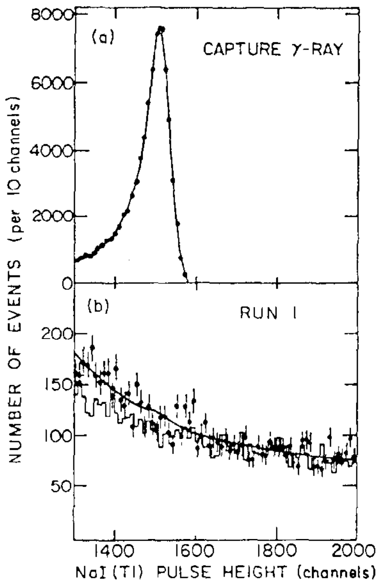

Fig. 12. In (a) is shown a calibration signal from 20 MeV capture γ rays and shows what the signal would look like. The observed energy spectrum is plotted in (b), using a sodium iodine detector located after the uranium filter. The data (points) as well as the expected cosmic ray background (histogram) are shown. The curve in (b) is a fit to the calibration spectrum shown in (a) superimposed on a smooth background.[19]

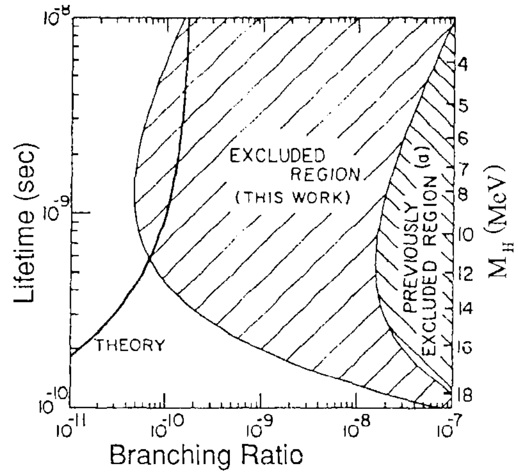

Fig. 13. Experimentally excluded region (at 2 sigma) in the life-time branching ratio plane. Figure is from experimental search for Higgs scalars emitted from the $J^P = 0^+$ to 0^+ forbidden transition in ^{4}He. The theoretical curve is for a standard model Higgs. The scale at right shows the correspondence with Higgs mass.[19]

5.4. SINDRUM Measurement of $\pi^+ \to e^+\nu_e H \to e^+\nu e^+ e^-$

Moving up in the mass range, a recent and very impressive experiment was performed at the Paul Scherrer Institute by the SINDRUM collaboration.[20] They have measured the rate for the decay for $\pi^+ \to e^+\nu_e\gamma^*$, where the photon decays to an electron-positron pair.

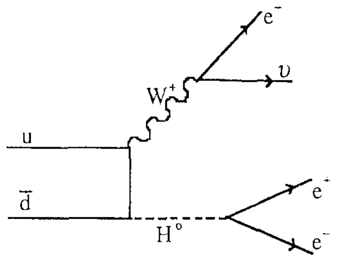

Fig. 14. Diagram for the process $\pi^+ \to e^+\upsilon_e H \to e^+\upsilon e^+e^-$.

This radiative decay is a standard model process that goes very slowly. The branching fraction is measured to be 3.2×10^{-9}. The interesting aspect about this experiment is that it is also sensitive to $\pi^+ \to e^+\upsilon_e H$ with the same final state electron-positron pair. The Feynman graph for this process is shown in Fig. 14. The branching ratio for $\pi^+ \to e^+\upsilon_e H$ is given below,[21]

$$
\begin{aligned}
BR(\pi^+ \to e^+\upsilon H^\circ) &\cong \frac{\Gamma(\pi^+ \to e^+\upsilon H^\circ)}{\Gamma(\pi^+ \to \mu^+\upsilon)} \\
&= \frac{\sqrt{2}G_F m_\pi^4 \cdot f(x)}{48\pi^2 m_\mu^2 (1 - m_\mu^2/m_\pi^2)} \qquad \text{where} \quad x = M_H^2/m_\pi^2 \\
&\cong 6.5\times10^{-9}\cdot f(x) \quad \text{and} \quad f(x) = (1-8x+x^2)\cdot(1-x^2) - 12x^2 \ln x.
\end{aligned}
$$

The only difficulty in performing this experiment is the long lifetime of a light Higgs, allowing it to completely evade detection in the apparatus for a sufficiently low mass Higgs. The long decay length for Higgs particles with mass below twice the muon mass is shown in Fig. 15.

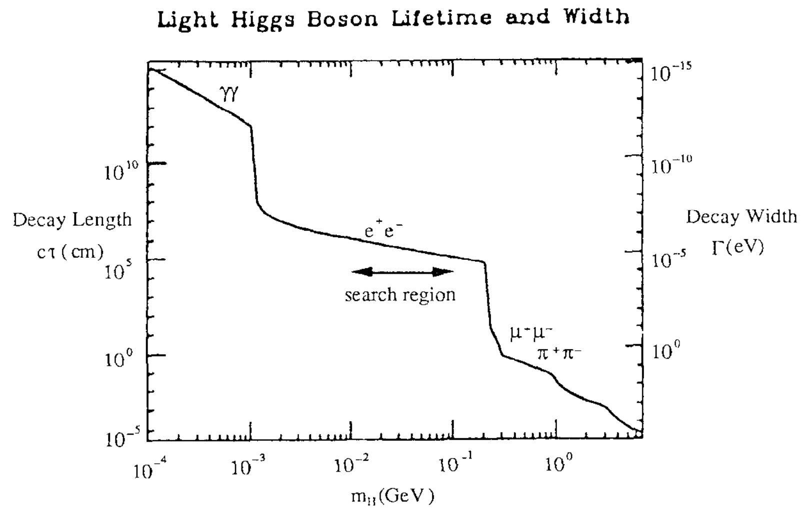

Fig. 15. Light Higgs boson lifetime and width. The figure shows the the decay length as a function of the Higgs mass. The right scale gives the corresponding decay width. The figure is from Ref. [2].

The long decay length somewhat limits the low end range of their search. However, it is fairly straightforward to search for two electrons forming a very narrow resonance, and in the search region of interest, which was about 10 MeV to 110 MeV, the branching ratio of Higgs to two electrons is very close to 100%.

In Fig. 16b), a Monte Carlo study shows the mass spectrum of what a 70 MeV Higgs in the SINDRUM detector would look like. The data, in Fig. 16a), shows the region searched by this experiment.

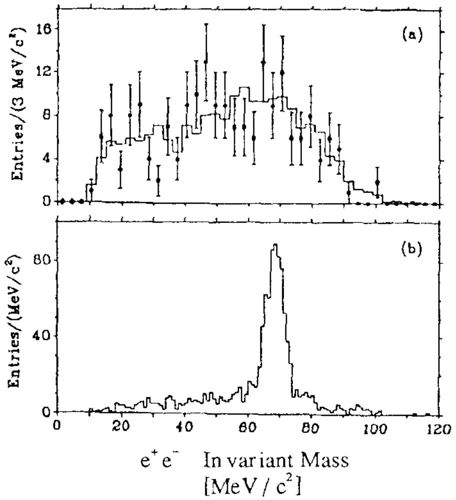

Fig. 16. In (a) the data for the process $\pi^+ \rightarrow e^+ \nu e^+ e^-$ are shown with error bars. The histogram is the Monte Carlo prediction for the standard model radiative decay process $\pi^+ \rightarrow e^+ \nu \gamma^*$. In (b) is shown the Monte Carlo prediction for $\pi^+ \rightarrow e^+ \nu H^\circ$ where M_{H°=70 MeV/c^2. The figure is from Ref. [20].

No corresponding peak is seen in the data, allowing them to set an experimental limit on the branching fraction at a level of 6.5×10^{-9} at a 90% confidence level. This excludes the presence of a Higgs in the mass region from 10 MeV up to 110 MeV.

5.5. NA-31 Search for $K_L^0 \rightarrow \pi^0 H$ $(H \rightarrow e^+ e^-)$

Beyond 110 MeV the searches are more complex. There is a preliminary measurement from CERN Experiment NA-31,[22] which has searched for the decay $K_L^0 \rightarrow \pi^0 H$ $(H \rightarrow e^+ e^-)$. They are limited in this experiment to the mass region below twice the muon mass. There is considerable theoretical uncertainty about the rate for $K_L^0 \rightarrow \pi^0\ H^0$. There are two Feynman graphs in Fig. 17 that contribute to this process and it is theoretically uncertain how to add the two amplitudes.[2]

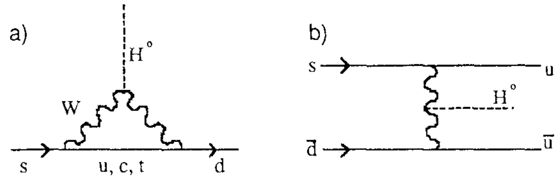

Fig. 17. Feynman graphs that contribute to the process $K_L^0 \rightarrow \pi^0\ H^0$.

The graph at left has a higher order loop with top quarks running around the loop, introducing an uncertainty due to our lack of knowledge of the top quark mass. In addition some of the Kobayashi Maskawa matrix elements are not well known and there are uncertainties in the relative phases of the two amplitudes. It suffices to say that there are a variety of theoretical predictions and in the worst case they give a branching ratio for $K_L^0 \rightarrow \pi^0\ H^0$ of 10^{-7}, although some predictions are as high as 10^{-4}. However even if one assumes the worst case, 10^{-7}, it is still possible to produce an experimental limit on the Higgs mass with this experiment. This limit given by NA-31 excludes Higgs masses from 15 MeV to 211 MeV, and they are able to exclude regions of Higgs production with branching fractions as low as 2×10^{-8}.

The results are plotted in Fig. 18 as a function of the mass of the Higgs vs. its lifetime. The solid diagonal line corresponds to a standard model Higgs; as the mass is lowered the lifetime becomes longer. In this experiment, as one gets to smaller masses and very long lifetimes, sensitivity to the Higgs is reduced, resulting in the lower end of their limit at 15 MeV. The upper end of the limit is the two muon threshold.

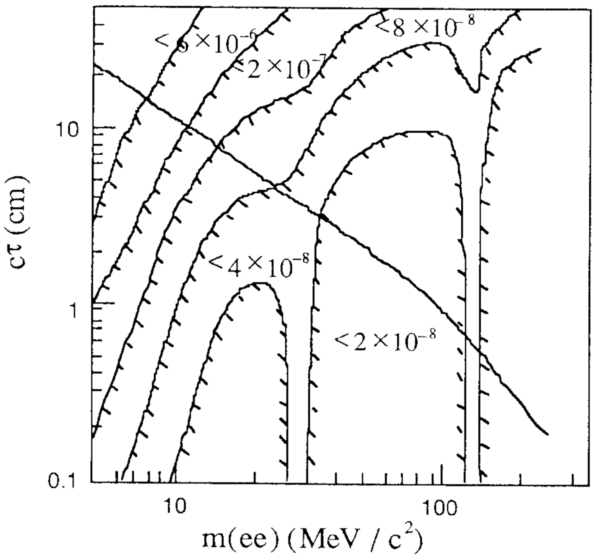

Fig. 18. Excluded regions for a light Higgs hypothesis for the process $K_L^0 \to \pi^0 H$ ($H \to e^+e^-$) as measured by the NA-31 collaboration. Shown in the figure are the contours for various excluded branching fractions as a function of the e^+e^- final state mass (Higgs mass) and the decay length. The results are plotted as a function of the mass of the Higgs vs. the lifetime of the Higgs. The diagonal line corresponds to a standard model Higgs. The lower limit on the expected theoretical branching fraction is 2×10^{-8} in this search region, which excludes Higgs masses in the region from 15 MeV to 211 MeV. Figure is from Ref. [22].

5.6. CLEO Search for $b \to sH$ Transitions

The CLEO experiment has looked for decays of B mesons to the standard model Higgs boson.[23] At the quark level, the transition $b \to sH$ is suppressed and can only occur through the higher order diagrams shown below.

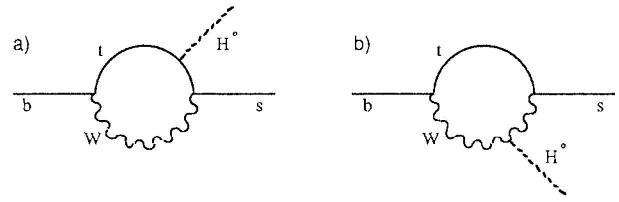

Fig. 19. Feynman graphs for the process $b \to sH$.

Since these graphs have heavy quarks in the loop, the branching fraction is dependent on the unknown mass of the top quark. The branching fraction is calculated to be 4.2% for a top mass of 50 GeV. The top mass appears to the fourth power,

$$BR(B \to H^\circ X) \cong 0.042\left[\frac{m_t}{50\,\mathrm{GeV}}\right]^4 \cdot \left[\frac{V_{ts}}{0.045}\right] \cdot \left(1 - \frac{M_H^2}{m_b^2}\right)^2$$

so for heavier masses the branching fraction is much larger. Such a substantial decay rate should not be difficult to detect. They have searched in a number of final states, including the inclusive modes $B \to H^0 X$ where the Higgs decays to $\mu^+\mu^-$, and the exclusive modes $B \to H^0 K$ or $B \to H^\circ K^*$, where the Higgs decays to $\mu\mu$, $\pi\pi$, or $K\bar{K}$. The most sensitive among these various modes is the inclusive process $B \to H^\circ X \to \mu\mu X$ and the exclusive processes $B \to H^\circ K(\text{or } K^*) \to K(\text{or } K^*)\mu\mu$ or $B \to K(\text{or } K^*)\pi\pi$.

The results of this experiment are used to exclude the mass region $2m_\mu < m_H < 2m_\tau$. This region is excluded using a number of different, overlapping decay modes as shown in Fig. 20. In the lower mass region the inclusive mode $B \to HK$ or K^* was used, assuming that the Higgs decays could be $H \to \mu\mu$ or $\pi\pi$. The upper mass region was excluded using the inclusive mode $H \to \mu\mu$. They had a little trouble around the J/ψ mass due to backgrounds; however the limits are still quite good even in that region. Given that we already know that the top mass is in excess of 77 GeV,[24] the CLEO limits are quite firm.

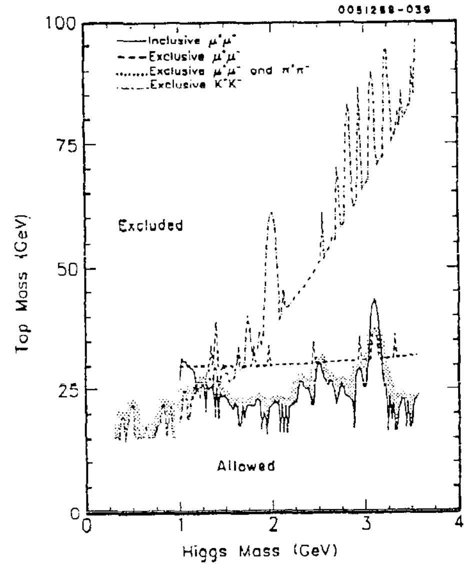

Fig. 20. Experimentally excluded regions of standard model Higgs boson mass as measured by the CLEO collaboration in the inclusive processes $B \to H^0X$ where the Higgs decays to $\mu^+\mu^-$, and the exclusive modes $B \to H^0K$ or $B \to H^0K^*$, where the Higgs decays to $\mu\mu, \pi\pi$, or $K\overline{K}$. The results of this experiment[23] are used to exclude the mass region $2m_\mu < m_H < 2m_\tau$.

6. Experimental Searches at SLC and LEP

Given these lower energy limits we know that the minimal Higgs is somewhere between 3.4 GeV and 1.7 TeV. How does one find the Higgs if it is above 3.4 GeV? First, we will look at some potential experiments at the e^+e^- colliders, SLC and LEP. Next we will consider what can be done at LEP-200, an upgrade to LEP scheduled to begin operations in 1995 at a center-of-mass energy of 200 GeV. Finally, at the end of this report we will discuss the search potential of the proposed accelerators TLC/CLIC which are e^+e^- machines and the SSC, a multi-TeV hadron collider currently under construction. The mass reach of the new and proposed accelerators is shown in the figure below.

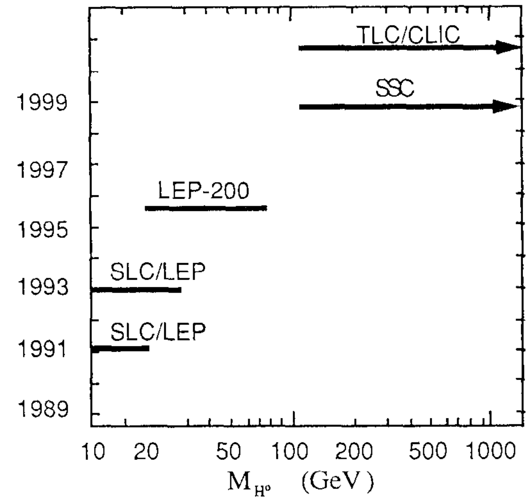

Fig. 21. The mass reach for minimal standard model Higgs boson searches of the new and proposed accelerators is shown in the figure. The dates shown are estimates of when such searches may be completed.

6.1. LEP/SLC Higgs Production Mechanism

The principal production mechanism of Higgs bosons at LEP/SLC is through bremsstrahlung off a Z^0. The diagram for this process and the production cross section are shown in Fig. 22. Higgs searches at these machines can be divided into three regions of interest as a function of the center-of-mass energy.[25] In region I of the figure, on the Z^0 resonance, Higgs bosons are produced in the process $e^+e^- \to Z^0 \to H^0 + Z^0$, where a real Z^0 is produced and decays into a Higgs and a virtual Z^0. Region II is defined as $M_z < \sqrt{s} < M_z + \sqrt{2}\, M_H$. In this region Higgs bosons can be produced by the same diagram, except that now both Z^0 propagators are virtual. When both Z^0's are off mass shell there is a dip in the production cross section, making it more difficult to perform searches in this region. The third region of interest, which really applies more to LEP-200, is at a center-of-mass energy $\sqrt{s} > m_Z + \sqrt{2}\, M_H$. In this case, the decay is through a virtual Z^0 propagator which in turn decays into a real Z^0 and a Higgs boson.

6.2. Production on the Z^0 Resonance

We'll begin with region I. In a high luminosity e^+e^- machine with $L \cong 10^{31}$ cm^{-2} sec^{-1}, which is approximately the design luminosity of SLC/LEP, one expects to produce on the order of 10^6 Z^0's per year. In a typical search scenario[25] the lepton tag is exploited by identifying events in which $Z^{0*} \to e^+e^-$ and the Higgs decays into $b\bar{b}$; thus the final state consists of $e^+e^-\, b\bar{b}$. Since the Z^0 is virtual in this region, the invariant mass of the e^+e^- pair will be substantially less than the Z^0 mass for Higgs boson masses in the region of interest. The relative production rate of this process is shown in Fig. 23 for a range of Higgs masses.

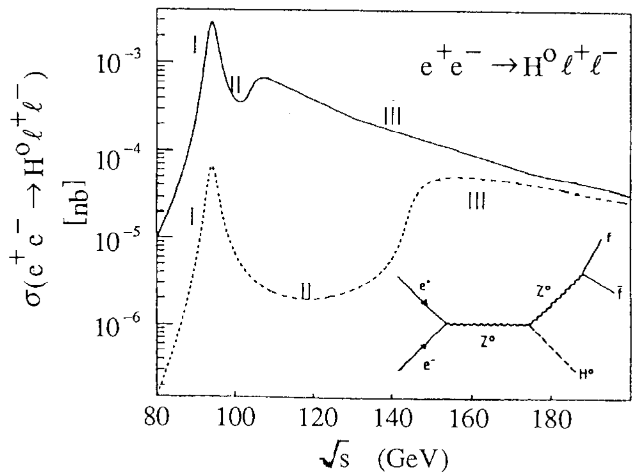

Fig. 22. Production cross section for the bremsstrahlung process $e^+e^- \to H^0Z^0 \to H^0\ell^+\ell^-$. The upper curve corresponds to a Higgs boson mass of 10 GeV, the lower (dashed) curve corresponds to a mass of 50 GeV. In region I marked on the curves a real Z^0 is produced and decays into a Higgs boson and a virtual Z^0. In region II marked on the curves both Z^0's are virtual. Finally, in region III only the final state Z^0 is on mass shell. Both curves assume that the Z^0 is detected through a charged lepton pair.[25]

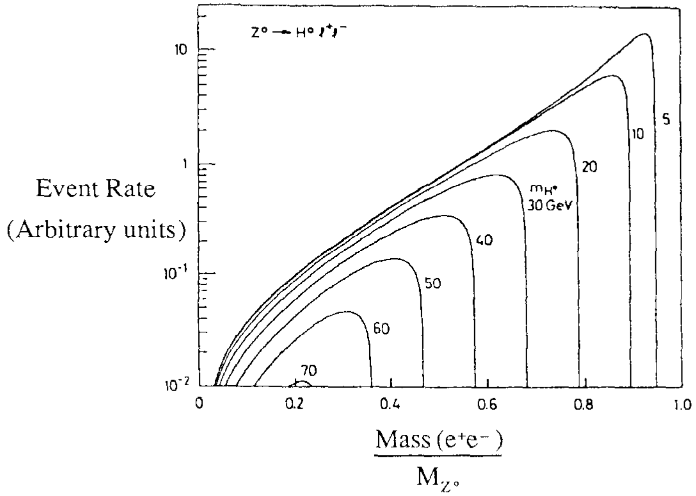

Fig. 23. The event rate for $e^+e^- \rightarrow H^oZ^{o*} \rightarrow H^o\ell^+\ell^-$ is compared on an arbitrary scale for different values of the Higgs boson mass and shown as a function of the invariant mass of the virtual Z^0 (e+e- pair mass). The production rate is seen to peak very closely to the kinematic threshold. The figure is taken from Ref. [25].

Unfortunately, the process, $e^+e^- \rightarrow H^oZ^{o*} \rightarrow H^o\ell^+\ell^-$ is severely rate limited, but it is the only way to make a Higgs at the SLC or LEP-1. The branching fraction for this process decreases rapidly from 10^{-4} for a massless Higgs to 10^{-6} at a mass of about 50 GeV as shown in Fig. 24. The dashed line in the figure marks the one event per 10^6 produced Z^0 rate (approximately one year of machine running), at design luminosity.

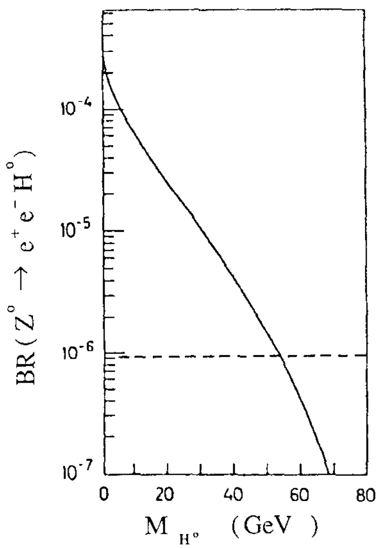

Fig. 24. Branching fraction for the on resonance production process $Z^o \rightarrow e^+e^-H^o$ as a function of the Higgs boson mass.[25] The dashed line corresponds to approximately one event produced in a canonical year of operation of a 10^{31} e+e- collider.

In a canonical year consisting of 10^7 sec of operation at an e+e- machine operating at full design luminosity of 10^{31}, 65 Higgs events are produced for M_H=10 GeV Higgs, but only one event for a Higgs boson mass of 50 GeV. So clearly the rate is inadequate somewhere in the region between 30 and 40 GeV. The following table shows the number of Higgs events produced with final states of $e^+e^- b\bar{b}$ from 10^6 initial state Z^0 events produced on resonance.

Higgs Mass (GeV)	10	20	30	40	50
Number of Events	65	26	11	4	1.5

Table 3. Number of Higgs bosons produced through the sequence, $e^+e^- \to Z^\circ \to Z^{\circ *}H^\circ \to e^+e^-b\bar{b}$ and into this specific final state as a function of the Higgs mass for 10^6 initial state Z^0 events produced on resonance.[25]

6.3. Mark II Simulation

Monte Carlo simulations of this process have been performed by groups at CERN and at SLAC. Here is a typical set of selection criteria from a Mark II study:[26] two electrons are required to have a total energy of $E_{e^+} + E_{e^-} > 30\,\mathrm{GeV}$, and the visible energy (sum of all observed energy in the detector) is required to be at least 85% of the center mass energy. The latter cut is made rather tight in order to reduce backgrounds to this process arising from the lower energy two photon exchange process, $e^+e^- \to \gamma^*\gamma^* \to e^+e^-q\bar{q}$. These cuts have an efficiency of about 65%. A simulation has been performed for three different postulated masses of the Higgs: 10 GeV, 20 GeV, and 35 GeV.

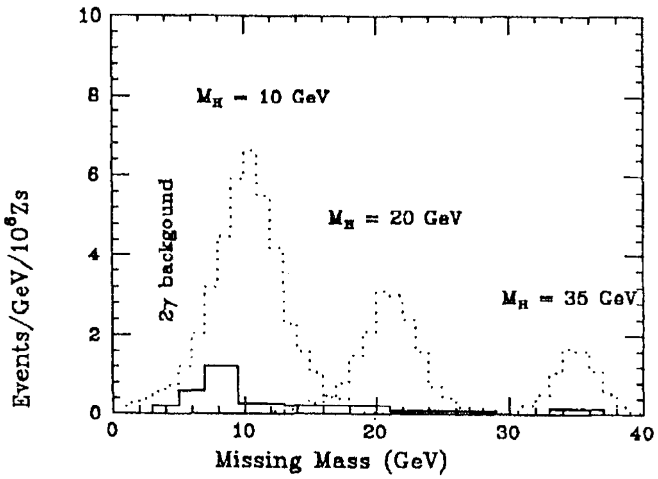

Fig. 25. A simulation by the Mark II collaboration for Higgs production through the sequence $e^+e^- \to Z^\circ \to Z^{\circ *}H^\circ \to e^+e^-b\bar{b}$ for three postulated masses of the Higgs boson as indicated. The signal is shown for each of the three Higgs masses (dotted histogram). The background, arising primarily from the two photon process $e^+e^- \to \gamma^*\gamma^* \to e^+e^-q\bar{q}$, is shown in the solid histogram. The figure is from Ref. [26].

In Fig. 25 the signal (dotted curves) and background (solid curves) are plotted in number of events per $10^6\ Z^0$, so this is a plot one might expect after a year of operation. When the missing mass, here defined as the mass recoiling against the Z°, is plotted one expects to see a resonance peak at the postulated Higgs mass. In the figure, the 10 GeV Higgs is readily apparent, as well as the 20 GeV Higgs, however a 35 GeV Higgs boson is clearly rate limited in this simulation.

The conclusion drawn from the Mark II simulation was that the range of observation for the Higgs, given $10^6\ Z^0$'s at LEP or SLC, would be from about 10 to 30 GeV. In a data sample of $10^7\ Z^0$'s, where this might be 10 years of operation or three years at a higher luminosity machine, one could extend the search up to M_H=50 GeV.

6.4. LEP Simulation

A LEP study tried to extend this range by expanding the search to include other Z° decay modes than to two electrons, which constitutes only 3% of all Z° decays.[25] They included final states in which the Z° decays to two neutrinos, $e^+e^- \to Z^\circ \to Z^{\circ *} H^\circ \to \nu\bar{\nu}b\bar{b}$, which has a branching ratio of about 19%, and should greatly improve the rate. The final state topology consists of two b jets recoiling against nothing, with the two jets being acoplanar. They therefore require two jets with less than half of the center-of-mass energy, because the Z° should carry away a majority of the energy. The event is required to be acoplanar, with missing transverse momentum of p_t > 3 GeV in order to reject QCD events. Finally, the calculated mass of the unobserved virtual Z° must be greater than 40 GeV. By applying a beam energy constraint to the observed system the invariant mass of the Higgs boson is obtained for M_H=30 GeV in Fig. 26a), and M_H=20 GeV in Fig. 26b).

The primary background to $e^+e^- \to Z^\circ \to Z^{\circ *} H^\circ \to \nu\bar{\nu}b\bar{b}$ is standard QCD production of two jets events. For the simulation of a 20 GeV Higgs mass there is an apparent peak, but there is also substantial $q\bar{q}$ background beneath it. Because of the cuts there is a kinematic cutoff at around 40 GeV. As the mass increases to 30 GeV there is a substantial reduction in rate due to the loss of phase space. Unfortunately, the peak begins to look a lot like the $q\bar{q}$ background. So although a more copious production mode, $Z^0 \to \nu\bar{\nu}$, is used in this search, one comes up with more or less the same answer as the Mark II analysis, and that is that one cannot extend the search region much higher than M_H=30 GeV at SLC or LEP-1. There is an advantage in using the mode, $Z^0 \to \nu\bar{\nu}$ if one only has for example 20,000 Z°'s, because one might still be able to do a Higgs search in the 5-15 GeV mass range. Therefore this is something that might be accessible to LEP or SLC during the very first year of operation.

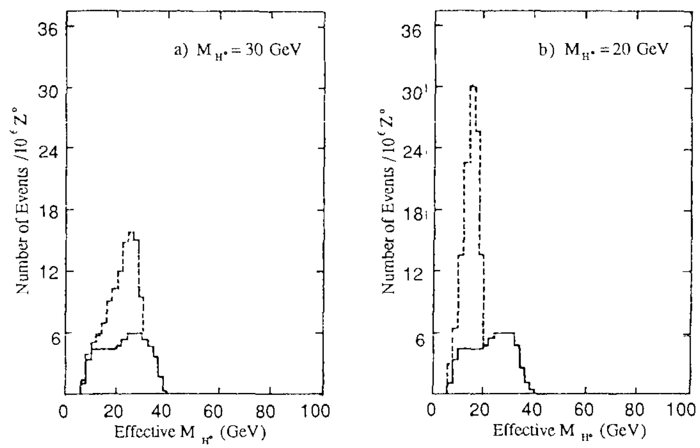

Fig. 26. Result of a LEP study for the Higgs production process $e^+e^- \to Z^\circ \to Z^{\circ *} H^\circ \to \nu\bar{\nu}b\bar{b}$. The figure (a) on the left is evaluated for a Higgs boson mass of M_{H°=30 GeV, the figure (b) on the right is evaluated for a mass of M_{H°=20 GeV. The signal (dashed histogram) is easily observed for the case of M_{H°=20 GeV over the QCD background (solid histogram). The figure is from Ref. [25].

7. Higgs Searches at LEP-200

We will now move up the mass scale range to LEP-200.[27] LEP-200 is a machine that will presumably come into operation in 1995, with a center-of-mass energy of 200 GeV and potentially a higher luminosity than the present LEP-1 machine. At LEP-200 the primary production mechanism for the Higgs boson is through the bremsstrahlung process $e^+e^- \to Z^{\circ *} \to Z^\circ H^\circ$.

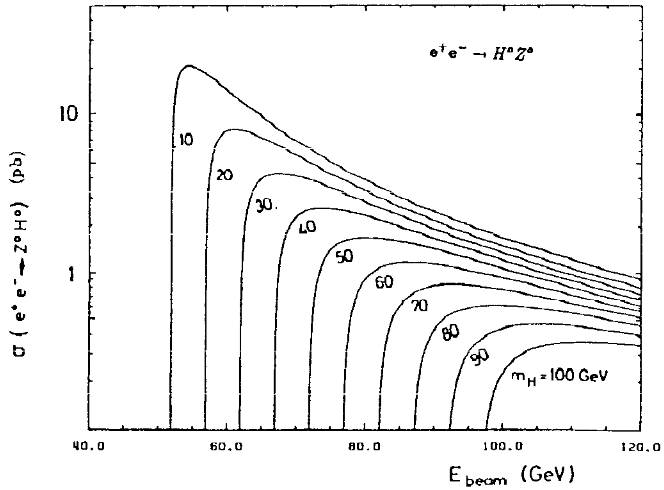

Fig. 27. Higgs production cross section for the bremsstrahlung process $e^+e^- \to Z^{\circ *} \to Z^\circ H^\circ$, as a function of the accelerator beam energy.[25]

In the figure above, the production cross section varies from 1 to 10 picobarns depending upon the mass of the Higgs. For example, at an accelerator operating at 200 GeV in the center-of-mass and for a 60 GeV Higgs mass the expected production rate is approximately 1 picobarn. The production cross section is summarized in Table 4.

E_{cm} (GeV)	M_{H° (GeV)	$\sigma(e^+e^- \to H^\circ Z^\circ)$	Expected Events in $500pb^{-1}$
160	20	3.34pb	1670
	40	2.30	1150
	60	0.89	446
200	20	1.47pb	735
	40	1.19	595
	60	0.92	460
	80	0.62	308
	100	0.23	114

Table 4. Higgs production cross section and event rate for the bremsstrahlung process $e^+e^- \to Z^{\circ *} \to Z^\circ H^\circ$, as a function of the accelerator center-of-mass energy and as a function of the Higgs mass.[28]

In a typical year of operation, at 200 GeV, if an experiment could accumulate a data sample of $500pb^{-1}$, then approximately 500 Higgs events at a mass of 60 GeV would be expected. The number of events drops precipitously as the Higgs mass increases; for a Higgs mass of 100 GeV there are only 100 events expected. Presumably a lower mass Higgs would have already been either discovered or ruled out up to 30 or perhaps even 40 GeV at LEP-1 or SLC by this time. If not, one would probably prefer to run the accelerator at a lower energy, around 160 GeV, in order to study the lower mass Higgs range.

At 200 GeV one is above the W^+W^- threshold, and W pairs or Z pairs become a potential new background to the signal process. There is also substantial QCD background and this has to be contended with as well. The production rate for these processes is summarized in Table 5.

E_{cm} (GeV)	Background Processes	Cross section (pb)
160	σ(QCD)	139.8
200	$\sigma(e^+e^- \to W^+W^-)$ $\sigma(e^+e^- \to Z^\circ Z^\circ)$ σ(QCD)	16.1 2.2 74

Table 5. Background production cross sections at LEP-200.[28]

At LEP-200 there are three possible final state detection channels for the bremsstrahlung production mechanism $e^+e^- \to Z^{\circ *} \to Z^\circ H^\circ$ (region III in Fig. 22). These channels are shown in Fig 28. In all cases the Higgs boson is assumed to decay into $b\bar{b}$, while the Z° can decay to either two neutrinos, two muons or electrons, or two quarks.

The mode $Z^0 \to \nu\bar{\nu}$ is promising due to the large branching fraction, approximately 19%. However, the number of events expected per 500pb^{-1} in the neutrino mode is no more than approximately 100 events for Higgs masses greater than 40 GeV, so this is a rate limited regime. The mode with the charged leptons is almost background free but even more rate limited. There are a significantly greater number of events in the $Z^\circ H^\circ \to q\bar{q}b\bar{b}$ (four-jet) final state, but this is a difficult mode because of QCD multi-jet backgrounds.

7.1. ALEPH Simulation of LEP-200 Higgs Search

As an example, we now discuss a simulation by the ALEPH collaboration of the case of $Z^0 \to \nu\bar{\nu}$ at LEP-200.[28] There are a number of backgrounds, due to any kind of a process that generates neutrinos. For example, in Z^0Z^0 production, which is now kinematically permissible, one Z can decay to $q\bar{q}$ while the other decays to two neutrinos. Also, two W's can decay into a final state consisting of a tau and its neutrino on one side and $q\bar{q}$ on the other. In the decay of the tau lepton additional neutrinos are produced. Two-jet production in QCD, in which heavy quarks decay semi-leptonically, can also produce background.

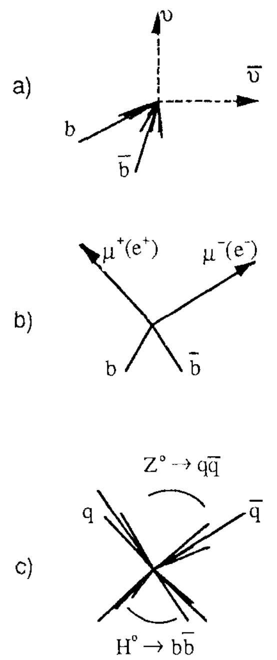

Fig. 28. Three final state production mechanisms considered by the LEP-200 study for the bremsstrahlung process $e^+e^- \to Z^{\circ *} \to Z^\circ H^\circ$. In (a) the Z° decays to $\nu\bar{\nu}$, (b) the Z° decays to charged leptons, and in (c) the Z° decays into $q\bar{q}$ jets. In all three cases shown the Higgs is assumed to decay exclusively to $b\bar{b}$ jets.

Typical cuts (see Table 6) to eliminate these backgrounds might be: 1) Cut on the missing mass to eliminate events without a Z^0 in the final state. This reduces backgrounds from W^+W^- and QCD, (see Fig. 29a) for the missing mass distribution for the case of a Higgs mass of 60 GeV. This is fairly effective in reducing these backgrounds. 2) Cut on missing momentum. That also rejects QCD events (see Fig. 29b), because one expects to see a substantial amount of missing p_t for Z° events with neutrinos in them. However, there is a substantial loss of efficiency with this requirement. 3) Cut on event sphericity in the rest frame of the final state $q\bar{q}$ system, sphericity is defined as the sum

$$S = \frac{2}{3} \mathrm{MIN} \left[\left(\sum_j (p_j^T)^2 \right) \right] \Big/ \left[\left(\sum_j (p_j)^2 \right) \right],$$

and where p^T is the momentum transverse to the sphericity axis, which minimizes this sum. The event sphericity is near zero for a two-jet event, and near one for an event without structure. One expects the $b\bar{b}$ jets to look broader because they are heavier than udsc quarks (see Fig. 30).

ALEPH LEP-200 Simulation Selection Requirements
Missing Mass > 92 GeV
Missing Momentum > 30 GeV
Sphericity in rest frame > 0.02
Apply Constraint $Z^\circ \to \upsilon\bar{\upsilon}$

Table 6. Summary of ALEPH Simulation Selection Criteria for Higgs Boson Searches in the Mode $e^+e^- \to Z^{\circ *} \to Z^\circ H^\circ \to \upsilon\bar{\upsilon}b\bar{b}$ at LEP-200.

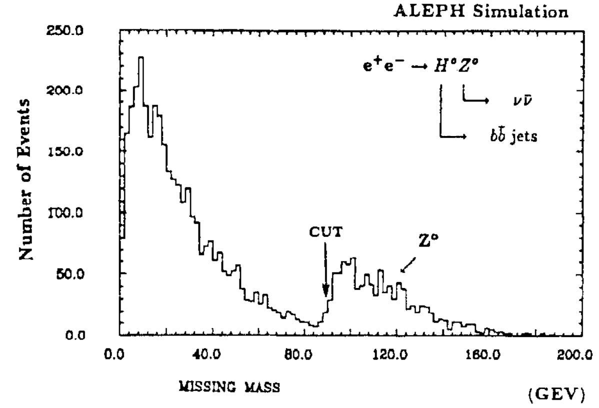

Fig. 29a. ALEPH simulation for LEP-200 ($\sqrt{s} = 200$ GeV) for the process $e^+e^- \to Z^{\circ *} \to Z^\circ H^\circ \to \upsilon\bar{\upsilon}b\bar{b}$. Shown in the figure is the missing mass distribution, the background from QCD and W^+W^- events are at left while signal events are to the right of the Z^0 mass (91 GeV). The figure is from a simulation for a Higgs mass of 60 GeV.[28] The curves are not normalized.

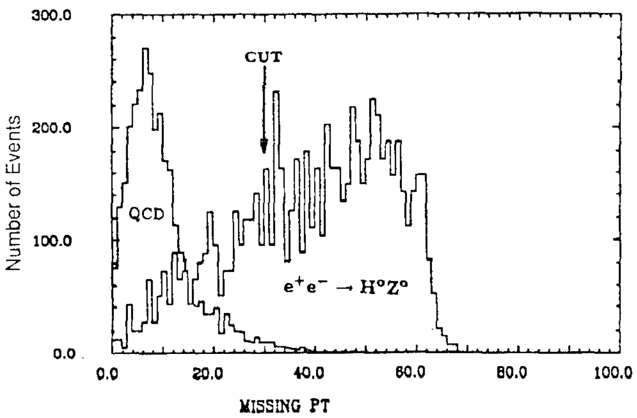

Fig. 29b. ALEPH simulation for LEP-200 ($\sqrt{s} = 200$ GeV) for the process $e^+e^- \to Z^{o*} \to Z^oH^o \to \nu\bar{\nu}b\bar{b}$. Shown in the figure is the missing momentum distribution, the background from QCD events are at left while signal events are to the right. The figure is from a simulation for a Higgs mass of 60 GeV.[28] The curves are not normalized.

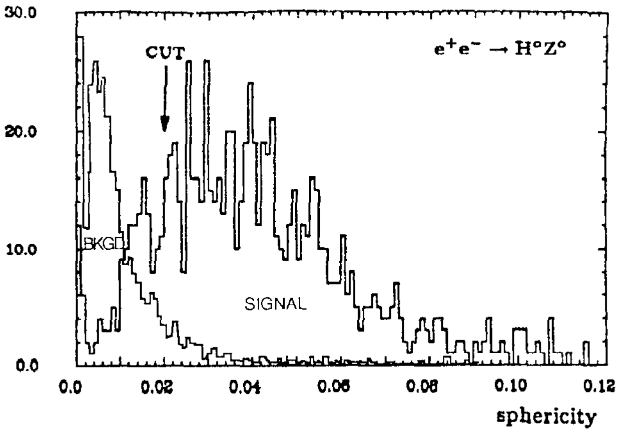

Fig. 30. ALEPH simulation for LEP-200 ($\sqrt{s} = 200$ GeV) for the process $e^+e^- \to Z^{o*} \to Z^oH^o \to \nu\bar{\nu}b\bar{b}$. Shown in the figure is the sphericity distribution. The background from QCD events are at left while signal events are to the right. The figure is from a simulation for a Higgs mass of 60 GeV.[28] The curves are not normalized.

After these event selection criteria are applied, an additional constraint is imposed that the missing particles in the event, i.e. the two neutrinos, come from a Z^o. Then one examines various postulates of what the Higgs mass might be. For example, for M_H=40, 60, and 80 GeV, the distribution shown in the figure below is obtained after all cuts and with the background and the signal normalized to an integrated luminosity of $500 pb^{-1}$ and $\sqrt{s} = 200$ GeV.

For M_H=40 GeV the signal is readily apparent over background. For increasing values of the Higgs mass, from 40 to 60 GeV, the signal begins to merge with the background and the rate is reduced. By 80 GeV the ratio of signal to background is only 3, and the peak may be difficult to resolve for a data sample of only 500 pb^{-1}.

The simulation for the ALEPH experiment concluded that in this mode, for 40, 60, and 80 GeV Higgs masses one would expect 49, 34, and 12 signal events, respectively. The signal to background ratio was computed, comparing the number of signal events on peak to the number of background events under that peak, as summarized in the table below. The invariant mass spectrum for these three different mass values is shown in Fig. 31.

$e^+e^- \to Z^\circ H^\circ$ where $Z^\circ \to \nu\bar{\nu}$ and $H^\circ \to b\bar{b}$				
M_{H° (GeV)	Total # of Events	# of Signal Events at Peak	# of Background Events at Peak	Signal/Background
40	107	49	2	25
60	83	34	7	5
80	56	12	4	3

Table 7. Conclusion for ALEPH simulation for LEP-200 for an integrated luminosity of 500pb-1 in the process $e^+e^- \to Z^\circ H^\circ$ where $Z^\circ \to \nu\bar{\nu}$ and $H^\circ \to b\bar{b}$.[28]

The ALEPH analysis also looked at $Z^\circ \to e^+e^-$ or $Z^\circ \to \mu^+\mu^-$. These modes are more or less background free, but are rate limited at the very high end of the mass range at 80 GeV. Here the signal to background is still only 3.7, not much better than the neutrino mode. The conclusions for this analysis are summarized in Table 8.

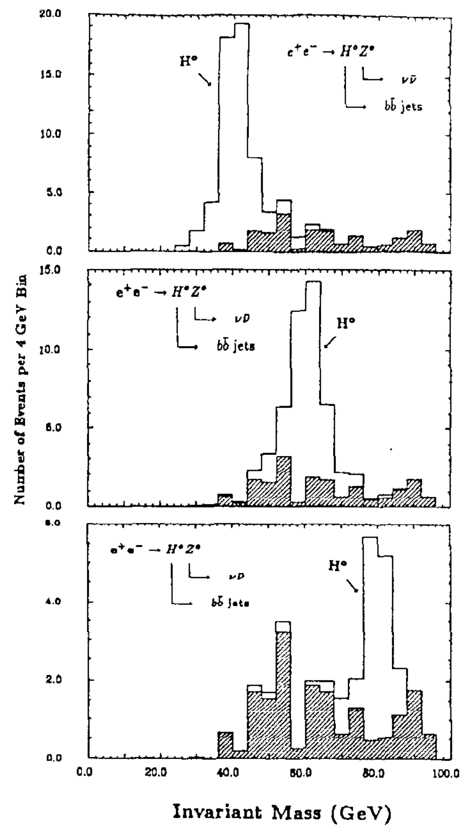

Fig. 31. ALEPH simulation for LEP-200 ($\sqrt{s}$ = 200 GeV) for the process $e^+e^- \to Z^{\circ*} \to Z^\circ H^\circ \to \nu\bar{\nu}b\bar{b}$. The plots are, from top to bottom, for M_H= 40, 60, and 80 GeV. Shown in the figure is the signal (solid histogram) normalized for a data sample of 500pb^{-1} and with all background sources (hashed histogram). The figure is taken from Ref. [28].

$e^+e^- \to Z^\circ H^\circ$ where $Z^\circ \to e^+e^-$ or $Z^\circ \to \mu^+\mu^-$ and $H^\circ \to b\bar{b}$				
M_{H° (GeV)	Total # of Events	# of Signal Events at Peak	# of Background Events at Peak	Signal/Background
40	36	24	0.2	Large
60	28	17	0.6	28
80	18	11	3	3.7

Table 8. Conclusion for ALEPH simulation for LEP-200 for an integrated luminosity of 500pb-1 in the process $e^+e^- \to Z^\circ H^\circ$ where $Z^\circ \to e^+e^-$ or $Z^\circ \to \mu^+\mu^-$ and $H^\circ \to b\bar{b}$.[28]

The other mode that was looked at, which I will just briefly mention here, is a four-jet final state, $Z^\circ H^\circ \to q\bar{q}b\bar{b}$. The background to this mode is from QCD multijets. Here the signal to background ratio is only 2 and is clearly not favorable as compared to the other modes. The conclusions for this analysis are summarized in Table 9.

$e^+e^- \to Z^\circ H^\circ$ where $Z^\circ \to q\bar{q}$ and $H^\circ \to b\bar{b}$				
M_{H° (GeV)	Total # of Events	# of Signal Events at Peak	# of Background Events at Peak	Signal/Background
40	430	54	23	2.3
60	340	60	31	2
80	-	-	-	-

Table 9. Conclusion for ALEPH simulation for LEP-200 for an integrated luminosity of 500pb^{-1} in the process $e^+e^- \to Z^\circ H^\circ$ where $Z^\circ \to q\bar{q}$ and $H^\circ \to b\bar{b}$.[28]

8. Higgs Searches at Future e^+e^- Colliders

Next we will discuss Higgs searches at future colliders, in particular TLC, CLIC and SSC. The TLC (TeV Linear Collider) is a linear e^+e^- machine that would operate at 1 TeV,[29] and CLIC (CERN Linear Collider), is a CERN design for a linear e^+e^- collider that would operate at 2 TeV.[30] The SSC (Superconducting Super Collider) is a pp machine which is planned to operate at 40 TeV.[31]

8.1. WW and ZZ Decays

At these, higher energy scales, new decay modes of the Higgs appear with couplings that are quite different from what we have discussed so far. For example, a very heavy Higgs can decay to two W's or to two Z's. This has important experimental consequences. The coupling is proportional to $G_F \times M_H^3$, so the decay width grows as the mass cubed. As expected this decay rate to two massive gauge bosons is almost identical to the rate we discussed earlier for $\Gamma(H^\circ \to \gamma\gamma) \propto G_F\alpha^2 M_H^3$ aside from the factor of α^2. The rate for the decay $H \to Z^\circ Z^\circ$ is about half that of the decay to two W's, where the factor of one-half arises from the final state summation over two identical particles:

$$\Gamma(H^\circ \to W^+W^-) = \frac{G_F M_H^3}{8\pi\sqrt{2}}\beta_w \cdot \left(\beta_w^2 + \frac{12m_w^4}{M_H^4}\right) \cong 328\,\text{GeV} \cdot [M_H(\text{TeV})]^3$$

$$\Gamma(H^\circ \to Z^\circ Z^\circ) = \frac{G_F M_H^3}{16\pi\sqrt{2}}\beta_w \cdot \left(\beta_w^2 + \frac{12m_w^4}{M_H^4}\right) \cong 164\,\text{GeV} \cdot [M_H(\text{TeV})]^3 .$$

Adding both of these decay widths, the total decay width of a very heavy Higgs is given by:

$$\sim 500\,\text{GeV}\left[\frac{M_H}{1\,\text{TeV}}\right]^3 .$$

Therefore a Higgs particle with a mass of 1.3 TeV has a width equal to its mass, and at that scale has a behavior that is more like a continuum than like a particle.

8.2. Decay Rate to Top Quarks

Another interesting phenomenon in the case of a high mass Higgs occurs if there is a very massive top quark. Normally, the Higgs likes to couple to the heaviest kinematically accessible fermion, but it happens that the coupling to gauge bosons is even stronger. So if one hypothesizes that $M_H > 2m_w$ and $M_H > 2m_{Top}$ then,

$$\frac{\Gamma(H \to W^+W^-)}{\Gamma(H \to t\bar{t})} \cong \frac{M_H^2}{2m_{Top}^2} > 2 \ .$$

Above the W-pair threshold, this ratio is always larger than two. Thus, although we do not know the top quark mass, we know that for the purposes of these high mass studies the decay $H \to W^+W^-$ will always dominate for a minimal standard model Higgs boson. A graphical representation of Higgs decay rate as a function of mass is shown in Fig. 32.

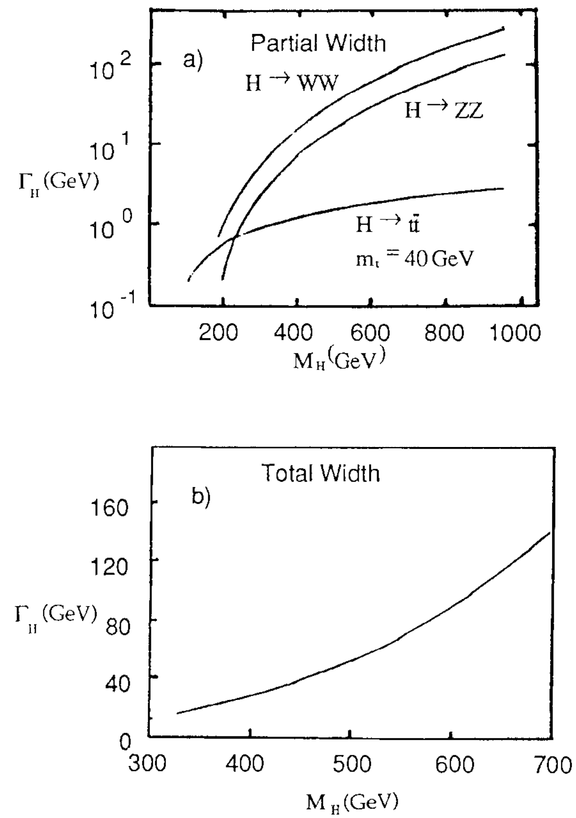

Fig. 32. In (a) the Higgs boson partial decay width to W^+W^-, $Z^\circ Z^\circ$, and $t\bar{t}$ (m_t=40GeV) final states. In (b) the Higgs boson total width is shown as a function of the Higgs mass.[25,32]

8.3. Longitudinally Polarized W Pairs

When a heavy Higgs decays into W or Z pairs, they will tend to be longitudinally polarized. The fraction of longitudinal decays, f_L, and transverse decays, f_T, are given by the following,[33]

$$f_L = \left[\frac{M_H^2}{2m_z^2} - 1\right]^2 \Bigg/ \left[\left(\frac{M_H^2}{2m_z^2} - 1\right)^2 + 2\right]$$

$$f_T = 2 \Bigg/ \left[\left(\frac{M_H^2}{2m_z^2} - 1\right)^2 + 2\right]$$

The fraction of polarized W's or Z's as a function of the mass of the Higgs is shown in the table below.

M_{H^0}(GeV)	Γ(GeV)	f_L	f_T
200	1.8	0.47	0.53
300	9.1	0.90	0.10
500	53.2	0.99	0.01
800	238	0.998	0.002
1000	474	0.999	0.001

Table 10. The total decay width for massive Higgs boson decays and the fraction of the decays into longitudinally (f_L) and transversely polarized (f_T) gauge boson pairs (W's and Z's) as a function of the Higgs boson mass. For M_H>300 GeV the heavy Higgs will decay primarily to longitudinally polarized states ($W_L^+W_L^-$ and $Z_L^\circ Z_L^\circ$).[33]

For example, a 300 GeV mass Higgs decays with a probability of 90% to longitudinally polarized pairs. For very massive Higgs almost 100% of the decays are into longitudinally polarized pairs. This has experimental ramifications if one considers angular distributions: a longitudinally polarized W will decay with a different angular distribution than a transversely polarized W.

8.4. WW Fusion

In addition to new decay modes, there is a new production process that takes place at these very high energies. Besides the bremsstrahlung mechanism that we have already discussed, shown in Fig. 33a) below, there is the WW fusion process, shown in Fig. 33b) below.

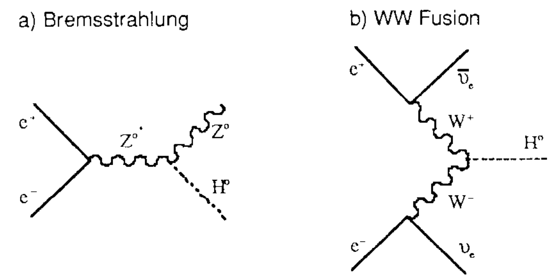

Fig. 33. Feynman graph for the bremsstrahlung process in (a) is supplanted by the WW fusion graph shown in (b) for heavy Higgs production.

The WW fusion process is analogous to the two-photon process shown in Fig. 34 that we know from low energy e^+e^- machines, in which a flux of virtual photons is radiated off the incoming electrons.

Two-Photon Process

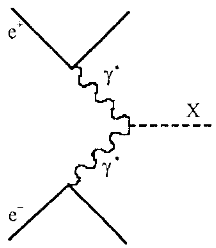

Fig. 34. Feynman graph for the two-photon process.

Two of these virtual photons can fuse to form a new state, a resonance for example. The formalism for this is well known, and the rate can be calculated using the equivalent photon approximation of Weizsacker and Williams.[34] In the equivalent photon approximation the energy spectrum of the emitted bremsstrahlung photons is given by,

$$\frac{dN}{dk} = \frac{N(k)}{k} \quad \text{and} \quad N(k) \approx \frac{2\alpha}{\pi} \ln \frac{E}{m_e} .$$

The production cross section is then obtained by integrating over the emitted photon flux and the $X \to \gamma\gamma$ width for the final state X. The following result is obtained,

$$\sigma(e^+e^- \to e^+e^-X) = \int \frac{dk_1}{k_1} \int \frac{dk_2}{k_2} N(k)N(k)\sigma_{\gamma\gamma\to X}(4k_1k_2)$$
$$\cong \frac{2\alpha^2}{\pi}\left[\ln\frac{E}{m_e}\right]^2 \int \frac{ds}{s}\sigma_{\gamma\gamma\to X} f\left(\frac{\sqrt{s}}{2E}\right)$$

where the function f is the form factor for the final state. For resonance production the simple form is obtained,

$$\sigma(e^+e^- \to e^+e^-X) = \frac{8\alpha^2}{M_x^3}\Gamma^x_{\gamma\gamma} \cdot \ln\frac{s}{M_e^2} \cdot f\left(\frac{M_x}{2E}\right) .$$

The fact that the rate increases as log s is important at the highest energies. Remember that the point cross section is falling like 1/s. If we now consider the case of WW or ZZ fusion we can again use the Weizsacker-Williams approximation. The decay width of $H \to W^+W^-$ or $H \to Z^\circ Z^\circ$ is given by:

$$\Gamma(H^\circ \to W^+W^-) = \frac{G_F M_H^3}{8\sqrt{2}\pi} \quad \text{and} \quad \Gamma(H \to Z^\circ Z^\circ) = \frac{G_F M_H^3}{16\sqrt{2}\pi} .$$

Using the form factors corresponding to both W's being transversely polarized or both longitudinally polarized, one obtains:

$$W_{TT}: \quad f \cong \ln\left(\frac{s}{m_w^2}\right)^2 \left[(2+\tau)^2 \ln\frac{1}{\tau} - 2(1-\tau)(3+\tau)\right]$$
$$W_{LL}: \quad f \cong (1+\tau)\ln\frac{1}{\tau} + 2(\tau - 1) \qquad \text{where } \tau \equiv \frac{M_H^2}{s} .$$

Then the total cross section for $M_H \gg m_w$, where the two W's are predominantly longitudinally polarized is[4]

$$\sigma(e^+e^- \to \nu\bar{\nu}H^\circ) \cong \frac{1}{16 m_w^2} \cdot \left[\frac{\alpha}{\sin^2\theta_w}\right]^3 \cdot \left[(1+\tau)\ln\frac{1}{\tau} - 2 + 2\tau\right]$$
$$\cong 0.13\text{pb} \times \ln\left(s/M_H^2\right) .$$

While for comparison, the bremsstrahlung cross section for $M_H \ll \sqrt{s}$ is

$$\sigma(e^+e^- \to Z^\circ H^\circ) \cong \frac{0.01}{s[\text{TeV}^2]} \text{pb}.$$

At sufficiently high energy the fusion process will overtake the bremsstrahlung process. In the figure below the production cross section for the bremsstrahlung mechanism in Fig. 35a) is compared to the WW fusion process shown in Fig. 35b) for a variety of Higgs masses. Also shown is the point cross section for e^+e^-.

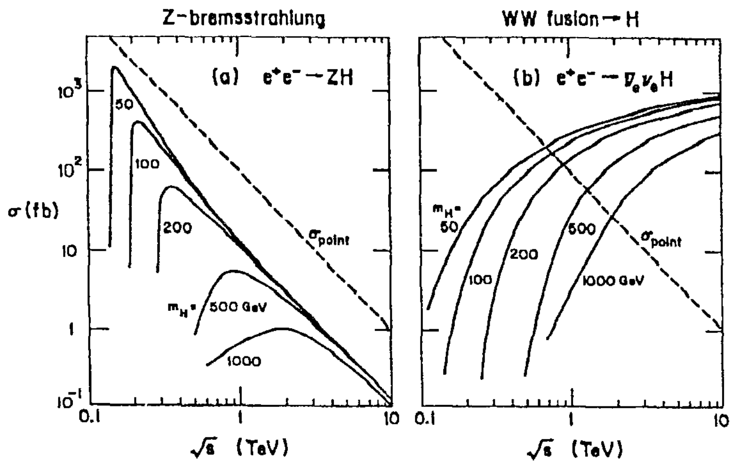

Fig. 35. In (a) the production cross section for the bremsstrahlung mechanism $e^+e^- \to Z^\circ H^\circ$ is compared to the WW fusion process $e^+e^- \to \upsilon_e \bar{\upsilon}_e H^\circ$ shown in (b) for a variety of Higgs masses.[35] Also shown is the point cross section for e^+e^-, $\sigma_{point} = 86.8\mathrm{nb}/s(\mathrm{GeV}^2)$.

8.5 High Energy e^+e^- Colliders

At a 1 TeV collider, we are already well into the regime where WW fusion dominates. For a Higgs mass of a 100 GeV, at 1 TeV center-of-mass, the production cross section is about 3.4 units of R, where a unit of R is given by the point cross section $86.8\mathrm{nb}/s(\mathrm{GeV}^2)$, which at 1 TeV is 86.8 fb. Enormous luminosities are required in order to obtain a measurable rate. For example at a luminosity of 1×10^{33}, with a cross section equal to one unit of R, 1000 events are produced in a canonical year of 10^7 seconds.

How can a luminosity of $10^{33}\mathrm{cm}^{-2}\mathrm{sec}^{-1}$ be achieved at 1 TeV center-of-mass? An e^+e^- storage ring with E_{cm}=1 TeV would be prohibitively expensive since the cost of such a storage ring scales with E^2_{cm}. On the other hand, a linear collider should scale linearly with energy, because you just make the collider longer to get to higher energy. The SLC, at SLAC, is the first example of such a linear collider. Electrons and positrons are accelerated in the same linear accelerator, then the electrons go around one arc and the positrons go around the other and they collide at the center. That is fine for center-of-mass collisions at 100 GeV, but there is a substantial synchrotron energy loss in the arcs that become a significant problem at 1 TeV. The solution is to have two linacs colliding head on, as illustrated in Fig. 36.

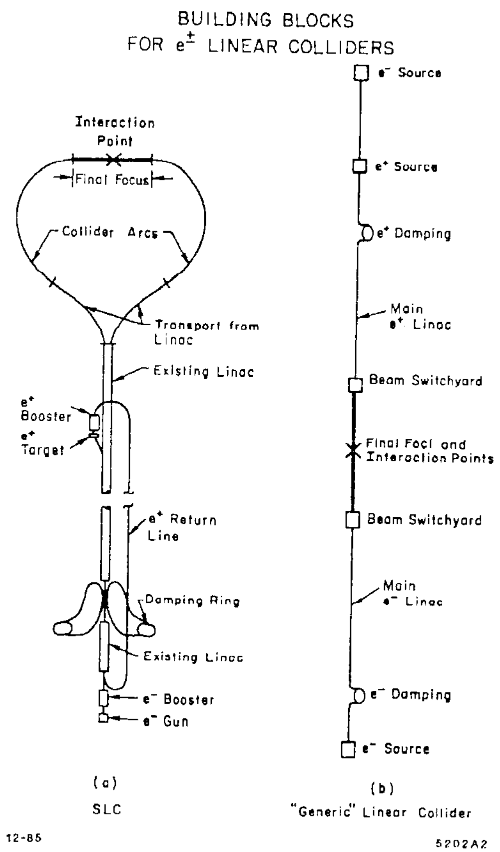

Fig. 36. In the figure at left (a) is shown a schematic of the linear collider at SLAC which accelerates both electrons and positron in the same accelerator. At right (b) a generic design of high energy collider is shown where electrons and positrons are accelerated in separate structures.

8.6. Linear e+e- Collider Parameters

What are the parameters of such a collider? The TLC design, conceived at SLAC, has a center-of-mass energy of 1 TeV and a design luminosity of 1×10^{33}. The CERN design, CLIC, has a center-of-mass energy of 2 TeV and a comparable luminosity. The properties of these colliders is shown in the following table.

	SLC	CLIC	TLC
E_{cm}	100 GeV	2 TeV	1 TeV
Power Source	Klystron	Superconducting Drive LINAC	Relativistic Klystron
Accelerator Gradient	17 MV/m	80 MV/m	196 MV/m
Accelerator Length	3 km	2x12.5 km	2x2.5 km
Luminosity ($cm^{-2}sec^{-1}$)	$6x10^{30}$	$1.1x10^{30}$	$1.2x10^{33}$

Table 11. Parameters of the existing e+e- collider SLC, and the proposed 1 TeV collider TLC and the 2 TeV collider CLIC.[32]

8.7 Background Processes at 1-2 TeV

At these very high energies a whole new realm of background processes appears which we need to understand. These backgrounds fall into two distinct classes, the first order standard model processes and the second order peripheral interactions. The standard model backgrounds are from the single photon or Z annihilation graphs in Fig. 37a) and b), and the electron, or neutrino exchange processes such as those shown in Fig. 37c) and d).

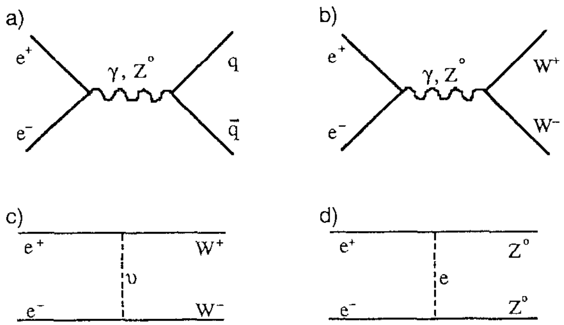

Fig. 37. Annihilation and standard model backgrounds to massive Higgs boson detection. Shown in the figure are the processes (a) $e^+e^- \rightarrow q\bar{q}$, (b) $e^+e^- \rightarrow W^+W^-$,(c) $e^+e^- \rightarrow W^+W^-$,and (d)$e^+e^- \rightarrow Z^oZ^o$.

The backgrounds due to the peripheral interactions are primarily from two photon interactions and the WW or Wγ fusion process. These processes are shown in the figure below.

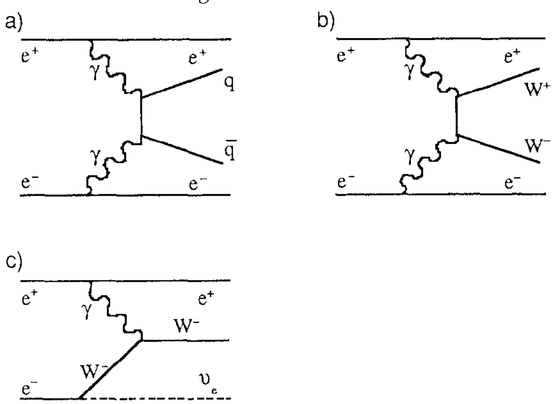

Fig. 38. Background processes to massive Higgs boson detection from second order processes. Shown in the figure are the processes (a) $e^+e^- \rightarrow e^+e^-q\bar{q}$, (b) $e^+e^- \rightarrow e^+e^-W^+W^-$, and (c)$e^+e^- \rightarrow e\upsilon W$.

There are numerous backgrounds to be contended with that are significantly larger than the signal process prior to analysis cuts, as can be seen in Fig. 39. For example there is the standard two-jet process, $e^+e^- \rightarrow q\bar{q}$, which has a cross section nine times the point cross section, or nine units of R, and there is the process $e^+e^- \rightarrow W^+W^-$ which has a rate of about 27 units of R.[36] There are actually two diagrams for the latter process, the s channel with a virtual γ or Z, and the t-channel where a neutrino is exchanged. At these high energies the t-channel diagram causes sharp peaking in the forward and backward direction along the beam line. In order to reduce this background one therefore makes restrictive cuts on the event axis. There is also the process $e^+e^- \rightarrow Z^oZ^o$, although at a reduced rate relative to W pair production. The process $e^+e^- \rightarrow e^+e^-W^+W^-$ is a background for high mass Higgs searches, as we will see later. This latter mode also has a very substantial production cross section, and it has the property that $p_T^{w^+w^-} \approx 0$. Another background process that is quite important is $e^+e^- \rightarrow e\upsilon W$. The final state W has a large p_T ($p_T^w \approx m_w$) which is much the same as the large p_T of the Higgs in the WW fusion process (also $p_T^w \approx m_w$). A fairly comprehensive list of backgrounds is shown in Table 12 along with their production cross sections.

Annihilation Process	σ (units of R)
$e^+e^- \to \ell^+\ell^-$	4
$e^+e^- \to q\bar{q}$	9
$e^+e^- \to W^-W^+$	27
$e^+e^- \to Z^oZ^o$	1.5
$e^+e^- \to \gamma\gamma$	10
$e^+e^- \to \gamma Z^o$	31
$e^+e^- \to W^+W^-Z^o$	0.4
$e^+e^- \to Z^oZ^oZ^o$	0.03

Peripheral Interaction	σ (units of R)
$e^+e^- \to e^+e^-q\bar{q}$	1
$e^+e^- \to e^+e^-W^+W^-$	9.3
$e^+e^- \to e\upsilon WZ^o$	3.4
$e^+e^- \to e\upsilon W$	140
$e^+e^- \to e^+e^-Z^o$	70

Table 12. Summary of background rates at a 1 TeV e^+e^- collider.[36]

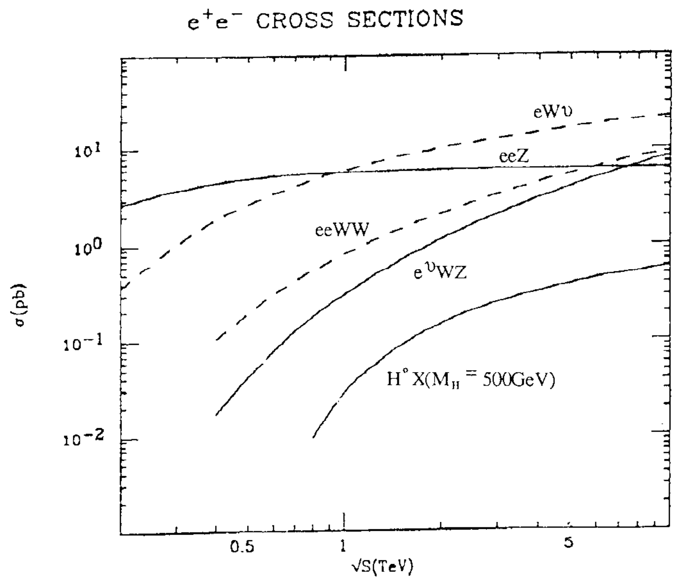

Fig. 39. Background processes compared to the Higgs production rate for the case of M_H=500 GeV as a function of e^+e^- collider center-of-mass energy.[37]

9. TLC/CLIC Design Studies

In order to be able to distinguish between signal and background one requires a very good detector. In the TLC design studies, a detector with very good hadronic calorimetry was assumed, with a resolution of $\sigma / E = 50\%/\sqrt{E} + 2\%$. The electromagnetic calorimeter was assumed to have $8\%/\sqrt{E} + 2\%$ resolution. This is a very difficult set of parameters to obtain simultaneously, in the real world. The TLC studies further assumed a very good tracking system, with a resolution of $\sigma_p/p = 0.3 \cdot p(\mathrm{TeV}/c)$.

The TLC is assumed to operate at a luminosity of $1\times10^{33}\,\mathrm{cm^{-2}s^{-1}}$, resulting in an integrated luminosity of 10 $\mathrm{fb^{-1}}$/year. The most important production process is the WW fusion process ($e^+e^- \to \upsilon\bar{\upsilon}H^o$), with a cross section 17 times greater than the bremsstrahlung process for M_H=100 GeV.

There are two analysis regions that are quite distinct and which we will consider separately. The first region concerns the intermediate mass Higgs, with $M_H < 2m_w$. The Higgs cannot decay into two W's, and decays instead to $b\bar{b}$. The dominant sources of background come from $e^+e^- \to e\upsilon W$ and $\upsilon\bar{\upsilon}H$. The second analysis region applies to the high mass Higgs, $M_H > 2m_w$, where the Higgs can decay into WW. There is background coming from other peripheral interactions such as $e^+e^- \to W^+W^-e^+e^-$ where both electrons go down the beam pipe. Other backgrounds are due to fusion processes producing ZZ and WZ.

9.1. Intermediate Mass Higgs Search Region

We will start with the intermediate mass Higgs search region, and assume that the Higgs boson does not decay to top, $M_H < 2m_{top}$, but rather exclusively to b quarks with $BR(H^0 \to b\bar{b}) \sim 100\%$. Finally, we assume that the Higgs boson is produced by either the fusion process, $e^+e^- \to \upsilon\bar{\upsilon}H^0 \to \upsilon\bar{\upsilon}b\bar{b}$, or by bremsstrahlung $e^+e^- \to Z^0 H^0 \to \upsilon\bar{\upsilon}b\bar{b}$.

The signature for production of an intermediate mass Higgs boson is two low mass jets corresponding to the $b\bar{b}$ system. There will be some missing transverse momentum in the event carried off by the neutrinos. Because the Higgs is produced primarily through WW fusion, the produced Higgs will also have a substantial transverse momentum due to the massive W propagators. The other important signature is that the b quark is relatively long lived, so one should be able to see a secondary vertex in the detector.

9.2. TLC Design Study

A comprehensive study of the intermediate mass region was performed as part of the TLC study at SLAC.[29,32,38] As we just discussed, the signatures for this mass region are two b quark jets and large missing transverse momentum. To select these events, a two cluster analysis was performed, requiring that the mass of each of the two jets be consistent with a b-quark and not consistent, e.g. with a W or Z. A substantial amount of missing transverse momentum was required: $|\sum_i \vec{p}_T^{\,i}| > 50$ GeV. To select events with a long lived particle they simply required that there be at least four tracks with a large (>3σ) impact parameter; δ:

$$3\times\left[(5\mu\mathrm{m})^2+(50\mu\mathrm{m}/p(\mathrm{GeV}))^2\right]^{\frac{1}{2}} < \delta < 3\,\mathrm{mm}.$$

This assumes that one has an excellent vertex detector with resolution given by the quantity in brackets. To avoid selection of K^{o}'s or other very long lived particles there was the further requirement that the impact parameter be less than 3 mm. Finally, the two b quark jets will not be coplanar since the Higgs is not produced at rest in the lab frame in the fusion process, so an acoplanarity greater than 10 degrees was required. If the mass of the top quark were low enough, e.g. 40 GeV, then $e^+e^- \to e^+\upsilon_e W^- \to e^+\upsilon_e t\bar{b}$ would be kinematically allowed, and would become the predominant background process for this intermediate mass search region, due to the high rate for this process and the similarity in the final state parameters. It is now known experimentally that m_{Top}>77 GeV, so this is not a concern.[39] However, at the time of this study, high mass limits on the top quark were not available.

In this study an integrated luminosity of $\int L dt = 30\,\mathrm{fb^{-1}}$ and $\sqrt{s} = 1$ TeV was assumed. This corresponds to three years at design luminosity or one year at three times the design luminosity. In Fig. 40 the signal for the process $e^+e^- \to \upsilon\bar{\upsilon}H^0 \to \upsilon\bar{\upsilon}b\bar{b}$ and $e^+e^- \to Z^0 H^0 \to \upsilon\bar{\upsilon}b\bar{b}$ is shown together with the main background due to $e^+e^- \to e^+\upsilon_e W^- \to e^+\upsilon_e t\bar{b}$. The

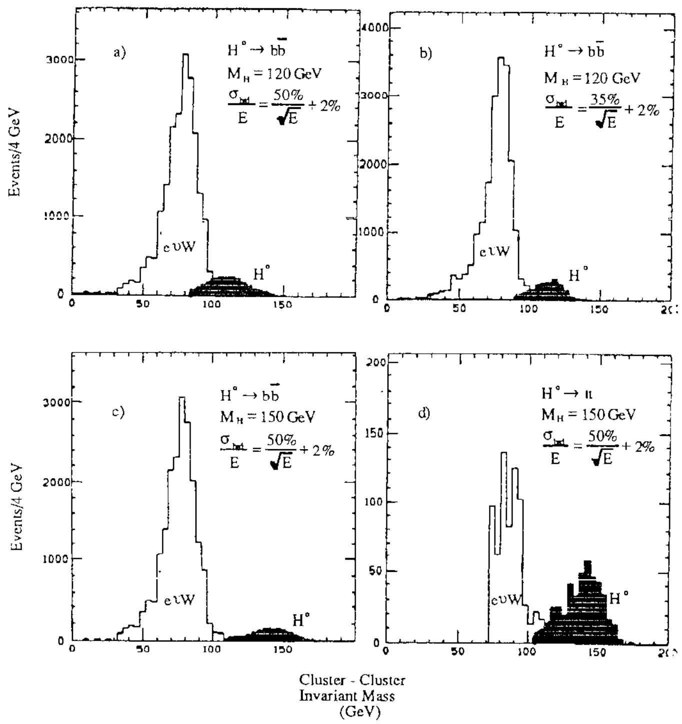

Fig. 40. The signal for the process $e^+e^- \to \nu\bar{\nu}H^0 \to \nu\bar{\nu}b\bar{b}$ and $e^+e^- \to Z^0 H^0 \to \nu\bar{\nu}b\bar{b}$ is shown together with the main background due to $e^+e^- \to e^+\nu_e W^- \to e^+\nu_e t\bar{b}$. The distribution of two-cluster invariant mass for the two b-jets is plotted in the figure. In (a) and (b) M_H=120 GeV, in (c) and (d) M_H=150 GeV. The detector resolution for hadrons is assumed to be $\sigma/E = 50\%/\sqrt{E} + 2\%$ in (a), (b), and (c), an improved resolution of $\sigma/E = 35\%/\sqrt{E} + 2\%$ is assumed in plot (b). In plot (d) it is assumed that the Higgs decay mode is $H \to t\bar{t}$, m_T=40 GeV, a four cluster analysis is then performed to detect the top decays.[40]

distribution of two-cluster invariant masses for the two b-jets is plotted in the figure. The study considered two possible intermediate mass Higgs, M_H=120 GeV and M_H=150 GeV. Assuming a canonical TLC generic detector with $50\%/\sqrt{E}$ hadronic resolution, the background tends to obscure the signal, but for a Higgs mass of 150 GeV the signal stands out quite clearly. If one could build an even better detector with a resolution of $35\%/\sqrt{E}$ even a 120 GeV mass Higgs stands out quite convincingly. One can also do a completely different analysis by assuming that the main Higgs decay mode is $H \to t\bar{t}$. Then one performs a four cluster analysis and can do quite well for example in finding a 150 GeV Higgs. This is of course at the edge of the kinematic limit given our present knowledge of the lower bound on the top quark mass.

The conclusion from the TLC study is that one can just marginally detect a M_H=120 GeV Higgs, but can detect a M_H=150 GeV Higgs quite well. If one were to assume a heavy top, so that the W cannot decay to $t\bar{b}$ then the background is dramatically reduced. It would be rather interesting to see this analysis repeated based on the new top quark mass limits. It is likely that the analysis could be extended to find Higgs bosons with masses below 120 GeV. Higgs bosons with masses close to the W or Z mass are nonetheless very difficult to discover since the detected signature is almost indistinguishable from these particles.

9.3. High Mass Higgs Search Region

The TLC study also examined the high mass Higgs search region, $M_H > 2m_w$, where we will assume that the Higgs decays exclusively to WW or ZZ and is produced through the fusion process $e^+e^- \to \nu\bar{\nu}H^\circ$. In this mass region one can more or less ignore the top quark since $\Gamma(H^\circ \to W^+W^-)/\Gamma(H^\circ \to t\bar{t}) \cong M_H^2/2m_T^2 > 2$ if $M_H > 2m_T$. Here one is looking for a final state consisting of 2 W's (or Z's) produced with substantial transverse momentum, $p_T^{WW} \approx O(m_w)$, since the produced Higgs obtains large transverse momentum in the fusion process due to the massive W propagators. The P_T spectrum of the final state WW pair is shown in the figure below; it peaks near the W mass of 80 GeV. One therefore performs an analysis to select this region, which is a novel signature for this process.

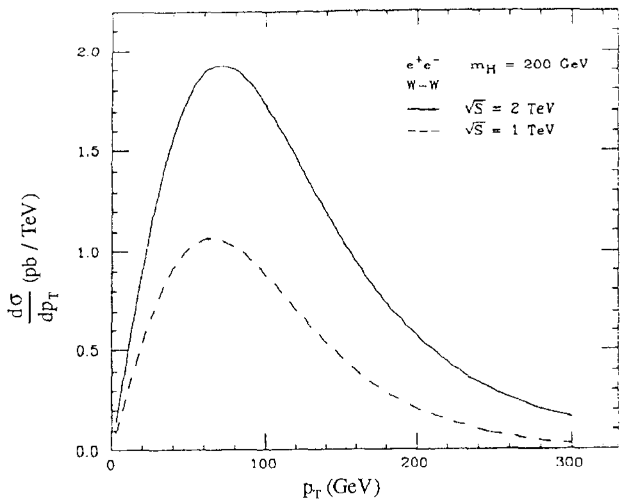

Fig. 41. Transverse momentum spectrum for Higgs bosons produced from WW fusion.[41]

The heavy Higgs selection for the TLC study is straightforward. The principal backgrounds due to $e^+e^- \to W^+W^-$ or $e^+e^- \to Z^\circ Z^\circ$ are t-channel processes and are therefore sharply peaked along the beam axis.[42] One therefore determines the thrust axis of the event and requires that the event be centrally produced by selecting $|\cos\theta_{thrust}| < 0.8$. A cut on the transverse momentum, $|\sum_i \vec{p}_T^{\,i}| > 50\,\mathrm{GeV}$, exploits the large expected P_T for the signal while rejecting two-photon backgrounds which peak at P_T=0. Then one performs a two-cluster analysis to detect two W's. The invariant mass of the smallest of the two clusters is required to be in the region $66 < M^{min}_{cluster} < 94$ GeV while the other must be in the region $75 < M^{max}_{cluster} < 100$ GeV. These cuts select a region that brackets the possibility that either of the two particles is a $W^\pm$ or a Z°. Finally, because of the large expected transverse momentum one requires the two W's or Z's to have an acoplanarity>10°. These cuts result in a very background free signal as can be seen in the figure below. In a data sample of 30 fb^{-1}, for M_H=300 GeV 125 signal events pass these selection requirements (for an efficiency of 7.9%). For M_H=500 GeV 46 events pass (for an efficiency of 12%).

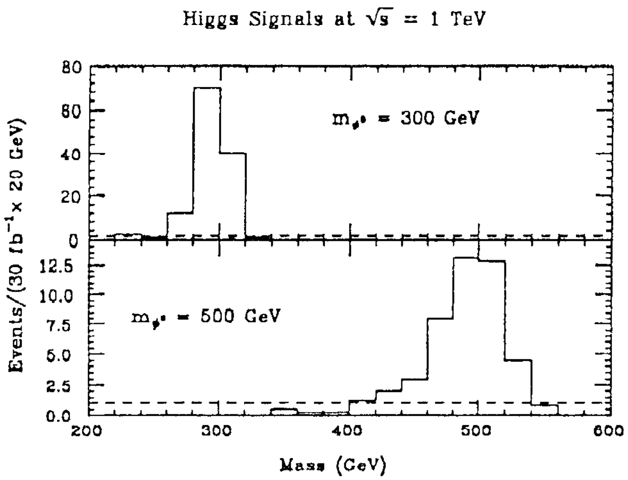

Fig. 42. The heavy Higgs signal from the fusion process $e^+e^- \to \nu\bar{\nu}H^\circ$, where the Higgs boson decays to W or Z pairs, is shown in the figure for the TLC study at $\sqrt{s} = 1$ TeV and a data sample of 30 fb^{-1}. The histogram at top is for M_H=300 GeV, 125 signal events appear in the peak after all selection requirements. The histogram at bottom is for M_H=500 GeV, 46 events appear in the peak. The dashed line shows the expected background level due to $e^+e^- \to W^+W^-$ or $e^+e^- \to Z^\circ Z^\circ$.[2]

9.4. Heavy Higgs Search Strategy for CLIC from the La Thuile Study

A similar analysis was performed in a CERN study at La Thuile where the CLIC design at $\sqrt{s} = 2$ TeV was considered.[37,43] For this study it was assumed that the accelerator would have a luminosity of $L \cong 10^{33}\,\mathrm{cm}^{-2}\mathrm{s}^{-1}$, or $10\,\mathrm{fb}^{-1}$/year. The analysis was preoccupied with backgrounds coming from the peripheral interactions $e^+e^- \to e\nu WZ$ and $e^+e^- \to eeWW$ which are relatively easy to reject as shown in Fig. 43 of the P_T spectrum of signal

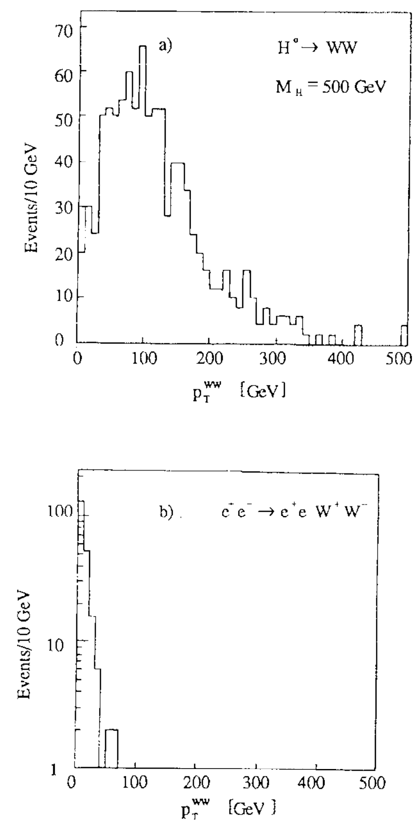

Fig. 43. P_T spectrum of signal and background processes from the La Thuile study of CLIC at $\sqrt{s} = 2$ TeV and $10\,\mathrm{fb}^{-1}$. In (a) is shown the p_T^{WW} for the signal process $e^+e^- \to \nu\bar{\nu}H^\circ$ where the M_H=500 GeV Higgs boson decays to W or Z pairs. In (b) the p_T^{WW} is shown for the background process $e^+e^- \to eeWW$.[37,43]

and background processes. Otherwise the analysis is very similar to the TLC study but with somewhat less restrictive cuts. The analysis cuts and the resulting data sample are shown in Table 13 for 10 fb^{-1} and for two cases of the Higgs boson mass, M_H=500 GeV and M_H=800 GeV.

In particular the CERN analysis required a net transverse momentum greater than 20 GeV, compared to the TLC cut at 50 GeV. From a total of 1400 produced events, for a 500 GeV Higgs mass, they end up with a signal of 420 events. This can be compared to a total background of 160 events. Because they used a less restrictive set of cuts the signal to background is not as good as in the TLC design study. However, due to the higher center-of-mass energy of the CLIC design a substantial Higgs signal (190 events) is obtained for M_H=800 GeV.

The conclusions of the CLIC study are illustrated in the simulated mass spectrum shown in Fig. 44 for the case of M_H=500, 800, and 1000 GeV. For a 500 GeV Higgs mass, in a data sample of 10 fb^{-1}, the WW mass peak corresponding to the Higgs is quite apparent over the background. For the 800 GeV Higgs, one sees that the signal is starting to look more and more like a continuum distribution due to the increasing width of the Higgs. At 1 TeV in Higgs mass there is still a very striking Higgs signal over the continuum background process, but to achieve this the CLIC study had to assume five times the design luminosity .

Heavy-Higgs Rates Per Year at CLIC

	Signal M_H = 500 GeV/c^2	Background m_{WW} = 450–550 GeV/c^2	Signal M_H = 800 GeV/c^2	Background m_{WW} = 600–1000 GeV/c^2
Produced	1400	3000	600	4650
Purely hadronic final state	660	1390	260	2140
After detector acceptance and jet reconstruction	530	460	240	500
Angular cut: $\lvert\cos\theta_W\rvert<0.8$	480	260	210	160
P_T^{WW} cut: $P_T^{WW}>20$ GeV/c	420	160	190	130

Table 13. Signal and background rates from the La Thuile study for CLIC at $\sqrt{s}=2$ TeV and 10 fb^{-1}. Shown are the rates for the signal process $e^+e^- \to \nu\bar{\nu}H^\circ$ where the M_H=500 GeV or 800 GeV Higgs boson decays to W or Z pairs. The background processes are primarily $e^+e^- \to eeWW$ and $e^+e^- \to e\nu WZ$.[37,43]

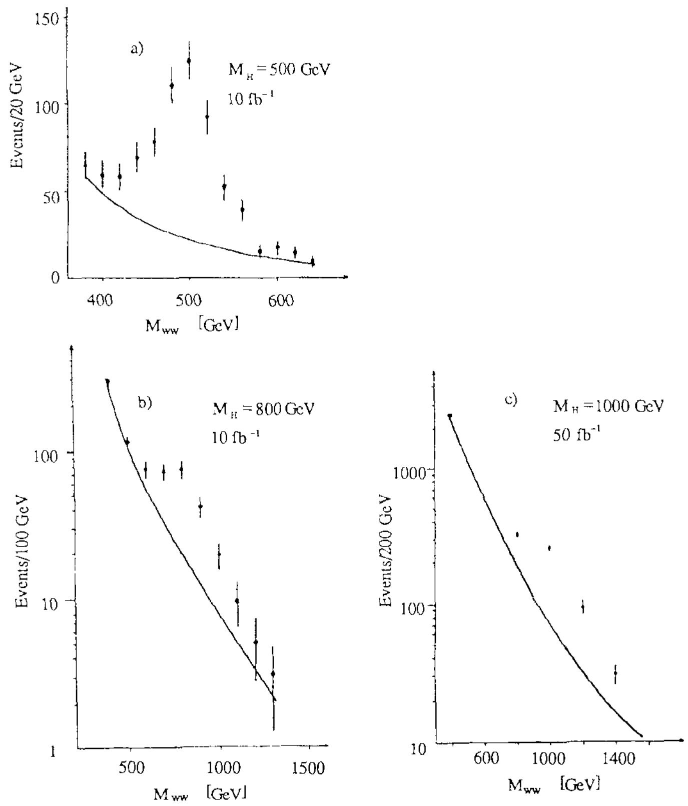

Fig. 44. Signal and background rates from the La Thuile study for CLIC at $\sqrt{s} = 2$ TeV and 10 fb^{-1} in (a) and (b), and 50 fb^{-1} in (c). Shown in the figure is the WW mass spectrum for the signal process (data points) $e^+e^- \to \upsilon\bar{\upsilon}H^\circ$ where the M_H=500, 800, and 1000 GeV Higgs boson decays to W or Z pairs in (a), (b), and (c), respectively. The background processes in this analysis are principally due to $e^+e^- \to eeWW$ and $e^+e^- \to e\upsilon WZ$, and are shown as the solid curves.[37,43]

10. Higgs Boson Searches at the SSC

10.1. SSC Accelerator and Detectors

This concludes the discussion of design studies at SLAC and CERN for linear e+e- colliders. Our next stop is in Waxihachie, Texas. The Superconducting Super Collider (SSC) is a pp collider 53 miles in circumference, designed to operated at 40 TeV in the center-of-mass and with a peak luminosity of 10^{33}cm^{-2}s^{-1}, or 10 fb^{-1}/year.

For Higgs studies at the SSC one has to assume that very good detectors will be available, perhaps better than what one can construct today. The generic detector which was used for the design studies which will be presented here came out of the Berkeley workshop[44] and is described in more detail in the references. The calorimeter has very small segmentation, 0.05x0.05 towers in units of $\Delta\varphi$ (azimuth) and $\Delta\eta$ (pseudorapidity, $\eta = -\ln\tan(\theta/2)$ where θ is the polar angle) and has calorimetric coverage that extends to $|\eta| = 5.5$. The electromagnetic resolution is taken to be $\sigma / E = 15\%/\sqrt{E} + 1\%$, and the hadronic resolution is $\sigma / E = 50\%/\sqrt{E} + 1\%$. The tracking system is assumed to have a resolution of $\sigma_{p_t} / p_t = 0.5 \cdot p_t[\mathrm{TeV}/c]$. It is not only a very good detector, it is also enormous by present-day standards, and would dwarf the CDF detector, for example. The tonnage has gone up dramatically, from 4000 tons for CDF, to perhaps 40,000 tons.

10.2. Gluon-Gluon Fusion

The high energy of the SSC accelerator can extend the possible search region for a minimal standard model Higgs to masses of almost 1 TeV. At these high masses the process that is important for massive Higgs production is WW fusion and gluon-gluon fusion.[45] Gluon-gluon fusion is very similar to the WW fusion process discussed earlier and shown in Fig. 45a), except that now instead of W's there are gluons radiated from the incoming quark lines. Although there is no mechanism for a Higgs to directly couple to a gluon, it can couple through higher order loops involving heavy quarks as shown in Fig. 45b).

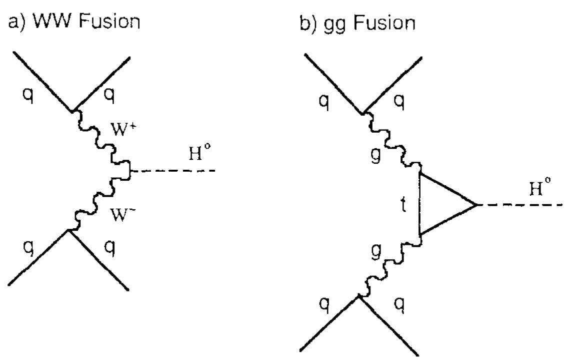

Fig. 45. Feynman diagram for WW fusion is shown in a). The Feynman diagram for gluon-gluon fusion is shown in b). This latter, high order process, is the highest rate production mechanism for heavy Higgs bosons at the SSC.

For a very massive top quark, the loop diagram will dominate over the WW fusion process. In Fig. 46 the production rates for gluon-gluon fusion and WW fusion are shown for various values of the top quark mass and the Higgs mass. For a 50 GeV top quark mass, gluon fusion dominates until very large Higgs masses, above 300 GeV. However, we do know that the top quark mass is greater than 77 GeV from CDF measurements[24]; if it is as high as 200 GeV the cross section for heavy Higgs will be dominated by gluon-gluon fusion. It is important to keep in mind when evaluating the various SSC studies that there is a substantial range of uncertainty about the Higgs production cross section due to uncertainty in the mass of the top quark.

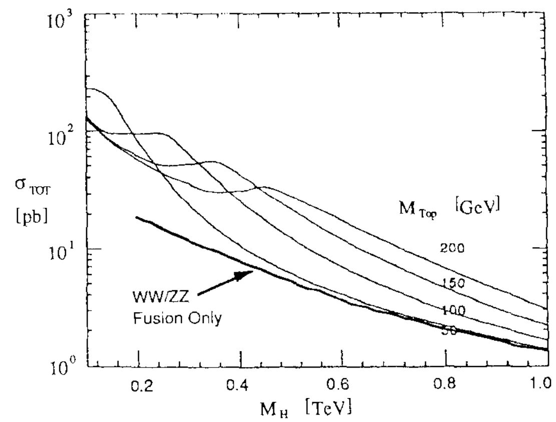

Fig. 46. Heavy Higgs production cross section for four different values of the top quark mass. Cross-section is strongly influenced by the gluon-gluon fusion mechanism where the gluon couples to the Higgs through a top quark loop.[46]

10.3. Higgs Search Regions at the SSC

There are three analysis regions considered in the SSC design studies. First is the intermediate mass Higgs search region, defined as 80 GeV<M_H<180 GeV. In this region the decay modes which are considered are $H^\circ \to b\bar{b}$ (assuming M_H<$2M_{Top}$), $H^\circ \to \gamma\gamma$, and through a virtual Z^o, $H^\circ \to ZZ^* \to 4\ell^\pm$.

In the heavy Higgs mass range, 180 GeV<M_H<600 GeV, the Higgs decay through $H^\circ \to ZZ \to 4\ell^\pm$ is the preferred mode of detection. Finally, in the obese Higgs mass range, 600<M_H<1000 GeV, the Higgs decays considered to have adequate rate are $H^\circ \to W^+W^- \to \ell^+\upsilon jj$ and $H^\circ \to Z^\circ Z^\circ \to \ell^+\ell^- jj$

(j=jet). The three regions and the decay modes of interest are summarized in the following table:

Minimal Standard Model Higgs Search Modes at the SSC

i) Intermediate Mass Higgs $80<M_H<180$ GeV

A) $H^\circ \rightarrow \gamma\gamma$

B) $H^\circ \rightarrow ZZ^* \rightarrow 4\ell^\pm$

C) $H^\circ \rightarrow b\bar{b}$

ii) Heavy Higgs Mass Range $180<M_H<600$ GeV

A) $H^\circ \rightarrow ZZ \rightarrow 4\ell^\pm$

iii) Obese Higgs Mass Range $600<M_H<1000$ GeV

A) $H^\circ \rightarrow W^+W^- \rightarrow \ell^+\nu jj$

B) $H^\circ \rightarrow Z^\circ Z^\circ \rightarrow \ell^+\ell^- jj$

Table 14. The minimal Higgs boson searches at the SSC are divided into three categories for the different mass ranges. Preferred modes for searches in each of the mass ranges are shown.

10.4. Intermediate Mass Higgs Searches

We will begin with the intermediate mass region. In the intermediate mass region the Higgs decays predominantly into $b\bar{b}$ but there is also a suppressed mode into $\gamma\gamma$. Towards the upper end of this mass region the ZZ^* decay mode increases substantially, this can be seen in Fig. 47.

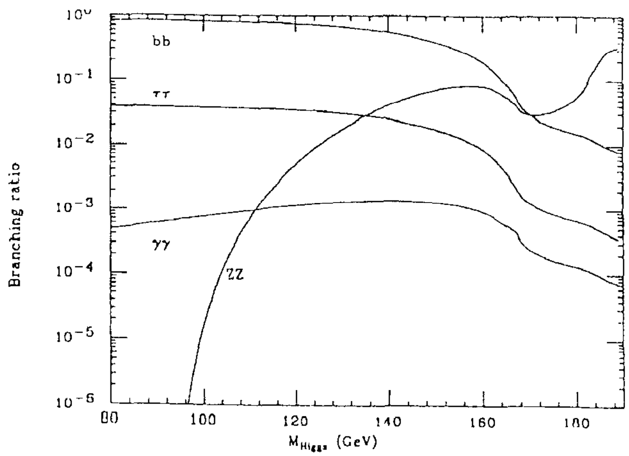

Fig. 47. Branching fraction of the intermediate mass Higgs boson assuming $M_H<2m_T$.[46]

10.5. $H \rightarrow \gamma\gamma$

The mode $H \rightarrow \gamma\gamma$ has a branching ratio of about 10^{-3}, so one expects about 500 produced events/year for a Higgs mass of 100 GeV and about 800 events/year for a Higgs mass of 150 GeV.[47] The dominant backgrounds are $q\bar{q} \rightarrow \gamma\gamma$ and $gg \rightarrow \gamma\gamma$; these are irreducible backgrounds because the final state is identical to the signal process. In addition there is background due to standard QCD jet-jet events which can fragment to look like $\gamma\gamma$; this particular background is not even considered in the analysis.

For this analysis two different detector resolutions have been assumed: 1) an "excellent" detector with $\sigma_E/E = 10\%/\sqrt{E} + 1\%$ electromagnetic resolution. This in itself would be an extraordinary achievement for a large scale SSC detector; 2) a detector with "extraordinary" electromagnetic resolution, $\sigma_E/E = 3\%/\sqrt{E} + 0.5\%$. This resolution is achievable only in a detector using sodium iodine, or BGO as the detection elements. This type of detector might be appropriate for a special purpose experiment devoted to analyzing this process.

With these assumptions, and assuming two choices for the Higgs boson mass, M_H=100 GeV and M_H=150 GeV, a simulated $M_{\gamma\gamma}$ mass spectrum is obtained as shown in Fig. 48. For either detector and M_H=100 GeV, there is no statistical significance for the signal. Only when M_H=150 GeV is there any statistical significance to the result, as summarized in Table 15.

Higgs Mass	Detector Resolution	Mass Resolution	Statistical Significance
100 GeV	$\frac{\sigma}{E}=\frac{10\%}{\sqrt{E}}+1\%$	1.44 GeV	None
100 GeV	$\frac{\sigma}{E}=\frac{3\%}{\sqrt{E}}+0.5\%$	0.55 GeV	2.8 σ
150 GeV	$\frac{\sigma}{E}=\frac{10\%}{\sqrt{E}}+1\%$	1.91 GeV	7.6 σ
150 GeV	$\frac{\sigma}{E}=\frac{3\%}{\sqrt{E}}+0.5\%$	0.80 GeV	12.0 σ

Table 15. Statistical significance of the $H \to \gamma\gamma$ signal over the irreducible background.[47]

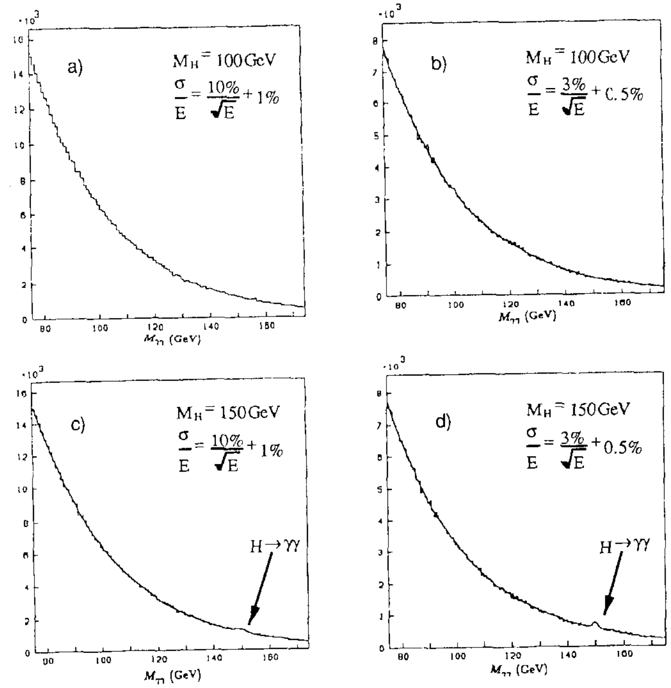

Fig. 48. Simulation of the process $H \to \gamma\gamma$. Shown is the number of events/1 GeV as a function of the $\gamma\gamma$ invariant mass. The background curve is due to the irreducible processes $q\bar{q} \to \gamma\gamma$ and $gg \to \gamma\gamma$. In (a) and (b) M_H=100 GeV, in (c) and (d) M_H=150 GeV. The signal is statistically significant only when M_H=150 GeV. In (b) and (d) the detector resolution of electromagnetic particles is set to $\sigma / E = 3\%/\sqrt{E} + 0.5\%$, and in (a) and (c) it is $\sigma / E = 10\%/\sqrt{E} + 1\%$.[47]

10.6. $H^\circ \rightarrow ZZ^* \rightarrow 4l^\pm$

The second search mode for the intermediate mass Higgs boson that we will discuss is through the process $H^\circ \rightarrow ZZ^* \rightarrow 4l^\pm$. In this mode one of the Z^0's will be off mass shell. Two analysis regions were considered in the simulations[48] for two conjectured top quark mass values, M_T=55 GeV and M_T=90 GeV. In view of the recent top quark mass limits the former is not a likely consideration. If the top quark is sufficiently light the Higgs will decay into it preferentially over the ZZ^* mode. When the results of the analysis are compared this assumption can affect the result by almost an order of magnitude. The rates for signal and backgrounds are listed in Table 16 for a variety of Higgs masses. For the case of M_H=140 GeV and a light top quark, there are only 16 signal events, so there is not a lot of room left to make cuts to eliminate the appreciable backgrounds. The situation is a little less bleak for the higher Higgs masses or higher top-quark masses with respect to signal vs. background; nonetheless, the detection of the intermediate mass Higgs through ZZ^* is clearly very difficult.

In order to reduce the backgrounds due to $gg \rightarrow Zb\bar{b}$, isolation cuts have to be applied on the leptons to insure that they are not due to QCD processes. Typically one sums up the energy in a cone around the lepton and limits the maximum energy allowed. Unfortunately this type of cut is known to be inefficient, so when this simulation was first attempted, at a time when the top quark was thought to be light, the simulation was never completed. Clearly for the high top quark mass the analysis warrants further study.

M_H (GeV)	Signal $10fb^{-1}$ m_T=90GeV	Signal $10fb^{-1}$ m_T=55GeV	$qg \rightarrow ZZ^*$ $10fb^{-1}$	$gg \rightarrow Zb\bar{b}$ $10fb^{-1}$
120	13	3	2	1000
140	110	16	3	550
160	248	44	2	300
180	143	84	8	300

Table 16. Signal and background rates for the process $H^\circ \rightarrow ZZ^* \rightarrow 4l^\pm$, for the case of the intermediate mass Higgs boson. The expected rate in this mode depends critically on the value of the top quark mass. The irreducible background due to $qg \rightarrow ZZ^*$ is small compared to the signal; however the background due to $gg \rightarrow Zb\bar{b}$ is sizeable. Numbers quoted are for a luminosity of $10fb^{-1}$ and are prior to any analysis cuts.[48,49]

10.7 $pp \rightarrow XWH^\circ \rightarrow X\ell^\pm b\bar{b}$

The analysis of the $b\bar{b}$ mode is the most complicated simulation that has been performed for the SSC, to my knowledge.[50] It assumes associated production of the Higgs with a W, $pp \rightarrow WH^\circ X$, which is a very different mechanism from what we have discussed so far, and a very difficult channel to observe. The final state consists of $b\bar{b}$ in association with a W. One must contend with enormous backgrounds from quark-gluon and $q\bar{q}$ production from W's and Z's. The production cross section for a Higgs through associated production with a W with a mass of 75 GeV is 3.9 pb, and only 1 pb for a 150 GeV Higgs mass. For comparison the background for W production is 27 nb. Thus the background starts out 10^4 times larger than the signal with a topology which is quite similar to the signal. These rate are summarized in Table 17.

Signal $q\bar{q} \to W^{\pm}H^{\circ}(H^{\circ} \to b\bar{b})$	
M_H=75 GeV	3.9nb
M_H=100 GeV	2.3nb
M_H=150 GeV	1.0nb

Background	
$qg \to W^{\pm}q$	27nb
$q\bar{q} \to W^{\pm}g$	1.8nb
$q\bar{q} \to W^{\pm}Z^{\circ}$	6.4nb

Table 17. Signal and background rate for associated production of intermediate mass minimal Higgs, where the Higgs is assumed to decay exclusively to b-quark pairs.[50]

Leptonic decays of the W are selected by requiring an isolated electron or muon with 25 GeV of transverse energy and missing transverse momentum greater than 40 GeV ($|\sum \vec{p}_T^{\,i}| > 40\,\mathrm{GeV}$). To tag the b-jets one must require that at least one of the b's undergoes a semileptonic decay, and that the leptons have P_T>1 GeV/c. The two b-jets should be rather narrow, and the lepton impact parameter, or distance of closest approach to the interaction point, δ, should be greater than 5σ, $\delta > 5 \cdot \left[(5\mu\mathrm{m})^2 + (80\mu\mathrm{m}/p(\mathrm{GeV}/c))^2\right]^{1/2}$, or at least greater than 50μm. Finally, the jet-jet invariant mass is required to be within 20 GeV of the expected Higgs mass. After applying these cuts, the raw production rate of 24,000 events per year is reduced to 41 events for the particular case of a 100 GeV Higgs, with a background of 107 events. The conclusion from this analysis is that the signal to background is about 1 to 2 over most of the intermediate mass range, so this is a tantalizing yet difficult analysis. The results of this analysis are summarized in the table below. This is one of the few analyses which is sensitive to Higgs masses near the mass of the Z^o.

M_H (GeV)	ΔM_H (GeV)	Signal	W+g W+q	Z^o
75	16	40	84	0
100	16	41	84	23
125	20	22	105	0
150	28	26	147	0

Table 18. Number of signal events expected after analysis cuts as a function of the Higgs mass, for $10\mathrm{fb}^{-1}$ at the SSC. Also shown are the number of background events from Wg and Wq, and from Z^o decays.[50]

10.8. Heavy Higgs Searches at the SSC, $H^{\circ} \to Z^{\circ}Z^{\circ} \to 4\ell^{\pm}$

While we have seen that the detection capabilities of an intermediate mass Higgs at the SSC are rather limited, such is not the case for a heavy Higgs, 180 GeV< M_H< 600 GeV. It has been suggested that a heavy Higgs can be detected at the SSC in the modes $H^{\circ} \to W^+W^- \to \ell^{\pm}\upsilon jj$ and $H^{\circ} \to Z^{\circ}Z^{\circ} \to 4\ell^{\pm}$. While the former has a high rate of production but serious background problems (which we will discuss further later on),[51] the latter mode is a straightforward detection channel with little background.[33,48] The branching ratio for a Higgs to decay into four charged leptons (electrons or muons only) is small, only $1.4\mathrm{x}10^{-3}$. The heavy Higgs will only decay to ZZ one third of the time, and the branching fraction of Z decays to two electrons is only 3% which accounts for the small combined branching ratio. A detector designed to study this mode would therefore have to have a large acceptance and efficient identification of leptons.

As we have discussed before, the heavy Higgs is produced through the gluon-gluon fusion process and therefore the expected event rates are sensitive to the top quark mass. The simulations of the four lepton detection channel have consequently considered two possible cases for the top quark mass, M_T=40 GeV and M_T=200 GeV. The rate dependence on this parameter can be seen in the table below, where the difference in the raw rates is striking for the highest masses. For M_H=600 GeV and m_T=40 GeV, 60 events are expected with a luminosity of $10\mathrm{fb}^{-1}$, but for m_T=200 GeV the rate jumps to 225 events.

Higgs Mass	Raw Rates	Detected Rates After Cuts
m_{top}=40 GeV		
M_H=200 GeV	575	70
M_H=400 GeV	144	89
M_H=600 GeV	60	40
m_{top}=200 GeV		
M_H=200 GeV	687	93
M_H=400 GeV	560	345
M_H=600 GeV	225	146
Background	1500	280
$q\bar{q} \to Z^\circ Z^\circ$		
$gg \to Z^\circ Z^\circ$		

Table 19. Higgs boson rates for the decay $H^\circ \to Z^\circ Z^\circ \to 4\ell^\pm$. The production of the heavy mass Higgs occurs through the gluon-gluon fusion process which is a higher order process that is sensitive to the top quark mass. Rates are given for a luminosity of $10fb^{-1}$ at the SSC $\sqrt{s} = 40$ TeV. Background rates are given for the irreducible continuum backgrounds $q\bar{q} \to Z^\circ Z^\circ$ and $gg \to Z^\circ Z^\circ$.[48]

To select the heavy Higgs decay mode, $H^\circ \to Z^\circ Z^\circ \to 4\ell^\pm$, the simulation assumed the following selection criteria.[48,52] The leptons are assumed to be visible and in the detector, meaning that they have transverse momentum p_T>10 GeV, and that they are centrally produced in the detector with $|\eta|$<2.5. For a high mass Higgs the two Z^0's will have substantial transverse momentum, so the reconstructed Z's are required to have $p_T^Z > 50$ GeV. Also the reconstructed invariant mass between the two leptons that make up each Z^0 must be consistent within ±10 GeV of M_Z.

After these 3 cuts are applied, there is still a substantial number of detected events in either scenario for the top-quark mass, as compared to the backgrounds as can be seen from the table above. The backgrounds are from continuum processes while the Higgs still has the shape of a resonance, at least in the lower mass range. The result of this simulation is shown in Fig. 49. For the case of M_H=400 GeV there is a substantial peak for M_T=40 GeV and it is even more significant for the M_T=200 GeV. However, for M_H=800 GeV the resonance width is so large and the rate so small that the signal is significant only if M_T=200 GeV. For these very high masses the resonance is so broad that the Higgs no longer looks like a particle.

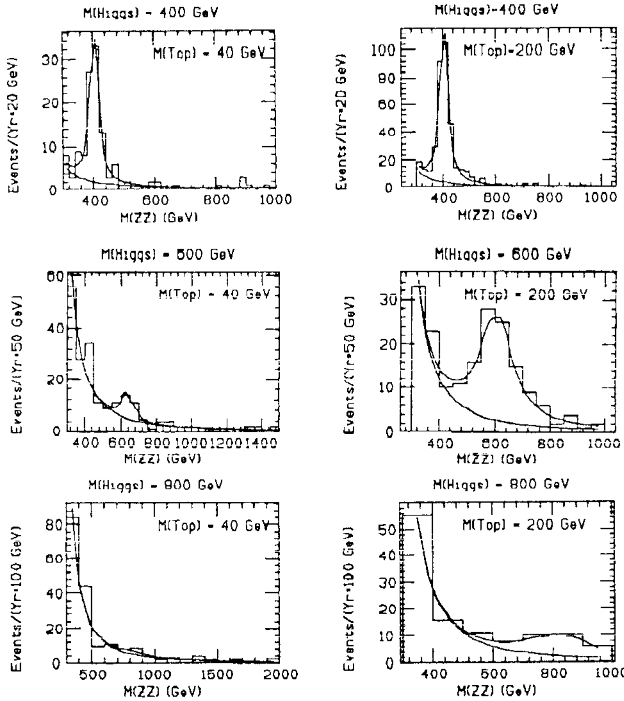

Fig. 49. Mass spectrum for the decay $H^\circ \to Z^\circ Z^\circ \to 4\ell^\pm$. The production of the heavy mass Higgs occurs through the gluon-gluon fusion process which is a higher order process that is sensitive to the top quark mass. Rates are shown for a luminosity of $10fb^{-1}$ at the SSC $\sqrt{s} = 40$ TeV. Background curves are given for the irreducible continuum backgrounds $q\bar{q} \to Z^\circ Z^\circ$ and $gg \to Z^\circ Z^\circ$.[52]

10.9. Obese Higgs Mass Regime

The final Higgs mass range that will be accessible to experiments at the SSC is the "obese" Higgs mass region, M_H>800 GeV. In this region the Higgs is difficult to detect because it no longer looks like a resonance. The rate is also very small. In the heavy Higgs mass range $pp \to H^\circ \to Z^\circ Z^\circ \to 4\ell^\pm$ is the preferred detection channel. For the obese Higgs, one would like to consider channels with higher rate, such as a $pp \to H^\circ \to Z^\circ Z^\circ \to \nu\bar{\nu}\ell^+\ell^-$, or $H^\circ \to W^+W^- \to \ell^\pm\nu jj$. These two modes have been considered rather extensively. However, the latter mode becomes increasingly difficult for higher top quark masses. In fact if M_{top}>M_W then the top quark will decay to W particles, rendering this mode unusable by high backgrounds from $pp \to t\bar{t} \to W^+W^-b\bar{b}$ and other high rate top quark production modes.

So the only mode seriously considered is $pp \to H^\circ \to Z^\circ Z^\circ \to \nu\bar{\nu}\ell^+\ell^-$. This requires a detector that is very hermetic, where you can effectively see the missing energy carried away by the neutrinos.[52] In Fig. 50 the transverse mass distribution is simulated for this process with M_H=800 GeV and 10fb^{-1} of data. The Higgs transverse mass distribution is defined to be

$$M_T = \left[2E_T^{Z\to\ell^+\ell^-} E_T^{Z\to\nu\bar{\nu}} - \vec{p}_T^{\,Z\to\ell^+\ell^-} \cdot \vec{p}_T^{\,Z\to\nu\bar{\nu}}\right]^{\frac{1}{2}}$$

where E_T^Z is the reconstructed Z^o transverse energy and p_T^Z the reconstructed Z^o transverse momentum.

The only background considered here was due to $q\bar{q} \to ZZ$. Additional but smaller backgrounds are expected from $gg \to ZZ$. The signal remaining after all selection cuts was only 17 events. Clearly a higher luminosity accelerator that would yield much more than 10fb^{-1} per year is required.

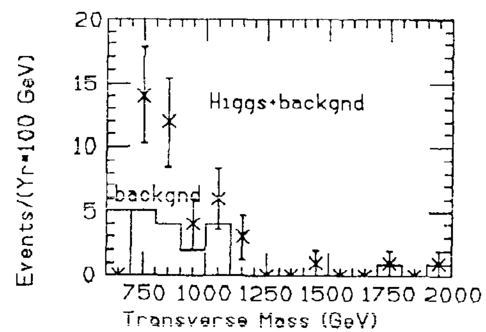

Fig. 50. The transverse mass distribution is simulated for this process $pp \to H^\circ \to Z^\circ Z^\circ \to \nu\bar{\nu}\ell^+\ell^-$ with M_H=800 GeV and 10fb^{-1}. The only background considered here was due to $q\bar{q} \to ZZ$ additional but smaller backgrounds are expected from $gg \to ZZ$. The signal remaining after all selection cuts is only 17 events. Figure is from Ref. [52].

10.10. Like-sign W Pair Production

In the obese Higgs mass region the Higgs sector becomes strongly interacting as the unitarity bound is approached.[53] In this regime the longitudinal component of the W, which was developed from the Higgs sector also becomes strongly interacting. So in the WW fusion process the Higgs can be produced by and decay into like sign WW's as shown in Fig. 51.

This is an even more interesting mode considering that there is an asymmetry in the production rate for W^+W^+ or W^-W^- which gives this production mode a distinctive signature. For example, for 10 fb^{-1}, 43 W^+W^+ events are expected but only 14 W^-W^- events. This is in part because in a proton there are twice as many u-quarks as there are d-quarks, However, there is a very substantial background to this process from single gluon exchange where like sign W pairs can also be produced through $uu \to ddW^+W^+$. This background is about two-thirds the signal from the most recent calculations. This is still actively discussed in the literature right now.

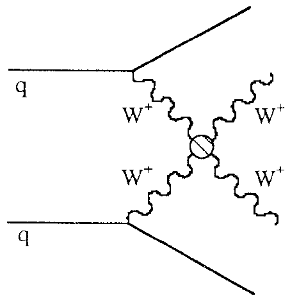

Fig. 51. Feynman graph for strongly interacting Higgs producing like-sign W pairs through a quartic interaction.

11. Conclusions

We began by looking at five experiments that have set limits on light Higgs:

(1)	X-ray transitions in μ-atoms	8 MeV< M_H
(2)	Forbidden transitions in $^4He^*$	3 MeV< M_H< 14 MeV
(3)	SINDRUM $\pi^+ \to e^+\upsilon_e H^\circ$	10< M_H< 110 MeV
(4)	NA-31 $K_L^\circ \to \pi^\circ H^\circ$	15< M_H< 211 MeV
(5)	CLEO $B \to H^\circ X$	210 MeV< M_H< 3.4 GeV

These three last experiments are all quite recent. The SINDRUM measurement was published just a few months ago, the NA-31 measurement is still preliminary and unpublished, and the CLEO result was published in February 1989. These experiments exclude Higgs masses between zero mass and twice the tau lepton mass. There are many other interesting experiments not covered here, including excellent limits from ARGUS, a very recent result by Mark II, and results from CUSB.

We then studied the capabilities of the existing machines to study minimal Higgs. SLC and LEP-1 are machines that are coming online, operating around the mass of the Z. LEP-200, in five years, will be operating at double that energy and possibly with higher luminosity. We also talked about the future machines: the TLC/CLIC Higgs simulation studies and the SSC studies. These are multi-TeV machines operating at high luminosity. The accelerators that we discussed in this review are summarized in Table 20.

Machine	ff	$\sqrt{s}$	L($m^{-2}\,s^{-1}$)
SLC/LEP-1	e^+e^-	M_Z	$\sim 10^{31}$
LEP-200	e^+e^-	200 GeV	$\sim 10^{31-32}$
TLC	e^+e^-	1 TeV	1×10^{33}
CLIC	e^+e^-	2 TeV	1×10^{33}
SSC	pp	40 TeV	1×10^{33}

Table 20. Summary of existing and proposed accelerators considered here.

We reviewed what the capabilities of the machines would be for minimal Higgs searches. In SLC/LEP-1 the preferred detection mode is $e^+e^- \to Z^\circ \to H^\circ Z^{\circ *} \to b\bar{b}\ell\bar{\ell}$. These two accelerators should be able to push Higgs searches up to 30 GeV and they might possibly reach 50 GeV. By the middle of the next decade with LEP-200 the search region could be extended to 80 GeV in the mode $e^+e^- \to Z^\circ \to H^\circ Z^\circ \to b\bar{b}\upsilon\bar{\upsilon}$.

We saw that the Higgs search range can be dramatically extended, perhaps to the TeV range, by TLC, CLIC, or SSC. In the TLC the preferred detection mode is in the fusion process $e^+e^- \to H^\circ\upsilon\bar{\upsilon} \to b\bar{b}\upsilon\bar{\upsilon}$ and

$e^+e^- \to H^\circ \nu\bar{\nu} \to WW\nu\bar{\nu}$. The search range examined here could find minimal Higgs in the range 120 GeV to 500 GeV. If the decay $W \to t\bar{b}$ is kinematically forbidden the search range could extend even closer to the Z^0 mass. In the CLIC studies, it was concluded that in the mode $e^+e^- \to H^\circ \nu\bar{\nu} \to WW\nu\bar{\nu}$, at five times design luminosity, the search region could be extended to 1 TeV.

In the SSC studies that we reviewed we saw how difficult the intermediate mass search region was, particularly how hard it was to find the Higgs decay into $b\bar{b}$. We also looked at the gluon fusion modes. In the decay $H^\circ \to Z^\circ Z^\circ \to 4\ell^\pm$ the search region extends to M_H=600 GeV, and if the top mass is quite heavy, as high as M_H=800 GeV. At a higher luminosity intersection region at the SSC one might be able to find the minimal Higgs up to one TeV, particularly in the interesting doubly charged mode $W^\pm W^\pm$.

There is a large body of literature and reviews which are well worth reading for further indepth study on the topic of minimal Higgs searches.[2,3,4,54] Not covered in these lectures was the topic of non-minimal Higgs such as those predicted by supersymmetric models. Extensive discussion of these models and studies of the experimental search possibilities are contained in the literature.[2,55]

REFERENCES

[1]P.W. Higgs, Phys. Rev. Lett. 13 (1964) 508.

[2]J. Gunion, H. Haber, G. Kane, S. Dawson, *The Higgs Hunter's Guide*, UCD-89-4, June, 1989, and references therein. J. Gunion, UCD-89-2, Feb. 1989.

[3]R. Cahn, Rep. Prog. Phys. 52 (1989) 389.

[4]M. Chanowitz, Ann. Rev. Nucl. Part. Sci. 38 (1988) 323.

[5]S. Glashow, Nucl. Phys. 22 (1961) 579.

[6]A. Salam and J.C. Ward, Phys. Lett. 13 (1964) 168.

[7]S. Glashow, J. Iliopolos, and L. Maiani, Phys. Rev. D2 (1970) 1285.

[8]M. Gell-Mann, Phys. Rev. 92 (1953) 833. K. Nishijima, Prog. Theor. Phys. 13 (1955) 285.

[9]E. Noether, Nachr. Kgl. Ges. Wiss. Goettingen, p.235 (1918).

[10]J. Goldstone, Nuovo Cim. 19 (1961) 154.

[11]J. Goldstone, A. Salam, and S. Weinberg, Phys. Rev. 127 (1962) 965.

[12]U. Amaldi, *etal*, Phys. Rev. D36 (1987) 1385.

[13]S. Dawson, Print-89-0156, Feb. 1989. S. Coleman and E. Weinberg, Phys. Rev. D7 (1973) 1988. P. Hasenfratz, BUTP-88/33, Nov. 1988.

[14]B. W. Lee, C. Quigg, and H. Thacker, Phys. Rev. D16 (1977) 1519.

[15]J. Steinberger, Phys. Rev. 76 (1949) 1180.

[16]J. Ellis, M. K. Gaillard, and D. Nanopoulos, Nucl Phys. B106 (1976) 292.

[17]A. I. Vainshtein, *et al.*, Sov. J. Nucl. Phys. 30 (1979) 711.

[18]I. Beltrami, *etal*, Nucl. Phys. A451 (1986) 679.

[19]S.J. Freedman, *et al.*, Phys. Rev. Lett. 52 (1984) 240. D. Kohler, B.A. Watson, and J.A. Becker, Phys. Rev. Lett. 27 (1974) 1628.

[20]S. Egli, *et al.*, Phys. Lett. 222 (1989) 533.

[21]S. Raby, G. West, and C. Hofman, Phys. Rev. D39 (1989) 828.

[22]H. Nelson, NA-31 Collaboration, Seminar at CERN, LBL, SLAC, April 1989. H.G. Sander, NA-31 Collaboration, *12th Int. Workshop on Weak Int. and Neutrinos*, Ginosar, Israel. H. Cheng, IP-ASTP-06-89, Jun. 1989.

[23]M. S. Alam, *et al.*, Phys. Rev. D40 (1989) 712.

[24]F. Abe, *et al.*, CDF Collaboration, UPR-0172E, Oct. 1989.

[25]H. Baer, *et al.*, "New Particles," *Physics at LEP*, CERN 86-02, Vol. 1, ed. J. Ellis and R. Peccei, Feb. 1986, p. 297.

[26]W. Innes, "Summary of Work on Z->Hff", SLAC-Report-306, Nov. 1986, p. 341. For Non-minimal Searches at this Energy see, S. Komamiya, "Searches for Higgs Pairs," SLAC-Report-315, July 1987, p. 253.

[27]G. Barbiellini, *et al.*, "Physics at LEP at High Energies," *Physics at LEP*, CERN 86-02, Vol. 2, ed. J. Ellis and R. Peccei, Feb. 1986, p.1.

[28]S. Wu, *et al.*, "Search for Neutral Higgs at LEP 200", CERN 87-08 Vol. 2, June 1987, p. 312.

[29]C. Ahn, *et al.*, SLAC-Report-329, May 1988.

[30]See *Proceedings of the 1987 La Thuile Workshop on Physics at Future Accelerators*, ed. J. Mulvey, CERN 87-07, Vol 1.

[31]See *Proceedings of the 1986 Snowmass Workshop on the Physics of the Superconducting Supercollider*, ed. R. Donaldson and Jay Marx.

[32]G. Feldman, *Proceedings of the 1987 SLAC Summer Institute on Particle Physics*, SLAC-Report-328, ed. E. Brennan, p.47.

[33]R. Thun, *et al.*, *Proceedings of the 1987 Berkeley Workshop on Experiments, Detectors, and Experimental Areas for the Supercollider*, ed. R. Donaldson and M. Gilchriese, p. 78.

[34]C. F. von Weizsaker, Z. Phys. 88 (1934) 612. E. J. Williams, Phys. Rev. 45 (1934) 729.

[35]V. Barger, *Proceedings of the 24th Int. Conf. on HEP*, Munich, West Germany, Aug. 1988, ed. R. Kotthaus and J. Kuhn, p. 1265.

[36]C. Baltay, *et al.*, *Proceedings of the 1988 Snowmass Workshop on High Energy Physics in the 1990's*, ed. S. Jensen, p. 182.

[37]G. Altarelli, *et al.*, *Proceedings of the 1987 La Thuile Workshop on Physics at Future Accelerators*, Vol 1, ed. J. Mulvey, p. 36.

[38]P. Burchat, D. Burke, and A. Petersen, Phys. Rev. D38 (1988) 2735, and erratum, Phys. Rev. D39 (1989) 3515. S. Komamiya, Phys. Rev. D38 (1988) 2158. J. Alexander, *et al.*, *Proceedings of the 1988 Snowmass Workshop on High Energy Physics in the 1990's*, ed. S. Jensen, p. 135.

[39]F. Abe, et al, UPR-0172E Oct. 1989, submitted to Phys. Rev. Lett.

[40]P. Burchat, SCIPP-89/27, Oct. 1989.

[41]G. Altarelli, N. Mele, and F. Pitolli, Nucl. Phys. B287 (1987) 205.

[42]M. Peskin, *Proceedings of the 1987 SLAC Summer Institute on Particle Physics*, SLAC-Report-328, ed. E. Brennan, p. 1.

[43]F. Richard, *Proceedings of the 1987 La Thuile Workshop on Physics at Future Accelerators*, Vol 2, ed. J. Mulvey, p 61; and D. Froidevaux, *ibid*, p. 61.

[44]G. Hanson, *et al.*, *Proceedings of the 1987 Berkeley Workshop on Experiments, Detectors, and Experimental Areas for the Supercollider*, ed. R. Donaldson and M. Gilchriese, p. 340. A. Bay, *et al.*, *Proceedings of the 1988 Snowmass Workshop on High Energy Physics in the 1990's*, ed. S. Jensen, p. 882; and I. Hincliffe and E. Wang, *ibid*, p.119.

[45]E. Glover and J. J. van der Bij, CERN-TH-5247/88, Dec. 1988; and CERN-TH-5248/88, Dec. 1988.

[46]I. Hinchliffe, *Proceedings of the 1987 Berkeley Workshop on Experiments, Detectors, and Experimental Areas for the Supercollider*, ed. R. Donaldson and M. Gilchriese, p. 1.

[47]C. Barter, *et al.*, *Proceedings of the 1988 Snowmass Workshop on High Energy Physics in the 1990's*, ed. S. Jensen, p. 98.

[48]E. Wang, *et al.*, *Proceedings of the 1988 Snowmass Workshop on High Energy Physics in the 1990's*, ed. S. Jensen, p. 109.

[49]J. Gunion, G. Kane, and J. Wudka, Nucl. Phys. B299 (1988) 231.

[50]J. Brau, K. Pitts, and L. Price, UTHEP-88-0601, June 1988; and *Proceedings of the 1988 Snowmass Workshop on High Energy Physics in the 1990's*, ed. S. Jensen, p. 103.

[51]G. Herten, *Proceedings of the 1987 Berkeley Workshop on Experiments, Detectors, and Experimental Areas for the Supercollider*, ed. R. Donaldson and M. Gilchriese, p. 110. H. Sadrozinski, A. Seiden, and A. Weinstein, *Proceedings of the 1988 Snowmass Workshop on High Energy Physics in the 1990's*, ed. S. Jensen, p. 124. W. J. Stirling, "Higgs Tagging at the LHC", CERN 88-02, May 1988, p. 67. R. Kleiss and W. Stirling, Phys. Lett. B200 (1988) 193.

[52]R. Cahn, *Proceedings of the 1987 Berkeley Workshop on Experiments, Detectors, and Experimental Areas for the Supercollider*, ed. R. Donaldson and M. Gilchriese, p. 20.

[53]M. Chanowitz and M. Golden, Phys. Rev. Lett. 61 (1988) 1053. M. Chanowitz, LBL-26547, Feb. 1989 (Heavy Flavor Physics Symposium, Beijing). M. Chanowitz and M. K. Gaillard, Nucl. Phys. B261 (1985) 379. M. Chanowitz, M. Golden, and H. Georgi, Phys. Rev. Lett. 57 (1986) 2344, and Phys. Rev. D36 (1987) 1490. M. Golden, FERMILAB-CONF/89-41-T, Feb. 1989. M. Chanowitz, LBL-26613, Mar. 1989. R. Cahn, LBL-27383, June 1989.

[54]R. Cahn, LBL-27134, *12th Int. Workshop on Weak Int. and Neutrinos*, Ginosar, Israel, April 1989. R. Cahn, LBL-25078, (8th Int. Workshop on Photon-Photon Collisions, Jerusalem), April 1988. A. Seiden, *Proceedings of the 1988 Snowmass Workshop on High Energy Physics in the 1990's*, ed. S. Jensen, p. 73.

[55]H. Haber, SCIPP-89/18, Jan. 1989, *Proc. of the Workshop on HEP Phenomenology*, Bombay India. J. Gunion, *et al.*, *Proceedings of the 1987 Berkeley Workshop on Experiments, Detectors, and Experimental Areas for the Supercollider*, ed. R. Donaldson and M. Gilchriese, p. 110. J. Gunion and H. Haber, Nucl. Phys. B272 (1986) 1.

Electroweak Symmetry Breaking: Higgs/Whatever [*]

Two lectures presented at
the SLAC Summer Institute
Stanford, California
July, 1989

Michael S. Chanowitz

Theoretical Physics Group
Physics Division
Lawrence Berkeley Laboratory
1 Cyclotron Road
Berkeley, California 94720

[*]This work was supported by the Director, Office of Energy Research, Office of High Energy and Nuclear Physics, Division of High Energy Physics of the U.S. Department of Energy under Contract DE-AC03-76SF00098.

1. Introduction

In these two lectures I will discuss electroweak symmetry breaking from a general perspective, stressing properties that are model independent and follow just from the assumption that the electroweak interactions are described by a spontaneously broken gauge theory.[1] This means I assume the Higgs mechanism[2] though not necessarily the existence of Higgs bosons.

The Higgs mechanism requires the existence of a new force and new quanta, which I refer to generically as

$$\mathcal{L}_{SB} = \mathcal{L}_{\text{Symmetry Breaking}}, \tag{1.1}$$

the Lagrangian of the still unknown symmetry breaking sector. We will see that the general framework is sufficient to tell us a good deal about the range of possibilities for $\mathcal{L}_{SB}$. In particular, general symmetry properties together with unitarity imply that the new physics of $\mathcal{L}_{SB}$ must emerge at or below ~ 1.8 TeV in the scattering of longitudinally polarized gauge bosons, $W_L W_L \to W_L W_L$.[3] If the quanta of $\mathcal{L}_{SB}$ are much lighter than 1 TeV, then there are narrow Higgs bosons and $\mathcal{L}_{SB}$ has a weak interaction strength that is amenable to perturbation theory. If the new quanta lie above 1 TeV then $\mathcal{L}_{SB}$ is a strongly interacting system with a rich spectrum, there are no narrow Higgs bosons and perhaps none at all, the theory cannot be analyzed perturbatively, and we say that the Higgs mechanism is implemented "dynamically".

I will argue that the SSC is a minimal collider with the assured capability to allow us to determine which possibility is realized in nature. The point is that the SSC is (just) sufficient to observe the signal of strong WW scattering that occurs if $\mathcal{L}_{SB}$ lives above 1 TeV. Therefore we will learn from the presence or absence of the signal in SSC experiments. If the signal does not occur it means that the physics lies below 1 TeV, in contrast to the more typical situation in high energy physics where a negative search at a given energy leaves open the possibility that still higher energies may be needed. This is the sense in which the SSC is a "no-lose" facility for the study of the symmetry breaking mechanism. Of course the technical challenges to realize this potential are enormous, both in accelerator physics (luminosity of $10^{33}\text{cm}^{-2}\text{s}^{-1}$ is essential) and especially in the experimental physics of the detectors. In the second lecture (Section 6) I will discuss some of the signals and backgrounds that must be mastered.

The first lecture (Sections 1-4) presents the general framework of a spontaneously broken gauge theory:

- the Higgs mechanism *sui generis*, with or without Higgs boson(s) (Section 2)
- the implications of symmetry and unitarity for the mass scale and interaction strength of the new physics that the Higgs mechanism requires (Section 3)

In addition I will review a "softer" theoretical argument based on the "naturalness" problem (Section 4) which leads to a prejudice against Higgs bosons unless they are supersymmetric. This is a prejudice, not a theorem, and it could be overturned in the future by a clever new idea. This is a good place to remember the slogan: **all theorists to be presumed guilty until proven innocent.**

In the second lecture I will illustrate the general framework by reviewing some specific models (Section 5):

- the Weinberg-Salam model of the Higgs sector
- the minimal supersymmetric extension of the Weinberg-Salam model
- technicolor as an example of the Higgs mechanism without Higgs bosons.

I will conclude the second lecture with a discussion of strong WW scattering (Section 6), that must occur if $\mathcal{L}_{SB}$ lives above 1 TeV. In particular I will describe some of the experimental signals and backgrounds at the SSC. A brief summary is presented in Section 7.

A more complete review and more extensive bibliography can be found in Ref. 4.

2. The Generic Higgs Mechanism

In this section we review the Higgs mechanism in its most general form. The basic ingredients are a gauge sector and a symmetry breaking sector,

$$\mathcal{L} = \mathcal{L}_{\text{gauge}} + \mathcal{L}_{SB}. \tag{2.1}$$

$\mathcal{L}_{\text{gauge}}$ is an unbroken *locally symmetric = gauge invariant* theory, describing massless gauge bosons that are transversely polarized, just like the photon. For instance, for $SU(2)_L \times U(1)_Y$ gauge symmetry the gauge bosons are a triplet

$\vec{W} = W_1, W_2, W_3$ corresponding to the generators $\vec{T}_L$ and a singlet gauge boson X corresponding to the hypercharge generator Y. If there were no $\mathcal{L}_{SB}$, the unbroken $SU(2)_L$ nonabelian symmetry would give rise to a force that would confine quanta of nonvanishing $\vec{T}_L$ charge, such as left-handed electrons and neutrinos.

In the generic Higgs mechanism $\mathcal{L}_{SB}$ breaks the *local* (or *gauge*) symmetry of $\mathcal{L}_{\text{gauge}}$. To do so $\mathcal{L}_{SB}$ must possess a *global* symmetry G that breaks spontaneously to a subgroup H,

$$G \to H. \tag{2.2}$$

In the electroweak theory we do not yet know either of the groups G or H,

$$G = ? \tag{2.3a}$$

$$H = ? \tag{2.3b}$$

We want to discover what they are and beyond that we want to discover the symmetry breaking sector

$$\mathcal{L}_{SB} = ? \tag{2.4}$$

including the mass scale of its spectrum

$$M_{SB} = ? \tag{2.5}$$

and the interaction strength

$$\lambda_{SB} = ? \tag{2.6}$$

Equation (2.4) is the 64 $\times 10^8$ dollar question (in then-year dollars, more or less).

We do already know one fact about G and H. The $SU(2)_L \times U(1)_Y$ gauge invariance of $\mathcal{L} = \mathcal{L}_{\text{gauge}} + \mathcal{L}_{SB}$ is *a local* symmetry, meaning that it is an invariance under transformations that depend on space-time,

$$e^{i\vec{f}(x)\cdot\vec{T}_L} e^{if_0(x)Y} \tag{2.7}$$

G and H are *global* symmetries of $\mathcal{L}_{SB}$, meaning that they are symmetries which do not depend on space-time (i.e., as Eq. (2.7) would be if $\vec{f}$ and f_0 were constants rather than functions of $x = \vec{x}, t$). Therefore G must be at least as big as $SU(2)_L \times U(1)_Y$ or $\mathcal{L}_{SB}$ would *explicitly* (as opposed to *spontaneously*) break the $SU(2)_L \times U(1)_Y$ gauge symmetry. Similarly H must be at least as big as $U(1)_{EM}$ or the theory after spontaneous breakdown will not accommodate the unbroken gauge symmetry of QED. That is, in order to be consistent with the desired pattern of breaking for the *local* symmetry

$$SU(2)_L \times U(1)_Y \to U(1)_{EM} \tag{2.8}$$

the spontaneous breaking of the *global* symmetry of $\mathcal{L}_{SB}$

$$G \to H \tag{2.9}$$

is constrained by

$$G \supset SU(2)_L \times U(1)_Y \tag{2.10a}$$

$$H \supset U(1)_{EM} \tag{2.10b}$$

STEP I:

There are two steps in the Higgs mechanism. The first has nothing to do with gauge symmetry—it is just the spontaneous breaking of a global symmetry as explained by the Goldstone theorem.[5,6] By *spontaneous* symmetry breaking $G \to H$ we mean that

$$G = \text{ global symmetry of } \textit{interactions} \text{ of } \mathcal{L}_{SB} \tag{2.11a}$$

while

$$H = \text{ global symmetry of the } \textit{ground-state} \text{ of } \mathcal{L}_{SB}. \tag{2.11b}$$

That is, the dynamics of $\mathcal{L}_{SB}$ are such that the state of lowest energy (the *vacuum* in quantum field theory) has a smaller symmetry group than the force laws of the Lagrangian. Goldstone's theorem tells us that for each broken generator of G the spectrum of $\mathcal{L}_{SB}$ contains a massless spin zero particle or Goldstone boson,

$$\begin{aligned} \#\text{ of massless scalars} & \\ &= \#\text{ of broken symmetry axes} \\ &= \text{dimension } G - \text{dimension H} \\ &= \#\text{ of energetically flat directions in field space.} \end{aligned} \tag{2.12}$$

The last line is the clue to the proof of the theorem: masses arise from terms that are quadratic in the fields,

$$\mathcal{L}_{\text{mass}} = -\frac{1}{2} m^2 \phi^2, \tag{2.13}$$

so a field direction that is locally flat in energy (i.e., goes like ϕ^n with $n \geq 3$) corresponds to a massless mode.

The classic example is the hypersombrero* potential. Consider a triplet of scalars

$$\vec{\varphi} = \varphi_1, \varphi_2, \varphi_3 \tag{2.14}$$

with interactions described by the potential $V(\varphi)$:

$$\begin{aligned} V(\varphi) &= \lambda(\vec{\varphi}^2 - v^2)^2 \\ &= \lambda(\vec{\varphi}^2)^2 - 2\lambda v^2 \vec{\varphi}^2 + \lambda v^4 \end{aligned} \tag{2.15}$$

λ is the dimensionless coupling constant and v is a real constant with dimension of a mass. The global symmetry group is

$$G = O(3), \tag{2.16}$$

like the symmetry of ordinary space. There are three symmetry axes, i.e., generators, so

$$\dim G = 3 \tag{2.17}$$

(in general for $O(N)$ the dimension in $N(N-1)/2$). Since $\mathcal{L} \propto -V$ we see comparing Eqs. (2.15) and (2.13) that our scalars are tachyons,

$$m^2_{\vec{\varphi}} = -4\lambda v^2 \,. \tag{2.18}$$

However (2.18) is not a true description of the spectrum because we have not identified the ground state of the system. Equation (2.18) is expressed relative to the state $\vec{\varphi} = \vec{0}$, but we see that (2.15) has its ground state (in lowest order) at

$$\vec{\varphi}^2 = v^2. \tag{2.19}$$

*You would recognize it as a sombrero if you plotted it in four dimensions with three axes for the $\vec{\varphi}$ and the fourth for V.

The classical ground state breaks the $O(3)$ symmetry, since one component of $\vec{\varphi}$ is singled out to be nonvanishing. We define the axes and that the special component is φ_3, and the classical ground state is given by

$$\varphi_3 = v \tag{2.20a}$$

$$\varphi_1 = \varphi_2 = 0. \tag{2.20b}$$

The ground state settles (spontaneously) on one of the infinity of possible equivalent directions. The fact that it could have equivalently picked any other direction means that the potential is locally flat under rotations that would carry φ_3 into a different direction, i.e., that there are massless modes associated with the axes (generators) of those rotations. These latter are precisely the broken generators, which are no longer symmetries in the ground state. Goldstone's theorem then follows.

For our hypersombrero the remaining symmetry is

$$H = O(2) \tag{2.21}$$

the rotations about the $\hat{n}_3$ axis, so

$$\text{dimension} \;\; H = 1 \tag{2.22}$$

and from (2.12) we expect $3 - 1 = 2$ massless particles. We easily check this by redefining φ_3 to vanish in the ground state:

$$\varphi_3 \to \varphi_3 + v. \tag{2.23}$$

In terms of the new field with $\varphi_3 = 0$ the potential V is

$$V(\varphi) = \lambda(\vec{\varphi}^2)^2 + 2\lambda v \varphi_3 \vec{\varphi}^2 + 4\lambda v^2 \varphi_3^2. \tag{2.24}$$

Notice that (2.24) clearly lacks the full $O(3)$ symmetry because of the last two terms but is only invariant under the $O(2)$ rotations that mix up φ_1 and φ_2. Notice also the absence of mass terms for φ_1 and φ_2, so that $m_1 = m_2 = 0$ as expected. Finally notice that φ_3 has a mass term with the correct sign (in contrast to the tachyonic masses in (2.15)), given by

$$m_3^2 = 8\lambda v^2 \,. \tag{2.25}$$

PLEASE DO NOT BE DECEIVED by the previous example however. The essential features are the symmetries of the Lagrangian (G) and the ground state (H). Elementary scalars are *not* essential: if it is necessary to make J. Goldstone happy, God makes composite scalars. He has (almost) already done so on at least one occasion. That is, we believe on the basis of strong theoretical and experimental evidence that QCD with two massless quarks is an example of his cooperation in this regard. The initial global (flavor) symmetry is

$$G = SU(2)_L \times SU(2)_R \tag{2.26}$$

since we can perform separate isospin rotations on the right and left chirality u and d quarks. The ground state is believed to have a nonvanishing expectation value for the bilinear operator

$$\langle \overline{u}_L u_R + \overline{d}_L d_R + h.c.\rangle_0 \neq 0 \tag{2.27}$$

where $h.c.$ = hermitean conjugate. Equation (2.27) breaks the global symmetry spontaneously, $G \to H$, where

$$H = SU(2)_{L+R} \tag{2.28}$$

is the ordinary isospin group of nuclear and hadron physics. That is, (2.27) is not invariant under independent rotations of left and right helicity quarks but only under rotations that act equally on left and right helicities. In this example, dim $G = 6$ and dim $H = 3$ so we expect $6 - 3 = 3$ Goldstone bosons. In nature we believe they are the pion triplet, π^+, π^-, π^0, which are much lighter than typical hadrons because the u and d quark masses are very small,[7] of order 10 MeV. (I refer to the "current" quark masses, the parameters that appear in the QCD Lagrangian.)

STEP II:

In step I we considered only the global symmetry breakdown induced by $\mathcal{L}_{SB}$ — Goldstone's territory. Now we consider the interplay of $\mathcal{L}_{SB}$ with $\mathcal{L}_{\rm gauge}$.

The essential point of the Higgs mechanism is that when a spontaneously broken generator of $\mathcal{L}_{SB}$ coincides with a generator of a gauge invariance of $\mathcal{L}_{\rm gauge}$, the associate Goldstone boson w and massless gauge boson W mix to form a massive gauge boson. The number of degrees of freedom are preserved, since the Goldstone boson disappears from the physical spectrum while the gauge boson acquires a third (longitudinal) polarization state. We will see how this occurs in general, without assuming the existence of elementary scalar particles.

By assumption the Goldstone boson w couples to one of the gauge currents, with a coupling strength f that has the dimension of a mass,

$$\langle 0|J^\mu_{\rm gauge}|w(p)\rangle = \frac{i}{2} f p^\mu \tag{2.29}$$

f is analogous to F_π, the pion decay constant. Equation (2.29) means that an effective representation of the current contains a term linear in w,

$$J^\mu_{\rm gauge}(x) = \frac{1}{2} f \partial^\mu w(x) + \cdots \tag{2.30}$$

In the Lagrangian $J^\mu_{\rm gauge}$ is by definition coupled to the gauge boson W^μ,

$$\mathcal{L}_{\rm gauge} = g W_\mu J^\mu_{\rm gauge} + \cdots \tag{2.31}$$

where g is the dimensionless gauge coupling constant. Substituting Eq. (2.30) we find

$$\mathcal{L}_{\rm gauge} = \frac{1}{2} g f W_\mu (\partial^\mu w) f \ldots \tag{2.32}$$

which shows that W_μ mixes in the longitudinal (parallel to $\vec{p}$) direction with the would-be Goldstone boson w.

We can use (2.32) to compute the W mass. Before symmetry breaking the W is massless and transversely polarized. Therefore as in QED we can write its propagator in Landau gauge,

$$D_0^{\mu\nu} = \frac{-i}{k^2}(g^{\mu\nu} - \frac{k^\mu k^\nu}{k^2})\ . \tag{2.33}$$

In higher orders the propagator is the sum of the geometric series due to "vacuum polarization", i.e., all states that mix with the gauge current. The vacuum polarization tensor is defined as

$$\begin{aligned}\Pi^{\mu\nu}(k) &= -\int d^4k e^{-ik\cdot x}\langle T J^\mu(x) J^\nu(0)\rangle_0 \\ &= i\frac{g^2 f^2}{4}(g^{\mu\nu} - \frac{k^\mu k^\nu}{k^2}) + \cdot\end{aligned} \tag{2.34}$$

In (2.34) I have indicated explicitly the contribution from the Goldstone boson pole: the factor $1/k^2$ is just the massless propagator and the factor $(gf/2)^2$ can be recognized from Eq. (2.32). The only subtle point is the $g^{\mu\nu}$ in (2.34). It is present since gauge invariance requires current conservation, $k_\mu \Pi^{\mu\nu} = 0$. Since it is a constant term with no absorptive part, its presence does not change the spectrum of the theory. (In theories with elementary scalars it arises automatically from the "seagull" interaction given by the Feynman rules.)

Finally we compute the W propagator from the geometric series (Fig. 2.1):

$$\begin{aligned} D^{\mu\nu} &= (D_0 + D_0 \Pi D_0 + \ldots)^{\mu\nu} \\ &= -\frac{i}{k^2}\left(g^{\mu\nu} - \frac{k^\mu k^\nu}{k^2}\right)\left(1 + \frac{g^2 f^2}{4k^2} + \cdots\right) \\ &= -i\left(g^{\mu\nu} - \frac{k^\mu k^\nu}{k^2}\right)\frac{1}{k^2}\frac{1}{1 - \dfrac{g^2 f^2}{4k^2}} \\ &= -i\frac{g^{\mu\nu} - \dfrac{k^\mu k^\nu}{k^2}}{k^2 - \dfrac{g^2 f^2}{4}}. \end{aligned} \tag{2.35}$$

The massless Goldstone boson pole induces a pole in the gauge boson propagator,

$$M_W = \frac{1}{2} g f. \tag{2.36}$$

From the measured value of the Fermi constant,

$$G_F = \frac{g^2}{4\sqrt{2} M_W^2} = \frac{1}{\sqrt{2} f^2} \tag{2.37}$$

we learn that

$$f \simeq 250\ GeV. \tag{2.38}$$

Customarily instead of f we refer to $v \equiv f$, the so-called vacuum expectation value. This custom, which I will also follow (though it is in general not appropriate), derives from theories with elementary scalar fields (see Section 5) where $v \equiv f$ is both the coupling strength of the Goldstone boson w to J_{gauge}, as in (2.29), and is also the value of the Higgs boson field in the ground state as in (2.19). However the above derivation shows that there is no need for any physical Higgs scalar to exist. The condensate that breaks the symmetry may in general be of a composite operator, as in (2.27), and may have no simple relationship to

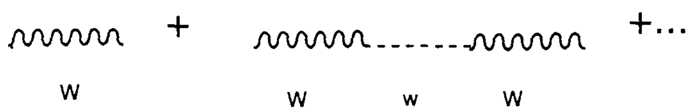

Figure 2.1: Geometric series for the W propagator corresponding to Eq. (2.35).

the parameter $f \equiv v$ defined in (2.29). For instance, in QCD there is no trivial relationship between F_π and $\langle \overline{u}u + \overline{d}d \rangle_0$ (though there is a nontrivial relation involving also the quark and pion masses[8]).

I will conclude this discussion of the Higgs mechanism with two more topics:

1. The significance of the ρ parameter for the global symmetries of $\mathcal{L}_{SB}$.

2. The equivalence theorem which allows us to connect the Goldstone boson dynamics of $\mathcal{L}_{SB}$ with the scattering of longitudinal gauge bosons in the laboratory.

First, what do we learn from the experimental observation that to within a few percent

$$\rho \equiv \left(\frac{M_W}{M_Z \cos\theta_W}\right)^2 = 1? \tag{2.39}$$

In deriving (2.36) I was careless with the T_{3L} indices and did not discuss the Z mass. More carefully, instead of (2.29) I should have written

$$\langle 0 | J^\mu_a | w_b \rangle = i p^\mu \frac{f_a}{2} \delta_{ab} \tag{2.40}$$

where $a, b = 1, 2, 3$. Choosing

$$w^\pm = \frac{1}{\sqrt{2}}(w_1 \pm i w_2) \tag{2.41}$$

we see that $U(1)_{EM}$ rotates the 1 and 2 components into one another, so that $U(1)_{EM}$ invariance implies

$$f_1 = f_2. \tag{2.42}$$

What about f_3? Is there an analogy to the isospin symmetry of hadron physics that ensures $f_1 = f_2 = f_3$?

As in the derivation of (2.36) we find that

$$M_{W^\pm} = \frac{1}{2} g f_1 \tag{2.43}$$

but for the W_3 and X bosons (associated with T_{3L} and Y) we find with an analogous calculation the mass matrix

$$\begin{pmatrix} M^2_{W_3} & M^2_{W_3-X} \\ M^2_{W_3-X} & M^2_X \end{pmatrix} = \frac{1}{4} f_3^2 \begin{pmatrix} g^2 & gg' \\ gg' & g'^2 \end{pmatrix} \tag{2.44}$$

where g and g' are the $SU(2)_L$ and $U(1)_Y$ couplings. The diagonalized matrix is then (since it has zero determinant)

$$\frac{1}{4} f_3^2 \begin{pmatrix} g^2 + g'^2 & 0 \\ 0 & 0 \end{pmatrix} \tag{2.45}$$

so that

$$M_Z = \frac{1}{4} f_3^2 (g^2 + g'^2) \tag{2.46}$$

$$M_\gamma = 0 \tag{2.47}$$

are the eigenvalues, the eigenstates being

$$Z = W_3 \cos\theta_w + X \sin\theta_w \tag{2.48a}$$

$$A = -W_3 \sin\theta_w + X \cos\theta_w. \tag{2.48b}$$

The mixing angle is

$$\cos^2\theta_w = \frac{g^2}{g^2 + g'^2} \tag{2.49}$$

and the ρ parameter is then

$$\rho = (f_1/f_3)^2. \tag{2.50}$$

Equation (2.50) teaches us that $\rho = 1$ is connected with the existence of an isospin-like symmetry in $\mathcal{L}_{SB}$. In particular if the global symmetry H of $\mathcal{L}_{SB}$ encompasses an $SU(2)$ under which $\vec{w}$ and J^μ_a are triplets, then it guarantees that $f_3 = f_1$ and that $\rho = 1$ to all orders in the (possibly strong) interactions of $\mathcal{L}_{SB}$. In this sense it functions as a "custodial" $SU(2)$ since it protects $\rho = 1$ against corrections from $\mathcal{L}_{SB}$.[9] Conversely, it can be shown that $\rho = 1$ implies that the low energy interactions of the Goldstone bosons $\vec{w}$ obey an effective custodial $SU(2)_{L+R}$ symmetry,[10] which need not however be an exact symmetry of $\mathcal{L}_{SB}$.

The custodial $SU(2)$ symmetry also underlies the upper bound on the top quark mass from one loop corrections to the ρ parameter[11] (or equivalently to a quantity called Δr in other renormalization schemes). The mass difference $m_t - m_b$ breaks the custodial isospin, resulting in a correction to ρ proportional to $G_F m_t^2$ for $m_t \gg M_{W'}$. Analyses[12] of the experimentally allowed deviations from $\rho = 1$ suggest an upper bound of ~ 200 GeV for m_t.

Finally I will describe the equivalence theorem, which relates the Goldstone boson physics of $\mathcal{L}_{SB}$ to observations that can be made in the laboratory and therefore suggests an experimental strategy to study the physics of $\mathcal{L}_{SB}$. The complete electroweak Lagrangian $\mathcal{L}$, Eq. (2.1), is of course $SU(2)_L \times U(1)_Y$ gauge invariant, so that physics does not depend on the choice of gauge. In the U (unitary) gauge only physical degrees of freedom appear in $\mathcal{L}$ and, in particular, the Goldstone boson fields vanish, $\vec{w} = 0$. In R (renormalizable) gauges, of which there are an infinite number, the Goldstone fields $\vec{w}$ do appear in $\mathcal{L}$ and in the Feynman rules, though gauge invariance ensures that they do not appear in the physical spectrum (i.e., they never generate poles in S-Matrix elements). Since they engender the longitudinal gauge boson modes, W_L and Z_L, it is plausible that W_L and Z_L interactions reflect the dynamics of $\vec{w}$. The equivalence theorem is the precise statement of this proposition,

$$\mathcal{M}(W_L(p_1), W_L(P_2), \ldots) = \mathcal{M}(w(p_1), w(p_2), \ldots)_R + 0\left(\frac{M_W}{E_i}\right). \tag{2.51}$$

The theorem was established in tree approximation[13] and used in a variety of calculations.[14–16] Reference 15 sketches a proof to all orders which is not however easily extended to matrix elements with more than one external W_L. A proof to all orders in both $\mathcal{L}_{SB}$ and $\mathcal{L}_{\text{gauge}}$ is given in Ref. 3, and alternative treatments have been given for the portion of the proof of Ref. 3 that is based on the BRS identities.[17] The suggestion has been made that the theorem may fail at higher orders, though not confirmed by an explicit calculation to one loop,[18] or that it may fail at higher orders in $\mathcal{L}_{\text{gauge}}$.[19] My own view is, coincidentally, that of Ref. 3: that the theorem is valid to all orders in all interactions when the Goldstone boson fields are appropriately renormalized.

The theorem (2.51) tells us that scattering of longitudinal gauge bosons at high energy reflects the dynamics of the underlying Goldstone bosons. We will use this connection in the next section to learn more about the general properties of $\mathcal{L}_{SB}$.

3. Symmetry and Unitarity

In this section we continue to extract the general properties of the Higgs mechanism. We will use the general symmetry properties of $\mathcal{L}_{SB}$, Eq. (2.10), and unitarity. The symmetry properties imply low energy theorems for $W_L W_L$ scattering[3,10] that correlate the unknown mass and interaction scales of $\mathcal{L}_{SB}$, (2.5) and (2.6), and allow us to estimate the scattering amplitudes if $\mathcal{L}_{SB}$ is strongly interacting. Unitarity then implies an upper limit on the energy scale at which the physics of $\mathcal{L}_{SB}$ must become visible and probably also an upper limit on the unknown mass scale M_{SB}. Experimental implications of these results will be discussed in Section 6.

Begin by considering $\mathcal{L}_{SB}$ in the absence of $\mathcal{L}_{\text{gauge}}$. The spontaneous symmetry breaking pattern $G \to H$ is sufficient to derive low energy theorems for Goldstone boson scattering in terms of the constants f_a that characterize the couplings of the Goldstone bosons to the symmetry currents. The earliest example is the Weinberg $\pi\pi$ low energy theorems.[20] Assuming the pion isotriplet to be the almost-Goldstone bosons associated with $SU(2)_L \times SU(2)_R \to SU(2)_{L+R}$ in hadron physics, Weinberg showed for example that

$$\mathcal{M}(\pi^+\pi^- \to \pi^0\pi^0) = \frac{s}{F_\pi^2} \tag{3.1}$$

where $F_\pi = 93$ MeV is the pion decay constant. Equation (3.1) neglects $O(m_\pi^2)$ corrections (which are in fact calculable) and is valid for low energy, defined as

$$s \ll \text{minimum}\{m_\rho^2, (4\pi F\pi)^2\}. \tag{3.2}$$

The low energy theorems can be derived by current algebra or effective Lagrangian methods. The proofs have two important features:

- they are valid to all orders in the Goldstone boson self-interactions. This is crucial since those interactions may be strong (as they are for the pion example) so perturbation theory is a non-starter.
- We needn't be able to solve the dynamics or even to know the Lagrangian of the theory. In fact the $\pi\pi$ low energy theorems were derived in 1966 before QCD was discovered. (And we still don't know today how to compute $\pi\pi$ scattering directly in QCD.)

The current algebra/symmetry method was important in the path followed in the 1960's that led in the early 1970's to the discovery that $\mathcal{L}_{HADRON} = \mathcal{L}_{QCD}$. What can it teach us about $\mathcal{L}_{SB}$?

If $G = SU(2)_L \times SU(2)_R$ and $H = SU(2)_{L+R}$ as in QCD, then we can immediately conclude that[3]

$$\mathcal{M}(w^+w^- \to zz) = \frac{s}{v^2} \tag{3.3}$$

at low energy,

$$s \ll \text{minimum}\{M_{SB}^2, (4\pi v)^2\}, \tag{3.4}$$

as in Eq. (3.2). Here M_{SB} is the typical mass scale of $\mathcal{L}_{SB}$ and $v \simeq \frac{1}{4}$ TeV, Eqs. (2.37–8). More generally, electroweak gauge invariance requires Eq. (2.10) from which we can deduce the more general result[10]

$$\mathcal{M}(w^+w^- \to zz) = \frac{1}{\rho}\frac{s}{v^2}. \tag{3.5}$$

Equation (3.5) is arguably more soundly based than (3.1) was in 1966, since (3.5) is a general consequence of gauge invariance and the Higgs mechanism while (3.1) was based on inspired guesswork as to the symmetries underlying hadron physics.

We can next use the equivalence theorem, (2.51), to turn (3.5) into a physical statement about longitudinal gauge boson scattering. In particular we have

$$\mathcal{M}(W_L^+W_L^- \to Z_LZ_L) = \frac{1}{\rho}\frac{s}{v^2} \tag{3.6}$$

for an energy domain circumscribed by (3.4) and (2.51) as

$$M_W^2 \ll s \ll \text{minimum}\{M_{SB}^2, (4\pi v)^2\}. \tag{3.7}$$

The window (3.7) may or may not exist in nature, depending on whether $M_{SB} \gg M_W$.

It is amusing that the low energy theorem (3.6) is precisely the famous "bad" high energy behavior that the Higgs mechanism is needed to cure — this emerges most clearly in the derivation of (3.6) given in Ref. 21. $\mathcal{L}_{SB}$ must cut off the growing amplitude in (3.6). Unitarity implies a rigorous upper bound on the energy at which this must occur.

The partial wave amplitudes for the Goldstone scalars (or for the zero helicity, longitudinal gauge bosons) are

$$a_J(s) = \frac{1}{32\pi}\int d(\cos\theta)P_J(\cos\theta)\mathcal{M}(s,\theta) \tag{3.8}$$

where θ is the center of mass scattering angle. Partial wave unitarily then requires

$$|a_J(s)| \le 1. \tag{3.9}$$

Putting $\rho = 1$, Eqs. (3.6-3.9) then imply

$$a_0(W_L^+W_L^- \to Z_LZ_L) = \frac{s}{16\pi v^2} \le 1 \tag{3.10}$$

so that the amplitude must be damped at a scale bounded by

$$\Lambda_{\text{Cutoff}} \le 4\sqrt{\pi}v \simeq 1.75\ TeV. \tag{3.11}$$

That is, new physics from $\mathcal{L}_{SB}$ must effect the scattering at an energy scale bounded by (3.11).

At the cutoff, $s \cong O(\Lambda)$, the $J = 0$ wave is

$$a_0(\Lambda) \cong \frac{\Lambda^2}{16\pi v^2} \tag{3.12}$$

which implies the promised correlation between the strength of the interaction and the energy scale of the new physics. If $\Lambda \lesssim \frac{1}{2}$ TeV then $a_0(\Lambda) \lesssim 1/4\pi$, well below the unitarity limit; then $\mathcal{L}_{SB}$ has a weak coupling and can be analyzed perturbatively. For $\Lambda \gtrsim 1$ TeV, we have $a_0(\Lambda) \gtrsim 1/3$, which is close to saturation; this means $\mathcal{L}_{SB}$ is a strong interaction theory requiring nonperturbative methods of analysis.

Though it is not rigorous, the most likely case is that $\Lambda_{\text{Cutoff}} = \Lambda_{SB}$ is of order the typical mass scale M_{SB} of the quanta of $\mathcal{L}_{SB}$,

$$\Lambda_{SB} \cong M_{SB}. \tag{3.13}$$

I can't prove (3.12) but can illustrate it with two examples. The first is the Weinberg–Salam model, in which s-channel Higgs exchange provides the contribution that cuts off (3.10). I assume that $m_H \gg M_W$ but that m_H is small enough that perturbation theory is not too bad — say $m_H \simeq 700$ GeV so that $\lambda/4\pi^2 = m_H^2/8\pi v^2 \simeq 1/10$ (see Section 5 below). Then I can calculate in tree approximation, with the result

$$a_0(s) = \frac{s}{16\pi v^2} - \frac{s}{16\pi v^2}\frac{s}{s - m_H^2} \tag{3.14}$$

where the first term arises from $\mathcal{L}_{\text{gauge}}$ and the second from the s-channel Higgs boson exchange given by $\mathcal{L}_{SB}$ now assumed to be the Weinberg-Salam Higgs sector (see Fig. 3.1). For $s \ll m_H^2$ the first term dominates, giving the low energy theorem as it must. But for $s \gg m_H^2$ the two terms combine to give

$$a_0\Big|_{s \gg m_H^2} = \frac{m_H^2}{16\pi v^2}. \tag{3.15}$$

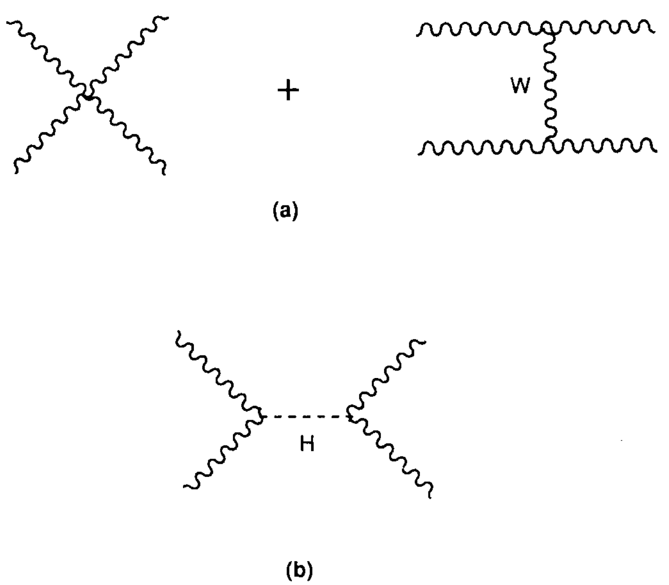

Figure 3.1: Leading diagrams for $W^+W^- \to ZZ$, including interactions from the gauge sector (a) and the s-channel Higgs boson exchange (b) — see Eq. (3.14).

Comparing (3.15) with (3.12) we see that (3.13) is indeed verified, i.e., $\Lambda \cong m_H$.

Consider next a strongly-coupled example. In this case we expect to approximately saturate the unitarity bound,

$$\Lambda_{\text{Strong}} \cong 4\sqrt{\pi}v \cong O(2)\ TeV. \tag{3.16}$$

I can't solve for M_{SB} in this case but I can relate the problem to one that has been studied experimentally. In hadron physics the saturation scale from (3.1) would be

$$\Lambda_{\text{Hadron}} \cong 4\sqrt{\pi}f_\pi \cong 650MeV. \tag{3.17}$$

Experimentally we know this is indeed of the order of the mass of the lightest hadrons, e.g., $m_\rho = 770$ MeV. This is not surprising: in strong coupling theories we expect resonances to form when scattering amplitudes become strong, as they do at the energy scale of the unitarity bound.

So we expect $\Lambda \cong M_{SB}$ for weak or strong $\mathcal{L}_{SB}$. The two generic cases are shown in Fig. 3.2. For weak $\mathcal{L}_{SB}$ we expect narrow resonances below 1 TeV — these are just the Higgs bosons. For strong $\mathcal{L}_{SB}$ we expect broad resonances in the vicinity of 1 to 2 TeV and strong $W_L W_L$ scattering, both of which can be observed at an appropriate collider.

4. The Naturalness Problem

In this section I will review the so-called "technical naturalness problem" that afflicts models with elementary Higgs bosons because of their quadratic divergences. I will also review two possible solutions: supersymmetry and technicolor. Both eliminate the offending quadratic divergences — supersymmetry by guaranteeing their cancellation and technicolor by doing away with elementary scalars. Both solutions also require new physics at or below the TeV scale, where it can be found at the SSC. The natural scale for technicolor is $\sim O(2)$ TeV since it is a strongly coupled theory which saturates the unitarity bound, Eq. (3.11). Supersymmetry must also appear at or below the TeV scale if it is indeed the explanation of the naturalness problem, since as the SUSY breaking scale grows beyond the TeV scale the problem begins to reappear.

There are two aspects of what is called the "naturalness" or "gauge hierarchy" problem. The first is the physical origin of the very small numbers $M_W/M_{GUT} \cong 10^{-12}$ or $M_W/M_{Planck} \cong 10^{-17}$. The second is a technical problem that is specific

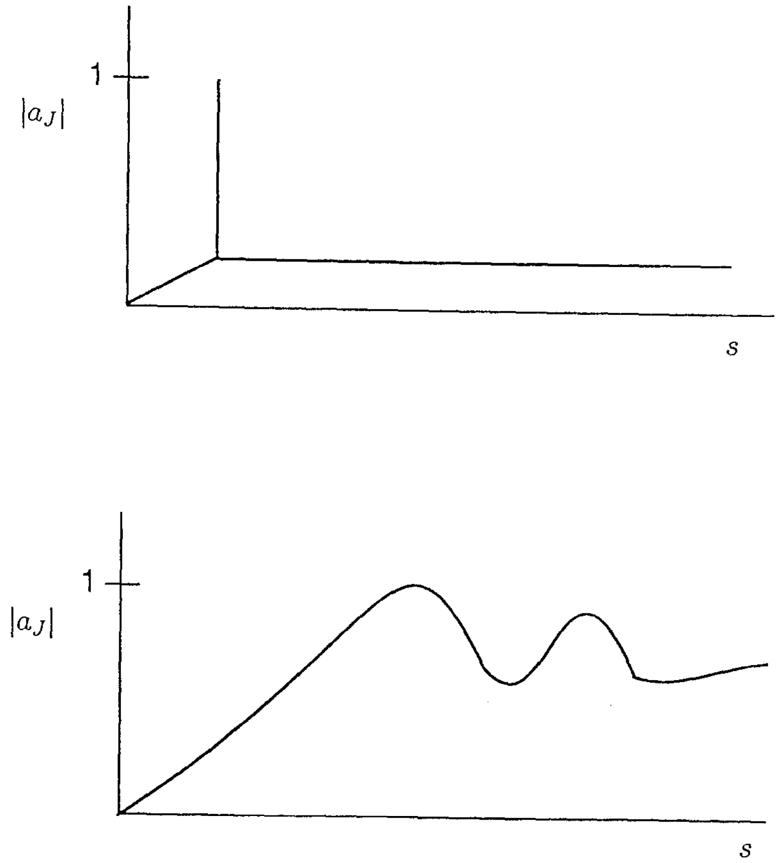

Figure 3.2: Typical behavior of partial wave amplitudes for $W_L W_L$ scattering for a weakly coupled model with narrow (Higgs) resonances (top figure) or a strongly coupled model with broad resonances in the 1-2 TeV region (bottom figure).

to Higgs boson models: even if the gauge hierarchy problem has a natural solution in lowest order, the quadratic divergences associated with scalar fields induce one loop corrections that destroy the hierarchy. In ordinary Higgs boson models these corrections require an order by order fine tuning of the subtraction constants that seems physically unnatural. In this section I will discuss this technical naturalness problem.

Consider the standard Higgs boson model, to be reviewed in Section 5. The potential V contains a wrong-sign (tachyonic) mass term for $\vec{w}$ and h, given by the coefficient of $\frac{1}{2}(\vec{w}^2+h^2)$ in Eq. (5.4) , equal to $-\lambda v^2$. Because of the tachyonic sign, the state of minimum energy has a condensate v, resulting in zero mass for the triplet $\vec{w}$ and a mass $+\sqrt{2\lambda v^2}$ for h. The one loop quantum correction (Fig. 4.1) is quadratically divergent,

$$\delta(\lambda v^2) = \frac{9\lambda}{2}\int \frac{d^4\ell}{(2\pi)^4}\,\frac{1}{\ell^2+\lambda v^2}. \tag{4.1}$$

Though expressions like Eq. (4.1) are shocking to novices in field theory, they lose their shock value as the student masters (i.e., is brainwashed by) the renormalization program, which shows that finite predictions can be extracted at the cost of a small number of subtractions or redefinitions. Most notably in the case of quantum electrodynamics this program has been extraordinarily successful. The divergence in Eq. (4.1) can be removed by introducing a counterterm that in effect shifts the initial value of λv^2 by an infinite constant cancelling the divergence generated in Eq. (4.1).

In the renormalization program we renounce any attempt to understand the physical origin of those parameters requiring subtraction — their values are simply fit to experiment — but we are then able to obtain finite predictions for all other physical quantities in the theory. To understand the naturalness problem it is necessary to go beyond this limited, though powerful, perspective and to ask questions about the origins of the subtracted quantities, assuming they will eventually be understood and calculable in the context of another theory formulated at a deeper level. The expectation is that the deeper theory introduces new physics at high energy that cuts off the divergent behavior of integrals like equation (4.1). Denoting the energy scale of the new physics by Λ, equation (4.1)

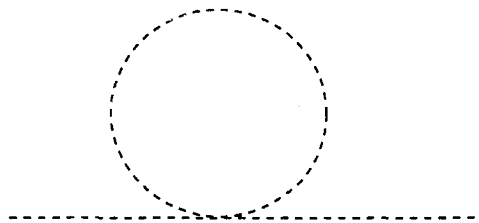

Figure 4.1: Quadratically divergent contribution to Higgs boson self–energy, as in Eq. (4.1).

would be replaced by

$$\delta(v^2\lambda) = C\frac{\lambda}{2\pi^2}\Lambda^2 \tag{4.2}$$

where C is a numerical constant of order unity.

Equation (4.2) tells us that the parameters of Higgs models are hypersensitive to the high energy scale of the deeper underlying theory. For example, the Higgs boson mass, given in lowest order by $m_H^2 = 2\lambda v^2$, might reasonably range from tens of MeV to perhaps the TeV scale. The scale Λ of the deeper theory might be the scale of Grand Unified Theories, $M_{GUT} = O(10^{14})$ GeV, or even the Planck scale suggested by superstring and supergravity models, $M_{\text{Planck}} = O(10^{19})$ GeV.

Writing the physical mass as the sum of a bare mass plus the one loop corrections

$$m_H^2 = m_{H,\text{bare}}^2 + \frac{C\lambda}{\pi^2}\Lambda^2 \tag{4.3}$$

we see that the bare mass must be tuned with exquisite precision to make the left side much smaller than the two terms on the right side. For instance, if $m_H =$ 1 TeV and $\Lambda = M_{\text{Planck}}$ then the cancellation on the right side must work to one part in 10^{17}! Of course the renormalization program allows us to arrange the cancellation to any desired precision, but viewed from the perspective of the deeper theory such a cancellation seems extremely unnatural — one might even say, in the absence of any principle requiring or explaining such a cancellation, that it is absurdly implausible.

Though the term is also used in other ways, this is the naturalness problem that uniquely afflicts Higgs boson models. It may be thought of us as an instability of the energy scale of the theory against quantum corrections that tend naturally to drive the scale to violently larger values. The problem uniquely affects Higgs models because in 3 + 1 dimensions the only renormalizable theories with quadratic divergences are those containing scalar fields. For instance in unbroken gauge theories like QED or QCD divergences are at most given by powers of logarithms. If instead of the quadratic dependence on Λ in Eq. (4.3) there were a logarithmic dependence,

$$m_H^2 = m_{H,\text{bare}}^2 + \frac{C\lambda}{\pi^2} m_{H,\text{bare}}^2 \ln\frac{\Lambda}{m_{H,\text{bare}}} \tag{4.4}$$

then no fine tuning would be needed even for Λ as large as M_{Planck}.

Two strategies have been proposed to deal with the naturalness problem. One is to suppose that the symmetry breaking sector, $\mathcal{L}_{SB}$, does not contain elementary Higgs bosons. In particular, in technicolor models[22] $\mathcal{L}_{SB}$ is presumed to be a confining gauge theory like QCD at a mass scale roughly $v/F_\pi \sim 2700$ times greater than the GeV mass scale of QCD. Since QCD is known to undergo spontaneous symmetry breaking, with $SU(2)_L \times SU(2)_R$ breaking to $SU(2)_{L+R}$, giving rise to three Goldstone bosons (the pions), it is plausible that a similar theory at a higher mass scale would contain the necessary ingredients for electroweak symmetry breaking.

The second strategy is to provide a principle for the cancellation of the quadratic divergences: supersymmetry.[23] In supersymmetric theories the quadratic divergences due to scalar boson loops are precisely cancelled by fermion loop contributions. The remaining finite difference is proportional to the scale of supersymmetry breaking e.g., the mass differences of the scalar and fermion superpartners. The absence of scalars degenerate with the known leptons and quarks tells us supersymmetry cannot be exact. Naturalness then implies an upper limit on the scale of supersymmetry breaking, since the naturalness problem returns if mass differences of fermion-boson superpartners are too large. To avoid fine-tuning at less than the few percent level, superpartners cannot be heavier than a few TeV.

Supersymmetry and technicolor are discussed in the next section. It is however important to recognize that nature may have found a way to solve the naturalness problem that has not yet occurred to us.

5. Models

In this section I will review three specific models of $\mathcal{L}_{SB}$, concentrating on how they illustrate the general features discussed in Sections 2 and 3. The models are

- the Weinberg-Salam model
- the minimal supersymmetric extension of the standard model
- technicolor

5.1 The Weinberg–Salam Higgs Sector

The Weinberg–Salam model is a minimal model in that it has the smallest number of fields needed to break the gauge symmetry from $SU(2)_L \times U(1)_Y$ to $U(1)_{EM}$. Four spin zero quanta are introduced, in a complex doublet of $SU(2)_L$:

$$\Phi = \frac{1}{\sqrt{2}} \begin{pmatrix} w_1 & + & iw_2 \\ H & + & iw_3 \end{pmatrix} \tag{5.1}$$

The Lagrangian is

$$\mathcal{L}_{SB} = |\mathcal{D}_\mu \Phi|^2 - V(\Phi) \tag{5.2}$$

where $\mathcal{D}$ is the gauge covariant derivative,

$$\mathcal{D}_\mu = \partial_\mu - ig\vec{T}_L \cdot \vec{W}_\mu - ig'YX. \tag{5.3}$$

The scalar self-couplings are just like the $O(3)$ model discussed in Section 2 (in fact the Weinberg-Salam model is just the extension to O(4)):

$$\begin{aligned} V &= \lambda(\Phi^+\Phi - \frac{v^2}{2})^2 \\ &= \frac{\lambda}{4}(H^2 + \vec{w}^2 - v^2)^2. \end{aligned} \tag{5.4}$$

The global symmetry group of (5.4) is

$$G = SU(2)_L \times SU(2)_R \tag{5.5}$$

(or equivalently $O(4)$). Defining $\vec{T}_L$ and $\vec{T}_R$ in terms of vector and axial-vector $SU(2)$ generators,

$$\vec{T}_{L,R} = \vec{V} \mp \vec{A} \tag{5.6}$$

the infinitesimal $SU(2)_L \times SU(2)_R$ rotations act on the fields as follows:

$$\delta_v(H, \vec{w}) = (0, \vec{\epsilon}_v \times \vec{w}) \tag{5.7a}$$

$$\delta_A(H, \vec{w}) = (\vec{\epsilon}_A \cdot \vec{w}, -\vec{\epsilon}_A H), \tag{5.7b}$$

i.e., as if $\vec{w}$ were a pseudoscalar and H a scalar.

As reviewed in Section 2 for the $O(3)$ model, the minimum energy configuration chooses a field condensate which we define to be H,

$$\langle H \rangle_0 = v. \tag{5.8}$$

Taking $H \to H + v$ the potential becomes

$$V = \frac{\lambda}{4}(H^2 + \vec{w}^2)^2 + \lambda v H(H^2 + \vec{w}^2) + \lambda v^2 H^2 \tag{5.9}$$

so that

$$m_H^2 = 2\lambda v^2 \tag{5.10}$$

$$m_{\vec{w}} = 0 \; . \tag{5.11}$$

Inspection of (5.9) reveals that the global symmetry has broken spontaneously from

$$\begin{aligned} G = SU(2)_L \times SU(2)_R \to H_{\text{The Group}} &= SU(2)_{L+R} \\ &= SU(2)_V \end{aligned} \tag{5.12}$$

(or equivalently $O(4) \to O(3)$). There are then $6 - 3 = 3$ Goldstone bosons, the $\vec{w}$ triplet, which become the longitudinal gauge boson modes as in Section 2. The only remaining quantum in $\mathcal{L}_{SB}$ is then the scalar H.

Notice that the symmetry structure $SU(2)_L \times SU(2)_R \to SU(2)_{L+R}$ is identical to the symmetry of QCD with two massless quarks, Eqs. (2.26) and (2.28). In fact $V(\Phi)$ as given in (5.4) is identical to the sigma model[24] with the substitutions $H \to \sigma$, $\vec{w} \to \vec{\pi}$, and $v \to F_\pi$. The sigma model was developed to model the low energy symmetries of hadron physics and played an important part in the history of the 1960's that led to the discovery and understanding of the underlying quark structure of hadrons. It is amusing that the Weinberg-Salam model could play a similar role in the effort to final $\mathcal{L}_{SB}$. In the sigma model the surviving $SU(2)_{L+R}$ symmetry is just the ordinary isospin of hadron physics. In the Weinberg-Salam model it is the custodial $SU(2)$ discussed in Section 2 that protects the ρ parameter against $O(\lambda)$ corrections.

The $|\mathcal{D}\Phi|^2$ term in (5.2) contains a contribution

$$\frac{1}{2} g v \vec{W}_\mu \cdot \partial^\mu \vec{w} \tag{5.13}$$

which is equivalent to Eqs. (2.31-2.32) with $f = v$. That is, the gauge current contains a term $\frac{1}{2} g v \partial^\mu \vec{w}$. We therefore see immediately from the discussion in Section 2 that the mixing of $\vec{w}$ with $\vec{W}^\mu$ results in a gauge boson mass

$$M_W = \frac{1}{2} g v. \tag{5.14}$$

A more familiar though less general derivation is by inspection of the term quadratic in $\vec{W}^\mu$ that is contained in $|\mathcal{D}W|^2$, i.e.,

$$\frac{1}{2}\left(\frac{gv}{2}\right)^2 \vec{W}_\mu \cdot \vec{W}^\mu \tag{5.15}$$

from which (5.14) may be read directly.

Taking $\lambda/4\pi^2$ as the quantity characterizing perturbative corrections, we find from (5.10) that

$$\frac{\lambda}{4\pi^2} = \frac{m_H^2}{8\pi v^2} \cong \left(\frac{m_H}{1\ TeV}\right)^2 \tag{5.16}$$

which shows that strong coupling sets in at roughly $m_H \geq 1$ TeV. This estimate agrees with the general analysis of Section 3, as discussed following Eq. (3.12), where we identify m_H with the cutoff Λ, as shown in Eqs. (3.14-3.15).

The Higgs boson decay width in lowest order is

$$\begin{aligned} \Gamma(H \to WW + ZZ) &= \frac{3\sqrt{2}}{32\pi} G_F m_H^3 \\ &\cong \frac{1}{2}\ TeV \cdot \left(\frac{m_H}{1\ TeV}\right)^3 . \end{aligned} \tag{5.17}$$

For $m_H \gtrsim 1$ TeV the width is so big that there is no discernible resonance peak. Since the theory is strongly coupled for such values of m_H, the spectrum need not correspond in a simple way to the degrees of freedom in the Lagrangian. It is in fact widely believed (the buzz word is "triviality") that the theory is inconsistent for m_H near or above 1 TeV. This conclusion was based first on a simple renormalization group analysis[25] and is supported by lattice computations.[26]

A lower bound on m_H follows from requiring the $SU(2)_L \times U(1)_Y$ broken vacuum (with $\langle H \rangle_0 = v \neq 0$) to be the lowest energy configuration in the one loop effective potential. The result is[27]

$$m_H^2 \geq \frac{3g^2}{64\pi^2}\left[2M_W^2 + \frac{1}{\cos^2\theta_w} M_Z^2 - 4m_t^2\right] \tag{5.18}$$

assuming the top quark is the only fermion as heavy as M_W. For $m_t \ll M_W$ the bound is $m_H \geq 7$ GeV but for $m_t > 80$ GeV the bound disappears. New bounds are obtained for $m_t > 86$ GeV from the requirement that the vacuum be stable against large Higgs field fluctuations, i.e., that the coefficient of $H^4 \ln H$ in the effective potential be positive.[28] The value of the bound depends on the value of a cutoff representing new physics beyond the Weinberg-Salam model. Consider for instance the possibility that $m_t > 120$ GeV. Then the renormalization group analysis of Lindner, Sher and Zaglauer[28] gives $m_H \gtrsim 50$ GeV for $\Lambda = 10^{15}$ GeV and $m_H \gtrsim 30$ GeV for $\Lambda = 10^3$ GeV.

Fermions acquire mass from a Yukawa interaction with the Higgs boson,

$$\mathcal{L}_{\text{Yukawa}} = y_f H \overline{\psi}_f \psi_f \tag{5.19}$$

where y_f is the dimensionless coupling constant. The fermion masses are then $m_f = yv$ so that the couplings are

$$y_f = \frac{m_f}{v} = g\frac{m_f}{2M_W}. \tag{5.20}$$

Except for the top quark the y_f are extremely small, which makes Higgs boson production cross sections extremely small as well.

This is not a satisfying description since all the mysteries of the quark and lepton spectrum are hidden in the y_f which are simply introduced by hand. In fact, fermion mass generation could prove much more difficult to understand than W and Z mass generation. Fermion and gauge boson masses could be due to different condensates rather than the single condensate of the Weinberg-Salam model. Unitarity allows very different scales. For a fermion of mass m_f the counterpart of the 1.75 TeV bound, Eq. (3.11), is

$$\Lambda \lesssim \frac{16\pi v^2}{\zeta m_f} \tag{5.21}$$

where $\zeta = 1$ for leptons and 3 for quarks. The right-hand side of (5.21) is much larger than the TeV scale, ranging from $5{\cdot}10^6$ TeV for the electron to ~ 10 TeV for a 100 GeV top quark.

5.2 Supersymmetry

The only known solution to the naturalness problem (Section 4) that allows elementary Higgs bosons is supersymmetry — that is the principal reason to believe supersymmetric partners of the known particles might be found at or below the TeV scale. In order to give mass to quarks and leptons of weak isospin $T_{3L} = \pm\frac{1}{2}$ the constraints of supersymmetry require a minimum of two complex doublet Higgs fields. In this section I will review the Higgs sector of the minimal supersymmetric extension of the standard model,[29] which has precisely two complex Higgs doublets,

$$\Phi_a = \frac{1}{\sqrt{2}}\begin{pmatrix} w_a^1 & + & iw_a^2 \\ H_a & + & iw_a^3 \end{pmatrix} \qquad a = 1, 2. \tag{5.22}$$

The scalar potential $V(\Phi_1, \Phi_2)$ has its minimum at

$$\langle H_a \rangle = v_a\ . \tag{5.23}$$

The W mass is

$$M_W = \frac{1}{2} g \sqrt{v_1^2 + v_2^2} \tag{5.24}$$

so that

$$v_1^2 + v_2^2 = v^2 = (\sqrt{2}G_F)^{-1}. \tag{5.25}$$

We choose H_1 to couple to $T_{3L} = +\frac{1}{2}$ and H_2 to $T_{3L} = -\frac{1}{2}$ fermions.

The two complex doublets contain eight degrees of freedom, of which three become the longitudinal $W^\pm$ and Z modes. The remaining five particles include three "pseudoscalars", $H^\pm$ and P', which are orthogonal to the "eaten" combinations of $\vec{w}_1$ and $\vec{w}_2$, and the two Higgs scalars H_1 and H_2. In general the eigenstates are mixtures with mixing angle α,

$$\begin{pmatrix} H \\ H' \end{pmatrix} = \begin{pmatrix} \cos\alpha & \sin\alpha \\ -\sin\alpha & \cos\alpha \end{pmatrix} \begin{pmatrix} H_1 \\ H_2 \end{pmatrix}. \tag{5.26}$$

In the Weinberg-Salam model, $\lambda_{SB} = \lambda$ is a free parameter so that the Higgs boson mass, $m_H^2 = 2\lambda v^2$, is also unconstrained. In the minimal supersymmetric model, the strength of the Higgs interactions is constrained (because the scalar potential arises from a "D-term") to be

$$\lambda = g^2 + g'^2 \tag{5.27}$$

where g and g' are the $SU(2)_L$ and $U(1)_Y$ gauge coupling constants. This means that the model is a weakly coupled $\mathcal{L}_{SB}$ in the sense of Section 3. It also means that Higgs boson masses are not completely arbitrary, but satisfy sum rules which in lowest order are

$$m_{H^\pm}^2 = m_P^2 + M_W^2 \tag{5.28}$$

$$m_{H,H'}^2 = \frac{1}{2}(m_P^2 + M_Z)^2 \pm \frac{1}{2}\sqrt{(m_P^2 + m_Z^2) - 4m_P^2 M_Z^2 \cos^2 2\beta} \tag{5.29}$$

where β is defined by the ratio of the vevs,

$$\tan\beta \equiv v_2/v_1. \tag{5.30}$$

We then see that

$$m_{H^\pm} > M_W \tag{5.31}$$

$$m_H < M_Z \tag{5.32}$$

$$m_{H'} > M_Z. \tag{5.33}$$

Equations (5.27–5.29) are not generally true for nonminimal supersymmetric models. In particular, models containing $SU(2)_L$ singlet Higgs fields can have arbitrary couplings λ. Because they mix with the doublet Higgs fields, all Higgs boson masses are then in general arbitrary.

The one loop corrections to the minimal model sum rules have been computed, both for the charged[30] (5.28) and neutral[31] (5.29) bosons. The corrections are typically small though they can be large for certain choices of the parameters.

The search for the lighter Higgs scalar H is similar to the search for the Weinberg-Salam Higgs boson below M_Z, as discussed by Michael Levi at this school.[32] Searches for the Weinberg-Salam Higgs boson can be used to exclude regions of the supersymmetric model's parameter space, which can be characterized by the angles α, β or, equivalently, by the masses of the scalars $m_H, m_{H'}$.

The heavy scalar H' has highly suppressed couplings to $WW + ZZ$ and is therefore probably undetectable at the SSC. However at the SSC we will be able to search directly for the superparticles, especially the squarks and gluinos which should be observable for masses as large as 1 TeV and perhaps even beyond.[33]

Charged Higgs bosons are of course pair-produced in e^+e^- annihilation, for $\sqrt{s} > 2\sqrt{M_W^2 + m_P^2}$. Since m_P is an arbitrary parameter, we cannot say what energy might be necessary.

5.3 Technicolor

Technicolor is the other known solution to the "technical" naturalness problem. In the context of a grand unified theory the logarithmic variation of the technicolor coupling constant might also explain[34] the "fundamental" naturalness problem, i.e., the origin of the electroweak : GUT or Planck hierarchy. Technicolor is a good example of a strongly interacting $\mathcal{L}_{SB}$ as defined in Section 3.

The basic idea is that the Goldstone bosons w and z of $\mathcal{L}_{SB}$ are bound states of an asymptotically free gauge theory with a confined spectrum at the TeV scale. The simplest example is an unbroken $SU(N_{TC})$ gauge theory which would resemble closely the familiar dynamics of QCD. For N_F massless techniquark flavors the global symmetry group is

$$G = SU(N_F)_L \times SU(N_F)_R. \tag{5.34}$$

As in QCD we expect the ground state to have a condensate

$$\left\langle \sum_{i=1}^{N_F} \overline{q}_L^i q_R^i + \overline{q}_R^i q_L^i \right\rangle_0 \neq 0 \tag{5.35}$$

which breaks G down to the diagonal, vector–like subgroup

$$H = SU(N_F)_{L+R}. \tag{5.36}$$

For $N_F \geq 2$, H includes a custodial $SU(2)_{L+R}$ symmetry so that $\rho = 1$ is protected against large corrections from strong technicolor interactions. Since there are $N_F^2 - 1$ broken $SU(N_F)_{L-R}$ generators, there are $N_F^2 - 1$ Goldstone bosons, $w^\pm, z, \{\phi_i\}$. The ϕ_i exist if $N_F > 2$; they acquire masses from the $SU(3)_{\text{color}} \times SU(2)_L \times U(1)_Y$ gauge interactions and are referred to as pseudo-Goldstone bosons. Choosing the "technicolor pion $= w, z$ decay constant"

$$F_\pi^{TC} = v \cong \frac{1}{4}\ TeV \tag{5.37}$$

referred to as f in Eqs. (2.29–2.38), we obtain the correct value of the W mass as shown in the general discussion of Section 2.

For $N_{TC} = 3$ the theory is precisely a rescaled version of QCD and we can reliably predict (up to small corrections due to the small masses of the QCD u and d quarks) the mass and width of the techni–rho vector meson:

$$m_{\rho_T} = \frac{v}{F_\pi} m_\rho = 2.04\ TeV \tag{5.38}$$

$$\Gamma_{\rho_T} = \frac{v}{F_\pi} \Gamma_\rho = 0.40\ TeV. \tag{5.39}$$

More generally (and less reliably) in the limit of large N_{TC} and large 3 (i.e., the large N limit assumed to be valid for QCD), we have

$$m_{\rho_T} = \sqrt{\frac{3}{N_{TC}}} \cdot 2\ TeV \tag{5.40}$$

$$\Gamma_{\rho_T} = \frac{3}{N_{TC}} \cdot 0.40\ TeV. \tag{5.41}$$

The techni-rho has a spectacular though small background free signal at the SSC, as discussed in the next section.

Technicolor has potential experimental problems, from possibly light pseudo-Goldstone bosons and from flavor-changing neutral currents. However it is far from dead.[35] Possible solutions are being actively studied, including composite models[36] and models with slowly running coupling constants and elevated mass scales.[37] The potential experimental problems and the theoretical repulsiveness of specific models both result from the effort to explain quark and lepton masses. If fermion masses arise by some other still unknown mechanism, technicolor (with two flavors) is an elegant mechanism for $SU(2)_L \times U(1)_Y$ breaking, with no experimental evidence presently against it.

6. Overview of Strong WW Scattering

In Section 3 we reviewed the low energy theorems for $W_L W_L$ scattering and showed that together with unitarity they require the dynamics of $\mathcal{L}_{SB}$ to affect the scattering at an energy scale $\Lambda_{SB} \lesssim 1.75$ TeV. The most probable mechanism is the exchange of particles from $\mathcal{L}_{SB}$, so that $\Lambda_{SB} \cong M_{SB}$, as shown in two examples in Section 3. In general just above the cutoff scale the $J = 0$ partial wave amplitude for scattering of the longitudinal modes $W_L^+ W_L^- \to Z_L Z_L$ is

$$a_0(W_L^+ W_L^- \to Z_L Z_L) \cong \frac{\Lambda_{SB}^2}{16\pi v^2} \tag{6.1}$$

so that the scattering is strong if $\Lambda_{SB} > 1$ TeV and weak if $\Lambda_{SB} \ll 1$ TeV.

In fact there are three independent reaction channels, which can be chosen as $a_{IJ} = a_{00}, a_{11}, a_{20}$ where I is the index of the custodial $SU(2)$ discussed in Section 3. In addition to (6.1) the complete list of $2 \to 2$ reactions is

$$W_L^+ W_L^- \to W_L^+ W_L^- \tag{6.2}$$

$$W_L^\pm Z_L \to W_L^\pm Z_L \tag{6.3}$$

$$W_L^+ W_L^+ \to W_L^+ W_L^+ \tag{6.4a}$$

$$W_L^- W_L^- \to W_L^- W_L^-. \tag{6.4b}$$

All these channels will exhibit strong scattering for $\sqrt{s} > 1$ TeV if $\Lambda_{SB} > 1$ TeV, and some will probably have s-channel resonances with masses M_{SB} of order Λ_{SB}.

Therefore by measuring the $W_L W_L$ scattering amplitudes at high energy, $\sqrt{s} > 1$ TeV, we will learn whether $\mathcal{L}_{SB}$ is a strongly or weakly interacting theory and whether the mass scale of its quanta is at the TeV scale or below. We will probably also begin to observe the quanta directly as resonance effects in some of the $2 \to 2$ channels. A general strategy to accomplish this is based on the $W_L W_L$ fusion reaction, Fig. 6.1, that can be studied at a pp or e^+e^- collider. The initial state W_L's are off-mass-shell and must rescatter to appear on-shell in the final state. The contribution from rescattering by $\mathcal{L}_{SB}$ is $O(g^2\lambda_{SB})$ where g is the $SU(2)_L$ gauge coupling constant and λ_{SB} the generic interaction strength of $\mathcal{L}_{SB}$. The dominant background from $\bar{q}q \to WW$ is $O(g^2)$. Therefore WW fusion contributes an observable increment if and only if the rescattering is strong, i.e., if and only if $\lambda_{SB}/4\pi = O(1)$ or equivalently $\Lambda_{SB} \gtrsim 1$ TeV.

Other backgrounds are $\mathcal{M}(gg \to W^+W^-, ZZ) \sim \alpha_S g^2$ via heavy quark loops[38] (e.g., top), WW bremsstrahlung with gluon exchange between the quarks,[39] $\sim \alpha_S g^2$, and WW fusion by $\mathcal{L}_{SU(2)\times U(1)}$ which is $\sim g^4$. These backgrounds are illustrated in Fig. 6.2. Though the backgrounds (except gg fusion) are dominated by transverse polarizations, polarization is not sufficient to separate them from the longitudinally polarized signal, though it can provide corroboration of a possible signal as discussed below.

The SSC is a minimal pp collider for this strategy. A collider of half the energy or less is not adequate, even with realistically likely higher luminosity. Because both the signal and the signal : background decrease at lower energy[40] and because the most important final states are inaccessible at high luminosity,[41] an upgrade in $\mathcal{L}$ of two to three orders of magnitude would be needed to offset a factor three loss in energy.[40] An e^+e^- collider of $\sqrt{s} \cong 2 - 3$ TeV is probably minimal for the strong WW scattering signal,[42] though more study is needed. See Fig. 6.3 for 1 TeV Higgs boson production cross sections at e^+e^- and pp colliders of various energies.[42a]

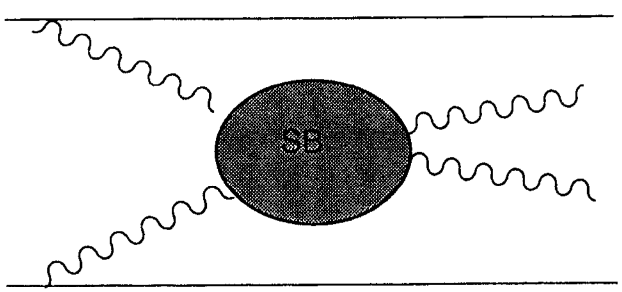

Figure 6.1: Generic $W_L W_L$ fusion via interactions of the symmetry breaking sector $\mathcal{L}_{SB}$.

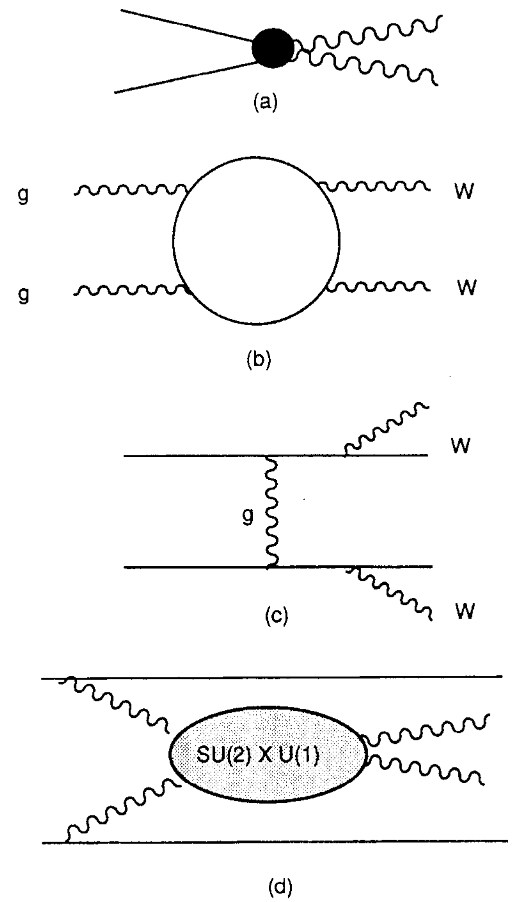

Figure 6.2: Backgrounds to $H \to WW$ signal from (a) $\bar{q}q \to WW$, (b) $gg \to WW$ via $\overline{Q}Q$ loops, (c) gluon exchange, and (d) higher order $O(g^4)$ electroweak interactions including WW fusion as shown.

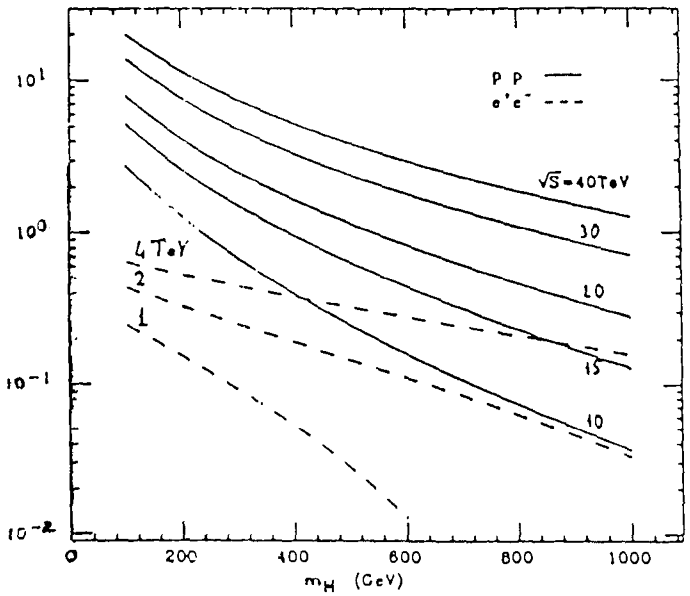

Figure 6.3: Higgs boson production cross sections in picobarns at e^+e and pp colliders with center of mass energies indicated (from Ref. 42a).

In this section I consider three examples of signals for strong symmetry breaking:

1. The 1 TeV Weinberg-Salam Higgs boson
2. Strong W^+W^+ and W^-W^- scattering
3. Techni-rho production

I will consider purely leptonic final states, since they are experimentally cleanest. Larger yields will be possible if detection of $WW \to \ell v + \bar{q}q$ proves feasible.[43–45]

The signals for examples 1) and 2) are excesses of events with no discernible structure. To detect this excess reliably we must understand the background to $\pm 30\%$, a goal consistent with the level at which we can expect to understand the nucleon structure functions and perturbative QCD.[46] Realization of this goal requires an extensive program of "calibration" studies at the SSC, to measure a variety of jet, lepton, and gauge boson final states in order to tune the structure functions and confirm our understanding of the backgrounds.[47]

6.1 The 1 TeV Weinberg-Salam Higgs Boson

In the Weinberg-Salam model the generic Fig. 6.1 is replaced by s-channel Higgs boson exchange, Fig. 6.4. I consider the leptonic final state,

$$H \to ZZ \to e^+e^-/\mu^+\mu^- + e^+e^-/\mu^+\mu^-/\bar{\nu}\nu \tag{6.5}$$

for which the branching ratio is 1.1%, of which 6/7 of the events have one Z decay to $\bar{\nu}\nu$.[3,48] I require any observed Z's to be central, $|y_Z| < 1.5$, and in addition require either $m_{ZZ} > 0.9$ TeV or $(m_{ZZ})_T > 0.9$ TeV, where $(m_{ZZ})_T$ is the transverse mass, $2 \cdot \sqrt{m_Z^2 + p_T^2}$, computed from the p_T of the observed Z when the second Z decays to $\bar{\nu}\nu$. The cuts are needed in order to see the signal above $\bar{q}q \to ZZ$ background. For this signal they are essentially equivalent to alternative cuts that have been suggested.[49]

An idea of the dependence of the signal on collider energy can be gotten from Fig. 6.5, which shows the signal alone. Figure 6.6, showing the signal over the background, illustrates the need for the cut on m_{ZZ} or equivalently on $p_T(Z)$.

Here and elsewhere I quote yields in events per $10^4 pb^{-1}$, the integrated luminosity accumulated with $10^{33} cm^{-2} sec^{-1}$ for 10^7 sec. For $m_t = 50$ GeV the signal

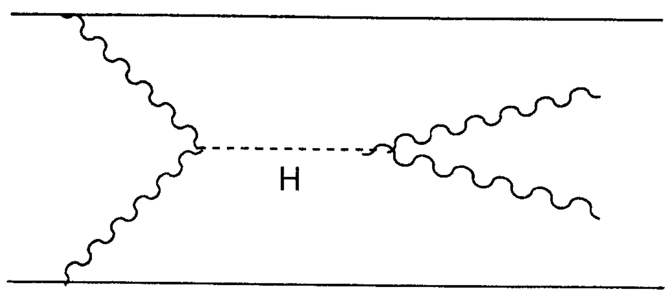

Figure 6.4: Higgs boson production via WW fusion and decay to WW.

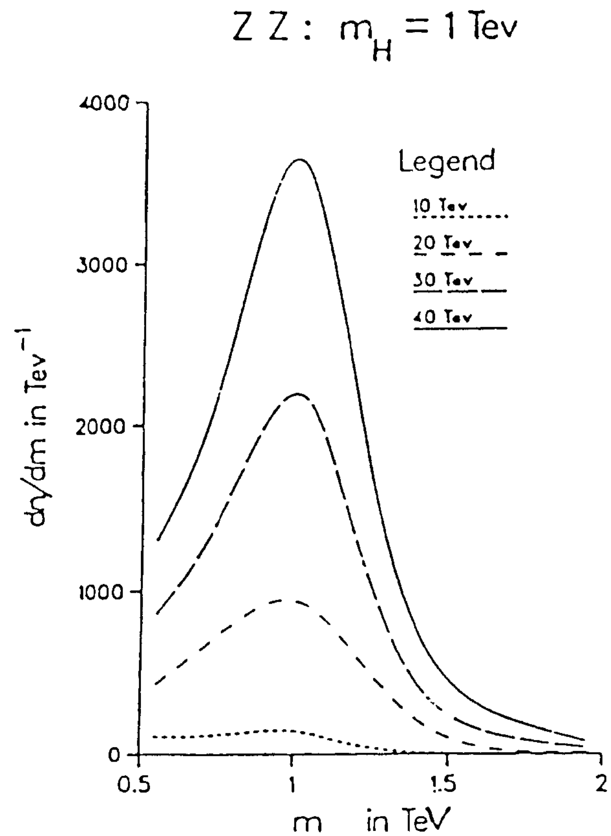

Figure 6.5: Yield dn/dm_{ZZ} in TeV^{-1} for $H \to ZZ$ at 10, 20, 30, and 40 TeV pp colliders, in events per $10^4 pb^{-1}$ with $|y_Z| < 1.5$ (from Ref. 3).

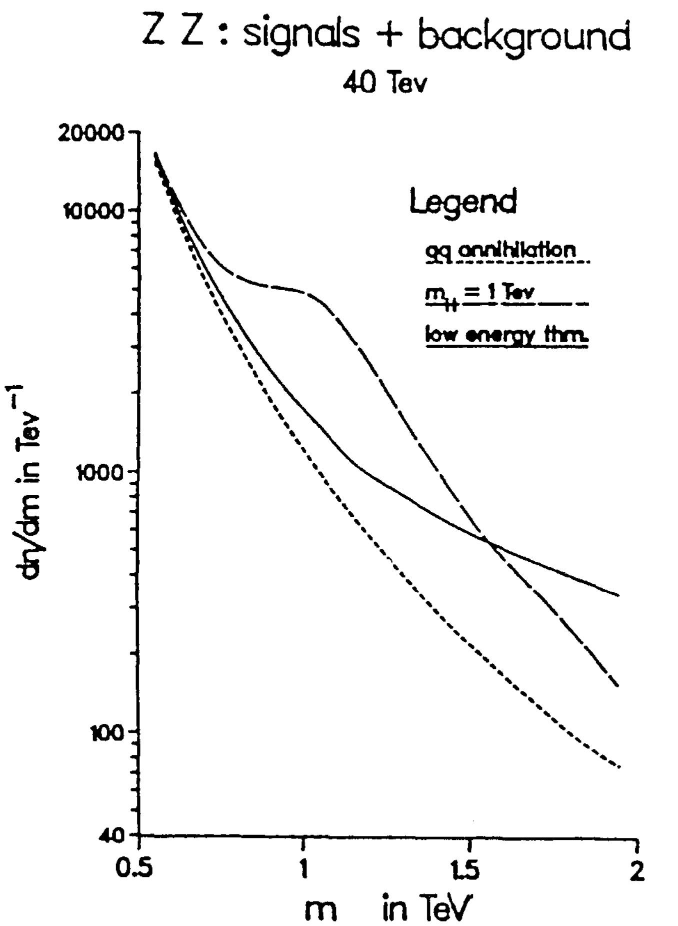

Figure 6.6: Yields defined as in Fig. 6.5 for a 40 TeV pp collider. The short dashed line is the $\bar{q}q \to ZZ$ background while the long dashed line is the sum of the background and the $H \to ZZ$ signal. The solid line represents the sum of signal plus background for an extrapolation of the low energy theorem as discussed in Section 6.2 (from Ref. 3).

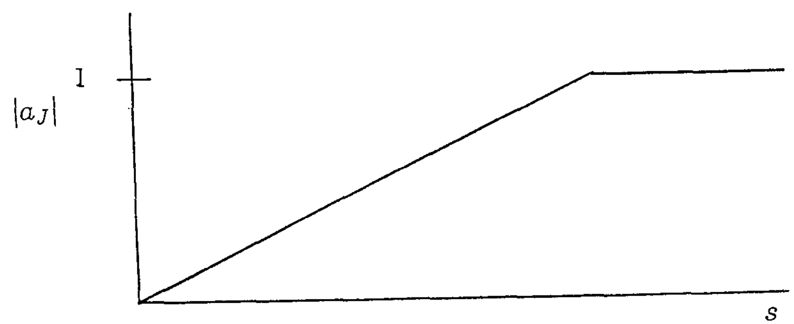

Figure 6.7: Extrapolated low energy theorem for strong W^+W^- scattering, Eq. (6.9).

is 34 events over a background (from $\bar{q}q$ and $gg \to ZZ$) of 16 events (i.e., 50 events total). The situation improves with a heavier top quark due to the additional production channel $gg \to H$ via a $\bar{t}t$ loop.[50] For $m_t = 200$ GeV the signal is 100 events over a background of 22 events. The $O(\alpha_s g^2)$ gluon exchange and $O(g^4)$ $qq \to qqZZ$ backgrounds have not yet been calculated, but will not be very important after the m_{ZZ} or $(m_{ZZ})_T$ cut is applied.

Except for $gg \to ZZ$, the backgrounds are predominantly transversely polarized Z's while the signal is purely longitudinal, resulting in different angular distributions for the decays $Z \to \bar{f}f$ where f is a lepton or quark. Define θ^* as the angle in the Z center of mass system between the fermion momentum $\vec{p}_f$ and the boost axis to the laboratory frame. Then the angular distributions for longitudinal and transverse polarizations are

$$P_L(\cos\theta^*) = \frac{3}{4}\sin^2\theta^* \tag{6.6}$$

$$P_T(\cos\theta^*) = \frac{3}{8}(1+\cos^2\theta^*)\ . \tag{6.7}$$

A strong cut against P_T throws out most of the P_L baby with the bath, and cannot be afforded given the small number of events. On the other hand, there are enough events to check that the signal is longitudinal as expected. For instance, a cut at $|\cos\theta^*| < 1/3$ reduces N_L by about 1/2 while reducing N_T by about 1/4 (see e.g. Ref. 51).

6.2 Strong W^+W^+ & W^-W^- Scattering

The like-charge W_LW_L channel is controlled by the $I_{\text{custodial}} = 2$ low energy theorem,[3]

$$a_{02} = -\frac{s}{32\pi v^2} \tag{6.8}$$

where I have put $\rho = 1$. This is analogous to the exotic $I = 2$ channel in QCD, in which no resonance structure is observed. A simple model[3] for the continuum scattering in this channel is obtained by extrapolating the low energy theorem (6.8) to the unitarity limit at $\sqrt{32\pi v^2} \cong 2.5$ TeV,

$$|a_{02}| = \frac{s}{32\pi v^2}\theta(32\pi v^2 - s) + 1\cdot\theta(s - 32\ piv^2) \tag{6.9}$$

as shown in Fig. 6.7. We then use the effective W approximation[52] to compute the yield from WW fusion.

The model (6.9) can be thought of as a kind of "insurance policy" against the possibility that the mass scale M_{SB} is much larger than the unitarity limit Λ_{SB}. As discussed in Section 3 this is physically implausible though not rigorously impossible. (Ultracolor[53] with a Higgs boson above 1 TeV might provide an example.) To see how this works, compare the analogous $\pi\pi$ scattering models with experimental data. For the three channels, $(I,J) = (0,0),(1,1),(2,0)$, the models analogous to (6.9) are labeled by the curves a in Fig. 6.8, compared there with experimental data.[53a] The model for $|a_{00}|$ describes the trend of the data well. For $|a_{11}|$ it underestimates the data because it fails to account for the ρ meson peak. For $|a_{02}|$ the model overestimates the data (note that since this is an exotic channel, $Im\ a_{02} \cong 0$ and $|a_{02}| \cong |Re\ a_{02}|$ to a good approximation), because it fails to include the effects of ρ exchange in the t and u channels. The model (6.9) is then a kind of worst case scenario: it should work best in the unlikely event that the resonances are much heavier than the unitarity bound for Λ_{SB}. For instance, if the ρ were heavier, say $\geq$ 1 GeV, then curve (a) in Fig. 6.8 would give a better fit (to larger s) than it now does. On the other hand, if the resonances are where we naively expect, $M_{SB} \cong \Lambda_{SB}$, then at least some channels will be dramatically enhanced relative to the model. We consider a resonant (technicolor) example below. First we consider strong WW scattering with no structure as in Fig. 6.7.

The signal is defined by two isolated like-charge leptons,

$$W^+W^+ \to e^+\nu/\mu^+\nu + e^+\nu/\mu^+\nu. \tag{6.10}$$

(Assuming $m_t > M_W$, the branching ratio is $(2/9)^2$.) Cuts imposed are $|y_\ell| < 2$ and $p_{T\ell} > 50$ GeV where $\ell = e,\mu$. In addition a "theorist's" cut of $M_{WW} > 800$ GeV is imposed to reduce background from $qq \to qqWW$ by gluon exchange, $O(\alpha_s g^2)$, and by higher order electroweak interactions, $O(g^4)$. This is a "theorist's" cut since the two ν's prevent it from being implemented experimentally. It can eventually be replaced by a set of cuts on observables, such as the dilepton mass and the transverse mass formed from the dilepton momenta.

The corresponding signal[54] for an SSC year (10^7 sec.) is 53 events, from both W^+W^+ and W^-W^-. The background is $\sim$ 34 events, of which 1/3 is from gluon exchange[54,55] and 2/3 is from $O(g^4)$ processes.[56] If instead of (6.9) we used a scaled version of the $I = 2$ $\pi\pi$ data shown in Fig. 6.8, the signal would be decreased by about a factor of 2.

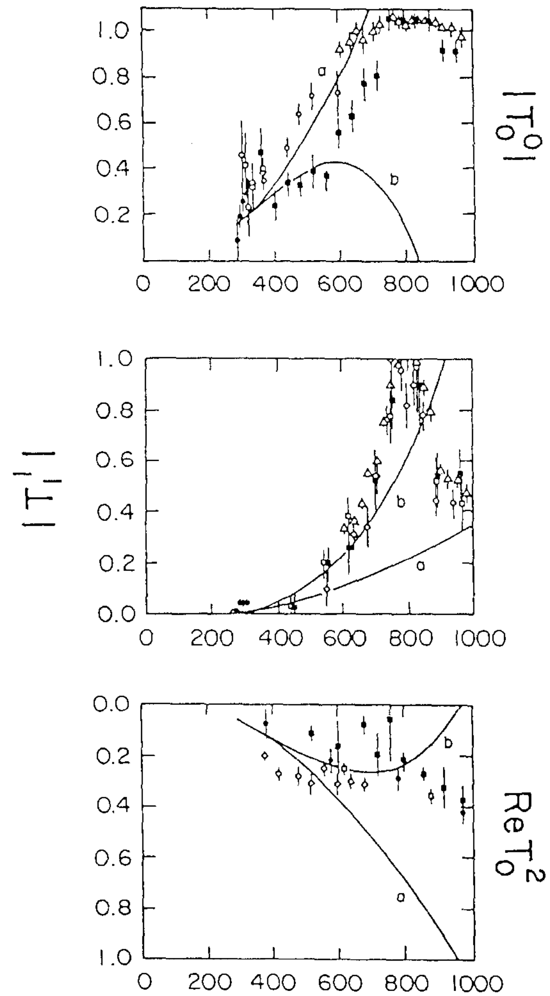

Figure 6.8: Data for $\pi\pi$ partial wave amplitudes compared with extrapolated low energy theorems (e.g., Eq. (6.9)) for the three channels $I, J = (0,0), (1.1), (2.0)$. The curves labeled a correspond to the naive extrapolation as in Eq. (6.9) and Fig. 6.6. The figures are from Ref. 53b.

6.3 Techni-rho meson

As an example of resonance production I will consider production of the techni-rho meson expected in $SU(4)$ technicolor. From Eqs. (5.40-5.41) we have

$$m_{\rho_T} \cong 1.8\,TeV \tag{6.11}$$

$$\Gamma_{\rho_T} \cong 0.3\,TeV. \tag{6.12}$$

There are two important production mechanisms: $W_L W_L \to \rho_T$ (Ref. (3)) and $\bar{q}q \to \rho_T$ Ref. (57)). I consider the easily observed purely leptonic final state

$$\rho_T^{\pm} \to W_L^{\pm} Z_L \to e^{\pm}\nu/\mu^{\pm}\nu + e^+e^-/\mu^+\mu^- \tag{6.13}$$

with branching ratio 0.014 (for $m_t > M_W$). With a central rapidity cut, $|y_{W,Z}| < 1.5$, and a diboson mass cut $M_{WZ} > 1.6$ TeV, I find a signal of 13 events and a background of 1.7 events. If $W \to \tau\nu$ events can also be recovered, signal and background both increase by $\sim 1\frac{1}{2}$ to 20 events over a background of 2.5.

7. Conclusion

The Higgs mechanism implies the existence of Higgs bosons below 1 TeV or strongly interacting particles above 1 TeV, though probably not much heavier than ~ 2 TeV. With the ability to observe strong WW scattering in the 1-2 TeV region, we can decide for certain if the symmetry breaking sector is strong or not. Unlike the usual situation where a negative result leaves open the possibility that we must search at higher energy, the observed absence of strong WW scattering would imply that symmetry breaking is due to Higgs bosons below 1 TeV. The SSC is a minimal pp collider with this "no-lose" capability. A minimal e^+e^- collider probably would need $\sqrt{s} \cong 3 - 5$ TeV and $\mathcal{L} \geq 10^{33} cm^{-2}\,\mathrm{sec}^{-1}$.

Presently approved world facilities would leave open an "intermediate mass" window for a Higgs boson of mass 70-80 GeV $< m_H <$ 120-140 GeV. The gap could be closed by an e^+e^- collider with $\sqrt{s} \gtrsim 300$ GeV and $\mathcal{L} \gtrsim 10^{32} cm^{-2}\,\mathrm{sec}^{-1}$. Motivation for closing this window would be strengthened by the discovery of supersymmetry or by evidence that strong WW scattering does not occur.

It should be clear from the small yields quoted in Section 6 and from the not much bigger yields reviewed by Michael Levi[32] for lighter Higgs bosons, that discovery of the symmetry breaking sector will not be the end but the beginning of a long process of detailed studies. The handful of events that provide the initial discovery will be completely inadequate as we begin our study of a fifth force of nature and an associated new world of particles. The experimental facilities needed for those studies will be awesome and are difficult for us even to imagine today.

References

1. S. Weinberg, *Phys. Rev. Lett.* **19:1264**, 1967; A. Salam, *Proc. 8'th Nobel Symp.*, ed. N. Svartholm, p. 367, (Almqvist & Wiksells, Stockholm, 1968).

2. P.W. Higgs, *Phys. Rev. Lett.* **12:132**, 1964; F. Englert and R. Brout, *ibid* **13:321**, 1964; P. W. Higgs, *Phys. Rev.* **145:1156**, 1966.

3. M. Chanowitz and M.K. Gaillard, *Nucl. Phys.* **B261:379**, 1985.

4. M. Chanowitz, *Ann. Rev. Nucl. Part. Sci.* **38:323**, 1988.

5. J. Goldstone, *Nuovo Cimento* **19:154**, 1961; Y. Nambu and G. Jona–Lassinio, *Phys. Rev.* **122:345**, 1961; J. Goldstone, A. Salam and S. Weinberg, *Phys. Rev.* **127:965**, 1962.

6. S. Coleman, *Aspects of Symmetry*, p.113 (Cambridge U. Press, 1985).

7. S. Weinberg, *Festschrift for I.I. Rabi*, Trans. N.Y. Acad. Sci. Ser. II, **38:185**, 1977; J. Gasser and H. Leutwyler, *Phys. Rep.* **C87**, 1982.

8. M. Gell Mann, R. Oakes, B. Renner, *Phys. Rev.* **175:2195**, 1968.

9. P. Sikivie et al., *Nucl. Phys.* **B173:189**, 1980.

10. M. Chanowitz, M. Golden, and H. Georgi, *Phys. Rev.* **D36:1490**, 1987.

11. M. Veltman, *Nucl. Phys.* **B123:89**, 1977; M. Chanowitz, M. Furman, and I. Hinchliffe, *Phys. Lett.* **78B:285**, 1978; *Nucl. Phys.* **B153:402**, 1979.

12. G. Costa et al., *Nucl. Phys.* **B297:244**, 1987; U. Amaldi et al., *Phys. Rev.* **D36:1385**, 1987.

13. J.M. Cornwall, D. Levin, and G. Tiktopoulos, *Phys. Rev.* **D10:1145**, 1974.

14. C. Vayonakis, *Lett. Nuovo Cim.* **17:383**, 1976.

15. B. Lee, C. Quigg, and H. Thacker, *Phys. Rev.* **D16: 1519**, 1977.

16. M. Chanowitz et al., *Nucl. Phys. B*,Ref. 11.

17. G. Gounaris, R. Kögerler, and H. Neufeld, *Phys. Rev* **D34:3257**, 1986; H. Veltman, LBL–27648, 1989 (submitted to *Phys. Rev. D*).

18. Y. Yao and C. Yuan, *Phys. Rev.* **D38:2237**, 1986.

19. K. Aoki, Tsukuba Meeting 1987:20 (QCD 161: M376, 1987) and RIFP–705, 1987; J. Bagger and C. Schmidt, HUTP–89/A030, 1989.

20. S. Weinberg, *Phys. Rev. Lett.* **17:616**, 1966.

21. M. Chanowitz, M. Golden, and H. Georgi, *Phys. Rev. Lett.* **57:2344**, 1986.

22. S. Weinberg, *Phys. Rev.* **D13:974**, 1976; **D19:1277**, 1979; L. Susskind, *Phys. Rev.* **D20: 2619**, 1979.

23. Y. Golfand and A. Likhtman, JETP Lett. **13:323**, 1971; D. Volkov and V. Akulov, *Phys. Lett.* **46B:109**, 1973; J. Wess and B. Zumino, *Nucl. Phys.* **B70:39**, 1974.

24. M. Gell Mann and M. Levi, *Nuovo Cimento* **16:705**, 1960.

25. R. Dashen and H. Neuberger, *Phys. Rev. Lett.* **50:1897**, 1983.

26. *Lattice Higgs Workshop*, eds. B. Berg et al. (World Scientific, Singapore, 1988).

27. S. Weinberg, *Phys. Rev. Lett.* **36:294**, 1976; A. Linde, *Phys. Lett.* **63B:435**, 1976.

28. M. Lindner, *Z. Phys.* **C31:235**, 1988; M. Lindner, M. Sher, W. Zaglauer, *Phys. Lett.* **228 B: 139**, 1989; M. Sher, *Phys. Rep.* **179:273**, 1989.

29. H. Haber and J. Gunion, *Nucl. Phys.* **B272:1**, 1986; **278:449**, 1986; **307:445**, 1988.

30. J. Gunion and A. Turski, UCD–89–5, 1989; UCD–89–6, 1989.

31. M. Berger, LBL–37539, 1989 (submitted to *Phys. Rev. D*).

32. M. Levi, these proceedings.

33. R. M. Barnett et al., *Experiments, Detectors, and Experimental Areas for the Supercollider*, p. 187, eds. R. Donaldson and M. Gilchriese (World Scientific, Singapore, 1987).

34. S. Weinberg, Ref. (22).

35. E. Eichten et al., *Phys. Rev.* **D34:1547**, 1986.

36. R. Chivukula and H. Georgi, *Phys. Lett.* **188B:99**, 1987; *Phys. Rev.* **D36:2102**, 1987; R. Chivukula, H. Georgi, and L. Randall, *Nucl. Phys.* **B292:93**, 1987.

37. B. Holdom, *Phys. Rev.* **D24:1441**, 1980; W. Bardeen et al., *Phys. Rev. Lett.* **56:1230**,1986; K. Yamawaki et al., *ibid* **56:1335**, 1986, T. Akiba and T. Yanagida, *Phys. Lett.* **169B:436**, 1986; T. Appelquist et al., *Phys. Rev.* **D35:774**, 1987; **D36:568**, 1987.

38. E. Glover and J. van der Bij, *Nucl. Phys.* **B321:561**, 1989.

39. M. Chanowitz and M. Golden, *Phys. Rev. Lett.* **61:1053**, 1988, **E 63:466**, 1989; D. Dicus and R. Vega, *Phys. Lett.* **B217:194**, 1989.

40. M. Chanowitz, LBL–26613, 1989 (to be published in Proc. of the INFN Eloisatron Workshop, Erice, 1988).

41. CERN 88–02, ed. J. Mulvey, 1988.

42. J. Gunion and A. Tofighi–Niaki, *Phys. Rev.* **D36:2671**, 1987.

42a G. Altarelli, p.36, Proc. Workshop on Future Accelerators, La Thuile, 1987, ed J. Mulvey, CERN 87–07, Vol.I.

43. R. Cahn et al., *Phys. Rev.* **D35:1626**, 1987; R. Kleiss and W. Stirling, *Phys. Lett.* **182B:75**, 1986.

44. J. Gunion and M. Soldate, *Phys. Rev.* **D34:826**, 1986.

45. J. Gunion et al., UCD–88–38, 1988.

46. R. Cahn et al., *Experiments, Detectors and Experimental Areas for the Supercollider*, op cit., p. 20.

47. M. Chanowitz, p. 183, *Observable Standard Model Physics at the SSC*, eds. H–U Bengtsson et al. (World Scientific, Singapore, 1986).

48. R. Cahn and M. Chanowitz, *Phys. Rev. Lett.* **56:1327**, 1986.

49. V. Barger, T. Han, and R. Phillips, *Phys. Rev.* **D37:2005**, 1988.

50. H. Georgi et al., *Phys. Rev. Lett.* **40:692**, 1978.

51. G. Kane and C. Yuan, ANL–HEP–PR–89–43, 1989.

52. M. Chanowitz and M. Gaillard, *Phys. Lett.* **142B:85**, 1984; M. Chanowitz and M. Gaillard, Ref. (3); S. Dawson, *Nucl. Phys.* **B29:42**, 1985; G. Kane, W. Repko, and W. Rolnick, *Phys. Lett.* **148B:367**, 1984.

53. H. Georgi and D. Kaplan, *Phys. Lett.* **B145:216**, 1984.

53a J. Donoghue, C. Ramirez, G. Valencia, *Phys. Rev.* **D38:2195**, (1988).

54. M. Chanowitz and M. Golden, Ref. (39).

55. D. Dicus and R. Vega,Ref. (39).

56. D. Dicus and R. Vega, UCD–89–9, 1989; *Phys. Rev.* **D37:2474**, 1988.

57. E. Eichten et al., *Rev. Mod. Phys.* **56:579**, 1984.

ELECTRON-POSITRON STORAGE RINGS AS HEAVY QUARK FACTORIES *

R. H. Siemann
Newman Laboratory of Nuclear Studies
Cornell University, Ithaca, N. Y. 14853

ABSTRACT: The physics of intensity limitations and the beam-beam interaction in low energy e^+e^- storage rings is presented at an introductory level. The progress in these subjects that are keys to the feasibility of heavy quark factories is discussed.

1. INTRODUCTION

1.1 Luminosity and Luminosity Requirements

There is tremendous interest in high luminosity e^+e^- storage rings for heavy quark and τ physics. These storage rings have come to be referred to as "τ-Charm Factories" and "B-Factories", names that reflect the (hoped for) prolific production of these particles. The luminosity, L, must be in the range of 10^{33} - 10^{34}cm^{-2}s^{-1} to earn the name. This range is determined by the particle physics that would be studied with these colliders and the performance of other facilities that could be used for this physics.

The general goals of a τ-Charm Factory are the testing of the Standard Model and the search for new physics through precise measurements and rare decays of the τ lepton and charmed particles. Examples of the capabilities of a τ-Charm Factory with $L = 10^{33}$cm^{-2}s^{-1} are[1]:

1) With center-of-mass energy W = 3.67 GeV, which is below the ψ', there would be 4×10^7 τ pairs produced per year. This would allow measurements of the τ mass to better than $\pm$ 1 MeV and place an upper limit on the ν_τ mass of 3 MeV.

2) By running on the ψ'' the number of tagged D-mesons per year would be 6×10^6 D^+D^-, 1×10^7 $D^0\bar{D}^0$, and 8×10^5 $D_s^+D_s^-$. Such a large, clean sample would allow more sensitive searches for D^0 mixing and measurements of weak decay constants in leptonic and semileptonic decays.

A luminosity of 10^{33}cm^{-2}s^{-1} is substantially larger than that of other colliders at the same energy. The BEPC storage ring has a design luminosity of 10^{31}cm^{-2}s^{-1} at W = 4 GeV, and the best luminosity obtained at SPEAR is 3×10^{30}cm^{-2}s^{-1} at W =

* Supported in part by the National Science Foundation.

3.77 GeV. The capability of colliders at other energies is being debated actively. A B-Factory would produce comparable numbers of τ and C events, but experiments at a τ-Charm Factory would have smaller systematic errors because they could be performed near thresholds and small changes in energy can be used to study the contamination of data samples.

The luminosity of a B-Factory should be well above $10^{33}cm^{-2}s^{-1}$. First, observing CP violation in B-meson decay would be a major objective of a B-Factory. The luminosity required to observe a three standard deviation effect in one year of running has been estimated to be between $5x10^{32}$ and $8x10^{34}cm^{-2}s^{-1}$. The range arises from uncertainty in weak decay parameters and different experiments at symmetric (equal beam energies) and asymmetric (unequal beam energies) colliders.[2]

Second, CESR has reached $10^{32}cm^{-2}s^{-1}$, and there are plans to raise the luminosity to possibly $5x10^{32}cm^{-2}s^{-1}$.[3] The B cross section at the Z is a factor of five larger than at the Υ(4S) where CESR operates, and the LEP I design luminosity is roughly $1.5x10^{31}cm^{-2}s^{-1}$.[4] Multibunch improvements based on the LEP II RF system and separated orbits could raise it to several times $10^{32}cm^{-2}s^{-1}$.[5] This would make LEP equivalent to a $10^{33}cm^{-2}s^{-1}$ B-Factory in this one regard. Of course, B physics will be only a part of a diverse physics program at LEP.

There are two views of luminosity. For the experimenter the luminosity is the proportionality constant between the event rate and cross section

$$\text{Rate } (\text{sec}^{-1}) = L \times \sigma(\text{cm}^2) \qquad (1)$$

while for the accelerator physicist the luminosity depends on properties of the beam

$$L = \frac{1}{4\pi}\frac{N^2 f_c}{\sigma_h \sigma_v} \quad . \qquad (2)$$

In this equation N is the number of particles per bunch which is assumed equal for the two beams, f_c is the collision frequency, and σ_h and σ_v are the rms horizontal and vertical sizes of the beams. The factor $4\pi\sigma_h\sigma_v$ is the effective area of the beam.

It is easy to see how to make the luminosity large in the absence of constraints, but there are constraints from space, cost, beam dynamics, technology, etc. These constraints are interconnected in a complex way as illustrated in Figure 1 which is a take-off of a similar diagram drawn for linear colliders by Bob Palmer.

The highest luminosity ever achieved in an e^+e^- collider is $10^{32}cm^{-2}s^{-1}$ at CESR which is one to two orders of magnitude below the interesting luminosities for factories. This raises the question that is a recurring theme of this paper:

Is the accelerator physics sufficiently well understood that two orders of magnitude in luminosity is conceivable?

In my opinion the answer is YES! That doesn't mean that all of the necessary research has been done at this time; rather, the basic accelerator physics is understood, and we must expand, develop, and apply that knowledge to the design of heavy quark factories.

After some further introductory material, the rest of this paper will concentrate on two beam dynamics issues that are the keys to designing heavy quark factories: i) beam current dependent effects, and ii) the beam-beam interaction.

1.2 A Typical Collider

Although parameters vary among designs, there are general features that all heavy quark factories have in common. It is useful to show a typical collider to put the discussion that follows in context. The τ-Charm Factory of John Jowett has been selected for this purpose.[6] It is illustrated in Figure 2, and parameters are given in Table 1.

There must be a large number of bunches to satisfy the constraints from beam current and beam-beam effects. Extraneous collisions, collisions anywhere but at the interaction point (IP), must be avoided to get the maximum luminosity, and, therefore, the beams are separated at either side of the IP and transported in separate rings. Jowett has chosen electrostatic separators, but RF separators and crossing at an angle are possibilities also. Separation methods are one of the open issues in designing heavy quark factories, and beam current and beam-beam effects influence the choice strongly. It is possible to have separated beams in a single ring. This is done at CESR and the SPS and is being proposed for the Tevatron. It has proved to be an excellent way to upgrade an existing collider. However, having separated beams in a single ring does affect performance, and it's not conservative to

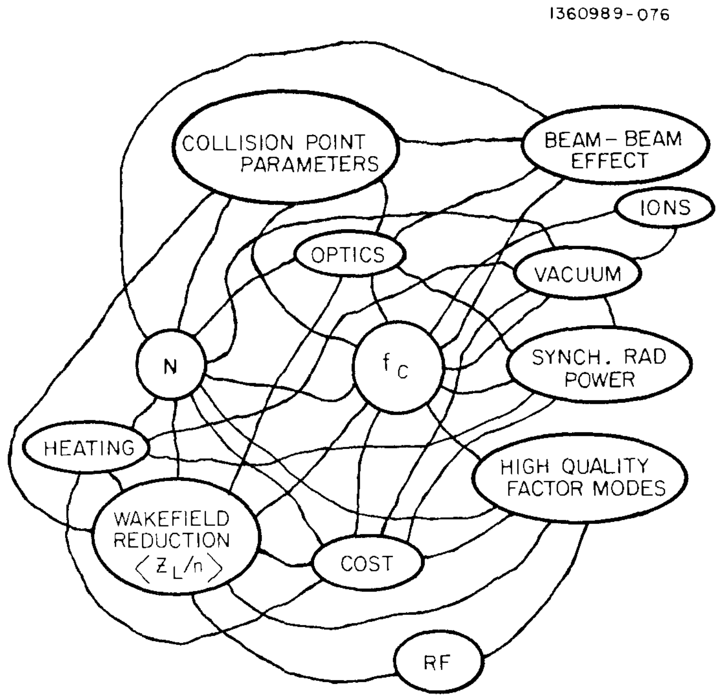

Figure 1: The *rats nest* of interdependencies that makes designing heavy quark factories a challenge.

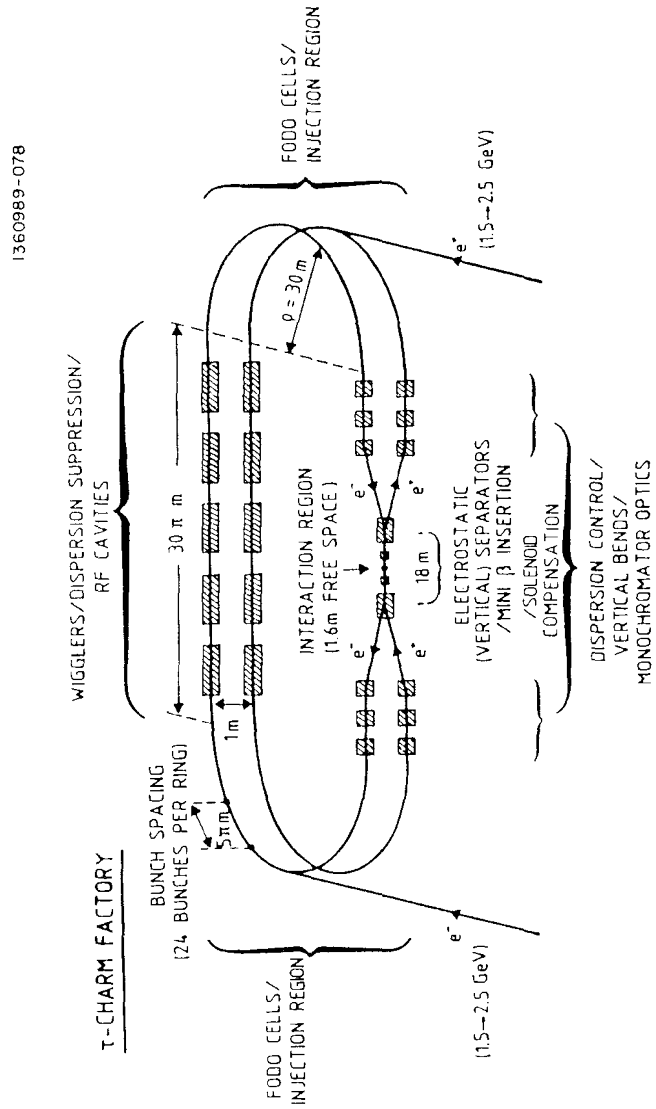

Figure 2: Schematic design of a τ-Charm Factory.[6]

Table 1: Parameters and Performance of a τ-Charm Factory[6]

Energy	$\gamma mc^2 = 2.5$ GeV	Luminosity	$L = 1.6\times10^{33} cm^{-2}s^{-1}$
Collision frequency	$f_c = 19.1$ MHz	Total current	$I_t = 0.5$ A
Number of bunches	$B = 24$	Particles/bunch	$N = 1.6\times10^{11}$
Average radius	$R = 60$ m	Bending radius	$\rho = 12$ m
β functions	$\beta_v = 1$ cm	Emittances	$\varepsilon_v = 3.0\times10^{-9}$ m
	$\beta_h = 0.8$ m		$\varepsilon_h = 0.25\times10^{-6}$ m
Betatron tunes	$Q_v \sim 9.3$	Synchrotron tune	$Q_s = 0.106$
	$Q_h \sim 9.4$	Momentum compaction	$\alpha = 0.0189$
RMS bunch length	$\sigma_L = 6.2$ mm	RMS energy spread	$\sigma_\delta = 5.8\times10^{-4}$
Beam-beam tune spread	$\xi_v = \xi_h = 0.04$	Energy loss/turn	$U_0 = 0.287$ MeV
Damping decrement	$\Delta = 1.1\times10^{-4}$	RF frequency	$f_{rf} = 1.5$ GHz
Synch. rad. power	$P_{sr} = 0.14$ MW	RF voltage	$V_{pk} = 5.0$ MV

incorporate it in the design of a new, high luminosity collider where many aspects of technology and accelerator physics will be stretched to new limits.

All heavy quark factories have "mini-β" optics which means that there is tight focusing at the interaction point.[7] This reduces the effective area in the denominator of eq. (2) without producing unwanted beam-beam effects. The τ-Charm Factory, in common with most designs, has a flat collision geometry, i.e. $R_\sigma = \sigma_v/\sigma_h << 1$; the rms sizes are shown in Figure 3. The rapid increase of vertical size away from the collision point is a consequence of the tight focusing of mini-β optics. The analog in geometrical light optics is a short focal length lens which can produce a small image but introduces a large angular divergence.

Continuing the analogy, the image size and angular divergence are determined by the focal length of the lens, the size of the object, and the angular divergence of light from the object. The product of the size and angular divergence is the "phase space" size of the object, and from Liouville's Theorem it is conserved.[8] The phase space size of a particle beam is called its emittance, ε. At a distance s from the IP (before any quadrupoles) the rms sizes are given by

$$\sigma_j = \left(\varepsilon_j\,(\beta_j + s^2/\beta_j)\right)^{1/2} \quad (j = h, v) \quad . \tag{3}$$

The variables β_j are the "betatron amplitude" functions at the nominal collision point. They are determined by the storage ring magnet configuration, the "lattice", and are independent of the beam emittances.

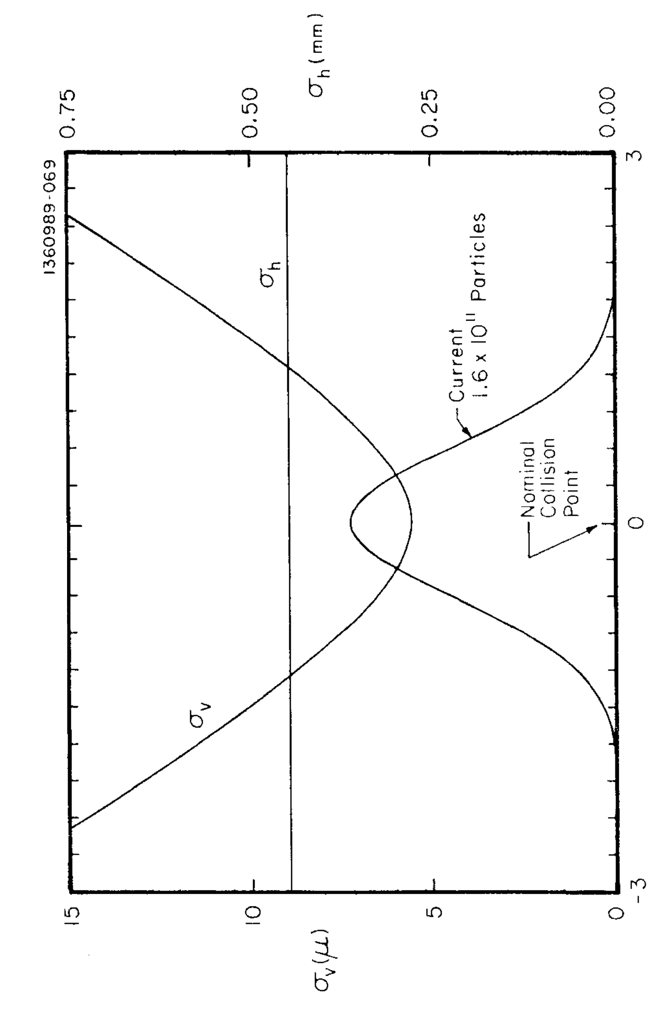

Figure 3: The rms beam sizes as functions of s, the distance from the nominal collision point. The β's and ε's in Table 1 are used. The beam current for σ_L = 6.2 mm is shown with the same horizontal scale.

A short bunch length is a general feature of heavy quark factories that follows from mini-β optics. One reason can be seen in Figure 3 where the charge density for a single bunch is plotted along with σ_V. The effective collision area increases and the luminosity is reduced if $\sigma_L \gtrsim \beta_V$. In addition to this geometric effect there are dynamical reasons associated with non-linear resonances that require $\sigma_L < \beta_V$. See section 4.2.

2. SINGLE PARTICLE MOTION

There is an extensive literature about single particle motion in storage rings and synchrotrons.[9] I have no intention of reproducing that well-known material here; instead, I would like to establish a few points that will be used in the discussions of intensity dependent and beam-beam effects.

Figure 4 is a sketch showing the basic components of a storage ring which are: i) dipole magnets that bend particles, ii) quadrupole magnets that focus particles, and iii) an RF cavity that makes up the energy lost to synchrotron radiation and, together with the magnets, determines the energy spread and bunch length. There is a mythical ideal particle (denoted as *IDEAL*) that travels on-axis and is at the nominal energy. Real particles deviate from the *IDEAL*, and the magnets and RF system provide restoring forces that make these particles oscillate about the *IDEAL*.

2.1 Betatron oscillations

The restoring forces in the horizontal and vertical dimensions come from the quadrupoles. A quadrupole that focuses in the horizontal dimension is defocusing in the vertical, and, therefore, particles see an array of alternating focusing and defocusing quadrupoles. The principle of "strong focusing" gives the conditions for stable oscillations in both transverse dimensions.[10]

The resulting oscillations are called "betatron oscillations", and the general form of the solution is

$$z(s) = \sqrt{A\beta(s)}\,\cos[\phi(s)] \tag{4}$$

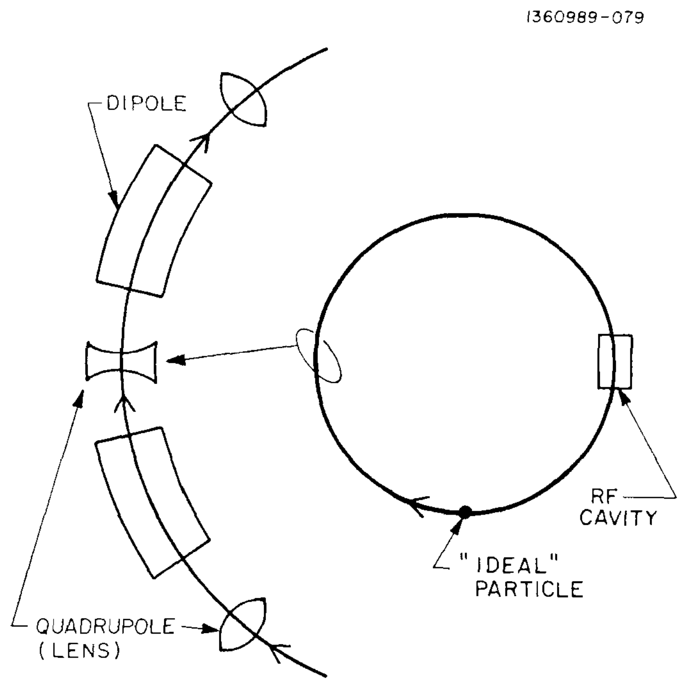

Figure 4: A sketch of a storage ring.

where A is a constant and s is the path length measured along the orbit of the *IDEAL*. The oscillation phase is

$$\phi(s) = \phi_0 + \int_0^s 1/\beta(s')\,ds' \qquad (5)$$

where ϕ_0 is a constant of integration. The β function is a periodic function with period $2\pi R$ that depends on the magnet lattice only. It determines:

1) The local amplitude of oscillation. The constant-of-the-motion A in eq. (4) is often called the amplitude of the oscillation. However, it is not the amplitude in the sense used for simple harmonic motion; $(A\beta(s))^{1/2}$ is closed to that amplitude. The typical value of A is the emittance, and when that typical value is combined with the variation of β near a minimum, eq. (3) results.

2) The rate of phase advance. The betatron tune, Q_β, is the number of betatron oscillations per revolution; it is related to the phase advance in one turn by

$$Q_\beta = \frac{1}{2\pi}\{\phi(2\pi R) - \phi_0\} = \frac{1}{2\pi}\int_0^{2\pi R} 1/\beta(s')\,ds' \ . \qquad (6)$$

These basic ideas about betatron motion are used through the rest of this paper.

2.2 Synchrotron Oscillations

Two effects combine to give synchrotron oscillations (called energy oscillations and longitudinal oscillations also):

1) the bending radius in a dipole is proportional to $|\vec{p}|/|\vec{B}|$, and for a particle with energy above that of the *IDEAL* the bending radius, the circumference, and the orbital period are larger, and

2) the energy gain from the RF cavity depends on the arrival time.

Let δ and τ denote the fractional energy and arrival time deviations from the *IDEAL*, respectively. The orbital period, T, depends on δ as

$$T = \frac{2\pi R}{c}(1 + \alpha\delta) \qquad (7)$$

where α is the momentum compaction which is a property of the lattice. From eq. (7) the change in τ per revolution is

$$\frac{d\tau}{dt} \simeq \frac{\Delta T}{(2\pi R/c)} = \alpha\delta \ . \qquad (8)$$

The RF voltage is shown in Figure 5. It undergoes an integral number of oscillations each time the *IDEAL* completes one revolution. The *IDEAL* arrives at the RF cavity at a phase stable point where the RF makes-up the energy loss due to synchrotron radiation. Particles with an arrival time different from the *IDEAL* have a fractional energy gain

$$\Delta\delta = \frac{1}{\gamma mc^2}\{eV - U_0\} = \frac{1}{\gamma mc^2}\{eV_{pk}\sin(2\pi f_{rf}\tau + \psi_s) - U_0\} \qquad (9)$$

where $V_{pk}\sin(\psi_s) = U_0/e$ gives the phase stable point. With the approximation $\tau \ll 1/f_{rf}$ eq. (9) becomes

$$\frac{d\delta}{dt} \simeq \frac{\Delta\delta c}{2\pi R} = \frac{eV_{pk}f_{rf}\cos\psi_s}{R\gamma mc}\tau \ . \qquad (10)$$

Combining eqs. (8) and (10) gives the equation of motion of a simple harmonic oscillator with a tune Q_s given by

$$Q_s^2 = -\frac{\alpha e V_{pk} f_{rf} R\cos\psi_s}{\gamma mc^3} \qquad (11)$$

provided $\cos\psi_s < 0$. Typical values of the synchrotron tune, Q_s, are in the range 0.01 to 0.10.

A particle undergoing synchrotron oscillations is continually exchanging time and energy deviations as shown in Figure 6. When the particle arrives at the same time as the *IDEAL* it has an energy deviation, and when it has the energy of the *IDEAL* it arrives early or late. When there are no instabilities the rms energy spread, σ_δ, is determined by synchrotron radiation and is a basic property of the lattice. The bunch length and energy spread are related because of synchrotron oscillations; the relation is

$$\sigma_L = \frac{\alpha R}{Q_s}\sigma_\delta \ . \qquad (12)$$

A short bunch length tends to require a high synchrotron tune and through eq. (11) a high V_{pk} and/or f_{rf}.

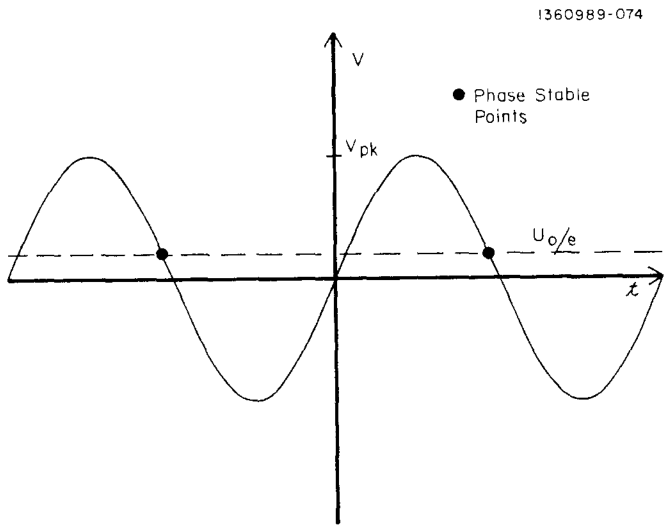

Figure 5: The RF voltage. The energy gain from the RF equals the average loss due to synchrotron radiation (U_0) at the phase stable points. The intersections where the slope of the RF is positive are points of unstable equilibrium.

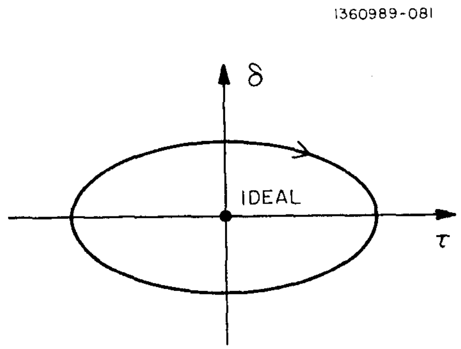

Figure 6: The longitudinal phase space path of a particle undergoing synchrotron oscillations.

3. INTENSITY DEPENDENT EFFECTS

3.1 Wakefields

A beam passing a change in vacuum chamber profile radiates electromagnetic fields that propagate down the beam pipe in waveguide modes and, if a structure is involved, excite normal modes. This is illustrated graphically in Figure 7.[11] At t = 0 the beam is entering the cavity, and the electric field is predominantly the space charge field of the beam. As time passes fields penetrate into the cavity, and cavity modes are excited. When the beam leaves at t ≈ 2.0 nsec, it has lost energy to electromagnetic fields in the cavity. These beam induced fields are called wakefields.

The "wake potential" is the beam induced voltage seen by a particle located at position t in the bunch (see the inset in Figure 8)

$$V(t) = \int_{-\infty}^{\infty} dz \int_{-\infty}^{\infty} dt'\, E_z(z,t')\,\delta(t'-(t+z/c)) \quad . \tag{13}$$

The direction of propagation is denoted by z in this equation, and it has been assumed that the structure producing the wakefield has rotational symmetry and that the beam and particle are traveling on the symmetry axis.[12] The quantity E_z is the longitudinal component of the beam induced electric field. It is proportional to N, the number of particles in the bunch, and depends on the rms bunch length and the structure geometry.

A wake potential for a CESR RF cavity is plotted in Figure 8. Several consequences of beam induced fields can be seen in this figure. First, the beam loses energy as is expected from a comparison of the electromagnetic field energies at t = 0 and t = 2 nsec in Figure 7. The energy loss is

$$\text{Energy change} = \int_{-\infty}^{\infty} dt\, I(t)\, V(t) < 0 \tag{14}$$

where I(t) is the bunch current. The wake potential and I(t) are each proportional to N, so the energy loss is proportional to N^2. The power lost due to beam induced fields is called Higher Order Mode power; it is given by

$$P_{hom} = k(\sigma_L)\, N^2 e^2 f_c = k(\sigma_L)\, I_t^2/f_c \quad . \tag{15}$$

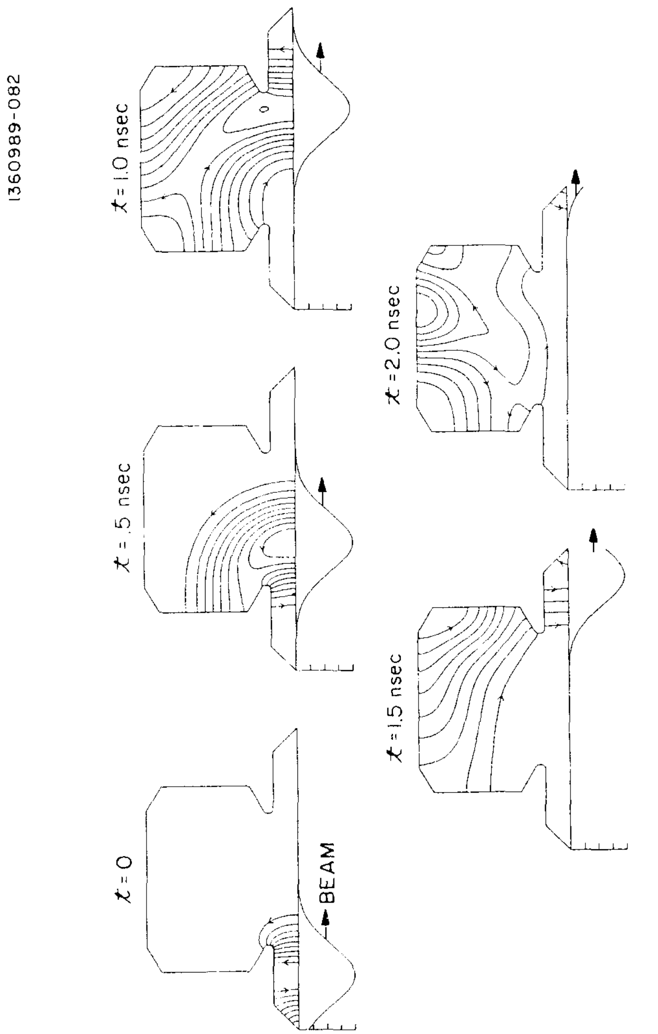

Figure 7: The electric field lines produced by a Gaussian bunch passing a LEP cavity. Ref. [11]

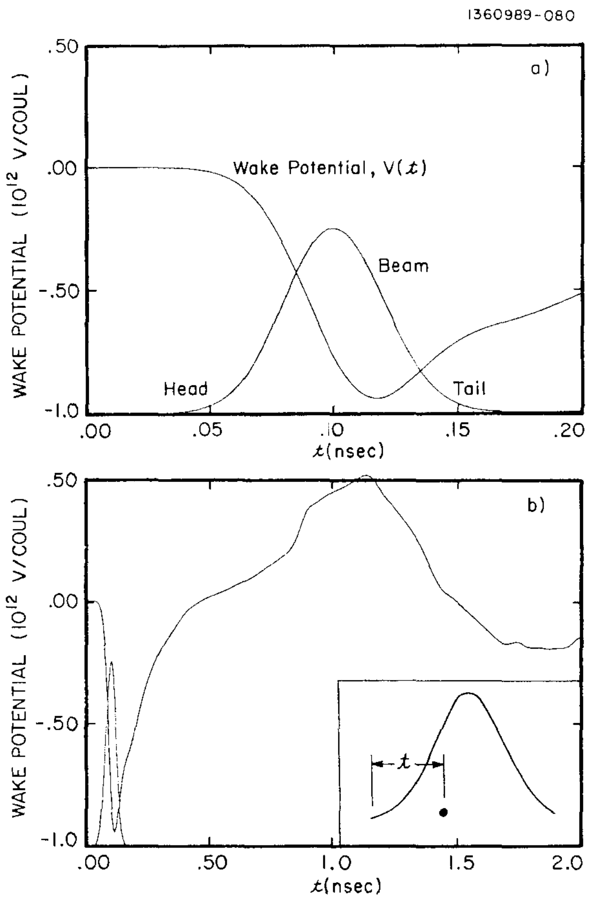

Figure 8: The wake potential for a 6 mm long, 1 C bunch traveling through a CESR cavity shown for two different time scales. The inset defines the time t as the elapsed time between the passage of the (arbitrarily chosen) origin and the particle located at t.

The quantity $k(\sigma_L)$ is the loss factor of the structure, and the bunch length dependence is shown explicitly. HOM losses are discussed further in section 3.2.

Instabilities are a second consequence of wakefields. Figure 8a shows that V(t) varies along the bunch; the wake potential is different at the head and tail. This introduces additional τ dependencies into eqs. (9) and (10); these can lead to the single bunch instabilities that are discussed in section 3.3. Figure 8b shows that the wake potential can be positive at longer times, and a particle passing through the cavity at those times will gain energy. Therefore, it is possible to transfer energy between bunches. This leads to coupled bunch instabilities that are discussed in section 3.4.

3.1.1 Longitudinal Impedance: Beam stability results are often presented in terms of the longitudinal impedance, Z_L. The reason is that stability calculations are done with the standard techniques of Green's functions and Fourier transforms. The Green's function is the wake potential from a unit charged δ-function bunch, $V_\delta(t)$. Its Fourier transform

$$Z_L(\omega) = -\int_{-\infty}^{\infty} V_\delta(t)\, e^{-i\omega t}\, dt \qquad (16)$$

is the longitudinal impedance.

3.2 Higher Order Mode (HOM) Losses

The HOM power, given by eq. (15), can be substantial for heavy quark factories because of the short bunch length and high current. The loss factor for a twenty convolution bellows has been calculated as an example and is shown in Figure 9. Taking the τ-Charm Factory parameters in Table 1 and $k = 3\times10^{11}$ V/C (a typical value for the bellows for $\sigma_L = 6.2$ mm) $P_{hom} \sim 4$ kW; the bellows would burn up! This example is gross, but it does point out the problem of localized heating. In fact, no one would use such a bellows; instead they are shielded to reduce the number and size of discontinuities.

A model of the storage ring vacuum system is needed to determine the total HOM power because it depends on the number, type, and geometry of individual components. Collider designs aren't sufficiently advanced to have such a model, but estimates can be made based on existing storage rings. One such estimate for a

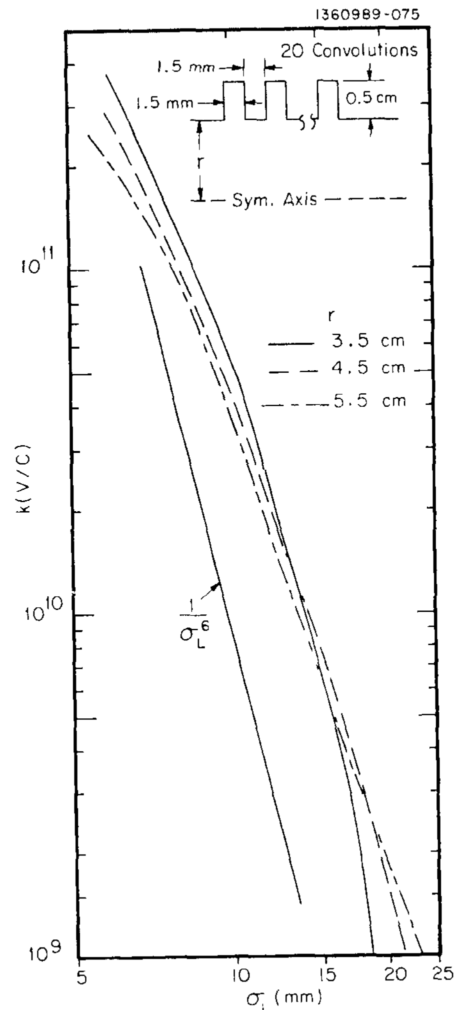

Figure 9: The loss factor for the 20 convolution bellows and three values of the inner radius.

B-Factory indicates that with present components the HOM power would be many times the synchrotron radiation power and could be over 20 MW per beam.[13] This is unacceptable!

Loss factors must be reduced because of localized heating and total HOM power. There are ways to do this: i) the number of discontinuities should be minimized, and ii) geometric factors should be considered for discontinuities that cannot be avoided. These factors are illustrated by referring to Figure 9. First, k has a strong bunch length dependence. The bunch has a spectrum that is proportional to $\exp\{-(2\pi f\sigma_L/c)^2\}$ where f is the frequency, and as σ_L becomes small the power extends to higher frequencies. In the bellows example, the loss factor becomes large when the bunch contains significant power at frequencies corresponding to the 3 mm period and 5 mm depth of the convolutions. Components that appear numerous times in the storage ring (bellows, pumping slots, etc) must be designed with discontinuities that are small on the length scale of the bunch.

Second, when the bellows loss factor is large ($\sigma_L < 10$ mm), it is roughly inversely proportional to the inner radius, r, and increasing r reduces k. This isn't nearly as effective as reducing the length scale of the discontinuities. However, it can be important because some components such as separators and RF cavities have geometric constraints imposed by their primary function; it helps to make their inner radius large. The implications for the RF system are discussed in section 3.4.

It is estimated that the total HOM power can be made comparable to or smaller than the synchrotron radiation power by employing the ideas above. The more serious remaining problem is heating of specific components where minimizing HOM power can be a significant design criterion. The separators at the IP are one place where this seems crucial. There must be gaps at the ends of electrostatic and RF separators to hold-off voltage, and there will be large HOM losses from these gaps. The HOM power of a specific RF separator being considered for a B-Factory has been calculated to be over 100 kW[14]; this amount of power presents considerable design and engineering problems. Asymmetric colliders have an advantage in this regard because magnetic separation can be used, and there is no need for a complicated separator.

3.3 Single Bunch Instabilities

Instabilities are classified as either longitudinal or transverse; the former are considered first. The total voltage is the sum of the applied RF voltage and the wake potential. Jowett suggests using a 1.5 GHz superconducting RF system for the τ-Charm Factory. Taking the wake potential for ten 1.5 GHz cavity cells for purposes of estimation, using the parameters in Table 1, and assuming a Gaussian bunch shape gives the voltage shown in Figure 10. The wake potential makes an appreciable contribution to the total voltage.

Wakefields have a fundamentally different character than the applied voltage. If the bunch shape changes, the wake potential changes, and a self-consistent picture has to have a distorted bunch shape and the fields that would be generated by a bunch of that shape. There are two possibilities:

1) The distorted bunch and its (self-consistent) wake potential are stable in time. The bunch shape is distorted, but the energy spectrum is unchanged from the Gaussian produced by synchrotron radiation.[15] This possibility is called "potential well distortion".

2) A stable self-consistent solution does not exist. Unstable structure develops on the bunch, and, if the sinusoidal RF voltage is approximated as linear, this structure grows exponentially in time. The non-linearity of the RF voltage limits the growth, and the result is increased bunch length and energy spread. Accelerator physicists call this possibility the "microwave instability".

Figure 11 shows these two regimes in SPEAR.[16] There is potential well distortion up to about 2 mA as evidenced by the constant energy spread, and then instability sets in with large increases in bunch length and energy spread.

The collider must be designed to avoid the microwave instability. Significant bunch lengthening is unacceptable because it is incompatible with mini-β optics. Energy spread increase affects experiments through a reduction in the effective cross section for experiments running on resonances and reducing the effectiveness of kinematic constraints for background rejection.[18] The instability threshold (particles per bunch) is

$$N_\mu \langle Z_L / n \rangle = \sqrt{\pi/2}\; Z_o \frac{\alpha\gamma\sigma_\delta^2\sigma_L}{r_e} \qquad (17)$$

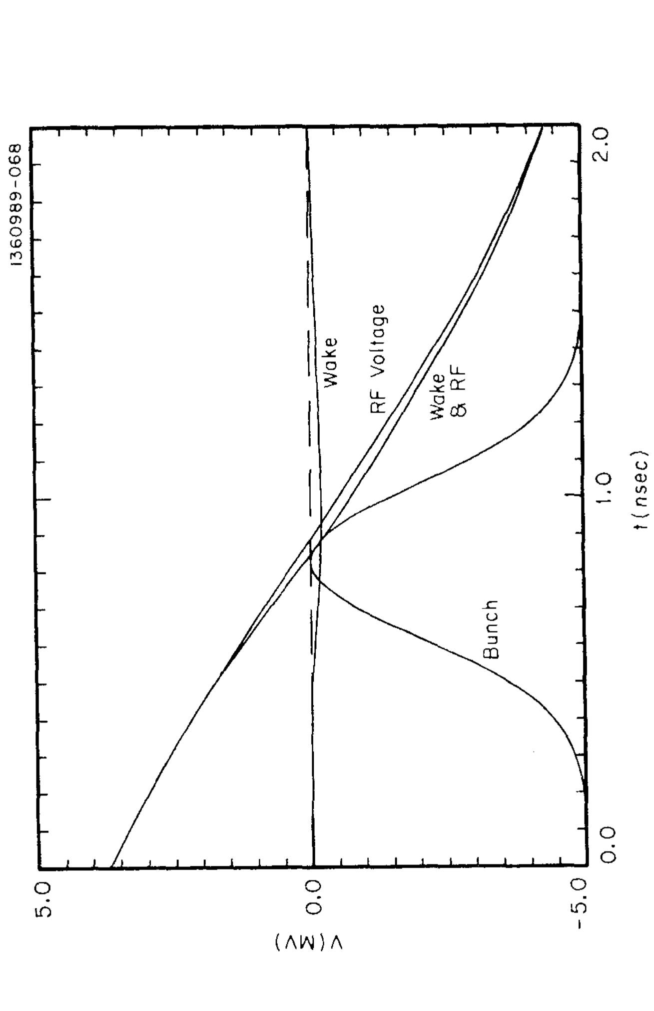

Figure 10: Wake potential, applied RF voltage, and total voltage for the τ-Charm Factory parameters in Table 1. The wake was calculated for ten 1.5 GHz RF cavity cells.

Figure 11: Bunch length, core energy spread, and synchronous phase shift in SPEAR at 1.55 GeV. The data which are represented by the solid points and the curves are from Wilson et al, [Ref. 16] and the open circles are the results of a simulation. [Ref. 17]

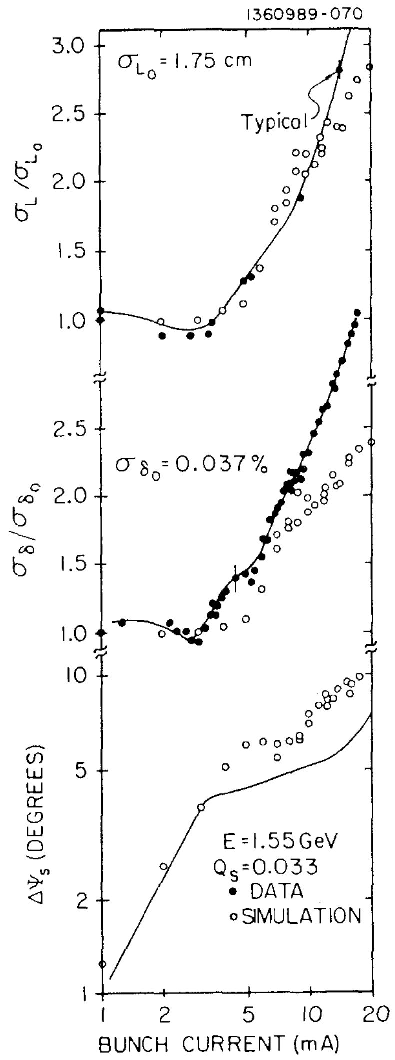

where $<Z_L/n>$ is the effective impedance of the storage ring

$$<Z_L/n> = \frac{Z_L(\omega)\,c}{\omega R} \tag{18}$$

averaged over the frequency spectrum of the bunch. There is a great deal of physics incorporated into $<Z_L/n>$; it contains information about the number and types of discontinuities, the frequency content of the bunch, the cut-off frequency for electromagnetic wave propagation, and even some unresolved questions associated with the high frequency behavior of the impedance. The value of eq. (17) is that it gives the dependences on accelerator parameters and it provides a rule-of-thumb for making estimates.

Existing machines have an effective impedance, $<Z_L/n> \sim 1\ \Omega$, but eq. (17) gives $<Z_L/n> < 0.2\ \Omega$ for the τ-Charm Factory at 2.5 GeV. This result is typical of all heavy quark factory designs, and it means that the effective impedance must be reduced by about an order of magnitude below that of existing machines. The steps required to do this are the same as those required to reduce the loss factor: minimizing the number of discontinuities and careful consideration of geometrical factors.

Transverse instabilities are produced by deflecting, rather than accelerating, wakefields. They limited the performance of PEP and PETRA, and it is anticipated they will be important for LEP also. However, rough estimates are that this will not be the case for heavy quark factories. The dominant transverse instability is expected to be the "fast transverse blow-up". The threshold (particles per bunch) when the vacuum chamber radius satisfies $b > \sigma_L$ is[19]

$$N_T = \frac{2\alpha\gamma\sigma_\delta R b}{r_e \beta_{avg}\sigma_L}\frac{Z_o}{<Z_T>} \ . \tag{19}$$

In this equation $<Z_T>$ is the effective transverse impedance and β_{avg} is the average β function given approximately by $\beta_{avg} \sim R/Q_\beta$. A rough relationship between the longitudinal and transverse impedances is

$$<Z_T> \sim \frac{2R}{b^2}<Z_L/n> \ . \tag{20}$$

The transverse impedance falls off more rapidly than the longitudinal impedance at high frequencies; eqs. (19) and (20) account for that in an approximate way.[20] Substituting

$$N_T<Z_L/n> = Z_o\,\frac{\alpha\gamma\sigma_\delta b^3 Q_\beta}{r_e R\sigma_L} \tag{21}$$

where $Q_\beta = Q_h$ or Q_v. The result is $N_\mu/N_T << 1$ for the τ-Charm and other heavy quark factories.

The approximations that give this result are crude, but it indicates that the microwave instability is dominant. The basic reasons for the difference from PEP, PETRA, and LEP are the short bunch length of heavy quark factories and the rapid high frequency fall-off of the transverse impedance.

3.4 Coupled Bunch Instabilities

The wake potential of a particular object like an RF cavity can be written as a sum over normal modes[21]

$$V(t) = -2\Theta(t)\left(\sum_\mu k_\mu(\sigma_L)\exp(-\omega_\mu t/2Q_\mu)\cos(\omega_\mu t)\right) \tag{22}$$

where $k_\mu(\sigma_L)$, ω_μ, and Q_μ are the loss factor, angular frequency, and quality factor for mode μ, respectively, and Θ(t) is the step function (Θ = 0 for t < 0; Θ = 1/2 for t = 0; Θ = 1 for t > 0). The quality factor of a mode depends on stored energy and energy losses due to wall resistance and external coupling. Examples of the latter are probes inserted specifically for reducing Q and waves propagating away from the structure in the beampipe. High frequency modes tend to have low Q's because wall losses are high and they are above the cut-off frequency of the beampipe. Therefore, at large t the wake is likely to be dominated by a few low frequency modes.

Modes with a high Q can cause coupled bunch instabilities because they can mediate energy transfer between bunches. Whether a particular mode causes an instability is sensitively dependent on its frequency, ω_μ. The bunch spacing is locked to the RF period, and the relative phase of the wake potential from different bunches is $n\omega_\mu/f_{rf}$ where n is the number of RF periods between bunches. When the phase is such that the wakes from successive bunches add constructively, an instability occurs. (This is an oversimplification because there are different coupled bunch modes distinguished by a relative phase between bunches, but the essential picture is correct.) There are three ways to cure potential coupled bunch instabilities: i) reduce the Q's of harmful modes so that the wakefield decays between bunches; ii) adjust the resonant frequencies so these modes do not cause instabilities; iii) use feedback to damp instabilities. Reduction of higher mode Q's is the preferred method.

The dominant high Q impedances usually come from the RF system. RF cavities have a high Q and strong coupling to the beam in the fundamental (accelerating) mode, and this leads to other modes with high Q's and large loss factors also. Many heavy quark factories have superconducting RF cavities as part of the design because a large V_{pk} is needed for a short bunch length (eq. (12)), and this is possible with a small number of superconducting cavities. This limits the contribution of the RF system to $<Z_L/n>$ by minimizing the number of discontinuities associated with the RF. In addition, the inner radius of the cavity can be larger than it would be for a normal conducting cavity, and this reduces $<Z_L/n>$ further.

The costs of using superconducting RF are the technical complexity and higher modes with $Q \sim 10^9$ in the absence of external coupling. These Q's must be reduced to about $Q \sim 100$ to avoid coupled bunch instabilities by Q reduction alone. This is one of the reasons that only single cell cavities are being considered for heavy quark factories; the explanation follows. Multipacting, a vacuum electronic phenomenon, used to limit the gradient of superconducting RF. This limit was removed by understanding the effects of cavity geometry and moving couplers (for reducing higher mode Q's) from the cavity body to the beampipe where the accelerating mode power is small.[22] RF systems with multiple cells per cavity module have normal modes with the field energy predominantly in a single cell. If that cell is an interior one, beampipe couplers can reduce the Q to $Q \sim 10^4$ only.

Heavy quark factories require greater Q reduction, and single cell cavities are attractive for this. The R&D for this remains to be done, and it may turn-out to be necessary to control coupled bunch instabilities with a combination of Q reduction and the other methods mentioned above.

3.5 Discussion

It's time to return to the central question raised in the introduction. The conclusion from looking at higher order mode losses and beam stability is that there needs to be an order of magnitude reduction of wakefields as compared to CESR, PEP, and PETRA. Therefore, with regard to intensity dependent effects the general question leads to two specific ones:

1) How complete is our knowledge of the causes and effects of wakefields; i.e. are we in for the surprise of encountering new accelerator physics when peak and total currents are raised substantially?

2) Do we have the tools and technology needed to specify, design, and build components that have the required wakefield reduction?

The answers to both questions rest on over two decades of experience with e^+e^- storage rings and on the progress during the last decade since CESR, PEP and PETRA were built.

3.5.1 Surprises: The role of wakefields in determining performance is increasingly appreciated with each new generation of accelerator. The "head-tail" instability (a single bunch, transverse instability) was encountered first at ADONE. The importance of sextupoles for curing this instability was understood there, and sextupoles were incorporated into all future storage rings. SPEAR has sextupoles, but it has a large impedance also, and the consequent bunch lengthening is shown in Figure 11. Wakefield reduction was carefully considered at CESR, PEP and PETRA. Impedance measuring techniques were developed, and there were "impedance czars" who ruled on the appropriateness of vacuum system components. Many practices that are now standard, such as shielding bellows, were perfected. Despite this, an unexpected instability, the "fast head-tail" instability (another single bunch, transverse instability) limited PEP and PETRA under some conditions.

The observations mentioned above and closely related ones in proton accelerators led to an explanation of beam instabilities based on the Vlasov equation.[23] This work became well-known and widely accepted by the early

1980's. All observed instabilities are explained. The principal limitations of these solutions are the simplified wakefields used to get results. Observations can be reproduced with simulations also. These can use realistic wakefields, but they don't lend themselves to giving a clear picture of the underlying physics. The combination of analytical work providing insight and simulations for detailed calculations gives the ability to make a realistic evaluation of intensity dependent effects. A recent success of this approach is the quantitative explanation of bunch lengthening in the SLC damping ring based on the vacuum system geometry![24]

Surprises have to arise from dynamics or impedances outside our present, comprehensive understanding. There are open questions about the high frequency behavior of the impedance from discontinuities and from coherent synchrotron radiation, and this satisfies the description of a possible surprise.[25] The problem of the high frequency impedance arises for accelerators ranging from synchrotron light sources to liner colliders, and it is the subject of some work. More may be required for heavy quark factories.

3.5.2 Tools: The theory and simulations needed for understanding the effects of wakefields have been mentioned above. They are well developed.

A second important set of tools are the computer programs for calculating wake potentials and loss factors. Ten years ago the only widely used program was one for calculating the loss factors of low frequency modes of rotationally symmetric structures.[26] Transverse wakefields, high frequency wakefields, and wakefields from structures without rotational symmetry could not be calculated. That is no longer the situation. About that time Tom Weiland began writing a comprehensive set of computer programs for solving Maxwell's equations; these can be used to calculate longitudinal and transverse loss factors and wake potentials in a large variety of situations. The programs include[27]: i) BCI and TBCI that integrate Maxwell's equations in time for rotationally symmetric objects (BCI was used to produce Figures 8 and 9), ii) URMEL and URMELT that find the normal modes of rotationally symmetric structures, and iii) the MAFIA group that generalizes the above programs for objects that don't have rotational symmetry. BCI, ..., URMELT can be used for calculating the wakefields of most components of a storage ring vacuum system, and they run on modest computers. The MAFIA programs can be used for components that are not approximated well enough by rotational symmetry, but they require extensive computer resources. In some cases that is a limitation.

Superconducting RF could be an important technology for heavy quark factories; here, again, there has been crucial advances in the last decade. Cavities with appropriate gradient (~ 5 MeV/m) and fundamental mode Q (~ $2x10^9$) are commercially available; they were barely in the laboratory ten years ago! The progress has come from controlling multipacting and improvements of niobium properties. In addition, large numbers of cavities are being employed in accelerators, and the systems aspects of large superconducting RF installations are understood. Heavy quark factories have special requirements, strong higher mode damping and high power RF windows, that are the focus of present development work. These developments must be successful for superconducting RF to be used, but most aspects of superconducting RF are proven already.

3.5.3 Summary: There is at least one possible accelerator physics surprise, and the tools aren't perfect. However, there has been tremendous progress in understanding and controlling intensity dependent effects since the CESR, PEP, PETRA generation. This progress is one of the reasons for my optimistic answer to the central question raised in the introduction.

4. THE BEAM-BEAM INTERACTION

The small impact parameter collisions that produce elementary particles are rare. Most of the time a particle interacts with the electric and magnetic fields of the other beam only. This is the beam-beam interaction that imposes important constraints on storage ring colliders.

4.1 Beam-Beam Tune Spread

Figure 12 shows the deflection of an electron passing through a Gaussian positron bunch with $R_\sigma << 1$. There are three distinct regions. When $|y|/\sigma_y \lesssim 1$ the deflection is linear in the displacement, $\Delta y' = y/f$. The opposing beam acts like a focusing lens with a focal length:

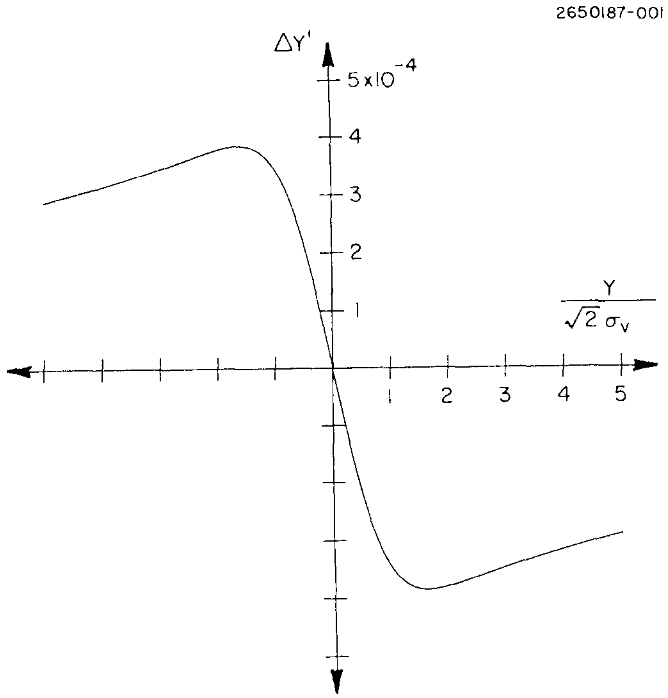

Figure 12: The vertical deflection of a typical electron in CESR passing through a positron bunch a distance y from the center.

$$\frac{1}{f} = -\frac{2r_e N}{\gamma\sigma_v(\sigma_v+\sigma_h)} \quad . \tag{23}$$

This focusing increases the vertical tune of particles with small betatron amplitudes ($A_v \leq \varepsilon_v$) from Q_v to $Q_v + \xi_v$ where

$$\xi_v = \frac{r_e}{2\pi}\frac{N\,\beta_v}{\gamma\sigma_v(\sigma_h+\sigma_v)} \quad . \tag{24}$$

When $|y|/\sigma_v \gtrsim 5$, the electron is above (or below) the positron bunch, and the fields fall-off as σ_h/y. Finally, there is an intermediate regime where the fields make a transition between the two limiting forms. In the intermediate and large $|y|$ regions the effective focal length, defined by $\Delta y' = y/f_{eff}$, is longer than it is for small displacements, and the focusing from the beam-beam interaction is weaker.

A particle with $A_v > 3\varepsilon_v$ is in the small $|y|$ region on some turns and outside it on others; it depends on the betatron phase in eq. (4). The tune of this particle is determined by averaging the focusing over all phases, and the result is that the tune is less than that of a small amplitude particle. A very large amplitude particle is outside the linear region on most turns, and its tune is unaffected by the beam-beam interaction. A summary is: i) at small amplitude $Q_p = Q_v + \xi_v$, ii) at intermediate amplitude $Q_p = Q_v + \chi\xi_v$ ($\chi < 1.0$), and iii) at large amplitude $Q_p = Q_v$; Q_p and Q_v denote the tunes with and without the beam-beam interaction, respectively.

The quantity ξ_v given by eq. (24) has a number of names. It is often called the "beam-beam tune shift", but this name is unfortunate because it evokes an incorrect picture. If all particles, not just the small amplitude ones, had the same tune shift, quadrupoles could be used to compensate for the beam-beam interaction. However, such compensation isn't possible because the beam-beam interaction introduces a tune spread. The second commonly used name, the "beam-beam tune spread", gives a better description, but it has a technical shortcoming outside the scope of this paper.[28] The third name, the "beam-beam strength parameter" doesn't have this shortcoming and is the most precise name. I will use beam-beam tune spread for the rest of this article.

Only vertical motion was considered in the discussion above, but particles oscillate in the horizontal and vertical. There is a beam-beam tune spread in both transverse dimensions, and the beam occupies an area in the betatron tune plane. Figure 13 shows an example of the beam's "footprint". The operating point is determined by the storage ring lattice; most particles have tunes shifted away from this point. The relation between the footprint and the resonance lines in the figure is discussed in the next section.

The horizontal and vertical beam-beam tune spreads characterize the beam-beam interaction. Years of experience have shown that the maximum tune spreads achievable are $\xi_v(\max)$, $\xi_h(\max) \sim 0.02$ to 0.06.[29] It is likely that the current will be limited by wakefields in heavy quark factories; then

$$\frac{L}{I_t} = \xi \frac{(1+R_\sigma)\gamma}{2\beta_v r_e e} \qquad (25)$$

where $\xi_v = \xi_h = \xi$ has been assumed. Large beam-beam tune spreads are important so that the beam current can be used efficiently.

4.2 Non-linearities

The maximum beam-beam tune spread is determined by the non-linearities of the beam-beam interaction. These lead to non-linear resonances that depend on the tunes as

$$kQ_v + lQ_h + mQ_s = n \qquad (26)$$

where k, l, m, and n are integers. The tune plane in Figure 13 has resonance lines given by eq. (26) crossing it. The maximum value of ξ is reached when the beam footprint is hemmed in by sufficiently strong resonances. These strong resonances are ones where the sum $|k| + |l| + |m|$ is below a critical value. Resonances can be caused by different effects. One of these is the departure from linearity ($\Delta y' = y/f$) in Figure 12; this leads to a minimum set of resonances that cannot be avoided. "Parametric" resonances are another class; they are driven by modulation of the beam-beam deflection. A simpler example of parametric driving is shown in Figure 14.

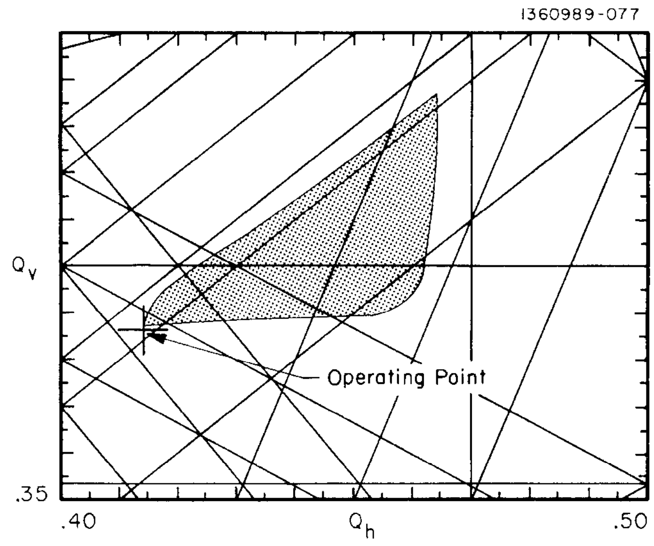

Figure 13: The betatron tune plane with the (shaded) beam footprint. The lines in the tune plane correspond to various resonances given by eq. (26). This figure is from ref. [30].

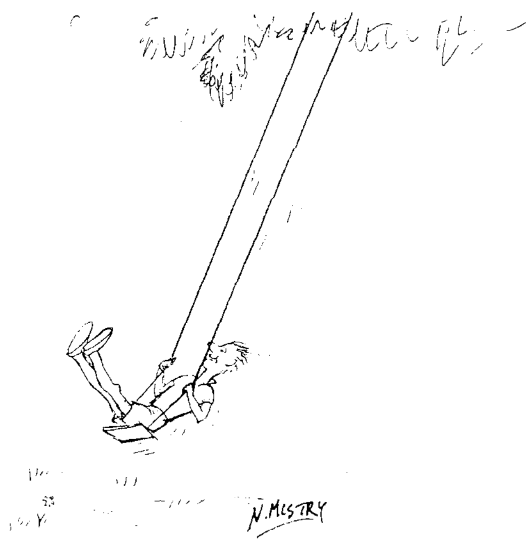

Figure 14: A parametric oscillator illustrated by Nari Mistry. Modulation of the restoring force allows this kid to reach large amplitudes.

Table 2: Beam-Beam Rules and Ideas

RULE	Ref.	EXPLANATION
$\beta_v, \beta_h > \sigma_L$	31	The betatron phase advance on successive turns is modulated by synchrotron oscillations. Recent work suggests that this rule may not be as stringent as once thought.[32]
$\eta_{IP} = 0$	31	The dispersion, η_{IP}, measures the energy dependence of the horizontal position at the IP. If $\eta_{IP} \neq 0$, the horiz. position is energy dependent; this modulates the beam-beam deflection at Q_s.
Head-on collisions	33	With non-zero crossing angle the beam-beam deflection is modulated by synchrotron oscillations.
IDEA	**Ref.**	**EXPLANATION**
Round beams	34	The modulation of the vertical deflection by horizontal betatron oscillations is removed.[35]
Crab crossing	36	Tilting the beam removes the modulation introduced by non-zero crossing angle.

The years of experience with e^+e^- storage rings have led to some empirical *rules* for getting large tune spreads. Most of these rules are ways to avoid parametric resonances. Table 2 gives the rules, brief statements about the physics, and the original references. Understanding the physics of the empirical rules leads to ideas about new modes of operation that have attractive features such as higher tune spreads. Two such ideas are included in Table 2. Crab crossing and head-on collisions are related closely, and they are discussed as an example.

Figure 15 shows two bunches colliding at an angle. Particle #1 at the head of its bunch passes through the head of the oncoming bunch while particle #2 passes through the center and particle #3 passes through the tail. Particle #2 is deflected more than #1 and #3 because the charge density of the opposing bunch is greater at the center than at the head or tail. One-quarter of a synchrotron oscillation period later the situation is different (Figure 16). Particles #1 and #3 are in the center of the bunch, and #2 is at the tail. Therefore, #1 and #3 experience larger deflections than #2. The beam-beam deflection is modulated by synchrotron oscillations, and collisions must be head-on to avoid this modulation. The beams in DORIS I crossed at an angle, and DORIS I had a low maximum tune spread.[33] That experience led to the rule that collisions must be head-on.

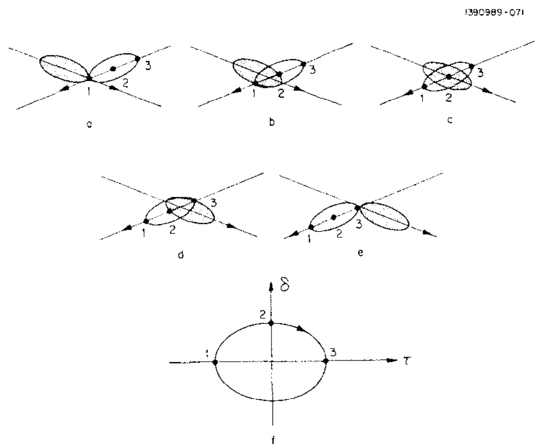

Figure 15: Two bunches colliding at an angle; particles 1, 2, & 3 are part of the unshaded bunch. Figures a) through e) show the passage of time during the collision, and f) shows the particles' positions in longitudinal phase space.

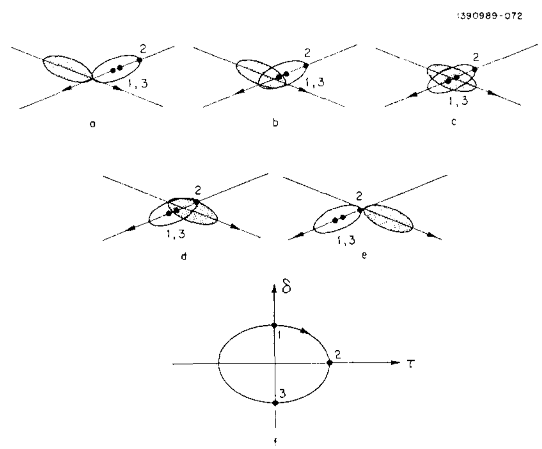

Figure 16: A collision one-quarter of a synchrotron oscillation period later.

Crossing at an angle could be attractive for heavy quark factories; complicated separators would be unnecessary, and high collision frequencies would be possible. Crab crossing is an idea for solving background problems in linear colliders[37] that has been adapted to storage rings to permit crossing at an angle.[36] It is illustrated in Figure 17. The bunches cross at an angle, but they are tilted with respect to their directions of propagation. Each of the three particles pass through the head, center, and tail of the opposing bunch, and they have the same beam-beam deflection. The source of the modulation is removed, and a crossing angle and large maximum ξ are possible at the same time! The cost is that RF cavities with deflecting fields are needed at each side of the IP to tilt the bunches before and remove the tilt after the collision.

4.3 Discussion

Heavy quark factories must be designed to get a large beam-beam tune spread. That simplifies many of the intensity dependent effects by lowering the total current, reducing the synchrotron radiation power, reducing the HOM heating, and relaxing the limit on $<Z_L/n>$. These could be crucial. Alternatively, an increase in ξ could mean a welcomed higher luminosity. Non-linearities and other effects that limit the tune spread must be understood. Work on the beam-beam interaction is not as advanced as that on intensity dependent effects, and history has shown the beam-beam interaction to be a *NOTORIOUSLY* difficult subject in which to make progress. The picture presented in the last section is one that I think summarizes the experience with e^+e^- storage rings, and that is another reason for my optimistic answer to the central question in the introduction.

However, it must be made clear that my opinion is not universally accepted, and the beam-beam interaction must be studied actively. A powerful combination for doing that has been developed. That combination is:

1) Theoretical work that has shown the importance of modulation effects in the beam-beam interaction by considering simplified situations.

2) Computer simulations and large computers for modelling the beam-beam interaction. These simulations have a mixed record of predicting performance,[38] but they are being improved by comparison with operating colliders.

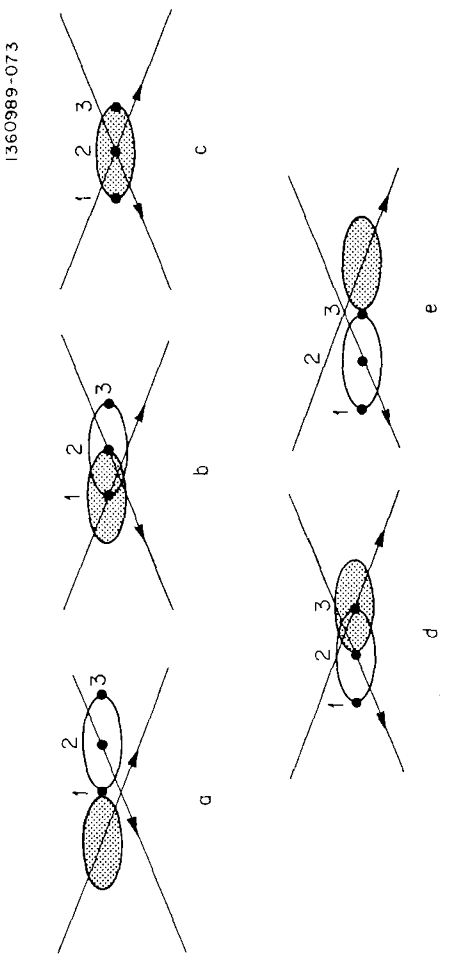

Figure 17: A collision with "crab-crossing" where the bunches have been tilted with respect to their directions of propagation.

3) Storage rings that can be used for beam-beam experiments. These are central for improving theories and simulations, and can be used for testing ideas. Experiments related to the ideas in Table 2 are under consideration. A first test of round beams will be made at CESR this fall,[39] and a crab crossing experiment is possible at PEP.[40]

This combination was not available ten years ago, but it is now! The work showing the importance of modulation was done during that time; there have been enormous increases in computer power, and storage rings that allow beam-beam experiments with parameters close to those of heavy quark factories are available. Given the motivation from Tau-Charm and B-Factories and our present insights and resources there can be progress in understanding the beam-beam interaction and increasing the beam-beam limit.

5. CONCLUDING REMARK

Is the accelerator physics sufficiently well understood that two orders of magnitude in luminosity (up to $10^{34}cm^{-2}s^{-1}$) **is conceivable?** There are good reasons to conclude that it is because of the progress during the last decade. Wakefields and their effects can be calculated, and there is new technology with important implications for wakefield reduction. A picture synthesizing beam-beam experience has emerged. It needs to be tested further, and if those tests are successful, we understand the beam dynamics that are key to a cost effective design of a heavy quark factory. This design is at the leading edge of accelerator physics and technology, and it offers challenging accelerator research, design and construction problems.

Moreover, heavy quark factories will be important instruments for particle physics research. The accelerator physics challenge coupled with the particle physics payoff make this an exciting area of physics.

This work was supported in part by the National Science Foundation.

APPENDIX A: DEFINITION OF SYMBOLS

VARIABLES*

Luminosity	L	Particles/bunch	N
Collision frequency	f_c	Beam energy/mc^2	γ
Center-of-mass energy	W	Betatron tunes	Q_β, Q_h, Q_v
Synchrotron tune	Q_s	Beam-beam tune spread	ξ_h, ξ_v
Transverse beam sizes	σ_h, σ_v	Beam size ratio	$R_\sigma = \sigma_v/\sigma_h$
Collision point β's	β_h, β_v	Emittances	$\varepsilon_h, \varepsilon_v$
Bunch length	σ_L	Energy loss per turn	U_0
Damping decrement	$\Delta = U_0/\gamma mc^2$	Momentum compaction	α
Number of bunches	B	Fractional energy spread	σ_δ
Longitudinal impedance	$<Z_L/n>$	Transverse impedance	$<Z_T>$
Average radius	$R = \text{Circum}/2\pi$	Bending radius	ρ
Vacuum chamber radius	b	Average β function	β_{avg}
Damping Partition numbers	J	Dispersion	η
Total current/ring	$I_t = Nf_c e$	Synch. radiation power	P_{sr}
Peak current	I_p	RF frequency	f_{rf}
Peak RF voltage	V_{pk}	HOM loss factor	k
HOM power	P_{hom}		

CONSTANTS

Electron classical radius	$r_e = 2.82\times10^{-15}$ m	Free space impedance	$Z_0 = 377\ \Omega$
Speed of light	$c = 3.00\times10^8$ m/sec	Electron charge	$e = 1.6\times10^{-19}$ C

* h and v denote horizontal and vertical, respectively.

REFERENCES

1. M. Perl, SLAC-PUB-4971 (SLAC, 1989).

2. G. J. Feldman et al, SLAC-PUB-4838 (SLAC, Jan. 1989); to be published in the proceedings of the 1988 Snowmass Workshop.

3. D. L. Rubin et al, to be published in the proceedings of the 1989 IEEE Particle Accelerator Conference.

4. LEP Design Report, CERN-LEP/84-01 (CERN, 1984).

5. J. Jowett, private communication.

6. J. M. Jowett, CERN/LEP-TH/88-22 (CERN, 1988).

7. K. W. Robinson & G. A. Voss, CEAL-TM-149 (Cambridge Electron Accelerator, 1965).

8. H. Goldstein, Classical Mechanics, (Reading, MA: Addison-Wesley, 1959).

9. The usual review for electron rings is:
M. Sands, The Physics of Electron Storage Rings, An Introduction, SLAC-121 (SLAC, 1970).
Aspects of single particle motion are treated in many articles in the Accelerator Summer School Proceedings:
R. A. Carrigan, F. R. Huson, M. Month, ed, AIP Conf. Proceed. **87**, (1982).
M. Month, ed, AIP Conf. Proceed. **105**, (1983).
M. Month, P. F. Dahl, M. Dienes, ed, AIP Conf. Proceed. **127**, (1985).
M. Month, M. Dienes, ed, AIP Conf. Proceed. **153**, (1987).
M. Month, M. Dienes, ed, AIP Conf. Proceed. **184**, (1989).

10. E. D. Courant & H. S. Snyder, Annals of Physics **3**, 1.

11. T. Weiland, CERN/ISR-TH/80-07 (CERN, 1980).

12. For a more general expression see R. H. Siemann, AIP Conf. Proceed. **127**, 368 (1985).

13. M. Billing, private communication.

14. R. Littauer, CON 89-7 (Cornell, 1989).

15. J. Haissinski, Nuovo Cimento **18B** 72 (1973).

16. P. B. Wilson, R. Servranckx, A. P. Sabersky, J. Gareyte, G. E. Fischer, A. W. Chao & M. H. R. Donald, IEEE Trans. Nucl. Sci. **NS-24**, 1211 (1977).

17. R. Siemann, Nucl. Inst. and Methods **203**, 57(1982).

18. D. G. Cassel, N. B. Mistry, J. A. Mueller & N. Katayama, CLNS 89-880 (Cornell, 1989); to be published in the proceedings of the 1988 Snowmass Workshop.

19. M. S. Zisman, S. Chattopadhyay & J. J. Bisognano, LBL-21270 (LBL, 1986).

20. J. Bisognano, private communication.

21. P. B. Wilson, AIP Conf. Proceed. **87**, 450 (1982).

22. H. Padamsee, Proceed. of 1987 IEEE Part. Accel. Conf., 1691 (1987).

23. Two reviews written for different audiences are:
A. Chao, AIP Conf. Proceed. **105**,353 (1983).
J. L. Laclare, Proceed. of 11th Inter. Conf. on High-Energy Accel., 526 (1980).

24. K. L. F. Bane & R. D. Ruth, SLAC-PUB-4905 (SLAC, 1989).

25. J. J. Bisognano, CEBAF-PR-88-006 (CEBAF, 1988).

26. SUPERFISH described in K. Halbach & R. F. Holsinger, Part. Accel. **7**, 213 (1976).

27. T. Weiland, IEEE Trans. Nucl. Sci. **NS-32**, 2738 (1985).

28. A. Chao, AIP Conf. Proceed. **127**, 201 (1985).

29. J. Seeman, Nonlinear Dynamics Aspects of Particle Accelerators (Berlin: Springer-Verlag, 1986, edited by J. M. Jowett, S. Turner & M. Month), p. 121.

30. S. Milton, Ph. D. Thesis (Cornell, 1990).

31. F. M. Izrailev & I. B. Vasserman, 7th All Union Conf. on Charged Part. Accel., 288 (1981).

32. D. Rice, CLNS 89/943 (Cornell, 1989).
S. Krishnagopal & R. Siemann, CLNS 89/936 (Cornell, 1989).

33. A. Piwinski, IEEE Trans. Nucl. Sci. **NS-24**, 1408 (1977).

34. S. Krishnagopal & R. Siemann, CBN 89-3 (Cornell, 1989).

35. S. Peggs & R. Talman, Phys. Rev. **D24**, 2379 (1983).

36. K. Oide & K. Yokoya, SLAC-PUB-4832 (SLAC, 1989).

37. R. B. Palmer, SLAC-PUB-4707 (SLAC, 1988).

38. R. H. Siemann, CBN 89-4 (Cornell, 1989).

39. P. Bagley, S. Krishnagopal, D. Rubin, R. Siemann, & J. Welch, CON 89-4 (Cornell, 1989).

40. K. Oide & G.-A. Voss, AAS Note-46 (SLAC, 1989).

PROSPECTS FOR NEXT-GENERATION e^+e^- LINEAR COLLIDERS*

RONALD D. RUTH

Stanford Linear Accelerator Center
Stanford University, Stanford, California 94309

1. INTRODUCTION

The purpose of this paper is to review progress in the U.S. towards a next generation linear collider. During 1988, there were three workshops held on linear colliders: 1.) "Physics of Linear Colliders," in Capri, Italy, June 14-18, 1988; 2.) Snowmass 88 (Linear Collider subsection) June 27-July 15, 1988; and 3.) SLAC International Workshop on Next Generation Linear Colliders, Nov. 28-Dec. 9, 1988. To obtain detailed current information, the reader is directed to Refs. 1-3 which are the proceedings of each of the workshops. In addition, the Snowmass proceedings for the linear collider working group are collected in Ref. 4. This paper will concentrate on U.S. efforts and will draw heavily from Refs. 3 and 4.

There is also much work ongoing in other parts of the world. The Soviet Union is planning a linear collider at Serpukov which is being designed at INP in Novosibirsk. CERN is working on CLIC (CERN Linear Collider). Finally, KEK is actively engaged in linear collider research towards a JLC (Japanese Linear Collider). Much of this work is covered in Refs. 1 and 3.

In this paper, I focus on reviewing the issues and progress on a next generation linear collider with the general parameters shown in Table 1. The energy range is dictated by physics with a mass reach well beyond LEP, although somewhat short of SSC. The luminosity is that required to obtain $10^3 - 10^4$ units of R_0 per year. The length is consistent with a site on Stanford land with collisions occurring on the SLAC site; the power was determined by economic considerations. Finally,

* Work supported by the Department of Energy, contract DE-AC03-76SF00515.

the technology was limited by the desire to have a next generation linear collider by the next century.

Table 1. General parameters.

Energy	0.5 – 1.0 TeV in center-of-mass.
Luminosity	$10^{33} - 10^{34}$ cm^{-2} sec^{-1},
Length	Each Linac $\lesssim$ 3 Km.
Power	$\lesssim$ 100 MW per Linac.
Technology	Must be realizable by 1990–92.

The basic configuration of such a linear collider is shown in Fig. 1. The beam is accelerated by an injector linac and then injected into a damping ring which damps the emittance of the beam and provides the beam with appropriate intensity and repetition rate. After extraction, the bunch must be compressed in length twice in order to achieve the short bunches suitable for the linac and final focus. The linac is used to accelerate the beams to high energy while maintaining the emittance. Finally, the final focus is used to focus the beams to a small spot for collision. This must yield a luminosity with tolerable beam-beam effects (disruption and beamstrahlung) and must also provide a reasonably background-free environment for the detector.

Before proceeding to a detailed discussion of the linear collider subsystem by subsystem, it is useful to discuss generally the overall results of the past few year's activities. Perhaps one of the most important developments is the increased interest in an Intermediate Linear Collider (ILC) with an energy of 0.5 TeV in the center-of-mass. This is a factor of two below the TeV Linear Collider (TLC) and thus would require a factor of four less peak power provided that the machines were the same length. From Fig. 1 an ILC could be upgradable in energy either by the addition of power sources or by increasing the linac length. The trombone shape lends itself well to increases in length.

If we begin the discussion of an ILC or TLC at the lower energy end, the damping ring and bunch compressor designs seem relatively straightforward with,

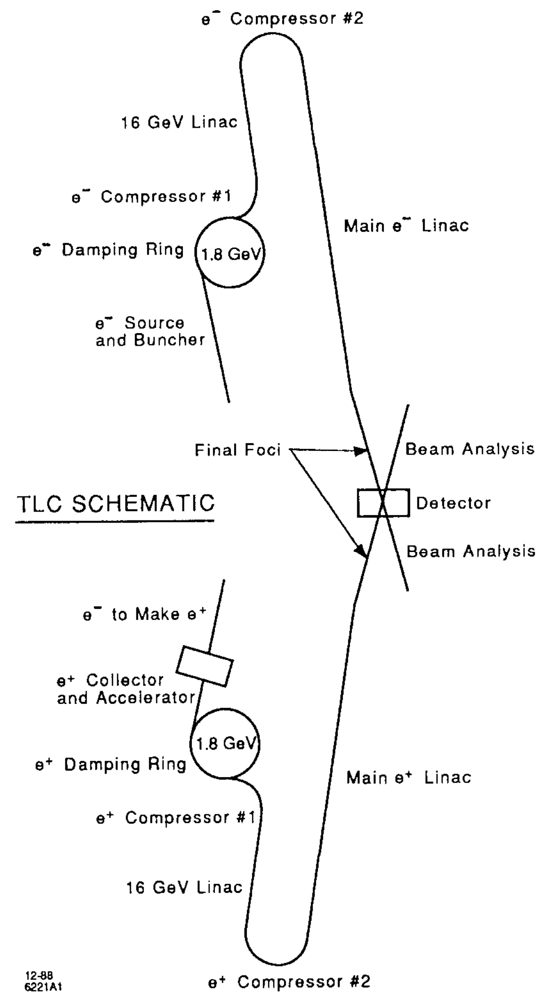

Fig. 1. Schematic layout of an ILC or TLC. The angles shown are exaggerated.

however, somewhat tighter tolerances than usual. The main linac will probably have a structure similar to SLAC, except at four times the frequency. The structure will be modified with holes coupled to waveguides in order to damp the transverse and longitudinal higher-order modes. This makes possible the use of multiple bunches per RF fill, which increases the luminosity by a factor of 10 for "free."

There is no definite power source as yet. The recent demonstration of binary pulse compression at SLAC has focused attention on more conventional approaches to long-pulse power production. A high-power klystron is under construction at SLAC to feed the RF pulse compressor, and there are many new ideas for power sources which would drive RF pulse compressors.

Once the power source problem is solved, we are still left with the luminosity problem. These two aspects are only partially decoupled due to the use of many bunches (a batch) per RF fill. To obtain the luminosity, we must preserve the emittance of the beam throughout the linac. The final focus demagnifies the beam to obtain a very flat beam at the final focus. The chromatic correction for this is quite delicate, and tolerances are tight. Finally, we must measure the beam size at the interaction point in order to tune the final focus. Many of these problems can be addressed via a model final focus at a lower energy. Towards this end, a Final Focus Test Beam is being constructed at SLAC by an international collaboration of SLAC, INP, KEK, and Orsay.

During the SLAC Workshop in December 1988 following Snowmass, there was one important discovery which should be emphasized here. Beamstrahlung photons create e^+e^- pairs upon interacting with the opposing bunch. One particle of the pair is deflected strongly by the field of the bunch. This, in turn, can cause serious background problems. This will be discussed more thoroughly in the later sections of this paper.

In the next sections, I first discuss parameters briefly and then discuss damping rings. The basic principles of bunch compression are treated in the next section. In the section on the linac, there are three subsections. First I discuss RF structures and power sources, and then I move to a discussion of emittance preservation in the linac. This is followed by a discussion of the final focus and beam-beam effects. Finally, I introduce some of the issues for multibunch effects.

2. PARAMETERS

The parameters for a next-generation linear collider are far from being fixed. However, initial studies have yielded global parameters in the neighborhood of those presented in Table 2.[5] The parameters shown are for an ILC with 0.5 TeV in the CM. To upgrade to a TLC with 1.0 TeV in the CM one can either increase the RF power by a factor of 4 or increase the length by a factor of 2. With the higher energy beams, the spot sizes will decrease, and the beamstrahlung energy loss increases to the level $\sim 20\%$.

The interaction point geometry is given with two options: no crab crossing means that the crossing angle is within the diagonal angle of the bunch, crab crossing allows a larger angle by giving the beams a time varying transverse kick which causes the beams to overlap almost completely when they cross.

In the next several sections we discuss many of the issues which are input into the design of a linear collider such as that presented in Table 2.

3. DAMPING RINGS

In Refs. 6 and 7, T. Raubenheimer *et al.* discuss many of the basic design considerations for the damping ring. The basic parameters are shown in Table 3 where they are compared to those of the SLC. The key differences are the decrease of the horizontal emittance by an order of magnitude, the increase of the repetition rate, and the requirement of $\epsilon_x/\epsilon_y = 100$. Although asymmetrical emittances have been measured in the SLC damping ring, they are not required for SLC operation.

The desired repetition rate is obtained by having many batches of bunches in the ring. Each batch of 10 bunches is extracted on one kicker pulse and accelerated on one RF fill in the linac. The remaining batches are left in the ring to continue damping while an additional batch is injected to replace the extracted

Table 2. Parameters for an ILC.

		ILC
General		
CM energy	TeV	.5
luminosity 10^{33}	cm^{-2} sec^{-1}	3.9
RF frequency	GHz	11.4
repetition rate	Hz	360
accel gradient	MV/m	93
number bunches		10
particles/bunch (at IP)	10^{10}	1.6
length	Km	7.2
Damping Ring		
emittance ϵ_x/ϵ_y		100
emittance $\gamma\epsilon_x$	μm	3.5
emittance $\gamma\epsilon_z$	m	.04
bunch spacing	m	.21
Linac RF		
loading η	%	2.5
iris radius a	mm	4.6
section length	m	1.5
v_g/c		0.06
pulse length	ns	82
peak power/length	MW/m	194
Final focus		
β_y^*	mm	.08
crossing angle (no crab)	mrad	4.8
crab crossing angle	mrad	30–100
free length	m	.52
Intersection		
σ_y	nm	3.1
σ_x/σ_y		180
σ_z	μm	70
disruption D_y		10
lum enhance H		1.5
beamstrahlung δ	%	6

one. The threshold current refers to the threshold for the "microwave instability" or "turbulent bunch lengthening."

The basic layout of a possible damping ring is shown in Fig. 2. Notice that there are several insertions which contain wigglers. In order to obtain the high repetition rate, it is necessary to decrease the damping time by the addition of wigglers in straight sections.

Table 3. Basic parameters of the SLC and TLC damping rings.

	TLC	SLC
Energy	$1 \sim 2$ GeV	1.15 Gev
Emittance, $\gamma\epsilon_x$	3.0 μmrad	36 μmrad
Emittance, $\gamma\epsilon_y$	30 nmrad	500 nmrad
Repetition rate	360 Hz	180 Hz
Bunch length	4 mm	5 mm[8]
Threshold Current	batches of 10 bunches of 2×10^{10}	1.5×10^{10}[8]

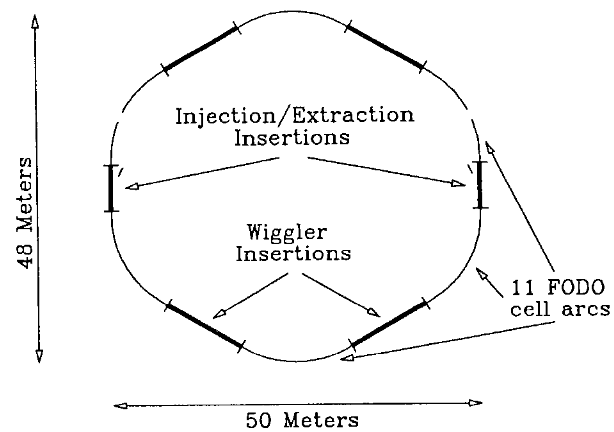

Fig. 2. Schematic of the TLC damping ring

In Tables 4 and 5, you see the basic parameters for the ring. The lattice is combined function which allows the partition of the damping times to trade horizontal damping time for longitudinal. The RF frequency for this example is necessarily 1.4 GHz since the bunch spacing in this example is about 20 cm. The threshold impedance $(Z/n)_t$ is that for the microwave instability. It is quite small due to the small momentum compaction factor, but is only about a factor of three below that obtained in the SLC damping rings.[8]

Table 4. TLC damping ring parameters.

Energy	$E_0 = 1.8$ GeV
Length	$L = 155.1$ meters
Momentum compaction	$\alpha = 0.00120$
Tunes	$\nu_x = 24.37, \quad \nu_y = 11.27$
RF frequency	$f_{RF} = 1.4$ GHz
Current	10 batches of 10 bunches of $2 \times 10^{10} e^+/e^-$

Table 5. TLC damping ring parameters.

	Wigglers Off	Wigglers On
Natural $\gamma\epsilon_x$	2.46 μmrad	2.00 μmrad
$\gamma\epsilon_x$ w/ intrabeam	3.33 μmrad	2.74 μmrad
Damping, τ_x	3.88 ms	2.50 ms
Damping, τ_y	9.19 ms	3.98 ms
Rep. rate, f_{rep}	155 Hz	360 Hz
Damp. partition, J_x	2.37	1.59
Energy spread, σ_ϵ	0.00128	0.00104
Radiation/turn, U_0	203 KeV	468 KeV
Bunch length, σ_z	5.6 mm	5.2 mm
Synch. tune, ν_s	0.0068	0.0058
$(Z/n)_t$	$\mathcal{F} \times 0.32\Omega$	$\mathcal{F} \times 0.20\Omega$
Natural chrom., ξ_x	-28.35	-28.07
Natural chrom., ξ_y	-25.10	-22.27

Another key aspect of the design is the small vertical emittance. The design calls for an emittance ratio $\epsilon_x/\epsilon_y = 100$. This size emittance ratio is quite common in $e^\pm$ storage rings. However, the tolerances for obtaining a small vertical beam size are proportional to the absolute size. In Ref. 6 , those tolerances which are related to maintaining the emittance ratio are calculated. The tolerances presented in Sec. 5 of Ref. 6 are in the 100 μm range and could be improved by adding correction skew quadrupoles in the ring.

4. BUNCH COMPRESSION AND PRE-ACCELERATION

In order to obtain the very short bunches necessary for the linac, it is necessary to perform at least two bunch compressions after the damping ring. Designs for bunch compression are presented in Refs. 9 and 10. A bunch length of about 50 μm in the linac puts a constraint on the longitudinal emittance of the damping ring. In addition, during the bunch compressions, it is necessary to keep the energy spread small to avoid the dilution of the transverse emittance. If we assume that we can transport 1% energy spread without diluting either transverse emittance, then at least two bunch compressions are needed. For example, if we consider a 1.8 GeV damping ring with energy spread $\Delta E/E = 10^{-3}$ and a bunch length of 5 mm, the two compressions are shown in Table 6. The first one decreases the bunch length by an order of magnitude. This is followed by a pre-acceleration section to decrease the relative energy spread in the beam by about an order of magnitude. One must avoid an increase of energy spread due to the cosine of the RF wave (and also due to beam loading). If this pre-acceleration is done at the present SLAC frequency and if the bunch current is as shown in Table 2, then the additional energy spread induced is about 5×10^{-4}. Neglecting this small increase, the next bunch compression happens around 18 GeV and serves to reduce the bunch length to about 50 μm. This is suitable for injection into the high frequency, high gradient structure.

Table 6. Bunch compression.

E	$\Delta E/E$	σ_z	Compress $\rightarrow$	$\Delta E/E$	σ_z
1.8 GeV	10^{-3}	5 mm	Compress $\rightarrow$	10^{-2}	0.5 mm
[pre-acceleration at long wavelength, $\lambda = 10.5$ cm]					
18 GeV	10^{-3}	0.5 mm	Compress $\rightarrow$	10^{-2}	50 μm

The two designs shown in Ref. 9 are for bunch compressors which have small bending angles. Reference 10 presents several designs in which the bend angle for the final compressor is 180° as shown in Fig. 1. This low energy bend allows easy upgrades in energy, and also makes it possible to do direct feedback to compensate jitter from the damping ring kicker magnet.

5. LINAC

The linac is envisioned to be similar to the SLAC disk-loaded structure with a frequency of four times the present SLAC frequency. The irises in the design are relatively larger to reduce transverse wakefields. The structure may have other modifications to damp long-range transverse wakefields. This would be driven by a power source capable of about 900 MW/m for a 200 MeV/m TLC or about 220 MW/m in the case of a 100 MeV/m ILC.

The remainder of this section is divided into three subsections. In the first subsection we discuss structures, the second deals with RF power sources, and finally the third treats emittance preservation in the linac.

5.1 STRUCTURES

Since the gradients being considered range from 100 MV/m to 200 MV/m, the first question that arises is RF breakdown. This question is treated in Refs. 11 and 12. In this paper G. Loew and J. Wang present results from many experiments at various frequencies. If the scaling laws thus obtained are extrapolated to 11.4 and 17.1 GHz, the breakdown limited surface fields obtained are 660 and 807 MV/m, respectively. To convert this to effective accelerating gradient, a reduction factor of 2.5 is typically used. In both cases, the accelerating gradient is above 200 MeV/m. However, the measurements also indicated significant "dark currents" generated by captured field-emitted electrons. The question of the effects of dark current on loading and beam dynamics is not yet resolved and needs further study.

As mentioned in the Introduction, in order to make efficient use of the RF power and to achieve high luminosity, it seems essential to accelerate a train of bunches with each fill of the RF structure. This leads to two problems: (1) the energy of the bunches in the train must be controlled and (2) the transverse stability of the bunch train must be ensured. Both of these problems are helped greatly by damping higher modes (both transverse and longitudinal) in the RF structure. In Ref. 13, R. Palmer describes a technique of using slotted irises coupled to radial waveguides to damp these modes: Q's as low as 10–20 have been measured in model structures. This encouraging evidence has led to a development program at SLAC and KEK to do more detailed studies of slotted structures. The beam dynamics consequences of damping the higher modes is explored in the section on Multibunch Effects.

5.2 RF POWER SOURCES

Before discussing results on power sources, it is useful to contrast and compare two basic approaches, RF pulse compression and magnetic pulse compression.

5.2.1 *RF Pulse Compression and Conventional Klystrons*

In Fig. 3(a), you see illustrated the basic principle of RF pulse compression. A long modulator pulse is converted by a high-power, 'semi-conventional' klystron or some other power source into RF power with the same pulse width. This RF pulse is then compressed by cleverly slicing the pulse using phase shifts and 3 db hybrids and re-routing the portions through delay lines so that they add up at the end to a high peak power but for a small pulse width. This scheme was invented by D. Farkas at SLAC and is presently under experimental investigation.[14] With a factor of 8 in pulse compression, a 100 MW klystron could power about 3 m of structure to achieve 100 MV/m.

In Ref. 15, P. Wilson describes RF pulse compression in some detail including estimates of efficiencies. An experimental test at SLAC of a low-loss, low-power system has been completed which yielded a factor of 3.2 power gain.[16] A 100 MW, 11.4 GHz "conventional" klystron, which has just been completed at SLAC, will be used to perform high-power tests of a pulse compression system designed to yield a power gain of 6.

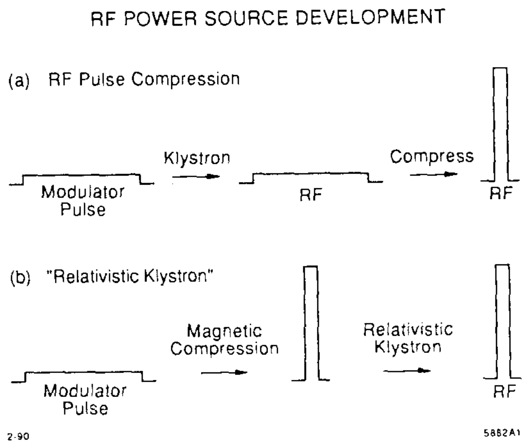

Fig. 3a. Illustration of RF pulse compression. 3b. Illustration of the relativistic klystron with magnetic compression.

5.2.2 *Magnetic Pulse Compression and the Relativistic Klystron*

In Fig. 3(b), you see the principle of magnetic pulse compression and the relativistic klystron illustrated. In this case, the pulse compression happens *before* the creation of RF. This technique makes use of the pulsed power work done at LLNL in which magnetic compressors are used to drive induction linacs to produce multi-MeV e^- beams with kiloampere currents for pulses of about 50 nsec. These e^- beams contain gigawatts of power. The object, then, is to bunch the beam at the RF frequency and then to extract a significant fraction of this power. This can be done either by velocity modulation or by dispersive magnetic "chicanes." After bunching, the beam is passed by an RF extraction cavity which extracts RF power from the beam.

Experiments on the relativistic klystron are described in Ref. 17. The best power output achieved to date is 330 MW. Although higher acceleration gradients have been achieved, the best break-down free acceleration gradient in this experiment is 84 MV/m with 80 MW of RF power input into a 30 cm long accelerator structure.

5.2.3 *Other RF Sources*

It is also possible to consider other sources driven by magnetic pulse compressors which directly produce short, high-power RF pulses. One example is a cross-field amplifier (CFA). This device has the geometry of a magnitron but is configured as an amplifier rather than an oscillator. SLAC is presently completing the construction of a 100 MW CFA which will be tested in early 1990. This device could also produce long RF pulses for RF pulse compression. Although it is a large extrapolation from existing sources, it holds the promise of being much cheaper than an equivalent power klystron.

Another interesting possible RF source is the cluster klystron. In Ref. 18, R. Palmer and R. Miller describe a multiple beam array of "klystrinos" which when coupled together can give impressive results. By dividing a single beam into many beams shielded from each other, the problems of space charge are effectively eliminated. This source could be used as a driver for RF pulse compression. Alternatively, with the addition of a grid and an oil-filled transmission line for energy storage, the device could directly produce short RF pulses. Thus far, there has been no experimentation; but calculations and cost estimates are encouraging.

Rather than separating the beam into separate beams, it is also possible to consider ribbon beam geometries. One possibility, the Gigatron, is presented in Ref. 19. This device makes use of the lasertron concept to produce a bunched beam directly at the cathode. Field emitting arrays are used for the cathode while a ribbon beam geometry is envisioned to control space charge effects. This device is another candidate for RF pulse compression and has an impressive efficiency on paper. Experimental tests are presently being prepared.

To conclude this section, it seems that if high-power tests of RF pulse compression show positive results, there are several candidates to provide the long pulse input RF. Such an RF source combined with RF pulse compression would be a possible power source for an ILC or TLC which could be realized in the near future.

5.3 Emittance Preservation

During the process of acceleration, we must take care not to dilute the emittance of the beam. There are several effects which can lead to emittance dilution. In the next few subsections, we discuss a few of the most important effects.

5.3.1 Chromatic Effects

The filamentation of the central trajectory in a linac can cause dilution of the effective emittance of the beam. If we first consider a coherent betatron oscillation down the linac, then to be absolutely safe, we must require that it be small compared to the beam size. If the spread in betatron phase advance is not too large, then this tolerance is increased to perhaps twice the beam size for the case shown in Table 2.

The chromatic effect of a corrected trajectory is rather different. In this case, it is the distance between an error and a corrector which matters, and the effects partially cancel yielding a growth $\propto \sqrt{N_{quad}}$. This yields a tolerance on magnet misalignment the order of 20 to 30 times the beam size in the linac (about 20 μm) for the case in Table 2. This is also the tolerance on BPM measurements. If the phase advance of the linac or some subsection is not too large, then this yields a linear correlation of position with momentum (dispersion) which can, in principle, be corrected since it does not vary in time. Therefore, it may be possible to have looser tolerances if such correction is provided.

5.3.2 Transverse Wakefields and BNS Damping

The wakefield left by the head of a bunch of particles, if it is offset in the structure, deflects the tail. If the transverse oscillations of the head and tail have the same wave number, the tail is driven on resonance. This leads to growth of the tail of the bunch.[20] This effect can be controlled by a technique called BNS damping.[21] The bunch is given a head-to-tail energy correlation so that the tail is at lower energy. The offset of the head by an amount $\hat{x}$ induces a deflecting force on the tail away from the axis. The tail, however, feels an additional force $\Delta K \hat{x}$, where ΔK is the difference in focusing strength. These two forces can be arranged to cancel, thereby keeping the coherence of the bunch as a whole. For the designs shown in Table 2, the spread in energy for BNS damping is much less than 1%. This correlation can be accomplished by moving the bunch slightly on the RF wave to obtain a linear variation across the bunch.

Recently, BNS damping has been tested at the SLC with great success.[22] It is now part of normal operating procedure.

5.3.3 Jitter

In order to maintain collisions at the interaction point, the bunch must not move very much from pulse to pulse. Since the optics of the final focus also demagnify this jitter, the tolerance is always set by the local beam divergence compared to the variation of some angular kick. The jitter tolerance on the damping ring kicker is thus related to the divergence of the beam at that point. This is discussed in Ref. 6. At the injection point to the linac, the offset caused by this jitter must be small compared to the local beam size.

If all the quadrupoles in the linac are vibrating in a random way, the effects accumulate down the linac and the orbit offset grows $\propto \sqrt{N_{quad}}$. This sets the tolerance on the random motion of quadrupoles to be much smaller than the beam size. In the examples in Table 2, the random jitter tolerances are $\simeq 0.01$ μm. On the other hand, tolerances for correlated effects are an order of magnitude less severe. In either case, this size motion from pulse-to-pulse is unlikely due to the large repetition rate of the collider. More gradual motion, which is larger, can be corrected with feedback.

Jitter in RF kicks can cause similar effects. These effects can be reduced by reducing the DC component of the RF kick by eliminating asymmetries in couplers and by careful alignment of structures.

5.3.4 *Coupling*

Finally, we discuss coupling of the horizontal and vertical emittance. The beam size ratio in the linac is 10:1. The tolerance on random rotations for a flat beam is given by

$$\Theta_{rms} << \frac{\sigma_y}{\sigma_x} \frac{1}{\sqrt{2N_q}} \quad .$$

For the example shown in Table 2, the right-hand side is about 3 mrad; this is straightforward to achieve. If the errors are not random, larger rotations can indeed result; however, because the beam size is so small, the effects are very linear. This means that skew quadrupoles can be used effectively as correction elements. Certainly, in the final focus, skew quads will be an integral part of the tuning procedure to obtain flat beams.

6. FINAL FOCUS

The final focus, as described in the parameters in Table 2, is a flat beam final focus with a crossing angle. The purpose of the flat beam is to increase the luminosity while controlling beamstrahlung and disruption. The crossing angle is to allow different size apertures for the incoming and outgoing beam. Another invention, "crab-wise crossing," discussed in Ref. 5, allows a much larger crossing angle than the diagonal angle of the bunch. As discussed in Ref. 5 and in Ref. 23, this type of geometry may now be essential due to the production of e^+e^- pairs by beamstrahlung photons in the field of the bunches.

6.1 Final Focus Optics and Tolerances

The first job in the final focus is to demagnify the beam to provide a small spot for collision. The design for such a system is presented in Ref. 24 by K. Oide. This is a flat beam final focus which achieves the parameters shown in Table 2 for vertical and horizontal beam size. The vertical size is limited by a fundamental constraint "the Oide limit" due to the synchrotron radiation in the final doublet coupled to the chromatic effect of a quadrupole. The quadrupole gradients necessary are very high and in Oide's design are obtained by conventional iron magnets with 1 mm pole-to-pole distance. Tolerances are very tight in such a final focus. The most restrictive vibration tolerance is on the final doublet which must be stable pulse-to-pulse to about 1 nm.

Since vibration of the final doublet is the most serious problem, it is considered in some detail in Ref. 25. In this paper, it is shown that passive vibration isolation seems to be more than adequate to handle the vibrations above 10 Hz at the high frequency end. For low frequencies, an interferometric feedback system can be used to control motion to about 1 μm. Beam steering feedback can then be used to control slow variations in the 1 nm to 1 μm region.

6.2 Beam-Beam Effects

When a small bunch of electrons collides with a small bunch of positrons, the fields of one bunch focus the other causing disruption. Since the opposing particles are strongly bent, they also emit radiation called beamstrahlung. These are the two basic beam-beam effects. The disruption enhances the luminosity by a small amount while the beamstrahlung causes significant energy loss during collision and increases the effective momentum spread for physics. These issues are discussed in more detail in Ref. 23.

In addition, there are several other important effects which should be mentioned here. If the beams are offset relative to each other, a kink instability develops. This effect actually causes the luminosity to be less sensitive to offsets because the beams attract each other and collide anyway when the disruption is not too severe. There is also a multibunch kink instability which is more serious since it can cause the trailing bunches to miss each other entirely. This places restrictions on the product of the vertical and horizontal disruption per bunch.

The final section of Ref. 23 is an addendum added after the SLAC Workshop in Dec. 1988. As mentioned earlier in the Introduction, it was discovered that the beamstrahlung photons pair-produce in the coherent field of the bunch.[26–29] The corresponding incoherent process has been known for some time, but its importance has only just been realized.[30] The problem is that low energy e^+e^- pairs are produced in an extremely strong field which then deflects the charge of the appropriate sign while confining the other. This leads to large angular kicks, as mentioned earlier in Section 2.

These stray particles can lead to more background problems, which must be addressed by further interaction point design. In Ref. 5, it is suggested that crab-crossing combined with large crossing angles and solenoidal fields would allow one to channel these electrons out through a large exit hole to a beam dump. Further studies of this option have indicated that crossing angles in the range 30–100 mrad would be necessary to avoid particle impact in the detector.[31]

The measurement of the final spot size is an extremely important, but as yet unsolved, problem. From SLC experience, it is probably possible to use beam-beam effects to minimize spot sizes. However, for the initial tune-up of the final focus, a single-beam method is almost essential. There was some initial work done at the workshop in June 1988 in Capri, Italy which was also reported at the SLAC workshop.[32] In addition, preliminary results were presented at the SLAC workshop on the use of beamstrahlung from an ionized gas jet.[33] Recently, there have been studies on the detection of the ions from a gas jet after beam passage.[34]

7. MULTIBUNCH EFFECTS

As mentioned earlier, in order to efficiently extract energy from the RF to obtain high luminosity, it is essential to have many bunches per RF fill. This, however, leads to transverse beam breakup. The invention of damped structures discussed in Section 5.1 helps but does not completely solve the problem for the linac. It is also necessary to tune the frequency of the first dipole mode of the accelerating structure.[35] In Ref. 36 the problem of multibunching is traced all the way through the linear collider subsystem by subsystem. Damped accelerating cavities are required for the main linac and the damping rings, while other systems can get by with very strong focusing. Thus, from the transverse point of view, stability seems possible.

In addition, it is necessary to control the energy spread from bunch to bunch very precisely ($\Delta E/E \lesssim 10^{-3}$). This can be accomplished by injecting the bunches before the RF structure is full to match the extraction of energy by the bunches to the incoming energy as the structure fills. This leads to tight tolerances on phase and amplitude of the RF, as well as tight control of the pulse-to-pulse number of particles in a batch of bunches.[37] However, the benefits of multibunching seem to far outweigh any difficulties they impose due to the order of magnitude increase in luminosity.

8. OUTLOOK

During the past few years, there has been tremendous progress towards a next generation linear collider. We now have a much clearer picture of how to obtain both the energy and luminosity required. An important development this past year was the increased interest in an ILC, that is, a linear collider with 0.5 TeV in the CM which would be upgradable to 1.0 TeV with additional power sources or length. We will probably see the development of a power source and structure during the next couple of years. This would yield the energy of the collider; what about the luminosity?

Designs of damping rings, bunch compressors and focus systems will continue. Studies of BNS damping in the linac and emittance dilution will continue both experimentally with the SLC and theoretically for the next generation high-frequency linac. However, to really understand tolerances, new measurement techniques, and final focus optics, it is probably essential to build a scale model final focus at SLC energy. This is being planned at SLAC (Final Focus Test Beam) and is being supported as a collaborative effort of SLAC, INP, KEK, and Orsay.

One key aspect of all linear collider design is background control. With the discovery of the swarm of e^+e^- pairs produced at the interaction point, there now needs to be detailed study of interaction point design to control backgrounds. This effort is underway at SLAC and KEK.

To conclude, it looks like we are on the path towards a next generation linear collider and with proper funding of R&D over the next few years we may see a detailed conceptual design in the early 1990's.

REFERENCES

1. *Proceedings of the Workshop on Physics of Linear Colliders*, Capri, Italy, June 1988.
2. *Proceedings of the Summer Study on High Energy Physics in the 1990's*, Snowmass, Colorado, July 1988, World Scientific, Singapore, 1989.
3. *Proceedings of the International Workshop on Next Generation Linear Colliders*, SLAC, Stanford, CA. Dec. 1988, SLAC-Report-335.
4. Linear Collider Working Group Reports From Snowmass '88, Ed. R. D. Ruth, SLAC-Report-334.
5. R. B. Palmer, *Energy Scaling, Crab Crossing and the Pair Problem*, SLAC-PUB-4707 (1988) and in Refs. 2 and 4.
6. T. O. Raubenheimer, L. Z. Rivkin and R. D. Ruth, *Damping Ring Designs for a TeV Linear Collider*, SLAC-PUB-4808 (1988) and in Refs. 2 and 4.
7. T. O. Raubenheimer, *et al.*, *Proc. of 1989 IEEE Part. Acc. Conf.*, p. 1316, and in SLAC-PUB-4912 (1989).
8. L. Z. Rivkin *et al.*, "*Bunch Lengthening in the SLC Damping Ring*," SLAC–PUB–4645 (1988).
9. S. A. Kheifets, R. D. Ruth, J. J. Murray and T. H. Fieguth, *Bunch Compression for the TLC. Preliminary Design*, SLAC-PUB-4802 (1988) and in Refs. 2 and 4.
10. S. A. Kheifets, R. D. Ruth and T. H. Fieguth, *Bunch Compression for the TLC*, *Proc. of Int. Conf. on High Energy Acc.* Tsukuba, Japan, 1989 and in SLAC-PUB-5034 (1989).
11. G. A. Loew and J. W. Wang, *RF Breakdown Studies in Room Temperature Electron Linac Structures*, SLAC-PUB-4647 (1988) and in Refs. 2 and 4.
12. G. A. Loew and J. W. Wang, *Field Emission and RF Breakdown in Copper Linac Structures*, *Proc. of the 14th Int. Conf. on High Energy Acc.*, Tsukuba, Japan (1989) and in SLAC-PUB-5059.
13. R. B. Palmer, *Damped Accelerator Cavities*, SLAC-PUB-4542 (1988) and in Refs. 2 and 4.
14. Z. D. Farkas, *IEEE Transcripts on Microwave Theory and Techniques*, **MTT–34**, No. 10 (1986) 1036, and also SLAC/AP–59.
15. P. B. Wilson, *RF Pulse Compression and Alternative RF Sources*, SLAC-PUB-4803 (1988) and in Refs. 2 and 4.
16. Z. D. Farkas, G. Spalek, and P. B. Wilson, *RF Pulse Compression Experiment at SLAC*, *Proc. of IEEE Part. Acc. Conf. 1989* and in SLAC-PUB-4911 (1989).
17. M. A. Allen et al., Phys. Rev. Lett. **63** (1989) 2472.
18. R. B. Palmer and R. Miller, *A Cluster Klystron*, SLAC-PUB-4706 (1988) and in Refs. 2 and 4.
19. H. M. Bizek *et al.*, *A Microwave Power Driver for Linac Colliders: Gigatron*, in Refs. 2 and 4.
20. A. Chao, B. Richter and C. Yao, *Nucl. Instr. Meth.* **178**, 1 (1980).
21. V. Balakin, A. Novokhatsky and V. Smirnov, *Proceedings of the 12th International Conference on High Energy Accelerators*, Fermilab, (1983) p. 119.
22. J. Seeman, SLAC-PUB-4968 (1990), to be published.
23. P. Chen, *Disruption, Beamstrahlung, and Beamstrahlung Pair Creation*, SLAC-PUB-4822 (1988) and in Refs. 2 and 4.
24. K. Oide, *Final Focus System for TLC*, SLAC-PUB-4806 (1988) and in Refs. 2 and 4.
25. W. W. Ash, *Final Focus Supports for a TeV Linear Collider*, SLAC-PUB-4782 (1988) and in Refs. 2 and 4.

26. R. Blankenbecler, S. D. Drell, and N. Kroll, *Phys. Rev. D*, **40**, 2462 (1989).

27. P. Chen and V. I. Telnov, *Phys. Rev. Lett.*, **63**, 1796 (1989).

28. M. Jacob and T. T. Wu, *Phys. Lett. B*, **221**, 203 (1989).

29. V. N. Baier, V. M. Katkov, and V. M. Strakhovenko, *Proc. 14th International Conf. on High Energy Particle Accelerators*, Tsukuba, Japan, 1989.

30. M. S. Zolotarev, E. A. Kuraev and V. G. Serbo, *Estimates of Electromagnetic Background Processes for the VLEPP Project,* Inst. Yadernoi Fiziki, Preprint 81-63, 1981; English Translation SLAC TRANS-0227, 1987.

31. J. Irwin, private communication.

32. J. Norem, presented at the *International Workshop on Next Generation Linear Colliders*, in preparation.

33. D. Burke, P. Chen, M. Hildreth and R. Ruth, *A Plasma Beam Size Monitor*, work in progress.

34. J. Buon, *Proceedings of the 14th International Conference on High Energy Accelerators*, Tsukuba, Japan, 1989.

35. K. A. Thompson and R. D. Ruth, *Controlling Transverse Multibunch Instabilities in Linacs of High Energy Linear Colliders*, *Phys. Rev. D*, **41**, 964 (1990), and in SLAC-PUB-4801 (1989).

36. K. A. Thompson and R. D. Ruth, *Multibunch Instabilities in Subsystems of 0.5 and 1.0 TeV Linear Colliders*, SLAC-PUB-4800 (1988) and in Refs. 2 and 4.

37. R. D. Ruth, *Multibunch Energy Compensation*, SLAC–PUB–4541 (1989) and in Ref. 1.

Hadron Colliders Beyond the SSC

Maury Tigner

Cornell University

Abstract

Extension of the storage ring collider technique to energies beyond the SSC is examined briefly and an example at $\sqrt{s}$ = 400 TeV given. At yet higher energies it is shown that the storage ring approach fails for power efficiency reasons and other approaches are needed. An approach with optimum efficiency is suggested and it is pointed out that the average power handling capability of detectors for the reaction products passing through will need to be in the megawatt region even at 400 TeV, rising as the cube of the beam energy.

Introduction

In hadron colliders the reaction rate, dn/dt is given by

$$dn/dt = \mathcal{L}\,\Sigma \qquad (1)$$

where Σ is the total cross section and is largely inelastic at energies of interest today. Since the primary behavior of the interesting cross section will have an s^{-1} dependence then, to be useful, $\mathcal{L}$ must be engineered to increase in proportion to s which we will adopt as our basic rule for extension of colliders to higher energies. The biggest part of Σ rises rather slowly[1] in the energy domain known to us.

From relation (1) we get directly the power radiated from the reaction zone in reaction products

$$P_R = \sqrt{s}\,\mathcal{L}\,\Sigma\,. \qquad (2)$$

When this is the dominant means by which the beam energies are dissipated, then the storage ring collider technique is a good one and the overall efficiency of the facility is governed by the mechanical and electrical efficiency of the accelerator apparatus.

To work out the energetics of an actual storage ring example there are three other basic relations needed. In what follows we shall assume, without much loss of generality, that the luminosity generating collisions are of circularly cylindrical Gaussian beams of equal and opposite energy colliding head-on with equal intensities. MKS units will be used unless noted specifically.

$$\mathcal{L} = \frac{N_B^2}{4\pi\sigma^2} \cdot \frac{c}{S_B} \tag{3}$$

N_B = number of particles per bunch
S_B = bunch separation along the beam line
c/S_B = bunch hitting frequency
σ = rms bunch radius at the collision point

In a storage ring environment this geometrical relation is constrained by the need to limit the self-focusing (defocusing) of the beams as they interpenetrate at the collision point. The strength of this focusing is characterized by a dimensionless "beam-beam tune spread" [2]

$$\xi = \frac{N_B r_p \beta^*}{4\pi\sigma^2\gamma} \tag{4}$$

r_p = 1.5 x 10^{-18} m
β^* = Betatron focusing strength parameter at the crossing, 1/2 -1 m typically in a proton collider
γ = Lorentz factor for beam particles in lab. frame.

Relations (3) and (4) can be combined to give a formula for the proton beam current required to give the desired luminosity

$$I = \frac{r_p e \beta^*}{\gamma\xi} \cdot \mathcal{L} \ . \tag{5}$$

In addition we need to incorporate the fact that each proton loses an energy U, each time it circuits the ring [3]

$$U[\mathrm{TeV/rev}] = 7.8\mathrm{x}10^{-12}\ E^4[\mathrm{TeV}^4]/\ R[\mathrm{km}]. \tag{6}$$

With these relations we can compute the total beam energy dissipation rate due to synchrotron radiation

$$P_\gamma = 2 \cdot I \cdot U \ \alpha\ E^6/R. \tag{7}$$

Example

As an illustration of these relations we imagine a machine with 10 times the SSC beam energy, i.e. 200TeV per beam. By our extension rule the luminosity must increase by 100 times to $1\mathrm{x}10^{39}\mathrm{m}^{-2}\mathrm{s}^{-1}$. In addition, for easy comparison, we will assume that before the machine is built superconducting magnet technology will improve to the point where the ring radius can remain the same as SSC, i.e. 10 km. Utilizing the above formulae

$$U = 7.8\mathrm{x}10^{-12}\mathrm{x}200^4/10 = 1.2\mathrm{x}10^{-3}\mathrm{TeV/rev} \quad \text{or}$$

$$U/E \sim O[10^{-5}] \quad \text{so } \xi \sim 10^{-2} \quad \text{and}$$

$$I \approx \frac{1.5\mathrm{x}10^{-18}\mathrm{x}1.6\mathrm{x}10^{-19}\mathrm{x}10^{39}\mathrm{x}0.5}{2.1\mathrm{x}10^{5}\mathrm{x}10^{-2}} = 0.057\mathrm{A}$$

$$P_\gamma = 2\mathrm{x}.057\mathrm{x}1.2\mathrm{x}10^{-3}\mathrm{x}10^{12} = 140\ \mathrm{MW}$$

which is indeed very large but perhaps not impossibly so. In an optimized design we might hope to achieve a total facility power of 200 MW. This is to be compared with the beam power dissipated in the physics reactions themselves

$$P_R = 2\mathrm{x}200\mathrm{x}10^{12}\mathrm{x}1.6\mathrm{x}10^{-19}\mathrm{x}10^{39}\mathrm{x}150\mathrm{x}10^{-31} \approx 1\ \mathrm{MW}.$$

From this one may draw two conclusions. First, as this power is less than 1% of the power dissipated in synchrotron radiation, the storage ring technique is beginning to fail at energies of 10 times that of SSC. From relation (7) we see that at higher energies the storage ring method is totally out of the question. Second, we see that any technique with an overall "wall plug" efficiency of greater than 1/2% would be competitive already at $\sqrt{s}$ = 400TeV.

Another interesting property of this example is the number of physics events per beam bunch crossing, a number that is fixed[4] by the choice to minimize I and thus P_γ

$$\langle n\rangle = \mathcal{L}\Sigma\cdot\frac{S_B}{c} \qquad (8)$$

$$\approx 10^{39}\times 150\times 10^{-31}\times 265/3\times 10^{8} \approx 10^{4}.$$

Note that $\langle n\rangle_{SSC} \approx 1$. Event reconstruction at energies beyond the SSC will be a significant challenge.

Other Approaches

The high synchrotron radiation dissipation rate of the storage ring can be avoided by adopting a linear accelerator approach much as is being discussed for electrons. We will thus not consider it further here other than to observe that a linear proton collider will be at an economic disadvantage by comparison with a linear electron collider because the proton beam energy must be at least 10 times that of the electron machine to provide the same elementary interaction energies.

In the storage ring method, the beam bunches interpenetrate cyclically for long enough to dissipate a significant part of the beam stored energy as wanted reaction products, normally a time of hours, unless, of course, synchrotron radiation intervenes to rob the energy as in our example. At the opposite extreme we might imagine engineering a situation in which the entire beam bunch energy is dissipated in reaction products each bunch interpenetration. Assume that we can confine the colliding beams into Gaussian circular cylinders of rms radius σ, N_B protons per bunch. The condition that all the particles interact with the oncoming bunch particles is approximately

$$\frac{N_B}{4\pi\sigma^2}\cdot\Sigma \approx 1\,. \qquad (9)$$

If we assume that at $\sqrt{s}$ = 400 TeV and that we have a means for making $\sigma\approx 1$Å then we would have

$$N_B \approx 4\pi\times 10^{-20}/150\times 10^{-31} \approx 8.4\times 10^{9}$$

events per collision. By hypothesis, at this energy the needed event rate is $\mathcal{L}\cdot\Sigma = 1.5\times 10^{10}s^{-1}$. Thus the bunch hitting rate needed to achieve the desired overall rate would be

$$F = \frac{\mathcal{L}\cdot\Sigma}{N_B} \approx 2 \text{ Hz}. \qquad (10)$$

For scale setting, note that if we could space the protons one beam diameter apart along the line of collision, i.e. 2Å, the bunch length would be $L_B = N_B\cdot dl \approx 1.6$m. Thus the collision zone would be about 2 meters long and emit about 10^{10} events in bursts of a few nano-seconds once or twice per second. Remember this represents an energy flux of 1MW at $\sqrt{s}$ = 400TeV. The length of the inter-penetration zone could be made longer, of course, by spacing the protons farther apart.

A technical means for carrying out the confinement conjectured above has been developing for more than 20 years and is called channeling in crystals.[5,6,7] In near perfect crystals there are certain directions, e.g. <110> in Si or Ge along which surrounding rows of ions form a strong potential minimum for positive particles thus acting as a strong lens for particles directed along these axes at sufficiently small angles characterized by a critical angle. While there are no ions in the channel, there are electrons which multiply scatter the channeled protons eventually driving them out of the channel. A characteristic "dechanneling length"[8] is proportional to momentum of the protons and is about one meter per TeV for protons in Si or Ge as measured at CERN and Fermilab. Thus, in our example we could have a 200 meter long interaction zone as the entering particles have 200TeV energy. The possible advantage of such a long zone would be to cut down the event density.

Accelerator Mechanisms

To take advantage of this potentially high efficiency scheme some relatively high efficiency acceleration mechanism must be found which is economical and capable of delivering beams of unprecedented brightness. The invariant admittance[9] of a single channel in Ge is about 3×10^{-13}meter whereas the emittance of beams from high energy accelerators are presently 10^{-6}to10^{-7} at best. One can easily imagine a source of the necessary brightness in which a crystal channel is used to filter a low energy beam. The challenge will be to accelerate that beam to high energy without emittance dilution.

Following the concept of completely absorbing, single pass collisions in a channel we can envision accelerating the beams in an external accelerator and introducing them into the confinement channel upon extraction from the accelerators. One example would be a pair of synchrotrons with counter rotating beams which are extracted at the simultaneous cycle peaks and directed into the confining crystal from opposite directions with optical matching systems designed for this purpose. This need not suffer the same energy dissipation due to synchrotron radiation that the storage ring does because the beam current is smaller and the duty factor, or time the beam spends at maximum energy is small.

Another possibility would be to accelerate the protons directly in the channel. This has been suggested by several authors and studied recently.[10,11] In the first reference it is suggested that a certain plasma wave mode be excited in the channeling crystal by an electromagnetic wave incident, thus providing the needed accelerating field for the protons. This method exploits the high inherent charge density in a crystal. The second reference exploits the periodic nature of the crystal lattice to support a "slow wave" at x-ray frequencies which is the s-ray analog of today's microwave linear accelerators which utilize periodically loaded waveguides. The technical difficulties to be overcome are perhaps best characterized by the dechanneling length, 1 meter per TeV. If the accelerating gradient doesn't exceed 1 TeV per meter the particles being accelerated will be dechanneled before reaching full energy and thereby lost. Today's accelerators achieve 10^8V/m at best, a shortfall of 10^4. Another way of saying it is that the needed power sources, which in the channeling accelerator case are in the ultra-violet and x-ray regimes, do not exist now. Further, the mode conversion efficiencies of the accelerating modes so far envisioned are very low meaning that overall efficiency would be low and that the needed excitation energy densities may exceed the damage threshold of the crystals.[12] Nevertheless thae basic idea has enough attractions that it deserves further study.

Summary

At this time there is no clear path to practical accelerators beyond SSC. It could well be that an improvement in current methods--storage rings-- will make one more step possible. There is, however, a great ferment of ideas only a few of which have been touched on here. It is hoped that the perspective given here will spawn a new idea or combination of ideas now circulating which will lead to a practical result.

In closing let us recall the basic challenge that we face. Rewriting relation (2) in terms of beam energy we have

$$P_R \propto E^3.$$

Thus at 10 x SSC energies, 1 MW is radiated from the ir zone in charged and neutral particles in contrast to the mere 1 kW at SSC energy. At 100 x SSC, $P_R >$ 1 GW. The challenge of extracting a useful signal from this background seems at least equal to producing the reactions in the first place.

References

1. M. Block, R. Kahn, Physics Letters, **B188**, 1987, p. 143.

2. Empirically, ξ has been O[10^{-3}] for proton machines and O[10^{-2}] for electron machines where radiation damping help ameliorate the diluting effects of the beam-beam interaction. We conjecture that the same thing will hold for protons when the damping decrement per collision reaches values comparable with that common in electron machines, i.e. 10^{-5}or greater. The limit to ξ is governed by non-linear effects not now understood. Thus design estimates can only be made by inserting the empirically derived values from foregoing machines.

3. M. Sands in "Physics with Intersecting Storage Rings," B. Touschek ed. Academic Press, 1971.

4. S_B/c is set by ξ and the beam emittance given by quantum fluctuations of the synchrotron radiation, op. cit. Ref. 3.

5. Sorensen and Uggerhoj, "The Channeling of Electrons and Positrons", Scientific American, June, 1989 p. 96.

6. R. Carrigan, J. Ellison, "Relativistic Channeling ," Plenum, 1987.

7. D. Gemmell, "Channeling and Related Effects", RMP **46**,1 Jan 1974, 129ff.

8. R. Carrigan, "Channeling and Dechanneling at High Energy," NIM **B33**, 1988, p. 43.

9. Admitttance = maximum amplitude times maximum angle of channeled particles.

10. P. Chen, R. Noble in Ref. 6.

11. T.Tajima and M.Cavenago, PRL **59**,13, 1987 p 1440.

12. See Ref. 8 for a good review.

Recent Results on Weak Decays of Charmed Mesons from the MarkIII Experiment

by Thomas E. Browder
Stanford Linear Accelerator Center, Stanford, CA, 94305
Cornell University, Ithaca, New York, 14853

Invited Talk at the SLAC Topical Conference, July 19-21, 1989

Recent results from the MarkIII experiment on weak decays of charmed mesons are presented. Measurements of the resonant substructure of $D^0 \to K^-\pi^+\pi^-\pi^+$ decays, the first model independent result on $D_s \to \phi\pi^+$, as well as limits on $D_s \to \eta\pi^+$ and $D_s \to \eta'\pi^+$ are described. The implications of these new results are also discussed.

* Work supported by Department of Energy Contract DE-AC-03-76SF00515

Resonant Substructure in $D \to K\pi\pi\pi$ Decays

A number of $D \to PP$ and $D \to PV$ decays[1] have now been measured and can be satisfactorily explained in two phenemenological models.[2] So far these models have not been tested for the case of $D \to VV$ decays. Using the decay mode $D^0 \to K^-\pi^+\pi^-\pi^+$ the branching ratio for $D^0 \to \overline{K^{*0}}\rho^0$ can be determined. In addition to the possibility of measuring the $V\ V$ components, it is also important to measure the resonant subcomponents of $D \to K\pi\pi\pi$ decays since these decays comprise a significant fraction of the total D width [35% of the D^0 width and 20% of the D^+ width].

Using the data sample [9.3 pb^{-1}] collected at the $\psi''(3.77)$ in 1982-1984, a complete resonant substructure analysis has been carried out for the decay modes $D^0 \to K^-\pi^+\pi^-\pi^+$ and $D^+ \to \overline{K^0}\pi^-\pi^+\pi^+$ by the MarkIII group.[3] A large clean signal for the all charged mode is shown in the recoil mass plot of Figure 1(a). The fitted signal contains 1281 ± 45 events. An equally clean signal, with 184 ± 21 events, for $D^+ \to \overline{K^0}\pi^+\pi^-\pi^+$ is shown in Figure 1(b).

An event by event maximum likelihood fit to the full five dimensional phase space defined by the four momenta of the D decay products is performed in order to determine the resonant content of the decay mode. A set of partial waves which describe the resonant substructure of the decay is chosen. The preferred fit includes contributions from $D^0 \to K^-\pi^+\pi^-\pi^+$ in a nonresonant state, $D^0 \to \overline{K^{*0}}\pi^-\pi^+$, $D^0 \to K^-\rho^0\pi^+$, $D^0 \to K^-a_1^+(1260)$, $D^0 \to K_1(1270)^-\pi^+$, $D^0 \to K_1(1400)^-\pi^+$, and $D^0 \to \overline{K^{*0}}\rho^0$. The $D^0 \to \overline{K^{*0}}\rho^0$ term contains two independent components in which either both vector mesons are polarized parallel or both vector mesons are polarized perpendicular to the direction of flight of the D^0 meson.

The amplitude for each of the above processes is expressed in terms of two body masses using the Lorentz invariant amplitude formalism or in terms of helicity angles using the helicity formalism. The amplitudes are symmetrized with respect to the labels of identical pions. The amplitudes so obtained are then multiplied by relativistic Breit Wigners and modulated by form factors. All the amplitudes are fully interfering. A Monte Carlo integration technique is used to

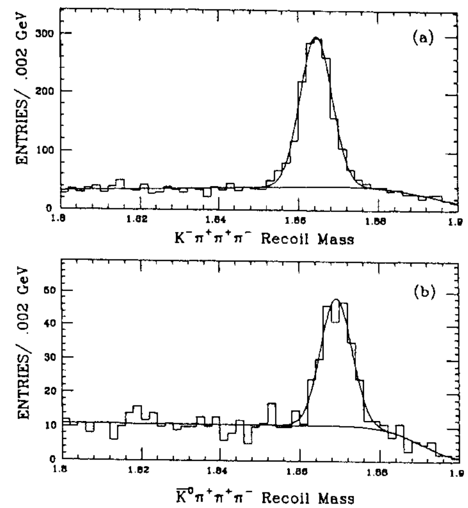

Figure 1. Recoil mass distribution for (a) $D^0 \to K^-\pi^+\pi^-\pi^+$ and (b) $D^+ \to K_s\pi^-\pi^+\pi^+$

take account of the dependence on detector acceptance and avoid the problem of parameterizing the acceptance in the five dimensional phase space.

The sidebands in recoil mass are used to determine the background likelihood function. The likelihood function allows for nonresonant, $\overline{K^{*0}}$, ρ^0, and $\overline{K^{*0}}\rho^0$ components in the background. These components are noninterfering.

The possibility that the choice of amplitudes may introduce some model dependence is one of the difficult issues that must be addressed in this analysis. A large number of decay modes could potentially contribute to the $D^0 \to K^-\pi^+\pi^-\pi^+$ final state. It is not practical to perform a fit that simultaneously includes all the possibilities. Instead, a large number of fits with different combinations of amplitudes were performed. Those fits which yielded a good likelihood were retained for further consideration. Fits which were physically implausible were discarded. The final set of fits give similiar results for the quasi two-body amplitudes and for the four-body nonresonant amplitude. The fits did not yield definitive results on which quasi three-body partial waves contribute. The range of variation among the final set of fits is used to estimate the systematic error.[4]

Since the a_1 is very broad, it is often difficult to distinguish it from nonresonant $\rho^0\pi$. The polarization of $D^0 \to K^-a_1$ $[P \to P\ A]$ leads to angular distributions which are distinctive. However, $D^0 \to K^-a_1$ cannot be separated from the reaction $D^0 \to K^-\rho^0\pi^+$ where the ρ^0 and π^+ are in relative s wave on the basis of angular information. The three pion mass distributions for these two possibilities are, however, significantly different; the $D^0 \to K^-a_1$ amplitude peaks about 100 MeV above the nonresonant amplitude. Fits in which the Ka_1 amplitude was replaced by the three-body amplitude resulted in a significantly smaller likelihood, with a difference in ln(L) of at least 12. Therefore it is assumed that this particular three-body amplitude does not contribute to the final states discussed here.

Projections of the five dimensional likelihood function for various submasses are shown in Figure 2. A large K^* contribution is evident in Figure 2(a). Similiarly, ρ production is evident in Figure 2(b). The enhancement at low $K^-\pi^-$ mass in Figure 2(e) is due to the polarization of the a_1. Evidence for $D^0 \to K_1(1270)\pi^+$

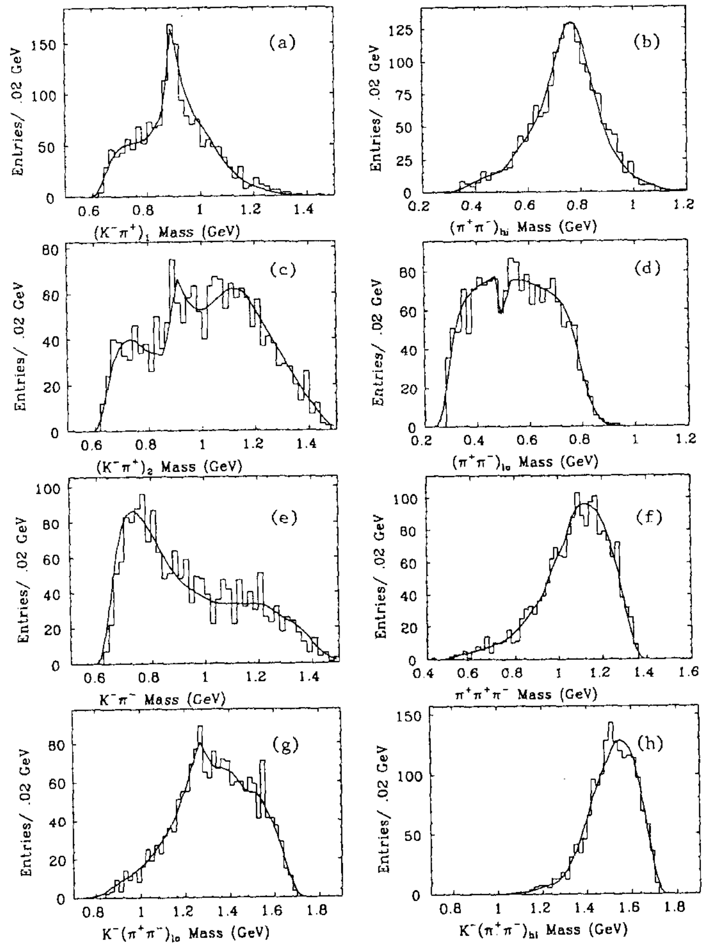

Figure 2. Projections of the likelihood function for $D^0 \to K^-\pi^+\pi^+\pi^-$. The solid lines, representing the projections of the likelihood function, are superimposed on histograms of the events in the signal region. The $\pi^+\pi^-$ combination with the higher mass is referred to as $(\pi^+\pi^-)_{hi}$, and the $K^-\pi^+$ combination formed with the π^+ not used in $(\pi^+\pi^-)_{hi}$ is referred to as $(K^-\pi^+)_1$. The deficit near .5 GeV in the $(\pi^+\pi^-)_{lo}$ mass plot is due to the rejection of $\pi^+\pi^-$ combinations which have a high probability of originating from a K_s decay.

is visible in Figure 2(g). In all the projections the fit is in good agreement with the data.

Table I Preliminary results for $D^0 \to K^-\pi^-\pi^+\pi^-\pi^+$

Amplitude	Fraction	Phase	Branching Ratio
4-Body Nonresonant	.233 ± .025 ± .10	-1.01 ± .08	.021 ± .003 ± .009
$\overline{K^{*0}}\rho^0$ Longitudinal	.014 ± .009 ± .01	-2.64 ± .28	Sum of L and T:
$\overline{K^{*0}}\rho^0$ Transverse	.152 ± .021 ± .05	-1.22 ± .11	.023 ± .003 ± .007
$K^-a_1(1260)$	.442 ± .021 ± .10	.0	.080 ± .008 ± .019
$K_1(1270)^-\pi^+$	.113 ± .028 ± .04	.44 ± .19	.031 ± .008 ± .011
$K_1(1400)\pi^+$	.011 ± .009 ± .03	.71 ± .43	< .012
$K^{*0}\pi^+\pi^-$	.091 ± .018 ± .04	-3.31 ± .11	.012 ± .003 ± .005
$K^-\rho^0\pi^+$	.088 ± .023 ± .04	-.62 ± .09	.008 ± .002 ± .004

The results of the fit are shown in Table I. A few qualitative features should be noted. There is a very large $D^0 \to K^-a_1(1260)$ $[D \to P\ A]$ contribution to this final state, consistent with the theoretical expectation from the BSW model [5.0%]. There is also a rather small $D^0 \to \overline{K^{*0}}\rho^0$ $[D \to V\ V]$ contribution, which is completely polarized transverse to the D^0 flight direction. There is some evidence for the final state $D^0 \to K_1(1270)^-\pi^+$ $[D \to A\ P]$. The four-body nonresonant contribution is also significant. In addition, there is a contribution from $D^0 \to \overline{K^{*0}}\pi^-\pi^+$ where the $\overline{K^{*0}}\pi^+$ system is in an axial vector state as well as $D^0 \to K^-\rho^0\pi^+$ where the $K^-\rho^0$ system is an axial vector state. It is not possible to determine whether the above three-body amplitudes are due to quasi two-body decays of broad resonances e.g. $D^0 \to K^-\pi(1300)^+$ or $D^0 \to K(1460)^-\pi^+$.

An analysis for the mode $D^+ \to \overline{K^0}\pi^-\pi^+\pi^-$ has been carried out using the same technique. The results of the fit are shown in Table II. There is a large contribution from the axial-vector pseudoscalar mode $D^+ \to \overline{K^0}a_1(1260)^+$. There is also some evidence for $D^+ \to K_1(1400)\pi^+$ $[D \to A\ P]$. There is no possible vector-vector mode that can contribute to this final state.

Resonant substructure analyses of the modes $D^0 \to K^-\pi^+\ \pi^0\pi^0$, $D^+ \to K^-\pi^+\ \pi^+\pi^0$, and $D^0 \to \overline{K^0}\pi^-\pi^+\pi^0$ channels will also be attempted in the near future. If the rates and phases for $D^0 \to \overline{K^{*0}}\rho^0$, $D^0 \to \overline{K^{*-}}\rho^+$, and $D^+ \to \overline{K^{*0}}\rho^+$ can be measured with sufficient accuracy, then the isospin sum rule[5]

Table II Results for $D^+ \to \overline{K^0}\pi^-\pi^-\pi^+$

Amplitude	Fraction	Phase	Branching Ratio
4-Body Nonresonant	.184 ± .052 ± .10	1.37 ± .17	.012 ± .004 ± .007
$\overline{K^0}a_1(1260)^+$	.612 ± .053 ± .15	.0	.081 ± .020 ± .027
$K_1(1270)\pi^+$	.010 ± .013 ± .02	1.30 ± .90	< .011
$K_1(1400)\pi^+$	.163 ± .048 ± .08	.24 ± .26	.024 ± .009 ± .013

$$\sqrt{2}A(D^0 \to \overline{K^{*0}}\rho^0) = A(D^+ \to \overline{K^{*0}}\rho^+) - A(D^0 \to K^{*-}\rho^+)$$

can be used to determine whether final state interactions play a significant role in these decays. If the above sum rule cannot be satisfied with relatively real amplitudes, then final state interactions are required. Examination of the other final states will also provide good consistency checks of the resonant substructure analysis since quasi two-body reactions can give rise to several distinct final states e.g. $D^0 \to \overline{K^{*0}}\rho^0 \to K^-\pi^+\pi^-\pi^+$ or $\overline{K^0}\pi^0\pi^-\pi^+$.

In addition to measurements of the absolute rates of $D \to V\ V$ decays, it is also possible to measure angular correlations between the two vectors in $D \to V\ V$ decays. This is useful for testing the factorization hypothesis.[6] If the two vectors are both polarized perpendicular to the D^0 direction, one expects that the angular dependence of the amplitude will have the form $A_T \propto \cos(\phi)\sin\theta_1\sin\theta_2$ where ϕ is the angle between the decay planes of the two vector mesons, and θ_1, θ_2 are the helicity angles of the ρ and K^* mesons, respectively. If the polarization is longitudinal, $A_L \propto \cos\theta_1\cos\theta_2$. If factorization is a valid assumption, longitudinal polarization is expected to be dominant. The analysis by the MarkIII group, however, indicates that $D^0 \to \overline{K^{*0}}\rho^0$ is transversely polarized. The observed angular correlation for $D^0 \to \overline{K^{*0}}\rho^0$ events is indicated in Figure 3.

Several recent observations appear to indicate that many of the VV decay rates are smaller than expected. For instance, the measured rate for $D^0 \to \overline{K^{*0}}\rho$ $(2.3 \pm 0.3 \pm 0.7\%)$ from MarkIII is almost three times smaller than the theoretical

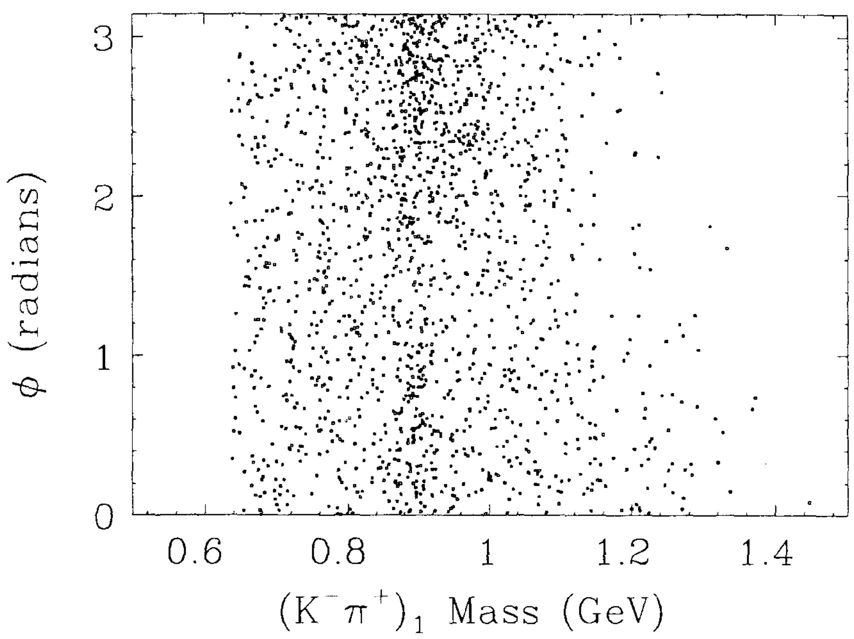

Figure 3. Scatter plot of $(K^-\pi^+)_1$ mass vs ϕ, where ϕ is the angle between the $\bar{K}^{*0}$ and ρ^0 decay planes as seen from the D^0 rest frame. In the $\bar{K}^{*0}$ band, an enhancement near ϕ=0 and a larger enhancement near $\phi = \pi$ are visible. The transverse $\bar{K}^{*0}\rho^0$ amplitude is proportional to $\cos\phi$ and accounts for this distribution. Since the sign of this amplitude reverses from $\phi = 0$ to $\phi = \pi$, there is more constructive interference near $\phi = \pi$.

expectation (6.1%). The branching ratio for the decay $D_s \to \phi\pi^+\pi^0$, which is expected to include a large $\phi\rho^+$ contribution, is 2.4 × Br($D_s \to \phi\pi^+$), nearly a factor of three smaller than the prediction [6.3 × Br($D_s \to \phi\pi$)]. Similiarly, even if the decay $D^+ \to K^-\pi^+\pi^+\pi^0$ is saturated by $D^+ \to \overline{K^{*0}}\rho^+$, the observed rate[7] [$3.7 \pm 0.8 \pm 0.8\% \; / Br(\overline{K^{*0}} \to K^-\pi^+)$] is still significantly lower than the BSW prediction[$\sim$ 13%]. These intriguing discrepancies may indicate the breakdown of the factorization Ansatz in decays with little energy release.[8] If the same models are used to extract information about the weak interaction in B decays, it is necessary to understand why these phenomenological models fail in the case of $D \to V\,V$.

The Absolute Branching Fraction B($D_s \to \phi\pi^+$)

All D_s decay measurements are normalized to $B(D_s \to \phi\pi^+)$. In addition, to extract $B(B \to D_sX_i)$ from a measurement of $B \to D_sX_i \to \phi\pi\ X_i$ for a final state X_i requires knowledge of the absolute branching fraction $B(D_s \to \phi\pi^+)$.[9]

There are three methods that can be used to extract the absolute branching fraction. For the majority of published results, one uses the measured quantity $\sigma_{D_s} \times Br(D_s \to \phi\pi^+)$ for $x_{D_s} >$ cut where $x_{D_s} = p(D_s)/p_{max}$. The measured D_s yield is extrapolated to all x_{D_s} using a model for the D_s fragmentation function. A theoretical value of σ_{D_s} is then calculated and the absolute branching fraction is determined. The theoretical value of σ_{D_s} depends on the probability of popping an $s\bar{s}$ quark pair from the vacuum and is sensitive to the details of D_s hadronization. The results obtained using this method range from 1.7% to 4.4%.[10 - 20]

A second method based on charm counting has been used recently as well. From the measured value of R in the continuum above the resonance region, the total charm cross section is inferred from the quark charges. The total charm cross section can then be decomposed into the following components:

$$\sigma_{\text{charm}} = \sigma_{D^0} + \sigma_{D^+} + \sigma_{D_s} + \sigma_{\Lambda_c} + \sigma_{\text{other baryons}}.$$

If the last term on the right-hand side can be absorbed into the other terms, then

$$\sigma_{D_s} = \sigma_{\text{charm}} - \sigma_{D^0} - \sigma_{D^+} - \sigma_{\Lambda_c}.$$

The cross section σ_{D^0} is obtained by dividing the observed quantity $\sigma_{D^0} \times Br(D^0 \to f_i)$ by the abolute branching fraction $Br(D^0 \to f_i)$ from MarkIII. The final states $f_i = K^-\pi^+$ and $K^-\pi^+\pi^-\pi^+$ are used. The cross section σ_{D^+} is obtained in a similiar way using the final state $D^+ \to K^-\pi^+\pi^+$. The cross section σ_{Λ_c} is determined from the measured Λ_c yield and the branching fraction for $\Lambda_c \to pK^-\pi^+$. The Λ_c branching fraction is in turn determined either from the measured $B \to$ proton X rate or from the MarkII continuum measurement. Using these cross sections, the absolute branching fraction is determined by the CLEO collaboration to be $2 \pm 1\%$.[21] This result is sensitive to the Λ_c branching fraction and assumptions about charmed baryon production.

The third method, which is used by the MarkIII experiment, employs the reaction $e^+e^- \to D_s^{\pm}D_s^{*\mp}$ decays where the full final state is completely reconstructed. This method was successfully used to extract absolute D^0 and D^+ branching fractions from the data sample collected at the $\psi(3.77)''$ resonance.[22]

The principle and advantages of this double tagging technique method are easy to understand. The number of double tags with $D_s \to f_i$ opposite $D_s \to \phi\pi$ will be given by

$$2\sigma_{D_sD_s^*}\ L\ B(D_s \to f_i)\ B(D_s \to \phi\pi)\ \epsilon_{f_i}\epsilon_{\phi\pi}.$$

The number of singly tagged $D_s \to f_i$ events will be given by

$$\sigma_{D_sD_s^*}\ L\ B(D_s \to f_i)\ \epsilon_{f_i}.$$

Therefore

$$N_{double}/(2N_{single}\epsilon_{\phi\pi}) = B(D_s \to \phi\pi^+).$$

This result is manifestly model independent. Clearly, the above derivation can easily be extended to any doubly tagged decay modes [f_i versus f_j] provided the branching ratios of $B(D_s \to f_i)$ and $B(D_s \to f_j)$ are known relative to $B(D_s \to \phi\pi^+)$.

The MarkIII analysis[23] is performed using the data sample [6.3 pb^{-1}] collected in 1986 at $\sqrt{s} = 4.14$ GeV. Candidates for the reaction $e^+e^- \to D_s^{\pm}D_s^{*\mp}$, $D_s^+ \to f_i$, $D_s^{*-} \to \gamma D_s^-$, $D_s^- \to f_j$ are selected using a six constraint kinematic fit. Energy momentum conservation for the exclusive final state leads to four constraints. The additional two constraints are due to the equal mass requirement $m(f_i) = m(f_j) = m(X)$ i.e. the two D_s candidates must have equal but unspecified masses. Candidates for the decay modes $D_s \to \phi\pi^+$, $D_s \to \overline{K^0}K^+$, $D_s \to \overline{K^{*0}}K^+$, $D_s \to f_0(975)\pi^+$, $D_s \to \phi\pi^+\pi^-\pi^+$, $D_s \to \phi\pi^+\pi^0$, and $D_s \to \overline{K^{*0}}K^{*+}$ are considered. There are a total of 28 possible final states.

A signal region which contains 95% of the signal events is determined for each of the combinations on the basis of Monte Carlo simulation. The observed M(X) distribution is the unshaded histogram in Figure 4(a). The expected M(X) distribution is the histogram shown in Figure 4(b). The arrows indicate the limits of the signal region for the combination of modes with the poorest resolution [± 20 MeV]. There are no candidate events inside the signal region. If $B(D_s \to \phi\pi^+) = 4\%$, we should observe three events in the signal region.

A likelihood function which depends on the $D_s \to \phi\pi^+$ branching ratio is used to obtain the upper limit. The likelihood function is integrated to obtain the 90% confidence level upper limit. After allowing for systematic error in the detection efficiency and Gaussian errors on the relative branching fractions of the tagging modes, the upper limit $B(D_s \to \phi\pi^+) < 4.1\%$ at the 90% confidence level is obtained.[24]

Search for D_s Decays to $\eta\pi$ and $\eta'\pi^+$ Final States

If the absolute branching fraction B($D_s \to \phi\pi$) $\sim 2\%$ then only $9 \times B(D_s \to \phi\pi)$ or 18% of all hadronic D_s decays have been measured. The existing measurements of D_s modes are summarized in Tables III and IV. It has been suggested that $D_s \to \eta\pi$ and $D_s \to \eta'\pi$ could account for a large fraction of the missing D_s modes. Two recent results from the MarkII[25] and NA14'[26] experiments appear to confirm this suggestion. Clearly, it is important to provide a definitive experimental resolution of this issue.

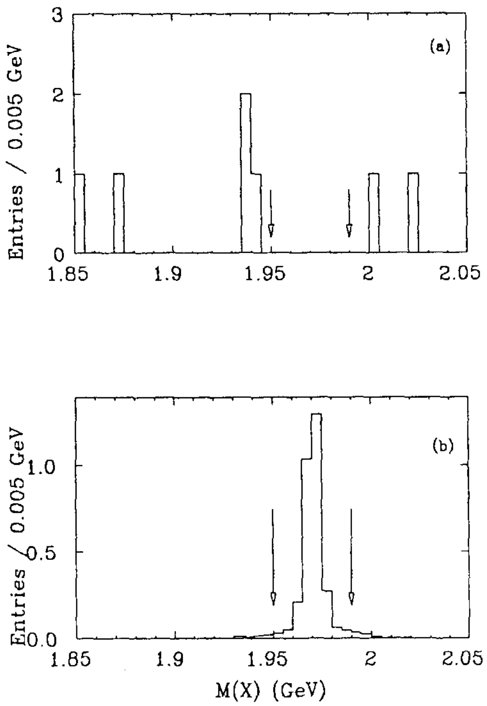

Figure 4. M(X) distribution for (a) data and (b) Monte Carlo events.

Table 3. Branching ratios of D_s modes with kaons relative to $\phi\pi$

Decay Mode	Experiment	Result or Limit
$D_s \to \overline{K^0}K^+$	MarkIII	$0.92 \pm 0.32 \pm 0.20$
	CLEO	$0.99 \pm 0.17 \pm 0.06$
$D_s \to \overline{K^{*+}}K^0$	CLEO	$1.2 \pm 0.21 \pm 0.07$
$D_s \to \overline{K^0}\pi^+$	MarkIII	< 0.21 at 90% CL
$D_s \to \overline{K^{*0}}K^+$	E691	$0.87 \pm 0.13 \pm 0.05$
	ARGUS	1.44 ± 0.37
	MarkIII	$0.84 \pm 0.30 \pm 0.22$
	CLEO	$1.05 \pm 0.17 \pm 0.06$
$D_s \to \overline{K^{*0}}K^{*+}$	NA32	2.3 ± 1.2
$D_s \to \phi\pi^+\pi^0$	E691	$2.4 \pm 1.0 \pm 0.5$
	NA14	< 2.6 at 90% CL
$D_s \to (K^-K^+\pi^+)_{NR}$	E691	$0.25 \pm .07 \pm .05$
	NA32	0.96 ± 0.32
$D_s \to \phi\pi^-\pi^+\pi^+$	E691	$0.42 \pm 0.13 \pm .07$
	NA32	0.39 ± 0.17
	Argus(a)	$1.11 \pm 0.37 \pm 0.28$
	Argus(b)	$0.41 \pm 0.13 \pm 0.11$
$D_s \to (K^-K^+\pi^+\pi^0)_{NR}$	E691	< 2.4 at 90% CL
$D_s \to (K^-K^+\pi^-\pi^+\pi^+)_{NR}$	E691	$< .32$ at 90% CL
	NA32	0.11 ± 0.07

Due to these surprising observations, there has been a great deal of theoretical interest in these D_s decay modes. The decay $D_s \to \eta\pi^+$ is expected to proceed via a spectator diagram and should therefore be comparable in rate to $D_s \to \phi\pi^+$. Predictions are available from Bauer, Stech and Wirbel(BSW),[27] Korner and Schuler(KS),[28] and Blok and Shifman(BS).[29] They find that $D_s \to \eta\pi^+/D_s \to \phi\pi^+$ should be 0.75–1.05(BSW), 1.35–1.89(KS), or 1.1(BS). The ratio of $B(D_s \to \eta'\pi^+)/B(D_s \to \eta\pi^+)$ is determined primarily by the $s\bar{s}$ quark content of the η and η' mesons, and by the amount of available phase space. Since the η' is more massive than η and has much less $s\bar{s}$ quark content, one expects naively: $B(D_s \to \eta'\pi^+)/B(D_s \to \eta\pi^+) < 1$. For this ratio, BSW predict $0.59 - 1.04$, while KS predict $0.62 - 1.09$. Blok and Shifman find 0.09. The range of the theoretical predictions in the first two cases is due to the possible choices of the $\eta - \eta'$ mixing angle (the two canonical choices are $\theta_p = 11$ or 19 degrees). The difference between the BSW and KS predictions is due to the method used for determining the hadronic form factors; BSW use relativistic harmonic oscillator wave functions to calculate the meson overlaps while KS use SU(4) symmetry.

Table 4. Branching ratios of D_s modes without kaons relative to $\phi\pi$

Decay Mode	Experiment	Result or Limit
$D_s \to \rho\pi^+$	E691	< 0.08 at 90% C.L.
	Argus	< 0.22 at 90% C.L.
$D_s \to f_0(975)\pi^+$	E691	$0.28 \pm 0.1 \pm .03$
	MarkIII	$0.58 \pm 0.21 \pm 0.28$
$D_s \to \eta\pi^+$	E691	< 1.5 at 90 % CL
	MarkII	3.0 ± 1.1
	MarkIII	< 2.5 at 90% CL
$D_s \to \eta'\pi^+$	MarkII	4.8 ± 2.1
	NA14	$6.9 \pm 2.4 \pm 1.4$
	MarkIII	< 1.9 at 90% CL
	E691	< 1.7 at 90% CL
$D_s \to \omega\pi^+$	E691	< 0.5 at 90% CL
	E564	seen
$D_s \to (\pi^-\pi^+\pi^+)_{NR}$	E691	$0.29 \pm .09 \pm .03$
$D_s \to (\pi^-\pi^+\pi^+\pi^-\pi^+)_{NR}$	E691	$< .29$ at 90% CL

In addition to the predictions listed above, Kamal and Sinha[30] have attempted a coupled channel treatment with three rescattering modes but were also unable to reproduce the large rates reported by MarkII and other experiments. Moreover, they note that the large ratio $D_s \to \eta'\pi^+/D_s \to \eta\pi^+ \sim 2$ cannot be accommodated within the standard range of $\eta - \eta'$ mixing for either a 10 or 19 degree pseudoscalar mixing angle. They claim that neither decay mode can be significantly enhanced by annihilation diagrams or penguins. The large rate for η modes, they speculate, is due to the presence of the decay $D_s \to$ glue π^+ or some other unconventional process. In contrast to Kamal and Sinha, L.L Chau concludes that the rates for $D_s \to \eta\pi^+, \eta'\pi^+$ demonstrate that annihilation is large in D_s decays.[31]

In a complementary approach using SU(3) flavor symmetry constraints, Rosen[32] derives the inequality $Br(D_s \to \eta\pi^+) < 9\%$ given the canonical choice $\theta_p = 19^0$ (or $Br(D_s \to \eta\pi^+) < 5.3\%$ for $\theta_p = 10^0$). He also finds that the ratio $Br(Ds \to \eta'\pi^+)/Br(D_s \to \eta\pi^+) < 0.22(0.43)$ for $\theta_p = 20^0$ (10^0). The large rates reported for the two reactions therefore indicate substantial SU(3) breaking effects.

The data sample collected at 4.14 GeV is used for the MarkIII analysis of $D_s \to \eta\pi^+$ and $D_s \to \eta'\pi^+$. The barrel and endcap shower counters are used to identify photon candidates. The MarkIII shower counter has a resolution $\sigma(\mathrm{E})/\mathrm{E} = 18\%/\sqrt{\mathrm{E}}$. The shower counter efficiency is 100% for photons with energies above 0.1 GeV. Both TOF and energy loss (dE/dx) information are used to identify charged pions.

In the analysis of the decay sequence $D_s \to \eta\pi^+$, $\eta \to \pi^+\pi^-\pi^0$, candidate π^0's are selected by performing a 1-C kinematic fit of all pairs of $\gamma\gamma$ candidates to the π^0 mass. Pairs for which the fit χ^2 confidence level (CL) is greater than 5% are retained for further consideration. The lower momentum pions from the η decay must be identified as pions. A 2-C kinematic fit to the hypothesis $e^+e^- \to \pi^+\pi^-\pi^0\pi^\pm D_s^{*\mp}$, $\pi^0 \to \gamma\gamma$ is then performed, using all combinations of three pion candidate tracks. The two constraints in the fit are the π^0 mass and the mass of the unobserved $D_s^{*\mp}$. After imposing the requirements CL $> 5\%$ for the 2-C fit, $E^{\gamma}_{fit} > 70$ MeV for the photons from the π^0, and $534 < M\left(\pi^+\pi^-\pi^0\right) < 564$ MeV, the $\eta\pi^+$ mass spectrum, shown in Figure 5(a) is obtained. The number of observed $D_s \to \eta\pi^+$ decays (16.6 ± 6.1) is determined by fitting the resulting mass spectrum. The signal shape is determined from a Monte Carlo simulation. The background shape is determined from the $\pi^+\pi^-\pi^0\pi^\pm$ mass distribution obtained when $M(\pi^+\pi^-\pi^0)$ is selected from the sideband region 0.5738 to 0.6038 GeV. After correcting for the detection efficiency (12.7%) and for the $\eta \to \pi^+\pi^-\pi^0$ branching ratio, this excess corresponds

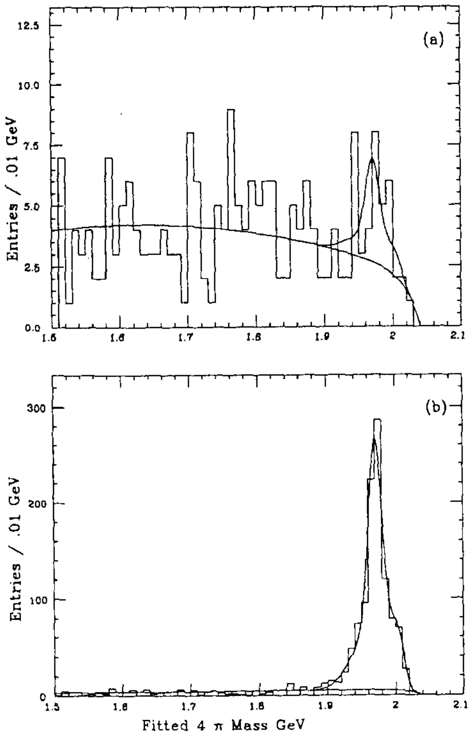

Figure 5. Mass spectrum for $\eta\pi^+, \eta\to\pi^+\pi^-\pi^0$ candidates after 2C kinematic fit: (a) for data events (b) for Monte Carlo events.

to $B(D_s \to \eta\pi^+)/B(D_s \to \phi\pi^+) = 1.7 \pm 0.7 \pm 0.6 \ < 3.3$ where the limits are calculated at the 90% confidence level. The estimate of the systematic error includes the uncertainties in the background shape (18%), the detection efficiency (13%), and the integrated luminosity (7%).

In the analysis of the decay sequence $D_s \to \eta\pi^+, \eta \to \gamma\gamma$, candidate η's are selected by performing a 1-C kinematic fit of all pairs of $\gamma\gamma$ candidates to the η mass. Pairs for which CL > 20% are retained. No particle identification is used. A 2-C kinematic fit to the hypothesis $e^+e^- \to \eta\pi^\pm D_s^{*\mp}$, $\eta \to \gamma\gamma$ is then performed. In order to reduce combinatorial background, more stringent requirements are imposed than in the preceding analysis: CL > 10% for the 2-C fit, $E_\gamma^{hi} > 0.5$ GeV and $E_\gamma^{lo} > 0.2$ GeV. When the resulting $\eta\pi^+$ mass distribution, shown in Figure 6(a) is fitted, no evidence for a D_s^+ signal is found. The signal shape is determined from a Monte Carlo simulation. The background shape is a second order polynomial. No sideband region is available since the two photons were constrained to the η mass. The resulting limit, obtained using a detection efficiency of 23.6%, a trigger efficiency of $92 \pm 4\%$, the $\eta \to \gamma\gamma$ branching ratio and allowing for systematic error (27%), is, $B(D_s \to \eta\pi^+)\ /B(D_s \to \phi\pi^+) <$ 1.6 (90% *C.L.*). The estimate of the systematic error includes the uncertainties in the background shape (20%), the detection efficiency (16%), the trigger efficiency (5%), and the integrated luminosity (7%).

The sensitivity of the two analyses is determined by the product of the detection efficiency and η branching ratios as well as the background levels. In this case, the sensitivity of the two methods are comparable. To combine the results from the two modes properly, a joint likelihood function which depends on the number of produced events is calculated. The joint likelihood function is integrated to determine the 90% confidence level upper limit on the number of produced events, $N_{\eta\pi} < 825$. This yields:

$$\sigma \cdot B\left(Ds \to \eta\pi^+\right) < 66 \text{ pb} \quad (90\% \text{ C.L.})$$

$$\frac{B\left(Ds \to \eta\pi\right)}{B(Ds \to \phi\pi)} < 2.5 \quad (90\% \text{ C.L.})$$

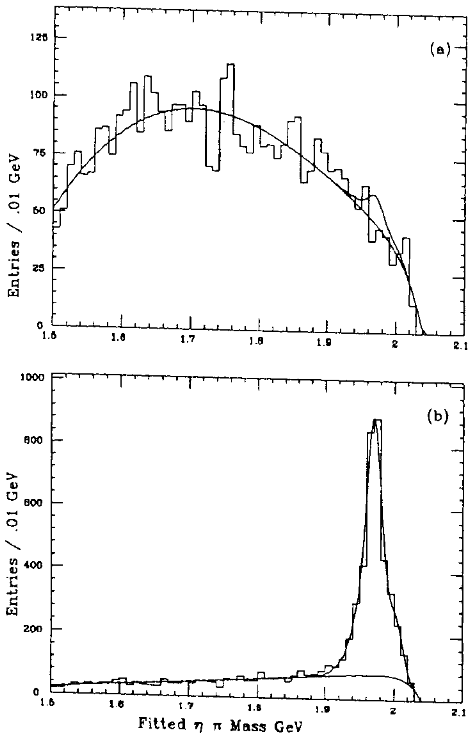

Figure 6. Mass spectrum for $\eta\pi^+$, $\eta\to\gamma\gamma$ candidates after 2C kinematic fit: (a)for data events (b)for Monte Carlo events.

The analysis presented here uses improved detector constants, fitting techniques, and background simulation than was previously used by the MARKIII in a preliminary analysis of this channel.[33]

The $\eta'\pi^+$ analysis uses the decay chain, $D_s \to \eta'\pi^+$, $\eta' \to \eta\pi^+\pi^-$, $\eta \to \gamma\gamma$. Photon candidates are selected with a 1-C fit to the η mass, requiring CL > 10%. The low momentum pions from the η' decay are required to be identified as pions. A 2-C kinematic fit to the hypothesis $e^+e^- \to \eta\pi^+\pi^-\pi^\pm D_s^{*\mp}$, $\eta \to \gamma\gamma$ is performed, where the masses of the η and the missing $D_s^{*\mp}$ are fixed. After imposing the requirements $E_\gamma^{\rm fit} > 0.15$ GeV, CL> 10% for the 2-C fit, and $|m(\eta\pi^+\pi^-) - m_{\eta'}| < 0.015$ GeV, the $\eta'\pi^+$ mass spectrum, shown in Figure 7 is obtained. The distribution is fitted using a background shape determined from sideband regions 0.922 to 0.937 and 0.977 to 0.992 GeV. No excess of events is observed at the D_s mass. The resulting limit, calculated using a detection efficiency of 11.2%, the $\eta' \to \eta\pi^-\pi^+$ and $\eta \to \gamma\gamma$ branching ratios, and allowing for systematic error (36%) is

$$\frac{\mathrm{B}(D_s \to \eta'\pi)}{\mathrm{B}(D_s \to \phi\pi)} < 1.9 \ (90\% \ \text{C.L.}).$$

The estimate of the systematic error includes the uncertainties in the background shape (25%), in the detection efficiency (26%), and in the integrated luminosity (7.3%).

The Monte Carlo photon efficiency is calibrated using the decay $J/\psi \to \rho^0\pi^0$. The efficiency for photon detection in the 4.14 GeV data sample is checked using $e^+e^- \to D^*\overline{D}^*$ events, which are abundant at this center-of-mass energy. A clear $D^0 \to K^-\rho^+$ signal is observed. The measured ratio, $\mathrm{B}(D^0 \to \mathrm{K}^-\rho^+)$ / $\mathrm{B}(D^0 \to \mathrm{K}^-\pi^+) = 2.5 \pm 0.4$, is in good agreement with the value $2.2^{+0.4}_{-0.3}$ from the Particle Data Group compilation.[34]

The results on $D_s \to \eta\pi^+$ are consistent with the measurement $\mathrm{B}(D_s \to \eta\pi)$ / $\mathrm{B}(D_s \to \phi\pi^+) \sim 3$ by Mark II[35] and the limit $\mathrm{B}(D_s \to \eta\pi^+)/\mathrm{B}(D_s \to \phi\pi^+) < 1.5$ (90% C.L.) set by E691.[36] The $\eta'\pi^+$ limit is lower than the ratio $\mathrm{B}(D_s \to \eta'\pi)/\mathrm{B}(D_s \to \phi\pi^+) \sim 4.8$ reported by Mark II,[37] as well as the ratio

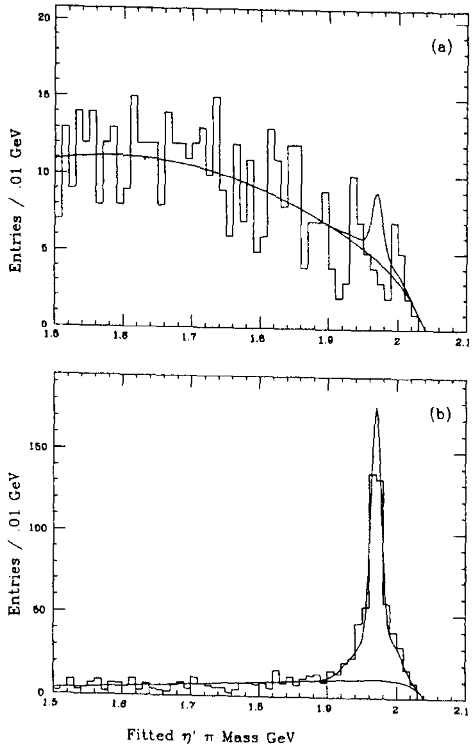

Figure 7. Mass spectrum for $\eta'\pi^+$, $\eta'\to\eta\pi^+\pi^-$, $\eta\to\gamma\gamma$ candidates after 2C kinematic fit: (a) for data events (b) for Monte Carlo events.

$B(D_s \to \eta'\pi)/B(D_s \to \phi\pi) = 6.9 \pm 2.4 \pm 1.4$ reported by NA14'.The results from MARKIII suggest that D_s branching ratios to $\eta\pi$ and $\eta'\pi$ may be much smaller than earlier indications, in agreement with the aforementioned phenomenological models of charm decay.

Summary

A resonant substructure analysis of the mode $D^0 \to K^-\pi^+\pi^-\pi^+$ has been performed. A large contribution from the quasi two-body pseudoscalar axial vector reaction $D^0 \to K^-a_1$ is found, in good agreement with the prediction of the BSW model. The rate for $D^0 \to \overline{K^{*0}}\rho^0$ is also measured and found to be smaller than the theoretical expectation. A similiar analysis of $D^+ \to \overline{K^0}\pi^+\pi^-\pi^+$ has also been carried out. A large contribution from the quasi two-body process $D^+ \to \overline{K^0}a_1(1260)^+$ is found in this final state.

Using fully reconstructed candidates for the reaction $e^+e^- \to D_s^\pm D_s^{*\mp}$, the model independent limit on the absolute branching fraction $B(D_s \to \phi\pi^+) < 4.1\%$ is obtained.

A search for the decay modes $D_s \to \eta\pi$ and $D_s \to \eta'\pi^+$ is performed. Upper limits for both decay modes are obtained. The branching ratios for these decay modes are much smaller than the branching ratios suggested by earlier measurements from the MarkII and NA14' experiments.

REFERENCES

1. $D \to P\ P$ will be used as an abbreviation for the decay of a D meson to a pseudoscalar-pseudoscalar final state. Similiarly, $D \to P\ V$ refers to the decay of a D meson to a pseudoscalar vector final state.
2. M. Bauer, B. Stech and M. Wirbel, Z. Phys. C **34**, 103 (1987). Revised values of $a_1 = 1.2$ and $a_2 = -0.5$ are taken from B. Stech, Heidelberg report HD-THEP-87-18, 1987 (unpublished). B.Yu.Blok and M.A. Shifman, Sov. J. Nucl. Phys. **45**, 135 (1987); **45**, 301 (1987); **45**, 522 (1987); **46**, 767 (1987)].
3. F. DeJongh, CALT-68-1578. To appear in the Proceedings of the 1989 International Symposium on Heavy Quark Physics, American Institute of Physics.
4. We also allow for systematic error in the parameterization of broad resonances and error in the Monte Carlo modeling of the detector.
5. This result follows from the isospin decomposition: $A(D^+ \to \overline{K^{*0}}\rho^+) = A_{3/2}e^{i\delta_{3/2}}$, $A(D^0 \to \overline{K^{*0}}\rho^0) = 1/3(\sqrt{2}A_{3/2}e^{i\delta_{3/2}} - A_{1/2}e^{\delta_{1/2}})$, $A(D^0 \to \overline{K^{*+}}\rho^-) = 1/3(A_{3/2}e^{i\delta_{3/2}} + \sqrt{2}A_{1/2}e^{\delta_{1/2}})$.
6. J.G. Korner and G.R. Goldstein, Phys. Lett. B **89**, 105 (1979).
7. G.P. Yost et. al. (Particle Data Group), Phys. Lett. B **204**, 1 (1988).
8. M. Bauer, B. Stech and M. Wirbel, Z. Phys. C. **42**, 671, 1989.
9. For instance, the luminosity required to observe CP violation in the decay $B^0 \to D^+D_s^-$ is uncertain by a factor of 2 (in addition to the uncertainty in KM angles and phases) due to the uncertainty in the value of the $B(D_s \to \phi\pi^+)$.
10. J.A. McKenna, Ph.D. thesis, University of Toronto, report RX-1191, 1987.
11. G.P. Yost et al. (Particle Data Group), Phys. Lett. B **204**, 1 (1988).
12. A. Chen et al., Phys. Rev. Lett. **51**, 634 (1983).
13. G. Moneti, in *Proceedings of the XXIII International Conference on High Energy Physics,* Berkeley, 1986, edited by S. Loken (World Publishing, Singapore, 1987).
14. M. Althoff et al., Phys. Lett. B **136**, 130 (1984).
15. W. Braunschweig et al., Z. Phys. C **35**, 317 (1987).
16. H. Albrecht et al., Phys. Lett. B **146**, 111 (1984).
17. H. Albrecht *et al.*, Phys. Lett. B **187**, 425 (1987).
18. M. Derrick et al., Phys. Rev. Lett. **54**, 2568 (1985).
19. S. Abachi et al., Argonne National Laboratory preprint ANL-HEP-CP-86-71, 1986 (unpublished).
20. The Particle Data Group's estimate is $B = (8 \pm 5)\%$ (Reference 11).
21. P. Avery et al., Phys. Lett. B **226**, 192, 1989.
22. J. Adler et al., Phys. Rev. Lett. **60**, 89, 1988.
23. S.R.Wasserbaech, Hadronic Decays of the D_s Meson, SLAC-Report-345, June 1989 and references therein.
24. If the unconfirmed modes $D_s \to \phi\pi^+\pi^0$ and $D_s \to \overline{K^{*0}}K^{*+}$ are omitted from the analysis, the upper limit will increase to 5.9%.
25. G. Wormser et al., Phys. Rev. Lett. **61**, 1057 (1988).
26. G. Wormser, LAL-89-10 (1989).
27. M. Bauer, B. Stech, and M. Wirbel, Z. Phys. C **34**, 103 (1987).
28. A. N. Kamal, N. Sinha, and R. Sinha, Phys. Rev. D **38**, 1612 (1988).
29. B. Yu. Blok and M. A. Shifman, Sov. J. Nucl. Phys. **45**, 522 (1987).
30. A. N. Kamal, N. Sinha, and R. Sinha, Phys. Rev. D **38**, 1612 (1988).
31. L.L. Chau, H.Y. Cheng, Phys. Lett. B **222**, 285, (1989) and UCD-88-9.
32. S. P. Rosen, Phys. Rev. D **39**, 1349 (1989).
33. J. C. Brient, SLAC-PUB-4607, March 1988.

34. T. Freese, Ph. D. Thesis, University of Illinois, unpublished (1990).

35. The measured cross section times branching fraction at $\sqrt{s} = 29$ GeV is $\sigma \cdot \mathrm{B}(D_s \to \eta\pi^+) = 5.2 \pm 2.2$ pb.

36. J. C. Anjos et al., Phys. Lett. B **223**, 267 (1989).

37. The measured cross section times branching fraction at $\sqrt{s} = 29$ GeV is $\sigma \cdot \mathrm{B}(D_s \to \eta'\pi) = 8.4 \pm 3.7$ pb.

Recent CLEO Results on Bottom and Charm

Philip S. Baringer

University of Kansas, Lawrence KS 66045

(Representing the CLEO collaboration)

Abstract

Recent results from the CLEO experiment are presented. A data sample corresponding to 428 pb^{-1} of e^+e^- annihilations taken at the Υ energy region is used in the analyses. Included in this report are results on: exclusive hadronic B meson decays; semileptonic B meson decays to charm; B decays into baryons; branching ratio measurements for continuum produced D^0, D_s^+, and Λ_c^+; and mass measurements of the charmed strange baryons Ξ_c^+ and Ξ_c^0. Also presented is the observation of an excess of leptons at the endpoint of the momentum spectrum from semileptonic B meson decay, which constitutes evidence for $b \to u$ transitions.

Invited talk presented at the Topical Conference
of the 1989 SLAC Summer Institute on Particle Physics
July 19-21, 1989, Stanford CA

1. Introduction

In this paper we discuss recent results from the CLEO experiment, which operates at the Cornell Electron Storage Ring (CESR). The data sample used in the analyses described here corresponds to 428 pb^{-1} of e^+e^- annihilation events taken at an average center-of-mass energy of 10.6 GeV. More specifically, data were gathered at three different energies: 212 pb^{-1} were gathered on the $\Upsilon(4S)$ resonance, 102 pb^{-1} were taken off-resonance (30 MeV below the $\Upsilon(4S)$ peak), and 114 pb^{-1} were gathered on the $\Upsilon(5S)$ resonance. The $\Upsilon(4S)$ data contain some 480,000 B (or $\bar{B}$) meson decays.

Data from the $\Upsilon(5S)$ were used in the charmed meson and baryou analyses discussed in section 5 of this report. The $\Upsilon(4S)$ and off-resonance data sets are used in all the analyses presented below. Because the $\Upsilon(4S)$ sits on a large non-resonant background, all B meson decay analyses are performed on both the $\Upsilon(4S)$ resonance data and the off-resonance data. The off-resonance data are then appropriately scaled and subtracted from the on-resonance data to remove the continuum backgrounds from the B meson decay data. This process will be refered to below as "continuum subtraction".

The CLEO detector[1] featured a 64-layer system of drift chambers in a 1 T magnetic field which provided a momentum resolution of $(\sigma_p/p)^2 = (0.23\%p)^2 + (0.7\%)^2$ (p in GeV/c). The central drift chamber[2] of this system had 51 tracking layers and provided a dE/dx measurement resolution of 6.5%. A 10-layer vertex detector was placed inside the central drift chamber, and extended from 8.5 to 16 cm in radius from the beam interaction point. A third chamber, the inner vertex detector, was located inside the 10-layer device, provided three additional layers of tracking, and extended down to a radius of 5.5 cm. Energy measurements were provided by a lead-PWC, electromagnetic shower detector which was located outside the magnet coil at a mean distance of 2.4 m from the beam interaction point and had a photon energy resolution given by $\sigma_E/E = 20\%/\sqrt{E}$ (E in GeV). Also outside the magnet coil were time-of-flight counters and additional dE/dx counters. Muons were identified using special tracking chambers which surrounded the outside of the detector. The CLEO detector has now been completely disassembled, and a new detector, CLEO II, has replaced it in the South interaction region of the CESR storage ring.

We present below a number of results from this data set taken with the old CLEO detector. First, new measurements of exclusive hadronic B decay branching ratios are discussed together with new values for the $\bar{B}^0$ and B^- masses. Second, we report measurements of exclusive semileptonic B decays to charm, in particular the decays $\bar{B}^0 \to D^{*+}l^-\bar{\nu}$ and $B^- \to D^0 l^- \bar{\nu}$. In the next section an excess of leptons is found at the endpoint of the momentum spectrum from semileptonic B meson decay. This constitutes evidence for $b \to u$ transitions, and model dependent values for the ratio of the KM matrix elements $|V_{ub}|/|V_{cb}|$ are given. In the next two sections we turn to the continuum production of charmed particles. Measurements of D^0, D_s^+, and Λ_c^+ branching ratios are given, together with mass measurements of the charmed strange baryons Ξ_c^+ and Ξ_c^0. And in the final section we discuss B decays into baryons.

2. Exclusive Hadronic B Decays

First we present new measurements of the masses of the $\bar{B}^0$ and B^- mesons. In the first step of this analysis, a heavy meson (D^{*+}, D^+, D^0, D_s^+, or Ψ) signal is found, candidates within two standard deviations of the known particle mass are selected, and a kinematic fit using the known particle mass is performed. These candidate heavy mesons are then combined with other tracks in the event in a search for B mesons. Since the $\Upsilon(4S)$ is known to decay only to either $B^0\bar{B}^0$ or B^-B^+, the energy of a true B meson candidate must be equal to the beam energy. A cut is therefore made on the energy of the B candidates requiring them to have an energy which is within two σ of the known beam energy, where σ is the experimental resolution for that particular decay mode. (The resolution varies with the decay mode is question, but is typically around 20 MeV.) A beam constrained mass is then calculated for combinations passing this energy cut. This mass is given by $M^2 = E^2_{beam} - (\Sigma\vec{p_i})^2$, where E_{beam} is the beam energy and the p_i are the measured 3-momenta of the tracks comprising the B candidate. By substituting the beam energy for the sum of the measured particle energies the resolution on the B mass is improved by an order of magnitude.

In Figure 1a. we show the beam constrained mass signals for eight exclusive modes of the $\bar{B}^0$, and in Figure 1b. is presented the corresponding plot for three B^- exclusive modes. Here and throughout this paper the charge conjugate modes are also implied. (So, for example, the $\bar{B}^0 \rightarrow D^+\pi^-$ data include also $B^0 \rightarrow D^-\pi^+$.) To obtain mass values, these data were fitted to a Gaussian signal on a flat background. The width of the Gaussian was fixed to the expected r.m.s. resolution of 2.6 MeV. Uncertainty in the beam energy contributes 2.0 MeV to this width, and the rest is from the momentum measurement resolution. A value of 5279.3 ± 0.4 MeV is obtained for the $\bar{B}^0$ mass, and 5278.9 ± 0.4 for the B^- mass. These values are preliminary and the errors quoted are statistical only. The mass difference $\Delta M = M(\bar{B}^0) - M(B^-) = 0.4 \pm 0.6$ MeV has a very small systematic error since the uncertainties in the beam energy cancel. A previous CLEO measurement from a separate data set gave $\Delta M = 2.0 \pm 1.1$ MeV. Combining these two measurements we get $\Delta M = 0.8 \pm 0.5$ MeV. This is in good agreement with the recently reported ARGUS measurement[3] of $\Delta M = 0.0 \pm 1.3 \pm 1.0$ MeV.

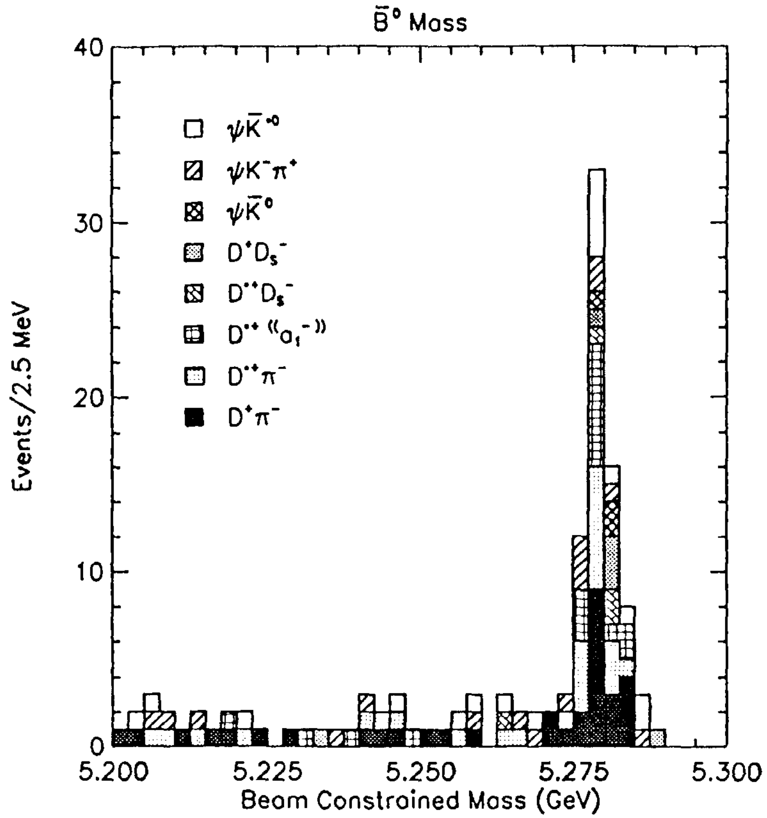

Fig. 1a. Beam constrained mass distribution for $\bar{B}^0$ mesons

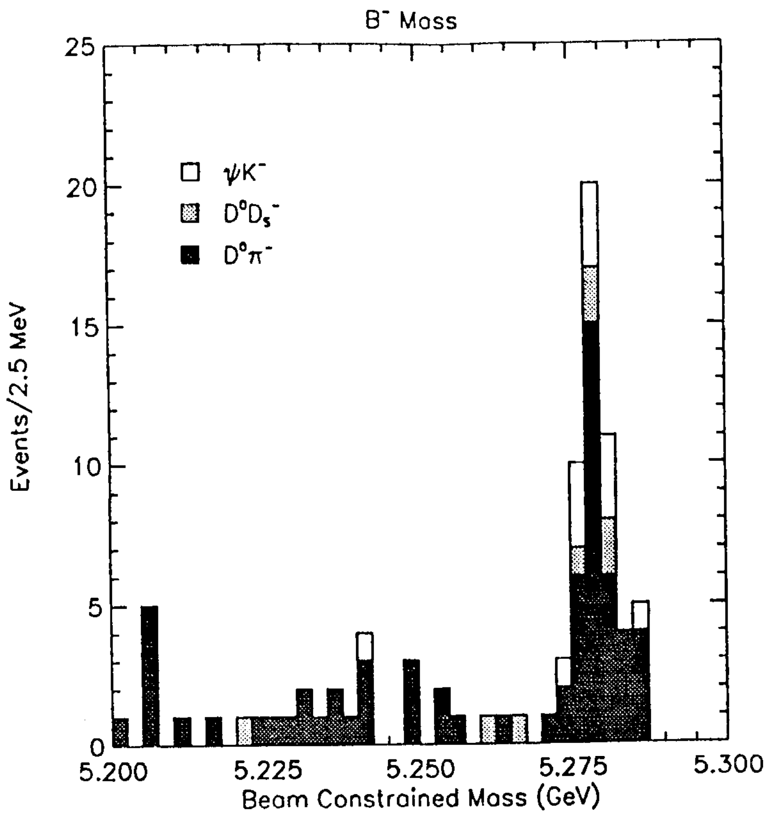

Fig. 1b. Beam constrained mass distribution for B^- mesons

Each decay mode shown in Fig. 1 was also plotted separately and fitted to a Gaussian on a flat background. The width of the Gaussian was fixed as before, and the mass was also fixed to the values obtained in the previous procedure. In this way a number of events is determined for each decay mode. Combining these numbers with calculated efficiencies, branching ratios are obtained for each mode. Preliminary values for these branching ratios are presented in Table 1. Results from the ARGUS experiment[4] are presented for comparison.

In calculating these branching ratios an assumption must be made about the fraction of $\Upsilon(4S)$ decays that go to the charged B mesons versus the neutral B's. In the past the CLEO group has taken the ratio of charged to neutral B's to be 57/43 based on a phase space argument, and ARGUS has used 55/45 for similar reasons. Given the new mass measurements and the possible invalidity of the phase space arguments, this ratio is now assumed to be 50/50. The ARGUS values have been rescaled from the values given in Ref. 4 for comparison purposes.

Among the items in Table 1, the double charm decay modes $D^+D_s^-$, $D^{*+}D_s^-$, and $D^0D_s^-$ are of particular note . These have been observed for the first time, and presumably arise from a spectator decay of b to c where the W^- forms the D_s^- and the c quark combines with the light spectator quark to form the other charmed meson. The D_s^- in these events have been observed in the decay mode $\phi\pi^-$, and the branching ratio into $\phi\pi^-$ has been taken to be 2% (see section 6 in this report).

Also of interest are the new data on $\bar{B}^0 \to D^{*+}\pi^-\pi^+\pi^-$. The first $D^{*+}\pi^-\pi^+\pi^-$ branching ratio quoted in Table 1 assumes non-resonant production of the three pions. If instead, the three pions come from the decay of the a_1^-, the calculated efficiency for this mode rises and the branching ratio drops to give the second reported value. The three-pion and two-pion mass distributions for these events

Decay Mode	Branching Ratio (%)	
$\bar{B}^0$	CLEO	ARGUS
$D^{*+}\pi^-$	$0.33 \pm 0.09 \pm 0.06$	$0.32 \pm 0.16 \pm 0.12$
$D^{*+}\rho^-$	$1.9 \pm 0.9 \pm 1.3$	
$D^{*+}\pi^-\pi^+\pi^-$ †	$1.5 \pm 0.4 \pm 1.0$	$3.9 \pm 1.1 \pm 1.8$
† if all $D^{*+}a_1^-$	$0.9 \pm 0.3 \pm 0.6$	
$D^+\pi^-$	$0.27 \pm 0.08 \pm 0.05$	$0.28 \pm 0.12 \pm 0.09$
$D^+D_s^-$	1.2 ± 0.7	
$D^{*+}D_s^-$	2.4 ± 1.4	
$\Psi \bar{K}^0$	$0.06 \pm 0.03 \pm 0.02$	
$\Psi \bar{K}^{*0}$	$0.11 \pm 0.05 \pm 0.03$	0.30 ± 0.16
$\Psi' \bar{K}^{*0}$	$0.14 \pm 0.08 \pm 0.04$	
$\Psi K^-\pi^+$(NR)	$0.10 \pm 0.04 \pm 0.03$	

B^-	CLEO	ARGUS
$D^0\pi^-$	$0.30 \pm 0.06 \pm 0.04$	$0.21 \pm 0.11 \pm 0.07$
$D^0D_s^-$	2.6 ± 1.3	
ΨK^-	$0.08 \pm 0.02 \pm 0.02$	0.08 ± 0.04
ΨK^{*-}	$0.13 \pm 0.09 \pm 0.03$	
$\Psi' K^-$	< 0.05	0.24 ± 0.19
$\Psi K^-\pi^+\pi^-$	$0.12 \pm 0.06 \pm 0.03$	0.12 ± 0.08

Table 1. B Meson Branching Ratios

are consistent with the hypothesis that all of the $D^{*+}\pi^-\pi^+\pi^-$ decays come via $D^{*+}a_1^-$, however, due to the broad width of the a_1 resonance and the limited statistics of our data we can not make any firm conclusion. Should all of this decay proceed via the a_1, the branching ratio for $\bar{B}^0 \to D^{*+}a_1^-$ would be $1.8 \pm 0.5 \pm 1.2\%$, correcting for the unseen decay $a_1^- \to \rho^-\pi^0$.

The decay $\bar{B}^0 \to D^{*+}\rho^-$ is also observed for the first time, as are the $\Psi'\bar{K}^{*0}$ and non-resonant $\Psi K^-\pi^+$ modes.

3. Semileptonic B Decays to Charm

We now change the focus of our discussion from the purely hadronic B meson decays to semileptonic decays. The simple spectator decay diagram for a semileptonic B meson decay is shown in Figure 2a. In the Standard Model of the weak interaction, the b quark can make a transition into either a c quark or u quark by emitting a W^- boson. In semileptonic decays, the W^- couples to a lepton (l^-) and an antineutrino. These decays are simpler to describe theoretically than the hadronic decays, so measurements of semileptonic decays can provide important constraints on models.

Leptons arise in the data from many sources and one must do some work to separate out the leptons that come from semileptonic B meson decays. Hadronic events are separated from leptonic QED processes by a series of selection cuts which have been described elsewhere.[5] The many sources of leptons in continuum produced hadronic events are removed from the B decay sample by the continuum subtraction technique described in the introduction. The size of this subtraction is reduced significantly by cutting on an event shape variable. Continuum produced hadronic events are jetlike, whereas the events containing decays of the massive B mesons are more spherical. The Fox-Wolfram event shape parameters[6] are

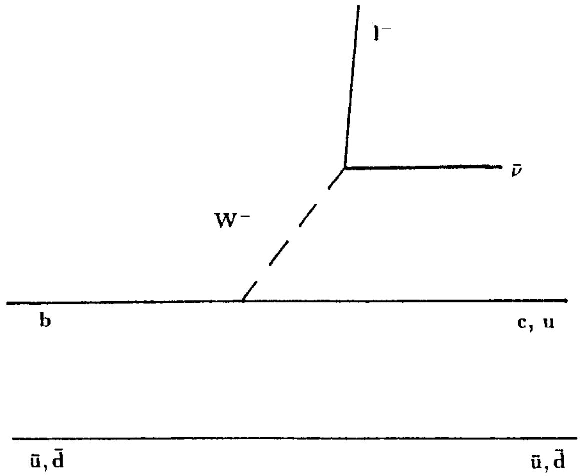

Fig. 2a. Diagram of semileptonic decay of B meson

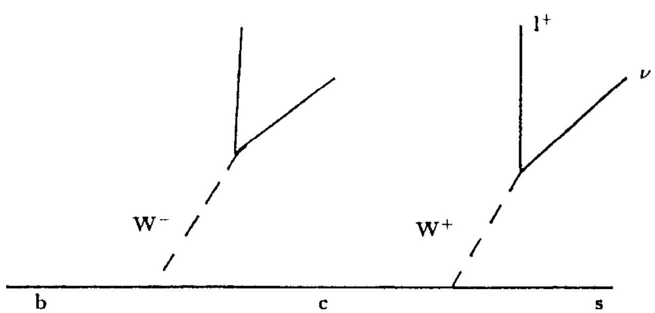

Fig. 2b. Diagram for production of "cascade" lepton in B meson decay

calculated and those events having $R_2 < 0.4$ are retained, where $R_2 = H_2/H_0$.

Other backgrounds come from B decays. For example, B mesons are known to decay to Ψ mesons which can in turn decay into lepton pairs. Events are rejected if the lepton candidate can be combined with any other track in the event to yield a mass within 60 MeV of the Ψ mass. The major background from B meson decay, however, is the so-called "cascade" leptons. These leptons are produced via the process depicted in Figure 2b. where a lepton is emitted in the decay of the secondary charmed quark. These leptons are in general much softer than the primary leptons and are largely removed with a momentum cut.

3.1 Lepton Identification

Lepton identification has been described elsewhere [7-8] for a CLEO detector with a different central drift chamber. The muon identification remains as described in Ref. 7. Charged tracks found in the drift chamber are matched to crossed hits in the muon chambers. The overall muon chamber efficiency, including geometrical acceptance, varies with the track momentum but plateaus at 60% for $p_l > 1.8$ GeV/c. Electron identification is provided by the dE/dx measurements of the central drift chamber, and by the outer octants which contain electromagnetic calorimetry, time-of-flight counters, and dE/dx counters. The drift chamber covers a region in solid angle of 80% of 4π, while the outer octants cover 47% of 4π. For tracks which pass through both the drift chamber and the outer octants, electrons with $2.6 > p_l > 1.4$ GeV/c are identified with 90% efficiency and a fake probability of 0.2%. For tracks passing through only the drift chamber and with $|\cos\theta| \leq 0.8$, the efficiency is 60% with a fake probability of 0.6%.

The continuum subtracted momentum spectrum for identified leptons coming from the $\Upsilon(4S)$ is presented in Figure 3. Electrons and muons are shown separately. The solid curve represents a fit to two components: direct leptons from the

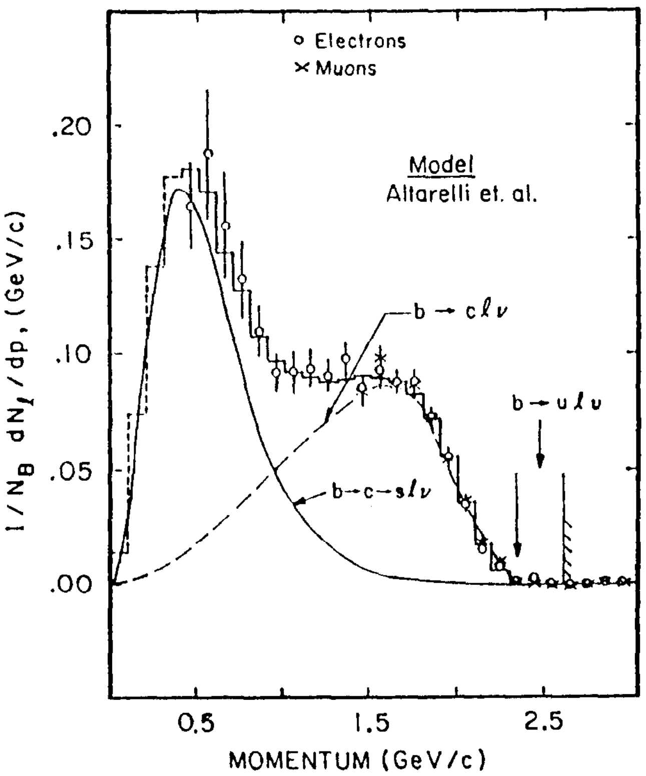

Fig. 3. Continuum subtracted momentum spectrum for identified electrons and muons coming from the $\Upsilon(4S)$

$b \to c$ transition and cascade leptons from the secondary $c \to s$ transition. The kinematic limit for leptons produced in the $b \to c$ transition is 2.4 GeV/c. For the exclusive semileptonic decay analyses presented below, leptons are selected in the range $1.4 < p_l < 2.4$ GeV/c, where the lower momentum bound is chosen to remove most of the cascade leptons. For $b \to u$ transitions the kinematic limit is $p_l = 2.7$ GeV/c, somewhat higher than for $b \to c$ due to the lighter accompanying hadron. The search for leptons coming from $b \to u$ transitions, presented in section 4, is made in the lepton momentum range of 2.2 - 2.6 GeV/c.

3.2 The Decay $\bar{B}^0 \to D^{*+}l^-\bar{\nu}$

In order to look for the exclusive decay $\bar{B}^0 \to D^{*+}l^-\bar{\nu}$,[9] one must first isolate a clean sample of D^{*+} mesons. These are identified from the decay chain $D^{*+} \to D^0\pi^+$; $D^0 \to K^-\pi^+$ or $D^0 \to K^-\pi^+\pi^-\pi^+$. Only D^{*+} mesons with $p_{D^*} < 2.5$ GeV/c are used in order to suppress those produced in continuum events.

One cannot use the B reconstruction technique of section 2 to search for a $\bar{B}^0 \to D^{*+}l^-\bar{\nu}$ signal due to the undetectable neutrino. Instead, we choose events with a D^{*+} and a lepton (l^-) and calculate a missing mass (MM). We know that the energy of our $\bar{B}^0$ is equal to the beam energy E_{beam}. If we make the approximation that the $\bar{B}^0$ is at rest, we obtain:

$$MM^2 = (E_{beam} - E_{D^*} - E_l)^2 - (\vec{p}_{D^*} + \vec{p}_l)^2,$$

where all of the quantities on the right-hand side are known. The $\bar{B}^0$ meson is not produced at rest in $\Upsilon(4S)$ decay, but rather with a momentum of roughly 300 MeV/c. The effect of this momentum on a MM^2 signal from $\bar{B}^0 \to D^{*+}l^-\bar{\nu}$ is to give it a broad width about its central value of zero. This width is determined by Monte Carlo simulation to be 0.8 GeV^2 (FWHM). In Figure 4 we see a large signal in the MM^2 data centered at zero, and with the expected width.

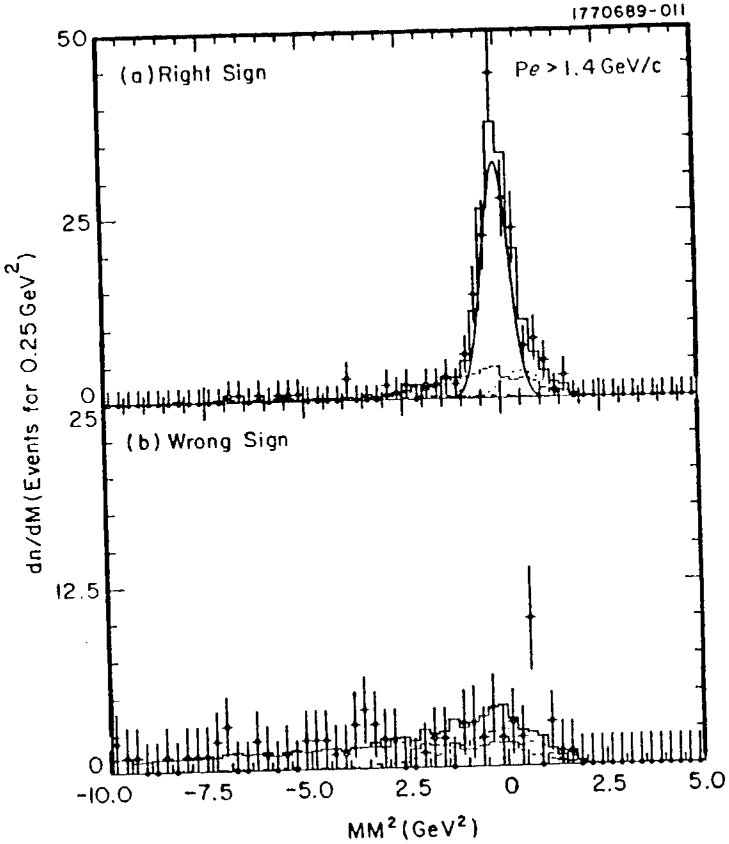

Fig. 4. Missing mass squared distributions for a) right sign $D^{*+}l^-$ and b) wrong sign $D^{*+}l^+$. Curves are described in the text.

There are a number of sources in the data of events containing both a D^{*+} and a charged lepton. Various background sources were considered and measured using both the data and Monte Carlo simulation. We consider processes that will produce the correct charge combination $D^{*+}l^-$, and as a check of our understanding we also consider sources of the wrong charge combination $D^{*+}l^+$. Right sign events can arise from five sources: 1) the $\bar{B}^0 \to D^{*+}l^-\bar{\nu}$ signal; 2) the decays $\bar{B}^0 \to D^{*+}\pi^0 l^-\bar{\nu}$ and $B^- \to D^{*+}\pi^- l^-\bar{\nu}$, where the $D^*\pi$ may be either non-resonant or come via a D^{**}; 3) fake l^- or fake D^{*+} production; 4) a cascade process with D^{*+} production from one B and l^- production from the semileptonic decay of the charmed daughter of the other B; 5) an event with $B^0\bar{B}^0$ mixing can produce a D^{*+} from one B, and a right sign l^- from the semileptonic decay of the other B. Sources of wrong sign events are: 1) a D^{*+} from one B and a l^+ from the semileptonic decay of the other B; 2) an event with $B^0\bar{B}^0$ mixing can produce a D^{*+} from one B, and a l^+ from the semileptonic decay of the charmed daughter of the other B; 3) fake l^+ or fake D^{*+} production. Each of these sources is accounted for in fits to the data. Right sign events due to $B \to D^{**} + X$ appear on the MM^2 plot as a skewed Gaussian centered at a small positive value of MM^2 and with a shape predicted by Monte Carlo. (The shape of non-resonant $D^*\pi$ is very similar and cannot be distinguished from D^{**} in the fit.) Processes involving $B^0\bar{B}^0$ mixing or cascade leptons are also described by Monte Carlo simulation. The shape of the contribution due to D^{*+} fakes is determined by an analysis of D^0 sidebands. The shape due to lepton fakes is obtained by combining a D^{*+} with another hadron in the event.

In Figure 4a. the continuum subtracted right sign data are shown together with a fit to the data. The solid histogram shows the overall fit and the various other curves show the components of that fit. In terms of the sources mentioned above, the solid curve represents the $D^{*+}l^-\bar{\nu}$ signal, the dotted curve represents source 2), the dashed curve represents the fakes, and the dot-dashed curve represents the cascade and mixing sources 4) and 5). Figure 4b. presents the continuum subtracted wrong sign data, an overall fit given by the solid histogram, a dot-dashed histogram representing wrong sign sources 1) and 2), and a dashed histogram representing the contributions from fakes.

In the fit to the right sign data 107 ± 12 events are attributed to the $\bar{B}^0 \to D^{*+}l^-\bar{\nu}$ signal. We obtain a branching ratio for this decay of $(4.6 \pm 0.5 \pm 0.7)\%$ after efficiency correction and using the ISGW[10] model to correct for the unmeasured portions of the lepton momentum spectrum. The contribution from the decays $\bar{B}^0 \to D^{**+}l^-\bar{\nu}$ and $B^- \to D^{**0}l^-\bar{\nu}$ is 18 ± 10 events. Assuming the branching ratios for these two processes are equal we obtain $B(\bar{B}^0 \to D^{**+}l^-\bar{\nu}) = (2.0 \pm 1.1)\%$. And lastly, the right sign and wrong sign data yield 7 ± 3 events attributed to $B^0\bar{B}^0$ mixing, which implies a mixing parameter $r = 0.15 \pm 0.07$, in good agreement with previous ARGUS[11] and CLEO[12] mixing measurements.

3.3 The Decay $B^- \to D^0 l^-\bar{\nu}$

The measurement of the branching ratio $B(B^- \to D^0 l^-\bar{\nu})$ is made in an analysis very similar to that described for $\bar{B}^0 \to D^{*+}l^-\bar{\nu}$. Here we calculate a missing mass squared for events containing a D^0 and l^-, whereas before we took $D^{*+}l^-$ events. There are some important differences between this analysis and the $D^{*+}l^-\bar{\nu}$ analysis. First of all, the D^0 signal sits on top of a much larger background than the D^{*+}. Only the relatively clean decay channel $D^0 \to K^-\pi^+$ is used here, but we must still perform a careful D^0 sideband subtraction to remove a sizable fake D^0 background. Another added difficulty in this analysis is the larger number of B decays that feed down into the $D^0 l^-$ signal. The decays $\bar{B}^0 \to D^{*+}l^-\bar{\nu}$ and $B^- \to D^{*0}l^-\bar{\nu}$ followed by $D^{*+} \to D^0\pi^+$ and $D^{*0} \to D^0\pi^0$ each contribute, as do the B to D^{**} semileptonic decays. We use our previously measured branching ratio to calculate the contribution from $\bar{B}^0 \to D^{*+}l^-\bar{\nu}$, but the $B^- \to D^{*0}l^-\bar{\nu}$ contribution must be treated as an unknown. The shape of the contribution of this process to the $D^0 l^-$ MM^2 plot is calculated from Monte Carlo simulations.

The $D^0 l^-$ MM^2 distribution is shown in Figure 5 where not only has a continuum subtraction been performed, but appropriately scaled D^0 sideband and fake lepton data have been subtracted as well. The solid histogram represents a fit to the data and the fitted contributions from $D^0 l^-\bar{\nu}$ (solid curve), $(D^{*0} + D^{*+})l^-\bar{\nu}$ (dashed curve), $D^{**}l^-\bar{\nu}$ (dotted curve), and background processes (dot-dashed curve) are shown separately. In the fit all shapes are predetermined from Monte Carlo simulations, the D^{**}/D^* ratio is fixed to the value found in the $D^{*+}l^-\bar{\nu}$ analysis, and only the numbers of $D^0 l^-\bar{\nu}$ and $D^{*0}l^-\bar{\nu}$ events are allowed to vary (and proportionately the $D^{**}l^-\bar{\nu}$). The background processes shown as the dot-dashed curve are calculated prior to the fit and fixed in shape and numbers of events. The dominant backgrounds come from "cascade" leptons and events with $B^0\bar{B}^0$ mixing. The numbers of events extracted from the fit are $N(B^- \to D^0 l^-\bar{\nu}) = 58 \pm 20$ and $N(B \to D^* l^-\bar{\nu}) = 214 \pm 24$. After correcting for detector acceptance, and using the ISGW[10] model to correct for the unmeasured portion of the lepton momentum spectrum, we obtain the (preliminary) branching ratios: $B(B^- \to D^0 l^-\bar{\nu}) = (2.4 \pm 0.8^{+0.7}_{-0.8})\%$ and $B(B^- \to D^{*0}l^-\bar{\nu}) = (3.9 \pm 0.8^{+1.1}_{-0.8})\%$.

Before concluding our discussion of exclusive semileptonic branching ratios we note a couple of interesting ratios. First, the ratio of vector to pseudoscalar production in semileptonic B decay is given by:

$$\frac{\Gamma_{SL}(D^*)}{\Gamma_{SL}(D)} = \frac{B(B^- \to D^{*0}l^-\bar{\nu})}{B(B^- \to D^0 l^-\bar{\nu})} = 1.6^{+1.2}_{-0.6}{}^{+0.7}_{-0.5}.$$

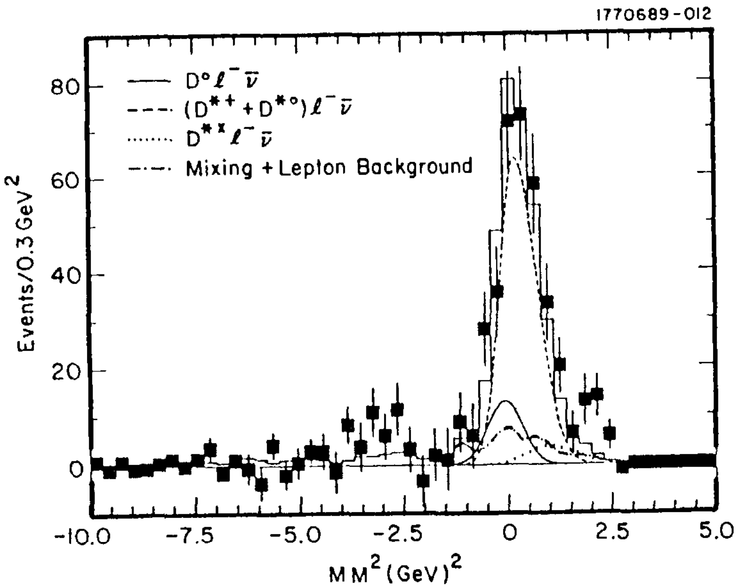

Fig. 5. Missing mass squared distribution for $B^- \to D^0 l^- \bar{\nu}$. Continuum and D^0 sidebands have been subtracted. Curves are described in the text.

Next, we have from isospin symmetry that $\Gamma(\bar{B}^0 \to D^{*+} l^- \bar{\nu}) = \Gamma(B^- \to D^{*0} l^- \bar{\nu})$, therefore the ratio of the lifetimes of the charged and neutral B is given by:

$$\frac{\tau(B^-)}{\tau(\bar{B}^0)} = \frac{B(B^- \to D^{*0} l^- \bar{\nu})}{B(\bar{B}^0 \to D^{*+} l^- \bar{\nu})} = 0.85 \pm 0.20 \begin{array}{l} +0.22 \\ -0.16 \end{array}.$$

This is the first measurement of this ratio of lifetimes. Note that the lifetime ratio depends on our assumption that the $\Upsilon(4S)$ decays to $B^0 \bar{B}^0$ and $B^+ B^-$ in equal amounts, and should this $\bar{B}^0/B^-$ production ratio decrease, the lifetime ratio would decrease in direct proportion.

4. Endpoint of the Lepton Momentum Spectrum

As mentioned in section 3.1, there is a kinematic limit to the momentum of leptons produced in the semileptonic decay of B mesons at the $\Upsilon(4S)$. For a $b \to c$ transition this limit is 2.4 GeV/c and for a $b \to u$ transition it is 2.7 GeV/c. A search for leptons having momentum beyond the kinematic limit for $b \to c$ is a very sensitive method of searching for $b \to u$. In this section we will show new data on the lepton endpoint spectrum which indicate that $b \to u$ transitions have been observed.[13]

The techniques used to identify electrons and muons have been discussed in section 3.1. The lepton momentum region which we will use in the search is 2.2 - 2.6 GeV/c. The search is cut off at 2.6 GeV/c because very little $b \to u$ signal remains in the 2.6 - 2.7 GeV/c region (1 - 2% in most models) and one expects a terrible signal to noise ratio given the high continuum background. The search is extended down to 2.2 GeV/c because there is a relatively small and calculable $b \to c$ background in the 2.2 - 2.4 GeV/c region and because one expects to roughly triple the statistics on any $b \to u$ signal.

Leptons from continuum processes are the largest background source. In this analysis the selection on the shape parameter R_2 is used as described in section 3. Here the effect is to reject 70% of continuum events while keeping 90% of the $B\bar{B}$ events of interest. The scaling factor by which the continuum data are multiplied to account for the ratio of $\Upsilon(4S)$ to continuum luminosities and the differences in cross section at the two energies is 2.08 ± 0.01.

Obviously, accurate momentum measurement is crucial to this analysis. The momentum resolution function for the charged particle tracking was presented in the introduction, and gives a resolution (δp) of around 20 MeV/c for the lepton endpoint region. This is perfectly adequate to prevent large numbers of $b \to c$ background leptons from appearing in the $b \to u$ signal region through measurement error. However, we must be careful to rule out large momentum mismeasurements due to systematic effects. Thus, in this analysis we impose strict track quality criteria on the candidate lepton tracks. We demand that each lepton track have at least 30 hits in the central drift chamber (out of a possible 51) and at least 5 hits in the two inner tracking chambers (out of a possible 13). The average residual of the hits is required to be less than 250 μm and the track is required to extrapolate to within 2.0 mm of the beam position.

The effect of these track quality cuts was checked in the data in two ways. First a large sample of μ-pair events was examined after imposing the cuts. It was found that fewer than 0.3% of the tracks were shifted by more than three σ from the known momentum and fewer than 0.01% were shifted by more than six σ. The isolated tracks in μ-pair events, of course, are unlikely to cause confusion in the software trackfinding procedure. In order to rule out large momentum shifts in the more complicated hadronic events, we took isolated tracks with $2.0 < p < 2.5$ GeV/c from radiative bhabha events and embedded their hits in randomly selected hadronic events. The trackfinding algorithm was then run on these embedded events and the new momenta were compared with the old. No non-Gaussian momentum tails were observed, implying that less than one $b \to c$ event will be shifted into the signal region above 2.4 GeV/c.

In Figure 6 we present the raw momentum measurements of the endpoint leptons. Electron and muon data are shown separately in the top and bottom portions (respectively) of Fig. 6. Data taken on the $\Upsilon(4S)$ are shown by the diamond shaped points and the scaled continuum data are shown by the crosses. Fits to the continuum data are shown by the solid curves in the figures. A large $b \to c$ signal is evident below 2.3 GeV/c in both the electron and muon data. Also, in both data sets some excess is observed is the $b \to u$ signal region 2.4 - 2.6 GeV/c.

The $b \to c$ background contribution is calculated using the ISGW model,[10] a model by Wirbel, Stech and Bauer,[14] and a model by Altarelli *et al.*[15] Charmed semileptonic decays are generated according to these models, the detector response is simulated, and QED effects are accounted for. For each model the Monte Carlo momentum spectrum is normalized to our data for leptons in the momentum region 1.5 - 2.2 GeV/c and the number of events that appear in our search region of 2.2 - 2.6 GeV/c is then determined by extrapolation. All three models give reasonable fits to the data. The number of events in the region 2.4 - 2.6 GeV/c is insensitive to the model used or to reasonable changes in the modeling procedure. In the 2.2 - 2.4 GeV/c region the models' predictions of the $b \to c$ contribution agree to within 10%.

Table 2 below presents the continuum subtracted yield of leptons in two bins of momentum together with the calculated backgrounds. For each entry, the first error quoted is statistical and the second systematic. The continuum data have

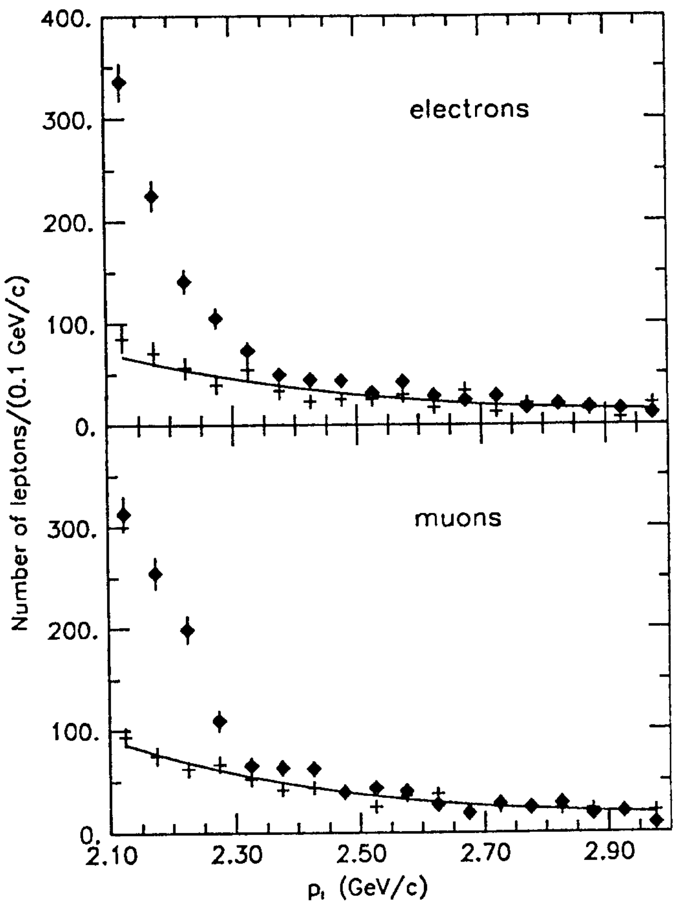

Fig. 6. Momentum spectrum in the endpoint region for electrons (top) and muons (bottom). Data on $\Upsilon(4S)$ (diamonds), continuum (crosses), and a fit (solid line) to the continuum data are shown.

been fitted to a smooth shape before subtraction, and the systematic errors given for the "l^- from $B\bar{B}$" reflect the uncertainties in this procedure.

Lepton Momentum: 2.2 – 2.4 GeV/c		
l^- from:	Electrons	Muons
$B\bar{B}$	$182 \pm 21 \pm 7$	$178 \pm 21 \pm 13$
Ψ	$2.7 \pm 0.9 \pm 0.5$	$1.7 \pm 0.6 \pm 0.4$
Ψ'	$1.7 \pm 0.6 \pm 0.6$	$1.7 \pm 0.6 \pm 0.6$
$b \to c$	$145 \pm 2 \pm 10$	$146 \pm 2 \pm 10$
$b \to u$	$33 \pm 21 \pm 14$	$29 \pm 21 \pm 21$
Lepton Momentum: 2.4 – 2.6 GeV/c		
l^- from:	Electrons	Muons
$B\bar{B}$	$49 \pm 15 \pm 6$	$26 \pm 14 \pm 9$
Ψ	$1.0 \pm 0.5 \pm 0.5$	$0.8 \pm 0.4 \pm 0.4$
Ψ'	$1.0 \pm 0.5 \pm 0.5$	$1.0 \pm 0.5 \pm 0.5$
$b \to c$	$0.4 \pm 0.1 \pm 0.3$	$0.6 \pm 0.1 \pm 0.3$
$b \to u$	$47 \pm 15 \pm 6$	$24 \pm 14 \pm 8$

Table 2. Endpoint Lepton Yields and Backgrounds

In Table 2, "l^- from $B\bar{B}$" represents the lepton yield after continuum and fake subtraction. The fakes background includes misidentified electrons and muons and the effects of spurious hits in the muon chambers. Other sources of background leptons have been considered including converted photons, leptonic decays of vector mesons, cascade leptons from B decay, π^0 Dalitz decays, and muons from pion or kaon decays. It is calculated that all of these sources together contribute less than one event to our selected sample.

In addition to measuring the numbers of leptons in the $\Upsilon(4S)$ data and the off-resonance data, a mean value of the shape parameter R_2 was calculated for each data set in each momentum interval. These mean values were $\langle R_2\rangle_{4S} = 0.250 \pm 0.003$ and $\langle R_2\rangle_{off} = 0.287 \pm 0.006$ in the 2.2 - 2.4 GeV/c interval, and $\langle R_2\rangle_{4S} = 0.278 \pm 0.005$ and $\langle R_2\rangle_{off} = 0.302 \pm 0.007$ in the 2.4 - 2.6 GeV/c interval. Monte Carlo simulations of $\Upsilon(4S)$ decays where at least one B decays semileptonically predict a mean R_2 for $B\bar{B}$ events of $\langle R_2\rangle_{B\bar{B}} = 0.213 \pm 0.007$ for the lower momentum range and $\langle R_2\rangle_{B\bar{B}} = 0.216 \pm 0.010$ for the higher momentum range. (The errors on $\langle R_2\rangle_{B\bar{B}}$ are entirely systematic and arise from uncertainties in the $b \to ul^-\bar{\nu}$ modeling.) The measured mean R_2 values support the assumption that the observed lepton excess is coming from B decay. Further, for each momentum interval we can take the three measured quantities, lepton yield for $\Upsilon(4S)$, n_{4S}, and mean R_2 for $\Upsilon(4S)$ and off-resonance, together with our $\langle R_2\rangle_{B\bar{B}}$, and calculate a yield of leptons from $B\bar{B}$ events from: $y = n_{4S}(\langle R_2\rangle_{off} - \langle R_2\rangle_{4S})/(\langle R_2\rangle_{off} - \langle R_2\rangle_{BB})$. After subtracting fakes and the backgrounds listed in Table 2, we get numbers of leptons (e^- plus μ^-) attributable to $b \to u$ transitions in each momentum range: $64 \pm 49 \pm 44$ for 2.2 - 2.4 GeV/c and $88 \pm 29 \pm 12$ for 2.4 - 2.6 GeV/c. Averaging these yields with the $b \to u$ yields of Table 2, and taking the correlations between them into account we get $62 \pm 28 \pm 28$ $b \to u$ leptons for 2.2 - 2.4 GeV/c and $76 \pm 18 \pm 8$ $b \to u$ leptons for 2.4 - 2.6 GeV/c. The $b \to u$ branching ratios we obtain from these averaged yields are: $B(2.2 - 2.4) = (1.6 \pm 0.7 \pm 0.7) \times 10^{-4}$, and $B(2.4 - 2.6) = (1.8 \pm 0.4 \pm 0.3) \times 10^{-4}$, where we have averaged over the e^- and μ^- branching ratios.

We can now extract values for the ratio of the KM matrix elements $|V_{ub}|/|V_{cb}|$ using our measured branching ratios, $B(p)$, and the relation:

$$\frac{|V_{ub}|^2}{|V_{cb}|^2} = \frac{B(p)}{B_0}\frac{1}{d},$$

where B_0 is the average of the semileptonic branching ratios for $b \to ce^-\bar{\nu}_e$ and $b \to c\mu^-\bar{\nu}_\mu$ (which has been previously determined to be $10.2 \pm 0.2 \pm 0.7\%$[16]), and d is a model dependent parameter which must account for the semileptonic decay width of $b \to u$ transitions and the fraction of the $b \to u$ momentum spectrum which is in the observed region. In Table 3 we have calculated d for each momentum interval from our three previously mentioned models and a model by Korner and Schuler,[17] and give the corresponding values of $|V_{ub}|^2/|V_{cb}|^2$. We note that the values derived from the 2.2 - 2.4 GeV/c interval are somewhat smaller than those for the 2.4 - 2.6 GeV/c range. This may be due to statistical fluctuations in our data, or to inadequate models of the $b \to c$ and $b \to u$ momentum spectra. We emphasize though that our evidence for an excess of leptons above 2.4 GeV/c is quite insensitive to the models.

model	(2.2 - 2.4) GeV/c $\times 10^{-2}$	(2.4 - 2.6) GeV/c $\times 10^{-2}$
ISGW[10]	1.3 ± 0.8	3.6 ± 1.0
WBS[14]	0.8 ± 0.5	1.8 ± 0.5
Alt.[15]	0.5 ± 0.3	1.4 ± 0.4
KS[17]	0.6 ± 0.4	1.1 ± 0.3

Table 3. $|V_{ub}|^2/|V_{cb}|^2$ for Various Models and Lepton Momentum Ranges

After this talk was presented in July, the ARGUS collaboration announced similar results[3] on the endpoint of the lepton spectrum. Using events with both single and double lepton tags, ARGUS observes a lepton excess of more than 3 σ in significance. They extract a value of $|V_{ub}|/|V_{cb}| = 0.10 \pm 0.03$ using the Altarelli model,[15] in good agreement with our values for the same model.

5. Continuum Production of Charmed Mesons and Baryons

We now turn from the subject of B meson decay to discuss new results on the continuum production of charmed mesons and baryons. For these analyses we use 428 pb^{-1} of data taken on the continuum and at the $\Upsilon(4S)$ and $\Upsilon(5S)$. In each analysis the selection $x > 0.5$ is made, where $x = p/p_{max}$, to remove particles produced in B meson decay. We first discuss our observation of the decay $D^0 \to K^0\bar{K}^0$, then we present new measurements of D_s^+ decay modes, and finally we present results on charmed baryon production.

5.1 The Decay $D^0 \to K^0\bar{K}^0$

The decay $D^0 \to K^0\bar{K}^0$ is of interest because it cannot proceed via a simple spectator process. The decay can occur via W exchange diagrams as illustrated in Figure 7. However, unless SU(3) flavor breaking occurs these two diagrams cancel. The other possible mechanism for the production of this decay is final state interactions. The E400 collaboration[18] has previously observed this decay with a branching ratio of $B(D^0 \to K^0\bar{K}^0) = (0.10 \pm 0.08)\%$.

We have been able to observe a very clean signal in our data by selecting for the decay chain $D^{*+} \to D^0\pi^+; D^0 \to K_s^0 K_s^0$. The K_s^0 candidates are observed via their decay to $\pi^+\pi^-$. The secondary decay vertex of the K_s^0 is required to be at least 0.5 cm from the primary event vertex, the secondary vertex is required to be well defined in the three spatial dimensions, and the neutral momentum vector of the K_s^0 is required to point back to the event vertex. A D^0 candidate is formed from two of these K_s^0 candidates, then a pion is added to form the D^{*+} candidate. A D^{*+} candidate is required to have $p_{D^*} > 2.5$ GeV/c, and a mass difference $m_{D^*} - m_D$ within 1.2 MeV of the known mass difference 145.5 MeV. The resulting $K_s^0 K_s^0$ mass spectrum is shown in Figure 8a. We see five events

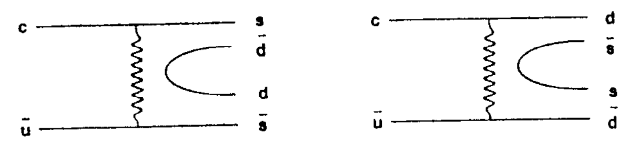

Fig. 7. Diagrams for $D^0 \to K^0\bar{K}^0$.

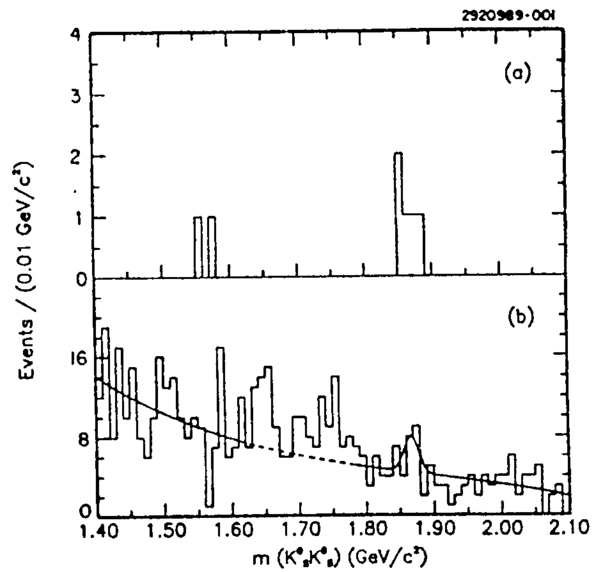

Fig. 8. $K_s^0 K_s^0$ invariant mass plot for a) D^0 produced via $D^{*+} \to D^0\pi^+$ and b) inclusive D^0 production.

on an estimated background of 0.3 event. Each of the five events yields a mass consistent within our experimental resolution with the D^0 mass.

A peak can also be seen at the D^0 in the $K_s^0 K_s^0$ mass spectrum without requiring that the D^0 come via a D^{*+}. This inclusive D^0 spectrum is shown in Fig. 8b. where $p_{D^0} > 2.5$ GeV/c. Fitting this distribution to a Gaussian on a polynomial background, 11 ± 5 events are seen on a comparably sized background. The region 1.6 to 1.78 GeV is excluded from this fit to avoid the effects of "satellite" peaks. To extract a branching ratio we take our result from the D^{*+} selection technique and normalize it to the decay $D^0 \to \bar{K}^0\pi^+\pi^-$. A signal of 457 $\pm$ 23 events is seen in our data for $D^0 \to K_s^0\pi^+\pi^-$ where the D^0 comes via a D^{*+}. After correcting for the detection efficiencies for these two decays and using the Mark III value[19] $B(D^0 \to \bar{K}^0\pi^+\pi^-) = (6.4 \pm 1.1)\%$, we obtain $B(D^0 \to K^0\bar{K}^0) = (0.13^{+0.07}_{-0.05}{}^{+0.02}_{-0.02})\%$. We obtain a consistent value from the alternate analysis which does not require the D^{*+} constraint. This result is in good agreement with the E400 result and constitutes evidence for either final state interactions or flavor SU(3) symmetry breaking in charmed meson decays.

5.2 D_s^+ Decays

Now we present new measurements of D_s^+ decay modes.[20] The observed modes are $\phi\pi^+, \bar{K}^{*0}K^+, K^{*+}\bar{K}^0$, and $\bar{K}^0K^+$. The $K^{*+}\bar{K}^0$ mode is observed here for the first time. Drift chamber dE/dx measurements are used to distinguish kaons from pions in the analysis of these modes. A candidate K^+ is considered "positively" identified if the measured dE/dx of the track is greater than two standard deviations away from the expected dE/dx for a pion. A K^+ or π^+ candidate track is called "consistent" with its particle type if its dE/dx measurement is within three standard deviations of its expected value. All charged particles are required to be "consistent"with their mass interpretations in the four analyses, except for the primary kaons in the $\bar{K}^{*0}K^+$ and $\bar{K}^0K^+$ decay modes where the K^+ is required to be "positively" identified. This stricter requirement minimizes the background to these two decay modes from the decays $D^+ \to \bar{K}^{*0}\pi^+$ and $D^+ \to \bar{K}^0\pi^+$.

In Figure 9 we present the invariant mass spectra for our four decay modes for $x_{D_s^+} \geq 0.5$. In Figure 9a. we present the $\phi\pi^+$ mass distribution, where the ϕ has been identified through its decay to K^+K^-. Two helicity angle cuts are made on these data: $|cos\theta_1| > 0.4$ and $cos\theta_2 > -0.8$, where θ_1 is the angle between the kaon and the D_s^+ in the rest frame of the vector meson ϕ, and θ_2 is the decay angle of the π^+ in the D_s^+ rest frame. In Figure 9b. and 9c. the mass plots for $\bar{K}^{*0}K^+$ and $K^{*+}K_s^0$ are shown, where the $\bar{K}^{*0}$ and K^{*+} are identified via their respective decays to $K^-\pi^+$ and $K_s^0\pi^+$. The K_s^0 is found via its long-lived decay to $\pi^+\pi^-$ in a manner similar to that described in the previous section. For these two decay modes the same helicity angle selection on θ_1 is made as in the $\phi\pi^+$ case. The mass plot for the fourth decay channel, $K_s^0K^+$ is shown in Figure 9d. The raw yield, efficiency corrected $\sigma\cdot$Br, and relative branching ratio to $\phi\pi^+$ are given in Table 4 for each of our four modes.

D_s^+ Decay Mode	Raw Yield	$\sigma\cdot$Br (pb)	Br/Br($D_s^+ \to \phi\pi^+$)
$\phi\pi^+$	405 $\pm$ 27	6.5$\pm$0.5$\pm$0.3	1
$\bar{K}^{*0}K^+$	149 $\pm$ 25	6.8$\pm$1.1$\pm$0.7	1.05$\pm$0.17$\pm$0.12
$K^{*+}\bar{K}^0$	40 $\pm$ 7	7.8$\pm$1.4$\pm$0.8	1.20$\pm$0.21$\pm$0.13
$\bar{K}^0K^+$	110 $\pm$ 19	6.4$\pm$1.1$\pm$0.6	0.99$\pm$0.17$\pm$0.10

Table 4. Results on $e^+e^- \to D_s^+X$ ($x_{D_s^+} \geq 0.5$).

For three of our four modes (the exception being $\bar{K}^{*0}K^+$) a prominent D^+ peak is observed in addition to the D_s^+. By fitting these three spectra each to two

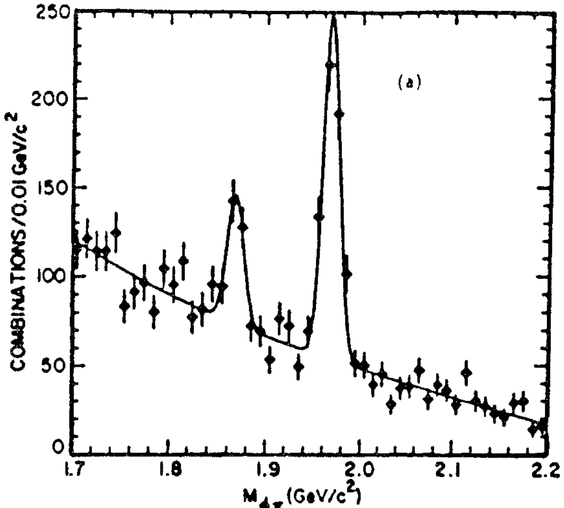

Fig. 9a. $\phi\pi^+$ invariant mass spectrum for $x_{D_s^+} \geq 0.5$.

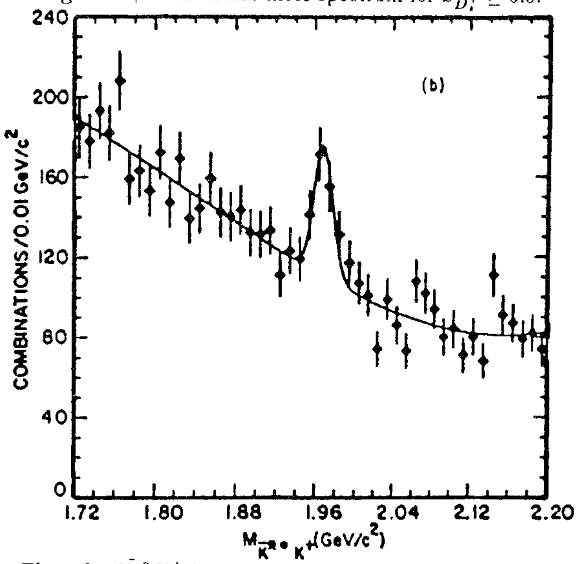

Fig. 9b. $\bar{K}^{*0}K^+$ invariant mass spectrum for $x_{D_s^+} \geq 0.5$.

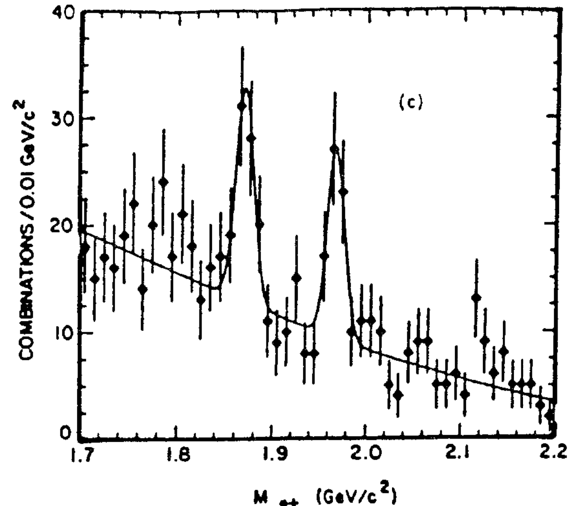

Fig. 9c. $K^{*+}K_s^0$ invariant mass spectrum for $x_{D_s^+} \geq 0.5$.

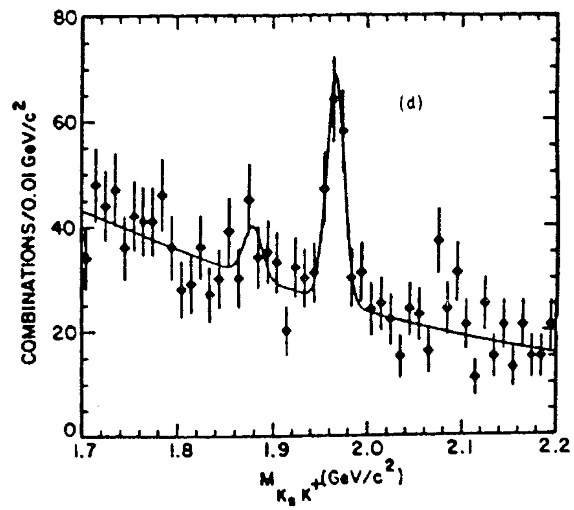

Fig. 9d. $K_s^0K^+$ invariant mass spectrum for $x_{D_s^+} \geq 0.5$.

Gaussians and a polynomial background shape, not only are the raw yields of Table 4 obtained, but mass values for the D^+ and D_s^+ are measured as well. The mass difference is of particular interest because it is relatively free from systematic error. The weighted average of the three mass difference determinations is $M(D_S^+) - M(D^+) = 98.5 \pm 1.5$ MeV.

5.3 CHARMED BARYON PRODUCTION

We now turn our attention to charmed baryons. We have observed several decay modes of the Λ_c^+, with one mode being observed for the first time. The observed yield in the data, the $\sigma\cdot$Br, and the relative branching ratio to $\Lambda_c^+ \to pK^-\pi^+$ are given in Table 5 for six different decay modes. The numbers in this table are all preliminary. As in the D_s^+ analyses described above, dE/dx measurements are used to identify the charged protons, kaons, and pions. The K^0 and Λ are identified via their long-lived decays to $\pi^+\pi^-$ and $p\pi^-$, respectively, in manners similar to that described above for the K^0. In the case of the Λ, the daughter proton is required to have a measured dE/dx consistent with the proton mass hypothesis. All data are again taken at $x \geq 0.5$.

Λ_c^+ Decay Mode	Raw Yield	$\sigma\cdot$Br (pb)	Br/Br($\Lambda_c^+ \to pK^-\pi^+$)
$pK^-\pi^+$	690 $\pm$ 70	5.7$\pm$0.6$\pm$0.6	1
$p\bar{K}^0$	132 $\pm$ 18	2.9$\pm$0.4$\pm$0.3	0.51$\pm$0.09$\pm$0.03
$p\bar{K}^0\pi^+\pi^-$	82 $\pm$ 23	2.9$\pm$0.8$\pm$0.6	0.51$\pm$0.15$\pm$0.03
$\Lambda\pi^+$	90 $\pm$ 13	1.0$\pm$0.2$\pm$0.1	0.18$\pm$0.04$\pm$0.02
$\Lambda\pi^+\pi^-\pi^+$	269 $\pm$ 34	4.3$\pm$0.5$\pm$0.4	0.75$\pm$0.12$\pm$0.08
$\Xi^-K^+\pi^+$	32 $\pm$ 7	0.9$\pm$0.2$\pm$0.2	0.16$\pm$0.04$\pm$0.02

Table 5. Results on $e^+e^- \to \Lambda_c^+ X$ ($x_{\Lambda_c^+} \geq 0.5$).

The decay $\Xi^-K^+\pi^+$ is observed here for the first time. The Ξ^- is found in the decay chain $\Xi^- \to \Lambda\pi^-; \Lambda \to p\pi^-$. The $p\pi^-$ invariant mass of the daughter Λ candidate is required to be within 6 MeV of the known Λ mass, and the intersection point between the Λ and the π^- is required to be inside the Λ decay vertex and at least 4 mm away from the primary event vertex. Ξ^- candidates having a reconstructed mass within 5 MeV of the known Ξ^- mass are accepted for further analysis. The number of Ξ^-'s so obtained is 1006 $\pm$ 43 over a background of 563. The $\Xi^-K^+\pi^+$ invariant mass spectrum is shown in Figure 10. The signal at the Λ_c^+ mass contains 32 $\pm$ 7 events.

The measured masses of the six Λ_c^+ decay modes are all in agreement. A preliminary average mass value of $M_{\Lambda_c^+} = 2285.2 \pm 0.7 \pm 3.0$ MeV is obtained from these data.

The Ξ^- sample described above was also used in a search for the charmed strange baryons Ξ_c^0 (csd) and Ξ_c^+ (csu),[21] via the decay modes $\Xi_c^0 \to \Xi^-\pi^+$ and $\Xi_c^+ \to \Xi^-\pi^+\pi^+$. In Figure 11a. we show the invariant mass plot for $\Xi^-\pi^+$, and in Figure 11b. we show the $\Xi^-\pi^+\pi^+$ distribution. As with the other charm analyses, we take $x_{\Xi_c} \geq 0.5$ in both plots. In the Ξ_c^0 analysis we require that $cos\theta > -0.8$, where θ is the decay angle of the π^+ in the Ξ_c^0 rest frame. The spectrum of Figure 11a. is fitted to a Gaussian signal with a fixed FWHM of 25 MeV on a polynomial background. This fit yields 18.8 $\pm$ 4.9 events with a mass of 2472$\pm$3$\pm$4 MeV. Fitting Figure 11b. to a Gaussian (FWHM = 22 MeV) and a polynomial background yields 23.0 $\pm$ 6.3 events and a mass of $2467 \pm 3 \pm 4$ MeV. The isospin mass splitting between the two states is found to be $M(\Xi_c^+) - M(\Xi_c^0) = (-5 \pm 4 \pm 1)$ MeV. The systematic error of 1 MeV comes from the uncertainty in the difference in the mass scales introduced by the additional pion in the Ξ_c^+ decay. The Ξ^0 state was observed by CLEO[22] for the first time, and this is the first measurement of

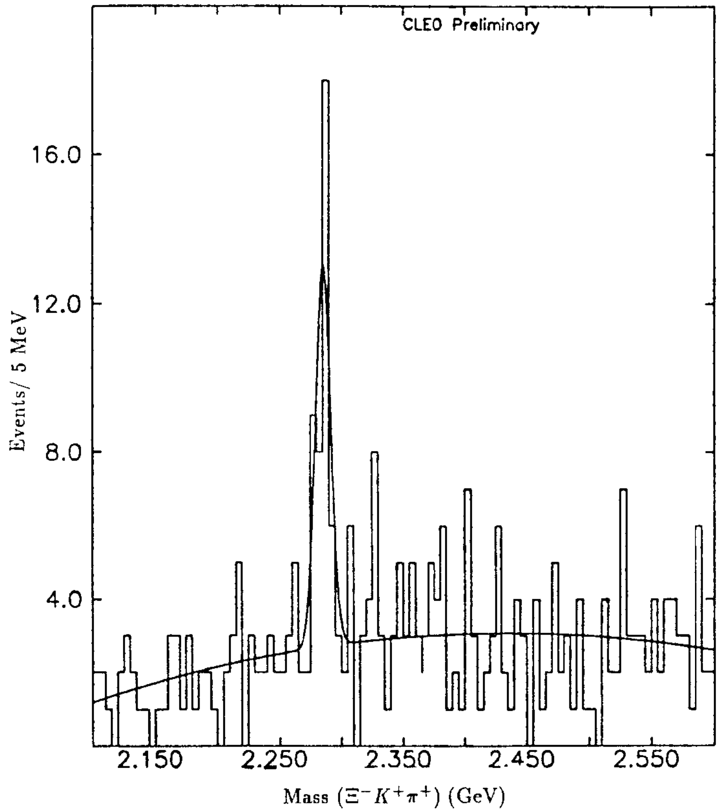

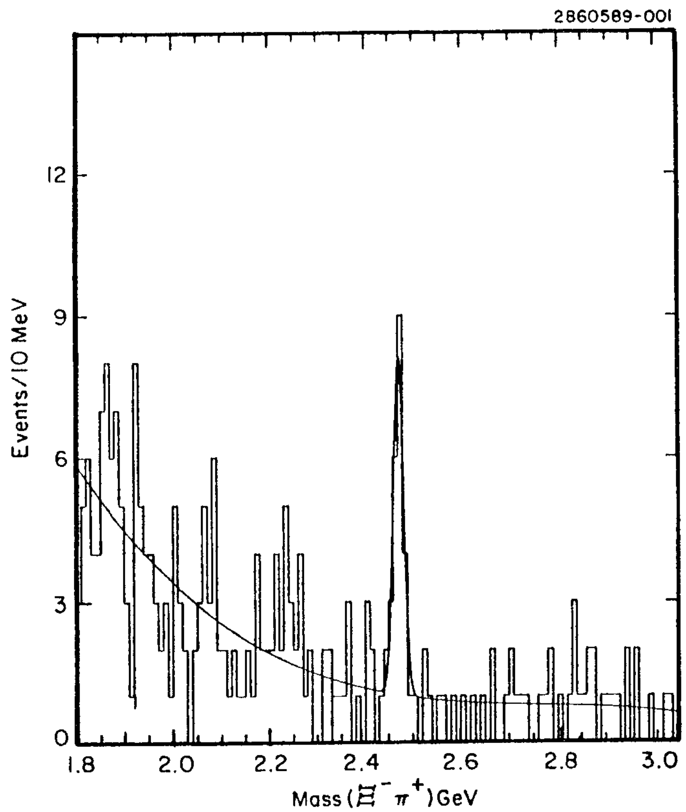

Fig. 10. $\Xi^- K^+ \pi^+$ invariant mass spectrum.

Fig. 11a. $\Xi^- \pi^+$ invariant mass spectrum.

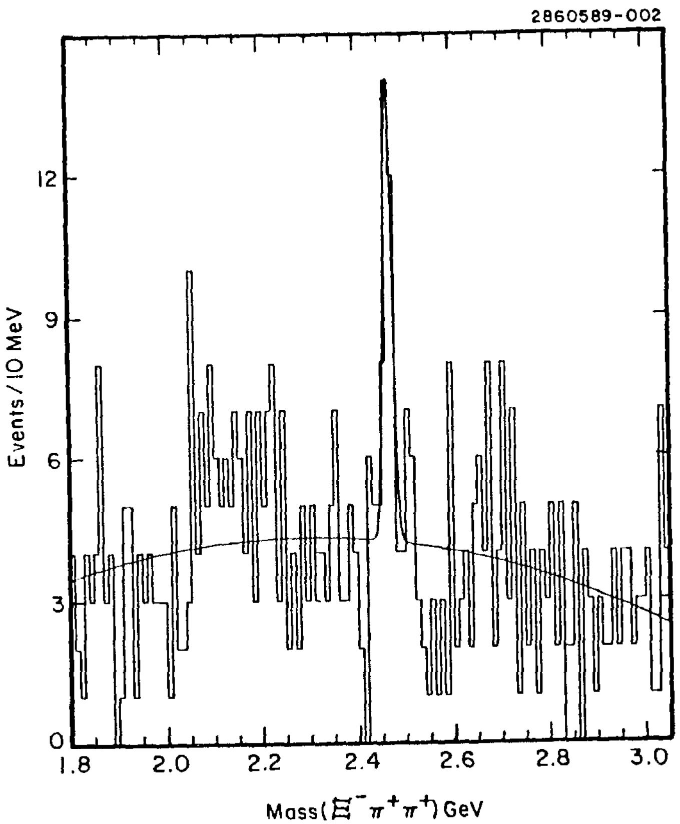

Fig. 11b. $\Xi^-\pi^+\pi^+$ invariant mass spectrum.

the isospin mass splitting by a single experiment.

6. *B* Meson Decays to Baryons

Our final subject is B meson decays into baryons. One mechanism for the production of baryon - antibaryon pairs in B meson decay is illustrated in Figure 12a. Here we have a spectator decay process with a diquark pair produced from the vacuum. The c quark combines with a diquark to produce a charmed baryon $\mathbf{B_c}$, while the light spectator quark combines with the anti-diquark to produce the compensating baryon $\bar{\mathbf{B}}$. If there is no $s\bar{s}$ popping from the vacuum, the diquark will be composed of two light quarks and the charmed baryon, $\mathbf{B_c}$, will either be a Λ_c^+, or a baryon that will decay via the Λ_c^+. The compensating baryon, $\bar{\mathbf{B}}$, will be either a $\bar{p}$ or $\bar{n}$ in this case. Should $s\bar{s}$ popping occur we will get $\mathbf{B_c} = \Xi_c$ and $\bar{\mathbf{B}} = \bar{\Lambda}$.

To explore the baryon production mechanism in B meson decay we make a series of inclusive measurements of single baryon and baryon-antibaryon pair production in our $\Upsilon(4S)$ data. The results of these measurements are presented in Table 6 below. The p, Λ, and Ξ^- are identified by the dE/dx and secondary vertex methods described in section 5. Protons are required to be "positively" identified, and for the $\bar{B} \to pX$ inclusive measurement only $\bar{p}$ data were used to avoid the large background of protons coming from beam-gas and beam-wall interactions. The large Λ/p ratio observed in the B decay data suggest that the Λ_c^+ is being produced. The Λ_c^+ is also seen directly. In Figure 12b. we show $pK^-\pi^+$ combinations for $x < 0.5$ for the $\Upsilon(4S)$ data, and the scaled continuum. There is an obvious signal in the $\Upsilon(4S)$ data, and none in the continuum where the charmed baryons are expected to be produced dominantly at high x. The product of branching ratios obtained from the continuum subtraction of these

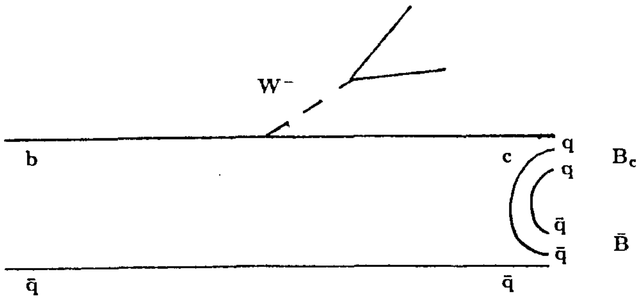

Fig. 12a. Diagram for B Meson decay into baryons.

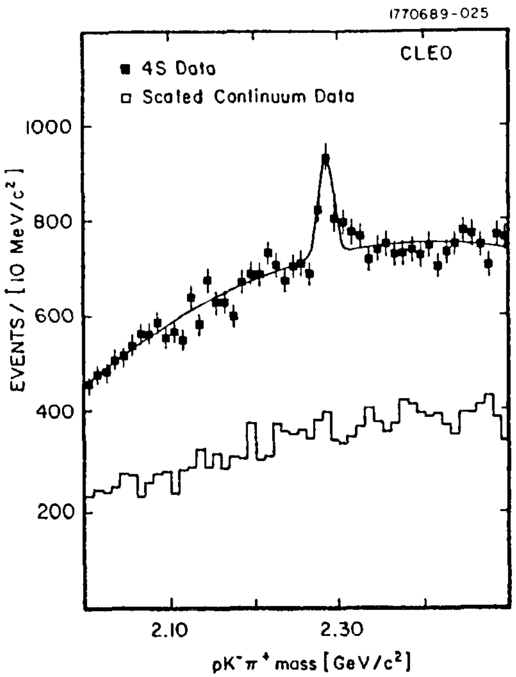

Fig. 12b. $pK^-\pi^+$ invariant mass plot for $x < 0.5$. Data points represent $\Upsilon(4S)$; histogram gives scaled continuum data.

data is presented in Table 6. Measurements from the ARGUS collaboration[23] are also presented in Table 6, and are in good agreement with the CLEO values.

Inclusive Branching Ratio	Branching Ratio (%)	
$\bar{B} \to$	CLEO	ARGUS
pX	$8.4 \pm 0.5 \pm 0.8$	$8.2 \pm 0.5^{+1.3}_{-1.0}$
$\Lambda^0 X$	$3.9 \pm 0.4 \pm 0.4$	$4.2 \pm 0.5 \pm 0.6$
$\Xi^- X$	$0.26 \pm 0.04 \pm 0.05$	0.28 ± 0.14
$\Lambda_c^+ X \cdot B(\Lambda_c^+ \to pK^-\pi^+)$	$0.28 \pm 0.05 \pm 0.05$	$0.30 \pm 0.12 \pm 0.06$
$p\bar{p}X$	$2.6 \pm 0.1 \pm 0.4$	$2.5 \pm 0.2 \pm 0.2$
$\Lambda^0 \bar{p} X$	$2.5 \pm 0.3 \pm 0.3$	$2.3 \pm 0.4 \pm 0.3$
$\Lambda^0 \bar{\Lambda} X$	< 0.4	< 0.9

Table 6. Inclusive Branching Ratios for B Meson Decays to Baryons

The momentum spectra we observe for $\bar{B} \to pX$, $\bar{B} \to \Lambda X$, and $\bar{B} \to \Xi^- X$ are consistent with what we would expect from our simple spectator process. Also, the lack of $\Lambda\bar{\Lambda}$ production and the small amount of Ξ^- production relative to Λ argues for little $s\bar{s}$ popping from the vacuum. (As we have seen in section 5.3, the Λ_c^+ does decay to Ξ^-, so the observation of Ξ^- production does not necessarily indicate $s\bar{s}$ popping in the B meson decay.) If we assume the spectator production mechanism of Figure 12a, and further assume that no strange quarks are produced from the vacuum, we can deduce the inclusive branching ratio for $B \to \Lambda_c^+ X$, inclusive Λ_c^+ branching ratios, and the exclusive branching ratio $B(\Lambda_c^+ \to pK^-\pi^+)$. These values are given in Table 7 below.

Decay Mode $\bar{B} \to$	Branching Ratio (%)
$\Lambda_c^+ X$	$6.8 \pm 1.0^{+2.3}_{-1.8}$
Decay Mode $\Lambda_c^+ \to$	Branching Ratio (%)
$pK^-\pi^+$	$4.1 \pm 1.1^{+1.6}_{-1.3}$
pX	$65 \pm 20 \pm 10$
$\Lambda^0 X$	$57 \pm 13 + 6$

Table 7. Branching Ratios Calculated from Results of Table 6.

We can stretch our string of deductions still further. We can use the continuum charm production cross sections of section 5, together with the results of Table 7, to get a value for the branching ratio $B(D_s^+ \to \phi\pi^+)$. The chain of reasoning goes as follows: using our measured σ_{Λ_c}·Br from continuum production, and the value $B(\Lambda_c^+ \to pK^-\pi^+) = (4.1 \pm 1.1)\%$ deduced from the B to baryons data, we obtain a value for σ_{Λ_c}, the continuum cross section for Λ_c^+ production. If we assume all charm production from the continuum goes eventually into either D^0, D^+, D_s^+ or Λ_c^+, we obtain:

$$\sigma_{D_s} = \sigma_c - \sigma_{D^0} - \sigma_{D^+} - \sigma_{\Lambda_c}.$$

The total charm cross section, σ_c is known, and measurements exist for the other three quantities on the right side of this equation. These numbers give $\sigma_{D_s} = 0.37 \pm 0.15 \pm 0.22$ pb, which together with the σ_{D_s}·Br from Table 4 yield $B(D_s^+ \to \phi\pi^+) = (2 \pm 1 \pm 1)\%$. The systematic error of 1% includes only the systematic errors involved in the cross section measurements, and not effects of the various assumptions that went into the calculation. Note that many of our assumptions would tend to make this an *overestimate* of the $\phi\pi^+$ branching ratio. For example, we have ignored the production in B decay of charmed baryons such as the Ξ_c which do not decay to Λ_c^+. Including this effect would decrease $B(\Lambda_c^+ \to pK^-\pi^+)$, decrease σ_{Λ_c}, increase σ_{D_s}, and decrease $B(D_s^+ \to \phi\pi^+)$. We have used this value of the $\phi\pi^+$ branching ratio, $(2 \pm 1)\%$, to determine the B meson branching ratios involving the D_s^+ which are presented in Table 1.

7. Conclusions

In this report we have presented a number of new results from the CLEO collaboration on B meson decays and continuum charm production. New values for the $\bar{B}^0$ and B^- masses were reported in section 2 together with branching ratios for exclusive hadronic decays of the $\bar{B}^0$ and B^-. In section 3 we reported on measurements of $B(\bar{B}^0 \to D^{*+}l^-\nu)$ and $B(B^- \to D^0 l^-\nu)$ obtained using a missing mass squared technique. Then in section 4 we discussed evidence for $b \to u$ transitions. An excess of leptons was observed beyond the $b \to c$ kinematic limit, and interpreting these data as coming from $b \to u$ transitions allowed us to determine model dependent values for the ratio of KM matrix elements $|V_{ub}|/|V_{cb}|$. In section 5 we presented results on the continuum production on charmed mesons and baryons. New measurements of $B(D^0 \to K^0\bar{K}^0)$, various D_s^+ and Λ_c^+ branching ratios, and the masses of the charmed strange baryons Ξ_c^0 and Ξ_c^+ were given. Finally, in section 6, inclusive measurements of baryon production in B decay were presented. Values for the branching ratios $B(\Lambda_c^+ \to pK^-\pi^+)$ and $B(D_s^+ \to \phi\pi^+)$ were shown to be consequences of the B to baryons measurements.

ACKNOWLEDGMENTS

I would like to thank my CLEO colleagues for enduring my numerous questions as I prepared this report. I would also like to thank the organizers of the SLAC Summer Institute for the opportunity to participate in a most enjoyable conference.

REFERENCES

1) D. Andrews *et al.*, Nucl. Instrum. Methods **211**, 47 (1983).

2) D. G. Cassel *et al.*, Nucl. Instrum. Methods **A252**, 325 (1986).

3) M. Danilov, "Recent ARGUS Results on B Mesons", talk presented at the XIV International Symposium on Lepton and Photon Interactions, Stanford CA, August 1989.

4) H. Albrecht *et al.*, Phys. Lett. **B185**, 218 (1987); K. Schubert, "Review of B-Meson Decay Results", talk presented at the Heavy Flavor Symposium, Ithaca NY, June 1989.

5) S. Behrends *et al.*, Phys. Rev. **D31**, 2161 (1985).

6) G. C. Fox and S. Wolfram, Phys. Rev. Lett. **41**, 1581 (1978).

7) Muon identification criteria are discussed in K. Chadwick*et al.*, Phys. Rev. **D27**, 475 (1983).

8) A. Chen *et al.*, Phys. Rev. Lett. **52**, 1084 (1984).

9) The $D^{*-}l^-\bar{\nu}$ analysis has been published in: D. Bortoletto *et al.*, Phys. Rev. Lett. **63**, 1667 (1989).

10) B. Grinstein and M. B. Wise, Phys. Lett. **B197**, 249 (1987); N. Isgur, D. Scora, B. Grinstein and M. B. Wise, Phys. Rev. **D39**, 799 (1989).

11) H. Albrecht *et al.*, Phys. Lett. **B192**, 245 (1987).

12) M. Artuso *et al.*, Phys. Rev. Lett. **62**, 2233 (1989).

13) This analysis has appeared in: R. Fulton *et al.*, preprint CLNS 89/951 (CLEO 89-14) (1989).

14) M. Wirbel, B. Stech and M. Bauer, Z. Phys. **C29**, 637 (1985).

15) G. Altarelli *et al.*, Nucl. Phys. **B208**, 365 (1982).

16) R. V. Kowalewski, Ph.D. thesis, Cornell Univ., 1988, (unpublished).

17) J. G. Korner and G. A. Schuler, Z. Phys. **C38**, 511 (1988).

18) J. P. Cumulat *et al.*, Phys. Lett. **B210**, 253 (1988); J. P. Cumulat private communication.

19) D. Hitlin, Nucl. Phys. **B3** (Proc. Suppl.), 179 (1988).

20) The D_s^+ analysis has been published in: W. -Y. Chen *et al.*, Phys. Lett. **B226**, 192 (1989).

21) This Ξ_c analysis has been published in: M. S. Alam *et al.*, Phys. Lett. **B226**, 401 (1989).

22) P. Avery *et al.*, Phys. Rev. Lett. **62**, 863 (1989).

23) H. Albrecht *et al.*, Phys. Lett **B210**, 263 (1988); H. Albrecht *et al.*, Z. Phys. **C42**, 519 (1989).

Recent Results on B-Decays from ARGUS

H. Kolanoski
Institut für Physik, Universität Dortmund, Fed. Rep. of Germany

Abstract

In this talk recent results from the ARGUS experiment are reported emphasizing semileptonic B-decays and the determination of CKM matrix elements. The analyses of exclusive B-decays into $Dl\nu$ and $D^*l\nu$ and of the inclusive lepton spectrum are shown to yield consistent results for V_{cb}. Also discussed is the measurement of the helicity structure of the $D^*l\nu$ final state and of the lifetime ratio of neutral to charged B mesons. Upper limits for charmless B decays into exclusive semileptonic and hadronic channels are given. Evidence for $b \to u$ transitions from the endpoint of the inclusive lepton spectrum is reported. The ARGUS results on $B^0 - \overline{B^0}$ mixing are updated and the resulting constraints on the standard model discussed. The report closes with an introduction of the new ARGUS Micro Vertex Drift Chamber, which is expected to improve the efficiency for the reconstruction of B-decays.

This work was supported by the German Bundesministerium für Forschung und Technologie under contract number 054DO51P.

1 Introduction

Over the last few years the investigation of the physics of b-quarks improved considerably our knowledge of the parameters of the Standard Model and posed stringent limits on the existence of new physics beyond the Standard Model [1]. With the top quark still missing, b-physics offers the unique possibility to determine the coupling of the third quark generation to the lighter quarks. The relative strength of the quark couplings are given by the Cabbibo-Kobayashi-Maskawa (CKM) matrix, which is unitary in the Standard Model with three generations [2]:

$$\begin{pmatrix} V_{ud} & V_{us} & V_{ub} \\ V_{cd} & V_{cs} & V_{cb} \\ V_{td} & V_{ts} & V_{tb} \end{pmatrix} \tag{1}$$

The matrix elements V_{ub} and V_{cb} can be determined from B-meson decays in combination with b lifetime measurements, while V_{td} and V_{ts} can be obtained from oscillations in the $B^0 - \overline{B^0}$ and $B_s - \overline{B_s}$ systems, respectively. Semileptonic B-meson decays (Fig.1) are best suited for the determination of CKM matrix elements, because the theoretical uncertainties are expected to be smaller than in purely hadronic decays. Note that the b quark decays into u or c quarks via emission of a W^- while the $\bar{b}$ emits a W^+. Hence, in semileptonic B-decays, a negative lepton tags a B^- or $\overline{B^0}$ and a positive lepton a B^+ or B^0.

In the spectator model the semileptonic width is the same for neutral and charged B-mesons. For current quark masses and next-to-leading order QCD corrections it is predicted to be [1]

$$\Gamma_{SL}(B) = \frac{G_F^2 m_b^5}{192\pi^3}\left(0.86\,|V_{ub}|^2 + 0.48\,|V_{cb}|^2\right). \tag{2}$$

This allows the determination of the lifetime ratio of neutral and charged B's from the measurement of the semileptonic branching ratio B_{SL} (see Sect. 2.4) using the relation

$$\Gamma_{SL}(B) = \frac{B_{SL}(B)}{\tau_B}. \tag{3}$$

Most results on b-physics have been obtained from e^+e^--experiments running on the $\Upsilon(4S)$ resonance. The $\Upsilon(4S)$ resonance is assumed to decay exclusively into $B\overline{B}$ pairs (Fig.2) with a branching ratio into neutral and charged B's given only by the phase space, i.e. by the masses of both charge states. Previously ARGUS assumed a production ratio $f^0/f^\pm = B^0\overline{B^0} : B^+B^- = 45 : 55$. Recent mass determinations by ARGUS and CLEO yield for the mass difference $M(B^0) - M(B^+) = 0.3 \pm 0.6\ MeV$ and thus a production ratio [3] :

$$\frac{f^0}{f^\pm} = B^0\overline{B^0} : B^+B^- = 50 \pm 2.5 : 50 \pm 2.5 = 1.00 \pm 0.08.$$

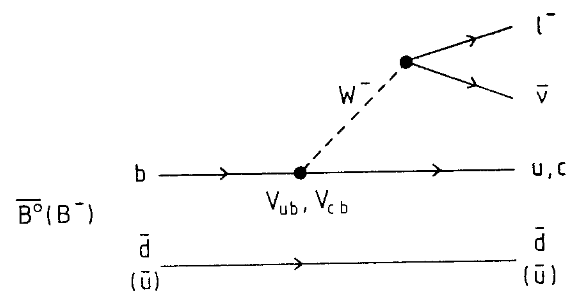

Figure 1: W-exchange diagram for semileptonic B-meson decays.

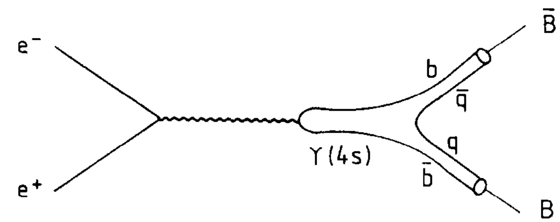

Figure 2: Diagram for $B\overline{B}$ pair production via the $\Upsilon(4S)$ resonance in e^+e^- annihilation.

This ratio was used for the results given in this writeup.

The results presented in the following were obtained from data taken with the ARGUS detector [4] on the $\Upsilon(4S)$ resonance and in the nearby continuum. The integrated luminosity of about 180 pb^{-1} collected at the $\Upsilon(4S)$ yields roughly 300K B-mesons. The continuum data, necessary for the subtraction of non-resonant background, correspond to an integrated luminosity of about 60 pb^{-1}.

2 Semileptonic B-Decays into Charmed Final States

2.1 The inclusive lepton spectrum from semileptonic B-decays

The semileptonic branching ratio for B-decays can be determined from the inclusive lepton spectrum measured at the $\Upsilon(4S)$ resonance. Figure 3 shows the continuum substracted spectrum which is well described by the contribution from primary B-decays (dominated by $b \to c$ transitions) according to

$$B \to l\nu X$$

and a softer component from secondary charm decays. As will be shown in the following section the dominant part of the semileptonic B-decays proceeds via the exclusive channels $Dl\nu$ and $D^*l\nu$. Since the theoretical models for these decays have now been tested experimentally, the uncertainty in the extrapolation of the lepton spectra to lower momenta is much reduced. Being consistent with the experiments the ACM model [5] has been used by ARGUS to obtain the semileptonic branching ratio of B-mesons [3]:

$$BR(B \to l\nu X) = (10.3 \pm 0.7 \pm 0.2)\%.$$

Similar results have been obtained by the CLEO and Crystal Ball experiments [6,7], yielding an average of $(10.9 \pm 0.6)\%$ [3]. This is somewhat low compared to spectator model predictions of about 12 to 15 % [8]. Since the semileptonic decays can be more safely estimated than the hadronic ones this result asks for more detailed investigation of the hadronic channels.

While the semileptonic branching ratio is nearly independent of the values of the CKM matrix elements the semileptonic width,

$$\Gamma_{SL} = \frac{B_{SL}}{\tau_B},$$

depends according to Eq. (2) on V_{ub} and V_{cb}. With the measured average beauty lifetime $\tau_B = (1.15 \pm 0.14)10^{-12}\ s$ [9] and for $|V_{ub}|/|V_{cb}| < 0.2$ we obtain:

$$|V_{cb}| = 0.046 \pm 0.005.$$

The main uncertainty in this value comes from the m_b^5 term in the width formula (2).

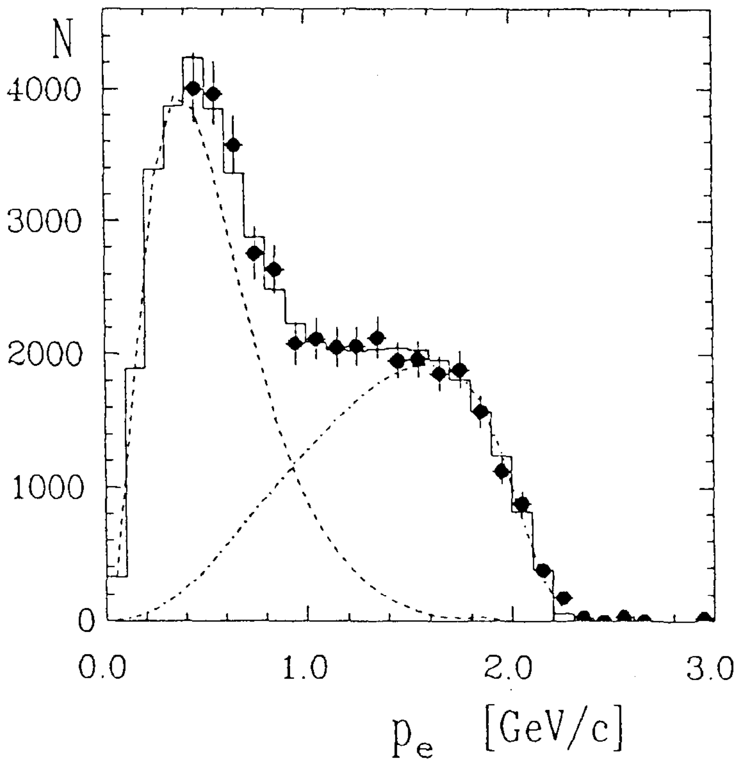

Figure 3: Inclusive electron spectrum at the $\Upsilon(4S)$ resonance after continuum subtraction (dashed-dotted curve: electrons from primary B-decays; dashed curve: electrons from secondary charm decays).

2.2 The decay $B^0 \to D^{*-}l^+\nu$

2.2.1 Branching ratio

The branching ratio for the decay[1]

$$B^0 \rightarrow D^{*-}l^+\nu$$

has first been measured by ARGUS [10]. With new values for the branching ratios involved in the analysis, $BR(D^{*-} \to \overline{D^0}\pi^-) = (57\pm6)\%$ [11] and $BR(\Upsilon(4S) \to B^0\overline{B^0}) = 50\%$ (see Sect.1) the experimental result is now:

$$BR(B^0 \to D^{*-}l^+\nu) \;=\; (5.4 \pm 0.9 \pm 1.3)\%.$$

The $D^*l\nu$ final state has been selected using a missing mass technique. With the approximation of zero B-meson momentum, $p_B = 0$, one can determine the mass recoiling against D^*l according to:

$$M^2_{rec}(D^*l) \;\approx\; [E_B - (E_{D*} + E_l)]^2 - [\vec{p}_{D*} + \vec{p}_l]^2 . \tag{4}$$

The recoil mass spectrum in Fig.4 peaks around zero, i.e. at the ν-mass. Only the background at positive M^2_{rec} can be due to B-decays into $D^*l\nu$ plus additional particles. From the measured spectrum the following upper limit for such a contribution, which would also include higher D^* excitations, was obtained:

$$BR(B^0 \to D^{*-}l^+\nu + X) \;<\; 1.4\% \text{ (90\% c.l.)}.$$

2.2.2 The helicity structure of the decay $B^0 \to D^{*-}l^+\nu$

The decay amplitude for $B \to D^*l\nu$ contains three form factors, $T_-(q^2)$, $T_+(q^2)$, $L(q^2)$, which determine the contributions from D^* helicities -1, +1 and 0, respectively. These formfactors depend on the invariant mass of the lepton pair, q^2, which is equal to the virtual mass of the W (Fig.1).

In the $l^-\overline{\nu}$ rest frame the angular momentum component in the direction of the lepton l^- is, for sufficiently light leptons, fixed to be -1 due to the V-A coupling (Fig.5a). Thus each D^* helicity (in the D^* rest frame) yields a distinct distribution of the D^* direction w.r.t. the lepton direction, in particular a forward-backward asymmetry for the ±1 contributions. This allows in principle to measure the three form factors separately.

The helicity of the D^* can also be determined from the decay angular distribution of the D^* which is observed in the decay mode

$$D^{*-} \;\rightarrow\; \overline{D^0}\pi^-.$$

[1]Reference to a specific charge state is understood to include also the corresponding charge conjugate state.

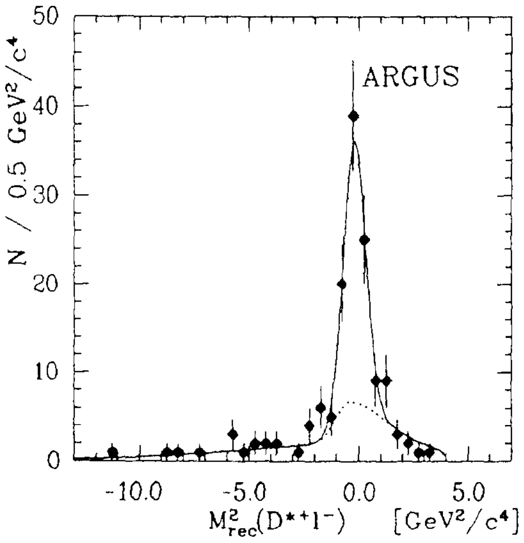

Figure 4: Invariant mass of the system recoiling against a D^*l combination.

The polar angular distribution of the pion in the D^* rest frame w.r.t the D^* direction (Fig.5b) can be written as:

$$\frac{dN}{d\cos\Theta^*} \sim 1+\alpha\cos^2\Theta^*; \quad \alpha = \frac{2\Gamma_L}{\Gamma_T} - 1. \tag{5}$$

Γ_L and Γ_T are the widths for the B's decaying into longitudinal and transverse D^*'s, respectively. Γ_T includes both helicities +1 and -1 (they can be separated by measuring the D^* production angular distribution as described above).

The Θ^* distribution measured by ARGUS (Fig.6) yields [12]

$$\alpha = 0.7 \pm 0.9$$

and

$$\frac{\Gamma_L}{\Gamma_T} = 0.85 \pm 0.45.$$

This measurement excludes theoretical models with a Γ_L/Γ_T ratio larger than 2 [13,14] and supports those with Γ_L/Γ_T around 1 [15,16,17].

Because of the correlation between the helicity and the production angle of the D^* the Γ_L/Γ_T ratio influences also the kinematical variables of the leptons. For example, dominance of T_- would yield a hard spectrum for the charged lepton which has to recoil in this case against the D^* and the ν (see Fig.7). Figure 8 shows theoretical distributions for the lepton energy E_l and the lepton pair invariant mass, q^2. The measured distributions in Fig.9 confirm the result $\Gamma_L/\Gamma_T \approx 1$ ([15,16,17]).

With this result on α, which was also confirmed by CLEO [18], we have obtained a better understanding of exclusive semileptonic B-decays. The systematic uncertainties in necessary extrapolations into unaccessible kinematical regions (leptons can only be identified above ~1 GeV) and in the description of the inclusive lepton spectra are now considerably reduced.

2.2.3 V_{cb} determination

The measured branching ratio can be related to the matrix element V_{cb}:

$$BR(B^0 \to D^{*-}l^+\nu) = \tau_B\,|V_{cb}|^2\,\hat{\Gamma}_T\,(1+\Gamma_L/\Gamma_T) \tag{6}$$

where $\hat{\Gamma}_T$ can be more reliably calculated theoretically than Γ_L, Γ_T separately. From the measured branching ratio and Γ_L/Γ_T one obtains

$$|V_{cb}| = 0.046 \pm 0.009.$$

Here $\hat{\Gamma}_T = 12 \cdot 10^{12} s^{-1}1$ [17,19] has been used; the model uncertainty is about 10%.

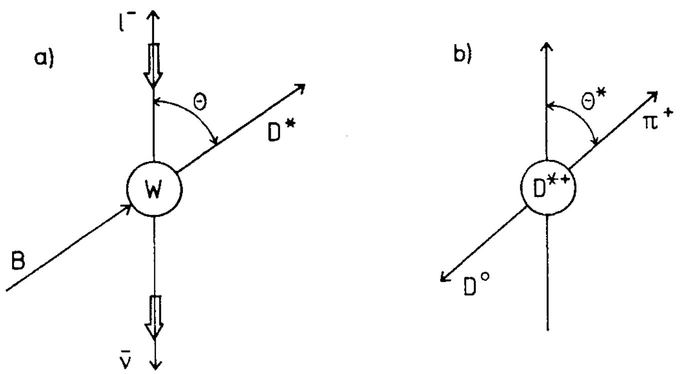

Figure 5: (a) Definition of the D^* production angle Θ in the $l\nu$ CM-system. (b) Definition of the D^* decay angle Θ^* in the D^* CM-system.

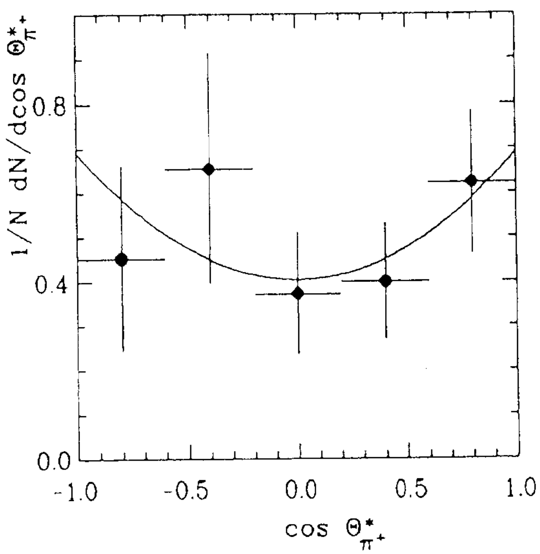

Figure 6: Measured D^* decay angular distribution.

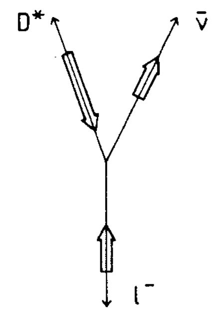

Figure 7: Sketch of helicities and kinematical constraints in the $D^*l\nu$ system in the case of T_- dominance.

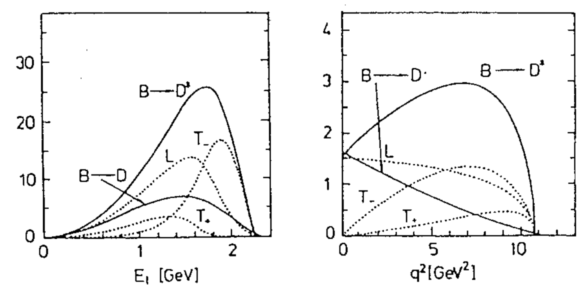

Figure 8: Theoretical prediction for the lepton energy and q^2 distributions for $B \to Dl\nu$ and $B \to D^*l\nu$ (from [16]).

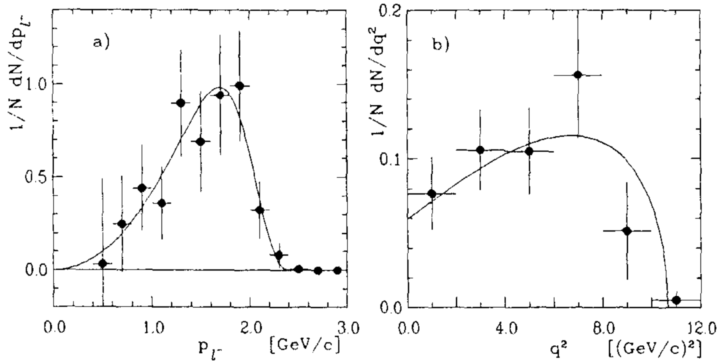

Figure 9: Measured lepton momentum and q^2 distributions for $B^0 \to D^{*-}l^+\nu$ compared to the predictions from [16].

2.3 The decay $B^0 \to D^- l^+ \nu$

Involving only one form factor the decay

$$B^0 \to D^- l^+ \nu$$

may be even more suited to determine V_{cb}. However, experimentally this channel is more difficult to analyse since the signal-to-noise ratio for the D mass reconstruction is much worse than for the D^*.

The ARGUS group reconstructed the D decay mode

$$D^- \ \to \ K^+\pi^-\pi^-.$$

For lepton momenta between 1 and 2.5 GeV and momenta of the D candidates between 1.5 and 2.5 GeV $K^+\pi^-\pi^-$ mass spectra are shown in Fig.10. The three plots are for different masses recoiling against the $K^+\pi^-\pi^-l^+$ system (recoil masses calculated as in the D^* case). A clear D^--signal is seen for recoil masses around zero, i.e. the neutrino mass. Fitting the $K^+\pi^-\pi^-$ spectra in M^2_{rec} bins yields the number of D's as a function of M^2_{rec} (Fig.11a). There is a background from the decay $B^0 \to D^{*-}l^+\nu$ where the D^* decays into a D^- and a π^0 or γ (note that this is the only way to get charged D's via D^* decays). This background has been determined by measuring the corresponding decay chain

$$B^0 \to D^{*-}l^+\nu, \ \ D^{*-} \to \overline{D^0}\pi^-.$$

The obtained recoil mass spectrum in Fig.11b has been subtracted after proper normalisation.

To determine the decay branching ratio the extrapolation to unobserved lepton momenta was done using the WBS model [15]. With $BR(D^- \to K^+\pi^-\pi^-) = (9.1 \pm 1.4)\%$ and $BR(\Upsilon(4S) \to B^0\overline{B^0}) = 50\%$ ARGUS obtains [20]:

$$BR(B^0 \to D^- l^+ \nu) \ = \ (1.7 \pm 0.6 \pm 0.4)\%$$

and

$$R \ = \ \frac{BR(B^0 \to D^{*-}l^+\nu)}{BR(B^0 \to D^- l^+\nu)} \ = \ 3.3^{+3.7}_{-1.1}.$$

The latter ratio is consistent with the models in [15,16,17,21]. Using the average B lifetime as before one obtains the partial width

$$\Gamma(B^0 \to D^- l^+ \nu) \ = \ 0.016 \pm 0.007$$

which yields for the WBS model [15]:

$$|V_{cb}| \ = \ 0.042 \pm 0.008.$$

The model dependence of this value is smaller than the experimental errors.

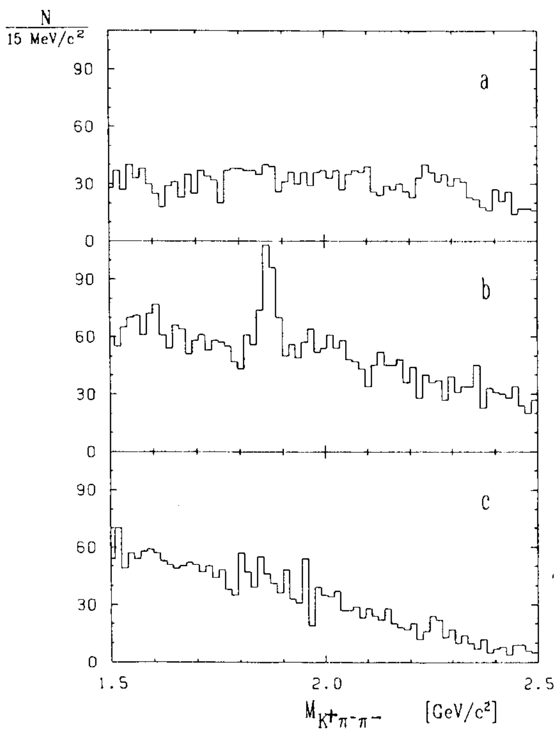

Figure 10: Invariant mass spectra of $K^+\pi^-\pi^-$ combinations in events which contain a l^+ lepton. The spectra are given for different invariant masses of the system recoiling against the the $K^+\pi^-\pi^-l^+$ combination:

(a) -1.5 < M^2_{rec} < -0.5 GeV^2,

(b) -0.5 < M^2_{rec} < 0.5 GeV^2,

(c) 0.5 < M^2_{rec} < 1.5 GeV^2.

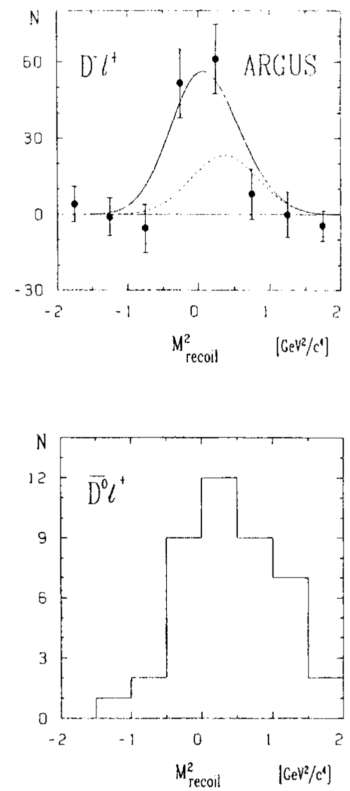

Figure 11: (a) Distribution of the invariant mass recoiling against the D^-l^+ system. The dashed curve shows the contribution from the cascade decay $B^0 \rightarrow D^{*-}l^+\nu \rightarrow D^-(\pi^0,\gamma)l^+\nu$.

(b) Distribution of the invariant mass recoiling against the $\overline{D^0}l^+$ system with the $\overline{D^0}$ originating from the cascade decay $B^0 \rightarrow D^{*-}l^+\nu$ (used to determine background in (a)).

2.4 The lifetime ratio of charged and neutral B mesons

The "average bottom lifetime" τ_B as used above has been measured at PEP and PETRA and is an average over all bottom hadrons as produced in b-jets. Since the knowledge of the lifetime is necessary to relate the measured branching ratios to the theoretically interesting partial widths it is important to know if neutral and charged B's have the same lifetime. Remember that the charged D mesons live about two times longer than their neutral partners. In B decays this ratio is expected to be closer to 1 [22]. Since in the spectator model no difference between neutral and charged B's is expected any deviation of the ratio from 1 signals non-spectator contributions due to strong interactions.

Excepting for the semileptonic width the spectator model prediction

$$\Gamma_{SL}(B^\pm) = \Gamma_{SL}(B^0)$$

one obtains with

$$\Gamma_{SL} = \frac{BR(B \to l\nu + X)}{\tau_B}$$

the lifetime ratio in terms of the semileptonic branching ratios:

$$\tau^\pm/\tau^0 = \frac{BR(B^\pm \to l\nu + X)}{BR(B^0, \overline{B^0} \to l\nu + X)}. \tag{7}$$

Since it is known that the exclusive channels $B \to D^* l\nu$ and $B \to D l\nu$ contribute a large fraction to the semileptonic decays it appears safe to assume that the ratio of semileptonic branching ratios is already determined by these exclusive channels:

$$\frac{BR(B^\pm \to l\nu + X)}{BR(B^0, \overline{B^0} \to l\nu + X)} \approx \frac{BR(B^\pm \to D^*/Dl\nu)}{BR(B^0, \overline{B^0} \to D^*/Dl\nu)}.$$

The ARGUS group considered the following decay chain:

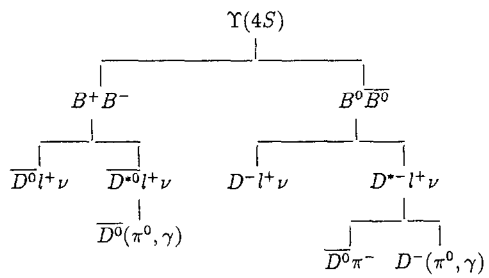

In this scheme charged B mesons always end up in neutral D mesons while neutral B's go mainly into charged D's with the exception of the path with $D^{*-} \to \overline{D^0}\pi^-$. Thus one finds the formula

$$\tau^\pm/\tau^0 = \frac{f^0}{f^\pm}\frac{N(\overline{D^0}l^+) - N(D^{*-}l^+, D^{*-} \to \pi^-\overline{D^0})}{N(D^- l^+) + N(D^{*-}l^+, D^{*-} \to \pi^-\overline{D^0})} \tag{8}$$

where the rates of $\overline{D^0}l^+$, $D^- l^+$ and $D^{*-}l^+$ ($D^{*-} \to \pi^-\overline{D^0}$) have to be measured. After the correction for continuum, fakes and uncorrelated pairs, ARGUS finds 363 ± 38, 193 ± 53 and 57 ± 12 pairs, respectively. Assuming $f^0/f^\pm = 1$ this yields:

$$\tau^\pm/\tau^0 = 1.00 \pm 0.23 \pm 0.14,$$

confirming the theoretical expectation of nearly equal lifetimes [22]. With the applied method the determined lifetime ratio is found to be rather insensitive to contributions of excited charm states to the semileptonic B-decays.

3 Charmless B-Decays (b $\rightarrow$ u Transitions)

B-decays with no charmed particles in the final state are a signal for $b \rightarrow u$ transitions (Fig.12). Examples for exclusive channels are the semileptonic decays $B \rightarrow \rho l \nu$ and $B \rightarrow \pi l \nu$ (corresponding to $B \rightarrow D^*/Dl\nu$ in $b \rightarrow c$ transitions) or the hadronic decay $B^0 \rightarrow \pi^+\pi^-$.

Involving a transition between the 3^{rd} and the 1^{st} generation, $b \rightarrow u$ decays are much rarer than $b \rightarrow c$ decays which connect two adjacent generations. Therefore, until recently only upper limits on $b \rightarrow u$ transitions were obtained. After the presentation of this talk ARGUS found evidence for $b \rightarrow u$ transitions from the inclusive lepton spectrum with a significance of more than 3 standard deviations (see below). In the following we discuss the different approaches to determine the matrix element V_{ub}.

3.1 V_{ub} determination from charm counting ?

The decay width of B-mesons is essentially given by the $b \rightarrow u$ and $b \rightarrow c$ transitions:

$$\Gamma(B) \sim f_u|V_{ub}|^2 + f_c|V_{cb}|^2 \qquad (9)$$

where f_u and f_c take into account phase space and hadronic effects. Since c quarks can also be produced at the second $W^\pm$ vertex, about 1.15 c or $\bar{c}$ quarks are expected per B-decay via $b \rightarrow c$ transition. ARGUS finds from all measured decay modes $0.98 \pm 0.10 \pm 0.08$ c or $\bar{c}$ per B-decay [23] (Table 1). That leaves room for about 20% $b \rightarrow u$ transitions but poses no real constraint compared to other limits.

Decay	Branching Ratio [%] ARGUS
$B \rightarrow D^0X$	$46.6 \pm 7.1 \pm 6.3$
$B \rightarrow D^+X$	$23.2 \pm 5.3 \pm 3.5$
$B \rightarrow D_sX$	$16 \pm 4 \pm 3$
$B \rightarrow "\Lambda_c"X$	$7.6 \pm 1.4 \pm 1.8$
$2 \times B \rightarrow J/\psi, \psi', \chi_cX$	4.2 ± 1.0
Σ	$98 \pm 10 \pm 8$

Table 1: Inclusive branching ratios for B mesons decaying into charmed particles.

3.2 Exclusive charmless B-decays

3.2.1 Exclusive semileptonic decays

The ARGUS group has searched for the decays

$$B^+ \rightarrow \rho^0 l^+ \nu,$$
$$B^0 \rightarrow \pi^- l^+ \nu$$

employing the missing mass technique as for $B \rightarrow D^*/Dl\nu$. Figures 13 and 14 show the distributions of masses recoiling against the $\rho^0 l^+$ and the $\pi^- l^+$ systems, respectively. A huge background at positive M^2_{rec} extends above the signal region. No excess above the background described by the wrong charge combination is observed around $M^2_{rec} = 0$. The upper limits on the branching ratios and on V_{ub} derived from these plots are model dependent and are listed for three different models in Table 2.

Decay		GISW [17]	WSB [15]	KS [16]
$B^+ \rightarrow \rho^0 l^+ \nu$	BR	$0.84 \cdot 10^{-3}$	$1.00 \cdot 10^{-3}$	$0.90 \cdot 10^{-3}$
	$\lvert V_{ub}\rvert$	$13.3 \cdot 10^{-3}$	$8.4 \cdot 10^{-3}$	$6.9 \cdot 10^{-3}$
	$\lvert V_{ub}\rvert/\lvert V_{cb}\rvert$	0.30	0.17	0.15
$B^0 \rightarrow \pi^- l^+ \nu$	BR	$1.04 \cdot 10^{-3}$	$0.77 \cdot 10^{-3}$	$0.77 \cdot 10^{-3}$
	$\lvert V_{ub}\rvert$	$21.0 \cdot 10^{-3}$	$9.6 \cdot 10^{-3}$	$9.7 \cdot 10^{-3}$
	$\lvert V_{ub}\rvert/\lvert V_{cb}\rvert$	0.47	0.19	0.21
Combined	$\lvert V_{ub}\rvert$	$13.2 \cdot 10^{-3}$	$7.4 \cdot 10^{-3}$	$6.7 \cdot 10^{-3}$
	$\lvert V_{ub}\rvert/\lvert V_{cb}\rvert$	0.29	0.15	0.15

Table 2: Upper limits (90% c.l.) on exclusive semileptonic B-decays.

3.2.2 Exclusive hadronic decays

The ARGUS group searched also for exclusive hadronic decays with n pions in the final state (n = 2,3,4,5). No signals were observed and the upper limits listed in Table 3 were obtained. As an example the search for the decay $B^0 \rightarrow \pi^+\pi^-$ is illustrated in Fig.15.

ARGUS previously reported the observation of the charmless decays $B^+ \rightarrow p\bar{p}\pi^+$ and $B^0 \rightarrow p\bar{p}\pi^+\pi^-$ [24]. This observation could not be confirmed by CLEO [25]. In a new data set (~60% of the old one) ARGUS also finds no signal.

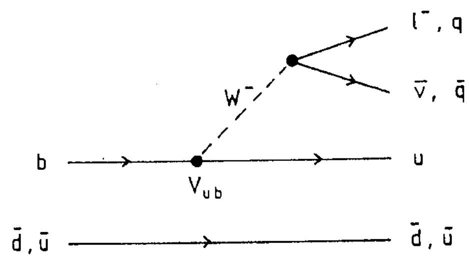

Figure 12: W-exchange diagram for $b \to u$ transitions.

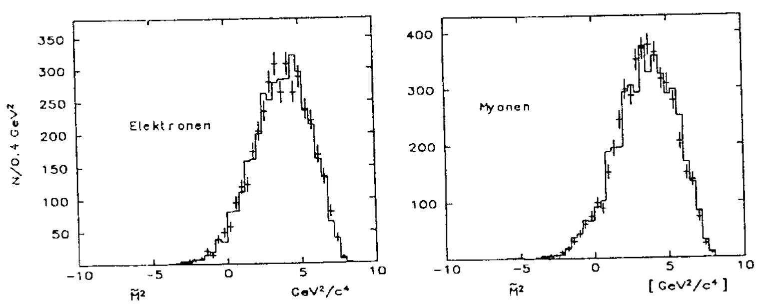

Figure 13: Invariant mass of the system recoiling against $\pi^+\pi^-e^-$ and $\pi^+\pi^-\mu^-$ combinations ($\pi^+\pi^-$-mass in ρ-band) in $\Upsilon(4S)$ decays. The histogram describes the background as obtained from like-sign pion pairs.

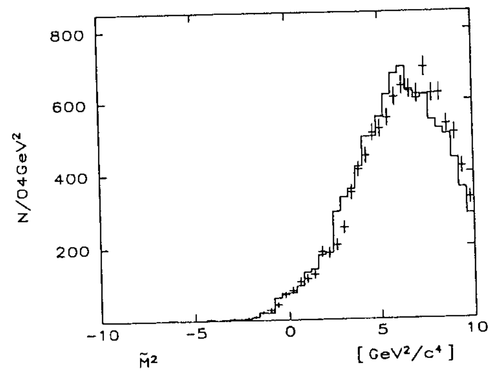

Figure 14: Invariant mass of the system recoiling against π^+l^- combinations in $\Upsilon(4S)$ decays. The histogram describes the background as obtained from like-sign pion-lepton pairs.

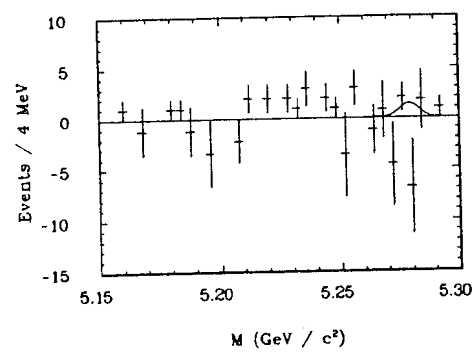

Figure 15: Search for the decay $B^0 \to \pi^+\pi^-$: continuum subtracted $\pi^+\pi^-$ mass distribution.

Decay	ARGUS	CLEO	Theory ($\lvert V_{ub}/V_{cb}\rvert = 0.1$)
$\pi^{\pm}\pi^{0}$	$5.0 \cdot 10^{-4}$	$2.6 \cdot 10^{-3}$	$0.6(1.3) \cdot 10^{-5}$
$\pi^{+}\pi^{-}$	$1.9 \cdot 10^{-4}$	$0.8 \cdot 10^{-4}$	$2.0(2.5) \cdot 10^{-5}$
$\pi^{\pm}\pi^{+}\pi^{-}$	$8.0 \cdot 10^{-4}$	$1.9 \cdot 10^{-4}$	$6 \cdot 10^{-5}$
$\rho^{0}\pi^{\pm}$	$1.9 \cdot 10^{-4}$	$1.7 \cdot 10^{-4}$	$2 \cdot 10^{-6}$
$\pi^{+}\pi^{-}\pi^{0}$	$1.8 \cdot 10^{-3}$	–	$2 \cdot 10^{-4}$
$\rho^{0}\pi^{0}$	$4.3 \cdot 10^{-4}$	–	$2 \cdot 10^{-6}$
$\pi^{+}\pi^{+}\pi^{-}\pi^{-}$	$1.0 \cdot 10^{-3}$	–	$1 \cdot 10^{-4}$
$\pi^{\pm}\pi^{+}\pi^{-}\pi^{0}$	$5.4 \cdot 10^{-3}$	–	$4 \cdot 10^{-4}$
$\pi^{+}\pi^{-}\pi^{0}\pi^{0}$	$5.7 \cdot 10^{-3}$	–	$5 \cdot 10^{-4}$
$\rho^{+}\rho^{-}$	$4.2 \cdot 10^{-3}$	–	$5 \cdot 10^{-5}$
$\pi^{\pm}2\pi^{+}2\pi^{-}$	$1.2 \cdot 10^{-3}$	–	$2 \cdot 10^{-4}$
$3\pi^{+}3\pi^{-}$	$3.3 \cdot 10^{-3}$	–	$2 \cdot 10^{-4}$

Table 3: Upper limits (90% c.l.) on B decay branching ratios into multi-pion final states.

3.3 The inclusive lepton spectrum from semileptonic B-decays

The kinematical limit for the momenta of leptons from semileptonic $b \to c$ transitions is 2.3 GeV/c, while the lepton momenta in the corresponding $b \to u$ transitions go up to more than 2.6 GeV/c. Thus an excess in the lepton spectrum (Fig.3) between 2.3 and 2.6 GeV/c is interpreted as a signal for $b \to u$ transitions. The analysis is complicated by a large background from the continuum. At the time when this talk was presented CLEO [26] and ARGUS had reported an enhancement for large lepton momenta with a significance of 2.2 and 1.7 standard deviations, respectively. Only a few weeks later a new ARGUS analysis was presented at the Lepton-Photon Conference yielding a 3.3 σ signal for $b \to u$ transitions. The determination of V_{ub} from this analysis is model dependent. Using the ACM model [5] yields:

$$|V_{ub}|/|V_{cb} = 0.10 \pm 0.02.$$

For more details see the Proceeding of the Lepton-Photon Conference [27].

4 Update of $\mathrm{B}^0 - \overline{\mathrm{B}^0}$ Mixing

4.1 Introduction

In the standard model $B^0 - \overline{B^0}$ transitions can occur via the box diagram (Fig.16). Including this interaction which mixes the flavour eigenstates B^0 and $\overline{B^0}$ the corresponding mass matrix becomes non-diagonal:

$$H \begin{pmatrix} B^0 \\ \overline{B^0} \end{pmatrix} = \begin{pmatrix} M - \frac{i}{2}\Gamma & M_{12} - \frac{i}{2}\Gamma_{12} \\ M_{12}^* - \frac{i}{2}\Gamma_{12}^* & M - \frac{i}{2}\Gamma \end{pmatrix} \begin{pmatrix} B^0 \\ \overline{B^0} \end{pmatrix} .$$

Diagonalizing this matrix leads to the mass eigenstates:

$$B_{1,2} = \frac{1}{\sqrt{2}} \left(|B^0\rangle \pm |\overline{B^0}\rangle \right) .$$

Vice versa, a pure B^0 (or $\overline{B^0}$) state (as produced in strong interactions) can be represented by

$$|B^0, \overline{B^0}\rangle = \frac{1}{\sqrt{2}} (|B_1\rangle \pm |B_2\rangle) .$$

Due to the different time evolution of B_1 and B_2 an initially pure B^0 ($\overline{B^0}$) state acquires $\overline{B^0}$ (B^0) components with an oscillation frequency proportional to ΔM, the difference in the masses of the B_1 and B_2 states. Figure 17 shows for an initially pure B^0 beam how many particles decay after a time t as B^0 or as $\overline{B^0}$ (the upper and lower shaded areas, respectively). The ratio of the time integrated number of $\overline{B^0}$ and B^0 depends on $x = \frac{\Delta M}{\Gamma}$, which is a measure for the number of oscillations per lifetime:

$$r = \frac{N(B^0 \to \overline{B^0})}{N(B^0 \to B^0)} = \frac{x^2}{2 + x^2}. \tag{10}$$

At the $\Upsilon(4S)$ the initial $B^0\overline{B^0}$ pair can oscillate into three possible configurations:

$$\Upsilon(4S) \to B^0\overline{B^0} \begin{array}{l} \to B^0\overline{B^0} \\ \to B^0 B^0 \\ \to \overline{B^0}\overline{B^0} \end{array}$$

The same r defined above for single B's is now given by

$$r = \frac{N(B^0B^0) + N(\overline{B^0}\overline{B^0})}{N(B^0\overline{B^0})} . \tag{11}$$

Before the discovery of $B^0 - \overline{B^0}$ mixing by ARGUS in 1986 the mixing parameter r was predicted to be of order 10^{-2}. ARGUS measured $r = 0.21 \pm 0.08$ using $\Upsilon(4S)$ data corresponding to an integrated luminosity of about 100 pb^{-1}

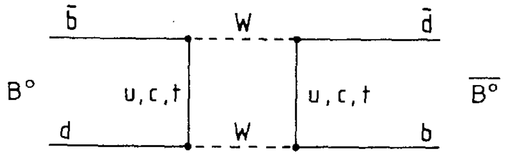

Figure 16: Box diagram for $B^0 - \overline{B^0}$ transitions.

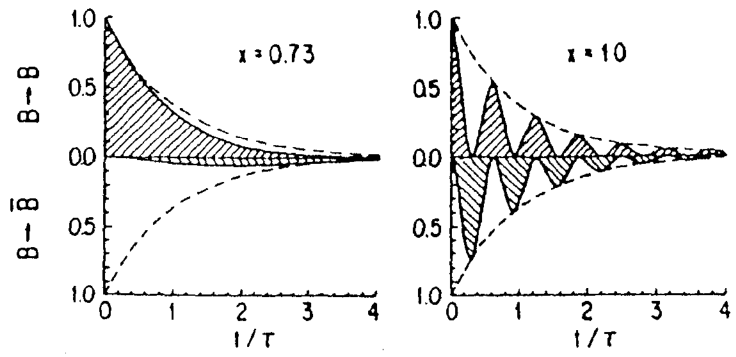

Figure 17: $B^0 - \overline{B^0}$ oscillations for (a) x=0.73 and (b) x=10.
Starting from pure B^0's at t=0 the shaded area under the full curves give the time dependent rate to decay as B^0 (upper part) or as $\overline{B^0}$ (lower part). The dotted curve gives the decay probability without oscillations. (From [29]).

[28]. Now the analysis has been updated and extended with an additional 70 pb^{-1}.

Basically the analysis method employs the semileptonic decays to determine from the charges of the observed leptons if a B^0 or $\overline{B^0}$ has decayed (Fig.1):

$$B^0 \to l^+ + X, \quad \overline{B^0} \to l^- + X.$$

Another possibility is to tag B^0, $\overline{B^0}$ by the charm content of D^* mesons observed in the decay. Spectator diagrams yield only charged D^*'s from the $b \to c$ transition:

$$B^0 \to D^{*-} + X, \quad \overline{B^0} \to D^{*+} + X.$$

4.2 Mixing analysis

To update the original result on $B^0 - \overline{B^0}$ mixing the ARGUS group has followed three approaches which differ in the systematic uncertainties involved. The data samples for these three analyses are mutually exclusive so that the results are statistically independent.

4.2.1 Lepton-lepton correlations

For this analysis events with two fast leptons are selected. The lepton spectrum in Fig.3 suggests to require for a "fast" lepton:

$$p_l > 1.4\ GeV/c\,.$$

This cuts off the background from secondary charm decays which contributes mainly to like-sign lepton pairs ($l^\pm l^\pm$). The remaining background is subtracted using a Monte Carlo simulation of B-decays. The dominant backgrounds for the unlike-sign lepton pairs (l^+l^-) are:

- converted photons,
- $J/\Psi \to l^+l^-$ decays,
- leptons from continuum $c\bar{c}$ jets.

The corrections are obtained from data and Monte Carlo simulations (Table 4). The mixing is then determined by the ratio of observed like-sign to unlike-sign lepton pairs. Correcting in addition for semileptonic decays of charged B's, $B^\pm \to l^\pm + X$, which do not show mixing, yields:

$$r = \frac{[N(l^+l^+) + N(l^-l^-)]\,(1+\lambda)}{N(l^+l^-) - [N(l^+l^+) + N(l^-l^-)]\,\lambda}. \tag{12}$$

	$e^\pm e^\pm$	$\mu^\pm\mu^\pm$	$e^\pm\mu^\pm$	e^+e^-	$\mu^+\mu^-$	$e^\pm\mu^\mp$
$\Upsilon(4S)$ + Continuum	15	21	34	102	97	204
Continuum	0	1	1	2	3	2
$\Upsilon(4S)$ direct	15.0	18.1	31.1	96.1	88.2	198.1
Corrected for J/ψ cut	15.0	18.1	31.1	112.3	103.2	198.1
	± 4.9	± 5.2	± 6.3	± 10.9	± 11.1	± 14.9
Background						
Fakes	1.8	4.0	6.7	3.6	7.0	13.2
Conversion	0.3	-	0.3	0.3	-	0.3
Secondary decays	4.6	2.9	7.2	1.9	1.2	3.0
J/ψ decays	0.6	0.3	0.8	0.6	0.3	0.8
Signal	7.7	10.9	16.2	105.9	94.7	180.7
	± 4.9	± 5.2	± 6.3	± 10.9	± 11.1	± 14.9

Table 4: Lepton - lepton correlation rates.

The charged B contribution is described by

$$\lambda = \frac{f^\pm}{f^0}\left(\frac{\tau^\pm}{\tau^0}\right)^2. \tag{13}$$

In the previous ARGUS analysis $\lambda = 1.2$ was used. With the experimental results $f^\pm/f^0 \approx 1$ (see Sect.1) and $\tau^\pm/\tau^0 \approx 1$ (see Sect.2.4) we now assumed $\lambda = 1.0$ and obtain

$$r = 0.20 \pm 0.06 \pm 0.05.$$

4.2.2 D*lν - lepton correlations

The uncertainty in the charged B contribution can be avoided by reconstructing one B^0 or $\overline{B^0}$. ARGUS used the reconstructed $B \to D^* l\nu$ sample described in Sect.2.2. In addition it is required that the D^*l pairs are correlated with a fast lepton ($p_l > 1.4$ GeV/c). After background subtraction only about 6 mixed and 25 unmixed events remain (Table 5) leading to

$$r = 0.24 \pm 0.12 \pm 0.02.$$

	N($D^{*+}l^-l^-$)	N($D^{*+}l^-l^+$)
$\Upsilon(4S)$ Background	8 1.9 ± 0.5	27 1.7 ± 0.5
Signal	6.1 ± 2.8	25.3 ± 5.9

Table 5: $D^{*+}l^-$ - lepton correlation rates.

	N($D^{*+}l^-$)	N($D^{*+}l^+$)
$\Upsilon(4S)$ Background	7 2.0 ± 0.5	23 2.3 ± 0.5
Signal	5.0 ± 3.1	20.7 ± 5.5

Table 6: D^{*+} - lepton correlation rates.

4.2.3 D* -lepton correlations

In the spectator model each charge state of a B-meson decays into a specific D^* charge state:

$$\begin{aligned} B^0 &\to D^{*-} + X; \\ \overline{B^0} &\to D^{*+} + X; \\ B^+ &\to \overline{D^{*0}} + X; \\ B^- &\to D^{*0} + X. \end{aligned}$$

Thus we pick out decays of neutral B's by correlating $D^{*\pm}$ with fast leptons, e.g.:

$$\begin{aligned} B^0\overline{B^0} &\to D^{*+}l^+ + X; \\ \overline{B^0}\overline{B^0} &\to D^{*+}l^- + X. \end{aligned}$$

To exclude D^*l pairs from the same B decay the recoil mass is required to be in the unphysical region, $M^2_{rec} <$ -2.5 GeV (Fig.18). The observed rates (Table 6) are as for the $D^*l\nu$- lepton correlations statistically not competitive with the lepton - lepton correlation. But in both methods the uncertainty due to the $B^\pm$ contributions is absent. The result from the D^*-lepton correlations is

$$r = 0.24 \pm 0.16 \pm 0.03.$$

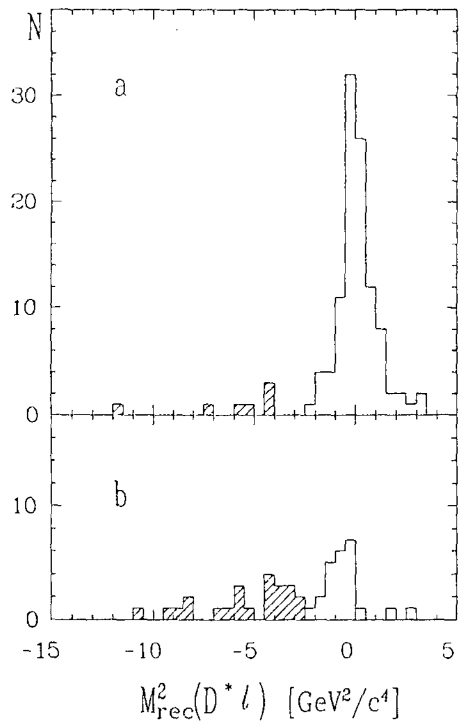

Figure 18: Invariant mass distribution of the system recoiling against (a) $D^{*-}l^{+}$ and (b) $D^{*-}l^{-}$ combinations.

4.2.4 The combined result on mixing

Combining the three different methods the average value for the mixing parameter becomes:

$$r = 0.21 \pm 0.06 \pm 0.04.$$

A similar result was obtained by CLEO ($r = 0.24 \pm 0.16 \pm 0.03$) [30].
With $r = x^2/(2 + x^2)$ follows:

$$x = \Delta M/\Gamma = 0.75 \pm 0.18,$$

and with Γ from the average B-lifetime:

$$\Delta M = (4.2 \pm 1.1) \cdot 10^{-4}\ eV.$$

Thus ΔM, the $B_1 - B_2$ mass difference, is about 100 times larger than the corresponding one in the K^0 system.

4.3 Implications of the mixing result

In the standard model with three generations the mixing parameter x is given by [31]

$$x = \frac{G_F^2}{6\pi^2} B_B f_B^2 m_b \tau_b |V_{td}|^2 m_t^2 F\left(\frac{m_t^2}{M_W^2}\right) \eta_{QCD}\,. \tag{14}$$

From this formula one can obtain a constraint for the CKM matrix element V_{td} as a function of the top mass m_t (Fig.19). Considerable efforts have been made both experimentally and theoretically to fix the other, a priori unknown, parameters in (14) (see the discussion in [32]).

Unitarity of the CKM matrix requires for three generations $|V_{td}| < 0.018$. This limit applied to the plot in Fig.19 yields

$$m_t > 60\ GeV.$$

The theoretical upper bound of the top mass, $m_t < 190$ GeV [33], requires:

$$|V_{td}| > 0.007.$$

Since for $B_s - \overline{B_s}$ mixing the same formula (14) applies with V_{td} replaced by V_{ts} one obtains rather reliable predictions for $B_s - \overline{B_s}$ mixing. The unitarity bounds of the CKM matrix yield

$$\frac{x_s}{x_d} = \frac{|V_{ts}|^2}{|V_{td}|^2} > 4.5\ .$$

The corresponding r-parameter is near its maximal value, i.e. the oscillation frequency is large compared to the scale set by the lifetime (Fig.17b)

$$r_s > 0.8.$$

With such fast oscillations the time integrated mixing effect becomes insensitive to the exact value of x_s or r_s, which can only be overcome by measuring the time evolution of the mixing. Such measurements are part of the physics programs for asymmetric B-meson factories (see e.g. [34]).

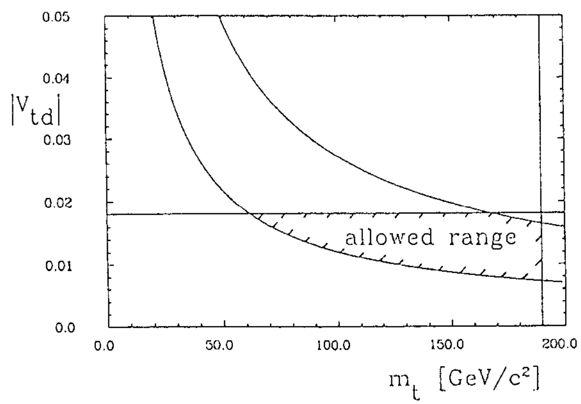

Figure 19: Allowed range for $|V_{td}|$ and m_t (from [1]).

5 A New Vertex Detector for ARGUS

In current experiments B mesons decays can only be reconstructed with efficiencies around 10^{-3}. This is mainly due to combinatorial background, since at the $\Upsilon(4S)$ the B-mesons are produced nearly at rest and thus the decay products of both B's are completely intermixed. With a very precise vertex measurement it should be possible to tag D decays (average decay length at the $\Upsilon(4S)$: 60 μm for D^0 and 130 μm for $D^{\pm}$) thus reducing the combinatorial background. (Separating the two B vertices (decay length about 25 μm) is much more difficult.) The ARGUS collaboration is currently building a new vertex detector, the Micro Vertex Drift Chamber (μVDC). The design of the chamber optimizes the following requirements :

- low multiple scattering
- high position resolution
- multi-track separation
- three-dimensional vertex reconstruction
- small lever arm to the interaction point.

These requirements are met in the following way :

- At the $\Upsilon(4S)$ the average momenta are about 0.5 GeV/c. This requires a particulary low mass detector to minimize multiple scattering. At the time of the design it was found that only a drift chamber could meet the requirements (sufficiently thin double-sided silicon strip detectors were not available).
- The precision in the position measurements is achieved with pressurized slow gases. For example: with CO_2-propane in a 90:10 mixture and 4 bar pressure resolutions down to 20 μm were reached [35].
- Track separation will be achieved by making the cells sufficiently small (5.2 mm × 5.3 mm , Fig. 20).
- Monte Carlo studies showed that a good track reconstruction in space is necessary to reduce false vertices [36]. This requires about equal resolutions in the projections perpendicular and parallel to the beam (r-ϕ and r-z). This requirement is met by an unconventional arrangement of the sense wires under extreme stereo angles (±45°). Figure 21 shows the mechanical realization of this concept: In 12 layers the wires wind at +45° or -45° around the beam pipe, supported by five Beryllium vanes which carry jewels as insulating feed-throughs. The two innermost and additional two intermediate layers have axial sense wires.

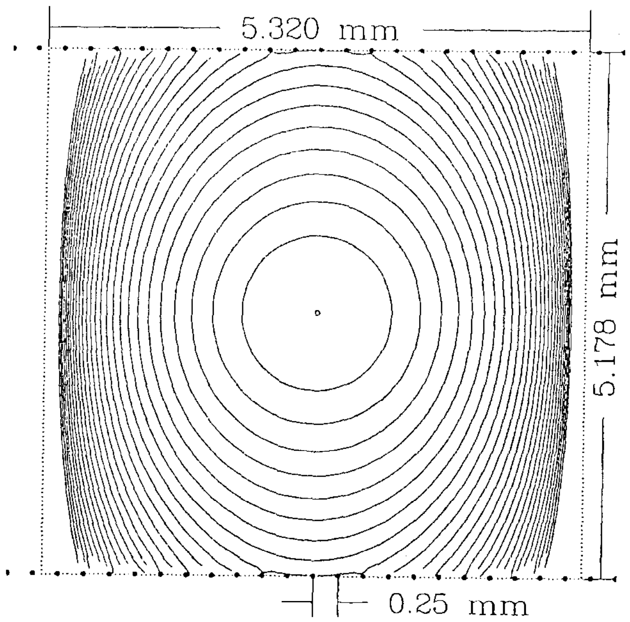

Figure 20: Drift cell of the ARGUS μVDC with isochrones for CO_2 - propane (90 : 10 , 4 bar).

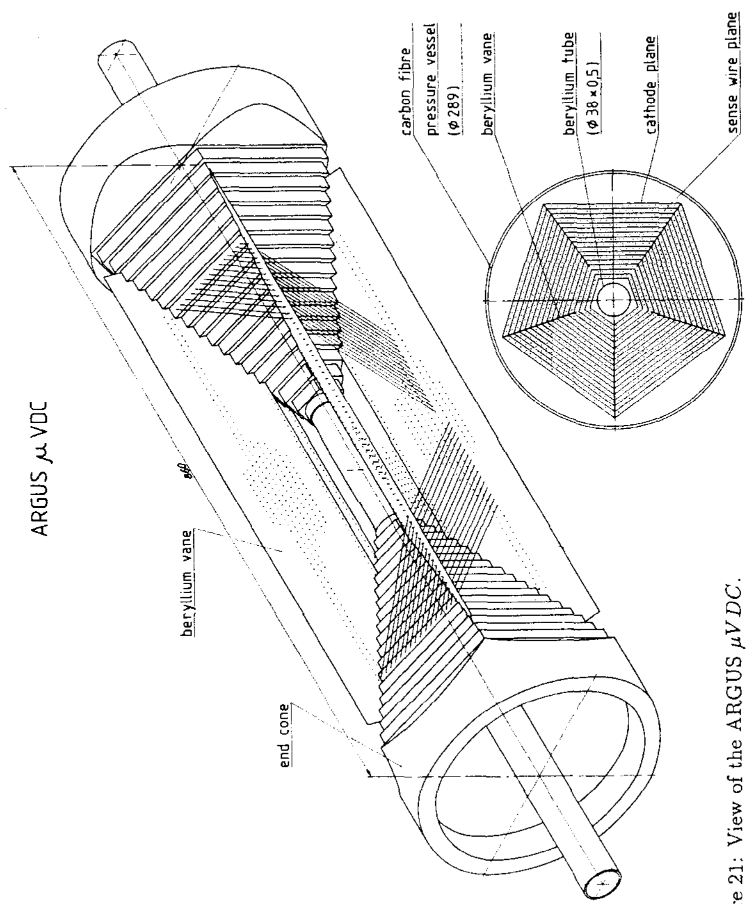

Figure 21: View of the ARGUS μVDC.

- A good vertex reconstruction requires a small lever arm from the detector to the vertex region. Therefore ARGUS wants to use an extremely narrow beam pipe, with a diameter of 38 mm made of 500 μm thick Beryllium (Fig. 22).

The beam pipe has been tested in the former Crystal Ball interaction region at DORIS. Most importantly, it was found that the beam pipe does not disturb the machine behaviour (this was still true for a 18 mm diameter tube tested later). However, the background from synchrotron radiation was found to be too large. This background is mainly due to backscatters of a moveable Cu-scraper which is necessary to shield the Be-tube from direct synchrotron light (Fig. 22). The tested Be-tube had a 8 μm Cu coating at the inside; a more favourable 50 μm Al coating was not possible for technical reasons. The collaboration decided on two measures to reduce the synchrotron radiation : Firstly, the Cu-scrapers will be coated with Titanium on the edges facing the interaction region. Secondly, additional dipole magnets, one on each side of the interaction region, will make the final bend smoother. This implies that the synchrotron radiation from the quadrupoles will now become the dominant background.

The new μVDC is currently built and will be installed at the end of this year to be available for the 1990 running of ARGUS.

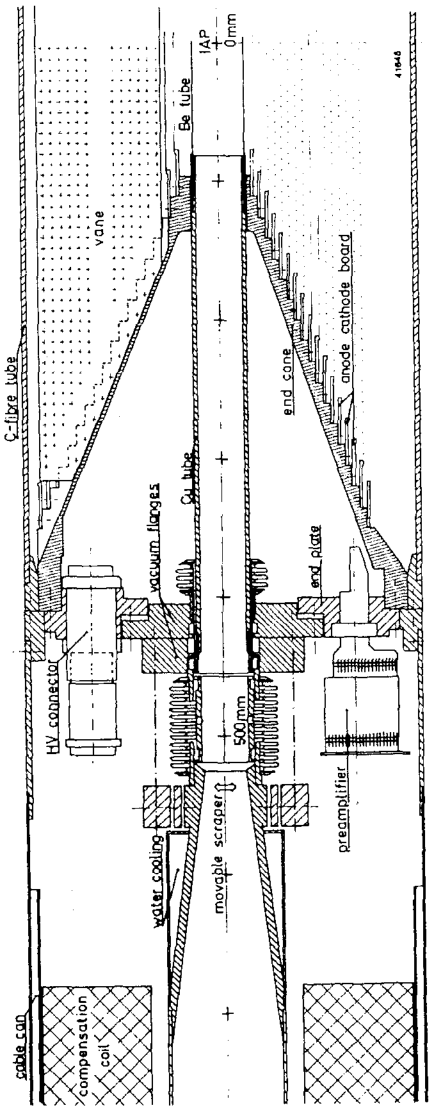

Figure 22: Design of the vacuum system near the interaction region for the new μVDC

6 Summary

The results from the ARGUS experiment reported in this talk are mainly on semileptonic B-decays. Since the dependence of semileptonic decay rates on the quark transition probabilities are expected to be reliably calculable, these decays are most frequently used to determine the CKM matrix elements.

The ARGUS collaboration determined the matrix element V_{cb} from three different semileptonic channels:

$$\begin{aligned} B \to D^* l\nu \quad &: \quad V_{cb} = 0.046 \pm 0.009, \\ B \to D l\nu \quad &: \quad V_{cb} = 0.042 \pm 0.008, \\ B \to l + X \quad &: \quad V_{cb} = 0.046 \pm 0.005. \end{aligned}$$

A study of the D^* helicity in the decay $B^0 \to D^{*-} l^+ \nu$ yields for the ratio of 0 to ± 1 helicity states: $\Gamma_L/\Gamma_T \approx 1$. This result discriminates between different models and allows for a more reliable description of the lepton spectra in semileptonic B-decays.

From semileptonic B-decays ARGUS determined also the lifetime ratio of charged to neutral B's:

$$\tau^{\pm}/\tau^0 = 1.00 \pm 0.23 \pm 0.14 \, .$$

(This result assumes the charged to neutral B production ratio at the $\Upsilon(4S)$ to be $f^{\pm}/f^0 \approx 1$).

In order to determine the CKM matrix element V_{ub} the ARGUS group searched for B decays into charmless final states. No such signal was found in exclusive channels. Upper limits were derived for the semileptonic decays $B^{\pm} \to \rho^0 l^{\pm} \nu$ and $B^0 \to \pi^- l^+ \nu$ and for B decays into n pions (n = 2,3,4,5). None of the limits is in conflict with standard model expectations.

Recently, the ARGUS group found evidence for $b \to u$ transitions from the inclusive lepton spectrum of $\Upsilon(4S)$ decays with a significance of 3.3 standard deviations. The result for the CKM matrix is

$$|V_{ub}|/|V_{cb}| = 0.10 \pm 0.02.$$

With improved statistics ARGUS updated the results on $B^0 - \overline{B^0}$ mixing. Mixing has been observed in lepton - lepton, D^* - lepton and $D^* l\nu$ - lepton correlations, leading to the combined result:

$$\begin{aligned} r &= 0.21 \pm 0.06 \pm 0.04 \\ \Delta M &= (4.2 \pm 1.1) \cdot 10^{-4} \, eV. \end{aligned}$$

This constraints standard model parameters (using in addition the theoretical bound $m_t < 190$ GeV and $|V_{td}| < 0.018$ from unitarity):

$$\begin{aligned} m_t &> 60 \, GeV \\ |V_{td}| &> 0.007. \end{aligned}$$

The ARGUS detector will be upgraded with a Micro Vertex Drift Chamber in order to improve the B reconstruction efficiency by tagging D's via their decay vertices. Novel features of the chamber are:

- extreme stereo angles ($\pm 45°$) to ensure optimal spatial resolution necessary to suppress fake vertices;
- a narrow beam pipe (37 mm diameter) allowing for a short lever arm for vertex reconstruction.

The new beam pipe has been tested to work in the environment of the DORIS machine.

References

[1] H.Schröder, 'Physics of B Mesons', DESY Report 88-101 (1988) .

[2] N. Cabibbo, Phys.Rev.Lett. 10 (1963) 531;
M.Kobayashi and T.Maskawa, Prog. Theor. Phys. 49 (1973) 652.

[3] K.Schubert, presented at the 1989 Int. Symposium on Heavy Quark Physics, Cornell, 1989 (Univ. Karlsruhe preprint IEKP-KA/89-6).

[4] ARGUS Coll., H.Albrecht et al., Nucl. Inst. Meth. A275 (1989) 1.

[5] G.Altarelli et al., Nucl. Phys. B208 (1982) 365.

[6] S.Stone, presented at the Int. Workshop on Weak Interactions and Neutrinos, Ginosar, Israel, April 1989.

[7] K.Wachs et al. (Crystal Ball Coll.), Z.Phys. C42 (1989) 33.

[8] R.Rückl, Habilitationsschrift, Universität München, 1984.

[9] D.Muller, Proc. of the 24th Int. Conf. on High Energy Physics, Munich, 1988.

[10] ARGUS Coll., H.Albrecht et al., Phys. Lett. 197B (1987) 452.

[11] Mark III Coll., J.Adler et al., Phys. Lett. 208B (1988) 152.

[12] ARGUS Coll., H.Albrecht et al., Phys. Lett. 219B (1987) 121.

[13] H.Pietschmann and F.Schöberl, Europhys. Lett. 2 (1986) 583.

[14] B.Grinstein, M.B.Wise and N.Isgur, Phys.Rev.Lett. 56 (1986) 298.

[15] M.Wirbel, M.Bauer and B.Stech, Z.Phys. C29 (1985) 637;
M.Bauer and M.Wirbel, Z.Phys. C42 (1989) 671.

[16] J.G.Körner and G.A.Schuler, Z.Phys. C38 (1988) 511.

[17] N.Isgur, D.Scora, B.Grinstein and M.B.Wise, Phys. Rev. D39 (1989) 799.

[18] CLEO Coll., D.Bortoletto et al., CLNS 89/922 (1989).

[19] T.Altomari and L.Wolfenstein, Phys. Rev. D37 (1988) 681.

[20] ARGUS Coll., H.Albrecht et al., DESY 89-082 (the results of this preprint have been modified assuming $f^0/f^{\pm}= 1$).

[21] J.M.Cline, W.F.Palmer and G.Kramer, DESY 89-029 (1989).

[22] M.A.Shifman, Proc. of the 1987 Int. Symposium on Lepton and Photon Interactions at High Energies, Hamburg, 1987.

[23] M.Danilov, Proc. of the 24th Int. Conf. on High Energy Physics, Munich, 1988.

[24] ARGUS Coll., H.Albrecht et al., Phys. Lett. 209B (1988) 119.

[25] D.L.Kreinick, Proc. of the 24th Int. Conf. on High Energy Physics, Munich, 1988.

[26] P.Baringer, these Proceedings.

[27] M.Danilov, Talk given at the 1989 Int. Symposium on Lepton and Photon Interactions, Stanford, 1989.

[28] ARGUS Coll., H.Albrecht et al., Phys. Lett. 192B (1987) 245.
[29] K.Hagiwara, Proc. of the 2nd Int. Conf. of Hadron Spectroscopy, KEK.
[30] CLEO Coll., M.Artuso et al., Phys. Rev. Lett. 63 (1989) 2233.
[31] J.S.Hagelin, Phys. Rev. D20 (1979) 2893.
[32] G.Altarelli, Proc. of the Intern. Europhysics Conf. on High Energy Physics, Uppsala, 1987.
[33] G.Costa et al., Nucl. Phys. B297 (1988) 244.
[34] H.Kolanoski, Proc. of the XVI Int. Meeting on Fundamental Physics, Peniscola, Spain, 1988;
D.Hitlin, Proc. of the Workshop on High Luminosity Asymmetric Storage Rings for B Physics, Pasadena 1989 (CALT-68-1552);
H.Nesemann et al., DESY 89-080 (1989).
[35] E.Michel et al., presented at the Wire Chamber Conf., Vienna 1989, DESY 89-044.
[36] ARGUS Coll., H.Albrecht et al., Internal Report DESY F15-86-01, Aug. 1986.

A REVIEW OF RECENT RESULTS ON THE HADRO- AND PHOTOPRODUCTION OF CHARM

JEFF SPALDING
Research Division, Fermilab, P.O. Box 500
Batavia, Illinois 60510, USA

ABSTRACT

The study of charm hadro- and photoproduction is a very active field with several fixed target experiments currently analyzing high statistics data samples and others preparing for data-taking. In this talk I will review some of the most recent results from Fermilab and CERN experiments, and discuss the prospects for the near future. In this brief review it will be possible only to point to some of the most interesting or controversial aspects of the results, not to discuss them in depth. I apologize for these shortcomings.

1. Introduction

In the study of heavy flavor production the goal is to understand the dynamics of quark and gluon interactions. In QCD the lowest order processes are photon-gluon fusion for photoproduction [$O(\alpha_s\ \alpha_{em})$], and quark-quark and gluon-gluon fusion for hadroproduction [$O(\alpha_s^2)$].

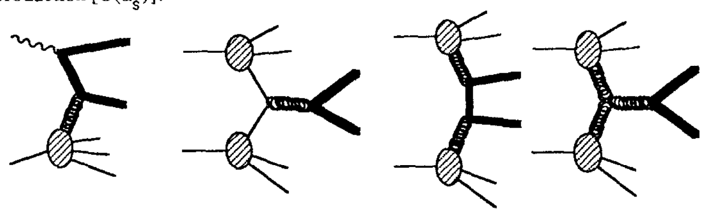

Photon-Gluon Fusion   Quark-Quark Fusion   Gluon-Gluon Fusion

In the last couple of years the next-to-leading order diagrams [$O(\alpha_s^3)$ and $O(\alpha_s{}^2\alpha_{em})$] have been calculated. (See K. Ellis contributions to this summer school.) The contribution of these diagrams does not change the differential shape of the cross section, but is larger in magnitude than the leading order contribution. At first glance this is disturbing behavior for a perturbation series which is expected to converge, however Ellis et al. point out that at the next-to-leading order level new processes involving gluon exchange diagrams can contribute, which don't exist at lowest order. Lowest-order calculations required either a low value for the charm quark mass (around 1.2 Gev)[1] or a higher value with an arbitrary "K-factor" to account for the magnitude of the cross section (eg. m_c = 1.7 GeV and K= 6)[2]. The next-to-leading order calculations can accommodate the data with a very reasonable mass of 1.5 GeV or higher without the need for a K-factor. Ellis and others stress that the charm quark mass may be too light for the reliable application of perturbation theory, but the agreement with the data is encouraging.

The data are usually described in terms of an energy dependence for the total charm cross section, and by the differential cross section, usually parameterized as: $d\sigma/dx_F = (1-x_F)^n$ and $d\sigma/dp_t^2 = e^{-bp_t^2}$. Most of our knowledge of the charm cross section comes from the dominant decay modes of D^0 and D^+ mesons, i.e. the high statistics channels for which the branching ratios are well measured. In photoproduction there are now high statistics experiments covering large overlapping ranges of photon energy, and the experimental situation is in relatively good shape. In hadroproduction, the situation is less clear. High statistics samples are only just becoming available, and the problem is compounded by the need to compare and combine the data from experiments with low statistics, typically in a limited number of charm modes, using different projectiles, and very different target materials. An understanding of the A-dependence is essential to compare these results, and is in itself an important measurement. The existence of a "leading particle effect", where charm particles which share a valence quark type with the beam particle are produced with a more forward x_F distribution, has been a much discussed issue lately. While the direct experimental evidence for such an effect is now weak, there are several reports of the forward production of charm baryons. The present and next generation of experiments are addressing these issues with higher statistics measurements from a variety of targets and beam particles.

Table 1 contains a list of the experiments discussed in this review. We will start by discussing two experimental issues in extracting the rare charm decays from the common or garden total cross section events. Then we will briefly review the status of the data in photoproduction and hadroproduction for the total charm cross section. Finally we will take a quick look at the controversial, but rather sparse data on charm baryon production.

Table 1: Experiments Discussed in this Paper

	Beam	Target	Trigger	Data Sample
E691	γ, 90-260 GeV	Be	Transverse Energy	100M
NA14	γ, 40-120 GeV	Si	Multiplicity	17M
E687	γ, 160-350 GeV	Be	Interaction/Energy	75M,*
BIS-2	n,<En> = 58 GeV	C (C,Al,Cu)	Multiplicity	11.4M
E400	n,<En>= 640 GeV	W,Si,Be	Multiplicity	45M
NA27	π^-,p 300 GeV	H	Interaction	200K
	p 400 GeV			1M
E743	p 800 GeV	H	Interaction	500K
NA32	π^-,K^-,p^- 200 GeV	Si	Interaction	40M
	230 GeV	Cu	x^+x^-, x = k/p	17M
WA82	π^-,K^-,p^- 340 GeV	Si,W	Impact Parameter	30M,*
E653	p, 800GeV	emulsion	Muon	5M
	π^-, 600 GeV			15M
E769	$\pi^\pm$,$K^\pm$,p^+ 250 GeV	Be,Al,Cu,W	Transverse Energy	500M
E791	π^-,K^- 500 GeV		Transverse Energy	*

* Further data-taking in the near future.

2. Two Experimental Issues: Triggering and Vertex Reconstruction

The charm cross section is 0.5% of the total cross section in photoproduction, and only 0.1% in hadroproduction, so, the experiment trigger is an important factor in enriching the charm content of a data set. Ideally for cross section studies the trigger should be as unbiased as possible, which unfortunately implies a small enrichment factor. The three photoproduction experiments in Table 1 all use relatively open triggers. In hadroproduction with the lower charm content, only E769 and E791 of the high statistics experiments take this approach. Table 2 illustrates three trigger philosophies, ranging from the relatively unbiased ET trigger of the experiments using the Tagged Photon

Spectrometer, to the more severe selection criteria (and higher enrichment) of the WA82 impact parameter trigger.

Table 2: Three Approaches to Triggering

Experiment	Trigger	Charm Enrichment in the Selected Sample	Comments
Tagged Photon Spectrometer E691/E769/E791	High Transverse Energy E_T> a few GeV	modest x 2 or 3	Accept ~ 1/4 or 1/3 of σ_{TOT} Less Biased
NA32	Cerenkov I.D. K^+/p and K^-/p^-	x 7 for Λ_c^+ and D_s^+	Biased for D decays where K or p from the other charm decay is needed. (Not so easy to correct.)
WA82	Impact Parameter ≥ one track between 0.1 and 1mm at primary vertex	x 15 for D^+	Biased against short lifetimes (relatively easy to correct).

Cuts must be applied either in the off-line analysis (TPS), or on-line (WA82). Certainly cutting off-line is safer and allows a thorough study of the effects of the cuts, but requires that the data acquisition system and at least the preliminary stages of the analysis handle a very large number of events. (E791 is expected to write up to 1 x 10^{10} events to tape.) With advances in computing and storage media this approach becomes more appealing.

Extracting a clean charm signal from the large combinatorial background is a severe problem. All but one of the experiments discussed here (BIS-2) use the separation of the charm decay vertex from the production vertex to reduce the combinatorial background. The methods employed are either visual (bubble chambers and emulsions) and slow (and thus very low statistics), but affording high resolution and large acceptance, or electronic (silicon vertex detectors and charge coupled devices).

The latter method allows the measurement of very high statistics samples. As an example of this technique, Figure 1 shows the separation between the production and decay vertices, divided by the error in that separation, versus the mass of $K\pi$ combinations in E691 data. The D^0 signal is clearly separated. Cutting on this separation variable can lead to a reduction by a factor of over 1000 in the combinatorial background. Without such a reduction a detailed study of charm production is not possible.

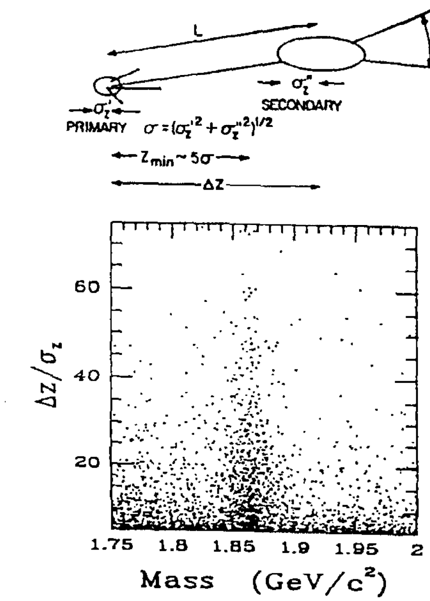

Figure 1: From E691

This requirement for observing a separation between the production and decay vertices is not entirely unbiased for production studies, since the selection efficiency is lower for events with lower charged multiplicity at the production vertex.

3. Photoproduction

Two experiments have recent results on charm photoproduction: E691 at Fermilab,[3] and NA14' at CERN.[4]

With 10,000 fully reconstructed charm decays, E691 can fully parameterize the differential cross section and is presently analyzing the shape in the context of the the next-to-leading order QCD calculations. Here we will only report on the measurement of total charm cross section. Using a photon-gluon fusion Monte-Carlo program with Lund fragmentation to extrapolate to all x_F, and all charm states, E691 derives σ_{cc} = 4.49±0.07±0.46 μb per Be nucleus using $A^{0.93}$ † this gives σ_{cc} =0.58±0.01±0.06 μb per nucleon (at $<E\gamma>$=145Gev). The D cross section rises by a factor 1.96±0.24 from 100 GeV to 200 GeV. NA14' derives σ_{cc}(event)=0.45±0.05±0.11μb per nucleon (at $<E\gamma>$=100Gev).

† The A-dependence for the total cross section and for ψ production are very similar in photoproduction:
α = 0.920±0.002 μb for σ Total (ref. 5)
α = 0.94±0.02 ±0.03 μb for ψ (ref. 6)

The energy dependence predicted by the next-to-leading order calculations of Ellis and Nason[7] for two charm quark masses is shown in Figure 2, compared to the data. The three curves represent the central value and the range for reasonable variation of the mass scale μ and QCD scale Λ. The gluon structure function used is $xG(x) = 3(1-x)^5$. The data prefers a charm quark mass between 1.5 and 1.8 GeV.

To really tie down the QCD parameters it is clearly necessary to have high statistics experiments covering a large energy region. E691 is the first such experiment, complemented now by NA14' at lower energies and E687, which is a new photoproduction experiment at Fermilab, at higher energies. E687 is presently analyzing their first data run, and has very recently presented their first charm signals. They expect a factor 10 increase in a luminosity for the next data run, and will be the first photoproduction experiment to have a chance at b-physics. The prediction for b-production of Ellis and Nason is shown in Figure 3. The cross section is rising steeply, but even so it is 0.1-0.2% of the charm cross section for the energy range of E687.

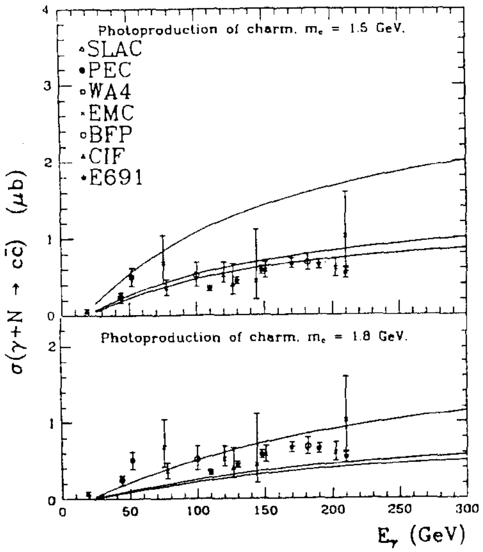

Figure 2: From Ellis & Nason

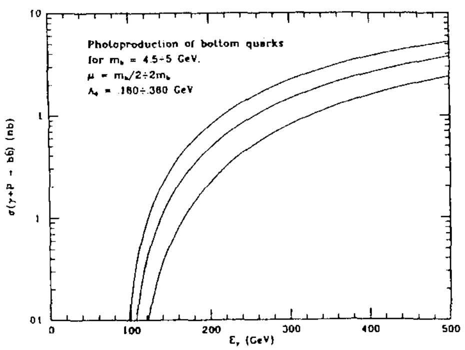

Figure 3: From Ellis & Nason

4. Hadroproduction

In Figure 4, Alterelli et al.[8] compare their prediction for the hadroproduction cross section at next-to-leading order, which is based on the work of R. K. Ellis, S. Dawson, and P. Nason,[9] with the results of several experiments. (The compilation of data is from reference 10.) The values plotted are for $\sigma_{c\bar{c}}$ (all x_F). A high charm quark mass is indicated without the need for a K-factor.

It is important to note that many of the experiments included in this plot have limited statistics, and use a variety of target materials. Some see charm decays directly, others are inclusive beam dump experiments. In order to combine these data for this plot, an A-dependence of $A^{1.0}$ is used. It is pointed out in reference 10 that the good agreement at $\sqrt{s}$~ 25-30 GeV deteriorates rapidly for α different from 1.0, as the beam dump (Fe) and LEBC (H) results diverge.

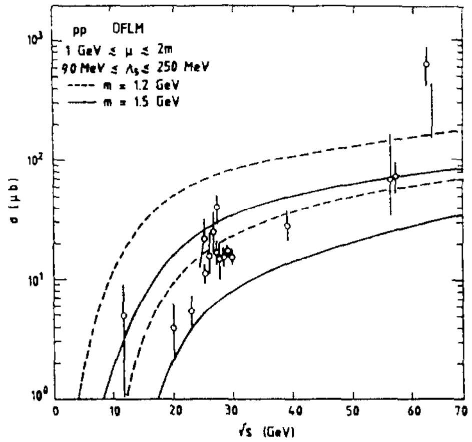

Figure 4: From Alterelli, et al.

Unlike photoproduction, the interpretation of hadroproduction results is impaired by the uncertainty in the A-dependence of the charm cross section. As discussed above there is indirect evidence that α~1, yet direct measurements have tended to prefer numbers nearer 0.75[11] (E613, WA78), although the full range between is covered. WA82 has a new result from a direct measurement of α. The experiment uses a target which is divided transverse to the beam direction into two materials, tungsten and silicon, and compares the yield of D^0 and D^+ from the two sides. Using 700 D-decays (one quarter of their full sample) they obtain α= 0.89 ± 0.05 ± 0.05 at $<x_F>$=0.2. The measurement is limited in systematic error by the uncertainty in the relative beam flux on the two sides of the target. This is determined using the relative rate of all triggers, and the known A-dependence for the total hadronic cross section. An improved measurement is expected from further data-taking.

It seems likely that α is close to 1 (0.9 or above) at central x_F, but smaller at forward x_F. This behavior is indeed the case for the total cross section.[12]

The x_F dependence of charm production is still a somewhat controversial issue. Table 3 compares the results of CERN experiment NA27[13] (LEBC with the EHS : pp at $\sqrt{s}$=27.4 GeV, pp, and πp at $\sqrt{s}$=26 GeV), and Fermilab experiment E743[14] (LEBC with the Fermilab MPS : pp at $\sqrt{s}$=39 GeV). We find a rise in total cross section with $\sqrt{s}$ consistent with QCD fusion models, and an increase in n, making the production more central at higher $\sqrt{s}$. This is attributed to lower x gluons having sufficient energy to contribute to the cross section.

Table 3: Summary of NA27 and E743 Results

	NA27 (pp)		E743 Preliminary
$\sqrt{s}$ (GeV)	26	27.4	38.8
$\sigma(D^o/\bar{D}^o+D^\pm)$ (μb)		30.2±2.2	48^{+10}_{-8}
n in $(1-x_F)^n$	1.8±0.8	4.9±0.5	8.6±2.0
b in $e^{-bP_t^2}$	1.1±0.3	1.05±0.10	0.8±0.2

The more central production at higher energies is confirmed by a preliminary result from E653 (pp at $\sqrt{s}$ of 38.8 GeV): n=11.2 ± 0.9. However both experiments have low statistics and there is clearly a need for more data. Another issue in the x_F dependence is the so called leading-particle effect. This was first reported in πp interactions by NA27 where n=1.8 ± 0.6 for leading and 7.9 ± 1.5 for non-leading D's. Such an effect may be related to the high cross-sections reported from ISR experiments for the diffractive-like production of Λ_c. We will touch on this issue again in discussing baryons production below. Two recent results, one from NA32[15] (n(leading)=2.93 ± 0.33, n(non-leading)=4.37 ± 0.44) and a preliminary result from WA82[16] (n(all D's)= 3.40 ± 0.45 with room for only a slight leading effect. Figure 5, suggests that if there is a leading effect it is much smaller than originally reported.

It is interesting to note that the calculations of Ellis et al.[9] do not produce this leading effect, but do predict a slightly more forward distribution for D^o and D^- over D^0 and D^+ (as compared to D^0 and D^- over D^o and D^+ for the valence quark effect). See Figure 6. Unfortunately, confirmation of this prediction will require statistics beyond the next generation of experiments.

5. Charm Baryons

The situation for charm baryons is more confused, due primarily to poor statistics, and there are clearly conflicting results. Some reports indicated large diffractive-like cross sections, others see no such effect.

ISR experiment R608[17] and Serpukhov experiment BIS-2[18] in a neutron beam have recently reported large measurements of σ.B for Λ_c. R608: σ.B ($\Lambda 3\pi$) = 2.84 ± 0.50 ± 0.72 μb/N (X_F > 0.5), BIS-2: σ.B ($\Lambda 3\pi$) ~ 3-7 μb/c nucleus (X_F>0). Neither experiment uses any vertex reconstruction and the backgrounds are large. In contrast, NA32, using silicon vertex detectors and CCD's, has a very clear signal (Figure 7) and finds σ.B (pKπ) = 0.17 ± 0.02 μb/N (X_F>0) [using $A^{1.0}$] for a π beam.

NA32 has six fully reconstructed Ξ_c^+ decays (e.g. Figure 8) and finds σ.B ($\Xi\pi\pi$) = 0.04 ± 0.02 ± 0.02 μb/N (X_F >0), well below the previously reported results of E400[19] (neutron beam), and WA62[20] (hyperon beam).

The QCD fusion models produce charm centrally with no enhanced forward

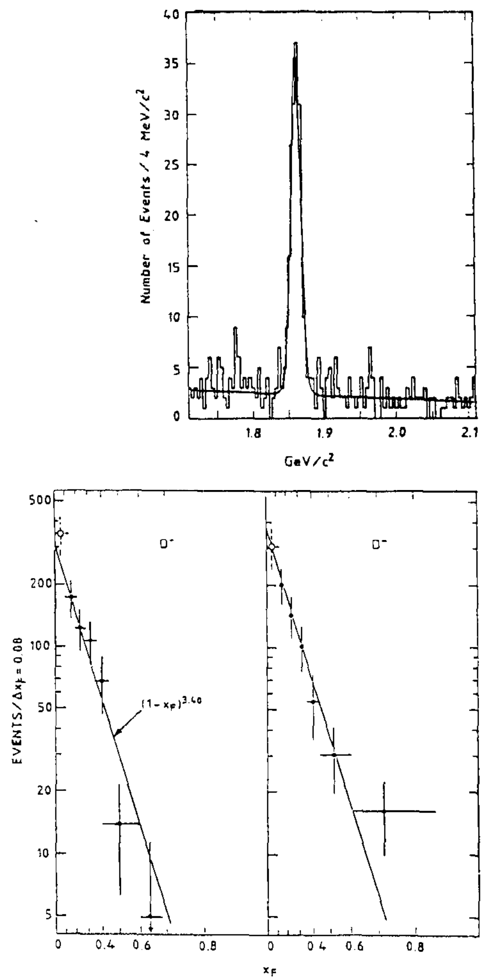

Figure 5: WA82 Preliminary (1/4 statistics) $D^\pm \rightarrow K\pi\pi$ and X_F distributions

production. If there is such an enhancement, it is due to some other mechanism, perhaps with a low multiplicity at the primary vertex, reducing the sensitivity of experiments requiring vertex separation.

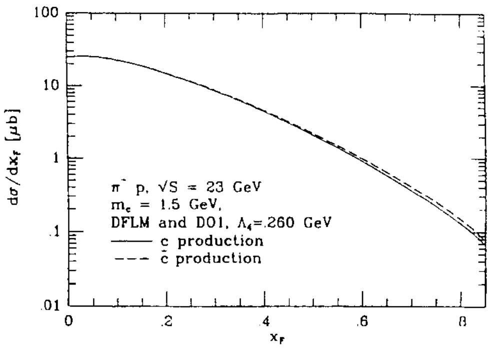

Figure 6: Nason, Dawson & Ellis

6. Future Experiments

The present data of E687 will extend the measurement of the photoproduction charm cross section up to 350 GeV. The overlap of the present generation of experiments (NA14': 40 - 120 GeV, E691: 90 - 260 GeV, E687: 160 - 350 GeV), each with high statistics, will tie down the QCD parameters. In the near future WA82 and E769 will analyze their hadro-produced samples. E769 has collected 500M events on tape using the ET trigger, with beam particle identification (π, K and p), and using four different target materials ranging from beryllium to tungsten. The experiment will address the issues of target A-dependence and beam flavor dependence.

In the next Fermilab fixed target run two experiments will aim for very high statistics (>100,000 fully reconstructed charm decays) ; E687 will run again (photoproduction), and E791 will follow E769 with the Tagged Photon Spectrometer (hadroproduction). Both experiments make use of extensive upgrades to their beamlines and data-acquisition systems. These very high statistics samples will finally allow a detailed parametrization of the differential cross sections of both D's and charm baryons, as well as the study of rare decay processes. Fermilab experiment E781 will run in the following period, looking for the forward production of charm-strange baryons using a hyperon beam, prompted by the large Ξ_c signal reported by WA62.

7. Concluding Remarks

There is continuing progress in measuring and modelling the production of charm. In the near future the data on photoproduction will allow the measurement of the QCD parameters, including the charm quark mass and the gluon structure function. In this

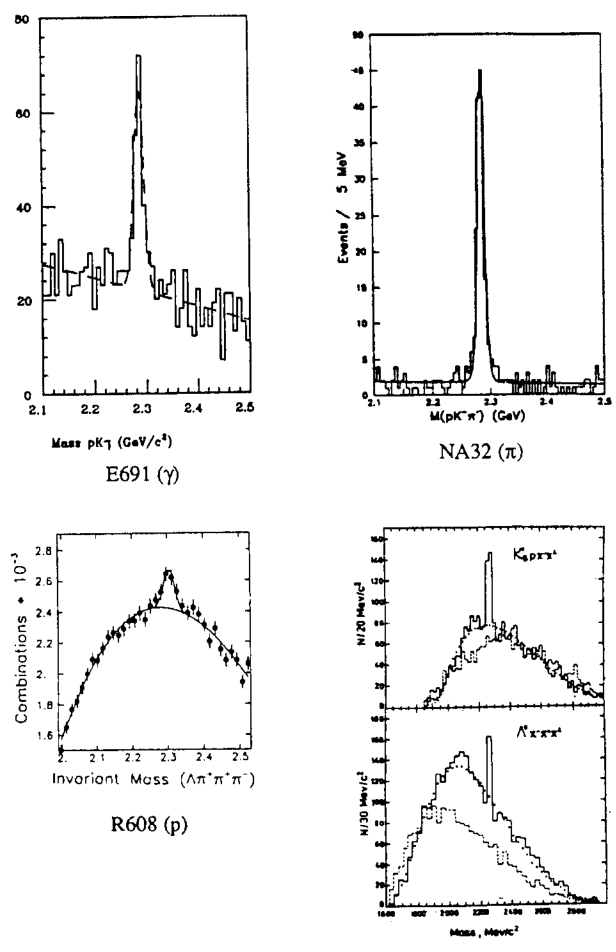

Figure 7: Λ_c Signals

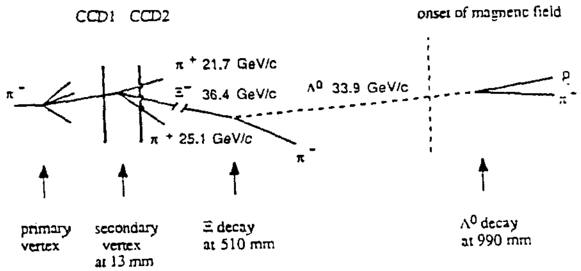

Figure 8: NA32 one of six events $\Xi_c \to \Xi\pi\pi$

regard hadroproduction lags behind somewhat, but this is because it has additional [interesting] issues and difficulties. These issues should be resolved with the present and next generation of experiments. Detailed measurement of charm baryon production will require the statistics of these next experiments.

8. Acknowledgements

This is an incomplete attempt to summarize the results of others, and many people have contributed information and ideas. The opinions, shortcomings and mistakes are mine. Special thanks are due to Laura Sedlacek for her work on the manuscript.

References

1. NA27 & E743: I. Leedom and S. Rencroft, presented at 4th DPF meeting of APS, Storrs, 1988.

2. HOBC: H. Cobbaert et al., *Z Phys.* **36C**(1987)577.

3. E691: J.C. Anjos et al., *Phys. Rev. Lett.* **62**(1989)513.

4. NA14: R. W. Forty et al., presented at the XXIV Conference on High Energy Physics (Munich).

5. D.O. Caldwell et al., *Phys. Rev. Lett.* **40**(1978)1222 and *Phys. Rev. Lett.* **42**(1979)553.

6. E691: M. D. Sokoloff et al., *Phys. Rev. Lett.* **57**(1986)3003.

7. QCD: R. K. Ellis and P. Nason, Fermilab-Pub-88/54-T.

8. QCD: G. Alterelli, M. Diemoz, G. Martinelli, and P Nason, CERN-TH.4978/88.

9. QCD: P. Nason, S. Dawson, and R.K. Ellis, Fermilab-Pub-87/222-T.

10. Review: S.P.K. Tavernier *Rep. Prog. Phys.* **50**(1987)1439.

11. W878: H. Cobbaert et al., *Phys. Lett.* **191B**(1987)456.

    E613: Duffy et al., *Phys. Rev. Lett.* **55**(1985)1816.

12. D.S. Barten et al., *Phys. Rev.* **D27**(1983)2580.

13. NA27: M. Aguilar-Benitez et al., *Phys. Lett.* **123B**(1983)103, *Phys. Lett.* **189B**(1987)476.

14. E743: R. Ammar et al., submitted to the XXIV Conference on High Energy Physics (Munich).

15. NA32: S. Barlag et al., CERN-EP/88-104.

    S. Kwan, presented at the International Symposium on Heavy Quark Physics, Cornell, 1989.

16. WA82: D. Barberis, presented at the International Symposium on Heavy Quark Physics, Cornell, 1989.

17. R608: P. Chamvat et al., *Phys. Lett.* **199B**(1987)304.

18. BIS-2: A.N. Aleev et al., *Z. Phys* . **37C**(1988)243.

19. E400: P. Coteus et al., *Phys. Rev. Lett.* **59**(1987)1530, C. Shipbaugh et al., *Phys. Rev. Lett.* **60**(1988)2117.

20. WA62: S.F.Biazi et al., *Z Phys.* **C28**(1985)175.

Search for the Top Quark at UA1

UA1 Collaboration, CERN, Geneva, Switzerland

Aachen - Amsterdam(NIKHEF) - Annecy(LAPP) - Birmingham - Boston - CERN - Harvard - Helsinki - Kiel - Imperial College, London - Queen Mary College,London - Madrid(CIEMAT) - MIT - Padua - Paris(College de France) - Riverside - Rome - Rutherford Appleton Lab - Saclay(CEN) - UCLA - Victoria - Vienna Collaboration.

Abstract

UA1 is continuing its search for new quarks in the muon channel with new data coming from the 1988 and 1989 runs. A description of the analysis done on a subsample of events (1.22 pb^{-1}) is given.

The properties of isolated muons accompanied by jets are consistent with the Standard Model prediction. The data do not show a signal for new quark production.

Using the UA1 data $\simeq 5.4\ pb^{-1}$ (1983-1989) and combining the electron and muon channels a lower limit on the mass is obtained at 61 GeV/c^2 (95% CL) for the t-quark and 41 GeV/c^2 (95% CL) for the b'-quark.

Presented by Teresa Rodrigo
at the Topical Conference of the XVII SLAC Institute on Particle Physics
July 10-21 1989, Stanford, California

Introduction

We report on the search for signals of the production and decays of the sixth quark (t-quark) in $p\bar{p}$ collisions at $\sqrt{s} = 630$ GeV using the UA1 detector at CERN.

A lower mass limit for the top quark of 41 GeV/c^2 (at 95% CL) has been published by UA1 [1],[2] based on the analysis of a data sample of $\simeq 0.7\ pb^{-1}$ accumulated between 1983 - 1985. The study was performed in the framework of the Standard Model and QCD.

We report here on the analysis of the data coming from the 1988 run, which represent $\simeq 1.22\ pb^{-1}$. As the UA1 detector is slightly changed with respect to previous data taking periods, first we describe in Section 1 the present UA1 detector and its performances. In Section 2 the characteristics of the 1988 run with ACOL are given.

The t-quark production and decay properties are revised in Section 3 together with the backgrounds expected for the experimental top signatures considered in the analysis.

In Section 4 we explain how a sample of muon + jet(s) events (control sample) is understood, mainly in terms of standard heavy flavour production. The agreement between the predicted contributions for this sample and the data gives confidence in the understanding of our data and detector, and allows us to go further in the top search with different samples where the sensitivity to top-quark production is improved.

The search for the t-quark in different channels, single muon and dileptons, is reported in Section 5. We explain briefly the top mass calculation used in the analysis. In this section, the overall sample (1983-1988) is summarised and a combined top mass lower limit is given.

In Section 6 we report on the extension of the present analysis to the search for a fourth generation quark, b'.

A search for non-standard top decay modes is under study. A preliminary study is presented in Section 7.

Updated results from a more complete analysis, using the full available statistics (1988 + 1989), are given in Section 8.

Finally, a summary and preliminary conclusions on m_t and $m_{b'}$ lower limits are set out in Section 9.

1 UA1 Detector and Performance

UA1 is a 4π detector, Fig. 1; a detailed description can be found in [3]. Only the major changes in the detector, compared to its previous configuration, are described here.

The detector consists of:

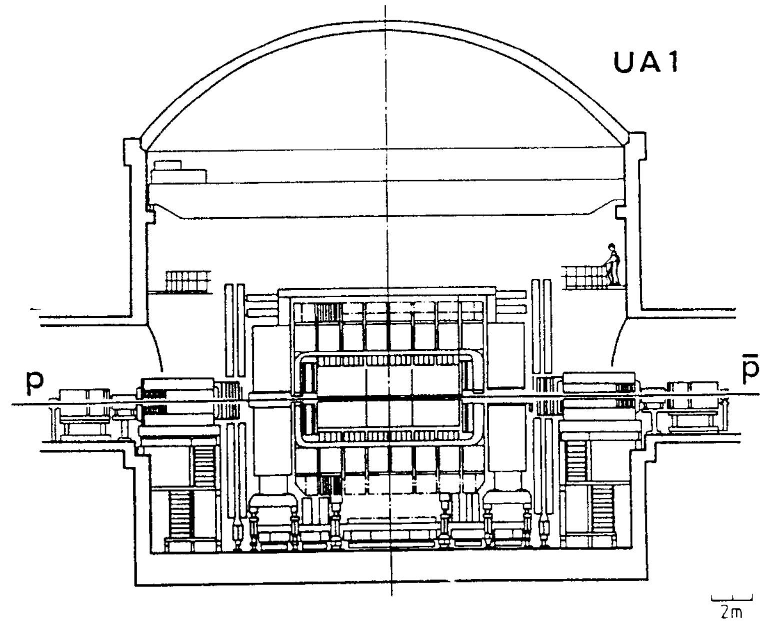

Figure 1: Schematic view of the UA1 detector

• The Central Detector

A Central Drift chamber (CD) inside a dipole magnetic field of 0.7 T transverse to the beam axis is used for measuring the momentum of charged particles. The CD is operated in a new mode in order to cope with the higher currents induced by the increased collider luminosity. The wire gain was lowered by a factor of 4, which was compensated by the same factor increase in the electronic gain. This resulted in a degradation of the charge division measurements.

The resolution in position along the wire for the longest wires (2m long) is now about 7 cm. The resolution in drift-time measurements is essentially unchanged at 300 μm on the average over the whole chamber volume.

• The Calorimeter

The old electromagnetic calorimeter (gondolas and bouchons) has been dismounted to be replace in the future by a new *Uranium / Tetramethyl-pentane* (TMP) calorimeter.

The present UA1 calorimetry consist only of the hadron calorimeter which is still in place. Therefore, we are no longer able to trigger on electrons and we concentrate, for the time being, on muon physics.

The hadron calorimeter (5 cm. Fe / 1 cm. scintillator), consist of two parts: central (C's) and endcaps (I's) covering 3 units in pseudorapidity. The C's cover $|\eta| < 1.5$. There are 16 C's, each with an azimuthal segmentation into 12 cells of $90 \times 90\ cm^2$. *They are sampled at two depths: after 2.5 and 5.0 nuclear* interaction lengths. The endcaps cover $1.5 < |\eta| < 3.0$. There are six vertical I modules per end-cap, each divided into six blocks of dimension $0.9 \times 0.9\ m^2$. The blocks nearest to the beam are further subdivided into four stacks of dimension $0.5 \times 0.4\ m^2$. The I's are also sampled at two depths: after 3.5 and 7.0 nuclear interaction lengths.

The performance of this calorimeter has been restudied. From 1988 test-beam data we have measured the electromagnetic and hadronic energy resolution to be $\sigma(E)/\sqrt{E}$ *of* $\simeq 50\%$ *and* $\simeq 80\%$ *respectively (Fig. 2). The calorimeter response* to electrons and hadrons has been parametrised and used in the Monte Carlo simulation of the calorimeter.

We used a large minimum-bias data sample taken in 1987, in the same detector conditions as at present, to study the resolution on missing transverse energy and jets measurements in the hadron calorimeter. We find, as shown in Fig. 3, that the missing transverse energy resolution can be parametrised as a function of ΣE_T: $\sigma(E_T^{miss}) = 0.8\ \sqrt{\Sigma E_T}$.

Concerning the jet measurement, Fig. 4a,b show *the transverse energy flow* around the calorimeter jet axis for $E_T^{jet} > 10$ GeV. These jet profiles can be compared with those (Fig. 4c,d) which show the transverse momentum flow around the jet as measured in the central tracking chamber.

The degradation in missing transverse energy resolution is about 15% compared with the previous calorimeter configuration. The jet recognition

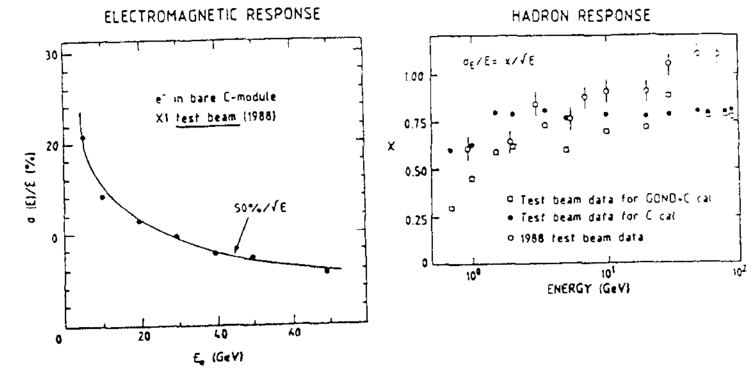

Figure 2: Electromagnetic and hadron energy resolution. In Fig. 2b the open squares represent the old calorimeter configuration (electromagnetic + hadron calorimeter). The hadron calorimeter alone (black dots) is compared with recent 1988 test beam data (open dots).

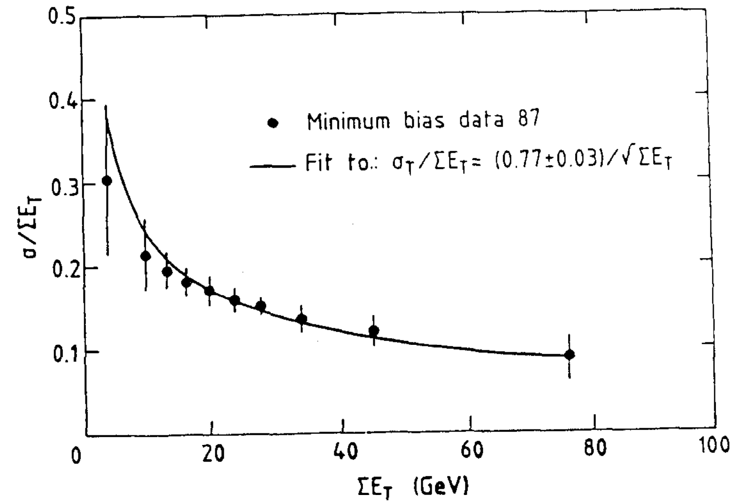

Figure 3: Missing transverse energy resolution.

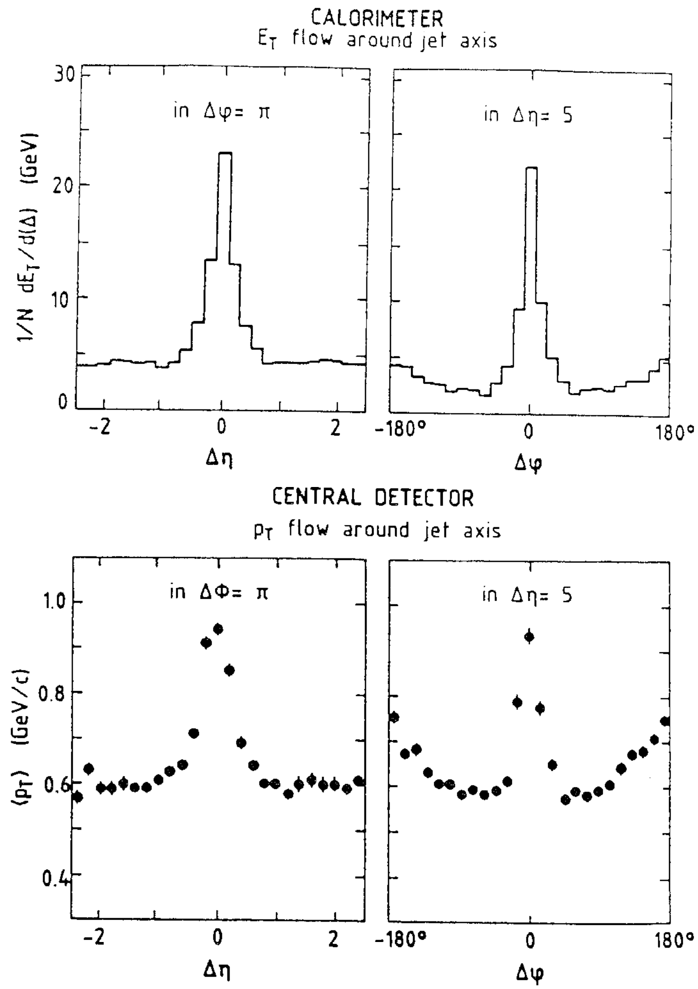

Figure 4: Jet Profiles : Transverse energy flow around the jet axis as measured in the calorimeter (a,b). Transverse momentum flow around the jet axis as measured in the central detector (c,d).

capability in the hadron calorimeter alone is still rather good, but systematic errors on the jet energy scale are also degraded.

During the 1988 run the calibration of the calorimeter was followed using different sources: cosmic muons for absolute calibration, laser for gain measurements and minimum-bias data for relative cell-to-cell variations and time-dependence monitoring. The systematic error on the absolute energy scale is $\simeq$ 7% in the central region.

• The Muon Chambers

The muon detection system was essentially unchanged compared to the earlier runs. The system of drift tubes used for muon detection covers 70% in ϕ angle for $|\eta| < 1.0$ and 90% for $1.0 < |\eta| < 2.3$. The acceptance as function of rapidity is shown in Fig 5.

Outside the hadron calorimeter, the shielding of the muon detection system has been improved with the installation of an additional 820 Tm of iron absorber in the forward region. A limited number of streamer-tube chambers were added [4].

2 1988 Run and Data Sample

During the 1988 data-taking period, the total integrated luminosity delivered by the SPS was 3.4 pb^{-1}, 3.0 pb^{-1} with the UA1 detector operational. A sample of $\simeq 1.33$ pb^{-1} was recorded by the experiment. The total data taking efficiency was about 55%.

The run was mainly dedicated to muon data. First and second-level muon trigger gave a single muon trigger in the region $|\eta| < 1.7$. The third-level trigger, using 11 emulators (3081E) in parallel, selected the most interesting events to be written on a special tape for early analysis.

The muon trigger chain was as follows (rate at $2 * 10^{30} cm^{-2} s^{-1}$) :

• Beam crossing :	260 kHz
• Pretriggers :	80 kHz
(inelastic, nondiffractive interactions)	
• 1st level muon trigger :	33 Hz
(pattern of tubes hit defines a 150 mrad cone in $\mid\eta\mid < 1.7$ or in $\mid\eta\mid < 2.0$ for dimuons)	
• 2nd level muon trigger :	10 Hz
(uses drift-time information to define narrower cone of $\simeq$ 70 mrad; efficient above $p_T^\mu > 6$ GeV/c for 1 μ and $p_T^\mu > 1.5$ GeV/c for 2 μ's)	
• third level muon trigger :	2 Hz
(3081E emulator farm: matching CD track, $p_T^\mu > 5$ GeV/c)	

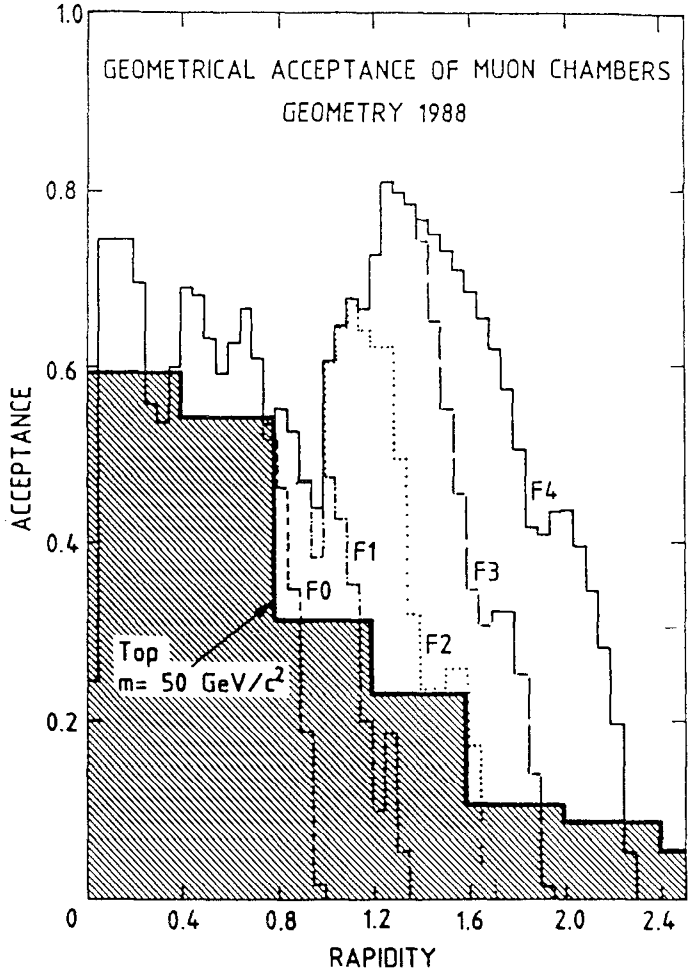

Figure 5: Geometrical acceptance of the muon chambers as a function of pseudorapidity (full line). The different active trigger areas are indicated (dashed and dotted lines). The shared area shows the acceptance for muons coming from top semileptonic decays (m_t = 50 GeV/c^2).

2.1 Data Sample

We recorded three sets of data: muon data used for muon physics (heavy flavour, W/Z production, top search, etc...), single jet data (QCD jet studies and background calculations) and minimum-bias data for calibration purposes.

The total number of events is divided as follows :

A) Muon trigger data : We took $\simeq 8.8 \times 10^6$ events corresponding to a total integrated luminosity of $\simeq 1.22 pb^{-1}$.

After the offline filter (third level trigger) and loose CD-muon chamber matching cuts, we selected the data samples used in the present analysis:

- single muon sample ($p_T^{\mu} > 10$ GeV/c) = 5984 events
- dimuon sample ($p_T^{\mu 1} > 8$ GeV/c, $p_T^{\mu 2} > 3$ GeV/c) = 200 events

B) Single jet data : $\simeq 2.3 \times 10^6$ events ($\simeq 3\ nb^{-1}$) were recorded using a first-level calorimeter trigger processor, efficient for clusters of transverse energy above 10 GeV. These data were used in the present analysis for background studies.

C) Minimum-bias data : A total of $\simeq 1.3 \times 10^6$ events, which represent $\simeq 0.3$ nb^{-1} were also recorded.

3 Production and Decay Properties of the t-Quark

3.1 Production Mechanism and Cross Section

In $p\bar{p}$ collisions at $\sqrt{s} = 630$ GeV, and in the framework of the Standard Model, there are two dominant mechanisms which produce t-quarks :

a) Decays of W's (if $m_W > m_t + m_b$) : $W^+ \to t\bar{b}$ ($W^- \to \bar{t}b$) where the cross section for $p\bar{p} \to W + X; W \to t\bar{b}$ is given by :

$$\sigma(p\bar{p} \to W \to t\bar{b}) = 3 * PS(m_t, m_b, m_W) * \sigma(p\bar{p} \to W \to e\nu) * C(m_t, m_W)$$

where 3 is the colour factor, PS is the phase space factor for which the dependence on the masses of the quarks and on the W mass is well known, and C(m_t, m_W) corresponds to QCD radiative corrections. For the cross section $\sigma(p\bar{p} \to W \to e\nu)$, we used the UA1 measurement [5].

b) Direct production of $t\bar{t}$ pairs : $p\bar{p} \to t\bar{t} + X$, via two QCD subprocesses $gg \to t\bar{t}$ and $q\bar{q} \to t\bar{t}$ at lowest order. The cross section for QCD heavy-flavour-production processes up to $\mathcal{O}(\alpha_s^3)$ has been calculated by P. Nason, S. Dawson and R.K. Ellis [6]. For the t-quark cross section, we used the calculation by G. Altarelli et al. [2] which includes all processes to $\mathcal{O}(\alpha_s^3)$, and uses the DFLM structure function parametrisation [7].

Figure 6 shows the relative contribution of the above processes for two different centre of mass energies. For $m_t < m_W + m_b$, the production of t-quarks via W decays dominates at $\sqrt{s} = 630$ GeV.

3.2 Top Decays

In view of the large background of events containing high p_T jets from QCD processes, the best way of identifying a new heavy quark in $p\bar{p}$ collisions is through its semileptonic decay modes; the branching ratio is $\simeq 11\%$ within the Standard Model.

We look for $t \rightarrow l^+\nu b$ ($\bar{t} \rightarrow l^-\bar{\nu}\bar{b}$) . As the top quark seems to be heavy, the decay lepton will be produced at high p_T and will have a high p_T relative to the other decay products, so that the lepton will be well separated from the accompanying jet.

3.3 Background Processes to the Top-Quark Signature

Apart from the instrumental background which is described below, there are essentially three processes which give high p_T leptons in the final state and can fake our experimental top production signature :

1) Semileptonic decays of charm and bottom quarks (mainly $p\bar{p} \rightarrow b\bar{b}g$).

2) Decays of $W^\pm$ and Z^0 bosons into leptons.

3) Lepton pair production via Drell-Yan, $J/\Psi \rightarrow \mu\mu$ and $\Upsilon \rightarrow \mu\mu$ processes.

To understand the behaviour of these events in the UA1 detector, all the processes have been simulated using the ISAJET Monte Carlo [8] and the UA1 detector simulation program, and finally studied with the same analysis programs as the real data. The cross section for the last two processes (2 and 3) are normalised to UA1 measurements. The cross sections for $W^\pm$ and Z^0 are taken from Ref. [5]. In the W case, in order to reproduce the measured $d\sigma/dp_T^W$ spectrum, the high p_T tail produced by ISAJET is weighted with the ratio of the observed cross section to the generated cross section in bins of p_T^W. The cross sections for J/Ψ, Υ and Drell-Yan production are taken from dimuon measurements [9],[10]. We generated Drell-Yan processes in two different regions: high-mass pairs at low p_T [9] and low-mass pairs at large p_T [11].

Charm and bottom quark production are not normalised at this stage. The absolute contribution of these processes is obtained later by normalisation to the muon + jet data. As heavy quark production is the most important contribution to the t-quark background, we discuss this process in more detail in the next section.

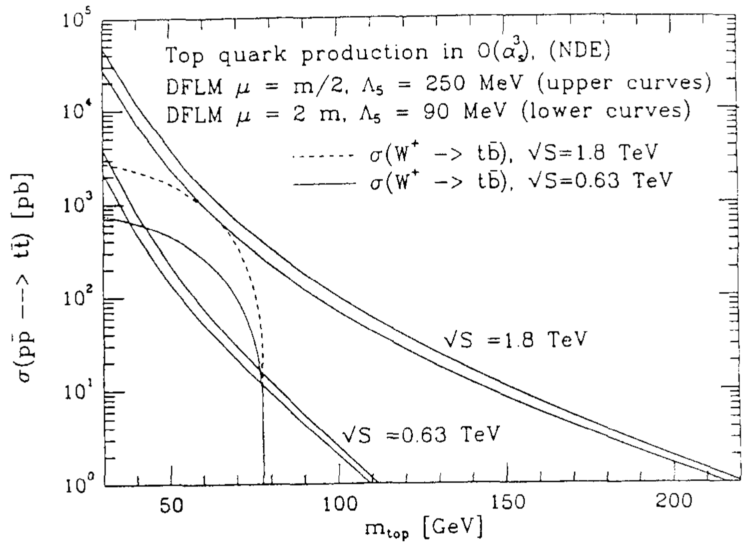

Figure 6: The $p\bar{p} \rightarrow$ t+X production cross section as function of m_t.

The Experimental Background

The only substantial source of background to the prompt muon signature is the decay in flight of charged pions and kaons. The inclusive muon p_T distribution is given by the convolution of the inclusive pion (kaon) p_T distribution and the probability density function of pion (kaon) to decay in flight. An extensive description of the method used to compute this background is given in Ref. [12]. As can be seen in Fig. 7, the p_T^μ distribution for the decay background is decreasing faster than the total inclusive p_T^μ distribution. Above $p_T^\mu > 15$ GeV/c this contribution is of $\simeq 25\%$.

In the present detector configuration (no electromagnetic calorimeter) the contribution from π/K decay background is slightly increased because of the longer decay path for hadrons. To estimate this contribution to the data sample used in the top search, we used the sample of single jet data : $\simeq 3\ nb^{-1}$.

4 Understanding of a Muon + Jet(s) Sample (Control Region)

Before starting the search for new quark production, we checked our understanding of heavy flavour production in the present UA1 detector. A similar study was already done earlier using UA1 data [13].

We defined a control sample of μ + jet(s) events and compared their properties with the Monte Carlo predictions. The sample is defined as follows:

- One μ with $12 < p_T^\mu < 15$ GeV/c
- At least one jet with $E_T^{jet} > 12$ GeV, we counted additional jets if $E_T^{jet} > 7$ GeV. Only jets outside a cone of ΔR = 1.0 around the μ, ΔR(μ,jet-axis) > 1.0, are counted. The ΔR is defined in azimuthal angle (around the beam direction) and pseudorapidity space: $\Delta R = (\phi^2 + \eta^2)^{1/2}$.

Under these conditions the possible top contribution is negligible. The decay background accounts for 23%, and therefore the main physics contribution comes from heavy flavour ($b\bar{b}, c\bar{c}$) production.

The missing transverse energy and the transverse energy of first and second highest E_T jets in the event are shown in Figs. 8 and 9, compared with the full Monte Carlo prediction (Section 3.3) and the π/K decay background. Some topological properties of these events are shown in Fig. 10. The variables used are : $\Delta\phi(\mu$, jet1), the angular separation between the muon and the highest jet in the event; the muon and jet 1 tend to be coplanar with the beam line (Fig. 10a); the $|\cos\theta^*_{jet2}|$ where θ^*_{jet2} is the angle between the second highest E_T jet and the incoming $\bar{p}$ beam. In $b\bar{b}/c\bar{c}$ events the second jet generally comes from initial state gluon bremsstrahlung and is produced with a large value of $|\cos\theta^*_{jet2}|$ (Fig. 10b).

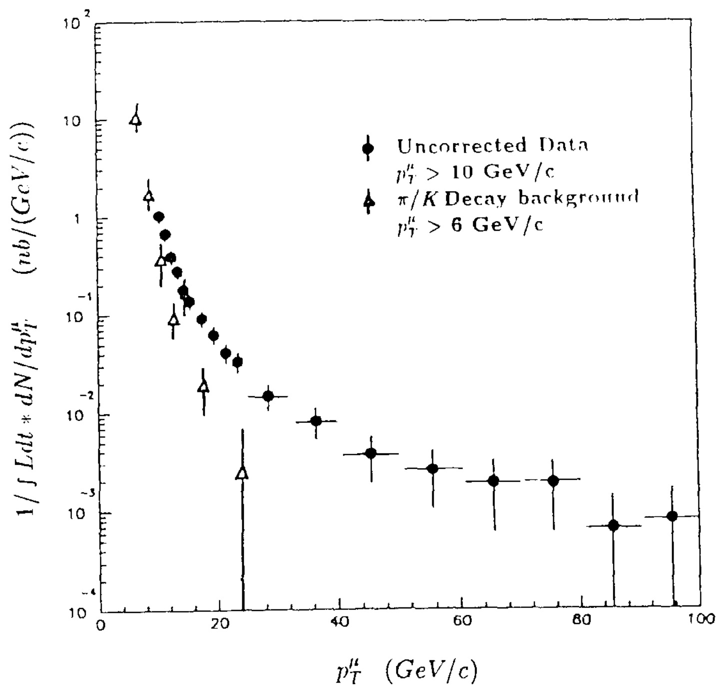

Figure 7: The inclusive p_T^μ distribution (black dots), not acceptance corrected and not background substracted, is compared with the p_T^μ distribution for π /K decay background alone (open triangles).

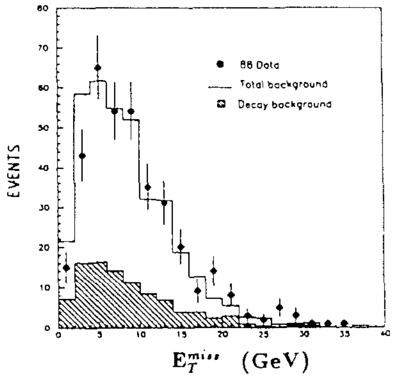

Figure 8: Missing transverse energy distribution. Comparison of 1988 data with a simulation of standard processes.

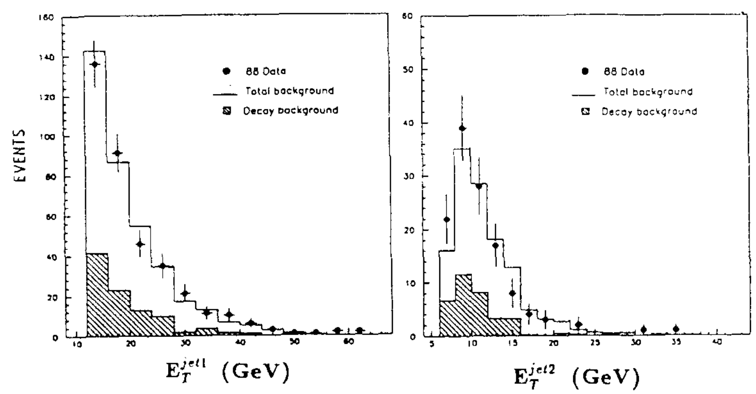

Figure 9: Comparison of 1988 data with a simulation of standard processes : E_T distribution for the highest (jet 1) and second (jet 2) jet in the event.

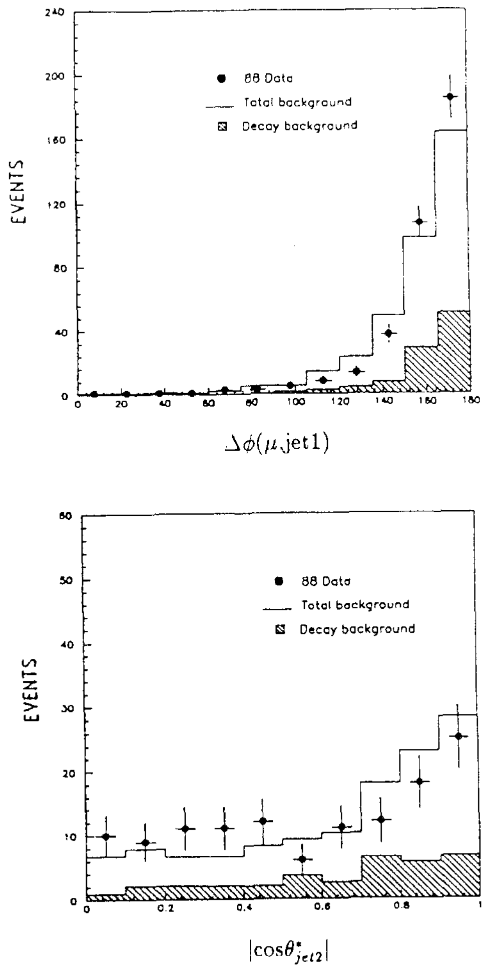

Figure 10: Comparison of 1988 data with a simulation of standard processes : a) Difference of azimuthal angles between the muon and jet 1. b) $|\cos\theta^*_{jet2}|$.

The muon isolation is shown in Fig. 11; the isolation variable is define as the activity measured around the muon in a cone $\Delta R = 0.7$:

$$I = ((\Sigma E_T/3)^2 + (\Sigma p_T/2)^2)^{1/2}$$

where ΣE_T is the transverse energy in the calorimeter (neutral and charged particles) and Σp_T is the sum of transverse momentum in the central detector (charged particles only). The ΣE_T and Σp_T are combined to take into account the different acceptance of the two detectors. As can be seen in Fig. 11, muons coming from $b\bar{b}/c\bar{c}$ production are mainly inside jets and therefore they are non-isolated.

In all these variables the behaviour of the data are rather well reproduced by the Monte Carlo. From the study of this control sample we conclude that the kinematic properties of μ + jet(s) events are understood with the present UA1 detector. This gives us confidence in our understanding of the main background to the top signal. We now try to select more appropriate samples to search for new quark production.

5 Search for Top

We describe in this section the search for the top quark in different samples : the single muon, dimuon and electron-muon channels. Each sample is define in such a way that the sensitivity to top is optimised.

From each individual channel a top mass lower limit is presented. The mass limit calculation used is briefly described. Combining all the available data 1983-1988 we obtain an upper limit for the top cross section and an improved mass limit.

5.1 Single Muon + $\geq$ 2 jets Channel

The sample is defined by the following cuts:

i) $p_T^{\mu} > 12$ GeV/c in $|\eta| < 1.5$
ii) $N_{jet} \geq 2$ with $E_T^{jet1} > 15$ GeV and $E_T^{jet2} > 7$ GeV in $|\eta| < 2.5$
(Jets are counted only if $\Delta R(\mu,\text{jet}) > 1.0$)
iii) A $m_T(\mu,\nu) < 60$ GeV/c^2 cut is applied to remove the W $\rightarrow \mu\nu$ contribution
iv) Finally, we ask for isolated muons I < 2.
(I = Isolation variable as it is defined in previous section)

After these cuts we are left with 19 top-like events. Figure 12 shows the muon isolation distribution for both isolated and non isolated muons. The agreement between the data and the background prediction is rather good. The total

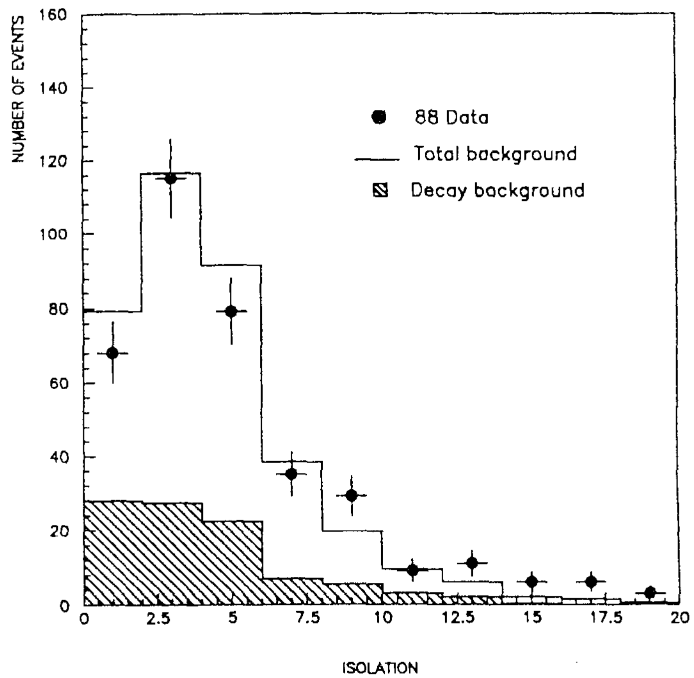

Figure 11: Isolation (I) distribution for muons ($12 < p_T^{\mu} < 15$ GeV/c) accompanied by at least one jet.

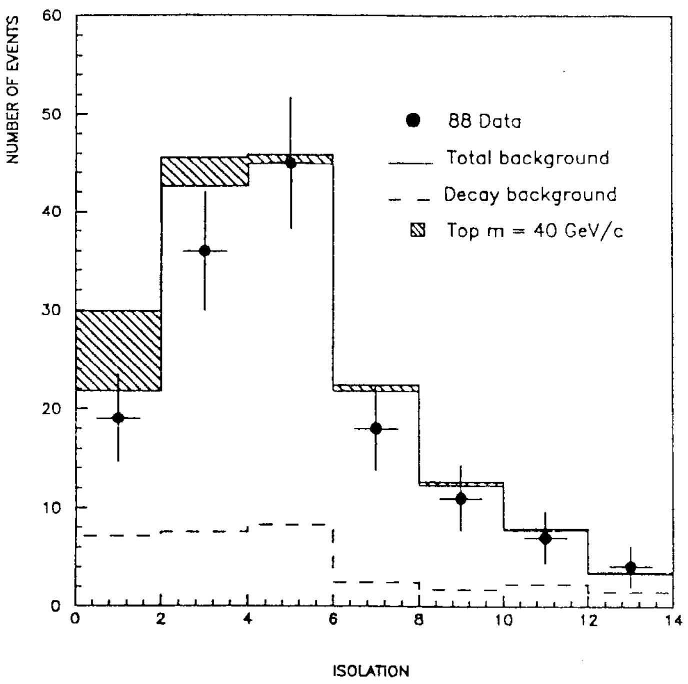

Figure 12: Isolation (I) distribution for muons ($p_T^\mu > 12$ GeV/c) accompanied by at least two jets.

background prediction for muons with $I < 2$ is 21.5. The largest contribution comes from $b\bar{b}/c\bar{c}$ processes. A detailed comparison between the data and Monte Carlo is given in Table 1. To improve the rejection against the $b\bar{b}$ and $c\bar{c}$ background without destroying the possible top signal (see Fig. 13 : $|\cos\theta^*_{jet2}|$ versus $\Delta\phi(\mu, jet1)$ for $b\bar{b}/c\bar{c}$ and top Monte Carlo events) we apply two additional topological cuts :

v) $|\cos\theta^*_{jet2}| < 0.8$
vi) $\Delta\phi(\mu, jet1) < 150^0$.

Five events remain after these cuts; the main source of background for isolated muons is now from decays in flight of charged pions and kaons (Table 1).

Table 1: Comparison Data and Monte Carlo

Monte Carlo	Isolated $\mu+ \geq 2$ jets	Isolated $\mu+ \geq 2$ jets + Topological cuts
π/K Decay	6.9	3.2
W/Z	2.3	1.1
D.Y., J/Ψ, Υ	2.2	0.1
$b\bar{b}/c\bar{c}$	10.1	1.2
Total Background	21.5	5.6
88 Data	19	5

The expectation from top for this sample is shown in Table 2 as function of the top mass.

Table 2: Top expectations ($t\bar{t} + t\bar{b}$)

Top Mass (GeV/c^2)	Isolated $\mu+ \geq 2$ jets	Isolated $\mu+ \geq 2$ jets + Topological cuts
40	8.9	5.5
50	6.5	4.0
60	3.9	2.5
70	1.3	0.8

The systematic uncertainties and the top mass limit calculation are explained below.

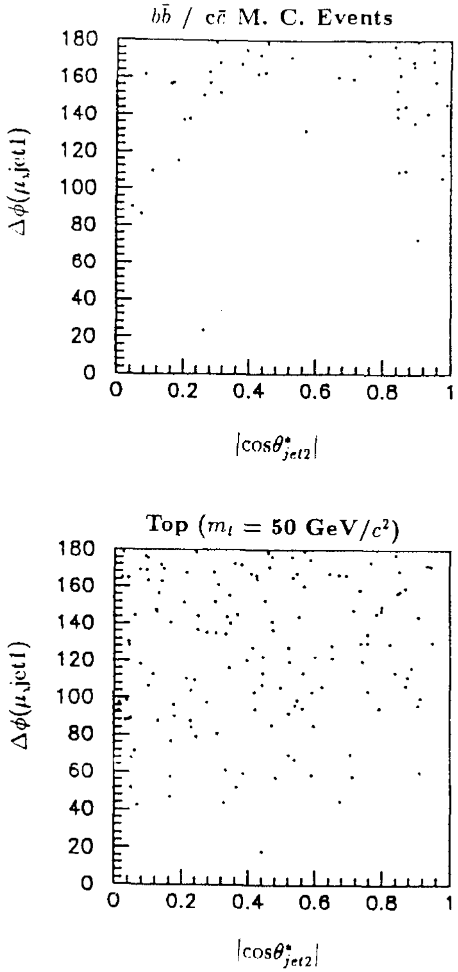

Figure 13: $|\cos\theta^*_{jet2}|$ versus $\Delta\phi(\mu, jet1)$ for $b\bar{b}/c\bar{c}$ and for top (m_t = 50 GeV/c^2) Monte Carlo events.

Top Mass Limit Calculation

In order to avoid the large uncertainties coming from the QCD prediction for the $b\bar{b}$ and $c\bar{c}$ production cross section, we obtain the absolute number of background contribution to the signal region I < 2 as follows: We normalise the total background (Monte Carlo + π/K decay) to the data in a control region (B) 2 < I < 10, then the knowledge of the isolation distribution shape allows us to predict the background contribution in the signal region (A). With this method we estimate our absolute background prediction with a 10% systematic error.

The number of events observed in the signal region A (= n) and in the control region B (= b) are governed by Poisson distributions, where E(b) = ν, E(n) = $\alpha\sigma + \rho\nu$ are the expectation values; α = integrated luminosity $\times$ branching ratio of considered channel $\times$ acceptances; σ = top cross section; ρ = ratio between the numbers of background events in regions A and B.

We obtain upper limits on the top cross section by folding the Poisson probabilities with Gaussian distributions for the number of background events predicted and the number of top events expected. The likelihood as a function of σ is expressed by :

$$L(\sigma) = \int_{\nu\alpha\rho} P(n \mid \alpha\sigma + \rho\nu) \times P(b \mid \nu) \times G(\alpha) \times G(\rho) d\nu d\alpha d\rho$$

where G(α) and G(ρ) are normal distributions which represent systematic uncertainties. The desired confidence level (CL) for a cross section limit is given by : $\int_0^{\sigma_T} L(\sigma)d(\sigma) / \int_0^{\infty} L(\sigma)d(\sigma)$ = CL.

Finally, to obtain a top mass lower limit, we need to include the systematic uncertainties in the top cross section. The systematic errors in the number of the top events expected are listed in Table 3.

Table 3: Systematic errors on the number of top events expected

Source of error	$t\bar{t}$ (%)	$t\bar{b}$ (%)
Theory	30	10
Eff. of jet cuts	12	12
Integrated Lum.	15	-
# W $\rightarrow \mu\nu$ observed	-	14
Eff. of μ cuts	10	10

From the μ + $\geq$ 2 jets channel, we obtain a lower limit on the t-quark mass of m_t > 42 GeV/c^2 (at 95% CL). From the same sample but without applying the additional topological cuts (v and vi in section 5.1) the top mass limit is m_t > 44 GeV/c^2 (at 95% CL).

5.2 Dimuon Channel

Since top production via W decays is dominant for m_t between 40 GeV/c^2 and 75 GeV/c^2, the dimuon analysis is optimised for this process. Based on the p_T^μ spectra from the different semileptonic decays of the quarks involved, the interesting channels are (for $p\bar{p} \to W + X$; $W \to t\bar{b}$) :

1)	$t \to \mu^+ \nu b$	1^{st} μ from t (1^{st} generation decay)
	$\bar{b} \to \mu^+ \nu \bar{c}$	2^{nd} μ from $\bar{b}$ (1^{st} generation decay)
2)	$t \to \mu^+ \nu b$	1^{st} μ from t (1^{st} generation decay)
	$b \to \mu^- \nu c$	2^{nd} μ from t (2^{nd} generation decay)

The muon coming from the t-quark, 1^{st} generation decay is expected to have the largest transverse momentum and be isolated, whilst the muons coming from $b/\bar{b}$ decay should be non-isolated.

The dimuon sample, which includes all the existing data from 1983 to 1988, accounts for an integrated luminosity of $\simeq 1.9\ pb^{-1}$. The followings cuts have been applied :

i) $p_T^{\mu_1} > 8$ GeV/c, in $|\eta(\mu_1)| < 1.6$; $p_T^{\mu_2} > 3$ GeV/c
ii) mass$(\mu_1, \mu_2) > 4$ GeV/c^2 to remove $b\bar{b}/c\bar{c}$ and J/Ψ contributions
iii) Loose isolation on 1^{st} muon I$(\mu_1) < 6$ in order to remove $b\bar{b}/c\bar{c}$ background. Non-isolation on the 2^{nd} muon I$(\mu_2) > 2$. This cut removes the Drell-Yan contribution existing in the data.
iv) Finally, we ask for at least one jet with $E_T^{jet} > 10$ GeV.

The reduction of the data as function of the different cuts is shown in Table 4. The calculation for π/K decay background is preliminary.

Table 4: Dimuon events as function of cuts

Cuts	Data (83-88)	π/K Decay	$b\bar{b}, c\bar{c}$	Top expected (m_t =40 GeV/c^2)
Total Events	263	36	163	11.7
I$(\mu_1) < 6$	221	27	136	10.5
I$(\mu_2) > 2$	84	21	88	6.5
$E_T^{jet} > 10$ GeV	43	13	48	5.2

To increase the sensitivity to t-quark production one can use the event properties that can differentiate between t and non-t events and combine the chosen set of variables in a function L, defined as $L = \Pi\ P_t(\mathcal{X}_i)/P_b(\mathcal{X}_i)$ where $P_t(P_b)$ is the probability density function for the variable $\mathcal{X}_i$ for top ($b\bar{b}/c\bar{c}$) events.

The set of variables used are shown in Fig. 14, for both $b\bar{b}/c\bar{c}$ Monte Carlo events and top (m_t = 50 GeV/c^2) events.

In terms of log(L), the 43 events selected have a similar distribution to the $b\bar{b}/c\bar{c}$ background events (Fig. 15). In the same figure the prediction for top (multiplied by a factor of 10) is shown.

A cut at log(L) > 1 gives us : 0 events in the data, 2.6 events for the background and 3.2 (2.1) t-quark events expected for m_t = 40 (50) GeV/c^2. This result can be converted into a lower t-quark mass limit of 43 GeV/c^2 (at 95% CL).

5.3 Electron-Muon Channel

The sample available for this channel comes from data taken before 1986 and corresponds to about 550 nb^{-1}.

The main difference with respect to the dimuon sample is that electrons need to be isolated in order to be recognised. The selection used requires one muon with $p_T^\mu > 3$ GeV/c and one electron with $E_T^e > 8$ GeV in a pseudorapidity range of $|\eta| < 1.5$. No jet activity is required. Figure 16 shows p_T^e versus p_T^μ for the 10 events selected, half of those events have at least one jet with $E_T^{jet} > 10$ GeV.

The main background contribution comes from $b\bar{b}/c\bar{c}$ processes, this contribution accounts for 12 events, the other backgrounds are significantly smaller : from $Z^0 \to \tau\tau$ 0.13 events and from Drell-Yan production of τ pairs 0.06 events.

The expected number of events from top are 5.7, 3.8 and 1.9 for m_t = 30,40 and 50 GeV/c^2 respectively.

Figure 17 shows p_T^μ for t-quark and $b\bar{b}/c\bar{c}$ events; p_T^μ tends to be harder for heavier mass of the quark. Requiring E_T^μ >10 GeV, no event remains (Fig. 17c). The $b\bar{b}/c\bar{c}$ prediction is reduced significantly by this additional cut : 1.6 events, whilst 1.74 and 1.23 events are expected from t-quarks for m_t = 40 and 50 GeV/c^2 respectively. We then derive a top mass lower limit of $m_t > 25$ GeV/c^2 (at 95% CL).

5.4 Combined Limit

The different channels have been combined to obtain an overall upper limit for the t-quark cross section. The results for the individual channel are summarised in Table 5.

We make the conservative assumption that all the systematic errors are correlated between channels. We add statistical and systematic errors in quadrature.

The combined upper limit for top quark production as function of the top mass is shown in Fig. 18 at 90% and 95% CL. To obtain the top mass lower limit we include the systematic errors from the theoretical top production cross section estimate.

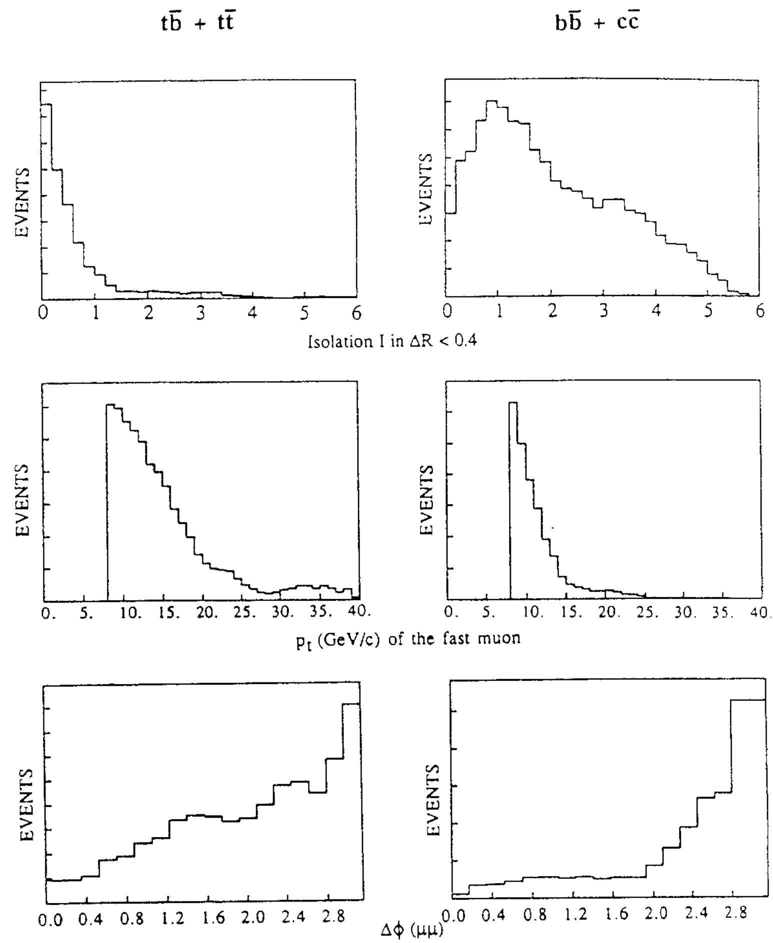

Figure 14: Dimuon events: Isolation of the fast muon, $p_T^{\mu 1}$ and $\Delta\phi(\mu\mu)$ for $b\bar{b}/c\bar{c}$ Monte Carlo events and for top ($m_t = 50$ GeV/c^2) Monte Carlo events.

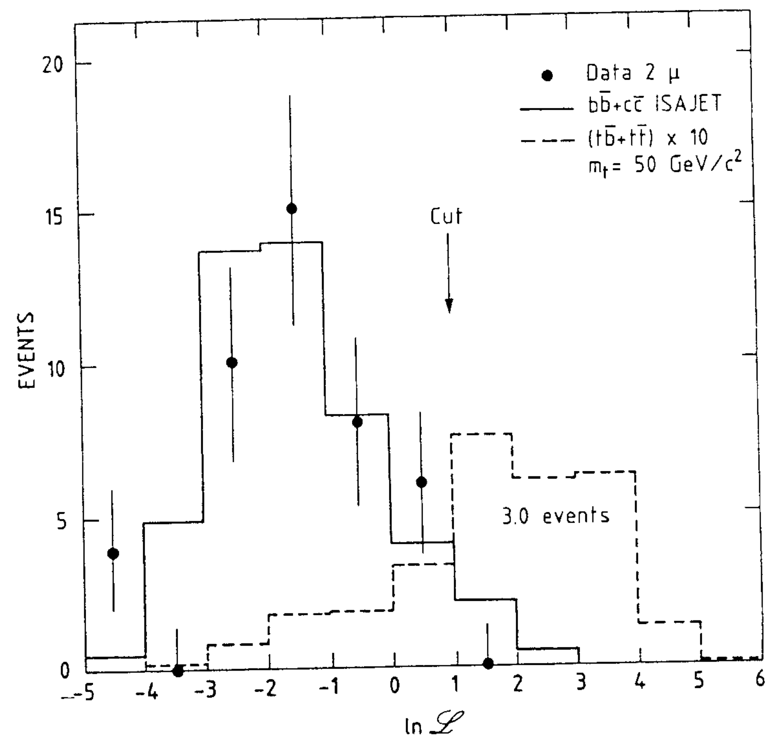

Figure 15: Distribution of the logarithm of L for muon pairs. Comparison of data with a simulation of standard processes and with the contribution from top multiplied by a factor of 10 ($m_t = 50$ GeV/c^2).

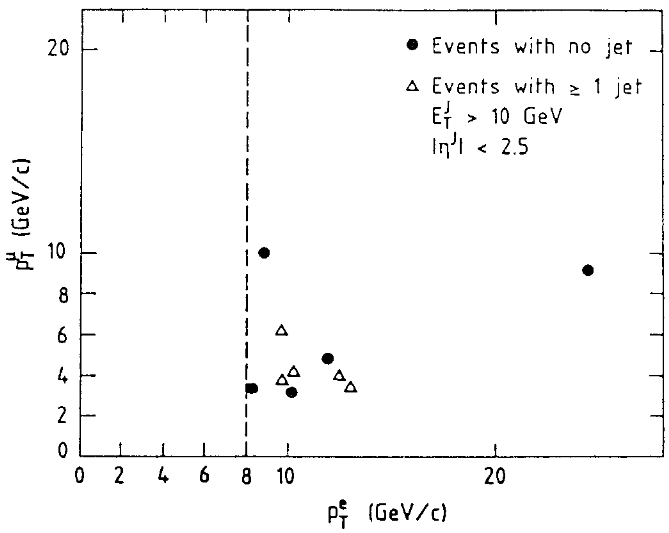

Figure 16: Muon-electron events: p_T^e versus p_T^μ for data ($\leq$ 1985).

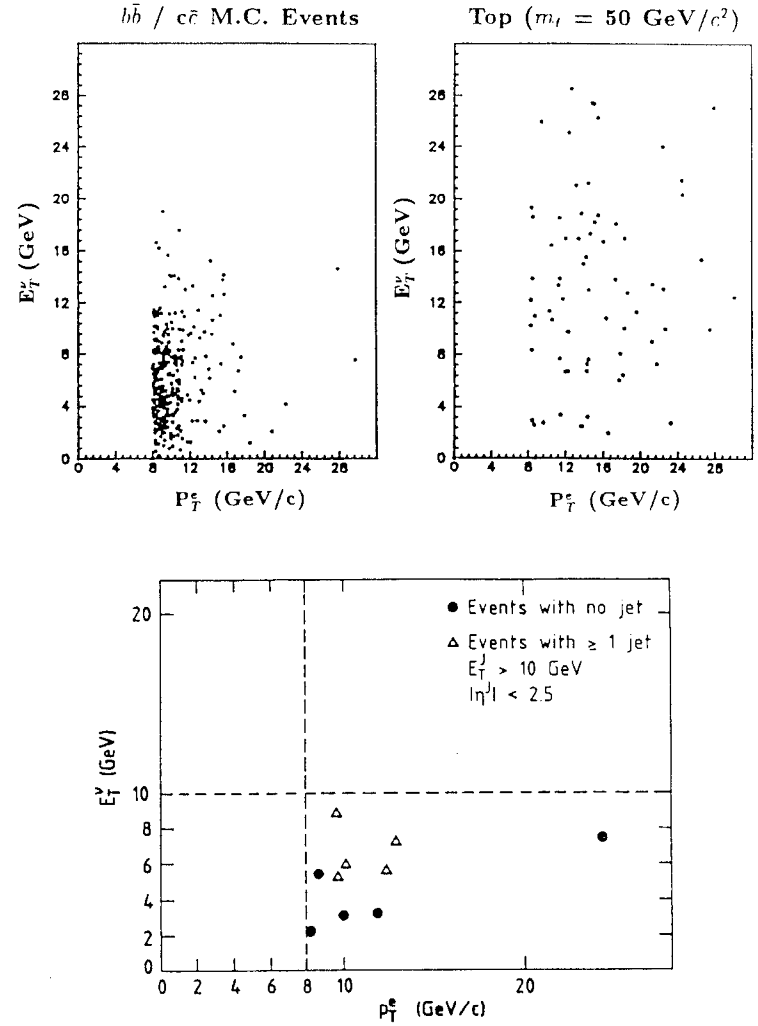

Figure 17: Muon-electron events: p_T^e versus E_T^μ for : a) $b\bar{b}/c\bar{c}$ Monte Carlo events, b) top (m_t = 50 GeV/c^2) M.C. events and c) data ($\leq$ 1985).

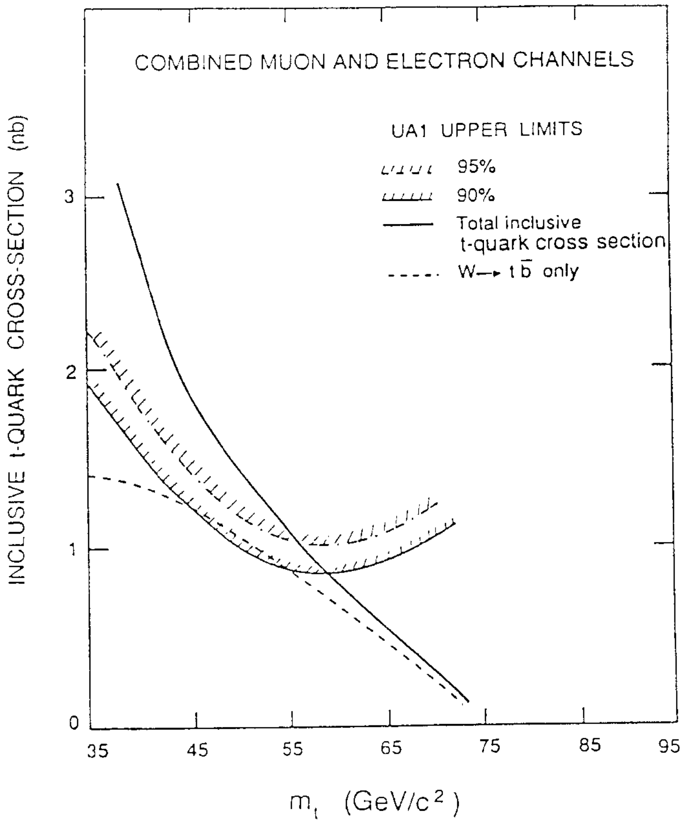

Figure 18: Combined muon and electron channel limits on the t-quark production cross section as function of the top mass. Comparison with theoretical prediction (full line).

Table 5: Summary of results on t-quark mass limit (95% CL)

Channel	$\int$ L dt (pb^{-1})	Data	Background	Top expected m_t=40 GeV/c^2	m_t Limit (GeV/c^2)
e + jets (84-85)	0.7	26	26.0±2.8	11.0	41
μ + jets (84-85)	0.6	10	11.4±1.2	7.4	40
e + μ (84-85)	0.6	0	1.6±0.1	1.7	25
μ + jets (88)	1.2	5	4.3±0.5	5.5	42
μ + μ(83-88)	1.9	0	2.6±0.3	3.2	43

We obtain :

$$m_t > 60 \text{ GeV}/c^2 \text{ (90\% CL)}$$
$$m_t > 56 \text{ GeV}/c^2 \text{ (95\% CL)}.$$

At 95% CL we are still not sensitive to top production via W $\rightarrow t\bar{b}$ decays alone.

6 b' Search

The search of fourth generation quark production has been done in parallel to the top search. For the fourth generation quark, b', we assume as in [1] :

- its electric charge is -1/3,
- its mass is lower that the top mass, so that it will not decay into top,
- it is not produced in W decays where $\sigma(b'\bar{b}')=\sigma(t\bar{t})$ for $m_{b'} = m_t$ as expected from QCD,
- b' $\rightarrow$ c predominates over b' $\rightarrow$ u,
- semileptonic branching ratio of $\simeq$ 11% to each lepton type.

A similar analysis to that performed in the top-quark (μ + $\geq$ 2 jets channel) search has been made. Figure 19 shows the b' upper cross section limit at 90% and 95% CL for the combined data sample : 1984-1988.

We obtain b' mass lower limits of 38 GeV/c^2 and 40 GeV/c^2 at 95% and 90% CL respectively.

7 Non-Standard Top Decays : Charged Higgs Search

In order to make a more complete analysis with the future data, we report here a preliminary study of possible top decay modes beyond the minimal Standard

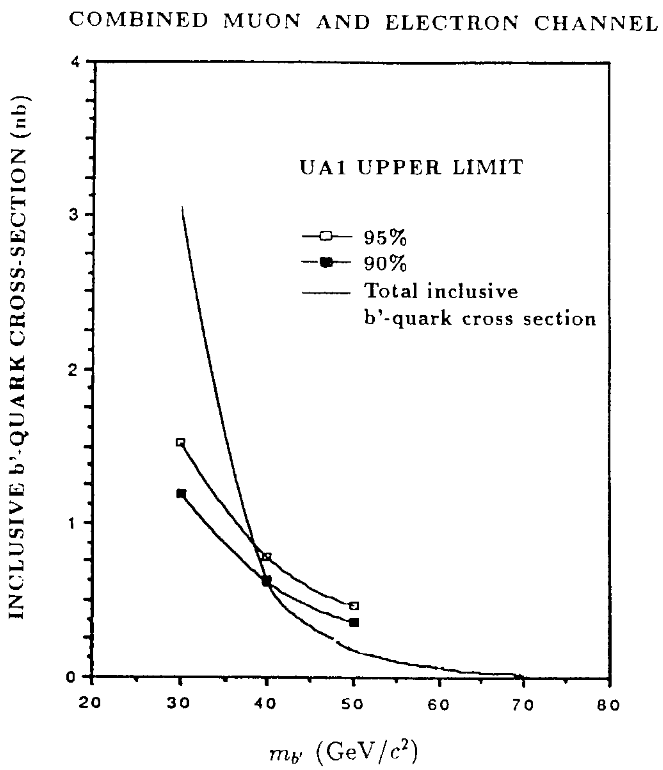

Figure 19: Combined muon and electron channel limits on the b'-quark production cross section as function of the b' mass. Comparison with theoretical prediction (full line).

Model. The sensitivity to charged Higgs t-quark decay with the standard analysis, which is optimised for the semileptonic decay of the heavy quark, is investigated.

In models with two Higgs doublets [14] one expects to observe a charged Higgs scalar. The present experimental lower mass limit for these particles is $m_{H^\pm} > 19$ GeV/c^2 [15].

If $m_t > m_{H^+} + m_b$ the top decay into a real Higgs is allowed. In fact, this decay becomes the dominant decay mode, and the top quark mass limit coming from hadron collider experiments and based on the Standard Model decays are no longer valid.

In this first approach we have assumed that top decays 100% into charged Higgs. Following S.L. Glashow and E.E. Jenkins [14], the decay modes and branching ratios of the Higgs are :

$$H^+ \rightarrow \tau\nu \text{ (31\%), } H^+ \rightarrow c\bar{s} \text{ (64\%)}$$

whilst the rest of the decay modes account for 5%. This is true only if $v_2/v_1 = 1$; v_1,v_2 being the vacuum expectation value of the two Higgs. If this ratio becomes higher the Higgs leptonic decay mode is strongly suppressed (2.9 for $v_2/v_1 = 2$). Therefore, only the $v_2/v_1 = 1$ case will be considered here.

We have implemented in the ISAJET Monte Carlo the above non-standard top decays for two sets of top/Higgs masses : $m_t = 40$ GeV/c^2, $m_H = 25$ GeV/c^2 and $m_t = 60$ GeV/c^2, $m_H = 40$ GeV/c^2. The Monte Carlo events have been simulated through the detector and analysed in the same way as the real data.

Considering single μ + ≥ 2 jets, only 1.5 events are expected from t $\rightarrow Hb$, H $\rightarrow \tau\nu$ with $m_t = 40$ GeV/c^2, $m_H = 25$ GeV/c^2 and 0.6 events and for $m_t = 60$ GeV/c^2, $m_H = 40$ GeV/c^2, to be compared with $\simeq 9$ and $\simeq 4$ events for Standard Model top decays.

With the present analysis, which is based on Standard Model top decays, we have little sensitivity to these decay modes. Further studies are going on, trying to optimise selection cuts for this type of search.

8 Updated Results from 1989 Data

A similar analysis to the one describe above has been preformed recently using the complete (1988 + 1989) data sample, 4.6 pb^{-1}.

For the more recent analysis we have improved the Monte Carlo statistics ($\simeq 15pb^{-1}$), and a more complete study of systematic errors has been done. Preliminary results have been presented [16] on the top quark mass limit. A summary of the new results is given in Table 6.

(*) For the 4.6 pb^{-1} sample, the topological cuts $\Delta\phi(\mu$,jet1) and $|\cos(\theta^*_{jet2})|$ have not been applied.

Combining all the different electron and muon channels, we obtain (for 5.4 pb^{-1}) :

Table 6: Updated results on t-quark mass limit (95% CL)

Channel	$\int$ L dt (pb^{-1})	Data	Background	Top expected (m_t=50 GeV/c^2)	m_t Limit (GeV/c^2)
μ + jets$^{(*)}$(88-89)	4.6	76	77.0±11.0	29.0	53
$\mu + \mu$ (83-89)	5.4	10	11.8±2.3	7.1	46

$$m_t > 61 \text{ GeV}/c^2 \text{ (95\% CL)}.$$

An updated b' mass lower limit has also been obtained with the complete sample :

$$m_{b'} > 41 \text{ GeV}/c^2 \text{ (95\% CL)}.$$

9 Summary and Conclusions

We have presented here a preliminary analysis done with the sample of muon events collected during 1988. A recently completed analysis of old electron-muon data ($\leq$ 1985) has also been reported.

We conclude that the UA1 detector in the present configuration (no electromagnetic calorimeter) is still operational for the study of heavy flavour quark production in the muon channel and the search for new heavy quarks (t-quark and b'-quark). From the analysis of the new data we do not find a signal for new quark production.

Using the available UA1 data (1983-1989), for 5.4 pb^{-1}, and combining the electron and muon channels, we obtain a lower mass limit for the top quark of :

$$m_t > 61 \text{ GeV}/c^2 \text{ (95\% CL)}$$
$$m_t > 66 \text{ GeV}/c^2 \text{ (90\% CL)}.$$

Considering W $\rightarrow t\bar{b}$ only :

$$m_t > 58 \text{ GeV}/c^2 \text{ (95\% CL)}.$$

A similar analysis for the b'-quark gives a new b' mass lower limit of :

$$m_{b'} > 41 \text{ GeV}/c^2 \text{ (95\% CL)}.$$

Acknowledgements

I should like to thanks all my colleagues in UA1 who helped to make these results possible and with special thanks to Michel della Negra and Nick Ellis.

References

[1] C. Albajar et al., (UA1 Collab.): Z. Phys. 37C(1988)505.

[2] G. Altarelli, M. Diemoz, G. Martinelli and P. Nason, Nucl. Phys. 308B(1988)-724.

[3] UA1 Collab.: Proposal CERN/SPSC/78-06(1978).
M.J. Corden et al., Physica Scripta 25(1982)5 and 11.
K. Eggert et al., Nucl. Instrum. Methods 176(1980)217 and 233.
G. Arnison et al., Phys. Lett. 107B(1981)304.

[4] G. Bauer et al., Nucl. Instrum. Methods 253A(1987)179.

[5] C. Albajar et al., (UA1 Collab.), Preprint CERN-EP/88-168(1988).

[6] P. Nason, S. Dawson and R.K. Ellis, Nucl. Phys. 303B(1988)607.

[7] M. Diemoz, F. Ferroni, E. Longo and G. Martinelli, Z. Phys. 39C(1988)31.

[8] F. Paige and S.D. Protopopescu, ISAJET Monte Carlo, BLN 38034(1986).

[9] C. Albajar et al., (UA1 Collab.), Phys. Lett. 168B(1987)237.
C. Albajar et al., (UA1 Collab.), Phys. Lett. 168B(1987)247.

[10] C. Albajar et al., (UA1 Collab.), Phys. Lett. 200B(1988) 380.

[11] C. Albajar et al., (UA1 Collab.), Phys. Lett. 209B(1988) 397.

[12] M.P. Jimack, Ph.D. Thesis, Birmingham University, 1987.

[13] C. Albajar et al., (UA1 Collab.), Z. Phys. 37C(1988)489.

[14] S.L. Glashow and E.E. Jenkins, Phys. Lett. 196B(1987)233.

[15] H.J. Behrend et al., (CELLO Collab.), Phys. Lett. 193B(1987)277.

[16] A. Nisati: Top search at UA1 with single muon + jets.
S. Lammel : Top search in the dimuon channel with UA1.
Eighth Topical Workshop on Proton Antiproton Collider Physics.
Castiglione della Pescaia, Italy. September 1989.

RECENT RESULTS FROM THE UA2 EXPERIMENT AT THE CERN $\bar{p}p$ COLLIDER

The UA2 Collaboration

Bern - Cambridge - CERN - Heidelberg - Milano
Orsay (LAL) - Pavia - Perugia - Pisa - Saclay (CEN)

presented by
Trivan Pal
University of Bern, Bern, Switzerland

Abstract

We present results on : (i) the cross section for W and Z production, and (ii) the search for the top quark, obtained with the UA2 detector at the CERN $\bar{p}p$ collider. The data sample corresponds to an integrated luminosity of 7.1 pb^{-1}.

Talk given at the 1989 Topical Conference,
SLAC Summer Institute on Particle Physics, Stanford, CA, USA,
10-21st July, 1989

1. INTRODUCTION

The UA2 detector has been extensively modified during the period 1985 to 1987, in order to achieve an improved performance at the upgraded CERN $\bar{p}p$ collider. With the successful operation of the new Antiproton Accumulator Complex (AAC), the UA2 detector collected a data sample corresponding to an integrated luminosity of 7.4 pb^{-1}, at a center of mass energy $\sqrt{s}$ = 630 GeV, during the 1988 and 1989 data taking periods.

In this article we present preliminary results on the cross section of the W and Z bosons, as well as a search for the top quark production and its subsequent semi-electronic decay. We note that the results presented here are preliminary, and may change slightly as further analysis of the systematic uncertainties proceeds.

2. THE UA2 DETECTOR

The details pertaining to the construction and performance of the various detector types can be found in the references given below. In the following sections, we recall the salient features.

2.1 *The Calorimeter*

An overall view of the *central* and *end-cap* calorimeters [1,2] is shown in Fig. 1. The central calorimeter covers a polar angle range $40° < \theta < 140°$, and the full azimuthal range. It consists of 240 electromagnetic and hadronic cells of size $\Delta\theta \times \Delta\phi$ = $10° \times 15°$. The electromagnetic part consists of a 17 radiation lengths thick, multilayer lead-scintillator sandwich; while the hadronic part consists of an iron-scintillator sandwich of thickness 4.5 absorption lengths (including the electromagnetic cells). For the upgrade, all the scintillator plates of the 2 hadronic compartments were replaced, and the thickness of the edge cell electromagnetic compartments was reduced. The latter was necessary in order to increase the radial space available to accommodate the new central detector.

The end-cap calorimeters cover the pseudorapidity (η) region $1 \le |\eta| \le 3$. There are a total of 24 modules (12 on each side of the detector), and each module is segmented into 16 cells. For each module, the two cells closest to the beam axis ($2.5 \le |\eta| \le 3.0$ and $2.2 \le |\eta| \le 2.5$) cover 30° in azimuth, whilst the other cells have a

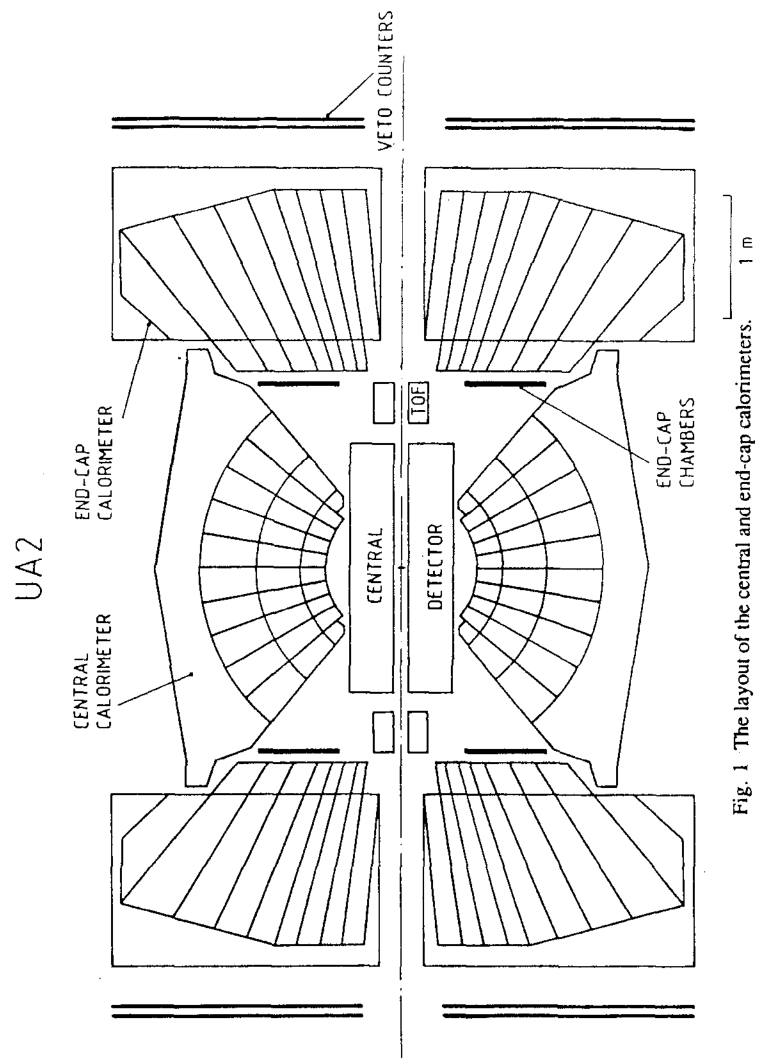

Fig. 1 The layout of the central and end-cap calorimeters.

constant segmentation of $\Delta\phi = 15°$, $\Delta\eta = 0.2$. All cells in the interval $1.0 \leq |\eta| \leq 2.5$, have one electromagnetic and one hadronic compartment. The electromagnetic compartment consists of a multi-layer sandwich of lead (3 mm thick) and scintillator (4 mm thick). The thickness varies from 17.1 to 24.4 radiation lengths, depending on the polar angle. The hadronic compartment is a multi-layer sandwich of iron (25 mm thick) and scintillator (4 mm thick), corresponding to approximately 6.5 absorption lengths (including the electromagnetic cells). The cells nearest to the beam have only a hadronic compartment. In addition, cells with only a hadronic compartment cover the interval $0.9 \leq |\eta| \leq 1.0$, to measure the particles escaping from the interface between the end-cap and the central calorimeters. The readout for each compartment is achieved via two wave-length shifting plates placed on the opposite sides of each cell. This introduces a dead space between adjacent cells of 7 mm for the electromagnetic compartments, and of 13 mm for the hadronic compartments. In order to minimize the effect of these dead spaces each module is rotated by 50 mrad around its symmetry axis normal to the beam directions.

From the energy deposited in the calorimeters, *clusters* are constructed by joining all cells with a transverse energy (E_T) greater than 400 MeV, that share a common edge. We label clusters as being electromagnetic if they have a small lateral size and an energy fraction leaking into the hadronic compartment that is consistent with a shower initiated by a single electron. Since the response of the calorimeter to showers depends on the fraction of the energy carried by hadrons, the observed energy depositions in each calorimeter compartment are multiplied by appropriate weights (of the order of 1.2 for the electromagnetic compartments), in order to compensate for the difference in response. The efficiency to reconstruct an electromagnetic cluster in the central calorimeter from an electron candidate with $E_T > 12$ GeV, was measured from test beam data to be $\varepsilon_{cal} = (91.3 \pm 2.0)\%$. This value is an average over the allowed impact points for electron candidates. The main sources of losses are for electrons incident upon an inter-cell boundary, or the truncated electromagnetic cells (at the edge of the calorimeter), giving an increased hadronic leakage.

2.2 *The Central Detector*

A schematic view of the layout of the central detector around the beam-pipe is shown in Fig. 2. It comprises the following elements :

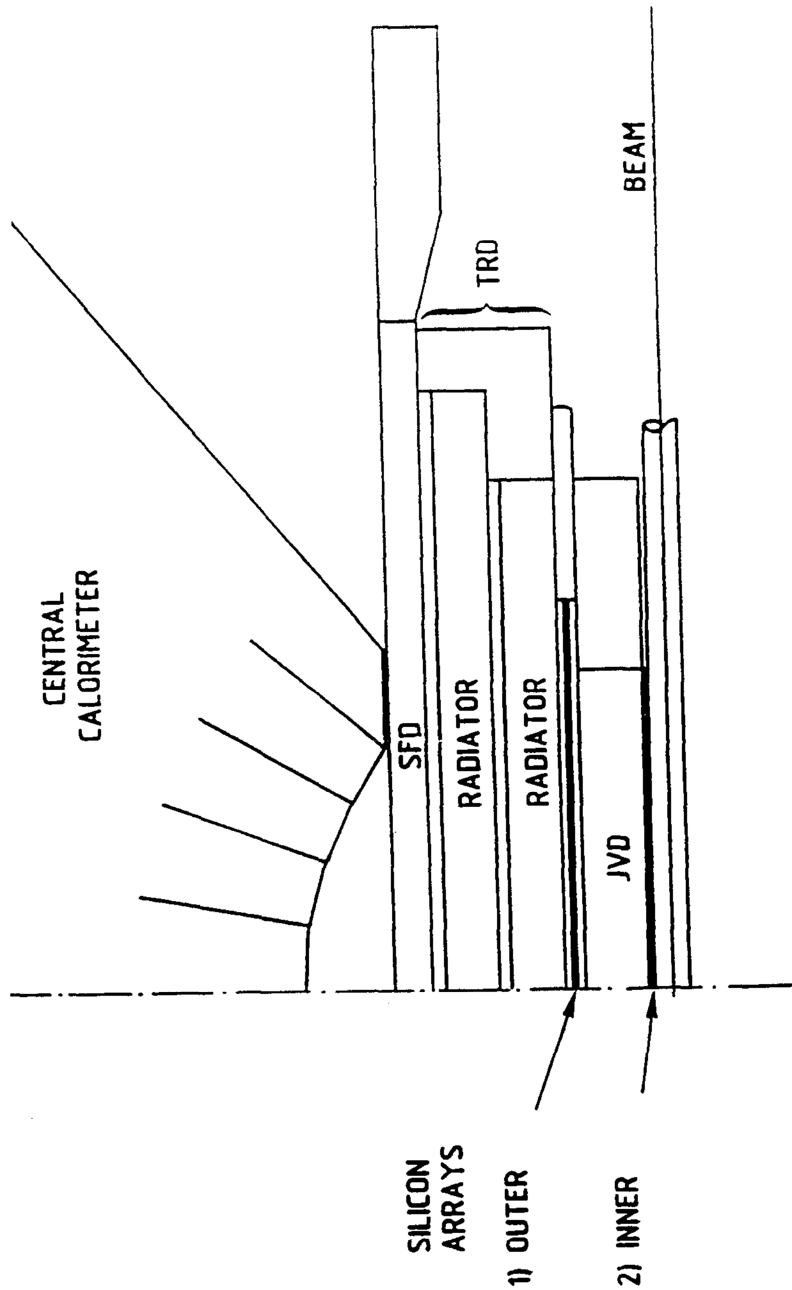

Fig. 2 The configuration of the central detectors.

- a set of *silicon hodoscope* counters located at radii of 3.5 cm (inner array) and 14.5 cm (outer array). Both arrays are used in the pattern recognition and provide ionisation measurements [3];
- a *Jet Vertex Detector* (JVD), consists of a cylindrical drift chamber [4], located between the two silicon arrays;
- a *Transition Radiation Detector* (TRD), located after the tracking devices, consisting of two sets of radiators and proportional chambers [5]. The TRD may be used to distinguish electron tracks from those of hadrons;
- a *Scintillating Fibre Detector* (SFD), which consists of fibres arranged on cylinders into 6 stereo triplets followed by a 1.5 radiation length thick lead convertor, facing the central calorimeter. A further 2 stereo triplets, after the radiator, serve as a preshower detector [6].

The reconstruction of charged particles tracks and the position of the event vertex are achieved using the SFD in conjunction with the Silicon hodoscopes as well as the JVD. The fraction of vertices within ± 300 mm (± 250 mm) of the detector center is measured to be $\varepsilon_V = (98 \pm 1)\%$, ($\varepsilon_V = (94.0 \pm 0.5)$ %) respectively. The tracking efficiency for isolated, high energy tracks, is measured to be $\varepsilon_{trk} = (90.6 \pm 1.1)\%$, using a sample of electrons produced in the decay of W bosons (referred to as "W electrons" hereafter).

The tracking and preshower sections of the SFD are used to match the impact point of candidate electron tracks with the position of the electromagnetic showers. The resolution in the r-ϕ plane (perpendicular to the beam axis) is $\sigma_{r\phi} = 0.4$ mm, and $\sigma_z = 1.1$ mm along the beam direction. The quality of a track-preshower match is defined by the quantity $d\sigma^2 = (\Delta r\phi/\sigma_{r\phi})^2 + (\Delta z/\sigma_z)^2$, where $\Delta_{r\phi}$, Δz are the displacements between the track and shower positions. Accidental overlaps between showers initiated by photons and charged particles generally give large values of $d\sigma^2$, whereas candidate electrons are required to have $d\sigma^2 < 25$. Furthermore, the preshower clusters for the electron candidates are required to have a charge of at least twice that expected from a minimum ionising particle, for each of the stereo views of the preshower detector. The efficiency of the track-preshower match, with the above cuts, is measured to be $\varepsilon_{ps} = (89.9 \pm 1.1)\%$ using the W electrons.

2.3 Tracking in the Forward Region

In front of the forward calorimeters, in the pseudorapidity range $1.1 < |\eta| < 1.6$, are located sets of End-Cap Proportional Tubes (ECPT), that provide tracking and preshower information. The ECPT detector consists of 16 modules ($\Delta\phi = 45^o$ each) of proportional tubes. Each module consists of two stereo triplets, with an additional stereo triplet positioned after a ~ 2 radiation lengths thick convertor acting as a preshower detector.

2.4 The Trigger System

The multi-level trigger system [7] is based on the calorimeter information and on signals from the Time-of-Flight (TOF) counters (see Fig. 1), and consists of the following main parts :

- *The first level* trigger uses the analogue sums of the signals from the photomultipliers of the electromagnetic calorimeter cells up to $|\eta| = 2$.
- *The second level* trigger employs a processor to reconstruct electron and jet clusters, using information from a fast digitization of the calorimeter cell signals.
- *The third level trigger* consists of a full calorimeter reconstruction algorithm, employing a complete set of calibration constants.

The TOF counters are used to generate a minimum bias trigger and to calculate the integrated luminosity.

3. THE W AND Z CROSS SECTIONS

In this section we report on the preliminary results for the W and Z cross sections, (σ_W, σ_Z).

3.1 The Data Samples

There are two data samples used in this analysis :

- *The "W sample"* consists of events containing an electromagnetic cluster with $E_T > 15$ GeV and with missing transverse momentum, P_T^{miss}, greater than 15 GeV/c, as reconstructed online :

$$P_T^{miss} = |\Sigma E_{cell} \times \vec{u}^{\,T}_{cell}|,$$

where E_{cell} is the sum of the electromagnetic and hadronic energies for each cell (weighted to compensate for the response of the electromagnetic compartments to hadron showers) and $\vec{u}^{\,T}_{cell}$ is the projection on the transverse plane of a unit vector from the center of the detector to the cell center. The sum extends over all the calorimeter cells.

- *The "Z sample"* consists of events containing at least two electromagnetic clusters with $E_T > 5$ GeV each, and with $\Delta\phi > 60°$. In addition, the invariant mass of the two clusters is required to be above 25 GeV/c^2.

Data were also taken with a single electron trigger which was used for background estimates.

3.2 *Electron Identification*

Electron candidates in the central region ($|\eta| < 1$) are selected by requiring a track-preshower match to lie within $d\sigma^2 < 25$, facing an electromagnetic cluster in the calorimeter. Furthermore, the lateral and longitudinal shower profiles are required to be consistent with those expected for a single, isolated electron incident along the track direction. For this purpose, a quality factor, $P(\chi^2)$, is defined using extensive test beam measurements. Candidates with $P(\chi^2) < 10^{-4}$ are rejected, as well as electrons hitting the truncated edge cells. The efficiency of this cut is measured to be $\varepsilon_{P(\chi 2)} = (96.9 \pm 0.5)\%$ for W electrons, in the fiducial regions of the calorimeter (i.e. excluding a 5 mm region near the inter-cell boundaries). The electron energy is corrected for the impact point dependence of the calorimeter response as determined from the test beam data. In the forward regions ($1 < |\eta| < 1.6$), an equivalent selection is made using the ECPT tracking and preshower information.

3.3 *Neutrino Identification*

The neutrino is identified using the missing transverse momentum, which is now calculated according to :

$$\vec{P}_T^{\nu} = -\vec{P}_T^{e} - \Sigma E_{cell} \times \vec{u}^{\,T}_{cell}$$

where $\vec{u}^{\,T}$ is now the projection on the transverse plane of a unit vector from the interaction vertex to the cell center, and the sum over all cells excluded the electron "core" cells. The P_T^e is corrected downwards by ~ 1% to take into account the electron energy that is deposited outside the core cells.

3.4 *The Cross Section Values*

The W sample

In addition to the cuts described above, we require $P_T^e > 20$ GeV/c and $P_T^{\nu} > 20$ GeV/c. The distribution of P_T^e and P_T^{ν} for the remaining sample of 1266 events is shown in Fig. 3, and shows the characteristic Jacobian peak structure expected from $W \to e\nu$ decays. The QCD background is estimated to be ~ 1%. In the forward regions, a similar selection resulted in a sample of 361 events. The acceptance was estimated using a simple Monte Carlo model for the detector response. A summary of the numbers is given in Table 1.

TABLE 1 : The efficiency and acceptance values for the W sample

	Central	Forward
Number of events	1266	361
Electron selection criteria efficiency	(78.1±1.2±1.6)%	(81.5±2.7±1.5)%
Acceptance	(38.3±0.8)%	(9.9±0.2)%

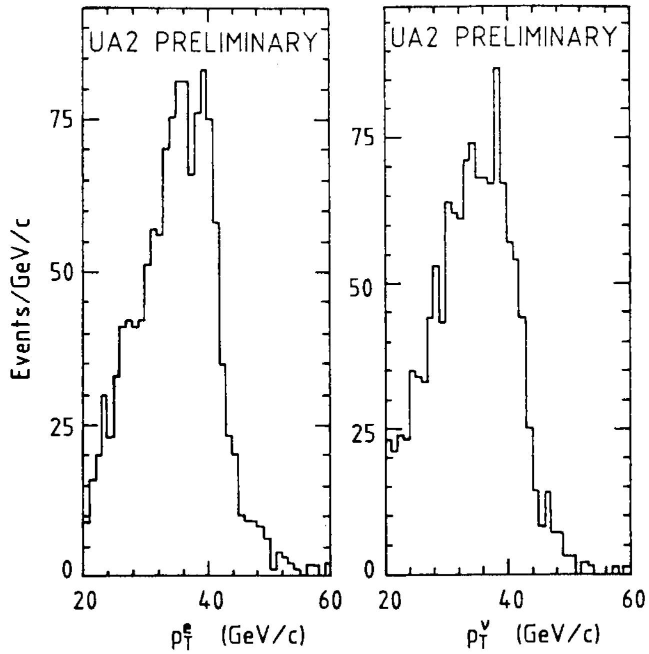

Fig. 3 Distribution of P_T^e and P_T^ν for the W candidates identified in the *central region.*

From the above values and the integrated luminosity of 7.1 ± 0.5 pb^{-1}, corresponding to this data sample plus small additional corrections due to the trigger efficiency, we measure the cross section to be :

$$\sigma_W = 630 \pm 20 \text{ (stat)} \pm 50 \text{ (syst) pb} .$$

The Z sample

In this preliminary analysis of the cross section, both electrons are required to be in the fiducial regions of the calorimeters where it is easier to evaluate the efficiencies. The invariant mass distribution, Mee, for this reduced sample of events is shown in Fig. 4. There are a total of 86 events with $M_{ee} > 76$ GeV/c^2. Employing a procedure similar to that described for the W sample, the cross section is calculated to be :

$$\sigma_Z = 61 \pm 7 \text{ (stat)} \pm 5 \text{ (syst) pb} .$$

The values for σ_W and σ_Z are in agreement with expectations from QCD calculations [8]. Likewise, the cross section ratio, $R_{exp} = \sigma_W/\sigma_Z$, can be compared to the QCD predictions, assuming three light neutrino generations. This measurement has the advantage that most of the theoretical and experimental uncertainties cancel in the ratio. The preliminary measured value is :

$$\text{Rexp} = 10.35\ ^{+1.2}_{-1.1} \text{ (stat)} \pm 0.3 \text{ (syst).}$$

4. SEARCH FOR THE TOP QUARK

In this section we give a brief description of the procedure used, and the results obtained concerning the search for the top quark.

At the $\bar{p}p$ Collider, the top quark can be produced from the following two dominant processes :

1) via the *weak interaction* : $p\bar{p} \rightarrow W + X$, $W \rightarrow t\bar{b}$, or

2) via the *strong interaction* : $p\bar{p} \rightarrow t\bar{t} + X$.

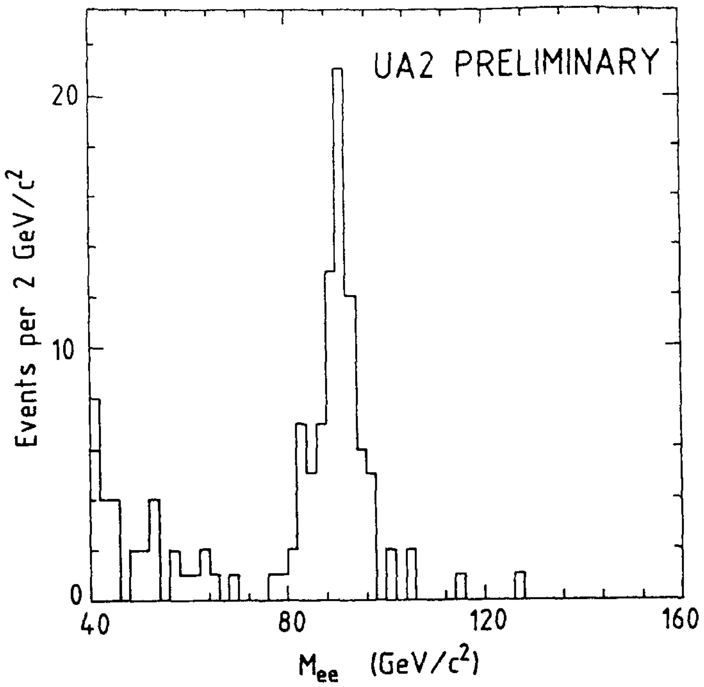

Fig. 4 The M_{ee} mass spectrum for the Z data sample (see text).

The production rate for the top quark in (1) is related to the W production cross section (see Section 3) via the equation :

$$\text{Ntop} = 3 \int L\, dt \times \sigma(\bar{p}p\, W \to e\nu_e) \times PS(m_t) \times F_{QCD},$$

where :

- 3 is the colour factor,
- $\int L\, dt$ is the integrated luminosity,
- $PS(m_t)$ is a phase-space factor depending on the top quark mass,
- F_{QCD} is a correction for higher order QCD processes, (which was set equal to 1, because of its large uncertainties for $m_{top} \sim M_W - m_b$ [9]).

The cross section for process (2) has been evaluated using the full next-to-leading order calculation [10,11]. The results for both processes are shown in Fig. 5.

The decays of the top quark into final states containing only hadronic jets are very difficult to distinguish from the large background due to QCD processes. We therefore restrict ourselves to the search using the semi-electronic decay mode : $t \to be\, \nu_e$, which has a branching ratio of 1/9 in the Standard Model. In this case, the experimental signature consists of events containing an electron, one or more hadronic jets (from the associated t or b quarks) and a P_T^{miss} imbalance from the neutrino.

4.1 The Data Sample

Two data sets were used in this analysis. The first one is from a total of 2.7 pb^{-1} of data collected during the 1988 run, and consisted of all events containing an electromagnetic cluster with $E_T > 12$ GeV. The second one is from an integrated luminosity of 4.4 pb^{-1}, collected during the 1989 run, with a trigger using the above cut, and in addition requiring a hadronic cluster with $E_T > 6$ GeV and $P_T^{miss} > 9.5$ GeV/c. Only electron candidates detected in the central calorimeter were considered.

In addition to the cuts described in Section 2 (common to both analyses), the pulse height information from the outer silicon array was used to reduce the large background from electron pairs, arising from photon conversions in the material closer to the beam pipe, and from Dalitz decays. The candidate electron tracks were required to match an outer silicon pad, with a measured charge between 0.6 and 1.6 times that expected from a minimum ionising particle. The efficiency of this cut was measured to be $\varepsilon_{sil} = (73.6 \pm 1.1)\%$, using W electrons.

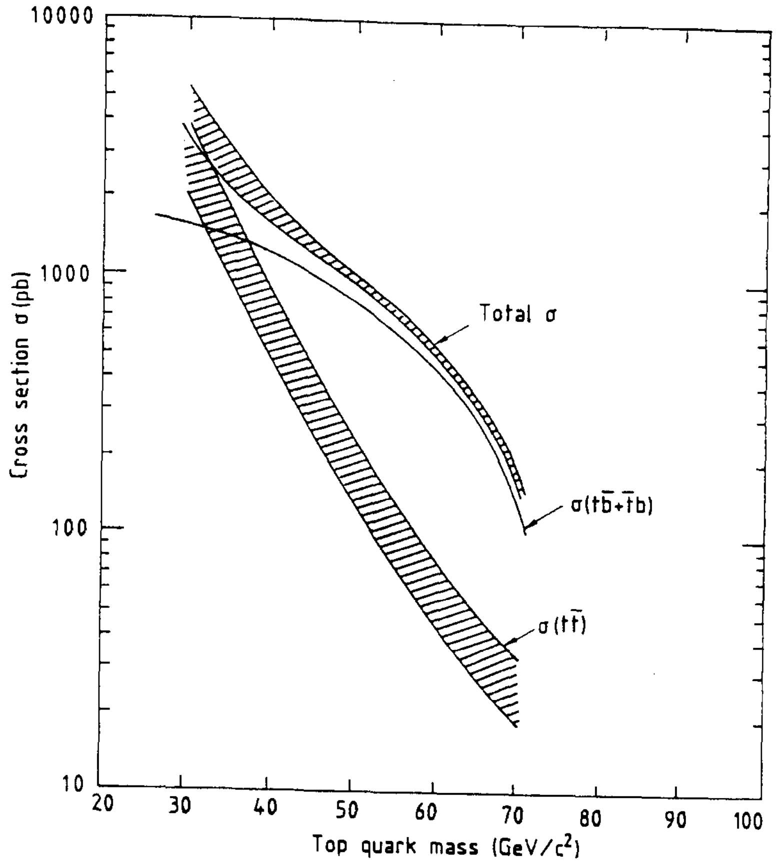

Fig. 5 Cross sections for top quark production in interactions at $\sqrt{s}$ = 630 GeV. The band indicates the theoretical uncertainties.

4.2 *Selection of the Top Candidates*

The *electron* and *neutrino* identification is essentially the same as for the W and Z analysis (see Sections 3.2 and 3.3), with some modifications. A summary of the electron selection criteria is given below :

- a track-preshower match is required to fulfill the criterion $d\sigma^2 < 25$,
- candidates with $P(\chi^2) < 10^{-2}$, or an energy greater than 1 GeV in the second hadronic compartment were rejected. The efficiency of this cut was estimated to be $\varepsilon_{P(\chi 2)} = (88.7 \pm 0.6)\%$ for W electrons.

The overall efficiency to find a W electron with the above cuts is : $\varepsilon_e^W = (47.6 \pm 1.6)\%$.

A useful variable for discriminating between various classes of events is the transverse mass of the electron - P_T^{miss} system (M_T) :

$$M_T = [2P_T^e \ P_T^{miss} \ (1 - \cos\Delta\phi_{e\nu})]^{1/2},$$

where $\Delta\phi_{e\nu}$ is the azimuthal angle between the electron and the P_T^{miss} vectors. The distribution of P_T^{miss} vs M_T is shown in Fig. 6 for a sub-sample which was selected by applying no cut on the missing transverse momentum. The events at low P_T^{miss} and small M_T are dominated by background processes in which a hadronic jet fakes the electron signature and the small P_T imbalance results from detector resolution effects or particles escaping the acceptance. The P_T^{miss} distribution of these events, integrated over all values of M_T, is shown in Fig. 7. Events consistent with the emission of a high energy neutrino were selected by requiring $P_T^{miss} > 15$ GeV/c for both samples.

4.3 *Jet Identification*

Any cluster failing to pass the electron cuts was considered to be a jet, and its energy was defined as the sum of the cell energies of all the cells in the cluster. We only retain jets with $|\eta| \leq 2.2$, so as to reduce the background from QCD processes for which the jet angular distribution peaks at large pseudo-rapidity. Events in which the highest E_T jet (jet1) was below 10 GeV are rejected. At this stage, the data sample still contains two-jet events in which a jet fakes the electron signature. Such events are expected to show an azimuthal difference between the electron and jet 1, $\Delta\phi_{e\text{-}jet1}$, close

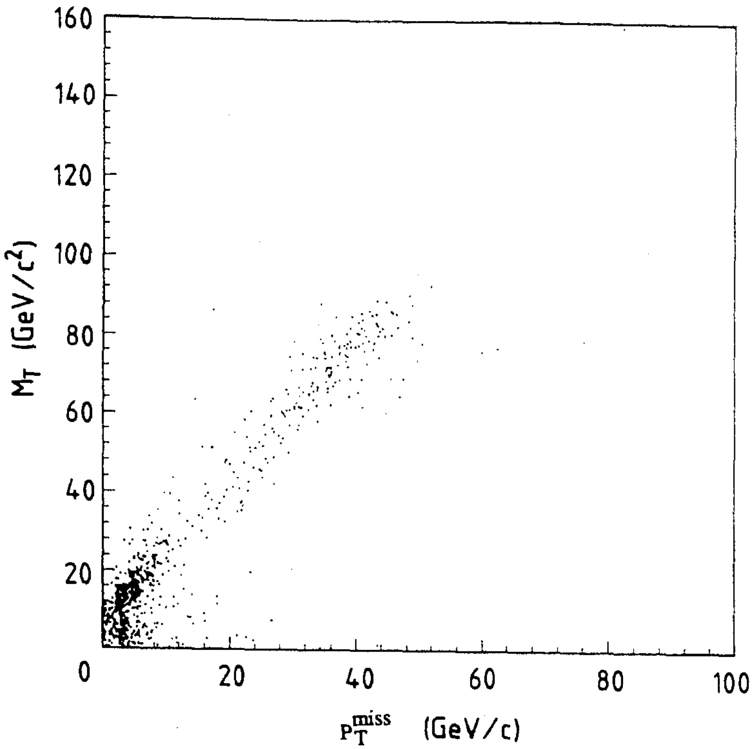

Fig. 6 M_T vs P_T^{miss} for events with an electron candidate (1988 data only).

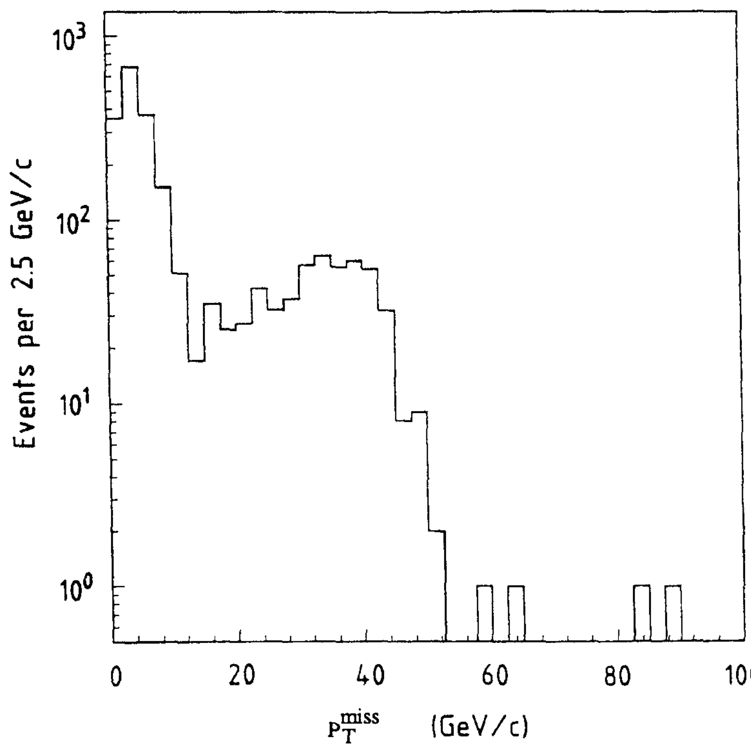

Fig. 7 The P_T^{miss} distribution for events with an electron candidate (1988 data only).

to 180°. We, therefore, discard events lying in the interval $160° < \Delta\phi_{e\text{-jet}1} < 200°$. After the above cuts, there remain a total of 137 events. The M_T distribution for these events is shown in Fig. 8.

4.4 Estimate of the Expected Signal

Events from the production and decay of the top quark are expected to have more complex topologies, and lower energy electrons than the W events which were used to determine the efficiencies of the electron cuts. The relative loss of efficiency was therefore studied for each cut :

- The cuts used to define an electromagnetic cluster have a lower efficiency for top events, depending upon the process considered and the top quark mass. For example, the loss of efficiency is approximately 28% for $t\bar{t}$.
- The loss of efficiency of the cut on the shower quality factor $P(\chi^2)$ was studied by overlaying the energy pattern of W electrons onto Monte Carlo simulations of top events. This was found to be between 1% to 6%.
- The loss of efficiency of the track-preshower match and the calorimeter was investigated using W events with underlying events characterized by either high total E_T or high charged track multiplicity. The loss was found to be (3±3)%.
- A loss of (2±1)% was associated with a decrease in response of the preshower detector for lower energy electrons. This was estimated using test beam data.

Taking into account the above losses the efficiency to find electrons in semi-electronic top decays is found to be ε_e^{top} = 44.4 % for $t\bar{b}$ and 34.1 for $t\bar{t}$, for a top quark mass, $m_{top} = 65$ GeV/c^2. The relative error on the efficiencies was estimated to be ±7%.

4.5 Monte Carlo Simulation of Top Events

The acceptance for top events and their expected M_T distribution were obtained using the Eurojet Monte Carlo [12]. This generator contains the matrix elements for the higher order tree level processes in heavy quark production (i.e. order α_s for $t\bar{b}$ and order α_s^3 for $t\bar{t}$). In the following, we give a brief summary of the results. A more complete discussion can be found in Ref. [9].

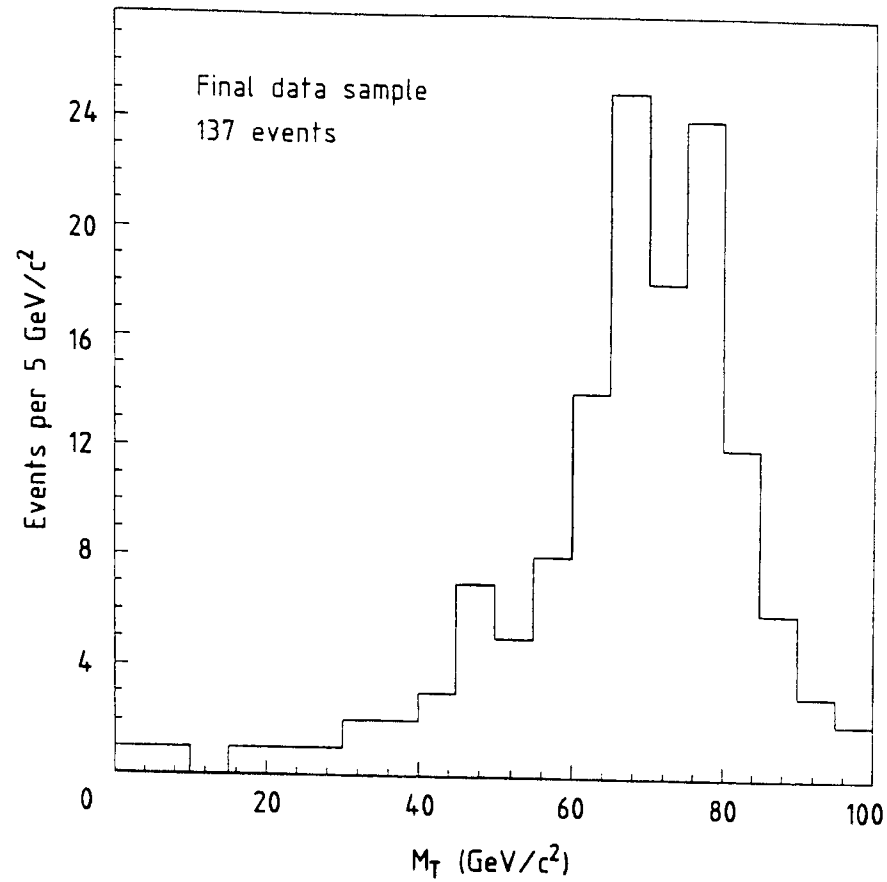

Fig. 8 The M_T distribution for the final event sample.

The top quark decay in Eurojet was simulated after hadronisation into a top meson or baryon, with the branching fractions as expected in the Standard Model for a free quark decay. The bottom and charm hadron decays were generated using extrapolations from known exclusive branching ratios, and the simulations were insensitive to the exact values used. After reconstruction in the UA2 calorimeter, the jets from hadronic bottom decays were found to be similar to those from gluons of the same parton energy, and only slighly broader than those from light quarks. Gluons were fragmented into light quark pairs, and the light quark fragmentation followed the parametrisation of Field and Feynman [13].

Finally, a full simulation was performed of the calorimeter response to all the generated particles, using test beam measurements, with hadron and electron beams, over an energy range from 300 MeV to 150 GeV. The Monte Carlo events were then analysed in the same way as the data.

4.6 *Systematic Uncertainties*

Several sources of systematic errors, affecting the acceptance were studied [9] :

- A comparison was made between the underlying event for the simulated top events, and the superposition of minimum bias events from the data. A systematic error of ±4% for $t\bar{b}$ and ±2% for $t\bar{t}$, for a top mass of 65 GeV/c^2, was estimated with the above procedure.
- The calorimeter response to hadron jets is sensitive to the response to low energy hadrons (< 1 GeV). The measured response curve was adjusted to give the lowest response consistent with the test beam data, thus reducing the acceptance for events with at least one jet with E_T > 10 GeV. The uncertainty in the absolute energy scale of the calorimeter (± 1% in the electromagnetic and ±2% in the hadronic compartments), was also taken into account by adjusting the response downwards. In the worst case, the loss in acceptance was 5% for $t\bar{b}$ and 2% for $t\bar{t}$ for a top quark mass of 65 GeV/c^2, the difference being due to the higher jet multiplicity in the $t\bar{t}$ final state.
- The parameters in the fragmentation functions were varied within limits consistent with the observed energy flow in jets with $E_T \sim 10$ GeV as measured in the data. In the worst case the loss in acceptance was 2% for both production processes.

The overall error on the acceptance was obtained by combining the above effects in the most pessimistic direction.

The expected numbers of events from both processes, after taking into account the electron detection efficiency and the semi-leptonic branching ratio, are given in Table 2 for a top quark mass of 65 GeV/c^2. These are given for the full transverse mass range, and the range $15 < M_T < 50$ GeV/c^2, where most of the signal is expected. The numbers in brackets refer to the lower limit, obtained using the lowest values for the production cross section and acceptance.

TABLE 2 : The estimated number of events for m_{top} = 65 GeV/c^2

All M_T	$15 < M_T < 50$ GeV/c^2
17.6 (13.4)	13.6 (10.6)

As an example the transverse mass distribution predicted for m_{top} = 65 GeV/c^2 is shown in Fig. 9.

4.7 *The Background Processes*

The main source of associated high energy electrons and neutrinos in the Standard Model is W boson production and decay via :

$$W \to e\nu_e \quad \text{or} \quad W \to \tau\nu_\tau,\ \tau \to e\nu_e\ \nu_\tau\ .$$

These events constitute a background if the W boson is produced in association with a high E_T jet. The Jacobian peak expected from W events is seen in the p_T^{miss} distribution of the data (Fig. 7). The transverse mass distribution expected for such events (Fig. 10), was obtained using the EKS Monte Carlo [14], which includes the full order α_s^3 calculations. The normalization is taken from the 105 events observed in the region M_T > 60 GeV/c^2, where the contribution from the top signal is expected to be small.

Other, smaller sources of background arise from the decays of the Z boson : $Z \to ee$, or $Z \to \tau\tau$, $\tau \to e\nu_e$, $\tau \to \nu\tau X$; which can simulate missing p_T if one of the electrons is misidentified as a jet. They were estimated using the EKS Monte-Carlo. Likewise, the process $\bar{p}p \to b\bar{b} + X$, $b \to e\nu_e\ c$ produces electrons from the

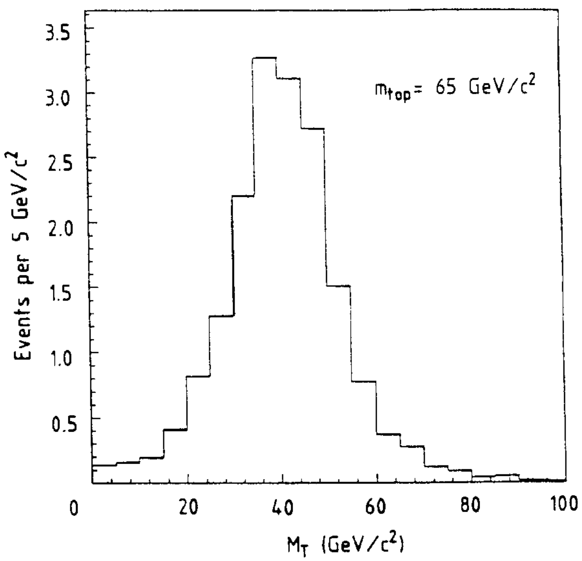

Fig. 9 The M_T distribution for the top decays with m_{top} = 65 GeV/c^2.

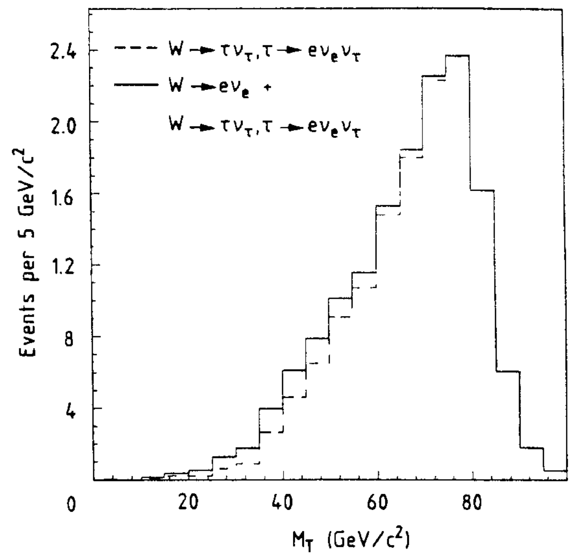

Fig. 10 The M_T distribution for W events obtained using the EKS Monte Carlo.

semileptonic b decays in association with a jet from the charm quark. The magnitude of this background is estimated [9] using the Eurojet Monte Carlo. Finally, the QCD background, due to jets misidentified as electrons, is estimated from the data [9].

A summary of the event sample and the estimated background is given in Table 3.

TABLE 3 : Event sample and backgrounds

	All M_T	$15 < M_T < 50$ GeV/c^2
$Z \rightarrow ee$,	2.5±0.6	1.6±0.4
$b\bar{b}$	1.0±0.6	0.5±0.3
QCD	2.4±1.5	2.1±1.5
W events	148.5±14.5	22.0±3.0
Total backgrounds	154.4±14.6	26.2±3.4
Observed events	137	17

4.8 *Mass Limits*

A brief summary of the technique used to determine the mass limit is given. Limits on the top mass were obtained by comparing the M_T distribution of the observed events with that expected from background sources alone, or in the presence of a top signal of a given mass. The M_T distribution for W events is taken from Fig. 10. The exact shape of the M_T distribution for the other background sources was uncertain, mainly due to their small numbers. However, the results were unchanged if the best estimate of the shape was replaced by a flat background distribution. The expected signal contribution was taken from the Eurojet simulation using the appropriate top mass (for example the distribution of Fig. 9 was used for a top mass of 65 GeV/c^2). A likelihood fit is performed to the observed events with two free parameters, giving the fraction of the event sample due to top decays and to background sources other than W events. No normalization was imposed on the number of W events, but for the other background sources the estimate of Table 3, with its error, was used. For each top mass considered, the fitted signal was consistent with no top production. The results of the fit yield the following limits :

$$m_{top} > 69 \text{ GeV}/c^2 \text{ (95 C.L.)},$$

or

$$m_{top} > 71 \text{ GeV}/c^2 \text{ (90 C.L.)}.$$

5. CONCLUSIONS

The UA2 detector has collected a data sample corresponding to 7.4 pb^{-1}, during the 1988 and 1989 data-taking periods. Preliminary results on the W and Z cross section are : $\sigma_W = 630 \pm 20(\text{stat}) \pm 50(\text{syst})$ pb, and $\sigma_Z = 61 \pm 7(\text{stat}) \pm 5(\text{syst})$ pb.

A search has also been performed for evidence for top quark production. We find no evidence for such a process, and obtain the following lower limits : $m_{top} > 69$ GeV/c^2 (95 C.L.), or $m_{top} > 71$ GeV/c^2 (90 C.L.).

ACKNOWLEDGEMENTS

I would like to thank the members of the SLAC committee for providing an exciting and lively atmosphere at the Summer Institute, and for their excellent organization.

REFERENCES

[1] A. Beer et al., Nuclear Instruments and Methods 224 (1984)360.

[2] F. Alberio et. al., The Electron, Jet and Missing Transverse Energy Calorimetry of the Upgraded UA2 Experiment at the CERN $\bar{p}p$ Collider (in preparation).

[3] R. Ansari et al., Nucl. Instr. Meth. A279 (1989) 388.

[4] F. Bosi et al., CERN-EP/89-82 (1989).

[5] B. Merkel, Proceedings 7th Topical Workshop on Proton-Antiproton Collider Physics (1988) 482.

[6] R.E. Ansorge et al., Nuclear Instr. Meth. A265 (1988) 33 and A273 (1988) 826.

[7] K. Einsweiler et al., Proc. Int. Conf. on the Impact of Digital Microelectronics and Microprocessors on Particle Physics (1988) 247.
S. Stapnes, ibid., 254.

[8] G. Altarelli et al., Z. Phys. C27 (1985) 617.

[9] L. DiLella, Talk given at the 1989 Lepton-Photon Symposium, Stanford, CA, USA (in preparation); and references contained therein.

[10] G. Altarelli et. al., Nucl. Phys. 308B (1988) 724.

[11] P. Nason, S. Dawson and R.K. Ellis, Nucl. Phys. B303 (1988) 607.

[12] A. Ali et al., Nucl. Phys. B292 (1987) 1.

[13] B. Anderson et al., Phys. Rep. 97 (1983) 34.

Selected Preliminary Results from CDF

The CDF Collaboration[1]

Presented by K.J. Ragan, University of Pennsylvania

Invited talk at the 1989 SLAC Topical Conference,
July 21-23, 1989, Stanford, CA.

Abstract

Preliminary results in the areas of heavy quark searches, precision electroweak measurements, and QCD tests are presented from the study of $\bar{p}p$ collisions at a center of mass energy of 1.8 TeV.

1 Introduction

The CDF experiment at Fermilab, studying $\bar{p}p$ collisions at a center of mass energy of 1.8 TeV, has recently completed a run during which 4.4 pb^{-1} of data was accumulated. Many analyses are underway, including heavy quark searches, precision electroweak measurements ($W^{\pm}$ and Z^0 masses, $\sin^2\theta_W$, ratio of W to Z production cross sections, *etc.*), and the study of jets of large transverse energy (single jet inclusive cross section, dijet angular distributions, trijet production, *etc.*). We present here a selected number of these analyses; the goal is not to give a comprehensive update of *all* analyses but rather to give a flavour for the *range* of physics topics that CDF is able to address. All analyses and results, unless noted otherwise, are preliminary.

This paper will be organized as follows: the parts of the detector relevant for the analyses discussed here will be presented in the next section, followed by a brief discussion of the trigger and data collection. Section 3 will discuss the calibration of the central electromagnetic calorimeter and the determination of the momentum scale, as well as jet energy corrections. Sections 4, 5 and 6 will be devoted to searches for the standard-model top quark, jet studies, and W and Z mass measurements, respectively. Conclusions are presented in Section 7. In keeping with the style of the SLAC Summer Institute, the forum for this presentation, this report will be somewhat pedagogical; those familiar with the detector may choose to skip directly to the physics results in sections 4 through 7.

2 Description of the Detector

The CDF detector [2] is a general purpose solenoidal detector with tracking and calorimetric coverage over nearly the full solid angle. An elevation view of one half of the detector (which is forward-backward symmetric) is shown in Figure 1. Moving from the interaction point outward in the central region (*i.e.* at pseudorapidities[1] $|\eta| < 1$), one encounters successively the vertex time projection chamber, the central tracking chamber (CTC), the central electromagnetic calorimeter, the central hadron calorimeter, and the central muon chambers. In the forward and backward regions ($|\eta| > 1$) the calorimetry is provided by the plug and forward calorimeters, and forward muon chambers with steel toroids provide muon measurements over a limited part of the solid angle. In the region in front of the forward and backward detectors are scintillators that cover the pseudorapidity region $3.2 < |\eta| < 5.9$. They are used to trigger the detector on inelastic $\bar{p}p$ interactions.

The Vertex Time Projection Chamber

The vertex time projection chamber (VTPC) [3] consists of eight time projection modules surrounding the beam pipe and mounted end-to-end along the beam direction (the z axis)[2]. The system provides precise r-z tracking for $|\eta| < 3.3$ in order to locate the interaction vertex and to recognize multiple beam-beam interactions (in six-bunch mode at a luminosity of $\mathcal{L} = 10^{30} cm^{-2} s^{-1}$, 7.5% of bunch crossings with interactions contain more than one interaction). The resolution on the z position of the vertex is typically a few millimeters.

Special care was taken to minimize the amount of material in the chamber in order to reduce photon conversions and multiple Coulomb scattering of charged particles. The conversion removal algorithm mentioned in subsequent sections uses the VTPC tracking, removing any electron candidate having fewer than 20% of the maximum possible number of VTPC space points.

The Central Tracking Chamber

The central tracking chamber (CTC) [4] is a large cylindrical drift chamber containing 60 (24) layers of axial ($\pm 3°$ stereo) sense wires organized into five (four) superlayers. The large tilt (45°) of the sense wire cells with respect to the radial direction ensures that every high transverse momentum (p_T) track must pass close to at least one sense wire in each superlayer, permitting a straight-forward 'prompt-hit' high-p_T charged track trigger. Operated in the 1.41 Tesla solenoidal magnetic

[1] Pseudorapidity η is defined as $\eta = -\ln(\tan(\frac{\theta}{2}))$, where θ is the polar angle measured from the proton direction.

[2] The CDF coordinate system uses the proton beam direction as the z axis, the radial distance r from the beams, and the azimuthal angle ϕ around the z axis.

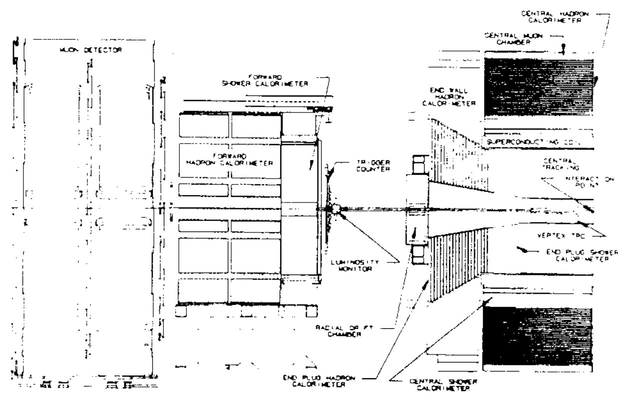

Figure 1: Elevation view of the CDF detector. Only the forward half is shown, the detector being forward-backward symmetric.

field[3], the CTC transverse momentum resolution is $\delta p_T/p_T = 0.002p_T\ (GeV/c)^{-1}$. Constraining track trajectories to pass through the beam position improves the momentum resolution to $\delta p_T/p_T = 0.0011p_T\ (GeV/c)^{-1}$.

The Central EM Calorimeter

The central electromagnetic calorimeter (CEM) [5] is a lead-scintillator sampling calorimeter of 18 radiation length thickness, segmented into 15° wedges in azimuthal angle ϕ. Each wedge contains 10 projective towers subtending 0.1 units of pseudorapidity. At $\eta = 0$, this geometry gives rise to a region of reduced calorimeter response approximately 8 cm wide. A strip chamber with wire and cathode strip read-out is embedded in the calorimeter after approximately 6 radiation lengths to provide shower position determination and longitudinal shower development information. The wires run in the z direction (parallel to the beams), and thus measure the shower shape in the r-ϕ plane (*i.e.* the bend plane of the solenoidal magnet); the cathode strips run in the ϕ direction.

The calorimeter was originally calibrated [6] in an electron test beam, and Cs^{137} sources are used to track the energy response to better than 1%. The final calibration is obtained using an inclusive electron sample from the $\bar{p}p$ collision data; the procedure will be described in detail below. The electron energy resolution of the CEM is well described by $\sigma(E)/E = 13.5\%/\sqrt{E_T} \ominus 1.7\%$ (for E_T in GeV), where the 1.7% term represents the average uncertainty in the individual tower calibrations. The strip chamber position resolution is measured to be ± 2.5 mm for 25 GeV electrons.

The Central Hadron Calorimeter

The central hadron calorimeter (CHA) [7] is a steel-scintillator sampling calorimeter approximately 5 absorption lengths deep. The tower geometry matches that of the CEM; *i.e.* wedges of 15° in azimuthal angle subdivided into towers of 0.1 units in pseudorapidity. The energy resolution is approximately $\sigma(E)/E = 80\%/\sqrt{E_T}$.

Each CHA photomultiplier tube is equipped with a 16-bit TDC in order to reject out-of-time energy from cosmic rays or background from the Fermilab main ring, which is near the roof of the collision hall, above the detector.

The Central Muon Chambers

Behind the central hadron calorimeter, for $|\eta| < 0.65$, is a series of drift chambers comprising the central muon system [11]. Each calorimeter wedge contains one chamber (four wire planes) of azimuthal dimension 12.6°, leading to azimuthal gaps in the central muon system amounting to 16% of the fiducial region. The chambers use single hit TDCs for position measurements in the azimuthal direction, and attain a position resolution of 250 μm. In the beam direction, charge division is used to attain a resolution of 1.2 mm. The geometry of the chambers also allows them to be used to form a first level trigger for penetrating tracks with a transverse momentum p_T greater than a given (programmable) value.

[3] For the 1987 data taking, the field value was 1.5 Tesla.

The Plug and Forward Calorimeters

In the region $1 < |\eta| < 4.2$ energy measurements are provided by the plug [8] and forward/backward [9, 10] calorimeter systems[4]. These are finely segmented gas sampling calorimeters with cathode pad readout, and are used in the analyses presented here only to extend the jet coverage of the detector and to measure the total transverse energy in the event (*i.e.* we do not use these systems for electron measurements). The hadronic energy resolution in these regions is approximately $\sigma(E)/E = 100\%/\sqrt{E_T}$.

The Trigger System

The CDF trigger system is a two-level FASTBUS-based system of micro-coded processors [12] followed by a Level-3 'farm' of VME-based processors [13] running offline-like algorithms written in high-level languages.

To signal an inelastic $\bar{p}p$ interaction, all triggers require a coincidence in the scintillator counters located between the central detector and the forward and backward arms.

The level-1 decision is based on global transverse energy deposition in the calorimeters, as well as the high-p_T track and high-p_T muon-candidate triggers mentioned above. The level-2 trigger incorporates a cluster finder and operates on calorimeter clusters and high-p_T tracks, correlating information across detector sub-system boundaries and permitting one to trigger on physics 'entities' such as electrons, muons, or jets. The cluster finder uses physical calorimeter towers ganged together into 'trigger towers'[5], thus retaining some of the detector granularity at the trigger level. The level-3 algorithms receive the data in the standard offline data structures and are used to improve background rejection; for example, EM strip chamber data, two-dimensional (r-ϕ) CTC tracking, and calorimeter noise rejection are all available to level-3 algorithms.

It is germane to this discussion to illustrate in some detail a few of the triggers that will be used in the analyses presented later.

[4] For $|\eta| > 3.6$, the calorimeter depth is reduced due to the presence of low-β quadrapoles.

[5] The trigger towers are 15° in ϕ by 0.2 units in η.

The Inclusive Central Electron Trigger

Much of the electroweak and heavy flavour physics accessible to CDF has as a possible signature a large transverse energy electron. The strong magnetic field, precision tracking, and finely segmented projective calorimeters of CDF are well suited to a clean, high-purity electron trigger.

The level-1 requirement is an E_T deposition in the central electromagnetic calorimeter of at least 6 GeV in a single trigger tower. The level-2 electron trigger requires a central cluster of E_T greater than 12 GeV, with a ratio of hadronic energy to electromagnetic energy less than 0.125. In addition the level-2 trigger requires a prompt-hit track with a p_T of at least 6 GeV/c (the threshold is the 90% efficiency point for this setting of the track processor), matched to the ϕ position of the cluster. The level-3 algorithm reclusters the energy using the physical segmentation of the calorimeter, and requires the cluster to have fewer than four towers in a single wedge. The wedge construction ensures that well measured electron showers do not cross wedge boundaries. The energy sharing among the towers is required to be consistent with that expected for an electron, as is the strip chamber pulse shape. For electrons of $E_T > 15$ GeV passing the offline criteria (see below), this trigger is $98 \pm 0.5\%$ efficient. It has a raw rate of approximately 250 nb, which could be substantially reduced online with no loss of efficiency by tightening the selection criteria in the level-3 algorithm.

The standard offline algorithm to identify electrons [14] uses tighter cuts on the above variables as well as the ratio of energy to measured track momentum (E/p) and geometrical matching of the measured strip chamber shower to the track trajectory. Distributions of some of these quantities and the cut values are shown in Figure 2 for an unbiased sample of electrons selected using the missing transverse energy $\not{E}_T$. The cuts can be seen to be very efficient. Inside the fiducial region (away from ϕ and η cracks) the overall efficiency is approximately 77%. The dominant losses are due to cuts on the strip chamber wire profile and the cut on E/p.

The resulting rate of electrons is approximately 5 nb; we will see below that this sample is dominated by physics processes (in particular QCD production of $b\bar{b}$ quarks and electroweak production of $W^{\pm}$) and *not* by non-electron background. Thus the trigger and the offline selection result in a small, very pure electron sample conducive to the study of QCD and electroweak processes.

The Inclusive Muon Trigger

The level-1 requirement for the inclusive muon trigger is a track in the muon chambers with a transverse momentum p_T above 3 GeV/c, using the chamber geometry for a rough momentum measurement as described above. The level-2 trigger requires a CTC prompt hit track with p_T greater than 9.2 GeV/c (90% efficiency point). Finally, the level-3 selection uses the 2-dimensional CTC tracking and requires a track with p_T above 11 GeV/c, matched to the position (in ϕ) of the muon chamber

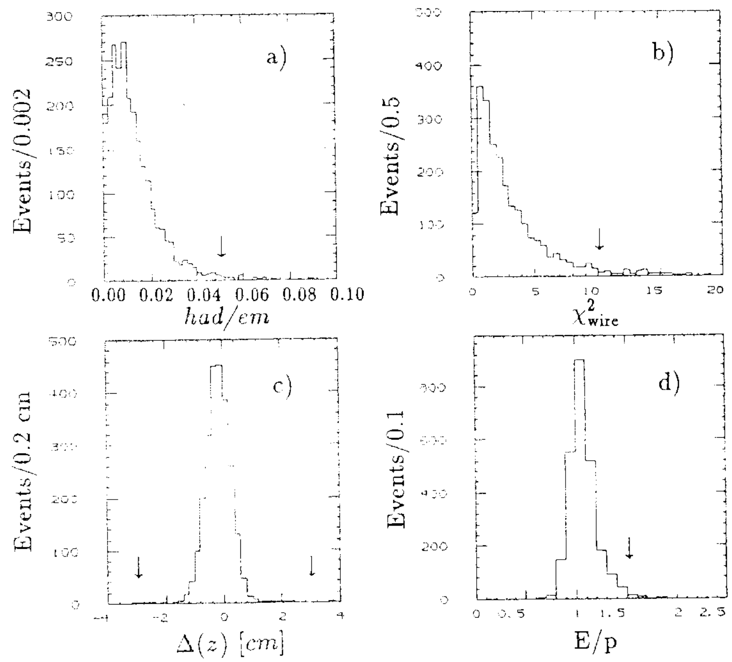

Figure 2: Distributions of some of the variables used in the standard CDF electron selection, for a sample of $W \to e\nu$ decays chosen using $\not{E}_T$ criteria. a) ratio of hadronic to electromagnetic energy; b) strip chamber shower shape χ^2 in the azimuthal (wire) direction; c) track to strip chamber position matching in the z direction; d) ratio of calorimeter energy to track momentum, E/p. In each case the cut value is indicated by an arrow.

track. The trigger has a rate of approximately 130 nb.

Offline, the criteria used to select muons are the CTC-muon chamber track matching in both position and angle and the energy deposition in the calorimeter (required to be consistent with a minimum ionizing particle). Figure 3 shows the distributions of these quantities and the cut values for an unbiased sample.

Jet Triggers

Jet triggers are based exclusively on calorimeter information. The level-1 requirement is at least 18 GeV of transverse energy in the entire detector (summed over towers having at least 1 GeV E_T each). The level-2 trigger cluster finder starts from a seed tower of at least 3 GeV E_T and finds all contiguous towers with at least 1 GeV E_T. Cluster thresholds are imposed at 20, 40, and 60 GeV, with the first two being prescaled by factors of 100 to 300 and 10 to 30, respectively. In addition, there is a trigger on the total transverse energy being greater than 120 GeV, and a multijet trigger requiring three or more clusters above 20 GeV E_T.

In the 1987 run, only the level-1 trigger was used, with E_T thresholds of 20, 30, and 40 GeV set over the central calorimeter only.

3 Calibration and Energy Scale Determination

This section has two main topics; one is the determination of the central electromagnetic calorimeter calibration and the momentum scale of the central tracking system, important for precise W and Z mass measurements. The other is a discussion of the energy corrections that must be applied to calorimeter clusters in order to relate the underlying parton (gluon or quark) energy to the cluster energy.

Energy and Momentum Calibration for Electrons

As mentioned above, the initial calibration of the central electromagnetic calorimeter was obtained using electron test-beam measurements, and the calibration for each wedge was tracked *in situ* using Cs^{137} sources. The accuracy of this calibration (of the order of 1%) is insufficient for high precision $W^{\pm}$ and Z^0 mass measurements, and a very large inclusive electron sample makes it possible to use the data itself to calibrate the detector with improved precision. First, the mean value of the ratio of energy to momentum for a sample of inclusive electrons, $\langle \frac{E}{p} \rangle$, was used to adjust the tower-to-tower calibrations and to tie the overall energy scale to the momentum scale as determined by the tracking chamber and the magnetic field map (the latter is known to better than 0.05%). The width of the E/p distribution and the number of electrons in each tower resulted in a (typically) 1.7% uncertainty on the calibration of each tower. This 1.7% is the tower-to-tower term quoted above which must be

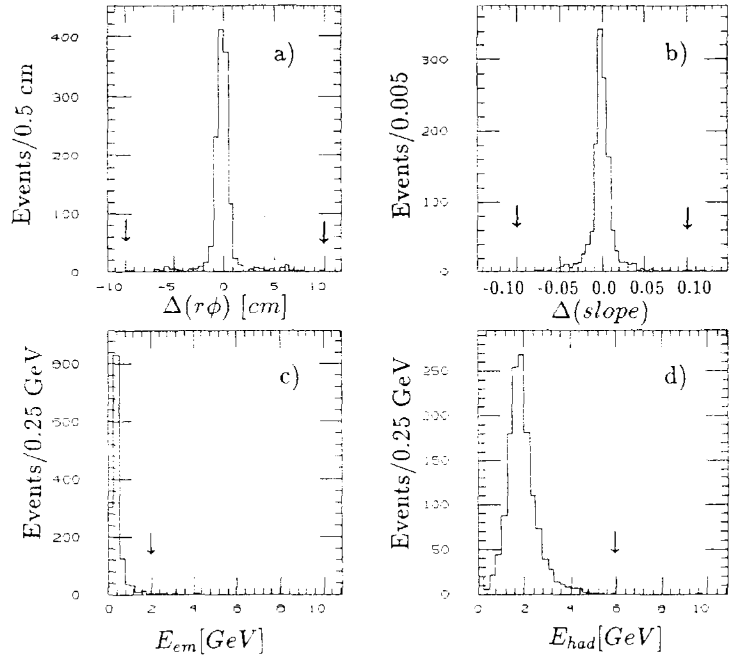

Figure 3: Distributions of some of the variables used in the CDF muon selection, for a sample of $W \to \mu\nu$ decays chosen using $\not{E}_T$ criteria. a) CTC track to muon chamber track position matching in r-ϕ; b) CTC track to muon chamber track angle matching in r-ϕ; c) energy deposited in the EM calorimeter; d) energy deposited in the hadron calorimeter. In each case the cut value is indicated by an arrow.

added in quadrature with the energy-dependent resolution term, and is a statistical (not a systematic) uncertainty. The results of the tower-to-tower adjustment (Figure 4) show a mean tower correction compared to the 1987 source calibrations of 1.6%, demonstrating the long-term stability of the source calibration. The width (rms) of the corrections is 2.7% and represents the convolution of the 1.7% tower-to-tower uncertainty and the error on the original source calibration.

The mean values of E/p for electrons and positrons were then used to precisely align the tracking chamber by wire-layer rotation. The wire-position corrections were typically 35 μm (a rotation of approximately 30 μrad), and the resulting alignment is accurate to better than 5 μm. The basis of this method is the observation that the absorptive process of calorimetric measurement cannot distinguish between charges, while any geometric distortions or alignment errors of the chamber lead to absolute sagitta errors and thus *charge-dependent* errors:

$$S^{\pm}_{measured} \quad = \quad S^{\pm}_{true} \quad \pm \quad \delta S \quad ,$$

where the superscripts indicate the charge of the particle and δS represents the effect of distortions or alignment errors. Note that *charge-independent* sagitta errors can be absorbed into the overall momentum scale uncertainty, which will be discussed below.

Finally, having adjusted the electromagnetic calibration based on $\langle\frac{E}{p}\rangle_+ + \langle\frac{E}{p}\rangle_-$, and aligned the central chamber based on $\langle\frac{E}{p}\rangle_+ - \langle\frac{E}{p}\rangle_-$ (where the subscripts indicate the particle charges) of an inclusive electron sample, we have two cross-checks on our absolute energy/momentum scale. One is the shape of the E/p distribution for electrons from the process $W^{\pm} \to e^{\pm}\nu$, shown in Figure 5. These electrons are affected by both internal and external *bremsstrahlung* which is precisely predicted by QED, and the distribution is neither centered on, nor symmetric about, a value of 1.0. Figure 5 shows the data and the results of a Monte Carlo calculation including calorimeter and tracking resolution as quoted above and the full effects of radiation. The agreement between the two is excellent. The statistical agreement between them introduces an uncertainty of 0.2% in the calorimeter energy scale. Additionally, there is a 0.3% uncertainty arising from possible uncertainties in the radiative calculation, so that the final uncertainty on the energy scale is smaller than 0.4%. The second check, which serves to establish the uncertainty on the absolute momentum scale, is the agreement of our measured masses of the K^0_S , J/ψ, and Υ with the accepted values (see Figure 6). We measure, using tracking information only, 0.4977 ± 0.0003 GeV/c^2, 3.096 ± 0.001 GeV/c^2, and 9.469 ± 0.010 GeV/c^2, respectively. The last of these is 1σ (0.1%) above the accepted value of 9.4603 ± 0.0002 GeV/c^2, allowing us to conservatively set an uncertainty on the momentum (mass) scale of 0.2%.

Jet Energy Corrections

The jet energy scale must be understood if one is to identify jets with initial partons and compare jet measurements to QCD predictions. For the jet studies discussed

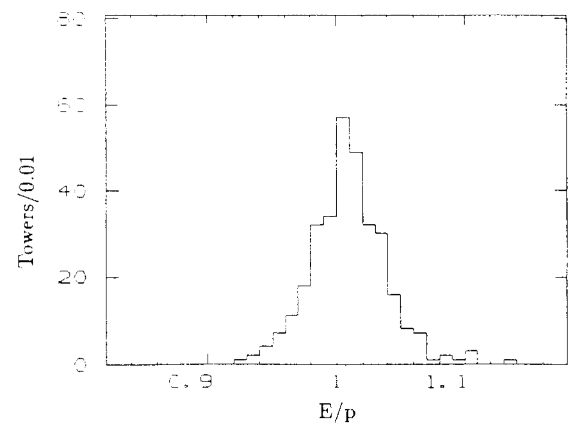

Figure 4: The mean value of E/p for each tower of the CEM for the inclusive electron sample, using the 1987 CEM source calibration. The correction factor for each tower is $1/\langle\frac{E}{p}\rangle$. The mean value of the corrections is 1.016, showing the long term stability of the original source calibration. The *rms* width of the distribution is 0.027 and is related to the residual tower-to-tower calibration uncertainty and the uncertainty on the original source calibration.

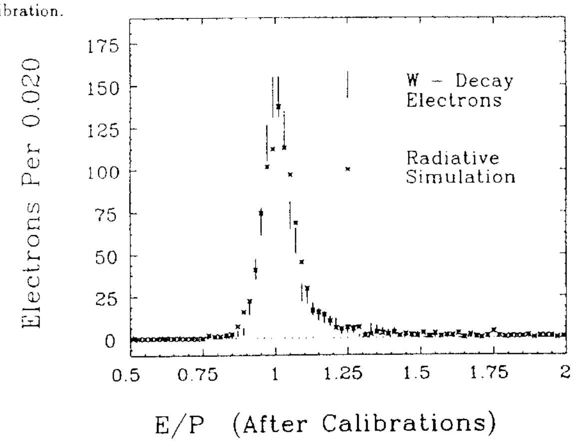

Figure 5: The E/p distribution for a sample of $W \to e\nu$ decays, showing the excellent agreement of the data (vertical bars) and a radiative Monte Carlo (points) including both calorimeter and tracking resolutions. The agreement between the two is used to set a limit on the systematic uncertainty of the electron energy scale determination.

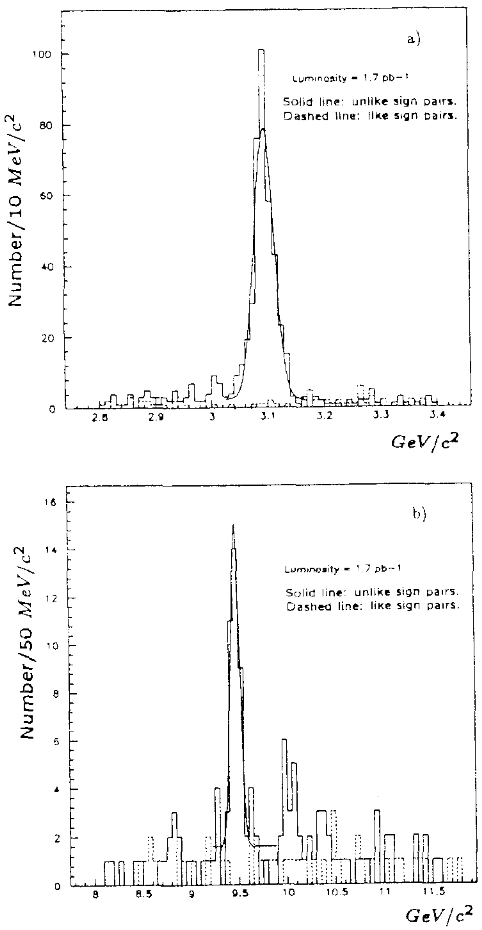

Figure 6: The $\mu\mu$ effective mass distribution a) in the region of the J/ψ, and b) in the region of the Υ. The solid lines are the $\mu^+\mu^-$ spectra, and the dashed lines are the like sign spectra. The agreements of the fitted masses with the known masses of the J/ψ and Υ are used to estimate the uncertainty on the momentum measurement.

below, an energy correction was applied that includes effects due to the non-linear low energy response of the calorimeter, energy from the underlying event, clustering effects, leakage, and energy in uninstrumented regions of the detector or regions of reduced response. The calorimeter response was determined from test beam data for pions with $p_T > 10$ GeV/c, and from isolated low p_T pions in minimum bias events. The non-linearity at low p_T is as large as 30%. The effects of the underlying event were studied by looking at the energy flow far from the jet. Leakage and cracks were studied by using the ISAJET [15] Monte Carlo event generator with a full detector simulation.

The final energy corrections (see Figure 7) vary from 33% to 17% for uncorrected cluster transverse energies between 20 and 400 GeV. The systematic uncertainty on the corrections varies from 12% to 4%. The largest single correction is due to the non-linear low-energy response of the calorimeter; the largest uncertainty on the correction comes from the uncertainty on the fragmentation function of the jets, combined with the calorimeter non-linearity.

4 Top Quark Searches

The Standard Model requires an SU(2) isodoublet partner of the bottom quark, commonly called the top or t quark:

$$\binom{u}{d}\binom{c}{s}\binom{t}{b}.$$

Experiments in e^+e^- annihilation at Tristan [16] and SLC [17] require the top quark to have a mass above 30.4 GeV/c^2 and 37.5 GeV/c^2 respectively. From $\bar{p}p$ collisions at CERN, mass limits of 65 GeV/c^2 [18] and 67 GeV/c^2 [19] have been inferred. Finally, consistency of the Standard Model parameters in low Q^2 (ν scattering) and high Q^2 (W and Z production and decay) processes [20] gives an upper limit[6] of 180 GeV/c^2.

The cross section for production of top quarks in $\bar{p}p$ interactions is shown in Figure 8. At $\sqrt{s}$ = 1.8 TeV, unlike the situation at the CERN $\bar{p}p$ collider, $t\bar{t}$ production is the dominant process for all top masses. The Standard Model decay of the top quark is via the charged current process $t \rightarrow W^+ + b$. The W, which may be virtual or real (depending on the top quark mass), decays into leptons or a $q\bar{q}$ pair. The 4-jet final state, where both W bosons decay to $q\bar{q}$ pairs, accounts for approximately 44% of events. The electron and muon one-lepton final states (one W decaying into e or μ) account for 30%. Finally, di-lepton (e or μ) final states account for 4% of events.

The backgrounds in the various channels are very different. The large QCD multi-jet cross section makes the use of the 4-jet final state a formidable task except

[6]This upper limit was calculated for a Higgs mass of 100 GeV/c^2; for larger Higgs masses the top mass limit becomes somewhat less restrictive.

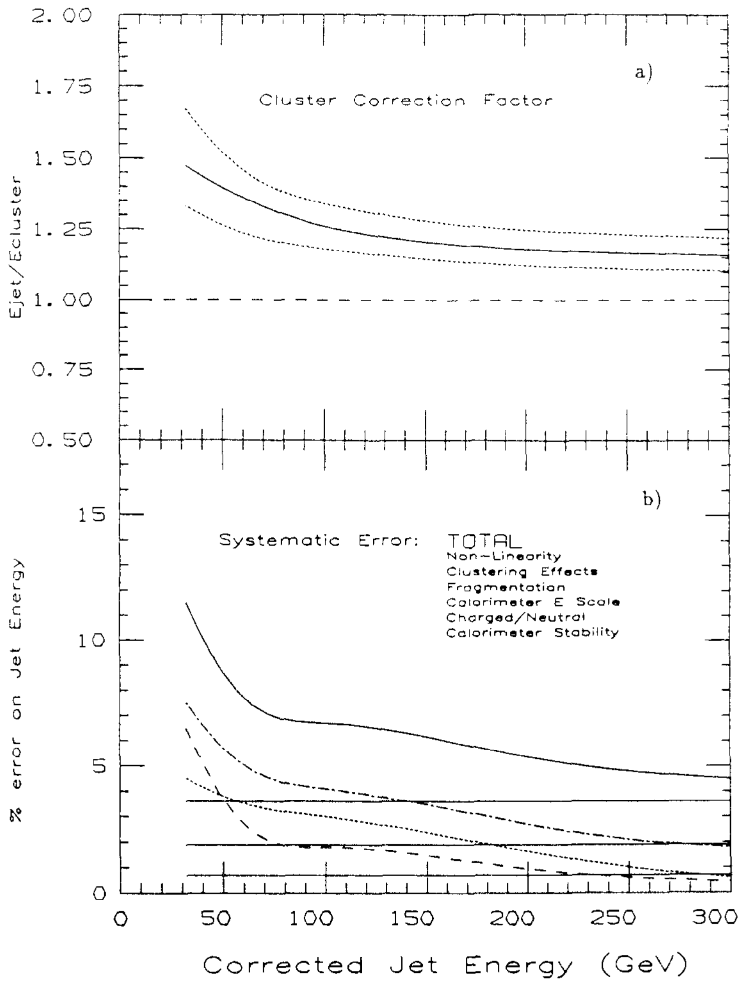

Figure 7: a) The overall cluster correction factor due to the effects discussed in the text, as a function of jet energy. b) The systematic uncertainty due to these corrections. The effects as listed correspond to the curves shown from top to bottom at the left edge of the plot.

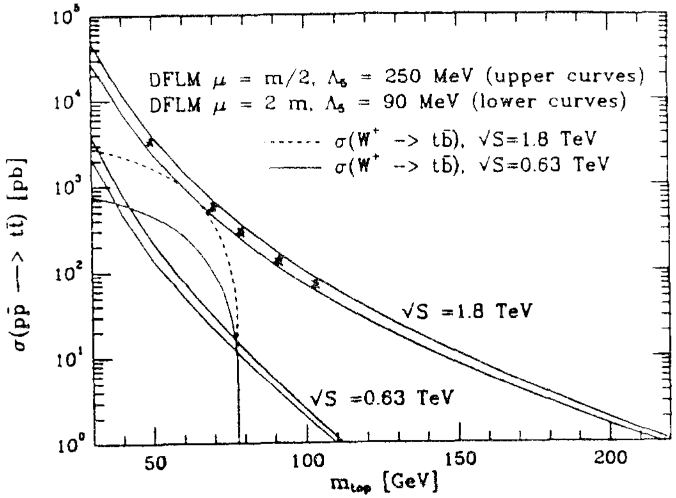

Figure 8: The predicted $t\bar{t}$ and $W \rightarrow tb$ production cross sections in $\bar{p}p$ collisions, as a function of top quark mass, based on calculations in references [23, 24]. The asterisks indicate the ISAJET 6.21 cross sections for $\sqrt{s} = 1.8$ TeV.

for very heavy top mass, and forces one to consider only final states containing at least one lepton. The single lepton final states will be dominated by electroweak production of W+2 jets and QCD production of $b\bar{b}$ pairs. The di-lepton final states have Drell-Yan and resonance backgrounds for the $e-e$ and $\mu-\mu$ channels which are present in the $e-\mu$ channel only through Drell-Yan and resonant production of $\tau^+\tau^-$. Here we will concentrate on the $e-\mu$ and $e+2$ jets final states.

Top Search in the $e+\mu$ Final State

Both the inclusive electron and inclusive muon triggers described above are sensitive to $e\mu$ events. There is also a special $e\mu$ trigger requiring both an electron candidate with $E_T > 5$ GeV and a μ candidate with $p_T > 5$ GeV/c. However, in this search for a heavy top, we use only the inclusive electron trigger.

The offline selection requires an electron of transverse energy $E_T > 15$ GeV using the standard cuts discussed above, together with a muon candidate. Photon conversions are removed by requiring a minimum number of VTPC space points, as discussed above, and by vetoing on electrons with an oppositely charged CTC track nearby forming a low mass e^+e^- pair. The algorithm is measured to be 88% efficient for photon conversions, and rejects approximately 7% of non-conversion electrons. The electron reconstruction efficiency of 77% quoted above is slightly reduced for a top quark search due to possible overlap between the electron and jets in the event. This has been studied using the Monte Carlo and reduces the electron selection efficiency to approximately 70%. The muon candidate is required to have $|\eta| < 1.2$ and to be minimum ionizing in the calorimeters (*i.e.* with greater than 0.1 GeV in the calorimeter but less than 2 GeV in the EM and 6 GeV in the hadronic compartments, respectively[7]) and must satisfy one of the following two criteria:

- Either have $p_T > 5$ GeV/c and a distance in ϕ of less than 30 mrad to a muon chamber track segment, *or*
- have $p_T > 10$ GeV/c, and be isolated in the calorimeter, having less than 5 GeV of transverse energy in a cone of $R = 0.4$ around the muon[8].

Fiducial cuts are also applied to avoid the regions of reduced calorimeter response around wedge boundaries. The second of the two criteria above is designed to increase the pseudo-rapidity acceptance for the muons from $|\eta| < 0.65$ (the coverage of the central muon system) to $|\eta| < 1.2$. For $|\eta| < 1.2$, the acceptance of the fiducial cuts is 84%. Within the fiducial cuts and for muons of $p_T > 20$ GeV/c, the efficiencies of the muon selection criteria have been measured using samples of $Z^0 \rightarrow \mu^+\mu^-$ and found to be $98 \pm 2\%$ ($96 \pm 2\%$) for muons with (without) a muon chamber track segment. As in the case of electrons, efficiencies for a top quark search are slightly smaller because of the possible overlap of the muon with a jet. Using the Monte Carlo, we estimate the top search muon selection efficiency to be approximately 85%.

[7]The typical transverse energy deposited by a minimum ionizing particle is 0.5 GeV in the EM calorimeter and 2 GeV in the hadron calorimeter.

[8]The cone radius R is defined as $R = \sqrt{(\Delta\phi)^2 + (\Delta\eta)^2}$. The tower traversed by the muon is excluded from the sum.

For these selection criteria, 45 opposite-charge $e\mu$ events are found in the data sample. Figure 9 shows the scatter plot of $E_T(e)$ *vs.* $p_T(\mu)$ for the data, as well as for ISAJET Monte Carlo samples of $b\bar{b}$ and $t\bar{t}$ production[9]. The decays of an intermediate mass top quark generate leptons with large transverse energies, whereas the leptons from $b\bar{b}$ production are concentrated at lower transverse energies. In a top quark signal region defined as

$$E_T(e) > 15 \text{ GeV}, \ p_T(\mu) > 15 \text{ GeV}/c,$$

we find a single event. In this region, background from $b\bar{b}$ production is negligible, and we expect approximately one event from $Z^0 \rightarrow \tau^+\tau^-$. However, the lepton momenta from $Z^0 \rightarrow \tau^+\tau^-$ events are generally low (below 20 GeV/c), and the probability for an event from this process to have transverse energies exceeding those of the candidate event is small. We also expect of order 0.2 events in the signal region from WW and WZ production.

In Figure 10 we show scatter plots of the minimum lepton transverse energy *vs.* $\Delta\phi$, the azimuthal angle between the leptons. The leptons from $b\bar{b}$ production are primarily back-to-back in azimuth, with some events close to $\Delta\phi = 0$ resulting from the gluon splitting diagrams. A small number of events are present between the forward and backward peaks, and come primarily from flavour excitation diagrams. Again, the decays of a heavy top quark produce leptons of higher transverse energy, less well correlated in $\Delta\phi$. Finally, in Figure 11 we show the electron isolation I, defined to be the ratio of the energy in a cone of $R = 0.7$ centered about the electron (excluding the electron E_T) to the electron transverse energy:

$$I = \frac{E_T^{\text{cone}} - E_T^{\text{electron}}}{E_T^{\text{electron}}}.$$

Well isolated electrons will have an isolation value close to 0. The heavy quark decays generate well isolated electrons, whereas the electrons from b quark decays are generally not well isolated. The shape of the data is consistent with that of the $b\bar{b}$ Monte Carlo sample.

Assuming that the single event in our signal region is from top decay, we may calculate an upper limit on the $t\bar{t}$ cross section. The efficiencies of the selection are shown in Figure 12 as a function of top quark mass. The selection criteria have a systematic uncertainty of 3% (electron) and 3% (muon) for top quarks in the mass range from 30 to 90 GeV/c^2. The uncertainty in the efficiency of the lepton E_T cuts arising from changes to the lepton transverse energy spectrum from t quark decays was estimated by varying the Peterson parameter [21] in the fragmentation

[9]The $b\bar{b}$ production takes into account all three processes thought to be important, *i.e.* direct production, gluon splitting, and flavour excitation.

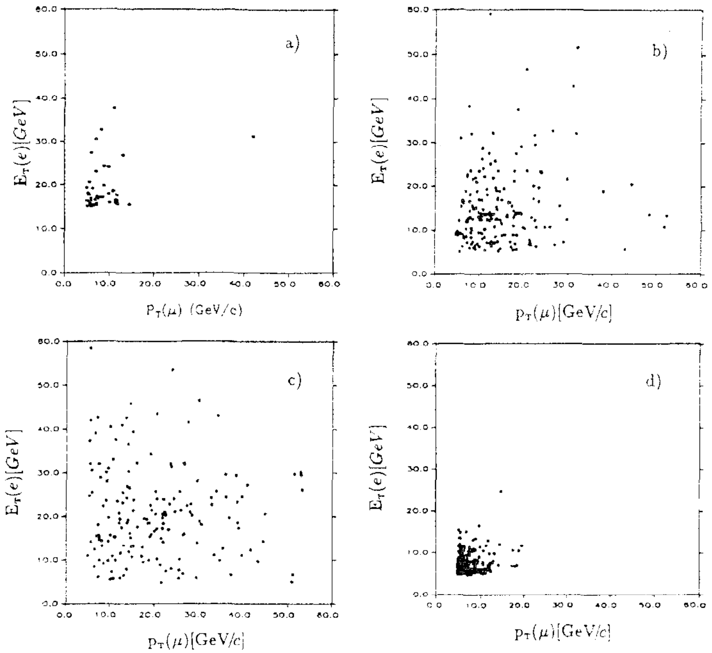

Figure 9: Scatter plots of electron transverse energy E_T *vs.* muon transverse momentum p_T. a) For the $e\mu$ sample described in the text; b) for a Monte Carlo $t\bar{t}$ sample with $m_{top} = 40$ GeV/c^2 (4.1 pb^{-1}); c) for a Monte Carlo $t\bar{t}$ sample with $m_{top} = 60$ GeV/c^2 (59 pb^{-1}); d) for a Monte Carlo $b\bar{b}$ sample (0.6 pb^{-1}). The Monte Carlo samples have not had the 15 GeV electron E_T cut applied, and represent very different integrated luminosities than the data; we present them here only for a qualitative comparison.

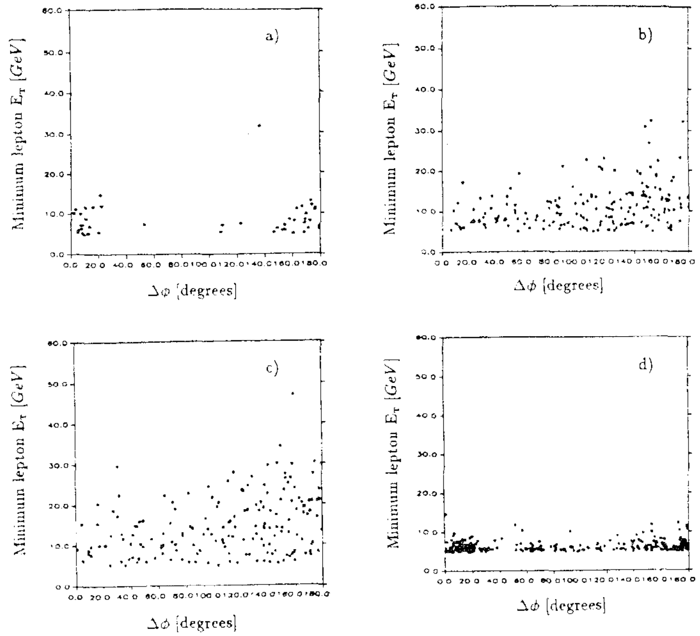

Figure 10: Scatter plots of the minimum lepton transverse energy *vs.* the azimuthal angle difference $\Delta\phi$. The samples in a) through d) are the same as in Figure 9.

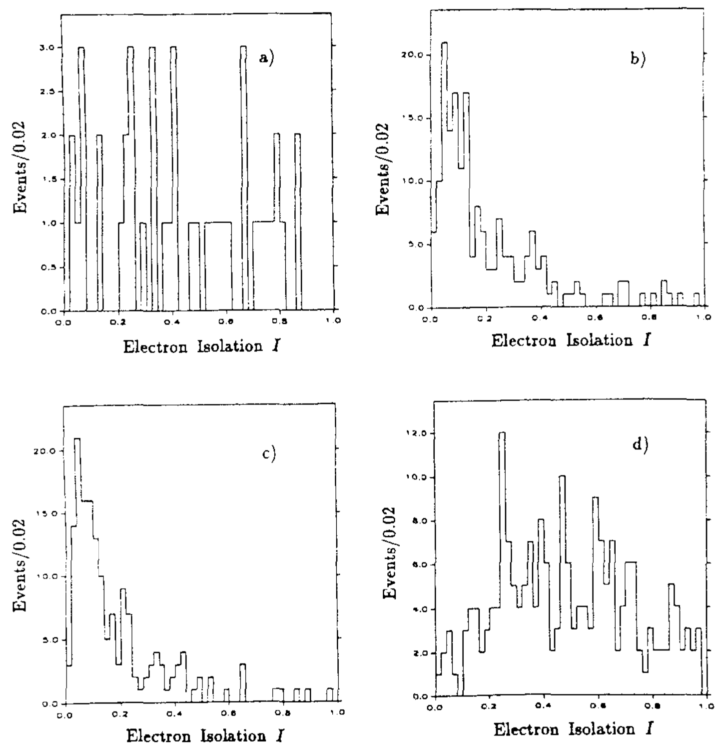

Figure 11: The electron isolation variable I as defined in the text, for the four samples a) through d) of Figures 9 and 10.

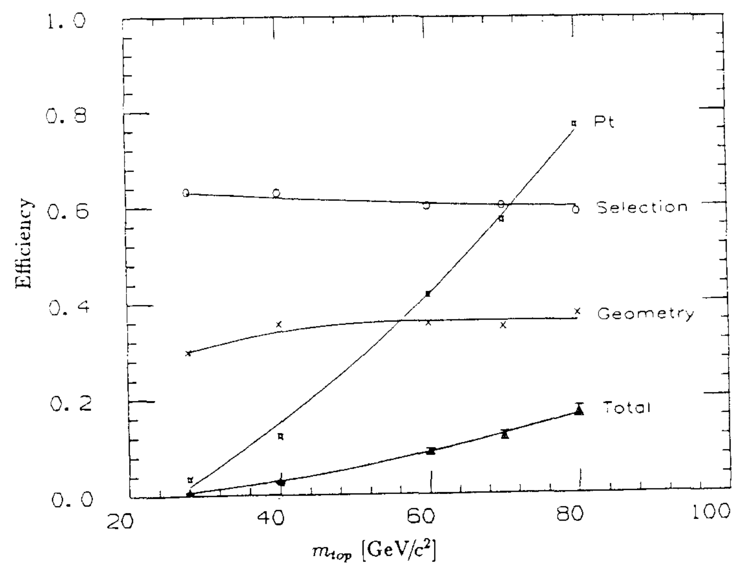

Figure 12: The efficiencies of the $e\mu$ selection criteria as a function of top quark mass. The points labelled 'Selection' refer to the electron and muon selection criteria, excluding fiducial cuts and E_T and p_T cuts. 'Geometry' refers to the effect of fiducial cuts (η and ϕ), whose efficiency decreases at lower top masses because the $t\bar{t}$ system is produced less centrally. The points labelled 'p_T' reflect the effects of the cuts on the electron energy and the muon momentum. 'Total' is the product of the three efficiencies. The curves are shown to guide the eye.

function, and varies from 30% for m_{top} = 30 GeV/c^2 to 10% for m_{top} = 70 GeV/c^2. The acceptance uncertainty was obtained by comparing ISAJET and PAPAGENO [22] Monte Carlo calculations, and varies from 30% for m_{top} = 30 GeV/c^2 to 4% for m_{top} = 70 GeV/c^2. The uncertainty in the integrated luminosity of the data sample is 15%, arising primarily from the extrapolation of the $\bar{p}p$ cross section to $\sqrt{s} = 1.8$ TeV from lower energies. The systematic uncertainties, assumed to be Gaussian, were convoluted with a Poisson probability distribution for the one observed event to calculate an upper limit on the number of events in the signal region. Using the Monte Carlo calculations of $t\bar{t}$ detection efficiency (as a function of m_{top}), the semi-leptonic branching ratio, and the integrated luminosity, we calculate the upper limits on the $t\bar{t}$ production cross section shown in Figure 13. The 95% confidence level upper limit intersects the lower bound of the theoretical predictions [23, 24] at m_{top} = 72 GeV/c^2. For top quark masses less than 30 GeV/c^2, the $t\bar{t}$ production cross section is very large but the efficiency of our cuts is very small, primarily due to the requirements on the electron E_T and the muon p_T, and we conservatively choose to use 30 GeV/c^2 as our lower bound on m_{top}.

Top Search in the e+jets Final State

In spite of a larger rate than the $e\mu$ final state, the search for top in the e+multi jets final state is complicated by considerable backgrounds from QCD $b\bar{b}$ production for low electron E_T and from W+jets for higher electron E_T. In particular for top masses above the W mass, the top quark decays to a real W and the $e\nu$ transverse mass[10] can no longer be used to discriminate between the two processes. As well, in this mass range the two b jets are very soft and not easy to detect.

The event selection required an electron candidate with $E_T > 15$ GeV, and at least two jets in the region $|\eta| < 2$ with $E_T > 10$ GeV. The electron was selected using the standard electron criteria, with photon conversions removed as described above. If the effective mass of the electron and any other electromagnetic cluster in the event is above 70 GeV/c^2, the pair is considered to result from the decay $Z^0 \rightarrow e^+e^-$ and the event is rejected. Finally, an explicit electron isolation requirement was applied to reduce the background from $b\bar{b}$ production: the total E_T in the calorimeter towers immediately adjacent to the electron was required to be less than 2 GeV. Studies using electrons from $W^\pm$decays and Monte Carlo samples of $b\bar{b}$ and $t\bar{t}$ events show that this is very efficient for heavy top while rejecting most of the $b\bar{b}$ events.

Figure 14 shows the scatter plot of $E_T(e)$ *vs.* missing tranverse energy $\not{E}_T$ for the 512 events in the resulting sample. There is an accumulation of events at small E_T and small $\not{E}_T$ due to residual $b\bar{b}$ events; the region at large E_T and large $\not{E}_T$ is populated by $W + 2$ jet events. The intermediate region is where one would expect

[10] The transverse mass is defined as:

$$m_T = \sqrt{2E_T\not{E}_T(1 - \cos\Delta\phi)} \;,$$

where $\Delta\phi$ is the azimuthal angle between the electron and the missing transverse energy vector $\not{E}_T$.

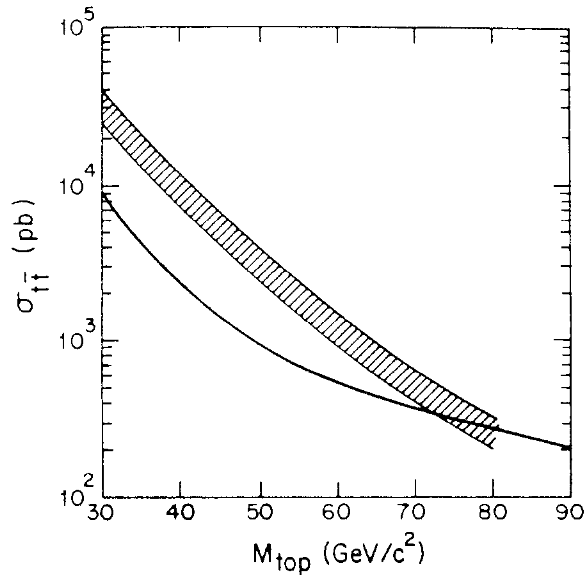

Figure 13: The 95% confidence level upper limits on the $t\bar{t}$ production cross section from the $e\mu$ channel (solid line). The shaded band is the predicted cross section from references [23] and [24].

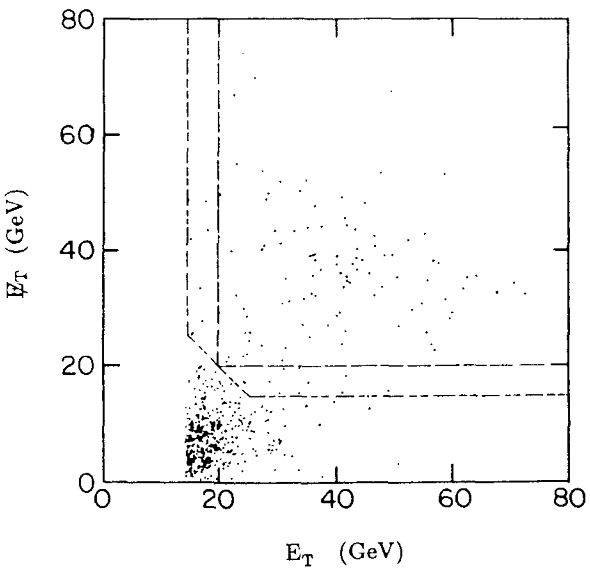

Figure 14: The distribution of electron E_T *vs.* missing tranverse energy $\not{E}_T$, for the $e+2$jet sample of 512 events. The lines show the two different top quark search regions as described in the text.

to see $t\bar{t}$ events. One of the more sensitive variables to the presence of $t\bar{t}$ events in our sample is the transverse mass m_T. The distribution of m_T is shown in Figure 15a for the data sample, a PAPAGENO Monte Carlo simulation of $W+2$ jet events, and an ISAJET Monte Carlo simulation of $t\bar{t}$ events, with $m_{top} = 70$ GeV/c^2. For these distributions, cuts on the electron transverse energy $E_T > 20$ GeV and on the missing transverse energy $\not{E}_T > 20$ GeV (shown as a dashed line in Figure 14) have been applied to remove the $b\bar{b}$ background[11], leaving a sample of 104 events. The W simulation shows a Jacobian peak near a mass of 80 GeV/c^2, while most of the events in the $t\bar{t}$ simulation have lower transverse masses. The data is very well explained by the W simulation alone, and shows no excess corresponding to top quark production and decay.

In order to unravel quantitatively the uncertainty in our transverse mass calculation, the possible signal from a top quark, and possible inadequacies in the $W+$ jets simulation, we turn to a sample of events containing an electron and a single jet, where we expect any top contribution to be negligible. The transverse mass distribution, again with the cuts $E_T > 20$ GeV, $\not{E}_T > 20$ GeV, is shown in Figure 15b together with the Monte Carlo distribution for $W+1$ jet events. The excellent agreement in shape of the Monte Carlo and data indicates that we understand the missing transverse energy measurement in events with electrons and jets, and that the Monte Carlo adequately models the $W+$ jets process; the normalization agrees with that predicted by PAPAGENO to within the theoretical uncertainties of the $W+$jets cross section calculation, typically $\pm 50\%$ [25].

The very different shapes of the $W+2$jet and $t\bar{t}$ transverse mass distributions, for $m_{top} < m_W + m_b$, allow us to place an upper limit on the number of $t\bar{t}$ events in our sample by fitting the observed transverse mass distribution (Figure 15a) to a linear combination of the expected spectra from the two processes $W+2$jets and $t\bar{t}$ production:

$$\frac{dN}{dm_T} = \alpha\left(\frac{dN}{dm_T}\right)_{t\bar{t}} + \beta\left(\frac{dN}{dm_T}\right)_{W+2\text{jets}} .$$

The mass interval 24 GeV/$c^2 < m_{top} <$ 120 GeV/c^2 is fit using a maximum likelihood technique. For top quark masses $m_{top} > 65$ GeV/c^2, the cuts

$$E_T > 20 \text{ GeV}, \quad \not{E}_T > 20 \text{ GeV}$$

are applied. For lower masses, we use instead the cuts

$$E_T > 15 \text{ GeV}, \ \not{E}_T > 15 \text{ GeV}, \ E_T + \not{E}_T > 40 \text{ GeV},$$

indicated in Figure 14 by the dot-dashed line. These cuts are more efficient for lower top quark masses, at the price of a slightly larger background[12]. We do not fit the transverse mass distribution below 24 GeV/c^2 because our cuts on E_T and

[11] For heavy top ($m_{top} \gtrsim 50$ GeV/c^2) these cuts provide good efficiency and leave b quark and non-electron backgrounds estimated to be approximately 12%.

[12] The b quark and non-electron background in this sample of 123 events is estimated to be approximately 20%.

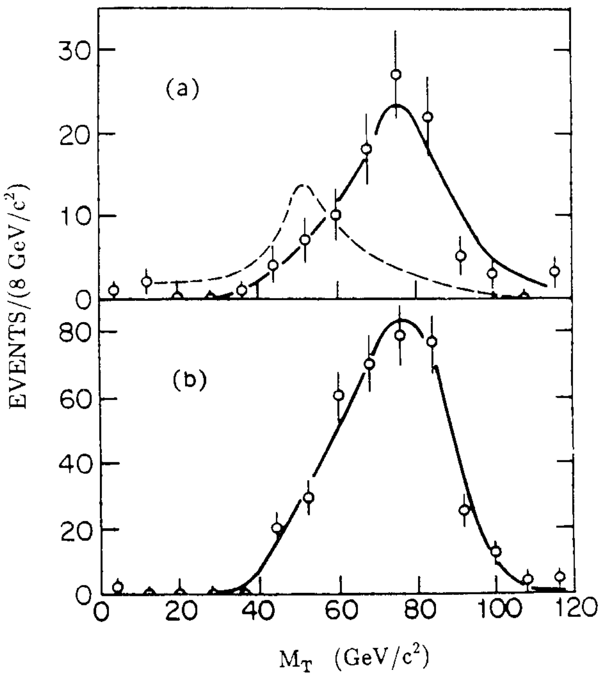

Figure 15: a) The transverse mass m_T distribution for the e + 2jet data sample (open points) with Monte Carlo $W+2$jet (solid line) and tt (dashed line) predictions. A top quark mass of 70 GeV/c^2 was used for the $t\bar{t}$ curve. b) The transverse mass distribution for the e + 1jet data (points) with a W + 1jet Monte Carlo prediction (solid line), normalized to equal area.

m_{top} (GeV/c^2)	$\alpha(\pm stat \pm sys)$	$n_{t\bar{t}}$ predicted	$\sigma_{t\bar{t}}$ (pb)
40	$0.07 \pm 0.05 \pm 0.02$	130 ± 44	< 2410
50	$0.06 \pm 0.05 \pm 0.03$	123 ± 31	< 648
60	$0.11 \pm 0.08 \pm 0.04$	101 ± 22	< 408
70	$0.00^{+0.12}_{-0.00} \pm 0.11$	43 ± 8	< 266
80	$0.00^{+0.27}_{-0.00} \pm 0.17$	32 ± 5	< 281

Table 1: The fitted $t\bar{t}$ contribution to the $e+2$jet sample, with the predicted number of $t\bar{t}$ events and the 95% upper limit on the $t\bar{t}$ cross section, as a function of top quark mass. See text for details on the quoted uncertainties.

$\not{E}_T$ leave few top events in this region. It is worth pointing out that any residual b quark, conversion, or non-electron backgrounds will tend to have low transverse mass. Because the $t\bar{t}$ transverse mass distribution peaks below the $W+$jets distribution, these backgrounds will tend to increase the fitted $t\bar{t}$ component and thus α will be an overestimate of the $t\bar{t}$ fraction in the data.

The fit results are shown in Table 1, expressed such that the observation of the number of events predicted by the standard model would result in both α and β equal to 1. The fitted top quark contribution is much smaller than the standard model prediction for all top quark masses less than 80 GeV/c^2. The systematic uncertainty on α shown in Table 1 arises from a number of sources. The jet energy scale was studied using direct γ events which are believed to be dominated by a γ recoiling against a single parton, with transverse energy balance between the γ and the parton-initiated jet. The low E_T electron sample, dominated by $b\bar{b}$ production, was also extensively compared to the Monte Carlo predictions to check the low energy jet reconstruction in these events. The uncertainty on the jet energy scale was estimated to be $\pm 20\%$, leading to an uncertainty on α of ± 0.13 for $m_{top} = 80$ GeV/c^2. The uncertainty in α due to differences in the underlying event between the data and the Monte Carlo leads to an uncertainty on α of ± 0.05 for $m_{top} = 80$ GeV/c^2. The exact choice of the transverse mass interval used in the fit leads to an uncertainty on α of ± 0.10 for $m_{top} = 80$ GeV/c^2. These uncertainties are added in quadrature and shown in Table 1.

There is a second class of uncertainties which do not affect the shape of the transverse mass distribution but nonetheless affect the calculation of an upper limit for $t\bar{t}$ production, due to the uncertainty they introduce on the acceptance. These include the acceptance calculation using the Monte Carlo, and uncertainties in the integrated luminosity of the data, top quark fragmentation, electron detection efficiency, and initial state gluon radiation. Acceptance, top quark fragmentation, and luminosity were treated as in the $e\mu$ case. The uncertainty in the electron detection efficiency is 5%. Initial state gluon radiation is a factor in this analysis due to the requirement that there be two observed jets; some of these may come from initial state radiation, and inadequacies in the modelling of this radiation may affect the acceptance. We take this into account in the systematic error by halving the contribution predicted by ISAJET. The resulting uncertainty in the acceptance is $\pm 4.5\%$

for $m_{top} = 80$ GeV/c^2. All of these systematic uncertainties are taken together in quadrature to calculate the predicted number of $t\bar{t}$ events we should observe as a function of t quark mass, shown in Table 1.

The systematic uncertainties are assumed to be Gaussian, and are convoluted with the likelihood function for α from the fit to obtain the upper limits on the cross section shown in Table 1 and Figure 16. We exclude top quark masses below 77 GeV/c^2 at the 95% confidence level. Again, at low top quark masses the systematic uncertainty on the detection efficiency increases rapidly, and we choose to conservatively quote 40 GeV/c^2 as our lower limit.

b quark Lepton Production

We have claimed repeatedly that $b\bar{b}$ production is responsible for the cluster of low energy ($E_T < 20$ GeV) electrons visible in the lower left hand corner of Figure 14. Indeed, we have studied many electron and jet variables and have found good agreement between an ISAJET $b\bar{b}$ Monte Carlo sample and the data. In an attempt to quantify these statements, we present here two distributions showing this agreement.

In Figure 17 we show the transverse energy in the calorimeter towers adjacent to the electron, for electrons satisfying the criteria applied above in the e+jets search (except for the explicit electron isolation requirement), and with $E_T < 20$ GeV or $\not{E}_T < 20$ GeV. The prediction of the $b\bar{b}$ Monte Carlo is shown, normalized to the data. The agreement in shape is excellent and the normalization is within the theoretical uncertainty on the QCD $b\bar{b}$ cross section[26, 27, 28] at our energies which arises primarily because of uncertainties in the low-x behaviour of the proton structure functions. Finally, if these electrons result from the semi-leptonic decay of B mesons formed from the $b\bar{b}$ quarks, the accompanying charm quark should be observable through its fragmentation into D mesons:

$$B\bar{B} + X$$
$$\quad \hookrightarrow D^0 e^- \bar{\nu}$$
$$\qquad \hookrightarrow K^- \pi^+$$

The charge of the electron 'tags' the expected decay; *i.e.* if we observe electrons, we expect to observe $D^0 \rightarrow K^-\pi^+$ but not $\bar{D}^0 \rightarrow K^+\pi^-$. Because there is no K/π identification in the CDF detector, we have looked at $K^\pm\pi^\mp$ mass combinations for all oppositely charged track pairs found in a cone of $R = 1.0$ around the electron. The mass spectra are shown (for a subsample of the data) in Figure 18, divided into 'right sign pairs' where the kaon charge is the same as the electron charge, and 'wrong sign pairs' where the kaon sign is opposite to the electron charge. On a smooth combinatorial background, we observe a signal at the D^0 mass of 63 ± 17

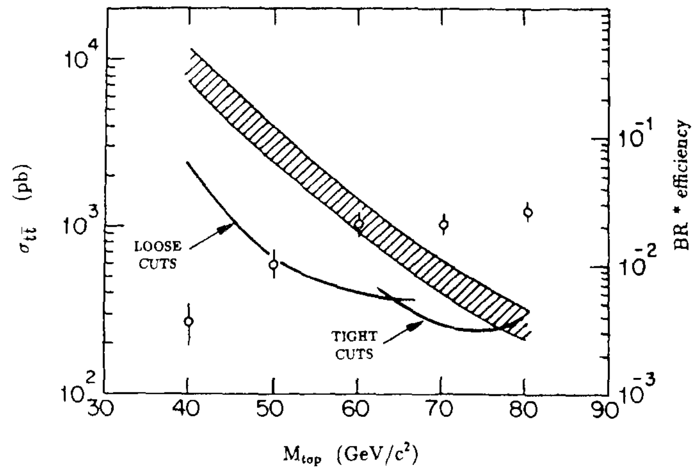

Figure 16: The 95% confidence level upper limits on the $t\bar{t}$ production cross section (solid lines). The curve labelled 'loose cuts' ('tight cuts') refers to the dot-dashed (dashed) line of Figure 14, as explained in the text. The shaded band is the predicted cross section from references [23] and [24], and the open points show the $t\bar{t}$ acceptance (right hand scale) as a function of top quark mass.

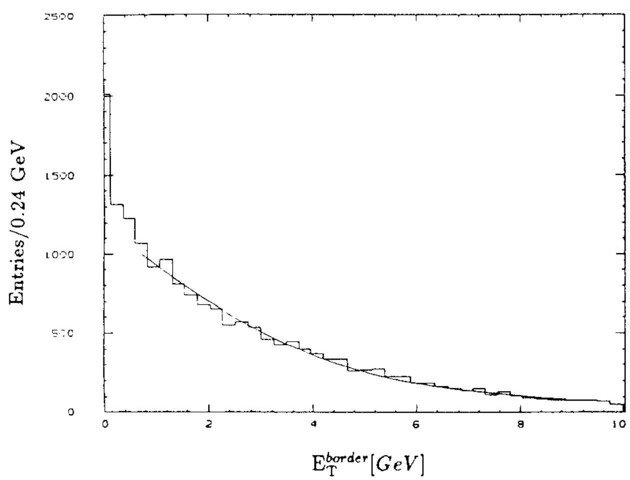

Figure 17: The total transverse energy in the towers adjacent to the electron, for an inclusive electron sample satisfying the cuts explained in the text. The histogram shows the data; the curve shows an ISAJET $b\bar{b}$ prediction normalized to the data above 1 GeV (below 1 GeV we expect a contribution from residual W events in the sample). The agreement in shape is excellent.

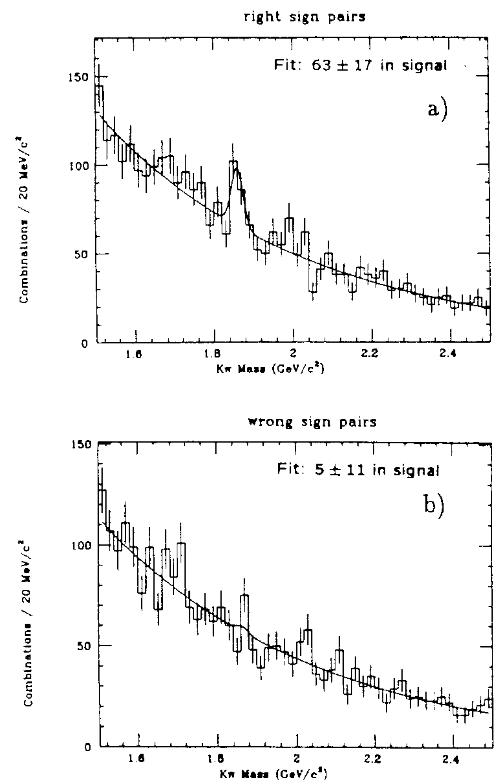

Figure 18: $K\pi$ effective mass distributions from a subsample of the inclusive electron sample: a) 'right sign' combinations *i.e.* $K^{\pm}\pi^{\mp}$ for an observed $e^{\pm}$; b) 'wrong sign' combinations. In both distributions, all pairs of oppositely charged tracks within R=1.0 of the electron were used because of the lack of K/π identification.

combinations in the right sign sample, and no excess in the wrong sign sample. Based on the CLEO measurements [29] of the ratio of B meson branching fractions:

$$\frac{\mathrm{B}(\bar{B}\to\ell^- D^0 X)}{\mathrm{B}(\bar{B}\to\ell^- X)} = 0.68 \pm 0.15$$

and the world average branching ratio $D^0 \to K^-\pi^+$ [30] of $3.8 \pm 0.4\%$, and assuming that B_s production and baryon production account for approximately 15% and 8% of $b\bar{b}$ quark production respectively, we expect to observe 87 ± 19 $D^0 \to K^-\pi^+$ and charge conjugate decays. The good agreement with our observed signal and the correlation of the signal with the electron charge support the hypothesis that the sample is composed primarily of $b\bar{b}$ events.

Top Search Conclusions

In conclusion, we have shown that both the $e\mu$ and e+jets samples in our data are consistent with known sources of leptons - QCD $b\bar{b}$ production and the production of W+jets. There is no evidence for the production of $t\bar{t}$ events. The resulting 95% confidence level limits on the top quark mass are:

$$30\ \mathrm{GeV/c^2}\ < m_{top} < 72\ \mathrm{GeV/c^2}\ (e\mu),\quad \text{and}$$

$$40\ \mathrm{GeV/c^2}\ < m_{top} < 77\ \mathrm{GeV/c^2}\ (e + \text{jets}).$$

These two analyses are in the course of publication[31, 32].

Work is also underway to combine the two results in order to exclude higher values of m_{top}, as well as to investigate the channels μ+jets, ee, and $\mu\mu$.

5 Jet Physics Results

Because of the very large Q^2 values attained - CDF has observed jets with transverse energies in excess of 400 GeV - jet physics at the Fermilab Tevatron provides a new and sensitive testing ground for QCD. Much of the observable cross section at these energies can be described well by a leading order perturbative calculation, and scale breaking effects associated with soft gluon radiation can be seen in the jet fragmentation function and in the comparison of our data to that taken at lower values of $\sqrt{s}$.

Here, we shall limit our discussion to three topics, in an effort to demonstate the breadth of QCD physics attainable at CDF. We present measurements of the inclusive jet cross section $d\sigma/d\mathrm{E_T}$, the double differential cross section $d^2\sigma/d\mathrm{E_T}d\eta$, and the jet fragmentation function $D(z)$.

All analyses presented here use the standard CDF jet clustering algorithm. This algorithm uses fixed-size cone clustering which sums all the energy inside a cone of radius $\mathrm{R} = \sqrt{(\Delta\phi)^2 + (\Delta\eta)^2} = 0.7$ centered on a seed tower with $\mathrm{E_T} > 1$ GeV. The cluster energy is the sum of the energies in the EM and hadron calorimeters.

The Inclusive Jet Cross Section

The inclusive jet cross section $d\sigma/d\mathrm{E_T}$ is dominated by the QCD $2\to2$ graphs but is sensitive to higher order QCD processes. As well, possible quark substructure or new 4-fermion (contact) interactions result in enhancements to the $\bar{p}p$ scattering cross section which flatten the inclusive jet cross section for large transverse energy jets.

The data sample used here is the full 4.4 pb^{-1} of the 1988 data. The event selection requires a level-2 cluster trigger. There is some smearing of the level-2 trigger thresholds due to differences between the online and offline algorithms and to the online transverse energy calculation which considers the event vertex to be at the center of the detector. Offline, the true event vertex (as determined by the VTPC) is used to correct the transverse energies, and required to be within 60 cm of the center of the detector. The three online triggers with thresholds of 20, 40, and 60 GeV are found to be fully efficient offline (with efficiency greater than 99.7%) for cluster thresholds of 28, 55, and 80 GeV respectively, and these transverse energy thresholds are applied. The clusters are energy corrected as explained in Section 3 in order to relate cluster energy to parton energy. Clusters are also required to be away from the region of low response near $\eta = 0$, and to be well contained in the central calorimeter: $0.1 < |\eta_{jet}| < 0.7$.

Two sources of background are present in the jet sample: cosmic rays which shower in the calorimeter, and particles from the main ring, which is situated above the detector and is used during $\bar{p}p$ data-taking for $\bar{p}$ production. Both backgrounds have flatter $\mathrm{E_T}$ spectra than the distribution expected from parton-parton collisions, and thus affect the high $\mathrm{E_T}$ part of the distribution sensitive to deviations from QCD. The timing information from the central hadron calorimeter is used to reject events with significant energy out-of-time with the beam crossing; however, no timing information is available from the central EM calorimeter, so additional cuts are applied to clusters with $\mathrm{E_T} > 80$ GeV. The electromagnetic fraction of the jet $\mathrm{E_{em}/E_{total}}$ is required to satisfy $0.1 < \mathrm{E_{em}/E_{total}} < 0.95$. The missing transverse energy significance, defined as $\not{E}_T/\sqrt{\mathrm{E_T}}$, is required to be less than 4.8; from a study of $\not{E}_T$ in minimum bias events, this is estimated to be equivalent to a very loose 6σ cut. These cuts reject 99% of the background and retain at least 97% of the true jet cross section.

The raw jet differential cross section is not the true cross section because of the steeply falling $\mathrm{E_T}$ spectrum. Finite resolution smears the observed jet energy and causes the more numerous jets at lower $\mathrm{E_T}$ to appear at higher $\mathrm{E_T}$, flattening the $\mathrm{E_T}$ spectrum. Thus we must deconvolute the energy resolution and the $\mathrm{E_T}$ spectrum shape. The energy resolution for jets has been measured using the transverse energy balancing technique [33] to be $\sigma(\mathrm{E_{jet}})/\mathrm{E_{jet}} = 110\%/\sqrt{\mathrm{E_{jet}}}$. The deconvolution procedure consists of iteratively generating an E_T spectrum and applying the jet energy resolution, then comparing the resulting smeared spectrum to the observed spectrum; when the two are in agreement, the data is corrected by the ratio of the Monte Carlo generated spectrum to the smeared spectrum. The jet energy smearing deconvolution results in a 70% increase in the jet cross section for low E_T, and a 12% increase at the largest jet energies.

The resulting jet cross section per unit rapidity in the central region is shown in Figure 19. Statistical and E_T-dependent systematic errors are plotted point-to-point. The normalization error includes the E_T-independent systematics expressed as an uncertainty in the cross section of (at most) 25%. In addition, there are systematic uncertainties from the luminosity measurement (15%), smearing corrections (10%), and energy scale uncertainty (50%). The solid line is a QCD 2→2 calculation using the Duke and Owens structure functions (set 2) [34]; the Q^2 value used to evaluate the strong coupling constant α_s and to evolve the structure functions was $Q^2 = E_T{}^2/2$. The dashed line indicates the flattening of the E_T spectrum expected in the presence of a 4-fermion contact term at the mass scale indicated. It is worth noting that the QCD prediction is *absolute*; *i.e.* the QCD curve has *not* been normalized to the data. The QCD prediction describes the data very well over six orders of magnitude. The deviation of the contact term predictions from the data allow us to derive a lower limit on the mass scale of new contact interactions[13]:

$$\Lambda_{\text{contact}} > 950 \text{ GeV}/c^2 \quad (95\%\text{C.L.}) \ .$$

The Double Differential Cross Section

The double differential cross section $d^2\sigma/dE_T d\eta$ is the product of the QCD 2→2 subprocess cross section (point-like scattering term) with the parton structure functions describing the parton momentum distributions in the initial state. The calculable point-like 2→2 cross section is divergent at very large η due to t-channel exchange; however the falling structure function at large x (large parton momentum) overcomes this rise and the physical cross section remains finite. Thus the double differential cross section allows us to investigate the proton structure function at large x.

This analysis was performed on the 28 nb^{-1} sample of data from the 1987 run, which had level-1 E_T trigger thresholds of 20, 30, 40, and 45 GeV. Studies with simulated events show that single jets in the region $|\eta| < 0.6$ satisfy the trigger criteria (with efficiency above 98%) if they have E_T above 45, 55, 65, or 75 GeV respectively. At least one jet above this threshold, in the region $|\eta| < 0.6$, was required; this jet is referred to as the trigger jet. The event vertex was required to be within 60 cm of the center of the detector, and a second jet anywhere in the

[13] Assumed to be unity strength isospin- and colour- singlet interactions between left-handed quarks[35].

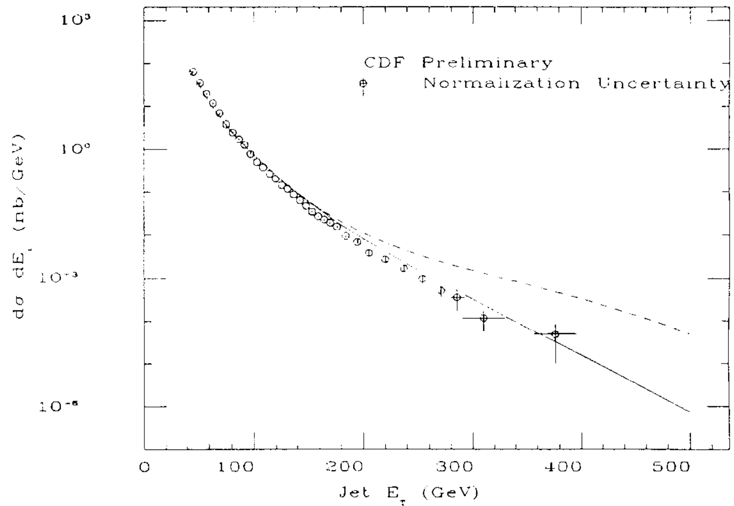

Figure 19: The single jet inclusive cross section per unit rapidity in the central region. The plotted errors include statistical and E_T-dependent systematic errors; the overall normalization uncertainty shown includes the E_T-independent systematic errors. The solid line is a QCD prediction (see text). The dashed line indicates the modification to the cross section expected in the case of a contact interaction at a mass scale of $\Lambda = 700$ GeV/c^2.

detector (the 'probe' jet), with $E_T > 2$ GeV, was required[14]. These criteria yield a sample of 5291 events.

The data are then binned in bins of E_T, the trigger jet transverse energy, and η_2, the probe jet pseudorapidity, and raw cross sections calculated for each bin. As in the previous section, this raw cross section must be corrected for the change of shape resulting from the detector E_T and η resolutions. These resolutions have been studied using the technique of reference [33], in which one assumes that the parton transverse momenta balance. The transverse energy imbalance along the jet axis and along a bisector to that axis (*i.e.* at 90° to the jets) are then related to the E_T and η resolutions together with deviations from 2→2 kinematics caused by higher order QCD processes (primarily gluon *bremsstrahlung*). The true cross section $d^3\sigma/dE_T d\eta_1 d\eta_2$, summed over the interval $|\eta_1| < 0.6$, is then obtained by a deconvolution procedure similiar to that discussed in the previous section: the E_T and η_2 spectra are parametrized, smeared, and compared to the data; the ratio of generated to smeared spectra is then used as a correction to the observed data. The correction ratios vary from 77±5% at low $|\eta_2|$ and high E_T to 21±9% for one of the high $|\eta_2|$ bins; the difference is caused by the steeper E_T spectrum at high $|\eta_2|$, causing more events to fluctuate into our sample from low E_T.

Figure 20 shows the resulting cross section as a function of $|\eta_2|$ for different E_T ranges, as well as leading order QCD calculations using the EHLQ structure functions (set 10) [36] and various choices of the Q^2 scale. Again, the QCD prediction is absolute and has not been normalized to the data. The cross section falloff at large values of $|\eta_2|$ due to structure function decrease at large x is clearly observed and in excellent qualitative agreement with the data.

The Jet Fragmentation Function

The jet fragmentation function $D(z)$ is the distribution of the fraction of the jet energy carried by charged particles:

$$D(z) = \frac{1}{N_{\rm jet}} \frac{dN_{\rm charged}}{dz}$$

where $z = p_{\parallel}/E_{\rm jet}$ is the momentum of the charged particle along the jet axis. The fragmentation function should reflect the effects of QCD scale breaking due to soft gluon emission, and should thus become softer at larger Q^2.

The analysis was performed using a dijet sample selected from the 1987 data. Events were chosen with two central $(0.1 < |\eta| < 0.7)$ jets whose summed transverse energies satisfied the trigger threshold. The jets were required to be back-to-back in azimuthal angle to within 30° $(150° < \Delta\phi < 210°)$ and any other jets in the event were required to have $E_T < 20$ GeV and $E_T < 0.2 \times (E_T^{\rm jet1} + E_T^{\rm jet2})$. For acceptance

[14] If the second jet was also in the central region ($|\eta| < 0.6$) then both jets were counted as trigger and probe jets.

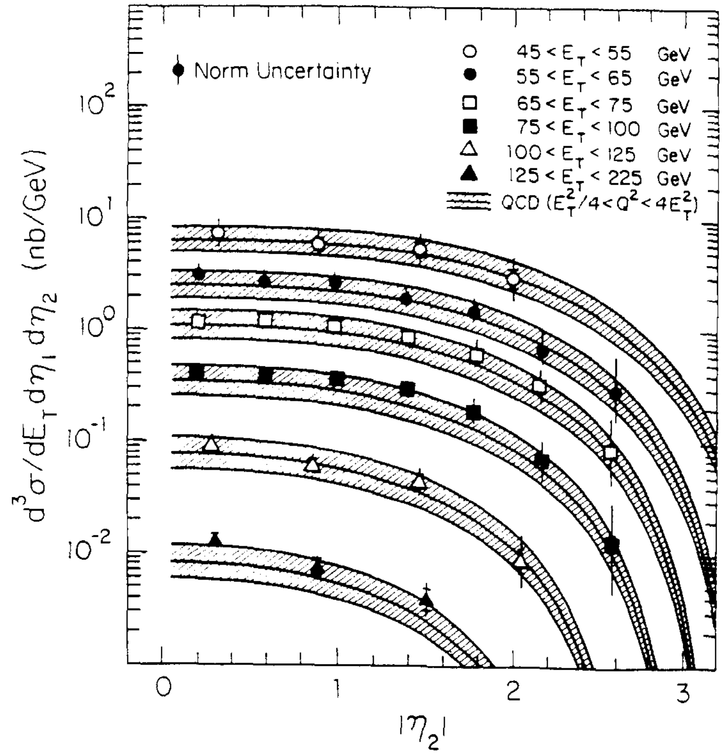

Figure 20: The two jet differential cross section, $d^3\sigma/dE_T d\eta_1 d\eta_2$, summed over the range $|\eta_1| < 0.6$. The inner error bars represent statistical errors; the outer error bars include the statistical errors and the E_T and η_2 dependent parts of the systematic errors. The remaining systematic errors are absorbed into the normalization error which is shown. The shaded bands represent QCD predictions for a range of Q^2 values (see text).

reasons, only events with a small jet-jet longitudinal momentum are used: we require

$$\eta_{\text{boost}} = \frac{1}{2}|\eta_1 + \eta_2| < 0.6 \ .$$

The events are boosted along the beam direction by the quantity η_{boost} as defined above. Tracks in the CTC are then associated with a jet if they have an angle with respect to the jet axis of less than 48° and a momentum along the jet axis of $p_{||} > 0.6$ GeV/c. The reconstruction efficiency (a function of the jet-jet mass m_{j-j} and the fragmentation variable z) was studied using Monte Carlo events and verified by inserting Monte Carlo tracks into real jet events. It was found to be greater than 85% for jet-jet masses below approximately 200 GeV/c^2. Small corrections are applied for tracks outside the pseudorapidity cone or outside of the CTC acceptance. The effect of the underlying event was studied by looking at the charged particle multiplicity at 90° in ϕ from the jets, and a small correction applied for these tracks. Finally, corrections are applied for the energy resolution of the calorimeter and the tracking momentum resolution, using a deconvolution procedure similiar to those described above.

The resulting fragmentation function $D(z)$ is shown in Figure 21 for jet-jet effective masses between 80 and 140 GeV/c^2. The statistical and z-dependent systematic errors have been plotted; there remains an overall normalization uncertainty which is shown. Figure 22 shows the same data plotted as a function of jet-jet mass, for various ranges of z. Also shown are the data from TASSO [37] showing the same trend to lower values of z as the jet-jet mass (or $\sqrt{s}$ in the case of the e^+e^- experiment TASSO) increases. This is due to the QCD scale breaking mentioned above. The fits to the data in Figure 22 are of the form $D(z) = \alpha + \beta \log(m_{j-j})$ expected from the Altarelli-Parisi Q^2 evolution of parton densities [38], and quantitatively explain very well the variation of $D(z)$ with m_{j-j}.

Jet Physics Conclusions

We have shown the single jet inclusive cross section as a function of the jet transverse energy E_T, the double differential cross section as a function of jet pseudorapidity and tranverse energy, and the jet fragmentation function as a function of di-jet mass. All of these distributions are compatible with QCD predictions which include scale breaking soft gluon emission. Using the single jet inclusive cross section to probe very small distances, we have excluded new contact interactions at energy scales below 950 GeV/c^{2}at the 95% confidence level.

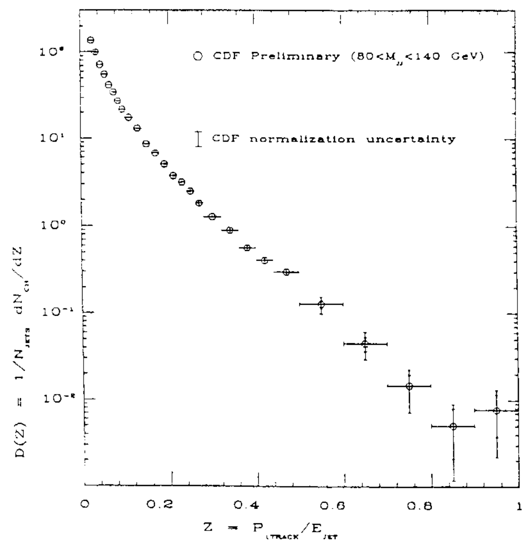

Figure 21: The jet fragmentation function $D(z)$, for the range of dijet effective masses shown. Statistical and E_T-dependent systematic errors are plotted as error bars; E_T-independent systematic errors are included with the overall normalization uncertainty shown.

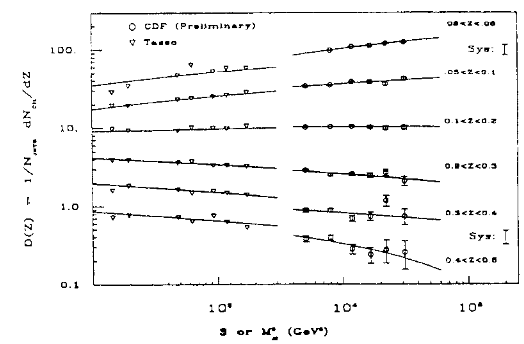

Figure 22: The evolution of the jet fragmentation function $D(z)$ with the dijet effective mass. Data from CDF and the e^+e^- experiment TASSO are shown, together with fits to the form suggested by the Altarelli-Parisi parton density evolution with Q^2 (see text).

6 W and Z Mass Measurements

The W and Z masses are fundamental parameters of the electroweak theory. Together they are used to define [39] the electroweak mixing angle $\sin^2\theta_W$:

$$\sin^2\theta_W = 1 - \left(\frac{m_W}{m_Z}\right)^2 \quad ,$$

i.e. the mixing is defined at the Q^2 value of W and Z production, $Q^2 \approx (90\ \text{GeV})^2$. All other measurements of $\sin^2\theta_W$ require non-trivial computations of radiative corrections, even those such as the Z^0 lepton decay asymmetry which occur at the same value of Q^2. In terms of the standard electromagnetic and Fermi coupling constants α and G_F, measured at low Q^2, we have:

$$m_W^2 = \frac{\pi\alpha}{\sqrt{2}G_F(1-\Delta r)\sin^2\theta_W}$$

where Δr represents the effect of radiative corrections. The uncertainty in these corrections arises principally from the uncertainties in the top quark and Higgs boson masses which affect the calculation of the boson propagators through internal loops. The top quark is the more important of the two effects; Figure 23a shows the dependence of Δr on the top quark mass, and Figure 23b shows the dependence on the Higgs mass. The crucial point is that precise electroweak measurements yield information, through the radiative corrections, on the as-yet-unobserved elements of the standard model.

Precise measurements of the Z^0 mass may be made at LEP or SLC where the limiting uncertainty will be the beam energy uncertainty. W mass measurements cannot be made at e^+e^- machines until the W^+W^- production threshold is reached. Direct measurements of the W mass can only be made at hadron colliders; hadronic production of the Z is copious enough in $\bar{p}p$ collisions at $\sqrt{s} = 1.8$ TeV to permit precision measurements of the Z mass, and thus mass difference measurements which are largely systematics-free.

The W Mass Measurement

The clearest signature for W production and decay is a high tranverse energy lepton accompanied by large missing transverse energy, signaling the presence of an undetected neutrino. Here, we concentrate on high E_T electrons, although a similiar analysis is underway for muons. The high-E_T-$\not{E}_T$ signature is sufficiently clean that the full power of the standard electron selection criteria (section 2) is not necessary. We require a cluster of energy in the central detector with a ratio of EM energy to total energy of greater than 0.85, associated with a single track such that E/p is less than 1.4. Fiducial cuts are applied using the CEM strip chambers, to ensure that the electron be well measured. Photon conversions are rejected using the algorithm described above. We require

$$E_T(e) > 25\ \text{GeV},\quad \not{E}_T > 25\ \text{GeV} \quad .$$

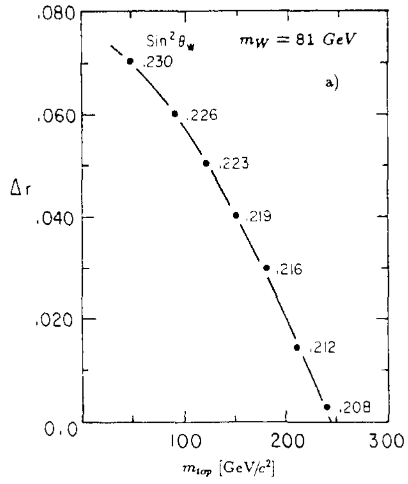

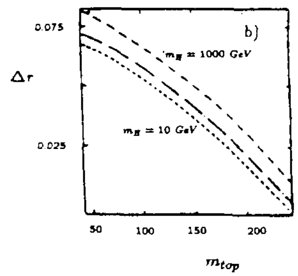

Figure 23: The dependence of the radiative correction term Δr on the top mass and the Higgs mass. In a) the curve shows the predicted radiative corrections as a function of the top mass, for a W mass of 81 GeV/c^2 and a Higgs mass of 100 GeV/c^2. The resulting values of $\sin^2\theta_W$ are also shown. In b) the variation of the curve with the Higgs mass is indicated.

Source of Uncertainty	Uncertainty (GeV/c^2)
Proton structure functions	0.3
E_T, $\not{E}_T$ resolutions and W p_T distribution	0.4
Background	≤ 0.05
Fitting procedure	0.25
Total Systematic Uncertainty	0.6

Table 2: Contributions to the W mass measurement systematic uncertainty. Not included is an overall energy scale uncertainty of 0.4% (0.3 GeV/c^2).

The background in this sample from QCD sources is estimated to be less than 1%. We also require that there be no other clusters of energy in the detector with $E_T > 7$ GeV, because mismeasurement of such clusters will affect the $\not{E}_T$ measurement. This selection leaves 1148 events.

The $e\nu$ transverse mass is shown in Figure 24, together with our best fit to the region between 66 and 88 GeV/c^2, which gives a mass of 80.0 ± 0.2 GeV/c^2, where the error is statistical. The mass determination in such a fit comes primarily from the peak of the distribution; the Jacobian edge of the distribution is related to both the W width and the mean p_T of the W. Finite E_T and $\not{E}_T$ resolution correlate these quantities, however, by smearing out the edge and changing the position of the peak. The quoted fit uses a W width fixed at the Standard Model value of approximately 2.5 GeV/c^2; a fit allowing both the width and the mass to vary is less precise statistically.

The systematic uncertainties on the W mass result from energy scale uncertainties, structure function uncertainties, uncertainties in the electron and $\not{E}_T$ resolutions and the W p_T distribution, effects due to the residual background in the sample, and the uncertainty introduced by the fitting procedure. They are summarized in Table 2 and explained below. The analysis is preliminary, and we have chosen to be conservative in our estimates of the systematic uncertainties, pending further study.

The energy scale uncertainty is explained in detail in Section 3, and is 0.4% (0.3 GeV/c^2). The proton structure function uncertainties enter because different structure functions give slightly different predictions for the shape of the transverse mass distribution. This arises because of the different W longitudinal momenta and the V − A decay of the W, together with our limited pseudorapidity acceptance for the W decay electron. We have tried many choices of structure functions; differences among them result in an estimate of 0.3 GeV/c^2 for the resulting uncertainty in the W mass. The $\not{E}_T$ resolution was studied using minimum bias data, and found to scale approximately according to $0.6 \times \sqrt{\Sigma E_T}$. In events with W bosons, the $\not{E}_T$ measurement is complicated by the energy flow into the electron cluster from the underlying event, studied using a comparison of the $\not{E}_T$ components parallel to and perpendicular to the electron direction. This study is in turn complicated by the correlation of the electron direction with the recoil energy direction for W bosons

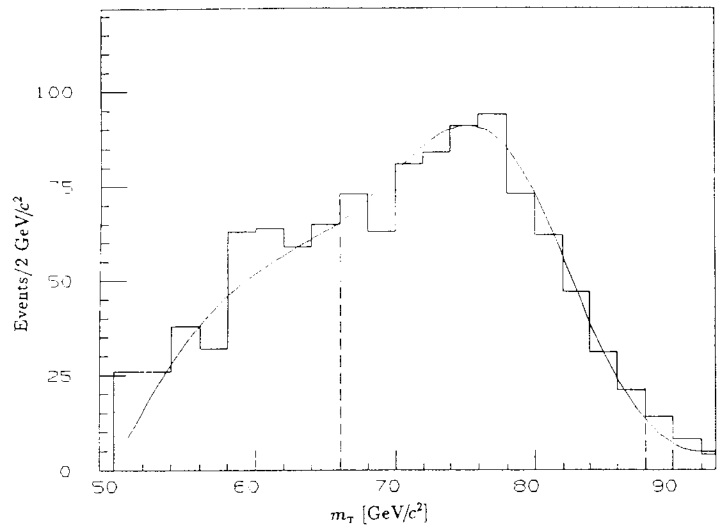

Figure 24: The transverse mass for the W sample (histogram) together with the fit discussed in the text (curve). The fitting range is indicated by the dashed lines.

produced at large p_T; this is one of the reasons we impose above the requirement that there be no additional clusters in the event. Thus, the uncertainties due to both the $\not{E}_T$ and the electron E_T resolutions are correlated to the uncertainty due to the W p_T distribution. Taken together, we estimate the resulting uncertainty on the W mass as 0.4 GeV/c^2, with the dominant contributions coming from the $\not{E}_T$ measurement and the W p_T distribution. Backgrounds in the sample include a small number of $W \to \tau\nu$, $\tau \to e\nu\bar{\nu}$ decays, and misidentified $Z^0 \to e^+e^-$ decays where one electron is lost or badly reconstructed in the detector. The 66 GeV/c^2 lower limit on the fit range was chosen to avoid the low transverse mass part of the spectrum where we expect the τ decays to contribute. Varying the backgrounds within reasonable limits leads to a small uncertainty (< 50 MeV/c^2) on the W mass. Finally, we have performed a binned fit. Binning variations and studies of the fit results on Monte Carlo samples lead to an uncertainty due to the fitting procedure of approximately 250 MeV/c^2.

The resulting $W^\pm$ mass measurement is thus:

$$m_W = 80.0 \pm 0.2 \pm 0.6 \pm 0.3 \text{ GeV}/c^2 \quad ,$$

where the first error is statistical, the second is the quadrature sum of the systematic errors discussed above, and the third is the overall energy scale uncertainty.

The Z Mass Measurement

The Z^0 mass is measured using a sample of $Z^0 \to e^+e^-$ decays, with the calorimeter measurement of the electron energies, and with a sample of $Z^0 \to \mu^+\mu^-$ decays using the muon momenta as determined from the tracking chambers. The $Z^0 \to e^+e^-$ decays using the electron momenta as measured in the tracking chamber are also presented for comparison, but are not used in the final determination of the Z^0 mass because of the large adjustments necessary to correct for electron *bremsstrahlung.*

The di-electron sample required two electrons, each in the central EM calorimeter inside the fiducial region of the detector (away from ϕ cracks), and used standard cuts on strip chamber shower shape and shower-track matching. The ratio of electromagnetic to total energy was required to be less than 0.10, and E/p was required to be less than 1.4. The sample contains 73 events with e^+e^- effective masses in the range from 50 GeV/c^2 to 150 GeV/c^2. As an indication of the background, there are no like-sign pairs in this mass range. The e^+e^- effective mass, using the calorimeter measurement of the electron energy, is shown in Figure 25. An unbinned maximum likelihood fit to the 65 events in the mass range between 80 GeV/c^2 and 100 GeV/c^2, using a Breit-Wigner form convoluted with the calorimeter resolution on an event-by-event basis, results in a fitted, uncorrected mass of 90.93 ± 0.34 GeV/c^2, and a width of $3.6 \pm 1.1 \pm 1.0$ GeV/c^2.

The di-muon sample required two tracks with p_T above 20 GeV/c, with energy depositions in the calorimeter towers associated with the tracks as explained above (*cf.* the $e + \mu$ channel in the top quark search). At least one muon candidate was required to have a track segment in the muon chambers, effectively restricting it to an η range of $|\eta| < 0.65$. The second was permitted to be outside of the muon chamber pseudorapidity coverage but was required to be well measured in the CTC and to be minimum-ionizing in the calorimeter. As in the case of the $e\mu$ channel, this is done only to increase the acceptance in pseudorapidity. Both muons were required to be further than 10° away from any jets with $E_T > 15$ GeV, in order to avoid di-jet punchthrough backgrounds. Events with two muons back-to-back within 0.1 units in η *and* 1.5° in ϕ were rejected as cosmic rays. The final sample contains 132 events with a $\mu^+\mu^-$ effective mass in the range 50 GeV/c^2 to 150 GeV/c^2; there are no like-sign muon pairs in this mass range. The muon tracks as measured in the CTC are beam constrained in order to obtain the best possible momentum resolution, measured to be $\delta p_T/p_T = 0.0011 p_T\ (GeV/c)^{-1}$. The $\mu^+\mu^-$ effective mass distribution is shown in Figure 26a. The 123 events in the mass range from 75 GeV/c^2 to 105 GeV/c^2 are fit using an unbinned maximum likelihood technique. The fit is to a Breit-Wigner convoluted with a Gaussian resolution in $1/p_T$, and gives a fitted, uncorrected mass of 90.41 ± 0.40 GeV/c^2, and a width of $4.0 \pm 1.2 \pm 1.0$ GeV/c^2.

Figure 26b shows the e^+e^- effective mass for the 64 events in the $Z^0 \to e^+e^-$ sample for which both tracks have sufficient quality to permit a beam-constrained fit to be performed. The radiative effects on the electrons are much larger than for the muons, and are clearly visible as a tail on the low side of the distribution. Performing the same fit as for the $Z^0 \to \mu^+\mu^-$ sample (there are 58 events in the fitted mass range) results in a fitted, uncorrected mass of 89.27 ± 0.80 GeV/c^2.

In order to obtain the physical Z^0 mass, the fitted masses must be adjusted for radiative corrections and structure function corrections (see Table 3). Radiative corrections were studied with a Monte Carlo simulation which used the exact electroweak matrix elements to order α^2 [40], and the events were processed through a full detector simulation to study external *bremsstrahlung.* The $Z^0 \to e^+e^-$ measurement using tracking information is the most sensitive to radiation because of external *bremsstrahlung* by the electrons, and the adjustment here is the largest. The $Z^0 \to e^+e^-$ measurement using the calorimeter energies is the least sensitive because most of the radiation is nearly collinear to the electron and thus is contained in the electron cluster and well measured in the calorimeter. We estimate the uncertainty on the radiative corrections to be less than 15%. Structure function corrections are necessary because it is more likely to have a parton-parton interaction with a center-of-mass energy slightly below the mass of the Z than it is to have an interaction at an energy slightly above the mass of the Z (*cf.* Figures 53 and 54 of reference [41]). Using various sets of structure functions, we find this correction to be approximately 80 MeV/c^2; the difference between various sets of structure functions gives an estimate of the uncertainty on this correction.

The $Z^0 \to e^+e^-$ calorimeter measurement has an energy scale uncertainty of 0.4%; all three measurements have the momentum scale (mass scale) uncertainty of 0.2% described in detail in Section 3. These corrections and uncertainties are listed

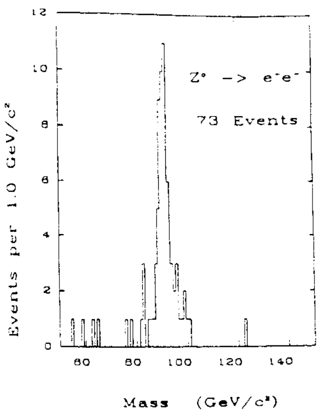

Figure 25: The $Z^0 \to e^+e^-$ effective mass distribution using the calorimeter energy measurements for the electrons.

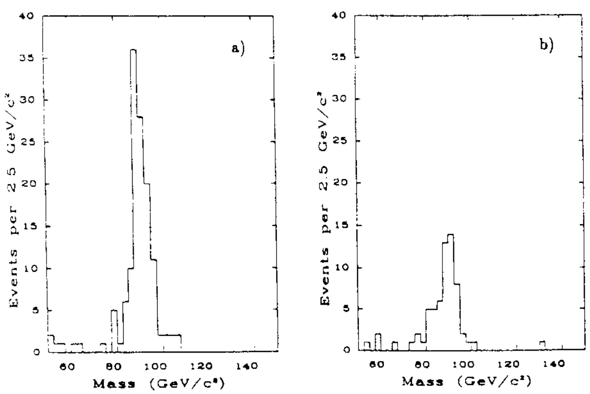

Figure 26: a) The $Z^0 \to \mu^+\mu^-$ effective mass distribution using the tracking measurements for the muons. b) The $Z^0 \to e^+e^-$ effective mass distribution using the tracking information for the electrons. The radiative tail on the low side of the peak is clearly visible.

	$Z^0 \to \mu^+\mu^-$ (tracking)			$Z^0 \to e^+e^-$ (tracking)			$Z^0 \to e^+e^-$ (calorimeter)		
Events in Fit	123			58			65		
Fitted Mass	90.41	±0.40		89.27	±0.80		90.93	±0.34	
Rad. Corr.	+0.22		±0.03	+2.19		±0.30	+0.11		±0.03
Struct. Func.	+0.08		±0.03	+0.08		±0.03	+0.08		±0.03
E/P Cal.									±0.38
Mom. Scale			±0.20			±0.20			±0.20
m_Z	90.7	±0.4	±0.2	91.5	±0.8	±0.4	91.1	±0.3	±0.4

Table 3: Corrections and uncertainties in the Z^0 mass, in GeV/c². The first uncertainty is statistical, the second systematic.

in Table 3. The resulting mass values are:

$$m_Z = 91.1 \pm 0.3 \pm 0.4 \text{ GeV/c}^2 \quad (e^+e^- \text{ cal.}),$$

$$m_Z = 90.7 \pm 0.4 \pm 0.2 \text{ GeV/c}^2 \quad (\mu^+\mu^- \text{ tracking}),$$

where the errors are statistical and systematic, respectively. Our best value for the Z^0 mass comes from a weighted mean of these two numbers, using for each an overall uncertainty formed by the combination (in quadrature) of the statistical and systematic uncertainties, excluding the common mass scale error. We obtain for our final result [42]:

$$m_Z = 90.9 \pm 0.3 \pm 0.2 \text{ GeV/c}^2 \quad ,$$

where the first error is the quadrature sum of the statistical and systematic uncertainties, and the second is the mass scale uncertainty. The MarkII experiment at the SLC has recently published a result [43] in good agreement with this number.

Electroweak Conclusions

In conclusion, we have measured the W and Z boson masses to be:

$$m_W = 80.0 \pm 0.6 \pm 0.3 \text{ GeV/c}^2 \quad ,$$

$$m_Z = 90.9 \pm 0.3 \pm 0.2 \text{ GeV/c}^2 \quad ,$$

where the first error is the quadrature sum of the statistical and systematic uncertainties, and the second is the mass or energy scale uncertainty. Together, these two precision measurements give a value for the electroweak mixing parameter of:

$$\sin^2\theta_W = 0.225 \pm 0.013 \quad ,$$

where the dominant contribution to the error is the systematic uncertainty on the W mass. This is in excellent agreement with a comprehensive analysis of all lower energy data (Amaldi *et al.*, [20]) which gives $\sin^2\theta_W = 0.230 \pm 0.0048$. Stated otherwise, one can use our measurements of the W and Z masses together with this value of $\sin^2\theta_W$ to calculate:

$$\rho \equiv \frac{m_W^2}{\cos^2\theta_W m_Z^2} = 1.006 \pm 0.018\ .$$

The ρ parameter is sensitive to the Higgs structure, and is identically one in the Standard Model and in any model where electroweak symmetry breaking occurs due to Higgs doublets. In extensions to the Standard Model with additional Higgs multiplets, ρ is not necessarily one. Clearly our measurements combined with the low Q^2 value of $\sin^2\theta_W$ are in good agreement with the standard model. In Figure 27 we show predictions for $\sin^2\theta_W$, based on the electromagnetic coupling constant α and the muon decay lifetime [44], as a function of the Z^0 mass for different values of the top quark mass (which enters because of the radiative corrections discussed at the beginning of this section). Our electroweak measurements do not yet seriously constrain the top quark mass, but more precise such measurements in the near future will help to constrain both the top quark mass and the standard model.

7 Conclusions

The analyses presented above give an overview of some of the medium and high p_T physics topics which CDF can address. We have ignored here many other interesting topics such as elastic and diffractive scattering, low p_T (minimum bias) physics, medium p_T heavy flavour (c and b quark) studies, and additional electroweak tests, but have shown that CDF is simultaneously exploring both the high precision and high energy frontiers that have traditionally been of interest in particle physics. The top quark continues to elude detection, large transverse energy jet production is well explained by QCD, and precise electroweak measurements have so far not uncovered anything in disagreement with standard SU(2)⊗U(1) electroweak theory. With an order of magnitude more data in the foreseeable future, we feel confident that we will continue to improve the precision of these tests in our efforts to further constrain the Standard Model.

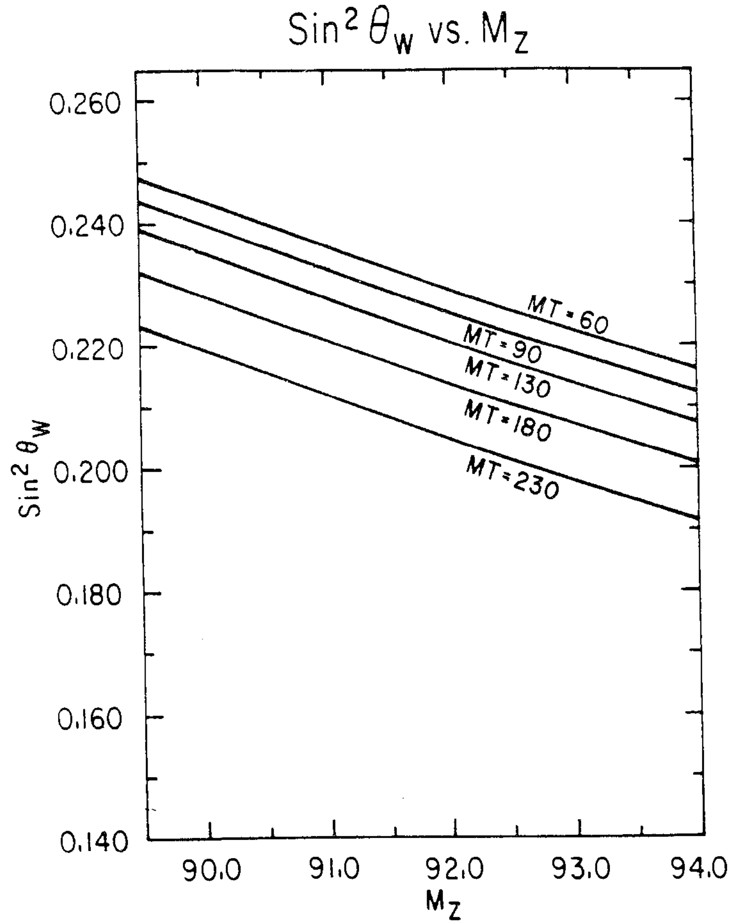

Figure 27: Predictions, based on α and the muon decay lifetime, for $\sin^2\theta_W$ as a function of m_Z and m_{top}. Adapted from Table 1 of reference [44]. A Higgs mass of 100 GeV/c^2 was assumed for these calculations.

References

[1] CDF is a collaboration of the following 18 institutions: Argonne National Laboratory, Brandeis University, University of Chicago, Fermi National Accelerator Laboratory, Laboratori Nazionali di Frascati, Harvard University, University of Illinois, National Laboratory for High Energy Physics (KEK), Lawrence Berkeley Laboratory, University of Pennsylvania, Istituto Nazionale di Fisica Nucleare (Pisa), Purdue University, Rockefeller University, Rutgers University, Texas A&M University, University of Tsukuba, Tufts University, and University of Wisconsin.

[2] The CDF Collaboration, F. Abe *et al.*, Nucl. Inst. Meth. **A271**, 387 (1988).

[3] F. Snider *et al.*, Nucl. Inst. Meth. **A268**, 75 (1988).

[4] F. Bedeschi *et al.*, Nucl. Inst. Meth. **A268**, 50 (1988).

[5] L. Balka *et al.*, Nucl. Inst. Meth. **A267**, 272 (1988).

[6] S. Hahn *et al.*, Nucl. Inst. Meth. **A267**, 351 (1988).

[7] S. Bertolucci *et al.*, Nucl. Inst. Meth **A267**, 301 (1988).

[8] Y. Fukui *et al.*, Nucl. Inst. Meth. **A267**, 280 (1988).

[9] G. Brandenburg *et al.*, Nucl. Inst. Meth. **A267**, 257 (1988).

[10] G. Cihangir *et al.*, Nucl. Inst. Meth. **A267**, 249 (1988).

[11] G. Ascoli *et al.*, Nucl. Inst. Meth. **A268**, 33 (1988).

[12] D. Amidei *et al.*, Nucl. Inst. Meth. **A269**, 51 (1988).

[13] E. Barsotti *et al.*, Nucl. Inst. Meth. **A269**, 82 (1988).

[14] J. Proudfoot, Proceedings of the Workshop on Calorimetry for the SSC, Tuscaloosa, March, 1989.

[15] F. Paige and S. Protopopescu, Brookhaven report BNL-29777 (1980).

[16] A. Maki, Proc. XIV Int. Symp. of Lepton and Photon Interactions, Stanford, 1989.

[17] A. Weinstein, Proc. XIV Int. Symp. of Lepton and Photon Interactions, Stanford, 1989.

[18] K. Eggert, Proc. XIV Int. Symp. of Lepton and Photon Interactions, Stanford, 1989.

[19] L. Di Lella, Proc. XIV Int. Symp. of Lepton and Photon Interactions, Stanford, 1989.

[20] U. Amaldi *et al.*, Phys. Rev. **D36**, 1385(1987).

[21] C. Peterson, D. Schlatter, I. Schmitt, and P.Z. Zerwas, Phys. Rev. **D27**, 105(1983).

[22] I. Hinchliffe, report in preparation.

[23] P. Nason, S. Dawson, and R.K. Ellis, Nucl. Phys. **B303**, 607(1988).

[24] G. Altarelli, M. Diemoz, G. Martenelli and P. Nason, Nucl. Phys. **B308**, 724(1988).

[25] M. Mangano and S. Parke, Fermilab-Pub-89/106-T.

[26] P. Nason, S. Dawson, and R.K. Ellis, ETH-PT/89-2 and Fermilab-Pub-89/91-T.

[27] F. Olness and W. Tung, Int. J. Mod. Phys. **A2**, 1413(1987).

[28] R.K. Ellis, Fermilab-Conf-89/168-T, lectures given at this Summer Institute.

[29] P. Tipton and E.H. Thorndike, CLEO internal report CBX 87-26; and E.H. Thorndike and R.A. Poling, Phys. Rep. **157**, 183 (1988).

[30] The Particle Data Group 'Review of Particle Properties', G.P. Yost *et al.*, Phys. Lett. **B204**, 1 (1988).

[31] The CDF Collaboration, F. Abe *et al.*, A Search for New Heavy Quarks in Electron-Muon Events at the Fermilab Tevatron Collider, in preparation.

[32] The CDF Collaboration, F. Abe *et al.*, A Search for the Top Quark in the Reaction $\bar{p}p \to$ Electron + Jets at $\sqrt{s} = 1.8$ TeV, submitted to Phys. Rev. Letters.

[33] P. Bagnaia *et al.*, Phys. Lett. **144B**, 283(1984).

[34] D. Duke and J. Owens, Phys. Rev. **D27**, 508(1984).

[35] E. Eichten, K. Lane and M. Peskin, Phys. Rev. Lett. **50**, 811(1983).

[36] E. Eichten, I. Hinchliffe, K. Lane and C. Quigg, Rev. Mod. Phys. **50**, 811(1983).

[37] M. Althoff *et al.*, Z. Phys. **C22**, 307(1984).

[38] G. Altarelli and G. Parisi, Nucl. Phys. **B126**, 298(1977).

[39] A. Sirlin, Phys. Rev. **D22**, 971(1980).

[40] R.G. Wagner, unpublished, based on calculations by: F. Berends *et al.*, Z. Phys. **C27**, 155(1985); F. Berends and R. Kleiss, Z. Phys. **C27**, 365(1985); G. Marchesini and B. Webber, Nucl. Phys. **B310**, 461(1988); G. Bonvicini and L. Trentadue, UM-HE-88-36.

[41] E. Eichten, I. Hinchliffe, K. Lane and C. Quigg, Rev. Mod. Phys. **56**, 580(1984).

[42] The CDF Collaboration, F. Abe *et al.*, Phys. Rev. Lett. **63**, 720(1989).

[43] G. Abrams *et al.*, Phys. Rev. Lett. **63**, 724(1989).

[44] B. Lynn and R. Stuart, Nucl. Phys. **B253**, 216(1985).

NEW MEASUREMENT OF THE PHASE DIFFERENCE $\Phi_{00} - \Phi_{+-}$ in CP – VIOLATING K^0 DECAYS

Bernd Panzer

J. – Gutenberg University Mainz, Germany

CERN – Edinburgh – Mainz – Orsay – Pisa – Siegen Collaboration [1]

Introduction

Neutral kaons are produced in hadronic reactions like $\pi^+ p \to \Sigma^+ \pi^+ K^0, K^+ p \bar{K}^0$. The particular feature of the K^0 and $\bar{K}^0$ particle consists in the fact that they differ only in one quantum number, the strangeness. Since weak interaction doesn't conserve strangeness, particle – antiparticle transitions can occur through intermediate decay states.

$$K^0\ (S=+1) \leftrightarrow \begin{bmatrix} \pi^0\pi^0 \\ \pi^+\pi^- \\ \pi^0\pi^0\pi^0 \\ \pi^0\pi^+\pi^- \end{bmatrix} \leftrightarrow \bar{K}^0\ (S=-1)$$

The new eigenstates of the neutral kaon system are therefore defined as

$$|K_1> = \frac{1}{\sqrt{2}}(|K^0> - |\bar{K}^0>)$$

$$|K_2> = \frac{1}{\sqrt{2}}(|K^0> + |\bar{K}^0>)$$

and these are also CP eigenstates (C = charge conjugation, P = parity). In 1964 the CP violation was discovered by Christenson et al. [6] with the consequence that the CP eigenstates are not anymore the eigenstates to mass and lifetime of the neutral kaons. This leads to the following description :

$$|K_S> = \frac{1}{\sqrt{2(1+|\varepsilon_S|^2)}}(|K_1> + \varepsilon_S|K_2>) = |K_S(0)> e^{-iM_St - \frac{\Gamma_S}{2}t}$$

$$|K_L> = \frac{1}{\sqrt{2(1+|\varepsilon_L|^2)}}(|K_2> + \varepsilon_L|K_1>) = |K_L(0)> e^{-iM_Lt - \frac{\Gamma_L}{2}t}$$

with $\varepsilon = \varepsilon_S = \varepsilon_L$ *assuming CPT – Invariance*

$$\varepsilon = \frac{\mathrm{Im}\Gamma_{12}/2 + i\ \mathrm{Im}M_{12}}{i\ (\Gamma_S - \Gamma_L)/2 - (M_S - M_L)} .$$

The CP violation manifests itself in the fact that the long living K_L state decays not exclusively in three pions but also, in 3‰ of all cases, in a two pion final state. The experimental accessible parameters of CP violation are η_{00} and η_{+-} defined as the ratios of decay amplitudes :

$$\eta_{+-} = |\eta_{+-}|e^{i\phi_{+-}} = \frac{<\pi^+\pi^-|H|K_L^0>}{<\pi^+\pi^-|H|K_S^0>} = \varepsilon + \varepsilon'$$

$$\eta_{00} = |\eta_{00}|e^{i\phi_{00}} = \frac{<\pi^0\pi^0|H_W|K_L^0>}{<\pi^0\pi^0|H_W|K_S^0>} = \varepsilon - 2\varepsilon' .$$

These variables again are connected with the two parameters describing the origin of CP violation

1. $\varepsilon \rightarrow$ CP violation through kaon state mixing

   $K_L \rightarrow \varepsilon K_2 \rightarrow \pi\pi$

2. $\varepsilon' \rightarrow$ CP violation in the decay ('direct' CP violation)

   $K_L \rightarrow K_1 \rightarrow \pi\pi$

and can be accommodated within quantized field theories such as the Standard Model. [2,3] The measured values for the complex parameters are summarized in the following table [8] :

$\lvert\eta_{+-}\rvert$	=	$(2.275 \pm 0.021)\times 10^{-3}$
$\lvert\eta_{00}\rvert$	=	$(2.299 \pm 0.036) \times 10^{-3}$
ϕ_{+-}	=	$(44.6 \pm 1.2)°$
ϕ_{00}	=	$(54.5 \pm 5.3)°$
Re ε	=	$(1.621 \pm 0.088) \times 10^{-3}$
$\lvert\varepsilon'/\varepsilon\rvert$	=	$(3.3 \pm 1.1) \times 10^{-3}$
Δm	=	$(3.521 \pm 0.014) \times 10^{-12}$ MeV

The first non – zero measurement of ε' came also from the NA31 group. [7] A graphical relation of all parameters is presented in figure 1, the so called Wu – Yang diagram.

CPT

A very important theorem in the framework of field theories is the CPT – theorem (C,P,T are abbreviations for the three symmmetry transformations charge conjugation, parity and time reversal). This theorem states that local Lorentz invariant quantum field theories are invariant under the combined transformation CPT.[4,5] This leads to the subsequent consequence : mass, lifetime and magnetic moment should be the same for a particle and its antiparticle. The most stringent limits on a possible CPT violation is delivered again by the neutral kaon system :

$$10^{-18} \geq \frac{M_{\bar{K}^0} - M_{K^0}}{M_{K^0}} .$$

The interesting factor in the formula is Δ which reveals the connection between CPT and the phases of the decay amplitude ratios using perturbation theory.[17,18]

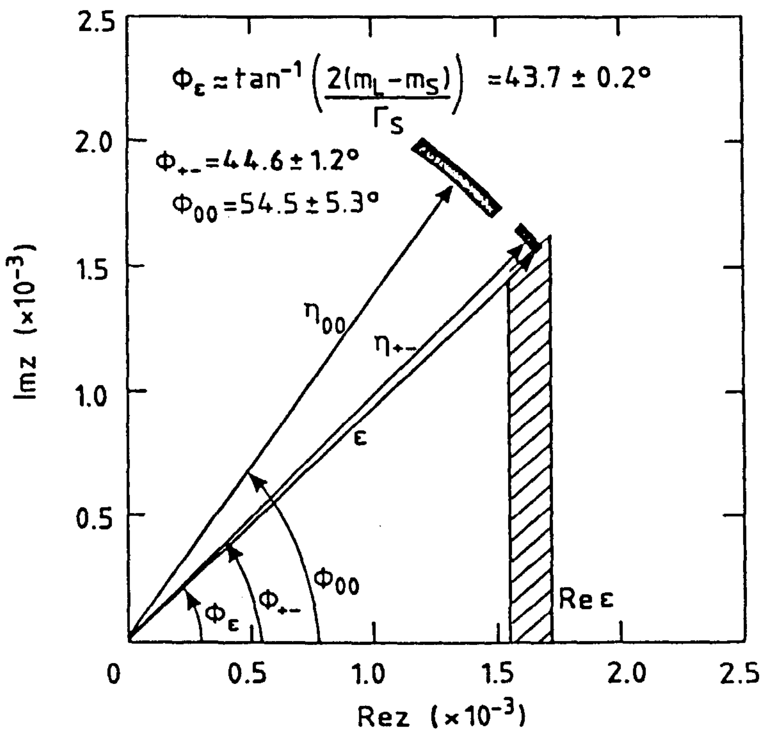

Figure 1: Wu – Yang diagram. Graphical representation of the different parameters of the CP violation.

$$\Delta = \frac{1}{2}\frac{<\bar{K}^0|H_W|\bar{K}^0> - <K^0|H_W|K^0>}{(M_L - M_S) + i(\Gamma_S - \Gamma_L)/2} \cong \frac{1}{2}\frac{M_{\bar{K}^0} - M_{K^0}}{M_L - M_S}\sin\phi_\varepsilon$$

$$\Delta \simeq = |\eta_{+-}|\left(\frac{1}{3}\Delta\phi + \phi_{+-} - \phi_\varepsilon\right)$$

$$\tan\phi_\varepsilon = \frac{2(M_L - M_S)}{\Gamma_L - \Gamma_S}, \quad \phi_\varepsilon = 43.7° \pm 0.2°$$

CPT invariance therefore requires some constraints on the values of ϕ_{+-} and ϕ_{00}, namely

$$\phi_{+-} \cong \phi_{00} \qquad \text{and} \qquad \phi_\varepsilon \cong \phi_{+-}$$

The value of the phase difference before the NA31 measurement was $\Delta\phi = \phi_{00} - \phi_{+-} = 12.6° \pm 6.2°$. (Christenson et al. [9])

To measure in an experiment the phase values one uses the phenomenon of interference in the neutral kaon system. Due to the CP violation the states K_L and K_S have decay channnels in common ($\to \pi^+\pi^-, \pi^0\pi^0$) and thus can interfere with each other. The calculation of the time dependent intensity of $K^0, \bar{K}^0$ decaying into two pion final states shows the usual exponential decay part and in addition a cosine term resulting from interference.

$$I_{\pi\pi}(t) = C\left[e^{-\Gamma_S t} + |\eta|^2 e^{-\Gamma_L t} + 2D|\eta|\, e^{-(\Gamma_S + \Gamma_L)\frac{t}{2}}\cos(\Delta m\, t - \phi)\right]$$

$$D = \frac{N(K^0) - N(\bar{K}^0)}{N(K^0) + N(\bar{K}^0)}$$

$N(K^0), N(\bar{K}^0)$ = number of created K^0 – , $\bar{K}^0$ – particle

C = norm

The dilution factor D takes into account the different amount of produced K^0 and $\bar{K}^0$ at the target. The maximum of information about the phases can be extracted from the intensity distribution at about 12 K_S lifetimes.

Principal of measurement

Figure 2 and enlarged figure 3 sketches the experimental setup of the NA31 experiment, a fixed target experiment at the CERN SPS accelerator in Geneva. The design of the interference beam was similar to that of the previous ε'/ε measurement in 1986. [14] A detailed description can be found in reference [15].

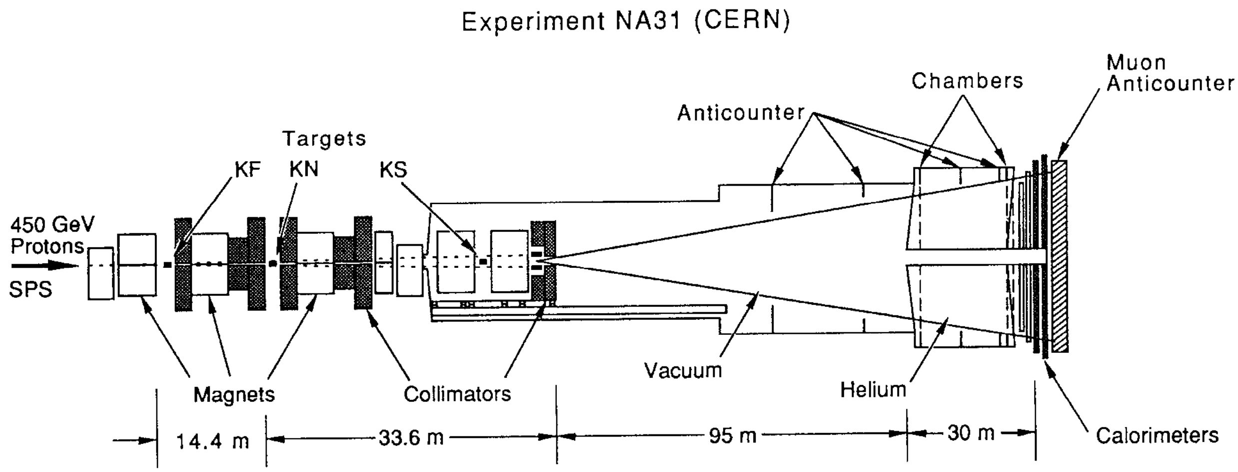

Figure 2: Experimental setup of the NA31 experiment. Display of the target region, the decay volume and the detector part with the helium tank.

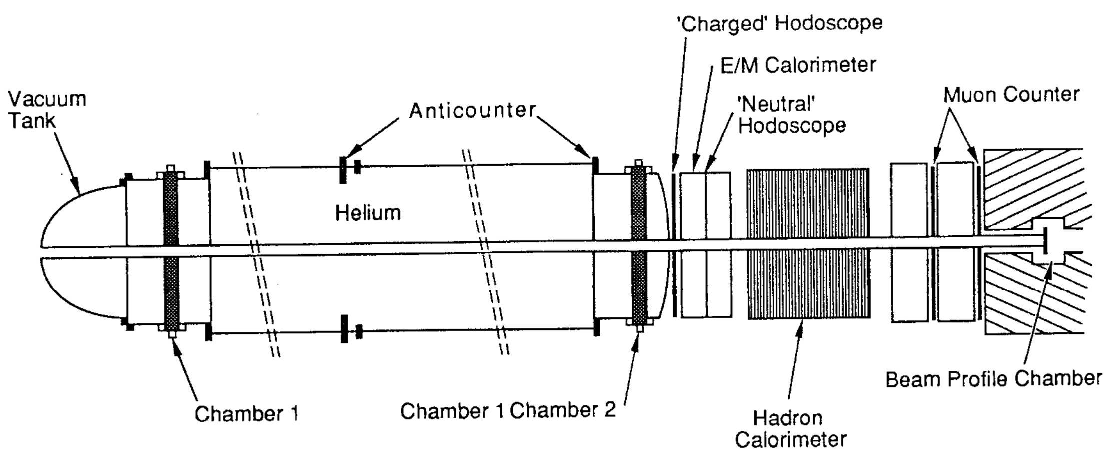

Figure 3: Enlarged view of the detector section.

The four main characteristics of the experiment are listed below:

1. the experiment NA31 relied on vacuum interference, no regenerator was used
2. the decay kinematic was measured with wirechambers and calorimeters
3. charged and neutral decay channels were measured simultaneously, so we determined ϕ_{00} and ϕ_{+-} at the same time
4. there was the possibility to record two time shifted intensity distributions by using targets in different distances from the decay volume (KF−target and KN−target 14.4 m apart, N for near − F for far). The advantage of this setup was that all acceptances cancel if one forms the ratio of the two intensity distributions at the same energy and vertex point. And thus get rid of a substantial systematic error.

The data collection of the NA31 experiment took place in 1987 where during 70 days a total of about 2400 magnetic tapes with $1.4\,10^{8}$ triggers were recorded. The following table shows the exact numbers of measured kaon decays, where the number in brackets include the lifetime downscaling weights :

Table 1

	$K \to \pi^0\pi^0$ ($\times 10^6$)	$K \to \pi^+\pi^-$ ($\times 10^6$)
KNEAR	1.81	2.24
KFAR	0.31	0.57

This lifetime downscaling was used online for events with a lifetime below $7\,\tau_S$ to reduce the data volume. To avoid systematic errors due to time variations in the detectors a special condition of running was chosen. In a repeating cycle 20 Tapes of KN−data (decays of kaons which were produced at the KN target), 11 tapes of KF−data and one tape with K_S decays were successively taken. In total we collected 57 of these cycles.

Reconstruction of the two decay modes

1. $K^0 \to \pi^0\pi^0 \to 4\gamma$

For the recording of photons an elm. calorimeter was used. The calorimeter consisted of 80 cells with 2.3 mm lead plates containing liquid argon as active material. Copper strips in X an Y direction were used to readout the pulseheights of the LAC, there existed in total 1536 readout channels. We achieved an energy resolution of $\frac{\sigma_E}{E} = \frac{0.075}{\sqrt{E}}$ and a spatial resolution of about 0.75 mm for gammas. The reconstructed kaon energy came from the sum of the 4 photon energies. While the vertex calculation ensued from geometric means under the assumption of a kaon decay :

$$Z_{\text{Vertex}} = Z_{LAC} - \frac{1}{M_K}\left\{ \sum_{i,j<i} E_i E_j \left[(x_i - x_j)^2 + (y_i - y_j)^2 \right] \right\}^{\frac{1}{2}}$$

Z_{Vertex} = vertex

Z_{LAC} = position of the elm. calorimeter = 12374.95 cm

M_K = kaonmass

$x_i y_i$ = X,Y position off photon i in the LAC

$E_{i,j}$ = energy of the photon

2. $K^0 \to \pi^+\pi^-$

Two multiwire proportional chambers served to extract the vertex from this decay mode. Each chamber consisted of 4 planes with 432 gold plated tungsten wires (size = 0.03 mm). The chambers contained an Argon/Isobutan gas mixture (70%/30%) and the cathode planes were connected to 2850 V of tension. These parameters resulted in a space point resolution in X,Y of 0.75 mm. The final vertex was reconstructed by fitting a plane through the four spacepoints and improved by using the drift time information from TDC's connected to each chamber.

The energy of the pions was measured with a combination of two calorimeters, the already described elm. calorimeter and a hadron calorimeter. The latter was composed of 48 2.5 cm iron plates and 49 planes of scintillator strips, alternately orientated in X and Y direction. The finally achieved energy resolution was $\frac{\sigma_E}{E} = \frac{0.65}{\sqrt{E}}$.

The energy of the kaon was not just the sum of pion energies but relied mostly on geometric calculations using the opening angle from the decay:

$$E = \frac{\sqrt{\left[M_K^2 - m_\pi^2 T\right] T}}{\Theta}$$

M_K = kaonmass , Θ = opening angle

m_π = pionmass

T = 2. + E_1/E_2 + E_2/E_1 $\quad E_1, E_2$ = pionenergies

With this method the resolution in kaon energy was very much improved leading to $\frac{\sigma_E}{E} \approx 1\,\%$.

Systematic errors

1. Energy scale

A very important point in this experiment was the determination of the energy scale, mainly in the neutral decay mode but also in the charged decay mode. In both reconstruction mechanism the kaon energy was coupled to the vertex calculation. This was the feature on which the energy scale determination was based.

During special runs kaon have been produced in a target (KS – target) directly at the beginning of the decay volume. Because of the long decay length of the K_L particle ($\gamma c t_L =$ 3000 m at 100 GeV) only K_S were decaying and their decay products recorded by the detectors. An anticounter was placed in the neutral kaon beam to record only decays which took place downstream of this detector, thus defining a zero point in the system. The physical Z – position of this anticounter was precisely known.

The procedure now was to fit an exponential distribution (folded with a Gaussian resolution function) to the measured vertex distribution of the K_S decays, taking the resolution and the anticounter position as free parameters. A comparison of the measured anticounter position with the physical position gave the shift in the vertex measurement and because of the described coupling also the shift in energy scale (Fig.4). Thus any time dependent shift could be corrected by using the information from the regularly K_S data taken during the 1987 run.

Figure 5 gives the final result for the precision of the energy scale for charged and neutral decays. Also one can see the very small nonlinearities in the experiment. A deviation of 10 cm in the anticounter position was equal to a 1 ‰ shift in energy scale which again would shift the phase values by one degree. This gives an indication of how important the energy scale measurement was and how well it was carried through.

2. Background events

a) $K^0 \rightarrow \pi^0 \pi^0$ mode

The only background to this decay channel came from the decay of $K_L \rightarrow \pi^0\pi^0\pi^0$ (B.R. 21.7 % compared to $K_L \rightarrow \pi^0\pi^0$ B.R. 0.091 %).To reduce these decays several conditions per event had to be fullfilled:

1. no signals from the ring anticounters surrounding the decay volume and the helium tank
2. only four photons reconstructed in the LAC
3. the center – of – gravity had to be within 10 cm around the beam axis.

The main cut, also used to extrapolate the amount of background into the signalregion, was a constraint on the reconstructed π^0 mass.

$$N_{Ellipse} = \left\{ \frac{(m_{\gamma_1\gamma_2} - m_{\gamma_3\gamma_4})}{(12MeV)} \right\}^2 + \left\{ \frac{(m_{\gamma_1\gamma_2} + m_{\gamma_3\gamma_4} - 2m_{\pi^0})}{(8MeV)} \right\}^2$$

$m_{\gamma\gamma}$ = invariant mass of the photons

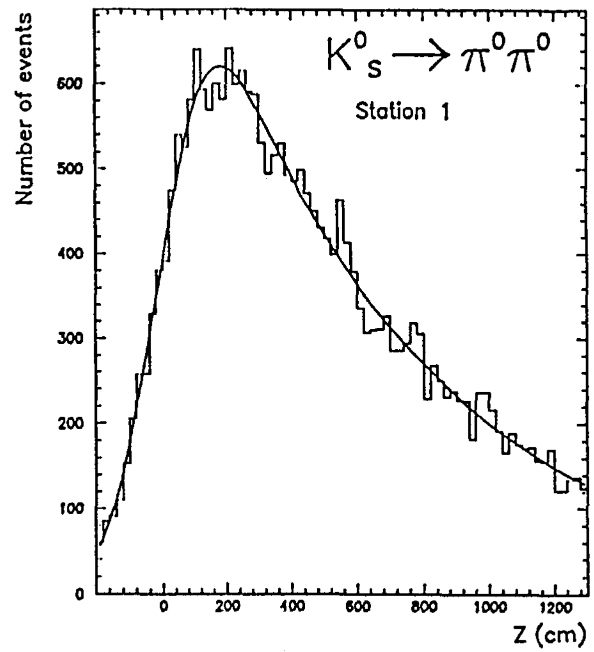

Figure 4: Vertex distribution KS data. Overlayed is the result from the fit procedure.

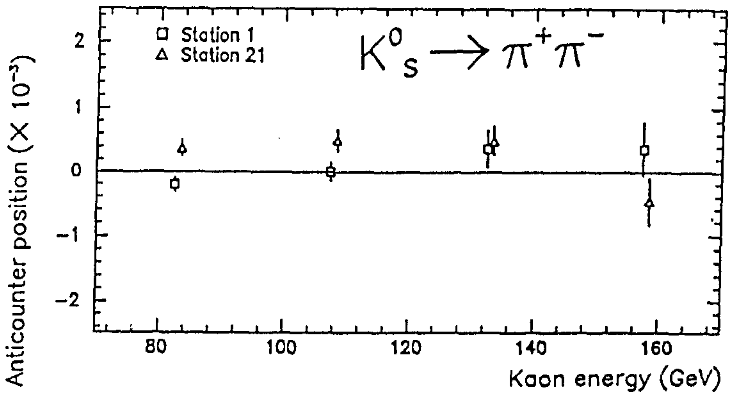

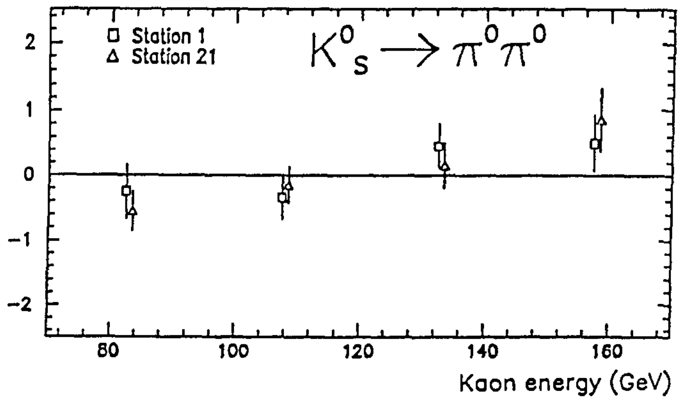

Figure 5: Final precision of the charged and neutral energy scale.

m_{π^0} = neutral pion mass (134.96 MeV)

For good events N should be less than one while the background region was defined as 7 < N < 12 (Fig.6). The number of background events was afterwards flat extrapolated into the signal region and than subtracted (Fig.7). The consequently ascertained background level was 1‰ for the KN data and 3‰ for the KF data (Fig.8). The total effect on the phase determination was − 0.6 ° when subtracting the neutral background.

b) $K^0 \to \pi^+\pi^-$ mode

The source of background in this decay mode consisted of different parts :

$K_L \to \pi e \nu$ B.R. 38.6 %

$K_L \to \pi \mu \nu$ B.R. 27.0 %

$K_L \to \pi^+\pi^-\pi^0$ B.R. 12.4 %

$\Lambda \to \pi^- p$

and kaon and lambda decays which took place before the collimators and then being bent by a magnetic field.

All these kinds of background were substantially (a factor 25) reduced by the following cuts and requirements :

1. no hits in the anticounters
2. no extra photons reconstructed
3. cut on electrons, using the longitudinal shower development
4. cut on the pion energy ratio (R < 2.5)
5. cut on the reconstructed kaon mass
6. rejecting events with a low vertex (< 120 cm)

The remaining background came mainly from K_{e3} decays. To get a handle on this events and to estimate at the same time the amount of background in the signalregion the variable D−target was utilized. The measurement of D−target revealed information about the transverse momentum of the decay. Figure 9 shows the distribution of D−target overlayed with a reference distribution of positive identified K_{e3} events. A background region was defined (6 cm < D−t < 10 cm) and with the help of the reference distribution this was extrapolated into the signalregion (0 cm < D−t < 3.25 cm (3.5 cm KF)). The influence of this background subtraction on the charged phase value was very small, it decreased ϕ_{+-} by 0.2 °.

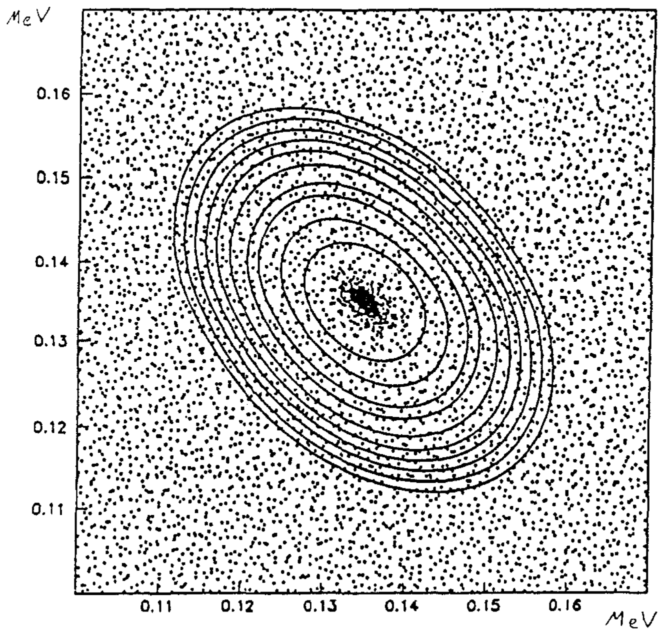

Figure 6: Reconstructed pion mass distribution for neutral events. Drawn are also the ellipse numbers 1 to 10.

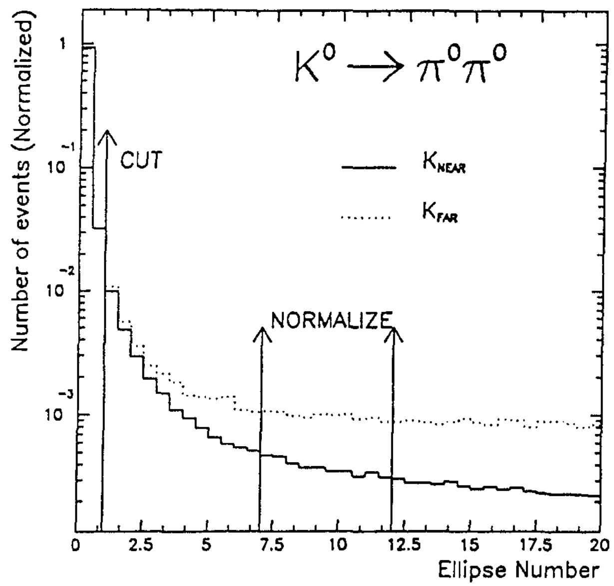

Figure 7: Ellipse distribution for neutral events, KN and KF data sets. Indicated is also the signal region and the background region.

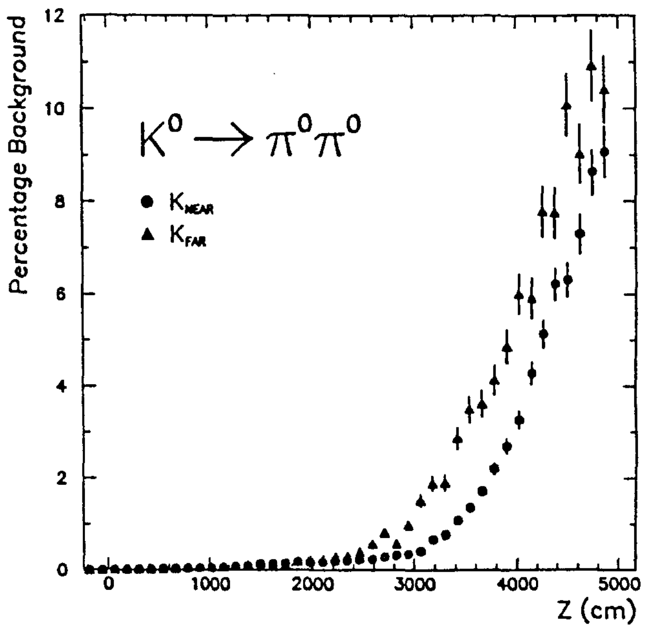

Figure 8: Z dependence of the amount of background in the neutral decays.

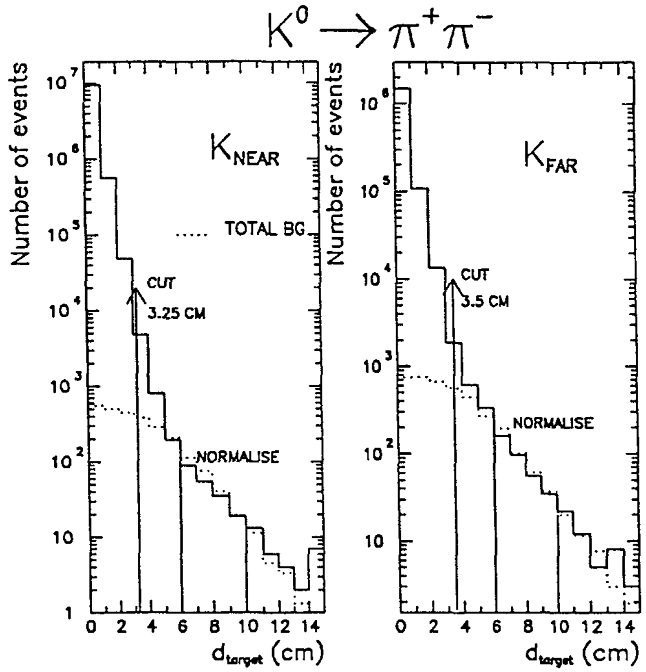

Figure 9: D – target distribution for charged events, KN and KF data sets. Indicated is the signal region and the background region and the solid line represents the distribution of the reference data sample used to subtract the background in the signal region.

Data analysis

The next figures reveal some information about the quality of the data taken in 1987. Figure 10 sketches the energy distribution of the decay modes in the data sets KN and KF. The collected statistics can be seen from figure 11, showing the uncorrected lifetime distributions for charged and neutral two pion decays, KN and KF data merged. To exhibit the clear interference feature in our data we started with a conventional treatment of the data. Figure 12 displays the lifetime distribution corrected for lifetime downscaling and acceptance, overlayed with a theoretical curve without interference term. One can see the distinct differences and the full feature of interference is exhibited when extracting the cosine interference term displayed in figure 13. But this conventional method was not used to extract the phase values from the data, because the experiment was designed to avoid the use of acceptance calculations thus omitting a strong source of systematic errors.

Determination of the phase values

The starting point of the phase analysis were 4 different data sets, charged decays and neutral decays from KN and KF running mode. Each of these were subdivided into 5 GeV energy bins in the energy range 70 – 170 GeV and into 0.5 τ_S lifetime bins in the vertex range 120 – 4920 cm (zero point = end point of the last collimator in the decay region). The crucial step in the procedure was to form now the ratio

$$R_{ij} = \left.\frac{\textit{number of events (KN mode)}}{\textit{number of events (KF mode)}}\right|_{E_i,\,\tau_j}$$

in each energy and τ_S bin separately for the two decay channels ($\pi^+\pi^-, \pi^0\pi^0$). This ratio R had the advantage of being independent from acceptances. The lifetime was calculated from the center between the two targets. The next step consisted in forming the same ratio calculated from the theoretical distribution

$$R_{Theorie} = \frac{\int_{E_i}^{E_{i+1}} f(E) \int_{\tau_j}^{\tau_{j+1}} I_{KN}(E,\tau)\, dE\, d\tau}{\int_{E_i}^{E_{i+1}} f(E) \int_{\tau_j}^{\tau_{j+1}} I_{KF}(E,\tau)\, dE\, d\tau}$$

$$I_{KN(KF)}(E,\tau) = N(E)\left[e^{-\tau_S} + |\eta|^2\, e^{-\tau_L} + 2\,D(E)\,|\eta|\, e^{-(\tau_S+\tau_L)/2} \cos(\Delta m\, \tau_S\, ct_S - \phi)\right]$$

$$f(E) = E^{1.671}\, e^{\frac{-E}{30.45}} \qquad (E \text{ in GeV}) \text{ energy spectrum}$$

$$\tau_{S,L} = \frac{(Z - Z_{Target})\, M}{E\, ct_{S,L}}$$

Z = vertexposition, M = kaon mass , E = kaon energy

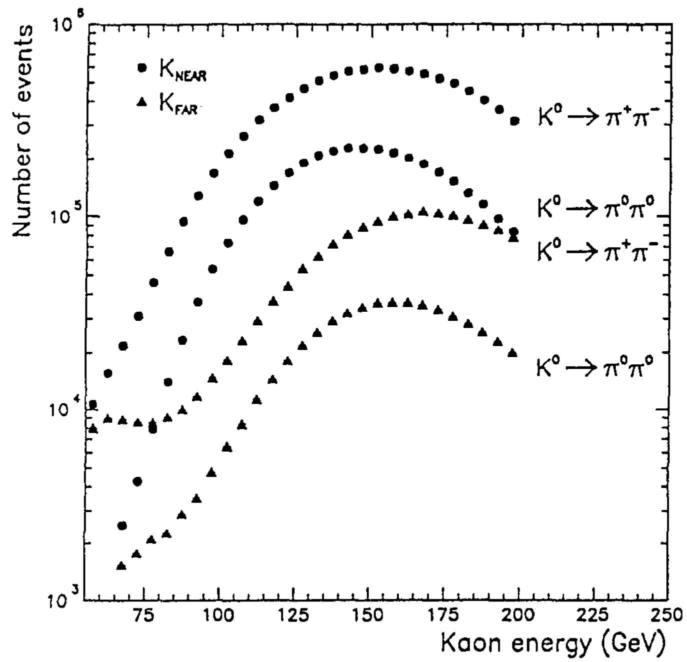

Figure 10: Energy spectra, charged and neutral decays, KN and KF data.

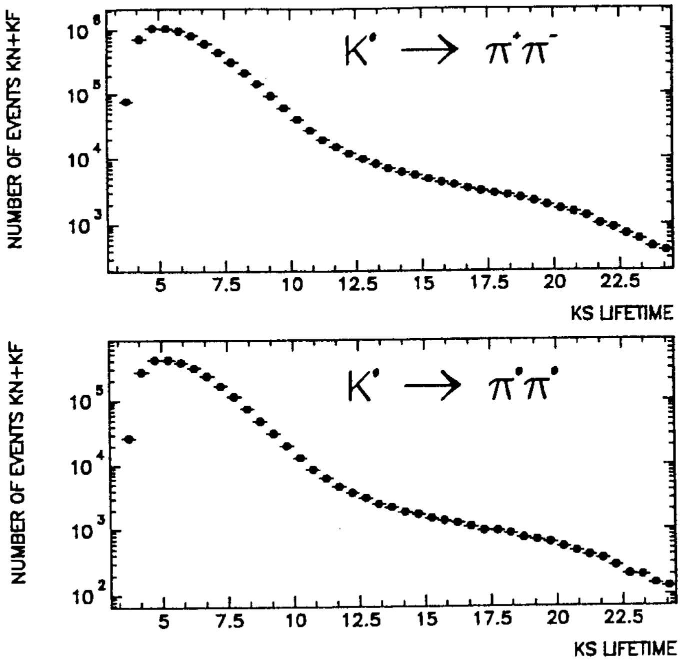

Figure 11: Uncorrected lifetime distribution.

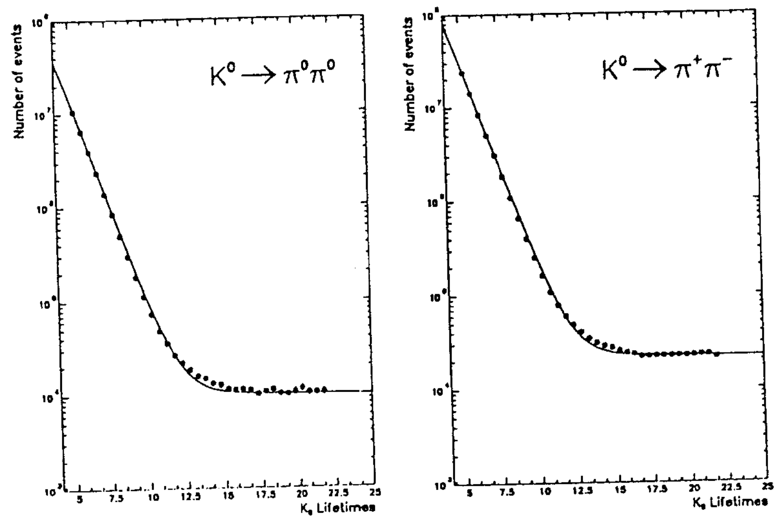

Figure 12: Acceptance corrected lifetime distribution. Also corrected for lifetime downscaling and overlayed with a theoretical distribution without interference term.

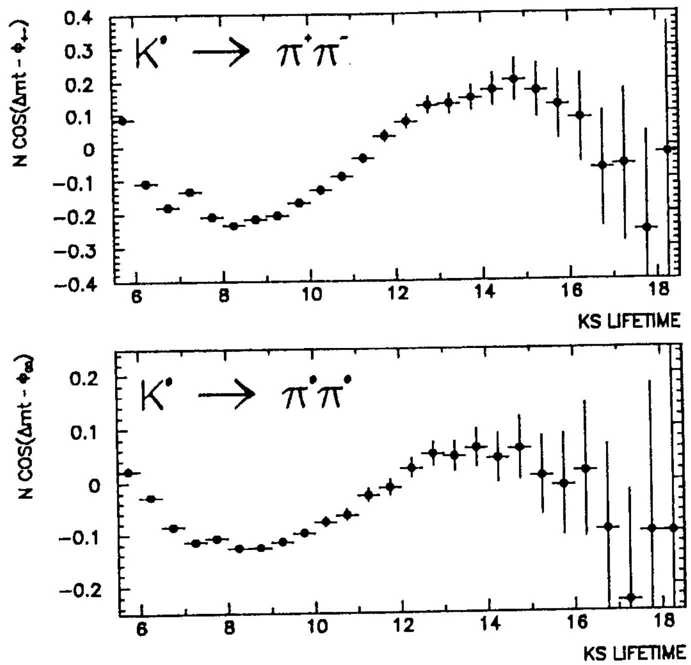

Figure 13: Extracted cosine interference term, KN and KF data merged.

$ct_{S,L}$ = decay length

Z_{Target} = Z − Position at the center between the targets KN → Z = −3360 cm, KF → Z = −4800 cm

A χ^2 − test was utilized to compare the ratio from the data with the ratio from theoretical assumptions. The following table shows the values used for the fixed input parameters.

Table 2

Massdifference	Δm	$= (3.521 \pm 0.014) \times 10^{-12}$ MeV
Lifetime K − short	t	$= (0.8923 \pm 0.0022) \times 10^{-10}$ s
Lifetime K − long	t	$= (5.18 \pm 0.04) \times 10^{-8}$ s
	η_{+-}	$= (2.275 \pm 0.021) \times 10^{-3}$
	$\lvert\eta_{00}\rvert$	$= 0.99 \times \lvert\eta_{+-}\rvert$

Both decay modes were fitted simultaneously taking ϕ_{+-} and $\Delta\phi = \phi_{+-} - \phi_{00}$ as free parameters. In addition 10 dilution factors (one per 10 GeV bin, the same for charged and neutral) and 20 normalization factors (one per 10 GeV bin, charged and neutral separately) were fitted. The result of the fit is visualized in the following pictures, showing data distributions for the decay modes in energy bins overlayed with the fitted curves (Fig.14). Figure 15 displays the distribution of the ratio, all energies included and normalized to 100 GeV, for charged and neutral decays overlayd with two theoretical distributions to exhibit again the measured interference in the neutral kaon system. More detailed descriptions can be found in references 10 − 13.

Figure 16 demonstrates the measured energy dependence of the dilution factor and in addition two predictions for the distribution of D are given. One extrapolating from K^+, K^- data to K^0, $\bar{K}^0$ and the other based on simple assumptions from the quark − parton model.[16] The agreement is much better for the second assumption but still not satisfying

The preliminary result for the phase measurement of the NA31 group is

$$\Delta\phi = \phi_{00} - \phi_{+-} = 0.3^\circ \pm 2.6^\circ \pm 1.1^\circ$$

$$\phi_{00} = 47.1^\circ \pm 2.1^\circ \pm 1.0^\circ$$

$$\phi_{+-} = 46.8^\circ \pm 1.4^\circ \pm 0.6^\circ$$

($\chi^2 = 800$ *with* 768 *degrees of freedom*)

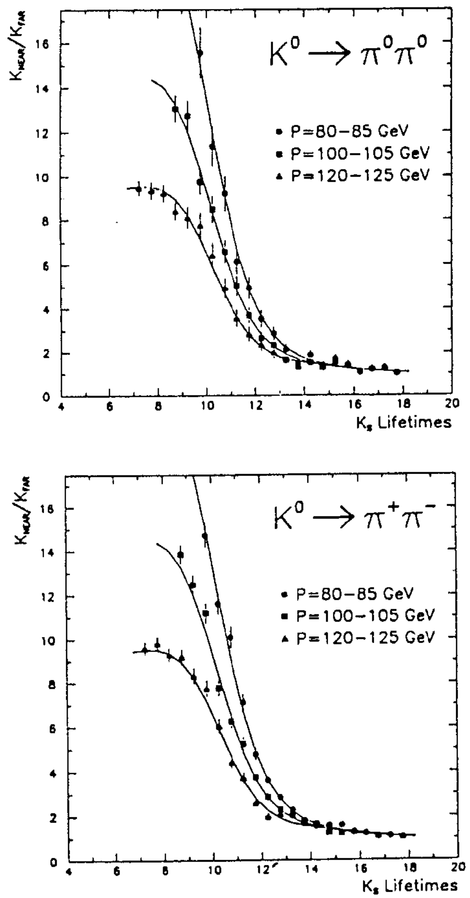

Figure 14: Results of the fit procedure in energy bins. The ratio distribution KN/KF for data and overlayed the fit results of the theoretical ratio.

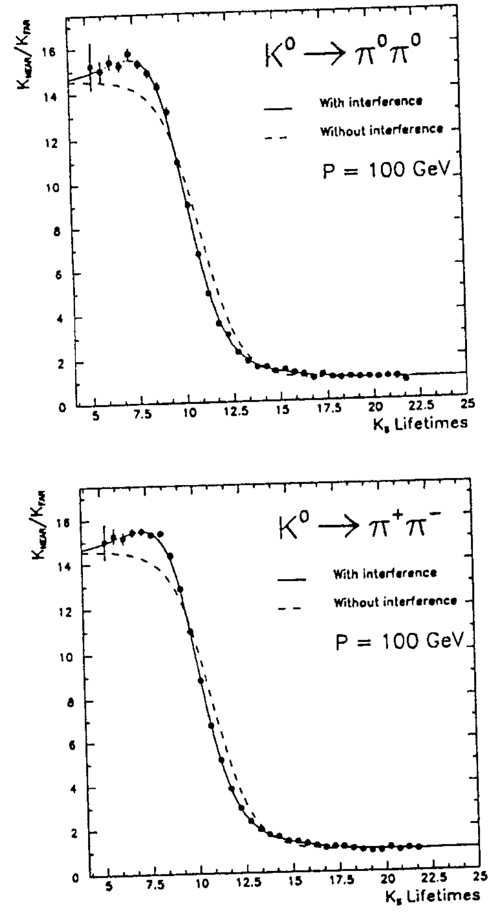

Figure 15: Results of the fit procedure. The ratio distribution KN/KF for data, all energies merged and normalized to 100 GeV, and overlayed the fit result with and without an interference term.

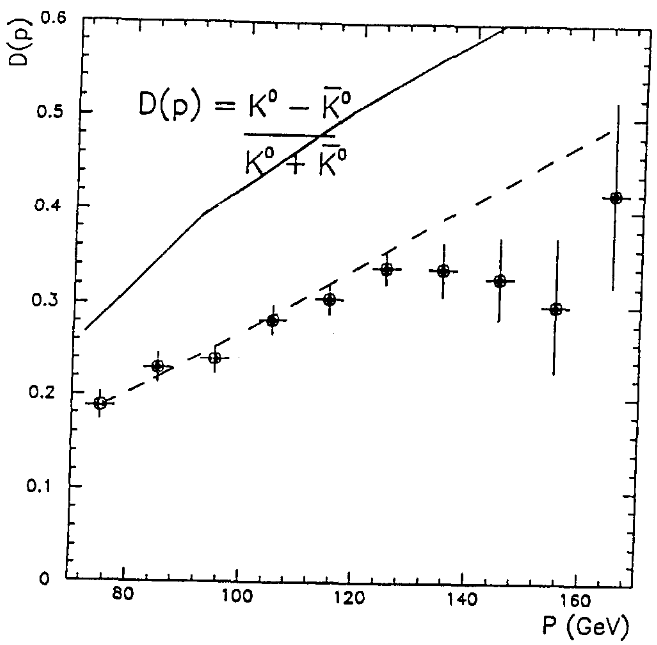

Figure 16: Energy dependence of the measured dilution factor. Solid line = prediction from charged kaon measurements, dashed line = predictions from the quark – parton model.

where the first error comes from statistics and the second error from systematics. A comparison of this result with previous measurements is shown in figure 17. The composition of the systematic error can be extracted from the following table :

Table 3

Contributions	ϕ_{+-}	ϕ_{00}	$\Delta\phi$
Energy scale	0.6	0.8	1.0
Nonlinearities	-	< 0.5	< 0.5
Background	0.1	0.1	0.1
Regeneration	0.1	0.1	-
MC acceptance	0.1	0.1	0.1
Resolution	negligible	0.2	0.2

The main error originated from the measurement of the energy scale in both decay modes. While all other errors are quite small, e.g. errors from second order effects in the MC acceptance calculations or errors from any background subtraction methods.

In addition to these systematic errors there existed another category due to the uncertainties in the external parameters ($c\tau_s$,Δm used in the fit procedure). The sensitivity of the phases on changes of the parameters can be represented in the following way (see also figure 18) :

	ϕ_{+-} [°]	ϕ_{00} [°]	$\Delta\phi$ [°]
$S(\Delta m)$	1.2	1.2	0.0
$S(\tau)$	0.6	0.4	−0.2
$S(\eta)$	0.2	0.2	0.1

$$\sigma_{ext} = \frac{(\tau - 0.8923\times10^{-10}s)}{0.0022\times10^{-10}s} S(\tau) + \frac{(\eta - 2.275\times10^{-3})}{0.021\times10^{-3}} S(\eta) + \frac{(\Delta m - 3.521\times10^{-12}MeV)}{0.014\times10^{-12}MeV} S(\Delta m)$$

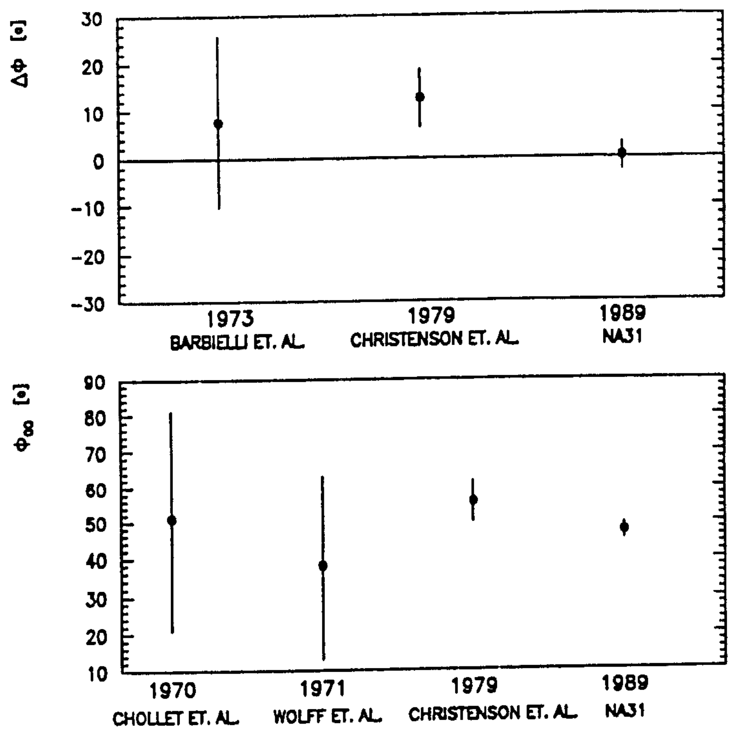

Figure 17: Comparison of the result with earlier measurements.

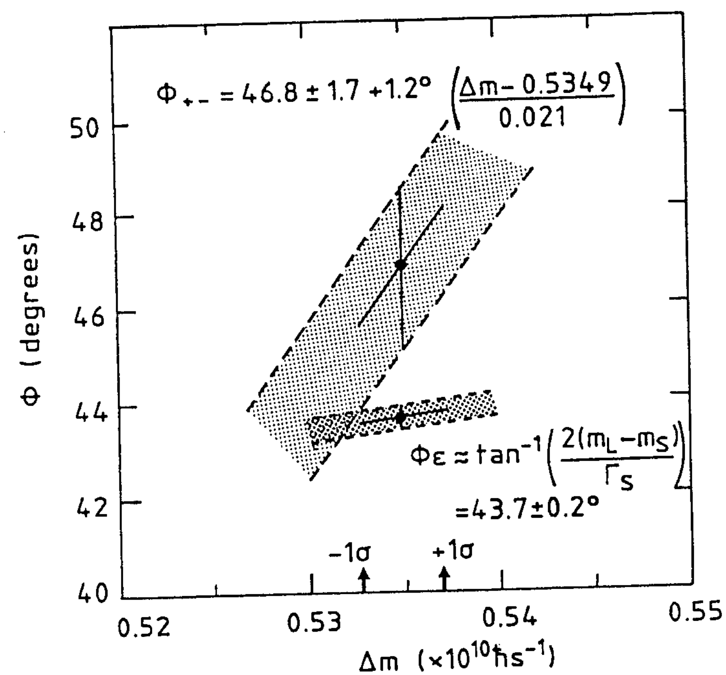

Figure 18: Dependence of the charged phase value on the mass difference.

This leads to the following manner of displaying the results of the phase measurement :

$$\Delta\phi \;= \left(0.3^\circ \;+ \sigma_{ext}(\Delta\phi)\right) \;\pm 2.6^\circ \pm 1.1^\circ \pm 0.2^\circ$$

$$\phi_{00} \;= \left(47.1^\circ + \sigma_{ext}(\phi_{00})\right) \;\pm 2.1^\circ \pm 1.0^\circ \pm 1.3^\circ$$

$$\phi_{+-} = \left(46.8^\circ + \sigma_{ext}(\phi_{+-})\right) \pm 1.4^\circ \pm 0.6^\circ \pm 1.4^\circ$$

Conclusion

The measurement of the NA31 group has substantially improved the precision of our knowledge about the values of the phases ϕ_{00} and the phase difference $\Delta\phi$ in the neutral kaon system. And the result is consistent with the conservation of CPT.

My personal thanks to Dr. V. Gibson and Prof. H.G. Sander.

REFERENCES

1) G.D. Barr, R. Carosi, P. Clarke, D. Coward, D. Cundy, N. Doble, L. Gatignon, V. Gibson, P. Grafström, R. Hagelberg, G. Kesseler, J. van der Lans, H.N. Nelson, H. Wahl (CERN); R. Black, D.J. Candlin, J. Muir, K.J. Peach (Edinburgh); H. Blümer, R. Heinz, M. Kasemann, K. Kleinknecht, P. Mayer, B. Panzer, B. Renk, H. Rohrer (Mainz); E. Augé, R.L. Chase, D. Fournier, P. Heusse, L. Iconomidou-Fayard, I. Harrus, A.M. Lutz, H.G. Sander, A.C. Schaffer (Orsay); L. Bertanza, A. Bigi, P. Calafiura, M. Calvetti, R. Casali, C. Cerri, G. Gargani, I. Mannelli, A. Nappi, G.M. Pierazzini (Pisa); C. Becker, H. Burkhardt, M. Holder, A. Kreutz, G. Quast, M. Rost, W. Weihs, R. Wertenbach, G. Zech (Siegen).

2) M. Kobayashi and K. Maskawa, Prog. Theor. Phys. **49** (1973) 652.

3) J. Ellis, M.K. Gaillard and D.V. Nanopolous, Nuc. Phys. **B109** (1976) 213.

4) G. Lüders, Ann. Phys. **2** (1957) 1.

5) W. Pauli, 'Niels Bohr and the Development of Physics', Pergamon Press (1955).

6) J.H. Christenson et al., Phys. Rev. Lett. **13** (1964) 138.

7) H. Burkhardt et al., Phys. Lett. **B206** (1988) 169.

8) Particle Data Group, Phys. Lett. **B204** (1988) 1.

9) J.H. Christenson et al., Phys. Rev. Lett. **43** (1979) 1209.

10) P. Clarke et al., CERN/SPSC/86-6 (1986).

11) R. Black, University of Edinburgh thesis, RALT-074 (1988).

12) P. Calafiura, INFN Pisa thesis, (1989).

13) B. Panzer, University of Mainz thesis, (1989).

14) M. Clément et al., SPS/EBS/Note 87-1 (1987).

15) H. Burkhardt et al., Nuc. Inst. Methods **A268** (1988) 116.

16) H.W. Atherton et al., CERN Report, CERN 80-07.

17) T.D. Lee and C.S. Wu, Ann. Rev. of Nuc. Sci. **16** (1966) 511.

18) V.V. Barmin et al., Nuc. Phys. **B247** (1984) 293.

A RECENT RESULT ON CP VIOLATION BY E731 AT FERMILAB

Hitoshi Yamamoto

Enrico Fermi Institute, The University of Chicago
Chicago, Illinois 60637

ABSTRACT

A measurement of the direct CP violation parameter Re(ε'/ε) by the E731 collaboration at Fermilab is reported. The technique that utilizes a double K_L beam is described and associated systematic errors are discussed.

Current members of the E731 collaboration are: A. Barker, R. Briere, L. Gibbons, G. Makoff, V. Papadimitriou, J. R. Patterson, S. Somalwar, Y. Wah, B. Winstein, R. Winston, and H. Yamamoto from The University of Chicago; E. Swallow from Elmhurst College and The University of Chicago; G. Bock, R. Coleman, J. Enagonio, B. Hsiung, R. Stefanski, K. Stanfield, and T. Yamanaka from Fermilab; M. Karlsson, R. Tschirhart, and G. Gollin from Princeton University; P. Debu, B. Peyaud, R. Turlay, and B. Vallage from Saclay.

INTRODUCTION

Ever since it was discovered 25 years ago,[1] the manifestation of CP violation has been confined to the neutral kaon system. Furthermore, until recently, all the observable effects of CP violation have been able to be accounted for by CP contamination (parametrized by $\tilde{\varepsilon}$) in K_S and K_L states which are eigenstates of mass and decay rate:

$$\begin{cases} K_S = K_1 + \tilde{\varepsilon} K_2 \\ K_L = K_2 + \tilde{\varepsilon} K_1 \end{cases},$$

where $K_1(K_2)$ is a CP plus(minus) eigenstate. If there is no direct CP-violating transition $K_2(CP-) \to 2\pi(CP+)$, then decays of K_S or K_L to 2π occur only through its K_1 component. In such a case, the observable parameter $\eta = \mathrm{amp}(K_L \to 2\pi) / \mathrm{amp}(K_S \to 2\pi)$ would be equal to $\tilde{\varepsilon}$ independent of whether the final state is $\pi^+\pi^-$ or $2\pi^0$ (i.e., $\eta_{+-} = \eta_{00} = \tilde{\varepsilon}$), and the isospin structure of the final state would be the same for K_S and K_L; namely, $\omega_S = \omega_L$ where $\omega_{S,L} = \mathrm{amp}(K_{S,L} \to I=2) / \mathrm{amp}(K_{S,L} \to I=0)$ are the $\Delta I=1/2$ enhancement factors in K_S and K_L respectively. Quite generally (without assuming CPT), the parameters η_{+-} and η_{00} can be written as[2]

$$\begin{cases} \eta_{+-} = \varepsilon + \dfrac{\varepsilon'}{1+\omega_S/\sqrt{2}} \\ \eta_{00} = \varepsilon - \dfrac{2\varepsilon'}{1-\sqrt{2}\omega_S} \end{cases}$$

with

$$\frac{\varepsilon'}{\varepsilon} = \frac{1}{\sqrt{2}}(\omega_L - \omega_S) \propto \frac{\mathrm{amp}(K_2 \to I=2)}{\mathrm{amp}(K_1 \to I=2)} - \frac{\mathrm{amp}(K_2 \to I=0)}{\mathrm{amp}(K_1 \to I=0)}.$$

The quantity $\mathrm{amp}(K_2 \to I=i)/\mathrm{amp}(K_1 \to I=i)$ is a measure of direct CP violation in decay to isospin=i final state; thus, the following three statements are equivalent and signal existence of direct CP violation: (1) rate of direct CP violation (defined by the amplitude ratio above) in I=0 is different from that in I=2. (2) $\Delta I=1/2$ enhancement in $K_S \to 2\pi$ (ω_S) is different from that in $K_L \to 2\pi$ (ω_L). (3) η_{+-} is different from η_{00}. If CPT symmetry is assumed, then one can make the fourth statement (which is more widely known) equivalent to the above three: the phase of $\mathrm{amp}(K_0 \to I=0)$ is different from the phase of $\mathrm{amp}(K_0 \to I=2)$ after phase shifts due to final state interaction are taken out.

Often, the difference between η_{+-} and η_{00} is studied by the double ratio R of the two pion decay rate of the K_S and K_L:

$$R = \frac{\Gamma(K_L\to\pi^+\pi^-)/\Gamma(K_S\to\pi^+\pi^-)}{\Gamma(K_L\to\pi^0\pi^0)/\Gamma(K_S\to\pi^0\pi^0)} \approx 1 + 6\mathrm{Re}(\varepsilon'/\varepsilon).$$

The superweak model of CP violation[3] proposed by Wolfenstein predicts essentially no direct CP violations; thus $\mathrm{Re}(\varepsilon'/\varepsilon) = 0$. In the standard model, however, CP violation is caused by an irreducible complex phase in the quark mixing matrix[4] and predicts non-zero values of order 10^{-3} for $\mathrm{Re}(\varepsilon'/\varepsilon)$.

In 1988, the NA31 collaboration at CERN reported[5] a value of $\mathrm{Re}(\varepsilon'/\varepsilon)$ three standard deviations away from zero (0.0033 ± 0.0011) which corresponds to the double ratio R being 2% above unity. There, K_S decays and K_L decays were taken separately. In the following, we present a determination of $\mathrm{Re}(\varepsilon'/\varepsilon)$ by the E731 collaboration at Fermilab[6] based on a data set in which all four decay modes are taken simultaneously.

APPARATUS

Figure 1 shows the side view of E731 detector. A double K_L beam is generated by a 800 GeV proton beam striking a Be target with a horizontal targeting angle of 5 mrad. The neutron flux reaching the detector is approximately the same as that for kaons and posed no problems. K_S is coherently generated by a B_4C regenerator placed at z = 123 m (z is the distance from the production target) in one of the beams which alternates between the two beams every spill (every minute) in

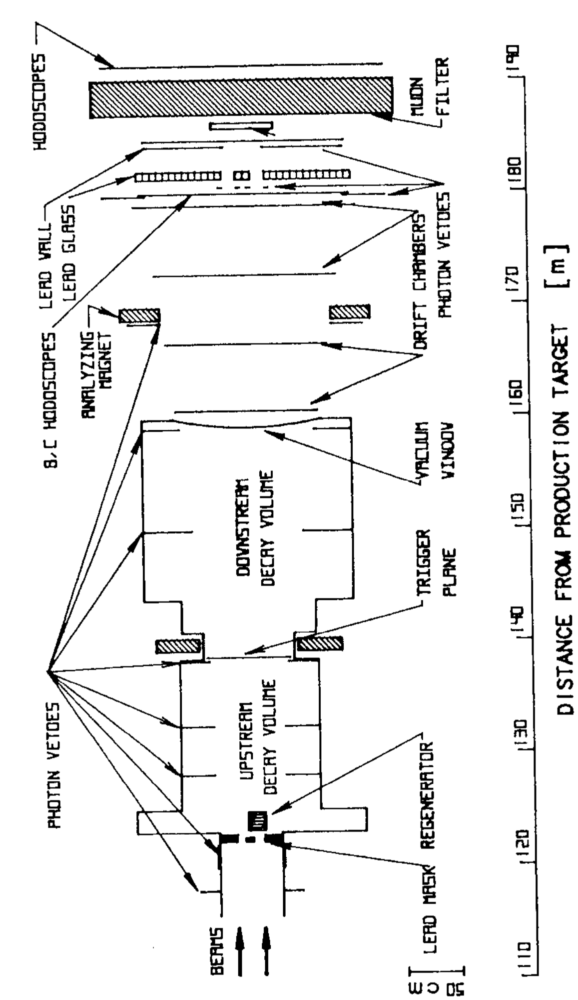

Figure 1. Side view of E731 detector.

order to symmetrize the beam fluxes and acceptances of K_S and K_L decays. The regenerator is implemented with four layers of scintillators to detect and veto inelastic interactions in order to suppress incoherently generated K_S. Also, a 1/2 inch thick piece of lead is placed just upstream of the last layer of the scintillators in order to sharply define the upstream edge of K_S decay region for the neutral mode as well as for the charged mode. The transverse shape of beams are defined by a two-hole beam dump that immediately follows the target and two sets of movable collimators. Actual beam profiles are well reproduced by adjusting the configuration of these components as used in the Monte Carlo simulation of the detector (Figure 2).

Neutral decays are reconstructed by a 804-block lead-glass array with photon energy resolution of $2.5 + 5/\sqrt{E(\mathrm{GeV})}\ \%$. The two beams pass the calorimeter through two holes (12 cm by 12 cm each). Charged tracks are detected and momentum-analyzed by a 200 MeV-kick magnet and 16 layers of drift chambers which are grouped into four sets. A typical single-hit position resolution was 100 microns which resulted in a typical single-track momentum resolution of 1% for $\pi^+\pi^-$ decays.

Eleven layers of photon veto counters are distributed along the apparatus to detect stray photons thereby reducing the background from $K_L \to 3\pi^0$ decays in the neutral mode. In the charged mode, a muon filter (3 m of steel) followed by a muon hodoscope is used to suppress the background from $K_L \to \pi\mu\nu$ decays.

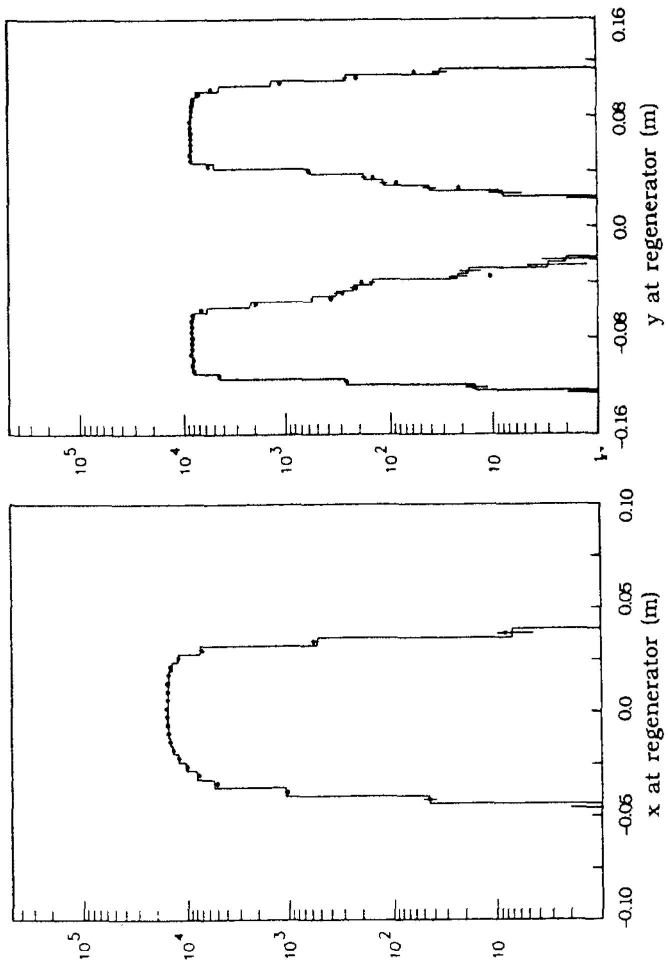

Figure 2. Beam profiles. The histograms are data and dots are the Monte Carlo. The parameter plotted is the transverse position of $K_S \to \pi^+\pi^-$ decay vertexes extrapolated back to the regenerator position.

The neutral mode trigger requires at least 30 GeV of energy deposit in the calorimeter and that four or six clusters are found by an online hardware cluster finder[7] which counts the number of groups of contiguous lead-glass blocks with more than 1 GeV energy deposit. The raw gain of each block was kept within 5% of each other so that the hardware cluster finder can directly process the raw pulse heights. The use of the hardware cluster finder was essential in enabling us to take data at a rate nearly 10 times higher than that of the previous run.[8] In addition, it is required that there be no hit in the trigger plane (see Figure 1) and some of the photon veto counters. Thus, $3\pi^0$ decays as well as $2\pi^0$ decays are accepted. The charged mode was triggered by any hits in the trigger plane and hits in the B,C hodoscopes consistent with 2 charged tracks. Also it was required that there be at least one drift chamber hits in both left and right sides of the second drift chamber set, and that there be no hit in the muon hodoscope. The accepted decay modes are then $\pi^+\pi^-$, $\pi^+\pi^-\pi^0$, and $\pi e\nu$.

DESIGN CONSIDERATIONS

If each decay mode is collected separately to form the double ratio R, then, one has to control the dead time caused by data acquisition and veto counters to an impossible accuracy: since the beam intensity invariably changes, the dead time caused by data acquisition can easily vary tens of percents, and the probability of accidental hits in veto counters also changes depending on the beam conditions and floating gains of counters. This can be solved by taking two modes each simultaneously: one in the denominator and the other in the numerator in forming R. Thus, one could take the two K_L modes simultaneously and the two K_S modes simultaneously; or, one can take the two charged modes simultaneously and the two neutral modes simultaneously. Either will work just as well in eliminating the dead time effects. Another important effect is due to efficiency/gain shifts in the calorimeter and drift chambers. For example, if some drift chamber wires are dead during $K_L \to \pi^+\pi^-$ data taking and not during $K_S \to \pi^+\pi^-$ data taking, then it will introduce a bias in R. This effect, however, cancels to the first order if, for each of the charged and neutral modes, K_S and K_L decays were taken simultaneously. Our entire data were taken in such manner; furthermore, in one-fourth of the data, all four modes were taken simultaneously, which has an added benefit of, among others, being able to use high-statistics charged mode events (such as electrons in $\pi e\nu$ mode) for neutral mode calibration and aperture surveys. About 80% of such data have been analyzed, and the result presented here is based on that portion of the data set.

EVENT RECONSTRUCTION AND BACKGROUND

A total of approximately 5000 tapes (6250 bpi) have been written, and the 20% reported here has been processed with the Fermilab Advanced Computer Project (ACP) system. In each of the charged and neutral modes, K_S decays and K_L decays are kept together throughout the data reduction chain; only in the final analysis job, each event is classified whether it originated from the regenerated beam (K_S) or the vacuum beam (K_L). This ensures that any loss of data due to damaged tapes etc. will not affect the result.

In the charged mode analysis, $\pi^+\pi^-$ decays were reconstructed by requiring two good tracks of opposite charges that originate from a common vertex, and forming an invariant mass assuming charged pion mass for the tracks. The tracking code was carefully designed to maximize the detection efficiency of genuine two track events including removal of out-of-time tracks using sum-of-time information of paired hits. The dead time in the drift time digitization was also studied in detail and implemented in the Monte Carlo simulation together with actual dead wires and plane-to-plane fluctuation of efficiency and resolution.

Figure 3 shows the reconstructed $\pi^+\pi^-$ invariant mass distributions for K_S and K_L. The mass resolution is about 3.5 MeV, and the signal region is defined to be ±14 MeV around the nominal kaon mass, which gives (after all cuts) 178803 K_S candidates and 43357 K_L candidates. There is virtually no background for K_S except for the lower-side tail which causes the discrepancy between the data (histogram) and the Monte Carlo (dots). The tail is due to the $\pi^+\pi^-\gamma$ radiative decay. For K_S, the gamma emission is completely dominated by internal bremsstrahlung

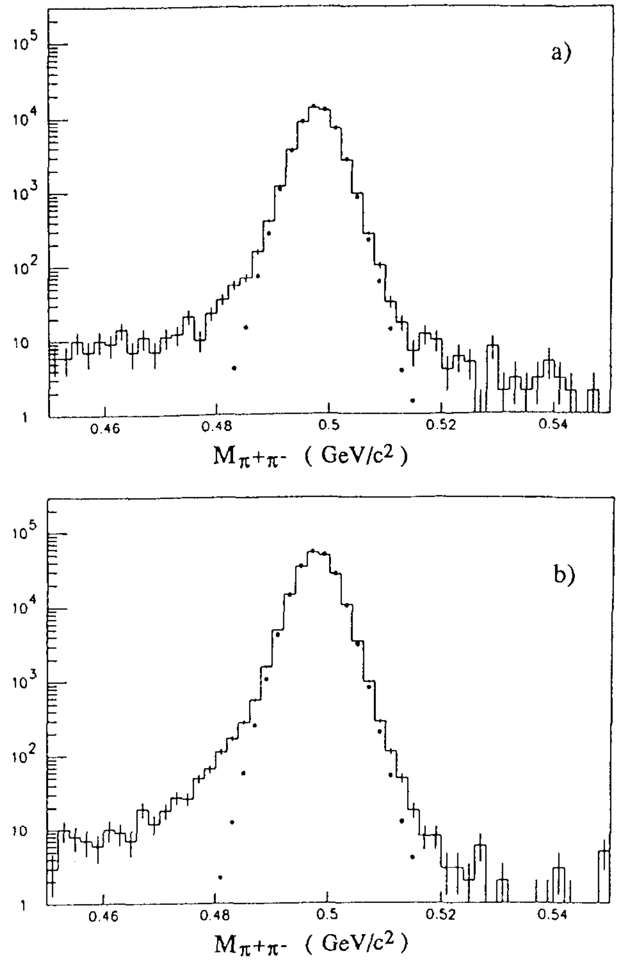

Figure 3. Reconstructed mass plots for K_L (a) and K_S (b) to $\pi^+\pi^-$. The data is shown by histogram and the Monte Carlo by dots.

with CP+ final state which is nothing but a soft radiative correction to the normal $K_S \to \pi^+\pi^-$ decay. For K_L, however,there is a substantial contribution from CP– final state as well as from CP+ final state. The latter is simply a soft radiative correction to the CP violating $K_L \to \pi^+\pi^-$ decay and has the same spectrum as for K_S, while the former has a much harder gamma energy spectrum. The CP– final states, which is present only for K_L, could in principle introduce bias in the double ratio. Owing to the good mass resolution, however, the CP– $\pi^+\pi^-\gamma$ contribution within the mass window is negligible, and the resulting bias is less than 2×10^{-4} in R.

Background due to $K_L \to \pi e \nu$ decays in $K_L \to \pi^+\pi^-$ sample is suppressed by requiring that the energy deposit in the calorimeter is less than expected for an electron of given track momentum. The residual background is seen in the mass side bands in Figure 3 b; this can be seen more clearly when plotted as a function of P_t^2 calculated at the regenerator[9] as shown in Figure 4 a. The peak at $P_t^2 = 0$ is the genuine $K_L \to \pi^+\pi^-$ decays and the $\pi e \nu$ background is estimated by extrapolating the distribution in $P_t^2 > 1000$ $(\mathrm{MeV/c})^2$ to the signal region of $P_t^2 < 250$ $(\mathrm{MeV/c})^2$ (solid line) and gives $(0.32\pm0.06)\%$. Background from $\pi\mu\nu$ decays are suppressed to an negligible level by vetoing on the muon hodoscope (momentum of each track was required to be greater than 7.5 GeV to ensure penetration by muons through the muon filter).

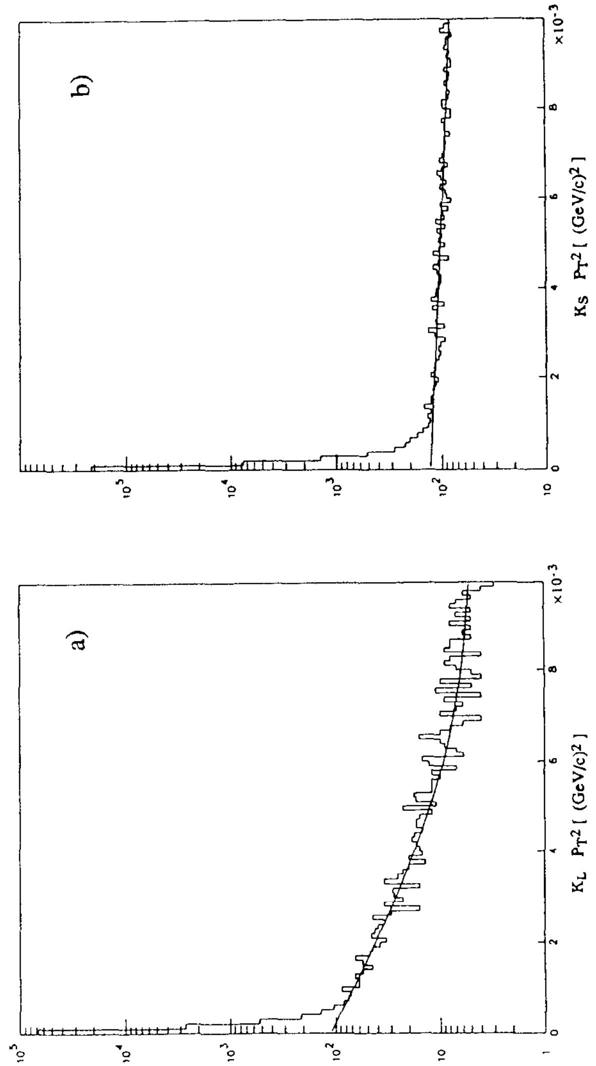

Figure 4. P_t^2 distributions for K_L (a) and K_S (b) to $\pi^+\pi^-$. The dotted lines show fits to the backgrounds.

The P_t^2 distribution for the regenerated beam is shown in Figure 4 b. In addition to the coherent peak at $P_t^2 = 0$, one can see a broad distribution due to K_S generated incoherently at the regenerator. The K_L beam passing through the regenerator can produce K_S in three ways: 1) by coherent regeneration which is well understood and is the part we use in this analysis, 2) by diffractive regeneration, and 3) by inelastic interactions. The contribution from inelastic interactions is substantially reduced by vetoing on the scintillators implemented in the regenerator. Both of the incoherent backgrounds (2 and 3 above) have almost flat P_t^2 distribution in the plot and the estimated incoherent contribution under the coherent peak is (0.13±0.01)%.

The neutral mode is reconstructed by combining four photon clusters in the calorimeter into two neutral pions. For each of the pion candidates, the longitudinal distance δz between the decay vertex and the calorimeter is given by

$$\delta z = d_{ij} \frac{\sqrt{E_i E_j}}{m_{\pi 0}},$$

where d_{ij} is the distance between the two clusters, E_i and E_j are energies of the two photons and $m_{\pi 0}$ is the nominal neutral pion mass. Out of three possible ways of pairing the four photons, the correct combination is the one for which the two pions have consistent decay vertexes. Once the longitudinal position of decay vertex is known, the kaon mass can be calculated by

$$m_K^2 = \frac{1}{\delta z^2} \sum_{i>j}^{4} E_i E_j d_{ij}^2.$$

In Figure 5 is shown the kaon mass distributions for the neutral modes. The signal region is defined to be within ±18 MeV around the nominal kaon mass, and the number of candidates is 201332 for K_S, and 52226 for K_L. The background seen in the side band for the K_L mass plot (Figure 5 a) is dominated by $3\pi^0$ decays for which two out of six photons are lost either by escaping the detector or by merging with other cluster in the calorimeter. In order to understand the shape of the background, a large amount of $3\pi^0$ decays have been fully simulated. The simulation employs a library of cluster patterns taken from real electron clusters and supplemented by an EGS simulation of electromagnetic showers.[10] The shape as well as amount of the background predicted by the simulation is shown by dots; the agreement is reasonable. The actual estimation of background is performed by normalizing the predicted shape in the side bands, giving (0.37±0.07)%. The corresponding mass distribution for the regenerated beam is shown in Figure 5 b. The non-kaon background for $K_S \to 2\pi^0$ is negligible.

Figure 6 shows the center of energy distribution at the calorimeter. For purpose of the plot, when the regenerator is in the top beam, the vertical axis is flipped so that the regenerated beam is always in the negative y region. Two beams are clearly separated; there are, however, decays of

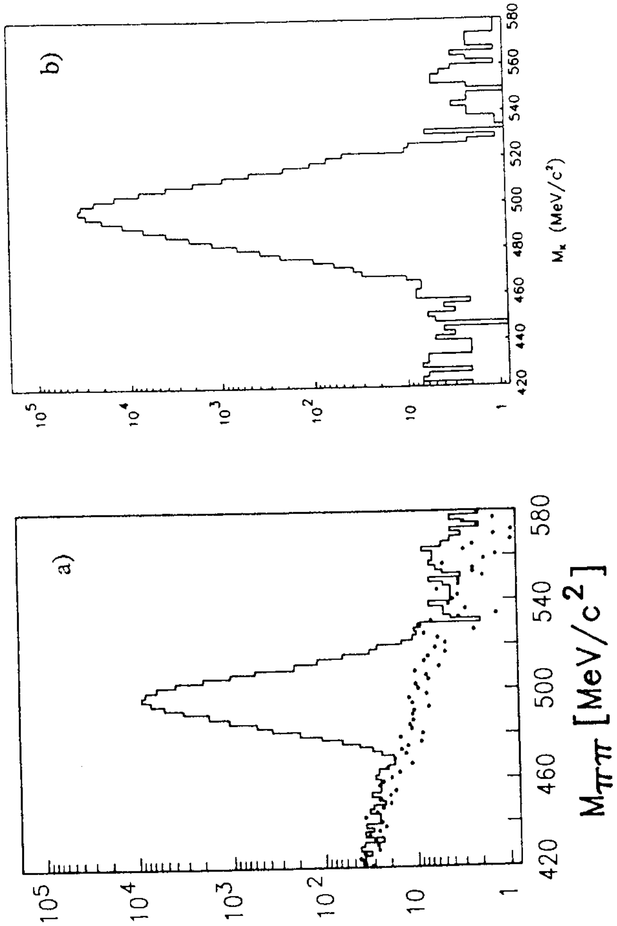

Figure 5. Distributions of $2\pi^0$ Invariant mass for K_L (a) and K_S (b). The Monte Carlo prediction background from $3\pi^0$ is shown by dots in (a). The amount is absolutely normalized.

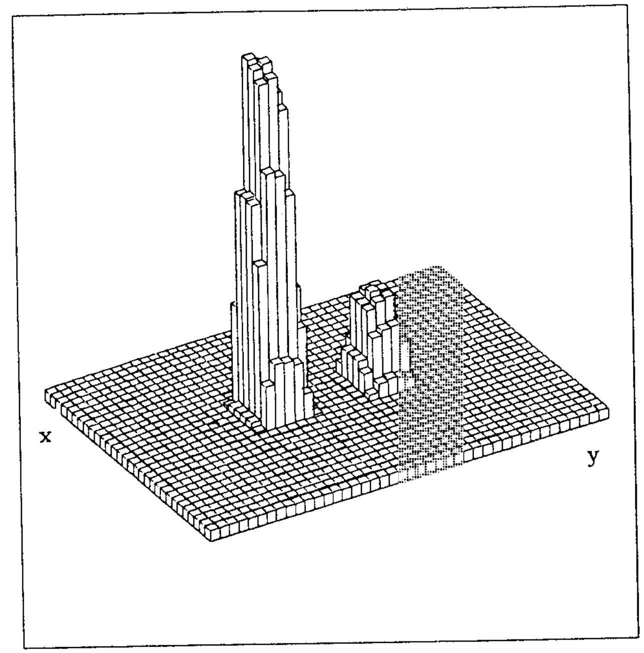

Figure 6. Center of energy distribution of $2\pi^0$ events at the calorimeter. The higher peak is K_S and the lower K_L. The region shown is 42 cm by 30 cm section of the calorimeter at the center.

K_S incoherently generated at the regenerator. Unlike the charged mode, it is not possible to trace the kaon direction back to the regenerator to find out which beam it originated; thus, there is a cross-over contribution from the regenerated beam to the vacuum beam due to the incoherently generated K_S. In order to estimate this background, we take equal-area concentric rings around the center of vacuum beam and plot the event density as a function of the ring number, which is simply the area in cm^2 inside the ring (Figure 7 a). Since the incoherently generated kaons are common to the charged and neutral modes, the P_t^2 distribution measured in the charged mode can be corrected for acceptance and then implemented in the neutral mode simulation. The dotted line shows the absolute prediction of the cross-over background by the simulation. The agreement is excellent; again, the final background is estimated by normalizing the predicted background shape in the incoherent region giving $(4.70\pm0.14)\%$. The incoherent contribution for K_S is estimated similarly by plotting the event density as a function of ring number around the regenerated beam (Figure 7 b). The absolute prediction of the simulation is quite good, and the estimated incoherent contribution for $K_S \to 2\pi^0$ is $(2.56\pm0.07)\%$.

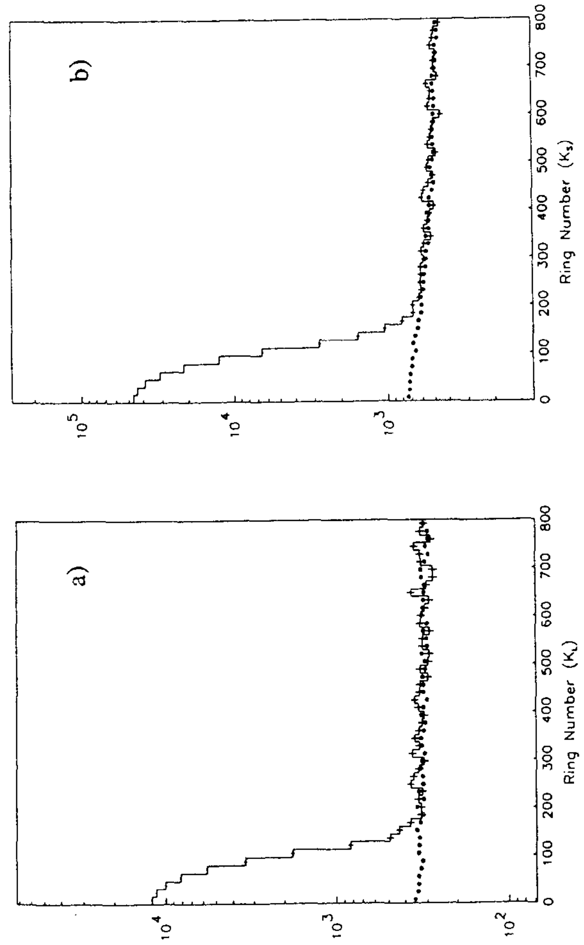

Figure 7. Distribution of $2\pi^0$ events plotted with respect to the 'ring number' (see text) around the K_L beam (a) and around the K_S beam (b).

ACCEPTANCE

The double beam method relies on the fact that the acceptance of a decay at a given longitudinal position is independent of which beam it occurs in. Alternating the regenerator between the beams ensures it to the first order; the higher order effects, however, could still remain. Thus, it is desirable that two beams be as close as possible. This makes it difficult to move the regenerator longitudinally to make the z distribution of K_S similar to that of K_L because K_L decays well upstream of the regenerator are obstructed by it. Furthermore, moving the regenerator longitudinally undermines the original purpose of simultaneously detecting K_S and K_L decays that occur at a same longitudinal position. With the regenerator at a fixed longitudinal position, however, the z distributions of K_S and that of K_L are different and thus it is important to understand the acceptance as a function of z position.

Figure 8 shows the z vertex distribution for $K_L \to \pi^+\pi^-$. The dots are Monte Carlo, and the ratio of data to Monte Carlo is shown in Figure 8 b. The agreement between data and Monte Carlo is good, and an error that would correspond to 2% shift in the double ratio is shown by a dotted line. Thus, if the acceptance error is linear in z (which is a good approximation locally), then 2% shift due to misunderstanding of the charged mode acceptance is comfortably ruled out. For extracting ε'/ε, we take events between z = 120 m (shown by the arrow) and 137 m. Corresponding plots for $K_S \to \pi^+\pi^-$ are shown in Figure 9. The sharp edge at the upstream end of the distribution is defined by the veto counter at the end of the regenerator. The vertex distribution for $K_L \to \pi^0\pi^0$ is shown in Figure 10. For this mode as well as for the charged mode, the suppression at the upstream end for the vacuum beam is due to a mask made of lead-scintillator sandwich which defines the aperture for

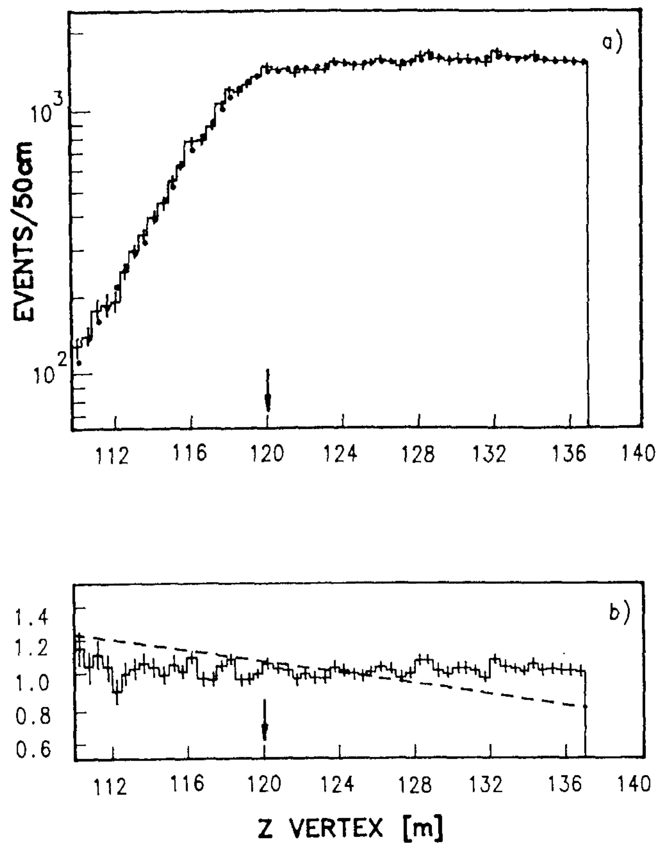

Figure 8. Distribution of z vertex for $K_L \to \pi^+\pi^-$ (a). Ratio of data to Monte Carlo is shown in (b). The arrow shows the upstream cut for the fiducial region.

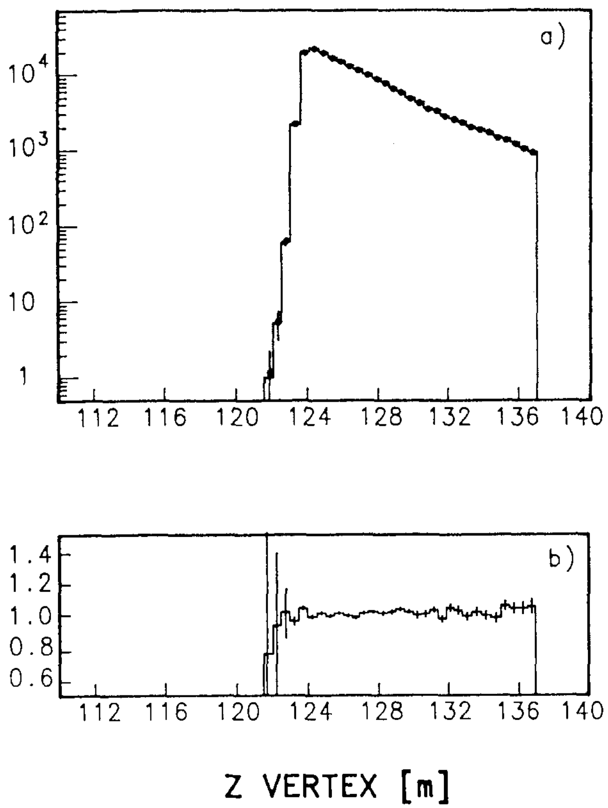

Figure 9. Distribution of z vertex for $K_S \to \pi^+\pi^-$ (a). Ratio of data to Monte Carlo is shown in (b).

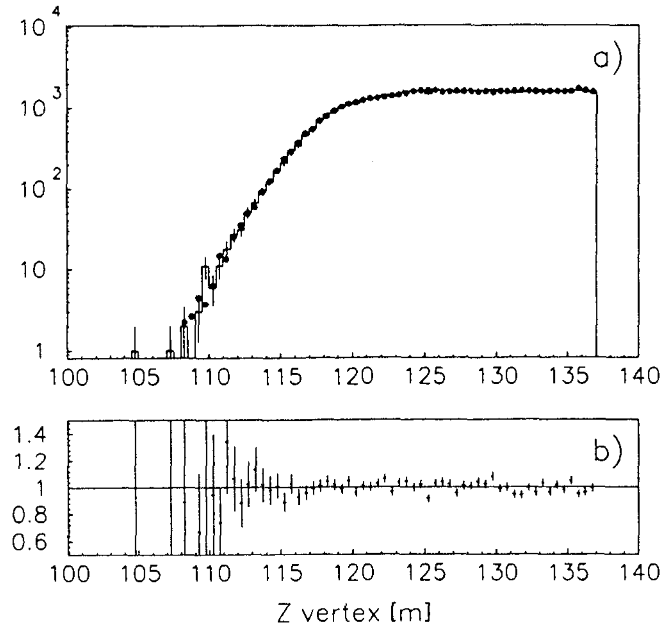

Figure 10. Distribution of z vertex for $K_L \to \pi^0\pi^0$ (a). Ratio of data to Monte Carlo is shown in (b).

photons as well as for charged particles. Another aperture-defining counter is located at the end of the decay region (z = 137.8 m); this and the active mask together with the drift chambers or the calorimeter define the geometrical acceptance of a given decay. That only a small number of fully active elements define the apertures facilitates the understanding of acceptances.

EXTRACTION OF $Re(\varepsilon'/\varepsilon)$

Downstream of the regenerator in the K_S beam, there is a transmitted component of K_L as well as the regenerated K_S, whose amplitude is the coherent regeneration amplitude ρ times the transmitted K_L amplitude. For a given kaon momentum, the decay rate as a function of proper time t from the regenerator $I_R(t)$ is then given by

$$I_R(t) = af\,\left|\rho/\eta\,\exp(-t/\tau_S + i\Delta m t) + 1\right|^2, \tag{1}$$

while the corresponding function for the vacuum beam $I_V(t)$ is flat:

$$I_V(t) = f \tag{2}$$

where τ_S is the K_S life time, Δm the K_L–K_S mass difference, and an approximation $\tau_L >> \tau_S$ is used. The parameter a is the relative attenuation of the K_L flux in the regenerated beam with respect to the vacuum beam flux f. The parameter f includes the partial decay rate of $K_L \to 2\pi$.

Typically, $|\rho/\eta|$ is of order 10; thus, the 2π decay yield is dominated by the K_S term and $R = 1 + 6Re(\varepsilon'/\varepsilon) \approx r^{+-}/r^{00}$, where r (+- for charged mode and 00 for neutral mode) is the yield ratio

$$r = \int_{t_1}^{t_2} I_V(t)dt \Big/ \int_{t_1}^{t_2} I_R(t)dt \tag{3}$$

within the fiducial region $t_1<t<t_2$ corresponding to 120 m $< z <$ 137 m for the given momentum. This approximation is sufficient in estimating systematic errors; in the actual fit, however, the full formulae are used (and without the approximation $\tau_L >> \tau_S$).

In each kaon momentum bin, ρ/η can be calculated from Equations (1) through (3). In order to derive a quantity that does not depend on geometric factor due to the finite thickness of regenerator, ρ is converted to $(f-\bar{f})/k$, difference of forward scattering amplitudes of K^0 and $\bar{K}^0$, by

$$\rho = \pi i N L \frac{1-e^{-x}}{x}\,\frac{f-\bar{f}}{k}, \quad \text{with} \quad x = \left(\frac{1}{2} - i\frac{\Delta m}{\Gamma_S}\right)\frac{L}{\Lambda_S},$$

where N is the density of scatterers, L the length of the regenerator, and Λ_S the K_S decay length. Assuming $\eta^{+-} = \eta^{00}$ = the world average,[13] Figure 11 shows $(f-\bar{f})/k$ as a function of kaon momentum for both charged and neutral mode. If Re(ε'/ε) is positive, then it will result in $(f-\bar{f})/k$ for the charged mode being smaller than that for the neutral mode by $1-3$Re(ε'/ε). The consistency between the charged and neutral mode indicates that Re(ε'/ε) is close to zero. Also, there is no indication of momentum dependence of Re(ε'/ε).

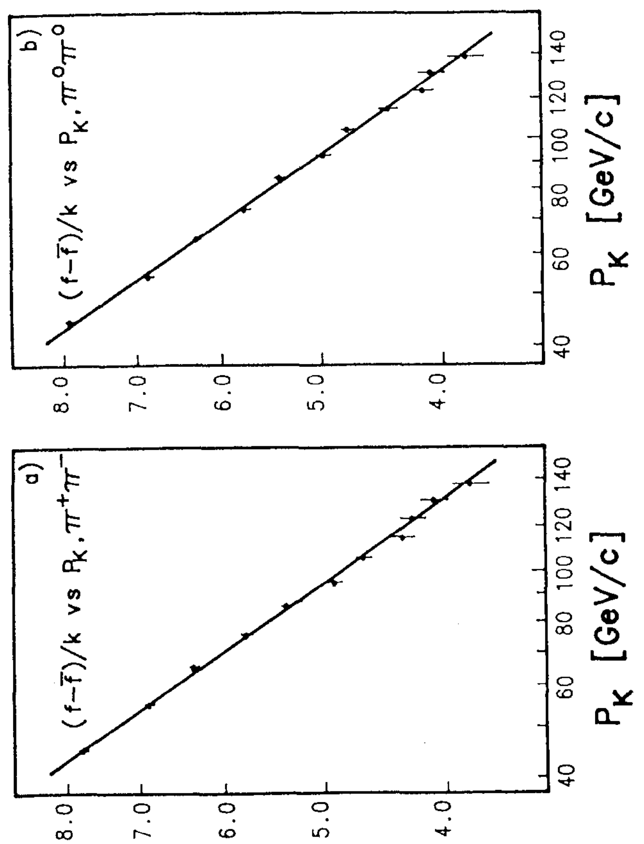

Figure 11. Forward scattering amplitude difference $(f-\bar{f})/k$ as a function of kaon momentum for the charged mode (a) and the neutral mode (b). It is assumed that $\eta^{+-} = \eta^{00}$.

In order to combine all the momentum bins, we use the fact that the momentum dependence of $(f-\bar{f})/k$ follows a power law $P^{-\alpha}$ (as seen in Figure 11) which is expected from a single Regge pole exchange model. These assumptions are well supported by experiments;[11] the use of them, however, is a matter of consistency check rather than of essence, and results are not affected when these assumptions are not made; namely, if one calculates Re(ε'/ε) in each momentum bin and statistically average them to obtain a final Re(ε'/ε) value, the result is consistent with that of the above method. When the power law coefficient α is fit separately for the charged and neutral modes, the result is 0.602 ± 0.010 (0.605 ± 0.010) with χ^2 of 11.5 (10.7) for 9 degrees of freedom for the charged (neutral) mode. The two values are consistent with each other and also with previous measurements.[12] The parameters of final fit are: α the power law coefficient of $(f-\bar{f})/k$, absolute value of $(f-\bar{f})/k$ at a reference momentum (70 GeV), and Re(ε'/ε). The values for τ_S, Δm,and η^{+-} are fixed to the world average.[13] The result is Re(ε'/ε) = -0.0004 ± 0.0014, where the error is statistical only.

SYSTEMATICS

Possible sources of systematic error are: 1) backgrounds, 2) energy scale/resolution, 3) acceptance, and 4) rate effects. They will be discussed in order.

The relevant backgrounds have been discussed already. The errors are due partly to statistics of background fits and partly to uncertainties of background shapes, with both sources contributing comparable amounts. The statistical parts can clearly be added in quadrature, while the parts due to uncertainties in background shapes tend to cancel in forming the double ratio. For example, main uncertainty in the shapes of two largest backgrounds, the incoherent backgrounds in the neutral mode, is the shape of the background under the coherent signal; if the geometry around the holes of the calorimeter is not simulated correctly then the amount of background can be biased. The bias, however, will affect K_S and K_L by the same amount to the first order, thus resulting in a unbiased value of R. To be conservative, we will add the background errors in quadrature to get 0.18% systematic error in R.

The energy scale for the charged mode is determined by masses of reconstructed $K^0 \rightarrow \pi^+\pi^-$ and $\Lambda \rightarrow p\pi^-$ decays. The accuracy is good enough not to cause any problems.

Calibration of the lead glass calorimeter for the neutral mode is a critical element of the analysis. The block-to-block gain variation is determined by special calibration runs where electron-positron pairs that are created upstream of the detector are steered by two magnets in the detector (the separator magnet and the analyzing magnet) to illuminate the entire surface of the calorimeter. Figure 12 shows E/P distribution for 1.3 million electrons used in the calibration, where E is the energy deposit in the calorimeter and P is the track momentum. The overall energy scale was then adjusted by about 0.5% so that the upstream edge of $K_S \rightarrow \pi^0\pi^0$ decays lines up with the nominal position of the regenerator (Figure 13). The residual uncertainty is 0.1%. The fiducial region of z vertex was chosen such that when the energy scale is slightly off, the total number of events in the region does not vary much. Figure 14 shows the effect of changing the energy scale in the analysis. The behavior of the data and that of the Monte Carlo are consistent and the uncertainty in the double ratio due to the energy scale error of 0.1% is 0.03%. The analysis, however, is sensitive to the uncertainty in resolution. The resolution is studied by the width of $\pi^0\pi^0$ invariant mass distributions and how well the z vertexes of two pions match when each photon pair is constrained to have π^0 mass, and lead to an 0.2% uncertainty in the double ratio.

The vertex distributions of 2π modes for data and Monte Carlo as shown in Figures 8 through 10 gives a measure of our understanding of acceptance as a function of z vertex. More sensitive check of acceptance, however, can be made using high statistics decay modes taken together with 2π modes; namely, 10 million $\pi e\nu$ events for the charged mode and

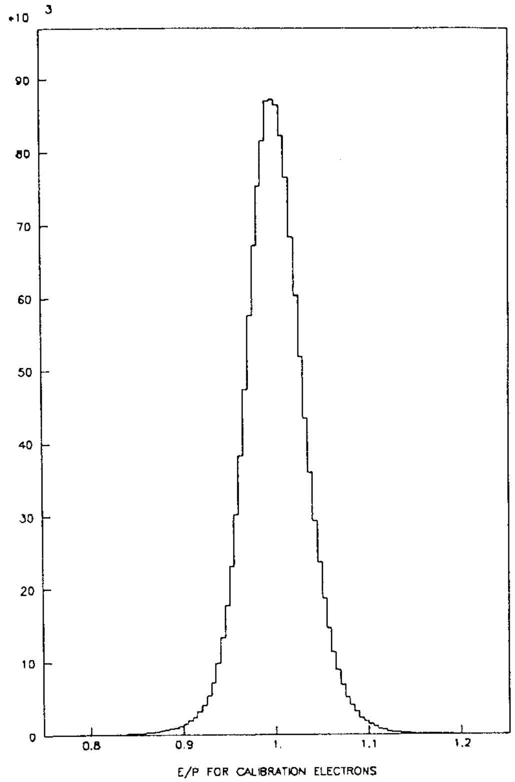

Figure 12. E/P distribution for electrons collected during a special calibration run.

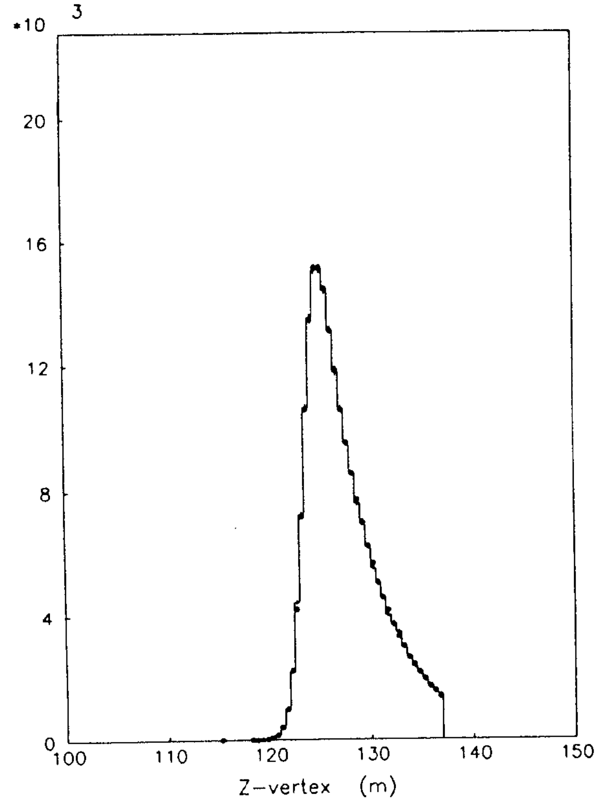

Figure 13. Decay vertex distribution for $K_S \rightarrow \pi^0\pi^0$. The sharp upstream edge of the distribution is used to determine the energy scale in the neutral mode.

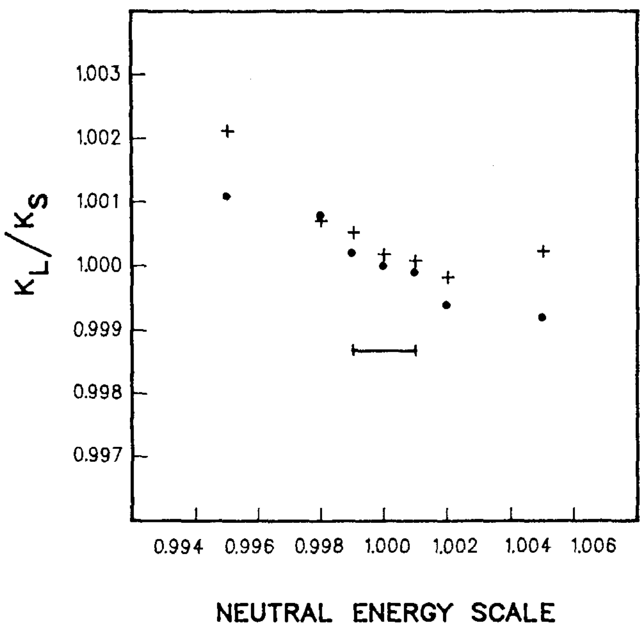

Figure 14. Effect of changing the neutral mode energy scale on the ratio K_L/K_S. The vertical scale is normalized to 1.0 at no energy scale change. The data is shown by pluses and the Monte Carlo by dots.

6 million $3\pi^0$ events for the neutral mode. Figure 15 shows the data and Monte Carlo comparison for the $\pi e\nu$ mode. The agreement is reasonably good within the fiducial region of 120 m < z < 137 m. The vertex distributions for the $3\pi^0$ are shown in Figure 16. Note that it shows the distribution down to z = 150 m; the agreement is good in the entire region shown. Acceptance uncertainty allowed in these high statistics modes is translated to uncertainty in R of 0.08%.

When the K_L-K_L yield ratio r (Equation 3) is calculated in small vertex bins as well as in kaon momentum bins, the uncertainty in acceptance cancels out, eliminating the need for acceptance corrections. The result is consistent with the standard fit, even though the systematic error due to resolution uncertainty increased, giving 0.2% uncertainty in R. We have also varied apertures, beam shapes, efficiencies of drift chambers, but the result is found to be insensitive to these changes. Combining all the above, we assign 0.25% systematic error in R due to acceptance.

An otherwise good event can be lost when accidental extra hits overlap with it. The ways they are lost can be divided into two categories: First, the accidental hit does not directly interact with the signal event. An accidental hit in a veto counter that kills the event belongs to this category. The probability that a given event is lost in this manner is independent of whether it is K_L or K_S, thus, it does not affect the double ratio. Second, the accidental hit interacts with the signal resulting in a loss of the event. An accidental hit in the calorimeter that overlaps with

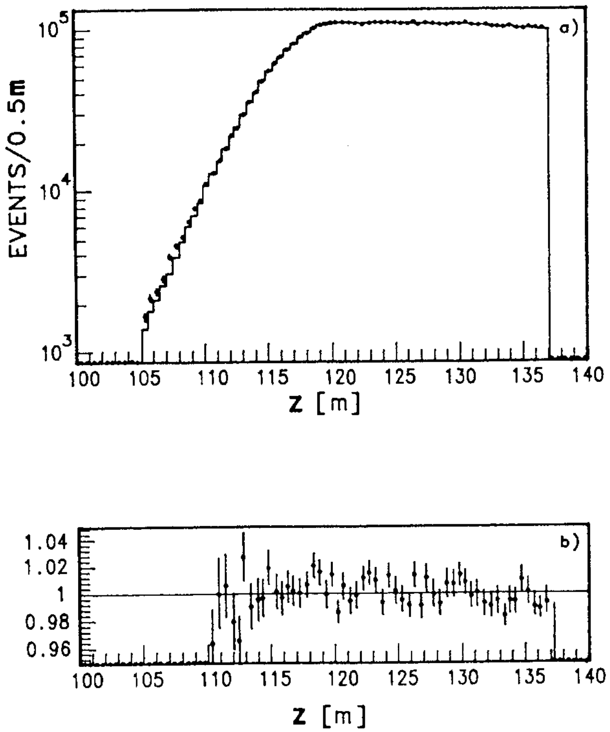

Figure 15. The vertex distribution of $\pi e \nu$ mode. A high statistics check of charged mode acceptance.

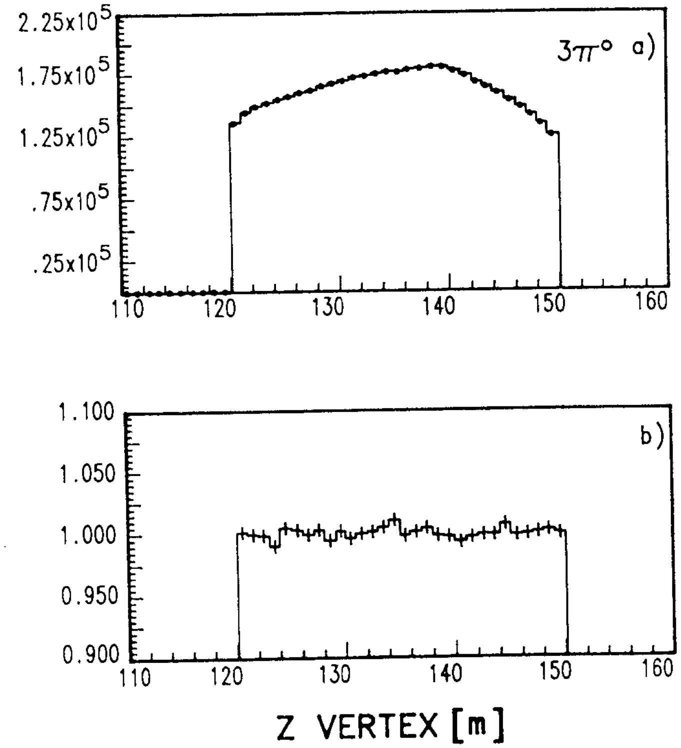

Figure 16. The vertex distribution of $3\pi^0$ mode, A high statistics check of neutral mode acceptance.

one of the photons from a kaon decay belongs to this category. This has a potential of coupling to slight topology differences between K_L and K_S biasing the double ratio.

In order to study such bias, a category of events have been taken simultaneously with the rest of the data which are triggered by a muon telescope pointing toward the proton target. The events triggered this way correctly represent the extra hits overlapping good kaon events including the effect of bunch-to-bunch intensity fluctuations. These 'accidental' events have on average 0.027 clusters in the calorimeter and 8.5 chamber hits. They are overlaid on Monte Carlo events to find out if there is any asymmetric loss between K_L and K_S. In overlaying chamber hits, idiosyncrasies of digitization electronics (dead time etc.) are correctly taken into account. The loss is about 3% for each of the four modes, and there is no bias observed beyond statistical uncertainty of 0.07%.

Figure 17a showsraw K_S-K_L yield ratios for the charged and neutral modes as a function of time, and beam intensity is plotted in Figure 17 b. The intensity varies with time considerably, but the yield ratio is consistent with being constant for both modes. As a final check, value of $Re(\varepsilon'/\varepsilon)$ as a function of beam intensity is shown in Figure 18. The beam intensity is monitored by muon rate which is a good measure of intensity of the beam hitting the target. The plot shows no indication of rate

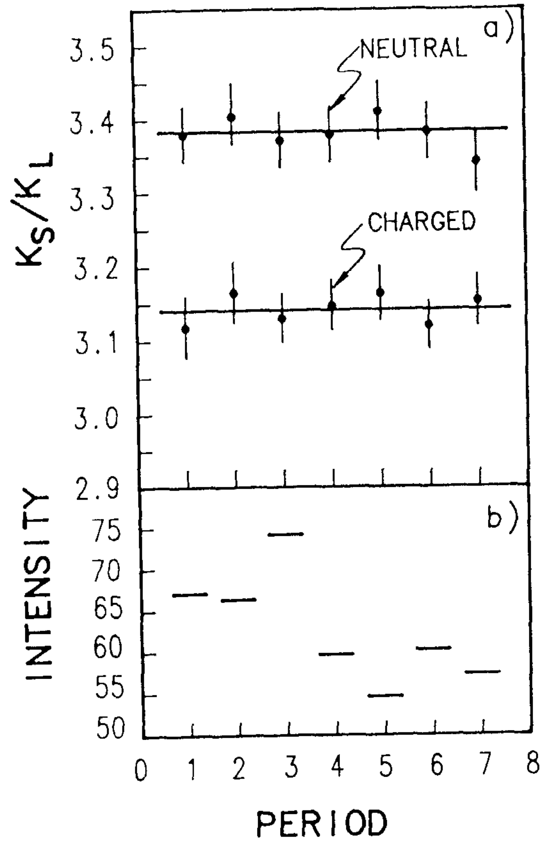

Figure 17. Raw ratio K_S/K_L with respect to time (20% of the whole data) for the neutral and charged mode (a). The beam intensity variation is shown in (b).

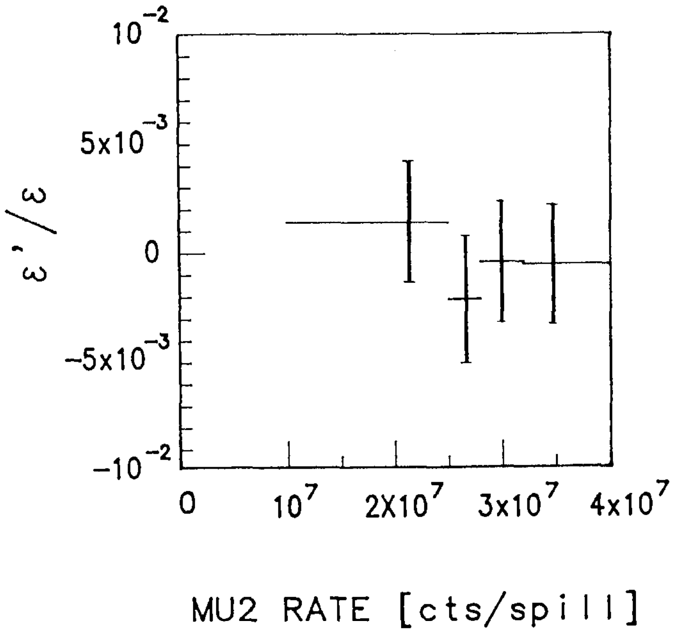

Figure 18. Re(ε'/ε) as a function of beam intensity (monitored by a muon counter rate).

dependence of the result. From the above studies, we set a systematic error of 0.10% in R due to accidental overlaps.

Error due to uncertainties in the fixed parameters of the fit, τ_S, Δm and η^{+-}, is small. On the other hand, as a self consistency check, we can fit for τ_S and Δm in the same analysis using small vertex bins to make the fit sensitive to the functional shape of vertex distribution. The fitted results for τ_S are 0.8909 ± 0.0063 (10^{-10} sec) for the charged mode and 0.8940 ± 0.0061 (10^{-10} sec) for the neutral mode, which are consistent with each other and with the world average of 0.8923 ± 0.0023 (10^{-10} sec). For Δm, we obtain 0.524 ± 0.018 (10^{10} sec^{-1}) for the charged mode and 0.524 ± 0.018 (10^{10} sec^{-1}) for the neutral mode,which can be compared with the world average of 0.535 ± 0.002 (10^{10} sec^{-1}).

CONCLUSION

Table 1 summarizes the systematic errors. The final result is then $\mathrm{Re}(\varepsilon'/\varepsilon) = -0.0004 \pm 0.0014 \pm 0.0006$ where the first error is statistical and the second systematic. Study of systematic errors are facilitated by taking all of the four 2π decay modes simultaneously and by high statistics modes such as $\pi e\nu$ and $3\pi^0$ modes which have also been taken at the same time. Our result is consistent with zero and thus with the superweak model, and does not confirm the NA31 result. The standard model, however, is not inconsistent with our result particularly with a rather high top quark mass.[14] With the whole data set analyzed, the

Table 1 Systematic Errors

source	(%)
backgrounds	0.18
acceptance	0.25
energy scale/resolution	0.20
accidental overlap	0.10
total	0.38

statistical error is expected to reduce to 0.0006 with a comparable or less systematic error.

REFERENCES

[1] J. H. Christenson, J. W. Cronin, V. L. Fitch, and R. Turlay, Phys. Rev. Lett **13** (1964) 138.

[2] The parameter ε in the expression is defined by amp($K_L \to I=0$)/amp($K_S \to I=0$) and not identical to $\tilde{\varepsilon}$ in general. They are related by $\varepsilon = \tilde{\varepsilon}$ + amp($K_2 \to I=0$) /amp($K_1 \to I=0$) (they are identical if there is no direct CP violation).

3 L. Wolfenstein, Phys. Rev. Lett. **13** (1964) 569.

[4] M. Kobayashi and T. Masukawa, Prog. Theor. Phys. **49** (1973) 652.

[5] H. Burkhardt *et al*, Phys. Lett. **B206** (1964) 569.

[6] J. R. Patterson *et al.*, submitted to Phys. Rev. Lett. For a detailed description of the analysis see: PhD thesis, J. R. Patterson, University of Chicago, 1990 (unpublished). The number of Re(ε'/ε) was not presented in the actual talk; it was announced two weeks later at Fermilab.

[7] H. Sanders *et al.*, IEEE Trans. Nucl. Sci. **36** (1988) 358.

[8] M. Woods *et al.*, Phys. Rev. Lett. **60** (1988) 1695.

[9] Even though there is no regenerator in the K_L beam, P_t^2 is calculated in the same way as in the regenerated beam; namely, by tracing the decay vertex back to the longitudinal position of the regenerator and drawing a line from there to the target.

[10] W. R. Nelson, H. Hirayama, D. W. O. Rogers, SLAC-Report-265 (1985).

[11] J. Roehrig *et al*, Phys. Rev. Lett. **38**, (1977) 1116.

[12] A. Gsponer *et al.*,Phys. Rev. Lett. **42**, (1979) 13.

[13] Particle Data Group, G. P. Yost *et al.*,Phys. Lett.,**B204**, (1988) 1.

[14] For example, see: J. M. Flynn and L. Randall, University of California Berkeley preprint UCB-PTH-89-3, to be published.

RARE KAON DECAY EXPERIMENTS*

Douglas Bryman
TRIUMF, 4004 Wesbrook Mall, Vancouver, B.C., Canada V6T 2A3

The status of new sensitive experiments searching for rare kaon decays is reviewed. Extensive experimental work on rare kaon decays is currently being performed at BNL, KEK and FNAL to search for exotic physics and to examine standard model predictions in great detail. Major advances spanning orders of magnitude are in progress in efforts to study allowed processes like $K^+ \to \pi^+\nu\overline{\nu}$ and $K_L^0 \to \mu\mu$. New insights into the origin of CP violation are being sought by studying $K_L^0 \to \pi^0 e^+ e^-$. Evidence for new particles and new interactions could appear in searches for $K^+ \to \pi^+ x$ where x represents a hypothetical neutral particle or system of neutral particles and in searches for lepton flavor violating processes $K_L^0 \to \mu e$ and $K^+ \to \pi^+ \mu e$.

1. Introduction

Rare decays of mesons and leptons play a significant role in challenging the standard model and in searching for effects which could indicate new directions. Kaon decays have been a rich and often surprising source of information at every stage in the development of the present picture of fundamental particles and their interactions. Parity violation, CP violation, neutral currents and the existence of charm are all effects in which kaon decays exhibited crucial or unique features. Kaon decays remain in the forefront of modern high precision attempts to test the accuracy of standard model predictions, to define the nature of CP violation, and to search for neutral flavor changing currents and lepton flavor violation (LFV) among other new interactions and particles. In this lecture, the latest results from the present round of rare kaon decay experiments at BNL and KEK will be discussed. For recent reviews of rare kaon decays see Refs. 1 and 2.

2. $K^+ \to \pi^+\nu\overline{\nu}$

Reactions which are allowed in the standard model can provide important, detailed information, and can also herald the presence of new effects. The process $K^+ \to \pi^+\nu\overline{\nu}$ offers a prime example of the unique opportunities available

*Sections of this paper were adapted from "Particle Physics Prospects at the KAON Factory", presented by D. Bryman at the International Meeting on Physics at KAON, Bad Honnef, W. Germany, June 1989, and from "Rare Kaon Decays", Douglas A. Bryman, Int. J. Mod. Phys. A 4, 79 (1989).

in the study of rare kaon decays because a reliable higher-order calculation assuming three generations can be confronted by experiment. Nonconformity with the standard model prediction could imply new physics in the form of extra generations or entirely new types of particles or interactions. The rate for $K^+ \to \pi^+\nu\bar{\nu}$ depends on parameters of the Cabbibo-Kobayashi-Maskawa (CKM) matrix as evidenced by the diagrams in Fig. 1. Constraints on the CKM mixing parameters $V_{ts}^*V_{td}$ have been derived from semileptonic B-meson decays, from the measured b-quark lifetime and from the large observed B_d^0-$\overline{B}_d^0$ mixing which, for example, fixes V_{td} (although with considerable uncertainty at present). The $K^+ \to \pi^+\nu\bar{\nu}$ branching ratio as a function of the t-quark mass with the dependence on uncertainties of B-meson decay observables lies in the region 1 to 7×10^{-10} for m_t in the range 50 to 200 GeV/c^2.[2] Ellis and Hagelin[3] calculated radiative QCD effects indicating that if the mixing angles and t-quark mass were known a firm prediction for the $K^+ \to \pi^+\nu\bar{\nu}$ branching ratio could be made. Conversely, a measurement of the branching ratio would be significant in constraining these parameters and would allow a direct test of higher order weak corrections in the standard model which is not significantly constrained by uncertain long distance effects[4] as in calculations of $K_L^0 \to \mu\mu$ and the $K_L^0 - K_S^0$ mass difference.

A precise standard model prediction for the $K^+ \to \pi^+\nu\bar{\nu}$ branching ratio allows the reaction to be used to search for new physics. The least exotic addition to the present picture would involve additional generations of quarks and leptons. Since experiments measuring $K^+ \to \pi^+\nu\bar{\nu}$ do not observe the weakly interacting decay products, it is possible that this reaction is accompanied by $K^+ \to \pi^+xx'$ or $K^+ \to \pi^+x$, which occur at comparable or even much higher rates. The window for exotic effects appearing unambiguously in the reaction $K^+ \to \pi^+xx'$ extends two orders of magnitude from the current limit $B(K^+ \to \pi^+xx') < 1.4 \times 10^{-7}$,[5*] to the upper level of the standard model value $B(K^+ \to \pi^+\nu\bar{\nu}) \sim 10^{-9}$. In supersymmetric theories a variety of new particles are hypothesized including the supersymmetric partners of the photon ($\tilde{\gamma}$), the Higgs particle ($\widetilde{H}$), the leptons and the quarks. These could contribute to the rate for $K^+ \to \pi^+xx'$, if the masses are sufficiently small. Schrock[6] estimated that if tree level graphs dominate in the decay $K^+ \to \pi^+\tilde{\gamma}\tilde{\gamma}$, then the branching ratio could be as large as 10^{-7}, near the current limit. Other possibilities for exotic reactions $K^+ \to \pi^+xx'$ and $K^+ \to \pi^+x$ involving scalar or pseudoscalar particles have been suggested. The Majoran (a massless Nambu-Goldstone boson), the axion, light Higgs particles, the familion and hyperphotons are all potential candidates for x above.

An experiment is now in progress at Brookhaven National Laboratory (BNL) to measure the process $K^+ \to \pi^+\nu\bar{\nu}$.[7] The apparatus for BNL E787, a BNL-

*All limits discussed in this paper will be at the 90% confidence level.

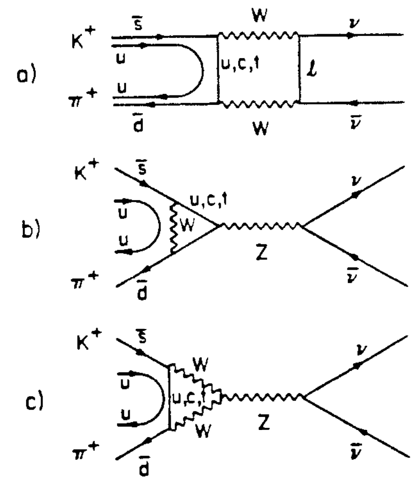

Fig. 1. Second-order weak diagrams for $K^+ \to \pi^+\nu\bar{\nu}$.

Princeton-TRIUMF collaboration, is pictured in Fig. 2. The E787 detector has a large geometrical acceptance (2π sr) for the $K^+ \to \pi^+\nu\bar{\nu}$ decay mode and has been designed to maximize the rejection of background processes such as $K^+ \to \pi^+\pi^0$ ($K_{\pi 2}$), $K^+ \to \mu^+\nu_\mu$ ($K_{\mu 2}$), $K^+ \to \mu^+\nu\gamma$, and others. Sensitivity for identification of unaccompanied pions from $K^+ \to \pi^+\nu\bar{\nu}$ is accomplished through measurements of momentum, kinetic energy, range, decay sequence $\pi \to \mu \to e$, and nearly 4π coverage for detection of photons. The 800 MeV/c K^+ beam is brought to rest in a 10 cm diameter target consisting of groupings of scintillating fibers 2 mm in diameter viewed by photomultiplier tubes. The decay pions pass through a cylindrical drift chamber which measures their momenta in a 1 T magnetic field. The pions then stop in a multi-layer plastic scintillator range stack which also contains multiwire proportional chambers. Each range stack counter (2 cm thick) is viewed from both ends by 5 cm diam phototubes read out by 500 MHz transient digitizers, so that the decay chain $\pi \to \mu \to e$ can be observed for particle identification. The total energy of the decay pions is measured by summing the pulse heights of the target and range array elements. The pion detector is completely surrounded by 12 to 15 radiation lengths of Pb-scintillator gamma veto (1 mm Pb, 5 mm scintillator). Figure 3(a) shows an example of a calibration event of the type $K^+ \to \pi^+\pi^0$. A blow-up of the target region is shown in Fig. 3(b). Energy and time for each target element are available at present from an ADC and a TDC, respectively, so that the incident kaon and outgoing pion elements can be identified. In Fig. 3(a) the momentum calculated from the track in the drift chamber is 198 MeV/c, determined with resolution $\sigma_p = 2.5\%$; the track energy is found by summing the range stack and target energies to be 97 MeV with a resolution of $\sigma_E = 3\%$ and the range is 31 gm/cm^2 with a resolution of $\sigma_R = 3\%$. Correlation of range, energy and momentum are used to verify that the particle is a pion. In addition, the $\pi \to \mu\nu$ decay pulse is observed using the transient digitizer (TD) in the last range stack counter hit as shown in Fig. 3(c). The energy and timing of the 4 MeV muon pulse can be obtained and checked for consistency of position using the two ends of the counter. The $\mu \to e\nu\nu$ decay is also observed with the TD during an inspection period of 5 μs. In this event, the two photons from π^0 decay are both observed. We have determined from data that the inefficiency of the photon veto system is $\bar{\epsilon}_{\pi 0} < 4 \times 10^{-6}$ for π^0's from $K_{\pi 2}$ which is consistent with expectations of Monte Carlo calculations.

The E787 experiment had a engineering run in 1988 and has just completed a 10-week run. From the 1988 exposure of 1.24×10^{10} kaon stops no candidate events were found in the accessible kinematic region above the $K_{\pi 2}$ peak which comprises approximately 17% of the available phase space for $K^+ \to \pi^+\nu\bar{\nu}$. With an overall acceptance of 0.0055 we obtain a new limit on the branching

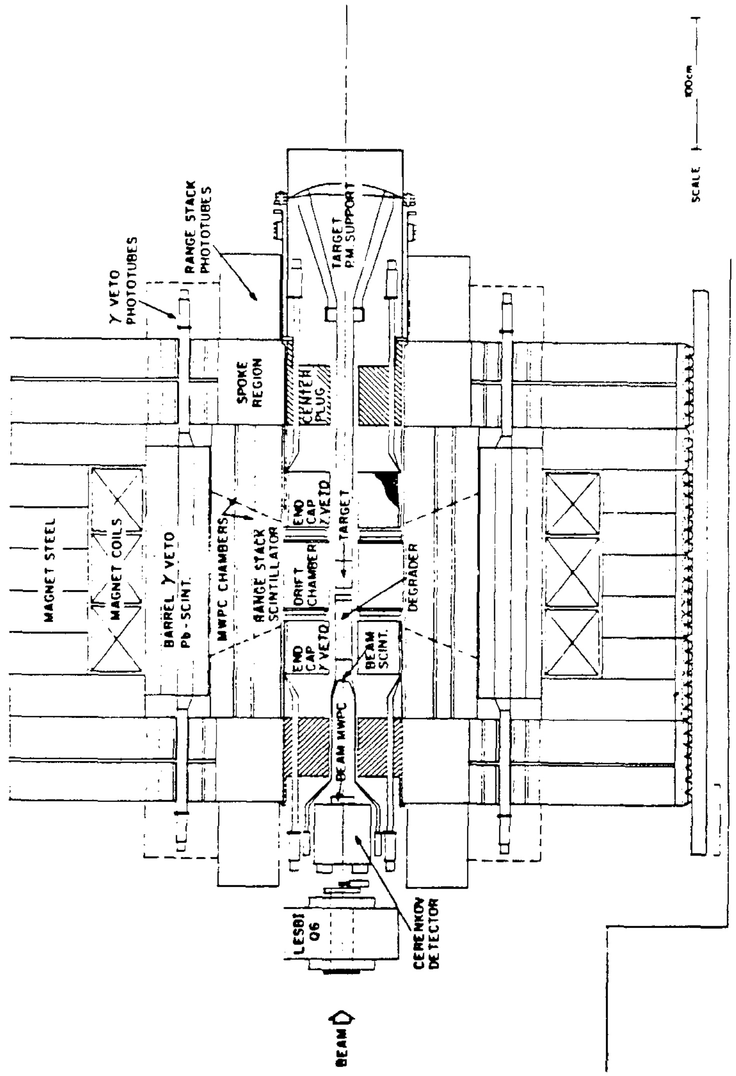

Fig. 2. Apparatus for BNL-787 measurement of $K^+ \to \pi^+\nu\bar{\nu}$.

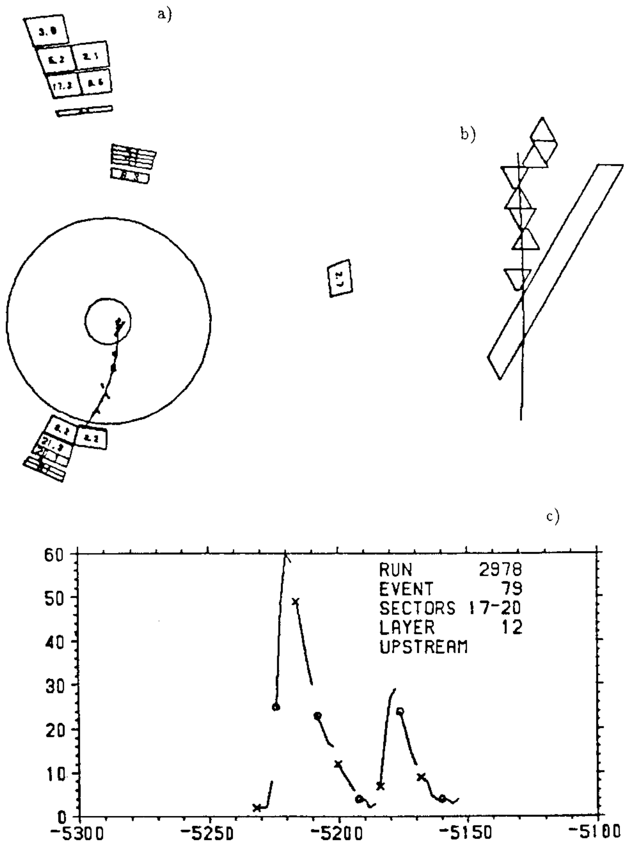

Fig. 3. $K^+ \to \pi^+\pi^0$ event in the BNL 787 detector (see text).

ratio for $K^+ \to \pi^+\nu\bar{\nu}$ (or $K^+ \to \pi^+ x x'$)

$$\frac{\Gamma(K^+ \to \pi^+\nu\bar{\nu})}{\Gamma(K^+ \to \text{all})} < 3.4 \times 10^{-8} \ .$$

For the hypothetical two-body decay $K^+ \to \pi^+ a$ the limit is

$$\frac{\Gamma(K^+ \to \pi^+ a)}{\Gamma(K^+ \to \text{all})} < 6.4 \times 10^{-9} \ ,$$

where a represents any light, non-interacting particle such as an axion or familon.

In addition to the primary search for processes like $K^+ \to \pi^+ x$, the 1988 data set from E787 was used to extract more sensitive limits on other processes including decays involving light Higgs particles[8] $K^+ \to \pi^+ H$; $H \to \mu^+\mu^-$ and direct (continuum) decays $K^+ \to \pi^+\mu^+\mu^-$ and $K^+ \to \mu^+\mu^-\mu^+\nu_\mu$. Three candidate events of the type $K^+ \to \pi^+\mu^+\mu^-$, shown in Fig. 4 and listed in Table I, were observed. They are consistent with being due to the direct decay $K^+ \to \pi^+\mu^+\mu^-$ for which the expected background (due to particle misidentification) is 0.3±0.3 events from $K^+ \to \pi^+\pi^- e^+\nu$. Based on these data we can set limits on the process $K^+ \to \pi^+ H$; $H \to \mu^+\mu^-$ for Higgs particles in the mass range $220 < m_H < 320$ MeV/c^2 as shown in Fig. 5. Table II lists (preliminary) limits for $K^+ \to \pi^+\mu^+\mu^-$ and $K^+ \to \mu^+\mu^-\mu^+\nu$. We have also searched for $K^+ \to \pi^+\gamma\gamma$ and $K^+ \to \pi^+\pi^0$; $\pi^0 \to \nu\nu$ and found no candidate events leading to the results shown in Table II.

Table I. The $\pi^+\mu^+\mu^-$ and $\mu^+\mu^-$ masses of the three $K^+ \to \pi^+\mu^+\mu^-$ candidates. The errors in $M_{\pi\mu\mu}$ and $M_{\mu\mu}$ are 7.5 MeV/c^2 and 5.0 MeV/c^2, respectively.

Candidate #	$M_{\pi\mu\mu}$ (MeV/c^2)	$M_{\mu\mu}$ (MeV/c^2)
1	498.4	298.7
2	495.0	255.6
3	491.0	256.1

2. $K_L^0 \to \pi^0 e^+ e^-$

CP violation has only been observed in the neutral kaon system in $K_L^0 \to 2\pi$ decays and in the charge asymmetry in $K_L^0 \to \pi e^\pm \nu$ (K_{13}^0) decays. In the standard model with at least three generations a CP-violating phase can be accommodated in the quark-mixing matrix. The magnitude of CP violation is

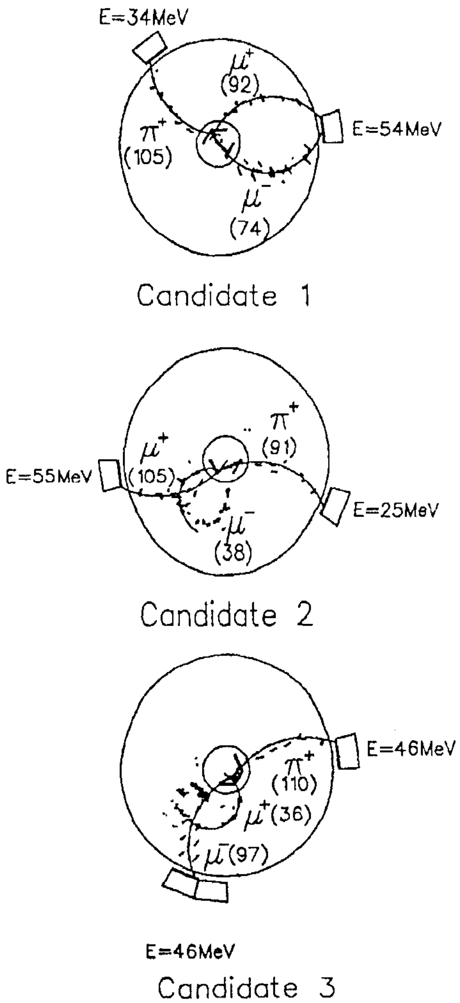

Fig. 4. Candidate events of the type $K^+ \to \pi^+\mu^+\mu^-$.

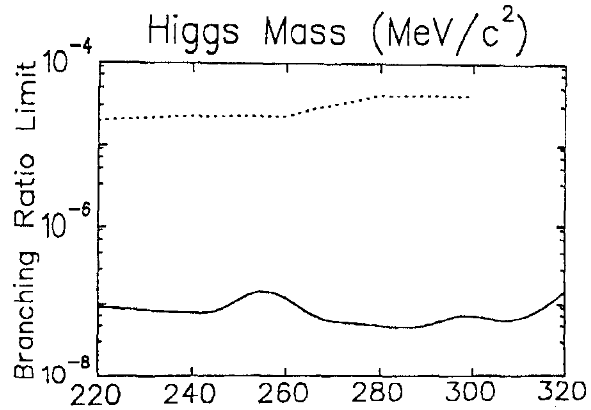

Fig. 5. The upper limits of the branching ratio for $K^+ \to \pi^+ H$; $H \to \mu^+\mu^-$ as a function of m_H (solid line). The dashed line is the result of an inclusive search for $K^+ \to \pi^+ X^0$ (Ref. 9).

Table II. Summary of (preliminary) results for the E787 1988 run.

Process	Branching ratio limits (90% C.L.)
$K^+ \to \pi^+\nu\bar{\nu}$	$< 3.4 \times 10^{-8}$
$K^+ \to \pi^+ a$	$< 6.4 \times 10^{-9}$
$K^+ \to \pi^+ H;\ H \to \mu^+\mu^-$*	$< 1.5 \times 10^{-7}$
$K^+ \to \pi^+\mu^+\mu^-$	$< 2.3 \times 10^{-7}$
$K^+ \to \mu^+\mu^-\mu^+\nu$	$< 4.1 \times 10^{-7}$
$K^+ \to \pi^+\gamma\gamma$	$< 10^{-6}$
$\pi^0 \to \nu\nu$	$< 8 \times 10^{-7}$

*$220 < m_H < 320$ MeV/c^2

indicated by the parameter $\epsilon \sim 10^{-3}$, which has as its source the K^0, $\bar{K}^0$ mass matrix. CP violation is manifested by the level of CP impurity of K_L^0 and K_S^0 states. A second possible source of CP violation originates directly from the $K \to 2\pi$ decay amplitude and is represented by the parameter ϵ'. A recent CERN experiment[10] (NA31) reported consistency with the CKM picture of CP violation, finding a non-zero value (at the three-standard deviation level) for the ratio $\epsilon'/\epsilon = (3.3 \pm 1.1) \times 10^{-3}$. Fermilab experiment E731[11,12] is expected to report a result for ϵ'/ϵ later this year with comparable or greater precision. Whether a non-zero value of ϵ'/ϵ is confirmed or (especially) if an inconsistency appears further experiments are needed to define or confirm the origin of CP violation.

The decay $K_L^0 \to \pi^0 e^+e^-$ is a rare example of a reaction which can proceed through both CP-conserving and CP-violating paths at potentially comparable rates. Since K_L^0 consists of the CP odd-state K_2 with a small admixture of the CP even state K_1, decays proceeding through two virtual photons and through a single virtual photon are, respectively, possible. Various calculations indicate the CP-conserving and CP-violating amplitudes may be comparable and, furthermore, that the CP-violating components due to the mass matrix ($\Delta S = 2$) and the direct 2π amplitude ($\Delta S = 1$) may also be comparable. Essential theoretical work is in progress to understand this reaction.[13] Because the ranges of calculated values for the CP-violating components and the CP-conserving components (both due to mixing and direct contributions) are wide and overlap, there would be considerable difficulty in interpreting an observation of $K_L^0 \to \pi^0 e^+e^-$ based on the rate alone. A measurement of $K_S^0 \to \pi^0 e^+e^-$ (estimated to be at the 10^{-10} to 10^{-8} level)[14] would provide the most reliable input for determining the CP-violating part of the $K_L^0 \to \pi^0 e^+e^-$ amplitude due to mixing (i.e., the K_1 component). There may be sufficient variation in Dalitz plots to enable one to distinguish the CP-violating from the CP-conserving components if adequate statistics were available (a formidable task in light of the small branching ratio expected). Sehgal[15] calculated the phase of the 2γ amplitude and the interference between the 1γ and 2γ contributions to arrive at another possible observable, a CP-violating asymmetry between e^+ and e^- energies. Littenberg (see Ref. 2) has suggested measurement of the time dependence. Although the branching ratio is expected to lie in the 10^{-12} to 10^{-11} region and significant statistics will be necessary to unravel the various contributions, $K_L^0 \to \pi^0 e^+e^-$ is certainly an important reaction for study to help elucidate the mechanism of CP violation.

Recent experiments at CERN[16] and FNAL[17] have resulted in branching ratio limits for $K_L^0 \to \pi^+e^+e^-$: $B(K_L^0 \to \pi^0 e^+e^-) < 4 \times 10^{-8}$. The present round of experiments at FNAL, BNL and KEK is aiming to reach the 10^{-11} to 10^{-10} level where initial observation of $K_L^0 \to \pi^0 e^+e^-$ may be possible. The experiments require high beam intensity and therefore detectors with fast response, large acceptance and excellent particle identification capabilities to distinguish electrons from pions. Potential backgrounds may arise from combinations of K_L^0 decays with accidentals such as $K_L^0 \to \pi e \nu$ plus two accidental gamma rays and misidentification of the charged pion as an electron. The decay chain $K^0 \to \pi^0\pi^0$ with $\pi^0 \to 2\gamma \to e^+e^-$ could also prove to be an important background.

The set-ups for the proposed experiments at KEK[18] and BNL[19] are shown in Fig. 6(a) and 6(b), respectively. (The FNAL experiment is described elsewhere in these proceedings.) In KEK E162 a 2 to 10 GeV/c beam of approximately 6×10^7 K_L^0/pulse enters a 3 m decay region closely followed by a magnetic spectrometer which includes a gas Čerenkov detector for particle identification. The spectrometer is to be followed by a 16 radiation length calorimeter composed of 500 blocks of pure CsI. Tests indicate that energy resolution $\frac{\Delta E}{E} \sim \frac{2\%}{\sqrt{E}}$ can be achieved in the calorimeter which uses the fast component ($\tau \sim 10$ ns) of the CsI scintillation light (the slow component will be partially removed by filters). Experiment E845 at BNL [Fig. 6(b)] is similar in concept to KEK E162; however, a lead glass calorimeter is being used. Both experiments are expected to take significant data by 1990.

4. Lepton Flavor Violation

Searches for rare kaon decays not expected in the standard model could also contribute dramatic new information. Lepton flavor violating (LFV) interactions are strictly absent in the standard model with massless neutrinos because neither the intermediate vector bosons nor the Higgs particle have LFV couplings. However, in many extensions of the standard model LFV interactions appear naturally, leading to decays like $K_L^0 \to \mu e$ and $K^+ \to \pi^+\mu e$. Among

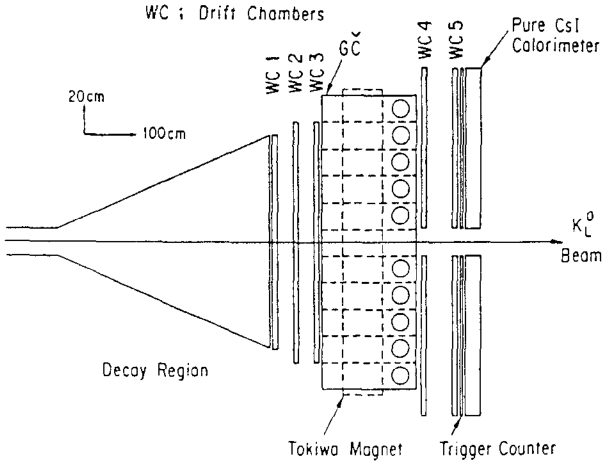

Fig. 6(a). Set-up for KEK E162 search for $K_L^0 \to \pi^0 e^+ e^-$ (Ref. 18).

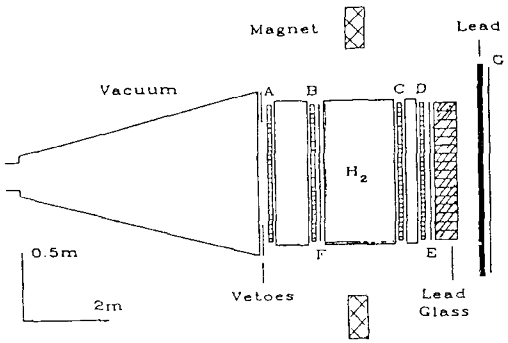

Fig. 6(b). Set-up for BNL E845 search for $K_L^0 \to \pi^0 e^+ e^-$ (Ref. 19).

these are models in which flavor violations are mediated by horizontal gauge bosons, additional neutral Higgs particles, vector or pseudoscalar leptoquarks and supersymmetric particles. The mass regions probed by rare kaon processes reach scales of order 100 TeV/c^2, which are inaccessible to direct experiments at any existing or planned high energy accelerator. Table III (see Ref. 1) gives a sample of the mass regions probed by current experiments. Thus, although kaon decay experiments are generally performed at relatively low energies, their implications are relevant and complementary to studies done at the highest energy facilities and beyond.

Table III. Mass bounds from different processes.

Process	Higgs scalars (GeV/c^2)	Pseudoscalar leptoquarks (TeV/c^2)	Vector leptoquarks (TeV/c^2)	Experimental value
$\frac{\Gamma(K_L^0 \to \mu \bar{e})}{\Gamma(K_L \to \text{all})}$	11	8	149	$<2.2 \times 10^{-10}$ [a]
$\frac{\Gamma(K_L^0 \to \mu \bar{\mu})}{\Gamma(K_L \to \text{all})}$	4.7	3.6	62	9×10^{-9} [b]
$\frac{\Gamma(K_L^0 \to e \bar{e})}{\Gamma(K_L \to \text{all})}$	8	2.6	108	$<3 \times 10^{-10}$ [c]
$\frac{\Gamma(K^+ \to \pi^+ \mu e)}{\Gamma(K^+ \to \text{all})}$	1	0.5	5.6	$<3 \times 10^{-10}$ [d]
$\frac{\Gamma(\mu \to e\gamma)}{\Gamma(\mu \to \text{all})}$	0.3	–	–	$<4.9 \times 10^{-11}$ [e]
$\frac{\Gamma(\mu \to ee\bar{e})}{\Gamma(\mu \to \text{all})}$	2.6	–	–	$<1.0 \times 10^{-12}$ [f]
$\frac{\Gamma(\mu Z \to eA)}{\Gamma(\mu Z \to \nu Z')}$	22	22	118	$<4.6 \times 10^{-12}$ [g]
$\Delta m(K_L^0 - K_S^0)$	150	–	–	3.5×10^{-15} GeV [b]

[a]Ref. 20; [b]Ref. 21; [c]Ref. 22; [d]Ref. 23; [e]Ref. 24; [f]Ref. 25; and [g]Ref. 26.

$K_L^0 \to \mu e$ is a prominent process with which to search for LFV, since it involves both quarks and leptons, has a large available phase space and occurs at a favorable rate in many models compared to some other LFV processes. The hadronic current for $K_L^0 \to \mu e$ must be either axial-vector or pseudoscalar unless the process is mediated by leptoquarks. $K_L^0 \to \mu e$ could also occur by means of constituent rearrangement in some substructure models.

Potential backgrounds in experiments searching for $K_L^0 \to \mu e$ arise from the decay $K_L^0 \to \pi e \nu_e (K_{e3})$ followed by $\pi \to \mu \nu_\mu$ decay-in-flight. In order to suppress this type of background, experiments are configured to perform high resolution tracking of the charged decay products in a magnetic field. From this information the decay vertex can be established and the kinematic reconstruction of the K_L^0 mass achieved. Requiring the reconstructed kaon momentum vector to point to the kaon production target can provide an additional constraint. High resolution and low mass in the decay region and tracking system enhance the ability to detect and identify kinks in the tracks due, for example, to pion decay. A redundant muon energy determination made by measuring the muon range allows the further identification of muons which result from the decay-in-flight of pions, since a mismatch with the apparent muon momentum will occur with high probability.

Two high sensitivity experiments are presently under way to search for $K_L^0 \to \mu e$ at branching ratio levels ranging from 10^{-10} to 10^{-11}. Set-ups for BNL E791 (Ref. 20) and KEK E137[27] are shown in Fig. 7(a) and 7(b), respectively. The approaches are similar in that the K_L^0 decay zone is followed by ultra-thin tracking chambers, two analyzing magnets, Čerenkov counters for particle identification, Pb-glass electron detectors and redundant massive muon energy detectors, which also serve to filter out hadrons. The use of two opposing equal bends is advantageous for identifying events in which pion decays occur inside the detector and for restoring the direction of the decay products to improve the ability to form an experimental trigger. Central vacuum chambers reduce the probability of beam neutron interactions (neutrons typically comprise 90% of the K_L^0 beams) and limit multiple Coulomb scattering of the kaon decay products. The experiments also include segmented muon range-stacks, which are designed to obtain muon energy measurements limited only by range straggling.

Initial results from both experiments have been reported recently (just following this Institute). No $K_L^0 \to \mu e$ candidate events have been identified from either search, thus far, resulting in the following branching ratio upper limits:

$$\text{KEK E137:} \quad B(K_L^0 \to \mu e) < 4.3 \times 10^{-10}$$
$$\text{BNL E791:} \quad B(K_L^0 \to \mu e) < 2.2 \times 10^{-10} \, .$$

BNL E791 has also recorded 87 $K_L^0 \to \mu\mu$ events resulting in a branching ratio $B(K_L^0 \to \mu\mu) = (5.8 \pm 0.6 \text{ (stat)} \pm 0.4 \text{ (syst)}) \times 10^{-9}$ (Ref. 28). KEK E137 has obtained 54 $K_L^0 \to \mu\mu$ events giving $B(K_L^0 \to \mu\mu) = (8.4 \pm 1.1) \times 10^{-9}$ (Ref. 27). In addition, limits on the branching ratio for $K_L^0 \to ee$ were $B(K_L^0 \to ee) < 3.1 \times 10^{-10}$ for BNL E791 and $B(K_L^0 \to ee) < 5.6 \times 10^{-10}$ for KEK E137. These experiments are continuing.

Even if $K_L^0 \to \mu e$ is absent, $K^+ \to \pi^+\mu^\pm e^\mp$ could occur, because it can be generated by vector or scalar currents. Experimentally, the three-body charged particle final state makes definite vertex reconstruction reliable and allows strict energy and momentum constraints to be imposed. The natural background, $K^+ \to \pi^+\pi^+\pi^-$ followed by reactions $\pi \to \mu\nu$ and $\pi \to e\nu$, which has correct final-state particles, is highly suppressed due to the 10^{-4} branching ratio for $\pi \to e\nu$ decay. All other potential background processes, such as $K^+ \to \pi^+\pi^0$

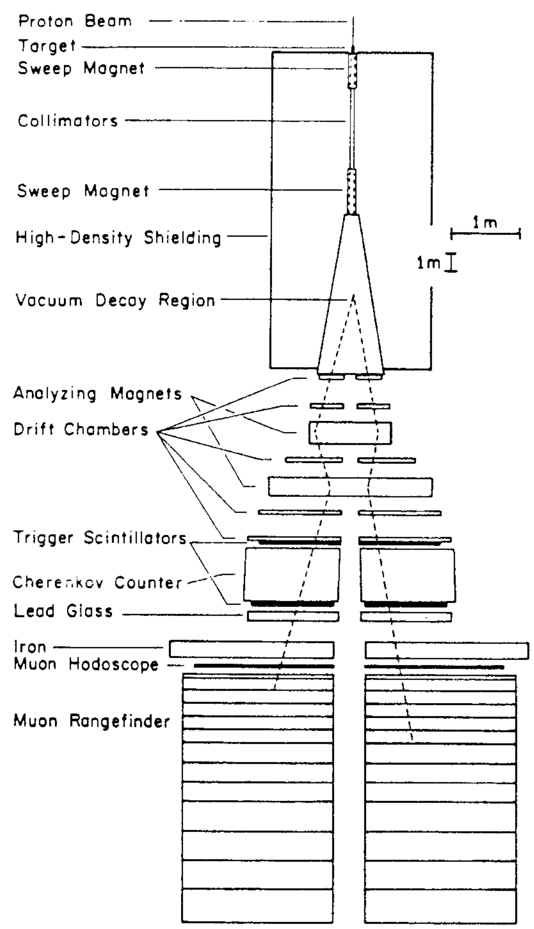

Fig. 7(a). Set-up for BNL E791 search for $K_L^0 \to \mu e$ (Ref. 20).

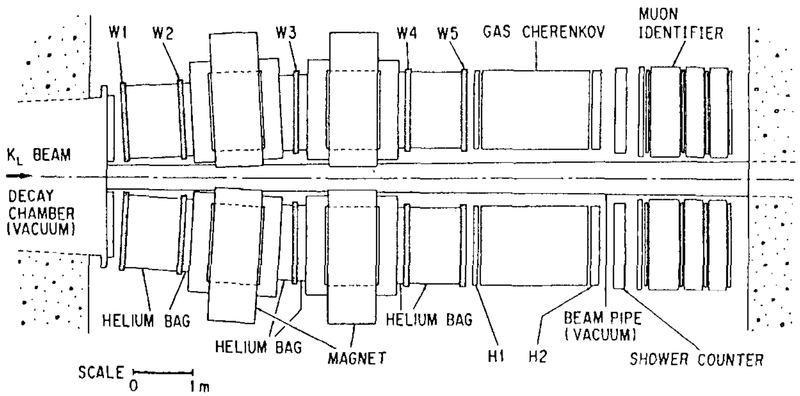

Fig. 7(b). Set-up for KEK E137 search for $K_L^0 \to \mu e$ (Ref. 27).

followed by $\pi^0 \to e^+e^-\gamma$, require particle misidentification.

An experiment is in progress at BNL to search for $K^+ \to \pi^+\mu^+e^-$ (see Ref. 23). The set-up for BNL E777 is shown in Fig. 8. The arrangement of detectors is asymmetric with positive particles directed to the right side and negative particles to the left. Multi-cell threshold Čerenkov counters perform the particle identification function along with the lead scintillator calorimeter.

BNL E777 has produced a new limit based on no observed candidate events

$$B(K^+ \to \pi^+\mu^+e^-) < 3 \times 10^{-10} ,$$

assuming a uniform phase space distribution. In addition, a limit was found on the branching ratio[29]

$$\frac{\Gamma(K^+ \to \pi^+ A^0)}{\Gamma(K^+ \to \text{all})} < 4.5 \times 10^{-7} ,$$

for a hypothetical A^0, which decays via $A^0 \to e^+e^-$ with lifetime shorter than 10^{-13} s and mass less than 100 MeV/c^2. Upper limits were obtained as a function of mass and lifetime of A^0 as shown in Fig. 9.

5. Conclusion

Major advances, spanning orders of magnitude, have recently been achieved in experiments dealing with rare kaon decays at BNL and KEK. Further significant improvements in sensitivity for $K^+ \to \pi^+\nu\bar{\nu}$, $K_L^0 \to \mu e$ and $K_L^0 \to \pi^0 ee$ are anticipated from current efforts. In the longer term, the upgraded booster at the AGS and the proposed kaon factory at TRIUMF may lead to a new era in high-precision and high-sensitivity particle physics experiments that have a unique role to play in examining the standard model and searching for new effects.

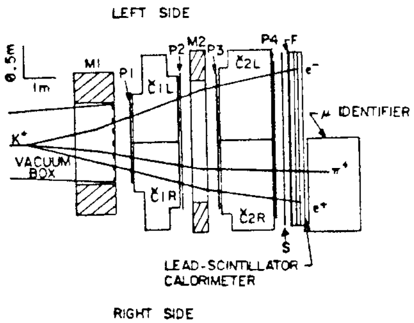

Fig. 8. Set-up for BNL E777 search for $K^+ \to \pi^+\mu^+e^-$.

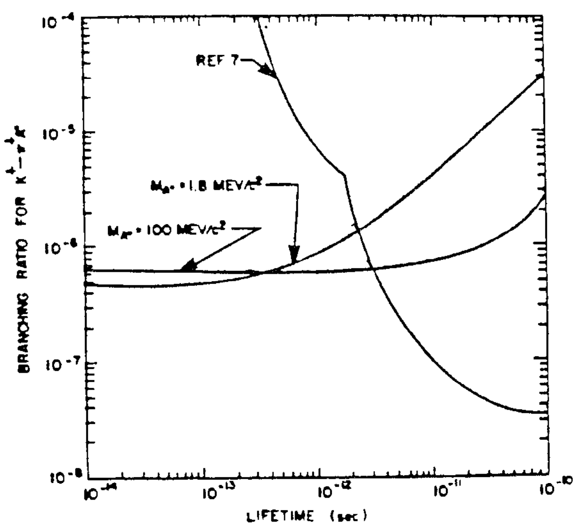

Fig. 9. Branching ratio for $K^+ \to \pi^+ A^0$ versus lifetime (from Ref. 29).

References

1. D.A. Bryman, Int. J. Mod. Phys. A **4**, 79 (1989).
2. L.S. Littenberg and J.S. Hagelin, BNL preprint 42423 (to be published).
3. J. Ellis and J.S. Hagelin, Nucl. Phys. **B217**, 189 (1983).
4. D. Rein and L.M. Sehgal, Phys. Rev. D **39**, 3325 (1989).
5. Y. Asano *et al.*, Phys. Lett. **107B**, 159 1981.
6. R. Shrock, *Proc. DPF Summer Study of Elementary Particle Physics and Future Facilities*, ed. R. Donaldson *et al.*, (Snowmass, 1982) p. 291.
7. See M. Atiya *et al.*, Proc. Rare Decay Symposium, ed. D.A. Bryman *et al.*, Vancouver, 1988 (World Scientific, Singapore, 1989), p. 61;
M. Atiya *et al.*, Proc. 2nd Int. Symposium on the 4th Family of Quarks and Leptons, Santa Monica, CA (to be published).
8. M.A. Selen, Ph.D. dissertation, Princeton University (1985) (unpublished).
9. T. Yamazaki *et al.*, Phys. Rev. Lett. **52**, 1089 (1984).
10. H. Burkhardt *et al.*, Phys. Lett. B **206**, 169 (1988).
11. FNAL E731; M. Woods *et al.*, Phys. Rev. Lett. **60**, 1695 (1988).
12. See the report on E731 in these proceedings.
13. See F.S. Gilman, these proceedings.
14. M.K. Gaillard and B.W. Lee, Phys. Rev. D **10**, 897 (1974).
15. L.M. Sehgal, Phys. Rev. D **38**, 808 (1988).
16. G.D. Barr *et al.*, Phys. Lett. B **214**, 303 (1988).
17. L.K. Gibbons *et al.*, Phys. Rev. Lett. **61**, 2661 (1988).
18. KEK E162, see N. Sasao, KEK report 89-7.
19. BNL E845, see W.M. Morse, Proc. Rare Decay Symposium, *op cit.*, p. 81.
20. C. Mathiazhagen *et al.*, UCI technical report 89-40.
21. Particle data group, Phys. Lett. **170B**, 1 (1986).
22. E. Jastrzembski *et al.*, Phys. Rev. Lett. **20**, 2300 (1988).

23. See H.J. Lubatti, Univ. of Washington preprint UWSE/A PUB 89–12.

24. R.D. Bolton *et al.*, Phys. Rev. Lett. **56**, 2461 (1986).

25. U. Bellgardt, Nucl. Phys. **B299**, 1 (1987).

26. S. Ahmad *et al.*, Phys. Rev. D **38**, 2102 (1988).

27. T. Inagaki *et al.*, Phys. Rev. D **40**, 1712 (1989)

28. C. Mathiazhagen *et al.*, UCI technical report 89–41.

29. N.J. Baker *et al.*, Phys. Rev. Lett. **59**, 2832 (1987).

CP VIOLATION

Frederick J. Gilman

Stanford Linear Accelerator Center
Stanford University, Stanford, California 94309

Abstract

Predictions for CP violation in the three-generation Standard Model are reviewed based on what is known about the Cabibbo-Kobayashi-Maskawa matrix. Application to the K and B meson systems is emphasized.

Introduction

It is now 25 years since the initial discovery of CP violation and we are still faced with the question of its origin and its ultimate significance:

- Is it a curiosity? Could it be physics from a much higher mass scale, at which we are allowed only a peek–a tiny remnant of new physics beyond the Standard Model?

or

- Is it a cornerstone? Does it originate inside the Standard Model? Indeed, is it the signal that there are three or more generations, all quark masses unequal, and all weak mixing angles nonzero? Is it then the single statement summarizing all of this, and yielding a characteristic pattern of CP violation which is tied to quark flavor?

These are the basic questions which we seek to answer experimentally, and then to delineate the details of whatever is the mechanism of CP violation. To do so, we need to know how CP violation is manifested in the Standard Model.

CP Violation in the Three-Generation Standard Model

The matrix[1] that describes the mixing of three generations of quarks has three real angles and one nontrivial phase. Any difference of rates between a given process and its CP conjugate process (or of a CP-violating amplitude) always has the form:

$$\Gamma - \bar{\Gamma} \propto s_1^2\, s_2\, s_3\, c_1\, c_2\, c_3\, \sin\delta_{KM} = s_{12}\, s_{23}\, s_{13}\, c_{12}\, c_{23}\, c_{13}^2\, \sin\delta_{13}\ , \quad (1)$$

where we express things first in the original parameterization of the quark mixing matrix[1] and then in the "preferred" parameterization adopted by the Particle

Data Group,[2] using the shorthand that $s_i = \sin\theta_i$ and $c_i = \cos\theta_i$. Our present experimental knowledge assures us that the approximation of setting the cosines to unity, which we often adopt in the following, induces errors of at most a few percent. In that case the combination of angle-dependent factors in Eq. (1), involving the invariant measure of CP violation,[3] becomes the approximate combination,

$$s_1^2\ s_2\ s_3\ \sin\delta_{KM}\ =\ s_{12}\ s_{23}\ s_{13}\ \sin\delta_{13}\ , \tag{2}$$

which was recognized earlier as characteristic of CP-violating effects in the three-generation standard model.[4] Equation (1) shows us immediately that all three generations of quarks are necessary for CP violation; in particular, none of the angles can be zero, nor can any of the Cabibbo-Kobayashi-Maskawa (C-K-M) matrix elements.

The C-K-M factors in Eq. (1) define the "price of CP violation" in the Standard Model. This "price" must be paid somewhere. It could be paid in a specific process by having many of these factors in both Γ and $\bar{\Gamma}$, corresponding to a very small branching ratio for that process: Then when we form the asymmetry,

$$A_{CP\ violation} = \frac{\Gamma - \bar{\Gamma}}{\Gamma + \bar{\Gamma}}\ , \tag{3}$$

the smallness of the denominator results in a large asymmetry. On the other hand, the price could be paid by having few of these factors in Γ and $\bar{\Gamma}$ separately (and hence in their sum), but only in their difference; the asymmetry is correspondingly small. There is therefore a very rough correspondence between rarer decays and bigger asymmetries. This rule-of-thumb is only that; it can be mitigated or exacerbated by other factors: hadronic matrix elements, dependence of one-loop amplitudes upon internal quark masses, and the possible presence of C-K-M factors in addition to those demanded by Eq. (1). A prime example of luck in this regard is provided by CP-violating effects which depend on $B - \bar{B}$ mixing, where the large top quark mass allows fairly big asymmetries between B and $\bar{B}$ decays to occur in modes which are themselves not suppressed in rate by C-K-M factors.

The Unitarity Triangle

In principle, measurement of just the magnitudes of the C-K-M matrix elements could tell us about the phase, δ_{13}, as well as the "rotation angles" θ_{12}, θ_{23}, and θ_{13} in Eq. (1). This is most easily seen for the case at hand, where the "rotation angles" are small, by using the unitarity of the matrix as applied to the first and third columns to derive that (c_{ij} have been set to unity):

$$1 \cdot V_{ub}^* - s_{12} \cdot V_{cb}^* + V_{td} \cdot 1 \approx 0\ . \tag{4}$$

This equation is represented graphically in Fig. 1 in terms of a triangle in the complex plane, the lengths of whose sides are $|V_{ub}^*|$, $|s_{12} \cdot V_{cb}^*|$, and $|V_{td}|$, and the nontrivial phase in different parameterizations is the indicated interior or exterior angle. This triangle appears explicitly in Ref. 4, and has been commented on by many people,[5] but has been particularly emphasized by Bjorken.[6]

According to an ancient theorem, perfect measurements of the lengths of all three sides could determine a nontrivial triangle, thereby completely fixing the mixing matrix, including the phase. Alternately, a set of measurements of the lengths could show that the triangle can not exist, forcing us beyond three generations. As a special case, the triangle could collapse to a line, and we must go beyond the three-generation Standard Model for an explanation of CP violation. Unfortunately, given our present experimental knowledge and our limited theoretical ability to compute hadronic matrix elements, the three sides are not known with sufficient accuracy to discriminate between these situations, let alone determine the value of δ_{13}. For now, to get information on the phase we are forced to consider a CP-violating quantity and assume it can be understood within the three-generation Standard Model.

Note that twice the area of the triangle is:

$$s_1^2 s_2 s_3 \sin\delta_{KM} \approx s_{12} s_{23} s_{13} \sin\delta_{13}\ . \tag{5}$$

This is "the price of CP violation," and reaffirms that if the triangle degenerates to a line, then CP is conserved.

With this representation of the ill-determined parameters of the C-K-M matrix, it is possible to see more directly the interplay of various pieces of experimental information. In Figs. 2 to 6 we have placed[7] the side $s_{12}\ V_{cb}^*$ along the horizontal and taken $|V_{cb}|$ at its central value[2] of 0.046, so that one vertex is at the origin and a second vertex is very near the point (0.010, 0). Constraints on the position of the third vertex follow from[8]

- $|V_{ub}|$ – An upper limit on this quantity forces the third vertex to lie inside a circle about the origin. A lower limit, taken here to be $|V_{ub}| > 0.04|V_{cb}|$, is implied by data indicating $b \to u$ transitions presented to this conference.[9]
- $B - \bar{B}$ Mixing – The combination of the experimental value of $\Delta M/\Gamma$ and an upper and lower limit on the hadronic matrix element[8] forces the third vertex to lie outside and inside, respectively, circles drawn with the second vertex as an origin.
- ϵ – Imposing the constraint of obtaining the experimental value of $|\epsilon|$ along with upper and lower limits on the hadronic matrix element forces the third vertex to lie between hyperbolas.

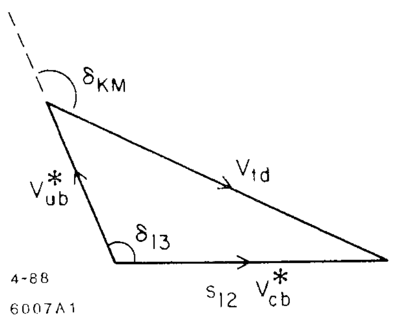

Figure 1. Representation in the complex plane of the triangle formed by the K-M matrix elements V^*_{ub}, $s_{12} \cdot V^*_{cb}$, and V_{td}.

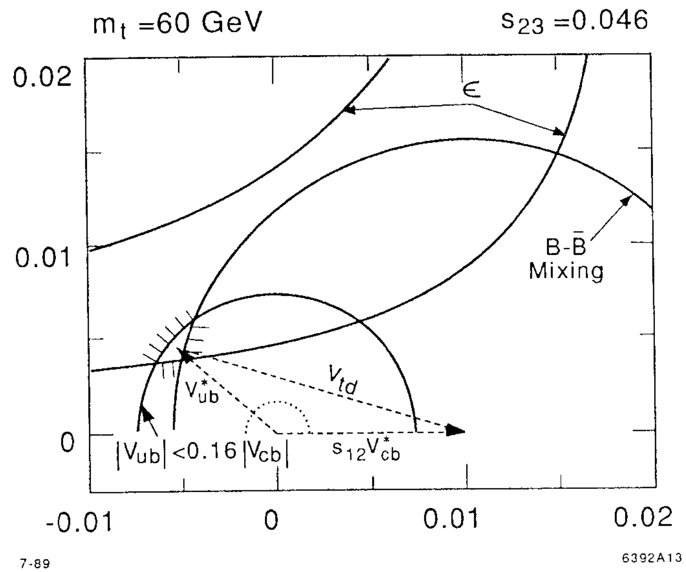

Figure 2. Constraints on the "unitarity triangle" for m_t = 60 GeV and $|V_{cb}| = 0.046$.

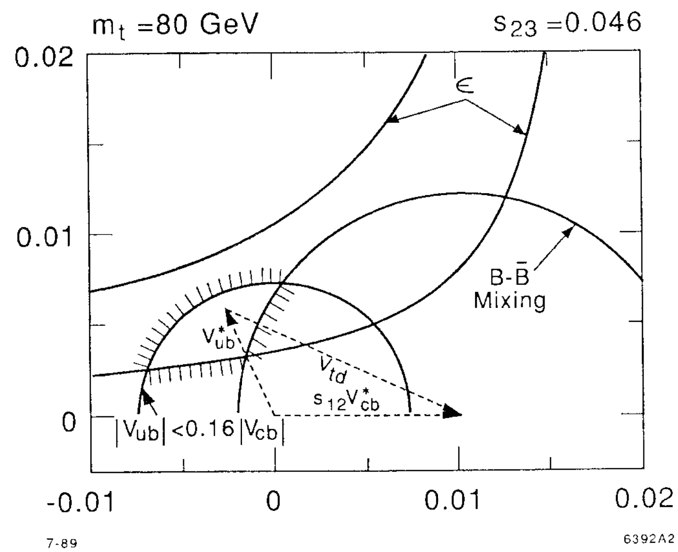

Figure 3. Constraints on the "unitarity triangle" for m_t = 80 GeV and $|V_{cb}| = 0.046$.

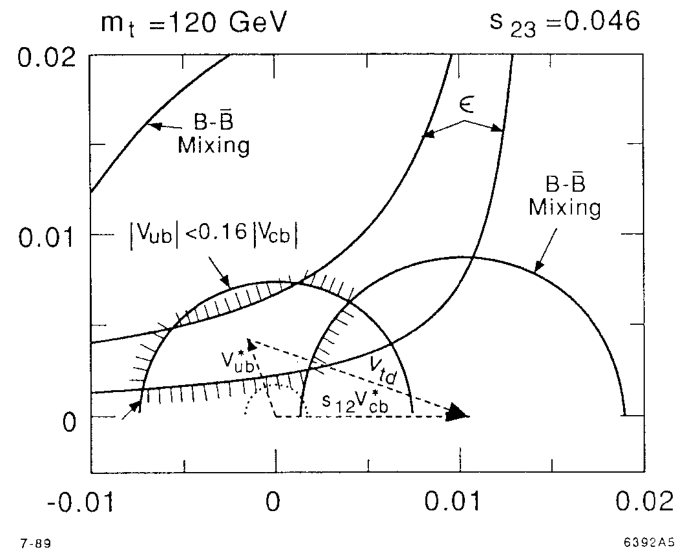

Figure 4. Constraints on the "unitarity triangle" for m_t = 120 GeV and $|V_{cb}| = 0.046$.

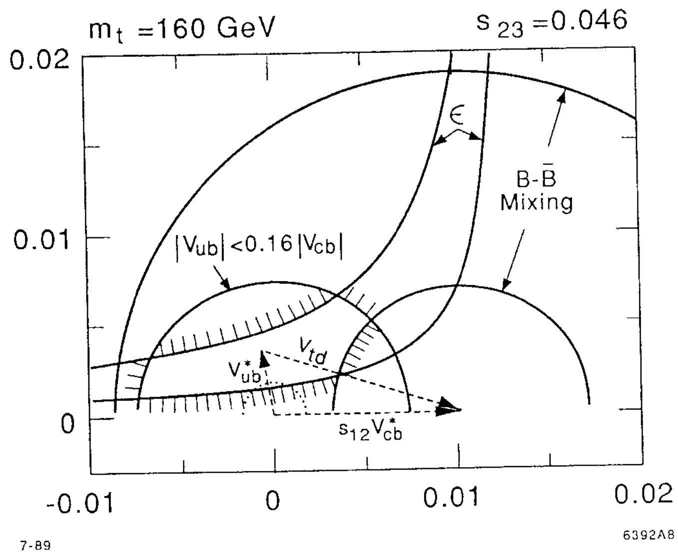

Figure 5. Constraints on the "unitarity triangle" for m_t = 160 GeV and $|V_{cb}| = 0.046$.

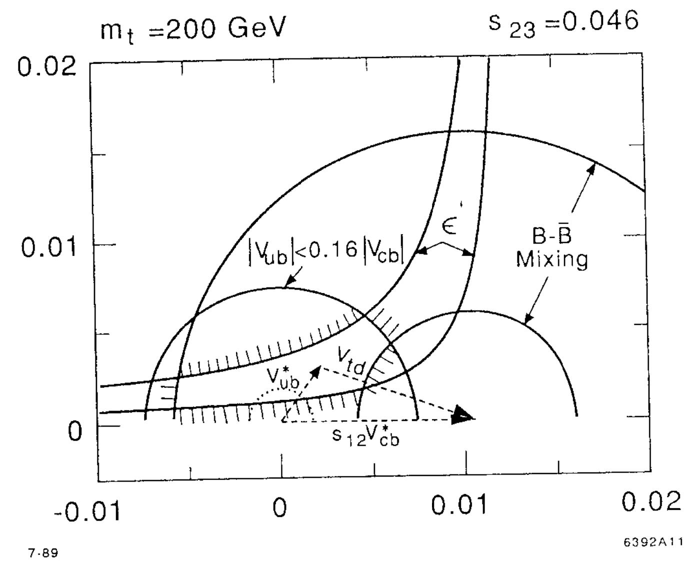

Figure 6. Constraints on the "unitarity triangle" for m_t = 200 GeV and $|V_{cb}| = 0.046$.

Figure 2 shows the situation for $m_t = 60$ GeV, where the position of the third vertex is quite limited by the solid curves indicating the various constraints. The dotted circle represents the lower limit on $|V_{ub}|$ from the observation of $b \to u$ transitions. A sample unitarity triangle is indicated by the dashed lines. For still lower values of m_t, the inner limiting circle due to $B - \bar{B}$ mixing moves outward and eventually becomes incompatible with the other constraints – this is precisely how a lower limit of around 50 GeV for m_t came about after the observation of large $B_d - \bar{B}_d$ mixing.

As we move to a top quark mass of 80 GeV in Fig. 3, the region permitted for the third vertex opens up. Values of $m_t = 120, 160$, and 200 GeV in Figs. 4, 5, and 6, respectively, show a progressively longer and lower allowed region, as both the upper and lower limits from $B - \bar{B}$ mixing and from $|\epsilon|$ enter the picture. Note in addition that the base of the triangle, $s_{12}V_{cb}^*$, is itself only moderately well determined: Figures 7 and 8 show what happens for $m_t = 200$ GeV when values of 0.036 and 0.056 are used for $|V_{cb}|$

The new lower limit we are using for $|V_{ub}|$ plays little role, except for the heaviest top masses, once the "ϵ constraint" is imposed. Of course, the latter assumes that CP violation originates in the C-K-M matrix; it is very important to ascertain without any such assumption that $|V_{ub}|$ is nonzero, and eventually, to pin down its value.

Of more import for high top masses is the constraint that follows from comparing recent experimental data[10,11] on $B(K \to \mu^+\mu^-)$ with the value expected from unitarity, *i.e.*, $K \to \gamma\gamma \to \mu^+\mu^-$, alone. The average of the two recent experiments is $B(K \to \mu^+\mu^-) = 7.0 \pm 0.6 \times 10^{-9}$, while the unitarity limit is $6.8 \pm 0.3 \times 10^{-9}$. If it is assumed that the short-distance contribution to the real part of the amplitude is not cancelled by long-distance contributions, then one obtains a bound on the charm and top quark short-distance contributions to the branching ratio of 2×10^{-9} at the 3σ level. While there is no fundamental reason that a cancellation between the short-distance and long-distance contributions cannot take place, any major cancellation would have to be "accidental." In any case, for large top masses this constraint becomes important, and in particular restricts ReV_{td}. After due account of QCD corrections (relevant to the small, but non-negligible, and constructively interfering charm contribution), the effect of this constraint[12] is shown for $m_t = 160$ and 200 GeV in Figs. 5 and 6 by the dashed-dot line. As is seen in the figures the third vertex of the unitarity triangle is forced to the right from the resulting upper bound[13] on $|ReV_{td}|$.

When viewed from the point of view of the "price of CP violation," *i.e.*, twice the area of the unitarity triangle, it is the altitude times the base that matters. This quantity clearly has a large range, especially once we have allowed m_t to vary all the way up to 200 GeV. A ballpark figure for $s_1^2 s_2 s_3 s_\delta$ is several times 10^{-5}, which means that $s_2 s_3 s_\delta$ is of order 10^{-3}.

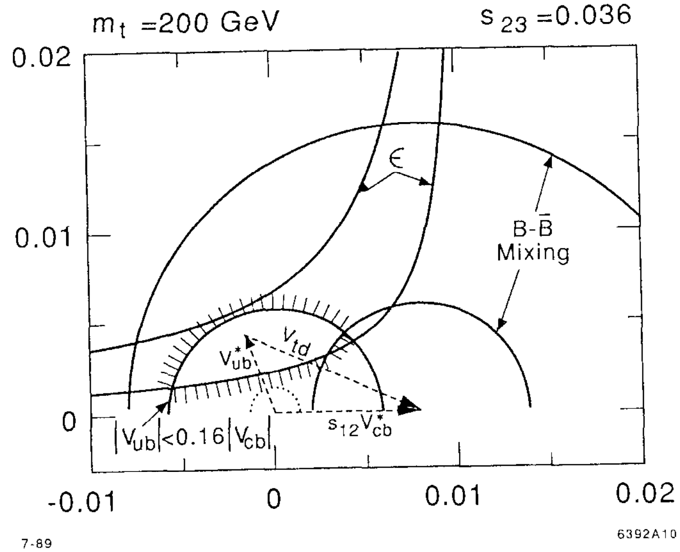

Figure 7. Constraints on the "unitarity triangle" for $m_t = 200$ GeV and $|V_{cb}| = 0.036$.

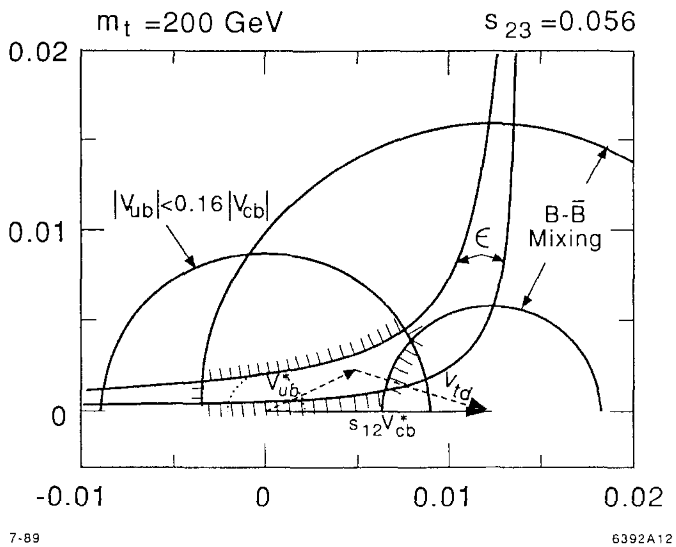

Figure 8. Constraints on the "unitarity triangle" for $m_t = 200$ GeV and $|V_{cb}| = 0.056$.

Status of CP Violation in the Standard Model

Given this "price of CP violation," we can "naturally" understand why

$$|\epsilon| \approx 2.28 \times 10^{-3} \tag{6}$$

is so small and CP seems to come so close to being a symmetry in K decays. When all the factors are put in, the size of $|\epsilon|$ is roughly governed by that of $s_2s_3s_\delta$. This is "naturally" of the right size in the technical sense that to have $s_2s_3s_\delta$ of order 10^{-3} does not require any angle to be fine-tuned to be either especially small or especially large.

This same factor of $s_2s_3s_\delta$ pervades all CP violation observables in the K system, so it is then not so surprising that after 25 years the total evidence for CP violation in Nature consists of a nonzero value of ϵ, and one statistically significant measurement[14] of a nonzero value of the parameter $\epsilon'/\epsilon = 3.3 \pm 1.1 \times 10^{-3}$, representing CP violation in the $K \to \pi\pi$ decay amplitude itself. Experiments at Fermilab[15] and at CERN[14] are continuing with the aim of reducing the statistical and systematic errors. The value of ϵ' from Ref. 14 is consistent[16–18] with the three-generation Standard Model. Unfortunately, this is not a very strong statement. Other values of ϵ' would be consistent as well because of our lack of knowledge both on the experimental and theoretical fronts:

- The hadronic matrix elements of the penguin operators, upon which the prediction of ϵ' depends, are fairly uncertain. Definitive results will presumably come from lattice QCD calculations which still seem several years away.
- The predictions depend on the value of $s_2s_3s_\delta$, which in turn depends (aside from another hadronic matrix element) on m_t through imposing the constraint of obtaining the experimental value of ϵ. Very roughly, as m_t goes up, the range allowed for $s_2s_3s_\delta$ goes down, and so does the prediction for ϵ'.
- Also as m_t rises, the contributions from "Z penguin" and "W box" diagrams begin to be significant. For sufficiently large m_t, a recent calculation[19] contends that most of the usual (strong) penguin contribution to ϵ' can be cancelled in this way.

Experimental and theoretical progress over the next few years should clarify these points. But even if the situation becomes that the value of ϵ' is in significant accord with the three-generation Standard Model, this single number is unlikely to be regarded as conclusively establishing that the origin of CP violation lies in the C-K-M matrix. We would demand additional evidence: A *single* set of C-K-M angles (including the phase) must be able to fit several different processes which exhibit CP-violating effects, providing a redundant check on the theory.

There are two main avenues being pursued in order to get this additional evidence. One is to look for CP-violating effects in the B meson system. Here the CP-violating asymmetries potentially can be very large – of order 10^{-1} or more. The second way is to consider other K decays where CP-violating effects, although very small, may occur with a different weighting (from that in $K \to \pi\pi$) between effects originating in the mass matrix and in the decay amplitude. Possible K decays which come to mind include $K \to 3\pi$, $K \to \gamma\gamma$, and $K \to \pi\pi\gamma$,[20–22] and especially $K_L \to \pi^0\ell^+\ell^-$ and $K_L \to \pi^0\nu\bar{\nu}$. We take up K decays in the next Section, saving the B system for last.

CP Violation in Rare K Decays

The late 1960s and early 1970s marked a peak in experiments on K decays, sparked by the discovery of CP violation.[23] This effort tailed off as many important measurements were completed and new areas of physics opened up in the 1970s at electron-positron and hadron machines.

Then in the late 1970s and early 1980s, both theoretical and experimental developments led to a "rebirth" of K physics. On the experimental side, great strides were made to create high flux beams, handle high data rates, incorporate "smart triggers," improve detectors (especially for photons), and be able to analyze enormous data samples. These matched, at least to some degree, the requirements in precision and rarity being demanded by the theory for incisive tests of the Standard Model. The last few years have seen the beginning of a parade of results which are the culmination of a decade of work in perfecting and performing the needed experiments. Much more is yet to come, and one can see the opportunity to make use of the beams and detectors which are already in existence, or are being developed, to attack the rare K decays which will give additional insight into CP violation.

On the theoretical side, the establishment of gauge theories for the strong and electroweak interactions provided a well-defined basis for calculations. The three-generation Standard Model could be used to make predictions of what, by definition, was inside, and, by its complement, outside the Standard Model. The question of "who ordered the muon" was generalized to "who ordered three generations with particular values of masses and mixing angles," and attention was directed at interactions which would connect quarks and leptons of different generations, producing flavor-changing neutral currents. It was realized that not only did the three-generation model provide an origin for CP violation in the nontrivial phase in the quark mixing matrix, but that CP violation should affect the K^0 decay amplitude as well as the $K^0 - \bar{K}^0$ mass matrix, resulting in values of ϵ'/ϵ in the 10^{-3} to 10^{-2} range.[24] There were also predictions for short-distance contributions to a number of other rare K decay amplitudes induced at one-loop, both CP-conserving and CP-violating.[25]

There has also been an associated experimental development which has important theoretical consequences: The *rise of the top quark*. Over the past decade, the "typical" or "best" value of the top quark mass used in theoretical papers has risen monotonically, somehow always remaining one step, or maybe one and a half steps, ahead of the experimental, then-current, lower bound. Values of 15, 25, 30, 45, . . . GeV have been used in various papers (some of them mine), and subsequently fallen by the wayside as experiments have been able to search at higher and higher masses. The present lower limit is around 60 GeV, below which a top quark is said[26] to be "unlikely." It seems that limits even higher than this will be quoted at high confidence within a month, as the analysis of the present round of collider data is completed. An upper limit of around 200 GeV follows from analysis of neutral and charged current data and the measured W and Z masses (i.e., consistency of the ρ parameter with unity).[27]

The rise of the top quark mass has important consequences when we go to calculate one-loop contributions. For the penguin diagrams in Fig. 9 involving a top and charm quark and a virtual photon (the "electromagnetic penguin"); the conserved nature of the current demands a factor of q^2, the square of the four-momentum carried by the virtual photon, be present in the numerator of the amplitude. This cancels the $1/q^2$ from the photon propagator; the leading term for small (compared to M_W^2) top mass in the coefficient of the appropriate operator behaves as $\ln\,(m_t^2/m_c^2)$. By contrast, the "Z penguin" or "W box" involve nonconserved currents: the factor q^2 in the numerator is replaced by the square of the quark mass in the loop and the propagator by $1/(q^2+M_Z^2) \approx 1/M_Z^2$ or $1/M_W^2$. The corresponding coefficient behaves like $[(m_t^2/M_W^2)\ln\,(m_t^2/M_W^2) - (m_c^2/M_W^2)\ln\,(m_c^2/M_W^2)]$ when the top mass is small. In the days when $m_t^2 << M_W^2$, it was completely justified to throw away the Z penguin and W box contributions to such amplitudes in comparison to that of the electromagnetic penguin. Not so any more. The various graphs give comparable contributions, as we will see below in a specific example. Moreover, the contributions from the top quark become the dominant ones to various rare K decays when $m_t^2 >> M_W^2$. In the three-generation Standard Model, as m_t rises farther and farther above M_W, more and more of one-loop K physics is top physics and we are in the interesting situation where those working at the highest energy hadron colliders are pursuing another aspect of the same physics as those working on the rarest of K decays at low energies.

Let us illustrate a number of the above remarks by looking in more detail at one particular rare K decay in which it is possible to observe CP violation and which has emerged as the object of concentrated theoretical and experimental study.

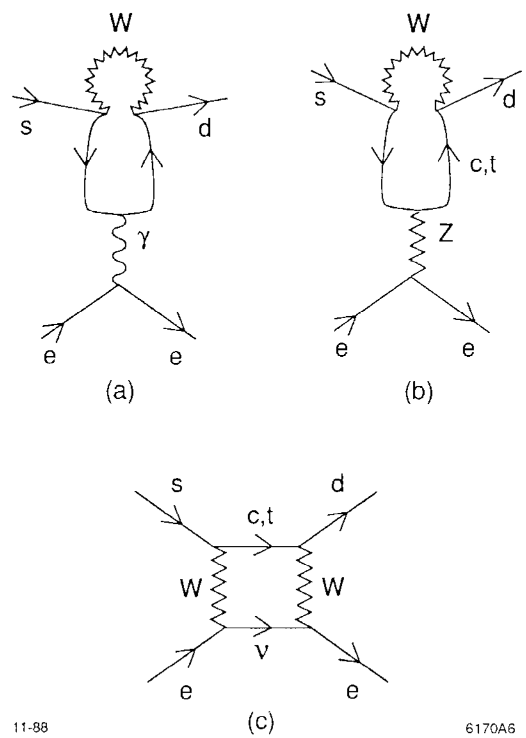

Figure 9. One-loop diagrams giving short distance contributions to K decays, and in particular, to the process $K \to \pi\ell^+\ell^-$: (a) the "electromagnetic penguin;" (b) the "Z penguin;" (c) the "W box."

$K_L \to \pi^0 e^+ e^-$.

If we define K_1 and K_2 to be the even and odd CP eigenstates, respectively, of the neutral K system, then $K_L \to \pi^0 e^+ e^-$ has three contributions:

(1) Through a two-photon intermediate state:

$$K_2 \to \pi^0\ \gamma\gamma \to \pi^0 e^+ e^- .$$

This is higher order in α, but is CP conserving. With two real photons there are two possible Lorentz invariant amplitudes for $K_L \to \pi^0\ \gamma\gamma$. One is the coefficient of $F^{(1)}_{\mu\nu}\ F^{(2)}_{\mu\nu}$, which corresponds to the two photons being in a state with total angular momentum zero. Consequently, it picks up a factor of m_e when contracted with the QED amplitude for $\gamma\gamma \to e^+e^-$, as the interactions are all chirality conserving, and its contribution to the $K_L \to \pi^0 e^+ e^-$ decay rate is totally negligible.[28] The other invariant amplitude is the coefficient of a tensor which contains two more powers of momentum and one might hope for its contribution to be suppressed by angular momentum barrier factors. In chiral perturbation theory, an order of magnitude estimate[29] for the resulting branching ratio of $K_2 \to \pi^0\ e^+e^-$ is 10^{-14}. However, a vector dominance, pole model predicts[30] a much bigger result: a branching ratio of order 10^{-11}, roughly at the level as that arising from the CP-violating amplitudes (see below). The experimental upper limit on the branching ratio for $K_L \to \pi^0\gamma\gamma$ has very recently been considerably improved,[31] and now is only a few times larger than some of the predictions.[29,30] In the future we might have not only a measurement of the branching ratio, but a Dalitz plot distribution which could help distinguish between models. The final answer for this contribution remains to be seen both theoretically and experimentally.

(2) Through the small (proportional to ϵ) part of the K_L which is K_1 due to CP violation in the mass matrix:

$$K_L \approx K_2 + \epsilon K_1$$
$$K_1 \to \pi^0\ \gamma_{virtual} \to \pi^0 e^+ e^- .$$

We call this "indirect" CP violation and may calculate its contribution to the decay rate once we know the width for the CP conserving process $K_1 \to \pi^0 e^+ e^-$. Eventually, there will presumably be an experimental measurement of $\Gamma(K_S \to \pi^0 e^+ e^-)$, which will take all the present theoretical model dependence away. For now, equating this width to the measured one for $K^+ \to \pi^+ e^+ e^-$ gives the estimate:

$$B(K_L \to \pi^0 e^+ e^-)_{\text{indirect}} = 0.58 \times 10^{-11} \quad . \tag{7}$$

(3) Through the large part of the K_L, *i.e.*, K_2, due to CP violation in the decay amplitude:

$$K_2 \to \pi^0 \; \gamma_{virtual} \to \pi^0 e^+ e^- \; .$$

We call this "direct" CP violation, and the amplitude for it arises from the diagrams shown in Fig. 9. For values of $m_t << M_W$, it is the "electromagnetic penguin" that gives the dominant short-distance contribution to the amplitude, which is summarized in the Wilson coefficient, C_{7V}, of the appropriate operator,

$$Q_{7V} \;=\; \alpha \left(\bar{s}\gamma_\mu(1-\gamma_5)d\right)\left(\bar{e}\gamma^\mu e\right) .$$

Values of $m_t \sim M_W$ allow the "Z penguin" and "W box" contributions to become comparable to that of the "electromagnetic penguin," and bring in another operator,

$$Q_{7A} \;=\; \alpha \left(\bar{s}\gamma_\mu(1-\gamma_5)d\right)\left(\bar{e}\gamma^\mu\gamma_5 e\right) .$$

The QCD corrections are substantial for the "electromagnetic penguin" contribution and have been redone for the case[32,33] when $m_t \sim M_W$. In contrast, the top quark contributions from the "Z penguin" and "W box" live up at the weak scale and get only small QCD corrections. Still, the coefficient C_{7V} comes largely from the "electromagnetic penguin," even after its reduction from QCD corrections. On the other hand, the "electromagnetic penguin" cannot contribute to C_{7A}, and here it is the "Z penguin" which gives the dominant contribution. The overall decay rate due to the "direct" CP-violating amplitude can be obtained by relating the hadronic matrix elements of the operators Q_{7V} and Q_{7A} to that which occurs in K_{e3} decay. Then we find that

$$B(K_L \to \pi^0 e^+ e^-)_{direct} \approx \; 1 \times 10^{-5} \; (s_2 s_3 s_\delta)^2 \; [|\tilde{C}_7|^2 + |\tilde{C}_{7A}|^2] \; . \tag{8}$$

The last factor, shown in Fig. 10, ranges[32] between about 0.1 and 1.0. As $s_2 s_3 s_\delta$ is typically of order 10^{-3}, the corresponding branching ratio induced by this amplitude alone for $K_L \to \pi^0 e^+ e^-$ is around 10^{-11}. Note that when $m_t \gtrsim 150$ GeV, the contribution from C_{7A} overtakes that from C_{7V}, and it is the "Z penguin" and "W box," coming from the top quark with small QCD corrections, which dominate the decay rate.

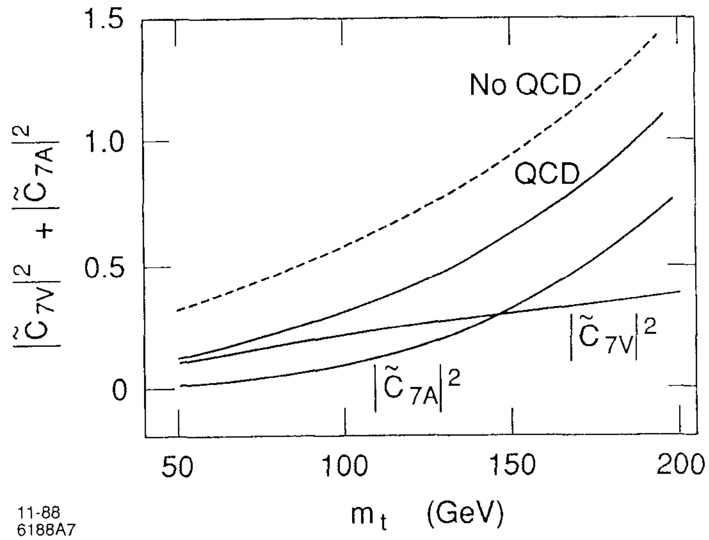

Figure 10. The quantity $|\tilde{C}_{7V}|^2 + |\tilde{C}_{7A}|^2$, which enters the branching ratio for the CP-violating decay $K_L \to \pi^0 e^+ e^-$, as a function of m_t for $\Lambda_{QCD} =$ 150 MeV, from Ref. 32 .

Thus it appears at this point that the three contributions from (1) CP conserving, (2) "indirect" CP-violating, and (3) "direct" CP-violating amplitudes could all be comparable. The weighting of the different pieces in $K_L \to \pi^0 e^+ e^-$ is entirely different from that in $K \to \pi\pi$. The present experimental upper limit[34,35] is 4×10^{-8}, with prospects of getting to the Standard Model level of around 10^{-11} in the next several years. Hopefully, the CP conserving and "indirect" CP-violating amplitudes will be pinned down much better by then, permitting an experimental measurement of this decay to be interpreted in terms of the magnitude of the "direct" CP-violating amplitude.

CP Violation in B Decay

The possibilities for observation of CP violation in B decays are much richer than for the neutral K system. The situation is even reversed, in that for the B system the variety and size of CP-violating asymmetries in decay amplitudes far overshadows that in the mass matrix.[36]

- To start with the familiar, however, consider the phenomenon of CP violation in the mass matrix of the neutral B system.

Here, in analogy with the neutral K system, one defines a parameter ϵ_B. It is related to p and q, the coefficients of the B^0 and $\bar{B}^0$, respectively, in the combination which is a mass matrix eigenstate by

$$\frac{q}{p} = \frac{1-\epsilon_B}{1+\epsilon_B} \,. \tag{9}$$

The charge asymmetry in $B^0\bar{B}^0 \to \ell^\pm\ell^\pm + X$ is given by[37]

$$\begin{aligned} \frac{\sigma(B^0\bar{B}^0 \to \ell^+\ell^+ + X) - \sigma(B^0\bar{B}^0 \to \ell^-\ell^- + X)}{\sigma(B^0\bar{B}^0 \to \ell^+\ell^+ + X) + \sigma(B^0\bar{B}^0 \to \ell^-\ell^- + X)} &= \frac{|p/q|^2 - |q/p|^2}{|p/q|^2 + |q/p|^2} \\ &= \frac{\mathrm{Im}(\Gamma_{12}/M_{12})}{1 + \frac{1}{4}|\Gamma_{12}/M_{12}|^2} \,, \end{aligned} \tag{10}$$

where we define $< B^0|H|\bar{B}^0 >= M_{12} - \frac{i}{2}\Gamma_{12}$. The quantity $|M_{12}|$ is measured in $B - \bar{B}$ mixing to be comparable in magnitude to the total width, while Γ_{12} gets contributions only from channels which are common to both B^0 and $\bar{B}^0$, *i.e.*, K-M suppressed decay modes. This causes the charge asymmetry for dileptons most likely to be in the ballpark of a few times 10^{-3}, and at best 10^{-2}. For the foreseeable future, it is inaccessible experimentally.

- Now we turn to where the excitement is: CP violation in decay amplitudes.

In principle, this can occur whenever there is more than one path, with different C-K-M factors, to a common final state. For example, let us consider the all-time favorite and paradigm: decay of a neutral B to a CP eigenstate, f, such as ψK_s^0 or D^+D^-. Since there is substantial $B^0 - \bar{B}^0$ mixing, one can consider two decay chains of an initial B^0 meson:

$$\begin{matrix} B^0 \to B^0 & \searrow & \\ & & f \\ B^0 \to \bar{B}^0 & \nearrow & \end{matrix} \,.$$

The second path differs in its phase because of $B^0 \to \bar{B}^0$ mixing, and because the decay of a $\bar{B}$ involves the complex conjugate of the K-M factors involved in B decay. The strong interactions, being CP invariant, give the same phases for the two paths. The amplitudes for these decay chains can interfere and generate nonzero asymmetries between $\Gamma(B^0(t) \to f)$ and $\Gamma(\bar{B}^0(t) \to f)$. Specifically,

$$\Gamma(\bar{B}^0(t) \to f) \sim e^{-\Gamma t}\left(1 - \sin[\Delta m\ t]\ \mathrm{Im}\left(\frac{p}{q}\rho\right)\right) \tag{11a}$$

and

$$\Gamma(B^0(t) \to f) \sim e^{-\Gamma t}\left(1 + \sin[\Delta m\ t]\ \mathrm{Im}\left(\frac{p}{q}\rho\right)\right) \,. \tag{11b}$$

Here we have neglected any lifetime difference between the mass matrix eigenstates (thought to be very small), set $\Delta m \equiv m_1 - m_2$, the difference of the eigenstate masses, and $\rho \equiv A(B \to f)/A(\bar{B} \to f)$, the ratio of the amplitudes, and then used the fact that $|\rho| = 1$ when f is a CP eigenstate in writing Eqs. (11). From this we can form the asymmetry:

$$A_{\text{CP Violation}} = \frac{\Gamma(B) - \Gamma(\bar{B})}{\Gamma(B) + \Gamma(\bar{B})} = \sin[\Delta m\ t]\ \mathrm{Im}\left(\frac{p}{q}\rho\right) \,. \tag{12}$$

Moreover, in the particular case of decay to a CP eigenstate with one combination of K-M factors contributing to the decay amplitude, the quantity

$$\mathrm{Im}\left(\frac{p}{q}\rho\right) = \mathrm{Im}\left(e^{2i\Phi}\right)$$

is given entirely by the C-K-M matrix and is independent of hadronic amplitudes, which cancel out in the ratio, ρ . Remarkably, the angles Φ turn out to be nothing but those of the unitarity triangle, as shown in Fig. 11, where the angles are labelled by examples of the neutral B decays to CP eigenstates whose asymmetries they govern.[38]

Figure 12 shows the potential size of the time dependent differences[39] between B_d and $\bar{B}_d$ decaying[40] to the same (CP self-conjugate) final state, ψK_s^0. The likely situation for B_s mixing is shown[41] in Fig. 13(c). The oscillations are so rapid that even with a very favorable difference in the time dependence for an initial B_s *versus* an initial $\bar{B}_s$, the time-integrated asymmetry is quite small. Measurement of the time dependence becomes a necessity for CP violation studies in this case.

We can also form asymmetries where the final state f is not a CP eigenstate. Examples are $B_d \to D\pi$ compared to $\bar{B}_d \to \bar{D}\bar{\pi}$; $B_d \to \bar{D}\pi$ compared to $\bar{B}_d \to D\bar{\pi}$; or $B_s \to D_s^+ K^-$ compared to $\bar{B}_s \to \bar{D}_s^- K^+$. There is a decided disadvantage here in theoretical interpretation, in that the quantity $\mathrm{Im}\left(\frac{p}{q}\rho\right)$ is now dependent on hadron dynamics.

In all the above cases, to measure an asymmetry one must know if one starts with an initial B^0 or $\bar{B}^0$, *i.e.*, one *must* "tag." This is one of the main difficulties experimentally, as the tagging efficiency is generally fairly low.[36]

A second path to the same final state could arise in several other ways besides through mixing. For example, one could have two cascade decays that end up with the same final state, such as:

$$B_u^- \to D^0 K^- \to K_s^0 \pi^0 K^-$$

and

$$B_u^- \to \bar{D}^0 K^- \to K_s^0 \pi^0 K^- \; .$$

Another possibility is to have spectator and annihilation graphs contribute to the same process.[42] Still another is to have spectator and "penguin" diagrams interfere.[43] These routes to obtaining a CP-violating asymmetry have the advantage that they do not require one to know whether one started with a B or $\bar{B}$, *i.e.*, they do not require "tagging." These decay modes are in fact "self-tagging" in that the properties of the decay products (through their electric charges or flavors) themselves fix the nature of the parent B or $\bar{B}$. Their disadvantage, which is theoretical, is that they generally bring poorly known hadronic matrix elements into the interpretation of an asymmetry, and so the association with specific combinations of K-M angles is not clean.

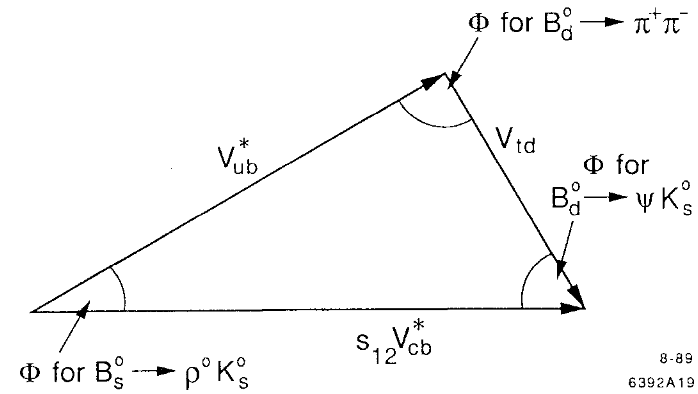

Figure 11. The quantity $|\tilde{C}_{7V}|^2 + |\tilde{C}_{7A}|^2$, which enters the branching ratio for the CP-violating decay $K_L \to \pi^0 e^+ e^-$, as a function of m_t for Λ_{QCD} = 150 MeV, from Ref. 32 .

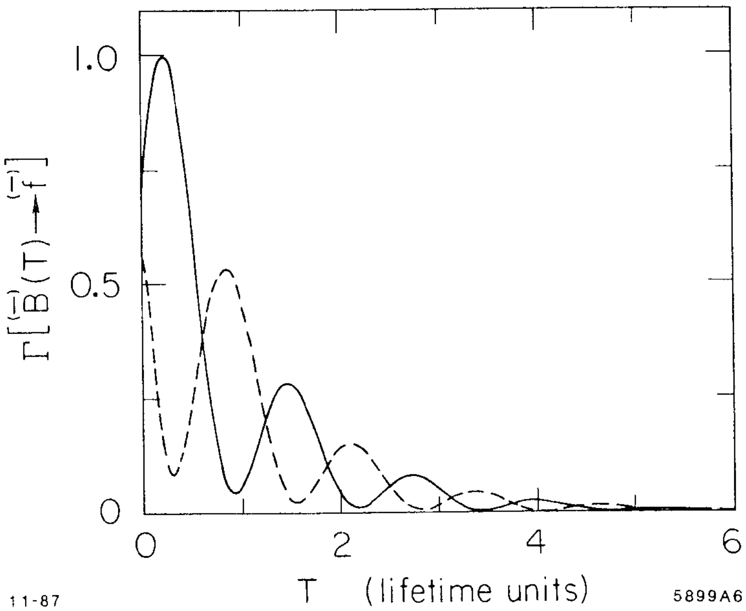

Figure 12. The time dependence for the process $B_d \to \psi K_s^0$ (dashed curve) in comparison to that for $\bar{B}_d \to \psi K_s^0$ (solid curve) for $\Delta m/\Gamma = \pi/4$, a value consistent with that measured experimentally.

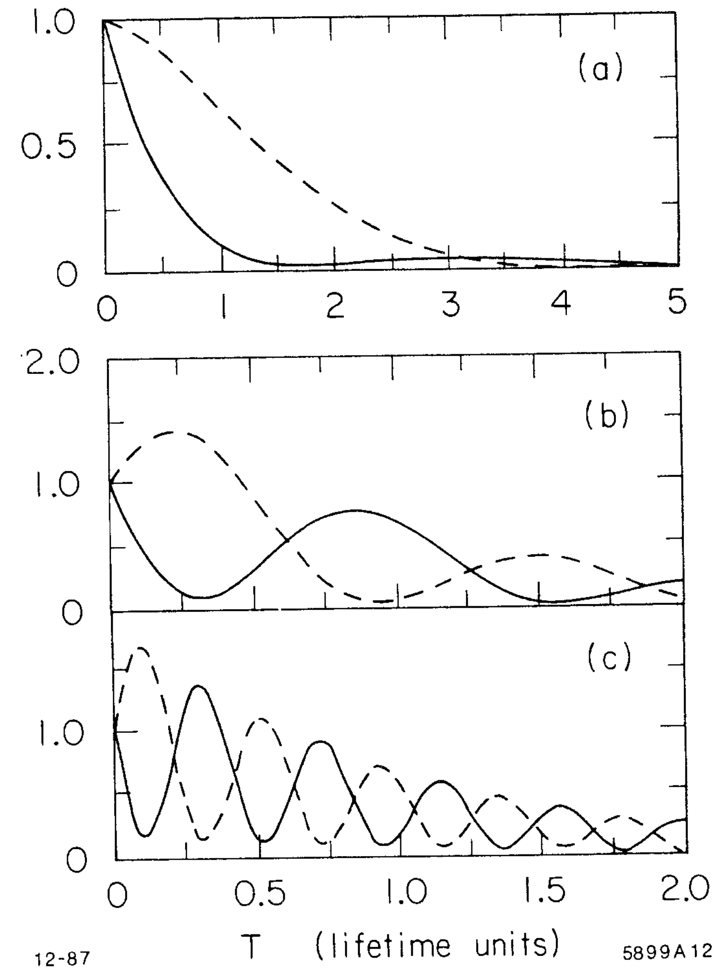

Figure 13. The time dependence for the process $B_s \to \rho K_s^0$ (solid curve) in comparison to that for $\bar{B}_s \to \rho K_s^0$ (dashed curve) for values of (a) $\Delta m/\Gamma = 1$, (b) $\Delta m/\Gamma = 5$, and (c) $\Delta m/\Gamma = 15$, from Ref. 41 .

Conclusion

In a sense, after 25 years we are still at the beginning of the study of CP violation; most CP-violating phenomena have yet to be explored, even those predicted by the Standard Model. The main thrusts in high energy physics are:

- K Decays: A strong effort is already underway at BNL, CERN, Fermilab, and KEK to pursue rare K decays. It includes measurements of ϵ'/ϵ and CP-violating effects in $K_L \to \pi^0 e^+ e^-$ and other K decays. With a number of groups proposing to get to sensitivity levels corresponding to the Standard Model, we are almost guaranteed interesting results over the next few years.
- B Decays: We have seen that there are many manifestations of CP violation to look at in the B system. It appears that one needs of order 10^7 B's to begin to see the large asymmetries that are predicted by the Standard Model in some channels, but I would be the last to tell someone not to look for such effects if they had, say, 10^6 B's. Any nonzero asymmetry is important, and part of the signature of the Standard Model is the flavor dependence of the effects, with generally much larger CP-violating asymmetries characteristic of B's than of K's. We want to know if this pattern is correct. Ultimately, CP violation in the B system is *the* way to measure the C-K-M angles in a redundant way. However, unlike the situation in K decays, we do not have the likelihood of significant results in the next few years. The prospects are longer term, but it seems clear what we must do: *Learn how to detect B's that are produced at hadron machines*, and *build electron-positron B factories.*

REFERENCES

1. M. Kobayashi and T. Maskawa, Prog. Theor. Phys. **49**, 652 (1973).
2. Particle Data Group, Phys. Lett. **204B**, 1 (1988) .
3. C. Jarlskog, Phys. Rev. Lett. **55**, 1839 (1985), and Z. Phys. **29**, 491 (1985).
4. L.-L. Chau and W.-Y. Keung, Phys. Rev. Lett. **53**, 1802 (1984).
5. C. Jarlskog and R. Stora, Phys. Lett. **208B**, 268 (1988);
   J. L. Rosner, A. I. Sanda, and M. P. Schmidt, in *Proceedings of the Workshop on High Sensitivity Beauty Physics at Fermilab*, Fermilab, November 11–14, 1987, edited by A. J. Slaughter, N. Lockyer, and M. Schmidt (Fermilab, Batavia, 1988), p. 165;
   C. Hamzaoui, J. L. Rosner and A. I. Sanda, in *Proceedings of the Workshop on High Sensitivity Beauty Physics at Fermilab*, Fermilab, November 11–14, 1987, edited by A. J. Slaughter, N. Lockyer, and M. Schmidt (Fermilab, Batavia, 1988), p. 215.
6. J. D. Bjorken, lectures, private communication, and Phys. Rev. **D39**, 1396 (1989).
7. C. O. Dib, I. Dunietz, F. J. Gilman, and Y. Nir, SLAC-PUB-5109, 1989 (unpublished).
8. We use $|V_{ub}| < 0.16|V_{cb}|$, $B_B^{1/2} f_B = 150 \pm 50$ MeV, $m_c = 1.4$ GeV, and $1/3 < B_K < 1$ for the parameters that enter the various constraints in Figs. 2–8.
9. P. Baringer, these Proceedings, describes data from CLEO for the inclusive lepton spectrum indicating $b \to u$ transitions at the 2.2σ level of significance.
10. C. Mathiazhagan *et al.*, University of California, Irvine, Report 89–41, 1989 (unpublished).
11. T. Inagaki *et al.*, KEK preprint, 1989 (unpublished).
12. C. O. Dib, I. Dunietz, and F. J. Gilman, unpublished.
13. The bound on the C-K-M matrix (and its effect on the decay $K \to \pi\nu\bar{\nu}$) has recently also been considered by C. Q. Geng and J. N. Ng, TRIUMF report TRIPP–89–84, 1989 (unpublished).
14. H. Burkhardt *et al.*, Phys. Lett. **206B**, 169 (1988).
15. M. Woods *et al.*, Phys. Rev. Lett. **60**, 1695 (1988);
    B. Winstein, invited talk at the Conference on CP Violation in Particle Physics and Astrophysics, Blois, France, May 22–26, 1989 reported a central value consistent with zero within the statistical error bars of $\pm 1.4 \times 10^{-3}$, based on 20% of the data from Fermilab experiment E731.

16. M. A. Shifman, in *Proceedings of the 1987 International Symposium on Lepton and Photon Interactions at High Energies*, Hamburg, July 27-31, edited by W. Bartel and R. Ruckl, (North Holland, Amsterdam, 1988), p. 289.

17. F. J. Gilman, in *International Symposium on the Production and Decay of Heavy Flavors*, Stanford, September 1-5, 1987, edited by E. Bloom and A. Fridman (New York Academy of Sciences, New York, 1988), vol. 535, p. 211.

18. G. Altarelli and P. J. Franzini, CERN preprint CERN-TH-4914/87, 1987 (unpublished).

19. J. M. Flynn and L. Randall, Phys. Lett. **224B**, 221 (1989).

20. L.-F. Li and L. Wolfenstein, Phys. Rev. **D21**, 178 (1980).

21. L.-L. Chau and H.-Y. Cheng, Phys. Rev. Lett. **54**, 1768 (1985) and Phys. Lett. **195B**, 275 (1987);
J. O. Eeg and I. Picek, Phys. Lett. **196B**, 391 (1987).

22. G. Ecker, A. Pich, and E. de Rafael, Nucl. Phys. **B303**, 665 (1988).

23. J. H. Christenson, J. W. Cronin, V. L. Fitch, and R. Turlay, Phys. Rev. Lett. **13**, 138 (1964).

24. F. J. Gilman and M. B. Wise, Phys. Lett. **83B**, 83 (1979), and Phys. Rev. **D20**, 2392 (1979).

25. See, for example, the recent review of J. S. Hagelin and L. S. Littenberg, Prog. Part. Nucl. Phys. **23**, 1 (1989).

26. UA1, UA2, and CDF, any talk in early 1989.

27. U. Amaldi *et al.*, Phys. Rev. **D36**, 1385 (1987);
G. Costa *et al.*, Nucl. Phys. **B297**, 244 (1988).

28. J. F. Donoghue, B. R. Holstein, and G. Valencia, Phys. Rev. **D35**, 2769 (1987).

29. G. Ecker, A. Pich, and E. de Rafael, Phys. Lett. **189B**, 363 (1987);
Nucl. Phys. **B291** 691 (1987); and Ref. 22.

30. L. M. Sehgal, Phys. Rev. **D38**, 808 (1988);
T. Morozumi and H. Iwasaki, KEK preprint KEK-TH-206, 1988 (unpublished);
J. Flynn and L. Randall, Phys. Lett. **216B**, 221 (1989).

31. V. Papadimitriou *et al.*, Phys. Rev. Lett. **63**, 28 (1989).

32. C. Dib, I. Dunietz, and F. J. Gilman, Phys. Lett. **218B**, 487 (1989);
Phys. Rev. **D39**, 2639 (1989).

33. Other recent work on the subject is found in J. Flynn and L. Randall, Nucl. Phys. **B326**, 31 (1989).

34. L. K. Gibbons *et al.*, Phys. Rev. Lett. **61**, 2661 (1988).

35. G. D. Barr *et al.*, Phys. Lett. **B214**, 1303 (1988).

36. K. J. Foley *et al.*, in *Proceedings of the Workshop on Experiments, Detectors, and Experimental Areas for the Supercollider*, Berkeley, July 7-17, 1987, edited by R. Donaldson and M. G. D. Gilchriese (World Scientific, Singapore, 1988), p. 701, review CP violation in B decay and give references to previous work.

37. A. Pais and S. B. Treiman, Phys. Rev. **D12**, 2744 (1975);
L. B. Okun *et al.*, Nuovo Cim. Lett. **13**, 218 (1975).

38. This is correct if, as stated in the text, there is just one combination of K-M factors contributing. This appears to be an excellent approximation for $B_d \to \psi K_s$ and a good one for $B_s \to \rho K_s$, while there may be significant corrections for $B_d \to \pi^+\pi^-$: See, M. Gronau, Max Planck Institute preprint MPI-PAE/PTh-27/89, 1989 (unpublished), and B. Grinstein, Fermilab preprint FERMILAB-PUB-89/158-T, 1989 (unpublished).

39. The importance of the time dependence has been particularly emphasized by I. Dunietz and J. L. Rosner, Phys. Rev. **D34**, 1404 (1986).

40. This graph was constructed by R. Kauffman, in accord with the paper of Dunietz and Rosner, Ref. 39, but with somewhat different parameters: $s_1 = 0.22, s_2 = 0.09, s_3 = 0.05$ and $\delta_{KM} = 150°$.

41. I. Dunietz, University of Chicago Ph.D. thesis, 1987 (unpublished).

42. This possibility has been particularly emphasized by L. L. Chau and H. Y. Cheng, Phys. Lett. **165B**, 429 (1985).

43. D. Silverman, and A. Soni, Phys. Rev. Lett. **43**, 242 (1979).

Inverse Muon Decay, Neutrino Dimuon Production, and a Search for Neutral Heavy Leptons at the Tevatron

S.R.Mishra, K.T.Bachmann, R.F.Bernstein, R.E.Blair,
C.Foudas, W.C.Lefmann, W.C.Leung, E.Oltman,
P.Z.Quintas, F.J.Sciulli, M.H.Shaevitz, W.H.Smith

Columbia University, New York, NY 10027;

F.S.Merritt, M.J.Oreglia, H.Schellman, B.A.Schumm

University of Chicago, Chicago, IL 60637;

F.Borcherding, H.E.Fisk, M.J.Lamm,
W.Marsh, K.W.Merritt, D.D.Yavanovitch

Fermilab, Batavia, IL 60510;

A.Bodek, H.S.Budd, W.K.Sakamoto

University of Rochester, Rochester, NY 14627

Talk Presented by M.H.Shaevitz for the CCFR Collaboration at the 1989 SLAC Summer Institute on Particle Physics July, 1989, Stanford, CA.

ABSTRACT

We report on three recent measurements by the CCFR collaboration using the Fermilab Tevatron quad-triplet neutrino beam with neutrino energies up to 600 GeV. In a sample of 666,000 neutrino and 132,000 antineutrino events, 1151 inverse μ−decay events, $\nu_\mu e^- \to \mu^- \nu_e$, were isolated corresponding to a rate with respect to ν_μ-N charged current interactions of $(0.125 \pm .009(stat.) \pm .003(sys.)) \times 10^{-2}$. The data also contain 1522 ν_μ and 275 $\overline{\nu}_\mu$ induced opposite sign dimuon events which are due predominantly to charm production at the hadronic vertex. Using this sample, we have measured the strange sea content of the nucleon, $\eta_s = \int dx(2xs(x))/\int dx(xu(x)+xd(x)) = .057^{+0.012}_{-0.008}$, the Cabbibo-Kobayashi-Maskawa matrix element, $|V_{cd}| = 0.220^{+.015}_{-.018}$, and the slow-rescaling model charm mass parameter, $m_c = 1.3^{+0.6}_{-0.5}$GeV. Finally, a search for neutral heavy leptons in our $\mu^-\mu^+$ sample excludes such particles with masses up to 18 GeV and muonic coupling greater than 10^{-3} with respect to standard Fermi coupling.

1. INTRODUCTION

With the advent of the Tevatron fixed target program, our CCFR collaboration (Columbia, Chicago, Fermilab, and Rochester) began a program of high statistic studies of neutrino and antineutrino interactions. We report here on three measurements from the first of two data runs at the Tevatron using the quadrupole triplet neutrino beam (QTB) and the CCFR neutrino detector.[1] The QTB produces both neutrinos and antineutrinos in the ratio $\approx 2/1$ with energies up to 600 GeV. The data sample used in this analysis, after fiducial and kinematic cuts on the outgoing muon ($E_\mu \geq 15$ GeV and $\theta_\mu \leq 150$ mrad), included 666,000 charged-current neutrino and 132,000 antineutrino events.

2. INVERSE MUON DECAY

The inverse μ-decay process, $\nu_\mu e^- \to \mu^- \nu_e$, offers an elegant test of the weak interaction theory.[2] Since this is a purely leptonic interaction, the theoretical predictions can be unambiguously tested. In particular, the Lorentz structure of the weak-current can be investigated and, in contrast to studies of muon decay, contributions from scaler currents can be probed. However, the extremely small cross-section, about 0.1% of the neutrino-nucleon cross-section, and the relatively high threshold ($E_\nu \geq 11$GeV) make the study of inverse muon decay difficult. Two previous experiments[3] have reported observation of this process. We present here a new high statistics measurement with neutrino energies up to 600 GeV.

The differential cross-section for the inverse μ-decay can be expressed in terms of two parameters, the admixture of the vector and the axial-vector weak current (λ) and the neutrino polarization (P), as follows:

$$\frac{d\sigma}{dy_\mu} = \frac{G_F^2(s-m_\mu^2)^2}{8\pi s}\left((1+P)(1-\lambda)y_\mu^2 + (1-P)(1+\lambda)\right)$$

where $y_\mu = \mathrm{E}_\mu/\mathrm{E}_\nu$ and $s = 2m_e\mathrm{E}_\nu$. Within the standard model with a left-handed two-component neutrino (P=−1.0) and a pure V-A coupling ($\lambda = 1.0$), the predicted cross-section for $s \gg m_\mu^2$, is $\sigma(\nu_\mu e^- \to \mu^- \nu_e) = G_F^2 s/\pi = 17.2 \times 10^{-42} E_\nu(\mathrm{GeV})\ \mathrm{cm}^2$.

Inverse μ-decay (IMD) events are selected by using kinematic variables that distinguish these from the much larger sample of ν_μ-N charged - current (CC) events. The distinguishing features are: IMD events have no associated hadron energy, E_{HAD}; the final state muon in an IMD event is kinematically limited in the lab to small outgoing muon angles, $\theta_\mu < \sqrt{2m_e/E_\mu}$, or momentum transfers, $\mathrm{Q}^2 < 2m_eE_\nu$; and only incident ν_μ's can produce IMD events due to the absence of positrons in the target material.

The dominant background mechanisms, from ν-N interactions that produce low hadron energy events, are quasi-elastic events, $\nu_\mu n \to \mu^- p(\overline{\nu}_\mu p \to \mu^+ n)$, Δ and N* resonance production, and coherent meson production off the nucleus. These processes, collectively referred to as quasi-elastic-like processes (QEP), are expected to be produced equally by high energy ν_μ and $\overline{\nu}_\mu$.[4] Since $\overline{\nu}_\mu$ cannot produce IMD events, low hadron energy $\overline{\nu}_\mu$ events provide a measure of the QEP background to the IMD signal when corrected for relative flux.

The IMD signal is found by separating the ν_μ and $\overline{\nu}_\mu$ events with $E_{HAD} \geq$ 1.5GeV into eight visible energy bins between 15 and 600 GeV. After a $Q^2 \leq$ .2GeV^2 cut, the $\overline{\nu}_\mu$ events, scaled by $\frac{\nu_\mu - flux}{\overline{\nu}_\mu - flux}$, are subtracted to remove any remaining QEP background in the ν_μ event sample. Figure 1 shows the Q^2 distribution for the low-E_{HAD} ν_μ and scaled-up $\overline{\nu}_\mu$ events. The ν_μ event excess below Q^2 of .2 GeV^2 is the raw IMD signal.

The corrections, due to the $E_{HAD} \leq$ 1.5GeV cut, the Q^2 - cut, reconstruction failures and the non-isoscaler target, range from 35% for the lowest energy bin to 24% for the highest. In addition, events in the lowest energy bin must be corrected for the $E_\mu \leq$ 15GeV cut. Finally, the signal is corrected for the threshold effect using a Monte Carlo simulation of IMD events in the detector. The corrected signal, when combined with results from our previous Narrow Band Beam run,[5] yields an asymptotic rate with respect to inclusive CC events of: R= $(0.125 \pm .009(stat.) \pm .003(sys.)) \times 10^{-2}$. Using the measured[6] $\sigma_{\nu N}(CC) = (0.680 \pm 0.015) \times E_\nu \times 10^{-38}$ cm^2, the absolute asymptotic cross-section for IMD is: $\sigma(\nu_\mu e^- \rightarrow \mu^- \nu_e) = (17.00 \pm 1.22 \pm 0.41) \times E_\nu \times 10^{-42}$ cm^2. The ratio of measured to predicted cross-section for IMD is $\sigma_{meas.}/\sigma_{pred.} = 0.988 \pm 0.071(stat.) \pm 0.023(sys.)$. With the restrictions on neutrino polarization, $P < .9975$, from studies[7] of π/K decay, this measurement restricts $\lambda > .78$ at 90% C.L. and implies that the mass of a possible right-handed boson mediating a V+A interaction would have a lower limit of $M_{W_R} > 1.8 M_{W_L}$. This results also limits scaler couplings to < .13 of the V-A coupling at 90% C.L. ($|g^S_{LL}|^2 < 0.52$ using the notation of Ref. 8). Compositeness of the interacting fermions would possibly lead to deviations of the IMD cross-section from a linear energy dependence. A two parameter fit to $\sigma_{meas.}/\sigma_{pred.} = \alpha + \beta E_\nu$ yields a value for β of $(-1.09 \pm 1.14) \times 10^{-3}$(GeV^{-1}) consistent with zero.

2. OPPOSITE SIGN DIMUON PRODUCTION

Dimuon production by neutrinos and antineutrinos predominantly originates

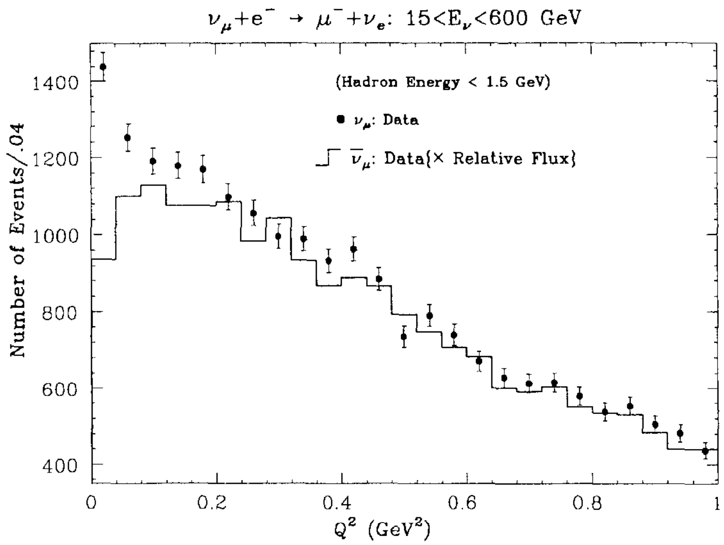

Fig. 1. Distribution of $Q^2 = E_\nu E_\mu \theta_\mu^2$ for events with $E_{HAD} \leq$ 1.5GeV. The ν_μ events are shown with solid circles. The $\overline{\nu}_\mu$ events, scaled by the relative ν_μ to $\overline{\nu}_\mu$ flux, are shown by the solid line.

from the production, off s or d quarks, of a charm quark at the hadronic vertex. The charm quark is assumed to fragment into charmed hadrons, typically D and D* mesons, which then decay semileptonically. Measurements of the rate and distribution of these events can be used to evaluate the strangeness content of the nucleon target, the effective charm quark mass in the $s(d) \rightarrow c$ quark transition, and the Cabbibo - Kobayashi - Maskawa matrix element, $|V_{cd}|$. The differential cross-section for ν-production of charm is given by:

$$\frac{d^2\sigma(\nu N \rightarrow cX)}{d\xi dy} = \frac{G^2 s}{\pi}\{\xi d(\xi)|V_{cd}|^2 + \xi s(\xi)|V_{cs}|^2\}\left(1 - \frac{m_c^2}{2ME_\nu \xi}\right)$$

where $d(\xi)[s(\xi)]$ represents the d(s)-quark number density within a proton target and ξ is the slow-rescaling modified Bjorken scaling variable, $\xi = x + m_c^2/2M\nu$. (A similar equation describes $\overline{\nu}_\mu$ production with $s \rightarrow \overline{s}$ and $d \rightarrow \overline{d}$.)

A sample of 1797 $\mu^-\mu^+$ events are extracted after fiducial and kinematic cuts, $E_\mu > 9$GeV , $\theta_\mu < 250$mrad and $E_{HAD} > 4$ GeV. An algorithm in which the leading muon is chosen to be the outgoing muon with the maximum P_T with respect to the hadron shower direction is used to separate the dimuon events into 1522 from ν_μ's and 275 from $\overline{\nu}_\mu$'s. With this algorithm the contamination from the wrong neutrino species in the ν_μ ($\overline{\nu}_\mu$) sample is 2%(26%).

The x-distributions of the data events are compared with predictions based on the above equation in order to determine the physics parameters, $\eta_s = \int(2xs(x)dx)/\int dx(xu(x) + xd(x))$, m_c, and $|V_{cd}|$. For this prediction, a Monte Carlo calculation is performed which allows the charm quark to fragment into D-mesons that decay semileptonically to muons with a branching ratio (BR) appropriate for the produced charm particle mixture. The predictions are sensitive to assumptions about: the light to heavy quark transition where we have used the "slow rescaling" formulation,[9] the fragmentation model for the charmed quark where the Peterson fragmentation function has been employed, and the $D^\circ/D^\pm/\Lambda_c$ production ratio taken from neutrino charm production measurements using an emulsion target.[10] Figure 2 shows the x-distribution for ν_μ and $\overline{\nu}_\mu$ induced $\mu^+\mu^-$ events. The individual contributions from the valence and sea components corre-

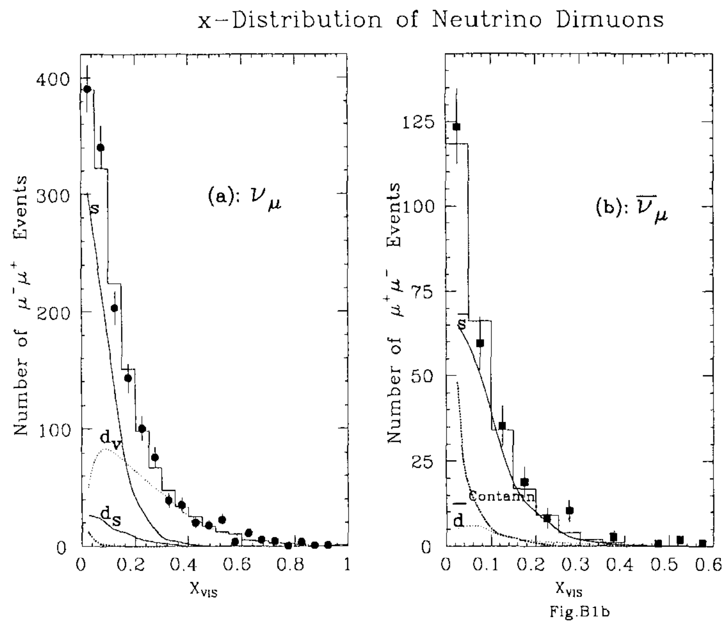

Fig. 2. The x_{vis}-distribution for a)ν_μ and b)$\overline{\nu}_\mu$ induced dimuons: data (solid circles) after background subtraction (from π/K decay), the histogram is the charm Monte Carlo prediction. The separate s-quark, $d_{valence}$, d_{sea}, and cross-over contamination are also shown.

sponding to the final parameters are shown as smooth curves along with the ν_μ cross-over contamination in the $\overline{\nu}_\mu$ sample.

The parameters are extracted by a simultaneous χ^2 fit of the Monte Carlo prediction to the data. The results are: $\eta_s = .057^{+.010+.007}_{-.008-.002}$, BR$= .109^{+.010+.005}_{-.010-.001}$, and $m_c = 1.3^{+.3+.6}_{-.4-.3}$ where the first error is statistical and the second systematic covering uncertainties in the Monte Carlo calculation. With a $\overline{Q}/Q$ ratio of .153 from our previous structure function analysis, this value of η_s corresponds to an approximate half SU(3) symmetric strange sea with $\kappa = 2s/(\overline{u}+\overline{d}) = .44^{+.11}_{-.07}$.

The matrix element $|V_{cd}|$ can also be extracted from a comparison of the observed ν_μ and $\overline{\nu}_\mu$ x_{vis} data and Monte Carlo distributions. Three quantities, representing the contributions of s, d-sea, and d-valence quarks to the dimuon production cross-section, are extracted assuming the above charm quark mass. This procedure yields: $\mathrm{BR}|V_{cd}|^2 = (0.534 \pm 0.050^{+0.015}_{-0.060}) \times 10^{-2}$, where the first error is statistical and the second is systematic. The latter is calculated by varying m_c and the fragmentation parameterization within allowed limits. The branching ratio of the ν -produced charmed hadrons can be independently calculated using emulsion data on neutrino production of charmed particles[10] and the muonic branching fractions for charmed hadrons,[11] giving a $\mathrm{BR}_{calc} = 0.109 \pm 0.009$. These two results can then be combined to give $|V_{cd}| = 0.220^{+.015}_{-.018}$ where the error includes systematic uncertainties in the BR, m_c, and the fragmentation.

3. SEARCH FOR NEUTRAL HEAVY LEPTONS IN ν-N INTERACTIONS

We have searched for indications of neutral heavy leptons (NHL) in our sample of $\mu^-\mu^+$ events. A NHL could be produced from an incident ν_μ by mixing followed by a weak neutral current interaction. In order to bypass a GIM suppression, the NHL would need to be a weak isospin singlet. Such NHL's have been proposed by various grand unified theories, left-right symmetric models, and models with mirror leptons.

The production of the NHL is suppressed by the mixing with the standard ν_μ, $|U_{\nu_\mu L^0}|$, and by a threshold factor due to the NHL mass. The relative production cross section is given by:

$$\frac{\sigma(\nu_\mu N \to L^0 X)}{\sigma(\nu_\mu N \to \nu_\mu X)} = |U_{\mu L^0}|^2 (1 - \frac{M^2_{L^0}}{2MxE_\nu})^2 .$$

Since the L^0 couples to standard neutrinos thru mixing, it can decay into a pair of muons via the charged or neutral current, $L^0 \to \mu^- + \mu^+ + \nu_\mu$, with a predicted branching ratio of 7% if the mixing to muons dominates.

The kinematics of NHL-induced dimuons are distinct from events due to conventional hadronic sources such as dimuons originating from charm or π/K decays. These later processes produce asymmetric μ-pairs: one at the lepton vertex and the other at the hadron vertex. In contrast, the μ^- and μ^+ from L^0 decay occur symmetrically at the lepton vertex. We use specialized kinematic cuts to isolate the L^0 events: i) The azimuthal angle, ϕ_{+-}, between the μ^- and μ^+ in a plane perpendicular to the beam direction must be less than 120°; ii) The transverse momentum, P_T^+, of the μ^+ with respect to the beam direction must be larger than 1.6 GeV. Figure 3a and 3b show the ϕ_{+-} and P_T^+ distributions respectively for the CCFR data (solid line) and for a Monte Carlo simulation of a 5 GeV L^0 (dashed line). As indicated in the figure, no data event survives these cuts.

The null result of the experiment when combined with Monte Carlo calculated efficiencies for different L^0 masses yields the 90% C.L. limits shown as curve a) of Fig. 4. Also shown are our previous limits from past experiments,[12] those imposed by the CHARM collaboration,[13] and an estimate of the sensitivity for a future monojet search of 10^5 Z° decays using the SLD detector at the SLC. Muon/electron universality tests put limits on couplings of the ν_μ to heavy neutrinos under certain model dependent assumptions. For example, a comparison[14] of nuclear beta decay to muon decay would restrict U^2 to below .008. With respect to this value, our dimuon limits are more stringent in the mass region from 0.5-10.0 Gev/c^2.

We acknowledge the gracious help of the Fermi National Accelerator Laboratory staff and the dedicated efforts of many individuals at our home institutions. This research was supported by the National Science Foundation and the Department of Energy.

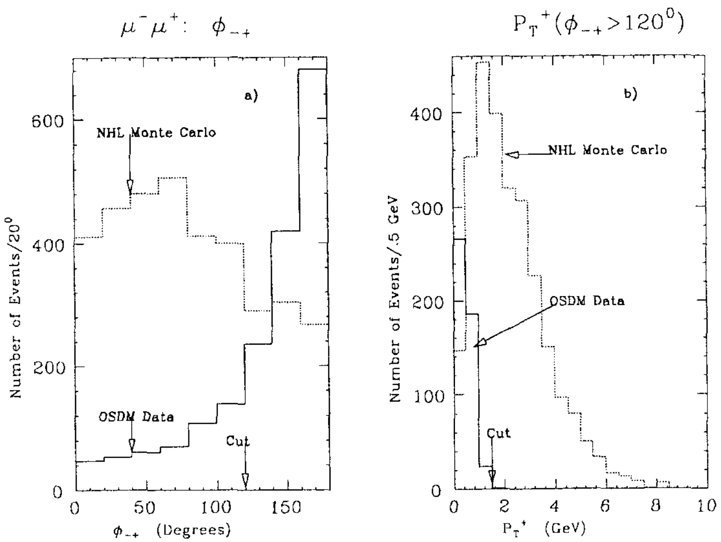

Fig. 3. a) Distribution of the azimuthal angle between the two muons, ϕ_{+-}. The solid line corresponds to the $\mu^-\mu^+$ data and the dashed line represents a Monte Carlo prediction for a 5 GeV/c^2 L° with $U^2 = 1.0$. b) Distribution of P_T^+ for events with $\phi_{+-} < 120°$.

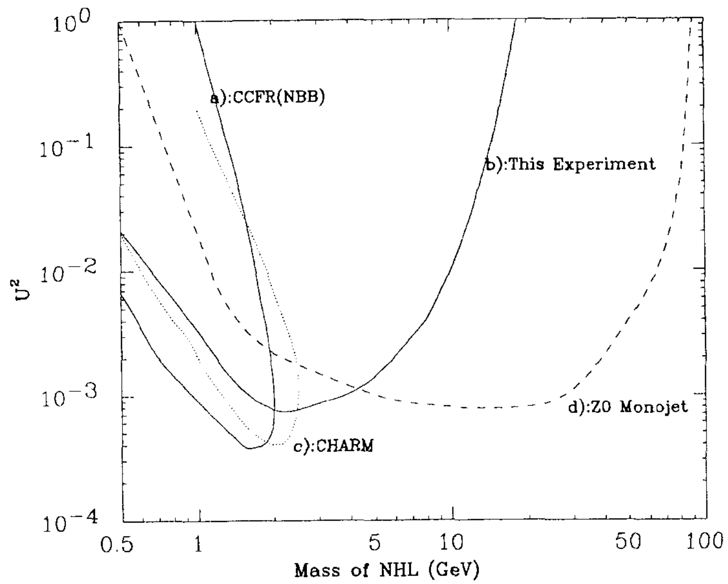

Fig. 4. Upper limits for NHL coupling to ν_μ; U^2 vs. L^0 mass. Curve a) Ref. 12, curve b) this measurement, curve c) Ref.13, and curve d) an estimate of the sensitivity of a future monojet search of 10^5 Z° decays in the SLD detector.

REFERENCES

1. F. S. Merritt et al., *Nucl.Inst.Meth.* **A245** (1986), 27.
2. E.C.G. Sudarshan and R.E. Marshak, *Phys. Rev.* **109** (1958), 1860 ; R.P. Feynman and M. Gell-Mann, *Phys. Rev.* **109** (1959), 193.
3. N.Armaenise et al., *Phy. Lett.* **B84** (1979), 137 ; M.Jonker et al., *Phy. Lett.* **B93** (1980), 203 ; F.Bergsma et al., *Phy. Lett.* **B122** (1983), 465.
4. D. Rhein and L.M. Sehgal, *Ann. Phy.* **133** (1981), 79.
5. S.R.Mishra etal.,, *Phys. Rev. Lett.* **63**(1989), 132.
6. The value is a weighted average of the CCFR measurement, R.E. Blair et al., *Phys. Rev. Lett.* **51**(1983), 343, and the CDHSW measurement, P. Berge et al., *Z. Phy.* **C35** (1987), 443.
7. R.Abela et al., *Nucl.Phys.* **A39** (1983), 413.
8. W.Fetcher, H.J. Gerber, and K.F. Johnson, *Phy. Lett.* **B173** (1986), 102.
9. H. Georgi and H.D. Politzer, *Phys. Rev.* **D14** (1976), 1829; R.M. Barnett, *Phys. Rev.* **D14** (1976), 70; A. DeRujula, *Rev. Mod. Phys.* **46** (1974), 391.
10. N. Ushida et al., *Phys. Lett.* **206B** (1988), 375.
11. D.G. Hitlin, *Nucl. Phys. (Proc. Suppl.)* **B3** (1988), 179.
12. S. R. Mishra, *Phys. Rev. Lett.* **59**(1987), 1397.
13. J. Dorenbach et al., *Phy. Lett.* **166B**(1986), 473.
14. R. Shrock and L. L. Wang, *Phys. Rev. Lett.* **41** (1978), 1692.

First Results from MACRO

THE MACRO COLLABORATION[1]
(Presented By Spencer Klein)

Department of Physics
Boston University
Boston, MA, 02215

ABSTRACT

MACRO (the Monopole Astrophysics Cosmic Ray Observatory) began collecting data this February. It is designed to: study the composition of high energy primary cosmic rays, search for point sources of cosmic rays, find or set limits on the cosmic magnetic monopole abundance, search for neutrino bursts associated with supernovae, search for point sources of high energy neutrinos, and to study neutrino oscillations with atmospheric neutrinos.

Results from the first three-month run are presented here. I will discuss throughgoing muons and give new limits on the magnetic monopole flux and on the rate of neutrino bursts from supernovae. For monopoles with velocities in the range $2.5 \times 10^{-4} < \beta < 1.5 \times 10^{-2}$, we find that the flux is less than $4 \times 10^{-14} cm^{-2} sec^{-1} sr^{-1}$ at a 90% confidence level. With the current supermodule, MACRO is sensitive to supernovae in the center of the galaxy, a distance of 10 parsecs. No supernovae candidates were observed during the run.

We have just started a new data run with this supermodule. Five more supermodules are now being built and instrumented; they should be complete next summer.

1. Introduction

MACRO is a large underground tracking detector located in Hall B of the Gran Sasso National Laboratory, 3000 feet (3800 m.w.e.) underground. It is situated under the Gran Sasso, the highest part of the Appenines, about 100 miles east of Rome, Italy.

The detector is optimized to study through going particles. It has three main subsystems: streamer tubes for particle tracking, liquid scintillator to measure particle time-of-flight and dE/dx, and a track etch detector which will be used to study any magnetic monopole candidates. The detector is being built by a collaboration of 15 U.S. and Italian institutions.[1] Because the detector is new, I will try to discuss the hardware in some detail. Further details are available elsewhere.[2]

One MACRO supermodule, measuring 12 meters square by 5 meters high began taking data this February. Results from the initial three-month run are presented here. We collected 245,000 muon triggers, and present a variety of studies of these single and multiple muon events. In addition, we have one solid candidate for an upward going, neutrino induced muon. We also present limits on the galactic abundance of GUTs monopoles and supernovae collapses.

2. Hardware

MACRO will eventually consist of 12 supermodules, as shown in Figure 1. Supermodule 1 is complete and taking data, 2-3 are mechanically complete, awaiting instrumentation, 4-6 are under construction, and 7-12 will be built in a year or two. Each supermodule is capable of independent operation, so it will not be necessary to turn off the entire detector for calibrations and maintenance. A cross section of one supermodule is shown in Figure 2. Each supermodule may be thought of as a core of pulverized rock, chosen for its low radioactivity, encased in steel containers, interspersed with streamer tubes, and surrounded by liquid

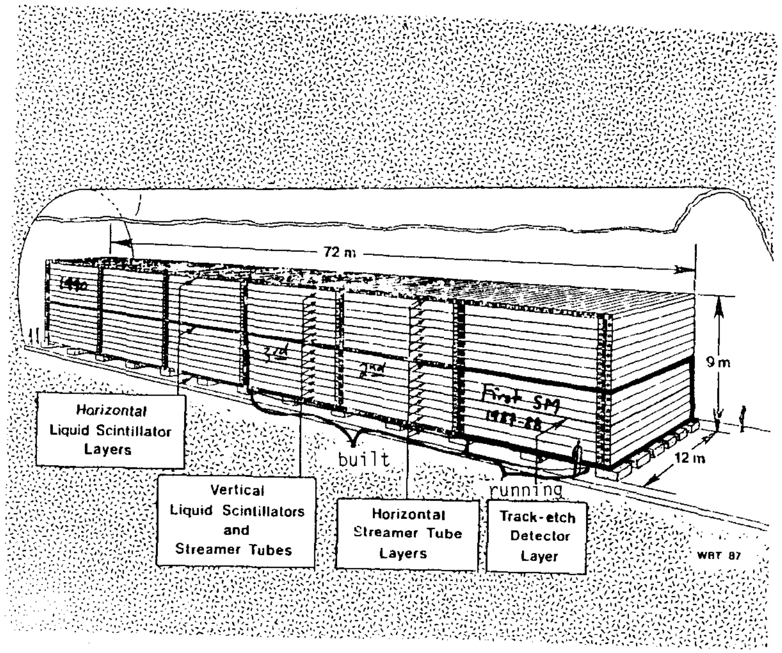

Figure 1. Layout of the MACRO detector. Supermodule 1 is operational; 2 and 3 are mechanically complete, and 4-6 are under construction.

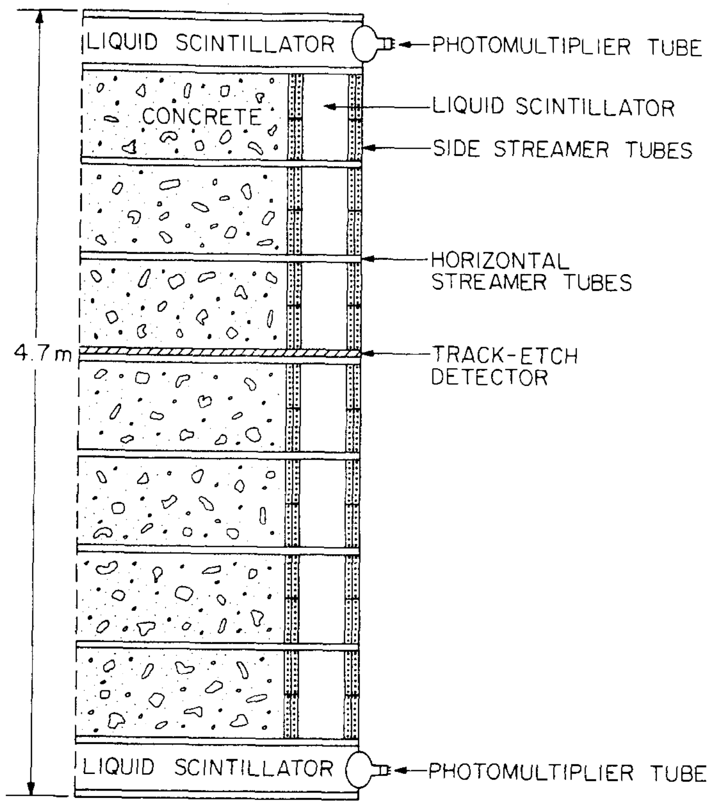

Figure 2. Cross Section of one supermodule.

scintillator. Supermodules 1-6 also contain a CR-39 and lexan track etch detector sandwich. Each supermodule is 12 meters square by 5 meters high, so that the complete detector will be 72 meters by 12 meters by 9 meters high.

The core of MACRO consists of a sandwich of streamer tubes and steel boxes containing ground up rock. This core is surrounded by PVC tanks filled with liquid scintillator. The scintillator tanks are themselves surrounded by more streamer tubes, giving a total of 10 streamer tube planes.

The streamer tubes are each 3 cm square by 12 meters long, with $100\mu m$ anode wires. The cathodes are graphite coating on plastic package. The present gas mixture is Argon, CO_2, and n-pentane. In future runs, helium will be added to the mixture, to allow for efficient detection of low velocity monopoles through the Drell effect.[3] Also, isobutane may replace the n-pentane for some of the running. The 5,000 anode wires are read out, along with the cathodes, which are divided into strips to give a 26^0 stereo view. The resolution is 1.1 cm in the x direction, and 1.2 cm in the D view. The minimum two-hit separation distance is about 3 cm. With 10 planes of tubes, the angular resolution is about 0.1^0. In comparison, downward going muons will multiple scatter by about 0.6^0 as they traverse the rock.

The liquid scintillator is a mixture of ultra pure mineral oil, pseudocumene, wavelength shifter, and anti-oxidants. The purity is necessary to maximize the attentuation length; the measured attenuation length is about 12 meters.

The liquid scintillator is held in 12 meter long tanks. Each supermodule has 16 top and 16 bottom tanks, and 7 on each side. Those on the horizontal layers have a 75 cm by 25 cm cross section; those on the vertical walls measure 50 cm by 24 cm. The boxes are lined with reflective FEP teflon. At each end of the boxes are 20 cm phototubes,[4] one per end in the vertical boxes, and two per end in the horizontal. For a typical muon passing through the center of the tank, the PMTs on each end currently detect roughly 400 photoelectrons. We are now improving the optics, and this will be increased by a factor of 3 in subsequent runs. The timing and amplitude of these pulses are measured with TDC's and ADC's. From the relative timing, we determine the position in the tank. Because of the 12 meter attenuation length, we can also determine the relative position based on the ratio of the amplitudes. By comparing these two positions, we can get a check on the quality of the data. A scatter plot of the positions determined by these two methods is shown in Figure 3. The resolution of the two methods is about 25 *cm*; most of the error is from the amplitude ratio. These positions can also be compared with the position determined from the streamer tubes. This will allow us to reject hits where the data is contaminated with a simultaneous radioactive decay. In addition, the tank ends are read out with a 100 MHz, 8 bit waveform digitizer; this is used for studying magnetic monopole candidates, stopping muons, multimuon events, and candidates for upward going muons.

The detector has a variety of triggers, each designed to detect different processes. Both the streamer tubes and scintillator have muon triggers. The streamer tube trigger searches for tracks; the scintillator trigger requires that tanks in two different faces be hit within 7 μsec. A muon will traverse the detector in less than 40 nsec; the wide time window is to trigger on possible 'fast' monopoles. For slower monopoles, a special monopole trigger searches for trains of photoelectrons in the scintillator. Another trigger detects neutrino interaction from gravitational collapse by monitoring and recording the rate of single tank hits.

The event times are determined from a rubidium-cesium clock, accurate to 1 μsec. It, and the other electronics are read out by a network of μVAXes, controlled by a VAX 8200.

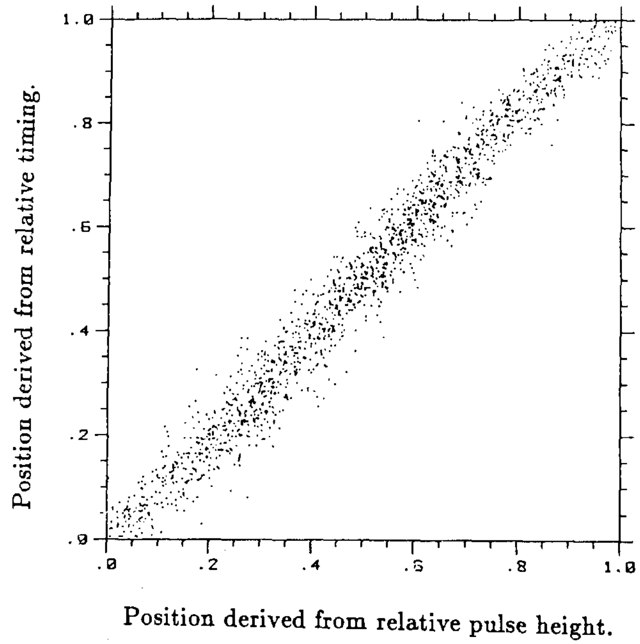

Figure 3. Scintillator tank position derived from TDC information versus position derived from ADC information. Both are on a scale which goes from 0 to 1.

3. Muon Physics

Studies of cosmic ray muons can contribute to a wide variety of physics topics. Downward going muons provide information about the cosmic ray spectrum. Muons may be detected from point sources.[5] Multiple muons, when two or more muons from a single interaction are detected, provide information about the cosmic ray primary composition. MACRO also has the capability to detect upward going muons from neutrino interactions. These can come from point sources, ushering in the field of neutrino astronomy, or from atmospheric neutrinos. The atmospheric neutrinos can be studied for evidence of neutrino oscillations. Finally, muons provide a good measurement of detector performance.

3.1. Detector Performance with Muons

The most obvious check of detector performance with muons is to measure their velocity, using the time-of-flight between the two scintillator layers. The flight time divided by the path length ($1/\beta$) is shown in Figure 4. The velocity resolution is 9.3% of c, corresponding to a time resolution of about 1.7 nsec. It is likely that this will be improved in the future, with improved calibration and algorithms. However, the final resolution is less important than the tails, since the tails of the distribution can form a background to a search for upward going muons. In MACRO, the measured time-of-flight is Gaussian over 4 orders of magnitude. The small remaining tails are due to events where there is a radioactive decay in one of the scintillator tanks during the muon traversal. These events can be controlled by careful streamer tube - scintillator matching and by study of the waveform digizer output, which will show the separate decay and muon pulses.

The overall muon rate is 1 every 40 seconds per supermodule, in agreement with predictions from other experiments, as shown in Figure 5. The rates as a function of azimuth and zenith angle are shown in Figure 6. The solid curves are predictions based on the rock thickness above the detector and the predicted

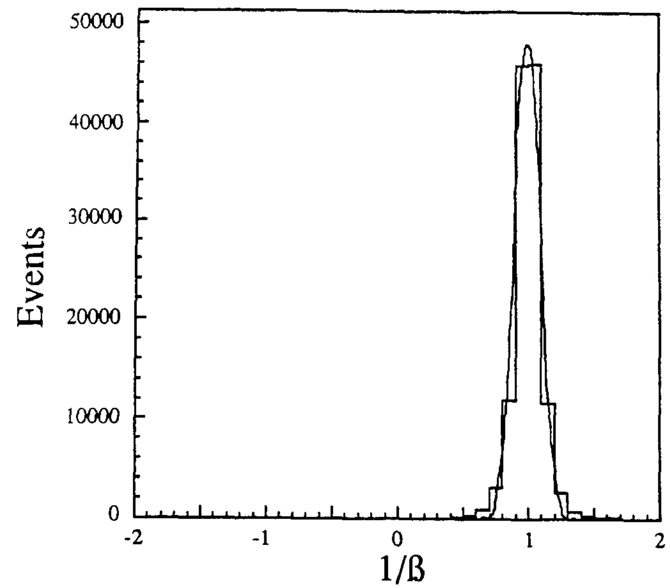

Figure 4. Measured μ time-of-flight, normalized to the path length.

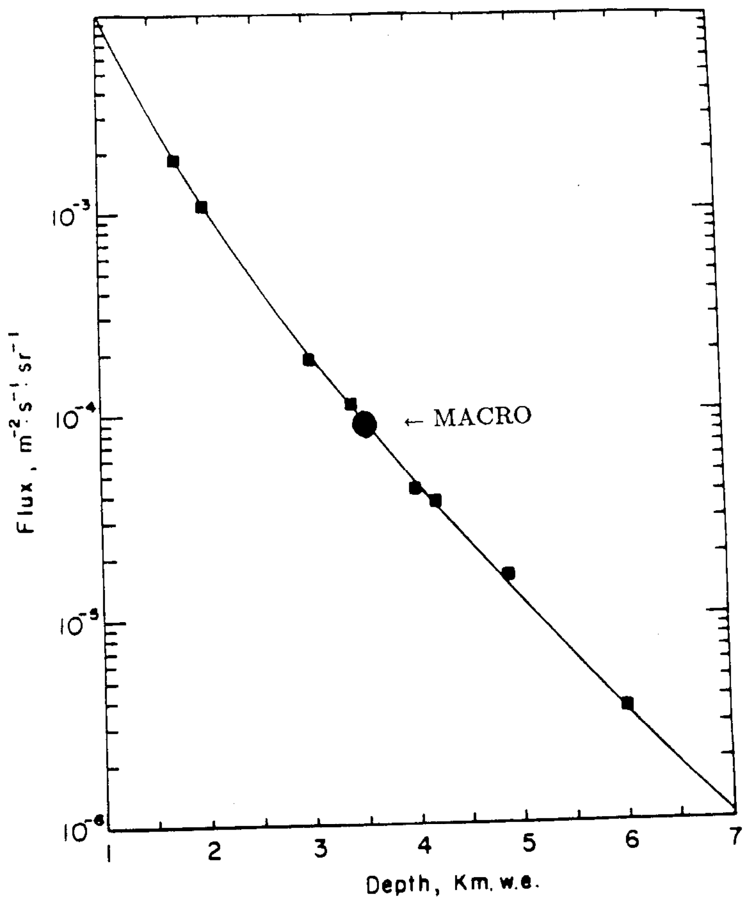

Figure 5. μ rate as a function of depth.

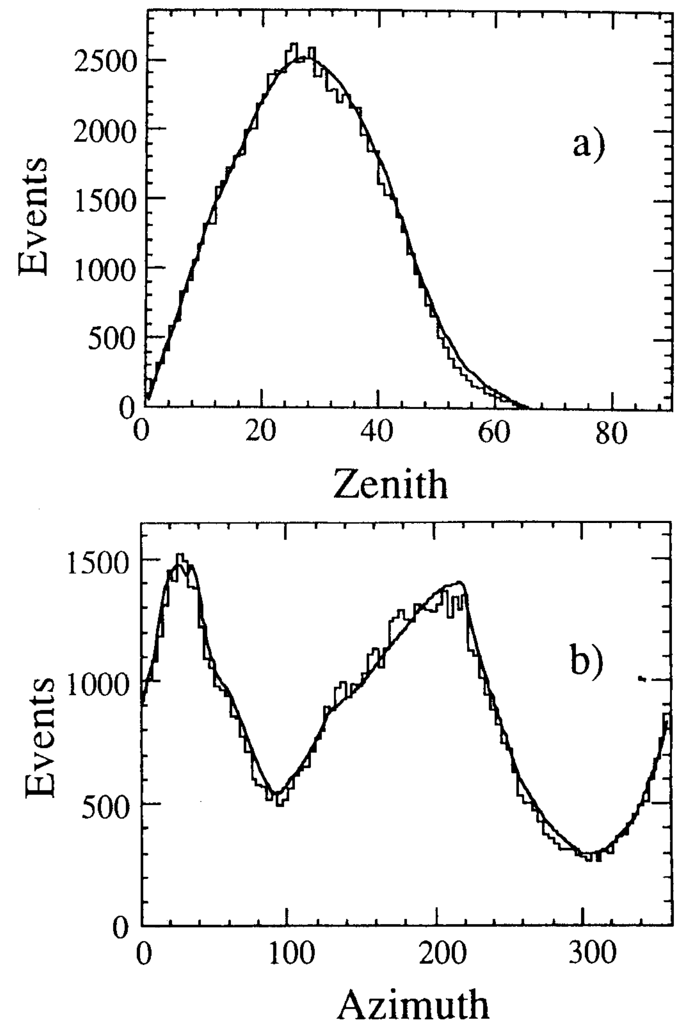

Figure 6. Muon rate as a function of (a) zenith angle and (b) azimuth. The solid lines are the result of a calculation including the rock thickness.

muon energy spectrum. This calculation checks the detector response, rock modelling, and the muon energy spectrum, since the muon energy needed to reach the detector varies with the rock thickness.

Muons need roughly 1.5 TeV to penetrate to MACRO. A detailed model of the mountain above MACRO is used to predict the effective rock thickness, and hence minimum muon energy, as a function of angle incidence. That energy 1.5 TeV corresponds to a minimum primary energy of 20 TeV, or a center of mass energy of 150 GeV, fitting nicely into the theme of this summer school. When a 20+ TeV proton (or heavier nucleus) hits the atmosphere and interacts, pions and kaons are produced. Since the upper atmosphere is thin, many of the pions and kaons have time to decay to muons before interacting. There are also a few muons from prompt sources, such as semileptonic heavy quark decays and Drell-Yan production.

In addition to the single muons, MACRO has seen a large number of multiple muon events. A typical six muon event is shown in Figure 7. The multiplicity distribution of muons is shown in Figure 8, not yet corrected for detector acceptance. There are about 3% as many di-muons as single muons, with the rate decreasing by a factor of 20-40 for each additional muon. Since, for a given energy, a heavier primary cosmic ray nucleus will, on the average, produce a larger number of muons,[6] it is, in principle, possible to determine the primary composition by studying the muon multiplicity distribution. With present statistics, MACRO can differentiate between the popular models of cosmic ray composition, such as the 'low energy' model,[7] where the cosmic ray composition at high energy matches that at lower energies, and the Maryland model,[8] which predicts a heavier composition. However, there are many theoretical uncertainties involved, and considerable Monte Carlo work is needed before we present any conclusions on this subject. In addition to the muon multiplicity, MACRO has an additional tool to study the subject: a surface air shower detector array located on the Gran Sasso above MACRO.

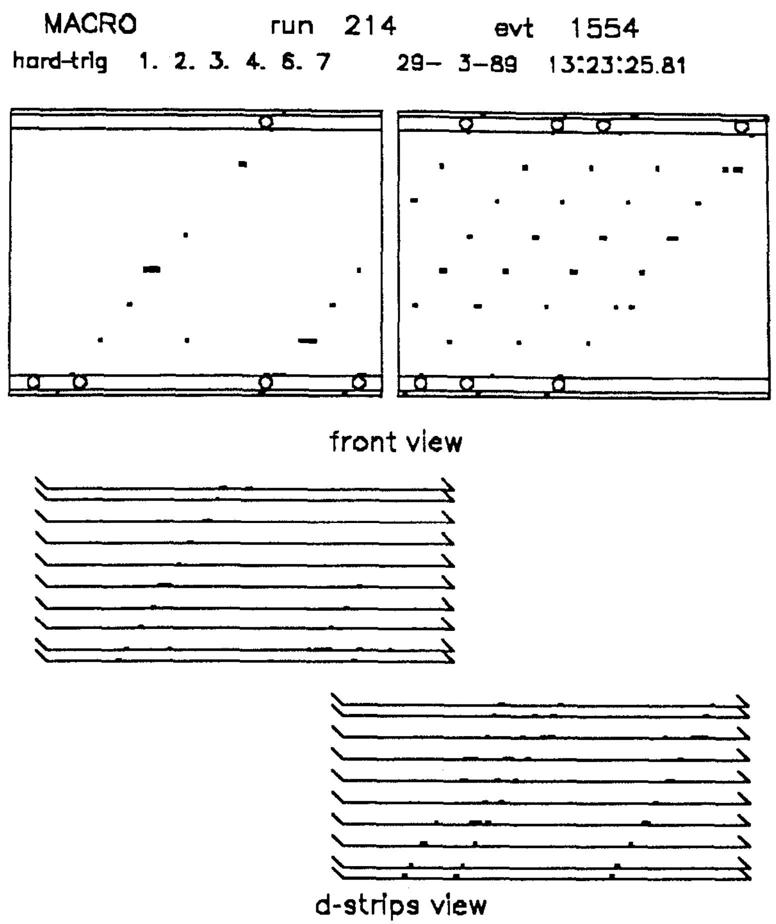

Figure 7. An event plot of a multiple μ event.

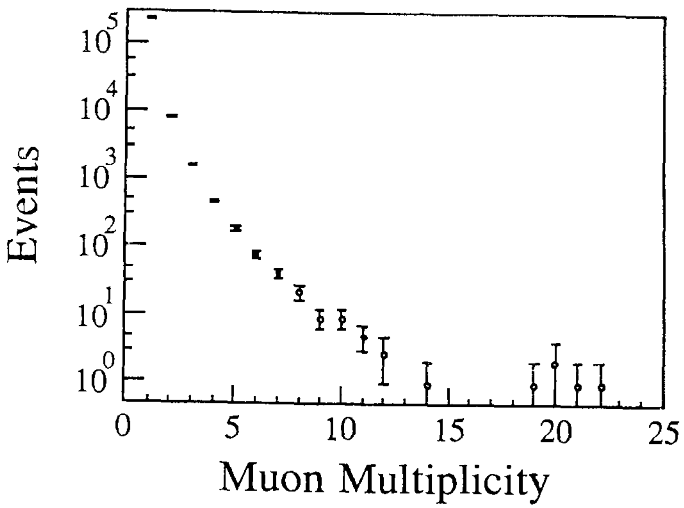

Figure 8. Observed MACRO μ bundle multiplicity.

3.2. Correlations with EASTOP

EASTOP is an extensive air shower array located on the mountain above MACRO. It is composed of 22 operating stations,[9] each comprising 10 m^2 of plastic scintillator. The detector array covers an area of 10^5 m^2. Because the mountain is rugged, the EASTOP collaboration[10] uses a small number of relatively sophisticated detectors, rather than a larger number of simple ones.

The array is triggered by a coincidence of at least 5-7 stations. This corresponds to a threshold of about 200 TeV, ten times the MACRO threshold of 20 TeV. The shower energy, found from the shower size and density, is measured to better than 200%. The shower direction, found from the relative arrival times of the shower front, is found to better than 2^0. Both of these numbers should improve as the analyses mature.

During the initial run, MACRO and EASTOP operated in coincidence for 1107 hours. Crude coincidences were found by requiring triggers to agree within 6 msec, and the MACRO muon to point back within a 17^0 by 40^0 rectangle around EASTOP. A total of 347 coincidences were found, with the relative time distributions shown in Figure 9. The peak has a width of 90 μsec, dominated by the uncertainty in the EASTOP clock.[11] The accidental coincidence rate, less than 3%, can be further reduced by tighter angle cuts.

Figure 10 shows the multiplicity distribution for these coincidence events. The average multiplicity is much higher than for MACRO only events. This is because of the much higher EASTOP trigger threshold.

The MACRO-EASTOP coincidences can be used to improve our determination of the cosmic ray spectrum as a function of energy. Knowing the muon multiplicity as a function of the independently measured shower energy will eliminate many of the theoretical uncertainties in the composition analysis.

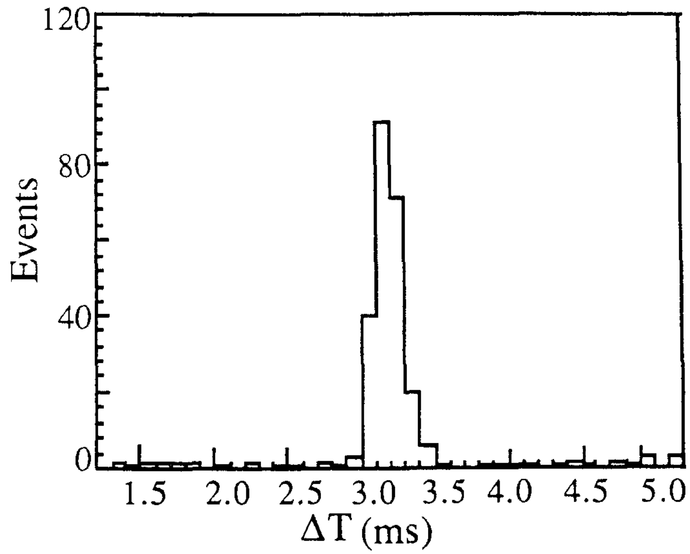

Figure 9. MACRO-EASTOP measured time difference for correlated events.

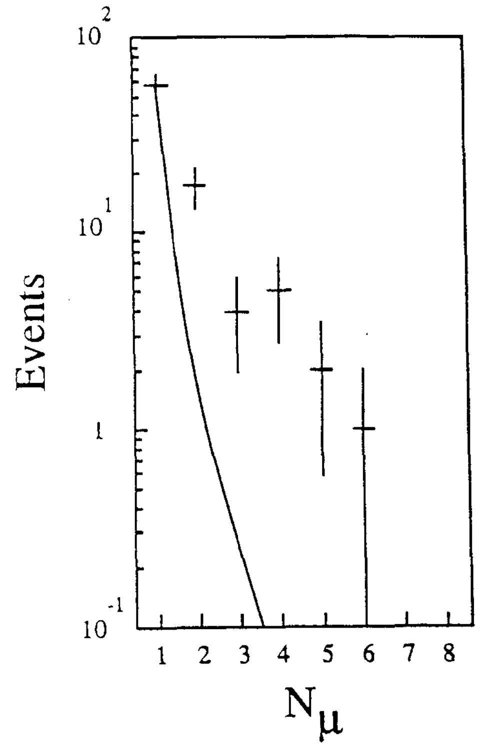

Figure 10. MACRO measured μ bundle multiplicity for MACRO-EASTOP correlated events. The smooth line is the measured multiplicity for all MACRO events, normalized to the EASTOP data for single muons.

3.3. Neutrino Events

MACRO can also detect upward going muons from neutrino interactions in the rock below the detector. One such event is shown in Figure 11. The muon hits two adjacent scintillator tanks in both the top and center layers. All of the adjacent tanks have consistent times, and the particle β is 0.995. These neutrino events are useful for two primary physics goals.

They can be used to search for point sources of neutrinos, to begin the field of neutrino astronomy. The theoretical predictions for expected neutrino flux are quite uncertain, but, with 6 supermodules operating, MACRO expects to see 1-10 events per year from southern hemisphere sources such as Vela X-1, the LMC, etc. The expected background from atmospheric neutrinos is about 400 events per year total, or about 1/40 per square degree. The expected resolution, limited by the scattering from the neutrino interaction, is about 1 degree.

Most of the background to the point source search is from atmospheric neutrinos, created in cosmic ray interactions. These neutrinos can be used to study neutrino oscillations,[12] extending the search for oscillations to much lower mass differences.

4. Magnetic Monopoles

A primary goal of MACRO is to search for magnetic monopoles. Since GUT (grand unified theory) monopoles are expected to be extremely heavy, they are not accessible to accelerator experiments, and can only be sought astrophysically. We expect to either find monopoles or to reach the Parker bound, the limit implied by the galactic magnetic field. MACRO is designed so that any monopole candidates will be detected in several independent ways. The streamer tubes, scintillator, and track etch are all sensitive to monopoles of varying velocities. The search presented here uses only the scintillator system.

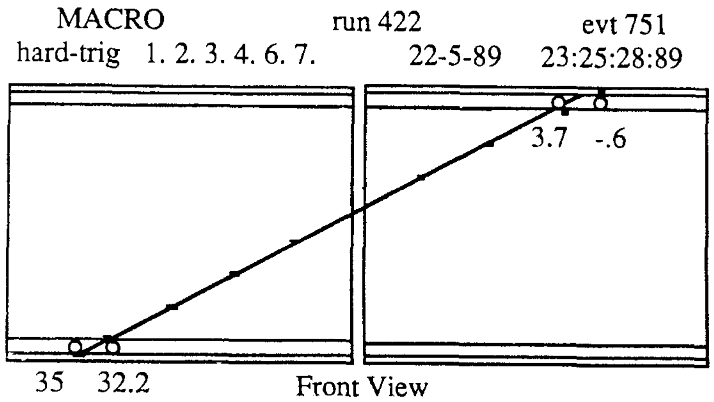

Figure 11. The first upward going muon event. The circles represent scintillation counter hits, and the dots are streamer tube hits. The numbers are the times in nsec, with an arbitrary offset. The particle β is 0.995.

Presently, we require monopole candidates to hit two scintillator planes, giving an acceptance of 800 m^2 sr. A special trigger circuit looks for long light pulses in the scintillator. For the slowest monopoles, these pulses will consist of individual single photoelectron pulses. When a trigger is detected, the tanks are read out with 50 MHz waveform digitizers which provide a graphic record of the pulse. LED's in the tanks can mimic fake monopoles; one such calibration pulse is shown in Figure 12.

With the waveform digitizers, we have searched 7.3×10^6 seconds of data, looking for pulses with length greater than 200 nsec, separated by at least 1 μsec. We found and hand scanned 2417 triggers. They were rejected on the basis of the recorded pulse shape and by requiring a match between the two ends of the tank. Roughly one-third of them were electrical breakdowns,[13] one-third were muons with electrical ringing, and one-third were one-sided (pulses visible in only one side of the counter). The latter are likely due to radioactive decays in the PMT itself. No candidates were observed.

From this, we find that, for velocities $2.5 \times 10^{-4} < \beta < 1.5 \times 10^{-2}$, the monopole flux is less than $4 \times 10^{-14} cm^{-2} sec^{-1} sr^{-1}$, at a 90% confidence level. Figure 13 compares this limit with other results.[14] The mica limit depends on the assumption that monopoles will bind to aluminum nuclei, with the nucleus leaving a track in the mica. The scintillator limit is from an experiment at Baksan searching for slow particles underground. The velocity limits come from electronics limitations.

In the future, MACRO will extend this limit to higher and lower velocities, and, of course, to lower fluxes. In addition, the streamer tubes will be integrated into the analysis. The ultimate lower velocity limit is a β of about 10^{-4}, while the upper limit be a β of 1, or close to it. For the higher velocities, a separate trigger looks for particles that look like slow muons.

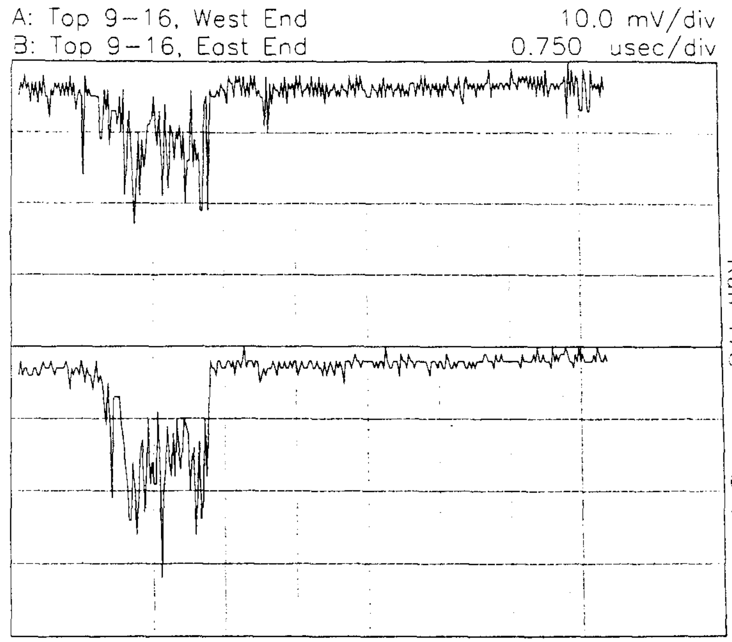

Figure 12. A calibration monopole, created with an LED pulse. A monopole with a β of 5×10^{-4} is being simulated. It takes 1.3 μsec to pass through the scintillator tank.

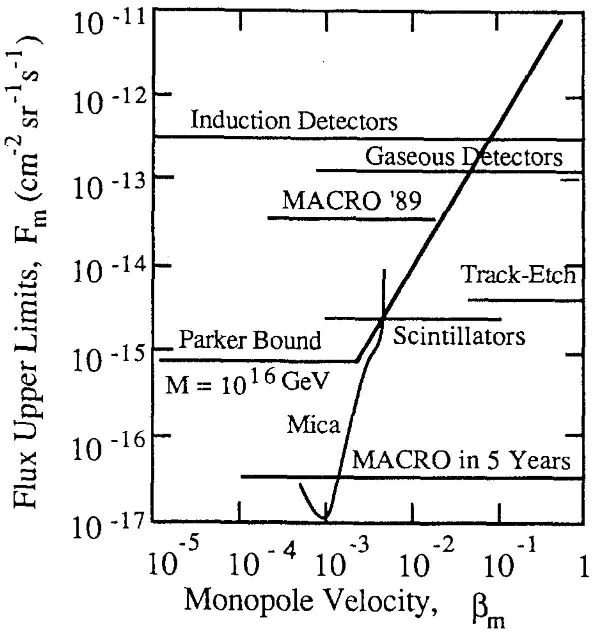

Figure 13. The MACRO monopole flux limit, compared with other limits. The induction limit is a combined limit; the others are representative 'best' limits for the various techniques. See the text for discussion and references.

5. Supernovae Search

MACRO has also searched for bursts of low energy neutrinos, a manifestation of a nearby supernova. These neutrinos have average 10 MeV in energy, and, when they interact, will deposit this energy in a single scintillator tank. MACRO searches for the bursts by monitoring the rate of single tank events. The active mass is 42 tons of scintillator.

MACRO has a two special triggers to search for the low energy, single tank interactions. Both measure the times and amplitudes of the scintillator pulses, to see if they are compatible with a single energy deposition. For accepted pulses, the tank data and the absolute time are stored in a gravitational collapse buffer. This buffer is read periodically by the computer. The major background is radioactive decay in the tanks. The energy threshold is about 5 MeV, which gives a trigger rate of roughly 1/40 Hz.

The gravitational collapse analysis covers 1.6×10^7 seconds live time. For the analysis, a 10 MeV software cut was imposed, and the number of single tank events in any two second period was counted. The data is shown in Figure 14; it is consistent with a Poisson distribution, with no supernovae. The largest number of detected events is four; a supernova like SN1987a occurring in the center of the galaxy would cause an average of eight interactions.

These statistics allow us to rule out any supernovae at the center of the galaxy (or within 10 parsecs) at a 90% confidence level during the MACRO running period.

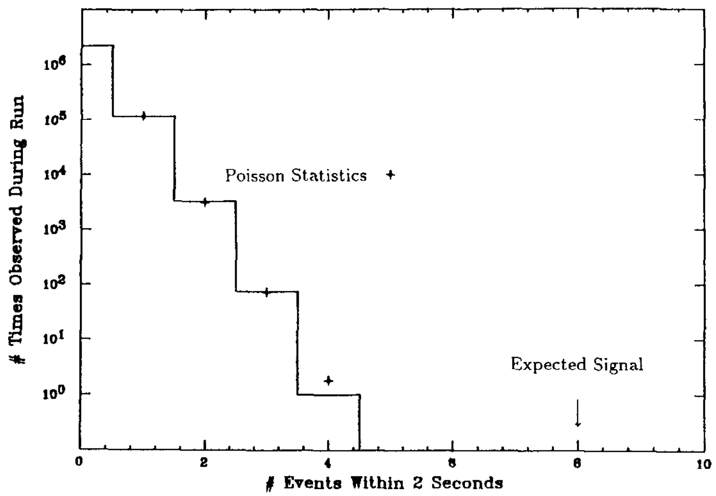

Figure 14. Plot of the number of tanks hit per two second interval versus frequency. The data fits a Poisson distribution. The expected signal for a supernova in the center of the galaxy is shown.

6. The Future

In September, after tuning up the detector, MACRO began a nine-month run with one supermodule. Meanwhile, we are hard at work building and instrumenting the remaining five supermodules. Numbers 2 and 3 are mechanically complete, while 4-6 are undergoing construction. We expect to have them complete and instrumented next summer. In 1990-91, we will begin the six upper deck supermodules. We plan to continue the same liquid scintillator arrangement, with the upper and lower decks sharing a single layer of scintillator in the center. Since the tracking resolution is already limited by multiple scattering, we are exploring alternatives to more rock and streamer tubes. Two of the most promising are an iron toroid magnet and a transition radiation detector (TRD). The iron toroids would allow us to measure the muon charge (and momentum) up to roughly 50 GeV momentum. Since many of the muons from atmospheric neutrinos are low momentum, this is useful for studying neutrino oscillations. The TRD will allow us to measure the muon momenta over a very wide range.

7. Conclusions

MACRO has just completed a three-month engineering run. Much muon data has been collected; analysis is proceeding.

We have set a limit on the galactic magnetic monopole flux. For monopole velocities $2.5 \times 10^{-4} < \beta < 1.5 \times 10^{-2}$, the monopole flux is less than $4 \times 10^{-14} cm^{-2} sec^{-1} sr^{-1}$ at a 90% confidence level.

We have also set a limit on the number of supernovae in the galactic center. At a 90% confidence level, the supernovae rate is less than 1 per month.

Data collection continues with the single supermodule. Next summer, we expect to commission five more supermodules, and to use them for exciting physics.

REFERENCES

1. The current members of the MACRO collaboration are: Bari, Bologna, Boston, Caltech, Drexel, Frascati, Indiana, L'Aquila, Lecce, Michigan, Napoli, Pisa, Roma, Texas A & M, and Torino.
2. M. Calicchio *et al.*, Nucl. Inst. and Meth. **A264**, 18 (1988).
3. S. D. Drell *et al.*, Phys. Rev. Lett. **50**, 644 (1983).
4. The PMT's are Hammamatsu R-1408 in the first supermodule, and will be Thorn-Emi D647 in the remainder of the detector.
5. This subject is controversial. For a good review, see D.E. Nagle, T.K. Gaisser and R.J. Proethroe, Ann. Rev. Nucl. Part. Sci **38**, 609 (1988).
6. L.G. Dedenko and Yu.N. Vavilov, in *Proceedings of the XXth International Cosmic Ray Conference*, Moscow, 1987.
7. M. Simon *et al.*, Astrophys J. **239**, 712, and references therein.
8. J. A. Goodman *et al.*, Phys. Rev. Lett. **35**, 854 (1979).
9. There were 29 originally; several were destroyed by various factors, including an avalanche.
10. A group at the University of Torino.
11. EASTOP will shortly acquire a new clock, improving the timing accuracy by a factor of close to 100.
12. G. Auriemma *et al.*, Phys. Rev. **D37**, 665 (1987).
13. This problem is now being corrected.
14. The gaseous detector limits is from T. Hara *et al.*, Phys. Rev. Lett. **56**, 553 (1986); the Induction detector limit is from Blas Cabrera, in the Proceedings of the 16th SLAC Summer Institute on Particle Physics, Stanford, CA, 1988. SLAC-Report-336. The scintillator limit is from A.E. Chudakov, Sov. J. Phys. Usp. **28**, 1054 (1985); the track etch limit is based on a nitrocellulose, given in T. Doke *et al.*, Phys. Lett. **129B**, 370 (1983); the mica limit is based on a track-etch technique, described in P.B. Price *et al.*, Phys. Rev. Lett. **52**, 1265 (1984).

A Superstring Theory Underview*

LANCE J. DIXON†

Stanford Linear Accelerator Center
Stanford University, Stanford, California 94309

ABSTRACT

I give a brief survey of the current status of superstring phenomenology, with an emphasis on the (currently unrealized) possibility of obtaining model-independent results.

Lecture presented at the
17th SLAC Summer Institute on Particle Physics
Stanford, California, July 10–21, 1989.

⋆ Work supported by the Department of Energy, contract DE-AC03-76SF00515.
† On leave from Joseph Henry Laboratory, Princeton University, Princeton, NJ 08544 until Sept. 1, 1989.

1. Introduction

This talk is meant to briefly and qualitatively summarize the current status of superstring phenomenology, and to mention what I think are the outstanding problems that must be solved before we can hope to get experimental predictions from string theory. The topic of this SLAC Summer Institute is "Physics at the 100 GeV Mass Scale", the region accessible to current accelerators. On the other hand, the characteristic mass scale for superstrings is the Planck mass $M_{\rm Pl} \simeq 10^{19}$ GeV/c^2. The Planck scale appears because strings provide a description of quantum gravity, and gravity is characterized by Newton's constant, which has mass dimension -2: $G_N = c\hbar/M_{\rm Pl}^2$. It will be useful to keep in mind throughout this talk the gap of 17 orders of magnitude in energy, because any predictions from superstrings will depend on analysis of effects over the entire range.

Recent work on superstrings has concentrated on answering questions in the following three areas:

(1) Fundamental understanding: Is string theory based on some new physical principle, in the same way that Yang-Mills theory, for example, is based on local gauge invariance?

(2) Formalism: Can we extend the calculational tools that have been developed for string theory to include non-perturbative effects?

(3) Phenomenology: Can we hope to make definite predictions of new (and old) phenomena at experimentally accessible energies?

I will focus on the third area in this talk (though I will digress to cover a little of the relevant formalism as well). Far below the Planck scale, strings appear to be pointlike, and string theory reduces to some *effective field theory.* At energies around 100 GeV this field theory should in turn reduce to approximately the standard model, if string theory is to describe experimental reality. At these energies, any predictions of string theory are therefore indirect, and can be summarized as predictions of the 18 or so input parameters of the standard model (or more accurately, *explanations* of those parameters that have already been measured), plus predictions of possible field theory extensions of the standard model and the parameters therein. Currently, string predictions also involve the rather arbitrary selection of a candidate string *vacuum*, or ground state, from a large set of degenerate vacua. Each such choice leads to a different effective field theory, and hence to a different model for physics at 100 GeV. Here I will describe the set of string vacua, and the prospects for obtaining "model-independent" predictions from string theory, and also (very briefly) summarize a few recent attempts to construct specific quasi-realistic[‡] models.

The three general areas of research are all related. In particular, a better fundamental understanding of string theory should lead to advances in the formalism, which should in turn lead to more concrete phenomenological predictions than at present.

Superstrings[1] generated much theoretical excitement in 1984, when it was realized that they had the potential for unifying all of the known gauge forces together with gravity, and for doing so in a practically unique way. Uniqueness is of particular importance due to the large discrepancy in energy scales between strings and current experiments: Since the signatures of string theory are so indirect, it would be nice if they were quite definite. At present, we still have the same limited number of string theories as were known in 1984: *bosonic strings*,[2] *superstrings*,[3] and *heterotic strings*.[4] The bosonic and superstring theories can contain either closed strings only, or else both closed and open strings; the strings can be either orientable (have an arrow along them specifying a direction) or non-orientable (no such arrow). The heterotic string theory is a hybrid of the bosonic and superstring theories, and as a consequence it contains only closed, orientable strings. Of these theories, only the heterotic string has any phenomenological promise, at least at our present level of understanding of string theory. A possible exception to this statement is the closed+open superstring with gauge group $SO(32)$;[5] this string

‡ A very fashionable adjective in string phenomenology.

theory has received much less attention than the heterotic string (due partly to a lack of any *obvious* phenomenological promise, and partly to a relative lack of open-string formalism), and I too will slight it here.

2. Vacuum Proliferation, Particle Spectrum, and Effective Lagrangians

So we still have in 1989 only one phenomenologically viable string theory, the heterotic string (with the possible exception of the $SO(32)$ superstring). However, there has been a recent proliferation of string *vacuum states*, which appear to be degenerate in energy to all orders in (string) perturbation theory. This non-uniqueness of the vacuum can play havoc with attempts to extract definite predictions from string theory, so I will spend some time describing it.

The vacuum proliferation has come through the realization that for any two-dimensional (2d) *conformal field theory*[6] (CFT) one can construct a vacuum state for classical string theory. I will describe the relation between CFT and string vacua in more detail later. For now, we just need to know that, in any particular string vacuum state, *the full spectrum of elementary particle masses and couplings are completely specified by the CFT for that vacuum.*

Elementary particles in string theory are identified as the different rotational and vibrational eigenmodes of a string as it oscillates around a vacuum state. The (mass)^2 of the particle is proportional to the frequency of vibration, and in the first approximation it is an integer multiple of some basic mass parameter M^2 of order $M_{\rm Pl}^2$. A typical spectrum is shown in Figure 1(a). Each of the mass levels shown in the figure is highly degenerate. The lowest level is of the most interest to us because it contains all the massless particles, where "massless" means having mass much less than $M_{\rm Pl}$. In particular, the massless level should contain all the particles that have been observed to date: the leptons, quarks and gauge bosons of the standard model. There must also be a "hyper-hyperfine" splitting of the mass degeneracy in Figure 1(a), as shown in Figure 1(b), in order to generate the observed particle masses of order M_W. The Higgs mechanism is usually invoked to explain this splitting, but a major task of string phenomenology is to explain *why M_W is so incredibly small relative to $M_{\rm Pl}$; the latter question is essentially the* familiar hierarchy problem. The remaining levels in the string spectrum contain particles with Planck-scale masses, which won't be produced in accelerators in the near future, and so they are of less direct interest. (If any of the massive particles are stable, however, they might have survived as relics of the Big Bang.)

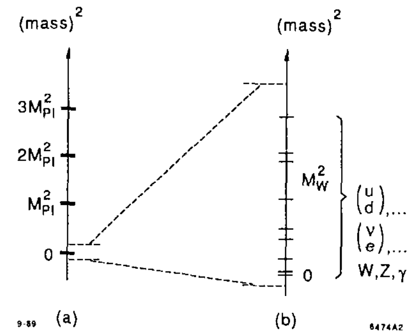

Figure 1. (a) A typical mass spectrum for a particular string vacuum state. (b) An enlarged view of the massless sector, showing the "hyper-hyperfine" splitting.

The couplings between particles in a given vacuum are found by studying how strings scatter. A four-string scattering process at tree level is shown in Figure 2(a), and at one loop (the next order in string perturbation theory) in Figure 3(a). For this process to describe the scattering of four massless particles, the four external strings should be prepared in the corresponding rotational/vibrational states. Remarkably, there is only one string scattering diagram for a particular process, at a given order in perturbation theory. For instance, the tree-level diagram in Figure 2(a) can be viewed as representing either s-, t-, or u-channel scattering, by stretching it either horizontally, vertically, or out of the page. (This property of string scattering amplitudes is called *duality*, and is the reason why string theories were termed "dual models" early in their history.) The one diagram summarizes the contributions of an infinite number of particles — both massless and massive — that can appear as intermediate states in the scattering, and in any of the channels. The individual particle contributions are represented by ordinary field theory Feynman diagrams, shown schematically in Figures 2(b) and 3(b). If the external states in a string scattering process are massless particles, and if the energy of the collision is much less than M_{Pl} (the usual case experimentally!), then the amplitude for the process can be reproduced using an *effective Lagrangian* $\mathcal{L}_{\text{eff}}$ which only involves the massless fields.[7] For example, to reproduce the amplitudes in Figure 2, one needs three-particle couplings of the type shown in Figure 4(a). In addition, an infinite set of *non-renormalizable terms* (terms in $\mathcal{L}_{\text{eff}}$ with dimension larger than four, whose coefficients contain inverse powers of M_{Pl}) results from exchanges of massive particles (Figure 4(b)). The latter terms are completely analogous to the four-Fermi interaction terms that reproduce the low-energy effects of W-exchange in the standard model. Similar considerations apply to loop- as well as tree-level string scattering amplitudes, as represented in Figure 3.

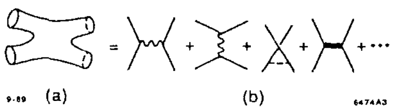

Figure 2. (a) A four-string scattering process at tree level. (b) The field theory Feynman diagrams that represent the contributions of individual particles to the amplitude. Thick lines denote massive particles; all other lines denote massless particles.

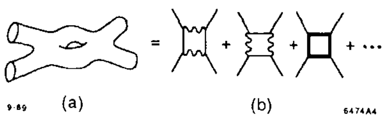

Figure 3. (a) A four-string scattering process at the one-loop level. (b) The Feynman diagrams contributing to it.

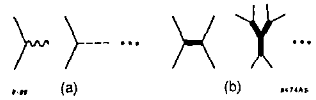

Figure 4. (a) Three-particle couplings needed to reproduce the four-string scattering amplitude at tree level. (b) Additional non-renormalizable interactions that are needed, due to exchanges of massive particles in the string amplitude.

To recap, if one chooses a particular string vacuum state (a CFT), then the string dynamics are fixed, and they can be used to obtain an effective Lagrangian $\mathcal{L}_{\text{eff}}$ for the massless particles in that vacuum. The effective Lagrangian describes physics at energies just below the Planck scale, where strings start to appear point-like, in terms of a conventional field theory (albeit including non-renormalizable terms). To describe physics at the electroweak scale, one then "just" renormalizes $\mathcal{L}_{\text{eff}}$ down to 100 GeV or so. All the non-renormalizable terms in $\mathcal{L}_{\text{eff}}$ can (in principle) be "renormalized" using the loop-corrected string amplitudes, because the latter are actually finite in the ultra-violet. The renormalization task is complicated by the presence of many light fields and many possible intermediate stages of symmetry breaking. Finally one compares $\mathcal{L}_{\text{eff}}|_{100\text{ GeV}}$ with the Lagrangian of the standard model, $\mathcal{L}_{\text{s.m.}}$. Usually they won't agree in sufficient detail for $\mathcal{L}_{\text{eff}}|_{100\text{ GeV}}$ to be considered realistic; in this case one can go back and pick another vacuum state, and go through the whole procedure again...!

Of course, in this *constructive* approach to string phenomenology, the results obtained may be highly model-dependent. Thus one should insist that a model give correct "postdictions" of old phenomena (namely, the host of standard model parameters that have already been measured) before taking seriously its predictions of new phenomena. I think it is fair to say that no model constructed to date satisfies this criterion. It is important to supplement the constructive approach with a *model-independent* approach, one that tries to determine the general low-energy properties common to *all* string vacua. In this way one may be able to test string theory rather than just testing specific string vacua. Unfortunately, there has been relatively little progress to date in the model-independent approach. Interplay between both approaches seems necessary in order to get the most complete understanding of what low-energy physics can be expected from strings.

3. The String Vacuum Landscape and Vacuum Cleaning

It would be nice to have a picture of what the space of string vacua looks like, in particular how different vacua are related to each other, in order to help understand how one of the vacua might be selected over the others (presumably by some non-perturbative string dynamics). Unfortunately our current picture of the string vacuum landscape is quite crude, and is only a local picture. That is, we understand the neighborhood of any particular vacuum reasonably well, through the effective Lagrangian described above, but we really have no idea of where the other vacua are in relation to it. The landscape near a vacuum state can be described roughly by plotting the effective potential $V_{\text{eff}}(\phi_i)$ for the massless scalar fields (particles) ϕ_i in that vacuum. (Note that $V_{\text{eff}}(\phi_i)$ is just a piece of the effective Lagrangian $\mathcal{L}_{\text{eff}}(\phi_i, \partial_\mu\phi_i, A_\mu, \ldots)$.) As an example, suppose there are only two massless scalars (usually there are many more), ϕ_1 and ϕ_2, with

$$V_{\text{eff}}(\phi_1, \phi_2) = \lambda_1\phi_2^4 + \lambda_2 M_{\text{Pl}}^{-2}\phi_1^2\phi_2^4 + \text{ higher order terms,}$$

such that V_{eff} vanishes identically whenever $\phi_2 = 0$. (See Figure 5.) Then any vacuum expectation value of ϕ_1 minimizes V_{eff} and provides a string vacuum state, so $\langle\phi_1\rangle$ parametrizes a line of vacua. Fields like ϕ_1 are called *moduli*, and occur frequently in string vacua.[8,9,10]

In Figure 6 I have embedded this example along with some others into what is supposed to be a more complete picture of the vacuum landscape. There is a great variety among the various vacua: they may feature different gauge groups, different numbers of moduli and/or massless fields, even different numbers of space-time dimensions. (We'll focus on those with four space-time dimensions!) The question marks in the figure reflect our almost total lack of knowledge about regions in the

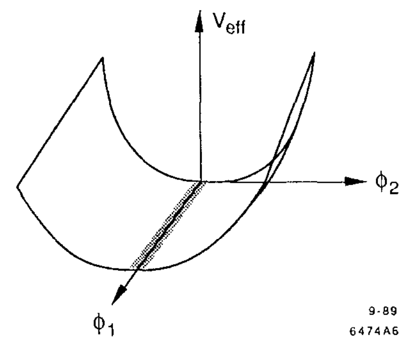

Figure 5. Plot of a simple effective potential, $V_{\text{eff}}(\phi_1, \phi_2) = (\lambda_1 + \lambda_2(\phi_1/M_{\text{Pl}})^2)\phi_2^4 + \ldots$. The line of vacua, parametrized by $\langle\phi_1\rangle$ and having $\langle\phi_2\rangle = 0$, is shaded.

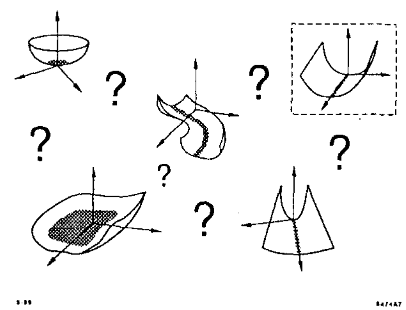

Figure 6. A rough sketch of the string vacuum landscape. The effective potential V_{eff} is plotted on the vertical axes, as a function of the massless fields in a given vacuum. The example of Figure 5 is in the dashed box. Again the vacua are shaded in. The question marks denote regions far from any vacua, which are not understood at all. (Here there be dragons!)

space that are not very close to any vacua. We don't even have a set of global coordinates with which to describe the space. In the neighborhood of the first example we may use the fields ϕ_1 and ϕ_2, but another vacuum (if not connected to the first one) will have another set of massless fields, say $\tilde{\phi}_i$, which bear no obvious relation to the first set ϕ_i. Similarly the effective Lagrangian describing the low-energy physics of the first vacuum, $\mathcal{L}_{\text{eff}}(\phi_i)$, has no obvious relation to that for the other vacuum, $\tilde{\mathcal{L}}_{\text{eff}}(\tilde{\phi}_i)$. The massive fields have been omitted from the picture, because including them would make the space infinite-dimensional; nevertheless, they will certainly play a role in our future understanding of the relation between the disconnected vacua, *i.e.* in filling in the question marks in the figure.

At present, there are no dynamical criteria for preferring any one vacuum over another. All the vacua (to be more precise, all the vacua with unbroken space-time supersymmetry) remain stable vacua to all orders in string perturbation theory.[11] One generally hopes that non-perturbative effects will lift this vacuum degeneracy, but without a formalism for calculating such effects, the best one can do at present is to apply phenomenological criteria to do the "vacuum cleaning". Here is a rather minimal set of criteria, which are also relatively easy to implement (or at least check) in a given string vacuum:

- Four-dimensional space-time.
- N=1 space-time supersymmetry at the Planck scale.
- A gauge group containing $SU(3) \times SU(2) \times U(1)$.
- Massless particles with the gauge quantum numbers of the standard model (quarks, leptons, *etc.*).

It should be noted that even these criteria are not completely free of theoretical prejudice. Four-dimensional space-time is on a pretty safe footing, but unbroken space-time supersymmetry at the Planck scale is put in so that it may play a role in explaining the naturalness/hierarchy problem of why M_W/M_{Pl} is so small.[12] (Vacua without space-time supersymmetry are also difficult to analyze because, unlike the supersymmetric ones, they are generally de-stabilized by radiative corrections.) Extended ($N > 1$) supersymmetry is excluded because it forces a non-chiral theory, *i.e.* one with no parity-violating gauge interactions[13]; it is assumed that parity is not spontaneously broken at some lower energy scale. The last two criteria assume that the observed gauge bosons and fermions are fundamental string excitations, rather than (say) composites of such excitations. There are of course many more criteria that could be applied, but they are generally much more difficult to implement. For example:

- No fast proton decay.
- The correct set of quark and lepton masses.

And so on.

4. Conformal Field Theory and String Vacua

I would now like to give a brief description of how two-dimensional (2d) conformal field theory (CFT) enters into string theory, and of how one actually implements the phenomenological criteria just discussed in terms of CFT's.

A string is a one-dimensional object, so as it moves through space-time it sweeps out a 2d surface, called the *world-sheet* — analogous to the one-dimensional world-line swept out by a point particle. (See Figure 7.) The equations of motion for a point particle can be obtained from an action, $S_{1d} = \int d\tau (ds/d\tau)$, equal to the

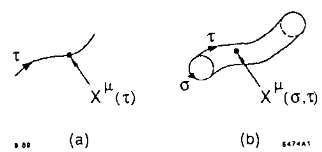

Figure 7. (a) The world-line swept out by a point particle moving through space-time. The position of the particle in space-time is given by $X^\mu(\tau)$. (b) The cylindrical world-sheet swept out by a closed string. The coordinates of the world-sheet are τ and σ; the position in space-time of a point on the world-sheet is given by $X^\mu(\sigma, \tau)$.

proper length of the world-line (parametrized by τ). Similarly, the equations of motion of the world-sheet are determined by a 2d field theory, $S_{2d} = \int d\tau d\sigma \mathcal{L}_{2d}(\tau,\sigma)$, where τ and σ parametrize the world-sheet. In the simplest case S_{2d} is the area of the world-sheet, but there are many other possibilities. The Lagrangian $\mathcal{L}_{2d}$ should not be confused with the space-time effective Lagrangian $\mathcal{L}_{\rm eff}$; also, the fields in the 2d field theory are called *world-sheet fields* in order to distinguish them from the space-time fields occurring in $\mathcal{L}_{\rm eff}$.

When the motion of the string is quantized, the world-sheet fields become operators in the 2d quantum field theory and create eigenstates of the string's oscillations. These states can be identified as particles moving in space-time. Thus the full particle spectrum — in particular the massless spectrum — can be determined by enumerating the world-sheet fields. (Note that the space-time fields, acting as operators in the quantized effective field theory $\mathcal{L}_{\rm eff}$, also create particle states, but only the massless particles, and only in accordance with the spectrum found by studying $\mathcal{L}_{2d}$.) It turns out that string *interactions* are also fixed uniquely by the choice of $\mathcal{L}_{2d}$; this means that $\mathcal{L}_{2d}$ determines not only the particle mass spectrum, but also all couplings between particles!

The simplest examples of world-sheet fields are those that represent the position of the world-sheet in space-time: $X^\mu(\sigma,\tau)$, where $\mu = 0,1,2,3$ labels the four space-time coordinates and σ,τ are the two world-sheet coordinates. (See Figure 7.)

In an arbitrary 2d field theory, most of the remaining world-sheet fields do not have such a simple geometrical interpretation. However, many string vacua can be described as *compactifications*, in which some space-time dimensions are taken to have sizes of order the Planck length. In the prototypical example of a compactification, one dimension X^i lives on a circle with a radius R of order the Planck length, and the rest X^μ parametrize space-time. If the X^μ are represented

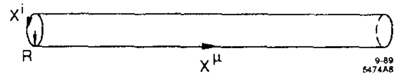

Figure 8. Compactification of a single extra coordinate X^i on a circle with radius R of order the Planck length. The four coordinates X^μ of Minkowski space-time are represented by the long direction of the "drinking straw".

by a single line, the result is the "drinking-straw" picture of Figure 8. When this compactification is used as a string vacuum, $X^i(\sigma,\tau)$ becomes a world-sheet field, just like $X^\mu(\sigma,\tau)$; it describes the position of the string in the compactified dimension. The moduli that parametrize string vacua also have a geometric interpretation in the case of a compactification: They represent the lengths of the internal dimensions, such as the radius R in the above example.

Not all 2d field theories give rise to *string vacua*. In a vacuum state, strings must not be created spontaneously — that is, all tadpole graphs must vanish. This non-trivial condition* on the 2d field theory will be satisfied if it is *conformally invariant*,[14,15] and has a few other properties to be described shortly.

I won't explain exactly why conformal invariance is required, but I should at least say what it is. The Lagrangian $\mathcal{L}_{2d}$ for the 2d field theory depends not only on the world-sheet fields X^μ, *etc.*, but also on the 2d metric $g_{\alpha\beta}$. Conformal invariance means that $\mathcal{L}_{2d}$ is invariant under a local change of scale on the world-sheet which preserves angles,

$$g_{\alpha\beta}(\sigma,\tau) \to e^{\phi(\sigma,\tau)} g_{\alpha\beta}(\sigma,\tau); \tag{1}$$

for example the transformation of Figure 9.

* The condition is somewhat trivial in the point-particle case, because one can adjust the particle interactions independently of S_{1d} so that particles are not created spontaneously. In the string case, however, the interactions are already fixed once S_{2d} is specified.

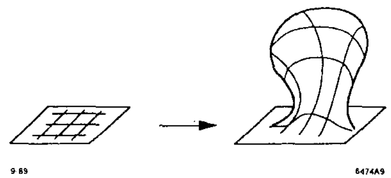

Figure 9. Example of a conformal transformation: a local change of scale on the surface that preserves angles.

In fact, 2d field theories with (1) as a classical symmetry generally develop a so-called *conformal anomaly* under the transformation at the quantum level. The details of this anomaly are not particularly important here. We just need to know that:

(*a*) The anomaly is characterized by a single real number c, which is additive in the sense that if a CFT consists of two non-interacting pieces, say $\mathcal{L}_{2d} = \mathcal{L}_{2d}^{(1)} + \mathcal{L}_{2d}^{(2)}$, then $c = c^{(1)} + c^{(2)}$.

(*b*) There is a contribution of $c = -26$ from the metric $g_{\alpha\beta}$ for the bosonic string, which must be cancelled by a contribution of $c = +26$ from world-sheet fields other than the metric $(X^\mu, \ldots)$; for the superstring $c = -15$ must be cancelled by $c = +15$.

(*c*) A single world-sheet field of the type $X^\mu(\sigma, \tau)$ contributes an anomaly $c = 1$, so if space-time is D-dimensional ($\mu = 0, 1, 2, \ldots, D-1$) the D fields will contribute $c = D$.

The "critical dimension" $D_c = 26$ for the bosonic string is obtained by assuming that there are no world-sheet fields other than X^μ (not counting the metric). For the superstring the critical dimension is $D_c = 10$. (It is 10 rather than 15 because each X^μ field has to be accompanied by a world-sheet superpartner ψ^μ which contributes an additional $c = \frac{1}{2}$). Four-dimensional (super)string vacua are constructed using only four fields X^μ that represent space-time coordinates (plus ψ^μ in the super case), but also using extra "internal" fields — like X^i — in such a way that the total anomaly from fields other than the metric continues to have the correct value, either $c = 26$ or $c = 15$.

The most important world-sheet fields in a CFT, which also have the simplest behavior, are those that move in only one direction on the string, either to the left or to the right; thus they depend only on $\sigma_L = \tau - \sigma$, or only on $\sigma_R = \tau + \sigma$, and are called *left-moving* fields or *right-moving* fields, respectively. The 2d Lorentz properties of any world-sheet field can be summarized by its *scaling* or *conformal dimension*,[6] which generally will get anomalous contributions at the quantum level, and which can be split into left- and right-moving parts, denoted h and $\overline{h}$ $(h, \overline{h} \geq 0)$. The left-moving fields all have $h > 0$, $\overline{h} = 0$, while the right-moving fields have $h = 0$, $\overline{h} > 0$.

In any conformal field theory, the energy-momentum tensor $T_{\alpha\beta}$ provides an important pair of left- and right-moving fields. While $T_{\alpha\beta}$ is present in any field theory, in a CFT it is traceless, $T^\alpha_\alpha = 0$, which allows it to be split into the left- and right-moving components

$$\begin{aligned} &T(\sigma_L) &&\text{with } (h, \overline{h}) = (2, 0), \\ &\overline{T}(\sigma_R) &&\text{with } (h, \overline{h}) = (0, 2). \end{aligned}$$

The short-distance behavior of $T_{\alpha\beta}$ also determines the conformal anomaly c, because $T_{\alpha\beta}$ generates conformal transformations, in addition to its usual role as generator of rigid translations of the world-sheet. *Any* CFT with an energy-momentum tensor $T_{\alpha\beta}$ giving rise to $c = 26$ provides a vacuum for the bosonic string (at the classical level).

A superstring vacuum has a few more restrictions on it — the 2d CFT must be supersymmetric as well. In this case the energy-momentum tensor $T_{\alpha\beta}$ will have a fermionic superpartner $(T_F)_{\alpha\theta}$, which can also be split into left- and right-moving pieces:

$$T_F(\sigma_L) \qquad \text{with } (h,\bar{h}) = (\tfrac{3}{2},0),$$
$$\overline{T}_F(\sigma_R) \qquad \text{with } (h,\bar{h}) = (0,\tfrac{3}{2}).$$

Any such *super*conformal field theory with conformal anomaly $c = 15$ provides a classical superstring vacuum.

The heterotic string is constructed by combining the left-moving world-sheet fields of the bosonic string with the right-moving fields of the superstring; hence it requires the presence of T, $\overline{T}$ and $\overline{T}_F$ but not necessarily T_F. The left- and right-moving conformal anomalies are now different from each other — $c = 26$ and $\bar{c} = 15$ respectively. In fact, a very large number of such superconformal field theories are now known to exist. This embarrassment of riches is precisely *the (heterotic) string vacuum degeneracy problem.*

5. Phenomenological Constraints

So far I have discussed the constraints on the CFT that come just from consistency of (super)string propagation. Now I would like to focus on the heterotic string, and impose some of the additional "phenomenological" constraints discussed above, in the hopes of reducing the vacuum degeneracy problem somewhat. Many of these constraints require the presence (or absence) of particular world-sheet fields, often the relatively simple purely left-moving (or purely right-moving) fields.

• **Four-dimensional space-time** is implemented by requiring the two-dimensional Lagrangian to have the form

$$\mathcal{L}_{2d} = \mathcal{L}_0(X^\mu,\psi^\mu) + \mathcal{L}_{\text{internal}}(\varphi_i), \tag{2}$$

where

$$\mathcal{L}_0(X^\mu,\psi^\mu) = \frac{1}{2\pi}\int d\sigma d\tau \{\partial_\alpha X^\mu \partial^\alpha X_\mu + \bar{\psi}^\mu(1-\gamma^3)\gamma^\alpha\partial_\alpha\psi_\mu\}. \tag{3}$$

The fields X^μ describing the string's position in space-time ($\mu = 0,1,2,3$), and their world-sheet superpartners ψ^μ, are free (non-interacting) fields due to Eq. (3); ψ^μ is a right-moving field, and X^μ can be split into left- and right-moving pieces, $\partial_{\sigma_L}X^\mu$ and $\partial_{\sigma_R}X^\mu$. The remaining "internal" fields φ_i do not interact with X^μ and ψ^μ. In the case where $\mathcal{L}_{2d}$ represents a compactification, they are the degrees of freedom associated with the (six) compactified dimensions: $X^i,\psi^i,\ldots$ The conformal anomalies associated with $\mathcal{L}_0(X^\mu,\psi^\mu)$ are $c = 4$ and $\bar{c} = 6$; hence $\mathcal{L}_{\text{internal}}$ must have

$$c_{\text{internal}} = 26 - 4 = 22, \qquad \bar{c}_{\text{internal}} = 15 - 6 = 9.$$

Additional constraints will now be imposed on $\mathcal{L}_{\text{internal}}$. The easiest constraints to implement have to do with the connection between massless particles (specifically, gravitinos, gauge bosons, quarks and leptons) and certain world-sheet fields having $(h,\bar{h}) = (1,\frac{1}{2})$ under the energy-momentum tensor for $\mathcal{L}_{2d}$. The contributions to $(h,\bar{h})$ coming from $\mathcal{L}_{\text{internal}}$ depend on the space-time Lorentz properties of the particles in question; they lead to the following restrictions on $\mathcal{L}_{\text{internal}}$:

- **Space-time supersymmetry** requires several additional right-moving fields; in particular, the right-moving component of the energy-momentum tensor $\overline{T}$ has a second superpartner $\overline{T}'_F$ in addition to $\overline{T}_F$:

  $$\overline{T}'_F(\sigma_R) \qquad \text{with } (h,\bar{h}) = (0,\tfrac{3}{2}).$$

  This means the internal CFT possesses an *extended* ($N = 2$) world-sheet supersymmetry.[16,17]

- **Not too much space-time supersymmetry** (which would destroy chirality) requires the *absence* of all right-moving fields with $(h,\bar{h}) = (0,\frac{1}{2})$.[18]

- **A gauge group containing** $SU(3)\times SU(2)\times U(1)$ requires left-moving fields, one for each gauge boson:

  $$J^a(\sigma_L) \qquad \text{with } (h,\bar{h}) = (1,0),$$

  where a labels the generators of the gauge group. (See *e.g.* Ref. 19.) The properties of the J^a are completely specified by the choice of gauge group, *i.e.* the structure constants f^{abc}, and of certain positive integers k_i (one for each non-abelian factor in the gauge group) which show up in the short-distance behavior of the J^a. The k_i are important in determining which representations of the gauge group can appear in the spectrum, and in the relation between different gauge couplings (see below).

- **Massless quarks and leptons** require world-sheet fields $\Phi_i(\sigma_L, \sigma_R)$ that are *not* purely left- or right-moving (they have $(h, \overline{h}) = (1, \frac{1}{2})$). (See *e.g.* Ref. 10.) They have specific charges under the fields $J^a(\sigma_L)$, corresponding to their gauge quantum numbers, but otherwise they are not terribly well specified.

And then there are the criteria that are much harder to implement, such as **no fast proton decay** and **reasonable quark and lepton masses**. Both these quantities are related to certain CFT correlation functions $\langle \Phi_i \Phi_j \Phi_k \rangle$, but they are also very sensitive to other possible fields, to radiative corrections, and to various stages of symmetry breaking below M_{Pl}, so in practice it is difficult to evaluate them for a specific model, let alone to implement them as general conditions.

Now that we have imposed some constraints on the CFT, we would like to see if the general properties of the allowed CFT's can in turn impose restrictions on the possible space-time effective Lagrangians. Unfortunately, not much progress has been made in this direction, at least for the heterotic string.* A primitive example of a restriction on $\mathcal{L}_{\mathrm{eff}}$ is the tree-level relation[20,19]

$$\frac{g_{SU(3)}}{g_{SU(2)}} = \sqrt{\frac{k_{SU(2)}}{k_{SU(3)}}} \,. \tag{4}$$

Here $g_{SU(3)}$, $g_{SU(2)}$ are the strong and weak gauge coupling constants, and $k_{SU(3)}$, $k_{SU(2)}$ are the integers associated with the world-sheet fields J^a that were mentioned above. In a given string vacuum, each k_i takes on one specific value, but that value can (in principle) be any positive integer. It is instructive to compare this prediction with that for the grand unified theory based on $SU(5)$[21] (or any gauge group containing $SU(5)$ and with the same embedding of $SU(3) \times SU(2)$):

$$\frac{g_{SU(3)}}{g_{SU(2)}} = 1. \tag{5}$$

The string theory prediction (4) is clearly much less definite than the GUT prediction (5). On the other hand, in the effective Lagrangians for many string vacua the standard model gauge group is not embedded into a simple Lie group (such as $SU(5)$, $SO(10)$ or E_6); under these circumstances a generic field theory would give no gauge coupling prediction at all! In fact, almost all of the attempts to date to build phenomenological string models have involved choosing $k_{SU(3)} = k_{SU(2)} = 1$, in which case one recovers the usual GUT prediction. There are, however, no arguments excluding $k > 1$ on phenomenological or other grounds (provided k is not too large); indeed, explicit models featuring $k = 2$ have recently been constructed.[22]

Both Eqs. (4) and (5) are tree-level relations that will get loop corrections. In particular they will change significantly under renormalization from M_{Pl} (M_{GUT}) down to M_W, and the change will depend on the masses of particles carrying $SU(3)$ and $SU(2)$ quantum numbers below M_{Pl} (M_{GUT}).[23] This change introduces further model dependence into the string prediction, beyond the choice of $k_{SU(3)}$ and $k_{SU(2)}$, but this kind of dependence is common to GUT's as well.

The model dependence of even the primitive string prediction (4) raises the more general question of the sensitivity of models to both *discrete* and *continuous* modifications. In Figure 6, discrete modifications jump the vacuum from one "known" patch to another, whereas continuous modifications involve changing the vacuum expectation values of moduli and slide the vacuum along the troughs in a given patch. In general, models are very sensitive to discrete modifications: The gauge group and matter content — even the number of generations — can change drastically. On the other hand, models are actually rather insensitive to continuous modifications. For example, tree-level relations like (4) between gauge couplings do

* For the closed superstring, on the other hand, one can show that there are *no* CFT's satisfying the combined constraints discussed above (though CFT's exist satisfying the individual constraints). This rules out *all* classical vacua of the closed superstring on phenomenological grounds.[18]

not change[20,17]; at least some of the matter content (usually including the quarks and leptons) remains the same[9,10]; and some of the Yukawa couplings among the matter fields even stay constant.[24] This insensitivity makes it difficult to tune low-energy predictions by continuous adjustments of the moduli, which I view as an encouraging result.

6. Specific Constructions

I would now like to make a few remarks about specific constructions of models. There are several different kinds of constructions, which overlap somewhat (different constructions can give rise to the same vacua), and which I will make no attempt to describe here.[25] They go under the names: Calabi-Yau compactifications,[8] orbifolds (symmetric[26,27] and asymmetric[28]), free fermions,[29] free bosons (or covariant lattices),[30] and tensor products of $N = 2$ superconformal field theories.[31,32] There are certainly at least thousands of models contained in these categories. Only a relative few have been analyzed in much detail. The more promising ones have certain features in common beyond the minimal criteria I mentioned previously:

- Three generations of light fermions. Four generations have been considered; one has then to prevent extra colored members of each generation from lurking at the 100 GeV scale (otherwise the $SU(3)_c$ coupling constant will fail to be asymptotically free and will blow up before the unification scale[33]). However, the very recent* measurements at SLC[34] and LEP[35] of the width of the Z^0 now seem to rule out four generations with light neutrinos.
- Space-time supersymmetry is broken by non-perturbative effects in a "hidden sector". (It is generally believed that supersymmetry will not be broken perturbatively if it is present at tree-level.) The hidden sector generally consists of a strongly-interacting gauge theory with some gauginos λ but no other charged matter fields, plus some gauge singlet matter fields. The supersymmetry breaking is supposed to be triggered by a condensate of the gauginos,[36] $\langle\lambda\lambda\rangle^{1/3} \sim 10^{14}$ GeV. The particles in the hidden sector interact with observable particles only through gravitational-strength interactions, and so the scale of supersymmetry breaking in the observable sector is reduced by a factor of $M_{\rm Pl}^{-2}$, to $\sim M_W$. The masses of the superpartners of the quarks and leptons then fall in the usual range $\lesssim 1$ TeV or so.
- There are no matter fields transforming under higher-dimensional representations of $SU(3)$ (that is, only singlets and triplets are present) or of $SU(2)$ (only singlets and doublets are present). This is a quite generic feature; it is true for any vacuum in which $k_{SU(3)} = k_{SU(2)} = 1$.
- There are also usually no light "exotic" ($SU(2)$ singlet) quarks, but for a different reason: They can cause fast proton decay if they are lighter than $\sim 10^{15}$ GeV, unless certain Yukawa couplings happen to vanish.
- There are often a few additional $SU(2)$ doublets and singlets around at TeV energies.
- The gauge group that acts on the observable particles is not necessarily unified anywhere below $M_{\rm Pl}$; typical gauge groups are $SU(3)^3$ (found in a particular Calabi-Yau/$N = 2$ tensor product construction[37,38,39]), $SU(3)\times SU(2)\times U(1)^n$ (found in various orbifold constructions[27]), or (flipped) $SU(5) \times U(1)$ (found in certain fermionic constructions[40]). Usually the gauge group is supposed to break spontaneously at a high "intermediate" mass scale $M_I \sim 10^{13\pm2}$ GeV, leaving at TeV energies only the standard model gauge group $SU(3)\times SU(2)\times U(1)$, plus perhaps one extra $U(1)$ factor (a Z' gauge boson).

* slightly postdating this talk, in fact!

7. Prospects

I will conclude by commenting on two of the major obstacles to extracting predictions from string theory. The first occurs in the analysis of any specific model — it is the question of how non-perturbative effects could lead to the breaking of space-time supersymmetry. As I mentioned earlier, there are often many fields (the moduli) whose potentials in V_{eff} are flat, *i.e.* their vacuum expectation values are undetermined to all orders in string perturbation theory. Some of the moduli can receive corrections to their potential from non-perturbative effects, in particular from interactions with the hidden sector gaugino condensate mentioned above, but perhaps also from other non-perturbative effects that have yet to be identified. In many cases the gaugino-induced corrections to the potentials cause vacuum expectation values for the moduli to run away to infinity! Thus we need to know: What is the full corrected potential? Does it have a stable minimum? If a minimum exists, is supersymmetry broken there? Finally, exactly how is the supersymmetry breaking manifested in the observable sector? There is a general understanding of the last question in supergravity (in terms of so-called "soft-breaking terms"), but the details can be sensitive to model-dependent parameters in $\mathcal{L}_{\text{eff}}$ (such as non-renormalizable kinetic-energy terms for observable fields, *etc.*).[12] The details can in turn be very important in determining many low-energy quantities, including the masses of superpartners but also the observed quark and lepton masses; the latter masses are sensitive to the pattern of supersymmetry breaking in models where there are additional scales of gauge symmetry breaking between M_W and M_{Pl}.[39]

A more fundamental obstacle to obtaining predictions from string theory is the issue of how one vacuum state is dynamically preferred over another. This issue cannot even be addressed until one has a formalism that can simultaneously describe two disconnected vacua, like two of the "islands" depicted in Figure 6. Until such a formalism is developed, the two ways one might hope to make phenomenological progress are: (1) to "get lucky" in finding "the right" vacuum, which would predict all the standard model parameters correctly; or (2) by trying to determine the general properties common to all the vacua, in the hopes of deciding whether *any* of them can lead to realistic physics at the 100 GeV scale. Clearly there is still a lot of theoretical work to be done before we know whether superstrings are a theory of everything or a theory of nothing.

Acknowledgements: I would like to thank the organizers of the SLAC Summer Institute for the opportunity to present this talk, and H. Haber, J. Louis, Y. Nir, M. Peskin and D. Schroeder for helpful comments on the manuscript.

REFERENCES

1. For a comprehensive introduction to the formalism and a little of the phenomenology of superstring theory, with references to the literature, see M. Green, J. Schwarz and E. Witten, *Superstring Theory*, Vols. I and II (Cambridge University Press, 1987).
2. Y. Nambu, in Symmetries and Quark Models, ed. R. Chand (Gordon and Breach, 1970);
   H.B. Nielsen, submitted to the 15th Int'l Conf. on High Energy Physics (Kiev, 1970);
   L. Susskind, *Nuovo Cim.* **69A** (1970), 457.
3. P. Ramond, *Phys. Rev.* **D3** (1971), 2415;
   A. Neveu and J. Schwarz, *Nucl. Phys.* **B31** (1971), 86;
   F. Gliozzi, J. Scherk and D. Olive, *Phys. Lett* **65B** (1976), 282, *Nucl. Phys.* **B122** (1977), 253;
   M. Green and J. Schwarz, *Nucl. Phys.* **B181** (1981), 502, *Nucl. Phys.* **B198** (1982), 252, *Phys. Lett.* **109B** (1982), 444.
4. D. Gross, J. Harvey, E. Martinec and R. Rohm, *Phys. Rev. Lett.* **54** (1985), 502, *Nucl. Phys.* **B256** (1985), 253, *Nucl. Phys.* **B267** (1986), 75.
5. M. Green and J. Schwarz, *Phys. Lett.* **149B** (1984), 117.
6. A. Belavin, A. Polyakov and A. Zamolodchikov, *Nucl. Phys.* **B241** (1984), 333.
7. See *e.g.* D. Gross and J. Sloan, *Nucl. Phys.* **B291** (1987), 41.
8. P. Candelas, G. Horowitz, A. Strominger and E. Witten, *Nucl. Phys.* **B258** (1985), 46.
9. M. Dine, N. Seiberg, X.-G. Wen and E. Witten, *Nucl. Phys.* **B278** (1986), 769, *Nucl. Phys.* **B289** (1987), 319;
   M. Dine and N. Seiberg, *Nucl. Phys.* **B293** (1987), 253.
10. L. Dixon, in *Superstrings, Unified Theories and Cosmology 1987*, ed. by G. Furlan *et al.* (World Scientific, 1988).
11. E. Martinec, *Phys. Lett.* **171B** (1986), 189;
    M. Dine and N. Seiberg, *Phys. Rev. Lett.* **57** (1986), 2625;
    J. Atick, G. Moore and A. Sen, *Nucl. Phys.* **B307** (1988), 221, *Nucl. Phys.* **B301** (1988), 1;
    O. Lechtenfeld and W. Lerche, preprint CALT-68-1551 (1989).
12. See *e.g.* H.P. Nilles, *Phys. Rep.* **110** (1984), 1, and references therein.
13. See *e.g.* J. Wess and J. Bagger, *Supersymmetry and Supergravity* (Princeton University Press, 1983).
14. A.M. Polyakov, *Phys. Lett.* **103B** (1981), 207, 211.
15. D. Friedan, *Phys. Rev. Lett.* **45** (1980), 1057, *Ann. of Phys.* **163** (1985), 318;
    C. Lovelace, *Phys. Lett.* **135B** (1984), 75, *Nucl. Phys.* **B273** (1986), 413;
    D. Friedan and S. Shenker, in *Proc. APS Div. Particles and Fields Conf.*, Santa Fe (1984);
    E. Fradkin and A.A. Tseytlin, *Phys. Lett.* **158B** (1985), 316, *Phys. Lett.* **160B** (1985), 64, *Nucl. Phys.* **261B** (1986), 1;
    C. Callan, D. Friedan, E. Martinec and M. Perry, *Nucl. Phys.* **B262** (1985), 593;
    A. Sen, *Phys. Rev. Lett.* **55** (1985), 1846, *Phys. Rev.* **D32** (1985), 2102.
16. C. Hull and E. Witten, *Phys. Lett.* **160B** (1985), 398;
    A. Sen, *Nucl. Phys.* **B278** (1986), 289.
17. T. Banks, L. Dixon, D. Friedan and E. Martinec, *Nucl. Phys.* **B299** (1988), 613.
18. L. Dixon, V. Kaplunovsky and C. Vafa, *Nucl. Phys.* **B294** (1987), 43.
19. See *e.g.* P. Ginsparg, in *Proc. of U.K. Summer Institute* (Cambridge, 1987).

20. P. Ginsparg, *Phys. Lett.* **B197** (1987), 139.

21. H. Georgi and S. Glashow, *Phys. Rev. Lett.* **32** (1974), 438.

22. D.C. Lewellen, preprint SLAC–PUB–5023 (1989).

23. H. Georgi, H.R. Quinn and S. Weinberg, *Phys. Rev. Lett.* **33** (1974), 451.

24. J. Distler and B. Greene, *Nucl. Phys.* **B309** (1988), 295.

25. See J. Schwarz, *Int. J. Mod. Phys.* **A4** (1989), 2653 for an overview.

26. L. Dixon, J. Harvey, C. Vafa and E. Witten, *Nucl. Phys.* **B261** (1985), 620, *Nucl. Phys.* **B274** (1986), 285.

27. L.E. Ibáñez, H.P. Nilles and F. Quevedo, *Phys. Lett.* **187B** (1987), 25;
L.E. Ibáñez, J.E. Kim, H.P. Nilles and F. Quevedo, *Phys. Lett.* **191B** (1987), 3;
A. Chamseddine and J.-P. Derendinger, *Nucl. Phys.* **B301** (1988), 381.

28. K.S. Narain, M.H. Sarmadi and C. Vafa, *Nucl. Phys.* **B288** (1987), 551.

29. H. Kawai, D. Lewellen and S.-H.H. Tye, *Phys. Rev. Lett.* **57** (1986), 1832, *Nucl. Phys.* **B288** (1987), 1;
I. Antoniadis, C. Bachas and C. Kounnas, *Nucl. Phys.* **B289** (1987), 87;
I. Antoniadis, J. Ellis, J.S. Hagelin and D.V. Nanopoulos, preprint CERN-TH.5442 (1989);
see J. Schwarz, *Int. J. Mod. Phys.* **A2** (1987), 593 for a review.

30. W. Lerche, D. Lüst and A. Schellekens, *Nucl. Phys.* **B287** (1987), 477;
see W. Lerche, A.N. Schellekens and N.P. Warner, *Phys. Rep.* **177** (1989), 1 for a review.

31. D. Gepner, *Phys. Lett.* **199B** (1987), 380, *Nucl. Phys.* **B296** (1988), 757.

32. Y. Kazama and H. Suzuki, *Nucl. Phys.* **B321** (1989), 232, *Phys. Lett.* **216B** (1989), 112.

33. M. Dine, V. Kaplunovsky, M. Mangano, C. Nappi and N. Seiberg, *Nucl. Phys.* **B259** (1985), 549.

34. J.M. Dorfan and J. Nash for the Mark II Collaboration, talks presented at the International Europhysics Conference on High Energy Physics, Madrid (1989).

35. ALEPH Collaboration, preprint CERN-EP/89–132; OPAL Collaboration, preprint CERN–EP/89–133; DELPHI Collaboration, preprint CERN–EP/89–134; L3 Collaboration, preprint L3–001 (1989).

36. S. Ferrara, L. Girardello and H.P. Nilles, *Phys. Lett.* **125B** (1983), 457;
M. Dine, R. Rohm, N. Seiberg and E. Witten, *Phys. Lett.* **156B** (1985), 55.

37. B.R. Greene, K.H. Kirklin, P.J. Miron and G.G. Ross, *Nucl. Phys.* **B278** (1986), 667, *Nucl. Phys.* **B292** (1987), 606.

38. D. Gepner, Princeton preprint (1987);
B.R. Greene, C.A. Lütken and G.G. Ross, preprint NORDITA-89/8-P (1989).

39. G.G. Ross, talk presented at Strings '89 Conference, Texas A&M Univ. (1989).

40. I. Antoniadis *et al.*, in Ref. 29.

Recent Results from TRISTAN

Shoji Uno
KEK
National Laboratory for High Energy Physics
Tsukuba, Ibaraki, Japan

Abstract

The three TRISTAN experiments(AMY,TOPAZ,VENUS) accumulated a data sample of about 30 pb^{-1} each in the energy range; 50.-61.4 GeV. Recent results from these experiments are presented. The R-ratio values were found somewhat higher than the five-flavor prediction above 56 GeV. Measured cross sections for leptons and forward-backward asymmetries for quarks and leptons are consistent with the standard model predictions. No new particles were observed and new mass limits were set.

1 Introduction

The TRISTAN ring has been providing beams without any serious trouble since the first collision as mapped in fig.1. After the installation of superconductive RF cavities, the CM energy rose up to 61.4 GeV.

AMY, TOPAZ and VENUS have searched for various new particles which are predicted both by the standard theory and by theories beyond it and quickly checked the standard theory using a data sample of about $30pb^{-1}$ each in the energy region between 50 and 61.4 GeV. This paper reports these results(results from SHIP can be found in ref.1). In the future, all three groups will precisely measure the electroweak and the QCD parameters and try to find small deviation from the standard theory with high luminosity.

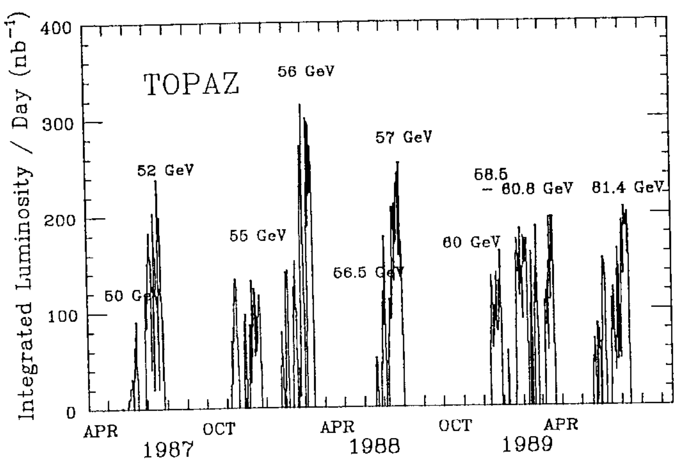

Figure 1 Integrated luminosity per day with TOPAZ detector.

2 Search for New Flavors (t and b')

2.1 Total Hadronic Cross Section

The R-ratio defined to be the ratio of the total hadronic cross section to the $\mu\mu$ cross section calculated in the lowest order QED. If quark masses are negligible, the R can be factorized as follows,

$$R = \sum_q Q_q^2(1 + C_{QCD})(1 + C_{EW})$$

where Q_q is a quark charge and C_{QCD} and C_{EW} are QCD and electroweak corrections, respectively.

If a new flavor threshold is crossed, the R-ratio is expected to jump up by 1.5(0.5) for full open top(b') production. This increase enables us to detect the new threshold. Experimentally the R-ratio is derived from the number of observed multi-hadronic events($N_{obs.}$) using the following formula,

$$R = \frac{N_{obs.} - N_{bg}}{\epsilon(1+\delta)\int Ldt\sigma_{QED}^{\mu\mu}}$$

where N_{bg} is the number of background events, ϵ is detection efficiency, δ is the radiative correction, $\int Ldt$ is integrated luminosity, and $\sigma_{QED}^{\mu\mu}$ is the $\mu\mu$ cross section calculated in the lowest order QED. To get $N_{obs.}$, TOPAZ selected multi-hadronic events by requiring the following criteria[2]. (1) The number of good tracks was greater than 4. (2) The total visible energy was greater than the beam energy. (3) The longitudinal momentum balance was less than 0.4. (4) The number of large energy clusters was less than 2(Bhabha rejection). (5) The invariant mass of each hemisphere was greater than 2 GeV($\tau\tau$ rejection). The criteria used by other groups are similar[3]. N_{bg} is a few percent mainly from $\tau\tau$ events. $\epsilon(1+\delta)$ is nearly equal to 1, which means that the efficiency is about 100% in the fiducial volume.

The radiative correction factor was calculated using the BKJ program[4] at PEP and PETRA. At TRISTAN, the FS program[5] was used. The FS includes all the electroweak diagrams up to α^3. The difference between the FS and the BKJ is less than 1% at PEP and PETRA. It is, however, 3% at 60 GeV(fig.2-a). The radiative correction factor in the FS depends on M_Z, M_{Higgs} and M_{top}. M_Z dependence is less than 1%. As for M_{Higgs} dependence, the deviation is very small in the wide mass range. For a M_{top} of less than 100 GeV, the deviation is also small, though a very high M_{top} may increase the R-ratio by about 1%. The origins of systematic errors summarized in table 1. The total systematic error is 4-5%.

Finally, the obtained R values are plotted in fig.3. Data from AMY, TOPAZ and VENUS are combined. The solid line is the prediction from the five-flavor, which was calculated with a Z^0 mass of 91 GeV. Clearly open top is ruled out. But the data points are somewhat higher than the five-flavor prediction. The R-ratio alone can not exclude b' possibility. In the next section, shape analyses are described as more sensitive methods for heavy flavor search.

Systematic Errors [%]	TOPAZ	AMY	VENUS
Luminosity	4.0	3.3	2.6
Radiative Correction	1.5	1.3	2.1
Acceptance	1.0	1.3	1.8
Event Selection	2.3	1.7	1.7
Total	5.5	4.2	4.2

Table 1 Systematic errors for R-ratio.

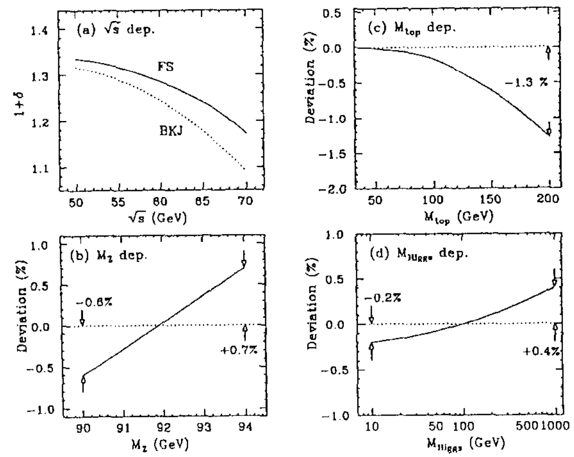

Figure 2 (a) The full electroweak radiative correction as a function of CM energy. The BKJ correction is also shown by a dashed curve. (b,c,d) The dependence of the correction factor on M_Z, M_{top} and M_{Higgs}n in the FS program.

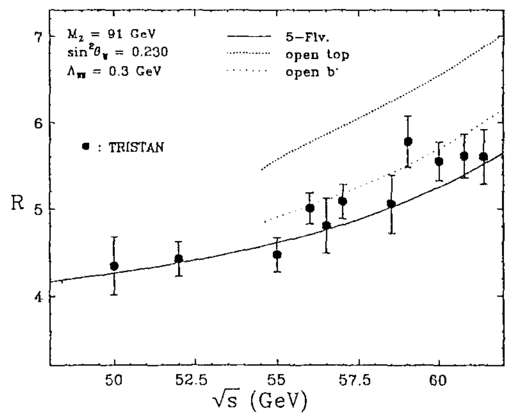

Figure 3 Measured R-ratio. The solid line represents five-flavor prediction.

2.2 Shape Analysis

Two modes must be considered for b' decay, charged current (CC) mode and flavor changing neutral current(FCNC) mode, because b' to $cf\bar{f}$ decay may be suppressed by the two-generation gap[6]. The CC decay may result in an isolated lepton event(fig.4-a), which is a clean signal of a new flavor production. So previous b' searches have been carried out assuming this mode[7,8]. However, the FCNC decay(fig.4-b) produces no isolated leptons. The CC decay mode leads to spherical and/or isolated lepton events. The FCNC decay mode is, on the other hand, characterized by the back to back planar four jet events near threshold and the events with high energy isolated photons, because of two-body decay of each b'. The FCNC to CC ratio is unknown. We should be prepared for any ratio.

2.2.1 CC Decay Mode

TOPAZ used aplanarity to search for new flavor production. This value is calculated from the minimum eigenvalue of the momentum tensor[9]. By selecting high aplanarity events, we can condense heavy flavor events. Figure 5 shows aplanarity distributions at 52 and 60 GeV. The data points are consistent with the five-flavor Monte Carlo at both CM energies. Figure 6 represents the production cross section of high aplanarity events as a function of CM energy. The solid line in the figure is five-flavor prediction. The dashed lines are for open top or b' productions. The data points are consistent with the five-flavor Monte Carlo. AMY and VENUS used other shape parameters and observed no excess.

TOPAZ analyzed isolated muon events[10]. The muon tracks were identified by muon chambers. They started from their hadronic sample and further required: (1) The muon track had to have a momentum greater than 2 GeV. (2) An energy flow less than 2 GeV(isolation criteria), where the energy flow was defined to the sum of track momenta and energy deposits in the electromagnetic calorimeter within the cone of a 30° half angle about the muon track. (3) Thrust had to be less than 0.9. One event survived these cuts. Since they expected a background of 1.43 events from the five-flavor Monte Carlo, their data were consistent with the background. Figure 7 shows the

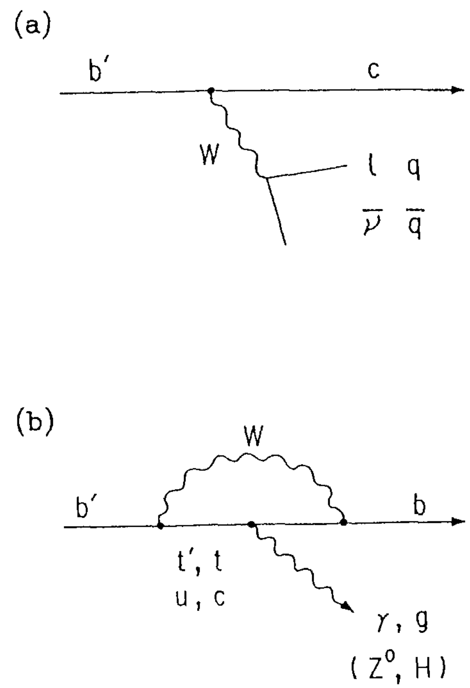

Figure 4 b' decay diagram for (a) charged current mode (b) neutral current mode.

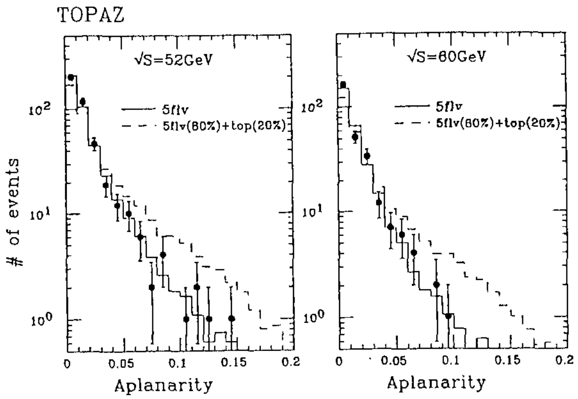

Figure 5 Aplanarity distribution at $\sqrt{s}$=52 and 60 GeV by TOPAZ.

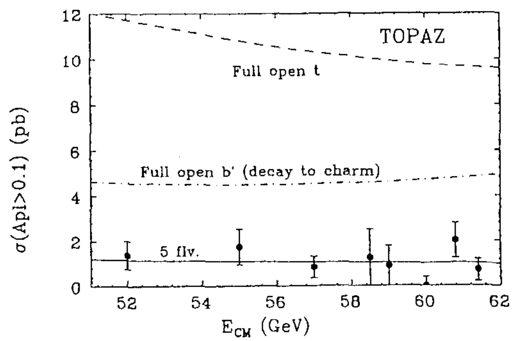

Figure 6 Total cross section produced high aplanarity events as a function of CM energy.

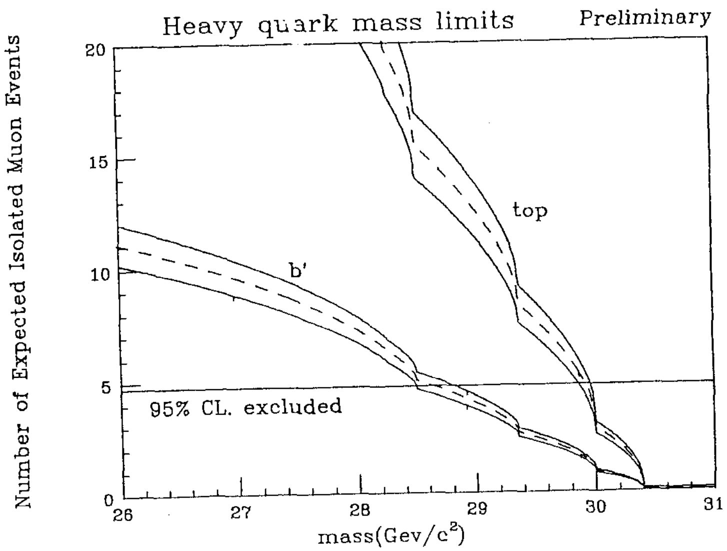

Figure 7 Number of expected isolated muon events as a function of new flavor mass. The horizontal line represents the 95% C.L. limit. The three lines for $t(b')$ production represent the number of events which is expected with errors.

number of expected events from open top or b' productions. The horizontal line in the figure represents the 95% C.L. limit. M_t and $M_{b'}$ should be greater than 29.9 and 28.4 GeV, respectively.

VENUS analyzed isolated muon and electron events. Muon and electron tracks were identified by muon chambers and the E/P method, respectively. Their analysis is similar to that of TOPAZ. They observed no events in the low energy region. However, five events were left at 60 and 60.8 GeV, through their expected background was only 1.0 event[11]. AMY and TOPAZ did not strongly support the VENUS observation at 60 and 60.8 GeV. Three groups did not observe any excess of isolated lepton events at the highest energy, 61.4 GeV. The statistical significance of the VENUS observation diminished.

2.2.2 FCNC Decay Mode for b'

If the CC decay is suppressed by two-generation gap, the FCNC decay mode is dominant. TOPAZ studied such case by two methods[12]. Method one is to search for isolated photon from b' to $b\gamma$ decay. The isolated photons were defined by (1) high energy photons (8.0 GeV< E_γ <22.0 GeV), (2) small charged track activity around the photons(E_{ch}(< 45°) <1 GeV), (3) large jet activity in the side ways. Method two is to look for the back to back jet pairs in four-jet events from b' to bg decay. Such events were selected by requiring (1) four-jet classification from the JADE cluster method[13]($Y_{cut} = 0.4$) and (2) the back-to-backness of opposite jet axes. The numbers of observed events were consistent with the five-flavor predictions in both methods. Then mass limits for b' quark were obtained as functions of branching ratios(fig.8). Independently of branching fractions b' lighter than 28 GeV was excluded. AMY and VENUS carried out similar analyses and observed no excess[14].

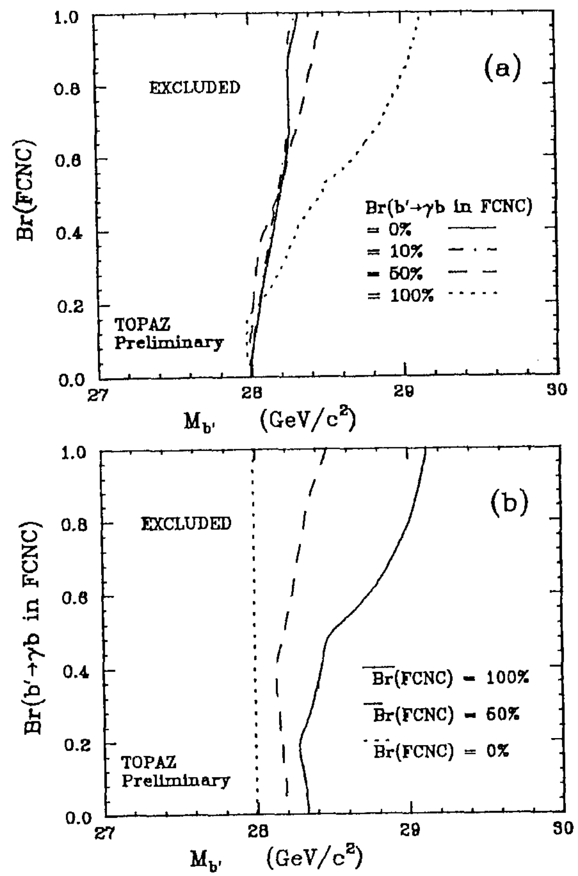

Figure 8 Mass limits for b' quark for various branching ratio.

3 Test of Standard Model

3.1 Electroweak Theory

The differential cross section of lepton pair production is given by the following formula,

$$\frac{d\sigma_{ll}}{d\Omega} = \frac{\alpha^2}{4s}[R(1+cos^2\theta) + Bcos\theta]; \beta = 1, l \neq e,$$

$$R = Q_l^2 - 2Q_l v_e v_l Re(\chi) + (a_e^2 + v_e^2)(a_l^2 + v_l^2)|\chi|^2,$$

$$B = 4a_e a_l[-Q_l Re(\chi) + 2v_e v_l|\chi|^2],$$

$$\chi = \frac{1}{16sin^2\theta_w cos^2\theta_w}\frac{S}{S - M_Z^2 + iM_Z\Gamma_Z}$$

where Q_l is lepton charge, a and v are axial vector and vector coupling constants, respectively. The normalized total cross section R_{ll} is equal to R. The standard model[15] predicts a small vector coupling constant $v_l = 0.1$. Then the second term in the formula R is smaller than the third term. The deviation of R_{ll} from one is small, about 7% at TRISTAN. Forward-backward asymmetry, A_{ll}, is calculated by the formula,

$$A_{ll} = \frac{\sigma_F - \sigma_B}{\sigma_F + \sigma_B} = \frac{3}{8}\frac{B}{R}.$$

In the standard model, the second term in the B expression is small. So A_{ll} is sensitive to axial vector coupling constants, $a_e a_l$. Asymmetry is large at about -0.4 at TRISTAN. Figure 9 shows observed $R_{\mu\mu}$ and $R_{\tau\tau}$. Data from AMY, TOPAZ and VENUS are combined. Solid line is the prediction of the standard model using the the best fit values of M_Z, $sin^2\theta_w$. The fitting procedure will be described in the next section. The data points are consistent with the standard model in both figures, through $R_{\mu\mu}$ is somewhat lower than the standard model prediction. The errors are dominated by statistical ones. More integrated luminosity is needed to confirm this observation. Figure 10 shows forward-backward asymmetries, $A_{\mu\mu}$ and $A_{\tau\tau}$. Again, the data points are consistent with the standard model prediction. The axial vector coupling constants were derived from these asymmetry data to be

$$a_\mu = -1.010 \pm 0.049,$$

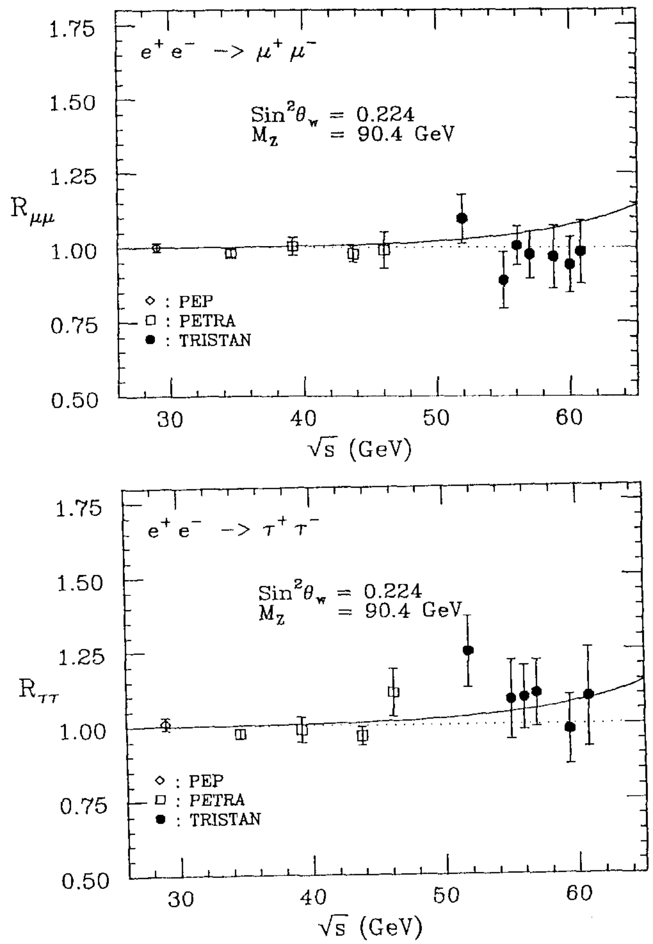

Figure 9 Normalized total cross section for $e^+e^- \to \mu^+\mu^-$ and $e^+e^- \to \tau^+\tau^-$.

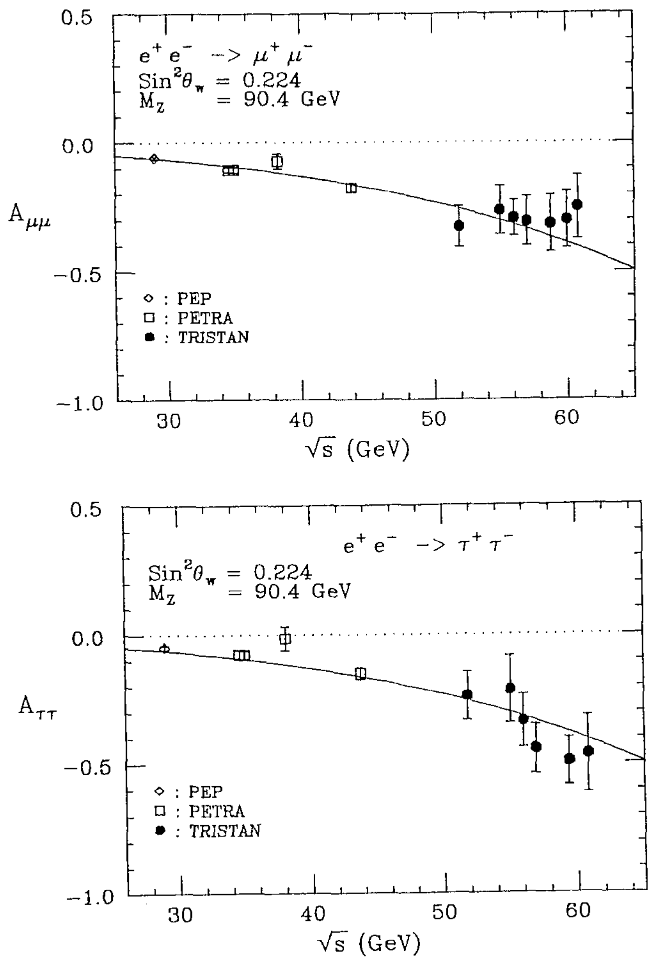

Figure 10 Forward-backward charge asymmetry for $e^+e^- \to \mu^+\mu^-$ and $e^+e^- \to \tau^+\tau^-$.

$$a_\tau = -0.913 \pm 0.072.$$

These values are consistent with -1. Inclusion of TRISTAN data moves a_l closer to the standard model value(fig.11). Assuming the lepton universality ($a_\mu = a_\tau$), we obtain

$$a_l = -0.980 \pm 0.041.$$

In fig.11, a_l values are shown for two different M_Z cases. If M_Z is fixed by SLC and LEP experiments, the axial vector coupling constant will be precisely measured at high luminosity TRISTAN.

In the quark sector, the differential cross section is represented by the following formula,

$$\frac{d\sigma_{qq}}{d\Omega} = \frac{\alpha^2}{4s} 3[R(1+cos^2\theta) + B cos\theta][1 + C_{QCD}]; \beta = 1.$$

The quark sector needs a color factor and a QCD correction. The normalized total cross section can be factorized at the formula in previous section. The QCD correction factor has been calculated up to $O(\alpha^3)$[16]. It is about 5% at TRISTAN. The electroweak term is larger than the lepton case, about 0.35 and 0.15 at 60 GeV for down type and up type quarks, respectively. In the forward-backward for quarks(A_{qq}), the QCD correction cancels and is given by the same formula as in the lepton case. Figure 12 is the R plot including low energy data[17,18]. The large effect of electroweak terms can be clearly seen at TRISTAN. We tried a global fit of these data to the standard model[17,19]. Free parameters were M_Z, $sin^2\theta_w$, and $\Lambda_{\overline{MS}}$ which is a QCD parameter. Used data were R_{qq}, R_{ll}, and A_{ll} at TRISTAN and PEP/PETRA. The results of the fit are the following,

$$M_Z = 90.4^{+1.69}_{-1.86} GeV,$$

$$sin^2\theta_w = 0.224^{+0.031}_{-0.020},$$

$$\Lambda_{\overline{MS}} = 372^{+283}_{-231} MeV.$$

The obtained M_Z is somewhat lower than world average 91.9 GeV[20]. A contour plot is given in fig.13. The solid lines are 1σ and 2σ contours. If G_F is used, the relation between M_Z and $sin^2\theta_w$ is given by the following formula,

$$M_Z^2 = \frac{\pi\alpha}{\sqrt{2} G_F (1+\Delta r) sin^2\theta_w cos^2\theta_w}$$

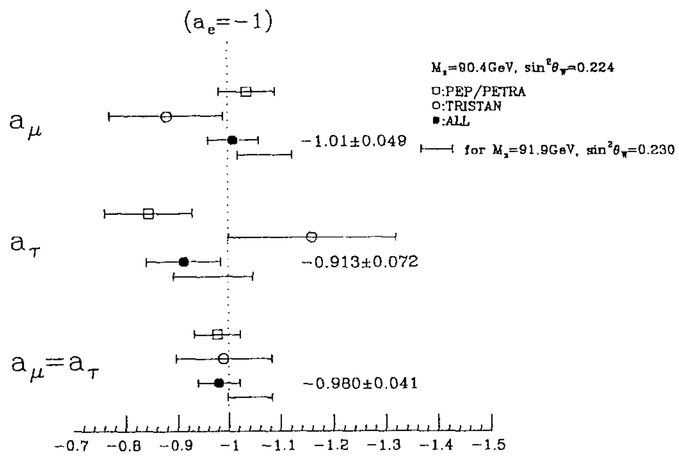

Figure 11 Axial vector coupling constants from $A_{//}$ data. a_e=1 is assumed.

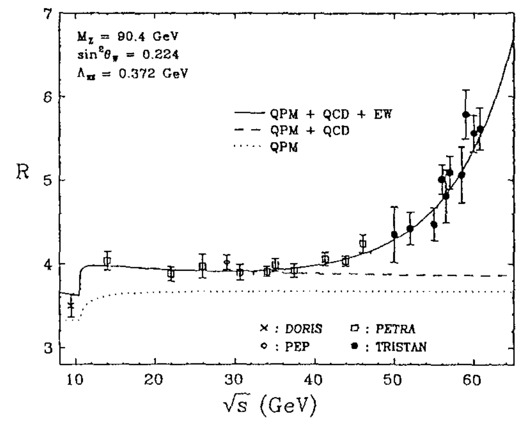

Figure 12 R-ratio including low energy data.

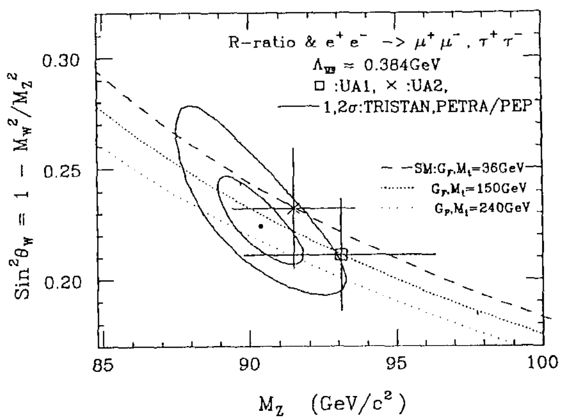

Figure 13 χ^2 contour plot in a global fit. The solid lines are 1σ and 2σ contours.

where Δr is a radiative correction factor and depends on M_{top} and M_{Higgs}. The effect of M_{Higgs} is small. The dashed lines in fig.13 are for M_{top} equal to 36, 150, and 240 GeV. The e^+e^- data favor a heavy top mass.

The forward-backward asymmetry for down type quark is minimum in the TRISTAN energy region. AMY measured b-quark forward-backward asymmetry[21]. Their analyzed data sample corresponds to an integrated luminosity of 18.6 pb^{-1} at CM energies between 52 and 57 GeV. b-quark events were selected from the hadronic events by requiring the following criteria. (1) The momentum of muon was greater than 1.9 GeV. (2) The p_t of muon was greater than 0.7 GeV, where p_t is the transverse momentum of muon with respect to the event thrust axis. Sixty events satisfied these criteria. The backgrounds were estimated to be about 30% and 20%, respectively, using the LUND 6.3 Monte Carlo simulation[22]. Figure 14-a is the resultant differential cross section after background subtraction. Data points are consistent with the standard model prediction. From the fit of the data in fig.14-a, the asymmetry and the cross section were obtained to be

$$A_b = -0.72 \pm 0.28 \pm 0.13,$$

$$R_b = -0.57 \pm 0.16 \pm 0.10$$

which were not corrected for the $B^0\bar{B}^0$ mixing. To compare with other data[23], the asymmetry value is plotted in fig.14-b. The data are consistent with the standard model prediction. The correction factor for the $B^0\bar{B}^0$ mixing is 6-56%[24], which depends on the parameters of $B^0_d\bar{B}^0_d$,$B^0_s\bar{B}^0_s$ mixing and semi-leptonic branching ratios of B mesons and B baryons. In any case, it will be possible to measure the $B^0_s\bar{B}^0_s$ mixing using precise measurements at the future high luminosity TRISTAN.

The b-tagging by leptons is clean but only at the cost of less events. In contrast to AMY's approach, VENUS took statistical merit rather than cleanliness and measured jet-jet asymmetry [25]. The jet-jet asymmetry is given by

$$A_{jet} = (f_d A_d + f_s A_s + f_b A_b) - (f_u A_u + f_c A_c)$$

where f_q is the fraction of the relative production rate of quarks. A_{jet} is about 10% at TRISTAN. To determine jet charge, all the tracks were divided

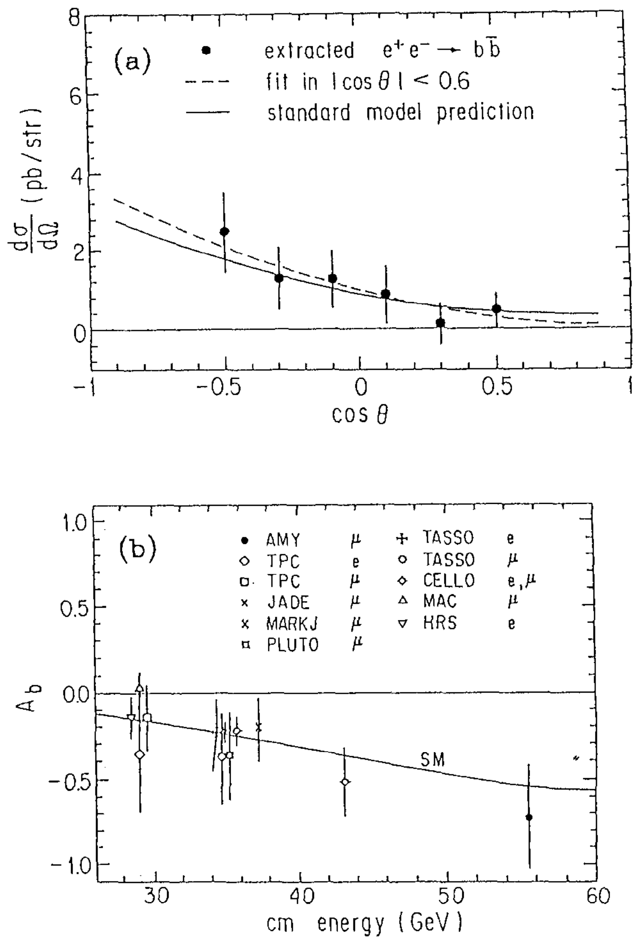

Figure 14 (a) Differential cross section $b\bar{b}$ production by AMY. (b) Forward-backward asymmetry including low energy data.

in to two jets by the plane perpendicular to the thrust axis. The charge of each jet was identified by a charge measure,

$$Q_{jet} = \sum Q_i (\frac{P_i}{E_{beam}})^{0.4}.$$

If Q_{jet1} is greater than Q_{jet2}, the charges of jet1 and jet2 are positive and negative, respectively. The charge identification probabilities by this method were 75% and 71% for up-type and down-type quarks, respectively, from studies using the LUND 5.3 Monte Carlo[26]. The integrated luminosity of the used data sample is 32.2 pb^{-1} accumulated between 52 and 61.4 GeV. The averaged center of mass energies is 57.6 GeV. All the hadronic events with a thrust greater than 0.85 were used. The differential cross section is shown is fig.15. As a result of fit, average quark asymmetry is

$$A_{jet} = 0.114 \pm 0.022 \pm 0.021.$$

The standard model prediction at 57.6 GeV is 8.7%, where no corrections were made for the effect of the $B^0\bar{B}^0$ mixing. If the $B^0\bar{B}^0$ mixing is considered, the asymmetry value ranges from 9.4% to 10.9% depending on the mixing parameters.

3.2 Search for Substructure of Fermions

If leptons and quarks are composite, their constituents is expected to be bound by a strong force. Since the compositeness scale, Λ, is very much higher than the CM energies we can cover, the binding force can be represented as a helicity conserving contact interaction [27],

$$L_{eff} = \frac{g^2}{2\Lambda^2}[\eta_{LL}\bar{\psi}_L\gamma_\mu\psi_L\bar{\psi}_L\gamma^\mu\psi_L + \eta_{RR}\bar{\psi}_R\gamma_\mu\psi_R\bar{\psi}_R\gamma^\mu\psi_R + 2\eta_{RL}\bar{\psi}_R\gamma_\mu\psi_R\bar{\psi}_L\gamma^\mu\psi_L]$$

where Λ is defined such that $g^2/4\pi = 1$ and the largest $|\eta| = 1$. The coefficients η are $\eta_{LL} = \pm 1$ and $\eta_{RR} = \eta_{RL} = 0$ for left-handed current(LL), $\eta_{RR} = \pm 1$ and $\eta_{LL} = \eta_{RL} = 0$ for right-handed(RR), $\eta_{RR} = \eta_{LL} = \eta_{RL} = \pm 1$ for vector(VV) and $\eta_{RR} = \eta_{LL} = -\eta_{RL} = \pm 1$ for axial vector(AA). The differential cross section now includes the L_{eff} effect as,

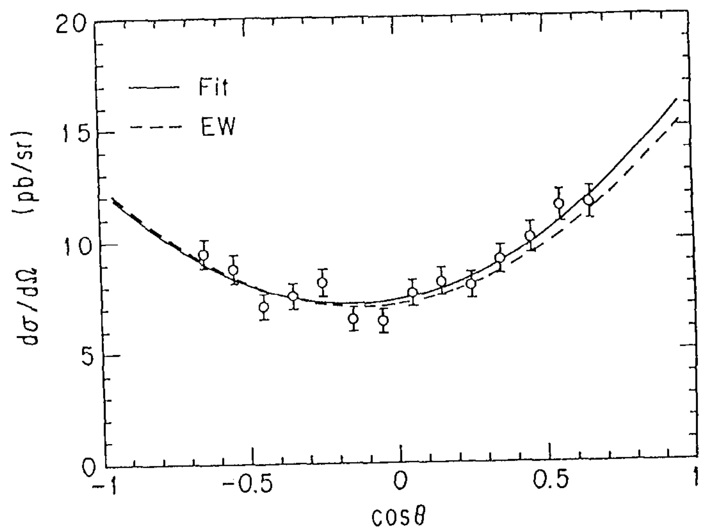

Figure 15 Differential cross section for $q\bar{q}$ production by VENUS.

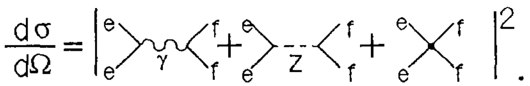

In the low energy region, the interference term is the dominant source of deviations from the standard model,

$$\frac{d\sigma}{d\Omega} \simeq \left(\frac{d\sigma}{d\Omega}\right)_{SM}\left(1 + O\left(\frac{s}{\alpha\Lambda^2}\right)\right); \Lambda \gg \sqrt{s}.$$

The differential cross sections for various $e^+e^- \to f\bar{f}$ processes were examined. As an example, fig.16 shows normalized $\mu\mu$ differential cross sections for various types of coupling. The data points are consistent with 1. Angular distributions were consistent with the standard model. Leptons and quarks seem point-like at our energies. Table 2 summarizes new lower limits of the compositeness scale parameters at 95% C.L.

3.3 Measurements of α_s or $\Lambda_{\overline{MS}}$

The QCD parameter α_s or $\Lambda_{\overline{MS}}$ has been measured by three methods, (1) derivation from the total hadronic cross section(see the previous section). This method is insensitive to fragmentation models. It is, however, also insensitive to $\Lambda_{\overline{MS}}$. (2) Three-jet fraction(R_3) are given by

$$R_3 = \frac{N_{3jet}}{N_{Total}} = C_1(y_{min})\alpha_s + C_2(y_{min})\alpha_s^2$$

where y_{min} is the minimum scaled invariant mass for parton pairs belonging to different jets[28]. Experimentally, three-jet events are usually selected by the JADE cluster method. If CM energy is high enough and y_{cut} is large enough, y_{min} is equal to y_{cut} and C_1, C_2 are almost independent of CM energy and selection cuts. Then if the R_3 decreases with CM energy, it means the α_s is running. (3) The asymmetry of energy-energy correlation(AEEC) is a powerful method to measure α_s[29]. Experimentally, EEC is given by the following formula,

$$EEC(\chi) = \frac{1}{N_{event}} \sum_{event} \sum_i \sum_j \frac{E_i E_j}{E_{vis}} \delta(\chi - \chi_{ij})$$

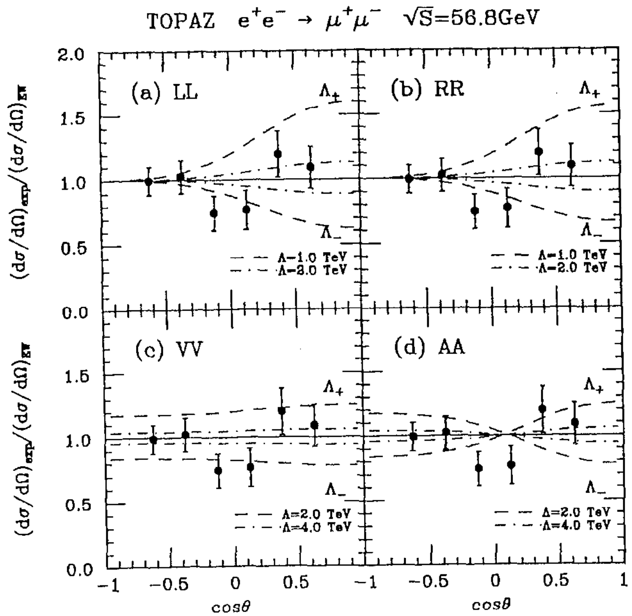

Figure 16 Normalized differential cross section for $e^+e^- \to \mu^+\mu^-$.

$e^+e^- \to e^+e^-$	LL [TeV]		RR [TeV]		VV [TeV]		AA [TeV]	
	Λ^+	Λ^-	Λ^+	Λ^-	Λ^+	Λ^-	Λ^+	Λ^-
VENUS	1.2	2.9	1.1	2.8	2.5	5.9	2.3	1.7
TOPAZ	1.1	1.0	1.2	1.0	2.7	2.5	2.3	1.4
AMY	1.3	1.3	1.3	1.3	1.8	4.0	3.9	0.7
$e^+e^- \to \mu^+\mu^-$								
VENUS	1.6	1.8	1.6	1.8	2.8	3.1	2.4	2.8
TOPAZ	1.5	1.6	1.4	1.5	3.3	2.4	2.0	3.8
AMY	1.9	1.0	1.9	1.0	3.1	2.6	3.0	1.9
$e^+e^- \to \tau^+\tau^-$								
VENUS	1.6	1.3	1.6	1.3	3.5	2.2	1.8	3.3
TOPAZ	0.9	2.2	0.9	2.1	1.6	7.2	2.1	1.6
$e^+e^- \to q\bar{q}$								
VENUS	0.9	1.8	1.5	2.5	3.9	2.4	3.4	5.5

Table 2 The 95% C.L. lower limits for compositeness scale parameters.

where i and j run over all the particle combinations in the event and χ_{ij} is the angle between i-th and j-th particles. The two-jet like events peak at 0 and π in the EEC distribution. For the AEEC defined by

$$AEEC(\chi) = EEC(\pi - \chi) - EEC(\chi)$$

the collinear effect is largely canceled. The AEEC enhances the effect of hard gluon emission and is good measure of α_s. TOPAZ determined α_s by comparing their AEEC data with Monte Carlo simulations using the matrix elements calculated by Gottshalk and Shatz[30] and the LUND string fragmentation[22]. The obtained $R_3(y_{cut} = 0.08)$ and α_s values were

$$\begin{aligned} R_3 &= 0.196 \pm 0.009 \quad at\ 55.1\,GeV\ (AMY); \\ &= 0.195 \pm 0.016 \quad at\ 53.3\,GeV\ (TOPAZ); \\ &= 0.184 \pm 0.010 \quad at\ 59.5\,GeV\ (TOPAZ); \\ &= 0.198 \pm 0.011 \quad at\ 57.3\,GeV\ (VENUS) \end{aligned}$$

and

$$\begin{aligned} \alpha_s &= 0.135 \pm 0.008 \quad at\ 55.1\,GeV\ (AMY); \\ &= 0.129 \pm 0.007 \pm 0.010 \quad at\ 55.3\,GeV\ (TOPAZ); \\ &= 0.120 \pm 0.008 \pm 0.010 \quad at\ 59.5\,GeV\ (TOPAZ); \\ &= 0.122 \pm 0.006 \pm 0.024 \quad at\ 57.3\,GeV\ (VENUS). \end{aligned}$$

Figures 17 and 18 shows the R_3 values and α_s from AEEC together with low energy data[31,32]. The data points in both figures are consistent with the running α_s predicted by the QCD theory.

4 Search for New Particles

Various new particles were searched for at TRISTAN. Signatures of heavy lepton, heavy neutrino, and SUSY particle productions are acoplanar leptons or jets or isolated leptons[33,34]. Excited leptons were searched in the $ll\gamma$ or $ll\gamma\gamma$ channels[35]. Any particle with abnormal dE/dx and scalar(X) and vector(Z') bosons were searched[36,37]. We cannot cover all of them. In what follows, only two examples of these searches are described.

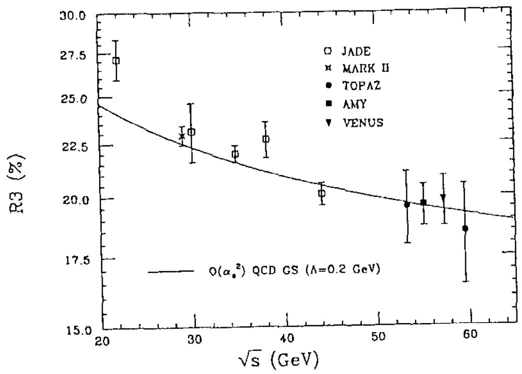

Figure 17 Three jet fraction for $y_{cut} = 0.08$ in comparison with the calculation with matrix elements(GS) for $\Lambda = 0.2GeV$.

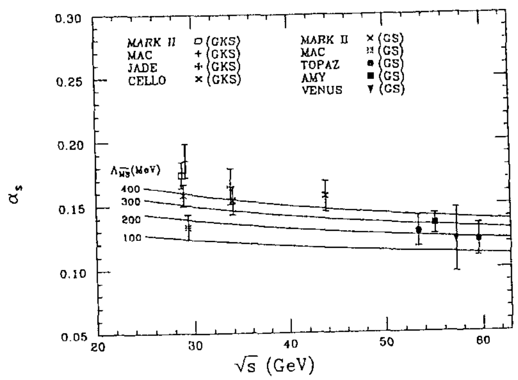

Figure 18 Measured α_s from AEEC analysis using matrix elements and LUND string fragmentation. Matrix elements were calculated with the GS and GKS[41].

Our first example is heavy lepton searches. Such leptons can be produced in pair and decay in to $f\bar{f}\bar{\nu}$. The neutrino carries away a large momentum leading to acoplanar jet-jet or lepton-jet events. AMY, TOPAZ and VENUS searched for such events. The data from all these groups were consistent with the five-flavor prediction, resulting in new mass limits. Figure19 shows the excluded region by AMY at the 95% C.L. The mass limit in the upper triangle from the analysis of low β tracks for the stable heavy lepton case.

Our second example is searches for particles with abnormal dE/dx[38]. Such search is sensitive to any new charged stable particles. Figure 20-a plots dE/dx as a function of momentum for tracks observed in the TOPAZ-TPC. The bands for e, μ, π, k, p, and deuteron are clearly seen. TOPAZ searched for pair productions of such particles. For the selected back to back tracks, dE/dx is plotted in fig.20-b. No events were observed in the two search regions. Limits were set on the production cross sections. The 95% C.L. limits were shown in fig.21 for various charge and spin hypotheses.

All the other searches ended up with negative results and, as a result, updated mass limits(table 3).

5 Search for Single Photon Events

The single photon events are used for neutrino counting and photino search. The main backgrounds are from radiative Bhabha and $\gamma\gamma$ events. To reject these backgrounds a small veto angle and hermetic calorimeters are essential. Having good hermetic calorimeters, VENUS searched for single photon events[39]. The integrated luminosity of their data sample is 28.2 pb^{-1} collected in the energy range $\sqrt{s} = 54. - 61.4$ GeV. Figure 22 plots the normalized transverse momenta($X_t = P_t/P_{beam}$) of single photons for a large veto and a small veto angle. The data points are consistent with the QED Monte Carlo. No events were observed in the region greater than the kinematical limit. The limits on the number of light neutrino type are obtained from calculated yield. The number limit is 11 at the 90% C.L. Combining with the ASP, CELLO, MAC and MARK-J data[40] VENUS obtained an upper limit of 3.9 for the number of light neutrino types at the 90% C.L.

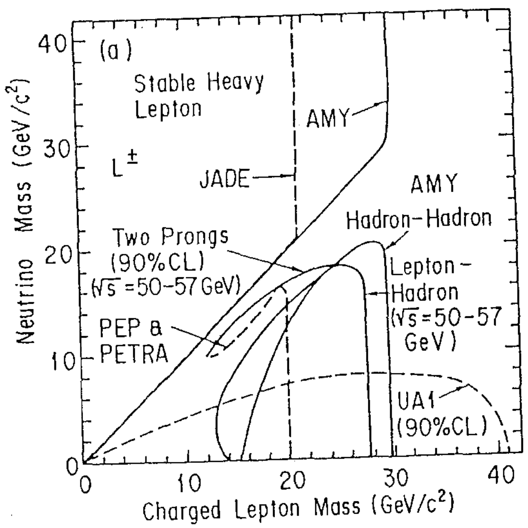

Figure 19 Mass limits for the charged heavy lepton by AMY.

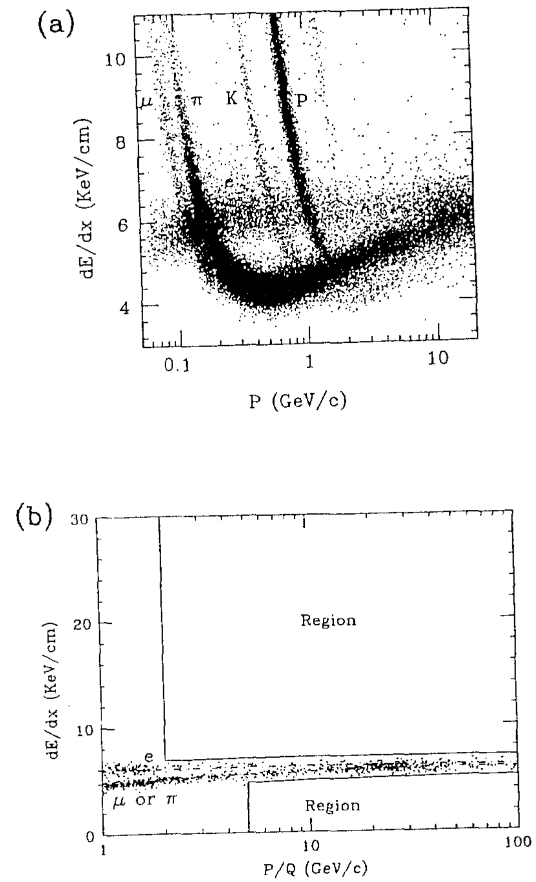

Figure 20 dE/dx for (a) tracks obtained by TOPAZ-TPC and (b) back to back tracks.

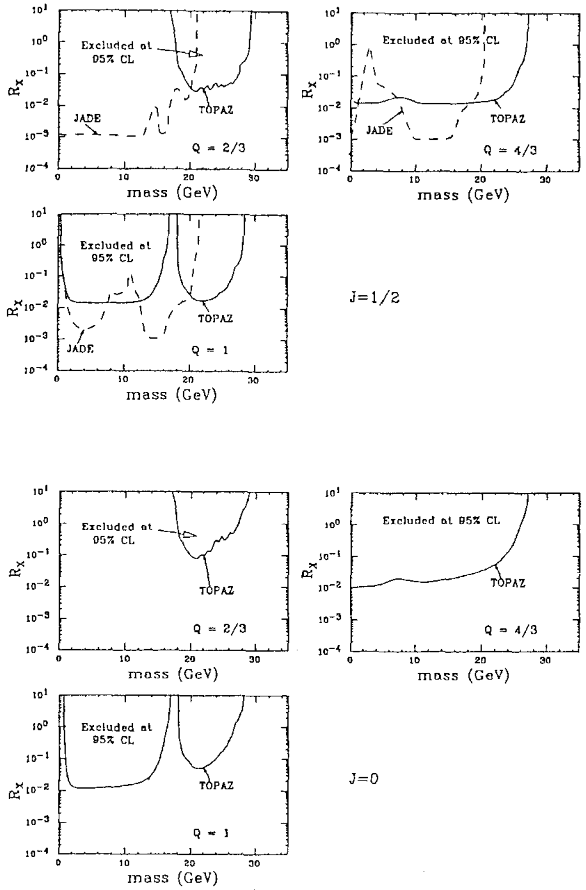

Figure 21 Mass limits for any particles with abnormal dE/dx.

Heavy Leptons and Neutrinos	
Heavy Lepton $m_\nu = 0$	> 29.9 GeV
Heavy Neutrino dirac type	> 26.8 GeV
Electron Type Heavy Neutrino V+A	>51.7 GeV or < 12.5 GeV
Electron Type Heavy Neutrino V-A	>48.5 GeV or < 17.3 GeV
Lepto-Quark (Second Generation) μ-s decay	>27.0 GeV or < 5.2 GeV
Lepto-Quark (Second Generation) c-ν decay	>27.0 GeV or < 7.8 GeV
Colored Lepton F(s)=1	>30.3 GeV or < 1.5 GeV
SUSY Particles	
$\tilde{e}$ ($M_{\tilde{f}_L} = M_{\tilde{f}_R}$)	> 29.5 GeV
$\tilde{\mu}$	> 25.8 GeV
$\tilde{\tau}$	> 24.7 GeV
$\tilde{q}$ Q = 2/3	> 27.7 GeV
Q = 1/3	> 26.2 GeV
Excited Leptons	
e^* pair	> 30.2 GeV
single	> 60.5 GeV
μ^* pair	> 30.1 GeV
single	> 53.0 GeV
τ^* pair	> 29.0 GeV
single	> 50.0 GeV
Bosons	
Scalar Boson (X)	Γ_{ee} < a few MeV for $54 < M_X < 60$ GeV
Vactor Boson (Z')	$(\lambda / \lambda_{SM})^2 < 2 \cdot 10^{-3}$ for $57 < M_{Z'} < 61$ GeV

Table 3 The 95% C.L. mass limits for searched new particles.

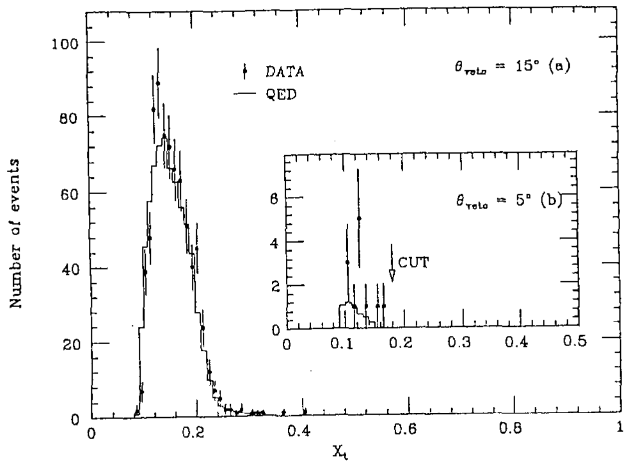

Figure 22 Normalized transverse momentum distribution of photons for (a) large veto angle(15°) and (b) small one(5°). The solid line is the prediction from QED processes.

6 Conclusion

Each of AMY, TOPAZ and VENUS accumulated data corresponding to 30 pb^{-1} in the energy range $\sqrt{s} = 50. - 61.4 GeV$. The measured R values were somewhat higher than five-flavor prediction. However, top and b' productions were excluded the shape analyses assuming the CC and the FCNC decay modes. The cross sections and the forward-backward charge asymmetries for quarks and leptons were consistent with the standard model predictions. The QCD parameter α_s was measured and was consistent with the running coupling constant predicted by the QCD theory. Various new particles were searched, but no excess was observed.

7 Acknowledgements

The author is grateful to experimental colleagues at TRISTAN for supplying materials presented in the talk and for helpful discussions.

References

[1] K.Kinosita et al.(SHIP), Phys.Rev.Lett. **60**(1988)1610 ; Phys.Lett. **B228**(1989)543.

[2] I.Adachi et al.(TOPAZ), Phys.Rev.Lett. **60**(1988)97.

[3] H.Sagawa et al.(AMY), Phys.Rev.Lett. **60**(1988)93; T.Mori et al.(AMY), Phys.Lett. **B218**(1989)499; H.Yosida et al.(VENUS), Phys.Lett. **B198**(1987)570.

[4] F.A.Berends and R.Kleiss, Nucl.Phys. **B178**(1981)141; F.A.Berends, R.Kleiss and S.Jadach, Nucl.Phys. **B202**(1982)63.

[5] J.Fujimoto and Y.Simizu, Mod.Phys.Lett. **A3**(1988)581.

[6] W.Hou and R.Stuart, Phys.Rev.Lett. **62**(1989)617.

[7] W.Bartel et al.(JADE), Phys.Lett. **B160**(1985)337; M.Althoff et al.(TASSO), Phys.Lett. **B138**(1984)441; H.-J.Behrend et al.(CELLO), Phys.Lett. **B144**(1984)297.

[8] C.Albajan et al.(UA1), Z.Phys. **C37**(1988)505.

[9] J.D.Bjorken and S.J.Brodsky, Phys.Rev. **D1**(1976)1416; E.Farki, Phys.Rev.Lett. **39**(1977)1587.

[10] I.Adachi et al.(TOPAZ), KEK Preprint 89-75.

[11] K.Ogawa, KEK Preprint 89-51, talk presented at KEK Topical Conference on e^+e^- Collision Physics, May 17-19, 1989, Tsukuba, Japan.

[12] I.Adachi et al.(TOPAZ), DPNU-89-39.

[13] W.Bartel et al.(JADE), Z.Phys. **C33**(1986)23.

[14] S.Eno et al.(AMY), KEK Preprint 89-46; K.Abe et al.(VENUS), KEK Preprint 89-39.

[15] S.Weinberg, Phys.Rev.Lett. **19**(1967)1264; A.Salam, Proc. Eight Nobel Symp, ed. by N.Svartholm (1968)p367; S.L.Glashow, Nucl.Phys. **B22**(1961)579.

[16] S.G.Gorishny, A.L.Kataev and S.A.Larin, Phys.Lett. **B212**(1988)238.

[17] H.-J.Behrend et al.(CELLO), Phys.Lett. **B183**(1987)400.

[18] R.Brandelik et al.(TASSO), Phys.Lett. **B113**(1982)499; W.Bartel et al.(JADE), Phys.Lett. **B129**(1983)145; Phys.Lett.**B160**(1985)337; E.Fernandey el al.(MAC), Phys.ReV. **D31**(1985)1537; D.P.Barber et al.(HRS), Phys.Rev. **D31**(1983)1.

[19] T.Tauchi, KEK Preprint 88-39.

[20] G.Arnison et al.(UA1), Phys.Lett. **B166**(1984)484; R.Ansari et al.(UA2), Phys.Lett. **B186**(1987)440.

[21] H.Sagawa et al.(AMY), KEK Preprint 89-38.

[22] T.Sjostrand and M.Bengtsson, Comp.Phys.Comm. **39** (1986)347; Comp.Phys.Comm. **43**(1987)367.

[23] W.Bartel et al.(JADE), Phys.Lett. **B146**(1984)437; M.Althoff et al.(TASSO), Phys.Lett. **B146**(1984)443; F.Ould-Saada, DESY report 88-177; H.R.Band et al.(MAC), Phys.Lett. **B218**(1989)369; C.R.Ng et al.(HRS), ANL-HEP-PR-88-11; S.L.Wu, Nucl.Phys.B (proc.Suppl.)3.

[24] K.Hagiwara et al., Phys.Lett. **B219**(1989)369.

[25] K.Abe et al.(VENUS), KEK Preprint 89-89.

[26] T.Sjostrand, Comput.Phys.Commum. **27**(1982)243.

[27] E.J.Eichten et al., Phys.Rev.Lett. **50**(1983)8.

[28] I.H.Park et al.(AMY), Phys.Rev.Lett. **62**(1989)1713; S.Bethke et al.(JADE), DESY 88-105; W.Braunschweig et al.(TASSO), DESY 88-046.

[29] C.Basham et al., Phys.Rev. **D17**(1978)2298.

[30] D.Gottschalk and M.P.Shatz, Phys.Lett. **B150**(1985)451.

[31] S.Bethke et al.(JADE), Phys.Lett. **B213**(1988)235; W.Braunschweig et al.(TASSO), Phys.Lett. **B214**(1988)286.

[32] D.R.Wood et al.(MARK-II), Phys.Rev. **D37**(1988)3091; E.Fernandez et al.(MAC), Phys.Rev. **D31**(1985)2724; W.T.Ford et al., SLAC preprint SLAC-PUB-4348(1989); W.Bartel et al.(JADE), Z.Phys. **C25**(1984)231; S.L.Wu., Intern. Symp. on Lepton and Photon Interactions at High Energies (Hamburg,1987) , eds. W.Bartel and R.Ruckel (North-Holland, Amsterdam)p.39.

[33] Y.Sakai et al.(AMY), KEK Preprint 89-42.

[34] G.N.kn et al.(AMY), Phys.Rev.Lett. **61**(1988)911; I.Adachi et al.(TOPAZ), KEK Preprint 89-31; Phys.Lett. **B218**(1989)105; A.Taketani et al.(VENUS), KEK Preprint 89-123.

[35] S.K.Kim et al.(AMY), KEK preprint 88-125; I.Adachi et al.(TOPAZ), Phys.Lett. B228(1989)553; K.Abe et al.(VENUS), Phys.Lett. **B213**(1988)400.

[36] K.Hagiwara, R.Najima, M.Sakuda and N.Terunuma, KEK Preprint 89-57.

[37] S.Suzuki, DPNU-89-32.

[38] K.Fujiwara, Ph.D.Thesis Kobe Univ. 1989.

[39] K.Abe et al.(VENUS), KEK Preprint 89-68.

[40] C.Hearty et al.(ASP), Phys.Rev. **D39**(1989)3207; H.-J.Behrend et al.(CELLO), Phys.Lett. **B215**(1988)186; W.T.Ford et al.(MAC), Phys.Lett. **D33**(1986)3472; H.Wu, Ph.D.Thesis Univ. Hamburg, 1986.

[41] F.Gutbrod,G.Kramer and G.Shierholz, Z.Phys. **C21** (1984)235.

Measurements of the Z Boson Resonance Parameters at SLC*

Christopher Hearty

Lawrence Berkeley Laboratory
University of California
Berkeley, California 94304

For the Mark II Collaboration

1. Introduction

This paper presents the measurement by the Mark II experiment at the SLAC Linear Collider of the parameters of the Z boson resonance. The results are updated from those presented at the SLAC Summer Institute to include all data presented in the most recent Mark II publication,[1] consisting of 19 nb^{-1} of data at ten different center-of-mass energies between 89.2 and 93.0 GeV.

The resonance parameters are extracted by measuring the Z production cross section at a series of center-of-mass energies (scan points) near the Z peak, then fitting these data with the theoretical cross section. The four major aspects of the analysis are the determination at each scan point of (1) the center-of-mass energy (E), (2) the integrated luminosity, (3) the number of Z decays and (4) the expected cross section as a function of the resonance parameters, such as mass and width. I will discuss each of these steps in turn, after a brief description of the Mark II detector, then conclude with the results of the analysis.

* This work was supported in part by the Director, Office of Energy Research, Office of High Energy and Nuclear Physics, Division of High Energy Physics of the U. S. Department of Energy under Contract Numbers DE-AC03-76SF00098 and DE-AC0376SF00515.

2. The Mark II Detector

The Mark II detector (Fig. 1) is described in detail in Ref. 2. The main components used to detect Z decays are the drift chamber and the electromagnetic calorimeters. The drift chamber, which has 72 layers and is located in a 4.75 kgauss axial magnetic field, tracks charged particles with $|\cos\theta| < 0.92$, where θ is the angle with respect to the beam line. The electromagnetic calorimeters cover the region $|\cos\theta| < 0.96$. The calorimeters in the central region ($|\cos\theta| < 0.68$) consist of alternating layers of liquid argon and lead, while the endcap calorimeters are layers of lead interspaced with proportional tube counters.

There are two detectors for the small-angle Bhabha events ($e^+e^- \rightarrow e^+e^-$) used to measure the integrated luminosity (Fig. 2). The small-angle monitors (SAMs) cover the angular region $50 < \theta < 160$ mr, where the acceptance at the inner (50 mr) edge is defined by a tungsten mask. Each SAM is 14.3 radiation lengths thick and consists of a tracking section with nine layers of drift tubes and a sampling calorimeter with six layer each of lead and proportional tubes (Fig. 3). The tracking sections have been used to determine the positional resolution of the calorimeter sections, but are not used to select events. The calorimeter sections are used to measure both the energy and position of the electron. The mini-small-angle monitors (MiniSAMs) detect Bhabha events in the angular region $15.2 < \theta < 25.0$ mr at one end of the detector and $16.2 < \theta < 24.5$ mr at the other. These angular regions, which are defined by tungsten masks, are asymmetric so as to substantially reduce the sensitivity of the Bhabha cross section to small movements in the interaction point (IP). Each MiniSAM is a 15 radiation length thick tungsten-scintillator sandwich divided into four azimuthal quadrants.

There are two major triggers for Z decays. The charged particle trigger requires two or more drift chamber tracks with transverse momentum greater than 150 MeV/c at $|\cos\theta| < 0.75$. The calorimeter trigger requires a single shower of at least 3.3 GeV in the barrel calorimeter or 2.2 GeV in the endcap calorimeter. The efficiencies for hadronic events are 97% and 95%, respectively, for these two

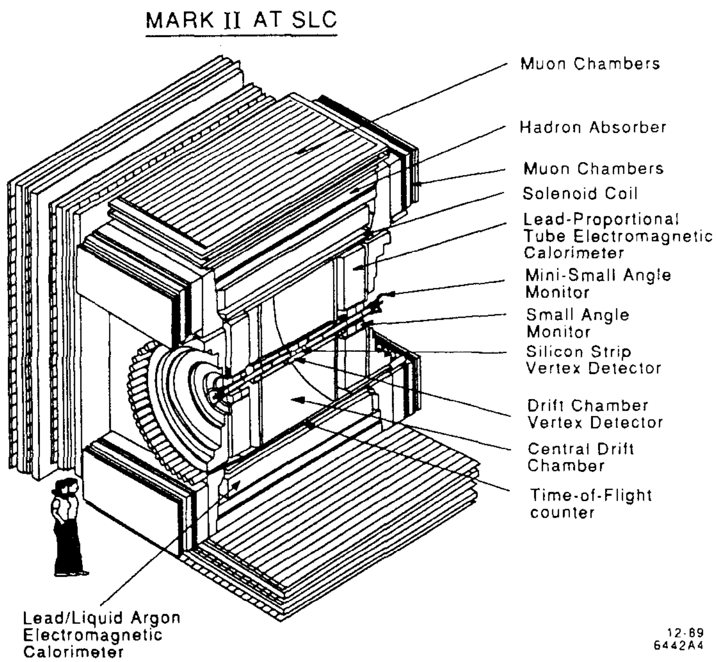

Figure 1. The Mark II detector.

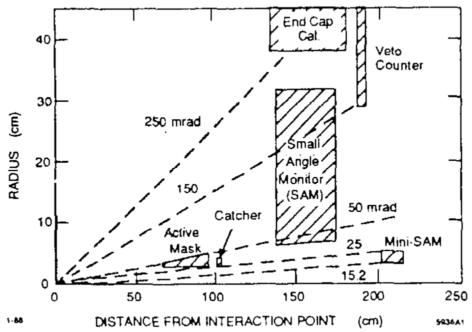

Figure 2. Locations of the SAM and MiniSAM. The relative luminosity is determined using the MiniSAM, while the absolute luminosity is found with the SAM.

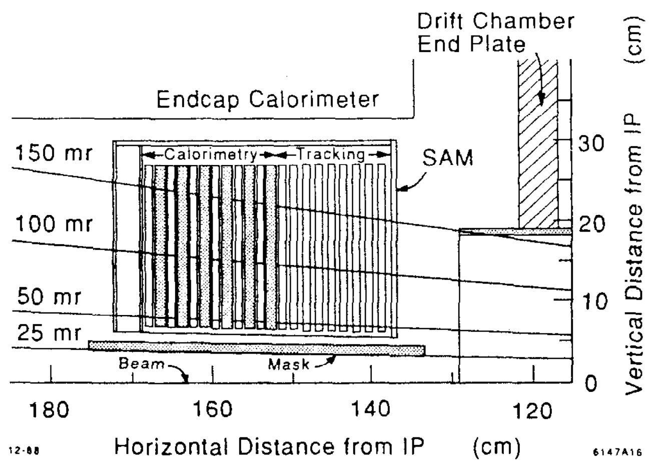

Figure 3. The small angle monitor. Bhabha events in the angular region $50 < \theta < 160$ mr are used in the integrated luminosity measurement.

triggers; together, the efficiency is 99.8%. Addition triggers record random beam crossings and cosmic rays for diagnostic purposes and low-angle Bhabha events for the luminosity measurement. At least 6 GeV of energy in each SAM or 20 GeV in each MiniSAM is required to trigger the data acquisition system.

3. Measurement of the Center-of-Mass Energy

The absolute center-of-mass energy (E) is measured on every pulse using an energy spectrometer in the extraction line of each beam.[3] The conceptual design of the extraction line is shown in Fig. 4. Dipole magnets before and after a precision spectrometer magnet bend the beam perpendicular to its direction, causing it to emit two swaths of synchrotron radiation. Phosphorescent screen monitors (Fig. 5) measure the distance between these swaths (approximately 27 cm) and hence the angle through which the beam was bent in the spectrometer magnet. This angle, which is proportional to $\int Bdl/E_{\text{beam}}$, is used with the known magnet strength to extract the beam energy E_{beam} with an uncertainty of 20 MeV. The contributions to the uncertainty are listed in Table I. There is an additional contribution to the uncertainty in E (but not in E_{beam}) due to momentum dispersion at the IP, giving a total uncertainty in E of 35 MeV. The center-of-mass energy spread, which is typically 250 MeV, is derived from the thickness of the synchrotron stripe to an uncertainty of approximately 30% of its value.

Table I. Systematic errors in the beam energy measurement.

Source of Error	Size of Error
Mapping of the spectrometer field	5 MeV
Rotational errors in dipole alignment	16 MeV
Determination of stripe position	10 MeV
Survey errors	5 MeV
Total Uncertainty	20 MeV

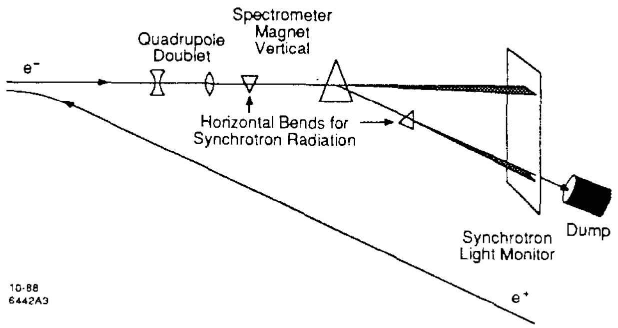

Figure 4. One of the two extraction line spectrometers used to measure the absolute beam energy.

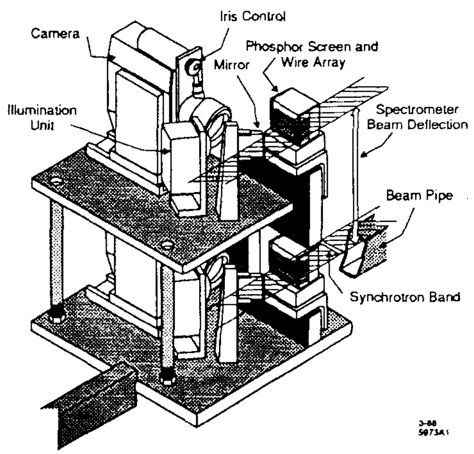

Figure 5. Phosphorescent screen monitor.

4. Integrated Luminosity Measurement

A typical Bhabha event in the SAM is shown in Fig. 6. Bhabha events are selected by requiring 40% of the beam energy in each SAM. There is essentially no background to these events. The position of the defining mask at 50 mr is not known accurately enough to permit the cross section for these "inclusive" events to be precisely calculated. Instead, the cross section is derived by scaling to a subset of events that fall into a fiducial volume that does have an accurately calculable acceptance. These "precise" Bhabha events are those in which $65 < \theta < 160$ mr for both e^+ and e^- showers, plus, with a weight of 0.5, events in which one shower has $65 < \theta < 160$ mr and the other has $60 < \theta < 65$ mr. The weighting reduces the effects of misalignments and detector resolution. The theoretically expected cross section[4] for events to be observed in the "precise" angular region is $25.2 \cdot (91.1/E(\mathrm{GeV}))^2$ nb. This includes a -1.9% correction from the nominal cross section for this region due to reconstruction inefficiency and a $+1.6\%$ correction due to detector resolution. (Events at $\theta < 60$ mr can be reconstructed as $\theta > 60$ mr.) We estimate a 2% systematic error from these detector effects and a 2% error from higher order radiative corrections, for a total systematic error of 2.8%. Multiplying this cross section by 815/484 — the ratio of "precise" to "inclusive" Bhabhas in the entire data sample — gives a cross section for events to be observed as "inclusive" Bhabhas of $\sigma_S = 42.6 \cdot (91.1/E(\mathrm{GeV}))^2$ nb, with a 2.9% statistical error due to the scaling error. A realignment of the 50 mr mask after the first seven scan points decreased σ_S by $1 \pm 2\%$. This factor is included in all of the following calculations.

Bhabha events in the MiniSAM are selected by requiring that a pair of quadrants of each side of the IP contain at least 25 GeV more deposited energy than the other pair of quadrants on that side. The pairs with significant energy must be diagonally opposite. In addition, all quadrants with greater than 18 GeV deposited energy must have timing information consistent with particles coming from the IP rather than striking the back of the detector 14 ns earlier. The efficiency (ϵ_M) depends on background conditions that can vary from scan point to scan point.

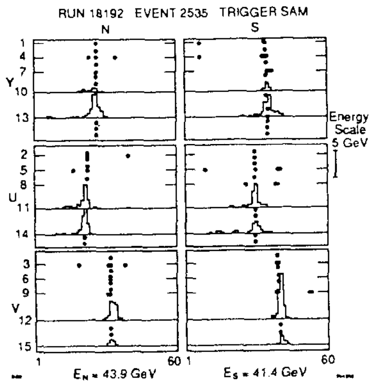

Figure 6. A Bhabha event in the small angle monitor.

It is measured for each scan point by combining random beam crossings at that energy with Monte Carlo Bhabha events and ranges from 91% to > 99%. Events in which the high energy pairs are not diagonally opposite are used to estimate the number of beam-related background events to be subtracted. The subtraction, which is 0.4% overall, ranges from 0% to 3.5% of the data at each scan point and is always less than the statistical error. The uncertainty in the number subtracted is taken to be the larger of 1% of the events at that scan point or the number itself. We cannot directly calculate the expected cross section for MiniSAM Bhabhas due to sensitivity to higher order radiative corrections and slight misalignments of the defining masks. Instead, we find it by scaling the number of events after background subtraction and efficiency correction to the number of "inclusive" SAM events. For the first seven scan points, $\sigma_M = 227 \cdot (91.1/E(\mathrm{GeV}))^2$ nb, while for subsequent data, $\sigma_M = 234 \cdot (91.1/E(\mathrm{GeV}))^2$ nb. In both cases, the statistical error due to the scaling factor is 4.5%. Because σ_M is substantially larger than σ_S, the MiniSAM dominates the measurement of relative luminosity between scan points, while the SAM determines the absolute luminosity.

5. Selection of Z Decay Events

We select hadronic decays of the Z and a subset of the leptonic decays based on charged tracks reconstructed by the drift chamber and showers found by the calorimeters. Charged tracks are required to emerge with transverse momentum greater than 110 Mev/c from within 1 cm of the beamline and 3 cm of the interaction point. The calorimeter showers are required to have at least 1 GeV in energy. The efficiencies of the selection criteria outlined below are measured by Monte Carlo (MC) simulation. Beam-related backgrounds are included in the detector simulation by combining data from random beam crossings with the MC data. They are found to have little effect on this analysis.

An example of a hadronic event is given in Fig. 7. Candidates for hadronic decays are required to have at least three charged tracks and at least $0.05E$ of energy visible in each of the forward and backward hemispheres. The cut on visible energy is designed to suppress beam gas and two-photon exchange interactions, which tend to deposit energy in only one hemisphere. A MC simulation indicates that we expect 0.02 events in our data from two-photon exchange interactions. The number of beam-gas interactions that satisfy these cuts is expected to be < 0.2 at the 90% confidence level (CL), since no events are found emerging from the beamline with $3 < |z| < 50$ cm. The efficiency for Z hadronic decays to satisfy these selection requirements (including trigger), is $\epsilon_h = 0.953 \pm 0.006$. Differences between QCD MC models account for the largest component of the uncertainty.

We also include in our fiducial sample μ and τ pairs with $|\cos\theta_T| < 0.65$, where θ_T is the thrust angle. We use this angular region to ensure high trigger and identification efficiency. Electron pairs are not included because of the interference from t-channel Bhabha events. Events are required to have at least $0.1E$ of visible energy, giving an efficiency of $99 \pm 1\%$ for muon events and $96 \pm 1\%$ for tau events.

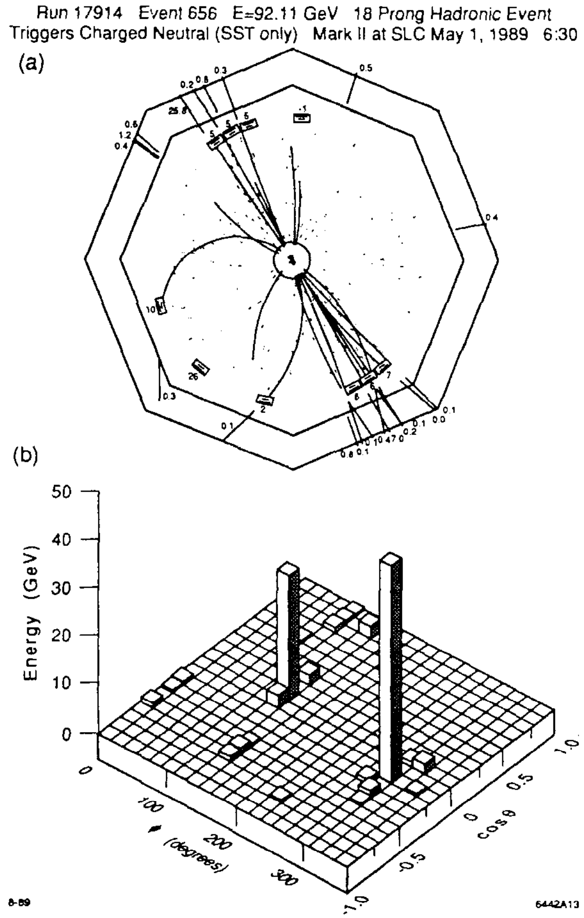

Figure 7. (a) A typical hadronic Z decay viewed along the beamline. (b) Detected energy of the event plotted as a function of phi and $\cos\theta$.

Tau events with $|\cos\theta_T| > 0.65$ that satisfy the hadronic selection criteria are rejected by a handscan.

Table II gives for each scan point the mean energy of the Bhabha events as measured by the energy spectrometer, the number of SAM "inclusive" (n_S) and MiniSAM (n_M) Bhabha events, ϵ_M, the integrated luminosity, the number of hadronic and leptonic Z decays passing the selection criteria, and σ_Z^m. The measured cross sections σ_Z^m are for the production of hadronic events and muon and tau pairs with $|\cos\theta_T| < 0.65$. The average σ_E generated by the energy spread of the beams and by the pulse-to-pulse jitter and drifts of the beam energies varies from 0.22 to 0.29 GeV. The cross sections contain corrections for this energy spread that vary from +3% near the peak to −3% in the tails. That is, σ_Z^m represents the cross section corresponding to a center-of-mass energy $< E >$ with $\sigma_E = 0$. Pairs of scan points that are very close in energy — such as points one and nine — have not been combined because the two points have different cross sections for SAM and MiniSAM Bhabha events.

6. Fitting the Data to Extract Resonance Parameters

We estimate Z resonance parameters by constructing a likelihood function from the probability of observing, at each energy, n_Z Z decays and n_L SAM and MiniSAM Bhabhas given that we have observed a total of $n_Z + n_L$ events. We obtain for the likelihood L

$$L = \prod \frac{(\epsilon\sigma_Z)^{n_Z}}{(\epsilon\sigma_Z + \sigma_L)^{n_Z+n_L}} \quad , \tag{6.1}$$

where the product is over energy scan points. The overall efficiency is $\epsilon = 0.954$, and $\sigma_Z(E)$ is the calculated production cross section for hadronic events and leptonic events with $|\cos\theta_T| < 0.65$. The likelihood function depends on the fit parameters, such as mass and width, through the dependence of σ_Z on these parameters. Terms that are constant with respect to σ_Z have been dropped from Equation (6.1).

Table II. Average energy, integrated luminosity, number of events, MiniSAM efficiency and σ_Z for each energy scan point. The luminosity for each scan point is given by Lum $= (N_S + N_M)/\sigma_L$, where $\sigma_L = \sigma_S + \epsilon_M \sigma_M$. The given error is the statistical error on N_S and N_M only; there are additional statistical errors on σ_L due to the scaling errors on σ_S and σ_M (see text). The total luminosity is calculated from the 485 "precise" SAM Bhabha events and has an overall 2.8% systematic error.

Scan Point	$< E >$ (GeV)	N_S	N_M	ϵ_M	Lum. (nb^{-1})	Z Decays			σ_Z (nb)
						Had.	Lep.	Tot.	
3	89.24	24	166	0.99	0.68±0.05	3	0	3	$4.5^{+4.5}_{-2.5}$
5	89.98	36	174	0.99	0.76±0.05	8	2	10	$13.5^{+6.0}_{-4.3}$
10	90.35	116	617	1.00	2.61±0.10	60	2	62	$24.8^{+3.8}_{-3.3}$
2	90.74	54	266	0.96	1.21±0.07	33	3	36	$31.7^{+6.8}_{-5.5}$
7	91.06	170	923	0.99	4.08±0.12	114	6	120	$31.6^{+3.4}_{-3.1}$
8	91.43	164	879	0.91	4.12±0.13	108	6	114	$29.8^{+3.3}_{-2.9}$
4	91.50	53	275	0.99	1.23±0.07	33	6	39	$34.3^{+7.0}_{-5.7}$
1	92.16	31	105	0.97	0.54±0.05	11	0	11	$21.5^{+9.2}_{-6.6}$
9	92.22	128	680	0.98	3.05±0.11	67	4	71	$24.3^{+3.4}_{-3.0}$
6	92.96	39	214	0.98	1.00±0.07	13	1	14	$14.6^{+5.4}_{-4.0}$
Totals		815	4299		19.3±0.9	450	30	480	

A relativistic Breit-Wigner resonance shape is used to represent σ_Z:

$$\sigma_Z(E) = \frac{12\pi}{m_Z^2} \frac{s\Gamma_e\Gamma_f}{(s - m_Z^2)^2 + s^2\Gamma^2/m_Z^2}(1 + \delta(E)), \tag{6.2}$$

where $s \equiv E^2$, δ is the substantial correction (~ -0.27 at the pole) due to initial state radiation calculated using an analytic form,[5] Γ_e is the Z partial width for electron pairs, and Γ_f is the partial width for decays in our fiducial volume. The partial widths for hadrons, muons and taus are related to Γ_f by $\Gamma_f = \Gamma_h + f(\Gamma_\mu + \Gamma_\tau)$, where $f = 0.556$ is the fraction of all muon and tau decays that have $|\cos\theta_T| < 0.65$. We take the total Z width to be $\Gamma = \Gamma_h + \Gamma_e + \Gamma_\mu + \Gamma_\tau + N_\nu\Gamma_\nu$, where N_ν is the number of species of neutrinos.

We have performed three fits to the data, which differ in their reliance on the minimal Standard Model. The first leaves only m_Z as a free parameter. The widths are those expected for Z couplings to the known fermions (5 quarks and 3 lepton doublets), including a QCD correction to the hadronic width.[6] The second fit leaves both m_Z and N_ν as free parameters but fixes Γ_ν and all other partial widths to their expected values. With this parameterization, N_ν is derived largely from the height of the resonance. Finally, the third fit does not assume any Standard Model partial widths. Instead, we write

$$\sigma_Z(E) = \sigma_0 \frac{s\Gamma^2}{(s - m_Z^2)^2 + s^2\Gamma^2/m_Z^2}(1 + \delta(E)), \tag{6.3}$$

and fit for m_Z, Γ and σ_0 (peak production cross section, in the absence of radiative corrections, for all hadronic events and for muon and tau pairs with $|\cos\theta_T| < 0.65$) as the three fit parameters. The extracted values of N_ν or σ_0 depend on the value of ϵ and the absolute luminosity normalization scale, while m_Z and Γ are not sensitive to these quantities.

7. Results of the Fits

The results of these fits are displayed in Fig. 8 and Table III. We conclude that $m_Z = 91.14 \pm 0.12$ GeV/c^2. The uncertainty includes systematic errors added in quadrature, the largest of which is the 35 MeV due to the absolute energy measurement. The systematic error in m_Z due to uncertainty in the initial state radiation correction is estimated to be less than 10 MeV/c^2.[5]

The second fit gives $N_\nu = 2.8 \pm 0.6$, which is equivalent to a partial width to invisible decay modes of $N_\nu\Gamma_\nu = 0.46 \pm 0.10$ GeV. The luminosity uncertainty

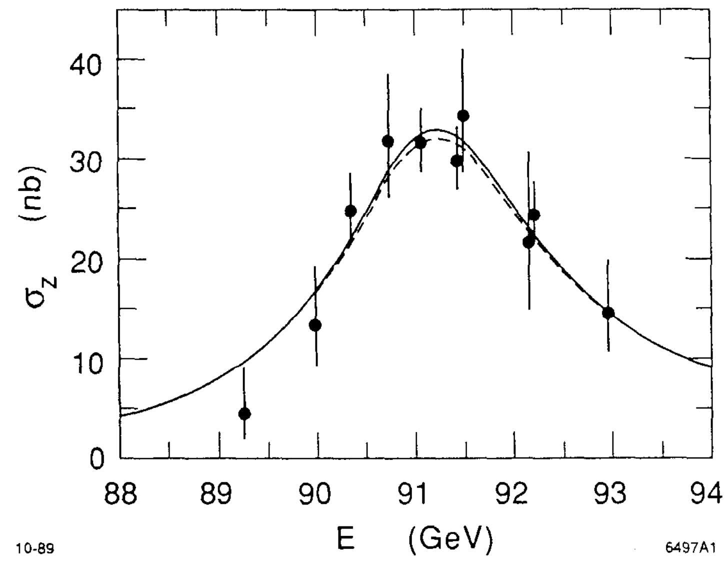

Figure 8. e^+e^- annihilation cross sections to all hadronic events plus μ and τ pairs with $|\cos\theta_T| < 0.65$. The dashed curve represents the result of the first fit, which assumes all standard model partial widths and $N_\nu = 3$ and leaves only m_Z as a free parameter. The solid curve represents the second and third fit results, which are indistinguishable. The second fit is similar to the first, except that both m_Z and N_ν are fit parameters, while the third fit includes no assumptions about partial widths.

contributes 0.45 to the error in N_ν. The 95% CL limit is $N_\nu < 3.9$, which excludes to this level the presence of a fourth massless neutrino species within the Standard Model framework.

Table III. Z resonance parameters. The three fits are described in the text.

Fit	m_Z GeV/c^2	N_ν	Γ GeV	σ_0 nb
1	91.14±0.12	–	–	–
2	91.14±0.12	2.8±0.6	–	
3	91.14±0.12	–	$2.42^{+0.45}_{-0.35}$	45±4

The third fit yields $\Gamma = 2.42^{+0.45}_{-0.35}$ GeV, in good agreement with the Standard Model value of 2.45 GeV. The MiniSAM background subtraction error, which is the largest systematic error, contributes 50 MeV to the uncertainty. The third fit value for σ_0 of 45±4 nb agrees well with the value of 43.6 nb calculated using $m_Z = 91.14$ GeV/$c^2$and Standard Model partial widths. The corresponding cross section for hadron decays is 42±4 nb. The maximum production cross section (including radiative corrections), which occurs approximately 90 MeV above the pole due to initial state radiation, is 33±3 nb for all events in our fiducial region, or 31±3 nb for hadronic events only.

The electroweak mixing angle, defined[7] as $\sin^2\theta_W \equiv 1 - m_W^2/m_Z^2$, is related to m_Z through

$$\sin 2\theta_W = \left(\frac{4\pi\alpha}{\sqrt{2}G_F m_Z^2(1-\Delta r)}\right)^{\frac{1}{2}}, \tag{7.1}$$

where Δr represents the effects of higher order radiative corrections. Because Δr is sensitive to the masses of heavy particles, the top quark mass and Higgs mass must be specified to calculate $\sin^2\theta_W$ from m_Z. For $m_t = m_H = 100$ GeV/c^2 and our value for the Z mass, $m_Z = 91.14 \pm 0.12$ GeV/c^2, we obtain

$$\sin^2\theta_W = 0.2304 \pm 0.0009. \tag{7.2}$$

The dependence of $\sin^2\theta_W$ on m_t and m_H is shown in Fig. 9.

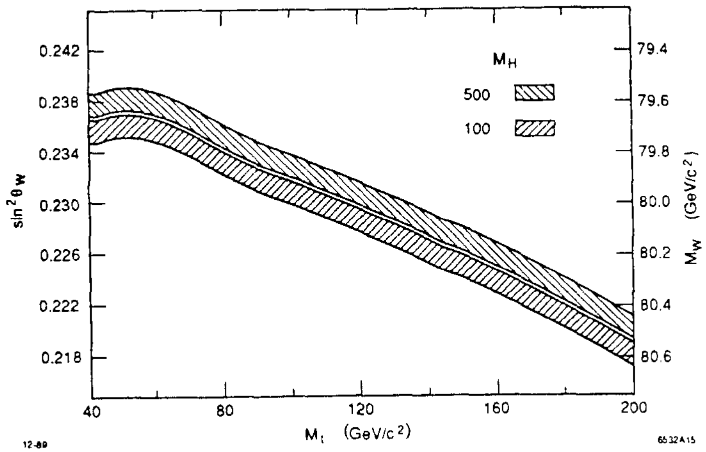

Figure 9. Value of $\sin^2\theta_W$ as a function of the top quark mass, for two Higgs boson masses. The widths of the bands are due to the uncertainty in the mass of the Z.

REFERENCES

1. G. S. Abrams *et al.*, *Phys. Rev. Lett.* **63**, 2173 (1989).
2. G. S. Abrams *et al.*, *Nucl. Instrum. Methods* **A281**, 55 (1989).
3. J. Kent *et al.*, SLAC-PUB-4922 (1989); M. Levi, J. Nash and S. Watson, *Nucl. Instrum. Methods* **A281**, 265 (1989); M. Levi *et al.*, SLAC-PUB-4921 (1989).
4. F.A. Berends, R. Kleiss, W. Hollik, *Nucl. Phys.* **B304**, 712 (1988), S. Jadach, B. F. L. Ward, *Phys. Rev. D* **40**, 3582 (1989).
5. R. N. Cahn, *Phys. Rev. D* **36**, 2666 (1987), Eqs. 4.4. and 3.1. See J. Alexander *et al.*, *Phys. Rev. D* **37**, 56 (1988) for a comparison of different radiative correction calculations.
6. Widths are calculated using the program EXPOSTAR, assuming m_{top} = 100 GeV/c^2. D. C. Kennedy *et al.*, *Nucl. Phys.* **B321**, 83 (1989).
7. A. Sirlin, *Phys. Rev. D* **22**, 971 (1980).

DECAYS OF THE Z BOSON

by

Tim Barklow

for

the Mark II Collaboration

ABSTRACT

We present results from the analysis of approximately 500 Z boson decays collected by the Mark II detector. Topics include the partonic structure of hadronic Z boson decays, charged particle inclusive distributions in hadronic decays, a measurement of α_S, properties of leptonic Z boson decays, and new particle searches.

1. INTRODUCTION

We present analyses of Z boson decay using data from the Mark II detector at the SLAC e^+e^- Linear Collider (SLC) operating in the e^+e^- center-of-mass energy ($E_{\rm cm}$) range from 89.2 to 93.0 GeV. We have studied the partonic structure of hadronic Z decays, measured the inclusive distributions of charged particles in hadronic decays, measured α_S, measured the ratio of leptonic decays to hadronic decays, and searched for new particles.

Our data sample consists of 528 events, of which 455 are hadronic Z boson decays, 41 are Z decays to μ pairs or τ pairs, and 32 are either Z decays to e^+e^- pairs or Bhabha scattering events. The luminosity integrated over all scan points is 19.7 $\rm nb^{-1}$.

Details of the Mark II detector can be found elsewhere.[1] A cylindrical drift chamber in a 4.75 kG axial magnetic field measures charged particle momenta. Photons are detected in electromagnetic calorimeters covering the angular region $|\cos\theta| < 0.96$, where θ is the angle with respect to the beam axis. Barrel lead-liquid-argon sampling calorimeters cover the central region $|\cos\theta| < 0.72$ and the remaining solid angle is covered by end-cap lead-proportional-tube calorimeters. The detector is triggered by two or more charged tracks within $|\cos\theta| < 0.76$ or by neutral-energy requirements of a single shower depositing at least 3.3 GeV in the barrel calorimeter or 2.2 GeV in an end-cap calorimeter.

2. HADRONIC Z BOSON DECAYS

2.1. Partonic Structure of Hadronic Decays

We test the underlying partonic structure of hadronic Z decays by studying the number of jets in an event (N_{jet}), the sphericity (S), the aplanarity (A) and the thrust (T). We compare the distributions for these variables to the predictions from several QCD–based models[2–5] which have had their parameters adjusted to fit Mark II data at E_{cm} = 29 GeV.[6] All event variables have been corrected for detector acceptance inefficiencies and machine–related backgrounds.[7]

The corrected distributions for the shape parameters sphericity, aplanarity and thrust are shown in Figs. 1 – 3 . Also shown are the predictions from several five-flavor QCD models for these quantities. These QCD model predictions are in good agreement with the data. The mean values of the shape quantities have been measured to be $< \mathrm{S} >= 0.070 \pm 0.007$, $< \mathrm{A} >= 0.0110 \pm 0.0009$ and $< \mathrm{T} >= 0.935 \pm 0.004$ where the corrections for detector acceptance have been applied and the errors are statistical only.

A cluster algorithm is used to estimate the number of jets (N_{jet}) observed in each event. The analysis method for calculating N_{jet} is described in detail elsewhere.[8,9] Briefly, in each event the quantities $y_{kl} = M_{kl}^2/E_{vis}^2$ are calculated for all pairs of particles k and l, where M_{kl} is the invariant mass of k and l, and E_{vis} is the sum of charged particle energies and shower energies. The pair with the smallest invariant mass is replaced by a pseudoparticle with four-momentum $(P_k + P_l)$. The procedure is repeated until the smallest y_{kl} exceeds a threshold value y_{cut}. The clusters formed by this procedure are called jets.

The corrected fractions of 2, 3, 4 and 5-jet events(R_2, R_3, R_4, R_5) are shown in Fig. 4 as a function of y_{cut}. In Fig. 4 each event contributes at all values of y_{cut} and hence the statistical errors for different values of y_{cut} are not independent. As illustrated in Ref. 9, the corrected jet multiplicity is expected to reproduce rather closely the produced jet (parton) multiplicity. At a standard value of $y_{cut} = 0.08$, the fraction of three jet events in hadronic events is 0.22 ± 0.03.

The mean values of the corrected quantities are compared in Fig. 5 to mean values from other experiments[10] at different center-of-mass energies and to the values from this experiment at 29 GeV.[6,9] For comparison, the solid curves show the expectations from the Lund parton shower model which follows the data over a wide range of energies.

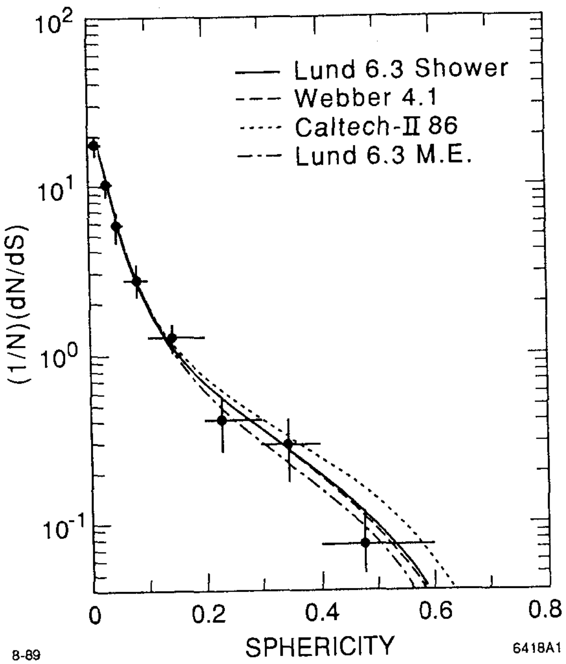

Figure 1. Event sphericity, for data (circles, with statistical errors) and four QCD Monte Carlo models (curves). Data points are plotted at the mean data value within each range and the horizontal bars show the extent of the range.

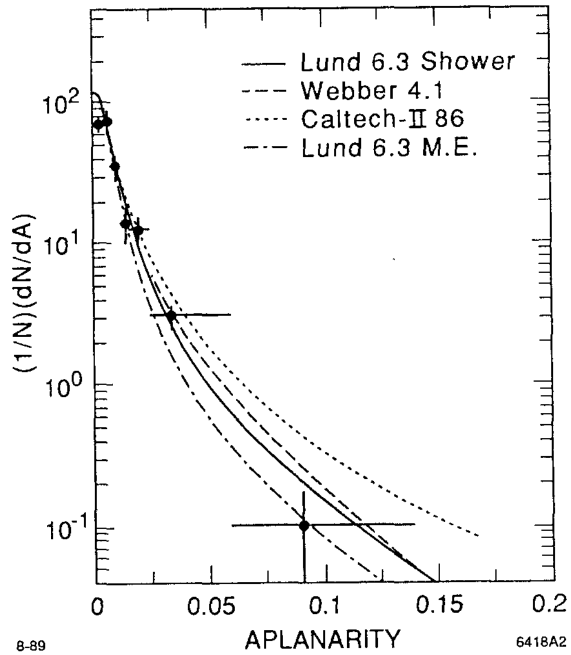

Figure 2. Event aplanarity, for data (circles, with statistical errors) and four QCD Monte Carlo models (curves).

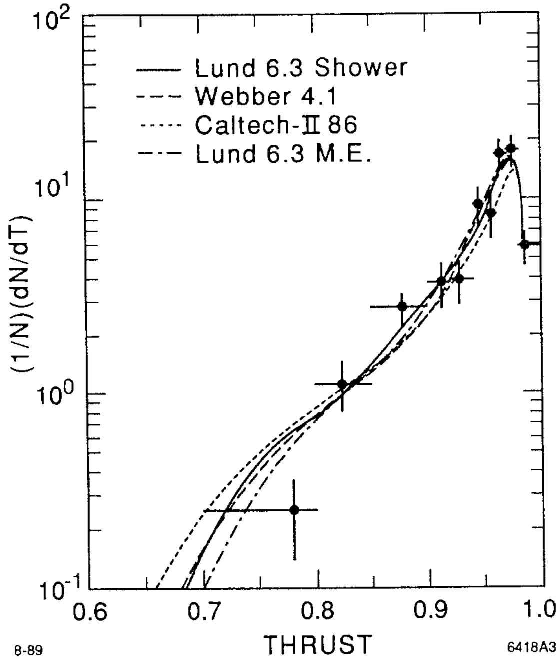

Figure 3. Event thrust, for data (circles, with statistical errors) and four QCD Monte Carlo models (curves).

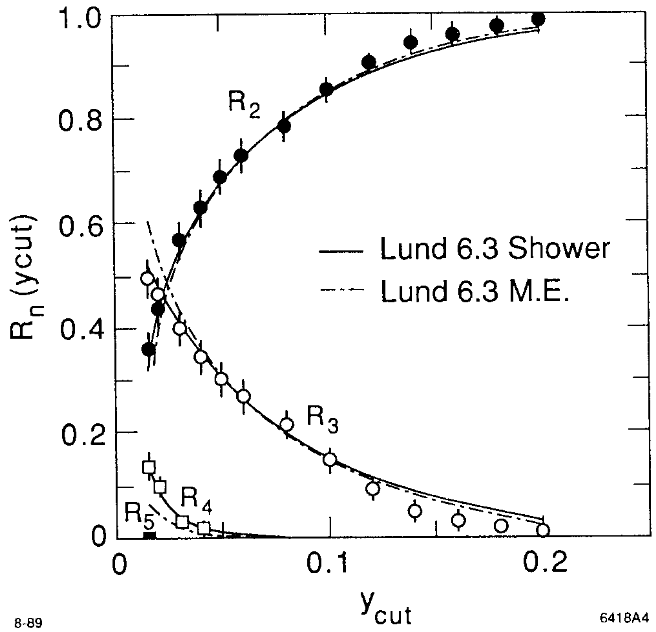

Figure 4. The observed 2, 3, 4 and 5-jet fractions for different values of y_{cut} (symbols, with statistical errors) and two QCD Monte Carlo model predictions (curves). For reasons of clarity, the other two models are not shown, but are also consistent with the data. Note that each event contributes at all values of y_{cut} and hence the statistical errors for different values of y_{cut} are not independent.

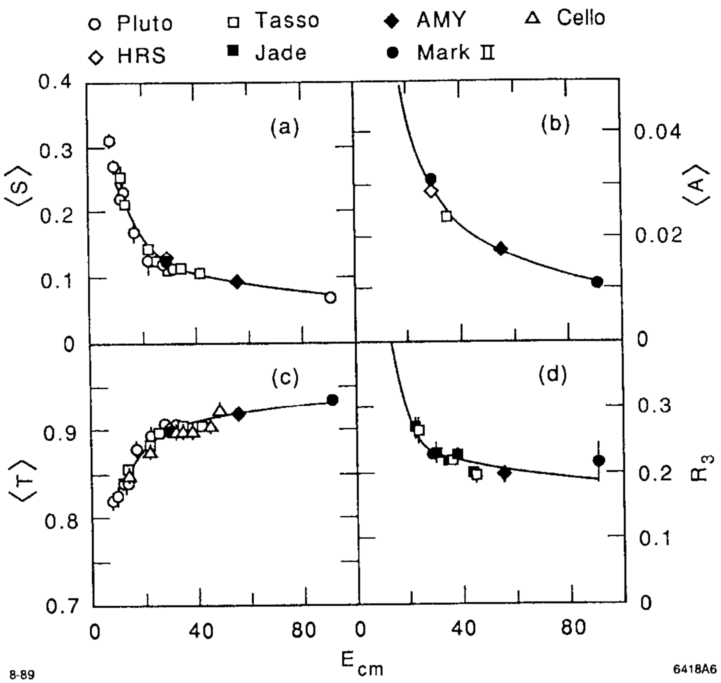

Figure 5. The mean values of (a) sphericity (b) aplanarity and (c) thrust and (d) the 3-jet fraction for a y_{cut} of 0.08 compared to data from several center-of-mass energies. The errors are statistical only. The curves are the predictions from the Lund parton shower model.

2.2. Charged Particle Inclusive Distributions

Inclusive charged particle distributions provide additional tests of hadronic Z boson decays. We study the charged multiplicity, the scaled momentum ($x \equiv 2p/E_{cm}$), the momentum transverse to the sphericity axis within the event plane $p_{\perp in}$, and the momentum out of the event plane $p_{\perp out}$.

All variables, with the exception of the charged multiplicity, are corrected for inefficiencies, detector resolution and machine backgrounds using bin-by-bin correction factors derived from the LUND 6.3 shower Monte Carlo with full detector simulation.[11] Charged particles from all K^0_S and Λ decays are included in the corrected distributions.

The uncorrected charged multiplicity distribution is shown in Fig. 6 (a). Also shown are the predictions of several QCD-based fragmentation models. The charged multiplicity was not corrected on a bin-by-bin basis because of large correlations between bins. We have, however, used an unfolding procedure[12] to measure the mean charged multiplicity of hadronic Z boson decays. Our corrected mean charged multiplicity is plotted in Fig. 6 (b) along with the mean charged multiplicities measured by other e^+e^- experiments[12,13] at various center-of-mass energies.

Figure 7 (a) shows the corrected distribution for $1/\sigma_{had}\, d\sigma_{trk}/dx$, where σ_{had} and σ_{trk} are the total hadronic and charged-particle inclusive cross sections, respectively, along with the predictions from several models. Figure 7 (b) shows $1/\sigma_{had}\, d\sigma_{trk}/dx$ *vs.* E_{cm} for several x bins, comparing the results of this analysis with data from other e^+e^- experiments at lower E_{cm}.[6,12,14] The small scaling violations in the largest and smallest x bins are accounted for by the LUND shower Monte Carlo.

The distributions for $p_{\perp in}$ and $p_{\perp out}$ are shown in Figs. 8 (a) and (b) respectively, together with predictions from several Monte Carlos. Mark II data from the Z boson resonance and from $E_{cm} = 29$ GeV[6] are shown. Figure 8 (c) shows the mean values of $p^2_{\perp in}$ and $p^2_{\perp out}$ from this experiment and from others[6,12,13,14] at a variety of center-of-mass energies along with the prediction from the LUND

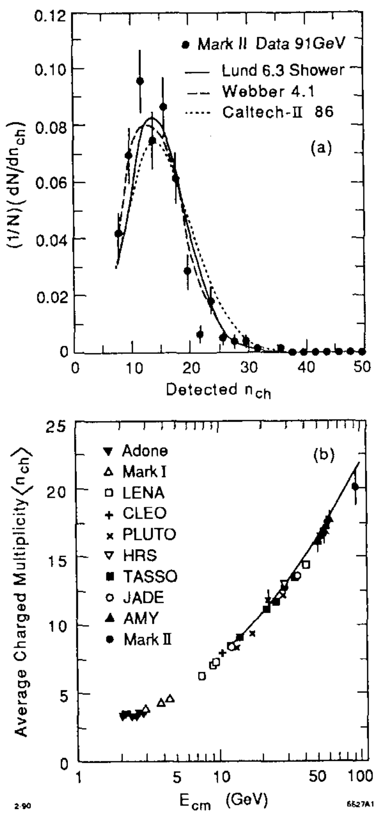

Figure 6. (a) Uncorrected charged particle multiplicity distribution for detected hadronic events. Comparisons with several QCD models are shown. (b) Mean corrected charged particle multiplicity *vs.* E_{cm} for various e^+e^- experiments. The solid line is the Lund Shower model prediction.

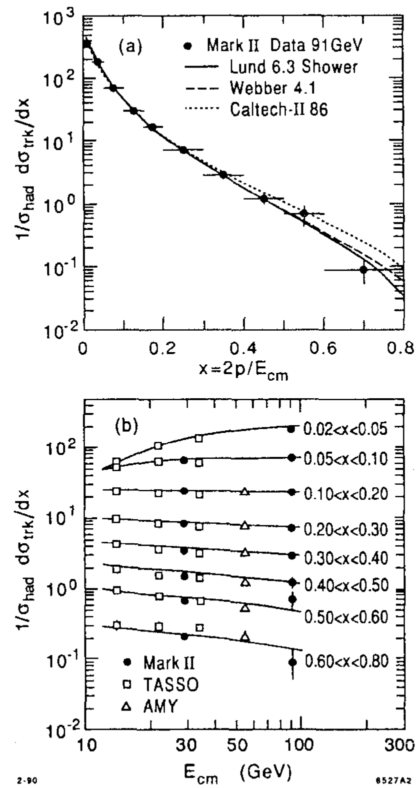

Figure 7. (a) Corrected charged-particle inclusive distribution $1/\sigma_{had}\ d\sigma_{trk}/dx$, where $x = 2p/E_{cm}$, compared with several models. (b) Comparison between charged-particle inclusive distribution in x for hadronic Z decays and various e^+e^- experiments at lower E_{cm}. The solid lines are the Lund Shower model prediction.

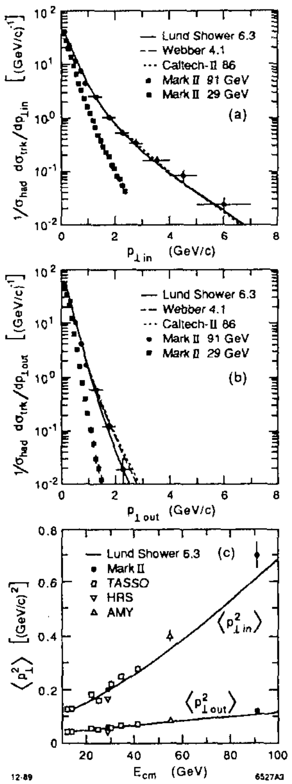

Figure 8. (a) Corrected charged-particle inclusive distribution $1/\sigma_{had}\, d\sigma_{trk}/dp_{\perp in}$ compared with the predictions of several models and with Mark II data at 29 GeV. (b) Corrected charged-particle inclusive distribution $1/\sigma_{had}\, d\sigma_{trk}/dp_{\perp out}$ compared with the predictions of several models and with Mark II data at 29 GeV. (c) Comparison between means of charged-particle inclusive distributions in $p^2_{\perp out}$ and $p^2_{\perp in}$ for hadronic Z decays and various e^+e^- experiments at lower E_{cm}. The solid lines are the Lund Shower model predictions.

shower Monte Carlo. The data at larger center-of-mass energies appears to be slightly higher than the Monte Carlo prediction.

2.3. Measurement of α_S

According to QCD the strong coupling constant α_S should decrease as the center-of-mass energy of e^+e^- collisions is increased. The Mark II is well-suited to test the running of α_S since the same detector has been used to observe hadrons produced through e^+e^- annihilation at $E_{cm} = 29$ and 91 GeV .

Examples of observables which are sensitive to α_S include the total hadronic cross section (σ_{tot}), the energy-energy-correlation asymmetry and the three-jet fraction R_3. The total hadronic cross section is free of fragmentation uncertainties, but depends only weakly on α_S (QCD corrections are approximately 5% of σ_{tot}). The energy-energy-correlation asymmetry has systematic errors from fragmentation uncertainties which are difficult to estimate.[15]

The three-jet fraction R_3 is insensitive to fragmentation effects for large enough values of the jet resolution parameter y_{cut}.[16] However, it is difficult to extract α_S by fitting the R_3 distribution since the same event can appear several times in the distribution. Instead of dealing with the complicated correlations of such a fit we have chosen instead to plot and fit the derivative of the R_2 distribution.[17]

The derivative of the R_2 distribution is defined as follows. For a given hadronic event, we define y_3 to be the largest jet resolution parameter y_{cut} for which the event can be classified as a three-jet event. We define $g_3(y_3)$ to be the distribution function of y_3. Integrating $g_3(y_3)$ over y_3 from 0 to y_{cut} yields $R_2(y_{cut})$, so that $g_3(y) = R_2{}'(y)$. Note that an event appears only once in the g_3 distribution.

The corrected $g_3(y_3)$ distribution is shown in Fig. 9 for (a) $E_{cm} = 91$ GeV and (b) $E_{cm} = 29$ GeV . Also shown are QCD predictions[18] for different values of the QCD scale parameter $\Lambda_{\overline{MS}}$. These predictions were obtained by differentiating the R_2 function calculated in Ref. 18. The dotted vertical lines at $y_3 = 0.04$ and $y_3 = 0.14$ are the boundaries of the region we fit to obtain α_S . The region with $y_3 < 0.04$ is not used because fragmentation effects are large for small values of

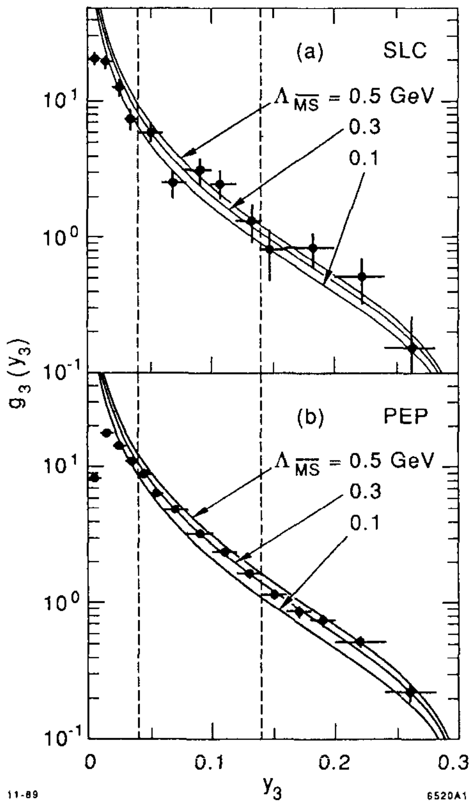

Figure 9. The experimental distributions of y_3 at (a) $\sqrt{s}$ = 91 GeV, and (b) $\sqrt{s}$ = 29 GeV. Only the statistical errors are indicated in the figures. The curves below $y_3 = 0.14$ indicate the QCD predictions with $\Lambda_{\overline{MS}}$ =0.1 GeV, 0.3 GeV and 0.5 GeV for $Q^2 = s$. The y_3 range used in the fit for the determination of α_s is defined by the two dashed lines. The curves above $y_3 = 0.14$ are extrapolated from the QCD predictions in the low y_3 range.

y_3, while the region with $y_3 > 0.14$ is not used because the $R_2(y)$ calculation in Ref. 18 is not valid for $y > 0.14$.

Choosing the renormalization point Q^2 to be s, we obtain

$$\alpha_S = 0.123 \pm 0.009 \pm 0.005 \text{ at } \sqrt{s} = 91\text{GeV}$$
$$\alpha_S = 0.149 \pm 0.002 \pm 0.007 \text{ at } \sqrt{s} = 29\text{GeV}.$$

Figure 10 shows our two measurements of α_S along with a QCD extrapolation[19] of our α_S measurement at $\sqrt{s}$ = 29 GeV to higher energies. The running of α_S from 29 GeV to 91 GeV is consistent with the QCD prediction.

Using the approximate solution to the renormalization group equation given in Ref. 19, we find that the corresponding QCD scale parameters are $\Lambda_{\overline{MS}} = 0.29^{+0.17+0.11}_{-0.12-0.06}$ at $\sqrt{s}$ = 91 GeV and $\Lambda_{\overline{MS}} = 0.28^{+0.02+0.08}_{-0.02-0.07}$ at $\sqrt{s}$ = 29 GeV .

3. LEPTONIC Z BOSON DECAYS

The ratio of the partial Z decay width into lepton pairs to the partial decay width into hadrons,

$$r_{ll} \equiv \frac{Br(Z \to ll)}{Br(Z \to hadrons)}, \quad l = e, \mu, \tau,$$

is expected to be 0.048 in the standard model.

We separate hadronic and leptonic decays on the basis of the number of tracks and the event thrust. For the purpose of measuring r_{ll}, hadronic events are selected by requiring at least seven charged tracks, while leptonic event candidates are required to have fewer than seven charged tracks. In addition, lepton candidates must have at least one charged track in each event hemisphere, defined by the plane perpendicular to the thrust axis calculated from the charged particles, and no tracks outside $|\cos\theta| < 0.82$. The separation of the leptonic Z decays into e, μ, and τ pairs requires additional criteria which are described in Ref. 20.

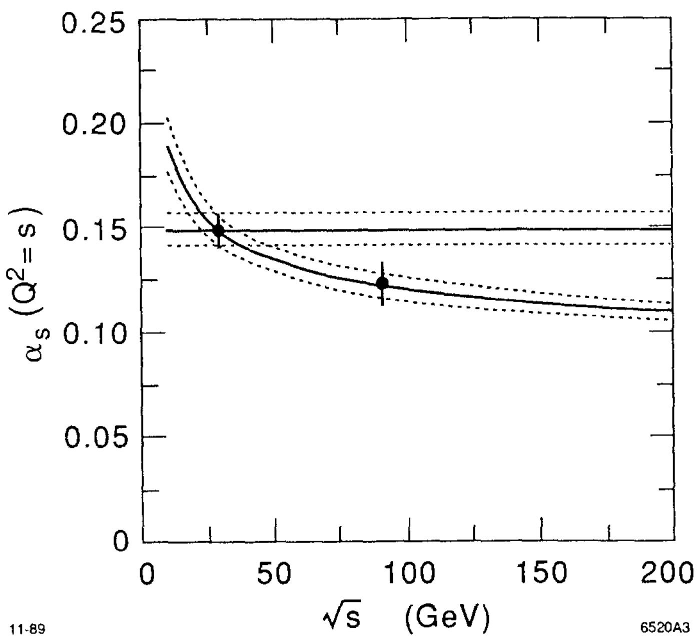

Figure 10. The strong coupling $\alpha_s(Q^2 = s)$ as a function of $\sqrt{s}$. The errors include statistical and systematic uncertainties added in quadrature. Also shown are the extrapolations of the α_s measurement at $\sqrt{s} = 29$ GeV to higher energies or assuming a constant α_s. The dotted lines indicate the extrapolation of the measured $\alpha_s \pm 1\sigma$ from 29 GeV.

The detection efficiency for the different classes of events are: 88% for hadronic events, 66% for τ pairs, 54% for μ pairs. The efficiency for electron pairs produced at the Z peak within $|\cos\theta| < 0.82$ is 93%. We find 397 hadronic events, 13 μ pairs, 21 τ pairs and 18 electron pairs. For the τ sample the estimated background from all sources is 1.6 events, for the μ sample the estimated background is 0.2 events, and for the electron sample the estimated background from all sources is less than 0.15 events.

The electron sample has a sizeable contribution from QED and weak–electromagnetic interference. To reduce this contribution we require that the positron scattering angle θ be in the range $-0.82 < \cos\theta < 0.68$, eliminating the forward region where the QED contribution is large. This cut leaves 12 events with a background of 1.4 ± 0.6 events due to QED and weak–electromagnetic interference. The overall electron efficiency after all cuts is 0.62.

After inclusion of all systematic and statistical uncertainties the resulting ratios of the partial decay widths are:

$$\frac{\Gamma_{ee}}{\Gamma_{had}} = 0.037^{+0.016}_{-0.012}$$
$$\frac{\Gamma_{\mu\mu}}{\Gamma_{had}} = 0.053^{+0.020}_{-0.015}$$
$$\frac{\Gamma_{\tau\tau}}{\Gamma_{had}} = 0.066^{+0.021}_{-0.017}.$$

These results are consistent with each other and agree well with the Standard Model prediction of 0.048. Under the assumption of lepton universality the combined lepton sample yields $\Gamma_{ll}/\Gamma_{had} = 0.053^{+0.010}_{-0.009}$.

4. NEW PARTICLE SEARCHES

4.1. New Heavy Quarks

Semi-leptonic Decays

Semi-leptonic heavy quark decays will produce isolated leptons. To maximize our detection efficiency for new heavy quarks and other new heavy particles decaying through a virtual W boson, we do not require that an isolated charged track be identified as an electron or muon.

An isolated track is one with isolation parameter $\rho_i > 1.8$ where ρ_i is defined as follows[21] : The Lund jet-finding algorithm is applied[22] to the charged and neutral tracks excluding the candidate track i. We then define

$$\rho_i \equiv \min_{jets\ j}[(2E_i(1-\cos\theta_{ij}))^{1/2}],$$

where E_i is the track energy in GeV and θ_{ij} is the angle between the track and each jet axis. The distribution of ρ, the maximum value of ρ_i of all charged tracks in an event, is shown in Fig. 11 for our data sample, for a five-flavor QCD Monte Carlo,[23] and for a 35 GeV/c^2 t quark .

There is one event with $\rho > 1.8$ while 0.9 events (Lund Shower with Peterson fragmentation) to 1.8 events (Webber 4.1[24]) are expected from QCD five-flavor processes. To be conservative, background subtraction is performed using the smallest value (0.9 events) expected. Using a standard approach,[25] we find the upper limit at 95% C.L. to be 4.2 events for one observed event and 0.9 expected background events.

From the above observation, we conclude that the mass of the top quark (t quark) is greater than 40.0 GeV/c^2 and the mass of a fourth generation down-type quark (b' quark) is greater than 44.7 GeV/c^2 at the 95% confidence level (C.L.) if t and b' decay 100% via a virtual W boson.

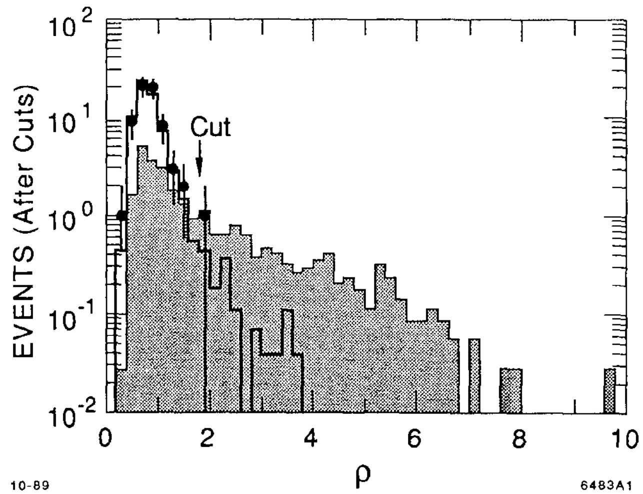

Figure 11. Maximum isolation parameter ρ of all the tracks in an event for data (circles, with statistical errors), *udscb* QCD Monte Carlo (solid line), and a 35 GeV/c^2 top quark (hatched area, normalized to data). The Monte Carlo simulation includes detector and beam background effects.

Loop Decays to Photons

A b' quark may not decay 100% of the time via a virtual W because of increased suppression of transitions which cross two generations.[26] Consequently, the flavor-changing neutral-current (FCNC) loop decays[27] of $b' \to b+gluon$ and $b' \to b\gamma$ must also be considered. We use isolated photons to search for the process $b' \to b\gamma$.

An isolated photon is defined to be a neutral shower with $\rho_i > 3.0$ where ρ_i is defined as for a charged track. A larger ρ cut is required because the calorimeters cannot resolve closely-spaced π^0's as well as the drift chamber can resolve closely-spaced charged pions. No events were found with an isolated photon. From this observation, we obtain $M_{b'} > 45.4$ GeV/c^2 (95% C.L.) if B.R.($b' \to b\gamma$) $\geq 25\%$.

Hadronic Decays

If the virtual W decays and direct photon decays of a heavy quark are suppressed, then isolated track techniques cannot be used to find a heavy quark. Hadronic decays might dominate if b' decays through $b' \to b + gluon$ are important. Also, in extensions of the Standard Model with two Higgs doublets, t and b' can decay into charged Higgs particles (H^+) by $t \to H^+b$ or $b' \to H^-c$ if $M_{H^\pm} < M_t$, $M_{b'}$. This two-body decay mode would dominate over decays through a virtual W.

To search for events in which both heavy quarks decay hadronically we take advantage of the fact that such events tend to be spherical and tend to have large momentum sums out of the event plane. We use the variable $M_{\rm out}$, defined to be

$$M_{\rm out} \equiv \frac{E_{\rm cm}}{E_{\rm vis}} \frac{1}{c} \sum |p_{\perp out}|,$$

where $p_{\perp out}$ is the momentum component of a charged track or neutral shower out of the event plane defined by the sphericity tensor, and the sum is over all charged tracks and neutral showers. The distribution of $M_{\rm out}$ is shown in Fig. 12 for the data sample, for a five-flavor QCD Monte Carlo, and for the process $b' \to cH^- \to c\bar{c}s$ for a 35 GeV/c^2 b'. We select heavy quark events by requiring that $M_{\rm out} > 18$ GeV/c^2 .

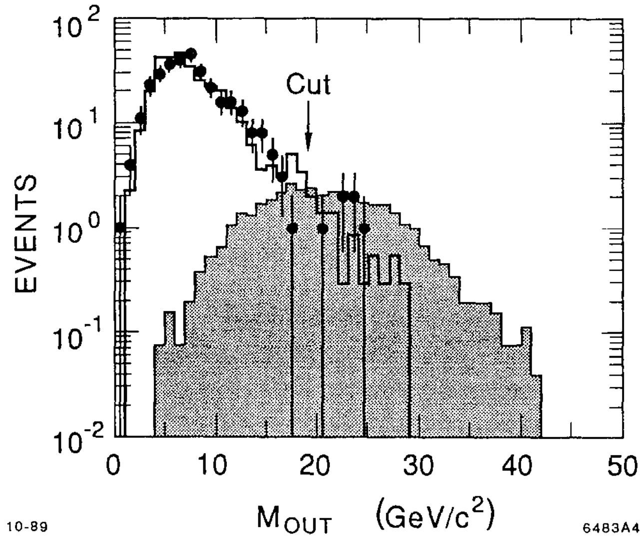

Figure 12. Mass out of the event plane $M_{\rm out}$ for data (circles, with statistical errors), *udscb* QCD Monte Carlo (solid line), and for a 35 GeV/c^2 b' quark decaying into cH^- (hatched area), with $M_{H^-} = 25$ GeV/c^2 and the H^- decaying 100% into $\bar{c}s$.

Six events are observed in the data with $M_{\rm out} > 18$ GeV/c^2 , while 4.8 events (Lund Matrix Element[24]) to 11.7 events (Webber 4.1[24]) are expected from QCD five-flavor processes. The tail of the QCD $M_{\rm out}$ distribution is very model dependent because of the different ways in which multiple-hard-gluon radiation is handled.[24] To be conservative, background subtraction is performed using the smallest value (4.8 events) expected. We find the upper limit[25] at 95% C.L. to be 7.4 events for 6 observed events and 4.8 expected background events.

The above observation allows us to set the following limits. If t and b' decay 100% via a virtual W, $M_t > 40.7$ GeV/c^2 and $M_{b'} > 44.2$ GeV/c^2 at 95% C.L. If b' decays 100% into $b + gluon$, then $M_{b'} > 42.7$ GeV/c^2 at 95% C.L. If t and b' decay 100 % through a charged Higgs boson of mass ≥ 25 GeV/c^2 , which in turn decays 100% hadronically into $c\bar{s}$, then $M_t > 42.5$ GeV/c^2 and $M_{b'} > 45.2$ GeV/c^2 at 95% C.L. The case of the H^- decaying partially into $\tau\bar{\nu}$ is found to weaken the above limits, but if B.R.$(H^- \to \tau\bar{\nu}) < 70\%$ both limits remain over 40 GeV/c^2 .

4.2. New Heavy Unstable Neutral Leptons

We restrict our neutral lepton (L^0) search to a sequential fourth generation Dirac neutral lepton. We assume that $M_{L^0} < M_{L^-}$ in the new lepton doublet (L^0, L^-), and that the weak eigenstates ν_ℓ and mass eigenstates L_i^0 of the four generations of neutrinos are mixed in analogy with the quark sector:

$$\nu_\ell = \sum_{i=1}^{4} U_{\ell i} L_i^0.$$

The possible decay modes of the L^0 are then $L^0 \to \ell + W^*, (\ell = e, \mu, \tau)$.

Limits on L^0 production are sensitive to the mixing parameter $U_{L^0\ell}$. For small enough values of the sum $\Sigma\ |U_{L^0\ell}|^2$ for $\ell = e, \mu, \tau$, the lifetime[28] of the L^0 will be sufficiently long that it will decay outside our fiducial vertex region. We therefore present our neutral lepton limits as a function of L^0 mass and $\Sigma\ |U_{L^0\ell}|^2$.

For short-lived neutral leptons with masses greater than about 20 GeV/c^2 we can use the isolated charged track analysis described in the previous section. From the fact that there is but one event with $\rho > 1.8$ we obtain the neutral lepton limits shown in Fig. 13.

4.3. Other New Particle Searches

The Mark II has searched for many other types of new particles. We have searched for long-lived neutral leptons,[29] short-lived neutral leptons with masses less than 22 GeV/c^2 ,[30] doubly charged Higgs bosons,[31] non-minimal neutral Higgs bosons,[32] heavy stable charged particles,[33] and supersymmetric particles.[34] All searches have been negative.

5. SUMMARY

All of our observations of Z boson decay are consistent with the standard model. QCD-based fragmentation models which have had their parameters adjusted at $E_{cm} = 29$ GeV describe hadronic Z decays very well. The strong coupling constant α_S runs between 29 GeV and 91 GeV as predicted by QCD. The ratio of leptonic to hadronic decays is consistent with the value predicted by the standard model. And we have seen no evidence for new particle production in Z boson decay.

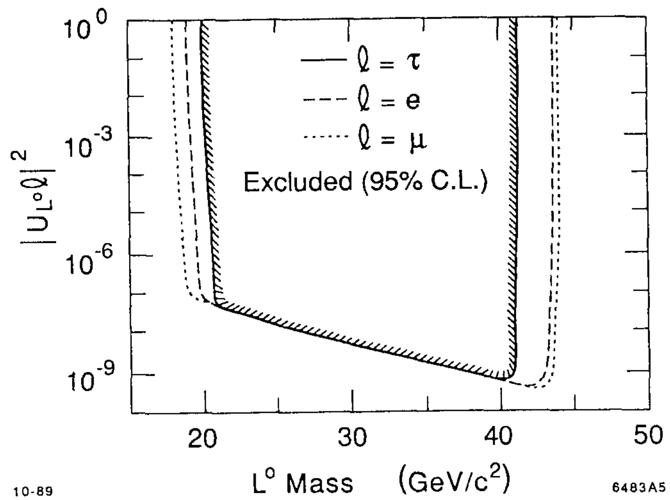

Figure 13. 95% C.L. mass limits for an unstable neutral heavy lepton L^0 as a function of mass and mixing matrix element $|U_{L^0\ell}|^2$ for B.R.$(L^0 \to \tau W^*) = 100\%$, B.R.$(L^0 \to eW^*) = 100\%$, and B.R.$(L^0 \to \mu W^*) = 100\%$, as indicated.

REFERENCES

1. G.S. Abrams *et al.*, Nucl. Instrum. Methods A **281**, 55 (1989).
2. T. Sjöstrand, Comp. Phys. Comm. **39**, 347 (1986); T. Sjöstrand and M. Bengtsson, Comp. Phys. Comm. **43**, 367 (1987); M. Bengtsson and T. Sjöstrand, Nucl. Phys. B **289**, 810 (1987).
3. G. Marchesini and B.R. Webber, Nucl. Phys. B **238**, 1 (1984); B. R. Webber, Nucl. Phys. B **238**, 492 (1984).
4. T.D. Gottschalk and D. Morris, Nucl. Phys. B **288**, 729 (1987).
5. T.D. Gottschalk and M. P. Shatz, Phys. Lett. B **150**, 451 (1985); T. D. Gottschalk and M. P. Shatz, CALT-68-1172,-1173,-1199 (1985) unpublished; T. D. Gottschalk (private communication).
6. A. Petersen et al., Phys. Rev. D **37**, 1 (1988).
7. G. S. Abrams *et al.*, Phys. Rev. Lett. **63**, 1558 (1989).
8. W. Bartel et al., Z. Phys C **33**, 23 (1986).
9. S. Bethke et al., Z. Phys C **43**, 325 (1989).
10. Ch. Berger et al., Z. Phys C **12**, 297 (1982); M. Althoff et al., Z. Phys C **22**, 307 (1984); D. Bender et al., Phys. Rev. D **31**, 31 (1985); S. Bethke et al., Phys. Lett. B **213**, 235 (1988); W. Braunschweig et al., Z. Phys. C **41**, 359 (1988); W. Braunschweig et al., Phys. Lett. B **214**, 286 (1988); I.H. Park et al., Phys. Rev. Lett. **62**, 1713 (1989); H.J. Behrend et al., DESY Preprint 89-019, to be published in Z. Phys. C; Y.K. Li et al., KEK Preprint 89-34 (1989), Y.K. Li,S. Olsen (private communication).
11. G. S. Abrams *et al.*, SLAC-PUB-5092 (1989).
12. M. Althoff *et al.*, Z. Phys. **C22**, 307 (1984).
13. C. Bacci *et al.*, Phys. Lett. **B86**, 234 (1979); J. L. Siegrist *et al.*, Phys. Rev. **D26**, 969 (1982); B. Niczyporuk *et al.*, Z. Phys. **C9**, 1 (1981); M. S. Alam *et al.*, Phys. Rev. Lett. **49**, 357 (1982); Ch. Berger *et al.*, Phys. Lett. **B95**,

313 (1980); D. Bender *et al.*, Phys. Rev. **D31**, 1 (1985); M. Derrick *et al.*, Phys. Rev. **D34**, 3304 (1986); W. Bartel *et al.*, Z. Phys. **C20**, 187 (1983); H. W. Zheng *et al.*, (AMY), in preparation.

14. Y. Li (AMY), private communication; KEK preprint 89-149.
15. Mark II Collab., D.R. Wood et al., Phys. Rev. D**37**, 3091 (1988).
16. S. Bethke et al., Phys. Lett. B**213**, 235 (1988); S. Bethke et al., Z. Physik C**43**, 325 (1989).
17. S. Komamiya *et al.*, SLAC–PUB–5137 (1989).
18. G. Kramer and B. Lampe, Fortschr. Phys. **37**, 161 (1989).
19. Particle Data Group, M. Aguilar-Benitez et al., Phys. Lett. B**170**, 78 (1986).
20. G. S. Abrams *et al.*, Phys. Rev. Lett. **63**, 2780 (1989).
21. G. S. Abrams *et al.*, Phys. Rev. Lett. **63**, 2447 (1989).
22. T. Sjöstrand, Comput. Phys. Comm. **28**, 229 (1983). In the algorithm, the jet-forming cutoff parameter d_{join} is changed from its default value to $d_{join} = 0.5$ GeV.
23. Lund 6.3 parton shower model, T. Sjöstrand, Comput. Phys. Comm. **39**, 347 (1986); M. Bengtsson and T. Sjöstrand, Nucl. Phys. **B289**, 810 (1987). In the hadronic decay of t and b' quarks, gluon emission effects are incorporated by the parton shower model based on a leading-log-approximation.
24. Lund 6.3 parton shower (Ref. 23) and Lund 6.3 matrix element (T.D. Gottschalk and M.P. Shatz, Phys. Lett. B **150**, 451 (1985)), both with Lund symmetric fragmentation (Ref. 23) and Peterson fragmentation (C. Peterson *et al.*, Phys. Rev. D **27**, 105 (1983)); and Webber 4.1 (G. Marchesini and B.R. Webber, Nucl. Phys. **B238**, 1 (1984); B.R. Webber, Nucl. Phys. **B238**, 492 (1984)).
25. Particle Data Group, Phys. Lett. B **204**, 81 (1988); O. Helene, Nucl. Inst. Meth. **212**, 319 (1983).
26. V. Barger *et al.*, Phys. Rev. D **30**, 947 (1984).
27. W. Hou and R.G. Stuart, Phys. Rev. Lett. **62**, 617 (1989); V. Barger *et al.*, Phys. Rev. Lett. **57**, 1518 (1986).
28. F. Gilman, Comments Nucl. Part. Phys. **16**, 231 (1986).
29. C. K. Jung *et al.*, SLAC–PUB–5136 (1989).
30. P. R. Burchat *et al.*, SLAC–PUB–5172 (1990).
31. M. Swartz *et al.*, SLAC–PUB–5176 (1990).
32. S. Komamiya *et al.*, SLAC–PUB–5175 (1990).
33. E. Soderstrom *et al.*, SLAC–PUB–5192 (1990).
34. T. Barklow *et al.*, SLAC–PUB–5196 (1990).

1989 SLAC SUMMER INSTITUTE LIST OF PARTICIPANTS

Iris Abt
University of Illinois
Dept. of Physics
1110 W. Green St.
Urbana, IL 61801
Bitnet: ABT@SLACVM

Andrew N. Acker
University of Hawaii at Manoa
Dept. of Physics
2505 Correa Road
Honolulu, HI. 96822
Bitnet: ACKER@UHHEP.G

Andre Aeppli
University Zurich
Inst. f. Theoretical Physics
Schonberggasse 9
CH-8006 Zurich
Switzerland
Bitnet: K626230@CZHRZU1A

Farhang Amiri
Weber State College
Physics Dept.
Ogden, UT 84408

Pierre Antilogus
SLAC
Mail Bin 62
P.O. Box 4349
Stanford, CA 94309
Bitnet: ANTILOG@SLACVM

Carlos G. Arroyo
Columbia University
Dept. of Physics
New York, NY 10027

David Aston
SLAC
Mail Bin 62
P.O. Box 4349
Stanford, CA 94309
Bitnet: DYAEB@SLACVM

William B. Atwood
SLAC
Mail Bin 96
P.O. Box 4349
Stanford, CA 94309
Bitnet: ATWOOD@SLACVM

Doris Averill
Indiana University
Dept. of Physics
Bloomington, IN 47405

Jayashree Balakrishna
Washington University
Dept. of Physics
St. Louis, MO 63130

Joseph Ballam
SLAC
Mail Bin 78
P.O. Box 4349
Stanford, CA 94309
Bitnet: JBALLAM@SLACVM

Varouzhan Baluni
SLAC
Mail Bin 81
P.O. Box 4349
Stanford, CA 94309

Philip Baringer
University of Kansas
Dept. of Physics and Astronomy
Lawrence, KA 66045
Bitnet: PSB@CRNLNS

Timothy L. Barklow
SLAC
Mail Bin 61
P.O. Box 4349
Stanford, CA 94309
Bitnet: TIMB@SLACVM

John E. Bartelt
SLAC
Mail Bin 78
P.O. Box 4349
Stanford, CA 94309
Bitnet: BARTELT@SLACVM

Andrew O. Bazarko
Columbia University
Dept. of Physics
New York, NY 10027
Bitnet: BAZARKO@SLACVM

Luis F.L. Bento
SLAC
Mail Bin 81
P.O. Box 4349
Stanford, CA 94309
Bitnet: LBENTO@SLACVM

Micheal Berger
Lawrence Berkeley Lab
University of California
Berkeley, CA. 94720

Maurizio Biasini
SLAC
Mail Bin 96
P.O. Box 4349
Stanford, CA 94309

Timothy L. Bienz
SLAC
Mail Bin 62
P.O. Box 4349
Stanford, CA 94309
Bitnet: BIENZ@SLACVM

Richard Blankenbecler
SLAC
Mail Bin 81
P.O. Box 4349
Stanford, CA 94309
Bitnet: RZBTH@SLACVM

Gerald C. Blazey
University of Rochester
Dept. of Physics and Astronomy
Rochester, NY 14627
Bitnet: Blazey@UORHEP

David Blockus
Indiana University
Department of Physics
Bloomington, IN 47405
Bitnet: DXBRA@SLACVM

Elliott D. Bloom
SLAC
Mail Bin 98
P.O. Box 4349
Stanford, CA 94309
Bitnet: ELLIOTT@SLACVM

Ben B. Brabson
Indiana University
Dept. of Physics
Swain Hall West
Bloomington, IN 47405
Bitnet: BBRABSON@SLACVM

Alan M. Breakstone
University of Hawaii
Dept. of Physics
Honolulu, HI 96822
Bitnet: ALANB@SLACVM

Stanley J. Brodsky
SLAC
Mail Bin 81
P.O. Box 4349
Stanford, CA 94309
Bitnet: SJBTH@SLACVM

Jean-Marie Brom
Centre de Recherches Nuclearies
Division Hautes Energies
B.P. no. 20 CRO
F-67037 Strasbourg Cedex,
France
Bitnet: BROM@CERNVM,
BROM@FRCPN11,
G0SSJB@FRCCSC21

Roger K. Brooks
SLAC
Mail Bin 81
P.O. Box 4349
Stanford, CA 94309
Bitnet: RBROOKS@SLACVM

Thomas Browder
SLAC
Mail Bin 65
P.O. Box 4349
Stanford, CA 94309
Bitnet: BROWDER@SLACVM

Karl Brown
SLAC
Mail Bin 72
P.O. Box 4349
Stanford, CA 94309
Bitnet: KLB@SLACVM

Douglas Bryman
TRIUMF
4004 Wesbrook Mall
Vancouver, B.C.
Canada V6T 2A3
Bitnet: DOUG@TRIUMFCL

Fatin Bulos
SLAC
Mail Bin 98
P.O. Box 4349
Stanford, CA 94309
Bitnet: FYBEC@SLACVM

David L. Burke
SLAC
Mail Bin 61
P.O. Box 4349
Stanford, CA 94309
Bitnet: DAVEB@SLACVM

Toby Burnett
University of Washington
Dept. of Physics FM-15
Seattle, WA 98195
Bitnet: THB@SLACVM

Marta Calvi
University di Milano
Istituto di Fisica
via Celoria 16
I-20133 Milan, Italy
Bitnet:
CALVI@MILANO.INFN.IT

Ronald E. Cassell
SLAC
Mail Bin 65
P.O. Box 4349
Stanford, CA 94309
Bitnet: CASSELL@SLACVM

George B. Chadwick
SLAC
Mail Bin 94
P.O. Box 4349
Stanford, CA 94309
Bitnet: GBC@SLACVM

Michael S. Chanowitz
Lawrence Berkeley Lab
50-A 3115
Berkeley, CA 94720
Bitnet: MSCHAN@LBL

Chia-Chu Chen
Texas A & M University
Dept. of Physics
Center for Theoretical Physics
College Station, TX 77843-4242
Bitnet: CHIACHU@TAMPHYS

Ting-Wai Chiu
Caltech 206-49
Pasadena, CA 91125
Bitnet:
TWC@HAMLET.CALTECH.EDU

Brajesh Chandra Choudhary
University of Delhi
Dept. of Physics and Astrophysics
Delhi 110007, India
Bitnet: BRAJESH@FNALB

James H. Cochran
State University of New York
Dept. of Physics
Stony Brook, NY 11794
Bitnet: COCHRAN@FNAL

Milciades Contreras
Brandeis University
Dept. of Physics
Waltham, MA 02254
Bitnet: FNALD::CONTRERAS

Adrian R. Cooper
SLAC
Mail Bin 81
P.O. Box 4349
Stanford, CA 94309
Bitnet: ADRIAN@SLACVM

Dieter Cords
SLAC
Mail Bin 78
P.O. Box 4349
Stanford, CA 94309
Bitnet: CORDS@SLACVM

David P. Coupal
SLAC
Mail Bin 95
P.O. Box 4349
Stanford, CA 94309
Bitnet: DPC@SLACVM

Ray F. Cowan
Massachusetts Inst. Tech.
Lab. for Nuclear Science
Cambridge, MA 02139
Bitnet: RFC@SLACVM

Paschal Coyle
University of California
SCIPP
Div. of Natural Sciences II
Santa Cruz, CA. 95064
Bitnet: PASCHAL@SLACVM

Nigel C.E. Crosland
University of Oxford
Dept. of Theor. Phys.
1 Keble Road
Oxford OX1 3NP, England
Bitnet:
CERN.VXCRNA::CROSLAND

Graham L.W. Cross
University of Victoria
Dept. of Physics
P.O. Box 1700
Victoria, BC, Canada V8W2Y2
Bitnet: GCROSS@SLACVM

Robert Danen
University of California
Dept. of Physics
Santa Barbara, CA 93106

Mourad Daoudi
University of California
Physics Department
Riverside, CA.
Bitnet: DAOUDI@SLACVM

Sridhara Dasu
SLAC
Mail Bin 62
P.O. Box 4349
Stanford, CA 94309
Bitnet: DASU@SLACVM

Patrizia De Simone
SLAC
Mail Bin 94
P.O. Box 4349
Stanford, CA 94309
Bitnet: PATRIZIA@SLACVM

Herbert DeStaebler
SLAC
Mail Bin 96
P.O. Box 4349
Stanford, CA 94309
Bitnet: HOBEY@SLACVM

Mourad Dhina
Eidgenossische Tech.
Hochsch., Zurich
Inst. of Physics
Honggerberg
CH-8093 Zurich,
Switzerland
Bitnet: DHINA@CZHETH1A

Marco A. Diaz
University of California
SCIPP
Div. of Natural Sciences II
Santa Cruz, CA. 95064

Claudio O. Dib
SLAC
Mail Bin 81
P.O. Box 4349
Stanford, CA 94309
Bitnet: DIB@SLACVM

Lance Dixon
SLAC
Mail Bin 81
P.O. Box 4349
Stanford, CA 94309
Bitnet: LANCE@SLACVM

Jonathan Dorfan
SLAC
Mail Bin 95
P.O. Box 4349
Stanford, CA 94309
Bitnet: JONATHAN@SLACVM

Richard Dubois
University of Victoria
Dept. of Physics
P.O. Box 1700
Victoria, BC, Canada V8W2Y2
Bitnet: RICHARD@SLACVM

Jean E. Duboscq
University of California
Dept. of Physics
Santa Barbara, CA 93106
Bitnet: DUBOSCQ@SBHEP

William Dunwoodie
SLAC
Mail Bin 62
P.O. Box 4349
Stanford, CA 94309
Bitnet: WMD@SLACVM

Stan D. Ecklund
SLAC
Mail Bin 55
P.O. Box 4349
Stanford, CA 94309
Bitnet: SDE@SLACVM

Helen Edwards
SSC
2550 Beckleymeade Ave.
Suite 260
Dallas, TX 75257

Yehudah Eisenberg
SLAC
Mail Bin 95
P.O. Box 4349
Stanford, CA 94309
Bitnet: EISENBER@SLACVM

Robert Elia
SLAC
Mail Bin 78
P.O. Box 4349
Stanford, CA 94309
Bitnet: ROB@SLACVM

Keith Ellis
Fermilab
MS 106
P.O. Box 500
Batavia, IL 60510
Bitnet: ELLIS@FNAL

Roger A. Erickson
SLAC
Mail Bin 55
P.O. Box 4349
Stanford, CA 94309
Bitnet: ROGER@SLACVM

Rahim Esmailzadeh
SLAC
Mail Bin 81
P.O. Box 4349
Stanford, CA 94309
Bitnet: RAHIM@SLACVM

Gary Feldman
SLAC
Mail Bin 78
P.O. Box 4349
Stanford, CA 94309
Bitnet: GARY@SLACVM

R. Clive Field
SLAC
Mail Bin 78
P.O. Box 4349
Stanford, CA 94309
Bitnet: SARGON@SLACVM

Carlos Figueroa
U.C. Santa Cruz
Cowell Number 838
Santa Cruz, CA. 95064

Carrie S. Fordham
SLAC
Mail Bin 95
P.O. Box 4349
Stanford, CA 94309
Bitnet: CARRIE@SLACVM

Ray Frey
University of Michigan
Physics Department
Ann Arbor, MI. 48109

Dietrich R. Freytag
SLAC
Mail Bin 94
P.O. Box 4349
Stanford, CA 94309
Bitnet: DRF@SLACVM

David Fryberger
SLAC
Mail Bin 20
P.O. Box 4349
Stanford, CA 94309
Bitnet: DAFRA@SLACVM

Donald H. Fujino
SLAC
Mail Bin 78
P.O. Box 4349
Stanford, CA 94309
Bitnet: DON@SLACVM

Pauline Gagnon
University of California
SCIPP
Div. of Natural Sciences II
Santa Cruz, CA. 95064
Bitnet: PAULINE @
SLACTBF

Kock-Kiam Gan
SLAC
Mail Bin 61
P.O. Box 4349
Stanford, CA 94309
Bitnet: KKG@SLACVM

Robert W. Gardner
University of Notre Dame
Dept. of Physics
Notre Dame, IN 46545
Bitnet: ROB@FNAL

Corrado Gatto
University of California
SCIPP
Div. of Natural Sciences II
Santa Cruz, CA. 95064
Bitnet: CARRADO@SLACVM

Roger A. Gearhart
SLAC
Mail Bin 20
P.O. Box 4349
Stanford, CA 94309
Bitnet: GEARHART@SLACVM

Earl Gero
University of Michigan
Dept. of Physics
Ann Arbor, MI 48109

Duncan Gibaut
Carnegie Mellon University
Dept. of Physics
Pittsburgh, PA 15213
Bitnet: GIBAUT@FNAL

Fred Gilman
SLAC
Mail Bin 81
P.O. Box 4349
Stanford, CA 94309
Bitnet: GILMAN@SLACVM

Thomas Glanzman
SLAC
Mail Bin 78
P.O. Box 4349
Stanford, CA 94309
Bitnet: DRAGON@SLACVM

Gary L. Godfrey
SLAC
Mail Bin 98
P.O. Box 4349
Stanford, CA 94309
Bitnet: GLGCB@SLACVM

Concepcion Gonzalez-Garcia
University de Valencia
Dept. de Fisica
Avda Dr. Moliner, 50
E-46100 Burjassot,
Valencia, Spain

Gunter Grindhammer
SLAC
Mail Bin 61
P.O. Box 4349
Stanford, CA 94309
Bitnet: GGG@SLACVM

Dave Gurd
University of Victoria
Dept. of Physics
P.O. Box 1700
Victoria, BC, Canada V8W2Y2
Bitnet: GURD@SLACSLD

Gregory Hallewell
SLAC
Mail Bin 62
P.O. Box 4349
Stanford, CA 94309
Bitnet: GREGH@SLACVM

Gail G. Hanson
SLAC
Mail Bin 78
P.O. Box 4349
Stanford, CA 94309
Bitnet: GAIL@SLACVM

Jens Harjes
DESY - F14
Notkestrasse 85
D-2000 Hamburg 52
West Germany
Bitnet: F14HAR@DHHDESY3

Katsuo Hasegawa
Tohoku University
Dept. of Physics
Sendai-shi, Miyagi 980,
Japan
Bitnet: HASEGAWA@SLACVM

Christopher Hearty
Lawrence Berkeley Lab
MS 50A - 2160
Berkeley, CA 94720
Bitnet: HEARTY@SLACVM

Ulrich Heintz
State University of New York
Dept. of Physics
Stony Brook, NY 11794
Bitnet: ULI@CUSB

Ralf Hempfling
University of California
SCIPP
Santa Cruz, CA 95064

Timothy L. Hessing
Texas A and M University
Dept. of Physics
College Station, TX 77843
Bitnet: HESSING@FNALD

Harold H. Hibbert
SLAC
Mail Bin 63
P.O. Box 4349
Stanford, CA 94309
Bitnet: HIBBERT@SLACVM

Mike D. Hildreth
SLAC
Mail Bin 61
P.O. Box 4349
Stanford, CA 94309
Bitnet: MIKEH@SLACVM

Paul Hill
DESY - Group F22
Notkestrasse 85
D-2000 Hamburg 52
West Germany
Bitnet: H01HIL@DHHDESY3

Thomas M. Himel
SLAC
Mail Bin 95
P.O. Box 4349
Stanford, CA 94309
Bitnet: TMH@SLACVM

Ian Hinchliffe
Lawrence Berkeley Lab
MS 3115
Berkeley, CA 94720
Bitnet: THEORY@LBL

Dean A. Hinshaw
University of Colorado
Dept. of Physics and Astrophysics
Boulder, CO 80309
Bitnet: DAH@SLACVM

John Hissong
Yale University
Dept. of Physics
New Haven, CT 06511
Bitnet: Hissong@FNAL

David Hochron
SLAC
Mail Bin 61
P.O. Box 4349
Stanford, CA 94309
Bitnet: DAVID@SLACVM

Robert Hollebeek
University of Pennsylvania
Dept. of Physics
Philadelphia, PA 19104
Bitnet: BOBH@PENNDRLS

Alan Honma
University of Victoria
Dept. of Physics
P.O. Box 1700
Victoria, BC, Canada V8W2Y2
Bitnet: HONMA@SLACVM

Alexander Hsieh
SLAC
Mail Bin 81
P.O. Box 4349
Stanford, CA 94309

Emlyn Hughes
SLAC
Mail Bin 96
P.O. Box 4349
Stanford, CA 94309
Bitnet: EMLYN@SLACVM

James Hylen
Johns Hopkins University
Dept. of Physics
Baltimore, MD 21218
Bitnet: JZH@SLACVM

Walter Innes
SLAC
Mail Bin 61
P.O. Box 4349
Stanford, CA 94309
Bitnet: WALT@SLACVM

George Irwin
SLAC
Mail Bin 63
P.O. Box 4349
Stanford, CA 94309
Bitnet: GMIEG@SLACVM

Jeffrey Isaacson
Massachusetts Inst. Tech.
Center for Theoretical Physics
Room 6-411A
Cambridge, MA 02139
Bitnet: JAI@MITLNS

Dieter Issler
SLAC
Mail Bin 81
P.O. Box 4349
Stanford, CA 94309
Bitnet: ISSLER@SLACVM

Bob Jacobsen
SLAC
Mail Bin 95
P.O. Box 4349
Stanford, CA 94309
Bitnet: JACOBSEN@SLACVM

Alexander M. Jahn
Max Planck Inst. fur Phys.
Fohringer Ring 6
Postfach 40 12 12
D-8000 Munich 40
West Germany
Bitnet: JAHN@VXCERN.CERN

John A. Jaros
SLAC
Mail Bin 61
P.O. Box 4349
Stanford, CA 94309
Bitnet: JOHN@SLACVM

Colin Jessop
Harvard University
Dept. of Physics
Cambridge, MA 02138
Bitnet: JESSOP@HUHEPL OR
JESSOP@HARVHEP

Chang-Kee Jung
SLAC
Mail Bin 95
P.O. Box 4349
Stanford, CA 94309
Bitnet: ALPINIST@SLACVM

Tom Junk
SLAC
Mail Bin 65
P.O. Box 4349
Stanford, CA 94309
Bitnet: TRJ@SLACVM

Uri Karshon
SLAC
Mail Bin 65
P.O. Box 4349
Stanford, CA 94309
Bitnet: URI@SLACVM

Russel Kauffman
SLAC
Mail Bin 81
P.O. Box 4349
Stanford, CA 94309
Bitnet: KAUFFMAN@SLACVM

Hideaki Kawahara
SLAC
Mail Bin 62
P.O. Box 4349
Stanford, CA 94309
Bitnet: KAWAHARA@SLACVM

Dallas Kennedy
SLAC
Mail Bin 78
P.O. Box 4349
Stanford, CA 94309
Bitnet: DON@SLACVM

Joel Kent
University of California
SCIPP
Div. of Natural Sciences II
Santa Cruz, CA. 95064
Bitnet: JKENT@SLACVM

Dong-Hee Kim
Syracuse University
201 Physics Building
Syracuse, NY 13244
Bitnet: KIM@SUHEP

Peter Chong-Ho Kim
SLAC
Mail Bin 65
P.O. Box 4349
Stanford, CA 94309
Bitnet: PKIM@SLACVM

Mary King
University of California
SCIPP
Div. of Natural Sciences II
Santa Cruz, CA. 95064
Bitnet: MARYK@SLACVM

Ross King
SLAC
Mail Bin 78
P.O. Box 4349
Stanford, CA 94309
Bitnet: ROSSKING@SLACVM

Spencer Klein
Boston University
Dept. of Physics
590 Commonwealth Ave.
Boston, MA 02215
Bitnet: SPENCER@BUPHY

Pyungwon Ko
Enrico Fermi Inst.
University of Chicago
5640 S. Ellis Ave.
Chicago, IL 60637

Herman Kolanoski
University of Dortmund
Inst. fur Physik
Otto Hahn Str.
Postfact 500 500
D-4600 Dortmund 50
West Germany
Bitnet: UPH026 at
DDOHR211

Sachio Komamiya
SLAC
Mail Bin 95
P.O. Box 4349
Stanford, CA 94309
Bitnet: SACHIO@SLACVM

Wayne A. Koska
SLAC
Mail Bin 78
P.O. Box 4349
Stanford, CA 94309
Bitnet: KOSKA@SLACVM

Lee Anne Kowalski
SLAC
Mail Bin 61
P.O. Box 4349
Stanford, CA 94309
Bitnet: ANNE@SLACVM

Witold Kozanecki
SLAC
Mail Bin 95
P.O. Box 4349
Stanford, CA 94309
Bitnet: WITOLD@SLACVM

Frederic Kral
Lawrence Berkeley Lab
MS 50A-2160
University of California
Berkeley, CA 94720

Robert S. Kroeger
University of Tennessee
401 Nielsen Physics Bldg.
Knoxville, TN 37996-1200
Bitnet: RKROEGER@SLACVM

Paul F. Kunz
SLAC
Mail Bin 62
P.O. Box 4349
Stanford, CA 94309
Bitnet: PFKEB@SLACVM

Youngjoon Kwon
SLAC
Mail Bin 62
P.O. Box 4349
Stanford, CA 94309
Bitnet: YKWON@SLACVM

Waikwok Kwong
Enrico Fermi Inst.
University of Chicago
5640 S. Ellis Ave.
Chicago, IL 60637
Bitnet: UCHEP::KWONG

Jonathan Labs
SLAC
Mail Bin 65
P.O. Box 4349
Stanford, CA 94309
Bitnet: JONLABS@SLACVM

Karol Lang
SLAC
Mail Bin 63
P.O. Box 4349
Stanford, CA 94309
Bitnet: LANG@SLACVM

Andrew Lankford
SLAC
Mail Bin 95
P.O. Box 4349
Stanford, CA 94309
Bitnet: LANKFORD@SLACVM

Francois LeDiberder
SLAC
Mail Bin 95
P.O. Box 4349
Stanford, CA 94309
Bitnet: DIBERDER@SLACVM

David W.G.S. Leith
SLAC
Mail Bin 62
P.O. Box 4349
Stanford, CA 94309
Bitnet: LEITH@SLACVM

Michael Levi
Lawrence Berkeley Lab
MS 50A-2160
Berkeley, CA 94720
Bitnet: LEVI@SLACVM

David C. Lewellen
SLAC
Mail Bin 81
P.O. Box 4349
Stanford, CA 94309
Bitnet: DCL@SLACVM

Willis Lin
University of California
Physics Department
Riverside, CA. 92521
Bitnet: LIN-WT@SLACPHYS

Bill Lockman
University of California
SCIPP
Div. of Natural Sciences II
Santa Cruz, CA. 95064
Bitnet: BILLY@SLACVM

Gabriel Lopes-Cardoso
University of Pennsylvania
Dept. of Physics
209 S. 33rd St.
Philadelphia, PA 19104-6396
Bitnet: MOLERA@PENNDRLS

Jan Louis
SLAC
Mail Bin 81
P.O. Box 4349
Stanford, CA 94309
Bitnet: LOUIS@SLACVM

Hung Jung Lu
SLAC
Mail Bin 81
P.O. Box 4349
Stanford, CA 94309
Bitnet: HLU@SLACVM

Vera Luth
SLAC
Mail Bin 95
P.O. Box 4349
Stanford, CA 94309
Bitnet: VGL@SLACVM

Doug A. MacIntire
University of California
Div. of Natural Sciences
Santa Cruz, CA 95064
Bitnet: DMACINT@UCSCC

Leon Madansky
Johns Hopkins University
Dept. of Physics
34th and Charles St.
Baltimore, MD 21218

Christophe Magneville
DPhPE/SEPh CEN Saclay
F-91191 Gif-sur-Yvette
France
Bitnet: CMV@FRSAC12 or
@CERNVM

Walid A. Majid
SLAC
Mail Bin 71
P.O. Box 4349
Stanford, CA 94309
Bitnet: WALID@SLACVM

Gianpiero Mancinelli
SLAC
Mail Bin 96
P.O. Box 4349
Stanford, CA 94309

Bill Marciano
Brookhaven National Lab
Building 510
Upton, New York 11973

Thomas Markiewicz
SLAC
Mail Bin 96
P.O. Box 4349
Stanford, CA 94309
Bitnet: TWMARK@SLACVM

Stuart Marshall
University of California
Dept. of Physics
Santa Barbara, CA 93106

Helmut Marsiske
SLAC
Mail Bin 98
P.O. Box 4349
Stanford, CA 94309
Bitnet: HMACB@SLACVM

Jose L. Martinez
University of Cincinnati
Dept. of Physics
Cincinnati, OH 45221
Bitnet: JLM@SLACVM

Mara Martini
Istituto Naz. Fiz. Nucleare
via Paradiso 12
I-44100 Ferrara, Italy
Bitnet: VAXFE::MARTINI

Hiroaki Masuda
SLAC
Mail Bin 96
P.O. Box 4349
Stanford, CA 94309
Bitnet: MASUDA@SLACVM

Laurent Mathys
University of California
Dept. of Physics
Santa Barbara, CA 93106
Bitnet: MATHYS@SLACVM

Tom S. Mattison
SLAC
Mail Bin 95
P.O. Box 4349
Stanford, CA 94309
Bitnet: MATTISON@SLACVM

John McGowan
University of Illinois
Dept. of Physics
1110 W. Green St.
Urbana, IL 61801

Stephen J. McMahon
Imperial Coll. Sci. Tech.
Blackett Lab
Prince Consort Road
London, SW7 2AZ, England
Bitnet: MACMAHON@CERNVM

Robert Messner
SLAC
Mail Bin 94
P.O. Box 4349
Stanford, CA 94309
Bitnet: ROM@SLACVM

Robert Michaels
Max Planck Inst. fur
Kernphysik
Saupfercheckweg 1
Postfach 103 980
6900 Heidelberg
West Germany
Bitnet: ROM@CRVXP173

Michiko Miyamoto
Kobe College
11-2, 1-chome, Yamato,
Nakasuji
Takarazuka City
Hyogo Prefecture
Japan 665

Kenneth C. Moffeit
SLAC
Mail Bin 78
P.O. Box 4349
Stanford, CA 94309
Bitnet: MOFFEIT@SLACVM

Patrick Mooney
Michigan State University
Dept. of Physics
East Lansing, MI 48824
Bitnet: MOONEY@FNAL

Mauro Morandin
INFN, Padova
via Marzolo 8
I-35131 Padova, Italy
Bitnet:
MORANDIN@PD.INFN.IT

Carlos Morgado
University of Bristol
H. H. Wills Physics Lab
Royal Fort, Tyndall Ave.
Bristol BS8 1TL, England
Bitnet:
MORGADO@UK.AC.RUTHER-
FORDVAX@(JANET)

David Robert Muller
SLAC
Mail Bin 62
P.O. Box 4349
Stanford, CA 94309
Bitnet: MULLER@SLACVM

Charles T. Munger
SLAC
Mail Bin 61
P.O. Box 4349
Stanford, CA 94309
Bitnet: CHARLES@SLACVM

Joe Murray
SLAC
Mail Bin 20
P.O. Box 4349
Stanford, CA 94309
Bitnet: JJMRA@SLACVM

William N. Murray
Indiana University
Dept. of Physics
Bloomington, IN 47405
Bitnet: MURRAY@SLACVM

Tadashi Nagamine
SLAC
Mail Bin 62
P.O. Box 4349
Stanford, CA 94309
Bitnet: NAGAMINE@SLACVM

Leslie F. Nakae
Brandeis University
Dept. of Physics
Waltham, MA 02254
Bitnet: LES@FNALD
Meenakshi Narain
State University of New York
Dept. of Physics
Stony Brook, NY 11794
Bitnet: MEENA@CUSB

Patrick Nedelec
College de France
Lab. de Physique Corpusculaire
11 Place Marcelin-Berthelot
F-75231 Paris CEDEX 05,
France
Bitnet: NEDELEC@CERNVM

Johnny S.T. Ng
Harvard University
Dept. of Physics
Cambridge, MA 02138
Bitnet: JNG@FNALD

Yosef Nir
SLAC
Mail Bin 81
P.O. Box 4349
Stanford, CA 94309
Bitnet: NIR@SLACVM

Sergio F. Novaes
Lawrence Berkeley Lab
50A-3115
University of California
Berkeley, CA 94720
Bitnet: NOVAES@LBL

Dietmar Nowotny
Max Planck Inst. fur Kernphysik
Saupfercheckweg 1
Postfach 103 980
6900 Heidelberg,
West Germany
Bitnet: NWY @ DHDMPI5U

H. Pierre Noyes
SLAC
Mail Bin 81
P.O. Box 4349
Stanford, CA 94309
Bitnet: NOYES@SLACVM

Mirko Nussbaum
University of Cincinnati
Dept. of Physics
Cincinnati, OH 45221
Bitnet: MMN@SLACVM

Stephen C. O'Day
University of Maryland
Dept. of Physics and Astronomy
College Park, MD 20742
Bitnet: FNAL::ODAY

Kathryn O'Shaughnessy
SLAC
Mail Bin 78
P.O. Box 4349
Stanford, CA 94309
Bitnet: KATHYO@SLACVM

Heungmin Oh
University of California
Physics Department
Riverside, CA 92521
Bitnet: OH@SLACVM

Trivan Pal
University of Berne
Sidlerstrasse 5
CH-3012 Berne
Switzerland
Bitnet: TRIVAN@CERNVM

Wolfgang K.H. Panofsky
SLAC
Mail Bin 76
P.O. Box 4349
Stanford, CA 94309
Bitnet: BEERBOHM@SLACVM

James T. Pantaleone
University of California
Physics Dept.
Riverside, CA 92521
Bitnet: PANTALEO@UCRPHYS

Bernd Panzer
CERN - EP Division
CH-1211 Geneva 23
Switzerland

Vittorio Paolone
University of California
Dept. of Physics
Davis, CA 95616
Bitnet:
FNAL:: V3223E653

Sherwood Parker
University of Hawaii
Dept. of Physics
Honolulu, HI 96822
Bitnet: SHER@SLACVM

Larry Parrish
University of Washington
Dept. of Physics
Seattle, WA 98195
Bitnet: PARRISH@SLACVM

Tomas Pavel
SLAC
Mail Bin 62
P.O. Box 4349
Stanford, CA 94309
Bitnet: PAVEL@SLACVM

Martin L. Perl
SLAC
Mail Bin 61
P.O. Box 4349
Stanford, CA 94309
Bitnet: MARTIN@SLACVM

Ida M. Peruzzi
INFN, Frascati
C.P. 13
I-00044 Frascati, Rome
Italy
Bitnet: IMP@SLACVM

Luca Pesando
INFN, Turin
Via Pietro Giuria 1
I-10125 Turin, Italy
Bitnet:
PESANDO@VAXTO.INFN.IT

Michael Peskin
SLAC
Mail Bin 81
P.O. Box 4349
Stanford, CA 94309
Bitnet: MPESKIN@SLACVM

Mina Petradza
SLAC
Mail Bin 78
P.O. Box 4349
Stanford, CA 94309
Bitnet: ANIM@SLACVM

Bo Pi
Michigan State University
Dept. of Physics
East Lansing, MI 48824
Bitnet: PI@MSUHEP

Marcello Piccolo
INFN, Frascati
C.P. 13
I-00044 Frascati, Rome
Italy
Bitnet: MXP@SLACVM,
MXP@IRMLNF

Andrew C. Pinsent
University of Oxford
Dept. of Theor. Phys.
1 Keble Road
Oxford OX1 3NP, England
Bitnet:
PINSENT@CERN.VXCRNA

Dale Pitman
SLAC
Mail Bin 65
P.O. Box 4349
Stanford, CA 94309
Bitnet: PITMAN@SLACVM

Rainer Pitthan
SLAC
Mail Bin 96
P.O. Box 4349
Stanford, CA 94309
Bitnet: RAINER@SLACVM

Richard Plano
Rutgers University
Dept. of Physics
New Brunswick, NJ 08903
Bitnet: PLANO@SLACVM

Charles Prescott
SLAC
Mail Bin 80
P.O. Box 4349
Stanford, CA 94309
Bitnet: PRESCOTT@SLACVM

Greg Punkar
University of California
Dept. of Physics
Santa Barbara, CA 93106
Bitnet: PUNKAR@SLACVM

Helen Quinn
SLAC
Mail Bin 81
P.O. Box 4349
Stanford, CA 94309
Bitnet: QUINN@SLACVM

Kenneth J. Ragan
University of Pennsylvania
Dept. of Physics
Philadelphia, PA 19104
Bitnet: RAGAN@PENNDRLS

Blair Ratcliff
SLAC
Mail Bin 62
P.O. Box 4349
Stanford, CA 94309
Bitnet: BLAIR@SLACVM

Stefania Ricciardi
SLAC
Mail Bin 96
P.O. Box 4349
Stanford, CA 94309

Jeffrey D. Richman
University of California
Dept. of Physics
Santa Barbara, CA 93106
Bitnet: RICHMAN@SLACVM

Burton Richter
SLAC
Mail Bin 80
P.O. Box 4349
Stanford, CA 94309
Bitnet: RICHTER@SLACVM

David M. Ritson
SLAC
Mail Bin 12
P.O. Box 4349
Stanford, CA 94309
Bitnet: DMR@SLACVM

Leon Rochester
SLAC
Mail Bin 96
P.O. Box 4349
Stanford, CA 94309
Bitnet: LSREA@SLACVM

Teresa Rodrigo
CERN
EP-Division
CH-1211 Geneva 23,
Switzerland
Bitnet: RODRIGO@CERNVM

Timothy F. Rohaly
University of Pennsylvania
Dept. of Physics
Philadelphia, PA 19104
Bitnet: ROHALY@FNCCF

Rogerio Rosenfeld
University of Chicago
Dept. of Physics
Chicago, IL 60637
Bitnet: UCHEP::ROSENFELD

Ronald D. Ruth
SLAC
Mail Bin 26
P.O. Box 4349
Stanford, CA 94309
Bitnet: RRUTH@SLACVM

Pamela H. Sandler
University of Wisconsin
Dept. of Physics
1150 University Ave.
Madison, WI 53706
Bitnet: SANDLER@WISCPSLB

Emanuele Santovetti
SLAC
Mail Bin 96
P.O. Box 4349
Stanford, CA 94309

Victor Scarpine
University of Illinois
Dept. of Physics
1110 W. Green St.
Urbana, IL 61801
Bitnet: SCARPINE@FNAL

Rafe H. Schindler
SLAC
Mail Bin 65
P.O. Box 4349
Stanford, CA 94309
Bitnet: RAFE@SLACVM

David M. Schmidt
University of California
Dept. of Physics
Santa Barbara, CA 93106
Bitnet: SCHMIDT@SBHEP

Ivan A. Schmidt
SLAC
Mail Bin 81
P.O. Box 4349
Stanford, CA 94309
Bitnet: SCHMIDT@SLACVM

Daniel Schroeder
SLAC
Mail Bin 81
P.O. Box 4349
Stanford, CA 94309
Bitnet: DVS@SLACVM

David C. Schultz
SLAC
Mail Bin 62
P.O. Box 4349
Stanford, CA 94309
Bitnet: DCS@SLACVM

Kunnat J. Sebastian
University of Lowell
Dept. of Physics
Lowell, MA 01854

Michael H. Shaevitz
Columbia University
Dept. of Physics
New York, NY 10027
Bitnet: SHAEVITZ@SLACVM

Marjorie D. Shapiro
Harvard University
Dept. of Physics
Cambridge, MA 02138
Bitnet: MDSHAPIRO@HUHEPL

Stephen L. Shapiro
SLAC
Mail Bin 62
P.O. Box 4349
Stanford, CA 94309
Bitnet: SHAPIRO@SLACVM

Rick L. Shypit
University of British Columbia
Dept. of Physics
6224 Agriculture Rd.
Vancouver, BC, Canada V6T2A6
Bitnet: SHYPIT@SLACVM

Hugues Sicotte
University of British Columbia
Dept. of Physics
6224 Agriculture Rd.
Vancouver, BC, Canada V6T2A6
Bitnet: SICOTTE@SLACVM

Robert Siemann
Cornell University
Newman Laboratory
Ithaca, NY 14853
Bitnet: SIEMANN@CRNLNS

Constantine Simopoulos
SLAC
Mail Bin 62
P.O. Box 4349
Stanford, CA 94309
Bitnet: CJS@SLACVM

Robert L. Singleton
SLAC
Mail Bin 81
P.O. Box 4349
Stanford, CA 94309
Bitnet: BOBS@SLACVM

Sarah J.P. Smith
Oxford University
Nuclear Physics Lab
Keble Road
Oxford OX1 3RH, England
Bitnet:
MITHS@UK.AC.OX.PH.VI

Stefan Soldner-Rembold
Max Planck Inst. fur Phys.
Fohringer Ring 6
Postfach 40 12 12
D-8000 Munich 40
West Germany
Bitnet: SSR@FNCCF

Jacob Sonnenschein
SLAC
Mail Bin 81
P.O. Box 4349
Stanford, CA 94309
Bitnet: COBI@SLACVM

Martin F. Spahn
Lawrence Berkeley Lab
50B-5239
University of California
Berkeley, CA 94720
Bitnet: SPAHN@LBL

Jeff Spalding
Fermilab, MS 222
P. O. Box 500
Batavia, IL 60510
Bitnet: SPALDING@FNAL

Daniel Sperka
University of California
Dept. of Physics
Santa Barbara, CA 93106
Bitnet: SPERKA@VOODOO

Florent Staley
Lab de Phys. des Particules
B.P. 110
F-74941 Annecy-le-Vieux
France
Bitnet: STALEY@CERNVM

Ransom W. Stephens
University of California
Dept. of Physics
Santa Barbara, CA 93106
Bitnet:
STEPHENS@SLACTBF

Claudia J. Stubenrauch
CERN
EP-Division
CH-1211 Geneva 23
Switzerland
Bitnet: STUBENRA@CERNVM

Dong Su
Rutherford and Appleton Labs
R1/1-53
Chilton, Didcot, Oxon OX11.02X
England
Bitnet: SUDONG@SLACSLD

Akira Sugiyama
SLAC
Mail Bin 96
P.O. Box 4349
Stanford, CA 94309
Bitnet: SUGIYAMA@SLACVM

Michael Sullivan
University of California
Physics Department
Santa Barbara, CA. 93106

Morris Swartz
SLAC
Mail Bin 78
P.O. Box 4349
Stanford, CA 94309
Bitnet: MORRIS@SLACVM

Anthony Szumilo
University of Washington
Dept. of Physics
Seattle, WA 98195
Bitnet: SZUMILO@SLACSLD

Andrew C. Tang
SLAC
Mail Bin 81
P.O. Box 4349
Stanford, CA 94309
Bitnet: ATANG@SLACVM

Gary Taylor
Imperial Coll. Sci. Tech.
Blackett Lab
Prince Consort Road
London, SW7 2AZ, England
Bitnet: TAYLORG@CERNVM

Richard Taylor
SLAC
Mail Bin 96
P.O. Box 4349
Stanford, CA 94309
Bitnet: RETAYLOR@SLACVM

William J. Thompson
State University of New York
Dept. of Physics
Stony Brook, NY 11794
Bitnet: JOEY@FNAL

Larus Thorlacius
SLAC
Mail Bin 81
P.O. Box 4349
Stanford, CA 94309
Bitnet: LARUS@SLACVM

Maury Tigner
Cornell University
Newman Laboratory
Ithaca, NY 14853-5001

Nobukazu Toge
SLAC
Mail Bin 62
P.O. Box 4349
Stanford, CA 94309
Bitnet: TOGE@SLACVM

Walter Toki
SLAC
Mail Bin 65
P.O. Box 4349
Stanford, CA 94309
Bitnet: TOKI@SLACVM

Donatella Torretta
Fermilab
E687-MS221
P.O. Box 500
Batavia, IL 60510
Bitnet: TORRETTA@FNAL

Yung-Su (Paul) Tsai
SLAC
Mail Bin 81
P.O. Box 4349
Stanford, CA 94309
Bitnet: YSTTH@SLACVM

Marc G. Turcotte
University of Victoria
Dept. of Physics
P.O. Box 1700
Victoria, BC, Canada V8W2Y2
Bitnet: MARC@SLACVM

Fumihiko Ukegawa
University of Tsukuba
Inst. of Physics
Sakura-mura
Niihari-gun Ibaraki-ken
305, Japan
Bitnet: FU@ANLHEP

Shoji Uno
KEK National Lab for High
Energy Physics
Department of Physics
Oho, Tsukuba-shi
Ibaraki-ken 305, Japan
Bitnet: TSJU@JPNKEKTR

Tracy Usher
SLAC
Mail Bin 96
P.O. Box 4349
Stanford, CA 94309
Bitnet: TUSHER@SLACVM

Jaroslav Va'vra
SLAC
Mail Bin 62
P.O. Box 4349
Stanford, CA 94309
Bitnet: JJV@SLACVM

Maarten W. Van de Guchte
Nat. Inst. Nucl., High
Energy Phys.
P. O. Box 41882
NL-1009 DB Amsterdam,
The Netherlands
Bitnet: VANDEGUC@CERNVM

Richard J. Van Kooten
SLAC
Mail Bin 95
P.O. Box 4349
Stanford, CA 94309
Bitnet: RICKV@SLACVM

Helene G.J. Veltman
Lawrence Berkeley Lab
University of California
Berkeley, CA 94720
Bitnet: VELTMAN@LBL

Marco Verzocchi
Universita degli Studi
"La Sapienza"
Via Spinoza 49/c
I-00137 Roma
Italy
Bitnet: VAXROM::SLUSER

David L. Wagner
University of California
Dept. of Physics
Los Angeles, CA 90024
Bitnet: WAGNER@BNLVMA

Christoph Wahl
University Freiburg
Fakultat fur Physik
Hermann-Herder Strasse 3
D-7800 Freiburg
West Germany
Bitnet: WAHL@CERNVM

Tony Waite
University of Victoria
Dept. of Physics
P.O. Box 1700
Victoria, BC, Canada V8W2Y2
2Y2
Bitnet: APW@SLACVM

Min-zu Wang
University of Iowa
Dept. of Physics & Astronomy
Iowa City, IO 52242
Bitnet: MINZU@SLACVM

Yao Wang
University of California
Physics Department
Santa Barbara, CA. 93106

Bennie F.L. Ward
University of Tennessee
Dept. of Physics
Knoxville, TN 37996
Bitnet: BFLW@SLACVM

Steven R. Wasserbaech
SLAC
Mail Bin 65
P.O. Box 4349
Stanford, CA 94309
Bitnet: SRW@SLACVM

Achim W. Weidemann
University of Tennessee
Dept. of Physics
Knoxville, TN 37996
Bitnet: ACHIM@SLACVM

William C. Wester
Lawrence Berkeley Lab
MS 50A-2129
1 Cyclotron Rd.
Berkeley, CA 94720
Bitnet:
WESTER@LBL

Judd Wilcox
University of California
Dept. of Physics
Davis, CA 95616
Bitnet: WILCOX@FNAL

Stephen H. Williams
SLAC
Mail Bin 60
P.O. Box 4349
Stanford, CA 94309
Bitnet: STEVE@SLACVM

Brian L. Winer
Lawrence Berkeley Lab
1 Cyclotron Road
Berkeley, CA 94720
Bitnet: WINER@LBL

Stan Wojcicki
Stanford University
Physics Department
Stanford, CA 94309
Bitnet: SGWEG@SLACVM

Michael Woods
SLAC
Mail Bin 78
P.O. Box 4349
Stanford, CA 94309
Bitnet: MWOODS@SLACVM

Jose Wudka
University of California
Dept. of Physics
Davis, CA 95616
Bitnet: WUDKA@UCDHEP

Jeffery L. Wyss
INFN, Padova
via Marzolo 8
I-35100 Padova
Italy
Bitnet: SLD::WYSS,
VAXFPD::WYSS

Hitoshi Yamamoto
Enrico Fermi Institute
University of Chicago
5640 S. Ellis Ave.
Chicago, IL 60637
Bitnet: HITOSHI@FNAL

Steve Yellin
University of California
Dept. of Physics
Santa Barbara, CA 93106
Bitnet: SJYP09@SLACTWGM

George P. Yost
University of California
421 LeConte Hall
Dept. of Physics
Berkeley, CA 94720

Charlie Young
SLAC
Mail Bin 96
P.O. Box 4349
Stanford, CA 94309
Bitnet: YOUNG@SLACVM

Michael V. Yurko
Indiana University
Dept. of Physics
Bloomington, IN 47405
Bitnet: MYURKO@SLACVM

Geordie Zapalac
SLAC
Mail Bin 98
P.O. Box 4349
Stanford, CA 94309
Bitnet: GEORDIE@SLACVM

Enrique Zas
University of Wisconsin
Dept. of Physics
1150 University Avenue
Madison, WI 53706
Bitnet: ZAS@WISCPHEN

Richard Zdarko
SLAC
Mail Bin 36
P.O. Box 4349
Stanford, CA 94309
Bitnet: RWZP06@SLACMAC

THE SLAC SUMMER INSTITUTES ON PARTICLE PHYSICS

1973 - 1988

1973 DEEP INELASTIC ELECTROPRODUCTION

"Hadron Production in Deep Inelastic Processes"	J. D. Bjorken
"Hadron Production in the Collision of Virtual Photons with Nucleons – an Experimental Review"	M. Perl
"Phenomenological Analysis"	F. J. Gilman
"Asymptotic Behavior and Short Distance Singularities"	Y. Frishman

WEAK CURRENTS AND INTERACTIONS

"Raw Notes of Lectures on Current Algebra and PCAC"	S. Drell
"Experimental Phenomenology"	M. Schwartz S. Wojcicki
"Gauge-Theories of Weak and Electromagnetic Interaction"	T. Appelquist
"How to Transform Current Quarks to Constituent Quarks and Try to Predict Hadron Decays"	J. Primack M. Kugler

1974 THE STRONG INTERACTIONS

"Diffractive Processes"	D.W.G.S. Leith
"Amplitude Structure in Two- and Quasi-Two-Body Processes"	M. Davier
"Resonances: Experimental Review"	R.J. Cashmore
"Resonances: A Quark View of Hadron Spectroscopy and Transitions"	F. J. Gilman
"Lectures on Inclusive Hadronic Processes"	D. Sivers
"Large Momentum Transfer Processes"	R. Blankenbecler
"Hadron Dynamics"	H.D.I. Abarbanel

1975 DEEP HADRONIC STRUCTURE AND THE NEW PARTICLES

"Leptons as a Probe of Hadronic Structure"	F. J. Gilman
"Lepton Scattering as a Probe of Hadron Structure"	E. D. Bloom
"High $p_\perp$ Dynamics"	J. D. Bjorken
"Hadronic Collision and Hadronic Structure (An Experimental Review)"	M. Davier
"The New Spectroscopy"	H. Harari
"The New Spectroscopy (An Experimental Review)"	G. H. Trilling

1976 WEAK INTERACTIONS AT HIGH ENERGY AND THE PRODUCTION OF NEW PARTICLES

"Weak Interaction Theory and Neutral Currents"	J. D. Bjorken
"Weak Interactions at High Energy"	S. G. Wojcicki
"ψ Spectroscopy"	G. J. Feldman
"A New Lepton?"	G. J. Feldman
"Lectures on the New Particles"	J. D. Jackson
"New Particle Production"	D. Hitlin

1977 QUARK SPECTROSCOPY AND HADRON DYNAMICS

"Quarks and Leptons"	H. Harari
"Quark Confinement"	S. D. Drell
"Hadron Spectroscopy"	F. J. Gilman
"Lectures on the Quark Model, Ordinary Mesons, Charmed Mesons, and Heavy Leptons"	M. L. Perl
"Quarks and Particle Production"	K. C. Moffeit

1978 WEAK INTERACTIONS – PRESENT AND FUTURE

"Accelerator Neutrino Experiments"	D. H. Perkins
"Weak Interactions at High Energies"	J. Ellis
"Gauge Theories of the Weak Interactions"	H. Quinn
"Weak Decays"	S. Wojcicki

1979 QUANTUM CHROMODYNAMICS

"Lepton Nucleon Scattering"	W. G. Atwood
"Massive Lepton Pair Production"	R. Stroynowski
"QCD Phenomenology of the Large P_T Processes"	R. Stroynowski
"Perturbative Quantum Chromodynamics"	S. J. Brodsky
"Elements of Quantum Chromodynamics"	J. D. Bjorken

1980 **THE WEAK INTERACTIONS**

"Gauge Theories of Weak Interactions"	M. J. Veltman
"Neutrinos and Neutrino Interactions"	F. J. Sciulli
"Weak Decays of Strange and Heavy Quarks"	D. Hitlin
"From the Standard Model to Composite Quarks and Leptons"	H. Harari
"Physics of Particle Detectors"	D. M. Ritson J. Jaros J. Marx H. A. Gordon R. S. Gilmore W. B. Atwood

1981 **THE STRONG INTERACTIONS**

"Quark-Antiquark Bound State Spectroscopy and QCD"	E. D. Bloom
"Meson Spectroscopy: Quark States and Glueballs"	M. S. Chanowitz
"Quantum Chromodynamics and Hadronic Interactions at Short Distances"	S. J. Brodsky
"Untangling Jets from Hadronic Final States"	G. Fox
"Heavy Flavor Production from Photons and Hadrons"	C. A. Heusch
"Design Constraints and Limitations in e^+e^- Storage Rings"	J. LeDuff
"Linear Colliders: A Preview"	H. Wiedemann

1982 **PHYSICS AT VERY HIGH ENERGIES**

"Expectations for Old and New Physics at High Energy Colliders"	R. N. Cahn
"Beyond the Standard Model in Lepton Scattering and Beta Decay"	M. Strovink
"Grand Unification, Proton Decay, and Neutrino Oscillations"	H. H. Williams
"e^+e^- Interactions at Very High Energy: Searching Beyond the Standard Model"	J. Dorfan
"The Gauge Hierachy Problem, Technicolor, Supersymmetry, and All That"	L. Susskind
"Composite Models for Quarks and Leptons"	H. Harari
"Electron-Proton Colliding Beams: The Physics Programme and the Machine"	B. H. Wiik

1983 **DYNAMICS AND SPECTROSCOPY AT HIGH ENERGY**

"Jets in QCD: A Theorist's Perspective"	S. Ellis
"Jets in e^+e^- Annihilation"	R. Hollebeek
"Jet Production in High Energy Hadron Collisions"	R. F. Schwitters
"Aspects of the Dynamics of Heavy-Quark Systems"	M. E. Peskin
"Heavy Particle Spectroscopy and Dynamics B's to Z's"	M. G. D. Gilchriese
"... And for Our Next Spectroscopy?"	J. Ellis
"Review of the Physics and Technology of Charged Particle Detectors"	A. H. Walenta
"A Review of the Physics and Technology of High-Energy Calorimeter Devices"	P. M. Mockett

1984 **THE SIXTH QUARK**

"The Last Hurrah for Quarkonium Physics: The Top System"	E. Eichten
"Developments in Solid State Vertex Detectors"	C. J. S. Damerell
"Experimental Methods of Heavy Quark Detection"	T. Himel
"Production and Uses of Heavy Quarks"	G. L. Kane
"Weak Interactions of Quarks and Leptons: Experimental Status"	S. Wojcicki
"The Experimental Method of Ring-Imaging Cherenkov (RICH) Counters"	T. Ekelöf
"Weak Interactions of Quarks and Leptons (Theory)"	H. Harari

PIEF-FEST

"Pief"	S. Drell
"Accelerator Physics"	R. R. Wilson
"High Energy Theory"	T. D. Lee
"Science and Technology Policies for the 1980s"	F. Press
"Inclusive Lepton-Hadron Experiments"	J. Steinberger
"Forty-Five Years of e^+e^- Annihilation Physics: 1956 to 2001"	B. Richter
"We Need More Piefs"	J. Wiesner

1985 **SUPERSYMMETRY**

"Introduction to Supersymmetry"	J. Polchinski
"Signatures of Supersymmetry in e^+e^- Collisions"	D. Burke
"Properties of Supersymmetric Particles & Processes"	R. M. Barnett
"Supersymmetry: Experimental Signatures at Hadron Colliders"	P. Darriulat
"Superworld/Hyperworlds"	M. E. Peskin
"Very High Energy Colliders"	B. Richter
"Some Issues Involved in Designing a 1 TeV (c.m.) $e^{\pm}$ Linear Collider Using Conventional Technology"	G. A. Loew
"Wake Field Accelerators"	P. B. Wilson
"Plasma Accelerators"	R. D. Ruth & P. Chen
"Collider Scaling and Cost Estimation"	R. B. Palmer

1986 **PROBING THE STANDARD MODEL**

"Electroweak Interactions —Standard and Beyond"	H. Harari
"CP and Other Experimental Probes of Electroweak Phenomena"	B. Winstein
"Pertubative QCD: K-Factors"	R. Field
"Experimental Tests of Quantum Chromodynamics"	J. Dorfan
"Phenomenology of Heavy Quark Systems"	F. Gilman
"Heavy Quark Spectroscopy and Decay"	R. Schindler
"Some Aspects of Computing in High Energy Physics"	P. Kunz
"Data Acquisition for High Energy Physics Experiments"	M. Breidenbach

1987 **LOOKING BEYOND THE Z**

"Theory of e^+e^- Collisions at Very High Energy"	M. E. Peskin
"Prospects for Physics at e^+e^- Linear Colliders"	G. J. Feldman
"Physics with Polarized Electron Beams"	M. L. Swartz
"Electron-Proton Physics at HERA"	G. Wolf
"Hadron Colliders Beyond the Z^0"	C. Quigg
"Physics at Hadron Colliders (Experimental View)"	J. L. Siegrist
"The Dialogue Between Particle Physics and Cosmology"	B. Sadoulet
"Requirements for Detectors at SSC"	M.G.D. Gilchriese*

1988 **PROBING THE WEAK INTERACTION: CP VIOLATION AND RARE DECAYS**

"Results on b-Decay in e^+e^- Collisions, with Emphasis on CP Violation"	K. Berkelman
"Precious Rarities—On Rare Decays of K, D and B Mesons"	I. Bigi
"Superconducting Detectors for Monopoles and Weakly Interacting Particles"	B. Cabrera
"Cosmic Relics from the Big Bang"	L. Hall
"Double Beta Decay"	M. S. Witherell
"Neutrino Masses and Mixings"	L. Wolfenstein
"The Bottom Quark: A Key to 'Beyond Standard' Physics"	H. Harari*
"b–Physics in Fixed Target Experiments"	J. Sandweiss*
"Experimental Searches for Rare Decays"	A.J.S. Smith*

*Manuscript was not received in time for printing.